www.jresm.org

Research on Engineering Structures and Materials









Volume 11
Issue 5
October 2025

P-ISSN: 2148-9807 E-ISSN: 2149-4088

The International Journal of **Research on Engineering Structures and Materials (RESM**) is a peer-reviewed open access journal (p-ISSN: 2148-9807; o-ISSN: 2149-4088) published by MIM Research Group. It is published in February, April, June, August, October, and December.

The main objective of RESM is to provide an International academic platform for researchers to share scientific results related to all aspects of mechanical, civil, and material engineering areas.

RESM aims the publication of original research articles, reviews, short communications technical reports, and letters to the editor on the latest developments in the related fields.

All expenditures for the publication of the manuscripts are most kindly reimbursed by *MIM Research Group*. Thus, authors do not need to pay for publishing their studies in the journal.

The scope of the journal covers (but not limited to) behavior of structures, machines and mechanical systems, vibration, impact loadings and structural dynamics, mechanics of materials (elasticity, plasticity, fracture mechanics), material science (structure and properties of concrete, metals, ceramics, composites, plastics, wood, etc.,), nano-materials performances of new and existing buildings and other structural systems, design of buildings and other structural systems, seismic behavior of buildings and other structural systems, repair and strengthening of structural systems, case studies and failure of structural systems, safety and reliability in structural and material engineering, use of new and innovative materials and techniques in energy systems and mechanical aspects of biological systems (biomechanics and biomimetics).

The topics covered in JRESM include:

- Structural Engineering
- Mechanical Engineering
- Material Engineering
- Earthquake Engineering
- Nano-technology
- Energy Systems (Focus on Renewable)
- Biomechanics and Biomimetics
- Environment (Material and Engineering System Related Issues)
- Computer Engineering and Data Science (Material and Engineering System-Related Issues)

Abstracting and Indexing
Please visit http://www.jresm.org for more information.

Graphics and Design

Mehmet Yılmaz myilmaz@jresm.net



RESEARCH on ENGINEERING STRUCTURES & MATERIALS

Research Group

RESEARCH on ENGINEERING STRUCTURES & MATERIALS

Editorial Board

Editor in Chief		
Hayri Baytan Özmen	Usak University	Türkiye
Editors		
Antonio F. Miguel	University of Evora	Portugal
Michele Barbato	University of California Davis	USA
Mehmet Palancı	Arel University	Türkiye
Francesco D'Annibale	University of L'Aquila	Italy
Chitaranjan Pany	Vikram Sarabhai Space Centre	India
Badrinarayan Rath	Wollega University	Ethiopia
Taymaz Tabari	Jagiellonian University	Poland
Tamer Saracyakupoglu	İstanbul Gelisim University	Türkiye
Ivan Banović	University of Split	Croatia
Rayah Nasr Al-Dala'ien	Al-Balqa Applied University	Jordan
Balasubramanian Ramesh	Dhanalakshmi Srinivasan University	India
Abbasali Sadeghi	Islamic Azad University	Iran
Srinivasan Anandhan	National Institute of Technology Karnataka	India
Huatian Zhao	Imperial College London	UK
Majid Pouraminian	Islamic Azad University	Iran
Blessen Skariah Thomas	National Institute of Technology Calicut	India
Ibrahim Alshaikh	University of Science and Technology	Yemen
Seyed Reza Samaei	Islamic Azad University Science and Research Branch	Iran
Uzair Aslam Bhatti	Hainan University	China
Tian Su	Shandong University of Technology	China
Pawel Skruch	AGH University of Krakow	Poland

Editorial Office

Publishing Manager		
Mehmet Yılmaz	MIM Research Group	Türkiye
Production Editor		
Damla Yalçıner Çal	MIM Research Group	Türkiye
Language Editors		
Gaye Kuru	Uşak University	Türkiye
Mete Çal	MIM Research Group	Türkiye

Editorial Board Members		
Farid Abed-Meraim	Arts et Metiers ParisTech	France
P. Anbazhagan	Indian Institute of Science	India
Raffaele Barretta	University of Naples Federico II	Italy
R.S. Beniwal	Council of Scientific and Industrial Research	India
Antonio Caggiano	University of Buenos Aires	Argentina
Noel Challamel	University of South Brittany	France
Abdulkadir Çevik	Gaziantep University	Türkiye
J. Paulo Davim	University of Aveiro	Portugal
Hom Nath Dhakal	University of Portsmouth	UK
Ali Faghidian	Islamic Azad University	Iran
S. Amir M. Ghannadpour	Shahid Beheshti University	Iran
Ali Goodarzi	Harvard University	USA
Jian Jiang	National Institute of Standards and Technology	USA
Ramazan Karakuzu	Dokuz Eylül University	Türkiye
Arkadiusz Kwiecien	Cracow University of Technology	Poland
Stefano Lenci	Universita Politecnica delle Marche	Italy
Silva Lozančić	University of Osijek	Croatia
Fabio Mazza	University of Calabria	Italia
Yuan Meini	North University of China	China
Stergios A. Mitoulis	University of Surrey	UK
Vinayagam Mohanavel	Anna University	India
Ehsan Noroozinejad Farsangi	Kerman Graduate University of Technology	Iran
Alaa M. Rashad	Shaqra University	Saudi Arabia
Mohammad Mehdi Rashidi	University of Tongji	China
Pier Paolo Rossi	University of Catania	Italy
Neritan Shkodrani	Polythecnic University of Tirana	Albania
Y.B. Yang	National Taiwan University	Taiwan

Advisory Board Members

A. Abdelbary	Alexandria University	Egypt
A. Karthik	SRM Institute of Science and Technology	India
Abbasali Sadeghi	Islamic Azad University	Iran
Abdelhalim Bensaada	University of Yahia Fares of Medea	Algeria
Abdellah Douadi	Ferhat Abbas University of Setif 1	Algeria
Abdel-Nasser Sharkawy	Faculty of Engineering, South Valley University	Egypt
Abdul Haseeb Wani	Presidency University, Bengaluru	India
Abid Ustaoglu	Bartın University	Türkiye
Abrham Gebre	Addis Ababa University	Ethiopia
Ahmed Maamoun	McMaster University	Canada
Aicha Rouabeh	University of Bouira	Algeria
Alaa M. Rashad	Housing & Building National Research Center (HBRC)	Egypt
Aleksandar Ašonja	University Business Academy	Serbia
Ameer Baiee	University of Babylon	Iraq
Amirreza Sadeghi	University of Birjand	Iran
Andi Yusra	Universitas Teuku Umar	Indonesian
Andriy Huts	Rzeszow University of Technology	Poland
Anthony N. Papathanassiou	National and Kapodistrian University of Athens	Greece
Arash Rahimi	University of Perugia	Italy
Arun KK	Kumaraguru College of Technology Coimbatore	India
ARUNKUMAR K	Mangalam College of Engineering	India
Ary A. Hoyos-Montilla	Construction School at Universidad Nacional de Colombia	Colombia
Ashhad Imam	National Institute of Technology Jamshedpur	India
Ayoub Souileh	University Mohammed V	Morocco
Azad A. Mohammed	University of Sulaimani	Iraq
Azzura Ismail	Universiti Tun Hussein Onn Malaysia	Malaysia
B.P.R.V.S. Priyatham	GMR Institute of Technology	India
Badrinarayan Rath	Wollega University	Ethiopia
Bengi Gözmen Şanlı	Mersin University	Türkiye
Berrin ikizler	Ege University	Türkiye
Bilge Demir	Karabuk University	Türkiye
Cagri Yardimci	Usak University	Türkiye
Canan Kandilli	Usak University	Türkiye
Caroline S. Sobhy	Fayoum University	Egypt
Catur Harsito	Universitas Sebelas Maret	Indonesia
Chau-Khun Ma	Universiti Teknologi	Malaysia
Christopher Fapohunda	Federal University Oye-Ekiti	Nigeria
Damilola Oyejobi	University of Botswana	Botswana
Daniel Cruze	Mohamed Sathak A J College of Engineering	India
Deep Tripathi	University of Sherbrooke	Canada
Dr Abhilash P P	Indian Institute of Technology (BHU)	India
E.R. Teixeira	University of Minho	Portugal
Ebrahim Sharifi Teshnizi	Ferdowsi University of Mashhad,	Iran
Edwin Klu	Virginia Tech	USA
Elavenil S	Vellore Institute of Technology	India
Emin Erdem	Pamukkale University	Türkiye
Ercan Isik	Bitlis Eren University	Türkiye
Eric M. Lui	Syracuse University	USA
Erion Bukaci	Polytechnic University of Tirana	Albania
Erion Bukaci	Polytechnic University of Tirana	Albania
Essam H. Mohamed	South Valley University	Egypt
Fatih Ahmet Senel	Süleyman Demirel University	Türkiye
Fokruddin Ahmad	Washington State University	USA

Advisory Board Members

Gaurav Dhadse	G. H. Raisoni Institute of Engineering and Business Management Jalgaon Maharashtra	India
Ghasan Fahim Huseien	Universiti Teknologi Malaysia	Malaysia
Gökhan Gece	Bursa Teknik University	Türkiye
Gururaj Hatti	KLS VDIT	India
Gustavo Bosel Wally	Federal University of Rio Grande do Sul	Brazil
Güneş Harman	Yalova University	Türkiye
Gür Emre Güraksın	Afyon Kocatepe University	Türkiye
Haithem Boumediri	Université Constantine 1	Algeria
Hakan Sarikaya	Uşak University	Türkiye
Halit Cetiner	Isparta University	Türkiye
Hamid Saberi	University of Eyvanekey	Iran
Hamoon Fathi	Islamic Azad University	Iran
Hasan ULUS	Selcuk University	Türkiye
Hasibullah Azizi	Andhra University	India
Hayri B. Ozmen	Usak University	Türkiye
HILTON AHMAD	Universiti Tun Hussein Onn Malaysia	Malaysia
Hossein Jarrahi	University of Birjand	Iran
Hossein Kabir	University of Illinois	USA
Hüsnügül YILMAZ ATAY	Izmir Katip Celebi University	Türkiye
Irina Volokitina	Karaganda Industrial University	Kazakhstan
J. Eswari	National Institute of Technology	India
J. Paulo Davim	University of Aveiro	Portugal
J. Paulo Davim	University of Aveiro	Portugal
Javad Vaziri	University of Semnan	Iran
Jayalalitha Subbaiah	SASTRA Deemed University	India
Jesús Castro	Universitat Politecnica de Catalunya	Spain
Kabiru Mustapha	Kwara State University	Nigeria
Kamel Chaoui	Badji Mokhtar University	Algeria
Kaplan Kaplan	Kocaeli University	Türkiye
Kourosh Mehdizadeh	Islamic Azad University	Iran
Lavanya Prabha	SRM Easwari Engineering College	India
Lawrence Zahemen Tuleun	University of Ilorin	Nigeria
Leonid Dvorkin	National University of Water and Environmental Engineering	Ukraine
Lomesh Mahajan	Dr. Babasaheb Ambedkar Technological University	India
Luiz Rocha	Federal University of Rio Grande do Sul	Brazil
Lyamine Briki	University of Batna2	Algeria
M. Jafaryar	Babol Noshirvani University of Technology	Iran
Madhulika Sinha	National Institute of Technology	India
Maheswaran Muthiah	Kalasalingam Academy of Research and Education	India
Majid M.A. Kadhim	University of Babylon	Iraq
Majid Pouraminian	Islamic Azad University	Iran
Matthew Martianus Henry	Bina Nusantara University	Indonesia
Md. Golam Kibria	Rajshahi University of Engineering & Technology	Bangladesh
Md. Zia ul haq	Panjab University	India
Mehdi Khorasani	Isfahan University of Technology	Iran
Mehdi Panji	Islamic Azad University	Iran
Mehmet Kaya	Bozok University	Türkiye
Melika Mahmoodabadi	Islamic Azad University	Iran
Mevlüt Gürbüz	Ondokuz Mayıs University	Türkiye
Mihir Mishra	Texas A&M University	USA
Mohammad Lesani	University of Tehran	Iran
Mohammad. I Al Biajawi	Universiti Malaysia Pahang Al-Sultan Abdullah	Malaysia

Advisory Board Members		
Mohammad Afrazi	Tarbiat Modares University	Iran
Mohammad Hossein Razmkhah	Semnan University	Iran
Mohammad Naeim Moradi	Amirkabir University of Technology	Iran
Mohammadreza Baghoolizadeh	Shahrekord University	Iran
Mohammed Jalal Al-Ezzi	University of Bilad Al-Rafidain	Iraq
Mohd Nasim	IPS Academy, Indore	India
Mohd Syahrul Hisyam Mohd Sani	Universiti Teknologi MARA (UiTM)	Malaysia
Mohsen Hajizamani	Graduate University of Advanced Technology	Iran
Moslem Paidar	Islamic Azad University	Iran
Motahhareh Nezafat Tabalvandani	Islamic Azad University	Iran
Mounika Ganta	Vignana Bharathi Institute of Technology	India
Mukaila Anifowose	Federal Polytechnic Offa	Nigeria
Murtala Namakka	Universiti Malaysia Sarawak	India
Mutluhan Akin	Nevşehir Hacı Bektaş Veli University	Türkiye
N. Arunachelam	Mepco Schlenk Engineering College	India
N.L.N. Kiran Kumar	Sri Venkateswara University	India
N.Venkata Sairam Kumar Namepalli	R.V.R & J.C College of Engineering	India
Nabil Bella	Tahri Mohamed University of Bechar	Algeria
Nahida Nazim Musayeva	Azerbaijan National Academy of Sciences	Azerbaijan
Naveen S	National Institute of Technology, Raipur	India
Nazime Seda Şaşmaz Karacan	Usak University	Türkiye
Neeraj SN	Visvesvaraya Technological University	India
Nermin Demirkol	Kocaeli University	Türkiye
Nhlanhla Nyembe	University of the Witwatersrand	South Africa
Nilesh Masne	GESCOEMSR	India
Ninu Praseetha N S		India
Ola Mazen Makki	University of Al-Qadisiyah	Iraq
Oladimeji Olatunji Ojo	Federal University of Technology Akure	Nigeria
Oleg V. Devitsky	Federal Research Centre Southern Scientific Centre of the Russian Academy of Sciences	Russia
Oleksii Hrechanyi	Zaporizhzhia National University,	Ukraine
Orhan Gülcan	General Electric Aerospace	Türkiye
Oritonda Muribwathoho	Cape Peninsula University of Technology	South Africa
P. Manoj Kumar	KPR Institute of Engineering and Technology	India
P. Marimuthu	SASTRA Deemed to be University	India
Parmo Parmo	UIN Sunan Ampel Surabaya	Indonesia
Partheeban Pachaivannan	Chennai Institute of Technology	India
Qasim M. Shakir	University of Kufa	Iraq
Qiang Ou	Chongqing University, Chongqing	China
Ramnarayan Sahu	Rajeev Gandhi Technical University	India
Rayeh Nasr Al-Dala'ien	Universiti Tenaga Nasional	Malaysia
Revathi Srinivasan	Mepco Schlenk Engineering College	India
Roberto Nascimbene	School of Advanced Studies IUSS Pavia	Italy
ROYAL MADAN	Chandigarh University	India
S. Ali Faghidian	Islamic Azad University	Iran
S. Ali Faghidian	Islamic Azad University	Iran
S. Gholizadeh	Urmia University	Iran
Saeid Foroughi	Selçuk University	Türkiye

Advisory Board Members

Sai Krishna Pinnamaneni	University of Texas at Arlington	USA
Saifulnizan Jamian	Universiti Tun Hussein Onn Malaysia	Malaysia
Saman Saadatfar	Islamic Azad University	Iran
Saman Mansouri	UNISTRAPG	Italy
Samuel Awe	Automotive Components Floby AB	India
Sangeetha Palanivelu	SSN College of Engineering	India
Sarmila Sahoo	Heritage Institute of Technology Kolkata	India
Sasikumar Palanisamy	Kumaraguru College of Technology	India
Sastri M V S S	Vasavi College of Engineering	India
Saumen Mandal	National Institute of Technology Karnataka	India
Selcuk Selimli	University of Karabük	Turkey
Serdar Gungor	Bilecik Şeyh Edebali University	Türkiye
Serkan Elcin	Pamukkale University	Türkiye
Seymur Bashirzade	Azerbaijan University	Azerbaijan
Shahazadi Begum	Baba Institute of Technology and Sciences	India
Shahrul Niza Mokhatar	Universiti Tun Hussein Onn Malaysia	Malaysia
Shaise K. John	College of Engineering Trivandrum	India
Shashi Prakash Dwivedi	G. L. Bajaj Institute of Technology & Management	India
Shoulong Zhang	Harbour Engineering Research Institute Co. Ltd.	China
Siti Aisyah Nurjannah	Universitas Sriwijaya	Indonesia
Somayyeh Pourbakhshian	Islamic Azad University	Iran
Srinivasan Anandhan	National Institute of Technology Karnataka	India
Sumanth Ratna Kandavalli	New York University	USA
Sunday Chukwuemeka	Ceramics Research and Production Dept. (CRPD)	Nigeria
Suriyaprakash Rajadesingu	SRM Institute of Science and Technology	India
Talha Taskanat	Erciyes University	Türkiye
Tasnia Ahmed	Military Institute of Science and Technology (MIST)	Bangladesh
Toufik Sebbagh	University of Skikda	Algeria
Upendra K. Mallela	Aerospace Vertical, Largy Services Limited	India
Utsav Koshti	Nirma University	India
Venkatesh Chava	CVR College of Engineering, India	India
Victor Rizov	University of Architecture	Bulgaria
Vijayasarathy Rathanasalam	ATRIA Institute of Technology	India
Vinicius Pepe	University Ritter dos Reis	Brazil
Waleed A Abbas	University of Technology	Iraq
Xiaojian Wang	Xinjiang University	China
Yamini Sreevalli I	Vellore Institute of Technology	India
Yuliang Chen	Guangxi University of Science and Technology	China
Yuvaperiyasamy M	Saveetha School of Engineering	India
Yuvaraj K	K.S.Rangasamy College of Technology	India
Zafer Kaya	Dumlupınar University	Türkiye
ZAINORIZUAN MOHD JAINI	Universiti Tun Hussein Onn Malaysia	Malaysia
Zainab Tolu Giwa	Kwara State University	India
Zeynep Ekincioğlu Küzeci	Kırşehir Ahi Evran University	Türkiye
Ziyauddin Seikh	Aliah University	India

In This Issue

Research Article
1889 **Habibe Gursoy Demir**
Effects of pipe vibration on roll angle of a quadrotor system with a vertical cantilever pipe conveying fluid

Research Article
1913 **Kalapala Vijay Babu, CH. Mallika Chowdary, Lingeshwaran N, Ikkurthi Siva Kishore**
Structural application of fiber reinforced concrete

Research Article
1947 **ShivaPrakash S, Santosh Kumar, Naveen Kumar B K, Madeva Nagaral, Narasimha Marakal, V Auardi, Manjunatha T H, Dileep B. P**
Mechanical characterization of alumina and graphite dual particulates reinforced hybrid aluminum alloy (Al2219) matrix composites

Research Article
1965 **Ashim Paul, Palash Dey, Mrinmoy Dhar**
Physico-mechanical properties of autoclaved aerated concrete block as an alternative to traditional bricks

Research Article
1981 **Sunday Albert Lawal, Rasaq Olawale Medupin, Victor Chiagozie Nwachukwu, Uzoma Gregory Okoro, Oyewole Adedipe, Joseph Abutu, Benjamin I. Attah, Jimoh Oladejo Tijani, Ambali Saka Abdulkareem**
Development and characterization of carbon nanotube/green titania as potential hybrid nanofiller in nanofluid for machining carbon fiber reinforced plastics

Research Article
1997 **Ola Mazen Makki**
Heat influence on sustainable rubberized concrete mixes

Research Article
2013 **Mahesh, M.S. Shobha, Poornima Hulipalled, Veerabhadrappa Algur**
ML driven optimization of mechanical properties in hybrid fiber-reinforced tertiary blended high-performance concrete

Research Article
2041 **Ghassan H. Humur, Hussein Hamada, Sarwar H Mohmmad, Abdulkadir Çevik, Farid Abed**
Thermomechanical properties of slag-based engineered geopolymer composite under a series of cooling and heating cycles

Research Article
2061 **Mohammad Sadegh Shahidzadeh, Mahbobeh Mirzaie Aliabadi, Hamid Mansouri Far, Amir Hossein Derakhshan Nezhad**
Mechanical and rheological performance of plastic concrete: Investigation of several properties

Research Article
2085 **Sudarsanam Mark, Jayaprabakar Jayaraman**
Experimental investigation on the effect of varied injection timings in a CRDI diesel engine driven by a biodiesel-diesel blend

Research Article
2097 **Satish Saini, Neeraj Sharma, Ranjeev Kumar Chopra, Monika Mehra, Ravi Kumar, Sushil Bhardwaj, Dinesh Kumar**
Data-driven prediction of mechanical properties in friction stir processed Al6061-Alumina composite using enhanced machine learning models

Research Article
2119 **Agus Susanto, Budi Setiyana, Rifky Ismail, Risma Alfiyani**
Design and construction of full octagonal transducer-based low-cost dynamometer for measuring cutting forces during turning process

Research Article
2139 **Muhammad Nura Isa, Hanizam Awang, Tan Ying Yi**
Physical and mechanical characteristics of lightweight POFA geopolymer concrete with timber clinker aggregate

Research Article
2161 **Giulia Martino, Claudia Naldi, Cesare Biserni, Sylvie Lorente**
Melting and solidification of a PCM in a bottom-heated/cooled cavity with and without metal fins

Research Article
2175 **Nilesh Masne, Akshay Pawar**
Experimental and numerical investigation of solid and hollow recycled aggregate concrete beams subjected to torsion

Research Article
2211 **Ahmed Amine Meraghni, Abderrezak Khellou, Saïd Abani**
Using sewage sludge ash as a replacement for cement in mortar applications

Research Article
2231 **Ram A, P D Jeya Kumar, Prince Arockia Doss**
Variable tube geometry micro channel heat exchanger (MCHX) using analytical and CFD analysis

Research Article
2253 **Antonio F. Miguel**
Flow of non-Newtonian fluids in self-similar networks across different scales

Research Article
2267 **V. Gayathri, C. Govardhan, S. Sruthi, Nabarun Dey**
Performance assessment of ternary blended fiber-reinforced recycled aggregate concrete

Research Article
2289 **Ashish Attari , Balwinder Lallotra**
Enhancing concrete mechanical properties using nano-silica, calcined clay, and glass fibers optimized by response surface methodology

Research Article
2307 **Yassine El Kiri, Laidi Zahiri, Khalifa Mansouri, Zakaria Mighouar**
Assessment of the harmfulness of corrosion defects in a pressurized pipeline with a single corrosion defect using FEA and ANN

Research Article
2331 **Abdulhamid Hamdan Al-Hinai, Karu Clement Varaprasad, V. Vinod Kumar**
Performance optimization of a horizontal axis wind turbine simulator under the effects of blade's pitch angle variation

Research Article
2351 **Kadir Sengun, Guray Arslan**
Investigation of CFRP strengthening efficiency experimentally and analytically on reinforced concrete beams

Research Article
2381 **Eduardo Henrique Taube Cunegatto, Flavia Schwarz Franceschini Zinani, Sandro Jose Rigo**
Predicting viscosity and yield surfaces for Bingham fluids in a lid-driven cavity employing a deep neural network

Research Article
2401 **Mariana Alvarenga Alves, Eduarda Machado Rodrigues, Vinícius Torres Pinto, Luiz Alberto Oliveira Rocha, Elizaldo Domingues dos Santos , Liércio André Isoldi**
Numerical simulation, constructal design, and systematic search applied to the geometrical evaluation of hat-stiffened plates under bending

Research Article
2421 **Rafael da Silveira Borahel, Giovani Dambros Telli, Augusto Antoniolli Bolzoni, Liércio André Isoldi, Elizaldo Domingues dos Santos, Luiz Alberto Oliveira Rocha**
Numerical analysis of the impact of PCM reservoir width on lithium-ion battery cooling: A constructal design study

Research Article
2437 **David Cotes-Prieto, Luis Zapata-Ordúz**
Prediction of the flexural capacity of steel fiber reinforced self-compacting concrete beams combining neural networks, the Barcelona test and the gravitational search algorithm

Research Article
2467 **Serdar Çilenmez, Yavuz Ergün, İbrahim Bulduk**
Removal of cytotoxic tamoxifen from aqueous solutions with hydroxyapatite adsorbent

Research Article
2481 **Tarek Djedid, Tahar Zerig, Messaoud Abbas, Mohamed Zohaïr Kaab, Mouloud Belachia**
Statistical modeling and optimization of recycled concrete properties enhanced with marble fines using response surface methodology

Research Article
2507 **Mohammed Dahmani, Ahcene Arbaoui, Billel Rebai**
Wavelet signal analysis for the detection of sand excess defects in hardened concrete

Research Article
2521 **Jamiatul Akmal, Adam Wisnu Murti, Asnawi Lubis, Masdar Helmi**
Development and validation of an accurate analytical solution for hoop stress distribution in cylindrical functionally graded materials

Research Article
2537 **Oussama Benmerabet, Salah Messioud, Rania Beghila, Daniel Dias**
Impact of the rigid piles on the dynamic response of the soil-inclusions-mattress-slab system under seismic excitations

Research Article
2559 **M N Rajesh, C Siddaraju, T Ram Prabhu, T S Sachit, R. Suresh**
Machine learning and Taguchi optimization technique for wear rate analysis of Al 2024/ SiC/CNT based hybrid metal matrix composites

Research Article
2581 **Sameh Fuqaha, Ahmad Zaki, Guntur Nugroho**
Bamboo in construction: Mapping global trends, strategic clusters, and future research pathways

Research Article
2605 **Idrissa Ouedraogo, Anas Bahi, Latifa Ouadif**
Enhancing structural integrity of plastic concrete diaphragm walls in dams on thick alluvium: A numerical study of geometry and construction sequencing

Research Article
2623 **E. Dhanesh, M. Shanmugasundaram**
Experimental evaluation on the durability characteristics of ternary blended concrete with ground granulated blast furnace slag and hydrated lime exposed to harsh environmental conditions

Review Article
2637 **Osamah Ali, Pinta Astuti**
Reimagining steel slag in sustainable concrete: A bibliometric and experimental review

Research Article
2667 **Parmo Parmo, Arqowi Pribadi, Noverma Noverma**
Enhancing mechanical properties of normal and lightweight concrete using ramie fiber-reinforced polymer

Research Article
2681 **Luma Ahmed Aday**
Experimental and predictive assessment of recycled rubber-modified lightweight mortars

Research Article
2701 **Sila Yaman**
Calibration of a general analytical model for the debonding strength of NSM-CFRP strip-concrete joints using particle swarm optimization

Research Article
2715 **Ke Ji, BoiYee Liao**
Investigation effect of metro entrance and exit construction on pedestrian overpass safety using numerical modelling and simulation

Free access to tables of content, abstracts and full text of papers for web visitors.

Copyright © 2023

Research on Engineering Structures & Materials
MIM Research Group Publications
P-ISSN: 2148-9807
E-ISSN: 2149-4088
http://www.jresm.org

ABSTRACTING / INDEXING

The international journal of Research on Engineering Structures and Materials (RESM) is currently Abstracted/Indexed by Asos Indeks, CiteFactor, Cosmos, CrossRef, Directory of Research Journal Indexing, Engineering Journals (ProQuest), EZB Electronic Journal Library, Global Impact Factor, Google Scholar, International Institute of Organized Research (I2OR), International Scientific Indexing (ISI), Materials Science & Engineering Database (ProQuest), Open Academic Journals Index, Publication Forum, Research BibleScientific Indexing Service, Root Indexing, Scopus, Ulakbim TR Index (Tubitak), Universal Impact Factor and under evaluation by many other respected indexes.

Check web site for current indexing info, www.jresm.org



Research on Engineering Structures & Materials
www.jresm.org

Research Article

Effects of pipe vibration on roll angle of a quadrotor system with a vertical cantilever pipe conveying fluid

Habibe Gursoy Demir [a]

Department of Aerospace Engineering, Iskenderun Technical University, Faculty of Aeronautics and Astronautics, Hatay, Türkiye

Article Info

Article History:

Received 15 May 2025

Accepted 18 June 2025

Keywords:

Quadrotor;
Pipe;
Vibration analysis;
Finite element method;
Fluid conveying

Abstract

A quadrotor + liquid conveying pipe system is used to transport liquids in applications where direct human intervention is impractical, such as firefighting, precision agriculture, industrial maintenance and cleaning. While the quadrotor provides mobility, the pipe acts as a conduit for continuous liquid transport from a reservoir. In this study, the coupled dynamics between quadrotor system and a vertical cantilever pipe conveying fluid were investigated. For this purpose, a coupled model was developed by connecting the pipe and the quadrotor model. It was assumed that the pipe vibrations affect the quadrotor but not the other way around. The effects of fluid speed and distribution impacts based uncontrolled pipe vibrations on the uncontrolled and PD controlled quadrotor were determined. The results show that fluid speed and pipe excitation significantly affect the stability of the quadrotor and cause variations in the roll angle and displacement at the free end of the pipe. It is observed that the pipe vibration and the torque applied to the quadrotor decrease as the fluid speed is increased until the critical speed is reached. It is observed that the flow velocity and the type of disturbance excitation affect the time domain performance criteria of the roll angle.

© 2025 MIM Research Group. All rights reserved.

1. Introduction

Quadrotor systems have a wide range of applications in aviation and robotics and are widely used in search and rescue operations, military reconnaissance missions and data collection in disaster areas. These systems offer high maneuverability in narrow spaces and can perform reconnaissance and surveillance in dangerous areas without human intervention. In addition, thanks to advanced sensor and camera systems, they are also quite successful in tasks such as mapping, object tracking and environmental analysis. Due to these successes, one of the most important areas of use of quadrotors, which are used in many areas, is the use of liquid transfer and application situations that need to be applied remotely. For this purpose, a liquid tank that can be carried by the quadrotor system or a hose for pumping liquid from the ground can be added. With all these additions, the liquid must be sprayed with the help of a pipe to transfer the liquid to the relevant area. For this purpose, the dynamics of the pipe added to UAVs such as quadrotors and through which the liquid flows create an effect together with the dynamics of the quadrotor, and external effects on the quadrotor occur in addition to pipe vibrations.

Using a UAV with a liquid delivery pipe is a method that increases efficiency in applications, improves safety, and expands accessibility in situations where traditional liquid delivery methods are impractical. This type of UAV is an advanced airborne system designed to transport and distribute fluids during flight and is useful in a variety of applications such as firefighting [1],

Corresponding author: habibe.gursoydemir@iste.edu.tr
[a]orcid.org/0000-0002-7705-9516
DOI: http://dx.doi.org/10.17515/resm2025-898st0515rs

precision agriculture [2], window cleaning of high-rise buildings [3] and industrial inspections [4]. Another application area is the cleaning of solar panels with water at a certain interval as their efficiency decreases as they get dirty. As seen in these application areas, UAVs connected to a land-based fluid source in particular guarantee continuous operation, reduce intervention time and provide time and cost savings while increasing occupational safety. In addition, these types of UAVs optimize resource use in all applications while minimizing environmental impact. They can reduce human exposure to hazardous conditions by transporting coolants, lubricants or decontaminants to remote machines, chemical spill areas or biohazard zones.

Generally, studies on this subject are focused on design and implementation, and these studies generally focus on UAVs with robot manipulators. There is one study in the literature where fluid-conveying pipes are integrated into the UAV. Lee et al. [5] investigated the effects of fluid-structure interaction (FSI) on the stability of a quadrotor when it is connected to a flexible hose that exhausts pressurized fluid. They derived an analytical solution to analyze the free-end response of the hose that affects the UAV stability. However, modeling of UAVs with manipulators in the literature is like this study due to the interaction between the UAV and the manipulator. Therefore, in the introduction section, we focused on modeling and analysis studies on UAVs with manipulators and vibration of fluid-conveying pipes. Omar and Mukras [6] presented a multi-rotor flying vehicle equipped with a crane and robotic arm to increase the efficiency and safety of date palm harvesting. Remotely controlled via a mobile app with live video feedback, the system cuts branches with precision, reducing reliance on dangerous traditional methods. A decoupled control scheme for an aerial manipulator consisting of a UAV and two robotic arms has been presented by Ruiz et al. [7]. Simulations confirm the ability of the system to perform complex tasks while maintaining synchronization with a predetermined audio signal, and the success of the controller implemented in structured aerial environments providing precise coordination between the UAV and the robotic arms has been demonstrated. A novel end effector mechanism designed to grasp and then place or throw objects using stored elastic energy was presented by Pasala et al. [8]. A mechanical design, simulation model and data-driven residual learning framework are developed to improve launch accuracy despite model uncertainties. Experiments are conducted to demonstrate the effectiveness of the end effector and algorithms for targeted launch. Choi and Jung [9] studied experimental studies on solar panel cleaning using a drone manipulator. A foldable and lightweight drone arm was designed that included a flexing mechanism to suppress vibration and hybrid force control to regulate contact force. Clustering algorithms were used to classify cleaning areas and efficient cleaning performance was achieved. In another application, Raj et al. [10] designed an autonomous drone with a robotic arm on top to inspect and repair faults in mobile towers. In this study, they developed an innovative matching algorithm that allows the drone to stabilize with less energy while the arm performs repair tasks. Suarez et al. [11] analyzed benchmarks for aerial manipulation robots performing physical interactions in high altitude workspaces. Various evaluation methods and criteria were defined to compare the performance considering different designs and applications, and experimental results obtained with a compliant joint aerial manipulator were compared for accuracy, execution time, manipulation ability, and impact response. Mendoza-Mendoza et al. [12] designed a new aerial manipulator based on multirotors, which uses yaw motion to generate and transmit forces through a serial chain of rigid links and drones. The experimental data were compared with existing technologies. They provided suggestions for further development along with potential application examples highlighting the scientific and social impact of the system. Readers who need more information on modeling, design, and applications of drones with robot manipulators can refer to the review works of Ramalepa and Jamisola [13] and Saunders et al. [14]. Ramalepa and Jamisola focused on collaborative robotic arms with fixed, mobile or drone bases to increase efficiency and safety [13]. They discussed the application areas of these robots, areas where they increase their efficiency, and collision avoidance, path planning and control.

Saunders et al. [14] reviewed research problems and state-of-the-art solutions for package delivery using aerial manipulators and grippers. The challenges associated with landing on both static and dynamic platforms were discussed, and risks such as weather conditions, attitude estimation and collision avoidance were examined. Another subsystem that needs to be addressed in accordance

with the content of the study is the fluid-conveying pipes. The dynamics and vibration analyses of these systems under different conditions are of great importance in terms of the effects they will have on the entire system. Fluid-conveying pipes are essential components of various engineering applications that facilitate the controlled [18] transportation of liquids and gases in industries such as oil and gas [15], water supply, chemical processing [16] and aviation [17]. These pipes play an important role in maintaining efficiency, safety and reliability in systems that require precise fluid transport at different pressures and temperatures. Advances in materials, design and monitoring technologies continue to increase their durability and performance, making them indispensable in modern engineering infrastructure.

Although generally perceived as static elements, these pipes are inherently dynamic systems that can exhibit complex vibration behaviors when subjected to dynamic interactions with the fluid in transit, external forces applied by supporting structures, or disturbances from the surrounding environment. Vibration in fluid-conveying pipes can be defined as the oscillatory motion of the pipe structure resulting from dynamic interactions with the fluid in transit, external forces applied by supporting structures, or disturbances from the surrounding environment. This phenomenon arises from the continuous and flexible nature of the pipe as a mechanical system. The primary source of vibration in fluid-conveying pipes is the dynamic interaction between the fluid flow and the pipe structure. This interaction is complex in nature and is influenced by a multitude of factors, including the velocity, density, and viscosity of the fluid, as well as the material properties, geometric configuration, and support conditions of the pipe. One of the primary mechanisms by which fluid flow causes vibration is the generation of inertial forces, particularly Coriolis and centrifugal forces. This complex relationship between fluid flow and the pipe structure brings fluid-structure interaction (FSI) to the forefront in the context of fluid-conveying pipe vibrations. This relationship between the fluid and the liquid has been addressed in the literature under many conditions and dynamic and vibration analyses of the fluid conveying pipe have been carried out. Detailed initial studies for modeling and dynamic examination of these systems have been made by Paidoussis and Issid [19] and Paidoussis and Li [20]. In these studies, the dynamics of the fluid conveying pipes have been examined and the extensive research carried out in this field has been emphasized. Various aspects including different boundary conditions, fluid types and linear or nonlinear behaviors have been analyzed. In these studies, it has been shown that the system exhibits complex dynamic behavior, and it has been stated that it is possible to examine it from both structural and control perspectives. Since the focus of the study is on the integration of the cantilever pipe to the quadrotor, the studies on the dynamic analysis of the cantilever pipe have been reviewed below.

Modarres-Sadeghi et al. [21] investigated the two-dimensional (2-D) and three-dimensional (3-D) fluttering of fluid-conveying cantilever pipes using a full set of nonlinear equations of motion. The stability behavior of horizontal and vertical systems was analyzed considering the effects of increasing flow velocity beyond the Hopf bifurcation. Liu et al. [22] presented a comprehensive study on the planar oscillations of a cantilever pipe conveying fluid under bottom excitation. The effects of flow velocity, excitation frequency and amplitude on the dynamic response of the pipe were investigated. Li et al. [23] proposed a feedforward vibration suppression method for fluid-conveying cantilever pipes. The dynamic equation was established using the Euler-Bernoulli beam model, and the vibration function of pipeline pressure was formulated by Fourier series to analyze the transient response. The effectiveness of optimizing the input signal parameters to minimize tip vibration was demonstrated through theoretical derivation and experimental verification. The dynamics of thin cantilever cylinders, plates and pipes subjected to internal or external axial flow have been studied extensively since the 1960s by Paidoussis [24]. The differences in behavior between conventional and reversed axial flow were analyzed and it was shown that reversed flow leads to weak flutter at low speeds and large amplitude static deflection at higher speeds. Semler and Paidoussis [25] investigated the nonlinear dynamics and stability of cantilever pipes conveying harmonic component fluid placed on a constant mean velocity. In this work, the effects of forcing frequency, disturbance amplitude and flow velocity on the pipe dynamics were analyzed, especially near the critical flutter instability. Some of the studies related to dynamic analysis of cantilever pipes are summarized and for more detailed information, readers can refer to references [26-30].

In addition, as seen in these studies, studies are carried out using both active and passive elements to cause vibrations in the pipe and to damp these vibrations. For this purpose, there are many studies in the literature using methods and equipment such as electromagnetic actuators [31], eddy-current dampers [32], mass dampers [33], piezoelectric actuators [34], artificial neural network-based control technique [35], adaptive modal control technique [36], feedforward control strategy based [37], LQR control technique [38], nonlinear energy sink [39] and feedback coupling [40]. The readers refer the review paper [41] for more details about control of the pipe vibration.

In this study, modeling and dynamic analysis of a vertically cantilever pipe connected quadrotor system will be performed based on the Euler and Euler-Bernoulli techniques for quadrotor and fluid conveying pipe, respectively. This paper extends the previous paper by adding coupled model between the quadrotor dynamics and fluid conveying pipe dynamics. The coupled model is developed in which the motion of the pipe affects the motion of quadrotor. Quadrotor+Pipe system, while spraying the liquid fed by the pump from the ground to a certain area, the effects of the pipe vibrations on the motion dynamics of the quadrotor will be examined in detail. The pipe vibrations and roll angle of the quadrotor are observed under controller, different fluid speed and different distribution impacts on the free end of the pipe such as unit step and sinusoidal inputs within a certain time period.

2. Mathematical Modelling

Quadrotor is a type of unmanned aerial vehicle with four rotors that provide lift, balance and precision maneuverability. It is widely used in various areas such as surveillance, delivery, agriculture and infrastructure maintenance with its ability to hover in the air, navigate in narrow areas and operate autonomously. In recent years, quadrotors have become frequently preferred due to their advantages in terms of cost, work safety and time, as they can perform tasks efficiently and safely in dangerous or hard-to-reach areas without requiring human intervention. For this purpose, they have begun to be frequently preferred in applications such as cleaning solar panels, irrigation or spraying from agricultural applications and remote intervention in fires.

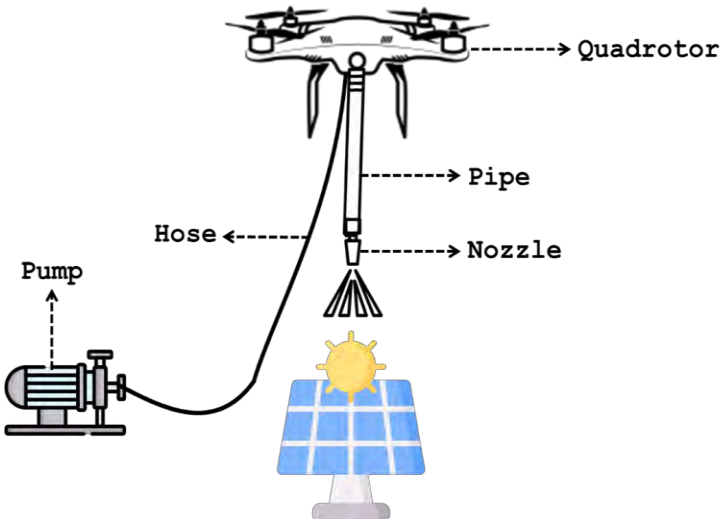


Fig. 1. The schematic diagram of Quadrotor+Pipe system

In all these applications, the liquid to be transferred is transferred via a pipe. This pipe is attached to the bottom of a quadrotor and is fed either from a tank mounted on the quadrotor or from a tank on the ground via a pump and hose. Since the liquid passing through this pipe flows in a non-uniform structure while being transferred, it causes vibrations in the pipe. These vibrations in the pipe cause the bending moment and force to occur at the point where the pipe is connected to the quadrotor, and the effects on the quadrotor also occur depending on the vibrations in the pipe. In order to analyze all this movement, the dynamics of the quadrotor and the fluid-conveying pipe were considered in this study. Then, a coupled model was created that combined these two dynamics. Figure 1 shows the schematic of the quadrotor+pipe system created in this study.

2.1. Quadrotor

The dynamics of a quadcopter include the mathematical and physical principles that govern its motion. These dynamics are based on aerodynamics to provide lift, steering and stability. For this reason, the motion of the quadrotor is modeled through translational and rotational motions affected by the forces and torques produced by the four rotors. Each of the four rotors is independently accelerated or decelerated to move in different directions. The basic motions of the quadrotor consist of four main parts: ascent-descent (thrust), forward-backward motion (pitch), right-left motion (roll) and rotation around its own block (yaw). The dynamic model is obtained using the Newton-Euler equations and this model determines the response of the system according to the force and torque balances. Figure 2 shows a schematic of a quadrotor and the forces and moments acting on it. Before calculating the dynamics of the quadrotor, some assumptions are needed to simplify the mathematical complexity [42].

- UAV structure and propellers are rigid and symmetrical
- Center of mass and body fixed frame origin are assumed to coincide with each other
- Thrust and drag are proportional to the square of the propeller speed
- Inertia matrix is time invariant.

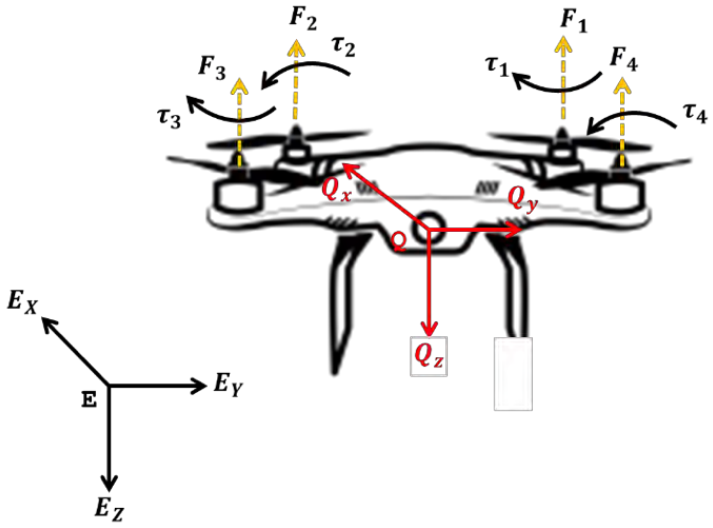


Fig. 2. The model of quadrotor system

As can be seen from the figure, the quadrotor has coordinated systems on the Earth and on itself. For this reason, the rotation matrix (R) is used to convert the observed motion on the Earth into the motion in the coordinate system on itself.

$$\begin{bmatrix} \dot{X} \\ \dot{Y} \\ \dot{Z} \end{bmatrix} = R \begin{bmatrix} U \\ V \\ W \end{bmatrix} \tag{1}$$

$$R = R_x R_y R_z = \begin{bmatrix} cos\psi cos\phi & cos\psi sin\theta sin\phi & cos\psi sin\theta cos\phi + sin\psi sin\phi \\ sin\psi cos\theta & sin\psi sin\theta sin\phi & sin\psi sin\theta cos\phi - sin\phi cos\varphi \\ -sin\theta & cos\theta sin\phi & cos\theta cos\phi \end{bmatrix} \tag{2}$$

In these equations, X, Y and Z indicate the position of the quadrotor on the Earth coordinate system. U, V and W indicate the position of the quadrotor with respect to its own coordinate system. In the equation, ϕ represents the roll angle, θ represents the pitch angle, and ψ represents the yaw angle. In this case, the dynamic equations of the quadrotor are given below. The readers looking for detailed information on modeling can refer to references [43] and [44].

$$\ddot{x} = -\frac{1}{M_{quad}}(u_1(sin\varphi sin\phi + cos\phi cos\varphi sin\theta)) \tag{3}$$

$$\ddot{y} = -\frac{1}{M_{quad}}(u_1(cos\varphi sin\phi - cos\phi sin\varphi sin\theta)) \tag{4}$$

$$\ddot{z} = \frac{1}{M_{quad}}(-M_{quad}g + u_1 cos\phi cos\theta) \tag{5}$$

$$\begin{bmatrix}\dot{p}\\ \dot{q}\\ \dot{r}\end{bmatrix} = \begin{bmatrix}I_{xx} & 0 & 0\\ 0 & I_{yy} & 0\\ 0 & 0 & I_{zz}\end{bmatrix}^{-1} + \left(-\begin{bmatrix}p\\ q\\ r\end{bmatrix} x \begin{bmatrix}I_{xx} & 0 & 0\\ 0 & I_{yy} & 0\\ 0 & 0 & I_{zz}\end{bmatrix}\begin{bmatrix}p\\ q\\ r\end{bmatrix} + \begin{bmatrix}u_2\\ u_3\\ u_4\end{bmatrix}\right) \tag{6}$$

$$\dot{\phi} = p + rcos\phi tan\theta + qsin\phi tan\theta \tag{7}$$

$$\dot{\theta} = qcos\phi - rsin\phi \tag{8}$$

$$\ddot{\varphi} = \frac{rcos\phi}{tan\theta} + \frac{qsin\phi}{cos\theta} \tag{9}$$

In these equations, u_i $(i = 1,2,3,4)$ shows the thrust force applied to the quadrotor system because of the rotation of the rotors and the moments that lead to Euler angular movements. These effects occur due to the rotation of the rotors depending on the voltage supply. For this reason, there is a connection between the angular velocities of the motors and the forces and moments generated.

$$\begin{bmatrix}u_1\\ u_2\\ u_3\\ u_4\end{bmatrix} = \begin{bmatrix}F_1 + F_2 + F_3 + F_4\\ F_4 - F_2\\ F_3 - F_1\\ F_2 + F_4 - F_3 - F_1\end{bmatrix} = \begin{bmatrix}b(w_1^2 + w_2^2 + w_3^2 + w_4^2)\\ b(w_4^2 - w_2^2)\\ b(w_3^2 - w_1^2)\\ d(-w_1^2 + w_2^2 - w_3^2 + w_4^2)\end{bmatrix} \tag{10}$$

F_i $(i = 1,2,3,4)$ forces seen Eq. (10) represent the forces produced by the rotors shown in Figure 2. The b and d parameters show the thrust and drag constants. These constants were determined under certain conditions and were taken constant throughout the study.

2.2. Fluid Conveying Cantilever Pipe

In the system under consideration, in addition to the quadrotor, a uniform vertical suspended pipe of length L and mass per unit length M_{fluid} and an incompressible fluid of axial velocity u and mass per unit length M_{pipe} are included. For the vertical suspended pipe, the z axis is in the direction of gravity and the y axis is the horizontal axis to be suitable for the quadrotor system. In the system under consideration, in addition to the quadrotor, a uniform vertical suspended pipe of length L and mass per unit length M_{fluid} and an incompressible fluid of axial velocity u and mass per unit length M_{pipe} are included.

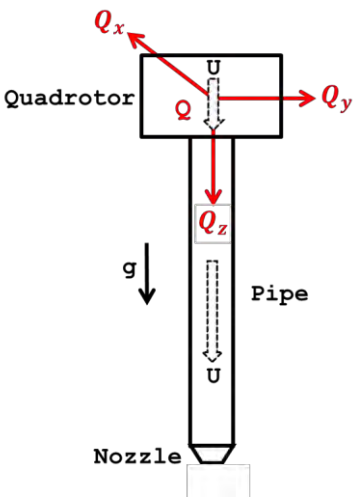


Fig. 3. The scheme of fluid conveying pipe

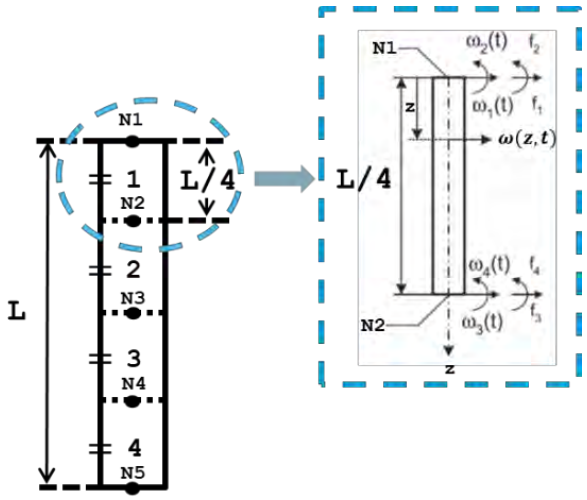


Fig. 4. Finite element model of the pipe and the applied forces on each element

For the vertical suspended pipe, the z axis is in the direction of gravity and the y axis is the horizontal axis to be suitable for the quadrotor system. A schematic representation of the pipe used in the system is given in Figure 3.

In this system, it can be assumed that the pipe free movements occur in the (y-z) plane and all movements are small. $y(z,t)$ represents the transverse deviation of the pipe from its equilibrium position. Other assumptions made to determine the forces acting on the pipe and the fluid motion are: i) the pipe does not change its shape due to pressure ii) the pipe material is elastic and linear. The equation of motion for the free transverse vibration of a vertically suspended pipe for different boundary conditions was obtained by Paidoussis and Issid [19] using the Newtonian approximation.

$$E^*I\frac{d^5y}{dz^4dt}+EI\frac{d^4y}{dz^4}+M_{pipe}uU_j\frac{d^2y}{dz^2}-\left(M_{pipe}+M_{fluid}\right)g\frac{d^2y}{dz^2}(L-z)+M_{pipe}\frac{du}{dt}(L-z)\frac{d^2y}{dz^2}+2M_{pipe}u\frac{d^2y}{dzdt}+\left(M_{pipe}+M_{fluid}\right)g\frac{dy}{dz}+c\frac{dy}{dt}+\left(M_{pipe}+M_{fluid}\right)\frac{d^2y}{dt^2}=0 \quad (11)$$

In Eq. (11), E is the elastic modulus of the pipe, and I is the sectional moment of inertia of the pipe. E^* represents the internal damping coefficient of the pipe material, and this material is assumed to be Kelvin-Voigt type viscoelastic. c represents the viscous damping coefficient due to the friction of the pipe with the surrounding stationary fluid medium, and g represents the gravitational acceleration. In this study, it is additionally assumed that the fluid flowing in the pipe has harmonics and that there is a nozzle at the end of the pipe that increases the exit velocity of the fluid. The flow rate is assumed to be in the form $U_0 = u(1 + \mu\, cos\, cos\, (w_d t))$. Here u is the average flow rate, μ is the amplitude of the added harmonic component and is assumed to be less than 1. w_d is the circular frequency. When it comes to the nozzle part, the weight of the nozzle is assumed to be small enough to be neglected and its length is quite short compared to the total length of the pipe. The exit speed is calculated with the formula $U_j = U_0 * A_1/A_2$. A_1 represents the cross-sectional area of the pipe and A_2 represents the nozzle exit area. Boundary conditions are needed to solve the general differential equation for pipe vibration given in Eq. (11). General boundary conditions for a fixed pipe are given in Eq. (12). The correct application of boundary conditions in cantilever beams is critical for the stability and convergence of the solution. While correct boundary conditions both increase accuracy and shorten the computational time, missing or excessive constraints can negatively affect the results. Therefore, boundary conditions that best reflect the physical situation and restrict only the necessary degrees of freedom were preferred.

$$y(0,t)=\frac{d^2y(0,t)}{dz^2}=0 \quad , \quad z=0$$
$$\frac{d^2y(L,t)}{dz^2}=\frac{d^3y(L,t)}{dz^3}=0 \quad , \quad z=L \quad (12)$$

Finite element analysis is used to solve the equation given by Eq. (11) with boundary conditions. In this analysis, firstly the main differential equation is discretized using the weak formulation. As shown in Figure 4, the cantilever pipe system is divided into four equal parts and contains a total of five nodes. Using more beam elements in FEM analysis provides more accurate modeling of structural behavior, especially in regions with high stress or displacement gradients. As the number of elements increases, the numerical solution gets closer to the analytical (real) solution and the quality of convergence increases. However, one of the disadvantages of using more elements is the increase in solution time and effort. This process increases the degrees of freedom and causes the system matrices to grow. Fine meshes that increase sensitivity are useful, but a balanced mesh structure should be preferred to avoid unnecessary computational load. For this reason, it was found appropriate to choose 4 elements for the pipe. According to the finite element method, these nodes of each element undergo both linear ($\omega_1(t)$ and $\omega_3(t)$) and rotational ($\omega_2(t)$ and $\omega_4(t)$) displacements. The linear joint forces $f_1(t)$ and $f_3(t)$ correspond to linear displacements, and the rotational joint forces $f_2(t)$ and $f_4(t)$ correspond to rotational displacements. In Figure 4, the forces and displacements of a pipe element of length L/4 are clearly shown. The system solution obtained using the weak formulation of the finite element method is obtained with the formula in Eq. (13). In this equation, $W_i(t)$ and $N_i(z)$express the displacement and shape functions.

$$y(z,t)=\omega(z,t)=\sum_{i=1}^{4}W_i(t)N_i(z) \quad (13)$$

It is extremely important to determine the shape functions that help to interpolate the variable values between two different nodes having discrete values of the variable, by considering that their derivatives can be taken depending on the boundary conditions. The selection of shape functions in FEM analysis directly affects the accuracy, convergence and computational efficiency of the solution. In order to obtain accurate results, it is important to use higher order shape functions, but higher order functions require more computational resources. In addition, appropriate shape functions provide faster convergence of the solution to the real solution as the mesh becomes thinner. For this reason, a balance must be established between accuracy and efficiency, and the differentiability and applicability of shape functions should not be controlled depending on the boundary conditions. For this reason, the shape function are determined as follows.

$$\begin{aligned} N_1(z) &= 1 - 3\left(\frac{z}{l}\right)^2 + 2\left(\frac{z}{l}\right)^3 \\ N_2(z) &= z - 2l\left(\frac{z}{l}\right)^2 + l\left(\frac{z}{l}\right)^3 \\ N_3(z) &= 3\left(\frac{z}{l}\right)^2 - 2\left(\frac{z}{l}\right)^3 \\ N_4(z) &= -l\left(\frac{z}{l}\right)^2 + l\left(\frac{z}{l}\right)^3 \end{aligned} \tag{14}$$

At the end of the finite element method, the mass, gyroscopic and stiffness matrices obtained for each element of the system are obtained and the displacements of each mode can be obtained by using Eq. (15).

$$M_e\ddot{\omega}(z,t) + G_e\dot{\omega}(z,t) + K_e\omega(z,t) = 0 \tag{15}$$

The mass, gyroscopic and stiffness matrices of each element seen in this equation are given in the Appendix. After this process, the matrices obtained for each element are combined to obtain the general equation of motion. Global matrices are obtained by combining the element matrices by applying the matrix operations given in Eq. (16) and then deleting the appropriate rows and columns in line with the boundary conditions.

$$M = \sum_{s=1}^{p} A_s^T M_e A_s \quad , \quad G = \sum_{s=1}^{p} A_s^T G_e A_s \quad , \quad K = \sum_{s=1}^{p} A_s^T K_e A_s \tag{16}$$

where A_s is rectangular matrix with four rows and its column number is equal to the selected number of joints displacements in the global coordinate system. General equation of motion is

$$M_G\ddot{w}(z,t) + G_G\dot{w}(z,t) + K_G w(z,t) = F = F_c + F_{ext} \tag{17}$$

where F_c and F_{ext} denote the control and external inputs, respectively. F_{ext} consists of the external forces (F_d) and the forces (F_{quad}), which is applied by the motion of the quadrotor.

2.3. Coupled Model

The system consisting of a quadrotor and a fluid conveying pipe provides the relationship between each other with the forces and moments created by both the quadrotor and the pipe on each other. The pipe applies a force and moment on the quadrotor at the connection point and these forces and moments change depending on the vibration of the pipe. The quadrotor creates inertial forces on the pipe due to translational and rotational accelerations depending on its movement. In addition, since the center of mass of the two interconnected systems shifts to different places, this causes a disruptive external effect on the vibrations of the pipe. However, since the movements of the quadrotor are assumed to be quite small in this study, the effect of the change of the center of mass is neglected.

The first part of this coupled equation of motion is the bending force and moment transferred by the pipe to the quadrotor. For this purpose, the force and moment at point $z = 0$ are obtained using the following equations.

$$M(x) = EI\left(\frac{d^2w}{dz^2}\right) = EI\left(\frac{d^2N}{dz^2}\right)\begin{Bmatrix}\omega_1(0,t)\\ \omega_2(0,t)\\ \omega_3(0,t)\\ \omega_4(0,t)\end{Bmatrix} \tag{18}$$

As can be seen here, since the second derivatives of the shape functions are linear, the bending moment $M(y)$ is also obtained linearly. Similarly, the shear force ($V(y)$) is also obtained as a constant since the third derivatives of the shape functions are constant.

$$V(x) = EI\left(\frac{d^3w}{dz^3}\right) = EI\left(\frac{d^3N}{dz^3}\right)\begin{Bmatrix}\omega_1(0,t)\\ \omega_2(0,t)\\ \omega_3(0,t)\\ \omega_4(0,t)\end{Bmatrix} \tag{19}$$

By using these two equations, the equations between Eq. (3) and Eq. (5) are rewritten as follows. In this equation, the force $V(y)$ acts in the y-direction and the weights of the pipe, fluid and hose act in the z-direction.

$$M_{total}\begin{bmatrix}\ddot{x}\\ \ddot{y}\\ \ddot{z}\end{bmatrix} = Ru_1 - M_{total}g\widehat{e_z} + V(y)\widehat{e_y} \tag{20}$$

$$M_{total} = M_{quad} + M_{pipe} + M_{fluid} + M_{hose} \tag{21}$$

where M_{hose} denotes the mass per unit length of the hose. Moreouver, $\widehat{e_y}$ and $\widehat{e_z}$ are the unit vectors along the y axis and z axis, respectively. Similarly, the bending moment exerted by the pipe also affects the Euler angles of the quadrotor. The Eq. (6) changes to the following general form.

$$I_{total}\begin{bmatrix}\ddot{\phi}\\ \ddot{\theta}\\ \ddot{\psi}\end{bmatrix} = -\begin{bmatrix}\phi\\ \theta\\ \psi\end{bmatrix} x\, I_{total}\begin{bmatrix}\phi\\ \theta\\ \psi\end{bmatrix} + \begin{bmatrix}u_2\\ u_3\\ u_4\end{bmatrix} + M(y)\begin{bmatrix}1\\ 0\\ 0\end{bmatrix} \tag{22}$$

$$\begin{bmatrix}\dot{p}\\ \dot{q}\\ \dot{r}\end{bmatrix} = \begin{bmatrix}I_{xx} & 0 & 0\\ 0 & I_{yy} & 0\\ 0 & 0 & I_{zz_{total}}\end{bmatrix}^{-1} + \left(-\begin{bmatrix}p\\ q\\ r\end{bmatrix} x \begin{bmatrix}I_{xx} & 0 & 0\\ 0 & I_{yy} & 0\\ 0 & 0 & I_{zz_{total}}\end{bmatrix}\begin{bmatrix}p\\ q\\ r\end{bmatrix} + \begin{bmatrix}u_2 - M(y)\\ u_3\\ u_4\end{bmatrix}\right) \tag{23}$$

$$I_{zz_{total}} = I_{zz} + I_{pipe} + I_{hose} \tag{24}$$

The expressions $I_{zz_{total}}$ and I_{zz} in the equations show the total moment of inertia in the z direction and the 3x3 dimensional moment of inertia matrix in all directions, respectively. In addition, in this study, the effect of pipe vibrations on the quadrotor fixed at a certain height was investigated. For this reason, the movements of the quadrotor are very small and the effects it creates on the pipe are assumed to be very small. In this case, it is assumed that the quadrotor does not create any force on the pipe dynamics. Then, the general equation of motion of the fluid-conveying pipe given in Eq. (17) can be rewritten as follows.

$$M_G\ddot{w}(z,t) + G_G\dot{w}(z,t) + K_G w(z,t) = F = F_c + F_d \;\; and \; F_{quad} = 0 \tag{25}$$

4. Results and Discussion

In this study, the quadrotor system is combined with a vertical pipe conveying fluid and the dynamics of this general system are investigated. In the considered system, the effects of pipe vibrations on the quadrotor are investigated for different conditions. The pipe vibrations and the effects of these vibrations on the quadrotor are discussed in detail for different fluid velocities and pipe-fluid parameters. Since the pipe is in the z direction and the pipe vibrations create a displacement in the x direction, it is assumed that all movements of the fluid-conveying pipe are in the x-z plane. For this reason, the effects of the displacements in the pipe, the shear force at the z=0

point and the bending moment at the same point on the quadrotor are in different directions. While the shear force caused by the pipe vibrations affects the movement of the quadrotor along the x-axis, the bending moment affects the roll rotation around the y-axis.

Based on these explanations, it is seen that pipe vibrations affect only the roll motion of the quadrotor. In the tests, the change in roll motion was observed for different pipe impulses. The parameter values used for the pipe, fluid and quadrotor during the process of obtaining the results are given in Table 1 and Table 2.

Table 1. The parameters of the quadrotor

Properties	Value
M_{quad} (kg)	1.2
l (m)	0.23
I_{xx} (kg. m^2)	$2.353x10^{-3}$
I_{yy} (kg. m^2)	$2.353x10^{-3}$
I_{zz} (kg. m^2)	$5.262x10^{-2}$

Table 2. The physical properties of the pipe, fluid and hose

Properties	Value	Properties	Value
M_{pipe}(kg/m)	0.1064	$I = I_{pipe} + I_{hose}$ (kg. m^2)	$8.97x10^{-9}$
M_{fluid} (kg/m)	0.0152	L (m)	3.2
M_{hose} (kg/m)	0.0842	A_j	2
E (Pa)	$6.89x10^{10}$		

In the tests performed, observations were made by applying disturbing impulses to the pipe after the quadrotor reached a certain height. Initially, an impulse was applied to the free end of the pipe for 1.5 seconds, lasting 0.05 seconds, without any control applied to the quadrotor. As a result, the roll motion of the quadrotor without any control was observed. Figure 5 shows the roll angle change of the quadrotor for different fluid velocities. As can be seen in these results, the vibrations occurring in the pipe due to the impulse cause instability in the roll motion even if the pipe is structurally damped. Figure 6 shows the pipe vibration under this impact for different fluid speeds. This shows that it would be easier to observe the effect of pipe vibrations on the roll motion by applying a simple controller to the quadrotor.

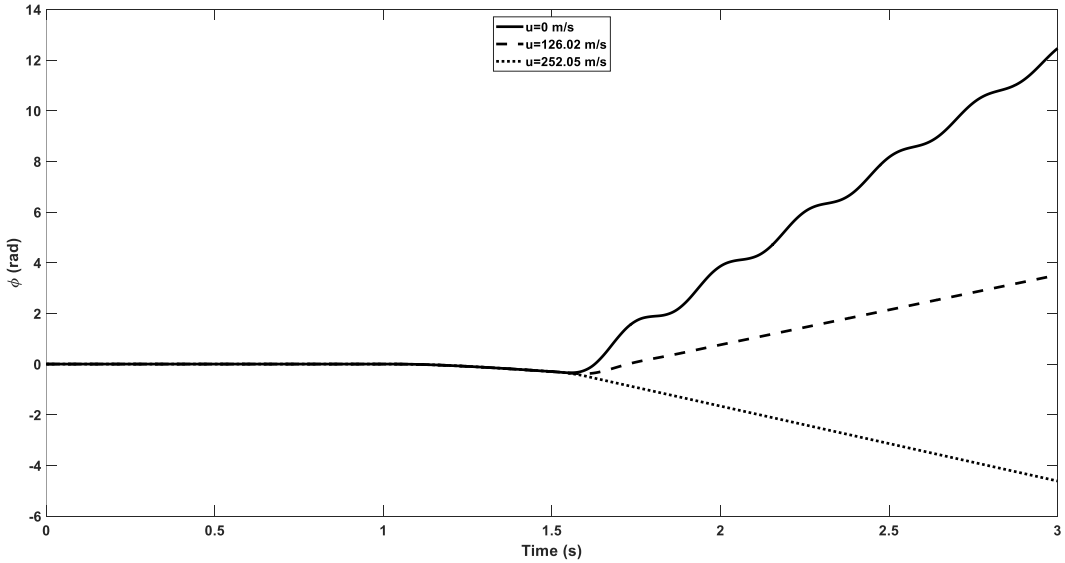


Fig. 5. Roll motion of uncontrolled quadrotor under pipe vibration at different fluid flow speeds

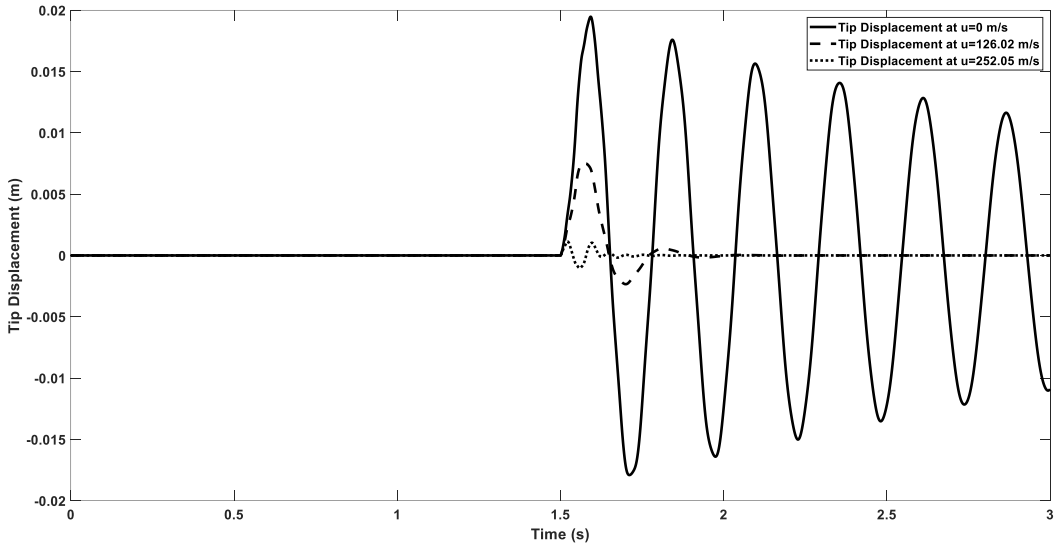


Fig. 6. Tip displacement of pipe at different fluid flow speeds

For this reason, a PD controller was designed to control the roll motion of the quadrotor. The primary reason for choosing PD control is that it is a simple and applicable controller. It also offers a good balance between speed and stability, making it ideal for dynamic systems that require fast response and reduced overshoot without the complexity of integral control. his controller has two basic control parameters: proportional gain (K_p) and derivative gain (K_d). While K_p directs the system according to the current error, K_d responds to the rate of change of the error, reducing oscillations and making the system more stable. The K_p value was selected as 0.8 and the K_d value as 0.4 for the PD controller. The selection of these controller values was made by trial and error. Because the situation observed in this study is the effects of pipe vibrations on the dynamics of the quadrotor rather than the control of the roll motion. Therefore, it is sufficient for the roll motion to reach the reference value within the desired time interval.

4.1. Test Scenario 1

In this scenario, the effect of an impulse acting on the free end of the fluid-conveying pipe after the reference value of the roll motion of the quadrotor has been reached under the PD controller has been investigated. For this, the unit step acting on the free end has been effective for 0.1 seconds.

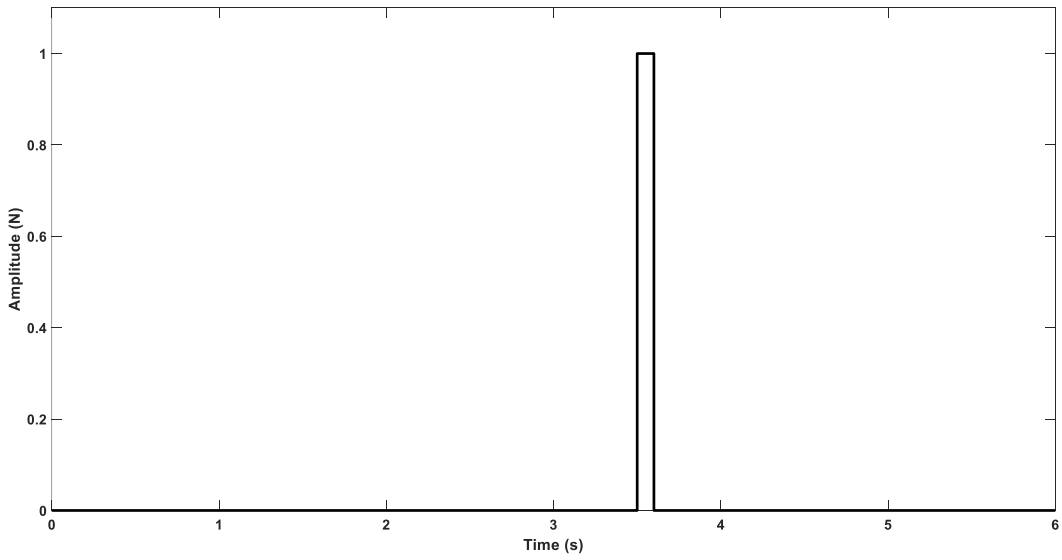


Fig. 7. The variation of the acting force at the free end of the pipe in Scenario 1

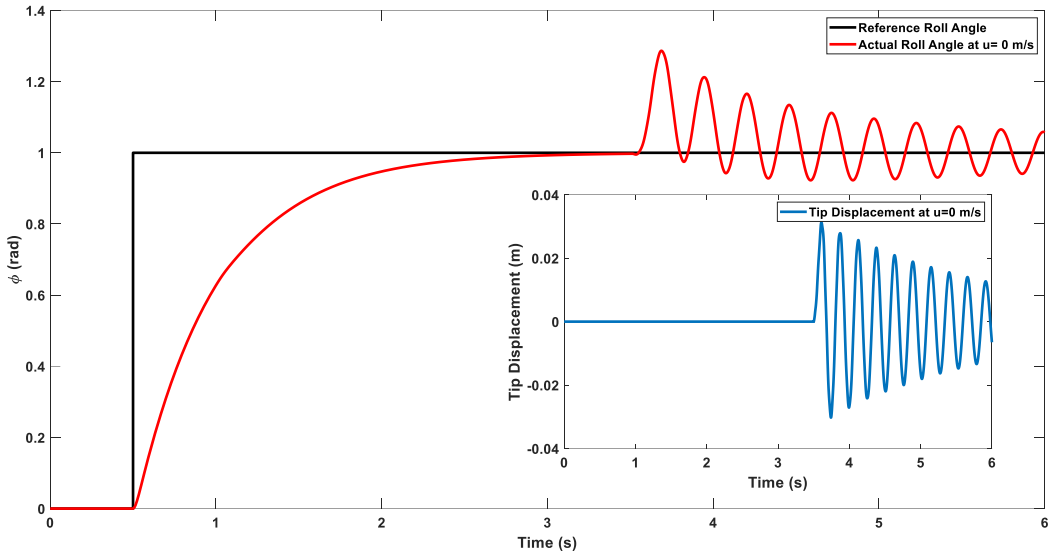
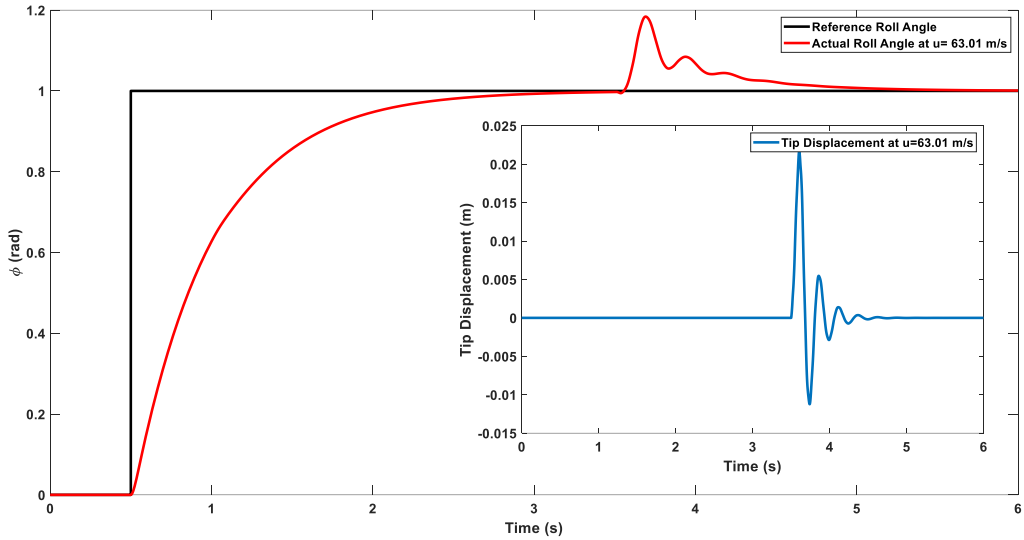


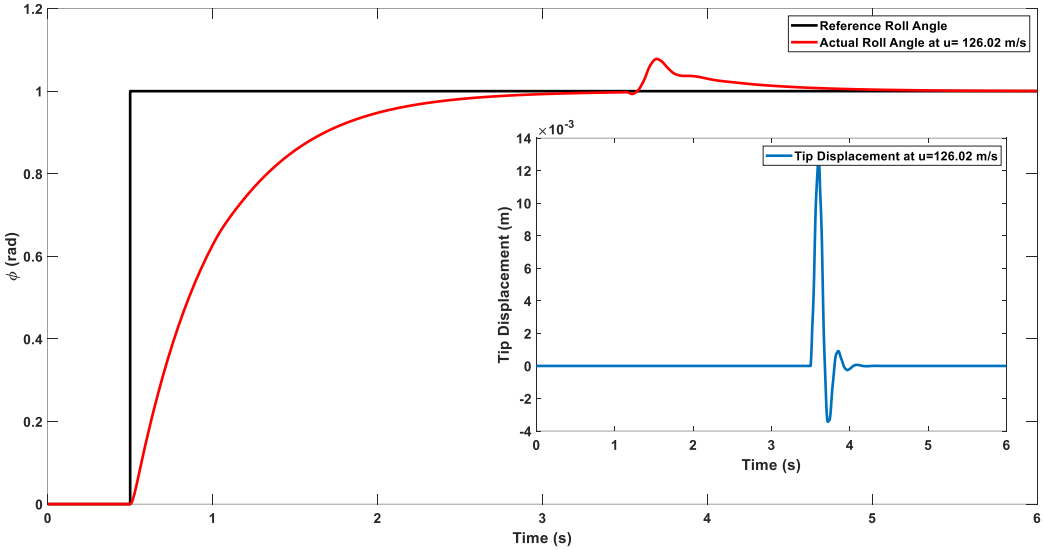
Fig. 8. Roll angle of PD controlled quadrotor under pipe vibration at u=0 m/s

The effect time of this impulse started at the t=3.5 sec of the movement. The acting force at the free end of the pipe is shown in Figure 7. Accordingly, the roll motion of the quadrotor, the free end vibrations of the pipe and the performance of the PD controller are observed in the following figures. Figure 8 shows the variation of the roll angle of quadrotor and the variation of the tip displacement of pipe when the fluid flow speed is 0 m/s. At this fluid velocity, the pipe behaves like a cantilever beam. The results show that the pipe oscillates for a long time in response to the applied force, which causes oscillation in the roll motion. The controller also takes time to dampen this oscillation, depending on the pipe vibrations. By designing a more successful controller, this damping time can be shortened, and thus, the vibrations of a pipe without fluid can be ensured to have a minimum effect on the quadrotor motion.

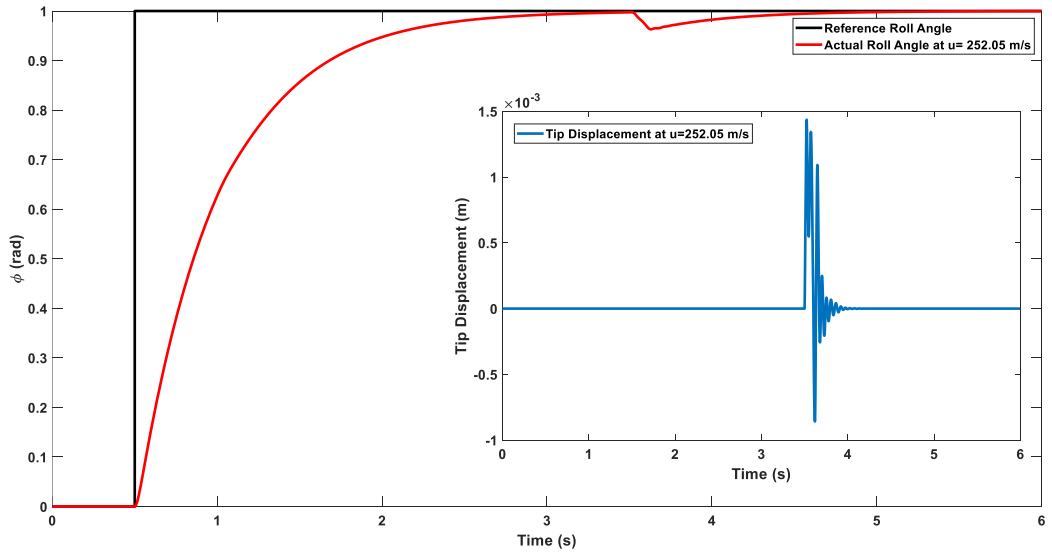
In Figure 9, the roll response of the quadrotor under this input effect is observed for different fluid velocities. The fluid velocity inside the pipe varies between 63 m/s and 346.57 m/s. At these velocities, the roll movement and pipe end displacement resulting from the disturbing effect applied to the free end of the pipe were observed.



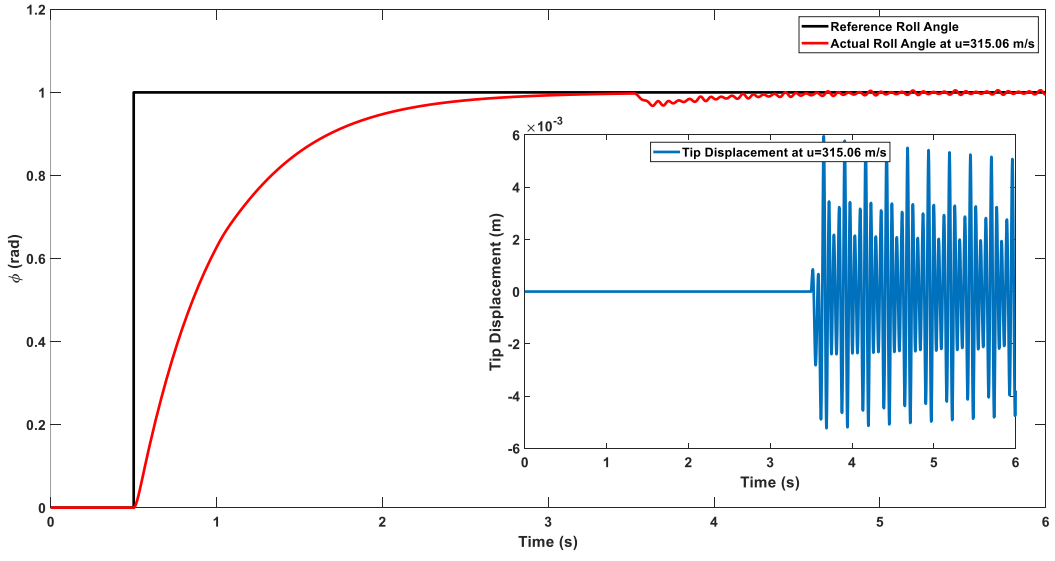
(a)


Reference Roll Angle
Actual Roll Angle at u= 126.02 m/s
Tip Displacement at u=126.02 m/s
×10^-3
Tip Displacement (m)
Time (s)
ϕ (rad)
Time (s)

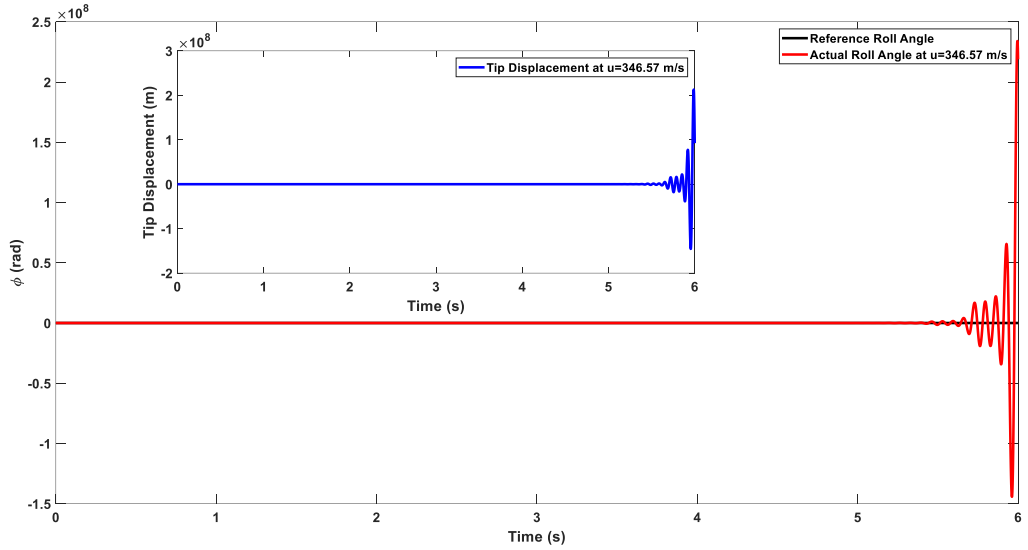
(b)


Reference Roll Angle
Actual Roll Angle at u= 252.05 m/s
Tip Displacement at u=252.05 m/s
×10^-3
Tip Displacement (m)
Time (s)
ϕ (rad)
Time (s)

(c)


Reference Roll Angle
Actual Roll Angle at u=315.06 m/s
Tip Displacement at u=315.06 m/s
×10^-3
Tip Displacement (m)
Time (s)
ϕ (rad)
Time (s)

(d)



(e)

Fig. 9. The variation of roll angle of PD controlled quadrotor and displacement of pipe's tip at (a) u=63.01 m/s, (b) u=126.02 m/s, (c) u=252.05 m/s, (d) u=315.06 m/s, (e) u=346.57 m/s

As seen from the figures, the pipe vibrations between Figures 9a-9d are damped after a certain period of time despite the disturbing input. These vibrations, whose oscillation and damping period change depending on the fluid velocity, create different effects on the quadrotor. According to the results between Figures 9a and 9d, the amplitude of the pipe vibrations decreases with the increase in speed at changing speeds and the effect on the roll movement decreases as the fluid velocity increases. Pipe vibrations and roll angle show a more stable movement depending on the increase in fluid velocity. At lower fluid velocities, the amplitudes of the pipe vibrations increase and the moment forcing the roll angle to change increases. With the increase in moment, the roll angle makes larger angular movements. However, as seen, the changes in the roll angle while the quadrotor is fixed at a certain height are successfully controlled by the PD controller used. When the fluid velocity is 315.06 m/s, small amplitude oscillations are observed in the pipe, and it is observed that these oscillations continue continuously. This shows that the critical fluid velocity that will make the pipe vibrations unstable is now approached [35, 40]. When this critical speed is approached, the oscillations in the pipe also cause oscillations in the quadrotor roll angle. However, as the speed of the fluid in the pipe increases, the pipe vibrations show a continuously increasing trend. After the fluid speed exceeds 315.06 seconds, the pipe system becomes unstable and the large amplitude vibrations that occur also cause instability for the quadrotor. As seen in Figure 9e, when the fluid speed is 346.57 m/s, both the quadrotor and the pipe system lose their stability.

4.2. Test Scenario 2

In this scenario, a disturbance effect similar to the previous scenario was applied to the fluid conveying pipe. However, in this scenario, the response of the quadrotor to this disturbance input acting on the pipe during the control process was examined. As mentioned above, before the effect was applied to the pipe, both the z and Euler angles were waited to reach the desired reference values. Thus, the response of a quadrotor standing still in the air to the effect was observed. In this scenario, the disturbance effect was applied to the pipe after the quadrotor took off and before it reached the desired reference values. For this purpose, a unit step input was applied to the free end of the pipe for 0.1 seconds, starting at the 1.5th second of the movement. In this scenario, both the change in the roll angle of the quadrotor and the performance of the applied PD controller were examined. Figure 10 shows the disturbance input applied to the pipe.

In Figure 11, the variation of roll angle of the quadrotor under the input in Figure 10 is observed for different fluid velocities. The fluid velocity inside the pipe varies between 0 m/s and 346.57 m/s. This input between 1.5 and 1.6 seconds was applied until the roll angle of the quadrotor

reached the reference value of 1 rad. As can be seen from the figures in Figure 11, it takes approximately 3.2 seconds for the roll angle to reach the reference value without pipe vibration. For this reason, the desired effect was applied to the pipe in half of this settling time.

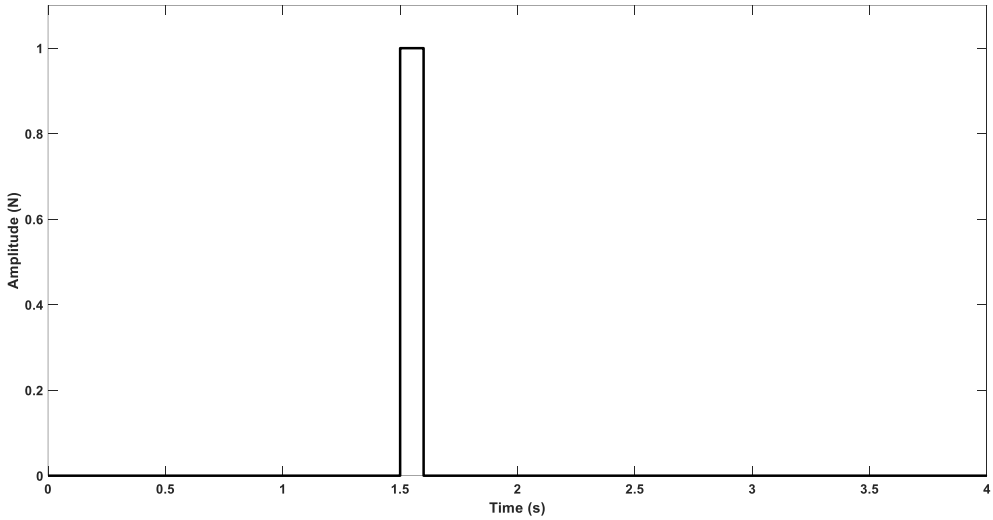
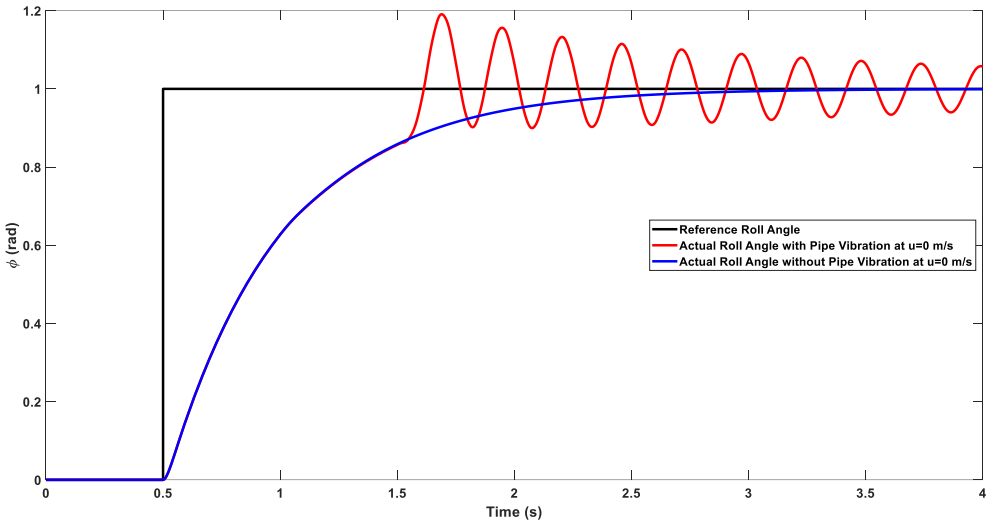
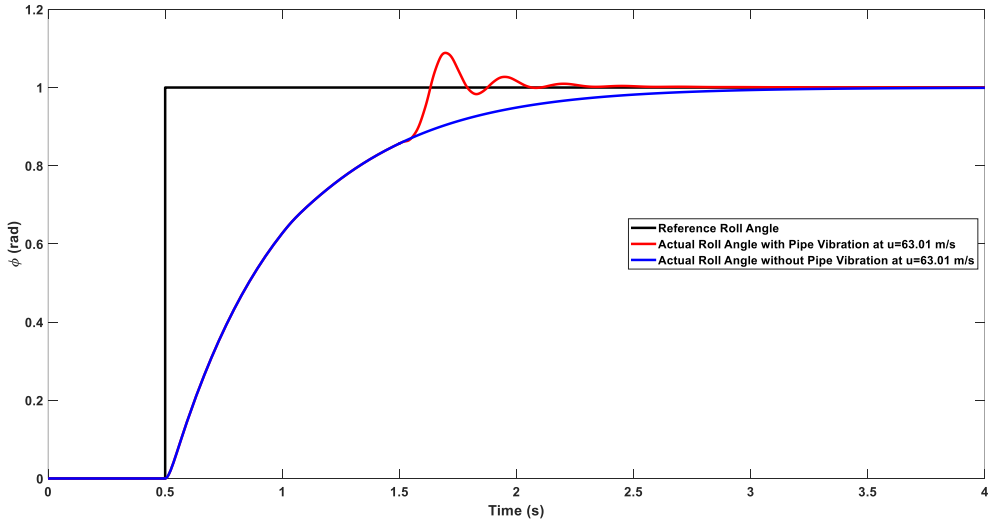


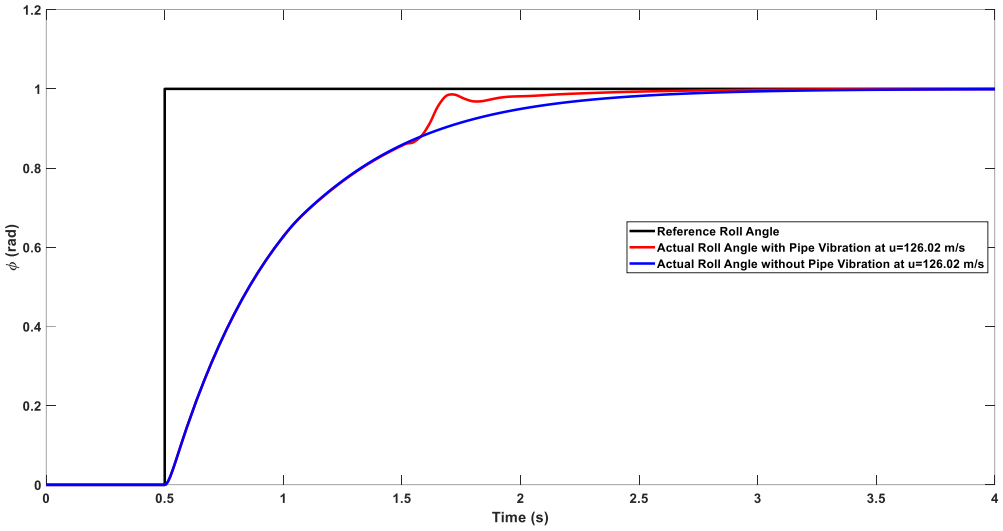
Fig. 10. The variation of the acting force at the free end of the pipe in Scenario 2



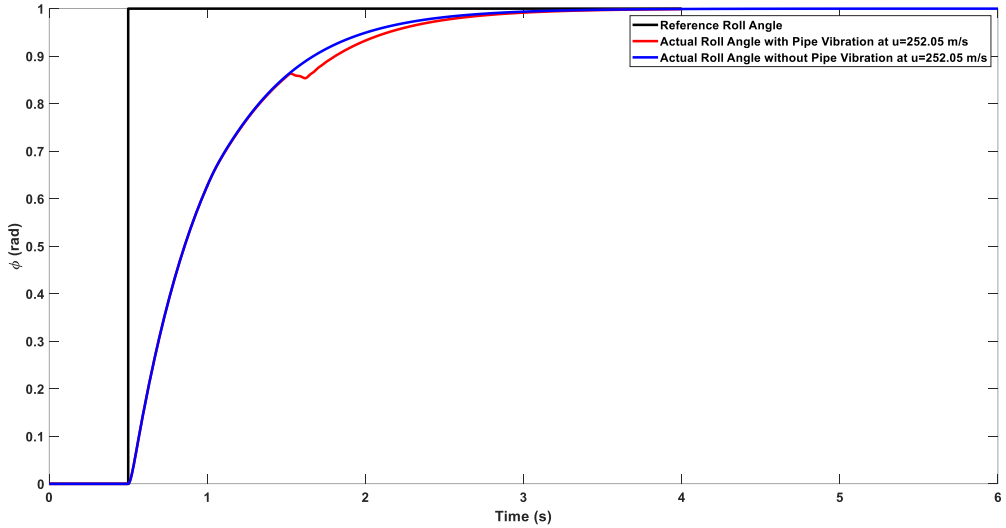
(a)



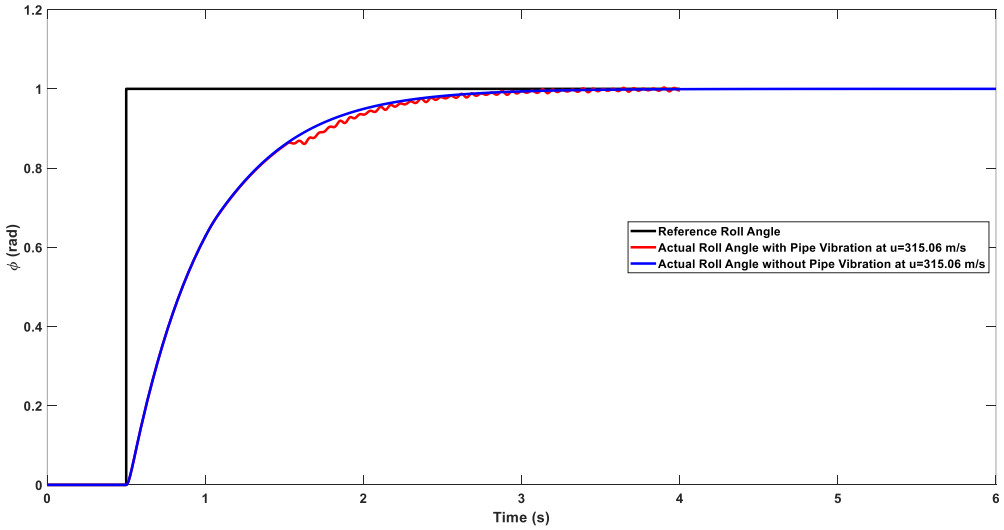
(b)



(c)



(d)



(e)

Fig. 11. Roll angle of PD controlled quadrotor under pipe vibration at a) u=0 m/s b) u=63.01 m/s, c) u=126.02 m/s, d) u=252.05 m/s, e) u=315.06 m/s

As can be seen from Figure 11, when the fluid velocity changes from 0 m/s to 315.06 m/s, the fluid conveying pipe and quadrotor maintain their stability. The PD controller has been successful in controlling the roll motion against pipe vibrations at all fluid velocities. When the disturbing effect is applied to the pipe, oscillatory changes in the roll angle are observed. When the fluid velocity is zero, there are oscillations around the reference value in the roll angle due to the oscillations in the pipe. In this case, it reveals the necessity of increasing the success of the PD controller used. In addition, by applying an additional control to the pipe, pipe vibrations can be eliminated or minimized, and it shows that significant decreases can occur in the vibration amplitude reaching the quadrotor. As in the previous scenario, the amplitudes of the pipe vibrations decrease as the fluid velocity increases, which causes less turning moment on the quadrotor. As seen in Figure 11b and Figure 11c, when the fluid speed is 63.01 m/s and 126.02 m/s, there is an upward change in the roll angle after t=1.5 s. This change, which is damped in time at these speeds, allows the roll angle to reach the reference value more quickly. As a result, the fluid speed in the pipe provides a positive contribution to the controller used at certain values and can ensure that the roll angle reaches the reference value earlier. From here, we can conclude that pipe vibrations at certain fluid speed ranges can contribute to the improvement of time domain criteria by helping the controller designed for the quadrotor. After a certain fluid speed, this effect reverses and the instability of the system increases again. As seen in Figure 11d, when the fluid speed is 252.05 m/s, the low amplitude oscillation in the pipe vibrations increases and can be structurally damped as in low speeds. The change in the roll angle shows that the PD controller is still successful, but it is observed that the settling time increases under the effect of pipe vibrations. In the previous scenario, when the fluid velocity is 315.02 m/s, it is observed that the vibrations in the pipe are small amplitude but continue as continuous oscillations. In this fluid velocity, like the previous scenario, small amplitude oscillations are observed after the effect is applied to the roll angle. For this scenario, tests with a fluid velocity greater than 315.06 m/s were not performed due to the instability of the pipe vibrations and the roll motion of the quadrotor.

4.3. Test Scenario 3

In this scenario, the change in the roll angle of the quadrotor was observed while the pipe was under a sinusoidal force. Unlike the previous scenarios, the reactions of both the pipe and the quadrotor to a disturbing input applied in a different form and for a longer period were examined. This type of disturbing effect may occur on the pipe under the influence of external factors such as weather conditions while the quadrotor is in the air. For this purpose, a force of 2*sin(10t) N acts on the free end of the pipe. This force, like the previous case, was applied without reaching the roll angle reference value with the help of the controller. For this purpose, analyses were performed at different fluid velocities as a result of the disturbing force applied for 0.5 seconds between t=1.5 and t=2 seconds. The force acting on the free end of the pipe in this scenario is shown in Figure 12.

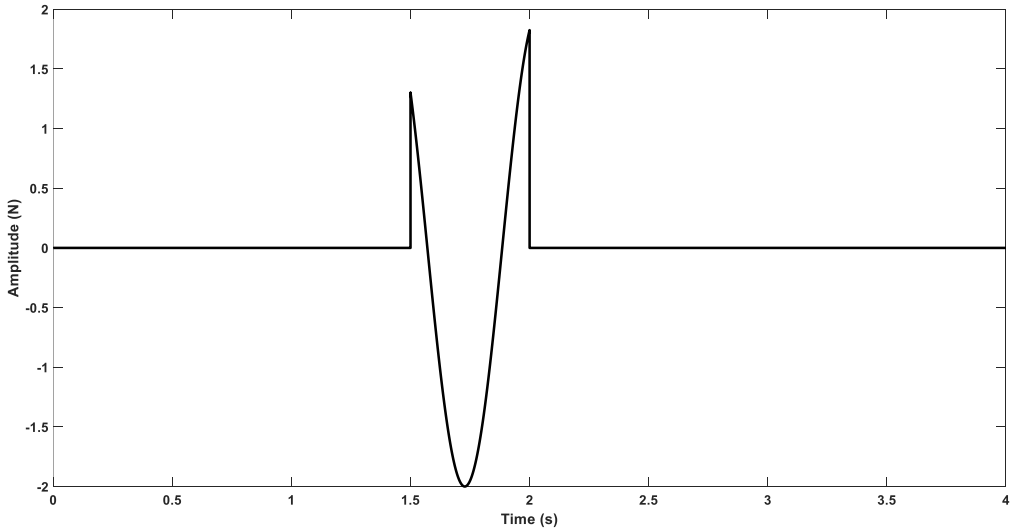
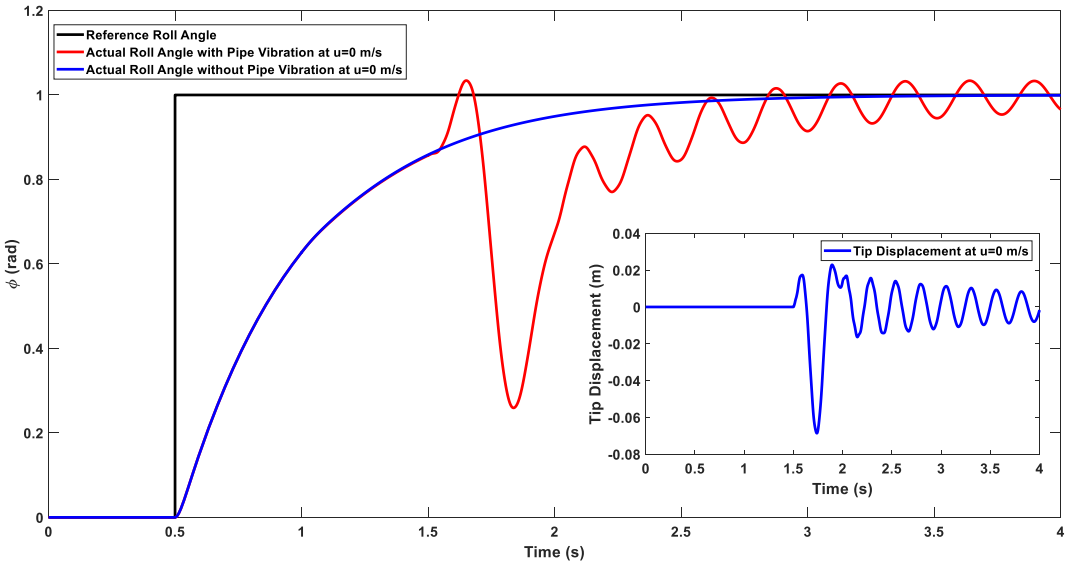


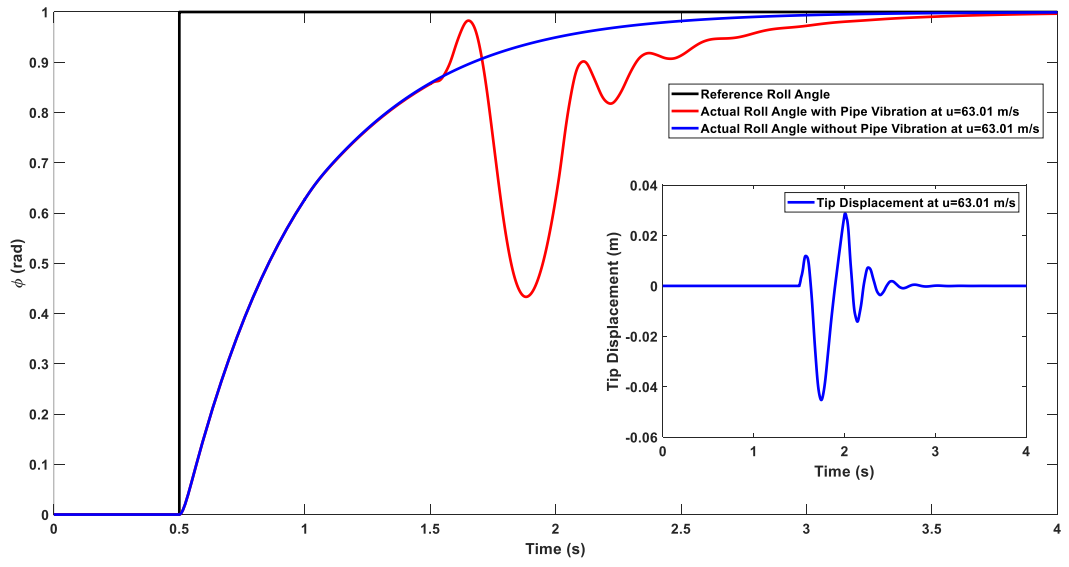
Fig. 12. The variation of the acting force at the free end of the pipe in Scenario 3

After this, the fluid conveying pipe vibrations and the change in roll angle corresponding to this disturbing input are investigated for different speeds. The control parameters of the PD controller used to control the roll angle of the quadrotor are the same for this scenario. Therefore, it takes approximately 3.2 seconds for the roll angle to reach the reference value of 1 rad without pipe vibrations. Figure 13 shows the pipe free end displacements and the roll angle changes caused by the moment caused by pipe vibrations on the quadrotor for the cases where the fluid speed varies between 0 m/s and 315.06 m/s.

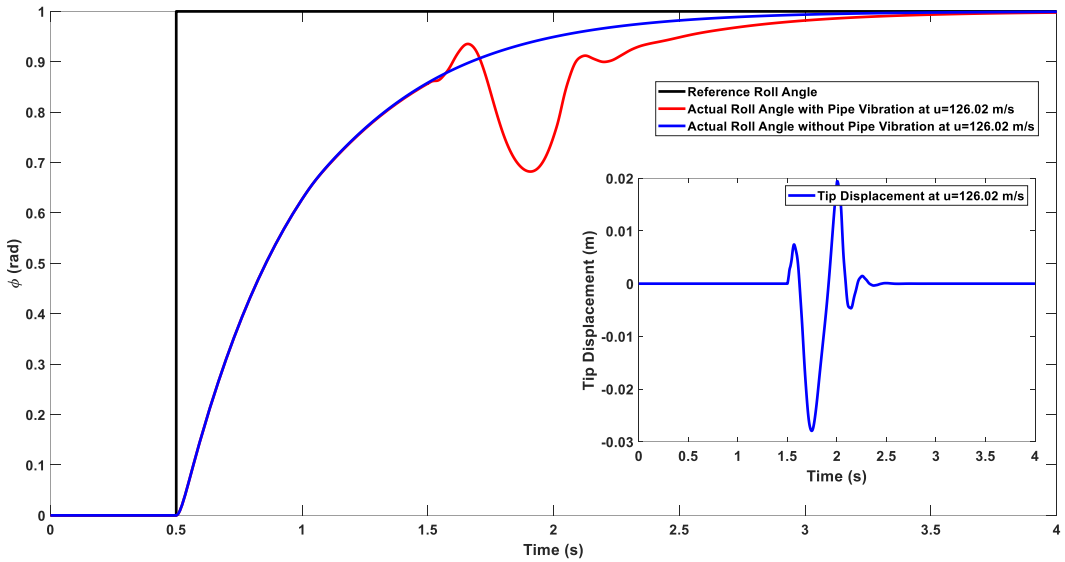
As seen in Figure 13, the vibrations of the free end of the pipe are observed to be compatible with the sinusoidal input in terms of both increase and form. Depending on the input applied at t=1.5 sec, an increase in amplitudes was observed for type displacement and roll angle change. In addition, this input applied before the roll angle reached the reference value caused the angle change to fluctuate more than in the previous scenario from the moment it was applied. Especially, the formation of these high amplitude oscillations can be observed more clearly at low fluid speeds. As seen in the figures, the amplitude of the pipe vibrations reaches the levels of 0.004 m with the increase in fluid speed and continues to decrease until the critical speed is reached. This decreases the input effect of the quadrotor on the roll angle depending on the increase in fluid speed. The effect of the sinusoidal input applied for lower speeds in Figure 13b and Figure 13c is seen together with the high amplitude initial fluctuations in the roll angle.



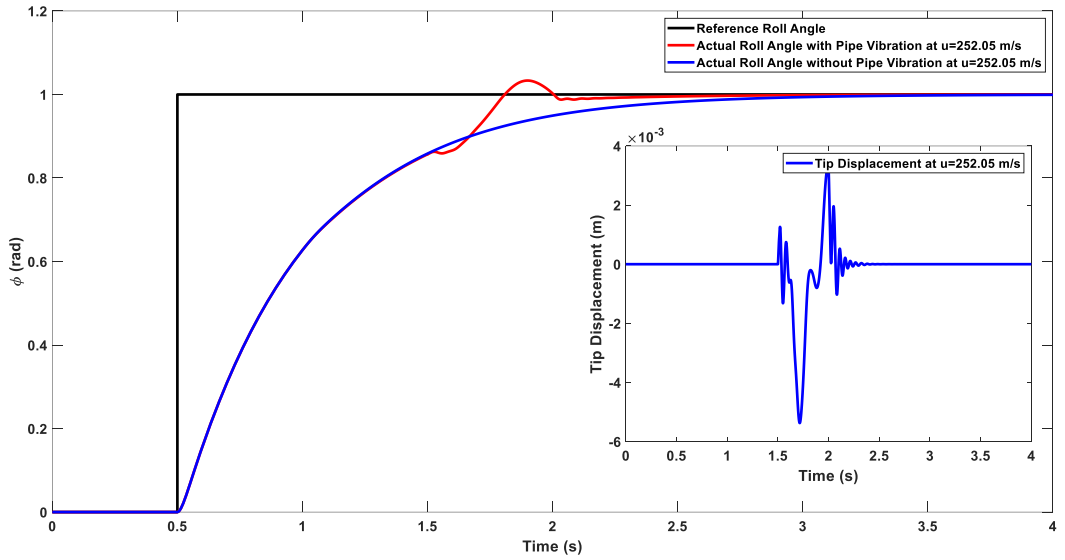
(a)



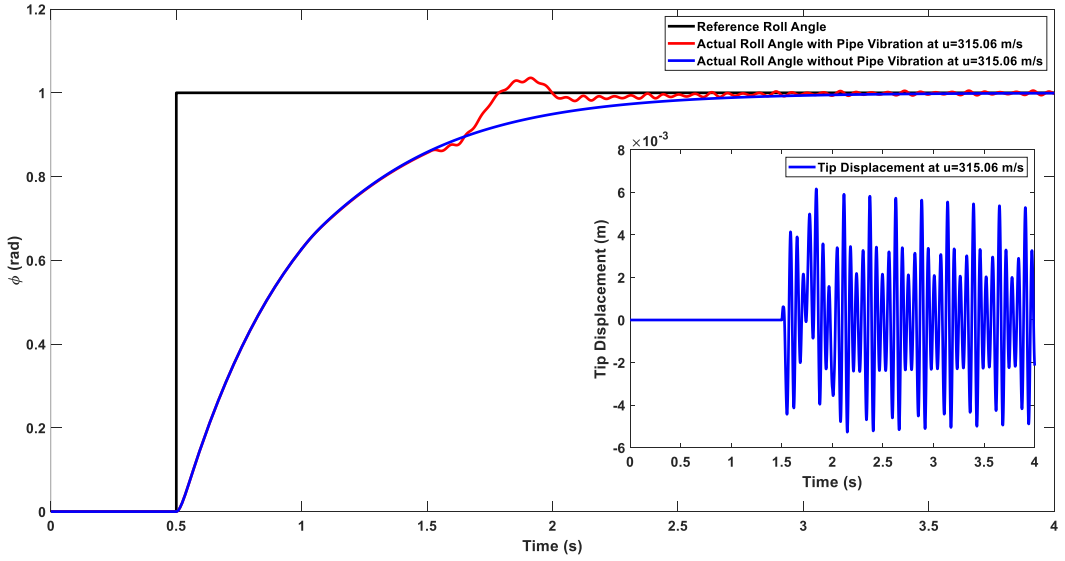
(b)



(c)



(d)



(e)

Fig. 13 The variation of roll angle of PD controlled quadrotor and displacement of pipe's tip at a) u=0 m/s b) u=63.01 m/s, c) u=126.02 m/s, d) u=252.05 m/s, e) u=315.06 m/s

This effect decreases significantly when the fluid speed reaches 252.05 m/s and 315.06 m/s as seen in Figure 13d and Figure 13e. This high amplitude angle change occurring at low fluid speeds also prolongs the time for the roll angle to settle to the reference value. It is observed that this time reaches 3.5 seconds when the fluid speed is 63.01 m/s and 126.02 m/s. For fluid speeds of 252.05 m/s and 315.06 m/s, a significant decrease is observed in the settling time due to the contribution of pipe vibrations. The settling time is around 2.5 seconds for both speeds. Despite the decrease in oscillation and the decrease in the settling time at high fluid speeds, an overshoot is observed in the change of the roll angle for 252.05 m/s and 315.06 m/s. This shows that the disturbance input, fluid speed and controller features are effective on the change of the roll angle.

5. Conclusion

In this study, the effects of fluid velocity and pipe vibration on the dynamic behavior of a quadrotor-fluid conveying vertical cantilever pipe system were investigated. A comprehensive system model was created to analyze quadrotor stability and pipe nonlinear vibrations by considering fluid-structure interaction and aeroelastic coupling. Euler method was used for the quadrotor model, and Euler-Bernoulli beam model based finite element method was used for modeling of the fluid conveying pipe. Both models were connected using the bending force and moment generated at the joint due to pipe vibrations. Observations were made under uncontrolled and PD control for the roll angle of the quadrotor, and no controller was applied for pipe vibrations. Then, tests were conducted at different fluid velocities and according to different pipe disturbance inputs.

According to the results obtained, it is shown that the fluid velocity and pipe excitation significantly affect the stability of the quadrotor and cause changes in the displacement of the free end of the pipe and the roll angle. It is observed that the amplitude of the pipe vibrations decreases with increasing the fluid velocity. However, this decrease continues until the fluid velocity reaches the critical level. For this reason, the roll angle of the quadrotor becomes more stable when the fluid velocity increases without exceeding the critical velocity. Therefore, the roll angle changes significantly at lower fluid velocities. However, when the critical fluid velocity is exceeded, both the pipe system and the quadrotor system lose their stability. When no control is applied to control the roll angle, the quadrotor behaves unstable for each fluid velocity. For this reason, in order to examine the effects of pipe vibrations more clearly, the U_2 force controlling the roll angle was controlled with the PD controller. It is seen that the performance of the PD controller is successful after the excitation applied before and after the roll angle settles at the desired reference value. In addition, the time domain criteria of the roll angle for the same inlet at different fluid velocities also vary. It has been determined that pipe vibrations occurring at certain speeds shorten the roll angle settling time to the reference value. This shows that pipe vibrations can provide positive contributions in the control phase. In addition, the type of distortion in the pipe significantly affects the rolling motion. When a sinusoidal-based disturbing input is applied, the roll angle follows this input and extends the settling time of the roll angle for low fluid velocities. For a 0.1 second step input, low fluid velocities shorten the settling time, and low fluid velocities lengthen the settling time for a 0.5 second sinusoidal input. As the fluid velocity increases, the settling time shortens by approximately 1 second, but the increase in the flow rate also causes an overshoot in the roll angle.

On the other hand, it has been observed that the PD controller applied yields successful results for different flow rates and drive types. As seen in this study, the use of such systems will increase and it is important to examine the interactions of the dynamics with each other in terms of efficiency. In addition, it has been determined that quadrotor-supported fluid transfer systems require optimized design and development of additional controllers for improved stability and performance. For this reason, it is planned to expand the system model of this study with future studies such as developing the quadrotor movement to affect pipe vibrations, adding an additional controller to the pipe to control pipe vibrations, preferring more adaptive controllers instead of PD controllers, and considering pipe vibrations in 3D.

Appendix

The element mass, gyroscopic and stiffness matrices are

$$M_e = \begin{bmatrix} \frac{13L(m+M)}{35} & \frac{11L^2(m+M)}{210} & \frac{9L(m+M)}{70} & \frac{-13L^2(m+M)}{420} \\ \frac{11L^2(m+M)}{210} & \frac{L^3(m+M)}{105} & \frac{13L^2(m+M)}{420} & \frac{-L^3(m+M)}{140} \\ \frac{9L(m+M)}{70} & \frac{13L^2(m+M)}{420} & \frac{13L(m+M)}{35} & \frac{-11L^2(m+M)}{210} \\ \frac{-13L^2(m+M)}{420} & \frac{-L^3(m+M)}{140} & \frac{-11L^2(m+M)}{210} & \frac{L^3(m+M)}{105} \end{bmatrix} \tag{A1}$$

$$G_1 = \begin{bmatrix} \frac{12E^*I}{L^3} + \frac{13cL}{35} + MU \\ \frac{6E^*I}{L^2} + \frac{11cL^2}{210} - \frac{LMU}{5} \\ \frac{-12E^*I}{L^3} + \frac{9cL}{70} - MU \\ \frac{6E^*I}{L^2} - \frac{13cL^2}{420} + \frac{LMU}{5} \end{bmatrix} \qquad G_2 = \begin{bmatrix} \frac{6E^*I}{L^2} + \frac{11cL^2}{210} + \frac{LMU}{5} \\ \frac{4E^*I}{L} + \frac{cL^3}{105} \\ \frac{-6E^*I}{L^2} + \frac{13cL^2}{420} - \frac{LMU}{5} \\ \frac{2E^*I}{L} - \frac{cL^3}{140} + \frac{L^2MU}{30} \end{bmatrix}$$

$$G_3 = \begin{bmatrix} \frac{-12E^*I}{L^3} + \frac{9cL}{70} + MU \\ \frac{-6E^*I}{L^2} + \frac{13cL^2}{420} + \frac{LMU}{5} \\ \frac{12E^*I}{L^3} + \frac{13cL}{35} + MU \\ \frac{-6E^*I}{L^2} - \frac{11cL^2}{210} - \frac{LMU}{5} \end{bmatrix} \qquad G_4 = \begin{bmatrix} \frac{6E^*I}{L^2} - \frac{13cL^2}{420} - \frac{LMU}{5} \\ \frac{2E^*I}{L} - \frac{cL^3}{140} - \frac{L^2MU}{30} \\ \frac{-6E^*I}{L^2} - \frac{11cL^2}{210} + \frac{LMU}{5} \\ \frac{4E^*I}{L} + \frac{cL^3}{105} \end{bmatrix} \tag{A2}$$

$$G_e = [G_1 \quad G_2 \quad G_3 \quad G_4]$$

$$K_1 = \begin{bmatrix} \frac{12EI}{L^3} + \frac{3g(m+M)}{5} - \frac{11M\dot{U}}{10} - \frac{6MUU_j}{5L} \\ \frac{6EI}{L^2} - \frac{LM\dot{U}}{10} - \frac{MUU_j}{10} \\ \frac{-12EI}{L^3} - \frac{3g(m+M)}{5} + \frac{M\dot{U}}{10} + \frac{6MUU_j}{5L} \\ \frac{6EI}{L^2} + \frac{gL(m+M)}{10} - \frac{MUU_j}{10} \end{bmatrix} \qquad K_2 = \begin{bmatrix} \frac{6EI}{L^2} + gL(m+M) - \frac{9LM\dot{U}}{10} - \frac{11MUU_j}{10} \\ \frac{4EI}{L} + \frac{gL^2(m+M)}{10} - \frac{L^2M\dot{U}}{10} - \frac{2LMUU_j}{15} \\ -\frac{6EI}{L^2} - \frac{LM\dot{U}}{10} + \frac{MUU_j}{10} \\ \frac{2EI}{L} - \frac{gL^2(m+M)}{60} + \frac{L^2M\dot{U}}{30} + \frac{LMUU_j}{30} \end{bmatrix}$$

$$K_3 = \begin{bmatrix} \frac{-12EI}{L^3} - \frac{3g(m+M)}{5} + \frac{11M\dot{U}}{10} + \frac{6MUU_j}{5L} \\ -\frac{6EI}{L^2} + \frac{LM\dot{U}}{10} + \frac{MUU_j}{10} \\ \frac{12EI}{L^3} + \frac{3g(m+M)}{5} - \frac{M\dot{U}}{10} - \frac{6MUU_j}{5L} \\ -\frac{6EI}{L^2} - \frac{gL(m+M)}{10} + \frac{MUU_j}{10} \end{bmatrix} \qquad K_4 = \begin{bmatrix} \frac{6EI}{L^2} + \frac{gL(m+M)}{10} - \frac{LM\dot{U}}{5} - \frac{MUU_j}{10} \\ \frac{2EI}{L} - \frac{gL^2(m+M)}{60} + \frac{LMUU_j}{30} \\ \frac{-6EI}{L^2} - \frac{gL(m+M)}{10} + \frac{LM\dot{U}}{5} + \frac{11MUU_j}{10} \\ \frac{4EI}{L} + \frac{gL^2(m+M)}{30} - \frac{L^2M\dot{U}}{30} - \frac{2LMUU_j}{15} \end{bmatrix} \tag{A3}$$

$$K_e = [K_1 \quad K_2 \quad K_3 \quad K_4]$$

where $m = M_{fluid}$ and $M = M_{pipe}$.

References

[1] Ando H, Ambe Y, Yamaguchi T, Konyo M, Tadakuma K, Maruyama S, Tadokoro S. Fire Fighting Tactics with Aerial Hose-type Robot "Dragon Firefighter". IEEE International Conference on Advanced Robotics and its Social Impacts (ARSO), Beijing, China, 2019. https://doi.org/10.1109/ARSO46408.2019.8948716

[2] Martinez-Guanter J, Aguera P, Aguera J, Pérez-Ruiz M. Spray and economics assessment of a UAV-based ultra-low-volume application. Precision Agriculture, 2020; 21:226-243. https://doi.org/10.1007/s11119-019-09665-7

[3] Uddin SMM, Hossain MR, Rabbi MS, Hasan MA and Rahman Zishan MS. Unmanned Aerial Vehicle for Cleaning the High Rise Buildings. International Conference on Robotics, Electrical and Signal Processing Techniques (ICREST), Dhaka, Bangladesh, 2019. https://doi.org/10.1109/ICREST.2019.8644476

[4] Nooralishahi P, Ibarra-Castanedo C, Deane S, López F, Pant S. Genest M, Avdelidis NP, Maldague XPV. Drone-Based Non-Destructive Inspection of Industrial Sites: A Review and Case Studies. Drones, 2021; 5(4): 106. https://doi.org/10.3390/drones5040106

[5] Lee SM, Ng WH, Liu J, Wong SK, Srigrarom S, Foong S. Flow-Induced Force Modeling and Active Compensation for a Fluid-Tethered Multirotor Aerial Craft during Pressurised Jetting. Drones, 2022; 6(4): 88. https://doi.org/10.3390/drones6040088

[6] Omar HM, Mukras SMS. Revolutionizing Palm Dates Harvesting with Multirotor Flying Vehicles. Applied Sciences, 2024; 14(22), 10529. https://doi.org/10.3390/app142210529

[7] Ruiz JP, Toazo ER, Naranjo CA, Ortiz JS, Silva FM, Andaluz VH. Aerial Manipulator Robot Trajectory Tracking for Rhythmic Entertainment Applications. Proceedings of the Future Technologies Conference (FTC) 2024;4: 17-31. Springer, Cham. https://doi.org/10.1007/978-3-031-73128-0_2

[8] Pasala HVS, Govindan N, Brahmbhatt S. Identification and Learning-Based Control of an End-Effector for Targeted Throwing. IEEE Robotics and Automation Letters, 2024; 9:11, 9558-9564, Nov. 2024. https://doi.org/10.1109/LRA.2024.3462250

[9] Choi, YJ, Jung S. Experimental Studies on Solar Panel Cleaning Task by a Foldable Robot Arm of a Drone. Journal of Institute of Control, Robotics and Systems, 2023; 29(11): 887-892. https://doi.org/10.5302/J.ICROS.2023.23.0076

[10] Raj DSS, Sethuraman TV, Shankar SS, Yashvanth VP, Perepu SK, Mohan S. An Autonomous Drone with Robotic End Effector for Maintenance Operation of 5G Mobile Towers. 3rd International Conference on Control and Robots (ICCR), 2020, Tokyo, Japan.

[11] Suarez A, Vega VM, Fernandez M, Heredia G, Ollero A. Benchmarks for Aerial Manipulation. IEEE Robotics and Automation Letters, 2020; 5(2): 2650-2657. https://doi.org/10.1109/LRA.2020.2972870

[12] Alberto J, Cervantes GS, Inanez CA, Mendez M. Air-arm: A new kind of flying manipulator. Workshop on Research, Education and Development of Unmanned Aerial Systems (RED-UAS). Cancun, Mexico, 2019.

[13] Ramalepa LP, Jamisola RS. A Review on Cooperative Robotic Arms with Mobile or Drones Bases. International Journal of Automation and Computing, 2021;18:536-555. https://doi.org/10.1007/s11633-021-1299-7

[14] Saunders J, Saeedi S, Li W. Autonomous aerial robotics for package delivery: a technical review. Journal of Field Robotics, 2024; 41: 3-49. https://doi.org/10.1002/rob.22231

[15] Xiao LJ, Liu Q. Analysis of the deep sea mining pipe transverse vibration characteristics based on finite element method. Mathematical Problems in Engineering. 2021. https://doi.org/10.1155/2021/8216439

[16] Kwag S, Eem S, Kwak J, Lee H, Oh J, Koo GH. Mitigation of seismic responses of actual nuclear piping by a newly developed tuned mass damper device. Nuclear Engineering and Technology. 2021; 53(8),:2728-2745. https://doi.org/10.1016/j.net.2021.02.009

[17] Wu CJ, Jiao ZX, Xu Y., Hu JH, Pan H. Developments in pogo suppression methods for liquid rockets. Progress in Aerospace Sciences. 2023; 140: 100931. https://doi.org/10.1016/j.paerosci.2023.100931

[18] Heng J, New T, Wilson P. Application of an Eulerian granular numerical model to an industrial scale pneumatic conveying pipeline. Advanced Powder Technology. 2019;30(2): 240-256. https://doi.org/10.1016/j.apt.2018.10.028

[19] Païdoussis, MP, Issid, NT. Dynamic Stability of Pipes Conveying Fluid. The Journal of Sound and Vibration. 1974; 33: 267-294. https://doi.org/10.1016/S0022-460X(74)80002-7

[20] Païdoussis MP, Li GX. Pipes Conveying Fluid: A Model Dynamical Problem. Journal of Fluids and Structures. 1993; 7: 137-204. https://doi.org/10.1006/jfls.1993.1011

[21] Modarres-Sadeghi Y, Paidoussis MP, Semle C. Three-dimensional oscillations of a cantilever pipe conveying fluid. International Journal of Non-Linear Mechanics. 2008;43: 18-25. https://doi.org/10.1016/j.ijnonlinmec.2007.09.005

[22] Liu ZY, Wang L, Sun XP. Nonlinear Forced Vibration of Cantilevered Pipes Conveying Fluid. Acta Mechanica Solida Sinica. 2018; 31: 32-50. https://doi.org/10.1007/s10338-018-0011-0

[23] Li J, Deng H, Jiang W. Dynamic response and vibration suppression of a cantilevered pipe conveying fluid under periodic excitation. Journal of Vibration and Control. 2019;2511: 1695-1705. https://doi.org/10.1177/1077546319837789
[24] Paidoussis MP. The dynamics of cantilevered structures subject to axial flow. Journal of Fluids and Structures. 2024;125: 104075. https://doi.org/10.1016/j.jfluidstructs.2024.104075
[25] Semler C, Païdoussis MP. Nonlinear Analysis of the Parametric Resonances of a Planar Fluid-Conveying Cantilevered Pipe. Journal of Fluids and Structures. 1996;107: 787-825. https://doi.org/10.1006/jfls.1996.0053
[26] Tang Y, Zhang HJ, Chen LQ, Ding Q, Gao Q, Yang T. Recent progress on dynamics and control of pipes conveying fluid. Nonlinear Dynamics. 2025; 113: 6253-6315. https://doi.org/10.1007/s11071-024-10486-1
[27] Ibrahim RA. Overview of mechanics of pipes conveying fluids-Part I: fundamental studies. Journal of Pressure Vessel Technology. 2010; 132: 034001. https://doi.org/10.1115/1.4001271
[28] Ibrahim RA. Mechanics of pipes conveying fluids-Part II: applications and fluid elastic problems. J Journal of Pressure Vessel Technology. 2011; 133: 024001. https://doi.org/10.1115/1.4001270
[29] Païdoussis, MP. Fluid-Structure Interactions: Slender Structures and Axial Flow, Vol. 1. Academic, London,1998. https://doi.org/10.1016/S1874-5652(98)80003-3
[30] Païdoussis, MP. Fluid-Structure Interactions: Slender Structures and Axial Flow, Vol. 2. Academic, London, 2004.
[31] Pisarski D, Konowrocki R, Szmidt T. Dynamics and optimal control of an electromagnetically actuated cantilever pipe conveying fluid. Journal of Sound and Vibration. 2018; 432: 420-436. doi:10.1016/j.jsv.2018.06.045. https://doi.org/10.1016/j.jsv.2018.06.045
[32] Szmidt T, Pisarski D, Konowrocki, R. Semi-active stabilisation of a pipe conveying fluid using eddy-current dampers: state-feedback control design, experimental validation. Meccanica. 2019; 54: 761-777. https://doi.org/10.1007/s11012-019-00988-3
[33] Ikbal M, Kumar A, Jaya MM, Bursi OS. Vibration control of periodically supported pipes employing optimally designed dampers. International Journal of Mechanical Sciences. 2022;234: 107684. https://doi.org/10.1016/j.ijmecsci.2022.107684
[34] Lin, YH, Chu CL. Active flutter control of a cantilever pipe conveying fluid using piezoelectric actuators. Journal of Sound and Vibration. 1996;1961: 97-105. doi:10.1006/jsvi.1996.0470. https://doi.org/10.1006/jsvi.1996.0470
[35] Demir MH, Yesildirek A, Yigit F. Control of a cantilever pipe conveying fluid using neural network. 6th International Conference on Modeling, Simulation, and Applied Optimization (ICMSAO). Istanbul, Turkey,2015. https://doi.org/10.1109/ICMSAO.2015.7152198
[36] Tsai YK, Lin YH. Adaptive modal vibration control of a fluid-conveying cantilever pipe. Journal of Fluids and Structures. 1997;11(5):535-547. doi:10.1006/jfls.1997.0092. https://doi.org/10.1006/jfls.1997.0092
[37] Li J, Deng H, Jiang W. Dynamic response and vibration suppression of a cantilevered pipe conveying fluid under periodic excitation. Journal of Vibration and Control. 2019;25(11):1695-1705. https://doi.org/10.1177/1077546319837789
[38] Zhang Y, Sun W, Zhang H, Du D, Xu K. Active vibration control of fluid-conveying pipelines: Theoretical and experimental studies. International Journal of Mechanical Science. 2024; 270: 109106. https://doi.org/10.1016/j.ijmecsci.2024.109106
[39] Philip R, Santhosh B, Balaram B, Awrejcewicz J. Vibration control in fluid conveying pipes using NES with nonlinear damping. Mechanical Systems and Signal Processing. 2023; 194: 110250. https://doi.org/10.1016/j.ymssp.2023.110250
[40] Yigit F. Active control of flow-induced vibrations via feedback decoupling. Journal of Vibration and Control. 2008; 14(4):591-608. https://doi.org/10.1177/1077546307082191
[41] Ding H, Ji JC. Vibration control of fluid-conveying pipes: a state-of-the-art review. Applied Mathematics and Mechanics. 2023; 44: 1423-1456. https://doi.org/10.1007/s10483-023-3023-9
[42] Bousbaine A, Wu, MH, Poyi GT. Modeling and Simulation of a Quad-Rotor Helicopter. University of Derby, UK,2021.
[43] Iyer A, Bansal HO. Modelling, Simulation, and Implementation of PID Controller on Quadrotors. International Conference on Computer Communication and Informatics (ICCCI). Coimbatore, India, 2021. https://doi.org/10.1109/ICCCI50826.2021.9402301
[44] Islam M, Okasha M, Idres MM. Dynamics and Control of Quadcopter Using Linear Model Predictive Control Approach. IOP Conf. Series: Materials Science and Engineering, 2017; 270: 012007. https://doi.org/10.1088/1757-899X/270/1/012007

Blank Page

Research on Engineering Structures & Materials
www.jresm.org

Research Article

Structural application of fiber reinforced concrete

Kalapala Vijay Babu [*,1,a], CH. Mallika Chowdary [1,b], Lingeshwaran N [1,c], Ikkurthi Siva Kishore [2,d]

[1]*Dept. of Civil Eng., Koneru Lakshmaiah Education Foundation (Deemed to be University), Guntur, India*
[2]*Dept. of Civil, Construction and Environmental Engineering, Iowa State University, Ames, IA, US*

Article Info

Article history:

Received 31 May 2024
Accepted 02 Dec 2024

Keywords:

Coir fiber;
Plastic fiber;
Stress- strain behavior;
Durability properties;
Flexural behavior;
Micro structural analysis

Abstract

This study investigates the structural application of fiber-reinforced concrete using coir and plastic fibers. The experiment incorporated various percentages of fibers in concrete: coir fiber and plastic fibers at 0.5%, 1%, 1.5%, and 2%. An over-all of 80 concrete cubes, 42 cylinders, and 40 prisms were cast and examined to assess various mechanical properties. Compressive strength, and durability tests were conducted on the concrete cubes. The cylinders were subjected to split tensile tests and stress-strain behavior evaluations. The prisms underwent flexural strength tests to determine their performance under load. Additionally, the study included reinforced concrete beams reinforced with steel and fibers, and one beam with fibers only. Flexural strength tests were conducted on these beams, resulting in stress-strain behavior and load-deflection. Advanced characterization techniques such as Scanning Electron Microscopy (SEM), Energy Dispersive X-ray (EDX), and Fourier Transform Infrared Spectroscopy (FTIR) were applied to end sample powders of both normal and optimized mixes The findings indicate that the incorporation of 1% coir and plastic fibers significantly enhances the mechanical performance of concrete. The results from compressive strength, tensile strength, and flexural strength tests recommend that fiber reinforcement improves the durability and structural integrity of concrete. The SEM, EDX, and FTIR analyses provided insights into the microstructural changes and bonding characteristics of the fiber-reinforced concrete, corroborating the mechanical test outcomes. In conclusion, the study demonstrates that fiber-reinforced concrete, particularly with 1% coir and plastic fibers, the 1% of coir sample increased tensile strength by 10% and flexural strength by 20%, while the 1% plastic fiber improved flexural strength by 50% and split tensile strength by 30%. It is a viable and sustainable option for enhancing the mechanical performance and durability of concrete structures. This creative approach has potential for building environmentally friendly concrete infrastructure.

© 2025 MIM Research Group. All rights reserved.

1.Introduction

The construction industry is heavily dependent on the extraction and use of natural resources, though, due to the materials' production and transportation to the construction site, which uses a considerable quantity of non-renewable resources and releases a substantial amount of carbon dioxide [1]. Concrete, a popular building material due to its strength, durability, and flexibility, has faced challenges in modern building processes. Low tensile and flexural strength, which increases the risk of breaking under strain, and the high CO_2 releases from concrete buildings have negative environmental impacts. Therefore, there is an increasing consumer demand for ecologically sustainable construction materials with higher quality. Research is being conducted to explore

*Corresponding author: kalapalavijay122@gmail.com
[a] orcid.org/0009-0000-4876-848X; [b] orcid.org/0000-0001-6888-0364; [c] orcid.org/0000-0003-2998-7315; [d] orcid.org/0000-0002-9143-0027
DOI: http://dx.doi.org/10.17515/resm2024.305st0531rs

alternative materials like industrial, home, and recyclable resources, which can support environmental harmony and contribute to sustainable development goals [2][3][4]. Aggregate, bound by slurry and water, forms a solid mass. It's an adaptable construction material, used for various purposes. Engineers can use additives and admixtures to modify concrete properties [5]. Certain loading stages influence how cementitious composites that include two or more blended fibers respond to the cracking process. The finished product that incorporates two or more fibers is referred to as "fiber reinforced concrete. Fibers perform better than the sum of their parts when combined, which is why fiber-reinforced concretes are constructed with a range of fiber types integrated [6].

FRC behaviour is influenced by fiber type, shape, orientation, aspect ratio, and content. Steel and basalt fibers are added to Ultra-High-Performance Concrete (UHPC) to improve tensile strength, hydration, and low pre-crack energy absorption [7]. CFRP composites offer numerous benefits over traditional materials, including durability, high strength, lightweight, and quick installation, making them increasingly used in the construction industry for infrastructure applications [8].

A brittle behaviour characterizes plain concrete in tension because of the low tensile strength, and the reduced strain capacity. The addition of randomly distributed fibers to plane concrete has been shown to provide higher ductility and strength. The fibers transfer stresses between the concrete matrix and tensile strains during the crack propagation, thus improving the post-cracking response. The main parameters affecting the design and performance of FRC are the fiber volume content (V_f), the ratio between the length and the diameter of fibers (l/d), and the fiber weight ratio (FWR), defined as the weight of the fibers in 1 m^3. In particular, the l/d ratio affects the number of fibers which cross the cracks under load, keeping constant V_f. Because of the importance of the fiber dimensions, the industry makes available different types and sizes of this reinforcement, ranging from 6 mm to a maximum length of 80 mm and from 0.1 to a maximum cross section area of 1.5 mm^2 [9].

C. Lin et.al[10]-classified features that include the reinforcement as well as the fibers as variables impacting the bonding among the fibers and the concrete matrix. Bonding strength may be increased by improving the concrete matrix's strength, which is directly related to how compact it is. By directly altering binder powder particle packing and wall effect, multiscale reinforcement of the environment with ingredients such as fly ash, silica fume, nanotubes, and micro or nanofillers can improve bonding characteristics and strengthen the fiber-matrix interface. Depending on the matrix and fiber characteristics, the ITZ's width can range from nanometers to micrometers. The surface area of the fiber is typically greater than its geometrical value because of these holes and microcracks. The efficiency of the method at the fiber-matrix interface is further examined using a variation of other micro-characterization methods, with scanning electron microscopy (SEM), Fourier transform infrared (FTIR) spectroscopy, nano-indentation, etc.

Jamal A. Abdalla et. al. [11] classify the constitutive behaviour of fiber reinforced composites at various strain rates as being shown to be greatly affected by the natural filler qualities, amounts, sizes, and kinds of matrix polymers.K. Sandeep Dutt et. al [12] Shows that Performance under varied strain rates can be enhanced by increasing the fiber-matrix stress-transfer efficiency by optimizing these variables. Composites reinforced with flax and jute fibres were found to be stiffer than those reinforced with cotton fibres, despite the fact that all materials have a potential to grow more rigid with rising strain rates.

The high concentration of natural fibers in many developing nations, together with additional relevant elements, demands that scientists and engineers use the right technology to maximize use of these fibers for structural upgrades and, additionally, other uses like housing and other requirements. There are plenty of natural resources available to us, and we must continue to explore them. The emergence of plant fiber composites is

quite new. Numerous different natural fibers, primarily produced in India, including jute, coir, banana, and sisal, are among the fiber-reinforced composites that are of special interest because they have moderate tensile and flexural properties in addition to strong impact resistance in comparison to other plant-based fibers [13, 15].

A. N. Kangu et.al [16] & U. Sharma et.al [17] added fibers to the concrete in specific portions, to improve its performance. The structural stability of concrete is increased by adding fibers. The fibers were cut into 40mm lengths and additional to the concrete at concentrations of 0.5%, 1%, 1.5%, and 2%. The mechanical properties, such as Tension, Flexure, and Compression strengths were examined to indicate the contribution of the fibers in concrete. The findings indicate prevention of cracks on adding fibers, thereby the stress-bearing capacity of concrete can be enhanced. Natural fiber-containing concrete mixes are ideal for civil construction, tunnelling, industrial floors, and foundation slabs. However, studies on high-strength concrete have not thoroughly examined the combined impacts of supplementary cementitious materials and natural fiber concentrations. These large, low-cost, and easy-to-manufactured composites are increasingly used in industries like paper fabrication, automobiles, and aircraft furniture due to their ecological benefits [18].

Bamboo leaf ash (BLA) is a renewable resource with pozzolanic reactivity, but its improper use leads to environmental harm. A sustainable solution is to activate Bamboo leaf ash (BLA) pozzolanic reactivity through controlled calcination. A study explores blending Portland-limestone cement and Bamboo leaf ash (BLA) in high performance concrete manufacturing to raise awareness among building industry experts about alternative materials in construction projects [19]. Fiber Reinforced Polymer (FRP) sheets are used, especially for seismic retrofitting, to boost the flexural capacity of reinforced concrete beams and columns. For FRP sheets, synthetic fibers are often utilized. However, because of their high cost and environmental problems arising from recycling issues, natural fibers are utilized to generate Natural Fiber Reinforced Polymer, or NFRP. NFRP provides a synthetic fiber substitute that is less harmful to the environment. The analysis of the bond strength between natural fiber reinforced polymer (NFRP) sheets and concrete [20,22].

The utilization of natural fibers resulting from plants such as jute, hemp, sisal, sugar cane, cannabis, bamboo, coconut, and banana are recommended for concrete because of their low cost, availability, and easy of handling. Coconut fiber is a biodegradable and renewable resource that might be used to strengthen concrete. This can improve the material's mechanical qualities, such as tensile strength and flexibility, and increase its resistance to damage and cracking [23]. The compressive strength of concrete with waste PET fibers is influenced by particle shape, concentration, and water cement ratio. Up to 1.0% of PET fibers can improve concrete performance due to their consistent fibrous structure. However, adding more than 1.0% was a reduction in the compressive strength of concrete, which is likely connected to PET surfaces' poor reactivity, low absorption qualities, reduced hydration, instability, and low friction coefficient. Waste polyethylene terephthalate (PET) can be used as recycled resin by depolymerizing it with nanocatalysts, reducing porosity and increasing durability. This study examined the flexural behavior of glass fiber reinforced polymer Reinforced polymer (GFRP RC) beams and concrete incorporating PET waste fiber. The results provide fresh directions for investigation into flexure structural elements. The study examined the effect of adding PET fiber to concrete on cracking behavior, ultimate load capacity, and mode of failure. Flexural analysis was shown for beams reinforced with PET bar to calculate strain and understand load-deflection response [24, 27].

Concrete's tensile strength has been improved by the use of various fibers over the past decade, including natural, synthetic, metallic, and mineral fibers. Steel fibers are the most

commonly used due to their excellent mechanical properties. The distribution of fibers in concrete is crucial for uniform reinforcing, as they can have various geometric characteristics. Steel fibers prevent crack formation and improve ductility, increasing tensile strength and post-crack reaction, making concrete more ductile and stronger under varied loads [28, 29]. This study explores the use of fibers like steel and glass fiber to improve the flexural strength and ductility of printed beams. These fibers are increasingly popular due to their financial and mechanical benefits. Glass fibers enhance mechanical properties, while steel fibers have been shown to affect the flexural strength and ductility of concrete components [30][31].

The study explores the relationship between fiber length and Ultra-high-performance fiber-reinforced concrete (UHPFRC's) tensile characteristics, finding that the type of fiber affects porosity and tensile strength distribution. The seismic performance of bridge piers is made of UHPFRC, using the modified Kent-Park model to describe the compressive stress-strain relationship of UHPFRC. The study emphasizes the importance of numerical simulation in designing UHPC/UHPFRC structures and suggests combining probabilistic analysis with UHPC fracture modelling for further investigation [32]. Salah Al-Jasmi et. al. research study on utilizes the ANSYS software and finite element analysis to design reinforced concrete beams for off-site oil and gas plants. The simulation environment aids in blast-resistant concrete structure design by generating beam models. The research fills gaps in engineering literature on blast-resistant concrete beam design, thereby enhancing scientific understanding and filling gaps in engineering literature [33][34]. Ultra-high-performance concrete (UHPC) uses steel fibers to withstand less tensile load at crack surfaces, enhancing the moment capacity of reinforced beams. The strong bond between rebar and UHPFRC reduces development length by 20-30% compared to ordinary concrete [35].

Layla K. Amaireh et. al. [36] classify the flexural strength of reinforced concrete beams has been enhanced by a number of methods, such as externally bonded steel plates, FRP strips, RC jacketing, and steel fiber reinforced concrete (SFRC). These techniques do have several drawbacks, though, including brittleness, limited fire resistance, low interfacial bond strength, and hazardous fume emission. A material with the necessary ductility and strength retention at high temperatures is required to reinforce for reinforced concrete structures. High ductility, fire resistance, and strength retention are characteristics of steel and polyvinyl-alcohol hybrid fiber-reinforced engineered cementitious composite (SPH-ECC) that indicate possibility. To look into these factors, ABAQUS finite element analysis and Experiments were conducted.

Seyed Fathollah Sajedi et. al. [37] research aims to determine the optimal arrangement and amount of CFRP composites for strengthening externally reinforced concrete beams, considering concrete strength and contact type. Various CFRP composite configurations were used, and nonlinear finite element analysis was conducted using ABAQUS to model and assess this behavior needed for reinforcing concrete structures.

Transverse rebars offer more confinement and avoid buckling, while increasing the longitudinal reinforcement ratio improves ductility in axially loaded GFRP-RC and CFRP-RC columns, according to research[38]. The numerical model's key aspects include determining the FE dimension, selecting constitutive models for steel fiber reinforced expanded-shale lightweight concrete (SFRELC), steel bars, and bond-slip behavior, defining the loading method, and establishing the convergence criterion. The FE dimension's accuracy and software efficiency depend on its size, with the smallest dimension being the size of coarse aggregate. [39].

This research fits well with many of the research gaps identified in the literature review, especially regarding fiber-matrix interaction, natural fiber performance, and comparative

studies between natural and synthetic fibers. However, there are opportunities for further research in areas like long-term durability, environmental impact assessment, and performance under extreme conditions. These additional investigations could significantly enhance the value of any research in the field of fiber-reinforced concrete.

This research attempted to assess the impact of incorporating fiber materials like coir and plastic in reinforced concrete beam construction to improve their structural properties. The research focused on evaluating how fibers affect the interaction of material and prevent tensile stresses. Fibers typically enhance the tensile strength of concrete and affect the ultimate shear capacity. To compare plastic and coir fibers, hemp coir rope was prepared with a thickness of 3 mm instead of adding coir fiber directly to the concrete. The physical characteristics of the plastic fibers resemble those of the coir hemp rope, similar to a 3 mm thick plastic rope cut into 50 mm length pieces. The coir fiber was divided into 50 mm × 3 mm pieces. Natural fiber reinforcements are a combination of matrix components and natural fibers, which are widely used in various fields due to their accessibility, abundance, and ease of use. These composites are thought to be eco-friendly. due to their production from plant waste, reducing their cost and being used in various industries.

2. Experimental Work

2.1. Materials

2.1.1. Concrete

To ensure the accuracy and quality of our concrete mixes, we strictly follow set norms and procedures in our trial work. OPC 53 Grade cement conforming to IS 12269: 2013, Cement properties are exposed in Table 1. Natural river fine aggregate meeting IS 383: 2016 Zone II requirements, and coarse aggregate with 30% of 10 mm and 70% of 20 mm sizes as per IS 383: 2016 are among our products.

Table 1. Properties of cement following laboratory testing

Test Performed	Value
Fineness (Sieving by 90 mm sieve)	225 m^2/kg
Specific gravity	3.15
Standard consistency	33%
Initial setting time	45 Minutes
Final setting time	8 hours 35 Minutes

Table 2. Physical properties of aggregates

Property	Fine Aggregates	Coarse Aggregate
Density kg/m^3	1.69	1.61
Water %	2	0.47
Fineness modules	3.26	3.2
Max Dia (mm)	-	20
Zone	II	-
Specific gravity	2.65	2.92

Table 2 provides the coarse and fine aggregate's properties. In accordance with IS 456: 2000, tap water is used to ensure uniformity. Furthermore, ~~our~~ mix designs are improved by adding HI FORZA 369 chemical admixture at 0.5% of the cementitious material, in compliance with IS 9103: 1999. ~~Our~~ The finalized mix proportions are carefully calculated

through repeated experiments in accordance with the strict requirements given in IS 10262: 2016, specifically for M40 grade. This ensures optimal performance and durability in our experimental objectives.

2.1.2. Coir Fiber

The coir fiber samples were extracted through cutting, maintaining a uniform size of 50 mm in length and 3 mm in diameter, resulting in an aspect ratio of approximately 16.67≃ 17. Each fiber sample was evaluated and maintained according to the required dimensions for further analysis. It is derived from coconut husks, is a biodegradable and renewable reinforcing material that reduces the carbon footprint in concrete manufacturing. It enhances flexural, tensile strength, crack resistance, shrinkage, and creep effects. Coir fiber also improves concrete's cohesiveness and workability, accelerating construction and resulting in better surface finishes. This sustainable addition aligns with sustainability goals, promoting robust and eco-friendly built environments in the construction industry. Coir fiber shown in Fig. 1a.

2.1.3. Plastic Fiber

Synthetic polymer nylon monofilament yarn is extracted through cutting, with 50mm x 3mm with aspect ratio of 16.67≃ 17. It is a multipurpose reinforcing material used in fishing lines, textile manufacture, and construction. It is essential for improving the structural integrity and lifespan of concrete constructions because of its remarkable tensile strength, resilience, and abrasion resistance. In addition to improving performance, this novel fiber helps promote sustainable building methods by lowering the need for conventional reinforcing materials like steel, which are prone to corrosion and environmental deterioration. Plastic fiber shown in Fig. 1b.

Table 3. Mix proportions of concrete

Constituents	Proportions
Cement	415 (kg/m^3)
Water	165.3 (kg/m^3)
Fine aggregate	725.2 (kg/m^3)
Coarse aggregate	1118.5 (kg/m^3)
20mm	894.8 (kg/m^3)
10mm	223.7 (kg/m^3)
Water /cement ratio	1: 2.5

2.2. Mix Design

As per the IS:10262-2019 standard, the concrete mixture is prepared. The mix ratio is shown in the Table 3 and the concrete strength grade was M40. The finalized mix proportions are the result of several trials conducted to ensure optimal outcomes. Concrete performance by volume using two types of fibers (coir and plastic). Hi-Forza 369 is a polycarboxylate-based additive that is used as a superplasticizer. During the production process, 0.5 percent of the cementitious material by weight is added to concrete as an admixture.



(a) (b)

Fig. 1. (a) Coir fiber (b) plastic fiber

2.3. Cast Specimens

A mix design was used to construct a concrete mix for the M40 grade. The ten mixes are cast out of concrete in order to examine its performance and the impact of fiber. Fig. 2 shown the schematic model for concrete mixing. Concrete performance by volume using two types of fibers (plastic and coir), one of which is a nominal mix with 0.5% superplasticizer in the M1 (Nominal Mix). The volume percentages of fiber were 0.5%, 1%, 1.5%, and 2% added by volume of concrete. Each and every mix compressive strength will compare to the nominal and each individual mixes.

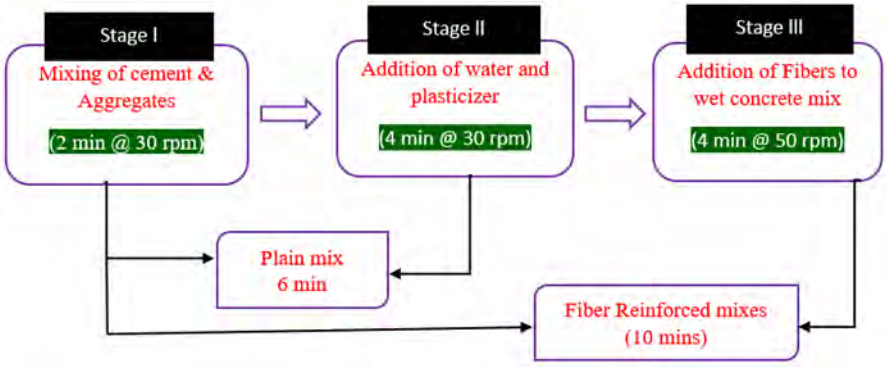


Fig. 2. Phases of mixing was carried out to generate batches of concrete [40]

The saturated, surface-dry-condition (SSD) coir fiber is used in the mixes to maintain the workability. As part of preparation, coir fiber (M1-0), (M2-0.5%C), (M3-1%C), (M4-1.5%C), (M5-2%C), and plastic fiber (M6-0.5%C), (M7-1%C), (M8-1.5%C), (M9-2%C) cast into cubes, cylinders, and prisms, etc. After 24 hours, the samples were taken out from the mould and subjected to proper curing conditions, as per standards IS 456:2000. This was done to prepare the specimens for the experimental testing. The specimens were assessed after 7, 14, 28, and 56 days of curing. Then, the split tensile, compressive, flexural, and stress strains of concrete were evaluated. On the basis of 28 days of flexural strength, split tensile strength, and compression strength, the combined mix of both the fibers, coir and plastic fibers (M10-1%CP), and 5 beams are cast to the size of 700 mm × 150 mm × 150 mm, and a nominal mix with steel reinforcement (B1-0), coir fiber (B2-1%C), plastic fiber 1% (B3-1%P), and a combined mix of both plastic and coir (B4-1%CP). B1, B2, B3, and B4

beams are cast with reinforcement and (B5-1%CP) beams without reinforcement, adding both types of fibers to the total volume of concrete.

2.4. Tests Conducted

2.4.1. Slump Test

It is a simple and widely used method to assess the workability or consistency of fresh concrete. It measures the ease with which concrete flows and is an important quality control test, especially for fiber-reinforced concrete (FRC), where the addition of fibers can affect the mix's fluidity. In the slump test, fresh concrete is placed into a conical mold (known as a slump cone) in three layers, with each layer being tamped to remove air pockets. The cone is then carefully lifted, and the vertical settlement or "slump" of the concrete is measured in millimeters.

2.5.2. Density of Concrete

This test helps in ensuring that the mix proportions are correct and that there are no significant air voids, which can reduce the strength and durability of the concrete. In the case of fiber-reinforced concrete, the inclusion of fibers may slightly alter the density, depending on the type and volume of fibers used, but it generally remains within the typical range for structural concrete. Firstly, measure the cylindrical jar (W_1). Fresh concrete is placed inside the cylinder. Until the jar is filled, compression is applied with the help of a tamping rod for at least 60 strokes for each 50mm layer. After the concrete's compression, the top surface should be level, and the fresh concrete should be weighed with the cylinder (W_2). The formula used to get the fresh concrete density $\left[\frac{[W_1 - W_2]}{[volume\ of\ the\ cylindrical\ jar]}\right] x\ 1000$.

2.5.3 Compressive Strength

2.5.3.1 Compression Strength Test for Cubes

It is one of the most important tests performed to assess the material's ability to withstand axial loads. This test measures the maximum compressive force that a concrete sample can bear before failure, giving an indication of the material's overall strength and suitability for structural applications. The compressive strength evaluation was performed on cube specimens with dimensions of 150 mm x 150 mm x 150 mm, which were tested following 7, 14, 28, and 56 days of curing. For each specified curing duration and for each concrete mix, three cubes were fabricated. Throughout the experimental procedure utilizing the compression testing apparatus, the well-prepared surface of the cube was oriented towards the upper section to facilitate the better compression process. The compression testing apparatus provides a quantifiable output reflecting the maximum load (in kN) that the concrete cube is capable of withstanding. The standard load rate for compressive strength tests of concrete according to IS 516 is 14 MPa per minute for cubes and 12 MPa per minute for cylinders.

2.5.3.2 Stress-Strain Behavior for Cylinders

It describes how concrete responds to applied loads, illustrating its mechanical properties, such as elasticity, stiffness, strength, and failure mechanisms. Concrete, being a brittle material, exhibits distinct stress-strain characteristics under different loading conditions, particularly in compression, which is its primary mode of operation in structural applications. To assess the stress-strain behavior of concrete, cylindrical specimens are tested after 28 days of curing. The specimens are placed in a compression testing machine with strain gauges to measure load and deformation. A controlled load is applied until the specimen fails, while stress and strain are recorded. Initially, the behavior is elastic, followed by a nonlinear phase as microcracks form. The test continues until the concrete

reaches its peak strength and then fails. This data is used to plot the stress-strain curve. Fig. 3 shows the experimental setup for stress-strain behavior for cylinders.



Fig. 3. Setup for stress- strain behavior

2.5.4. Split Tensile Strength

It is conducted to evaluate the tensile strength of concrete, which is important since concrete is typically weak in tension. This test measures the concrete's ability to resist tension indirectly by subjecting it to compressive forces along its side, which causes tensile stresses to develop in the specimen, leading to its splitting along the vertical axis. The split tensile strength was performed on cylinder specimens with dimensions of 150 mm diameter with a length of 300mm, which was tested following 7, 14, 28, and 56 days of curing. The constant load rate for the split tensile strength of concrete, as per IS 5816:1999, is 1.2 to 2.4 MPa/min. For each specified curing duration and for each concrete mix, three cubes were cast. The cylinder is placed horizontally between the platens of a compression testing machine. Formula for calculating split tensile strength $((\pi/4)\ (d^2)\ (h))$. A compressive load(kN) is applied along the length of the cylinder at a constant rate. This load generates tensile stress across the vertical plane through the center of the cylinder, causing it to split vertically into two halves. Three specimens were tested for every mix, and the average of those results was taken.

2.5.5. Flexural Strength

It is used to determine the ability of concrete to resist bending or flexural stress. It is especially important for structural elements like beams and slabs, which are often subjected to bending in real-life applications. The test measures the tensile strength of concrete in bending and is commonly known as the modulus of rupture. Rectangular concrete beams, typically with dimensions of 150 mm × 150 mm × 500 mm, are cast and cured, usually for 28 days. The beams must be properly prepared to ensure uniformity and accurate results. The beam is placed on two supporting rollers, with a specified span length. A load is applied either at the midpoint. In a three-point test, the load is applied at the center of the beam, while in a four-point test, the load is applied at two points equidistant from the center. As the load is applied, the beam will experience tensile stress at the bottom and compressive stress at the top until it fractures. Three specimens were tested for every mix, and the average of those results was taken.

2.5.7. Water Absorption

It is used to determine the porosity of the material, which affects its durability and performance. High water absorption can lead to increased permeability, which can, in turn, lead to issues like reduced resistance to increased risk of corrosion in reinforcement. The

test measures how much water concrete absorbs over a specified period, giving an indication of the material's porosity and density. The saturation water absorption rate of concrete cubes measuring 150 mm × 150 mm × 150 mm was measured after 28 days of age of curing. The specimen initial weight is shown as W1 before to the specimen being completely submerged in water at room temperature for a certain amount of time, usually 24 hours or more. In order to eliminate any extra water that remains on the cube, the specimens are removed from the water after the submersion period and allowed to dry on the surface. Specimens are marked as W2 after surface drying.

2.5.8. Water Permeability

Concrete water permeability is crucial for its effectiveness and long-term sustainability in environments with high water exposure. The Fig. 5 shows concrete permeability setup. Factors such as compaction quality, water-to-cement ratio, pore size distribution, porosity, and curing conditions influence permeability. It is used to measures the ability of concrete to resist the penetration of water under pressure. This property is crucial for assessing the durability and longevity of concrete structures, as high permeability can lead to increased moisture ingress, which can cause issues like reinforcement corrosion and degradation of the concrete matrix. They are typically 150 mm × 150 mm × 150 mm cubes or 150 mm diameter × 300 mm cylinders. After being cured for 28 days in water at 20°C ± 2°C, the specimens are removed 24 hours before testing and stored in a controlled environment.

The test uses a permeability cell connected to a water source applying pressure between 0.5 MPa and 1 MPa. Specimens are dried at 105°C to a constant weight, cooled to room temperature, and placed in the cell. Water is then applied under pressure for 72 hours to assess permeability.



Fig. 5. Concrete permeability test setup

2.5.9. Acid Attack (H_2SO_4)

When assessing the resistance of concrete to sulfuric acid attack, a common method involves immersing 150 mm concrete cubes in a sulfuric acid solution after a standard curing period, typically 28 days. The solution used usually consists of a 4% concentration of sulfuric acid in water. This concentration is chosen to simulate realistic conditions of acid exposure that concrete structures may encounter in certain industrial or environmental settings. Over the course of the immersion period, which can extend up to 28 days, the concrete cubes are subjected to the corrosive effects of the sulfuric acid solution. They are two common forms of chemical deterioration that can significantly impact the durability and longevity of concrete structures. Acid attack occurs when

concrete is exposed to acidic environments, leading to the degradation of the concrete matrix. Acids can react with the calcium hydroxide ($Ca(OH)_2$) in the concrete, which is a key component of the cement paste, leading to its dissolution and weakening. Sulfate attack occurs when concrete is exposed to sulfate-rich environments, such as soils or groundwater with high sulfate content.

2.5.9. Sulfate Attack ($MgSO_4$)

After a 28-day curing period, 150mm cubes are submerged in a 5% magnesium sulphate solution as part of the magnesium sulphate assault on concrete. Sulfates react with the calcium aluminate phases in the cement paste, leading to the formation of expansive products that can cause cracking and deterioration. Samples cured in water for 28 days were then cured for 56 days in solutions containing 2% magnesium sulphate (MgSO4) and 5% sodium sulphate (Na2SO4). Samples are tested for a period of 90 days. Samples are weighted after being cured in MgSO4 and Na2SO4 solutions. Before conducting the compressive test, the samples are cleaned with tap water after curing and weighed. Three samples are tested for every mix, and the results are averaged.

2.5.10 Microstructural Analysis

Microstructural analysis of the fiber-reinforced concrete using coir and plastic fibers will involve examining the internal structure of the concrete at the microscopic level.

2.5.10.1 Scanning Electron Microscopy (SEM)

Scanning Electron Microscopy (SEM) was employed to examine the microstructure of fiber concrete, featuring images of the control mix and an optimized mix containing 1% each of coir and plastic fibers after twenty-eight days of curing, as depicted in Figs. 13 & 14. These SEM images illustrated the distribution, formation, and hydration products of the hydrated cement paste within the concrete. In contrast, the mix with fiber additions displayed abundant white crystals with tiny granular crystals on the surface, indicating enhanced concrete strength. The control concrete mix image of SEM revealed that the surfaces were laminated with voids and layers unhydrated products in the concrete. SEM analysis of powdered concrete end samples provides detailed insights into the material's microstructure and composition, facilitating observation of features such as aggregate distribution, porosity, hydration products, and potential defects or degradation mechanisms. This analytical process involves grinding concrete samples into a fine powder, mounting them onto SEM stubs, coating them with a conductive material, and placing them inside the SEM chamber. The focused electron beam interacts with the sample's atoms, generating signals used to produce high-resolution images revealing the morphology and composition of concrete components.

2.5.10.2 Energy Dispersive X- Ray (EDX)

The analytical method known as energy dispersive X-ray spectroscopy, or EDS, is crucial for determining the elemental composition of several scientific fields. When used in conjunction with scanning or transmission electron microscopy (TEM or SEM), it causes a sample to be bombarded with electrons, causing it to release distinctive X-rays that are specific to each element. Identified and measured elements are present in these X-rays, which are detected by sensors. Atomic-level qualitative and quantitative material analysis is made possible by EDX, which is widely used in many different sectors.

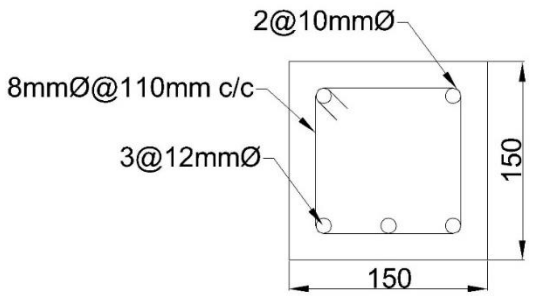
2.5.10.3 Fourier Transform infrared Spectroscopy (FTIR)

Fourier Transform Infrared Spectroscopy (FTIR) is a strong analytical technique that is widely applied in many different domains to examine the molecular makeup of materials. Through the evaluation of a substance's absorption of infrared light at different

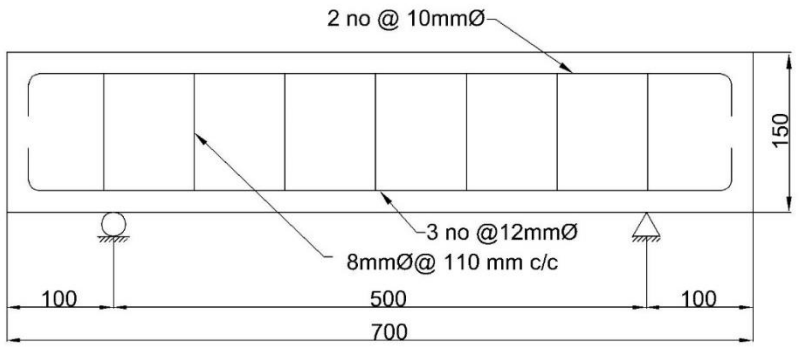
frequencies, Fourier transform infrared spectroscopy (FTIR) provides crucial information about the chemical bonds present in a sample. Defining the molecular structures is made easier by this absorption spectrum, which provides a thorough look at the functional groups that are present.

2.5.11. Flexural Behavior of Beams

Beam specimens are arranged in a simply supported condition by supporting one end by roller support and other end with hinge. Flexural test is conducted using UTM (universal Tensing Machine) with utilizing standard support conditions and standard test procedure (IS 9399: 1979). Specimens include a sample with nominal mix with steel reinforcement (B1-0), coir fiber (B2-1%C), 1% plastic fiber (B3-1%P), and a mixture of plastic and coir (B4-1%CP). In addition to these samples, a concrete beam without reinforcement (B5-1%CP) utilizing coir and plastic fibers is examined. Beam samples of dimension 700 x 150 x 150 mm are placed in water tank for 28 days for curing, and the beam is marked with a grid to visualize precise crack distance. Beam samples are arranged in a simply supported condition and gauges are fixed to measure flexural strength with proper loading arrangement is utilized to complete the investigation. Fig. 6 shows the reinforcement details provided for the RCC beam samples utilized in this research.



(a)



(b)

Fig. 6. Beam detailing

3. Results and Discussion

This section discusses the tests conducted for this research work. The detailed discussion is as follows:

3.1. Fresh Properties and Density of Concrete

Table 4 shows the fiber content of each concrete mix together with its workability and unit weight (UW). However, a superplasticizer dose of 0.5% was necessary for all combinations to achieve a design slump between 9 cm and 10.5 cm, which is important for efficiently pumping concrete. The fibers included in these new concrete mixes ranged widely, from artificial fiber like plastic to natural alternatives like coir. The range of fiber content levels to maintain a constant workability that was equivalent to the reference mix was 0.5% to 2.0%. The effectiveness of incorporating fibers into concrete formulations has been demonstrated by earlier studies, which also highlights the Fibers beneficial effects on performance.

The specimen's density was measured in accordance with code C-11249. The empty mould was first thoroughly oiled, then weighed, filled with concrete, and then weighed one more time. To calculate the wet density, the weight of the filled concrete (W_2) was subtracted from the weight of the empty weighed (W_1) mould and divided by the specimen volume (V_s). The density of concrete specimens (M1-0) is 2625.511 kg/m^3.

Table 4. Density of concrete specimens

Aspect ratio (17)	Coir Fiber				Plastic Fiber				Combined mix (coir +plastic)
	0.5%	1.0%	1.5%	2.0%	0.5%	1.0%	1.5%	2.0%	1.0%
Density (Kg/m^3)	2599	2573	2547	2520	2605	2586	2566	2547	2572
Slump (cm)	10.3	10.1	9.5	9.0	10.2	9.8	9.4	9.0	9.9

3.2. Compressive Strength

3.2.1 Compressive Strength for Cubes

The M-40 concrete underwent compressive strength testing for varying durations, following the IS Code guidelines. The mean compressive strength of concrete for each mix and each day of curing was obtained from the arithmetic average of the compressive strength obtained from twelve specimens fabricated for every specific mix, and three specimens were cast on each corresponding day of curing. We present concrete mixes with a superplasticizer of 0.5% to achieve the M-40 target mean strength after 28 days. Fig. 7 shows that, in comparison with fiber mixtures, conventional concrete has the highest compressive strength. The compressive strengths of conventional concrete for 7 days, 14 days, 28 days, and 56 days are 38.5 MPa, 40.88 MPa, 50.66 MPa, and 53.55 MPa, respectively. The compressive strength of the concrete specimens was observed with the use of two types of Fibers (coir and plastic) mixed differently. Almost all the fibers carried compression strengths very close to each other, which will lead to not reaching the target strength in 28 days. The 1% and 1.5% concentration mixes of compressive strength have not achieved a strength of 35 MPa. The compressive strength of 2% coir fiber mix will not reach 20 MPa. Comparing mixtures with different fiber percentages, we found that the compressive strength dropped as the fiber percentage increased. Conversely, though a rise in early-age strength was noted. In particular, the higher fiber concentration of coir fiber could prevent the fiber and cement mixture from properly bonding. The reduction in compressive strength seen with increased coir fiber percentages in concrete mixes can be caused by a number of factors, including weaker fibers, inefficient bonding with the cement matrix, in the introduction of voids, and workability difficulties. The compressive strength of the plastic fiber mixes is nearly the same for 7 days, 14 days, 28 days, and 56 days with

values of 0.5% plastic fiber mix are 32.66 MPa, 34.22 MPa, 38.66 MPa, and 42.22 MPa respectively. The combined mix of 1% both coir and plastic fibers is 31.33MPa, 34.66 MPa, 37.77 MPa, and 42 MPa respectively. Because of Plastic fibers in concrete fail to achieve the target mean strength while maintaining constant compressive strength across mix percentages and testing durations. This is due to factors in their composition and behavior within concrete matrices. While plastic fibers enhance concrete's ductility and toughness, their mechanical properties may not be optimized for achieving the desired target strength, potentially due to limitations in the plastic material's tensile strength.

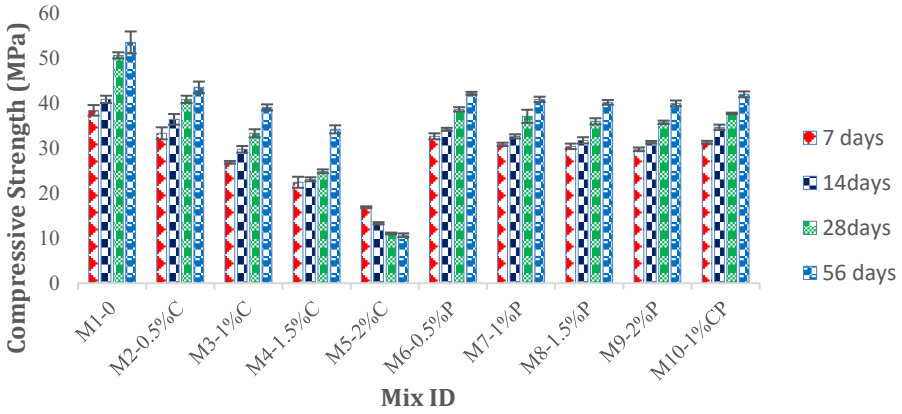
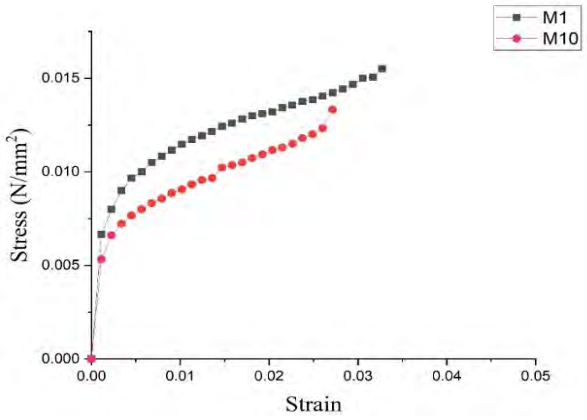


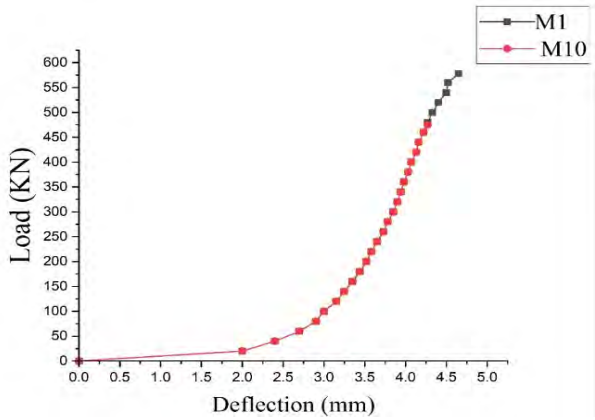
Fig. 7. Compression strength graph

3.2.2. Stress-Strain Behavior for Cylinder

The outcomes of the study, which was carried out over the course of 28 days on the nominal mix specimen and the optimized specimen (1% coir fiber and 1% plastic fibers). Fig. 8a presents the stress vs strain Load vs Deflection graphs for M1 & M10 providing comparative data. The stress-strain curve compares the performance of two concrete mixes, M1 and M10. M1 demonstrates higher stress values across the strain range compared to M10, indicating that M1 has greater strength and stiffness. The curve for M10, represented by red dots, is consistently lower than M1's, suggesting that M10 deforms more easily under the same load.



(a)



(b)

Fig. 8. Structural Behavior of M1 & M10 mixes

This could be due to different compositions or fiber additions in M10, which may reduce its load-bearing capacity and stiffness. The difference in curves highlights that M1 offers better mechanical properties under stress. Fig. 8b represents the load-deflection behaviour of two different materials, labelled M1 and M10. Both materials exhibit a non-linear relationship between load and deflection, indicating that they do not follow Hooke's law. The curve for M1 is steeper than that of M10, suggesting that M1 is stiffer and can withstand higher loads before reaching a certain deflection compared to M10.

3.3. Split Tensile Strength

Under code IS 5816, a split tensile strength test was performed for 7 days, 14 days, 28 days, and 56 days. The findings are shown in Fig. 9. The purpose of this test is to determine the tensile strength of concrete, which is critical for applications involving bending forces.

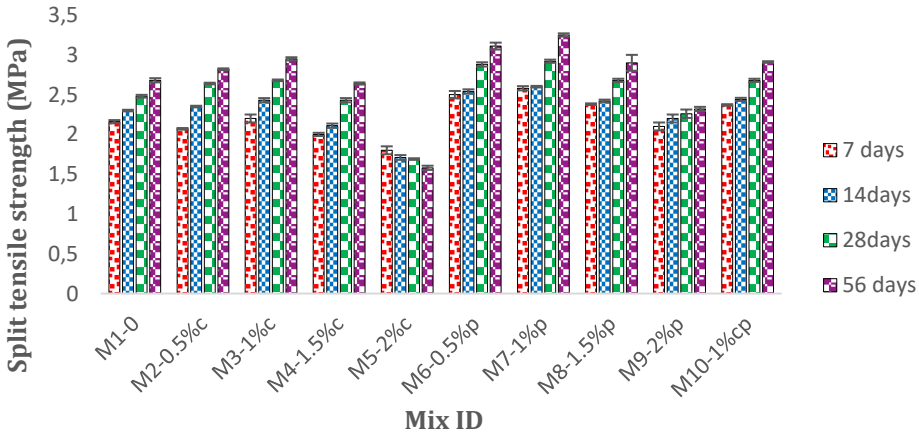


Fig. 9. Split tensile strength graph

It demonstrates how splitting plane tensile stresses can be applied to concrete while still maintaining its integrity, particularly in situations where higher durability is indicated by the tensile stresses. The split tensile strength of M3-1%C of the coir fiber used specimen is 2.95 MPa higher than the nominal mix of M1-0 split tensile strength of 2.68 MPa for the 56-day natural age curing period. The split tensile strength of M7-1%P of the plastic fiber specimen is increased to 3.25 MPa, M6-0.5%P is 3.11 MPa, and M8-1.5%P is 2.9 MPa when compared to nominal mix and coir fiber percentages. The split tensile strength of plastic fiber percentages of 0.5%, 1.0%, and 1.5% will increase while the age of curing will increase the strength is also increasing. The combined mix of both coir and plastic 1% is 2.91 MPa. The plastic fiber mixes strength will increase because ~~of~~ the plastic fiber made of synthetic polymers like polyester and polypropylene are used to create strong, durable plastic fibers. Their homogenous structure enhances tensile strength and provides excellent resilience to environmental deterioration, ensuring extended durability over time. Coir fibers, derived from coconut husk, are a natural substitute for artificial materials but may not match their tensile strength due to natural oscillations in the fiber structure. They also pose challenges for certain processing and treatment techniques and may deteriorate over time due to exposure to moisture, making them less durable.

3.4. Flexural Strength

The results of the Flexural strength tests performed on the concrete specimens are shown in the Fig. 10. Flexural strength findings for all types of fiber mixtures show good results when compared to the nominal mix and comparing the results between coir fiber and plastic fiber. The flexural strength of M3-1%C of the coir fiber used in the specimen is 7.95 MPa higher than the nominal mix of M1-0. The flexural strength was 6.21 MPa for the 56-day natural age curing period. The split tensile strength of M7-1%P of the plastic fiber specimen is increased to 9.48 MPa, M6-0.5%P is 9.16 MPa, M8-1.5%P is 8.94 MPa, and M9-1.5%P is 8.56 MPa when compared to nominal mix and coir fiber percentages. The flexural strength of plastic fiber percentages of 0.5% to 2% will increase while the age of curing will increase. The combined mix of both coir and plastic 1% is 7.58 MPa. The flexural strength got increased because plastic fibers are strong and durable due to their uniform structure and resistance to environmental deterioration. In contrast, coir fibers obtained from coconut husks have inherent structural differences and are less resistant to moisture, resulting in reduced tensile strength and durability.

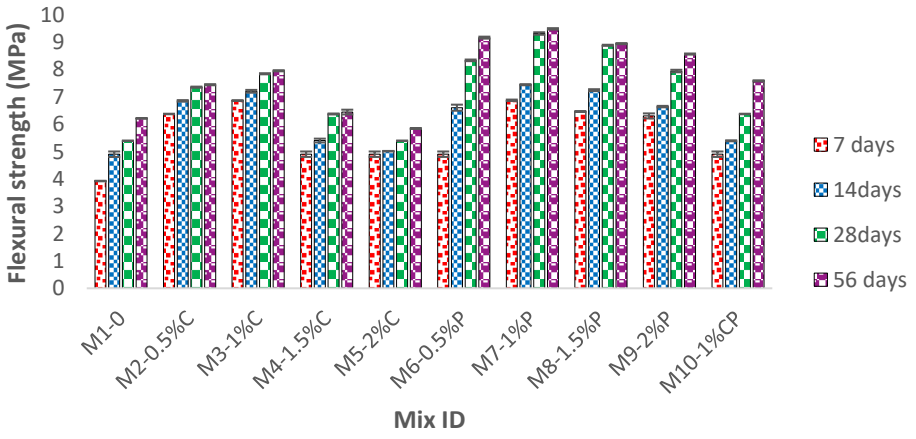


Fig. 10. Flexural strength graph

3.6 Durability properties

For this experiment on fiber-reinforced concrete using coir and plastic fibers, assessing the durability properties of the concrete is crucial. The following durability properties will be evaluated:

3.6.1 Water Absorption

One of the most important factors influencing concrete long-term performance and durability is water absorption. Concrete absorbs water via pore structure and capillary action; the amount of absorption is determined by several parameters such as ingredient quality, porosity, curing conditions, and mix design. Because of variations in moisture content, high water absorption can shorten lifespan, raise the danger of corrosion, and alter dimensions. Effective curing and mix design are two strategies to reduce water absorption. The long-term performance and structural integrity of concrete depend on the efficient regulation of water absorption. The test results of water absorption in every combination are shown in the Fig. 11. The water absorption percentages for various concrete mixes with different compositions of coir fiber ("C") and plastic fiber ("P") at 28 and 56 days of curing. Overall, most mixes show an increase in water absorption from 28 to 56 days, indicating that permeability may rise over time, possibly due to changes in the concrete's microstructure or fiber interactions. The M1-0, likely a control with no added fibers, has relatively low water absorption at both ages, suggesting a denser and less permeable matrix. In contrast, mixes containing coir fiber the percentage of coir fiber is adding to concrete it exhibit higher water absorption, especially at 56 days, indicating that increasing coir fiber content could lead to higher porosity, allowing more water ingress over time. This could be due to the natural characteristics of coir fiber, which may create additional voids or pathways in the concrete matrix.

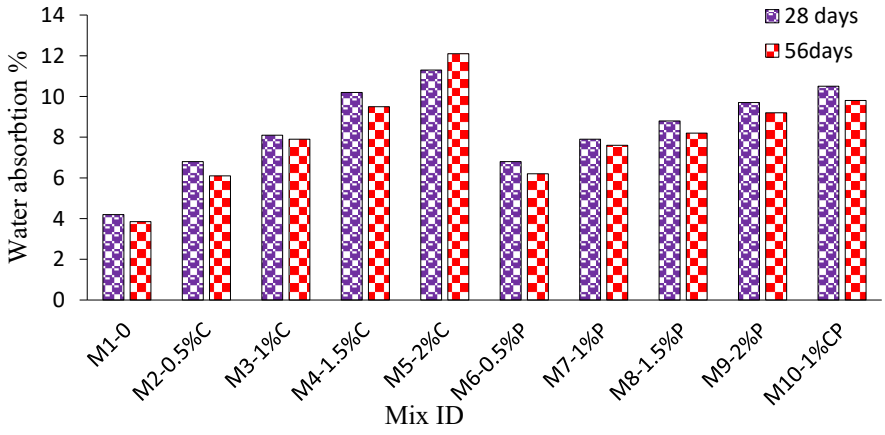


Fig. 11. Water absorption with respect to design mixes

On the other hand, mixes that include plastic fiber alone or in combination with coir fiber, like M6-0.5%P to M10-1%C&P, generally display lower water absorption. This suggests that plastic fiber may help reduce permeability, possibly by reinforcing the matrix or filling voids more effectively. The effect is particularly evident in mixes with lower coir and balanced plastic fiber content, where water absorption remains lower, even at 56 days. This observation indicates that plastic fiber might enhance durability by reducing the concrete's porosity and resistance to water absorption. For the applications where low water absorption and durability are critical, mixes with reduced coir fiber content or a combination of plastic and coir fibers appear beneficial. These compositions exhibit

improved resistance to water ingress, potentially reducing issues related to chemical attack, and steel corrosion over the structure's lifespan.

3.6.2. Water Permeability

The graph shows the water penetration depth for various concrete mixes, each containing different proportions of coir fiber ("C") and plastic fiber ("P"). This measurement reflects the concrete's resistance to water ingress, with lower penetration depths indicating better water resistance and durability. Significant variation in penetration depth across the mixes reveals that the type and proportion of fibers greatly influence permeability. Mixes with higher amounts of coir fiber, such as M5-2%C, exhibit the deepest water penetration (around 100 mm), suggesting that higher coir content increases porosity, allowing more water to penetrate and potentially reducing durability. In contrast, mixes containing plastic fiber, like M6-0.5%P and M7-1%P, display notably lower penetration depths, with M6-0.5%P having a penetration depth below 40 mm. This indicates that plastic fibers help to reduce permeability, likely by filling voids and creating a denser matrix that hinders water movement.

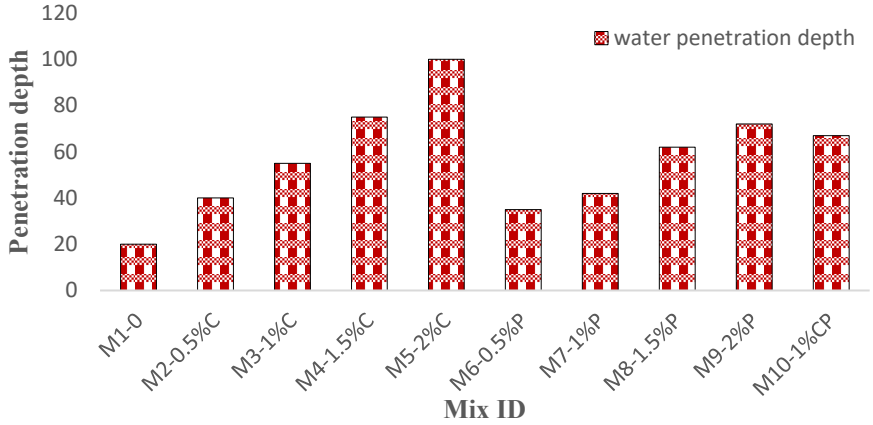


Fig. 12. Water penetration depth for design mixes

Table 5. Concrete permeability

Mix ID's	Permeability Coefficient, K (m/s)
M1-0	3.108×10^{-12}
M2-0.5%C	1.243×10^{-11}
M3-1%C	2.351×10^{-11}
M4-1.5%C	4.371×10^{-11}
M5-2%C	7.772×10^{-11}
M6-0.5%P	9.520×10^{-12}
M7-1%P	1.370×10^{-11}
M8-1.5%P	2.987×10^{-11}
M9-2%P	4.029×10^{-11}
M10-1%CP	3.488×10^{-11}

Mixes that combine both coir and plastic fibers, such as M10-1%C&P, show intermediate penetration depths, suggesting that plastic fibers can offset the increased permeability associated with coir fiber to some extent. Overall, the control mix M1-0, which likely contains no fibers, has one of the lowest penetration depths, showing that a standard

concrete matrix may have better water resistance than those with high coir content. In terms of durability, mixes with lower penetration depths particularly those with plastic fiber or balanced fiber content—are preferable, as they are more resistant to moisture-related damage, including reinforcement corrosion and freeze-thaw cycles. For applications needing high durability, mixes with plastic fiber alone or a lower proportion of coir fiber are recommended due to their reduced water permeability. The permeability coefficient is shown in Table 5, calculated using Darcy's law, provides valuable insights into concrete quality and suitability for various applications. Fig. 12 presents graph for water penetration depths for different mixes.

3.6.3. Acid Attack (H_2SO_4)

This exposure allows researchers and engineers to evaluate the performance of the concrete under conditions of chemical attack, assessing factors such as degradation, mass loss, surface roughness, and changes in mechanical properties. When curing concrete in acidic conditions, compressive strength and density decrease, particularly noticeable in exposed aggregates prone to acid corrosion. Immersing concrete cubes in acid solutions significantly reduces their compressive strength compared to standard curing. Acid attacks intensify with higher cement proportions, targeting hydrated lime and weakening the bond between cementitious aggregates, leading to mass loss and decreased durability.

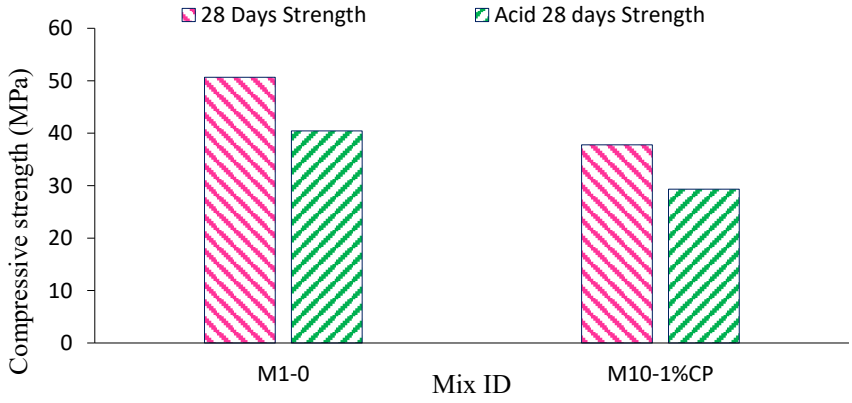


Fig. 13. Compressive strength graph for Acid attack (H_2SO_4)

Fig. 13 illustrates the graph of compressive strength for sulfuric attack of two concrete mixes, M1-0 and M10-1%CP, under different conditions at 28 days. The M1-0 mix serves as the reference mix, while M10-1%CP includes a 1% addition of coir-plastic (CP) fibers. The results reveal that the M1-0 mix achieves a higher compressive strength compared to M10-1%CP under standard conditions, suggesting that the addition of 1% CP fibers slightly reduces compressive strength. This reduction might indicate that, at a low content level, CP fibers do not significantly contribute to compressive strength. Both mixes exhibit a decrease in compressive strength after exposure to acid, which aligns with expectations, as acid exposure generally weakens concrete. Interestingly, the relative reduction in strength due to acid exposure is similar between the two mixes, implying that the inclusion of CP fibers does not notably enhance acid resistance at this 1% level.

3.6.4 Sulfate Attack ($MgSO_4$)

Researchers can assess deterioration, mass loss, surface roughness, and mechanical property changes in concrete thanks to this corrosive action. Comprehending the influence of magnesium sulphate on the longevity of concrete is essential for enhancing mix designs,

choosing suitable building materials, and putting preventive measures in place against degradation. In sulfate-rich settings, this aids in the development of strong infrastructure solutions for long-term performance and safety. Sulphates react with the calcium-silicate-hydrate gel in concrete, causing the gel to disintegrate and impair the cohesiveness of the material. Ettringite crystals are produced throughout this procedure. and push on the paste, producing fissures and affecting structural integrity. Concrete loses strength due to major changes in its chemical and physical characteristics. Following exposure to the magnesium sulfate solution, all of the concrete sample displayed deterioration.

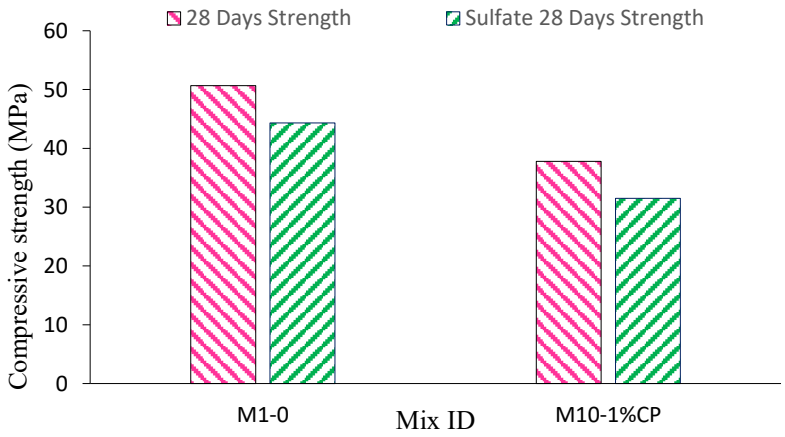


Fig. 14. Compressive strength graph for Sulfate attack ($MgSO_4$)

Fig. 14 displays the presents graph of compressive strength for sulfate attack ($MgSO_4$) of two concrete mixes, M1-0 and M10-1%CP, at 28 days under standard conditions and after sulfate exposure. M1-0, the reference mix, shows higher compressive strength compared to M10-1%CP under both conditions, indicating that adding 1% coir-plastic (CP) fibers slightly reduces compressive strength. Both mixes experience a drop in strength after sulfate exposure, as expected due to sulfate's corrosive effects on concrete. However, the reduction in strength is similar in both mixes, suggesting that 1% CP fiber content does not significantly enhance sulfate resistance. Thus, optimizing fiber content or other mix adjustments may be necessary to improve durability against sulfate exposure.

3.7. Microstructural Analysis

Microstructural analysis of the fiber-reinforced concrete using coir and plastic fibers will involve examining the internal structure of the concrete at the microscopic level. This analysis helps to understand the interaction between the fibers and the cement matrix, the distribution and orientation of the fibers, and the overall impact on the concrete's mechanical properties. The following techniques will be employed:

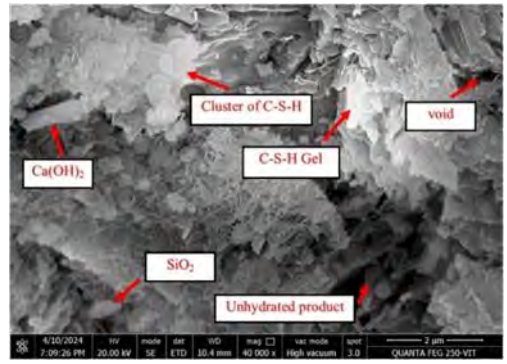
3.7.1. Scanning Electron Microscopy (SEM)

The SEM image reveals the microstructure of concrete, showcasing key components like C-S-H gel, Ca $(OH)_2$, and unreacted silica. The dense C-S-H gel indicates good hydration and potential strength. However, the presence of voids and unreacted materials might impact the concrete's long-term durability and permeability. Further analysis is needed to fully assess the material's properties. At this high magnification, we can observe individual particles and their interconnections. Fig. 15 and 16 shown the SEM images of the normal mix (M1) show a dense microstructure with some porosity at high magnifications, indicating good strength and durability, though the porosity may affect permeability and

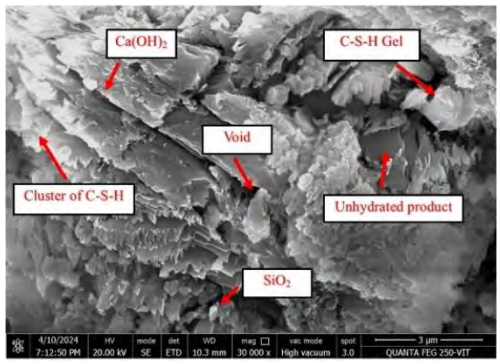
degradation resistance. Particle distribution is generally uniform, but some agglomeration could impact homogeneity and mechanical properties.



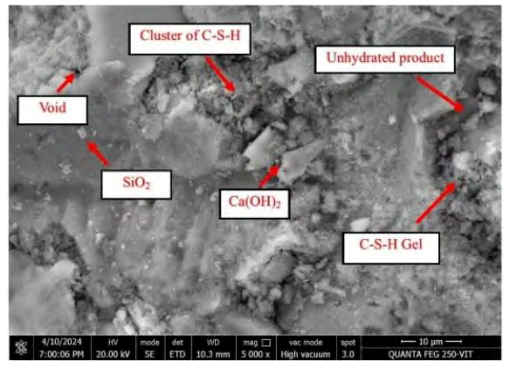
(a) SEM image at 20 kv, 60000 x



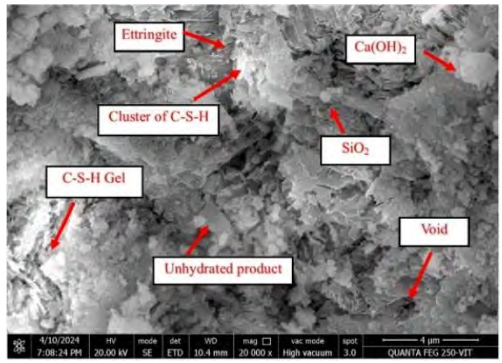
(b) SEM image at 20 kv, 40000 x



(c) SEM image at 20 kv, 30000 x



(d) SEM image at 20 kv, 5000 x

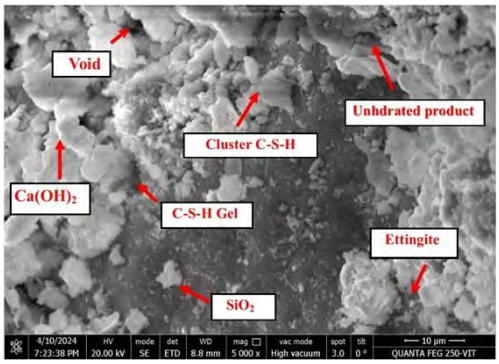


(e) SEM image at 20 kv, 20000 x

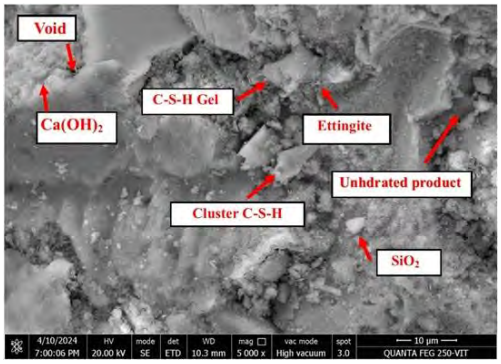
Fig. 15. SEM image for normal mix (M1)

Larger pores observed at lower magnifications may influence strength and durability under cyclic or harsh conditions. Overall, the mix has a relatively uniform particle arrangement with interlocked particles, suggesting strong mechanical properties. Further analysis and comparisons with other mixes would help assess the material's performance in specific applications. For the concrete samples M1 and M10 SEM analysis was carried

out. In the analysis process, it is observed C-S-H Gel was arranged in cluster which shows interfacial transition zone for these two mixes are strong which concludes this sample shows good strength.



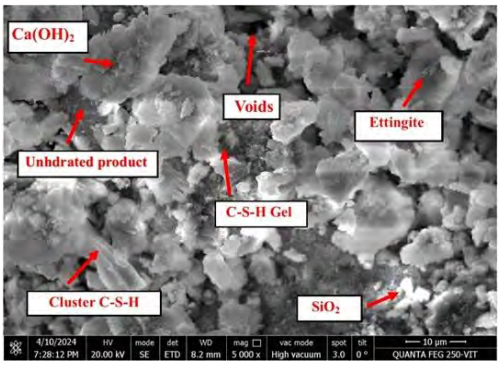
(a) SEM image at 20 kv, 5000 x



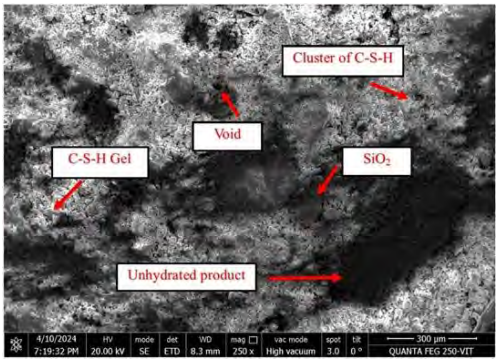
(b) SEM image at 20 kv, 5000 x



(c) SEM image at 20 kv, 10000 x



(d) SEM image at 20 kv, 5000 x



(e) SEM image at 20 kv, 250 x

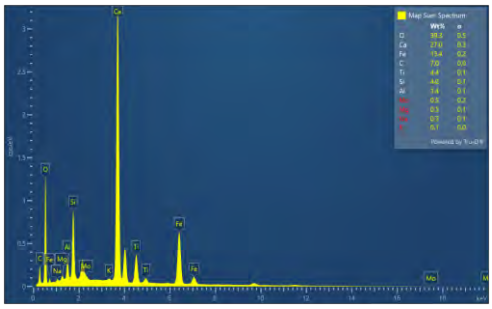
Fig. 16. SEM image for optimized mix (M10)

3.7.2. Energy Dispersive X-Ray (EDX)

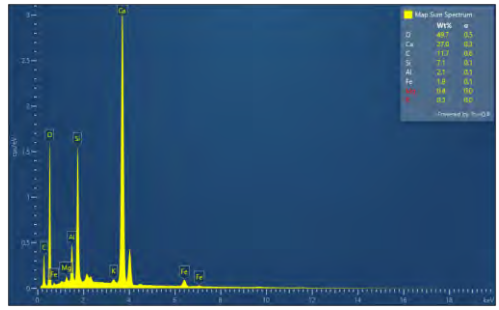
Microstructure analysis of EDX is shown in the below Fig. 17 a & b. The presence of calcium, aluminum, silicon, carbon, and oxygen was found using EDS analysis in the research of fiber concrete. The EDS analysis of fiber-reinforced concrete reveals key elements such as calcium, aluminium, silicon, carbon, and oxygen, which are integral to the material's composition and its interaction with reinforcing fibers. Calcium (Ca) is a major component

of cement and forms calcium silicate hydrates (C-S-H), which provide the primary binding strength. Aluminium (Al) contributes to the formation of calcium aluminate hydrates (C-A-H), improving early strength and durability. Silicon (Si) combines with calcium to form C-S-H, further strengthening the concrete. Carbon (C) is present from reinforcing carbon fibers or carbon-based additives, while oxygen (O) plays a vital role in the hydration process and the formation of C-S-H.

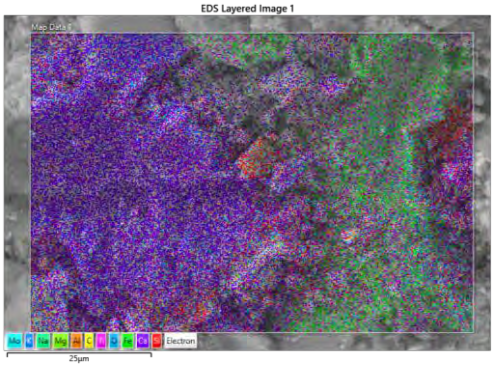
The detection of these elements through EDS confirms the presence of the typical concrete constituents and their interaction with fibers, particularly highlighting the incorporation of carbon fibers into the matrix. To optimize the performance of fiber-reinforced concrete, further research should focus on the distribution and orientation of fibers, the fiber-matrix interface, and the microstructural analysis. These factors influence load transfer, mechanical properties, and durability, which are crucial for achieving improved strength, ductility, and overall performance. Fig. 17 c and d shows EDS covered image for M1 and M10 mixes. In order to offer comprehensive insights into material composition and support microstructural investigation and quality evaluation, this technique combines electron microscopy with X-ray analysis. When combined with microstructural characteristics, the resulting "EDS layered image" helps to facilitate spatial comprehension and association with elemental composition. Electron images are shown in Fig. 17 e and f



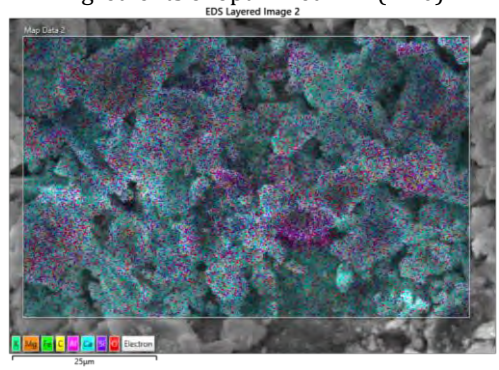
(a) EDX image showcasing properties of ingredients of nominal mix (M1)



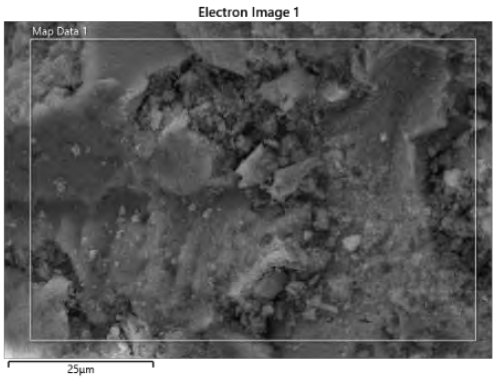
(b) EDX image showcasing properties of ingredients of optimized mix (M10)



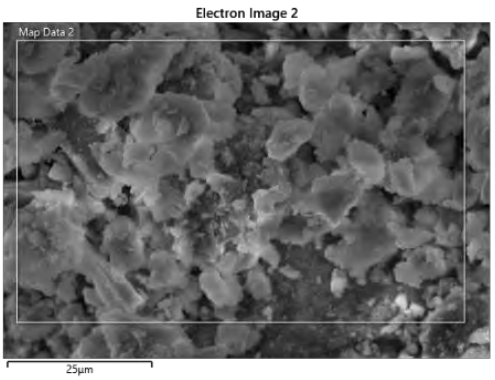
(c) EDS image at 25microns for nominal mix (M1)



(d) EDS image at 25microns for optimized mix (M10)



(e) Electron image at 25 microns for nominal mix (M1)



(f) 20 Electron image at 25 microns for optimized mix(M10)

Fig. 17. EDX, EDS & Electron images for nominal mix (M1) and optimized mix(M10)

3.7.3. Fourier Transform infrared Spectroscopy (FTIR)

The FTIR spectra of different concrete mixes with varying percentages of carbon fiber (C) and polypropylene fiber (P) reveal key insights into the chemical composition and molecular structure of the materials. The spectra show a general trend of increasing transmittance with rising wavenumbers, typical for concrete materials. The addition of carbon and polypropylene fibers has minimal impact on the overall spectral features, though slight variations in peak intensities and positions suggest potential changes in fiber distribution, fiber-matrix interface, and concrete microstructure.

These FTIR results indicate that the fibers do not significantly alter the fundamental chemical composition of the concrete, but their presence might influence the microstructure and bonding mechanisms, as seen in the variations of peak intensities. Further analysis, such as quantitative peak intensity measurements, and correlation with mechanical properties, would provide a clearer understanding of how fiber addition affects the concrete's performance. Combining FTIR with techniques like SEM and EDS can offer a more comprehensive view of the material's structure and properties.

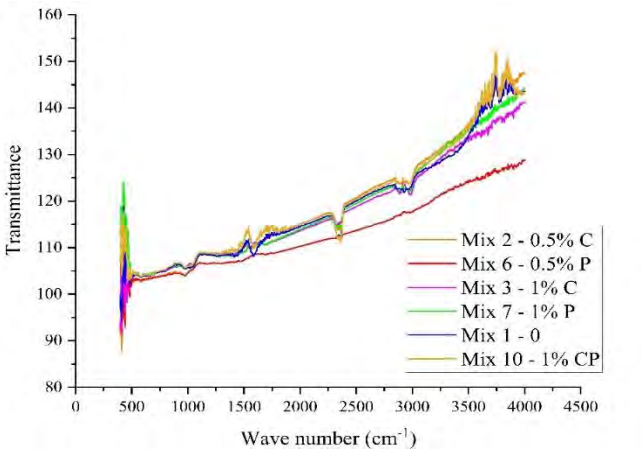


Fig. 18. FTIR analysis graphs for all concrete mixes

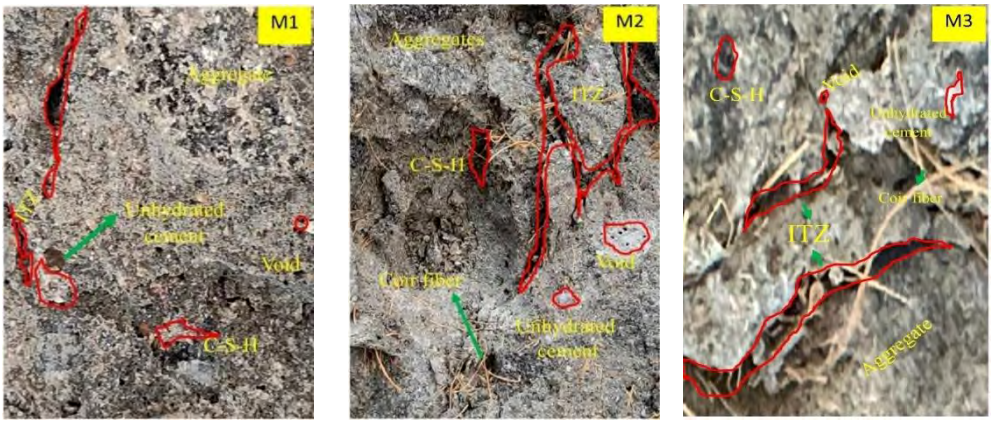
It is applicable in a wide range of fields, including chemistry, materials science, pharmacology, and forensic investigation. It supports both qualitative and quantitative examinations of both organic and inorganic compounds. FTIR is a mainstay in analytical chemistry and materials research because of its reputation for sensitivity, rapidity, and non-destructiveness. Microstructure analysis of FTIR is shown in the below Fig. 18

3.7.4. Interfacial Transition Zone

Interfacial Transition Zones (ITZs), aggregates, cement matrix, COIR fiber, and plastic fiber constitute fiber-reinforced composite (FRC), a non-homogeneous material with four distinct phases. The mechanical properties of this material on a macroscopic scale are intricately linked to its microstructure. Consequently, a thorough investigation into the microstructures of the cement paste-aggregate and cement paste-steel fiber ITZs is imperative. To facilitate this investigation, ten samples were meticulously prepared for microscopic imaging tests, designated as M1 (Nominal Mix), M2 (0.5%C), M3 (1.0%C), M4 (1.5%C), M5 (2%C), M6 (0.5%P), M7(1%P), M8 (1.5%P), M9(2%P), AND M10 (1%CP). The manufacturing process of these using microscopic samples is clarified in Fig. 17, all samples were meticulously crafted prior to any loading, ensuring that the test results accurately portray the initial morphology of the interfacial transition zone.

3.7.4.1. ITZ at fiber-cement paste and aggregate-cement paste

The study examines the microstructure of the Interfacial Transition Zones (ITZ) between the aggregate and cement paste in M1. The ITZ between the fiber and mortar matrix in specimens M2 to M5. The matrix is firmly bonded to the coir and plastic fiber, and the cement composite around the fibers is sufficiently hydrated. Dense ITZs and harmful crystals are observed on the fiber surface, but a small amount of microcracks exist in the transition zone. In specimens M6 to M10, the fiber surface is covered with a small number of harmful crystals, and the fibers are smoother with fewer cracks. The ITZ thickness of the fibers and mortar matrix is small, and the content of fibers has a small effect on ITZs. A distinct interfacial transition zone is generated between the fiber and matrix, resulting in a compact interfacial transition zone around the fiber in Fig. 19. The microstructural image of the all-concrete mix, which incorporates coir fiber, reveals several important features that contribute to the properties of the composite. Aggregates are visible within the matrix, providing bulk and contributing to the mix's mechanical strength, while the calcium-silicate-hydrate (C-S-H) phase, crucial for binding, can be seen surrounding these aggregates. Coir fibers, embedded within the mix, play a significant role in enhancing toughness by bridging microcracks and helping to reduce stress concentrations. The Interfacial Transition Zone (ITZ), situated between the aggregates and the cement paste, appears to be less porous in this fiber-reinforced mix.



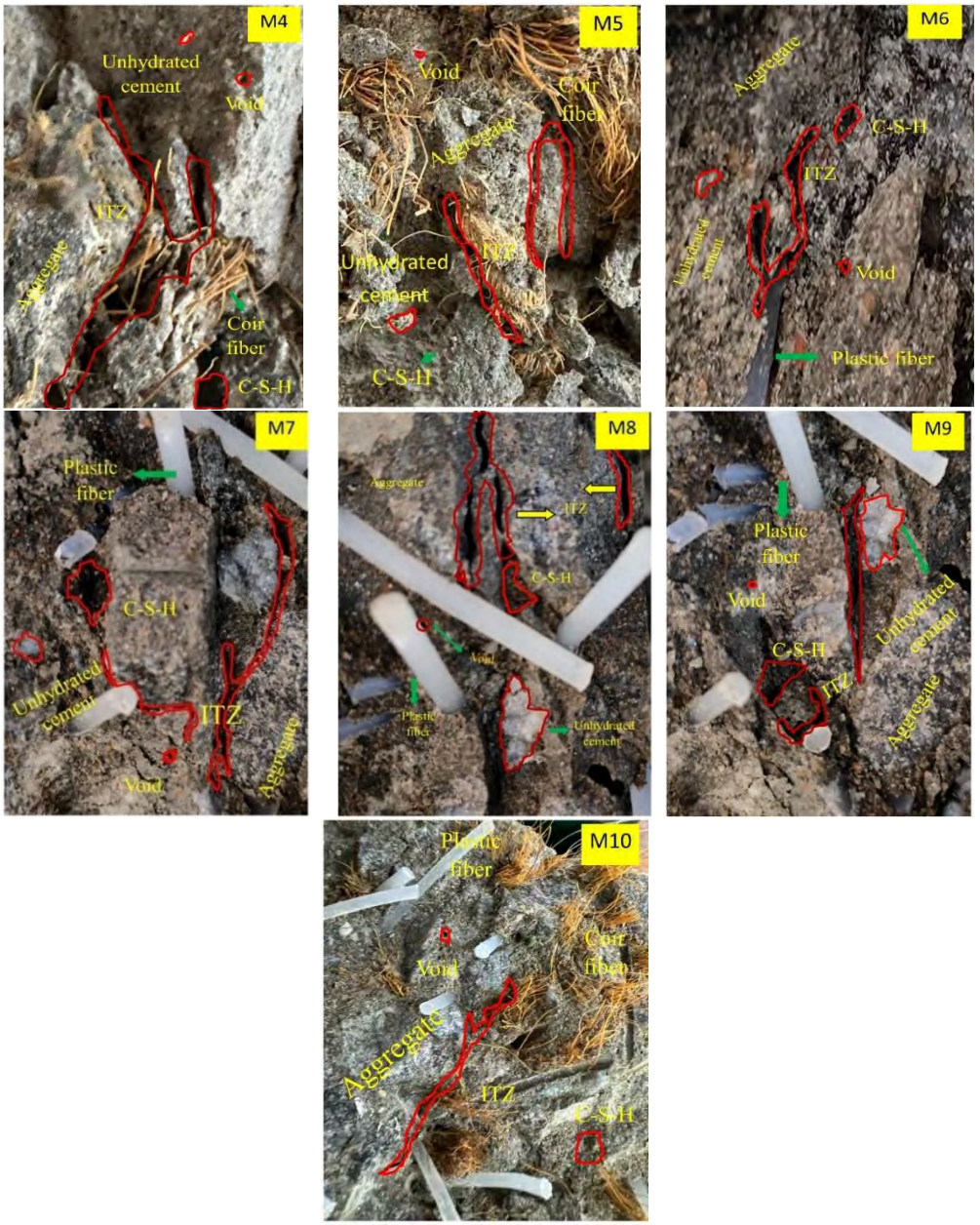


Fig. 19. ITZ images for different mixes

The addition of coir fibers seems to improve the ITZ quality, likely by minimizing voids and reducing microcracking around the aggregate-matrix interface, resulting in stronger bonding. However, some unhydrated cement particles are still present, indicating incomplete hydration, which could be due to limited water or mixing conditions and might slightly impact the concrete's strength. Although voids are present, the distribution appears more controlled due to the coir fibers, which help reduce crack propagation.

3.8. Flexural Behavior of Beams

From Fig. 20a presents the experimental configuration for flexural strength test and observed crack pattern of B1-0. In Fig. 20b support conditions are clearly shown for B2-1%C with observed crack patterns. Fig. 20c depicts the crack patterns observed on the B3-1%P with support condition. In Fig. 20d crack patterns of B4-1%CP is shown. For B5-1%CP, Fig. 20e shows the observed crack pattern. From the above Fig. 20, It has been noted that the crack patterns vary for reinforced and non-reinforced samples.



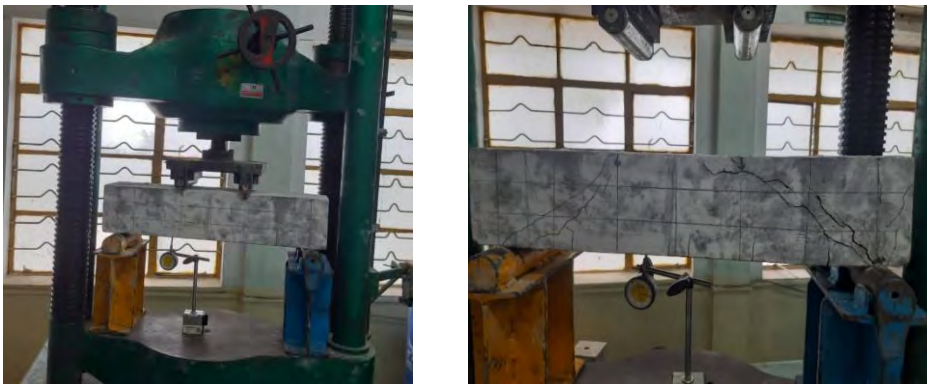

(a) Beam setup for B1-0




(b) Beam setup for B2-1%C




(c) Beam setup for B3-1%P



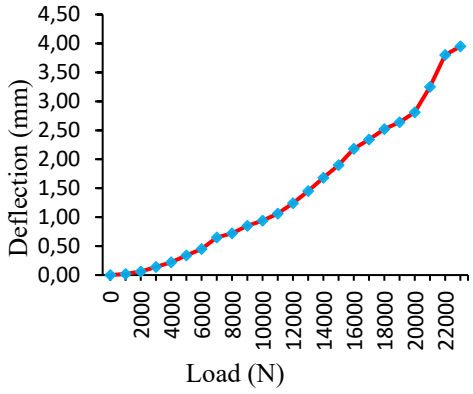
(d) Beam setup for B4-1%CP



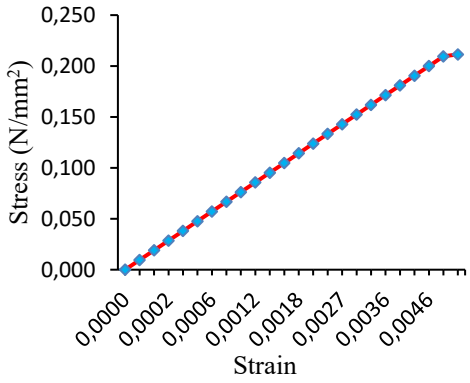
(e) Beam setup for B5-1%CP

Fig. 20. Experimental setup and crack patterns for Beams (B1, B2, B3, B4, and B5 mixes)

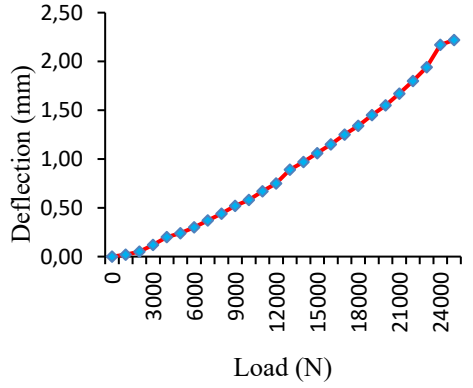
In reinforced and non-reinforced concrete beams, crack behaviour differs significantly due to the presence of reinforcement. In non-reinforced beams, cracks initiate at stress concentration points, such as corners or edges, and propagate rapidly along paths of least resistance, resulting in an irregular and unpredictable crack pattern. This often leads to an abrupt, brittle failure due to the uncontrolled crack progression. In the reinforced beams exhibit more controlled crack initiation, with the reinforcement restraining crack width and propagation. Consequently, the cracks in reinforced beams are finer, more evenly spaced, and aligned with the reinforcement direction, contributing to a more predictable crack pattern. This controlled cracking and gradual failure mode provide the beam with a ductile failure mechanism, allowing for greater deformation and warning before ultimate failure. Factors such as material properties, loading conditions, and reinforcement details impact crack patterns. For instance, overloading, design deficiencies, or environmental degradation can lead to cracking in reinforced beams, but these cracks are typically limited by the reinforcement, which provides additional load-carrying capacity. Observing crack patterns, especially in the tension zone where the cracks concentrate, and inspecting the exposure of reinforcement can reveal essential information about structural health. Therefore, understanding and monitoring crack behaviour are critical for designing durable structures, conducting inspections, and performing maintenance to ensure long-term structural serviceability.



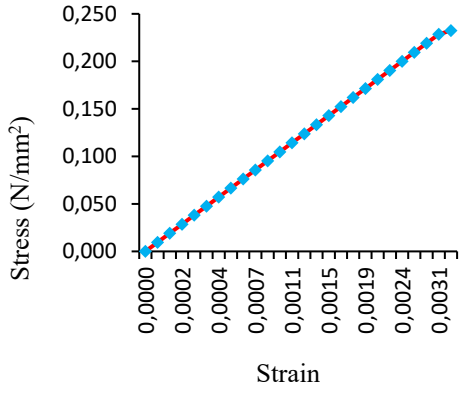
(a) load vs deflection graph for B1-0



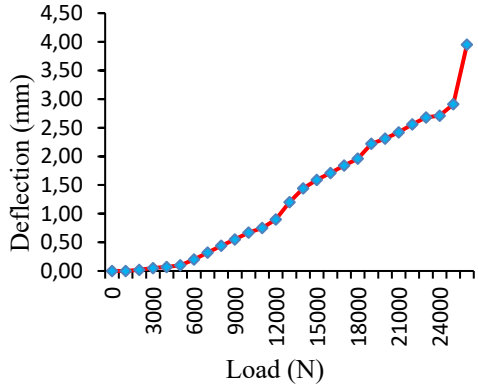
(f) stress vs strain graph for B1-0



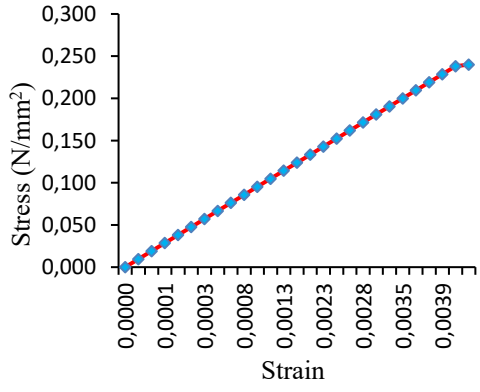
(b) load vs deflection graph for B2-1%C



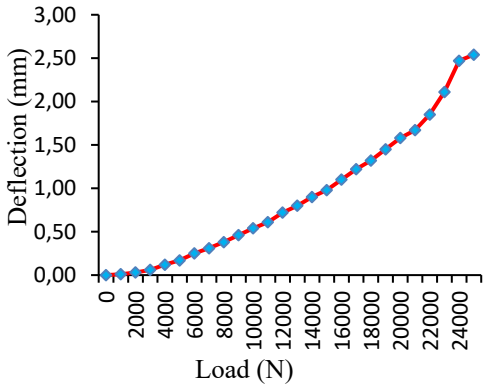
(g) stress vs strain graph for B2-1%C



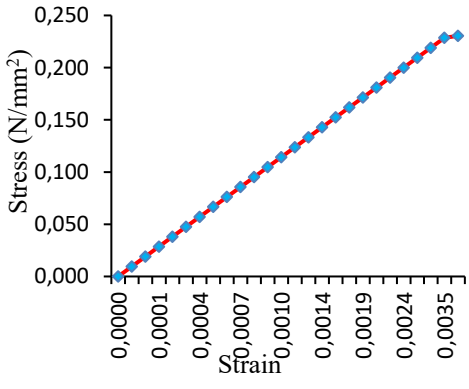
(c) load vs deflection graph for B3-1%P



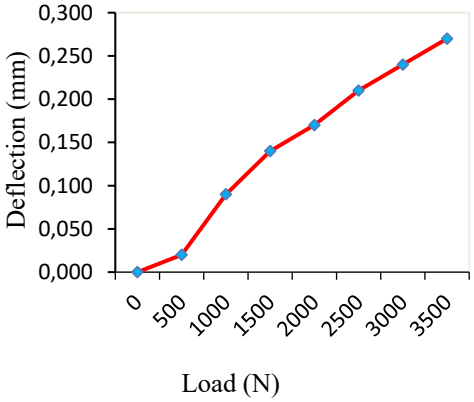
(h) stress vs strain graph for B3-1%P



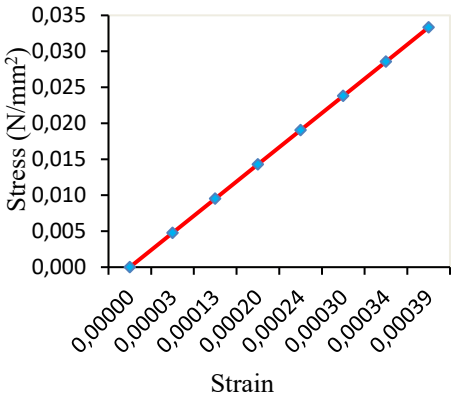
(d) load vs deflection graph for B4-1%CP



(i) stress vs strain graph for B4-1%CP



(e) load vs deflection graph for B5-1%CP



(j) stress vs strain graph for B5-1%CP

Fig. 21. Load table vs Deflection and Stress vs Strain graphs

Fig. 21 shows the load vs deflection and Stress vs Strain graphs; it represents the flexural strength of B1-0 of 3.288 MPa for 28 days of natural curing. The flexural strength of B2-1%C is 3.61 MPa, B3-1%P is 3.73 MPa, B4-1%CP is 3.58 MPa, and B5-1%CP is 0.6 MPa. The above sentence state that B1, B2, B3, and B4 are cast with reinforcement, and B5 beams are cast with reinforcement-free. While comparing each mix, the plastic fibers added to concrete is higher than coir, and coir is superior to the nominal mix. The comparison of B5 and B1 to reduce the 84.22% of steel was reduced. Optimized mix of B4 also gives better strength than nominal mix. While adding fibers to the concrete, the compressive strength of the concrete was reduced compared to the nominal mix. Comparing mixtures with different fiber percentages, we found that the compressive strength dropped as the fiber percentage increased.

4. Conclusion

This study examined the consequences of coir and plastic fibers the mechanical characteristics, durability properties, microstructural study, and structural applications of Fiber reinforced concrete by evaluating experimental results. From the results got, the following conclusions are as follow.

- While adding fibers to the concrete, the compressive strength of the concrete ~~was~~ reduced in fiber mix of M2-0.5%C and M6-0.5%P by 25.9% at 28 days and 29.96% at 56 days age of curing, the strength decreases when compared to the nominal mix of M1-0. The strength decreases in fiber mix of M2-0.5%C and M6-0.5%P 34.12% at 28 days, and 27.5% at 56 days age of curing compared to the nominal mix of M1-0 Comparing mixtures with different fiber percentages, we found that the compressive strength dropped as the fiber percentage increased. Conversely, however, a rise in early-age strength was noted. In particular, the higher fiber concentration fiber and cement mixture has improperly bonding. It caused by a number of factors, including weaker fibers, inefficient bonding with the cement matrix, the introduction of voids, and workability difficulties. when compare to individual fiber mixes optimized mix strength are better.
- The split tensile strength was increased in the concentration of 1% mixes of both coir and plastic fibers when compared to the nominal mix. The coir fiber mixes of M3-1%C of 8% at 28 days and 10% at 56 days of curing, the strength will increase than normal mix M1-0. For the plastic fibers of M7-1%P was 17.7% at 28 days and 21.2% at 56 days will increase the strength than normal mix. When compared to coir fiber and plastic fiber, the plastic fiber strength increases of M7-1%P by 9%.
- Flexural strength was increased in the concentration of 1% mixes of both coir and plastic fibers when compared to the nominal mix. The coir fiber mixes of M3-1%C of 45% at 28 days and 28% at 56 days of curing, the strength will increase than normal mix M1-0. For the plastic fibers of M7-1%P was 72% at 28 days and 52% at 56 days will increase the strength than normal mix. In the comparison between fibers the concentrations of plastic fiber will give better strength than coir fiber concentrations. The strength increases of plastic fiber of M7-1%P by 30%, because the plastic fiber has strong and durable in nature due their uniform texture and it has flexible in nature than coir fiber.
- The optimized concentration of M10-1%CP the strength increased by 20% than normal mix M1-0. The optimizes mix will give good mechanical performance by effectively strengthening the link between fiber to fiber it has meshing the components with concrete. It provides a stronger tensile bond than nominal mix.
- The SEM analysis shows the coir and plastic fiber with porous structure and it bonded strongly with the concrete matrix. It resulting the better mechanical characteristics.
- The EDS shows the optimizes mix had a lower Calcium/Silicon (Ca/Si) and Sodium/Titanium (Na/Ti) than nominal mixture, indicating the higher mechanical strength results good C-S-H gel formation. EDX investigation revealed the properties in concrete.
- The results of FTIR indicated that the good molecular structure and it indicates the carbonation bonding in fiber reinforced concrete, it enhancing the strength characterizes of mixes.
- The ITZ shows the effectiveness of concrete concentration the surface layer laminated with voids, week hydration products as C-S-H.
- The fiber reinforced concrete beams give good flexural strength compared to nominal mix.
- The study highlights the potential of using waste fibers into the concrete mixes to promote sustainability goals, while considering specific applications requirements.

The study's conclusions suggest that adding of 1% of coir and plastic fibers enhances the mechanical performance of concrete. These investigation shows that the concrete reinforced with fibers is promising for creating sustainable concrete structures.

5. Acknowledgements

The author would like to express gratitude for the help that was provided by the civil engineering department, faculty and staff at KL University, Vaddeswaram.

References

[1] Chen L, et al. Recent developments on natural fiber concrete: A review of properties, sustainability, applications, barriers, and opportunities. Dev Built Environ. 2023;16:100255. https://doi.org/10.1016/j.dibe.2023.100255
[2] Ja'e IA, et al. Experimental and predictive evaluation of mechanical properties of kenaf-polypropylene fibre-reinforced concrete using response surface methodology. Dev Built Environ. 2023;16:100262. https://doi.org/10.1016/j.dibe.2023.100262
[3] Akinpelu MA, Salman AS, Jimoh YA, Yahaya IT, Salami HM. Impact of treatment temperature of metakaolin on strength and sulfate resistance of concrete. Res Eng Struct Mater. 2024;x(x):1-19. https://doi.org/10.17515/resm2024.06ma1012rs
[4] Kumar RV, Prabaghar A. Evaluation of strength of self-compacting concrete having dolomite powder as partial replacement for cement. Res Eng Struct Mater. 2023;x(x):1-15. https://doi.org/10.17515/resm2023.48ma0725rs.
[5] Sahib Q, Marshdi R, Dakhil AJ, Al-khafaji Z. Investigation of strength and durability performance of concrete with varying crude oil waste ratios. Res Eng Struct Mater. 2024;x(x):1-17.
[6] Vairagade VS, Dhale SA. Hybrid fibre reinforced concrete-A state of the art review. 2023. https://doi.org/10.1016/j.hybadv.2023.100035
[7] Prakash R, Mukilan M. Impact of various fibers on the mechanical and durability performance of fibre-reinforced concrete with SBR latex. 2024.
[8] Sharhan ZS, Rad MM. Elasto-plastic analysis of two-way reinforced concrete slabs strengthened with carbon fiber reinforced polymer laminates. 2024. https://doi.org/10.3390/computation12050093
[9] Cucuzza R, Aloisio A, Accornero F, Marinelli A, Bassoli E, Marano GC. Size-scale effects and modelling issues of fibre-reinforced concrete beams. Constr Build Mater. 2023;392:131727. https://doi.org/10.1016/j.conbuildmat.2023.131727
[10] Lin C, Kanstad T, Jacobsen S, Ji G. Bonding property between fiber and cementitious matrix: A critical review. Constr Build Mater. 2023;378:131169. https://doi.org/10.1016/j.conbuildmat.2023.131169
[11] Abdalla JA, et al. A comprehensive review on the use of natural fibers in cement/geopolymer concrete: A step towards sustainability. Case Stud Constr Mater. 2023;19:e02244. https://doi.org/10.1016/j.cscm.2023.e02244
[12] Dutt KS, Kumar KV, Kishore IS, Chowdary CM. Influence of natural fibers as an admix in normal concrete mix. Int J Eng Trends Technol. 2016;35(1):1-5. https://doi.org/10.14445/22315381/IJETT-V35P201
[13] Sen T, Reddy HNJ. Strengthening of RC beams in flexure using natural jute fibre textile reinforced composite system and its comparative study with CFRP and GFRP strengthening systems. Int J Sustain Built Environ. 2013;2(1):41-55. https://doi.org/10.1016/j.ijsbe.2013.11.001
[14] Elbehiry A, Elnawawy O, Kassem M, Zaher A, Mostafa M. FEM evaluation of reinforced concrete beams by hybrid and banana fiber bars (BFB). Case Stud Constr Mater. 2021;14:e00479. https://doi.org/10.1016/j.cscm.2020.e00479
[15] Suresh S, Charan MS, Kishore IS. Strength and behaviour of concrete by using natural and artificial fibre combinations. Int J Civ Eng Technol. 2017;8(4):1652-8.
[16] Kangu AN, Shitote SM, Onchiri RO, Matallah M. Effects of waste tyre steel fibres on the ultimate capacity of headed studs in normal concrete. Case Stud Constr Mater. 2023;18:e02166. https://doi.org/10.1016/j.cscm.2023.e02166

[17] Sharma U, Sheikh IM. Investigating self-compacting concrete reinforced with steel & coir fiber. Mater Today Proc. 2021;45(x):4948-53. https://doi.org/10.1016/j.matpr.2021.01.386
[18] Rajkohila A, Chandar SP, Ravichandran PT. Assessing the effect of natural fiber on mechanical properties and microstructural characteristics of high strength concrete. Ain Shams Eng J. 2024;102666. https://doi.org/10.1016/j.asej.2024.102666
[19] Nduka DO, Olawuyi BJ, Ajao AM, Okoye VC, Okigbo OM. Mechanical and durability property dimensions of sustainable bamboo leaf ash in high-performance concrete. Clean Eng Technol. 2022;11:100583. https://doi.org/10.1016/j.clet.2022.100583
[20] Saidi T, Hasan M, Amalia Z, Salsabila S. The analysis of the bond strength between natural fiber reinforced polymer (NFRP) sheets and concrete. Results Eng. 2023;18:101124. https://doi.org/10.1016/j.rineng.2023.101124
[21] Yinh S, et al. Strengthening effect of natural fiber reinforced polymer composites (NFRP) on concrete. Case Stud Constr Mater. 2021;15:June. https://doi.org/10.1016/j.cscm.2021.e00653
[22] Al Ghali AE, El Ezz NE, Hamad B, Assaad J, Yehya A. Comparative study on shear strength and life cycle assessment of reinforced concrete beams containing different types of fibers. Case Stud Constr Mater. 2023;19:e02497. https://doi.org/10.1016/j.cscm.2023.e02497
[23] Althoey F, Zaid O, Majdi A, Alsharari F, Alsulamy S, Arbili MM. Effect of fly ash and waste glass powder as a fractional substitute on the performance of natural fibers reinforced concrete. Ain Shams Eng J. 2023;14(12):102247. https://doi.org/10.1016/j.asej.2023.102247
[24] Ahdal AQ, et al. Mechanical performance and feasibility analysis of green concrete prepared with local natural zeolite and waste PET plastic fibers as cement replacements. Case Stud Constr Mater. 2022;17:e01256. https://doi.org/10.1016/j.cscm.2022.e01256
[25] Mohammed AA, Muhammad MA, Mohammed BK. Effect of PET waste fiber addition on flexural behavior of concrete beams reinforced with GFRP bars. Case Stud Constr Mater. 2023;19:e02564. https://doi.org/10.1016/j.cscm.2023.e02564
[26] Abdulateef LA, Hassan SH, Ahmed AM. Exploring the mechanical behavior of concrete enhanced with fibers derived from recycled plastic bottles. Eng Technol Appl Sci Res. 2024;14(2):13481-6. https://doi.org/10.48084/etasr.6895
[27] Sharma L, Viradiya J, Gupta R, Baker S. Converting other flexible plastic packaging into fiber reinforcement for concrete structures. Lect Notes Civ Eng. 2024;359:885-901. https://doi.org/10.1007/978-3-031-34027-7_59
[28] Yıldızel SA, et al. Experimental investigation and analytical prediction of flexural behaviour of reinforced concrete beams with steel fibres extracted from waste tyres. Case Stud Constr Mater. 2023;19:June. https://doi.org/10.1016/j.cscm.2023.e02227
[29] Kishore IS, Chowdary CM. Influence of steel fibers as admix in normal concrete mix. Int J Civ Eng Technol. 2016;7(1):93-103.
[30] Pham LT, Trinh TD, Do QT, Huang JY. Flexural behavior of printed concrete wide beams with dispersed fibers reinforced. Res Eng Struct Mater. 2023;x(x):1-16.
[31] Zhang Y, Xin H, Correia JAFO. Fracture evaluation of ultra-high-performance fiber reinforced concrete (UHPFRC). Eng Fail Anal. 2021;120:September.
[32] Al-Jasmi S, Ariffin NF, Abu Seman M. Model analysis of carbon fiber reinforcement properties for reinforced concrete beams to resist blast loads. Mater Today Proc. 2023;xxxx. https://doi.org/10.1016/j.matpr.2023.06.326
[33] Kishore IS, Chowdary CM, Rao VR. Effect of debonding on stiffness and long-term creep of sandwich panels. IOP Conf Ser Mater Sci Eng. 2020;993(1). https://doi.org/10.1088/1757-899X/993/1/012169

[34] Yoo DY, et al. Strain-hardening effect on the flexural behavior of ultra-high-performance fiber-reinforced concrete beams with steel rebars. Dev Built Environ. 2024;17:100343. https://doi.org/10.1016/j.dibe.2024.100343
[35] Qasim M, Lee CK, Zhang YX. Flexural strengthening of reinforced concrete beams using hybrid fibre reinforced engineered cementitious composite. Eng Struct. 2023;284:115992. https://doi.org/10.1016/j.engstruct.2023.115992
[36] Amaireh LK, Al-Tamimi A. Optimum configuration of CFRP composites for strengthening of reinforced concrete beams considering the contact constraint. Procedia Manuf. 2020;44:350-7. https://doi.org/10.1016/j.promfg.2020.02.284
[37] Sajedi SF, Saffarian I, Pourbaba M, Yeon JH. Structural behavior of circular concrete columns reinforced with longitudinal GFRP rebars under axial load. Buildings. 2024;14(4):988. https://doi.org/10.3390/buildings14040988
[38] Li C, Li Q, Li X, Zhang X, Zhao S. Elasto-plastic bending behaviors of steel fiber reinforced expanded-shale lightweight concrete beams analyzed by nonlinear finite-element method. Case Stud Constr Mater. 2020;13(36). https://doi.org/10.1016/j.cscm.2020.e00372
[39] Farooq MA, Fahad M, Ali B, Ullah S, El Ouni MH, Elhag AB. Influence of nylon fibers recycled from the scrap brushes on the properties of concrete: Valorization of plastic waste in concrete. Case Stud Constr Mater. 2022;16:e01089. https://doi.org/10.1016/j.cscm.2022.e01089

Research on Engineering Structures & Materials
www.jresm.org

Research Article

Mechanical characterization of alumina and graphite dual particulates reinforced hybrid aluminum alloy (Al2219) matrix composites

ShivaPrakash S [1,a], Santosh Kumar [2,b], Naveen Kumar B K [3,c], Madeva Nagaral [*,4,d], Narasimha Marakal [5,e], V Auardi [6,f], Manjunatha T H [7,g], Dileep B. P [8,h]

[1]*Department of Mechanical Engineering, New Horizon College of Engineering, Bangalore-560103, India*
[2]*Department of Industrial and Production Engineering, The National Institute of Engineering, India*
[3]*Department of Mechanical Engineering, M S Ramaiah Institute of Technology, Bengaluru, India*
[4]*Aircraft Research and Design Centre, Hindustan Aeronautics Limited, Bangalore-560037, Karnataka, India*
[5]*Department of Mechanical Engineering, Nitte (Deemed to be University) NMAM Institute of Technology, Nitte, Karkala, Udupi-574110, Karnataka, India*
[6]*Department of Mechanical Engineering, Siddaganga Institute of Technology, Tumkur-572103, India*
[7]*Department of Mechanical Engineering, Ballari Institute of Technology and Management, Ballari-583104, Karnataka, India*
[8]*Department of Mechanical Engineering, Amrita School of Engineering, Amrita Vishwa Vidyapeetham, Bangalore, 560035, India*

Article Info

Article history:

Received 21 June 2024
Accepted 24 Dec 2024

Keywords:

Al2219 alloy;
Graphite particles hybrid composite;
Microstructure;
Mechanical behavior

Abstract

The current study involved the production of hybrid composites employing a liquid metallurgical technique, combining Al2219 alloy with Al_2O_3 and graphite. The Al2219 alloy was employed to fabricate hybrid composites consisting of Al_2O_3 particles, ranging from 3 to 6 weight percent, and a constant 2 weight percent of graphite particles. The generated composites underwent microstructural investigation using scanning electron microscopy (SEM) and energy-dispersive X-ray spectroscopy (EDS). The density, hardness, ultimate strength, yield strength, and elongation were determined according to ASTM standards. The SEM revealed that both graphite and Al_2O_3 particles were uniformly distributed within the Al2219 alloy. The EDS revealed the presence of hybrid particles in the Al2219 alloy. The incorporation of dual particles into the matrix resulted in a decrease in the density of aluminium alloy composites. The incorporation of dual particles enhanced the hardness of Al2219 alloy by 22%, ultimate strength by 36.7%, and yield strength 38.5%. The EDS results indicated that the Al2219 alloy contains hybrid particles. The incorporation of dual particles into the matrix resulted in a decrease in the density of aluminium alloy composites. The unique fracture characteristics of the Al2219 alloy and its composites were further demonstrated through the use of tensile force micrographs.

© 2025 MIM Research Group. All rights reserved.

1. Introduction

Composites consist of many materials that possess different chemical or physical properties. Upon combining these components, a novel product is formed, exhibiting distinct features from its individual constituents [1, 2]. Usually, the material's strengthening is done on a large scale [3, 4]. In the end result, the materials are easily recognisable, but they are joined together to enhance durability, reduce weight, and decrease overall expenses in comparison to the conventional material. Due to its enhanced

*Corresponding author: madev.nagaral@gmail.com
[a] orcid.org/0000-0001-5279-3522; [b] orcid.org/0000-0002-6129-4466; [c] orcid.org/0000-0002-3774-4551; [d] orcid.org/0000-0002-8248-7603; [e] orcid.org/0000-0003-4644-7361; [f] orcid.org/0000-0001-6549-6340
DOI: http://dx.doi.org/10.17515/resm2024.328me0621rs

customised characteristics, the final composite material surpasses its constituent components [5, 6]. These composites are attractive alternatives due to their improved mechanical, thermal, electrical, and environmental properties. Ceramic matrix composites and metal matrix composites are in great demand for many construction applications, such as bridges, buildings, boats, swimming pools, race car parts, tanks, and innovative materials for spacecraft, aviation, and buildings [7, 8].

Typically, metal matrix composites (MMCs) consist of two phases [9, 10, 42]. The process consists of two distinct phases: the matrix phase and the reinforcing phase, with the latter often being a metal alloy. To enhance the mechanical properties of composites and achieve material qualities that cannot be achieved by a single phase, it is customary to combine the two phases [11, 12]. Researchers are intensifying attempts to develop powerful reinforcements that augment the strength of MMCs. The integration of reinforcements into the matrix phase facilitates the enhancement of attributes including wear resistance, stiffness, thermal expansion coefficient, and high-temperature conductivity. The selection of suitable filler material is essential for developing a high-quality metal matrix composite [13, 43].

Aluminum possesses several beneficial characteristics, including its low density and its ability to resist corrosion due to passivation [14]. Aluminum and aluminum alloys are essential in the aerospace and automotive industries because they are inexpensive, have a high strength-to-weight ratio, are easy to machine and shape, and are relatively lightweight. Extensive research is being carried out in this field to discover methods of enhancing the strength-to-weight ratio of aluminum alloys by incorporating exceptionally robust elements, a quality that is in high demand [15, 16]. These reinforcing materials can be utilized to modify the mechanical properties according to your requirements. Metal matrix composites (MMCs) are a recently developed material resulting from continuous research on the incorporation of reinforcing elements with base materials such as aluminum alloy [17, 18].

Raj Kumar et al. [44] and co-authors conducted a study using SEM and EDS micrographs, which distinctly demonstrated the presence of B_4C and graphite particles embedded within the Al2117 matrix. The reinforcing particles significantly enhanced the hardness of the aluminum matrix. The incorporation of 3% and 6% B_4C-5% graphite particles increased the hardness of the Al2117 alloy by 3.1% and 10.41%, respectively. Additionally, the ultimate tensile strength of the Al2117 alloy improved by 4.06% and 9.6% with the incorporation of 3% and 6% B_4C-5% graphite particles, respectively. The use of B4C and graphite particles enhanced the yield strength of the Al2117 alloy. Nevertheless, as the concentrations of B_4C and graphite particles increased, the elongation of Al2117 diminished. Fractographic analysis of tensile fracture surfaces demonstrated a combination of ductile and brittle mechanisms in both the Al2117 alloy and its composites, highlighting the intricate mechanical behaviors influenced by reinforcing particles.

Raksha et al [45] utilized Two-stage melt stirring was employed to fabricate Al2011 alloy composites containing 2 and 4wt% graphite particles (50 to 60μm). SEM micrographs demonstrated a uniform distribution of graphite particles devoid of aggregation, corroborated by EDS examination. Augmenting the graphite content led to diminished hardness, concurrently enhancing ultimate tensile and yield strengths. The incorporation of 2 and 4 wt% graphite enhanced tensile strength by 17.64% and 21.15%, respectively, while simultaneously augmenting ductility. Tensile testing revealed distinct fracture mechanisms for the Al2011 alloy and graphite composites.

Pankaj [46] and his team conducted a study. Hybrid composites were fabricated by A two-stage stir casting method was employed to integrate 4 wt.% graphite (Gr) and 12 wt.% boron carbides (B_4C) into A356 alloy, then comparing it to the standard A356 alloy.

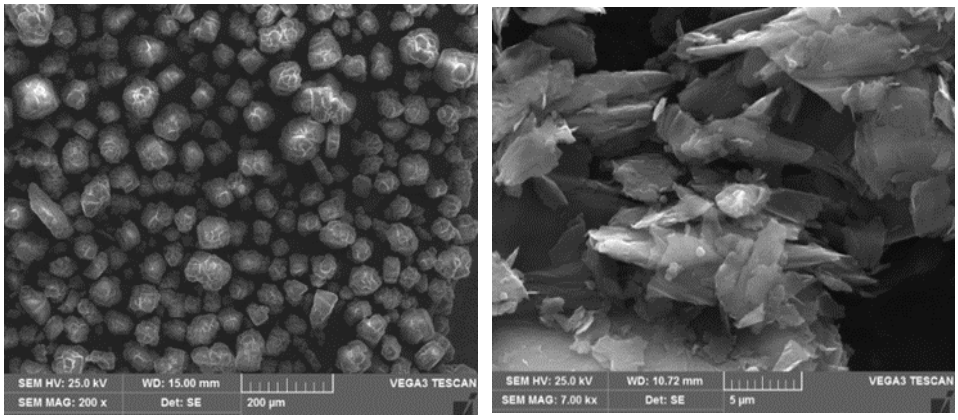
Microstructural study with SEM and EDS revealed a uniform distribution of graphite and B_4C particles throughout the matrix. The hybrid composites exhibit reduced densities owing to the lighter weights of graphite and B4C in comparison to the matrix. The mechanical properties, such as hardness and tensile strength, exhibited substantial enhancement relative to the A356 base alloy. Nonetheless, the elongation of the hybrid material under tensile stress decreased from 13.23% to 9.41%, indicating enhanced strength but reduced ductility. From the above literature various particles used to study the impact of dual particles addition on the mechanical behavior of Al alloy composites.

The primary objective of this research is to construct hybrid composites by including Al_2O_3 particles with a size range of 25 microns and graphite particles with a consistent weight percentage of 5 microns. The objective of this study is to investigate the impact of different concentrations of Al_2O_3 particles (ranging from 3 to 6 weight percent) and graphite particles (maintaining a constant 2 weight percent) on the mechanical behavior and tensile fractography of Al2219 composites. Additionally, the study will examine the microstructure, mechanical properties, and wear parameters of the alloy.

2. Experimental Details

2.1 Matrix and Reinforcement Materials

The procurement of Al alloy Al2219 ingots from FENFE Metallurgical in Bengaluru, India, is intended solely for this purpose. The chemical composition of the Al2219 alloy used in the study is presented in Table 1. The Al2O3 and graphite particles obtained from Bio-aid Scientific Industries Pvt. Ltd. in Bangalore, India were used as reinforcements. Their dimensions were 25 μm and 5 μm, respectively. Table 2 provides a comprehensive overview of the properties of the reinforcements and matrices. Fig. 1(a-b) illustrates the hybrid composites consisting of Al2219, Al2O3, and graphite. This is a scanning electron microscope image of the Al2O3 and graphite particles that were utilized in the fabrication of the material.



(a) (b)

Fig. 1. SEM micrographs of (a) 25-micron sized Al_2O_3 particles (b) 5 micron sized graphite particles

Table 1. Chemistry of Al2219 alloy by wt. %

Si	Fe	Cu	Mn	Mg	Zn	Ti	Al
0.20	0.28	6.50	0.30	0.02	0.10	0.15	Balance

Table 2. Properties of Al2219 alloy, Al_2O_3 and Graphite particles

Material	Hardness (BHN)	Density (g/cm^3)	Elastic Modulus (GPa)	Tensile Strength (MPa)
Al2219	70	2.82	70	220
Al_2O_3	2700	3.96	400	325
Graphite	1.7*	2.20	16	160

*Mohs hardness

2.2. Composite Fabrication

The sample was created using the conventional stir-casting procedure. Aluminium 2219, weighing one kilogramme, was melted in an electric furnace at a temperature of 700˚C. The furnace contained a graphite crucible and was filled with argon gas. The purpose of this process was to generate composites. To produce the homogenised melt, the furnace was heated to a temperature of 750˚C and kept at that level for a duration of 25 minutes. Continuous flow of heated graphite and alumina particles was added to the liquid metal. The reinforcement was thoroughly blended for 15 minutes at a speed of 500 revolutions per minute to provide uniform dispersion. Once the temperature of the cast-iron die had decreased to match that of the surrounding room, the slurry made from a combination of synthetic materials and aluminium was poured into it. An identical technique was utilised to fabricate Al2219 alloy composites including Al_2O_3 particles in the range of 3 to 6 weight percent, while keeping the graphite particles at a constant 2 weight percent. Figure 2 (a-d) represents the furnace set up used for the study, cast iron die, casting in the cast iron die and a sample of casting with tensile specimen respectively. Various sample prepared for the study are detailed in Table 3.



(a)



(b)



(c)



(d)

Fig. 2. Showing the (a) Furnace set up (b) Cast iron die (c) Casting in die (d) Sample of casting and tensile test specimen

Table 3. List of various composites prepared

Sl. No.	Material Code	Compositions of composites prepared
1	A	As-cast Al2219 Alloy
2	C1	Al2219 + 3 wt.% Al_2O_3 + 2 wt.% Graphite composites
3	C2	Al2219 + 6 wt.% Al_2O_3 + 2 wt.% Graphite composites

2.3. Testing of Composites

The study's composite casting was meticulously polished using polishing materials with abrasive particles smaller than three microns at a low speed, after being disassembled into many pieces from various locations. Polishing was employed to eradicate the superficial abrasions from the composites. The final steps of the polishing procedure involved the use of emery sheets that contained abrasives made from SiC and Al_2O_3. In order to enhance the optical clarity, Kellar's reagent was employed, comprising of hydrochloric acid, hydrofluoric acid, nitric acid, and water. Once the surface was thoroughly cleaned and polished, cotton swabs saturated with etchant were employed to administer Kellar's reagent [19, 20]. Subsequently, the SEM pictures were generated by delicately rotating the surface to evenly distribute the reagent.

The ASTM D792 [21] approach use standard test pieces with a diameter of 12 mm and a length of 30 mm for density calculations. In order to determine the mass of the sample, we immerse it in distilled water at the ambient temperature and employ a digital balance with a precision of 0.001 g. The density of a composite can be empirically evaluated by employing a physical offset and calibrating the equipment in accordance with ASTM D792-66.

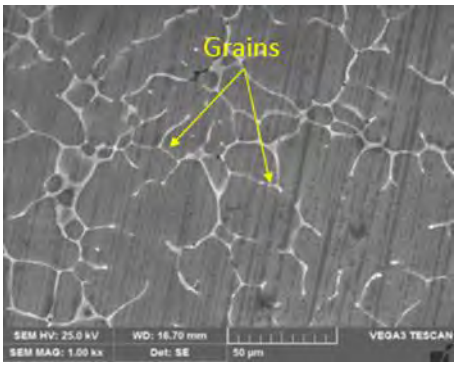
This investigation utilises a Brinell hardness tester that has been calibrated in accordance with the requirements outlined in ASTM E10 [22]. The Brinell test is generally required for surfaces that are excessively rough for standard testing equipment to handle. The hardness of both the as-cast and composited Al2219 alloy with Al_2O_3 particles was measured using a 5 mm ball indenter. Different durations were employed to exert a force of 250 kgf on each sample. The tension test is conducted using a Universal Testing Machine (UTM) that complies with the standards set by ASTM E8 [23]. The sample is subjected to controlled circumstances and stretched until it fractures. This test provides crucial information, such as the metal's response to tensile stress. A tension test can determine the failure point of a material by subjecting it to a significant amount of tensile stress. This method simplifies the process of determining the safety factor of a material and its maximum load capacity

prior to failure. Furthermore, engineers can employ it to determine whether a material is suitable for a certain application. Specimens were subjected to uniaxial tensile testing following preparation according to ASTM E8 standards for tension testing. The specimen is 45 millimetres in length and has a diameter of 9 millimetres. The tensile test was performed using an Instron servo-hydraulic apparatus with a cross head speed of 0.28 mm/min. Composites undergo testing at normal room temperature conditions.

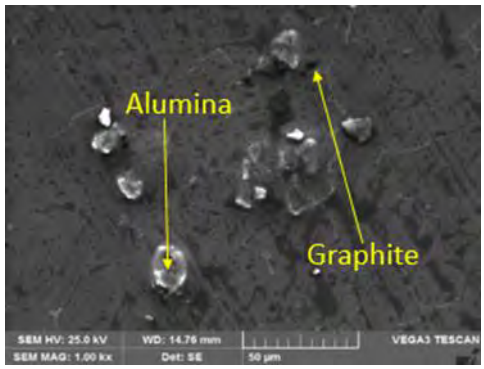
3. Results and Discussion

3.1 Microstructural Analysis

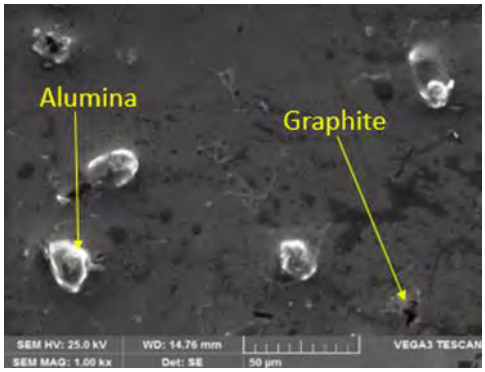
The synthesised hybrid composites demonstrate a notable reduction in porosity, as observed in scanning electron micrographs of Al2219 mixed with Al_2O_3 and graphite particles. Scanning electron microscopy was used to analyse composites containing varying quantities of Al_2O_3 and a fixed proportion of graphite. Fig. 3 (a) displays the scanning electron microscope (SEM) photos of the pure Al2219 alloy. Fig. 3 (b) exhibits the same alloy with 3% Al_2O_3 and 2% graphite reinforcement. Fig. 3 (c) showcases the same alloy with 6% Al_2O_3 and 2% graphite reinforcement. These photographs provide a visual representation of the microstructure of these artificial aluminium hybrid composites.



(a)



(b)

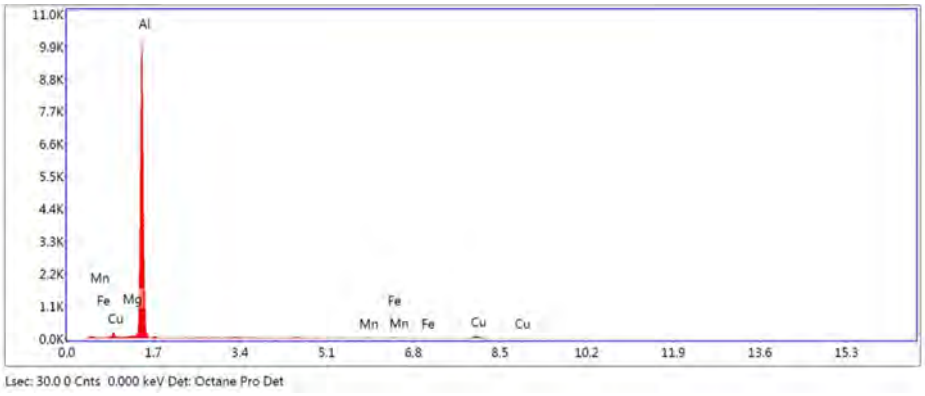


(c)

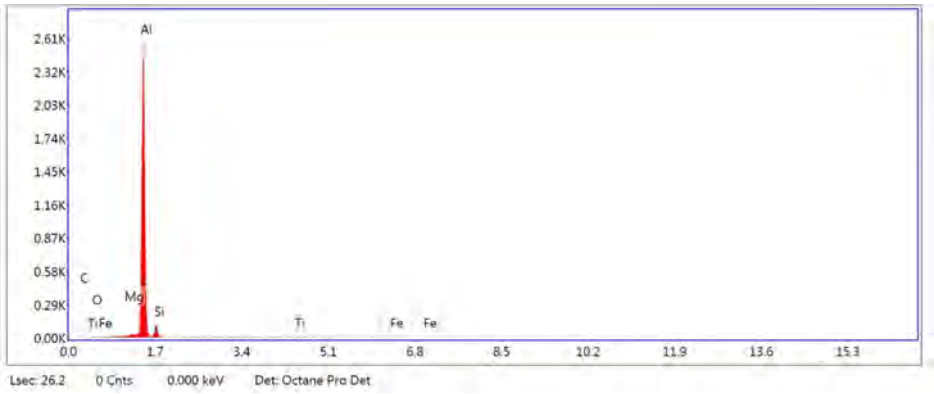
Fig. 3. SEM micrographs of (a) as-cast Al2219 alloy (b) Al2219 alloy with 3 wt. % of Al_2O_3 and 2 wt. % of Graphite composite (c) Al2219 alloy with 6 wt. % of Al_2O_3 and 2 wt. % of Graphite composite

Temperature differences between the solid matrix and the reinforcing particles help in the development of aluminium composites. Because ceramic particles have lower heat conductivity than the Al2219 melt, the molten matrix is at a higher temperature. During the development of dendrites in the first generation of Al2219 grains, the microstructure of the Al2219 silicate eutectic reveals the presence of an inter-dendritic zone between the Si and Al grains. The surface of Al-cast composites can be polished to achieve a highly reflective appearance. Increased magnification will allow for the observation of the grain boundary and secondary phases that are visible under a microscope (Fig. 3(a)). The properties of the composites are determined by the microstructure and features of the reinforcement-to-Al edge. Fig. 3(b-c) shows the scanning electron microstructures of MMCs reinforced with Al_2O_3 and graphite. Microstructure examination did not provide any evidence of aggregated or grouped reinforcements in the MMCs. The causes for this were the continuous contact time between Al_2O_3 and the graphite particle in the liquid Al during the production of the composites, as well as the circulation of the same reinforcement throughout the stirring process.

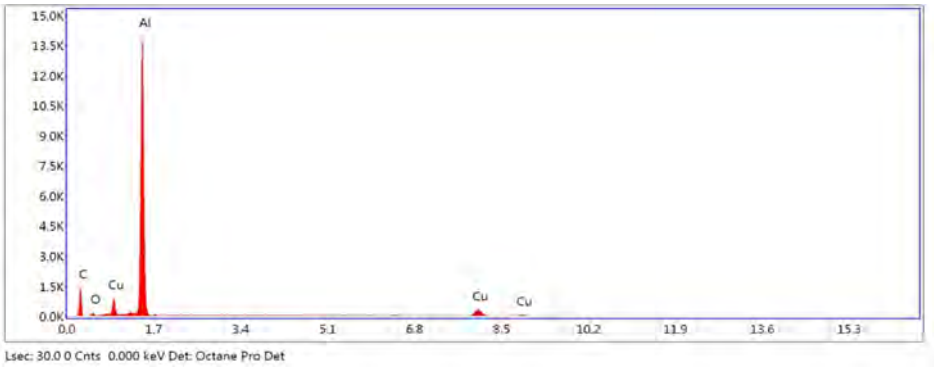
The reinforcing components seem to be uniformly distributed. The results and variable composition exhibited strong concordance, while the microstructure analysis of the composites had more limitations than those of the matrix alloy when all conditions were taken into account. In addition, the Al_2O3 and graphite are consistently dispersed throughout the aluminium matrix. The Gr particles maintain their polygonal shape as the quantity of Al_2O_3 particles increases. However, Fig. 3 (c) demonstrates the aggregation of Al_2O_3 particles in the composite region. The reinforcing components seem to be uniformly distributed. The results and variable composition exhibited a high level of concordance. However, when considering all conditions, the microstructure analysis of the composites imposed greater limitations compared to the matrix alloy. The Gr particles maintain their polygonal shape as the quantity of Al_2O_3 particles increases; however, the aggregation of Al_2O_3 particles in the composite region is depicted in Fig. 3 (c). By utilizing EDS, a pragmatic and efficient technique, it is possible to determine the comparative frequencies of constituents and confirm their existence. Chemical analysis can identify the composition of a sample, but quantifying the exact amount of each element can be challenging. The composite material depicted in Fig. 4 b and Fig. 4C consists of an Al2219 alloy combined with 3 and 6 wt.% Al_2O_3 and 2 wt.% graphite. Si, Fe, Mg, Cu, and Zn are essential alloying elements in Al2219, as depicted in Fig. 4 (a). Fig. 4 (b and c) displays the EDS spectra of composites reinforced with 3 and 6 weight percent Al_2O_3 particles, as well as a constant 2 weight percent graphite comprised of Al2219. Graphite and alumina particles include C and O elements as shown in the EDS composites spectra.



(a)



(b)



(c)

Fig. 4. EDS spectrums of (a) as-cast Al2219 alloy (b) Al2219 alloy with 3 wt. % of Al_2O_3 and 2 wt. % of Graphite composite (c) Al2219 alloy with 6 wt. % of Al_2O_3 and 2 wt. % of Graphite composite

3.2 Density Measurements

Fig. 5 displays the densities of three different materials: Al2219 aluminium alloy (A), Al2219 with 3% Al_2O_3 and 2% graphite (C1), and Al2219 with 6% Al_2O_3 and 2% graphite (C2) hybrid composites. The graph displays a comparison between the theoretical and experimental densities. A study has been conducted to investigate the impact of Al_2O_3 and graphite particles on the Al2219 alloy. The cumulative impacts of these hybrid particles are illustrated in Fig. 5. The theoretical values computed using the standard rule of mixture exhibit a greater abundance of values compared to the experimental data. The density of aluminium alloy 2219 has been determined to be 2.80 g/cm^3. The densities of the reinforcing components, Al_2O_3 and Gr, are 3.96 g/cm^3 and 2.52 g/cm^3, respectively. The graph demonstrates the Al2219—2% graphite and 6% Al_2O_3 (C2) composites had lower densities when compared to the base matrix and other hybrid composites. The proximity between the predicted and experimental densities, as observed in Fig.5, suggests that the stir approach is a feasible technique for manufacturing hybrid composites. Several studies [24] have analysed the impact of Al_2O_3 and Gr on the density of various Al alloys.

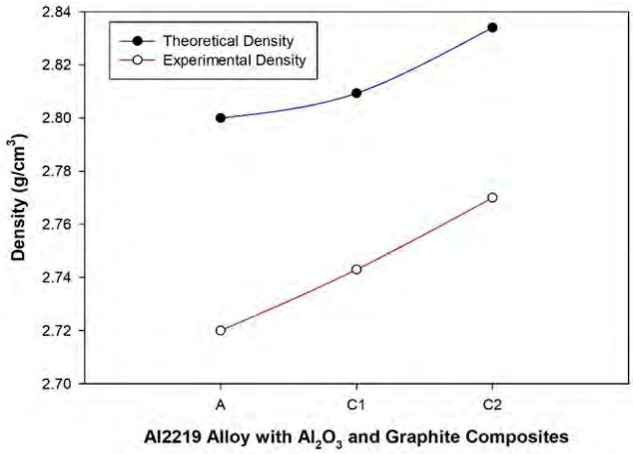


Fig. 5. Theoretical and experimental densities of Al2219 alloy and its Al_2O_3-Graphite composites

3.3 Hardness Measurements

Fig. 6 displays the hardness of the hybridised composites and the substrate metal Al2219. Composites that are reinforced exhibit a greater level of hardness compared to those that are not reinforced, and the level of hardness increases in proportion to the weight % of the reinforcement. This statement is accurate, as evidenced by the primary study sources [25, 26]. Incorporating robust reinforcing particles enhances the strength and toughness of the matrix. Due to the increased graphite content, the composites exhibit a larger percentage of softness in the 2 weight percent Gr and 3 weight percent Al_2O_3 particles. Based on the graphs, increasing the amount of Al_2O_3 in the matrix results in an enhancement of the hardness of the hybrid composite. The alloy's hardness was enhanced by including various proportions of Al_2O_3, which possesses greater hardness compared to most other materials. The improved hardness of hybrid composites may be attributed to the reduced porosity observed in scanning electron micrographs. Table 4 presents the hardness and standard deviation values for the Al2219 alloy and its hybrid composites.

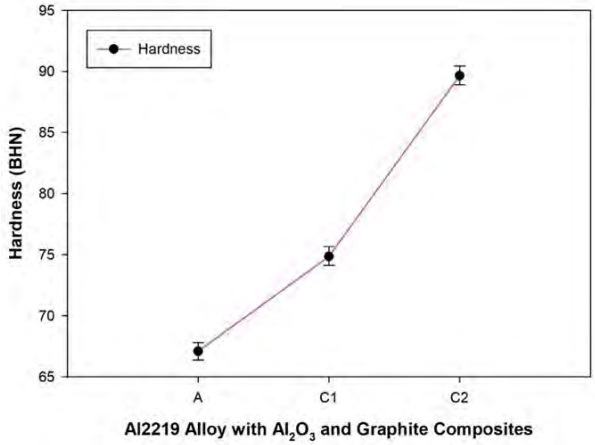


Fig. 6. Hardness of Al2219 and its Al_2O_3-graphite reinforced hybrid composites

The increased hardness value of the Al-Gr-Al_2O_3 hybrid composite can be accredited to the uniform dispersion of Al_2O_3 particles, which sets it apart from other made composites. The presence of fine Gr and hard Al_2O_3 particles made grain boundary sliding more difficult. The addition of Al_2O_3 to a composite enhances its hardness by elevating the dislocation density at the interfaces between the particles and the matrix. This phenomenon results from a disparity in thermal expansion between the matrix and the reinforcement. These components considerably limit the degree to which indentation induces localised deformation. Hardness testing revealed that the composites displayed enhanced hardness with an increase in the amount of Al_2O_3 reinforcement. Additionally, Gr was incorporated into the mixture to enhance its lubricating properties. Furthermore, studies have demonstrated that the presence of a larger Al_2O_3 component enhances the toughness of the material in comparison to a solid aluminium alloy. This is achieved by creating a barrier that hinders the movement of dislocations [27, 28].

3.4 Tensile Properties

Tensile testing of hybrid composites was performed at ambient temperature in accordance with the protocols specified in ASTM E-8. To reduce the margin of error, we used interpolation to determine the average value based on three sets of standard specimens. The data presented in Figures 7 and 8 clearly indicate that the synthetic composites exhibit higher tensile and yield strengths compared to the monolithic Al2219 alloy.

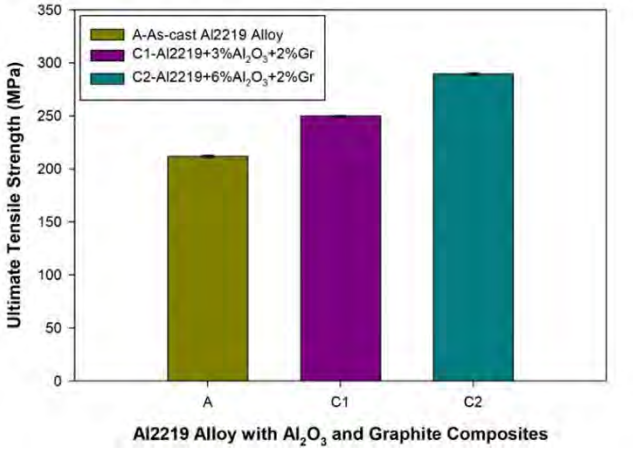


Fig. 7. Ultimate tensile strength of Al2219 with Al_2O_3-graphite reinforced hybrid composites

The microstructure encompasses the selection of the optimal grain size, the interfacial bonding between the Al2219 and reinforcement, and the uniform distribution of the reinforcement. Strain gradients play a role in strengthening composites. The recrystallization of Al2219 aluminium alloy is facilitated by the presence of a robust ceramic reinforcement, which serves as a site for nucleation. When a strengthened particle emerges from the nucleation process, it impedes the movement of the grain boundary, resulting in this occurrence. As a result, when compared to the Al2219 alloy without reinforcement, the size of the matrix grains is significantly larger. Grain boundaries play a dominant role in the movement of dislocations in artificial aluminium hybrid composites. The uninterrupted immobilisation of dislocations inside the matrix has resulted in a decrease in grain size [29]. This reduces the strengthening impact of dislocation movement in hybrid composites. The addition of Gr and Al_2O_3 to an aluminium matrix alloy enhances the properties of the alloy, thereby impacting the results of the tensile test.

The high strength values of Al-Gr Al_2O_3 hybrid composites can be accredited to the occurrence of dislocation pile-up, which arises from the existence of equally scattered Al2O3 in the composite matrix. As the strength of the composite increases, both the density of dislocations and the density of dislocation interactions at matrix/reinforcement contacts also rise. The Hall-Petch relationship, which is dependent on the Gr particles, elucidates this phenomenon. The integration of Al_2O_3 particles enhances the strength and ductility of typically brittle hybrid composites [30, 31].

The enhancements in the ultimate tensile strength (UTS) are achieved in the Al2219 matrix following reinforcement with rigid alumina particles. This improvement is attributed to the increased incorporation of alumina in the base Al2219, while maintaining a consistent graphite concentration. The matrix strength is enhanced by the inclusion of reinforcing particles, resulting in greater resistance to tensile stress. Moreover, due to the superior strength and rigidity of alumina particles compared to Al2219, these alumina and graphite particles initially endure significant stress with minimal deformation. The geometric constraints imposed by dual particles result in the inclusion of particles in the alloy, which enhances work hardening and hence improves tensile strength.

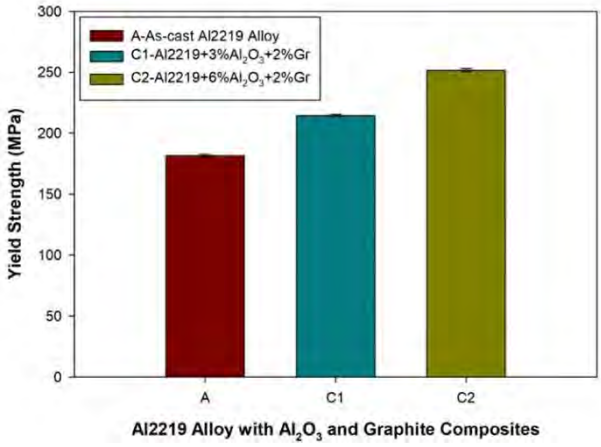


Fig. 8. Yield strength of Al2219 alloy and its Al_2O_3 -graphite reinforced hybrid composites

The dislocation hypothesis elucidates the relationship between the size of particles and the tensile strength. The critical strain required for plastic deformation can be attributed to a significant quantity of dislocations that possess the ability to move freely. Dislocations at the grain boundary might collect and travel at a reduced velocity. Once the quantity of dislocations above a specific threshold, the movement of the dislocations will be driven by their content [32, 33]. The dislocation pile-up, size of Al_2O_3 particles, and dislocation force all increase. Consequently, alloys that possess tiny grain sizes have significant strength. As the size of particles reduces, it becomes simpler to count the borders between particles, which in turn facilitates the prevention of dislocation migration. Hence, the dimensions of the Gr particles have a crucial role in determining the ultimate strength during plastic deformation [34, 35].

Fig. 9 demonstrates the impact of Al_2O_3 and graphite reinforcement on the ductility of Al2219. The existence of rigid Al_2O_3 particles has decreased the ductility in the Al2219. The addition of 3 weight percent Al_2O_3 (C1) particles and 2 weight percent soft graphite particles to the Al2219 alloy results in a substantial enhancement of its ductility. Fig. 9 demonstrates that the composites with the smallest percentage of elongation were the

ones that had a composition of 2 weight percent graphite and Al2219-6 weight percent Al_2O_3. Other researchers who have examined these composites reinforced with particles have reached same findings. When hard, brittle particles are present, they impede deformation and reduce ductility [36, 37]. The primary cause of decreased elongation in the Al2219 matrix is the existence of hard and brittle particles.

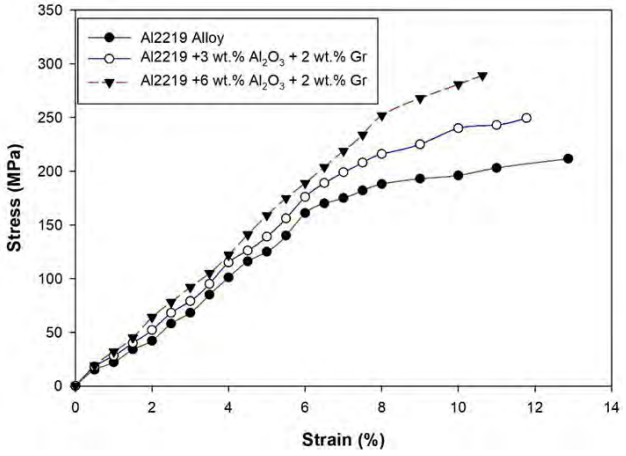


Fig. 9. Elongation of Al2219 alloy and its Al_2O_3-graphite reinforced hybrid composites

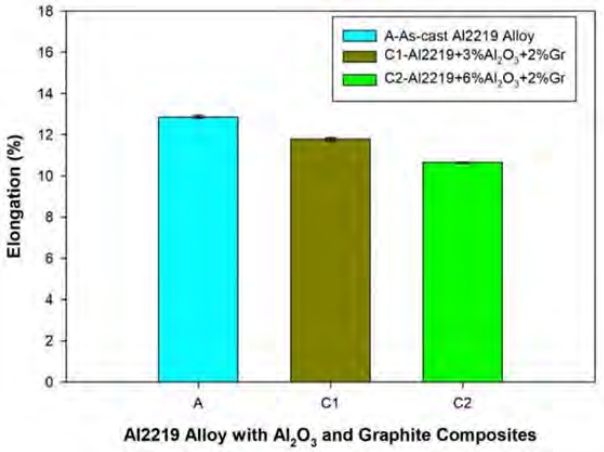


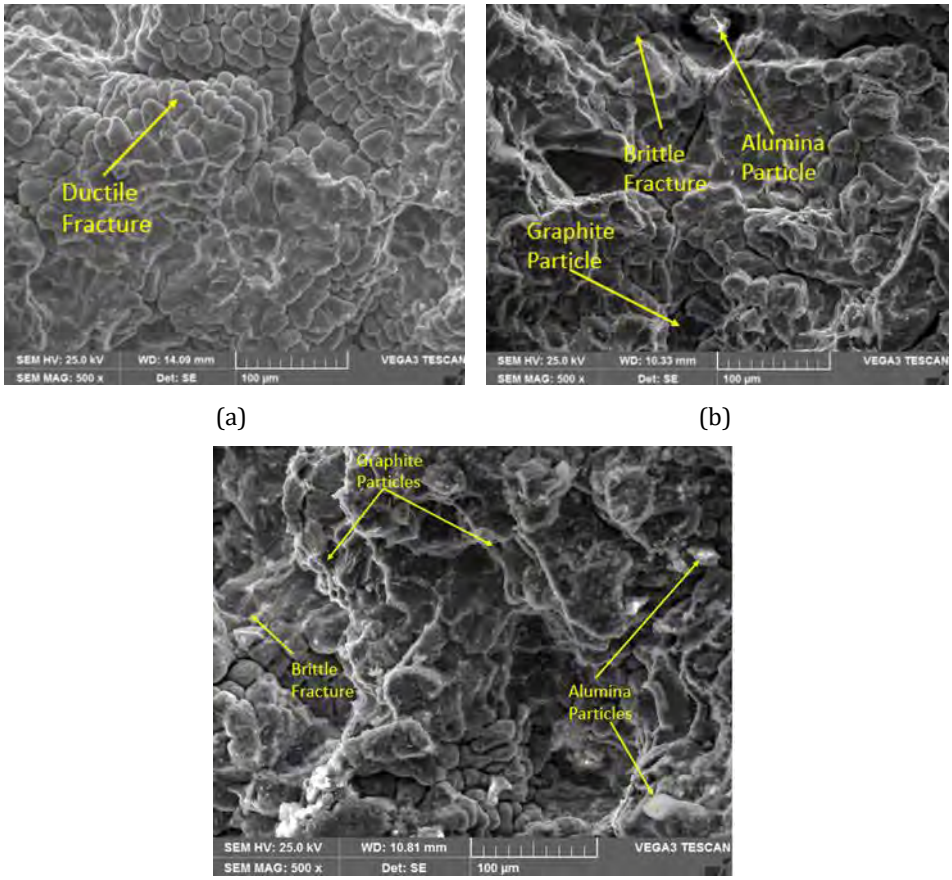
Fig. 10. Stress-strain plots of as-cast Al2219, Al2219 with 3 wt. % of Al_2O_3 and 2 wt. % of Graphite composite and Al2219 with 6 wt. % of Al_2O_3 and 2 wt. % of Graphite composite

The results demonstrate that the mechanical strength and tensile strength of Al2219 are improved by the inclusion of 3% graphite and 6% Al_2O_3. Fractures, perforations, and fractures are indications of brittle fracture. If the amounts of Gr particles remain constant and the concentration of Al_2O_3 increases, the occurrence is more probable. The composites are exhibiting increased brittleness, as shown by the visible surface fracture and crack propagation. One potential reason is because the percentage of elongation reduces as the final tensile strength increases, as stated in reference [38]. Fig. 10 is showing the stress-strain plots of as cast alloy, Al2219 alloy with 2 wt.% of graphite and varying 3 and 6 wt.%

of alumina composites respectively. The resistance to deformation has been enhanced with the inclusion of particles.

3.5 Tensile Fractography

The tensile fracture surfaces of Al2219 alloy, Al2219-3 % Al_2O_3-2 % of graphite and Al2219 -6 % & Al_2O_3-2 % of graphite composites studied as shown in Fig. 11 (a-c). Fig. 11 (a) shows that the superficial of the Al sample cracks in a fibrous manner. Fig. 11 (b, c) displays the fractures in the Al2219 with a weight percentage of 3%. The composition consists of 2 weight percent graphite and 3 weight percent Al_2O_3 in Al2219 alloy, and 6 weight percent Al_2O_3 and 2 weight percent graphite in the same alloy. By incorporating rigid Al_2O_3 particles into the matrix, the ductility of the material diminishes while its strength increases, resulting in enhanced stiffness and strength.



(a) (b)

(c)

Fig. 11. Tensile fractured surfaces SEM images of (a) of (a) as-cast Al2219 (b) Al2219 with 3 wt. % of Al2O3 and 2 wt. % of Graphite composite (c) Al2219 with 6 wt. % of Al2O3 and 2 wt. % of Graphite composite

SEM micrographs of composite materials exhibit a combination of shear and brittle fracture modes. The varying sizes of the matrix dimples on the fracture surface can be observed in Fig. 11 (b, c). The inclusion of soft graphite in the matrix enhances the ductility of composites. However, the presence of alumina particles diminishes this effect. SEM

micrographs [39, 40] reveal that composites exhibit a fracture mode that is a combination of ductile and brittle behaviour, which is attributed to the combined influence of graphite and Al_2O_3 particles.

4. Conclusion

The current study examined the mechanical characteristics of composites reinforced with graphite and Al_2O_3 particles manufactured of Al2219 matrix. The conclusions that followed were as follows:

- Using the stir cast method, hybrid composites of Al2219 with graphite and Al_2O_3 reinforcement were created. Al2219 with 3 and 6 wt.% of Al_2O_3 and constant 2 wt. % of graphite hybrid composites were studied.
- The scanning electron microscope images revealed a consistent distribution of Al_2O_3 and graphite within the Al2219. The EDS spectra indicate the presence of Carbon and Oxygen in the composites of Al2219 with Al_2O_3 and graphite.
- With an incorporation of alumina and graphite particles, the density of Al2219 alloy was increased. Al2219 composites containing 2% graphite and 6% Al_2O_3 had the highest density. The hardest composites are made of Al2219 with 2% graphite and 6% Al_2O_3.
- Al2219 alloy hardness was increased with the addition of Al_2O_3 and graphite. Al2219 with 6 wt.% of alumina and 2 wt. % of graphite composites exhibited highest hardness and improvement in the hardness was 33.6%.
- The ultimate and yield strengths of Al2219 were improved by using graphite and Al_2O_3 reinforcements. The maximum ultimate and yield strength was recorded in the composites reinforced with 6 wt.% alumina and 2 wt.% graphite. The addition of Al_2O_3 particles (6% by weight) and graphite (2% by weight) results in an increase of 36.7% in ultimate tensile strength (UTS) and 38.5% in yield strength (YS) of the Al2219 alloy.
- Graphite and Al_2O_3 have slightly reduced the ductility of the Al2219 matrix. The impact of hard alumina particles on the ductility of Al2219 alloy was more and hence caused in the reduction of elongation.
- According to a surface microscopic investigation of tensile fractures, the as-cast Al2219 exhibits ductile fracture behaviour, while the hybrid composites containing Al_2O_3 and graphite particles, displayed brittle fracture behaviour.

References

[1] Bharath V, Nagaral M, Auradi V. Preparation of 6061Al-Al2O3 metal matrix composite by stir casting and evaluation of mechanical properties. International Journal of Metallurgical & Materials Science and Engineering, 2012;2 (3): 22-31.

[2] Nagaral M, Auradi V, Kori SA. Microstructure and mechanical properties of Al6061-Graphite composites fabricated by stir casting process. Applied Mechanics and Materials, 2015;766: 308-314. https://doi.org/10.4028/www.scientific.net/AMM.766-767.308

[3] Pankaj RJ, Sridhar BR, Nagaral M, Jayasheel IH, Evaluation of mechanical properties of B4C and graphite particulates reinforced A356 alloy hybrid composites, Materials Today: Proceedings, 2017; 4(9), 9972-9976. https://doi.org/10.1016/j.matpr.2017.06.304

[4] Siddesh M, Shivakumar BP, Shashidhar S, Nagaral M. Dry sliding wear behavior of mica, fly ash and red mud particles reinforced Al7075 alloy hybrid metal matrix composites, Indian Journal of Science and Technology, 2021;14 (4): 310-318. https://doi.org/10.17485/IJST/v14i4.2081

[5] Nagaral M, Hiremath V, Auradi V, Kori SA. Influence of Two-Stage Stir Casting Process on Mechanical Characterization and Wear Behavior of AA2014-ZrO2 Nano-composites, Transactions of the Indian Institute of Metals, 2018; 71: 2845-2850. https://doi.org/10.1007/s12666-018-1441-6
[6] Veeresh Kumar GB, Gude VC, Mandadi SV, Jayarami R, Nagaral M, Naresh K. Effects of addition of Titanium Diboride and Graphite Particulate Reinforcements on physical, mechanical and tribological properties of Al6061 Alloy based Hybrid Metal Matrix Composites, Advances in Materials and Processing Technologies, 2022; 8 (2), 2259-2276. https://doi.org/10.1080/2374068X.2021.1904370
[7] Nagaral M, Attar S, Reddappa HN, Auradi V, Kumar S, Raghu S. Mechanical behavior of Al7025-B4C particulate reinforced composites. Journal of applied mechanical engineering, 2015; 4(6), 1-4.
[8] Bharath V, Auradi V, Nagaral M, Satish BP. Experimental Investigations on Mechanical and Wear Behaviour of 2014Al-Al2O3 Composites. Journal of Bio-and Tribo-Corrosion, 2020;6: 1-10. https://doi.org/10.1007/s40735-020-00341-2
[9] Nagaral M, Auradi V, Parashivamurthy KI, Kori SA, Shivananda BK. Synthesis and characterization of Al6061-SiC-graphite composites fabricated by liquid metallurgy. Materials Today: Proceedings, 2018; 5(1): 2836-2843. https://doi.org/10.1016/j.matpr.2018.01.073
[10] Nagaral M, Auradi V, Kori SA, Reddappa HN, Jayachandran, Veena S. Studies on 3 and 9 wt.% of B4C particulates reinforced Al7025 alloy composites. AIP conference proceedings, 2017;1:1859. https://doi.org/10.1063/1.4990172
[11] Sallahauddin A, Madeva N, Reddappa HN, Auradi V. Effect of B4C particulates addition on wear properties of Al7025 alloy composites. American Journal of Materials Science, 2015;5(3C): 53-57.
[12] Bharath V, Auradi V, Nagaral M, Satish BB, Ramesh S, Palanikumar K. Microstructural and wear behavior of Al2014-alumina composites with varying alumina content, Transactions of the Indian Institute of Metals, 2021;75: 133-147. https://doi.org/10.1007/s12666-021-02405-4
[13] Vasanth Kumar HS, Kempaiah UN, Nagaral M, Revanna K. Investigations on mechanical behaviour of micro B4C particles reinforced Al6061 alloy metal composites. Indian Journal of Science and Technology, 2021; 14 (22): 1855-1863. https://doi.org/10.17485/IJST/v14i22.736
[14] Nagaral M, Auradi V, Kori SA, Veena S. Mechanical characterization and wear behavior of nano TiO2 particulates reinforced Al7075 alloy composites, Mechanics of Advanced Composite Structures, 2020; 7(1): 71-78.
[15] Zeeshan A, Muthuraman V, Rathnakumar P, Gurusamy P, Nagaral M. Studies on mechanical properties of 3 wt% of 40 and 90 µm size B4C particulates reinforced A356 alloy composites. Materials Today: Proceedings, 2022;52: 494-499. https://doi.org/10.1016/j.matpr.2021.09.260
[16] Raj Kumar, Deshpande RG, Gopinath B, Jayasheel H, Nagaral M, Auradi V. Mechanical Fractography and Worn Surface Analysis of Nanographite and ZrO2-Reinforced Al7075 Alloy Aerospace Metal Composites. Journal of Failure Analysis and Prevention, 2021; 21: 525-536. https://doi.org/10.1007/s11668-020-01092-5
[17] V Bharath, Santhrusht S Ajawan, Madev Nagaral, Virupaxi Auradi, Shivaputrappa Amarappa Kori, Characterization and Mechanical Properties of 2014 Aluminum Alloy Reinforced with Al2O3p Composite Produced by Two-Stage Stir Casting Route, Journal of The Institution of Engineers (India): Series C, 100, 2019, 277-282. https://doi.org/10.1007/s40032-018-0442-x
[18] Pathalinga GP, Chittappa HC, Nagaral M, Auradi V. Influence of B4C Reinforcement Particles with Varying Sizes on the Tensile Failure and Fractography of LM29 Alloy Composites, Journal of Failure Analysis and Prevention, 2020;20 (6): 2078-2086. https://doi.org/10.1007/s11668-020-01021-6

[19] Zeeshan A, Muthuraman V, Rathnakumar P, Gurusamy P, Nagaral M. Investigation on the tribological properties of copper alloy reinforced with Gr/ZrO2 particulates by stir casting route. Materials Today: Proceedings, 2020; 33: 3449-3453. https://doi.org/10.1016/j.matpr.2020.05.351
[20] Nagaral M, Auradi V, Parashivamurthy KI, Kori SA. Wear behavior of Al2O3 and graphite particulates reinforced Al6061 alloy hybrid composites. American Journal of Materials Science, 2015; 5 (3C): 25-29.
[21] Samuel D, Satish BB, Virupaxi A, Nagaral M, Udaya MR, Bharath V. Evaluation of Wear Properties of Heat-Treated Al-AlB2 in-situ Metal Matrix Composites, Journal of Bio-and Tribo-Corrosion, 2021;7,(40): 1-11. https://doi.org/10.1007/s40735-021-00476-w
[22] Nagaraj N, Mahendra KV, Nagaral M. Microstructure and evaluation of mechanical properties of Al-7Si-fly ash composites, Materials Today: Proceedings, 2018; 5 (1): 3109-3116. https://doi.org/10.1016/j.matpr.2018.01.116
[23] Nagaral M, Shivananda BK, Virupaxi A, Kori SA. Development and mechanical-wear characterization of Al2024-nano B4C composites for aerospace applications, Strength, Fracture and Complexity, 2020;13 (1):, 1-13. https://doi.org/10.3233/SFC-190248
[24] Nagaral M, Shivananda BK, Auradi V, Parashivamurthy KI, Kori SA. Mechanical behavior of Al6061-Al2O3 and Al6061-graphite composites, Materials Today: Proceedings, 2017; 4(10): 10978-10986. https://doi.org/10.1016/j.matpr.2017.08.055
[25] Fazil N, Venkataramana V, Nagaral M, Auradi V. Synthesis and mechanical characterization of micro B4C particulates reinforced AA2124 alloy composites, International Journal of Engineering and Technology UAE, 2018; 7 (2.23): 225-229. https://doi.org/10.14419/ijet.v7i2.23.11954
[26] Krishna D, Prashanth L, Nagaral M, Mathapati R, Hanumantharayagouda MB. Microstructure and mechanical behavior of B4C particulates reinforced ZA27 alloy composites, Materials Today: Proceedings, 2017;4,8: 7546-7553. https://doi.org/10.1016/j.matpr.2017.07.086
[27] Veerabhadrappa A, Poornima H, Lokesha V, Nagaral M, Auradi V. Machine learning algorithms to predict wear behavior of modified ZA-27 alloy under varying operating parameters, Journal of Bio-and Tribo-Corrosion, 2022; 8: 1-10. https://doi.org/10.1007/s40735-021-00610-8
[28] Balaraj V, Nagaraj K, Nagaral M, Auradi V. Microstructural evolution and mechanical characterization of micro Al2O3 particles reinforced Al6061 alloy metal composites, Materials Today: Proceedings, 2021; 47: 5959-5965. https://doi.org/10.1016/j.matpr.2021.04.500
[29] Varadaraj KR, Kumar S, Vitala HR, Ravishankar MK, Dileep BP. Effect of Chromium on Mechanical and Corrosion Behaviour of Ferrous Metal Matrix Composites by Using Powder Metallurgy Route, Lecture Notes in Mechanical Engineering, 2023: 225-234. https://doi.org/10.1007/978-981-19-4140-5_19
[30] Sundararaj CP, Math MM, Girisha, Annigeri AR, Dileep BP. Machinability Study of Multilayer Coated Tungsten Carbide Inserts Using Chemical Vapor Deposition Techniques, Journal of The Institution of Engineers (India): Series D, 2023. https://doi.org/10.1007/s40033-023-00604-5
[31] Anjan Kumar, Hanumantharayappa B, Chaithra P, Chethana CR, Chandrasekhar SB, Latha SB, Nagaral M, Suresh R. Synthesis and mechanical characterization of Si3N4 reinforced copper-tin matrix composites. Journal of the Mechanical Behavior of Materials, 2021;30 (1): 199-206. https://doi.org/10.1515/jmbm-2021-0020
[32] Bharath V, Auradi V, Nagaral M, Satish BB. Influence of alumina percentage on microstructure, mechanical and wear behavior of 2014 aluminium alumina metal matrix composites, Jurnal Tribologi, 2020;25 (1): 29-44.
[33] Krishna SP, Samuel D, Rajesh M, Nagaral M, Auradi V, Rabin S. Preparation and mechanical characterization of TiC particles reinforced Al7075 alloy composites,

Advances in Materials Science and Engineering, 2022: 7105189. https://doi.org/10.1155/2022/7105189

[34] Pankaj RJ, Nagaral M, Shivakumar R, Jayasheel IH. Impact of boron carbide and graphite dual particulates addition on wear behavior of A356 alloy metal matrix composites, Journal of Metals, Materials and Minerals, 2020;30 (4): 106-112. https://doi.org/10.55713/jmmm.v30i4.642

[35] Bharath V, Auradi V, Veeresh Kumar GB, Nagaral M, Chavali M, Mahmoud H, Rokayya S, Aljuraide, Jong WH, Ahmed MG. Microstructural Evolution, Tensile Failure, Fatigue Behavior and Wear Properties of Al2O3 Reinforced Al2014 Alloy T6 Heat Treated Metal Composites, Materials, 2022: 15 (12): 4244. https://doi.org/10.3390/ma15124244

[36] Xie H, Fouad Y, Dileep BP, Kumar RS, Kannan S. Fabrication of high-performance LaFeO3/CuCo2O4 nanocomposite for X-band stealth application Colloids and Surfaces A: Physicochemical and Engineering Aspects, 2023; 677:132414. https://doi.org/10.1016/j.colsurfa.2023.132414

[37] Vasanth Kumar HS, Kempaiah UN, Nagaral M, Auradi V. Impact, tensile and fatigue failure analysis of boron carbide particles reinforced Al-Mg-Si (Al6061) alloy composites, Journal of Failure Analysis and Prevention, 2021;21 (6): 2177-2189. https://doi.org/10.1007/s11668-021-01265-w

[38] Nagaral M, Auradi V, Parashivamurthy KI, Shivananda BK, Kori SA. Dry sliding wear behaviour of aluminium 6061-SiC-graphite particulates reinforced hybrid composites, IOP Conference Series: Materials Science and Engineering, 2018;310: 012156. https://doi.org/10.1088/1757-899X/310/1/012156

[39] Bharath V, Auradi V, Nagaral M. Fractographic characterization of Al2O3p particulates reinforced Al2014 alloy composites subjected to tensile loading, Frattura ed Integrità Strutturale, 2021;15(57): 14-23. https://doi.org/10.3221/IGF-ESIS.57.02

[40] Nagaraj N, Mahendra KV, Nagaral M. Investigations on mechanical behaviour of micro graphite particulates reinforced Al-7Si alloy composites, IOP conference series: materials science and engineering, 2018; 310(1): 012131. https://doi.org/10.1088/1757-899X/310/1/012131

[41] Bharath V, Ashita DH, Auradi V, Nagaral M. Influence of variable particle size reinforcement on mechanical and wear properties of alumina reinforced 2014Al alloy particulate composite, FME Transactions, 2020;48 (4), 968-978. https://doi.org/10.5937/fme2004968B

[42] Paulo Davim J. Metal Matrix Composites, Materials, Manufacturing and Engineering, De Gruyter, 2014. https://doi.org/10.1515/9783110315448

[43] Paulo Davim J. Modern Mechanical Engineering, Springer Publications 2014. https://doi.org/10.1007/978-3-642-45176-8

[44] Kumar R, Deshpande RG, Shilpa RS, Rao KN, Nagaral M. Investigations on Mechanical Behavior of B4C and Graphite Particles Reinforced Al2117 Alloy Hybrid Metal Composites. PalArch's Journal of Archaeology of Egypt/Egyptology, 2021;17(6): 8052-8062.

[45] Raksha MS et al. Impact of micro graphite particles addition on the mechanical behavior of Al2011 alloy metal composites. Engineering Reports, 2023;6(2): 1-10. https://doi.org/10.1002/eng2.12746

[46] Pankaj Jadhav, Sridhar BR, Nagaral M, Harti JI. Mechanical behavior and fractography of graphite and boron carbide particulates reinforced A356 alloy hybrid metal matrix composites. Advanced Composites and Hybrid Materials, 2020;3(1):114-119. https://doi.org/10.1007/s42114-020-00143-7

Blank Page

Research on Engineering Structures & Materials
www.jresm.org

Research Article

Physico-mechanical properties of autoclaved aerated concrete block as an alternative to traditional bricks

Ashim Paul [1,a], Palash Dey [*,1,b], Mrinmoy Dhar [2,c]

[1]*Civil Engineering Department, ICFAI University Tripura, Kamalghat, Tripura – 799210, India*
[2]*Mechanical Engineering Department, ICFAI University Tripura, Kamalghat, Tripura – 799210, India*

Article Info

Article History:

Received 11 Aug 2024
Accepted 01 Jan 2025

Keywords:

Autoclaved aerated concrete;
Fly ash;
Clay bricks;
Microstructural analyses;
Cost analysis

Abstract

Autoclaved aerated concrete (AAC) can be treated as a sustainable construction material as it decreases environmental impact while enhancing urban development quality, aligning with sustainable development goal (SDG) 11 of United Nations. The present study aims to compare the properties of the AAC blocks with that of traditional bricks such as fly ash brick and clay brick to emphasize the distinct advantages and limitations of AAC blocks, proposing AAC as a potential alternative in construction sector. AAC blocks of different aluminum powder (0.025 % and 0.05 % Al) and the masonry prisms of these AAC blocks as well as fly ash bricks and clay bricks were prepared in the laboratory. The compressive strength of AAC block was found to be 5.01 N/mm2 which is higher than the minimum strength according to IS code. The compressive strength of a masonry unit was observed greater than that of masonry prisms in all cases. It was found that the AAC blocks contain minimal moisture, thus suitable for the walls subjected to damp environments continuously as compared to the walls prepared by using fly ash bricks and clay bricks. The microstructural morphology was also obtained using scanning electron microscope (SEM) equipment. It had been observed that the pore size enlarged with the inclusion of Al powder in AAC. As a result, the weight of AAC block reduced, thereby the density and compressive strength also decreased. Due to this characteristic, a masonry structure constructed with AAC blocks is recommended to perform well during earthquake in terms of seismic resistant compared to a structure prepared with traditional bricks. Furthermore, resource-based cost analysis method had been adopted to demonstrate with an example of model room that the cost of building construction can be reduced with the employment of AAC blocks by 29% and 36% as compared to clay bricks and fly ash bricks respectively.

© 2025 MIM Research Group. All rights reserved.

1. Introduction

Due to the rapid expansion of urban areas, development of infrastructure is progressing quickly despite the global resource crisis. The rising demand for housing increases the need for walling materials, which is supplied by brick production in kilns. After China, India is the largest producer of burnt clay bricks, with around 100,000 brick manufacturing plants generating 250 billion bricks annually. These plants together burn approximately 35 million tonnes of coal every year, which is depleting coal reserves and also polluting the environment [1]. At the local level, traditional clay brick kilns pose significant environmental concerns due to the emission of harmful pollutants, including hazardous suspended particulate matter, carbon monoxide, and sulfur oxides. These pollutants negatively impact human health, as well as the health of animals and plants. Additionally, the substantial use of fertile topsoil in brick production presents major environmental issues, such

*Corresponding author: palashdey@iutripura.edu.in
[a]orcid.org//0009-0008-2943-241X; [b]orcid.org/0000-0002-0151-9707; [c]orcid.org/0000-0003-1504-8771
DOI: http://dx.doi.org/10.17515/resm2025-392me0811rs

as, erosion and land degradation, loss of agricultural productivity and impact on biodiversity [2, 3]. Fertile topsoil is necessary for the growth of crops, providing plants with vital nutrients and organic matter. Removing this layer for brick production reduces the agricultural potential of the land and can decline crop yields, thereby impacting food security and causing higher food prices in regions with severely eroded topsoil. Further, topsoil is rich in microorganisms and nutrients that support a variety of plant species. Its exclusion disrupts local ecosystems, leading to habitat loss and adversely affecting biodiversity that depends on the soil for survival.

On a global scale, emissions from brick manufacturing plants significantly contribute to global warming and climate change. The problem of global warming and environmental pollution has become critically important worldwide. Hence, it is crucial to prioritize finding environmentally friendly solutions and policies [4]. Several alternatives (namely AAC block and fly ash brick) to clay bricks [5-7] can help to mitigate pollution and the negative effects of global warming.

Autoclaved aerated concrete (AAC) block may be a good alternative to the clay bricks. The details of aerated lightweight concrete can be found in the refs. [8-9]. AAC was first commercially produced in Sweden in the year 1923 [10]. Since then, till date the research is going on AAC for its advancement. Narayanan and Ramamurthy [11] reviewed structure and properties of aerated concrete. The influence of waste materials and fibres addition on AAC has been studied by several researchers [12-18].

Most of the studies related to seismic analysis found that the in-plane, out-of-plane and combined in-plane and out-of-plane failure risk of AAC infill walls during earthquake are very low due to their lighter weight. On the other hand, fly ash bricks are a kind of brick prepared from fly ash, a byproduct of coal fired power plants. These bricks are sustainable alternative to traditional clay bricks [19, 20]. However, the AAC blocks are often preferred over fly ash bricks in seismically most active zones for seismic design due to their lighter weight and superior ability to absorb vibrations [21]. Costa et al. [22] assessed the seismic performance of autoclaved aerated concrete masonry buildings. Sucuoğlu and Siddiqui [23] demonstrated the influence of AAC infills on the seismic performance of frames and developed an AAC strut model. Kasapgil et al. [24] studied the seismic behavior of AAC infill walls insulated with cementitious lightweight panels in frames.

While existing works extensively discuss the conventional bricks, the comprehensive research on AAC blocks are lacking in the literature. Most of the previous studies report the properties of clay brick and fly ash brick individually, whereas the comparison of the properties of these bricks with AAC is scanty in the literature. The authors are comparing the properties of the blocks to emphasize the distinct advantages and limitations of AAC blocks relative to traditional bricks. This comparison is crucial to demonstrate how AAC blocks stand out in terms of physical and mechanical properties, and cost-effectiveness. A discussion on microstructural morphology is also presented. The authors aim to underline the potential of AAC blocks as an innovative and efficient alternative for contemporary construction needs, offering insights that are both practical and impactful for the construction industry.

2. Materials

2.1. Raw Materials

In the current investigation, the traditional burnt clay bricks and fly ash bricks were brought from the local market. The process of brick manufacturing started with the careful material selection, where natural clay is often mixed with additives like sand, lime or iron oxide to reach desired properties. The fly ash bricks were prepared by combining fly ash, cement, sand, lime and water.

On the other hand, AAC blocks were manufactured in the laboratory. These three different varieties of masonry blocks or units are shown in Figure 1. Further, physical and mechanical properties of the ACC blocks were compared with traditional bricks. The raw materials used in this research work for the preparation of autoclaved aerated concrete were sand, cement, lime, aluminum powder and water.

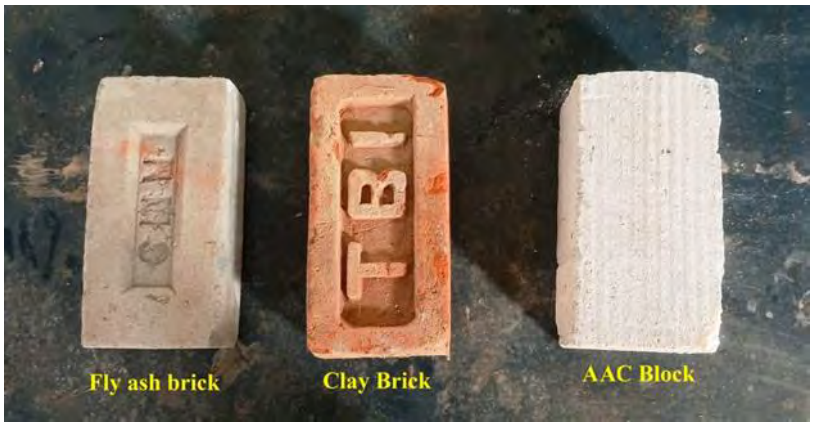


Fig. 1. Three different varieties of masonry blocks

2.1.1. Cement and Water

The testing of Ordinary Portland Cement had been conducted as per IS: 4032(1985). The percentage of Chemical compositions was verified based on IS: 8112 (2013). The fineness of the cement was 225 m^2/kg and the specific gravity 3.15. Chemical compositions of cement were presented in Table 1. Tap water was added to cement for creating a paste that glued all of the aggregates together. The measured pH value of water obtained from the laboratory experiment was equal to 7.7 [25].

Table 1. Chemical compositions of OPC 43 grade

Chemical composition	% (by weight)
CaO	60.22
SiO_2	20.86
Al_2O_3	5.84
Fe_2O_3	3.68
MgO	2.48
SO_3	3.35
Loss on ignition	3.57

2.1.2. Fine Aggregate

Locally available washed natural river fine aggregate or sand was utilized in the matrix of mortar. The specific gravity of the sand was 2.66 as obtained from the experiment. The zone III of the fine aggregate was confirmed by sieve analysis. The grading curve of fine aggregate or sand is depicted in Figure 2.

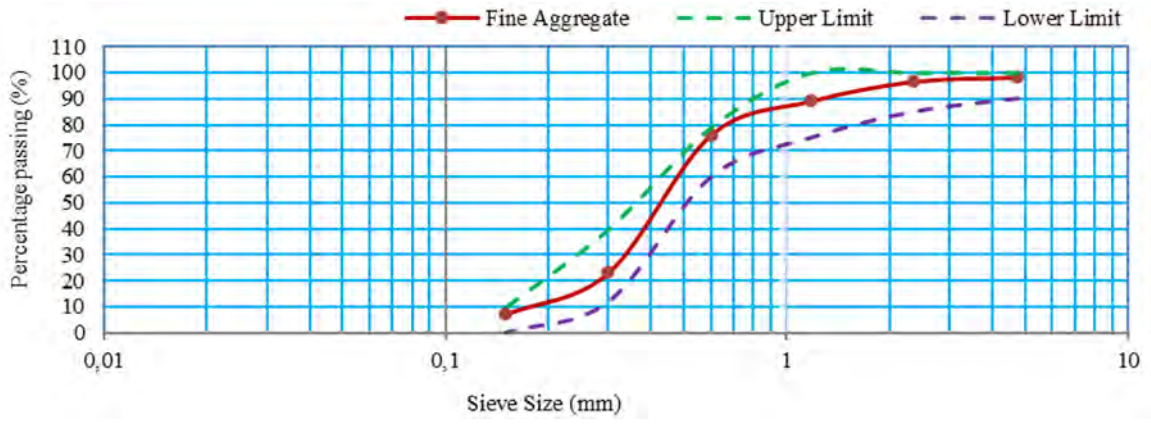


Fig. 2. Grading curve of fine aggregate

2.1.3. Lime

Lime is serving as a binding agent. This calcareous material reacts with SiO_2 and Al_2O_3 in siliceous materials under hydrothermal environments to produce hydrated calcium silicate and then built the strength of AAC blocks. It was prepared from limestone either by crushing to fine powder or by purchasing it in powder form from a local merchant.

2.1.4. Aluminum Powder

Aluminum is working as an expansion agent, which will affect the density of the AAC block. When aluminum powder was introduced in the raw materials, air bubbles were formed due to reaction between calcium hydroxide, aluminum and water; and released hydrogen gas. The aluminium powder used in the processes is presented in the Figure 3.



Fig. 3. Aluminium powder

3. Manufacturing Methods and Tests

The clay was collected from mines and then handled to eliminate impurities, developing a malleable paste or slurry. The clay was shaped into bricks through hand molding or machinery, and then dried under controlled conditions to eliminate moisture. The dried bricks were then fired in a kiln at temperatures between 800°C and 1100°C which strengthens and hardens them through chemical changes. Once cooled, the bricks were sorted by size, shape and strength, and underwent rigorous testing to meet safety and durability standards before being released to the market.

Fly ash bricks were prepared by mixing fly ash, cement, sand, lime and water. The mixture is poured into molds, compacted and cured for 7 to 14 days using either water or steam. After curing, the bricks were dried to decrease moisture and achieve strength. Finally, the bricks were tested for strength and durability, and if meeting the required standards, bricks were ready for use. In the present work a total of 1.055 kg of mixture was used based on ref. [26] for filling a single mould to prepare AAC block. Table 2 illustrates the material compositions of AAC block. Total 33 numbers of AAC blocks were manufactured. The prepared raw materials of mixture were weighed by using digital weighing machine with three decimal places of accuracy.

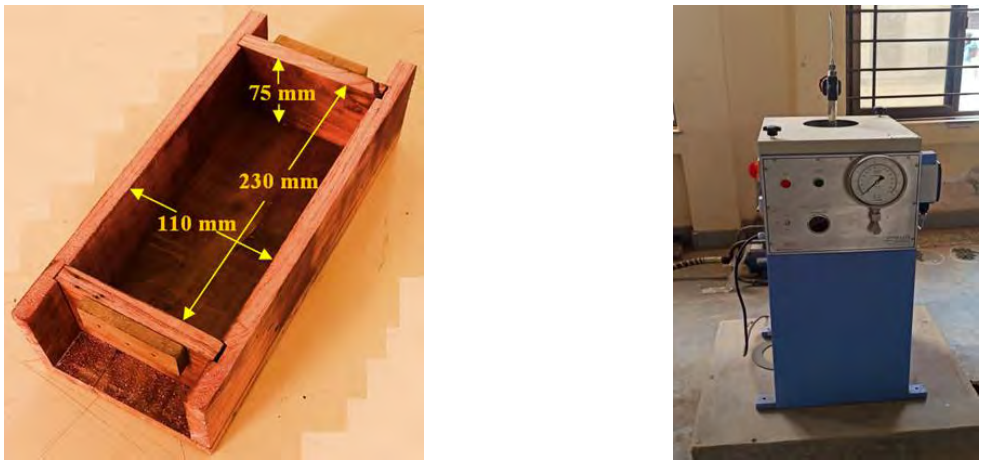
Table 2. Compositions of autoclave aerated concrete

Composition	% (by weight)
Sand	44.00
Cement	14.50
Lime	6.50
Water	36.50
Al powder	0.025 and 0.05

Thereafter, mixture of AAC was needed to pour in a wooden mould (Figure 4(a)). It had been observed that the poured material started to rise by producing air voids in it. This is due to the fact that when aluminum powder reacted with calcium hydroxide, it produced calcium aluminate hydrate ($3CaO.Al_2O_3.6H_2O$) as well as hydrogen gas (air voids), as shown in Eq. (1).

$$2Al+3Ca(OH)_2+6H_2O \longrightarrow 3CaO.Al_2O_3.6H_2O+3H_2 \quad (1)$$

Next step was demoulding of AAC block and this uncured block then sent to the autoclave for curing. Autoclave machine has been shown in Figure 4(b). It consists of one high pressure steam chamber 600 mm long, prepared of seamless stainless-steel tube with bolted steel cover, which is enclosed in heat insulated metal housing. The sample was then placed in an autoclave at 185°C, with a high steam pressure of 8 bar. It was maintained under these conditions for 5 hours. Thereafter, the AAC products within 24 hrs were ready for use.



(a) (b)

Fig. 4. Instrument used for manufacturing: (a) wooden mould and (b) autoclave

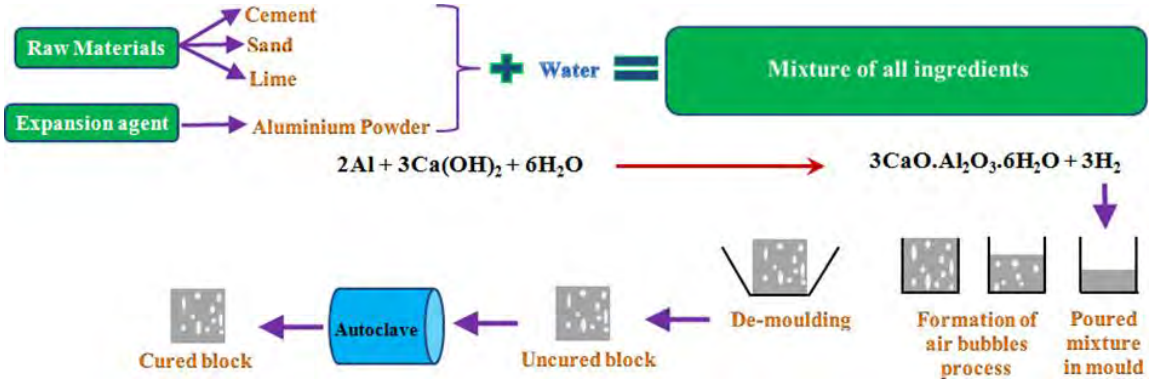


Fig. 5. AAC manufacturing process

In this case, the strength was usually equivalent to 28 days under ambient curing [27]. The flow diagram of AAC manufacturing process in laboratory has been shown in Figure 5. After manufacture process ends, the testing of AAC blocks begins. The tests listed below had been carried out to assess the physical and mechanical properties of three different types of masonry blocks - clay bricks, fly ash bricks and AAC blocks. For the AAC blocks, two different percentages of aluminum powder had been considered. The physical properties, namely, dry density and wet density had been calculated using following formulas:

$$Dry\ Density = \frac{Mass\ of\ the\ brick}{Volume\ of\ the\ brick} \quad (2)$$

$$Wet\ Density = \frac{Wet\ \ mass\ of\ th\ e\ brick}{Volume\ of\ the\ brick} \tag{3}$$

Other physical properties such as moisture content and water absorption were evaluated using Eq. (4) and Eq. (5). Water absorption measures the amount of water that can be absorbed by a material when submerged in water for 24 hours with respect to its dry weight. The moisture content is the amount of water already exists in the material in its natural state relative to its dry weight.

$$Moisture\ Content\ (\%) = \frac{Natural\ \ weight\ \ of\ \ the\ \ material\ \ -\ \ Dry\ weight\ \ of\ \ the\ \ material}{Dry\ weight\ \ of\ \ the\ \ material} \times 100 \tag{4}$$

$$Water\ \ Absorption\ (\%) = \frac{Wet\ weight\ \ after\ \ water\ \ immersion\ \ -\ \ Dry\ weight\ \ of\ \ the\ \ material}{Dry\ weight\ \ of\ \ the\ material} \times 100 \tag{5}$$

The mechanical property such as compressive strength was determined by placing brick/block in compression testing machine (CTM) or universal testing machine (UTM). Load is applied through the machine on it until brick breaks. In the present study, UTM with 600 kN capacity had been used in the laboratory. A test setup has been shown in the Figure 6(a). It is required to note down the value of failure load to find the compressive strength (Eq. (6)) of brick or block.

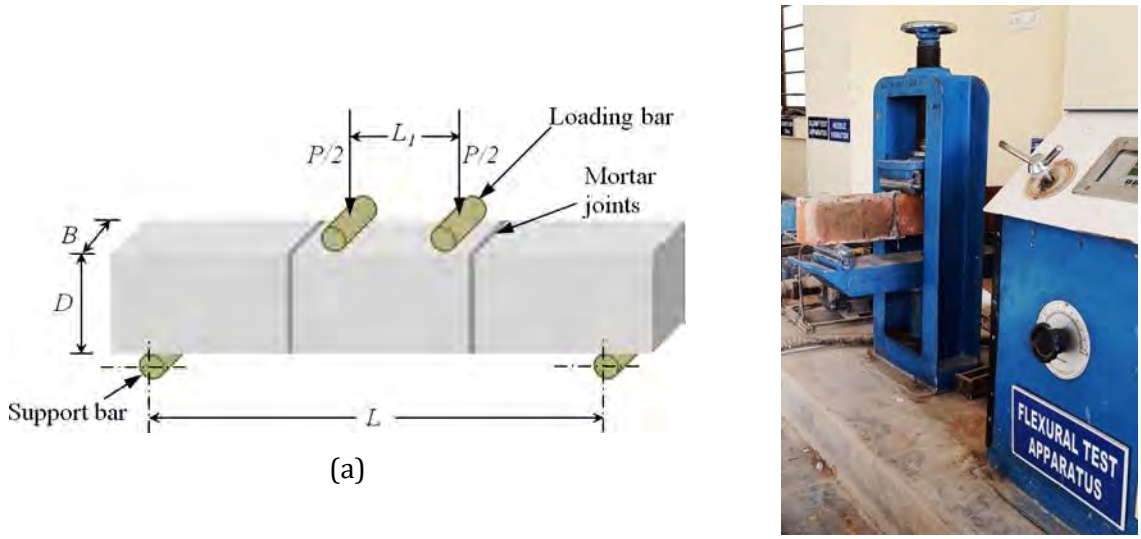
$$Compressive\ \ strength = \frac{Failure\ load}{Area\ over\ which\ \ failure\ load\ applied} \tag{6}$$

This mechanical property of masonry prisms was evaluated by testing three prisms of each variety (clay brick, fly ash brick and AAC block with 0.025% and 0.05% Al powder) subjected to monotonic uniaxial compression. The prisms, measuring 230 × 110 × 415 mm with a height to thickness ratio of 3.77, were built using a 1:3 cement-sand mortar mix with a bed-joint thickness 10 mm. The testing setup for the masonry prisms is presented in Fig. 6(b). The compressive strength of the prisms was determined by dividing the maximum recorded compressive load of each specimen by its gross cross-sectional area. Failure of masonry under compression occurred due to the interaction between the brick units and the mortar joints, which displayed differing deformation behaviors. Vertical compression caused the masonry assembly (bricks and mortar combined) to expand laterally. Since bricks were much stiffer than mortar, their lateral expansion was minimal, constraining the mortar which underwent triaxial compression.



(a) (b)

Fig. 6. Setup for compressive strength test for masonry: (a) unit and (b) prism



(a) (b)

Fig. 7. Flexural strength test for masonry: (a) Schematic diagram and (b) test set-up

This confinement resulted in the mortar pulling the bricks laterally, subjecting the brick units to biaxial tensile forces in addition to the vertical compressive load. A four-point beam bending test was used for estimating the flexural strength of masonry units. The specimen consisted of three bricks or blocks bonded lengthwise with a 1:3 cement-sand mortar mix and 10 mm thick joints. A schematic diagram of the test setup is shown in Fig. 6(c). This configuration (Fig. 6(d)) is particularly applicable to unreinforced masonry walls subjected to out-of-plane bending, such as those influenced by wind or seismic forces. Finally, methods used to analyze costs for masonry brick buildings often depends on the scope, scale and purpose of the project. The resource-based cost analysis method was adopted to estimate the expenses by separately considering labor, materials and overheads. The details of cost analysis have been presented in the later section for masonry work constructed using different types of blocks.

4. Results and Discussions

The physical and mechanical properties as well as cost analysis results of different variety of masonry blocks, namely, fly ash brick, clay brick, AAC blocks prepared with 0.025% and 0.05% aluminum powder had been compared as well as discussed in this section.

4.1. Physical properties

The dimension and average weight of blocks are presented in Table 3. Subsequently, influence of physical properties, namely, weight, pore diameter, density, moisture content, water absorption and color on masonry blocks are demonstrated in this subsection.

Table 3. Details of different variety of masonry blocks

Variety of blocks	Length (mm)	Breadth (mm)	Height (mm)	Dry weight (kg)	Moist weight (kg)
Fly ash brick	230	110	75	3.850	4.380
Clay brick	230	110	75	3.670	4.100
AAC blocks with 0.025%	230	110	75	1.190	1.250
AAC blocks with 0.05%	230	110	75	1.182	1.260

The average dry weight of AAC block was 1.19 kg whereas the fly ash brick 3.85 kg and clay brick 3.67 kg. It implies that the traditional fly ash brick and clay brick were 3.24 and 3.08 times heavier than AAC block. The average percentage difference between moist and dry weight (Table 3) for fly ash brick, clay brick, AAC blocks with 0.025% and 0.05% aluminum powder were 12.10%, 10.49%,

4.80% and 6.19% respectively. The existence of bigger pores in AAC block makes it lighter than other two varieties. These pore sizes were observed (Figure 8) to be increasing with the rise in Al powder percentage. The inspection of grain size of any materials can be conducted using inverted metallurgical microscope (IMM). In this work, IMM had been employed to measure the average pore sizes which were present in the different masonry blocks. The average pore diameters are depicted in the Figure 8. The pore diameter can be calculated by using Eq. (7).

$$D_{avg} = \frac{\sum_{i=1}^{n} D_n}{\sum n} \tag{7}$$

where D_n is the pore diameter, n is the number of the pores and D_{avg} is the average pore diameter.

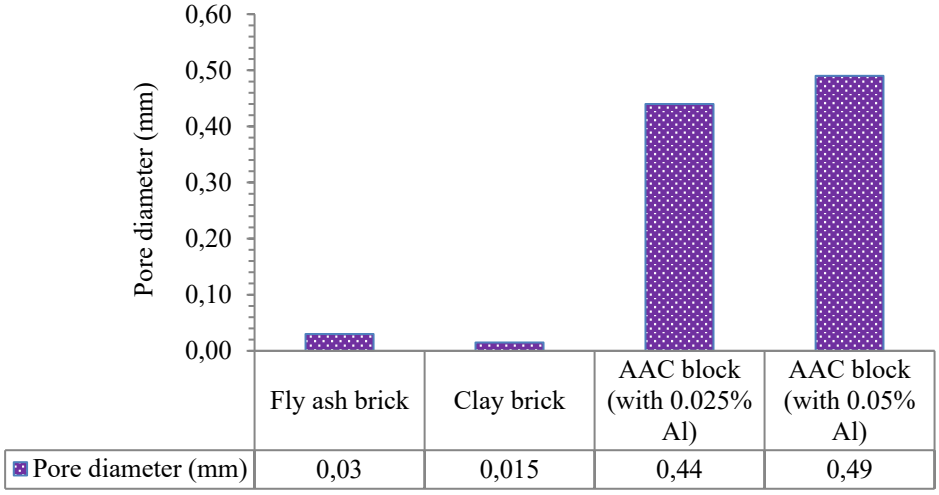


Fig. 8. Average pore diameters

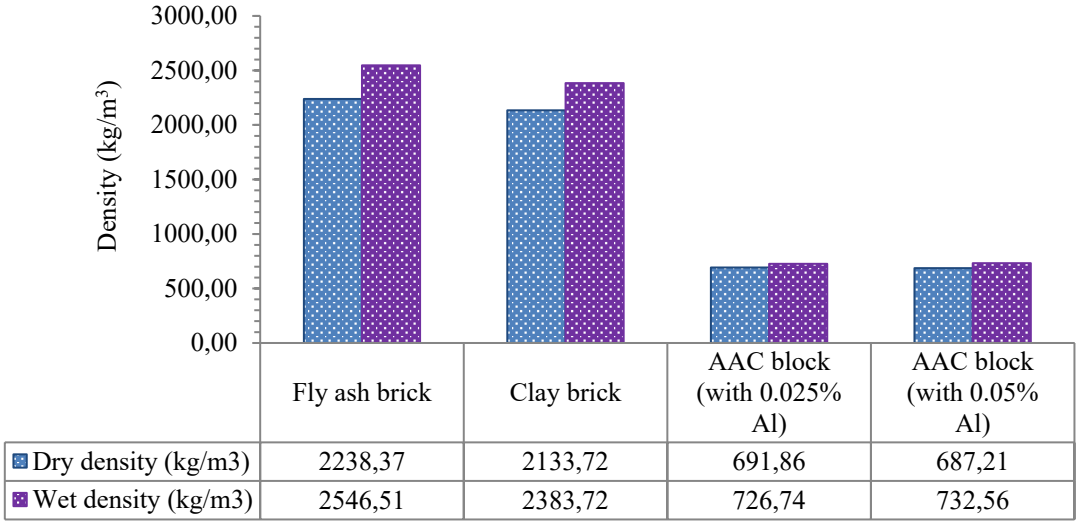


Fig. 9. Comparison of density

The dry density and wet density of different variety of blocks are shown in the chart data table and Figure 9. It can be observed from the figure that the dry and wet densities fly ash and clay bricks were more than three times higher than the AAC blocks. The traditional bricks and AAC block were taken for the moisture content test as per IS 6441 [28]. Fly ash brick and clay brick had average moisture content of 13.77% and 11.71% respectively.

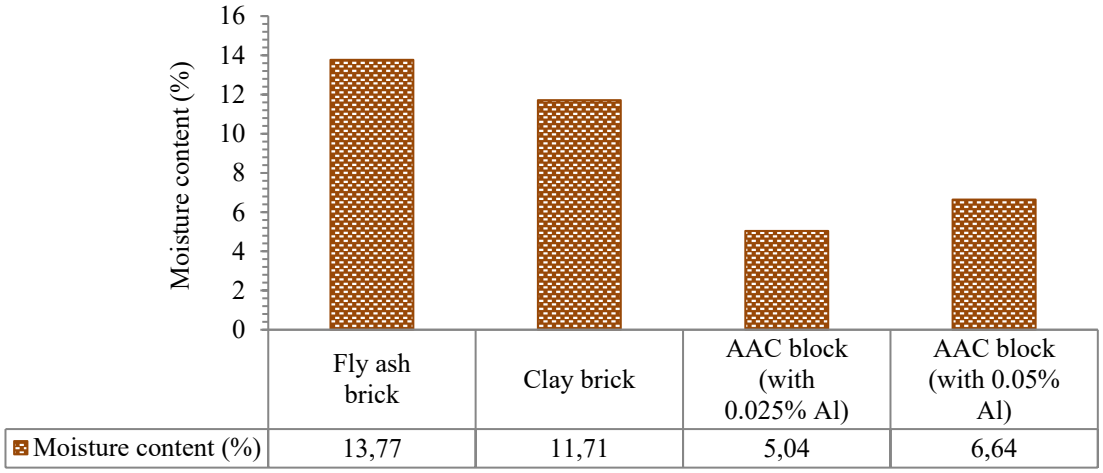


Fig. 10. Comparison of moisture content

On the other hand, AAC blocks with 0.025% and 0.05% aluminum powder hold the moisture content of 5.04% and 6.64% respectively (see Figure 10). Bhosale et al. [29] had reported the moisture content in their findings, ranging from 2.36% to 17.67%. It implies that the AAC block masonry wall does not hold water during curing process. This is particularly beneficial in situations where the wall is consistently exposed to damp conditions as a result of rain penetration. The pores existed in traditional bricks were capillary pores which bound water more tightly. Coarse pores present in AAC block were formed through the entrapment of air during the mixing process. The dry AAC blocks tended to entrain more air than wetter blocks [30] which resisted the water to entrain in those pores and this is the reason to hold less moisture in AAC blocks. Similarly, the water absorption of different types of masonry units is illustrated in Figure 11. It has been observed that the fly ash brick, clay brick, AAC blocks with 0.025% and 0.05% Al powder have average water absorption of 18.86%, 17.60%, 27.56% and 28.35% respectively. These water absorption values align fairly well with the results reported by previous researchers [7, 19, 29].

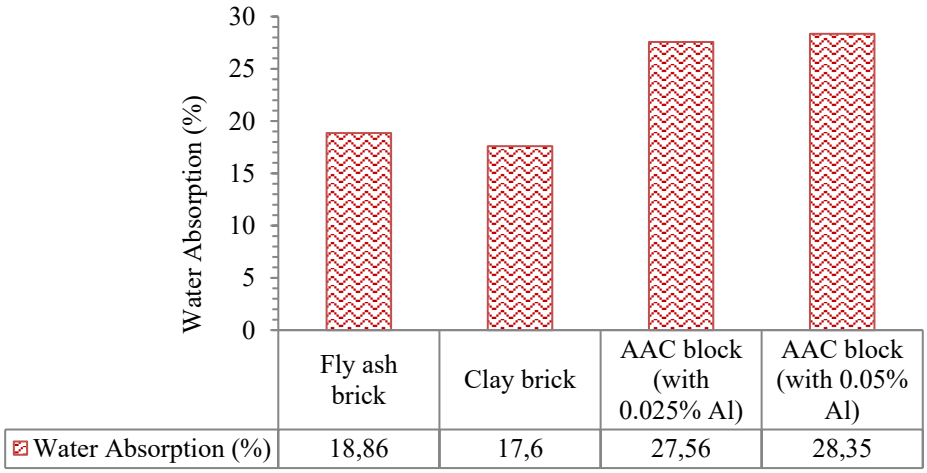
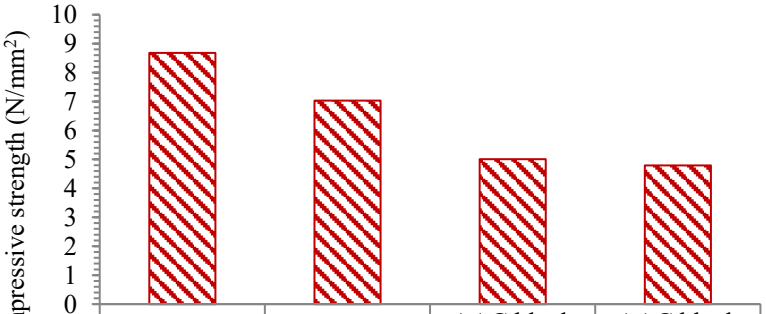


Fig. 11. Comparison of water absorption

Color testing is also performed to evaluate the physical properties of block. The color test is generally conducted under natural light, relying solely on visual inspection. In this study, the clay bricks exhibited a uniform red color. In contrast, the fly ash bricks and AAC blocks revealed a consistent pale gray tone and white to light gray shades respectively. These appearances served as indicators of good quality samples.

4.2. Mechanical Property

The compressive strength of concrete is closely related to its physical property like pore diameter and density. It had been observed that the presence of great numbers of pores highly reduced the strength of AAC. Subsequently, if the traditional bricks were compared with AAC blocks, it can be found that the density also greatly influence the compressive strength, that means less density implies lesser value of compressive strength.

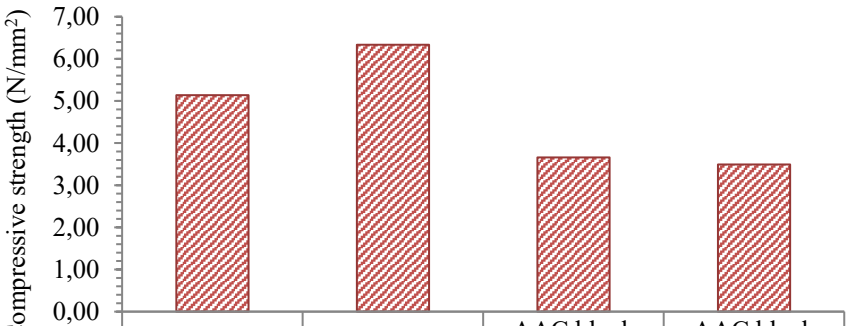


	Fly ash brick	Clay brick	AAC block (with 0.025% Al)	AAC block (with 0.05% Al)
Average Compressive strength	8,68	7,03	5,01	4,79

Fig.12. Comparison of compressive strength values of masonry units or blocks

The obtained average compressive strength for different variety of blocks is presented in the Figure 12. It can be observed that the strength of the AAC block was lesser compare to other two varieties of bricks. If it fails to achieve the required value, it is not useful for construction works. As per IS 1077 [31], masonry brick must achieve the compressive strength value equals to 3.5 N/mm^2. The compressive strength of AAC was found to be 5.01 N/mm^2 from the laboratory test. According to IS 2185-3 (1984), AAC blocks also fall under grade one. Thus, without any uncertainty, the AAC blocks can be easily utilized for construction purposes.

Checking hardness, alongside compressive strength, is also significant. Generally, this mechanical property test was conducted using a nail or a steel knife. If a scratch or dent found on the surface during testing, it designates inadequate hardness. However, in this work, no such imperfections were observed on any of the bricks or blocks samples. Thus, it can be concluded that all types of blocks exhibit good hardness.



	Fly ash brick	Clay brick	AAC block (with 0.025% Al)	AAC block (with 0.05% Al)
Average Compressive strength of masonry prism	5,14	6,34	3,66	3,49

Fig. 13. Comparison of compressive strength values of masonry prism

The average compressive strength of masonry prisms prepared by fly ash bricks, clay bricks and AAC blocks with 0.025% and 0.05% of Al powder have been illustrated in the Figure 13. In this work, the compressive strength obtained from the brick unit was higher than that of the masonry prism in case of all types of bricks. A similar pattern had been reported in ref. [7]. The prisms are generally expanded in lateral direction due to Poissons effect when subjected to axial load. However, this lateral expansion was restrained at the top and bottom surfaces because of friction between the steel plates of the loading machine and the prism surfaces. Consequently, the top and bottom of the prism experienced confined compression, while the central portion of the prism experienced tensile force. The depth of the compressive zone was influenced by the dimensions of the loading surface. Since masonry is weak in tension due to the fragile brick-mortar interface, this tensile zone becomes susceptible to cracking.

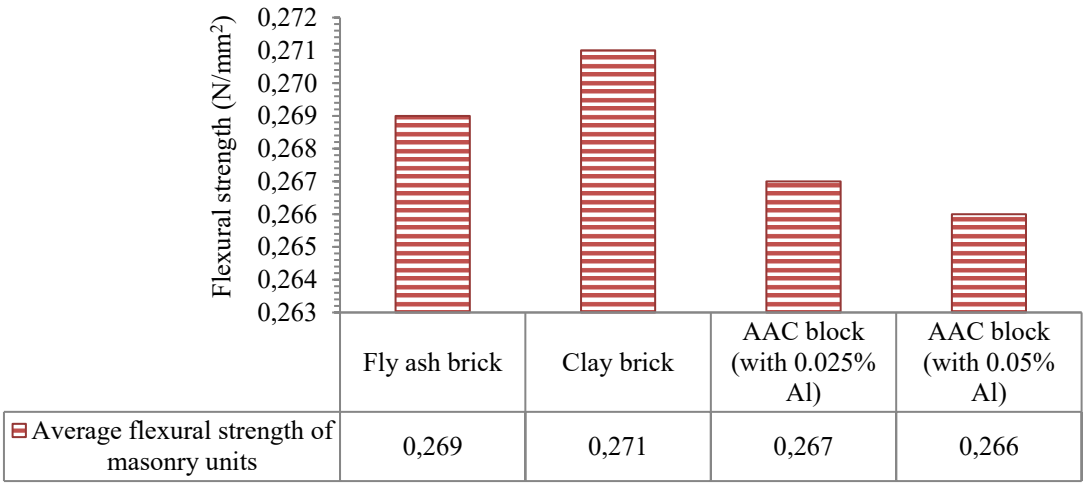


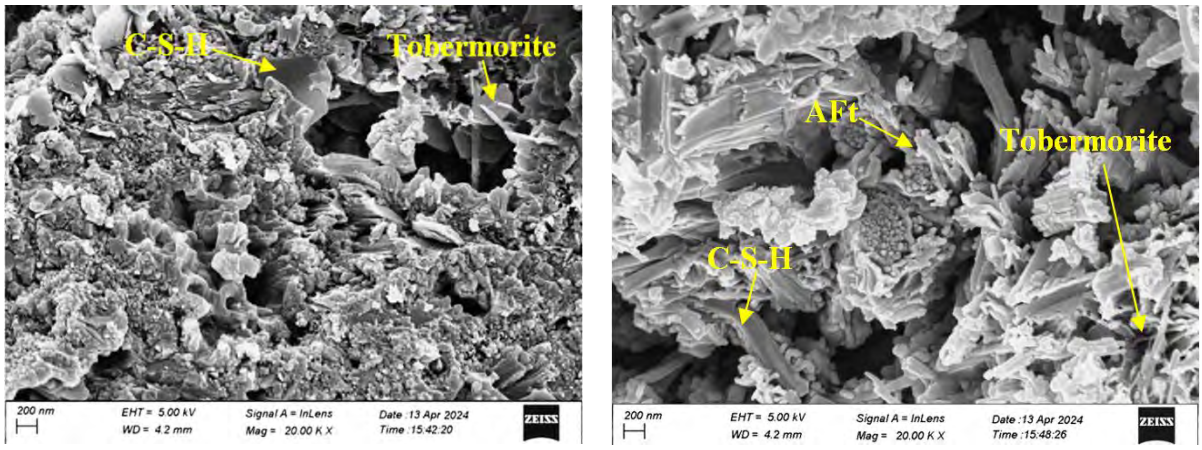
Fig. 14. Comparison of flexural strength values of masonry prism

On the other hand, the average flexural strength of masonry prisms prepared by fly ash bricks, clay bricks and AAC blocks with 0.025% and 0.05% of Al powder have been illustrated in the Figure 14. The flexural strength of fly ash bricks, clay bricks, and AAC blocks masonry was comparable, showing similar performance under bending forces. However, AAC blocks are gaining preference in the construction sector, particularly in seismically active areas, due to their exceptional technical advantages. In addition, their lightweight nature increases seismic performance by reducing the inertia forces subjected on a building during an earthquake. The lesser weight minimizes structural stress, decreasing the possibility of collapse.

4.3. Microstructural Analyses

The principal hydration products of AAC are tobermorite and C-S-H gel. Figures 15 (a) and (b) illustrate the scanning electron microscopy (SEM) images of the AAC samples containing 0.025% and 0.05% of aluminum powder by weight, respectively. As compared to AAC with 0.05 % aluminum powder (Figure 15(b)), AAC with 0.025% aluminum powder (Figure 15(a)) had greater hydration products. AAC sample with 0.025% aluminum powder interlaced to form a comparatively strong body.

It can be observed from Figure 15(b) that the surface morphology was uneven, and the structure was loose rather than densely packed. When more aluminum powder was added, the combination of micro and macro pores became more apparent. The porous nature of the AAC samples may result in a high-water demand during the experiment. As a result, increasing the amount of aluminum powder reduced the compressive strength. A similar tendency can be noticed in terms of density. This density reduction is helpful to the lightweight properties of AAC blocks, making them easier to handle and decreasing the load on structural components. However, it had been found from the literature [32, 33] that the microstructure of fly ash and clay brick had the minimal number of extremely small pores, thus the structure was densely packed and provided higher compressive strength.



(a) (b)

Fig.15. SEM images of the AAC samples containing: (a) 0.025% and (b) 0.05% of Al powder

4.4. Cost Analysis

The cost analysis of brick work included the expenses associated with materials such as brick, sand, and cement, as well as the expenses related to labor. To demonstrate that which variety of brick work is cost effective, an example had been considered in this study for cost analysis purpose. Assumed that a room of 3.6 m x 3.6 m internal dimensions. Wall thickness was considered 250 mm.

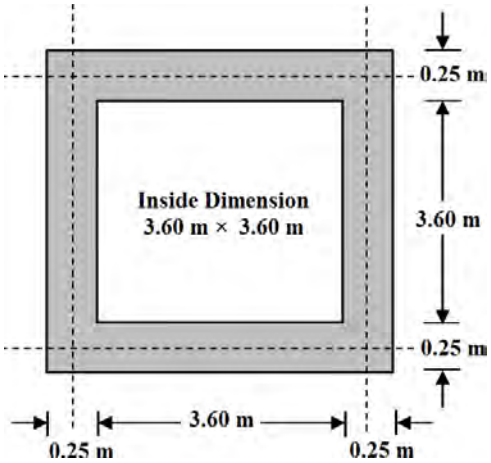


Fig. 16. Plan view of the room

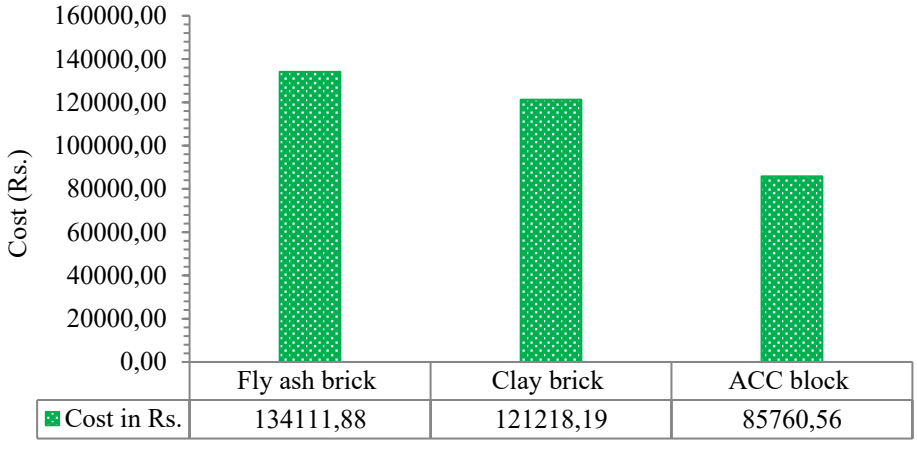


Fig. 17. Total cost for the estimated plan construction

Two windows of 1.5 m x 1.2 m and one door of 1.5 m x 2.1 m dimensions were provided to the room. The height between bottom of slab and top of plinth beam was taken 3.75 m. The plan view of the room has been shown in Figure 16. The detail estimation of the room has been given in Appendix A. The total cost comparison for the estimated plan is shown in the Figure 17. It has been observed from the cost analysis that the total cost for constructing the estimated plan using ACC blocks was 1.56 and 1.41 times lesser than fly ash bricks and clay bricks respectively.

5. Conclusions

The current work presents potentials of AAC block as an alternative in construction sector and compares it with traditional bricks such as fly ash brick and clay brick. AAC blocks of different percentage (0.025 % and 0.05 %) of aluminum powder and the masonry prisms of these AAC blocks as well as fly ash bricks and clay bricks were prepared in the laboratory. Masonry prism is a small-scale assemblage of masonry units and mortar, constructed to represent the material behavior of a larger masonry structure. As because of large pore diameters, AAC blocks exhibit lesser density and weight as compared to traditional bricks, causing it suitable for decreasing the structural self-load. A masonry structure constructed with AAC blocks thus performs well in terms of earthquake resistant compared to a structure prepared with fly ash bricks or clay bricks. The compressive strength of AAC block was observed to be 5.01 N/mm^2 higher than the minimum strength according to IS code. In addition, both the compressive strength and flexural strength of all varieties of masonry prisms were investigated. The compressive strength of a masonry unit was found higher than that of the masonry prisms in all cases. It was found that the AAC blocks contain minimal moisture, thus suitable for the walls subjected to damp environments continuously as compared to the walls prepared by using fly ash bricks and clay bricks. The microstructure analysis performed using SEM equipment, depicted that the inclusion of aluminum powder in the AAC led to formation of a greater number of micro and macro pores. Moreover, it had been observed that the pore size increased with the rising amount of Al powder in AAC. Finally, the study illustrated with an example the cost effectiveness of AAC. With the use of AAC, the construction cost was reduced by 29% and 36% as compared to clay bricks and fly ash bricks respectively.

Acknowledgment

Authors acknowledge the ICFAI University, Tripura and Tripura University for providing the laboratory facilities for this work.

Appendix A: Detail Estimation of The Room

First of all, the calculation has been done for 1 m^3 of brickwork volume.

The size of brick with mortar = 0.24 m × 0.12 m × 0.085 m

The actual size of brick = 0.23 m × 0.11 m × 0.075 m

Numbers of brick required in 1m^3 with mortar = 1/(0.24 × 0.12 × 0.085) = 408 Nos.

The only volume of brick = 408 × (0.23 × 0.11 × 0.075) = 0.7742 m^3

Mortar quantity required = 1 – 0.7742 = 0.2258 m^3

Including 10% wastage of mortar (wet volume) = 0.2258 + (0.2258 × 10/100) = 0.2484 m^3

Dry volume of mortar = wet volume + 33% of wet volume

= 0.2484 + (0.2484 × 33/100) = 0.3304 m^3

Cement Mortar ratio taken = 1:3

Volume of cement = (1×0.3304)/4= 0.0826 m3

Number of cement bags = 0.0826/0.0347 = 2.38

Volume of sand = (3× 0.3304)/4= 0.2478 m^3

Once the material quantity is evaluated, the subsequent step involves calculating the material cost. This is then monitored by adding the labor charges to arrive at the total expense of the room brick or block work. Assumed that the brick or block price = X Rs. The cost analysis for the room brick work shown in the Figure 13 has been presented in the Table A. Hence, the total quantity of the masonry works for that particular room = 11.81 m3.

Table A. Cost Analysis for the room brick work

Cost Analysis for 1 m^3 of brick work	Unit	Quantity	Rate (Rs.)	Amount (Rs.)
Material for 1 m^3 of brickwork				
Bricks/Blocks	Nos.	408	X	408X
Cement for mortar	Bag	2.38	450	1071.00
Sand for mortar	m^3	0.2478	1130	280.01
Labor rate for brickwork per m^3				
Mason (brick layer) 1stclass	Day	0.4	700	280.00
Mason (brick layer) 2ndclass	Day	0.4	620	248.00
Coolie	Day	1.43	550	786.50
Bhisti/ Waterman	Day	0.20	550	110.00
Total				408X + 2775.51
Add for Water charges	@	1.00%		4.08X + 27.76
Total				412.08X + 2803.27
Add GST (multiplying factor)		0.1405		57.90X + 393.86
Total				469.98X + 3197.13
Add for contractor's profit and overheads	@	15%		70.50X + 479.57
Total				540.48X + 3676.70
Add cess	@	1.00%		5.40X + 36.77
Total cost of 1 m^3 of brickwork				545.88X + 3713.47

Fly ash brick price per piece = 14.00 Rs.
Clay brick price per piece = 12.00 Rs.
ACC block price per piece = 6.50 Rs.
Cost of 1 m3 of brickwork using fly ash brick = (545.88 × 14.00) + 3713.47 = 11355.79 Rs.
Cost of 1 m3 of brickwork using clay brick = (545.88 × 12.00) + 3713.47 = 10264.03 Rs.
Cost of 1 m3 of brickwork using ACC block = (545.88 × 6.50) + 3713.47 = 7261.69 Rs.
Total cost of 11.81 m3 of brickwork using fly ash brick = 11.81 × 11355.79 = 134111.88 Rs.
Total cost of 11.81 m3 of brickwork using clay brick = 11.81 × 10264.03 = 121218.19 Rs.
Total cost of 11.81 m3 of brickwork using ACC block = 11.81 × 7261.69 = 85760.56 Rs

References

[1] Wanjule PB, Chandanshiv SB, Aswale S. Brick making in India - history. International Journal of Marketing, Financial Services & Management Research. 2015; 4(11):11-16.
[2] Biswas D, Gurley ES, Rutherford S, Luby SP. The drivers and impacts of selling soil for brick making in Bangladesh. Environmental Management. 2018; 62:792-802. https://doi.org/10.1007/s00267-018-1072-z
[3] Brunel N, Meza F, Ros R, Santibáñez F. Effects of topsoil loss on wheat productivity in dryland zones of Chile. Journal of Soil Science and Plant Nutrition. 2011; 11(4):129-137. https://doi.org/10.4067/S0718-95162011000400010
[4] Joseph P. Brick: sustainability through policy. Urban Research & Practice. 2021; 14(2):201-211. https://doi.org/10.1080/17535069.2020.1819724
[5] Thaickavil NN, Thomas J. Behaviour and strength assessment of masonry prisms. Case Studies in Construction Materials. 2018; 8:23-38. https://doi.org/10.1016/j.cscm.2017.12.007
[6] Danso H, Akwaboah M. Assessment of the quality of burnt bricks produce in Ghana: The case of Ashanti region. Case Studies in Construction Materials. 2021; 15:e00708. https://doi.org/10.1016/j.cscm.2021.e00708
[7] Padalu PKVR, Singh Y. Variation in compressive properties of Indian brick masonry and its assessment using empirical models. Structures. 2021; 33:1734-1753. https://doi.org/10.1016/j.istruc.2021.05.063
[8] Mindess S, Young JF, Darwin D. Concrete, 2nd edition, USA: Pearson Education, 2003: 656 pages.
[9] Hamad AJ. Materials, production, properties and application of aerated lightweight concrete. International Journal of Materials Science and Engineering. 2014; 2(2):152-157. https://doi.org/10.12720/ijmse.2.2.152-157

[10] Matthys JH, Nelson RL. Structural properties of autoclaved aerated concrete masonry. Masonry: Materials, testing, and applications. ASTM STP 1356. West Conshohocken, PA: ASTM, 1999.
[11] Narayanan N, Ramamurthy K. Structure and properties of aerated concrete: A review. Cement and Concrete Composites. 2000; 22(5):321-329. https://doi.org/10.1016/S0958-9465(00)00016-0
[12] Kurama H, Topçu IB, Karakurt C, Properties of the autoclaved aerated concrete produced from coal bottom ash. Journal of materials processing technology. 2009; 209(2):767-773. https://doi.org/10.1016/j.jmatprotec.2008.02.044
[13] Kunchariyakun K, Asavapisit S, Sombatsompop K, Properties of autoclaved aerated concrete incorporating rice husk ash as partial replacement for fine aggregate. Cement and Concrete Composites. 2015; 55:11-16. https://doi.org/10.1016/j.cemconcomp.2014.07.021
[14] Rózycka A, Pichór W. Effect of perlite waste addition on the properties of autoclaved aerated concrete. Construction and Building Materials. 2016; 120:65-71. https://doi.org/10.1016/j.conbuildmat.2016.05.019
[15] Pachideh G, Gholhaki M. Effect of pozzolanic materials on mechanical properties and water absorption of autoclaved aerated concrete. Journal of Building Engineering. 2019; 26:100856. https://doi.org/10.1016/j.jobe.2019.100856
[16] Shams T, Schober G, Heinz D, Seifert S. Rice husk ash as a silica source for the production of autoclaved aerated concrete - A chance to save energy and primary resources. Journal of Building Engineering. 2022; 57:104810. https://doi.org/10.1016/j.jobe.2022.104810
[17] Quan W, Huang W, An Y, Miao X, Chen Z. The effect of natural bamboo fiber and basalt fiber on the properties of autoclaved aerated concrete. Construction and Building Materials. 2023; 377:131153. https://doi.org/10.1016/j.conbuildmat.2023.131153
[18] Lv L., Guo M, Wang P, Zhang B, Liu M, Lin H, Liu C, Zhang X. Preparation of autoclaved-aerated concrete with waste ash of petroleum coke gasification. Materials Research Innovations. 2024; 1-6. https://doi.org/10.1080/14328917.2024.2304953
[19] Balasubramaniam T, Sharan Karthik PM, Sureshkumar S, Bharath M, Arun M. Effectiveness of industrial waste materials used as ingredients in fly ash brick manufacturing. Materials Today: Proceedings. 2021; 45:7850-7858. https://doi.org/10.1016/j.matpr.2020.12.410
[20] Yadav AK, Rawat K. Characterization of fly ash based bricks, alternative to normal clay bricks in building materials and other construction. In IOP Conference Series: Materials Science and Engineering 2021 Mar 1 (Vol. 1126, No. 1, p. 012045). IOP Publishing.
[21] Thakur A, Senthil K. Seismic performance of confined masonry walls with different infill materials: a comparative study. Asian Journal of Civil Engineering. 2024; 25:1587-1599. https://doi.org/10.1007/s42107-023-00863-3
[22] Costa A, Penna A, Magenes G, Galasco A. Seismic performance assessment of autoclaved aerated concrete (aac) masonry buildings. The 14th World Conference on Earthquake Engineering, October 12-17, 2008, Beijing, China.
[23] Sucuoglu H, Siddiqui UA. Pseudo-dynamic testing and analytical modeling of aac infilled rc frames. Journal of Earthquake Engineering. 2014; 18(8):1281-1301. https://doi.org/10.1080/13632469.2014.932723
[24] Kasapgil SM, Binici B, Canbay E. Seismic behavior of AAC infill walls insulated with cementitious lightweight panels in reinforced concrete frames. Engineering Structures. 2021; 248:113215. https://doi.org/10.1016/j.engstruct.2021.113215
[25] Dey P, Deb N, Roy S, Das D. Variations in water quality and their impacts on mechanical properties and microstructure of cement-based building materials. Innovative Infrastructure Solutions. 2023; 8:250. https://doi.org/10.1007/s41062-023-01194-7
[26] Raj A, Borsaikia AC, Dixit US. Manufacturing of autoclaved aerated concrete (AAC): present status and future trends. in Advances in Simulation, Product Design and Development. Springer, Singapore, 2020, pp. 825-833. https://doi.org/10.1007/978-981-32-9487-5_69
[27] Yazal A, Kavas T, Soyal AD. Effects of different autoclaving pressure on mechanical properties of AAC. Ce/Papers. 2018; 2(4):591-594. https://doi.org/10.1002/cepa.829
[28] IS 6441-5 (1972): Methods of Test for Autoclaved Cellular Concrete Products, Part V: Determination of Compressive Strength.
[29] Bhosale, A., Zade, N.P., Davis, R., Sarkar, P., 2019. Experimental Investigation of autoclaved aerated concrete masonry. J. Mater. Civ. Eng. 31(7), 04019109. https://doi.org/10.1061/(ASCE)MT.1943-5533.0002762
[30] Thomson M, Lindqvist JE, Elsen J, Groot C. Chapter 2.5 Characterisation: Porosity of mortars. In Characterisation of Old Mortars with Respect to their Repair; RILEM publications SARL: Paris, France, 2007.
[31] IS 1077 (1992): Common Burnt Clay Building Bricks -Specification.

[32] Munir MJ, Abbas S, Nehdi ML, Kazmi SM, Khitab A. Development of eco-friendly fired clay bricks incorporating recycled marble powder. Journal of Materials in Civil Engineering. 2018; 30(5):04018069. https://doi.org/10.1061/(ASCE)MT.1943-5533.0002259

[33] Ahmad M, Rashid K, Hameed R, Ul Haq E, Farooq H, Ju M. Physico-mechanical performance of fly ash based geopolymer brick: Influence of pressure-temperature-time. Journal of Building Engineering. 2022; 50:104161. https://doi.org/10.1016/j.jobe.2022.104161

Research on Engineering Structures & Materials
www.jresm.org

Research Article

Development and characterization of carbon nanotube/green titania as potential hybrid nanofiller in nanofluid for machining carbon fiber reinforced plastics

Sunday Albert Lawal [1,a], Rasaq Olawale Medupin [*,2,b], Victor Chiagozie Nwachukwu [1,c], Uzoma Gregory Okoro [1,d], Oyewole Adedipe [1,e], Joseph Abutu [3,f], Benjamin I. Attah [4,g], Jimoh Oladejo Tijani [5,h], Ambali Saka Abdulkareem [6,i]

[1]*Dept. of Mechanical Eng., Federal University of Technology, Minna, 920101, Nigeria*
[2]*Dept. of Mechanical Eng., Federal University Lokoja, Lokoja, 260101, Nigeria*
[3]*Dept. of Mechanical Eng., Taraba State University, Jalingo, 660213, Nigeria*
[4]*Dept. of Mechanical Eng., African University of Science and Technology, Abuja, 900107, Nigeria*
[5]*Dept. of Chemistry, Federal University of Technology, Minna, 920101, Nigeria*
[6]*Dept. of Chemical Engineering, Federal University of Technology, Minna, 920101, Nigeria*

Article Info

Article History:

Received 15 Aug 2024
Accepted 27 Nov 2024

Keywords:

Synthesis;
Characterization;
Cabon nanotube;
Green titania;
CFRPs;
Nanocomposites

Abstract

In the industry, removing heat from cutting zones during machining presents a major challenge. Consequently, there is increased demand for reasonably priced and environmentally safe cooling agents during carbon fiber reinforced polymers (CFRPs) machining for high-performance applications. This work synthesized and characterized green titania (TiO_2) and carbon nanotubes (CNTs) to create TiO_2/CNTs nanocomposites (NCs) with varying proportions (9:1, 7:3, and 5:5). To investigate the NCs' stability as potential fillers in base oils for creating nanofluids for machining carbon fiber reinforced plastics (CFRPs), a variety of analytical techniques was used to characterize them, including Brunauer-Emmett-Teller (BET), high resolution SEM/EDS, high resolution TEM, XRD, and FTIR. The FTIR spectra of the NCs indicate absorption peaks that are consistent with C=C and Ti-O bonds, generating peaks allocated to Ti-O-C and C-O bonds. Because primary peaks of CNTs and TiO_2 overlap, the peaks attributed to CNTs are hardly visible and those of anatase are easily identifiable. Due to their larger surface area, pore volume, and stability as a nanosuspension, TiO_2/CNTs (5:5) offers significant benefits over other NCs for heat removal: here lies the novelty of this research article utilizing green titania. The challenges associated with uncontrollable agglomeration of individual NCs are addressed by these hybrid NCs. Thus, it is concluded that TiO_2/CNTs NCs are potential reinforcing fillers in base oils for machining.

© 2025 MIM Research Group. All rights reserved.

1. Introduction

For many years, carbon fiber reinforced polymers, or CFRPs, have been recognized as essential materials for a wide range of engineering applications. Their current prominence in manufacturing technology is a result of their exceptional performance in the fields of aircraft, luxury consumer goods, and national defense [1]. Their enhanced mechanical qualities and increased competitiveness as high-performance materials in automotive and structural applications are attributed to the reinforcing strength of carbon fibers. Nevertheless, as a material with comparative

*Corresponding author: rasaq.medupin@fulokoja.edu.ng
[a]orcid.org/0000-0002-2818-9146; [b]orcid.org/0000-0002-9822-041X; [c]orcid.org/0009-0004-7076-1283; [d]orcid.org/0000-0002-4798-1876; [e]orcid.org/0000-0002-1840-7031; [f]orcid.org/0000-0003-1494-9201; [g]orcid.org/0009-0008-6877-7648; [h]orcid.org/0000-0002-1707-0078; [i]orcid.org/0000-0003-0049-3186
DOI: http://dx.doi.org/10.17515/resm2024.399ma0815rs

benefits, CFRP machining has not gotten nearly as much attention as it should until lately [2,3]. Scholars who have examined the machining of CFRPs using traditional cutting fluids have criticized the difficulties involved and have called for additional research to unravel the uncharted waters [4-6]. It has been demonstrated that the majority of conventional cutting fluids have continually failed to maintain their relevance in the present efforts to comply with SDG #12 of the United Nations (UN) on responsible consumption and production.

The degree of process success regarding tool life, cutting speed, and surface smoothness is impacted by the prompt and simple removal of heat from cutting zones during machining [7]. In pursuit of sustainable green manufacturing, Lawal et al. [8] reported on the preference for bio-oil-based cutting fluids to offer answers to various health problems connected with synthetic cutting fluids. While both vegetable and synthetic oils serve as effective temporary coolants during machining, the possibility of a chemical imbalance initiating corrosion process raises many concerns in today's eco-aware society [9]. Because of this, nanofluids are now being developed to use the quality and huge surface areas offered by nanoparticles (NPs) to address difficulties related to rapid heat removal from the tool/workpiece interface. This is expected to speed up heat evacuation and assist in lowering the amount of fluid required for a certain machining procedure [10]. Environmental pollution is effectively addressed in the same way that cost is adequately managed since both the volume of cutting fluids required and the volume released into the surrounding environment after usage are significantly decreased [11-13]. The Minimum Quantity Lubrication (MQL) technique was developed to further optimize machining settings in accordance with this principle [14]. MQL is a more economical and environmentally beneficial solution than flooding and the use of dry cutting fluid [15]. In the context of sustainable manufacturing, this machining procedure is congruent with more ethical and cleaner production.

But more recently, a better method of carrying out the complementary tasks of lubrication and heat removal during machining has been introduced, and the scientific community is now paying greater attention to it [16]. The fluid lubricates the cutting interface, and the nanofillers transfer heat away from the cutting zone, resulting in a smooth and quick machining process that improves surface finish and prolongs tool life [17,18]. This is referred to as nMQL, or nanofluid-MQL. In a recent study, Kumar et al. [19] referred to nMQL as the novel chapter in sustainable machining. Low cutting forces are produced by the method of spraying nanofluid mist over the tool-work contact during machining, which changes, sliding into rolling friction between the tool pieces and drastically lowers friction coefficient [20–23]. Assessment research on specific machining parameters under dry and MQL conditions was carried out by Venkatesan et al. [24]. Examination of turning operations under nMQL conditions demonstrates that MQL inhibits the wear mechanism, a typical shortcoming of dry machining. This suggests that using nMQL for sustainable machining of challenging materials for industrial purposes is a positive move [25]. While also investigating the approach, Gao et al. [16] observed that the optimization of the nanofluids under high pressure air flow addresses the challenge of unsatisfactory capability of MQL to transfer of heat in the machining area and advances the lubrication performance of the boundary between the tool and the metals. While acknowledging the likelihood of taking advantage of different properties of NPs to form hybrid nanofluids, Gao et al. [26] submitted that using nMQL technique, processing impairment such as resin covering, multi-fiber block pull-out, and pits can be lowered. Therefore, it can be concluded that nMQL is the future of CFRPs machining.

As good as the nMQL technique appears to be, there are a few issues with the hybrid nanofluid production process. Standard nanosuspension production is still a long-standing procedural difficulty. Because of the van der Waals interactions between individual NPs, Abubakre et al. [27] concurred with one of the previous research studies by Urmi et al. [28] regarding the challenges in achieving lasting equilibrium of hybrid nanofluids, which is a condition for hybrid nanofluid applications. This characteristic of the nanofluids is significant since it enhances the way it behaves thermally when used. As a result, solving the stability problem is essential to performing high-quality machining. According to the literature, if the length of each action is taken into consideration, then external force, stirring, and ultrasonication can be used to disrupt the bonds holding NPs together [29,30]. Therefore, there is still a great vacuum in the literature about the subject of time, particularly when the major goal of the exercise is commercialization.

Therefore, considering how essential NPs can be to achieving exceptional clean machining using the nMQL approach, the procedures involved in producing NPs should receive all the attention they require. In light of this, the objective of this work is to synthesize and characterize high-quality carbon nanotubes (CNTs), green titanium dioxide (TiO_2), and their nanocomposites (NCs) in order to develop hybrid nanofluids that may be used to machine CFRPs.

2. Materials and Methods

2.1. Materials

Chemicals with percentage purity ranging between 95% and 99.98% were used in this work. They were utilized without further purification after being obtained from Sigma Aldrich, a renowned first-class distributor of chemicals in the world. The materials for the studies comprise distilled water, extract from *Terminalia catappa*, sodium hydroxide (NaOH) pellets, methanol (CH_3OH), titanium (IV) isopropoxide ($Ti(OCH(CH_3)_2)_4$, hydrochloric acid (HCl), and sodium dodecyl sulfate (SDS). A few of the tools used are an electric weighing scale, an ultrasonic oscillator (version KQ3200DB), a muffle furnace, a UV-Visible spectrophotometer (UV-1800), a viscometer (NDJ-5S), a 78 HW-1 steady temperature mixer, and other necessities.

2.2. Materials

2.2.1 Production of Green TiO_2 Nanoparticles

Tables 1 and 2 illustrate how an extract of *Terminalia catappa* was used for biosynthesis of titania NPs through the green method. Using a magnetic stirrer, a known volume of titanium isopropoxide was measured and added to a 250 cm^3 beaker holding a predetermined volume of plant extract. Using a solution of NaOH and HCl, the mixture was continuously stirred until the required pH was reached. After that, the mixture was cleaned with deionized water, oven-dried for 12 hours at 105 ^oC, and then calcined for three hours at 450 ^oC. In Fig. 1, the process is depicted in detail.

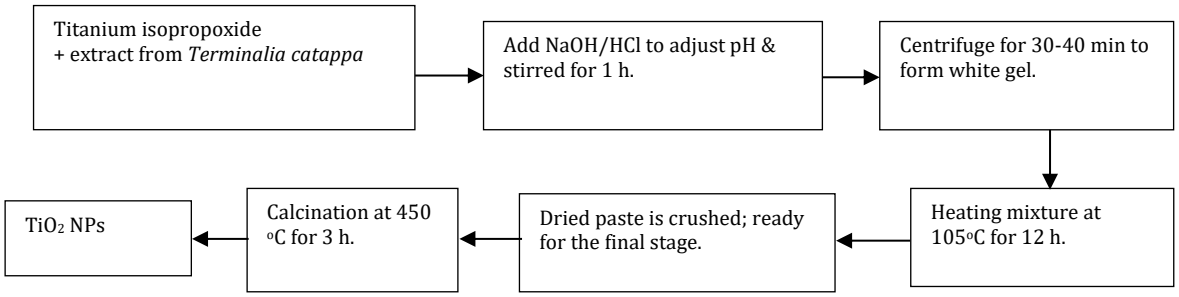


Fig. 1. Procedure for biosynthesis of titania nanoparticles

Table 1. 2^4 Factorial design matrices

Coded value	Volume of extract (cm^3)	Volume of precursor (cm^3)	Mixing time (min)	pH
– Level	50	5	100	2
+ Level	80	8	200	12

Table 2. 2^4 Experimental runs for biosynthesis of titania NPs

Run	Volume of extract (cm^3)	Stirring period (min)	Volume of precursor (cm^3)	pH
1	80	150	8.0	7
2	65	150	5.0	12
3	65	100	6.5	12
4	65	150	8.0	2
5	65	100	5.0	7

6	50	100	6.5	7
7	65	200	6.5	12
8	80	200	6.5	7
9	80	150	6.5	12
10	50	200	6.5	7
11	80	100	6.5	7
12	80	150	6.5	2
13	65	200	6.5	2
14	50	150	8.0	7
15	65	200	8.0	7
16	65	150	6.5	7
17	65	100	8.0	7
18	50	150	5.0	7
19	65	150	5.0	2
20	65	100	6.5	2
21	50	150	6.5	12
22	80	150	5.0	7
23	65	150	8.0	12
24	50	150	6.5	2
25	65	200	5.0	7

2.2.2 Carbon Nanotube Synthesis

After dissolving 14.53 g of Ni and 20.2 g of Fe in 100 ml of distilled water, 10 g of kaolin was introduced. The mix was then stimulated for one hour at 200 rpm using an orbital shaker. Before being decanted, the mixture was allowed to cool and then dried for 12 hours at 120 °C in the oven. A 150 μm sieve was used to screen and grind the dried mixture. After that, the fine powder (catalyst) was removed from the mixture by calcining it for 16 hours at 500 °C. In order to prevent agglomeration, which could impair the interaction between the carbon source and the surface mixture, the dried catalyst was then grounded. Subsequently, acetylene, the carbon source, was broken down in a cylindrical quartz reactor that was located horizontally inside a furnace to synthesize carbon nanotubes (CNTs). The reaction temperature, gas flow rates, and heating rate were all properly managed thanks to the electrical controls inside the furnace.

A thin layer of 1.0 g catalyst was applied in an 11 cm by 2.6 cm quartz boat and located midway in the quartz tube. Heat was supplied to the furnace at 10 °C/min, and at the same time, 30 ml of argon (Ar) was fluxed through the system. This was done to guarantee a furnace environment devoid of inert contaminants and to prevent oxidation, both pre- and post-reaction. Argon flow rate was raised to 230 ml/min at 750 °C. After that, C_2H_2 was added at 150 and 200 ml/min flow rates to start the growth of CNTs. Following a 90-minute reaction time, the C_2H_2 flow was stopped while the furnace cooled to room temperature and argon was continuously passed through the furnace at a rate of 30 milliliters per minute. In order to collect the catalyst and carbon deposit, the boat was removed from the reactor. CNTs yield (%) was computed using Eq (1) as a basis for the relationship.

$$CNTs\ yield(\%) = \frac{W_{product} - W_{catalyst}}{W_{catalyst}} \times 100\ \% \quad (1)$$

Using a 2.0 g measure of CNTs, the support material (kaolin) and the transition metal (Fe-Ni) catalysts were removed from a beaker filled with 200 ml of 3M NaOH solution. After using a magnetic stirrer for three hours, the solution was left to settle. To guarantee a neutral pH, the mix

was then sieved and rinsed in distilled water. After that, it was dried for 24 hours at 120 °C. After being finally sonicated, the CNTs were stored on the shelf for further usage.

2.2.3 Synthesis of Nanocomposites

In a ceramic mortar, a known quantity of CNTs and TiO_2 (TiO_2/CNTs) at various ratios were weighed, and a pestle was used to adequately crush the material. Prior to analysis, the mixes for TiO_2/CNTs at ratios of 9:1, 7:3, and 5:5 were compounded. TiO_2/CNTs at 9:1, 7:3, and 5:5 ratios were disseminated in propanol and sonicated until a homogenous solution was formed in order to create TiO_2/CNTs NCs. Concurrently, the TiO_2 was dissolved in an appropriate solvent and introduced in droplets to the distributed CNTs while sonication was carried out for a prolonged period, immediately succeeded by magnetic stirring. The suspension was poured into a round-bottom flask and heated to 200 °C in an oil bath while being stirred magnetically. The mix was then filtered, left to lose heat naturally to ambient condition, and repeatedly cleaned with ethanol and distilled water. The final composite was then calcined at 550°C and dried at 100°C.

2.3 Characterization of Nanomaterials

2.3.1 X-Ray Diffraction (XRD)

Bruker AXS D8 Advanced X-ray diffractometer, laden with Cu Kα radiation, was used to examined the phase and crystallite sizes of the nanoparticles. The diffractograms were obtained in the two-theta range of 20 – 90° with the powdered sample put on an aluminum sample holder. Next, phase identification was looked into.

2.3.2 High Resolution TEM

The samples were studied using Zeiss Auriga HRTEM to understand their morphology and structure. After the synthesized sample (0.02 g) was completely dispersed, it was floated in 10 cm^3 of methanol and ultrasonicated. Using a micropipette, two drops of the nanosuspension were applied to a perforated carbon lattice. Later, this was exposed to photo light to dry.

2.3.3 High Resolution SEM and EDS

Zeiss Auriga HRSEM in conjunction with EDS was deployed to examine the morphologies of the nanomaterials. Using the Quorum T15OT Analyzer, the sample (0.05 mg) was spread on carbon adhesive tape and sputter-coated with Au-Pd in five mins. After the coated sample was placed within the sample holder, imaging was performed at 5 kV with a high electron tension. The constituent elements of the samples were ascertained by operating the EDS at EHT for 20 kV, which is how the constituting elements of the materials were found.

2.3.4 Brunauer-Emmett-Teller (BET)

To eliminate any remaining water and volatile chemicals from the samples, a predefined mass (0.1 g) was first degassed for four hours at 95 °C. Plotting volume adsorbed against relative pressure yielded the BET surface area and pore size spread. Using Scherrer Debye equation (Eq 2), average crystallite size was calculated using total width at half maximum of the corresponding anatase peak. An acidic medium yielded the smallest confirmed crystallite size (Table 2: run 19).

$$D = \frac{k\lambda}{\beta \cos\theta} \tag{2}$$

where D is crystallite size, k represents shape factor (0.94), λ signifies wavelength of the X-ray source, and β is the full width at half maximum (FWHM). Fig 2 illustrates the crystallite sizes of some selected TiO_2 at varied runs.

3. Results and Discussion

3.1 Characterization of Optimized Materials and Their Nanocomposites via XRD

Tables 1 and 2 display the factorial design of 2^4 factorials and experimental runs, which were utilized to examine the impact of synthesis parameters on NP yield, including mixing duration, pH, precursor size, and volume of the extract. Cu Kα radiation was used as the X-ray source for the XRD examination, which yielded the crystallite size of the investigated TiO_2. As shown in Fig 3, the phase configuration according to estimated peak intensities was anatase.

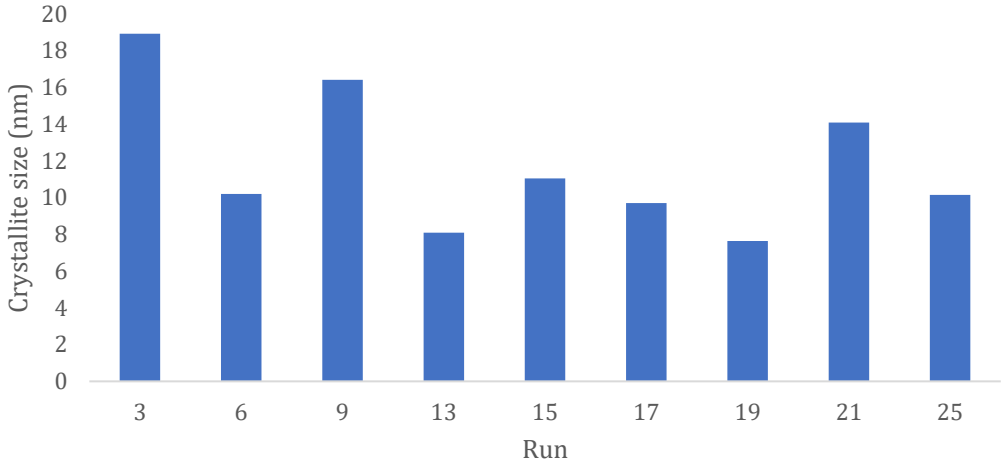


Fig. 2. Crystallite size of selected TiO2 at varied runs

The XRD data of individual material and their composites at various ratios of compounding are illustrated in Fig 3. The patterns indicate that TiO_2 is primarily composed of anatase peaks at 2θ = 25.2°, 37.7°, 48°, and 54°. Because of the anatase phase's enormous surface area, surface chemistry, and redox characteristics, catalytic activities occur there [31]. The XRD patterns of CNTs are displayed in Fig 4, which indicates that the sample exhibits two distinct peaks at approximately 31.6° and 52.1°. These peaks are indexed to the graphite reflections of (002) and (100), respectively. The peaks attributed to CNTs are hardly visible for the TiO_2/CNTs NCs (see Fig 4(A)), but anatase peaks are readily detected [31].

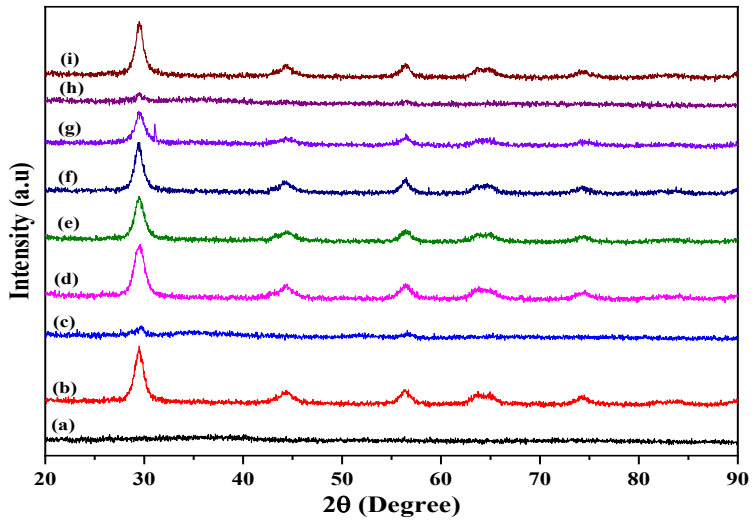


Fig. 3. XRD of TiO2 NPs for runs in Table 2

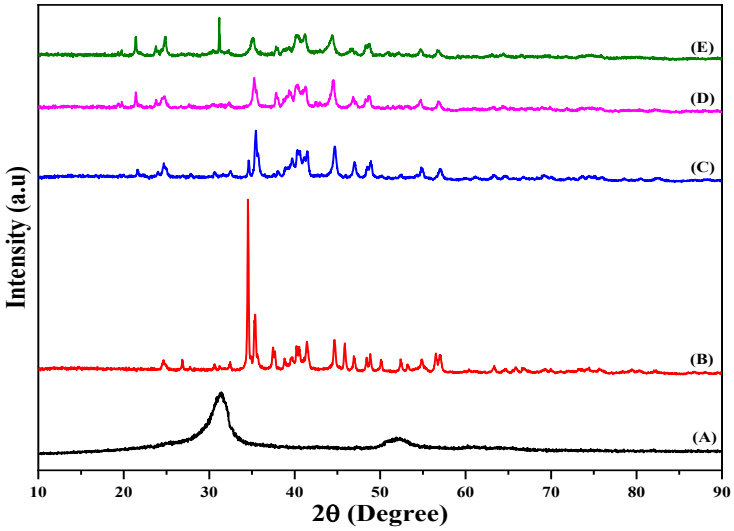
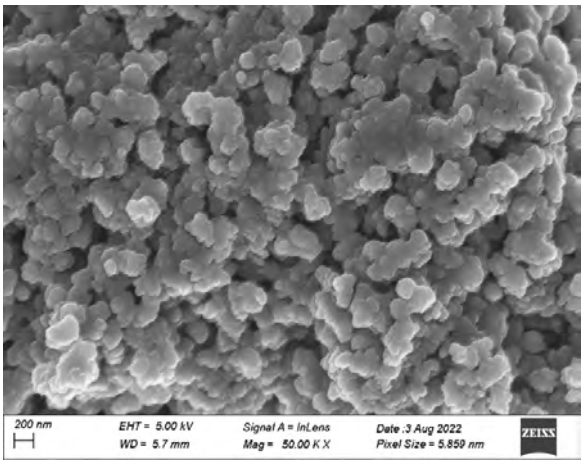


Fig. 4. XRD of CNTs (A), TiO2 (B), TiO2/CNTs (9:1; 7:3; 5:5)

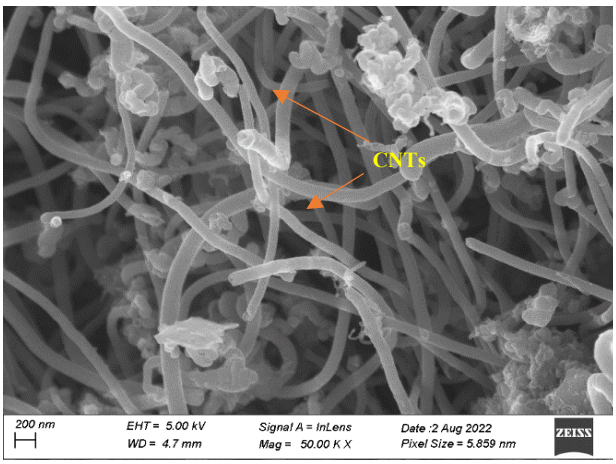
The possible cause of this scenario could be the overlap between the TiO_2 and CNT major peaks. This could also be explained by low concentration of CNTs and the strong intensity of TiO_2 peaks. Notably, with CNTs, the breadth of the XRD peaks at 35.03° and 57.5° was somewhat widened. This procedure suggests significant alteration of the crystalline size of TiO_2-based NCs by the addition of CNTs.

3.2 HRSEM of Individual Materials and Their Nanocomposites

HRSEM pictures of individual materials and their nanocomposites at various ratios are shown in Fig 5. TiO_2 NPs form a fleck-like structure in Fig 5(a) and alternatively, Fig 5(b) reveals HRSEM image of tube-like CNTs with diameters ranging from 20 to 30 nm. The magnified images in Fig 5(c-e) establish uniform distribution of TiO_2 NPs on the reactive sites provided on the treated CNTs surfaces. CNTs are hardly identified in consistency with the NC's content ratios, prompting homogeneous dispersion of TiO_2 on CNTs in the NC (9:1) as seen in Fig 5(c). When comparing the TiO_2 NPs and their NCs, the HRSEM picture of the NPs shows gaps or voids which may indicate inter-particulate porosity. The morphologies observed for the NCs could have resulted from the intermolecular interaction between TiO_2 and defect sites on the surface of the CNTs.



(a)



(b)

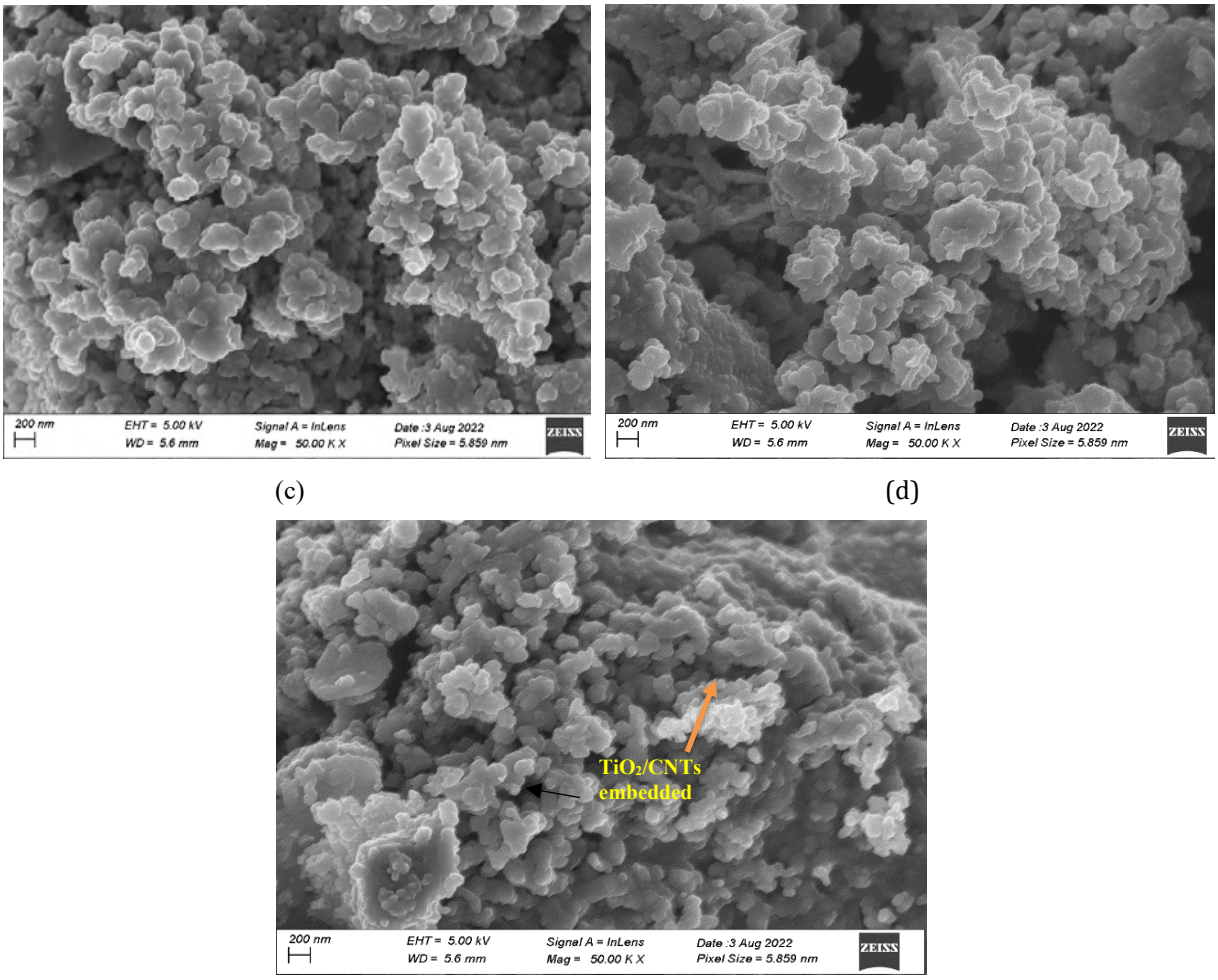


Fig. 5. (a) HRSEM pictures of TiO_2, (b) CNTs, (c)TiO_2/CNTs (9:1), (d) (7:3), and (e) (5:5)

3.3 HRTEM of Individual Materials and Their Nanocomposites

HRTEM pictures of TiO_2, CNTs, and varied NCs ratios are shown in Fig 6. The TiO_2 NPs are clearly spherical, as shown in Fig 6(a), and the CNTs that are formed are multi-walled, hollow, and have several inner diameters, as seen in Fig 6(b). The HRTEM pictures of NCs illustrated in Fig 6(c-e) show homogeneous dispersion with separate CNTs coated in TiO_2 and no aggregates between the TiO_2 and CNTs that resemble jams. While the TiO_2 distribution of the NCs steadily decreases, the mean size distribution of TiO_2 is 14.02 nm. The joining of the titania's hydroxyl group with the surface chemical groups of the CNTs may have caused this event by creating additional reaction sites during the CNTs' acid pretreatment. The visible locations of grain development for nanoparticles in the NCs are the surface flaws on the CNTs. On the other hand, as Fig 6(e) illustrates, adding more CNTs to TiO_2/CNTs NCs may decrease the magnitude of the crystallized TiO_2 on the CNTs and hence prevent the agglomeration of TiO_2 NPs. The polycentric ring of TiO_2 as witnessed in the EDS spectra is supported by the diffraction for anatase; nonetheless, the corresponding SAED patterns are characteristic of MWCNTs (Fig 7). The XRD analysis verified these as well. Additionally, the NCs exhibit polycentric rings with various reflection planes that resemble titania distributed in carbon nanotubes and create Ti-O-C and Ti-O-Ti networks. Ti, C, and O are the main constituents of the NCs, according to the EDS spectra (Fig 6), along with trace elements from kaolin catalysts and Ni salt. The Ti content in the composed NCs came after the mass ratio of the composites, according to the EDS study.

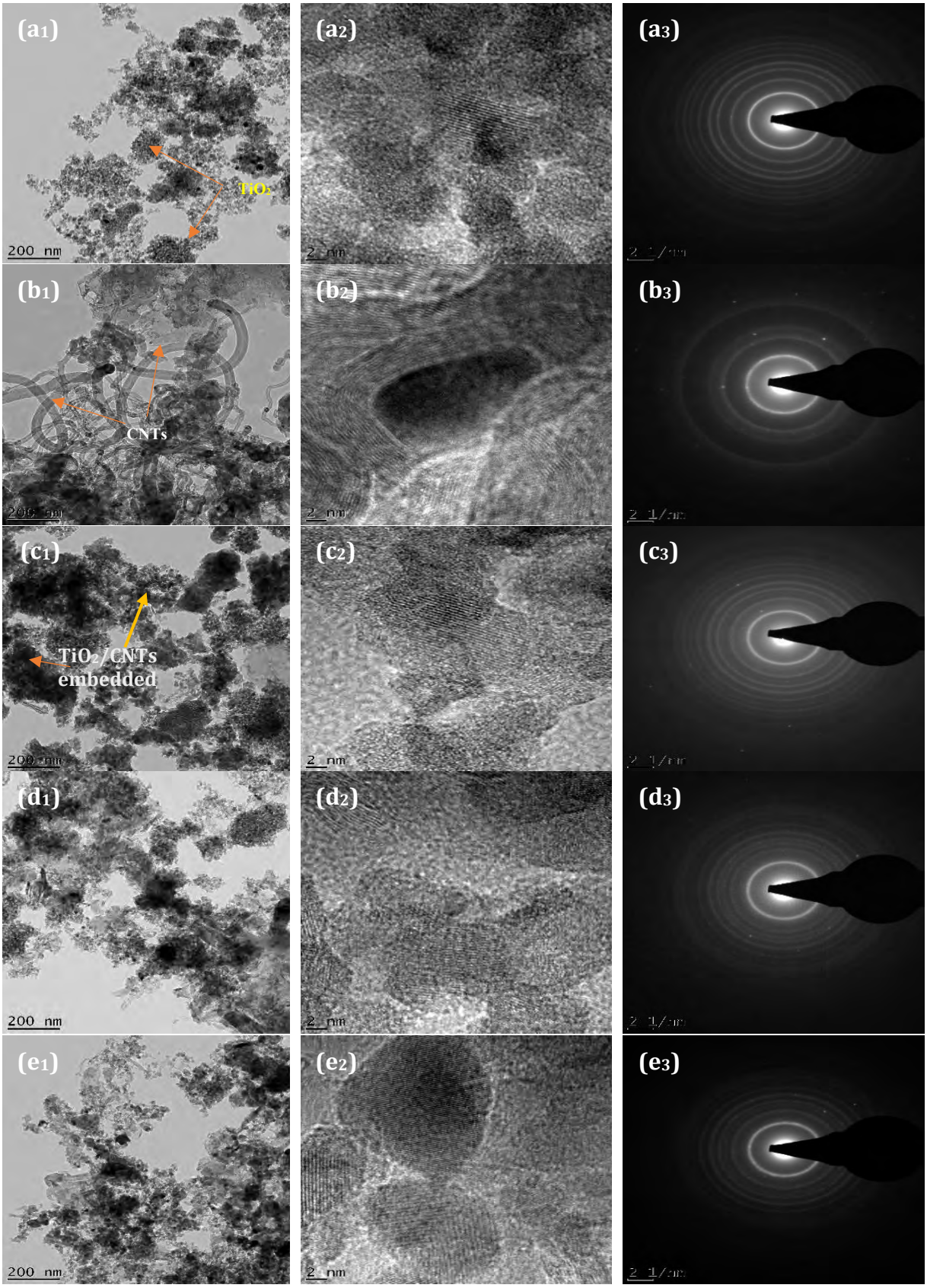
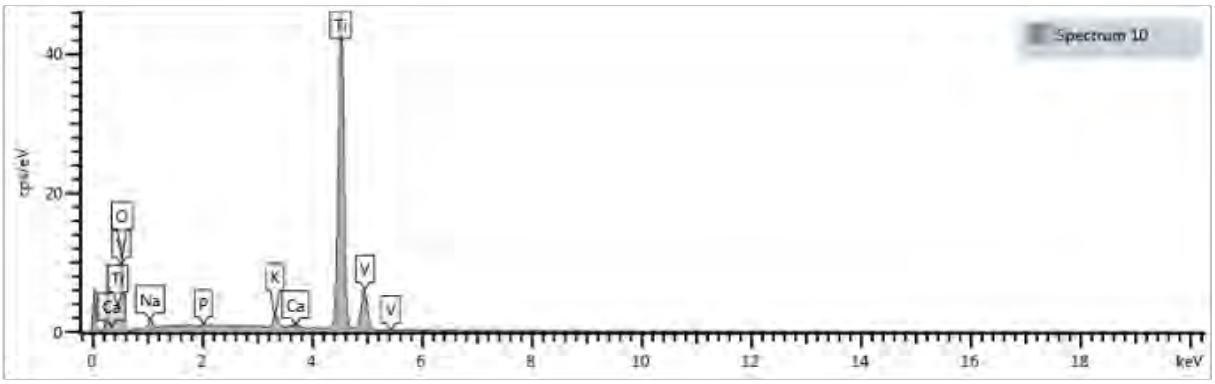
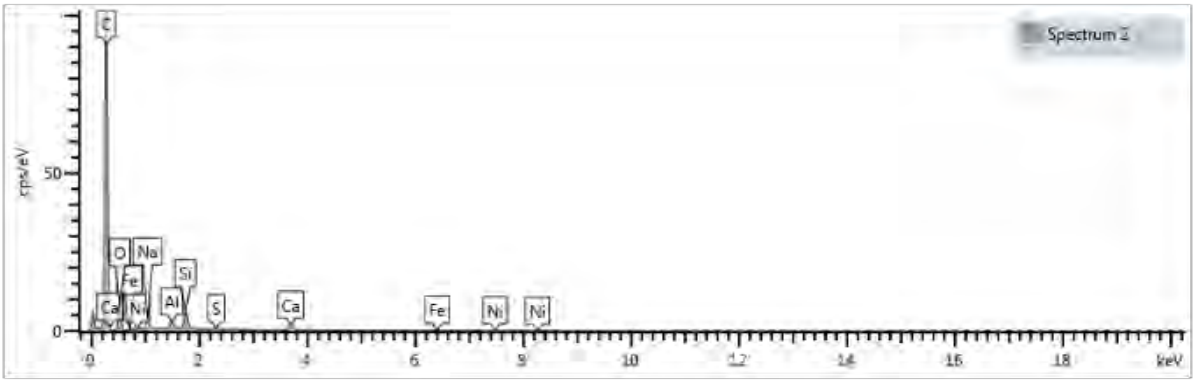


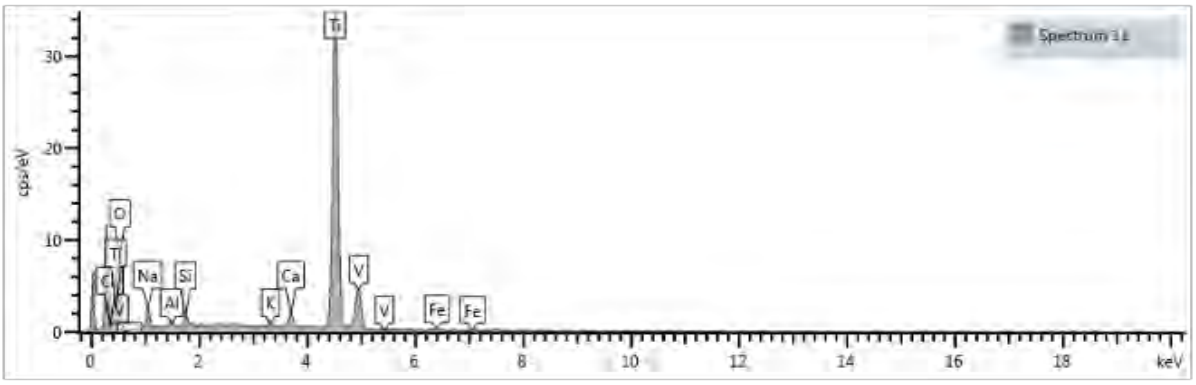
Fig. 6. (a) HRTEM images of TiO_2, (b)CNTs, (c)TiO_2/CNTs (9:1), (d) TiO_2/CNTs (7:3), (e)TiO_2/CNTs (5:5)


Spectrum 10
cps/eV
keV
O
Ti
Na
P
K
Ca
V

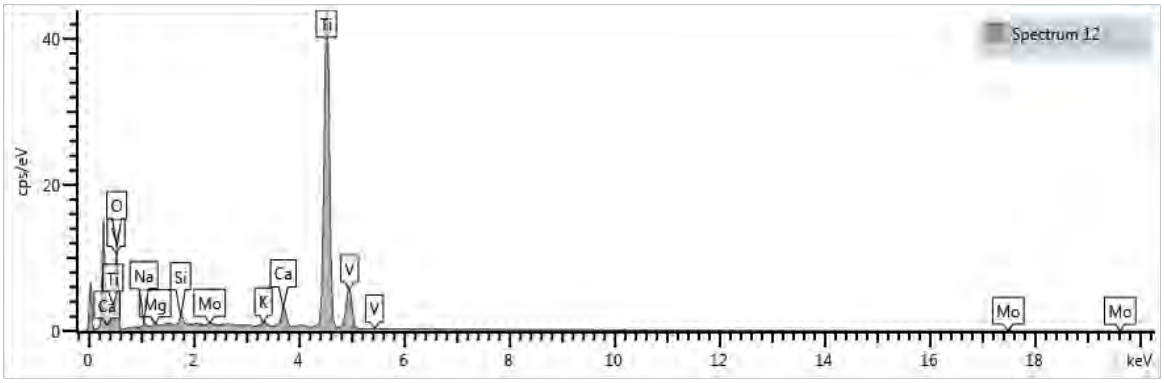
(a)


Spectrum 2
cps/eV
keV
C
O
Na
Fe
Si
Ca
Al
S
Ni

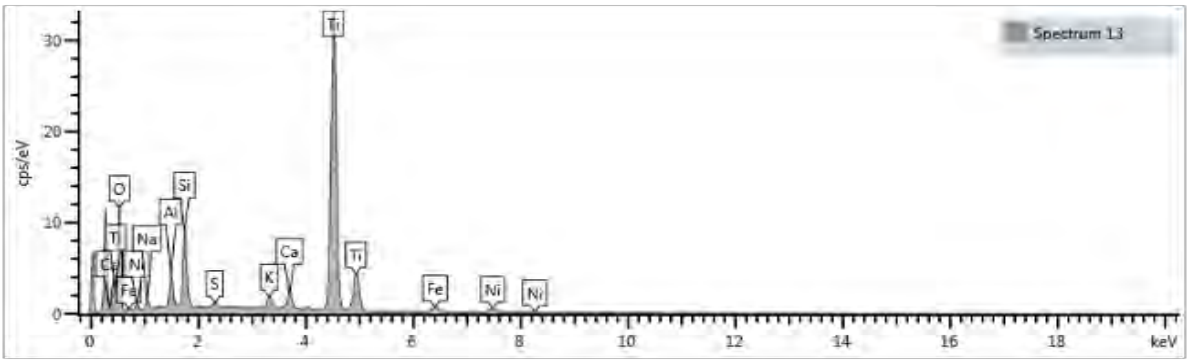
(b)


cps/eV
keV
O
Ti
Na
Si
Al
Ca
K
V
Fe

(c)


Spectrum 12
cps/eV
keV
O
Ti
Na
Si
Ca
Mg
Mo
K
V

(d)



(e)

Fig. 7. (a)EDS results of TiO_2, (b)CNTs, (c)TiO_2/CNTs (9:1), (d) (7:3), (e) (5:5)

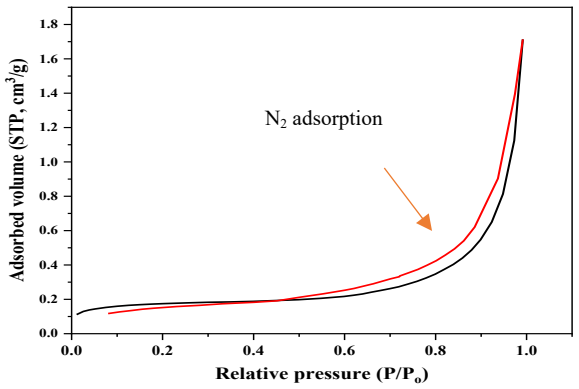
3.4 BET of Individual Materials and Their Nanocomposites

The N_2 adsorption-desorption isotherms of CNTs, TiO_2, and NCs are displayed in Fig 8, and Table 3 displays the BET-specific surface area, pore size, and pore volume. It is possible to identify the isotherms as intermediate cases between hysteresis loops of type I, where the two branches are almost vertical and parallel of a range of gas uptake, and type IV, where the branches stay virtually horizontal and parallel over a wide P/Po range, owing to the N_2 adsorption-desorption isotherm of TiO_2 [32]. The isotherm recognized for CNTs is type III isotherm (Fig 8(a)).

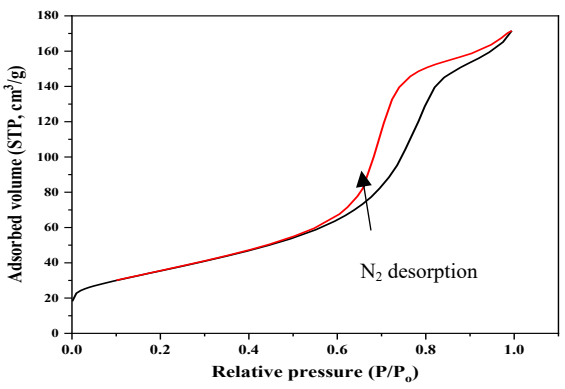
Table 3. Summary of BET results of individual materials and their nanocomposites

Sample	Surface area (m^2/g)	Pore size (nm)	Pore volume (cc/g)
CNTs	0.65	16.79	0.00276
$gTiO_2$	127.62	6.648	0.296
CNTs/$gTiO_2$ (1:9)	57.84	7.637	0.155
CNTs/$gTiO_2$ (3:7)	71.19	8.412	0.195
CNTs/$gTiO_2$ (5:5)	103.42	7.451	0.259

Type II isotherms, which can be linked to the merger of type I and type IV loops, are the isotherms originating from the NCs [33]. This can be explained by the fact that, in comparison to both TiO_2/CNTs (9:1) and TiO_2/CNTs, the isotherm shown in Fig 8(e) is closer to type II. The nanomaterials' BET surface areas are shown in Table 3. Compared to CNT, TiO_2 has a much bigger surface area, which suggests superior textural qualities and a greater variety of uses. Additionally, as TiO_2 falls in relation to the samples' CNT concentrations, the NCs' surface areas rise. The severing of TiO_2 NPs brought on by the inclusion of CNTs may be responsible for these phenomena. Moreover, mesoporous nanomaterials that may facilitate mass transfer are reflected in the pore sizes [34]. The NCs' pore volume increased as the CNT concentration increased, following the same trend as the surface area. This is understood by TiO_2's continuous filling of the reaction sites on CNT walls, according to previous study by Medupin et al. [35].



(a)



(b)

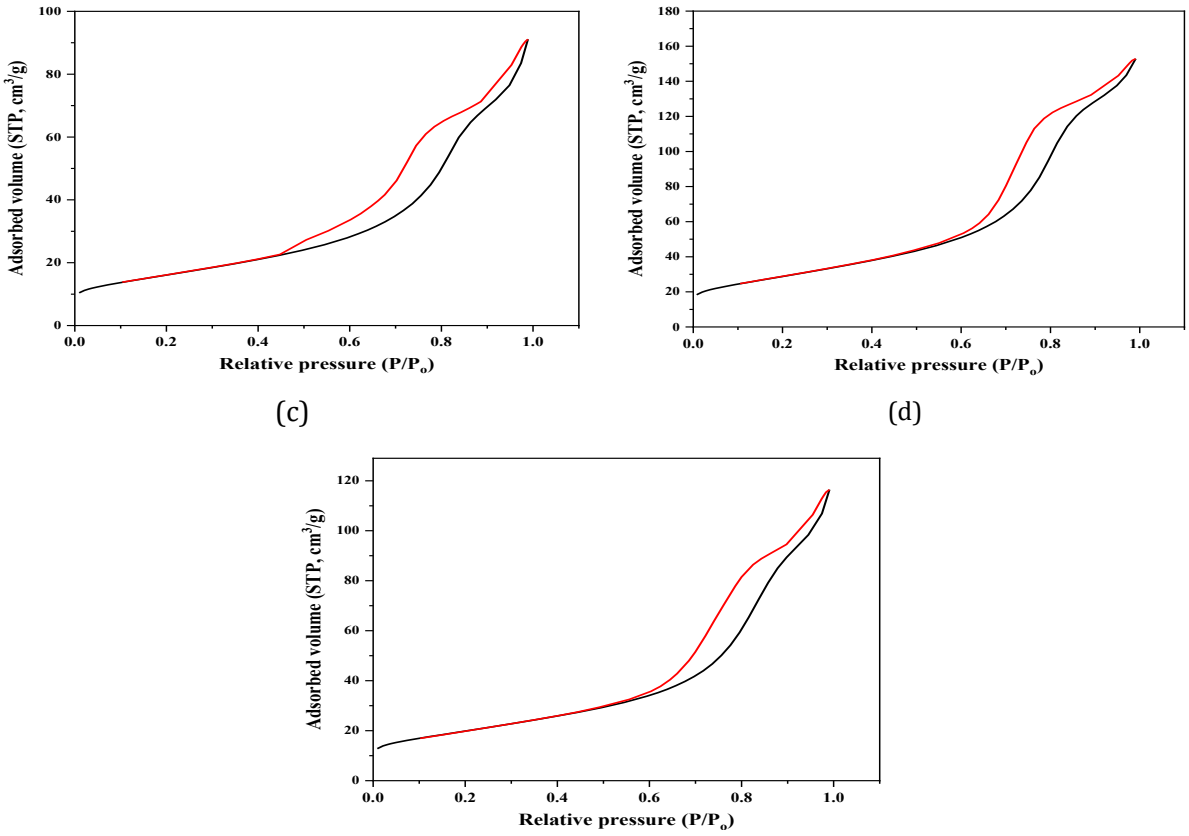


Fig. 8. (a)N_2 Adsorption-desorption curves of CNTs, (b)TiO_2, (c)TiO_2/CNTs (9:1), (d) (7:3), (e) (5:5)

3.5 FTIR of Separate Materials and Their Nanocomposite

FTIR helps to detect the characteristic vibration of chemical bonds between atoms of the nano components. Specific functional groups that indicate the presence and type of bonding in the nanocomposite can be identified by analyzing the adsorption peaks. The spectra in this research are recorded, then displayed in Fig 9. The bending vibration of adsorbed water molecules is responsible for the absorption at around 1630 cm^{-1} (Fig 9(a)).

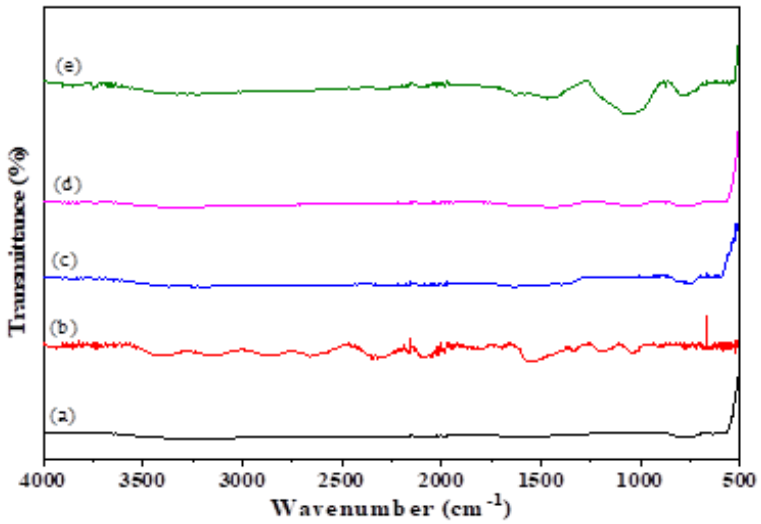


Fig. 9. (a)FTIR spectra of TiO_2, (b)CNTs, (c)TiO_2/CNTs (9:1), (d) (7:3), (e) (5:5)

The TiO_2 sample's broad band at 950 cm^{-1} is associated with the distinctive vibration of the Ti–O–Ti network. The CNTs (Fig 9(b)) exhibit C–C stretching bonds at 1650 cm^{-1}, which are identified as CNT modes. The peak at 1705 cm^{-1} is linked to the carboxyl group's C=O stretching, which is a feature of -COOH group [36–38]. The peaks at 3500–3300 cm^{-1} show a significant concentration of hydroxyl and carboxyl groups and correlate to their –OH stretching bonds. The composites include peaks consistent with C=C and Ti-O links, producing peaks allocated to Ti-O-C and C-O bonds, according to the FTIR spectra for the NCs, which are displayed in Fig 9(c, d, and e) [39]. These findings show that the growth produced a heterojunction at the gTiO_2 and CNT surfaces, creating interfacial connections in the matrices [34].

5. Conclusions

In conclusion, this research successfully synthesized and characterized green titania (TiO_2) and carbon nanotubes (CNTs) to develop TiO_2/CNTs nanocomposites with potential as hybrid nanofillers in nanofluids for machining carbon fiber reinforced plastics (CFRPs). Its findings demonstrate that carbon nanotubes (CNT) and green titania (TiO_2) nanocomposites could be dependable filler options for blending hybrid nanofluids for machining operations. After the analyses of the produced CNTs, TiO_2, and their NCs, it was discovered that the NPs were in good condition to be used as filler materials in both organic and inorganic base oils, for the creation of nanofluids intended for CFRP machining. The TiO_2 (particles) are observed to fill the sites formed after the CNTs (fibre) were purified and functionalized, which lessens the inherent difficulty of formulating the nanosuspension system. Three different nanofiller ratios were investigated under the same conditions, and it was found that adding fillers could significantly improve the stability of the nanofluids for machining application, with TiO_2/CNTs (7:3) NCs being the most stably dispersed of the three as could be noticed with the HRTEM micrographs. Agglomeration tendency, which has been identified by many earlier authors as the innate challenge with CNT system, is significantly reduced as TiO_2 nanoparticles occupy certain sites on the walls of the CNTs and break the van der Walls attractions between individual CNTs. The clustering merely shows that the TiO_2 in the suspension is drawn to the CNTs' wall apertures. However, the TiO_2/CNTs (5:5) NC has a distinct benefit over other NCs in that it could remove heat faster from the machining zone, according to the results of HRSEM/EDS, HRTEM, XRD, and BET. This is because it has the largest surface area for heat removal, the largest pore volume, and, indeed, the most stable nanosuspension of all the NCs studied in this research article. It is, therefore, anticipated that the hybrid nanosuspension that is produced after this study's successful synthesis, characterisation, and optimization will be useful as filler materials of improve the capacity of base oils to remove heat from cutting zones during machining operations. This work paves the way for further advancements in the use of nanocomposites in eco-friendly machining fluids, with broader implications for sustainable industrial practices.

Acknowledgement

The authors thankfully recognize the funding received from the TETFund, Nigeria, through the NRF with grant number: TETF/ES/DR&D/CE/NRF2020/SETI/113/VOL.1 for funding this research.

References

[1] Zheng H, Zhang W, Li B, Zhu J, Wang C, Song G, Wu G, Yang X, Huang Y, & Ma L. Recent advances of interphases in carbon fiber-reinforced polymer composites: A review, Composites Part B: Engineering, 2022;233, https://doi.org/10.1016/j.compositesb.2022.109639

[2] Erturk AT, Yarar E, Vatansever F, Sahin AE, Kilinçel M, & Alpay YO. A comparative study of mechanical and machining performance of polymer hybrid and carbon fiber epoxy composite materials, Polymer & Polymer Composites, 2021;29(9):S655–S666. https://doi.org/10.1177/09673911211020620

[3] Binali R, Ribeiro da Silva RR, Limenov DY, Kuntoglu M, Machado AR, Linul E. A review of progress trends of machining of carbon fibre reinforced plastics, Journal of Materials Research and Technology, 2024; In Press, https://doi.org/10.1016/j/jmrt.2024.10.050

[4] Elgnemi TSM, Jun MBG, Songmene V, & Samuel AM. Milling performance of CFRP composite and atomised vegetable oil as a function of fibre orientation, Materials, 2021;14(8), https://doi.org/10.3390/ma14082062

[5] Wang JJ, Zhang JF, Feng PF, & Guo P. Damage formation and suppression in rotary ultrasonic machining of hard and brittle materials: A critical review, Ceramics International, 2018;44(2): 1227–239, https://doi.org/10.1016/j.ceramint.2017.10.050
[6] Zhang MJ, et al. Analysis of flow field in cutting zone for spiral orderly distributed fibre tool, International Journal of Advances in Manufacturing Technology, 2017;92(9–12), 4345-354
[7] Lawal SA, Medupin RO, Yoro KO, Okoro UG, Adedipe O, Abutu J, Tijani JO, Abdulkareem AS, Ukoba K, Ndaliman MB, Sekoai PT, & Jen T-C. Nanofluids and their application in carbon fibre reinforced plastics: A review of properties, preparation, and usage, Arabian Journal of Chemistry, 2023;16(8):104908, https://doi.org/10.1016/j.arabjc.2023.104908
[8] Lawal SA, Medupin RO, Yoro KO, Ukoba KO, Okoro UG, Adedipe O, Abutu J, Tijani JO, Abdulkareem AS, Ndaliman MB, Abdulrahman AS, Eterigho-Ikelegbe O, Jen T-C. Nano-titania and carbon nanotube-filled rubber seed oil as machining fluids, Materials Chemistry & Physics, 2024;316:129126, https://doi.org/10.1016/j.matchemphys.2024.129126
[9] Medupin RO, Ukoba K, Yoro KO, & Jen T-C, Sustainable approach for corrosion control in mild steel using plant-based inhibitors: A review, Materials Today Sustainability, 2023;22:100373, https://doi.org/10.1016/j.mtsust.2023.100373
[10] Patole PB, Pol GJ, Desai AA, & Kamble SB. Analysis of surface roughness and cutting force under MQL turning using nano fluids, Materials Today: Proceedings, 2021;45:5684–688, https://doi.org/10.1016/j.matpr.2021.02.501
[11] Ni J, Cui Z, Wu C, Sun J, & Zhou J. Evaluation of MQL broaching AISI 1045 steel with sesame oil containing nano-particles under best concentration, Journal of Cleaner Production, 2021;320(May):128888, https://doi.org/10.1016/j.jclepro.2021.128888
[12] Haq MA, Hussain S, Ali MA, Farooq MU, Mufti NA, Pruncu CI & Wasim E. Evaluating the effects of nano-fluids based MQL milling of IN718 associated to sustainable productions, Journal of Cleaner Production, 2021;310(May):127463, https://doi.org/10.1016/j.jclepro.2021.127463
[13] Iruj M, Yaqoob S, Ghani Ja, Jaber H, Saibani N, Alkhedher M. State-of-the-art hybrid lubrication (cryo-MQL) supply systems, performance evaluation, and optimization studies in various machining process, Results in Engineering, 2024;22:102090.
[14] Usha M, & Srinivasa Rao G. Optimisation of Parameters in Turning Using Herbal Based Nano Cutting Fluid with MQL, Materials Today: Proceedings, 2019;22:1535-544 https://doi.org/10.1016/j.matpr.2020.02.115
[15] Agrawal SM, & Patil NG. Experimental study of non-edible vegetable oil as a cutting fluid in machining of M2 Steel using MQL, Procedia Manufacturing, 2018;20: 207–212, https://doi.org/10.1016/j.promfg.2018.02.030
[16] Gao T, Zhang Y, Li C, Wang Y, An Q, Liu B, Said Z, & Sharma S. Grindability of carbon fiber reinforced polymer using CNT biological lubricant, Scientific Reports, 2021;11(1);1–14, https://doi.org/10.1038/s41598-021-02071-y
[17] Singh Y, Negi P, Yadav A, & Tripathi R. Euphorbia lathyris: A novel feedstock for bio based lubricant application with titanium dioxide nanoparticles as additives, Materials Today: Proceedings, 2021;46;10518–522, https://doi.org/10.1016/j.matpr.2020.12.1237
[18] Zhang Y, Li L, Cui X, An Q, Xu, P, Wang W, Jia D, Lui M, Dambata YS, Li C. Lubricant activity enhanced technological for sustainable machining: Mechanisms and processability, Chinese Journal of Aeronautics, 2024; In Press, https://doi.org/10.1016/j.cja.2024.08.034
[19] Kumar A, Sharma AK, & Katiyar JK. State-of-the-art in sustainable machining of different materials using nano minimum quality lubrication (NMQL), Lubricants, 2023;11(64), https://doi.org/10.3390/lubricants11020064
[20] Bai X, Li C, Dong L, & Yin Q. Experimental evaluation of the lubrication performances of different nanofluids for minimum quantity lubrication (MQL) in milling Ti-6Al-4V, International Journal of Advances in Manufacturing Technology, 2019;101:2621–632
[21] Osman KA, Yılmaz V, Ünver HO, Seker U, & Kılıç, S. Slot milling of titanium alloy with hexagonal boron nitride and minimum quantity lubrication and multi-objective process optimization for energy efficiency, Journal of Cleaner Production, 2020;258:120739.
[22] Jamil MKhan AM, & Hegab H. Milling of Ti–6Al–4V under hybrid Al2O3-MWCNT nanofluids considering energy consumption, surface quality, and tool wear: A sustainable machining, International Journal of Advances in Manufacturing Technology, 2020;107:4141–4157
[23] Cui X, Li C, Ding W, Chen Y, Mao C, Xu X, Liu B, Wang D, Li HN, Zhang Y, Said Z, Debnath S, Jamil M, Ali HM, & Sharma S. Minimum quantity lubrication machining of aeronautical materials using carbon group nanolubricant: From mechanisms to application. Chinese Journal of Aeronautics, 2021;September. https://doi.org/10.1016/j.cja.2021.08.011
[24] Venkatesan K, Devendiran S, Sachin D, & Swaraj J. Investigation of machinability characteristics and comparative analysis under different machining conditions for sustainable manufacturing, Measurement:

Journal of International Measurement Confederation, 2020;154:107425, https://doi.org/10.1016/j.measurement.2019.107425
[25] Shokrani A, Arrazola PJ, Biermann D, Matevenga P, Jawahir IS, Sustainable machining: recent technological advances, CIRP Journal of Manufacturing Sciences and Technology, https://doi.org/10.1016/cirp.2024.06.001
[26] Gao T, et al. Surface morphology assessment of CFRP transverse grinding using CNT nanofluid minimum quantity lubrication, Journal of Cleaner Production, 2020;277:123328. https://doi.org/10.1016/j.jclepro.2020.123328
[27] Abubakre OK, Medupin RO, Akintunde IB, Tijani JO, Abdulkareem AS, Muriana RA, James JA, Ukoba KO, Jen T-C, & Yoro KO. Carbon nanotube-reinforced polymer nanocomposites for sustainable biomedical applications: A review, Journal of Science: Advanced Materials and Devices., 2023;8(2):100557, https://doi.org/10.1016/j.jsamd.2023.100557
[28] Urmi WT, Shafiqah AS, Rahman MM, Kadirgama K, & Maleque MA. Preparation Methods and Challenges of Hybrid Nanofluids: A Review, Journal of Advanced Research in Fluid Mechanics and Thermal Sciences, 2021;78(2):56–66, https://doi.org/10.37934/ARFMTS.78.2.5666
[28] Medupin RO, Abubakre OK, Abdulkareem AS, Muriana RA, & Abdulrahman AS. Carbon Nanotube Reinforced Natural Rubber Nanocomposite for Anthropomorphic Prosthetic Foot Purpose, Scientific Reports, 2019;9(1):20146, https://doi.org/10.1038/s41598-019-56778-0
[28] Ma C, Wen R, Zhou F, Zhao H, Bao X, Evelina A, Long W, Wei Z, Ma L, Liu J, & Chen S. Preparation and application of an environmentally friendly compound lubricant based biological oil for drilling fluids, Arabian Journal Chemistry, 2022;15(3):103610, https://doi.org/10.1016/j.arabjc.2021.103610
[28] Mustapha S, Ndamitso MM, Abdulkareem AS, Tijani JO, Shuaib DT, Ajala AO, & Mohammed AK. Application of TiO2 and ZnO nanoparticles immobilized on clay in wastewater treatment: a review, Applied Water Science, 2020;10(1), https://doi.org/10.1007/s13201-019-1138-y
[28] D'Aloia AG, Di Fransesco A, & De Santis V. A novel computational method to identify/analyses hysteresis loops of hard magnetic materials, Magnetochemistry, 2021;7(10).
[28] Brockmann EC, Pyykko M, Hannula H, Khan K, Lamminmaki U, & Huovinen T. Combinatorial mutagenesis with alternative CDR-L1 and H2 loop lengths contributes to affinity maturation of antibodies, New Biotechnology, 2020;60:73-182
[28] Paumo HK, Dalhatou S, Katata-Seru LM, Kamdem BP, Tijani JO, Vishwanathan V, Kane A, & Bahadur I. TiO2 assisted photocatalysts for degradation of emerging organic pollutants in water and wastewater, Journal of Molecular Liquids, 2021;331:115458, https://doi.org/10.1016/j.molliq.2021.115458
[28] Medupin RO, Abubakre OK, Abdulkareem AS, Muriana RA, & Lawal SA. Dimensional and Thermal Reliability of Multi-Walled Carbon Nanotube Filled Natural Rubber Nanocomposites, International Journal Engineering Resources in Africa, 2020;51:177-189, https://doi.org/10.4028/www.scientific.net/jera.51.177
[28] Medupin RO, Abubakre OK, Abdulkareem AS, Muriana RA, Kariim I, & Bada SO. Thermal and physico-mechanical stability of recycled high-density polyethylene reinforced with oil palm fibres, Engineering Science & Technology, an International Journal, 2017;20(6):1623–631, https://doi.org/10.1016/j.jestch.2017.12.005
[28] Gopiraman M, Selvakumaran N, Kesavan D, Kim IS, & Karvembu R. Chemical and physical interactions of 1-benzoyl-3,3-disubstituted thiourea derivatives on mild steel surface: Corrosion inhibition in acidic media, Industrial & Engineering Chemical Research, 2012;51(23):7910–7922, https://doi.org/10.1021/ie300048t
[28] Shaban MM, Eid AM, Farag RK, Negm NA, Fadda AA & Migahed MA. Novel trimeric cationic pyrdinium surfactants as bi-functional corrosion inhibitors and antiscalants for API 5L X70 carbon steel against oilfield formation water, Journal Molecular Liquids, 2020;305:112817, https://doi.org/10.1016/j.molliq.2020.112817
[28] Khadom AA, Abd AN, Ahmed NA, Kadhim MM, & Fadhil AA. Combined influence of iodide ions and Xanthium Strumarium leaves extract as eco-friendly corrosion inhibitor for low-carbon steel in hydrochloric acid, Current Research in Green and Sustainable Chemistry, 2022;5(December):100278, https://doi.org/10.1016/j.crgsc.2022.100278

Blank Page

Research on Engineering Structures & Materials
www.jresm.org

Research Article

Heat influence on sustainable rubberized concrete mixes

Ola Mazen Makki *,a

Dept. of Civil Engineering, College of Engineering, University of Al-Qadisiyah, Al-Qadisiyah, Iraq

Article Info

Article history:

Received 16 Aug 2024
Accepted 27 Jan 2025

Keywords:

Rubcrete;
Rubberized concrete;
Heat exposing;
Crumb;
Sustainable;
Chips

Abstract

Rubberized concrete (Rubcrete) usually minimizes concrete brittleness and increases conventional concrete's energy absorption as well as the brittleness. Exposing elevated heat deteriorates the strength of traditional concrete and causes rubber dilution. The article investigated replacing aggregate with rubber to enhance the dynamic properties of concrete and discussed many parameters like replacement type, replacement amount, effect of heat and heat increment. Also, many properties, such as unit weight, compressive strength, tensile strength and modulus of rupture, were investigated and discussed for two types of rubber versus aggregate replacement and 10%,20% and 30% percentages. It was concluded that the rubcrete strength was reduced more than the normal concrete due to the presence of rubber, which made the rubber melt inside the concrete pores and caused internal residual stresses due to the hydrostatic pressure. It's not recommended to use rubberized concrete in construction sites exposed to high-temperature rise, like baking ovens or nearby, because the rubberized concrete loses its strength to the fourth or half after exposure to heat.

© 2025 MIM Research Group. All rights reserved.

1. Introduction

Concrete is the most used construction material in the world. It has sufficient mechanical properties to resist static loads but does not meet the requirement for dynamic loading [1–3]. There are many ways to improve the dynamic properties of concrete, such as adding steel fibres, raising its strength with any additives, and using rubber (the best damper between materials) [4, 5]. Using scraped tiers rubbers gets the natural ride of its pollution besides the enhancement to concrete properties, especially after knowing that the pollution in scraped tiers becomes a serious problem against the environment. Because of that, the rubber is a non-biodegradable material and burning it causes effective air pollution[6]. The world produces Millions of tons of tyres per year, about 303 million each year in the United States [6] due to its repeated production and consumption worldwide. The biggest waste tire landfill lies in Arhyyah, Kuwait [7]. It is named Tires' graveyard and can be seen on satellites. Google Maps GPS showed it clearly, as shown in Fig.1. 90% of the recycled tiers rubbers in Mexico are reused in civil engineering applications, and 75% in Canada [8]. It could be used for floor units, walking paths, electricity floor isolation, healthy sports lands, and reinforced dampers for bridges.

Rubber particles produced by recycling factories in many sizes match the grades of sand and gravel particles, so replacing them with the same grades is possible. The factories cleaned the scraped tiers from dust and other unwanted objects and then chopped them for fine and coarse sizes. The fine grades are named crumbs, while the course is called chips, as explained in Fig.2. Effect of heat on rubberized concrete has been investigated previously, and it was concluded that the thermal conductivity of rubcrete is significantly affected by temperature due to porosity changes and water evaporation [9].

*Corresponding author: ola.mazen@qu.edu.iq
[a]orcid.org/0009-0008-0839-0716
DOI: http://dx.doi.org/10.17515/resm2025-400ma0116rs

Recycled tiers of rubber could also be used in concrete mixes as a partial replacement for sand, gravel, or even both [9–18], and some researchers used it as a partial replacement for cement. At the same time, other researchers put rubber bars with the primary reinforcement of concrete beams. The replacement may be from the mix volume or maybe from its weight. The volumetric replacement keeps the volume of the mix from changing after replacement. Replacing rubber with aggregate enhances the concrete mix's dynamic properties and makes the concrete absorb more energy and rest many impact loads. But the bad thing is that the concrete compressive strength and the other mechanical properties deteriorate [6, 10–18]. Conventional concrete was tested under heat in many types of research previously, and it was concluded that the concrete keeps the same behaviour in a degree of heat ranging from 65 °C to 93 °*c* [19], then it may be changed.

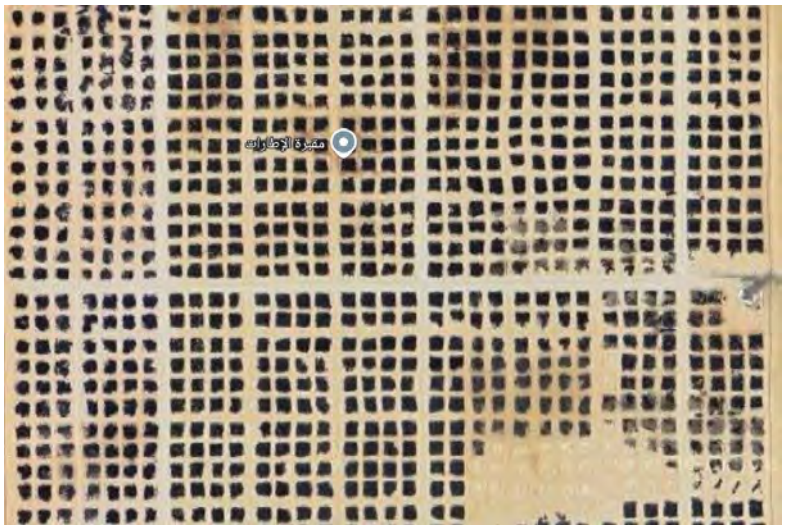


Fig. 1. The most enormous scraped tyres stacks in the world, from Google maps



(a) (b) (c)

Fig. 2. Recycled scraped tyre rubber, which products from recycling factories (a) ground rubber, (b) crumb rubber and (c) chip rubber [9]

The effect of heat on rubberized concrete was investigated in a few articles and in a manner different from this article, in which the researchers applied heat on the rubber before using it in the concrete mix [20, 21], or some papers studied the thermal conductivity of the rubberized concrete [1, 21–24]. This article discusses the effect of heat on the properties of rubcrete after drying and curing; in other words, studying the impact of heat when a fire occurs besides rubberized concrete. As the previous research has approved, conventional concrete loses its strength at a temperature starting from 38 °C [28], and the degree of strength dropping has a lower and upper bound limit, depending on the chart. At a temperature equal to 21 °C , the dropping in strength equals zero for both upper and lower bounds limits for both compressive and tensile strengths [19].

Abdelrahman Swilam et al. [20] and Osama Youssef et al. [25] investigated the effect of treating the rubber with heat before casting. It was concluded that, compressive strength recovery of 74% and impact resistance enhancements of 2.2 times at the first crack and 92% at the ultimate failure when

using rubber content of 40%. The microstructural analyses showed that rubber heat pre-treatment burnt out most of the unwanted materials in rubber aggregate, creating an outer hard shell on the rubber particles [25]. Heating the rubberized concrete after casting and curing has not been investigated yet. So, this study initially discussed the effect of heating the rubberized concrete after curing.

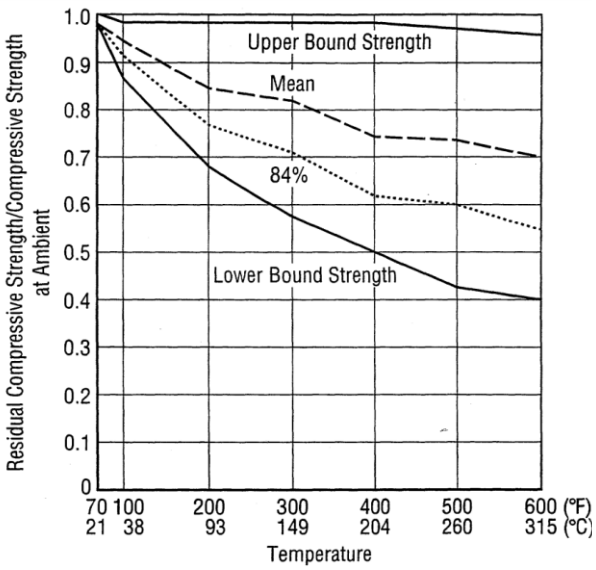


Fig. 3. Lower and upper limits in decreasing the concrete compressive strength after heat [19]

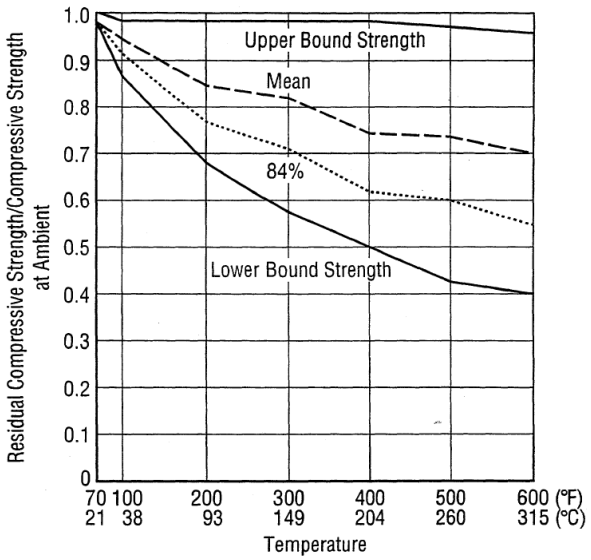
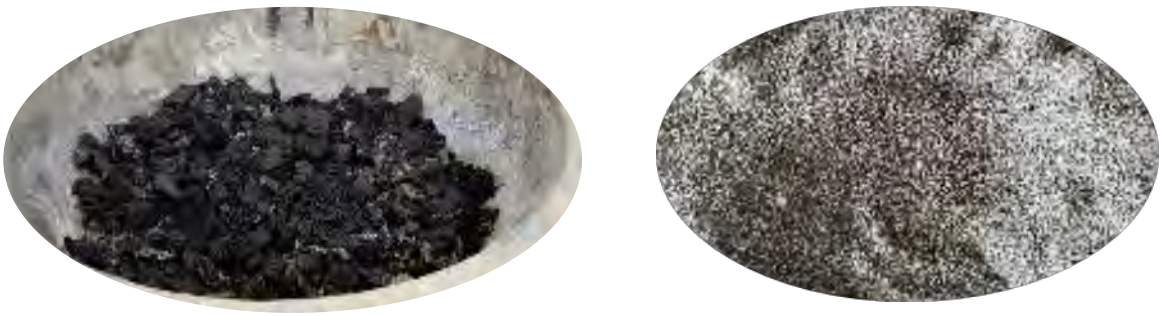


Fig. 4. Tensile strength decrement after elevated heat [19]

2. Test Methodology

Replacing the aggregate with rubber, even if it was totally or partially replaced, led to the introducing of a new material called rubcrete (rubberized concrete). Regular Portland cement was used, a well-graded aggregate and the used rubber was graded in the same gradient. Chips rubber (which partially replaced gravel) was 650 kg/m3, the crumb density was 720 kg/m3, and carbon black equals 20%. The maximum gravel and rubber aggregate size was 10 mm, and passing from 4.75 mm sieve for fine aggregate. The gravel density was 1650 kg/m^3, and the sand was 1600 kg/m^3. The cement used was Cement-Basian type, with a mortar compressive strength of 33 MPa for water-to-cement ratio (w/c) equals 0.25. Fig.5. showed the rubber used.



(a) (b)

Fig. 5. Rubber used in mix casting (a) chips rubber, (b) crumb rubber

The study investigated the mechanical and dynamic properties of rubcrete under heat, such as density, water absorption, compressive strength, tensile strength, bending capacity, and impact resistance. All the tests were investigated after 28 days of curing, and all the values were based on the average of three specimens. A slump test for all mixes was made using a 300 mm high cone-

shaped trunk, as explained in Fig.6.a. The base is 200 mm (8 in) in diameter and has a smaller opening at 100 mm. Each layer is tempered 25 times with a standard 16 mm.



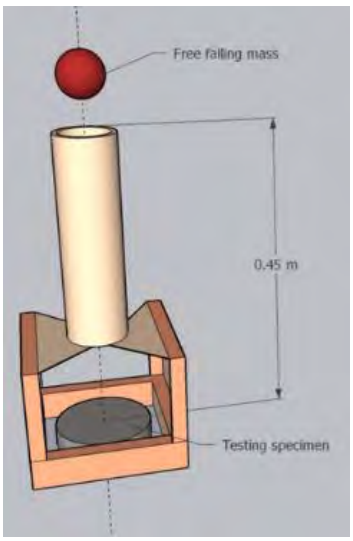
(a)



(b)



(c)



(d)





(e)



(f)

Fig. 6. Represent experimental work (a) Slump test, (b) Compressive strength machine, (c)Splitting strength, (d) Impact load device sketch, € casted impact load specimens and (f) dry samples

The same compressive machine press system was used to test the compressive strength of cubes and the cylinders' splitting. The cubes are inserted into the machine on a face perpendicular to the

casting direction with a loading rate equal to 0.2 MPa/sec, as explained in Fig.6.b. and c. Fig.6.d Explained the testing method, while Fig.6.e illustrated mould casting. Some samples after casting are illustrated in Fig. 6.f.
Following ACI committee 544 [26], the impact resistance of concrete may be obtained by casting cylindrical specimens of 65*152 mm (diameter * length) and applying a drop mass (m) simulated of 4.54 Kg. The number of hits that caused the first crack (N1) and the total number of hits that caused the final failure (N2) were recorded. The total energy applied to the specimen could be calculated from the following equations:

$$\text{energy at first crack} = N_1 mgh \quad (1)$$

$$\text{the energy at failure} = N_2 mgh \quad (2)$$

3. Experimental Mix Preparation

Seven mixes were cast, three of them of sand replacement, the other three of gravel replacement, and one conventional concrete without any replacement. Based on several trial mixes, the mix was of (1:1.4:2) percentages, which means that, for each quantity of cement, the sand amount equals 1.4 multiplied by cement quantity, and gravel equals twice the quantity of cement. The water-to-cement ratio was equal to 0.365. Superplasticizer Gelimum G54 was also utilized. Mix details for one cubic meter are illustrated in Table 1. Note that the names of specimens started with Gr for gravel replacement and Sr for sand replacement, followed by the volumetric percentage of replacement, which is 10, 20 or 30%.

The exact mix investigated in reference [15, 27] was used, so the study concentrated on the prisms' bending capacity after heating, slump test, unit weight after heat, water absorption, and concrete cube's compressive strength. The investigated heat applied on specimens was selected to be 100 ℃ and 200 ℃ for two hours.

Table 1. Mixes weights (kg/m^3) [15, 29]

Mix	Cement	Sand	Gravel	Rubber	water	G54
RF	475	760	1119	0	124	2.33
Sr10	475	684	1119	76	124	2.33
Sr20	475	608	1119	152	124	2.33
Sr30	475	532	1119	228	124	2.33
Gr10	475	760	1008	111	124	2.33
Gr20	475	760	896	223.8	124	2.33
Gr30	475	760	784	335	124	2.33

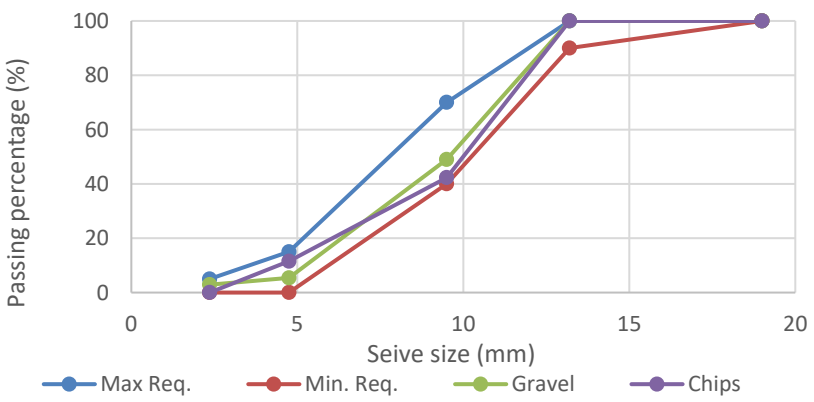


Fig. 7. Gradient of coarse aggregate and chip sizes

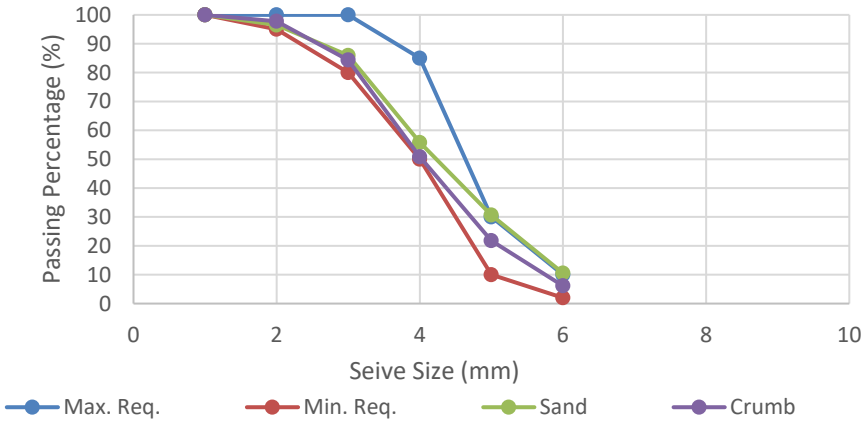


Fig. 8. Sieve analysis for fine aggregates

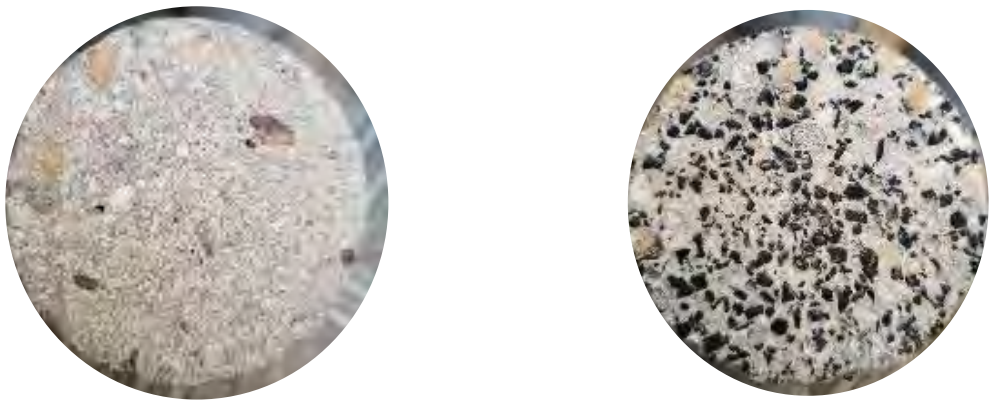


Fig. 9. Conventional versus rubberized concrete face

The dry content is mixed till get a homogenous dry mixture. It was noted that, despite the dark concrete dry mix colour, the fresh rubcrete mix appears darker than traditional concrete due to the presence of rubber. It's recommended by the previous research that, when replacing, it prefers to replace a thoroughly graded rubber with the same fully graded aggregate to avoid a massive loss in concrete strength [6]. So, sieve analysis for all materials was investigated. The gradients of gravel, chips, sand and crumb were used, matching with the maximum and minimum requirement of the recommended sieve analysis provided by ASTM C33-10 [28]; all results were shown in Fig.7 and Fig.8. Fig.9 showed the surface of rubberized concrete of 30% chips content.

4. Rubcrete Properties Result After Heating

4.1. Slump Test

Generally, after reviewing many studies, it was observed that the replacements deteriorate the workability of the mix for various reasons. Since the rubber particles have a hydrophobic surface, water particles do not stick on, contrary to aggregate particles with an absorption capacity [30]. Emam [31] investigated the fact that water covers rubber particles, decreasing the friction between concrete mixes. The fresh rubberized concrete mix flow matches the results at reference [15] because it is the same mix, but slight differences could be noted due to the weather conditions. It can be concluded that the presence of rubber reduces the workability of concrete in magnitudes increases with replacement percentages increment as explained in Table 2, which tested by the ASTM 143M-12 [32]. It also could be noted that the acceptable aggregate replacement is more workable than the coarse aggregate replacement because the chip rubber has many angles that can restrict the water between its particles.

Table 2. Workability results for conventional and rubberized mixes

Specimens	Slump (mm)	Reduction %
NC	105	------
Sr10	92.5	11.9
Sr20	80	23.81
Sr30	65	38.1
Gr10	67	36.19
Gr20	46	56.19
Gr30	37	64.76

4.2. Unit Weight

Replacement generally was proved by the previous research to minimize the unit weight of concrete due to replacing the heavier material (aggregate) with a lighter material (rubber), and this reduction depends on many factors, which are replacement method, the amount of replacement and replacing. In other words, the reduction in unit weight is a result of less rubber density than aggregate, where the density of sand (1450 kg/m3), gravel (1650 kg/m3), and natural rubber (500 kg/m3). After applying heat to the concrete cubes, three cubes from each mix were weighed before and after using heat of 100 °C for two hours. The results (which are shown in Fig.10) introduce that, the weight of rubberized concrete reduces more after heating due to the evaporation of free water from the cubes. Sand replacement specimens lost (1.28% to 1.95 %) of their weight after 100 C of heating and lost (1.8% to 2.98%). Gravel versus chips replacement weight was reduced by (0.74% to 0.97%) after heating for 100 C, while for 200 C of heat, the reduction ranged from (1.5% to 2.77%) according to rubber amounts. Whatever the heat was, and the amount of replacement occurred, the reduction in weight due to heat is so slight and does not reach 5%.

4.3. Water Absorption

Exposing heat to specimens working on emptying the concrete voids from water could cause the voids to receive more water. It was concluded previously from the literature that [6] the water absorption capacity of rubcrete enhanced when increasing the rubber amount; the same behaviour was observed for the heated specimens but with more significant absorption because its voids were dried by heat from free water.

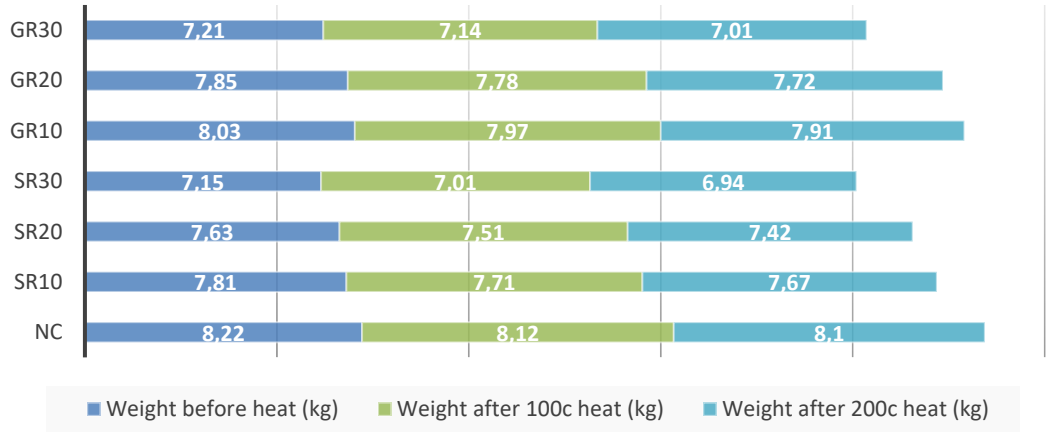


Fig. 10. Weight loss before and after heating

Three cubes from each mix were tested to show the water absorption, and it was concluded from the results listed in Fig. 11 that the water absorption rises gradually after any heat increment; also, it can be noted that the increment reached 8% for 30% sand versus crumb replacement and 8.5% for 30% gravel-chips replacement at 100 C°. At 200 C°, the increment reaches 6.7% and 8.5% for the 30% replacement of sand and aggregate, respectively. The water absorption increases after

heat due to evaporating free water mix from pores after heating, emptying the mix cavities and increasing the ability for absorbance.

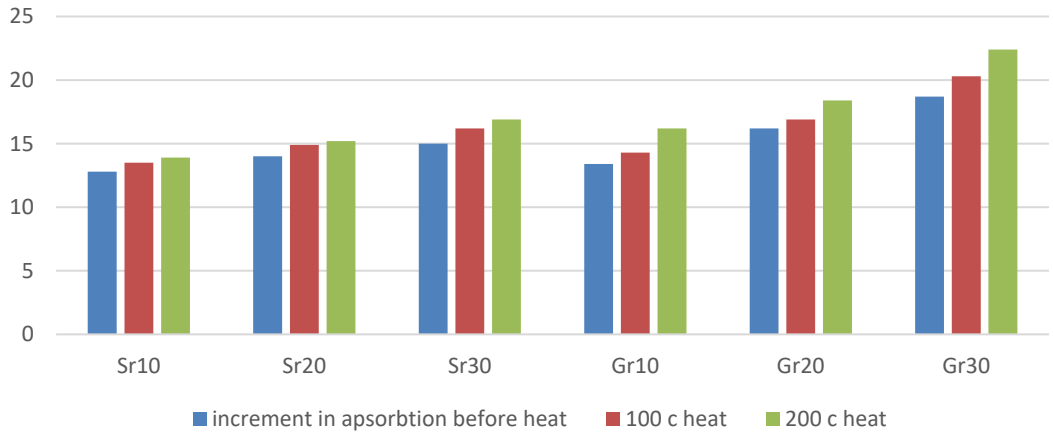


Fig. 11. Water absorption before and after heating

4.4. Concrete Compressive Strength

The average of three cubes by BS 1881 -116 [33] to get the British compressive strength Fcu. The drop in concrete compressive strength after a replacement was proved by many previous types of research. It was indicated that this drop happened due to forming micro-cracks between the cement paste and the rubber particles (considered an intruder material on the mix) [6]. The same drop observed previously from literature has been noticed in this study, and the decrement amount depends on replacing type and amounts. After heating, the concrete compressive strength also reduces capacity due to factors relenting on concrete and rubber.

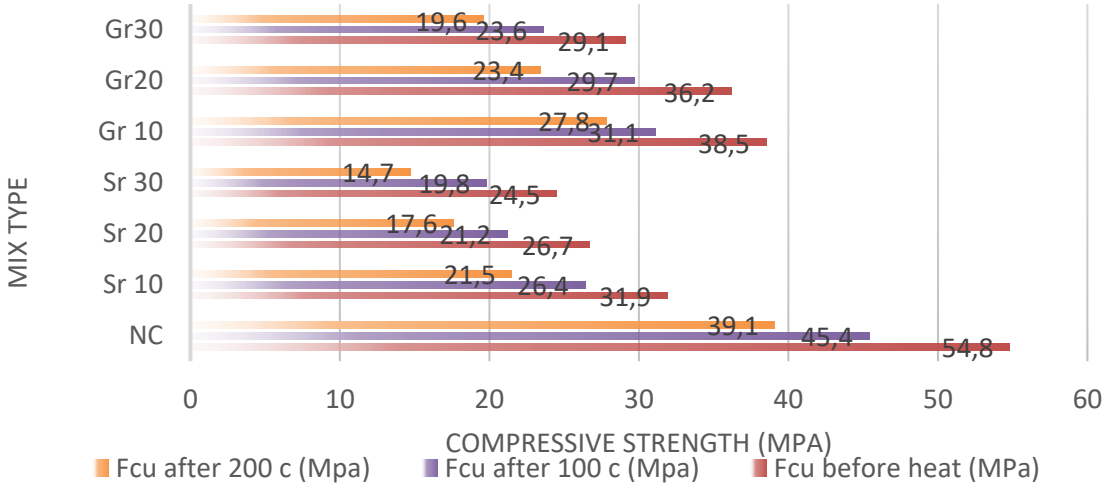


Fig. 12. Concrete compressive strength results

After exposing heat to concrete cubes, a drop in compressive strength was expected for both conventional and rubberized concrete. As could be concluded from the results listed in Fig.12, the traditional concrete strength drops after heating in the range of expectation introduced by the reference [19]. The expected degree of reduction for 100 ℃ and 200 ℃ of heat are (0.87-0.68) and (0.96-0.85), respectively, for lower- upper bounds. When the concrete strength was 54.8 MPa without heating, it is expected (by the chart) to drop the strength in the range between (41.03 MPa to 50.496 MPa) for 100 c and (35.76 MPa to 44.71 MPa) for 200 C, while experimentally it was 45.4 MPa and 39.1 MPa for 100 C and 200 C respectively. The specimen results showed a matching percentage drop compared to the previous articles [19].

For rubcrete material, the decrement accedes 0.84, and it deteriorates more than the conventional concrete. The philosophy of rubcrete reduction could be as follows: the rubber particles start to soften or maybe melt and form some gases inside the concrete, which cause a hydrostatic pressure inside the cube, and a residual pressure will develop inside the concrete block. The results could also be concluded that the sand replacement specimens suffer more heat than the gravel replacement due to the finer size of crumb particles, which made it melt faster than the chips' particles. Fig.13 shows some of the tested specimens after failure.



Fig. 13. Compressive strength failure for some specimens

4.5. Splitting Strength

As usual, splitting strength depends on the concrete compressive strength at the first degree. So, it's logically expected to be dropped after replacement and heating. After heating the specimens (three cylinders from each mix- of 200mm length and 100 mm diameter) in accordance with ASTM VC39/C39M − 15a [34] specification and testing them directly the results were obtained. It could be noted from the results (which listed in Table 3) that, the dropping in strength after replacement ranged from 20% to 47% for acceptable aggregate replacement and 16% to 40.75% for coarse aggregate replacements. After heating under 100 C, the reduction rises by 24% to 52% for crumb specimens and 21% to 48% for chip replacements. At the same time, the reduction in strength gets worse after 200 C° of heating. The decrease in splitting strength comes from the weakness of rubberized concrete due to heating; conventional concrete is affected negatively by heat and rubber, so the decrement occurred from both the weakening and rubber dilution.

It can also be noted that, when comparing sand and aggregate replacements, the gravel replacement introduced a deterioration in strength better than the sand samples, which means that the chips replacement is safer for strength than a crumb. Specimens after failure are shown in Table 3. Fig.14 viewed cylinder failures, which were typically repeated for all specimens.

Table 3. Tensile strength of concrete after and before heating

Mix	Ft (MPa)	Redaction (%)	Ft (MPa) after 100 c	reduction (%)	Ft (MPa) after 200 c	Reduction (%)
Nc	5.12	-----	4.67	-----	3.91	-----
Sr10	4.21	20.21	3.54	24.19	2.67	31.71
Sr20	3.78	35.03	2.98	36.18	2.31	40.92
Sr30	2.95	47.25	2.24	52.03	1.65	57.80
Gr10	4.61	16.12	3.67	21.41	2.84	27.36
Gr20	3.67	32.33	3.04	34.90	2.45	37.34
Gr30	3.21	40.75	2.41	48.39	1.88	51.91



(a) (b) (c)

Fig. 14. (a) Typical shape of cylinder failure. (b) Splitting face of Sr.10 sample. (C) failure face of SR.30 specimen

4.6 Modulus of Rupture

Prisms of (100*100*400 mm) dimensions were cast for the seven mixes to test the modulus of rupture at 28 days according to the ASTM C133-97 [35]. The tested specimens' results were clarified in Fig.15, and accordingly, the rupture strength of rubcrete was reduced due to the reduction in concrete compressive and tensile strength. Results show that the flexural strengths of sand replacement are slightly higher than gravel replacement because sand provides higher ductility than gravel. Rupture test for rubcrete was also investigated widely at reference [36]. For heating results, it can be quickly clarified that the flexural strength of rubcrete prisms deteriorates after the effect of heat in a magnitude depending on the temperature applied. Sand versus crumb specimens lost (17.6-29%) of the flexural capacity, while the chips versus gravel replacement lost (17.2-22%) of the bending capacity after 200 C of heat application. Applying heat on prisms worked on deteriorating the strength of concrete and rubber, which caused the dropping in rupture strength.

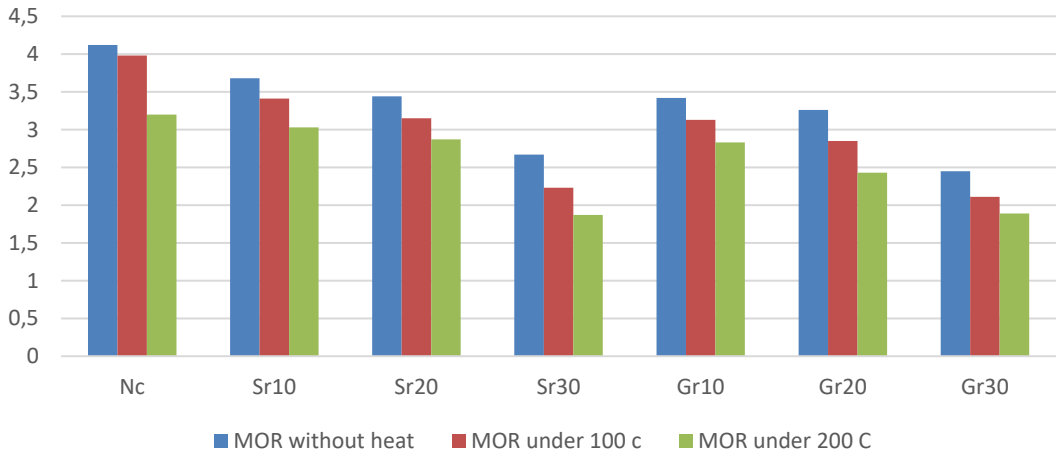


Fig. 15. Modulus of rupture results (MPa)

Fig.16. illustrated the rubberized specimens after failure and before heating; during the test, it was observed that the gravel particles worked as fibres matched between the cracked sides of the prism till completely cutting for the model by the load.

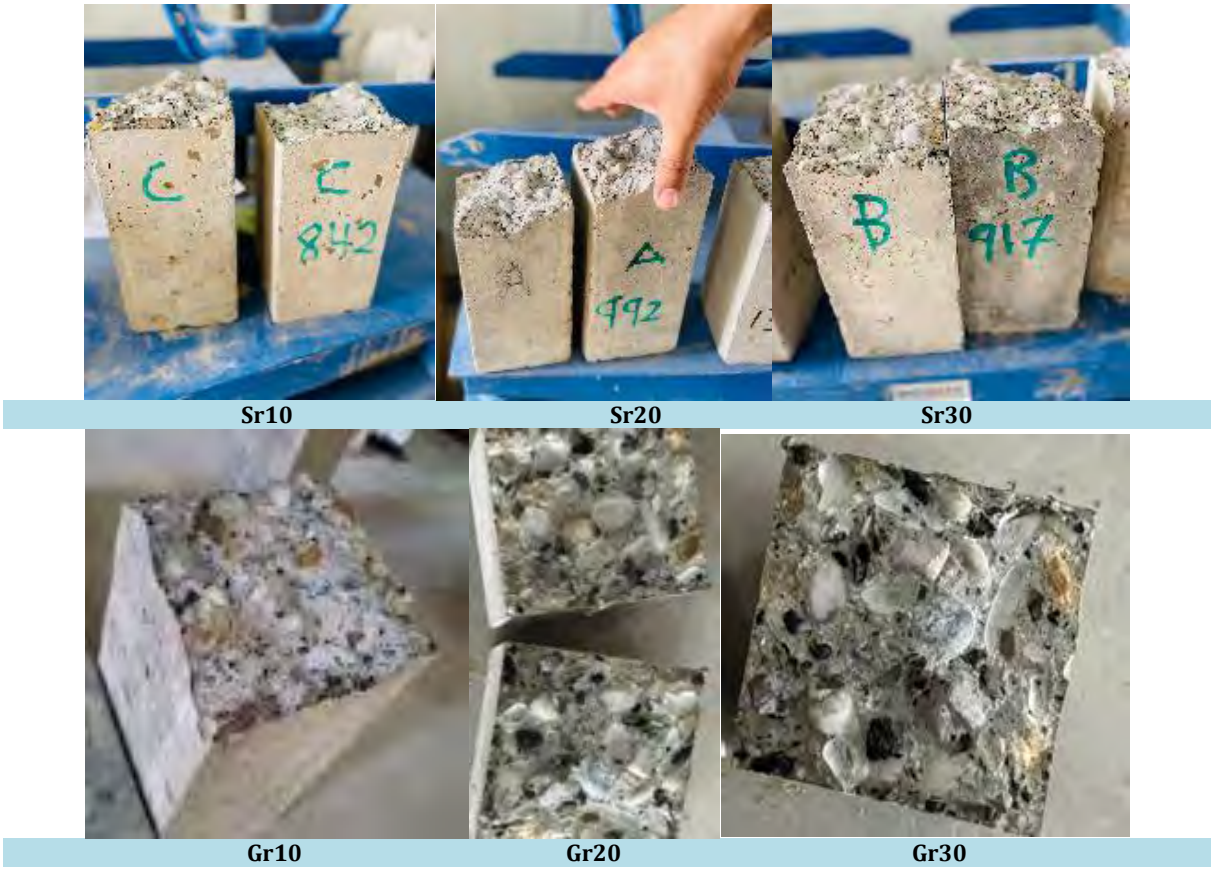


Fig. 16. Rubberized prisms after failure

Fig. 17 illustrates the modulus of rupture (MOR) decrement for the different mixes. Mathematical equations for the decrement in rupture strengths have been discussed. After investigating the best fitting curve, a polynomial from the second degree presented the results accurately for all samples but approaches to be linear at chips versus gravel replacement at 200 C; the equations are shown in Table 4. The reliability factor of the equations equals 1, which means that the equation precisely fits with the results and without error percentage as explained in Table 4.

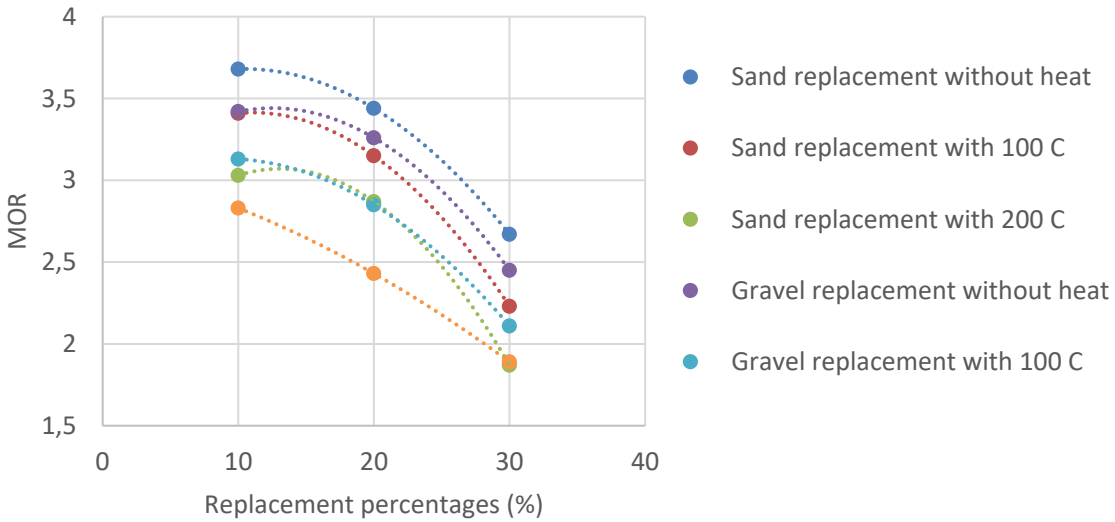


Fig. 17. Decrement in MOR and the suitable equation for the dropping

Table 4. Mathematical model of modulus of rupture for rubberized concrete

Specimen	Equation	Reliability factor
Gravel replacement without heat	y = -0.0032x2 + 0.0815x + 2.93	R2=1
Gravel replacement with 100 C	y = -0.0023x2 + 0.041x + 2.95	R2=1
Gravel replacement with 200 C	y = -0.0007x2 - 0.019x + 3.09	R2=1
Sand replacement without heat	y = -0.0027x2 + 0.0555x + 3.39	R2=1
Sand replacement with 200 C	y = -0.0033x2 + 0.073x + 3.01	R2=1
Sand replacement with 200 C	y = -0.0042x2 + 0.11x + 2.35	R2=1

4.7. Impact Load

Adding rubber into the conventional concrete mix dynamically works as micro springs fixed inside the concrete particles, and applying heat melts the rubber and destroys these springs. The results showed that rubberized specimens lose their impact resistance capacity and suffer from weaker absorbing energy. That was concluded from Table 5, which illustrated the capacity of heated and unheated rubcrete under impact loads per the ASTM C496 specifications [37]. The worst matter is that melting rubber minimizes concrete's compressive strength, which also decreases the impact strength of rubberized concrete. From the results, it could be noted that the sand versus crumb replacement specimens lost an impact capacity ranging from 54% to 88% at heat 100 C° and 65% to 92% for heat equals 200 C° which is due to melting the rubber particles and returning the rubberized concrete behaviour to the conventional concrete behaviour. 64% to 84% was the reduction in impact resistance after 100 C of heat subjected to gravel versus chips replacement; for 200 C°, the deterioration in energy absorption was 74% to 88%.

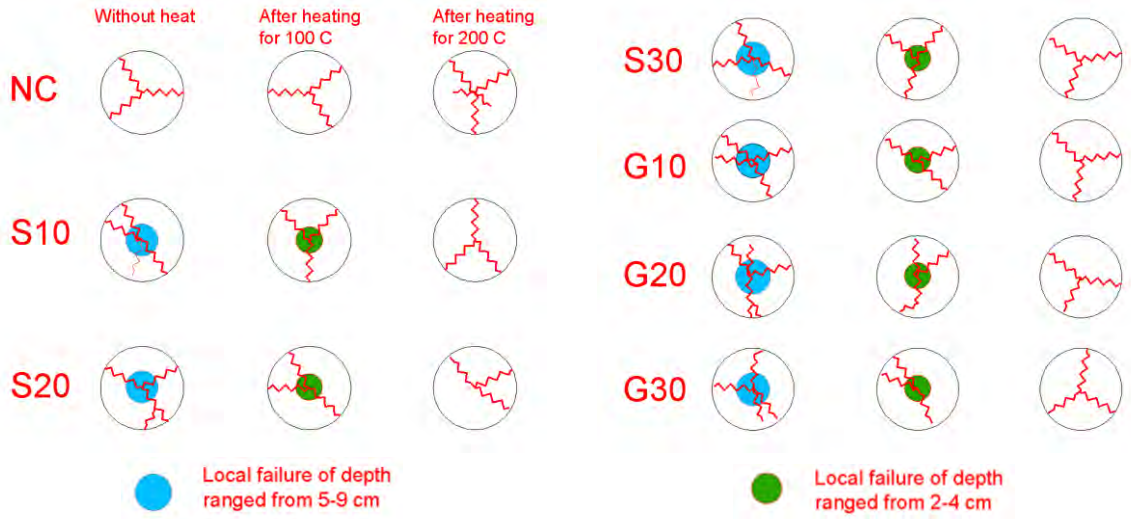


Fig. 18. Failure modes of different impacted specimens

Fig.18 illustrates the crack patterns for all impacted specimens. It can be noted that, before heating, the conventional concrete did not suffer from local failure in contrast to rubber specimens, which showed local failures ranging from 5 mm to 9 mm in depth. The local failure occurs due to rubber particles working on fending off the hit to crack the concrete; after each impact, a small local failure occurs and is cumulative till the final cracking failure happens. The local failure depth decreases for heated specimens at 100 C due to the melting of some rubber particles. In contrast, at 200 C° of heat, the crashing failure does not appear, and the specimen backs to the conventional concrete behaviour because the rubber lost its impact resistance property after melting.

Table 5. Impact resistance values

Specimen	The impact energy of the sample before the heat	Impact energy after 100 C° of heat	Impact energy after 200 C° of heat	Reduction percentage due to 100 C° heat	Reduction percentage due to 200 C° heat
NC	171.2	170.3	169.5	0.52	0.99
Sr 10	352.3	161.4	120.1	54.18	65.9
Sr 20	720.5	155.2	105.8	78.45	85.3
Sr 30	1285.2	142.8	98.7	88.88	92.3
Gr 10	493.6	175.3	125.6	64.48	74.5
Gr20	785.2	167.3	112.3	78.6	85.6
Gr30	2403.7	135.2	101.7	84.8	88.6

5. Conclusions

The effect of heat on rubberized concrete has been investigated using many parameters, such as replacement type, replacement percentages, heat effect, and heat increment. After testing the specimens, it could be concluded the following:

- Rubcrete compressive strength, in general, deteriorates after heat. Rubber particles start to soften or may be melting and form some gases inside concrete which what cause a hydrostatic pressure inside the cube and residual pressure inside the concrete block.
- Sand replacement specimens suffered from heat more than gravel replacement due to the finer size of crumb particles, which made them melt faster than the chip particles. This led to the conclusion that chip replacement is better than crumb replacement for structural members exposed to temperature.
- Dropping in tensile strength after replacement and without heating ranged from 20% to 47% for acceptable aggregate replacement and 16% to 40.75% for coarse aggregate replacements.
- At 100 c, the reduction in tensile strength ranged from 24% to 52% for crumb specimens and 21% to 48% for chip replacements. While the decrease in strength gets worse after 200 C° of heating
- The same behaviour, which appears in compressive strength, appears again in tensile strength; the chip replacement shows more resistance against heat than the crumb samples.
- The sand versus crumb replacement specimens lost an impact capacity ranging from 54% to 88% at heat 100 C° and 65% to 92% for heat equals 200 C°, which is due to melting the rubber particles and returning the rubberized concrete behaviour to the conventional concrete behaviour. 64% to 84% was the reduction in impact resistance after 100 C of heat subjected to gravel versus chips replacement; for 200 C°, the deterioration in energy absorption was 74% to 88%.
- It's not recommended to use rubberized concrete in construction sites exposed to a high temperature rise like baking ovens or nearby because the rubberized concrete loses its strength to the fourth or half after exposure to heat.

The suggested work after such a manuscript is to investigate enhancing rubberized concrete strength to avoid significant loss in strength after heat.

References

[1] Pongsopha P, Sukontasukkul P, Zhang H, Limkatanyu S. Results in Engineering Thermal and Acoustic properties of sustainable structural lightweight aggregate rubberized concrete. Results in Engineering. 2022;13:100333. https://doi.org/10.1016/j.rineng.2022.100333

[2] Roychand R, Gravina RJ, Zhuge Y, Ma X, Youssf O, Mills JE. A comprehensive review on the mechanical properties of waste tire rubber concrete. Construction and Building Materials. 2020;237:117651. https://doi.org/10.1016/j.conbuildmat.2019.117651

[3] Jawad EK, Makki OM, Al-Ajeel AI. Rubberized continuous deep beams under monotonic and repeated loads. Al-Qadisiyah Journal for Engineering Sciences.
[4] Youssf O, Hassanli R, Mills JE, Skinner W, Ma X, Zhuge Y, Roychand R, Gravina R. Influence of mixing procedures, rubber treatment, and fibre additives on rubcrete performance. Journal of Composites Science. 2019;3(2):41. https://doi.org/10.3390/jcs3020041
[5] Feng W, Liu F, Yang F, Li L, Jing L. Experimental study on dynamic split tensile properties of rubber concrete. Construction and Building Materials. 2018;165:675-687. https://doi.org/10.1016/j.conbuildmat.2018.01.073
[6] Al-Mutairee HMK, Makki OM. Rubberized concrete mix - discussions for literature review. Journal of Physics: Conference Series. 2021. https://doi.org/10.1088/1742-6596/1895/1/012011
[7] Aljarida magazine. Available at: https://www.aljarida.com/articles/1479573124876400300/. Accessed January 2025.
[8] Aslani F. Mechanical properties of waste tire rubber concrete. Journal of Materials in Civil Engineering. 2016;28(3):04015152. https://doi.org/10.1061/(ASCE)MT.1943-5533.0001429
[9] Guo J, Huang M, Huang S, Wang S. An experimental study on mechanical and thermal insulation properties of rubberized concrete including its microstructure. Applied Sciences. 2019. https://doi.org/10.3390/app9142943
[10] Shtayeh S, Abaza OA, Shtayeh SM. Crumbed rubber for non-structural Portland cement concrete applications. Dirasat, Engineering Sciences. 2010;37(2):201-221.
[11] Liu H, Wang X, Jiao Y, Sha T. Experimental investigation of the mechanical and durability properties of crumb rubber concrete. Materials (Basel). 2016;9(3):1-12. https://doi.org/10.3390/ma9030172
[12] Noaman AT, Bakar BHA, Akil HM. The effect of combination between crumb rubber and steel fiber on impact energy of concrete beams. Procedia Engineering. 2015;125:825-831. https://doi.org/10.1016/j.proeng.2015.11.148
[13] Kadhim AA, Al-Mutairee HMK. Experimental investigation of rubberized reinforced concrete continuous deep beams. Journal of King Saud University. 2021.
[14] Li Z, Huang X, Liang J. Experimental investigation on rubberized concrete mixed proportion design. Advanced Materials Research. 2012;399-401:385-389. https://doi.org/10.4028/www.scientific.net/AMR.399-401.385
[15] Makki OM. Mechanical and dynamical properties of structural rubcrete mixes. International Journal of Engineering. 2022;35(09):1744-1751. https://doi.org/10.5829/IJE.2022.35.09C.10
[16] Radhy ZH, Neamah MW, Makki OM, Al-Mutairee HMK. Experimental and statistical capacity of rubberized continuous deep beams under monotonic and repeated load. IOP Conference Series: Earth and Environmental Science. 2023;1232(1). https://doi.org/10.1088/1755-1315/1232/1/012022
[17] Beiram AAH, Al-Mutairee HMK. The effect of chip rubber on the properties of concrete. Materials Today: Proceedings. 2022. https://doi.org/10.1016/j.matpr.2022.01.209
[18] Sgobba S, Marano GC, Borsa M, Molfetta M. Use of rubber particles from recycled tires as concrete aggregate for engineering applications. 2nd International Conference on Sustainable Construction Materials and Technologies. 2010:465-475.
[19] Kassir MK, Bandyopadhyay KK, Reich M. Thermal degradation of concrete in the temperature range from ambient to 315 °C. ACI Materials Journal. 1996. https://doi.org/10.2172/432891
[20] Tahwia AM, Youssf O. Effect of rubber heat treatment on rubberized-concrete mechanical performance. 2022.
[21] Sukontasukkul P. Use of crumb rubber to improve thermal and sound properties of precast concrete panel. Construction and Building Materials. 2009;23(2):1084-1092. https://doi.org/10.1016/j.conbuildmat.2008.05.021
[22] Paine KA, Dhir RK. Research on new applications for granulated rubber in concrete. Construction Materials. 2009:7-17. https://doi.org/10.1680/coma.2010.163.1.7
[23] Suchat S, Aditapsatit P. On the performance of hybrid natural rubber rubberized concrete. Advanced Materials Research. 2014;844:186-189. https://doi.org/10.4028/www.scientific.net/AMR.844.186
[24] Bani-Hani EH, El Assad H, Al-Muqahwi Z. Overview of the effect of aggregates from recycled materials on thermal and physical properties of concrete. Cleaner Materials. 2022;4:100087. https://doi.org/10.1016/j.clema.2022.100087
[25] Youssf O, Swilam A, Tahwia AM. Performance of crumb rubber concrete made with high contents of heat pre-treated rubber and magnetized water. Journal of Materials Research and Technology. 2023;23:2160-2176. https://doi.org/10.1016/j.jmrt.2023.01.146
[26] ACI Committee 544. Guide to design with fiber-reinforced concrete. 2018.
[27] Makki OM, Al-Mutairee HMK, Jawad EK. Reinforced rubberized continuous deep beams under cyclic loadings. Al-Qadisiyah Journal for Engineering Sciences. 2024.
[28] ASTM C33. Standard specification for concrete aggregates. 2010.

[29] Dynamic response of sustainable rubberized reinforced concrete continuous deep beams. University of Babylon. 2023.
[30] Abdulameer A, Al-Mutairee HMK. An experimental study on behavior of sustainable rubberized concrete mixes. International Journal of Engineering. 2020;6(7):1273-1285. https://doi.org/10.28991/cej-2020-03091547
[31] Emam E, Saleh Y. Experimental study on enhanced crumb rubber concrete. International Journal of Scientific and Engineering Research. 2018;9(February):1240-1247.
[32] ASTM C143M. Standard test method for slump of hydraulic-cement concrete. ASTM International. 2012.
[33] BS 1881-116. Testing concrete - part 116: method for determination of compressive strength of concrete cubes. British Standards. 2010.
[34] ASTM International. Standard test method for compressive strength of cylindrical concrete specimens. Annual Book of ASTM Standards. 2010.
[35] ASTM C133-97. Standard test methods for cold crushing strength and modulus of rupture of refractories. 2015.
[36] Mohammed TJ, Breesem KM. Enhancement of the shear-flexural strength of the rubberized concrete prism beam by external reinforcement. International Journal of Engineering Transactions B: Applications. 2022;35(5):1017-1023. https://doi.org/10.5829/IJE.2022.35.05B.17
[37] ASTM C469-11. Standard test method for splitting tensile strength of cylindrical concrete specimens. ASTM International. 2008.

Blank Page

Research on Engineering Structures & Materials
www.jresm.org

Research Article

ML driven optimization of mechanical properties in hybrid fiber-reinforced tertiary blended high-performance concrete

Mahesh [1,a], M.S. Shobha [1,b], Poornima Hulipalled [2,c], Veerabhadrappa Algur [*,3,d]

[1]*Department of Civil Engineering, Rao Bahadur Y Mahabaleswarappa Engineering College, Ballari, Visvesvaraya Technological University, Belagavi, Karnataka, India*
[2]*Department of Master of Computer Applications, Kishkinda University, Ballari, Karnataka, India*
[3]*Department of Mechanical Engineering, Rao Bahadur Y Mahabaleswarappa Engineering College, Ballari, Visvesvaraya Technological University, Belagavi, Karnataka, India*

Article Info

Article History:

Received 24 Aug 2024
Accepted 29 Nov 2024

Keywords:

Hybrid fiber concrete;
Combined tertiary mineral admixture;
Machine learning;
Structural construction

Abstract

This study focuses on optimizing the mechanical properties of hybrid fiber-reinforced tertiary blended high-performance concrete (HFRTHPC) by integrating CSF and polypropylene fibers (PPF) into a mix of silica fume (SF), metakaolin (MK), and fly ash (FA). These mineral admixtures replace Ordinary Portland Cement (OPC) at varying levels of 0%, 15%, 22.5%, and 30%. A comprehensive analysis was conducted on 80 different concrete mixes, each with W/B ratios ranging from 0.275 to 0.375, and a total fiber content of 1.25% (0.5%-1% CSF and 0.25% PPF). The results showed a significant increase in compressive strength, with a maximum improvement of 30.24% after 28 days of curing. The optimal mix was identified as containing 5% SF, 5% MK, 5% FA, 1% CSF, and 0.25% PPF at a W/B ratio of 0.275. Additionally, regression equations were developed to predict the mechanical properties. The study also utilized three machine learning techniques—AdaBoost Regressor, Random Forest, and Extreme Gradient Boost Regressor—to model compressive, split tensile, and flexural strengths. Among these, the Extreme Gradient Boost Regressor exhibited superior predictive accuracy and generalization capabilities. This research offers valuable insights for optimizing sustainable concrete compositions and provides a foundation for future advancements in concrete technology.

© 2025 MIM Research Group. All rights reserved.

1. Introduction

In contrast to normal concrete, high-performance concrete (HPC) is developed with superior characteristics such as enhanced strength, durability, workability, and improved resistance to environmental factors. These qualities are achieved by incorporating low water-to-cement ratios and high-quality pozzolanic materials such as FA, SF, ground granulated blast furnace slag (GGBS), MK, and superplasticizers. High-performance concrete can involve up to 10 ingredients, focusing on strength and durability. The partial replacement of cement with one, two, or three pozzolanic materials can be termed binary, ternary, and tertiary/quaternary concrete mixes, respectively. Tertiary systems combining the pozzolanic materials offer advantages, blending silica fume and metakaolin with fly ash improves early strength, while fly ash enhances workability. This synergy is crucial for HPC development. Tertiary mixtures, including fly ash/GGBS, silica fume, and metakaolin, provide high strength, low permeability, corrosion and sulfate resistance, ASR resistance, and reduced thermal cracking. HPC represents a specialized form of concrete engineered for specific applications and environmental conditions, ensuring optimal performance

*Corresponding author: veereshalgur@gmail.com
[a]orcid.org/0009-0009-8110-7267; [b]orcid.org/0009-0001-1059-9606; [c]orcid.org/0000-0003-4680-8120; [d]orcid.org/0000-0001-6094-6197
DOI: http://dx.doi.org/10.17515/resm2024.409me0829rs

over the structure's design lifespan and exposure to varying loads and environments [1]. The blended concretes use fly ash, silica fume, ground granulated blast furnace slag, and metakaolin as partial cement replacements. These admixtures lower cement content, reducing the environmental impact of cement production. Reviewed research articles highlight improvements in mechanical properties, durability, workability, enhanced thermal performance, and long-term strength. The use of industrial by-products and potential cost savings are also noted [2]. In quaternary binders made with GGBS, FA, MK, and SF as partial replacements for Ordinary Portland Cement (OPC), the study focused on standard consistency, initial and final setting time. SF significantly increases water requirements due to its high surface area, while GGBS reduces the water/binder ratio. SF and GGBS extend setting time at various replacement levels, whereas SF and MK initially increase setting time but decrease at higher replacements. On the whole, the admixtures in the quaternary binder mix impact independently, with SF and MK notably enhancing consistency [3]. The effects of incorporating mineral admixtures such as FA, SF, GGBS, MK, and rice husk ash (RHA) on the properties of fresh concrete have been reviewed. The study compares normal and high-strength concrete partially replaced with these admixtures. The admixtures are classified into two types: chemically active (decreased workability and setting time but increased heat of hydration and reactivity) and micro fillers (increased workability and setting time but reduced heat of hydration and reactivity). While the small particle size and higher specific surface area of these admixtures improve concrete density and impermeability, they also lower workability, necessitating the use of superplasticizers [4]. Fly ash concrete typically had lower compressive strength. In contrast, binary combinations of Portland cement with silica fume or slag, as well as ternary combinations including both slag and silica fume, exhibited significantly higher compressive strengths. The addition of mineral admixtures also resulted in reduced water permeability values [5]. The quaternary binders with 50% partial replacement of OPC and 30% FA with 10% M/GGBS showed the highest compressive strength with a low water/binder ratio. An enhancement of about 25% and 10% higher flexural strength and around 11.9% and 11.2% in split tensile strength at longer ages were noted [6]. Enhanced compressive, split tensile and flexural strength was noticed for a quaternary blend of cement with 20% fly ash, 10% Lime powder, and 10% rice husk ash, for this same blend the corrosion resistance also levelled up [7]. Incorporating pozzolanic materials enhances concrete's resistance to aggressive agents, such as sulfuric acid. These additions reduce the amount of calcium hydroxide, which is most susceptible to acid attacks [8]. Concrete is brittle and weak in tension; early concrete hardening is prone to microcracks caused by environmental and load fluctuations. These limitations lead to the development of fiber-reinforced concrete (FRC). Initial studies on FRC focused on using single fiber types, demonstrating enhanced concrete properties, particularly in strength and durability, as fibers prevent surface cracking and improve impact strength. Current research has driven interest toward fiber hybridization, combining metallic and non-metallic fibers to leverage their respective advantages. Steel fibers enhance tensile strength, toughness, and stiffness, while fibers like PPF contribute to elasticity, mixability, and resistance. Combining these fibers results in composite fiber-reinforced concrete exhibiting superior strength properties compared to individual fibers [9-13]. Studies suggest that reinforced concrete containing 0.3% PPF demonstrates superior flexural and compressive strength compared to content levels up to 0.5%. The research reveals that the mix design with 0.3% PPF achieved the highest strength, with minimal variance (1.0% - 3.0%) from mixes with 0.25% PPF. As a result, 0.25% PPF was chosen for the experiment [14-15]. In examining CSF mechanical properties with an aspect ratio of 50, the research revealed that 3.0% CSF blends outperformed mixes with 0% to 2.0% fibers. Among all aspect ratios studied, CSF with an aspect ratio of 50 showed statistically better results in terms of strength. The study concluded that adding CSF up to 1% improved HPC strength meanwhile higher levels led to decreased compressive and tensile strengths, accompanied by drawbacks such as diminished ductility, increased cost, and reduced workability. CSF's primary role is crack prevention [16-17]. Research on enhancing structural strength and seismic resistance through fiber integration in concrete found that a composite blend of 80% crimped steel fiber and 20% polyolefin fiber showed robust qualities [18]. With the incorporation of CSF at levels of 0.55, 1.0% and 1.5%, HPC exhibited enhanced impact strength. The initiation strength for the first failure crack rose to 139%, 268%, and 366% and to 129%, 238%, and 321%, respectively, compared to normal concrete [19-20]. For a combined mix of cement, 20% GGBS, 10% MK, steel and glass fiber

at 2% showed an increase in compressive and split strength for a grade of M60 [21-22]. Optimal results were observed by replacing 10.0% of the cement with Metakaolin (MK), leading to increased compression strength at rates of 7%, 16.75%, 11.42%, and 6.0% for partial cement replacements of 5%, 10%, 15%, and 20% with MK, respectively [23]. The study highlights the importance of understanding the effective utilization of mineral admixtures in mortar. The findings are significant for optimizing the use of mineral admixtures in engineering applications, ensuring that they contribute to the desired properties of the mortar without remaining unreacted. Under a curing temperature of 30°C, when the replacement ratio exceeded 30%, the change in $Ca(OH)_2$ amount with replacement ratio was nearly linear. At this point, the excess fly ash essentially stopped consuming $Ca(OH)_2$. [24]. This study explored the strength and durability of HFRHPC with SF as an admixture. Using fixed PF and varying CF, it achieved significant gains in compressive (35.18%), split tensile (40.35%), and flexural strengths (71.54%) at 28 days [25]. This study examined HFRHPC incorporating FA as an admixture, with polypropylene and varying crimped steel fibers. Testing different FA levels and water-to-binder ratios, results revealed 1.25% hybrid fibers with 10% FA provided optimal strength, durability, and acid resistance, sustaining performance for 90 days [26]. This study assessed the effects of MK and hybrid fibers on High-Performance Concrete. With 0.25% polypropylene and varying steel fibers, results showed significant strength gains. Optimal mix—1.25% hybrid fibers with 10% MK—achieved peak compressive (37.05%), split tensile (42%), flexural (74.41%), and impact (68.32%) strengths after 28 days [27]. This study investigated the effects of combining Fly Ash, Silica Fume, Glass Fibers, and Polypropylene Fibers in Composite-Fiber Reinforced High-Performance Concrete. The optimal mix—5% FA and SF, with 1% GF and 0.25% PPF at a 0.275 W/B ratio—achieved maximum strength [28].

The ANOVA analysis revealed that different substitution levels of all three components significantly impacted the fresh and hardened properties of SCLCs. The findings showed that adding CS or MS to SCLC specimens improved the previously mentioned parameters, while ternary mixes with both MS and CS delivered the best performance [29]. The application of machine learning (ML) techniques, which make a significant contribution to the field of civil engineering by accurately predicting the mechanical properties of concrete, is particularly important. In recent times, the growth of soft-computing methodologies has given rise to ML as a reliable and accurate instrument for computer modeling. ML has become widely acknowledged as an effective methodology that can be implemented across diverse research domains, including concrete structures [30-31]. Studies have employed ML methods. During the training phase, the R-square value of the deep learning models was roughly 0.960, and during the testing phase, it was slightly above 0.940. But when it came to performance, the GRU model outperformed the others, as evidenced by an R-square value that was extremely greater than 0.990 in the learning phase and close to 0.961 in the testing phase. These findings point to the GRU model's excellent efficacy and accuracy in both phases [32]. The findings of the investigation showed that the suggested equations performed better at properly predicting than traditional techniques such as the linear regression model (LRM). In contrast to the LRM, the suggested equations produced lower values for MAE and RMSE and showed a higher coefficient of determination (R2) [33]. Compared to conventional approaches, ML provides better predictions for required mechanical characteristics [34-35]. Several studies have employed ML methods to predict the strength properties of conventional concrete [36-39]. ML methods are employed to forecast concrete strength [40-57] and the durability of concrete [58-59]. Nevertheless, the use of ML methods to predict compressive, flexural, and splitting tensile strengths in fiber-reinforced concrete is still not widely explored.

While extensive research has examined binary and ternary pozzolanic material combinations, limited studies explore the complex interactions and optimal mix proportions in tertiary/quaternary blends. More research is needed on the synergistic effects of materials like fly ash, silica fume, GGBS, and metakaolin across various proportions and environmental conditions. Regarding fiber optimization and hybridization in high-performance concrete (HPC), studies have shown enhanced properties with hybrid fibers, such as steel and polypropylene. However, the ideal fiber types, contents, and ratios for maximizing performance metrics like compressive strength, splitting tensile strength, flexural strength, and impact resistance are still underexplored,

especially in HPC applications. Further research is also required on the long-term effects of fiber hybridization in HPC.

Machine learning (ML) has been applied to predict mechanical properties in both conventional and HPC, yet its application to fiber-reinforced high-performance concrete (FR-HPC) is limited. There is a clear research gap in using ML techniques to accurately predict FR-HPC's compressive, flexural, and splitting tensile strengths. Additionally, achieving meaningful results with ML will require substantial input data collection. In order to get the desired findings, ML methods require the collection of an input dataset. To achieve this objective, we utilized eight input parameters, including W/B, cement, metakaolin, silica, fly ash, crimped steel fibers, polypropylene fibers, and the age of the specimens. The experiments were conducted using an absolute volume methodology for concrete mix design, while data points comprising the results of the experiments were gathered for algorithm implementation.

2. Experimental Program

2.1 Materials Used

In the current experimental study, OPC grade 43 as per IS 8112:1989, along with mineral admixtures such as FA, SF, and MK, were utilized. The physical and chemical properties of these materials are detailed in Tables 1. Local river sand served as the fine aggregate, while the crushed stone as coarse aggregate was also sourcing from local. Fine and Course aggregate physical properties provided in Table 2. To produce the concrete mix, the superplasticizer SP-430 was employed. Additionally, CSF and PPF were incorporated into the experiment, with their characteristics listed in Table 3.

Table 1. Physical and chemical properties of cement and mineral admixtures

Physical Properties	Cement	Fly ash	Metakaolin	Silica fume
Specific gravity.	3.12	2.17	2.61	2.21
Mean grain siz(μm)	8 -210	20-25	2.53	1.14
Specific area (cm^2/g)	2947	3988	15,000 to18,000	18,000 to30,000
Color	Grey.	Tan to dark grey.	Ivory to cream.	light to darkgrey.
Chemical Properties	Fly Ash (FA)	Metakaolin (MK)	Silica Fume (SF)	Code IS 3812 Requirement
Silica (SiO_2)	59.16	60-65	92.3	(SiO_2)+
Aluminum (Al_2O_3)	30.64	43.18	1.3	(Al_2O_3)+
Iron oxide (Fe_2O_3)	4.70	0.6	1.0	(Fe_2O_3) = 70.0 (min)
Calcium oxide (CaO)	2.85	1.06	1.6	--
Magnesium oxide(MgO)	0.36	0.61	0.9	5.0 (Max)
Loss on ignition	0.21	0.70	1.53	6.0(Max)

Table 2. Physical properties Fine and Coarse aggregate

Properties	fine aggregate	coarse aggregate
Specific gravity	2.68	2.75
Fineness modulus	2.74	6.73
Bulk density		
i) Loose	14.67 kN/m^3	13.291 kN/m^3
ii) Compacted	16.04 kN/m^3	15.001 kN/m^3
Grading	Zone – II	--

Table 3. Physical properties fibers

Properties	CSF	PPF
Specific Gravity	7.85	0.912
Tensile strength (MPa)	1050	530
Density (kg/m^3)	7850	910
Length of fiber (mm)	30	12
Equivalent diameter (mm)	0.60	0.35
Shape	crimped	monofilament



Fig. 1. Crimped steel fibers



Fig. 2. Polypropylene fibers



Fig. 3. The materials employed in the current study include

2.2 Materials and Mix Proportioning

In this experiment, mix proportions were assessed using an absolute volume approach. Ingredients were measured by volume and then converted to weight to ensure a uniform mixture. All ingredients were dry-mixed initially, with steel and polypropylene fibers added in this phase. Water and a superplasticizer were then introduced to achieve a homogeneous concrete mix. Table.4 provides the percentage dosage of each component in the sample. Mix identification employed a coding system: the first three Alphabets CTM represents combined tertiary mineral admixture, MK, SF, and FA. The subsequent number indicated the collective percentage of cement replaced by combining MK, SF, and FA. Alphabets P, Q, R, and S represented composite fiber matrices with varying CSF and PPF percentages: P (0% CSF +0% PPF), Q (0.50% CSF + 0.25% PPF), R (0.75% CSF + 0.25% PPF), and S (1.0% CSF + 0.25% PPF). The final letter indicated the A/B ratio (A = 1.75), the W/B ratios were depicted by the last number (1= 0.275, 2 = 0.300, 3 =

0.333, 4 = 0.350, and 5 = 0.375). For instance, a reference mix with A/B = 1.75 and W/Bof 0.275 and 788.29 kg/m^2 of cement was denoted as CTM0PA1, signifying the absence of fibers and mineral admixtures. Another mix, CTM15PA1 used 660.37 kg/m^2 of cement and 38.85 kg/m^2 of each MK, SF, and FA, indicating a specific combination of fibers and mineral admixtures. The nomenclature and compositions of various mixes are detailed in Table 4, maintaining consistent design principles across different W/B ratios to ensure a comprehensive assessment.

Table. 4 Mix. proportions of HFRHPTC mix for W/B= 0.275.

Mix designation	Cement (%)	MK (%)	SF (%)	FA (%)	CSF (%)	PPF (%)	Total percentage of tertiary mineral composition
CTM0PA1	100	0	0	0	0	0	0
CTM15PA1	85	5	5	5	0	0	15
CTM22.5PA1	77.50	7.50	7.50	7.50	0	0	22.5
CTM30PA1	70	10	10	10	0	0	30
CTM0QA1	100	0	0	0	0.50	0.25	0
CTM15QA1	85	5	5	5	0.50	0.25	15
CTM22.5QA1	77.50	7.50	7.50	7.50	0.50	0.25	22.5
CTM30QA1	70	10	10	10	0.50	0.25	30
CTM0RA1	100	0	0	0	0.75	0.25	0
CTM15RA1	85	5	5	5	0.75	0.25	15
CTM22.5RA1	77.50	7.50	7.50	7.50	0.75	0.25	22.5
CTM30RA1	70	10	10	10	0.75	0.25	30
CTM0SA1	100	0	0	0	1.00	0.25	0
CTM15SA1	85	5	5	5	1.00	0.25	15
CTM22.5SA1	77.50	7.50	7.50	7.50	1.00	0.25	22.5
CTM30SA1	70	10	10	10	1.00	0.25	30

*Similarly designs of constituents are used for other W/B ratios W/B= 0.300(2), 0.325(3), 0.350(4), and 0.375(5)

2.3 Experimental Methods

The compressive strength of concrete-cubic specimens (100 x 100 x 100 mm) was tested as per ASTM C39. The split tensile strength of concrete-cylinder specimens (150 mm diameter, 300 mm height) was evaluated following ASTM C496, and the flexural strength of concrete-prism or beam specimens (500 x 100 x 100 mm) was tested in accordance with ASTM C78. After demolding, all specimens were cured for 28 days. Cubic and cylindrical specimens were tested using a digital compression testing machine as per IS 14858, while prism or beam specimens were tested using a universal testing machine as per IS 516-1959. Each test was conducted with three samples per combination, and the average values are reported.

2.4 Machine Learning Approach

Within the scope of this investigation, the experiment yielded a total of 320 data samples and was utilized for the purpose of training ML methods. During data collection, the proportions of the combination and the output that was intended were taken into consideration. This was carried out to satisfy the requirements because the models needed the same input variables for every mixture to reliably estimate the outcomes.

The distribution of data trials used in testing and training the model was 30% and 70%, respectively. The levelof accuracy of a model can be assessed by examining the R^2 result of the projected outcome. Values closer to zero indicate a greater degree of variance, while values that are closer to one show a close alignment between the prediction model and experimental data. The statistical measures, including mean absolute error (MAE), mean square error (MSE), and root mean squared error (RMSE), were employed to measure the exactness of a model. Further details about the machine learning (ML) models and optimization techniques used in this investigation are covered in the sections that follow.

2.4.1 Ensemble Machine learning

In contrast to conventional machine learning, which typically employs a single model, ensemble learning makes use of multiple models. Ensemble methods construct a final prediction by combining the predictions of multiple models, as opposed to relying on the estimates of a single model. It results in enhanced efficacy in comparisonto standalone models. Through the utilization of three ensemble methods, namely Ada Boost (AdaB), random forest (RF), and extreme gradient boost (XGB), they have the capacity to significantly diminish errors, enhance precision, and augment generalizability. The important tuning parameters of the three ML models are listed in Table 5 to produce better performance.

2.4.2 Ada Boost

The AdaB regressor approach starts by training a weak learner on the original dataset with identical weights for each data point. In future rounds, it concentrates on misclassified occurrences, modifying the weights to emphasize difficult cases. It distributes weights to each weak learner based on their performance, and their predictions are combined in a weighted sum to get the final prediction. The mentioned iterative approach persists until the desired number of weak learners has been reached [52]. AdaB's adaptability to complicated datasets and ability to reduce overfitting make it an effective tool for regression tasks. In Python, the scikit-learn library includes the AdaBoost Regressor class for the implementation, which commonly uses decision trees as weak learners. AdaBoost Regressor stands out for its ensemble method, which provides robustness and increased generalization across a variety of regression settings. The final prediction for a new input X is the weighted sum of weak learner predictions:

$$\hat{y}(X) = \sum_{t=1}^{T} \alpha_t h_t(X) \tag{1}$$

Where; $\hat{y}(X)$ is anticipated output for input X, T represents the total count of weak learners, α_t is the weight assigned to the t-th weak learner, $h(X)$ is the prediction of the t-th weak learner for input X. AdaB creates a resilient and accurate ensemble model for regression tasks by combining weak learners thatfocus on different parts of the data.

2.4.3 Random Forest

RF is an ensemble learning approach for regression tasks that combines predictions from various decision trees to increase accuracy and decrease overfitting. In this model, decision trees serve as base learners, and the algorithm incorporates randomization by taking only a subset of characteristics at each split and using bootstrapped sampling [50]. The training procedure entails creating numerous trees independently, and during prediction, the final output is frequently an average of individual tree forecasts. This method improves resilience and handles non-linear connections effectively. RF provides insights regarding feature relevance, which helps with feature selection. In Python, the scikit-learn library provides the Random Forest Regressor class for easy implementation. For a given input X, the RF prediction is the mean of predictions from all the individual trees:

$$\hat{y}(X) = \frac{1}{N} \sum_{t=1}^{N} T_t(X) \tag{2}$$

Where; $\hat{y}(X)$ is the predicted output for input X, N is number of trees, (X) is prediction of the t-th tree for input X.

2.4.4 XG Boost

XGB Regressor, a gradient-boosting extension, is efficient, scalable, and regularized for regression applications.For better prediction, the system creates decision trees sequentially, correcting earlier errors. To avoid overfitting, the function minimizes the difference between the expected and actual values while penalizingmodel complexity using a regularization factor. The final forecast is the sum of all tree predictions. Regularization terms control tree complexity in XGB, improving

generalization to fresh data [54]. XGBoost efficiently handles massive datasets and uses feature-important insights to choose features. The number of trees, learning rate, tree depth, and minimum child weight must be tuned. The XGB Regressor class from the XGBoost package in Python is used for implementation. XGB is used for varied regression scenarios that require accurate and robust predictions due to its versatility. The XGB minimizes an objective function that combines a loss function measuring the difference between the actual and anticipated values with a regularization term. The function for XGB is defined as follows:

$$Objective = \sum_{i=1}^{n} L(y_i, \hat{y}_i) + \sum_{k=1}^{K} \Omega(f_k) \quad (3)$$

Where; n is the number of samples used for training, y_i is the actual value for the i-th sample, $\hat{y}_i$ is the predicted value for the i-th sample, $L(y_i, \hat{y}_i)$ is the loss function measuring the difference between the true and predicted values, K represents leaves in the tree, f_k is the score associated with the k-th leaf, $\Omega(f_k)$ is the regularization.

The regularization term and loss function are parameter and hyperparameter sensitive. Mean Squared Error andAbsolute Loss are two popular loss functions used in regression applications.

2.4.5 Validation of models

Evaluation metrics quantify a machine learning model's performance on a regression task. They help to assess model prediction accuracy and impact model selection and optimization. Evaluation metrics provide quantitativeperformance data to the machine learning pipeline, assisting in the creation, optimization, and deployment of models. The ML algorithms were verified using statistical error assessments like MAE, MSE, RMSE, and R^2 onthe test dataset and the k-fold approach while training the models. In this study, we have used 10-fold validations. The k-fold technique utilizes multiple train-test splits and averages the results to reduce the variancein the performance estimate and provide a more robust assessment of the model's effectiveness.

$$MAE = \frac{1}{N}\sum_{i=1}^{n} |F_i - V_i| \quad (4)$$

$$MSE = \frac{1}{N}\sum_{i=1}^{n} (F_i - V_i)^2 \quad (5)$$

$$RMSE = \sqrt{MSE} \quad (6)$$

$$R^2 = 1 - \frac{\sum_{n=1}^{n}(V_i - F_i)^2}{(V_i - V)^2} \quad (7)$$

Where n = number of data points, V_i F_i = predicted findings, and V_i = actual results, V = mean of actual values

3. Results and Discussion

3.1 Experimental Approach

3.1.1 Compression Strength

The cube compressive strength at 7 and 28 days cuing of combined tertiary mineral admixture-based HFRHPTC concrete mix results are presented in Table 6.

Table 6. Cube compressive strength of Tertiary mineral admixture based HPC mix

Mix Designation	Cube compressive strength MPa		Mix Designation	Cube compressive strength MPa	
	7 days	28 days		7 days	28 days
CTM0PA1	59.04	73.9	CTM0RA3	59.34	75.17
CTM15PA1	67.99	85.18	CTM15RA3	70.03	88.23

CTM22.5PA1	62.99	78.57	CTM22.5RA3	63.64	78.44
CTM30PA1	57.85	71.93	CTM30RA3	57.31	71.72
CTM0QA1	60.84	75.84	CTM0SA3	61.24	76.34
CTM15QA1	72.55	91.55	CTM15SA3	72.23	90.32
CTM22.5QA1	65.24	81.83	CTM22.5SA3	65.42	80.72
CTM30QA1	59.69	74.29	CTM30SA3	59.06	73.08
CTM0RA1	62.56	79.68	CTM0PA4	53.29	68.63
CTM15RA1	74.99	93.47	CTM15PA4	60.72	78.42
CTM22.5RA1	67.94	83.34	CTM22.5PA4	55.99	71.39
CTM30RA1	61.2	76	CTM30PA4	52.71	66.71
CTM0SA1	64.5	80.1	CTM0QA4	55.03	70.33
CTM15SA1	76.89	95.69	CTM15QA4	64.28	83.58
CTM22.5SA1	70.15	85.55	CTM22.5QA4	57.42	75.29
CTM30SA1	63.09	76.29	CTM30QA4	53.98	68.13
CTM0PA2	57.09	72.39	CTM0RA4	57.2	73.44
CTM15PA2	65.1	83.04	CTM15RA4	66.3	86.3
CTM22.5PA2	60.79	76.54	CTM22.5RA4	61.04	77.04
CTM30PA2	55.66	69.99	CTM30RA4	56.21	70.41
CTM0QA2	58.77	73.63	CTM0SA4	58.03	75.37
CTM15QA2	69.9	88.93	CTM15SA4	68.16	88.72
CTM22.5QA2	62.98	79.28	CTM22.5SA4	62.25	78.39
CTM30QA2	57.22	72.08	CTM30SA4	57.22	72.04
CTM0RA2	61.14	75.6	CTM0PA5	52.72	66.98
CTM15RA2	72.22	91.03	CTM15PA5	60.24	76.04
CTM22.5RA2	65.55	81.15	CTM22.5PA5	53.43	69.43
CTM30RA2	59.02	74.02	CTM30PA5	50.75	64.75
CTM0SA2	62.53	78.42	CTM0QA5	54.34	68.24
CTM15SA2	73.88	93.2	CTM15QA5	63.53	81.13
CTM22.5SA2	67.62	83.59	CTM22.5QA5	55.57	73.02
CTM30SA2	60.92	75.01	CTM30QA5	52.18	66.93
CTM0PA3	55.6	70.82	CTM0RA5	55.66	72.56
CTMF15PA3	63.28	81.47	CTM15RA5	65.28	84.08
CTM22.5PA3	58.86	74.16	CTM22.5RA5	57.09	75.19
CTM30PA3	53.98	67.88	CTM30RA5	52.96	68.66
CTM0QA3	57.33	71.37	CTM0SA5	57.46	73.12
CTM15QA3	67.25	86.15	CTM15SA5	67.01	86.54
CTM22.5QA3	61.11	76.87	CTM22.5SA5	59.12	77.05
CTM30QA3	55.47	70.07	CTM30SA5	55.19	69.29

3.1.1.1 Effect of Water-Binder Ratio on Cube Compressive Strength Of Tertiary Mineral Admixture Based HPC Mix With Hybrid-Fibers

The variation of cube compressive strength for blended tertiary mineral admixture-based HPC mix with different W/B ratios is shown in Figures 4 and 5, with results detailed in Table 6 for 7-day and 28-day compressive strength. It can be observed that the compressive strength of HFRHPTC mix declines as the W/B ratio increases from 0.275 to 0.375, which is similar to the behavior of plain HPC mix. The highest compressive strength of HFRHPTC mix at both 7 and 28 days for all W/B ratios is observed with 15% cement replaced by blended tertiary mineral admixture. The maximum cube compressive strength attained at 7 days is 76.88 MPa for the CTM15SA1 mix with a W/B ratio of 0.275. For the same mix, with W/B ratios ranging from 0.300 to 0.375, the strength was reduced by 6.07% to 15.10%, respectively. Similar trends are observed for the 28-day compressive strength, which was 95.68 MPa for the CTM15SA1 mix with a W/B ratio of 0.275. For the same mix, with W/B ratios ranging from 0.300 to 0.375, the strength was reduced by 4.87% to 12.13%, respectively.

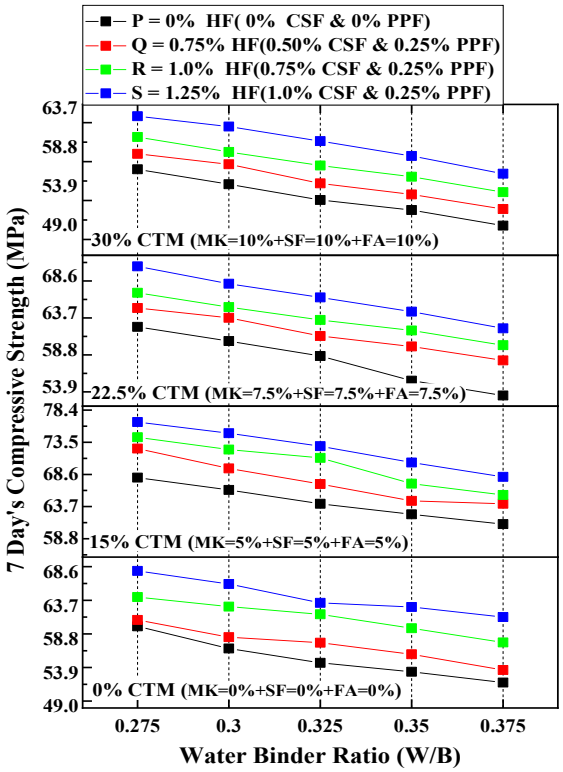


Fig. 4. Seven days Cube compression strength Vs. W/B ratio for HFRTHPC mix

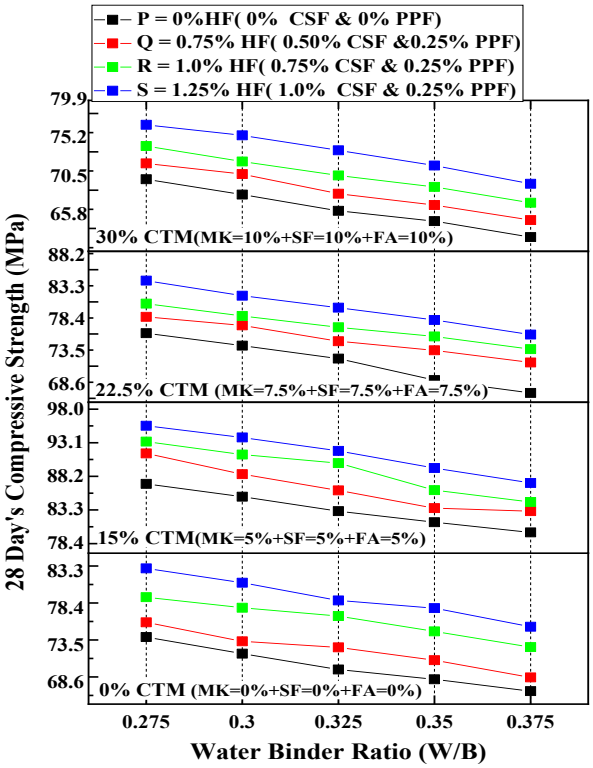


Fig. 5. Twenty-eight days Cube compression strength Vs. W/B ratio for HFRTHPC mix

3.1.1.2 Effect of Replacement Percentage of Cement by Combined Tertiary Mineral Admixture on Cube Compressive Strength of Tertiary Mineral Admixture Based HPC Mix with Hybrid-Fibers

To better understand the strength deviation caused by replacing cement with blended tertiary mineral admixtures in each mix, Figures 6 and 7 plot the cube compressive strengths for testing at 7 and 28 days for all water/binder ratios against the percentages of three combined mineral admixtures for various volumes of composite fibers. The correlation between the total percentages of tertiary mineral admixture and the 28-day cube compressive strength demonstrates that using a mixed tertiary mineral addition in place of cement increased the 28-day cube compressive strength. The addition of MK, SF, and FA enhances the mix's load-carrying capacity. The maximum cube compressive strength was obtained when 15% of the cement was replaced with mixed tertiary mineral additives across all composite materials. Beyond this 15% replacement, the compressive strength decreased. The CTM15SA1 mix outperformed the CTM0PA1 mix in 28-day cube compressive strength for high-fiber-reinforced high-performance concrete up to 29.49%. The fine mineral admixtures MK, SF, and FA, along with the filling of the interfacial transition zone with fine mineral admixture particles, generated pozzolanic reactions, which increased strength by up to 15% replacement due to the micro-filler effect [2,4,7,24]. At dosages greater than 15%, there was insufficient $Ca(OH)_2$ for the pozzolanic process, reducing the cube compressive strength as MK, SF, and FA then acted solely as fillers.

In comparing HPC mixes at a 20% replacement level, metakaolin in binary mixes achieved the highest compressive strength 91.70 MPa (A. gouda et al., 2022) [27], followed by silica fume 90.22 MPa (A. gouda et al., 2021) [25] and fly ash 87.40 MPa (A. gouda et al., 2020) [26]. The ternary mix of fly ash and silica fume improved strength to 92.32 MPa (S. Patil et al., 2021) [28]. However, the highest performance was observed in the tertiary blend of fly ash, metakaolin, and silica fume, reaching a compressive strength of 95.95 MPa. This superior performance is attributed to the synergistic effect of combining all three mineral admixtures, which enhances the concrete's microstructure through better particle packing, reduced porosity, and improved bonding, resulting in an overall increase in strength and durability.

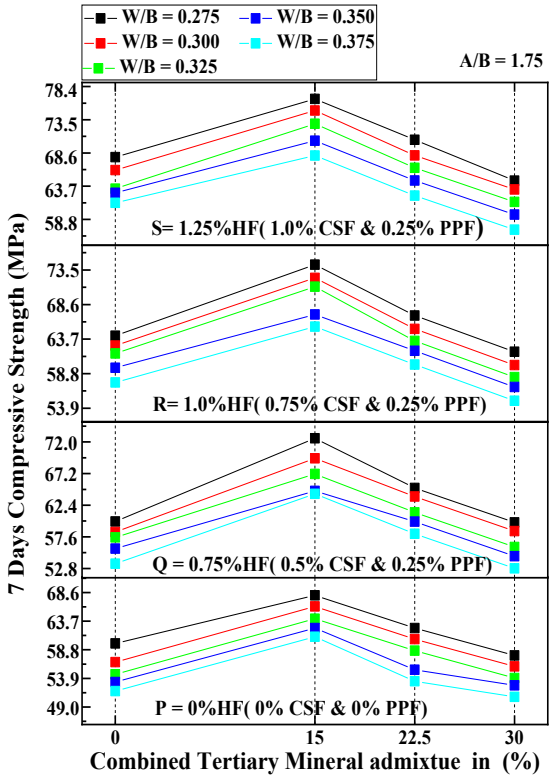


Fig. 6. Seven days cube compression strength Vs. % of combined tertiary mineral admixture

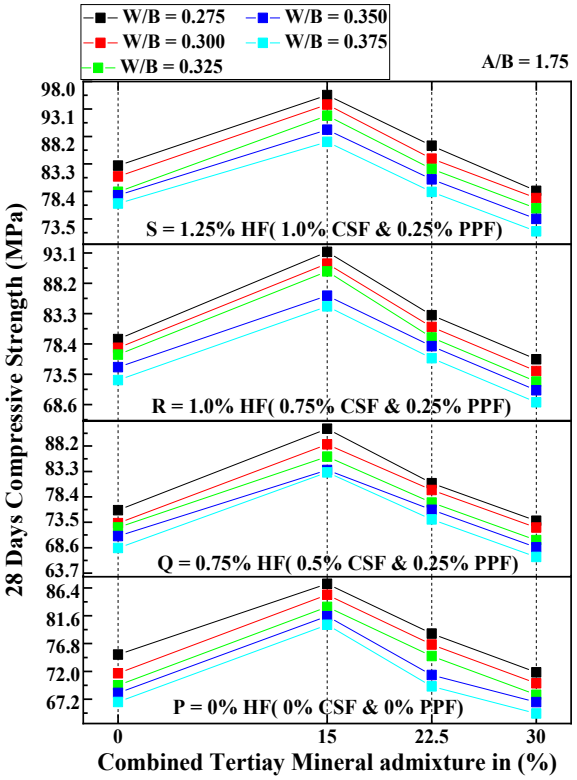


Fig. 7. Twenty-eight days cube compression strength Vs. % of combined tertiary mineral admixture

3.1.1.3 Effect of Composite Fiber Volume Percentage on Cube Compressive Strength of Tertiary Mineral Admixture Based HPC Mix with Hybrid-Fibers

Figs. 8 and 9 plot the cube compressive strengths against the volume percentages of composite fibers for various percentages of blended tertiary mineral admixture across different ages and water/binder ratios. This analysis aims to understand how composite fibers impact the compressive strength of each mix. The figures show that the compressive strength of the HFHPTC mix increases as the percentage of composite fibers is added. Specifically, the 28-day cube compressive strength improved with the addition of 0, 0.5, 0.75, and 1% CSF combined with a constant 0.25% PPF. This increase in cube compressive strength suggests a strong relationship between the fiber and the cement concrete matrix. The addition of composite fibers enhances the mixture, with the maximum cube compressive strength achieved at 1% CSF and 0.25% PPF for various amounts of mixed tertiary mineral admixture. For the PL0PA1 mix, the 28-day cube compressive strength increased by 23.89%, 26.49%, and 29.49% for the CTM15QA1, CTM15RA1, and CTM15SA1 mixes, respectively. The ability of these fibers to act as reinforcement at both macro and micro levels contributes to this performance. At the microscopic level, the fibers prevent the growth of microcracks, significantly influencing how microcracks form in the matrix. With more fibers in the matrix, the capacity for energy absorption increases, reducing the likelihood of micro and macro cracks forming and thus boosting the concrete's strength. While adding mono fibers to regular concrete enhances only ductility, the use of composite fibers and mixed mineral admixtures in this experiment significantly boosted the strength over plain HPC concrete due to the strain-hardening response of hybrid fiber-reinforced concrete [13-16, 18-22]. The greatest cube compressive strengths of the CTM15SA1 mix were 76.88 MPa and 95.68 MPa at 7 and 28 days, respectively

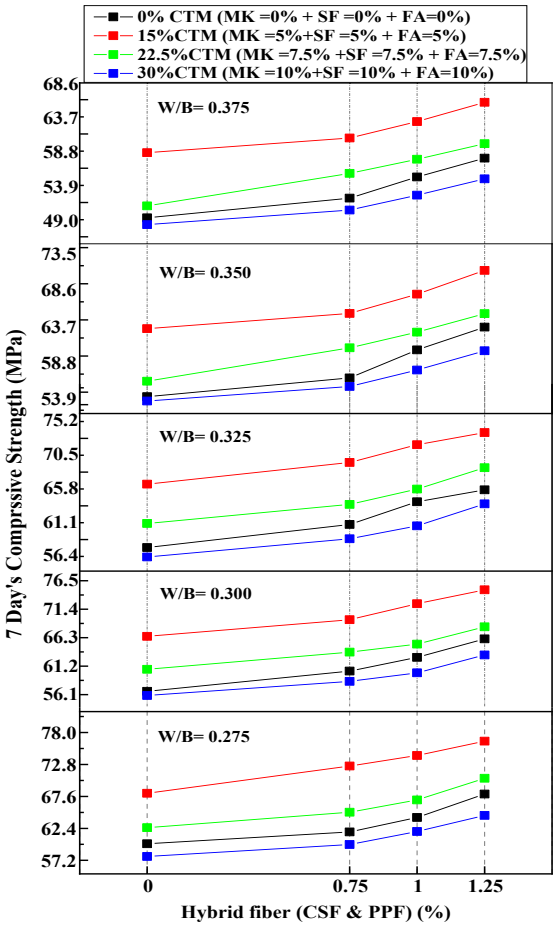


Fig. 8. 7 days Cube compressive strength Vs. volume % of composite fibers

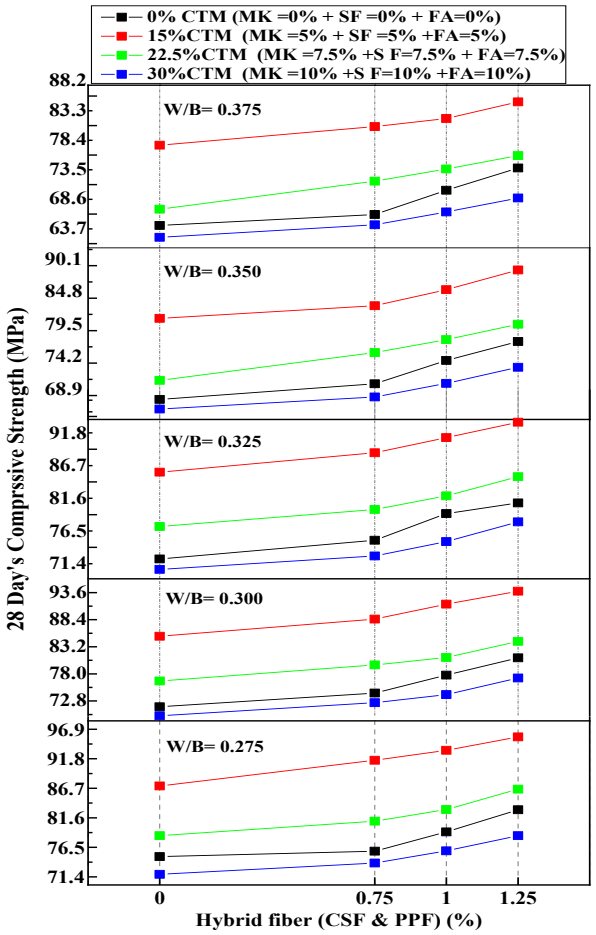


Fig.9. 28 days Cube compressive strength Vs. volume % of composite fibers

3.1.2 Split Tensile and Flexural Strength.

Figures 10 and 11 show the effect of replacing cement with varying percentages of combined tertiary mineral admixture on the 28-day curing split tensile and flexural strength. With a 15% replacement of cement by combined tertiary mineral admixture, the split tensile and flexural strengths of the mixture improved by 40.70% and 38.22% respectively, compared to the reference mix. For the CTM15SA1 mix, the highest split tensile and flexural strengths achieved were 7.04 MPa and 11.21 MPa respectively, indicating that 15% is the optimal substitution level. Beyond this percentage, insufficient availability of $Ca(OH)_2$ for the pozzolanic process reduces strength [2,4,24]. Figures 12 and 13 illustrate the effect of composite/hybrid fiber volume percentage on the split tensile and flexural strengths of high-performance concrete with blended tertiary mineral admixture. The load-carrying capacity of the mixture is enhanced by the inclusion of mixed steel and polypropylene fibers [13-16]. The current experiment shows that the greatest split tensile and flexural strengths were achieved with a combination of 1% crimped steel fiber and 0.25% polypropylene fiber, totalling a 1.25% hybrid fiber ratio.

In comparing split tensile and flexural strengths across HPC mixes at a 20% cement replacement level, the binary mix with metakaolin achieved the highest split tensile 7.0 MPa and flexural strengths 9.94 MPa (A. gouda et al., 2022) [27] among individual admixtures. However, the ternary mix of fly ash and silica fume offered only a slight improvement over other binary options, with split tensile and flexural strengths of 6.16 MPa and 9.12 MPa, S. (Patil et al., 2021) [28] respectively. The proposed tertiary mix, combining fly ash, metakaolin, and silica fume, delivered the most significant enhancements, reaching 7.04 MPa in split tensile strength and 11.21 MPa in flexural strength, the highest values in both categories.

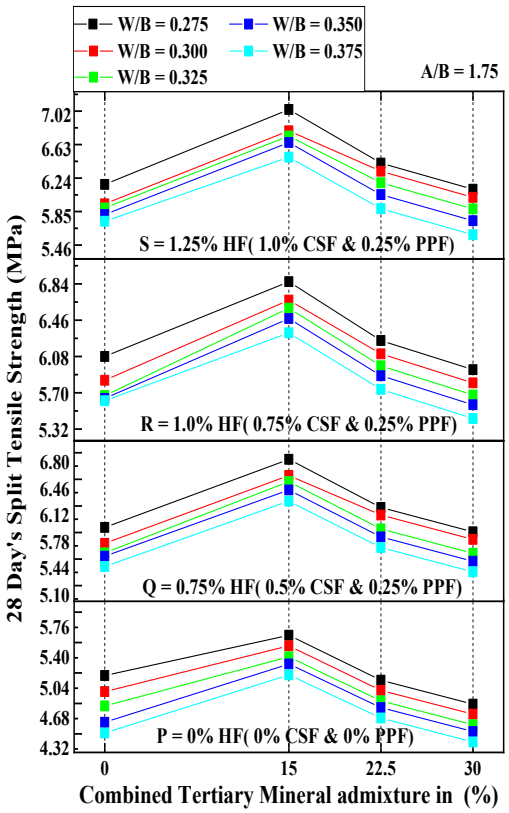


Fig. 10. Twenty-eight days Split Tensile strength Vs. % of combined tertiary mineral admixture

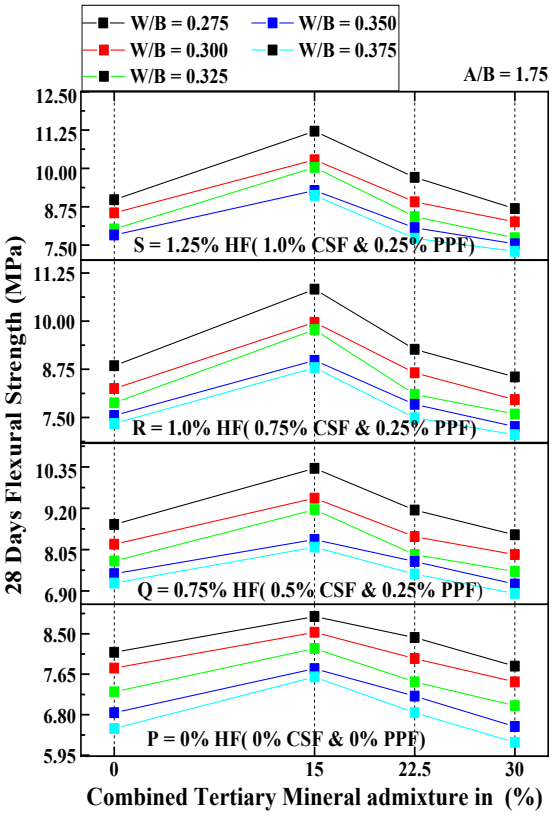


Fig. 11. Twenty-eight days Flexural strength Vs. % of combined tertiary mineral admixture

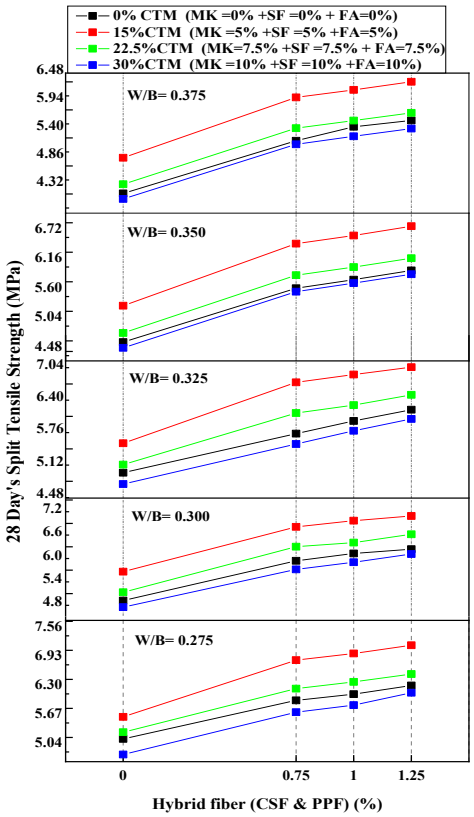


Fig. 12. Twenty-eight days Split Tensile strength Vs. volume % of composite fibers

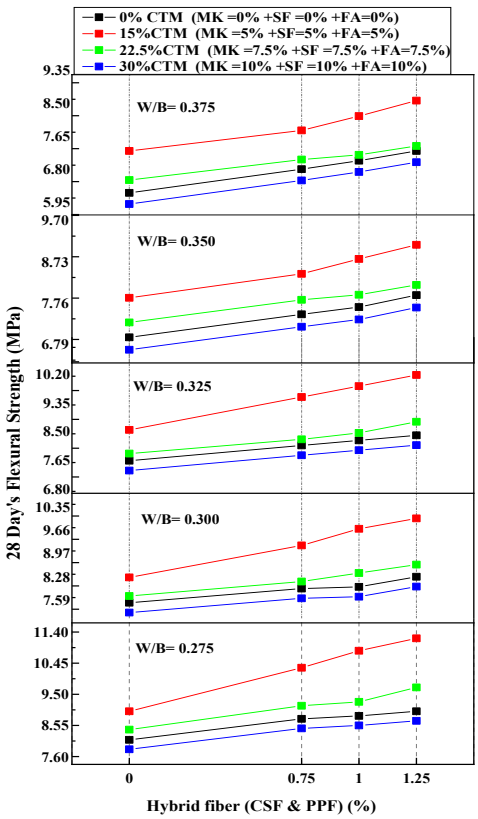


Fig.13. Twenty-eight days Flexural strength Vs. volume % of composite fibers.

3.1.3 The Inter-Relation Among Different Mechanical Properties of Tertiary Mineral Admixture Based HPC Concrete Mix with Hybrid Fibers

The interrelationships between cub compression strength and split-tensile strength, and cub compression strength and flexural strength, are depicted in Fig. 14 and Fig. 15 for specimens that were cured for 28 days. The formula $f_t = 0.7\sqrt{f_{ck}}$ MPa for normal concrete is prescribed by the BIS code IS:456-2000. This relationship was determined to be applicable for the hybrid fiber-reinforced tertiary blended HPC at 28 days of curing, the connection between split tensile strength and cub compressive strength was found to be $f_{ct} = 0.689\sqrt{f_{ck}}$ MPa, with a higher correlation value of 0.98756. Furthermore, a stronger correlation coefficient of 0.98588 was found for the link between cub compression strength and flexural strength for the hybrid fiber-reinforced tertiary mix at 28 days of curing, which is $f_r = 0.98\sqrt{f_{ck}}$ MPa.

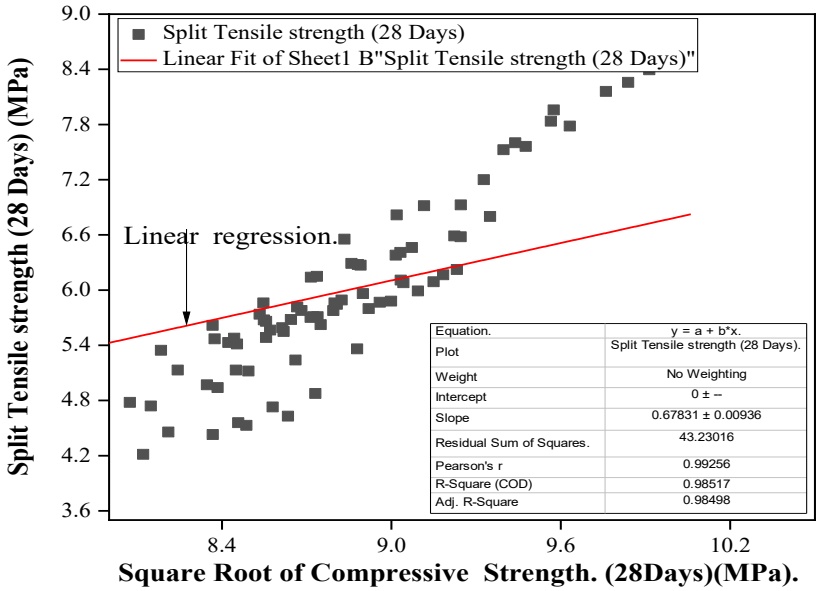


Fig. 14. Relationship between cube compression and split tension strength.

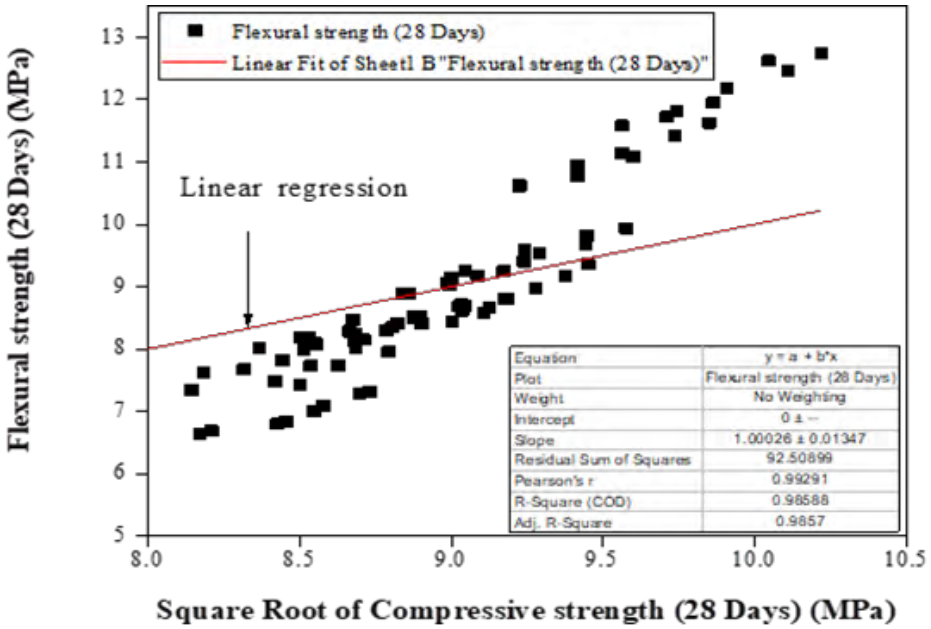


Fig. 15. Relationship between cube compression and flexural strength

3.2 Machine Learning Approach

The AdaBoost regressor was used to estimate the compressive strength of HFRTHPC, as illustrated in Fig. 16, which compares predicted and actual results. The model had an R-squared score of 0.903 for the training datasetand 0.897 for the test dataset. Despite its performance, with MAE = 0.6884, MSE = 0.8388, and RMSE = 0.9998 (Table 5), the errors appear to be outside the intended range when compared to other methods. The error distribution map in Fig. 17 shows the differences between the anticipated and practical results of HFRTHPC compressive strength using AdaBoost. Notably, the cumulative error estimates continue to be below 6 MPa. We recorded a maximum error of 5.72 MPa, a minimum error of 0.25 MPa, and an average error of 2.64 MPa.

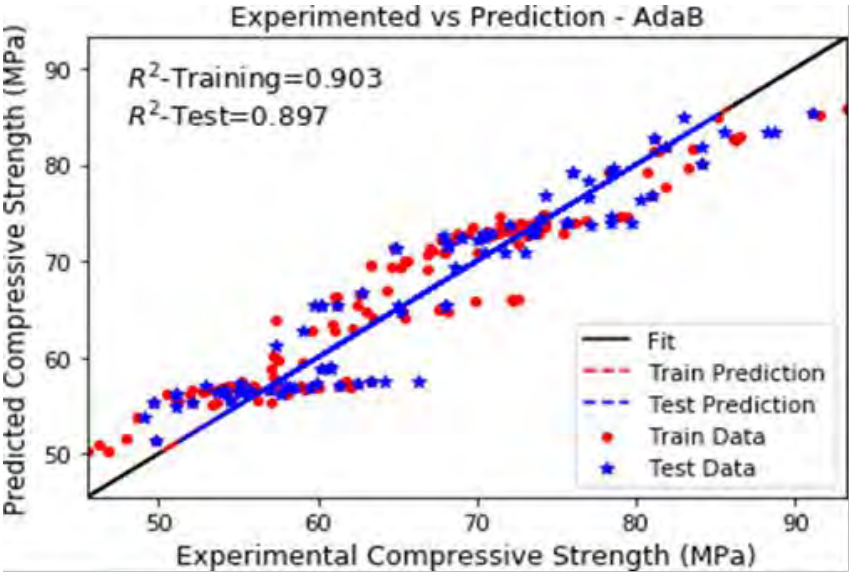


Fig. 16. Predicted V/s Experimental results for HFRTHPC CS – AdaB model

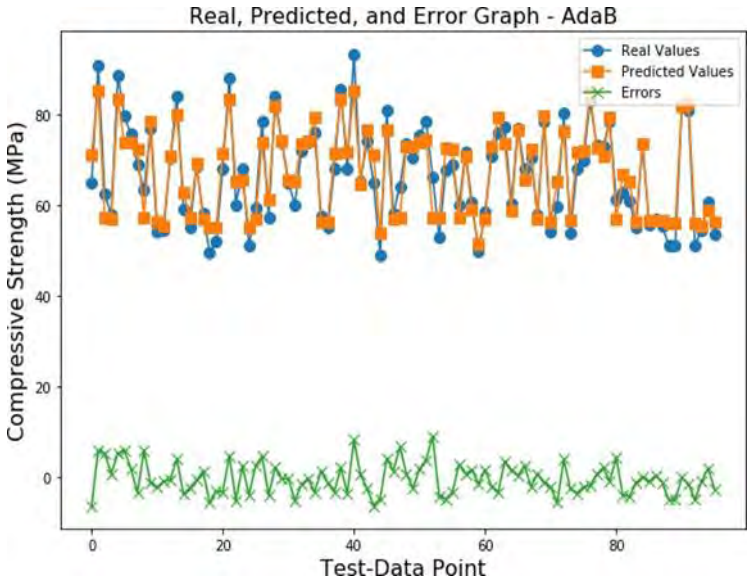


Fig. 17. Real, Predicted and Error distribution for AdaB model

Regression between the anticipated values and experimental values for HFRTHPC was conducted by adopting the RF algorithm, as illustrated in Fig.18. The RF shows less error variance and better-estimated outcomes than AdaB. The adequacy of the RF model is represented by an acceptable R2 value for training and testing of 0.997 and 0.962, respectively, and MAE = 0.4247, MSE = 0.420, and RMSE = 0.648. The error distribution of RF predicted and experimental for HFRTHPC compressive strength is illustrated in Fig.19.The total error values are below 6 MPa. Based on this distribution, the highest, lowest, and average values are 5.788, 0.032, and 1.546 MPa, respectively. As a result, the RF prediction findings are more precise than the AdaB model.

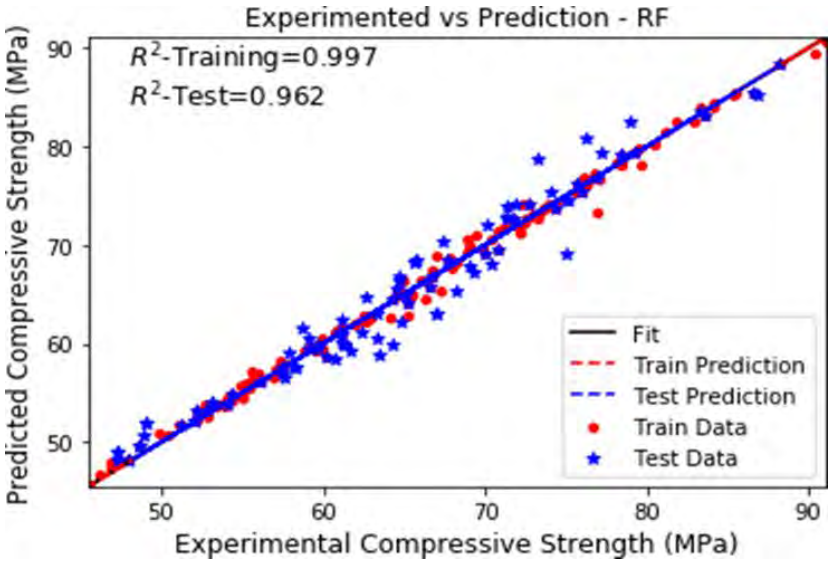


Fig. 18. Predicted V/s Experimental results for HFRTHPC CS – RF

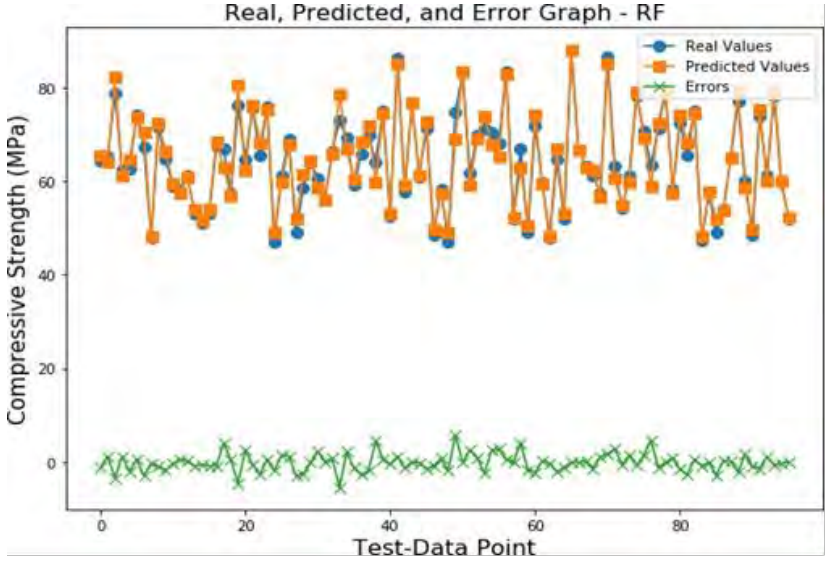


Fig. 19. Real, Predicted and Error distribution for RF model

Fig. 20 and Fig. 21 depicts the predicted results and error pattern representing the expected and experimental results for the compressive strength of HFRTHPC. Based on this distribution, the highest, lowest, and mean values are 4.004, 0.002, and 0.613 MPa, respectively. The cumulative error values are below 5 MPa. The XGB model demonstrates more precision, as seen by its higher R2 and lower error values. In contrast, the obtained XGB models' R2 and error values are adequate. Therefore, the finding suggests that the precision of XGB prediction results surpasses that of AdaB and RF models illustrates the anticipated and empirical results pertaining to the cub compressive strength of high-performance concrete reinforced with mixed fibers, as determined through the utilization of XGB. The R2 value training and test data sets are 1.000 and 0.994, respectively, and MAE = 0.0108, MSE = 0.0004, and RMSE = 0.0212 show highly precise results with better accuracy. At the same time, the estimated outcomes for HFRTHPC compressive strength are in the adequate.

The presented Fig. 22 illustrates the anticipated and empirical results pertaining to the split tensile strength of high-performance concrete reinforced with composite fibers, utilizing the AdaBoost algorithm. The R^2 values fortraining and testing are 0.924 and 0.912, respectively.

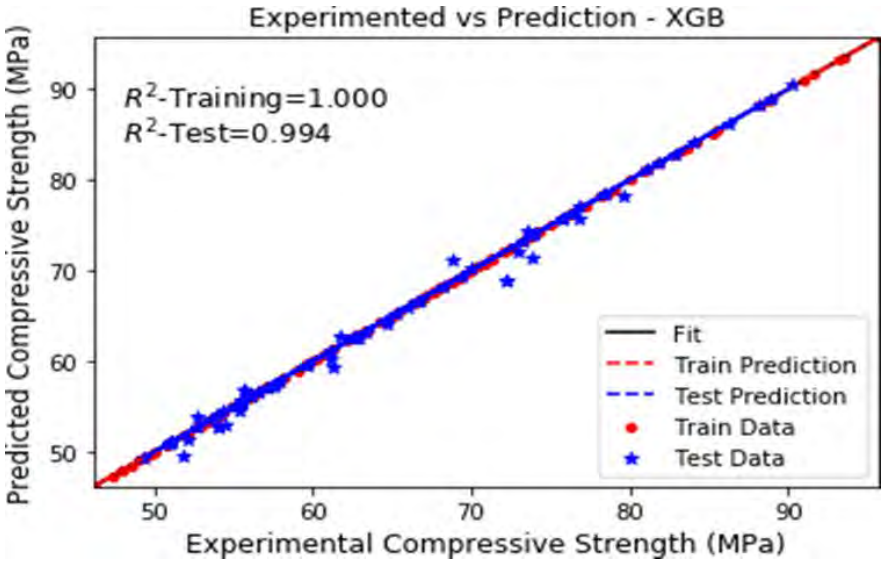


Fig. 20. Predicted V/s Experimental results for HFRTHPC CS – XGB model

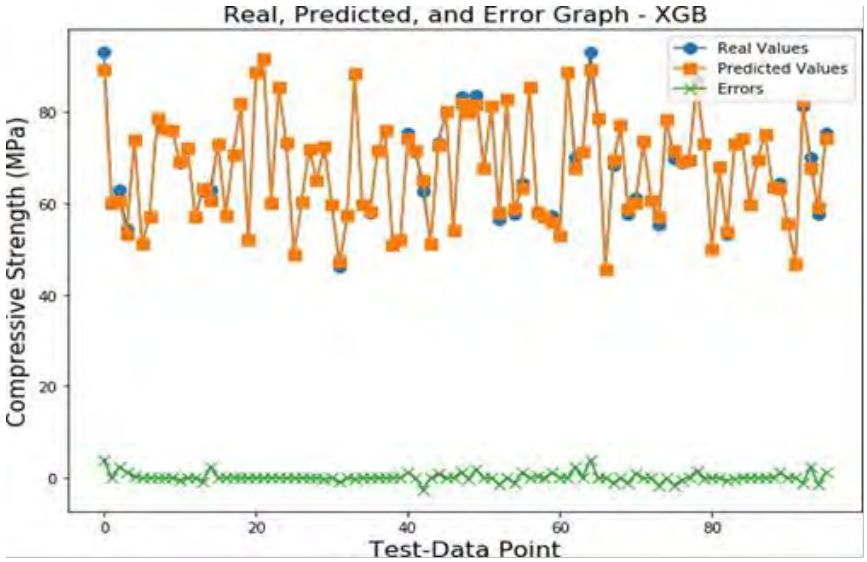


Fig. 21. Real, Predicted and Error distribution for XGB model

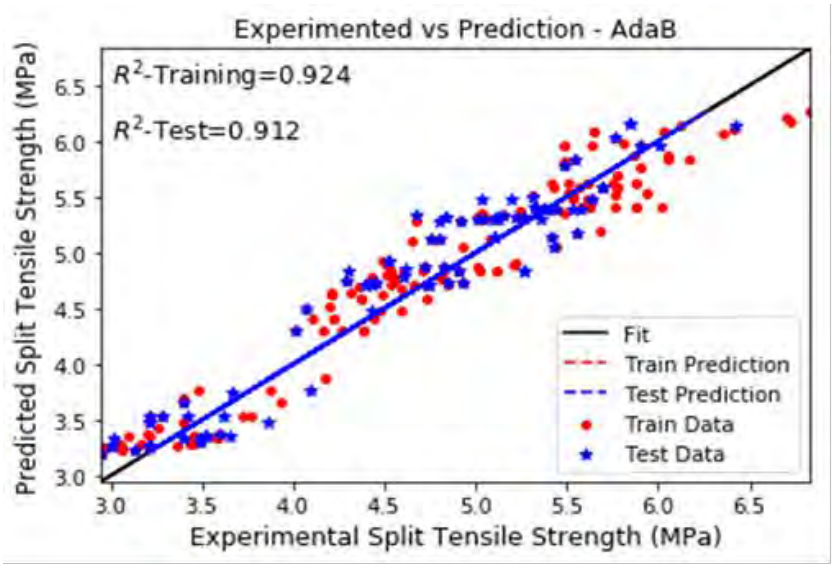


Fig. 22. Predicted V/s Experimental results for HFRTHPC TS – AdaB model

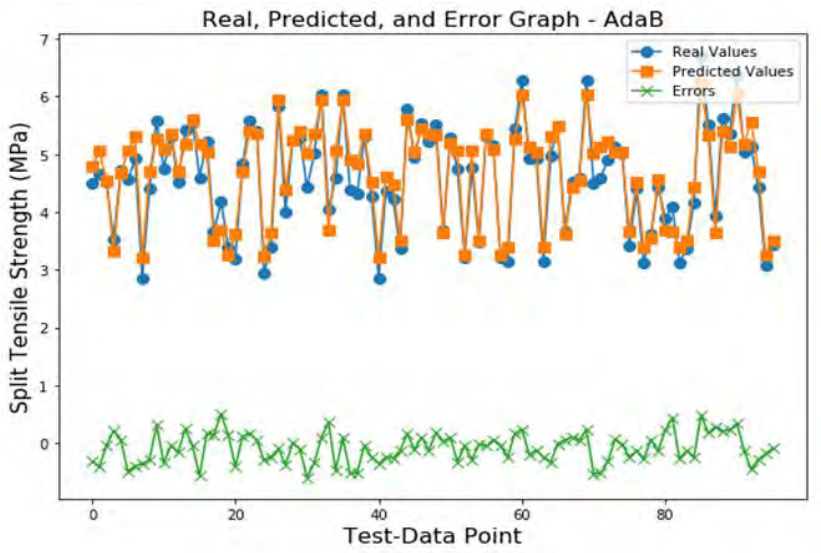


Fig. 23. Real, Predicted and Error distribution for AdaB model

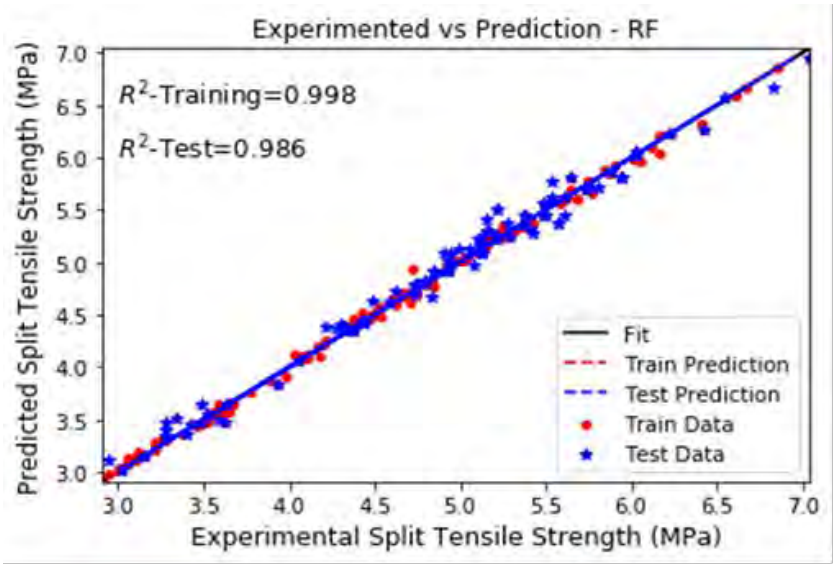


Fig .24. Predicted V/s Experimental results for HFRTHPC TS – RF model

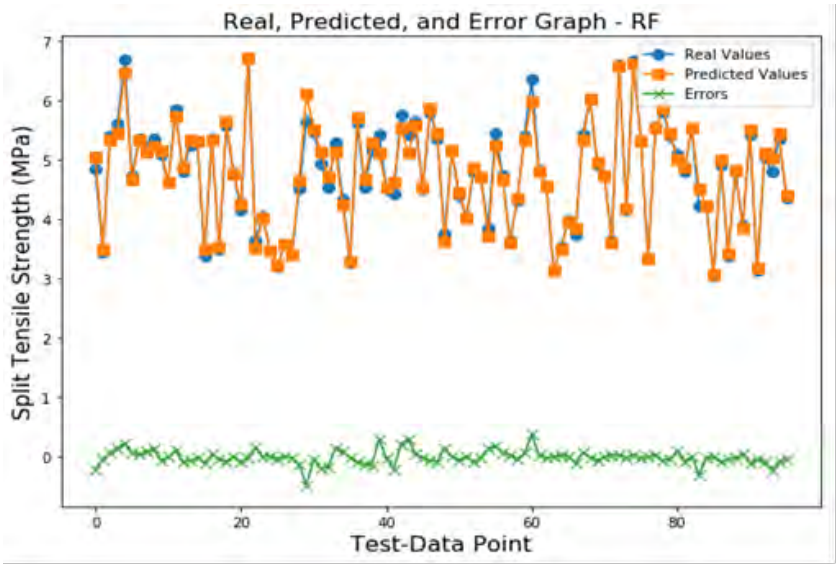


Fig. 25. Real, Predicted and Error distribution for RF model

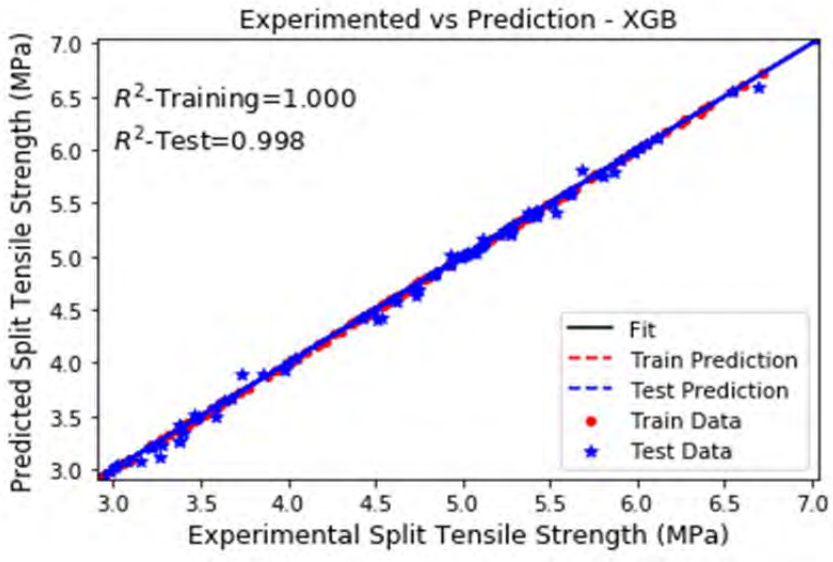


Fig. 26. Predicted V/s Experimental results for HFRTHPC TS – XGB model

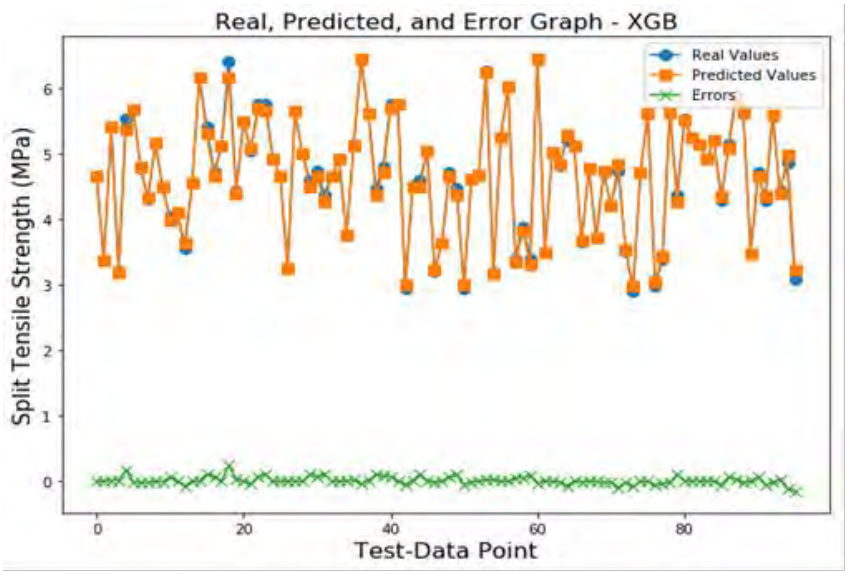


Fig. 27. Real, Predicted and Error distribution for XGB model

The MAE = 0.1921, MSE = 0.0568, and RMSE = 0.2384 confirm that AdB was unable to make reasonable predictions of tensile strength. Fig. 23 illustrates the errors between predicted and experimental values of split tensile strength via AdB. The minimum error was 0.008 MPa, the maximum error was 0.503 MPa, and the average error was 0.186 MPa in the AdB prediction. Figs. 24 and Fig. 25 indicate the predicted and experimental split tensile strength for composite fiber-reinforced tertiary blended high-performance concrete using RF and the errors between the experimental and estimated results using RF, respectively. The R^2 = 0.998 (training), R^2 = 0.986 (test), MAE = 0.0301 MPa, MSE = 0.0618 MPa, and RMSE = 0.0434 MPa in RF, showing the minimum errors in both AdB and RF. RF was more precise than AdB in the prediction of split tensile strength. The maximum and minimum error between practical and anticipated split tensile strength results using RF were 0.3754, 0.0008 MPa, and 0.0928, respectively.

Split tensile strength has been predicted using the XGB algorithm. The R^2 = 1.000 (training), R^2 = 0.998 (test), MAE = 0.0033 MPa, MSE = 0.02757 MPa, and RMSE = 0.0051 MPa using this algorithm show that XGB was more accurate than RF and AdB in predicting tensile strength. Fig. 26. Experimental and anticipated values and error distribution for XGB and Fig. 27 showed that the maximum and minimum errors were 0.24 MPa, 0.0001 MPa, and an average error of 0.049 MPa, respectively.

Fig. 28 presents the results of the AdB algorithm in predicting the HFRTHPC flexural strength. The AdB approach is estimated to have a moderate level of accuracy and divergence among experimental and estimated findings. The R^2 of 0.916 (training) and 0.894 (test) suggests that the AdB method for calculating the HFRTHPCflexural strength is satisfactory, and the experimental and predicted results reasonably agree. The error values MAE = 0.3933, MSE = 0.2204, and RMSE = 0.4695 are not in the adequate range for the remaining algorithm. Fig. 29 presents the actual, estimated, and error values distribution for the AdB model, and the maximum and minimum errors were 1.072 MPa, 0.008 MPa, and an average error of 0.367 MPa, respectively. The analysis of errors indicated that the AdaB model was estimated reasonably.

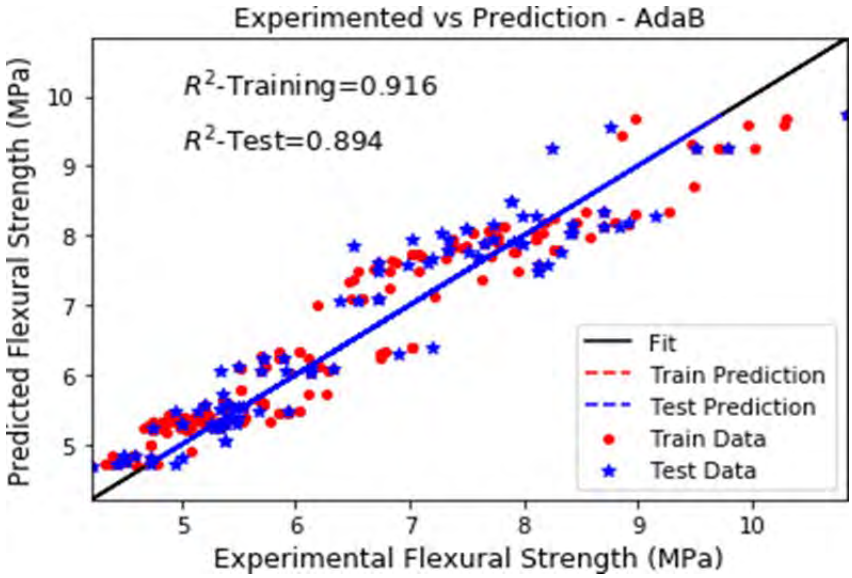


Fig. 28. Predicted V/s Experimental results for HFRTHPC FS – AdaB model

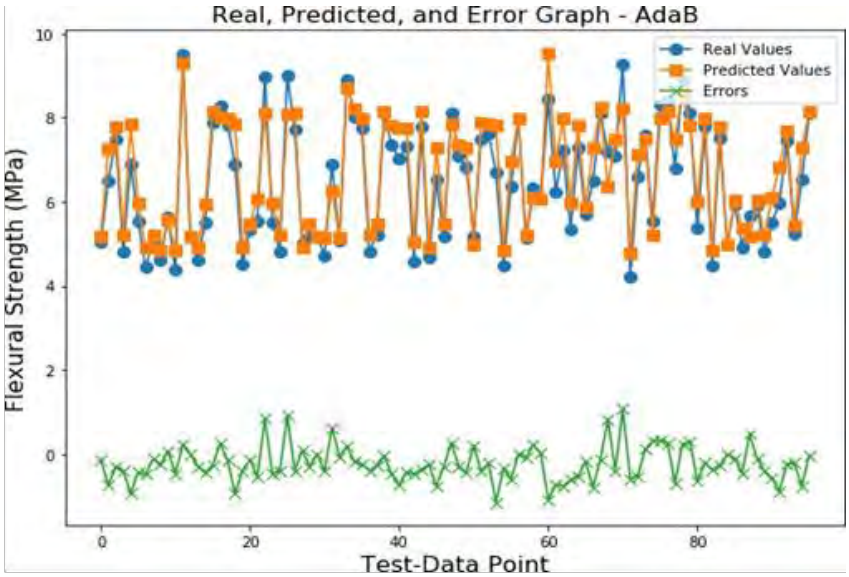


Fig. 29. Real, Predicted and Error distribution for AdaB model

Fig. 30 illustrates the correlations between the estimated and observed flexural strength values of HFRTHPC. This relationship provides 0.996 (training) and 0.982 (test) as the determination coefficient (R^2) values, as well as MAE = 0.0511 MPa, MSE = 0.0082 MPa, and RMSE = 0.0796 MPa. It is important to mention that the vertical axis represents the anticipated values, while the horizontal axis represents the experimental data for flexural strength. Fig. 31 shows the difference between the actual and predicted outcomes.

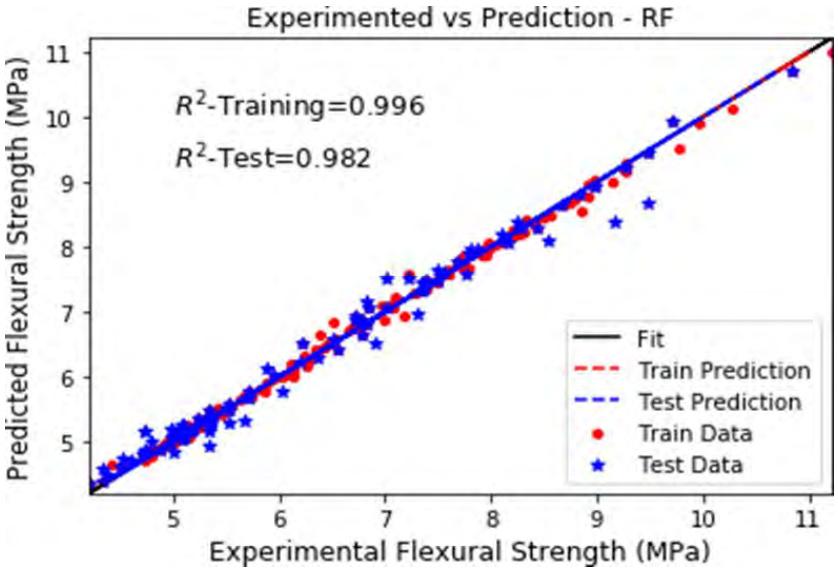


Fig. 30. Predicted V/s Experimental results for HFRTHPC FS – RF model

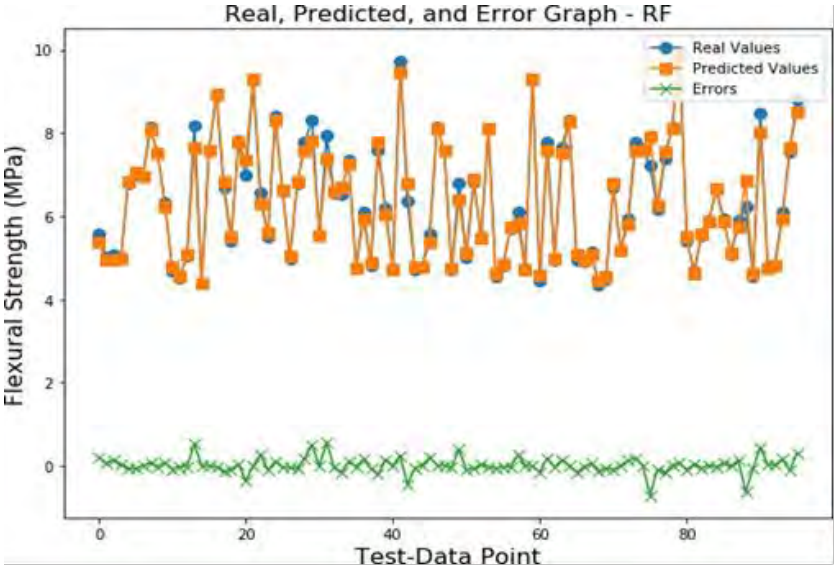


Fig. 31. Real, Predicted and Error distribution for RF model

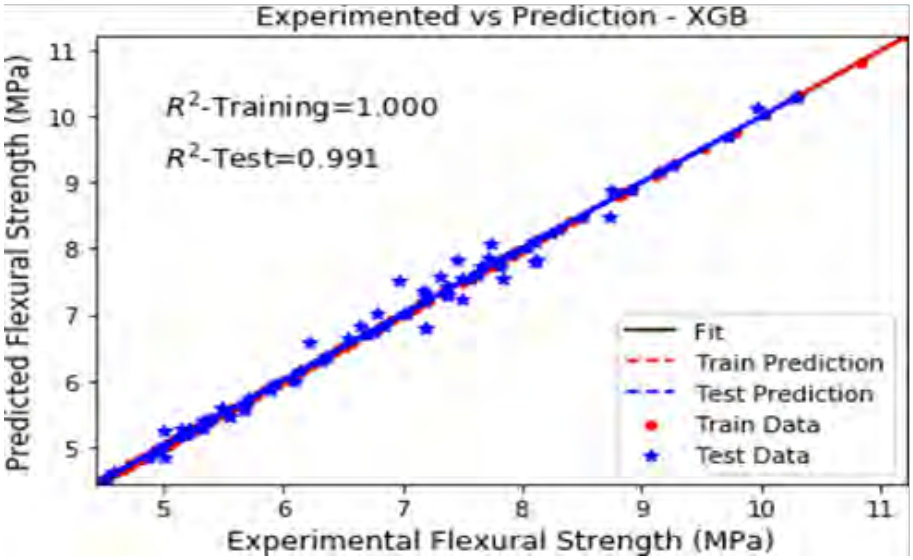


Fig. 32. Predicted V/s Experimental results for HFRTHPC FS – XGB model

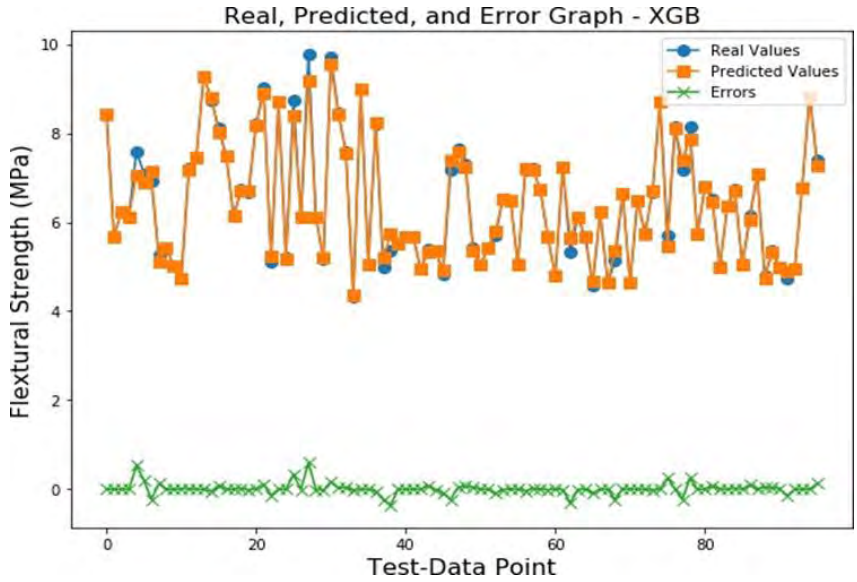


Fig. 33. Real, Predicted and Error distribution for XGB model

Here, the horizontal axis depicts the dataset for testing, whereas the anticipated flexural strength results are shown on the vertical axis. The difference shows the higher values, i.e., 0.574 MPa, the lower values, i.e., 0.003 MPa, and the average values, i.e., 0.145 MPa. Moreover, it has been determined that the total error values are below 1 MPa. Fig. 32 depicts that the XGB model offers a more precise relationship between the practice and anticipated HFRTHPC flexural strength results, which results in R^2 = 1.00 (training), R^2 = 0.991 (test), MAE = 0.025 MPa, MSE = 0.0063 MPa, and RMSE = 0.0042 MPa. The vertical and horizontal axes show expected and experimental flexural strength values. Fig. 33 shows the data distribution, showing actual versus projected outcomes. Here, the horizontal axis depicts the dataset for testing the models, whereas the anticipated flexural strength results are deciphered on the vertical axis. Based on this distribution, the highest, lowest, and average values are 0.599, 0.0001, and 0.0073 MPa, respectively. It is also found that total error values are below 01MPa.

Table 7. Statistical evaluation for the models

Models			AdaB	RF	XGB
Compressive Strength	R^2	Training	90.3	99.7	100
		Test	89.7	96.2	99.4
	MAE		0.6884	0.4247	0.0108
	MSE		0.8388	0.42	0.0004
	RMSE		0.9998	0.648	0.0212
Split Tensile Strength	R^2	Training	92.4	99.8	100
		Test	91.2	98.6	99.8
	MAE		0.1921	0.0301	0.0033
	MSE		0.0568	0.0618	0.02757
	RMSE		0.2384	0.0434	0.0051
Flexural Strength	R^2	Training	91.6	99.6	100
		Test	89.4	98.2	99.1
	MAE		0.3933	0.0511	0.025
	MSE		0.2204	0.0082	0.0063
	RMSE		0.4695	0.0796	0.0042

In contrast to the AdaB approach, the RF model produced more accurate results and the minimum difference between actual and estimated findings. Since the RF model had a smaller deviation of errors and was more accurate than the AdaB model, as a result of the usage of an endless number of decision trees during training and its initial decision tree's emphasis on incorrectly categorized input, the RF model achieves better accuracy. Another model also makes use of the same data. This

process is repeated until a sufficient number of basic learners have been created. The error distribution demonstrated that the XGB model outperformed the RF and AdaB models. The performance of the other models used is also satisfactory. The XGB model is more precise because it employs a tree-based ensemble learning strategy that optimizes output by generating sub models.

Fig. 34 shows the evaluation of predictive models for compressive strength. AdaB, RF, and XGB all demonstrated commendable performance across both training and test datasets. Notably, XGB emerged as the top performer, consistently surpassing AdaB and RF. With flawless R^2 scores of 100% on both training and test datasets, XGB showcased exceptional predictive capabilities. Moreover, its superiority was further evidenced byachieving the lowest error metrics (MAE, MSE, and RMSE) compared to AdaB and RF. These findings underscore XGB's remarkable accuracy and precision in forecasting compressive strength, positioningit as the preferred model for such predictions.

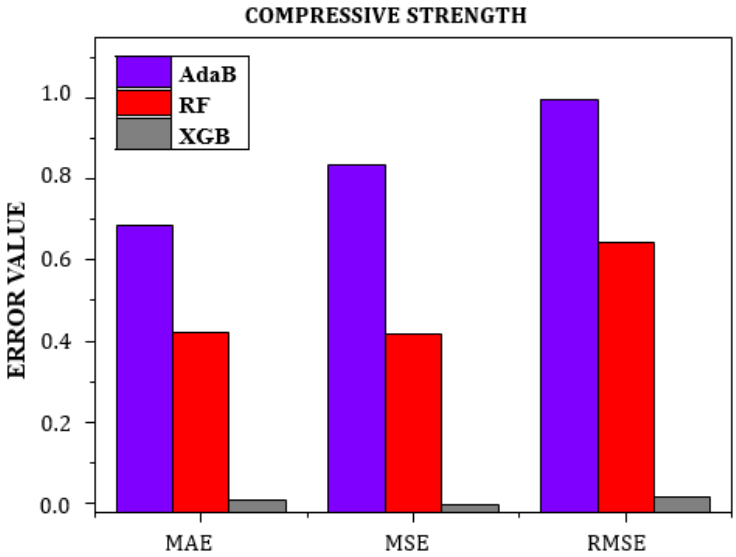


Fig. 34. Error analysis- Compressive strength

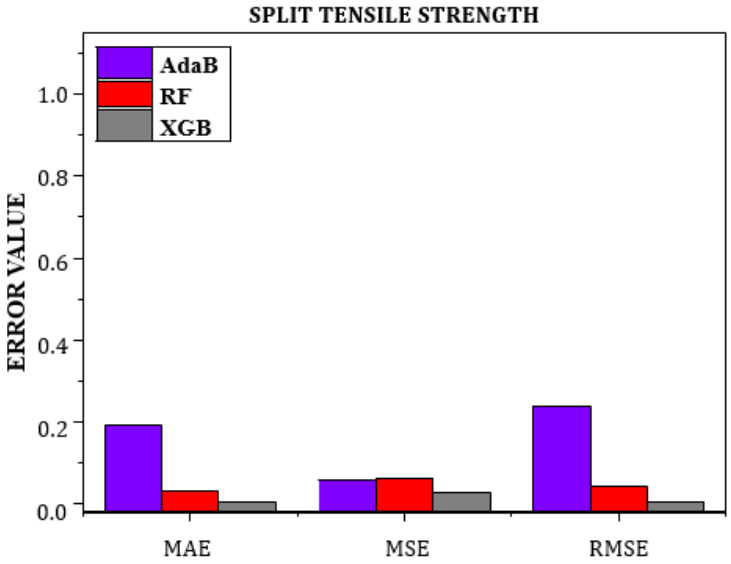


Fig. 35. Error analysis- Tensile strength

Fig. 35 depicts assessing the predictive models for tensile strength. AdaB, RF, and XGB each demonstrated commendable performance. However, XGB consistently emerged as the standout performer. Impressively, XGBattained perfect R^2 scores of 100% on both training and test datasets,

indicating its exceptional predictive prowess. Furthermore, XGB showcased the lowest error metrics (MAE, MSE, and RMSE) compared to AdaB and RF, underscoring its unmatched accuracy and precision in predicting tensile strength.These findings emphasize XGB's superiority and its potential as the preferred model for such predictive tasks.

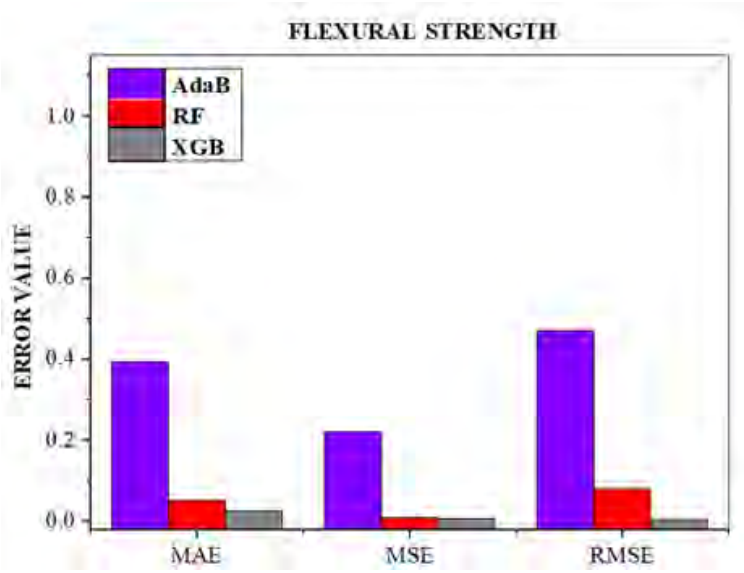


Fig. 36. Error analysis- Flexural strength

Fig. 36 represents the evaluation of predictive models for flexural strength. All models demonstrated satisfactory performance; however, XGB emerged as the standout performer. Remarkably, XGB attained perfect R^2 scores of 100% on both training and test datasets, showcasing its exceptional predictive capabilities. Additionally, XGBexhibited the lowest error metrics (MAE, MSE, and RMSE) compared to other models, indicating superior accuracy and precision in predicting flexural strength. These findings underscore XGB superiority and highlight its potential as the preferred model for accurate predictions of flexural strength in practical applications.

4. Conclusions

- The study successfully demonstrates that the incorporation of hybrid fibers (crimped steel fibers and polypropylene fibers) significantly enhances the mechanical properties of concrete. The optimal mix identified includes 1% crimped steel fiber and 0.25% polypropylene fiber.
- A notable increase in compressive strength of up to 30.24% was achieved with the Hybrid Fiber-Reinforced Tertiary Blended High-Performance Concrete (HFRTHPC) mix compared to the reference mix, with the highest compressive strength recorded at 28 days.
- The study revealed that as the W/B ratio increased from 0.275 to 0.375, the compressive strength of the HFRTHPC mix decreased. The highest strengths were consistently observed at the lowest W/B ratio, confirming the importance of maintaining a low W/B ratio for high-performance concrete.
- The results indicate a substantial improvement in split tensile strength (up to 40.70%) and flexural strength (up to 38.22%) when 15% of the Ordinary Portland Cement (OPC) is replaced with combined tertiary mineral admixtures (silica fume, metakaolin, and fly ash).
- Among the mixtures analysed, the Hybrid Fiber-Reinforced Tertiary Blended High-Performance Concrete (HFRTHPC) demonstrated optimal performance at a hybrid fiber volume of 1.25% with a 15% addition of combined mineral admixture. This combination led to significant improvements in compressive, splitting tensile, and flexural strength compared to the reference mix, highlighting the effectiveness of this hybrid approach.
- The proposed tertiary mix of cement with mineral admixtures outperformed other configurations, such as binary and ternary mixes, due to the combined benefits of fly ash,

metakaolin, and silica fume, which enhance particle packing, reduce porosity, and improve bonding in the concrete matrix.

- The research successfully applied three machine learning techniques—AdaBoost, Random Forest, and Extreme Gradient Boost—to model the mechanical properties of concrete. Among these, the Extreme Gradient Boost (XGB) model exhibited superior predictive accuracy and generalization capabilities, achieving R^2 scores of 1.000 for both training and testing datasets for compressive strength. This indicates the potential of machine learning as an effective tool for predicting concrete properties.
- This research highlights the potential for optimizing concrete compositions to create more sustainable construction materials, reducing the environmental impact associated with traditional concrete production by effectively utilizing industrial by-products like silica fume, metakaolin, and fly ash.
- The findings of this study provide a foundation for future research into hybrid fiber-reinforced concrete, suggesting avenues for further exploration in the optimization of fiber types, dosages, and the incorporation of additional sustainable materials.

References

[1] Patel V, Shah N. A survey of high-performance concrete developments in civil engineering field. Open J Civil Eng. 2013;3(2):69-79. https://doi.org/10.4236/ojce.2013.32007

[2] Juenger MCG, Siddique R. Recent advances in understanding the role of supplementary cementitious materials in concrete. Cem Concr Res. 2015;10:1016. https://doi.org/10.1016/j.cemconres.2015.03.018

[3] Dave N, Misra AK, Srivastava A, Kaushik SK. Experimental analysis of strength and durability properties of quaternary cement binder and mortar. Constr Build Mater. 2016;12:195. https://doi.org/10.1016/j.conbuildmat.2015.12.195

[4] Khan SU, Nuruddin MF, Ayub T, Shafiq N. Effects of different mineral admixtures on the properties of fresh concrete. Sci World J. 2014;1:986567. https://doi.org/10.1155/2014/986567

[5] Gesoğlu M, Güneyisi E, Özbay E. Properties of self-compacting concretes made with binary, ternary, and quaternary cementitious blends of fly ash, blast furnace slag, and silica fume. Constr Build Mater. 2009;23(5):1847-54. https://doi.org/10.1016/j.conbuildmat.2008.09.015

[6] Dhrangadharia S, Vishwakarma S, Kumar A, Saran B. Effect of quaternary binder systems on mechanical properties of concrete. Int J Eng Sci Res. 2018;6(1):2347-6532.

[7] Kathirvel P, Saraswathy V, Karthik SP, Sekar ASS. Strength and durability properties of quaternary cement concrete made with fly ash, rice husk ash, and limestone powder. Arab J Sci Eng. 2012;38(3):589-98. https://doi.org/10.1007/s13369-012-0331-1

[8] Makhloufi Z, Bouziani T, Hadjoudja M, Bederina M. Durability of limestone mortars based on quaternary binders subjected to sulfuric acid using drying-immersion cycles. Constr Build Mater. 2014;71:579-88. https://doi.org/10.1016/j.conbuildmat.2014.08.086

[9] Soroushian P, Khan A, Hsu JW. Mechanical properties of concrete materials reinforced with polypropylene or polyethylene fibers. ACI Mater J. 1992;89(6):535-40. https://doi.org/10.14359/4018

[10] Pierre P, Pleau R, Pigeon M. Mechanical properties of steel microfiber reinforced cement pastes and mortars. J Mater Civil Eng. 1999;11(4):317-24 https://doi.org/10.1061/(ASCE)0899-1561(1999)11:4(317)

[11] Jain A, Singh B, Shrivastava Y. Investigation of kerf deviations and process parameters during laser machining of basalt-glass hybrid composite. J Laser Appl. 2019;31(3):032017. https://doi.org/10.2351/1.5111369

[12] Anandan S, Alsubih M. Post-elastic deformation characteristics of hybrid fiber reinforced concrete composites. Lat Am J Solids Struct. 2020;17(1):1-20. https://doi.org/10.1590/1679-78255851

[13] Sharma KK, Shrivastava Y, Neha E, Jain A, Singh B. Evaluation of flexural strength of hybrid FRP composites having three distinct laminates. Mater Today Proc. 2020;38:418-22. https://doi.org/10.1016/j.matpr.2020.07.599

[14] Zhong H, Zhang M. Experimental study on engineering properties of concrete reinforced with hybrid recycled tyre steel and polypropylene fibres. J Clean Prod. 2020;259:120914. https://doi.org/10.1016/j.jclepro.2020.120914

[15] Eidan J, Rasoolan I, Poorveis D, Rezaeian A. Effect of polypropylene short fibers on energy absorption capacity and durability of concrete. J Test Eval. 2020;49(5):1-8. https://doi.org/10.1520/JTE20190778

[16] Afroughsabet V, Ozbakkaloglu T. Mechanical and durability properties of high-strength concrete containing steel and polypropylene fibers. Constr Build Mater. 2017;94:73-82. https://doi.org/10.1016/j.conbuildmat.2015.06.051

[17] Gupta AK. Experimental studies of strength and durability analysis of concrete incorporating ultrafine slag [doctoral dissertation]. Solan (HP): Jaypee Univ Inf Technol; 2018.
[18] Annadurai A, Ravichandran A. Strength prediction of hybrid fiber reinforced high strength concrete. Int J ChemTech Res. 2015;8(12):675-81.
[19] Alavi Nia A, Hedayatian M, Nili M, Sabet VA. An experimental and numerical study on how steel and polypropylene fibers affect the impact resistance in fiber-reinforced concrete. Int J Impact Eng. 2012;46:62-73. https://doi.org/10.1016/j.ijimpeng.2012.01.009
[20] Murali G, Santhi AS, Ganesh GM. Impact resistance and strength reliability of fiber reinforced concrete using two-parameter Weibull distribution. J Eng Appl Sci. 2014;9(4):554-59.
[21] Nagaraja K, Sudarshan Rao H, Shiva Shankar Reddy T. Study on performance of ternary blended high-strength hybrid fiber reinforced concrete. Int J Civil Eng Technol. 2018;9(11):925-33.
[22] Sreenu R, Hajarath K, Madhukar M. An experimental study on performance of ternary blended high-strength fiber reinforced concrete. Int Res J Eng Technol. 2018;5(8):1-7.
[23] Malagavelli V, Angadi S, Prasad JSR, Joshi S. Influence of metakaolin in concrete as partial replacement of cement. Int J Civil Eng Technol. 2018;9(7):105-11.
[24] Liu G, Guo Y, Li Q, Wang L. The threshold value of effective replacement ratio of fly ash mortar based on amount of calcium hydroxide. IOP Conf Ser Earth Environ Sci. 2020;455(1):012125. https://doi.org/10.1088/1755-1315/455/1/012125
[25] Gouda A, Somasekharaiah HM. Strength and durability studies on hybrid fiber reinforced high-performance concrete for silica fume-based mineral admixture. IOP Conf Ser Earth Environ Sci. 2021;822(1):012041. https://doi.org/10.1088/1755-1315/822/1/012041
[26] Gouda A, Somasekharaiah HM, Mallikarjuna HM. Mechanical properties and acid attack test of hybrid fiber reinforced high-performance concrete for fly ash-based mineral admixture. Mater Today. 2022;51:742-49. https://doi.org/10.1016/j.matpr.2021.06.220
[27] Gouda A, Somasekharaiah HM, Mallikarjuna HM. Combined effect of metakaolin and hybrid fibers on the strength properties of high-performance concrete. Mater Today. 2022;49:1527-36. https://doi.org/10.1016/j.matpr.2021.07.310
[28] Patil S, Somasekharaiah HM, Sudarsana Rao H, Vaishali G. Effect of fly ash, silica fume, glass fiber, and polypropylene fiber on strength properties of composite fiber reinforced high-performance concrete. Int J Eng Trends Technol. 2021;69(5):69-84. https://doi.org/10.14445/22315381/IJETT-V69I5P212
[29] Afzali-Naniz O, Mazloom M. Assessment of the influence of micro- and nano-silica on the behavior of self-compacting lightweight concrete using full factorial design. Asian J Civil Eng. 2019;20:57-70. https://doi.org/10.1007/s42107-018-0088-2
[30] Chen L, Wang Z, Khan AA, Khan M, Javed MF, Alaskar A, Eldin SM. Development of predictive models for sustainable concrete via genetic programming-based algorithms. J Mater Res Technol. 2023;24:6391-410. https://doi.org/10.1016/j.jmrt.2023.04.180
[31] Abdul-Jabbar H, Khan M, Awan HH, Eldin SM, Alyousef R, Mohamed AM. Predicting ultra-high-performance concrete compressive strength using gene expression programming method. Case Stud Constr Mater. 2023;18:e02074. https://doi.org/10.1016/j.cscm.2023.e02074
[32] Islam N, Kashem A, Das P, Ali MN, Paul S. Prediction of high-performance concrete compressive strength using deep learning techniques. Asian J Civil Eng. 2023;1:1. https://doi.org/10.1007/s42107-023-00778-z
[33] Albostami AS, Al-Hamd RKS, Alzabeebee S, Minto A, Keawsawasvong S. Application of soft computing in predicting the compressive strength of self-compacted concrete containing recyclable aggregate. Asian J Civil Eng. 2024;25(1):183-96. https://doi.org/10.1007/s42107-023-00767-2
[34] Shahani NM, Ullah B, Shah KS, Hassan FU, Ali R, Elkotb MA, et al. Predicting angle of internal friction and cohesion of rocks based on machine learning algorithms. Mathematics. 2022;10(20):3875. https://doi.org/10.3390/math10203875
[35] Zada U, Jamal A, Iqbal M, Eldin SM, Almoshaogeh M, Bekkouche SR, Almuaythir S. Recent advances in expansive soil stabilization using admixtures: current challenges and opportunities. Case Stud Constr Mater. 2023;18:e01985. https://doi.org/10.1016/j.cscm.2023.e01985
[36] Caglar N, Pala M, Elmas M, Eryılmaz DM. A new approach to determine the base shear of steel frame structures. J Constr Steel Res. 2009;65(1):188-95. https://doi.org/10.1016/j.jcsr.2008.07.012
[37] Solhmirzaei R, Salehi H, Kodur V, Naser MZ. Machine learning framework for predicting failure mode and shear capacity of ultra-high-performance concrete beams. Eng Struct. 2020;224:111221. https://doi.org/10.1016/j.engstruct.2020.111221
[38] Behnood A, Golafshani EM. Machine learning study of the mechanical properties of concretes containing waste foundry sand. Constr Build Mater. 2020;243:118152. https://doi.org/10.1016/j.conbuildmat.2020.118152

[39] Shang M, Li H, Ahmad A, Ahmad W, Ostrowski KA, Aslam F, et al. Predicting the mechanical properties of RCA-based concrete using supervised machine learning algorithms. Constr Build Mater. 2022;647:1-13. https://doi.org/10.3390/ma15020647
[40] Ni HG, Wang JZ. Prediction of compressive strength of concrete by neural networks. Cem Concr Res. 2000;30(8):1245-50. https://doi.org/10.1016/S0008-8846(00)00345-8
[41] Sarıdemir M. Predicting the compressive strength of mortars containing metakaolin by artificial neural networks and fuzzy logic. Adv Eng Softw. 2009;40(9):920-7. https://doi.org/10.1016/j.advengsoft.2008.12.008
[42] Sobhani J, Najimi M, Pourkhorshidi AR, Parhizkar T. Prediction of the compressive strength of no-slump concrete: A comparative study of regression, neural network, and ANFIS models. Constr Build Mater. 2010;24(5):709-18. https://doi.org/10.1016/j.conbuildmat.2009.10.037
[43] Hodhod OA, Ahmed HI. Modeling the corrosion initiation time of slag concrete using the artificial neural network. HBRC J. 2014;10(3):231-4. https://doi.org/10.1016/j.hbrcj.2013.12.002
[44] Awoyera PO, Kirgiz MS, Viloria A, Ovallos-Gazabon D. Estimating strength properties of geopolymer self-compacting concrete using machine learning techniques. J Mater Res Technol. 2020;9(4):9016-28. https://doi.org/10.1016/j.jmrt.2020.06.008
[45] Deifalla AF, Zapris AG, Chalioris CE. Multivariable regression strength model for steel fiber-reinforced concrete beams under torsion. Materials. 2021;14(14):3889. https://doi.org/10.3390/ma14143889
[46] Nafees A, Khan S, Javed MF, Alrowais R, Mohamed AM, Mohamed A, et al. Forecasting the mechanical properties of plastic concrete employing experimental data using machine learning algorithms DT, MLPNN, SVM, and RF. Polymers. 2022;14(8):1583. https://doi.org/10.3390/polym14081583
[47] Salem NM, Deifalla A. Evaluation of the strength of slab-column connections with FRPs using machine learning algorithms. Polymers. 2022;14(8):1517. https://doi.org/10.3390/polym14081517
[48] Azam R, Riaz MR, Farooq MU, Ali F, Mohsan M, Deifalla AF, et al. Optimization-based economical flexural design of singly reinforced concrete beams: a parametric study. Materials. 2022;15(9):3223. https://doi.org/10.3390/ma15093223
[49] Li Y, Zhang Q, Kamiński P, Deifalla AF, Sufian M, Dyczko A, et al. Compressive strength of steel fiber-reinforced concrete employing supervised machine learning techniques. Materials. 2022;15(12):4209. https://doi.org/10.3390/ma15124209
[50] Nafees A, Javed MF, Khan S, Nazir K, Farooq F, Aslam F, et al. Predictive modeling of mechanical properties of silica fume-based green concrete using artificial intelligence approaches: MLPNN, ANFIS, and GEP. Materials. 2021;14(24):7531. https://doi.org/10.3390/ma14247531
[51] Khan M, Lao J, Dai JG. Comparative study of advanced computational techniques for estimating the compressive strength of UHPC. J Asian Concr Fed. 2022;8(1):51-68. https://doi.org/10.18702/acf.2022.6.8.1.51
[52] Anwar MK, Shah SAR, Azab M, Shah I, Chauhan MKS, Iqbal F. Structural performance of GFRP bars based high-strength RC columns: an application of advanced decision-making mechanism for experimental profile data. Buildings. 2022;12(5):611. https://doi.org/10.3390/buildings12050611
[53] Shah SAR, Azab M, Seif ElDin HM, Barakat O, Anwar MK, Bashir Y. Predicting compressive strength of blast furnace slag and fly ash-based sustainable concrete using machine learning techniques: an application of advanced decision-making approaches. Buildings. 2022;12(7):914. https://doi.org/10.3390/buildings12070914
[54] Hulipalled P, Algur V, Lokesha V. An approach of data science for the prediction of wear behaviour of hypereutectoid steel. J Bio Tribo-Corros. 2022;8(3):69. https://doi.org/10.1007/s40735-022-00668-y
[55] Hulipalled P, Algur V, Lokesha V, Saumya S. Interpretable ensemble machine learning framework to predict wear rate of modified ZA-27 alloy. Tribol Int. 2023;188:108783. https://doi.org/10.1016/j.triboint.2023.108783
[56] Hulipalled P, Algur V, Lokesha V, Saumya S. Intelligent retrieval of wear rate prediction for hypereutectoid steel. Multiscale Multidiscip Model Exp Des. 2023;6(4):629-41. https://doi.org/10.1007/s41939-023-00172-x
[57] Hulipalled P, Lokesha V. Optimized machine learning algorithms to predict wear behavior of tribo-informatics. 2022. https://doi.org/10.21203/rs.3.rs-2159217/v1
[58] Hulipalled P, Lokesha V. Intelligent prediction of wear loss based on ensemble learning in dual-phase steel. J Int Acad Phys Sci. 2023;27(2):161-70.
[59] Carmichael RP. Relationships between young's modulus, compressive strength, poisson's ratio, and time for early age concrete. Swarthmore College. 2009.
[60] Bal L, Buyle-Bodin F. Artificial neural network for predicting drying shrinkage of concrete. Constr Build Mater. 2013;38:248-54. https://doi.org/10.1016/j.conbuildmat.2012.08.043

Blank Page

Research on Engineering Structures & Materials
www.jresm.org

Research Article

Thermomechanical properties of slag-based engineered geopolymer composite under a series of cooling and heating cycles

Ghassan H. Humur [1,a], Hussein Hamada [*,2,b], Sarwar H Mohmmad [3,c], Abdulkadir Çevik [4,d] Farid Abed [5,e]

[1]*Department of Civil Engineering, University of Kirkuk, Kirkuk, Iraq*
[2]*Al-Qalam University College, Kirkuk 36001, Iraq*
[3]*Technical College of Engineering, Sulaimani Polytechnic University, Sulaymaniyah 46001, Iraq*
[4]*Department of Civil Engineering, Gaziantep University, Gaziantep, Türkiye*
[5]*Department of Civil Engineering, College of Engineering, American University of Sharjah, UAE*

Article Info

Article History:

Received 25 Aug 2024

Accepted 09 Jan 2025

Keywords:

Geopolymer composite;
Polyvinyl alcohol;
Polypropylene fiber;
Engineered cementitious composite;
Thermal cycling;
Microstructure

Abstract

Using Polyvinyl alcohol (PVA) fiber and micro silica sand has adverse effects on the economic and sustainable advantages of Engineered Geopolymer Composites (EGCs). This study suggests replacing PVA fiber with polypropylene fiber (PP) in producing sustainable reinforced slag-based-engineered geopolymer composites (SEGC) subjected to thermal cycling and repeated loads. PP and PVA fibers, with a 2% content as a volume fraction were selected to reinforce the EGCs. The study examined mass loss, microstructural characterization, static (monotonic) and cyclic loading measurements, tensile properties, and flexural properties. The results obtained indicate a substantial reduction in the strength of lightweight SEGC under thermal cycling. The density of LW-EGC and ECC composite ranged between 1758 for ECC and 1870 kg/m3 for PVA-EGC, while the statistic stress ranged between 37.35 for PVA-ECC and 63.78 for PVA-EGC. However, the flexural strength under static and cyclic loading of LW-ECC (LW-ECC) samples showed substantial improvement due to the increased reaction rate of fly ash particles under high temperatures. Microstructure analysis revealed that SEGC samples suffered more severe damage than ECC specimens when subjected to various cooling and heating cycles. These micro-cracks contributed to defects in the residual mechanical behavior of lightweight SEGC specimens.

© 2025 MIM Research Group. All rights reserved.

1. Introduction

During In recent times, there has been an increase in the popularity of ductile fiber-reinforced geopolymer composites (DFRGC) in various construction applications [1, 2]. However, these composites are susceptible to exposure to different environmental factors during their curing process and service life, including heat and cooling cycles, fire incidents, freeze and thaw cycles, weather deterioration, and chemical attacks [3, 4]. These factors can pose significant risks to the performance and longevity of these materials in construction projects. Building components are subject to temperature variations throughout their lifespan, ranging from sub-zero degrees Celsius to approximately 80°C, depending on the geographical location. As a result, assessing the durability and service life of construction elements must take into account the effects of thermal cycling, which is a crucial aspect of evaluating serviceability in the construction industry.

*Corresponding author: enghu76@gmail.com
[a]orcid.org/0000-0002-4915-2887; [b]orcid.org/0000-0001-9911-8639; [c]orcid.org/0000-0002-7249-7760; [d]orcid.org/0000-0001-6700-0126; [d]orcid.org/0000-0002-9202-694X
DOI: http://dx.doi.org/10.17515/resm2025-412me0825rs

Ping et al. [5, 6] conducted a study to investigate the performance of fly ash in geopolymer concrete (FAGPC) under the influence of cooling and heating cycles. The researchers studied the influence of adding Iron ore tailing (IOT) and Silica fume (SF) in different ratios of 0%, 10%, 20%, and 30% by weight. The FAGPC specimens mixed with varying IOT and SF content were subjected to heating and cooling sequences for 7, 28, and 56 days at temperatures of 200, 400, and 800 °C. The study focused on recording the residual mechanical properties, weight loss, and microstructural characteristics of the specimens. The addition of SF and IOT led to the refinement of pores in the geopolymer and the optimization of microstructural cracks under thermal cycling. As a result, there was a reduction in porosity and micro-cracks, leading to an increased density of the microstructure and enhanced thermal resistance of the FAGPC specimens [7]. However, it was observed that the FAGPC specimens experienced an increase in mass and a loss of compressive strength, especially after undergoing 56 thermal cycles. Another study by Lin et al. [8], observed that thermal cycles hurt gas permeability. This effect was attributed to the enlargement of pores within the aggregates and cementitious materials. An et al. [9] examined the microstructural and mechanical behavior of high-performance concrete (HPC) under different thermal cycling conditions. The evaluation of HPC involved analyzing parameters such as compressive strength, elastic modulus, capillary water absorption, and splitting tensile strength. The researchers observed that as the number of heating and cooling cycles increased, there was a decrease in the compressive strength, splitting tensile strength, and elastic modulus of high-performance concrete (HPC). The uniaxial tensile test of HPC under varying strength grades was particularly sensitive to thermal treatment. With an increase in the number of thermal cycles, macroscopic cracks were observed in HPC, leading to weakened performance. This crack propagation was attributed to the existence of micro-cracks in the cement matrix and interfacial transition zone.

Geopolymers are a new type of inorganic material without cement, alkali-activated structure that has gained substantial attention in sustainable construction [10]. İt was produced from different aluminosilicate materials like slag and fly ash with alkali solutions like sodium or potassium hydroxide and silicate [11, 12]. Geopolymer and other cementitious materials have gained popularity due to their sustainability. Alkali-activated materials have been used as a replacement for Ordinary Portland Cement (OPC) and consist of aluminosilicate materials like slag and fly ash (FA) at normal or elevated temperatures [13]. Geopolymer composites have been found to reduce carbon footprint by about 80% and decrease the energy required by 60% compared to clinker-based cement production [14]. Engineered Geopolymer Composites (EGCs), a novel type of ductile fiber-reinforced geopolymer composite, contain a small ratio of short fibers (2% by volume) [15]. These materials offer significant advantages, such as being eco-friendly, reducing greenhouse gas emissions, and exhibiting high strain in uniaxial tensile tests. The use of landfill materials like fly ash, rice husk ash, and slag contributes to greener production with a lower carbon footprint and reduced environmental hazards [16]. Strain-hardening geopolymer composites display a high deformation capacity of about 74.3 mm and a relatively high flexural strength of approximately 12.7 MPa, demonstrating strong deformation performance [17]. Additionally, they exhibit high tensile ductility (up to 4.69%) and compressive strength (up to 64.11 MPa) [18].

Alrefaei and Dai [15] conducted an evaluation of the influence of combined fibers on the microstructural and tensile strength properties of one-part EGC treated at controlled temperatures. They studied the impact of hybrid combinations of steel fiber (SF) and polyethylene fiber (PE), with different precursor material ratios (100% slag and 50% FA-50% slag), along with the addition of micro-silica sand. The results revealed that the addition of steel fibers in the EGC composites led to an increase in dry density, slump, compressive strength, and fracture properties. However, it also resulted in a considerable decrease in the tensile strain and led to the formation of cracks in both hybrid mixes of EGC. In a separate study, Ling et al. [18] investigated the effect of the strong bond and slag content on the properties of EGC containing FA. The outcomes showed the presence of numerous small cracks in all EGC specimens. The inclusion of slag in EGC composites increased the spacing between cracks while reducing their number. During tensile loading and flexural strength tests, all EGC samples, regardless of slag content, exhibited fine cracks. However, the presence of slag reduced the number of cracks and increased the spacing between them.

Another study by G. Humur and A. Çevik [19] reported on the impact of high temperature on the deflection and strain-hardening behavior of EGC. The load-deflection responses showed that both ECC and EGC specimens maintained their deflection-hardening behavior at a thermal treatment of 200°C. Additionally, slag/fly ash-based EGC and fly ash-based EGC composites demonstrated higher flexural strength and deflection properties at 100°C and 200°C compared to control samples heated under normal conditions. However, the flexural strength and deformation properties of all EGC and ECC specimens degraded with increasing heat treatment up to 800°C. G. Humur and A. Çevik also investigated the effects of nano-silica, PP, and PVA fibers in slag/fly ash-based lightweight EGC (S-FA-EGC) [7]. The incorporation of polypropylene fibers in lightweight S-FA-EGC specimens enhanced tensile ductility and reduced tensile stress at ambient temperature. Moreover, the reinforcement of lightweight S-FA-EGC specimens with polyvinyl alcohol fibers eliminated fragmentation and explosive spalling, significantly enhancing the fire resistance of ECC and EGC under high temperatures. This is because the melted fibers create additional routes for vapor pressure to escape without damaging the EGC and ECC matrices [7].

To date, limited studies have investigated the influence of slag-based EGC under elevated temperatures. Most studies have focused on normal EGC, while the behavior of reinforced slag-based LW-EGC (SEGC) under cyclic heating-cooling programs has not been widely explored. Therefore, it is essential to study the changes in microstructural evolution and engineering properties of SEGC. Additionally, the influence of thermal cycles on the behavior of conventional ECC has not been extensively studied in the literature. This study aims to systematically examine the behavior of SEGC reinforced with polypropylene and polyvinyl alcohol fibers that are exposed to cooling-heating cycles (room temperature and 10, 20, and 30 cycles.) The study examines the influence of combined fibers on mass loss, density, static (monotonic) and cyclic loading responses, failure mode, strain hardening behavior, deflection hardening behavior, and microstructural characterization of lightweight SEGC and ECC composites. The outcomes acquired from this study will provide a fundamental database of the durability properties and mechanical behavior of SEGC exposed to heating-cooling cycles.

2. Experimental Program

2.1 Materials and Mix Preparations

In this research, ground granulated blast furnace slag (GGBFS) was chosen to produce lightweight SEGC mixes, while Ordinary Portland Cement (OPC) and low calcium fly ash (FA) were used to create LW-ECC as control samples. Table 1 provides the chemical composition and physical properties of GGBFS, OPC, and FA analyzed through X-ray Fluorescence (XRF). Expanded glass granule aggregate (EGGA) from HAbbe, a company located in the Kocaeli region of Turkey, was adopted as the fine aggregate in all concrete mixes. EGG is characterized by its creamy or white color, with a breaking resistance, bulk density, and granular size of 3.1 N/mm2, 450 kg/m^3, and 0.1-0.25 mm, respectively. NaOH and water glass were selected as alkaline activators for this study.

Table 1. Properties of OPC, GGBFS, and FA%

Chemical composition	GGBFS %	FA %	OPC %
SiO_2	36.4	62.53	19.69
CaO	34.12	1.57	62.12
Al_2O_3	10.39	21.14	5.16
MgO	10.3	1.76	1.17
Fe_2O_3	0.69	7.85	2.88
Na_2O	0.35	2.45	0.17
K_2O	0.97	0.73	0.88
SO_3	0.49	0.10	2.63
Loss on ignition %	1.64	2.07	2.99
Blaine fineness (m^2/kg)	418	227	394
Specify gravity	2.79	2.04	3.15

One day before casting, a 12 M NaOH solution was prepared, and a water glass with a molar ratio (Ms) of 3.10 was also prepared before the casting process. The Na2SiO3/NaOH ratio was set at 2.5 to fix the alkaline activator solutions. Table 2 presents the XRF analysis of the EGG materials. Polypropylene (PP) fibers with a length and diameter of 12 mm and 40 μm, respectively, were employed. Additionally, polyvinyl alcohol (PVA) fibers with a diameter of 39 μm, a volume fraction of 2%, and a length of 12 mm were used in this study. Table 3 provides the properties of PP and PVA fibers. A polycarboxylate-based high-range water-reducing admixture (PHRWRA) was used to improve the workability of the concrete mixes.

Table 2. Chemical composition of EGGA

Constituent	%
SiO_2	72.95
CaO	4.35
MgO	0.89
Al_2O_3	0.41
Fe_2O_3	0.09
Mn_2O_3	0
TiO_2	0.03
K_2O	0.2
Na_2O	18.74
Loss on Ignition (LOI)	2.33

Table 3. Characteristics of PVA and PP fibers

Type of fiber	Diameter (μm)	Length (mm)	Aspect ratio	Specific density (g/cm^3)	Elastic modulus (GPa)	Tensile strength (MPa)
PP	40	12	300	0.91	5	450
PVA	39	12	300	1.30	42.8	1620

Table 4 presents the mix proportions for LW-ECC and EGC. The Na_2SiO_3/NaOH ratio was fixed at 2.5 for all LW-EGC mixes, and the proportion of alkali activator/binder was maintained at 0.45. The proportion of EGG to binder was also set at 0.2 to ensure that the overall combinations have a density lower than that of the control mass. In total, six mixes were included in the testing program. Mix proportions Mix1, Mix2, and Mix3 were prepared to investigate the effect of microfibers (PVA and PP) on the properties of slag-based LW-EGC when exposed to thermal cycling. These mixes included different fiber contents while keeping a total volume of 2%. Additionally, two mixes without PVA and PP fibers were prepared to examine the influence of fiber type on the physical, thermal, and mechanical properties of SEGC and ECC composites.

Table 4. Characteristics of LW- ECC and EGCs mixtures (units)

Mixtures	GGBFS	FA	OPC	NaOH	Na_2SiO_3	Liquid/ binder	Sand/ binder	PP	PVA	Extra water	HRWR
PP-EGC	1.0			0.128	0.321	0.45	0.2	0.02		0.02	0.025
PVA-PP-EGC	1.0			0.128	0.321	0.45	0.2	0.01	0.01	0.02	0.035
PVA-EGC	1.0			0.128	0.321	0.45	0.2		0.02	0.02	0.046
PVA-ECC		0.5	0.5			0.29	0.2		0.02	0.02	0.02
EGC	1.0			0.128	0.321	0.45	0.2			0.018	0.025
ECC		0.5	0.5			0.29	0.2			0.018	0.02

2.2 Mixing and Curing

To prepare the NaOH solution with the desired molarity of 12M, accurately weighed sodium hydroxide beads were dissolved in drinking water. As the ingredients were mixed, an exothermic reaction occurred, leading to an increase in temperature. The solution was allowed to reach its equilibrium state at room temperature before use. This step is crucial to ensure the proper preparation of the NaOH solution. Next, the required materials were dried for about six minutes. Afterward, additional water with the alkaline activator solution was added to the LW-SEGC mix. Wet mixing was carried out for 3 minutes to ensure proper distribution. The polycarboxylate-based high-range water-reducing admixture (PHRWRA) was gradually added to obtain a workable mix. PVA fibers were incorporated and mixed for another six minutes until a homogeneous mix was achieved. The entire mixing process took approximately 15-20 minutes for each mix proportion.

The lightweight SEGC and ECC mixes were then cast and properly compacted using a vibrating table for 1 minute. In this study, an oven was chosen for the curing process, as previous research has shown that oven curing enhances the tensile ductility and mechanical properties of EGC [20, 21]. Fresh SEGC samples were wrapped to prevent moisture loss and placed in the oven at 70°C for 24 hours. Then, all SEGC samples were removed from the oven and kept at ambient room temperature. As for the LW-ECC samples, they were demolded after the 24-hour resting period and submerged in a water bath for 28 days.

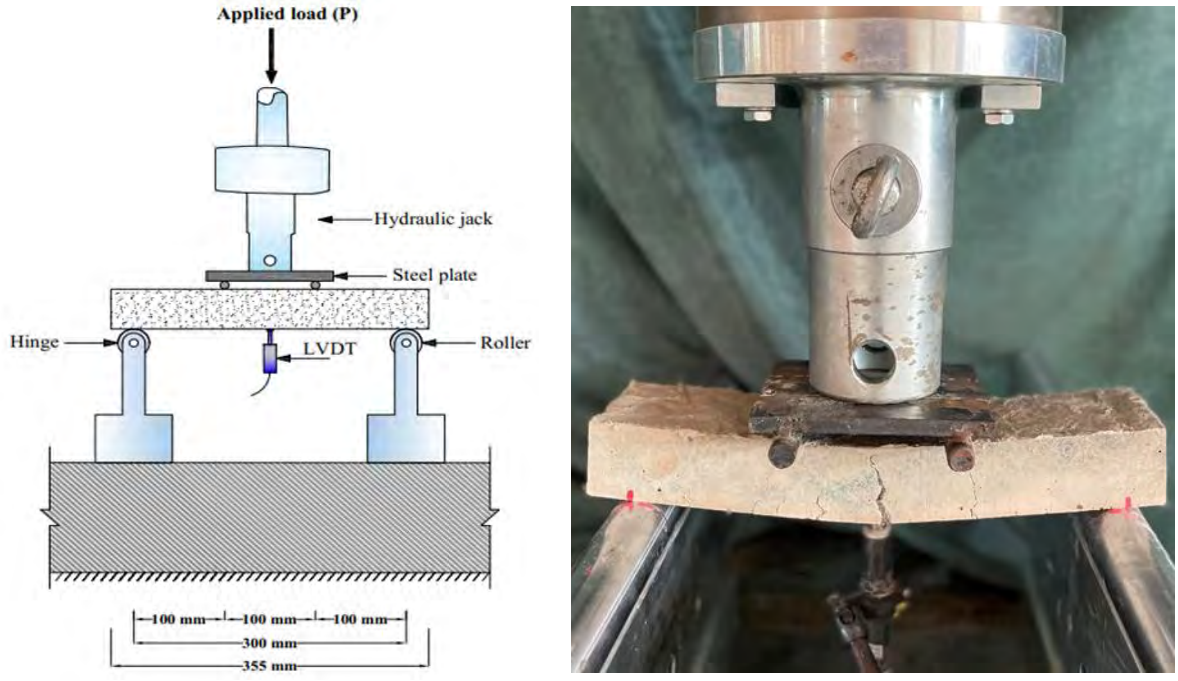
2.3 Test Program

2.3.1 Compressive Strength

The compressive strength test of LW-ECC and EGC specimens was conducted using ASTM C109 [20] standards. The concrete cubes had dimensions of 70 × 70 × 70 mm^3, and at least three specimens were tested to obtain an average result.

2.3.2 Direct Tensile Strength

For the tensile strength test, coupon specimens with dimensions of 330 mm x 60 mm x 13 mm were utilized to assess the tensile properties of the lightweight composites. The test was conducted at a loading rate of 0.2 mm/min to control the deformation, following the guidelines of the Japanese code [22].



(a) (b)

Fig. 1. Test set of four-point flexural test (a) Test set up and (b) SEGC specimen

2.3.3 Flexural Strength

To assess the flexural strength, the lightweight composites were subjected to a four-point bending test using prism specimens with dimensions of 50 mm x 76 mm x 355 mm at a loading rate of 0.2 mm/min, as specified in previous studies [23]. Fig. 1 illustrates the flexural testing machine used, with a capacity of 500 kN.

2.3.4 Scanning Electronic Microscopy

After mechanical testing, scanning electron microscopy was used to investigate the reason for changes in the strength of SEGC and ECC microstructures after exposure to various thermal cycles. SEM technique (ZEISS Gemini SEM 300) was adapted to assess the changes in the microstructure of all studied samples under thermal cycles, as shown in Fig.2.



Fig. 2. SEM device

2.3.5 Exposure to Thermal Cycling

In order to examine the behavior of the specimens under thermal cycling, all the tested samples were subjected to high temperatures up to 200°C at 28 days of age. Subsequently, the specimens were slowly cooled back to room temperature. Each heating and cooling cycle was considered as one step of thermal curing. The mechanical properties of the SEGC and ECC composites were evaluated at intervals of 10 cycles up to a maximum of 30 cycles. At the age of 28 days, all the lightweight SEGC specimens were subjected to a temperature of 200 °C in a computer-controlled, electrically heated furnace at a heating rate of 10°C/minute till the target temperature was attained and the temperature was maintained constant for 2 hr (heating time) After that, the samples were allowed to cool naturally to ambient temperature (cooling time). This heating-cooling cycle is hereafter referred to as one thermal cycle.

3. Results and Discussions

3.1 Microstructural Analysis

To gain detailed insights into the influence of cooling and heating cycles on the microstructural behavior of SEGC and ECC specimens, Scanning Electron Microscopy (SEM) analysis was conducted on cores extracted from 70 mm specimens. These specimens were cured at room temperature, subjected to 10 thermal cycles, and subjected to 30 thermal cycles before compressive strength testing. Figure 3 presents the SEM images of LW-ECC and SEGC composites at different thermal cycles. The integration of slag in the EGC mix appears to improve the density of the matrix and decrease the void ratio of the EGC mix (Fig. 3a, b, and c). The microstructure of LW-ECC specimens also contains several unreacted fly ash (FA) particles in spherical forms. When these LW-ECC specimens are exposed to various cooling and heating cycles at a temperature of 200°C, it significantly affects the microstructural properties. On the other hand, the ECC mix exhibits a

homogeneous and well-compacted microstructure. Furthermore, the materials undergo accelerated chemical reactions and leaching due to thermal cycling.

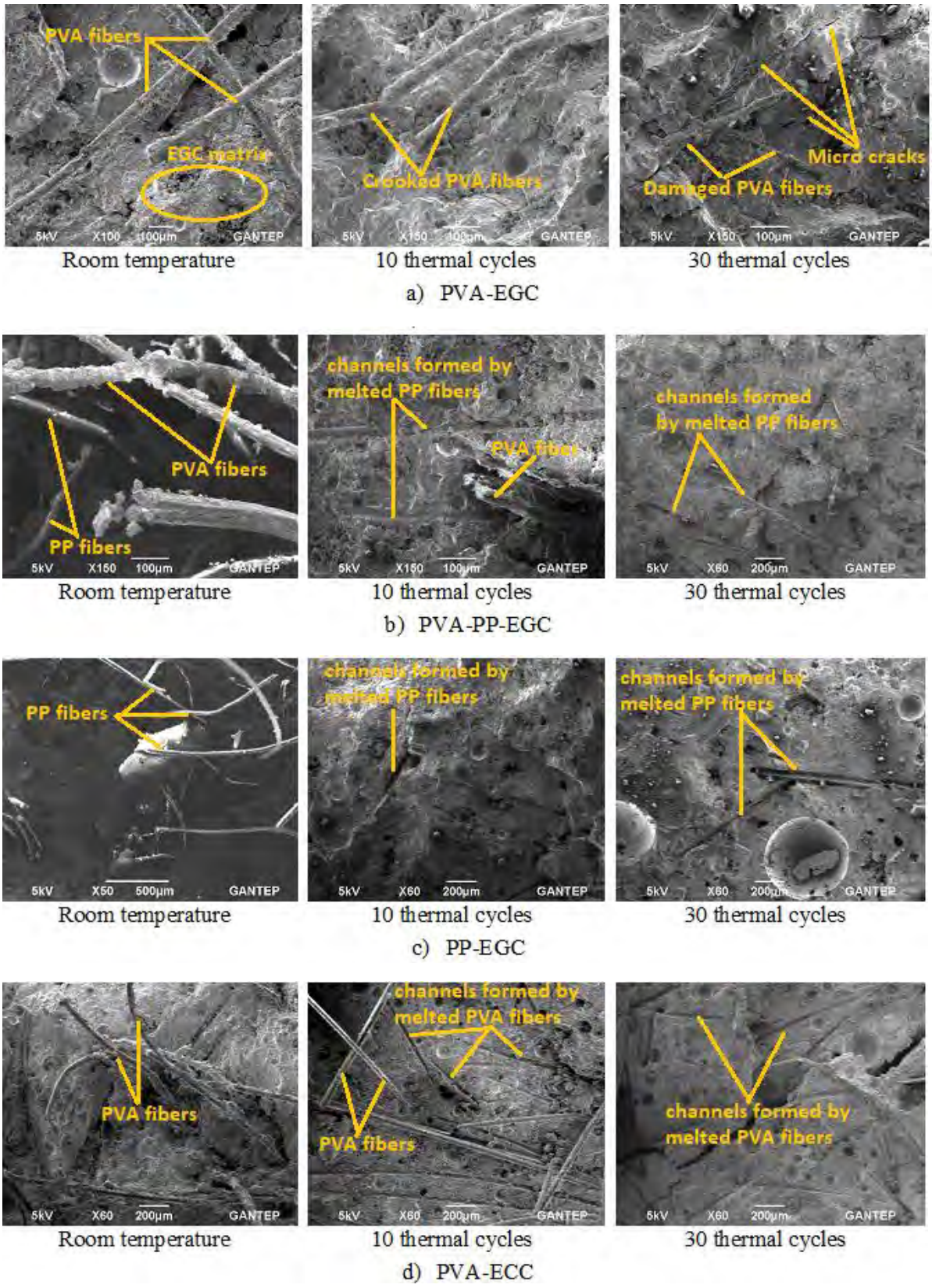


Fig. 3. SEM images of the green LW (ECC and EGC) composites both before and after being subjected to heating-cooling cycles

The spreading of fibers in the PVA-EGC specimens appears to be more homogeneous compared to the PP-EGC and PVA-PP-EGC specimens. As a result, the PVA fiber-reinforced specimens exhibit

higher mechanical properties than the specimens reinforced with PP fibers, as reported by previous studies [24, 25]. The thermal cycling treatment somewhat affected the PVA-EGC and PVA-ECC specimens. The PVA fibers did not melt when exposed to the thermal cycles between 10 and 30 cycles, particularly at 200 °C. On the other hand, the PP fibers in the PP-EGC specimens completely melted and disappeared after 10-30 thermal cycles, resulting in a noticeable significant number of capillary pores and micro-cracks in the microstructure. This is attributed to the low softening point of PP fibers, which induces minor cracks in the EGC mix and adversely affects the residual strength of LW-EGC specimens (Fig. 3b and c).

In the case of the microstructure of PVA-PP-EGC, no significant modification was observed after heat treatment until approximately 10 thermal cycles. However, after 30 cycles, an increase in crack spacing was observed in the hybrid composite. Channels may form, and cracks may develop as a result of PP fiber melting. This suggests that the microstructure of the hybrid composite is influenced at this stage, and additional cracks were observed on the surface of the specimens (Fig. 3b). The porosity considerably increased, and interconnected open pores were observed after 30 thermal cycles. The increased porosity and pore connectivity in the microstructure of the specimens are attributed to the softened PP fibers, resulting in a notable degradation in the strength of LW-EGC specimens. Compared to PVA-EGC specimens, PP-EGC specimens exhibited higher porosity and additional micro-cracks, mainly due to the melting of PP fibers within the SEGC matrix. This results in an increase in porosity and voids within the EGC mix, leading to structural flaws and a considerable loss in strength due to thermal treatment [26]. The micromorphology of PVA fibers in PVA-ECC and PVA-EGC samples deteriorated when exposed to higher heating and cooling cycles, and their microstructure was somewhat affected, with additional surface irregularities observed on the specimens (Fig. 3a and d). However, PVA-EGC specimens exhibited greater damage compared to PVA-ECC specimens after 30 thermal cycles. This is attributed to the higher number of voids and greater porosity in the microstructure of ECC compared to SEGC, which makes the internal microstructure of ECC less susceptible to the impact of thermal treatment. After being subjected to various thermal cycles, the higher the cooling and heating cycles, the course the pore structure and the higher the total intruded porosity of SEGC and ECC mixtures. Sahmaran and Li (2010) stated that the average pore diameter of ECC specimens dramatically enlarges to 2–10 times its original size after ECC has been exposed to 400 and 800°C. microstructural analyses revealed that physical change (increase in total intruded porosity, the average pore diameter, and surface cracking was greatly changed after the exposure of ECC composites to different temperatures.

3.2 Characteristics of Compressive Strength Under Static and Cyclic Loading

Table 5 presents the properties of static and cyclic loading of SEGC and ECC specimens at room temperature. The average test results, based on at least three specimens, are provided. The findings indicate that thermal cycling has a positive influence on the compressive strength of ECC mortar samples (without fiber), while SEGC samples experienced a significant strength loss with an increase in thermal cycles. The retained strength of ECC specimens can be attributed to the sintering process of non-reacted fly ash particles, which contributes to the strength improvement of ECC specimens [27]. The influence of fiber type on static and repeated loads is illustrated in Figure 4. The compressive strength of SEGC specimens gradually decreases with an increase in polypropylene fiber content. For example, the behavior of static and cyclic loading for both PP-EGC and PVA-PP-EGC specimens decreases by approximately 10% 40.1%, 13.1%, and 41.5%, respectively. When comparing the static and cyclic loading of PP-EGC and PVA-EGC specimens, it is evident that PVA fibers, with their higher modulus of elasticity compared to PP fibers, exhibit outstanding elongation and bridging connections at the fiber breakage points. These PVA fibers can absorb the energy generated by matrix cracking, preventing crack propagation and contributing to high mechanical properties [27, 28].

The residual strengths of PVA fiber-reinforced specimens were higher compared to specimens reinforced by PP fibers after being subjected to various thermal cycling conditions. The partially improved mechanical features of PVA-EGC specimens were observed after being removed from the oven and cooled to room temperature. Conversely, PP fibers melted totally and reduced its

strength. Additionally, the residual compressive strength of LW-ECC specimens significantly improved with an increase in the number of heating and cooling cycles. The static and cyclic loading of PVA-ECC specimens increased from 37.35 MPa to 51.02 MPa and from 36.86 MPa to 48.29 MPa, respectively, as the number of thermal cycles increased from 0 to 10. The improvement in compressive strength can be attributed to the large amount of fly ash in the LW-ECC mix, which undergoes a pozzolanic reaction even after 28 days. The reaction of fly ash is enhanced through thermal curing, resulting in improved compressive strength [21]. The residual strengths of LW-ECC specimens subjected to 20 and 30 thermal cycles remain higher than that of unheated specimens, owing to the existence of a large number of voids and a more permeable microstructure in the ECC mix. This mitigates the influence of thermal curing on the microstructure of the ECC matrix and serves as a protective coating for preserving the integrity of the PVA fibers against the effects of thermal curing.

Table 5. Density, cyclic, and static compressive strength of LW-EGC and ECC composite

mix code	Density (Kg/m^3)	Static stress MPa	Cyclic stress MPa
PVA-EGC	1870	63.78	62.24
PVA-PP-EGC	1848	57.96	55.02
PP-EGC	1839	45.51	43.97
PVA-ECC	1790	37.35	36.86
EGC	1799	51.02	48.64
ECC	1758	41.25	37.85

PVA-EGC exhibits the highest compressive strength among the EGC composites, often reaching 60 MPa for high-strength concrete [29]. However, in the case of slag-based LW-EGC mixes, the cement content is reduced, distinguishing it from typical high-strength concrete. As a result, it has a significantly reduced environmental footprint compared to high-strength concretes (HSC) [29]. The strengths of LW-PVA-EGC specimens for both static and cyclic loading are 70.8% and 68.9% higher, respectively than that of the corresponding lightweight PVA-ECC specimens.

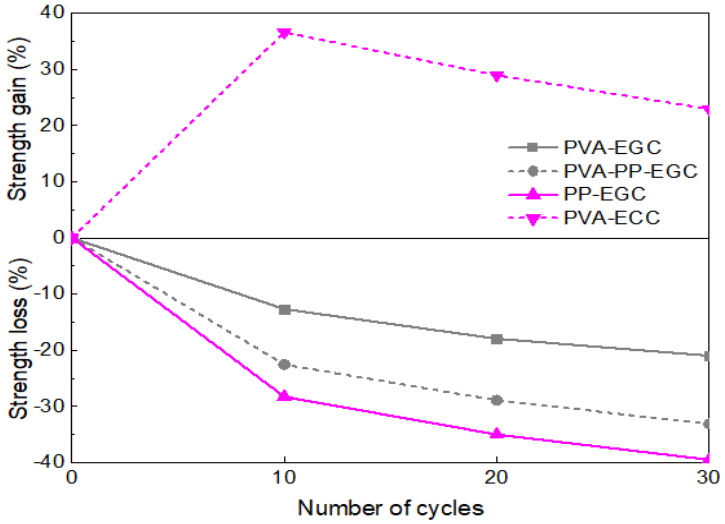


Fig. 4. Compressive strengths improvement and loss of green LW-ECC and LW-EGC specimens subjected to different thermal cycles

The significant effect of slag on the compressive strength of LW-EGC can be attributed to its improved cementing properties compared to FA. The high amount of CaO has a significant effect on the early strength development of concrete [30]. Additionally, the high CaO content can contribute to the formation of C-S-H/C-A-S-H gels, which can alter the microstructural elements of the EGC mix and further improve its strength [31]. The development of C-A-S-H gels also reduces the porosity and improves the microstructure of the EGC mix [32]. These findings are consistent with the SEM observations of LW-EGC composites mentioned earlier (section 3.1).

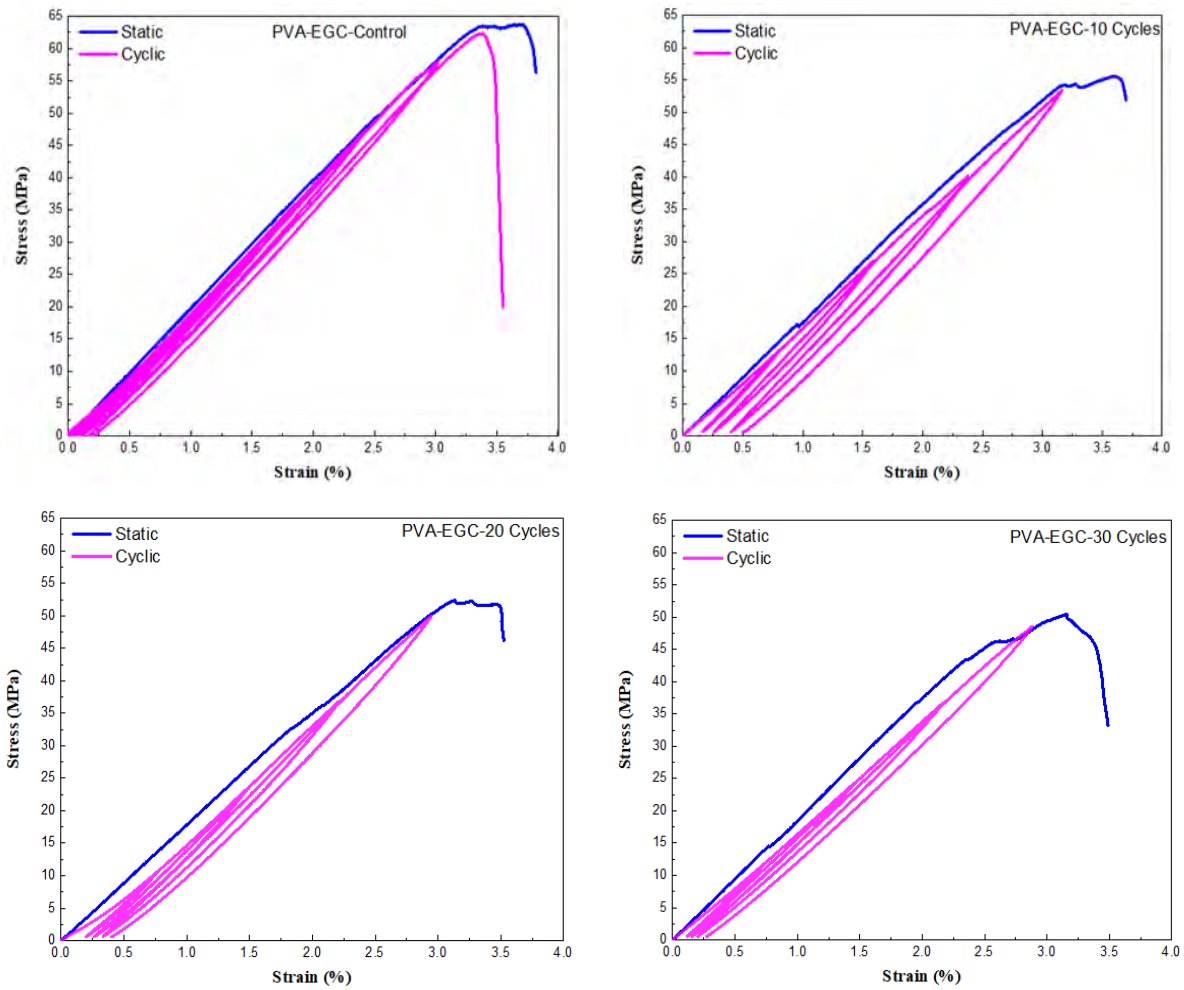


Fig. 5. Static and cyclic stress strain responses for PVA-EGC specimens at different thermal cycles

Figures 5-8 depict the influence of thermal cycling on the stress-strain behavior of the green LW-EGC and ECC specimens under static and cyclic loading. The behavior of both LW-ECC and EGC specimens exhibited nearly linear pre-peak behavior up to the maximum loads, even for specimens subjected to thermal cycles. Minor deviations were observed in the post-peak region of the static and cyclic curves for both lightweight specimens, as the elastic modulus decreased with increasing loading/unloading cycles. Similar properties have been reported in previous studies [33, 34]. Upon investigating the LW-EGC specimens under cooling and heating cycles, it was observed that both static and cyclic loadings decreased as the number of thermal cycles increased. The strength of PVA-PP-EGC, PP-EGC, and PVA-EGC specimens decreased by 28%, 23%, and 13%, respectively, after 10 thermal cycles. Further deterioration in the compressive strengths of LW-EGC specimens was observed as the heating and cooling cycles increased from 10 to 30. This reduction is due to the dense mix of the slag-based EGC, which promotes the accumulation of vapor pressure, leading to internal cracking. The different particle sizes, irregular flake-shaped particles, and high density of slag contribute to the denser microstructure of the slag-based EGC mix, resulting in reducing the pore size and thickness of the interfacial transition zone (ITZ) between PVA fibers and the EGC matrix. Additionally, the melting point and thermal cycling of polypropylene fibers significantly degrade the quality of the materials. Polypropylene fibers melt totally at a temperature of about 160 °C, rendering them unable to mitigate the detrimental effect of micro-cracks. The existence of voids in melted fiber in the EGC mix effectively decreases the compressive strength [35].

Figure 9 illustrates the failure modes of the green LW-ECC and EGC specimens after subjecting to various heating and cooling cycles. Irrespective of the compound type, the specimens exhibited a higher level of reliability before undergoing thermal curing owing to the inclusion of PP and PVA fibers in their mix proportions. The specimens reinforced by PVA fibers showed a more aggressive

failure compared to the specimens reinforced with PP fibers, primarily due to the high bond availability provided by the PVA fibers. This resulted in cracks propagating throughout the mid-lengths of the specimens. During thermal treatment, the failure pattern of the PVA fiber-reinforced specimens remained consistent with increasing thermal cycles, maintaining the integrity of the specimens.

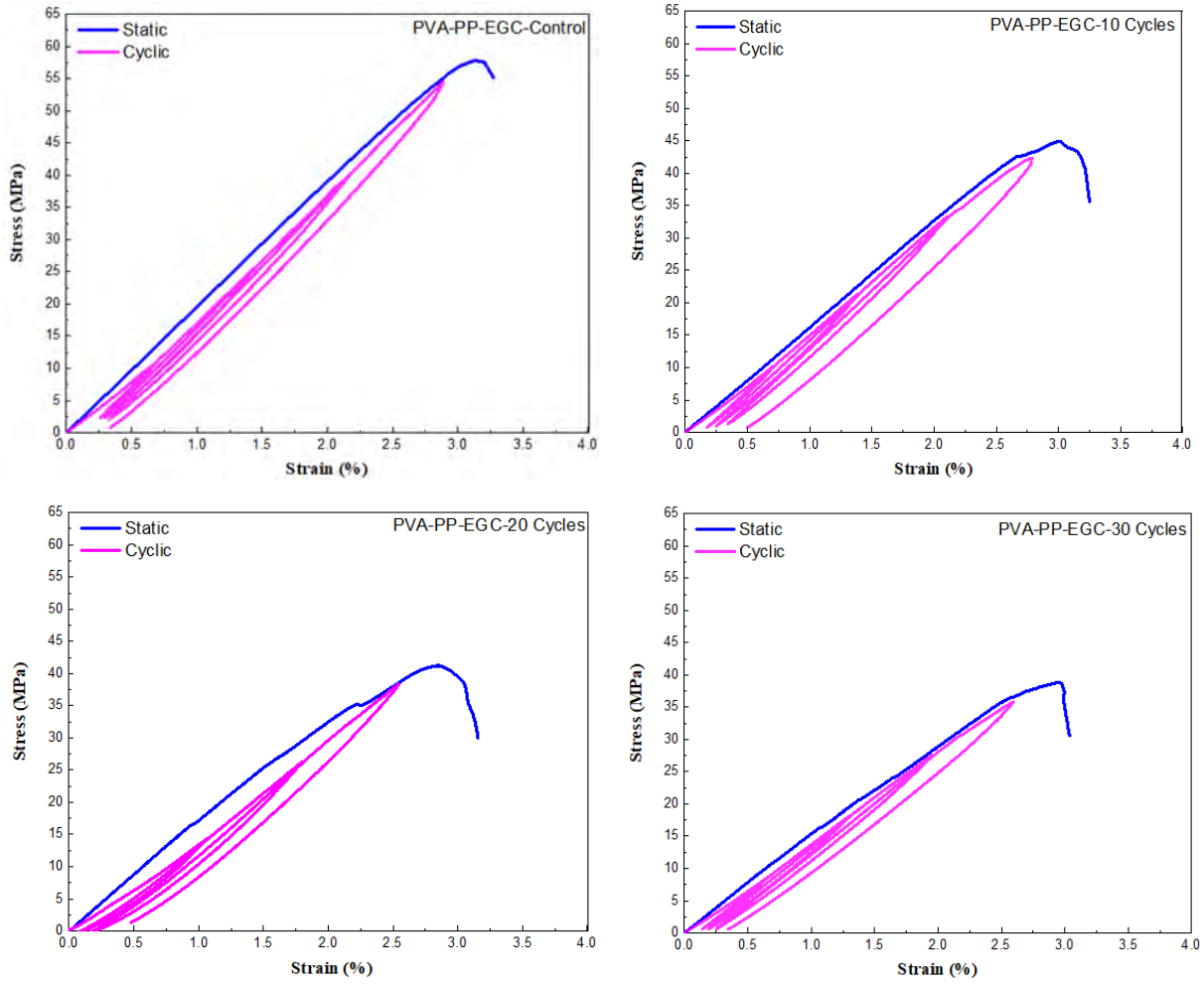
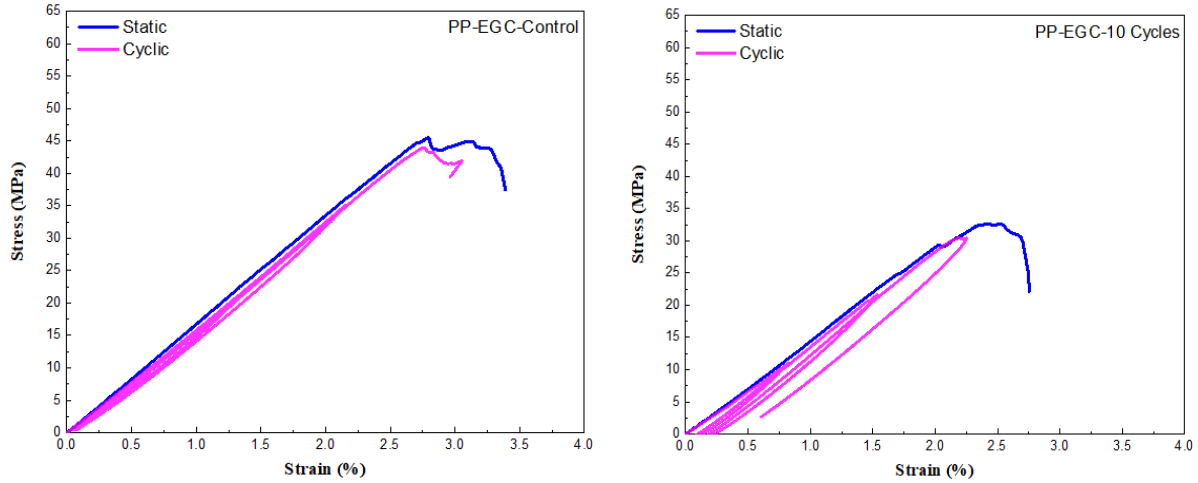


Fig. 6. Static and cyclic stress strain responses for PVA-PP-EGC specimens at different thermal cycles



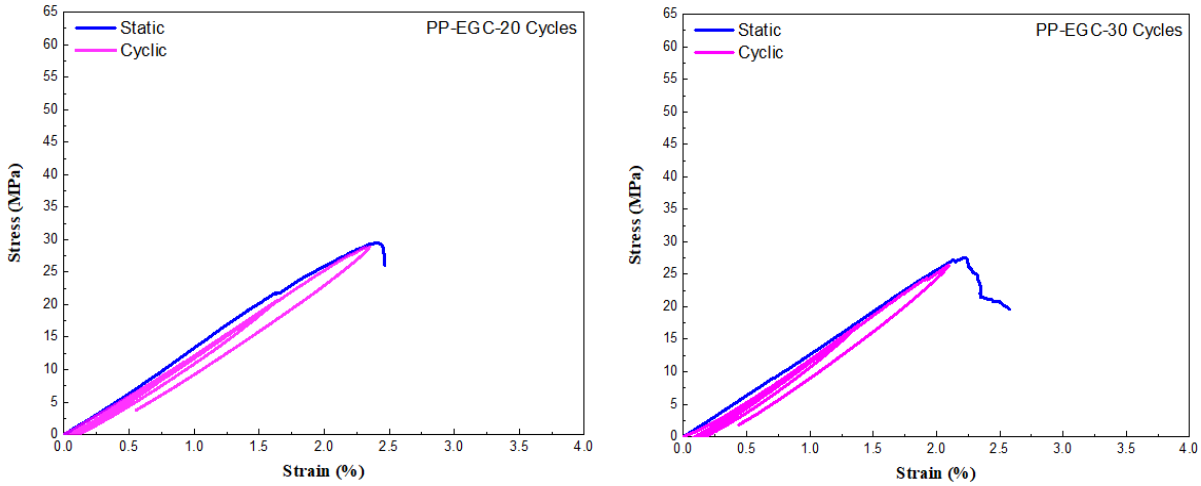


Fig. 7. Static and cyclic stress-strain responses for PP-EGC specimens at different thermal cycles

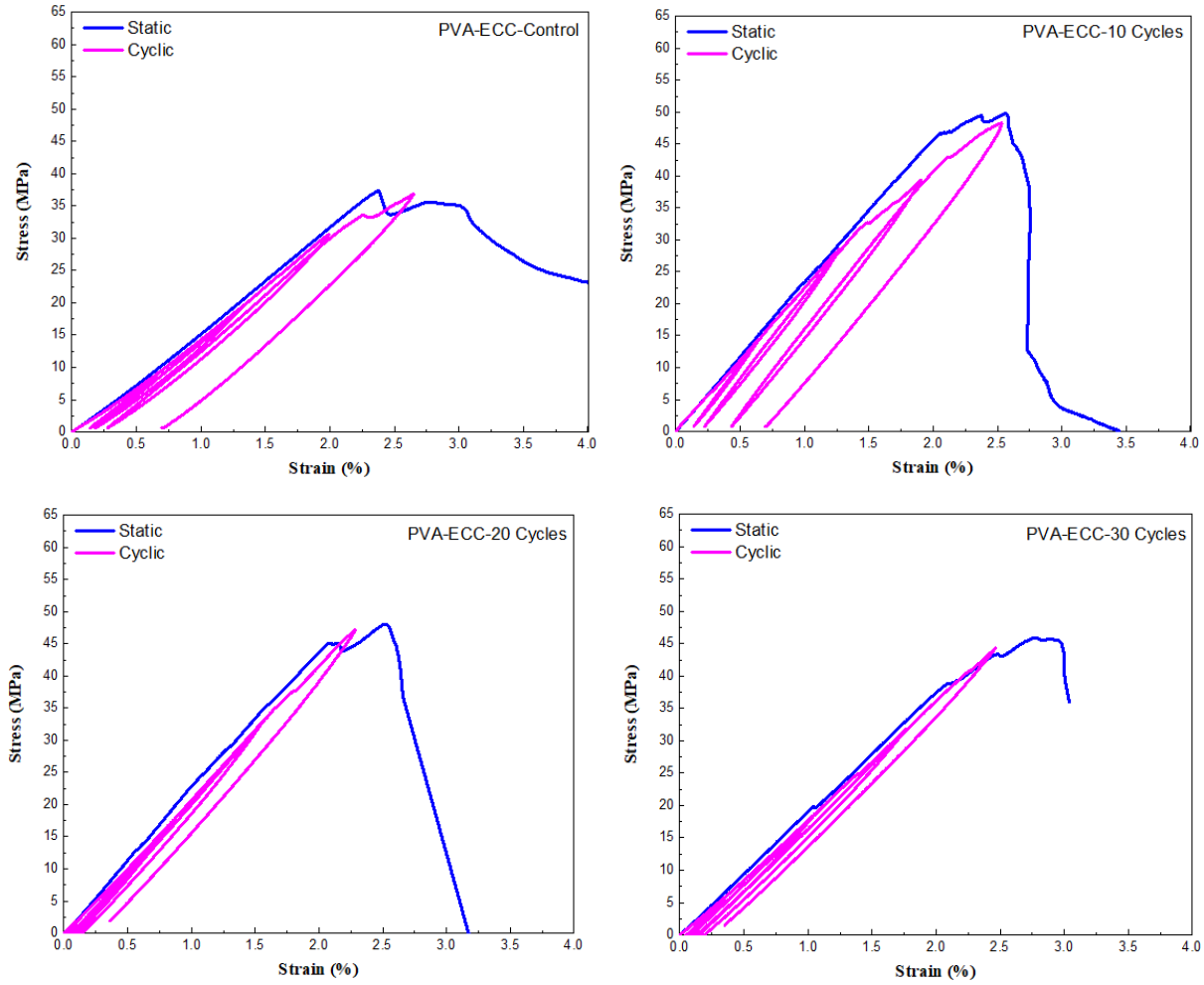


Fig. 8. Static and cyclic stress-strain responses for PVA-ECC specimens at different thermal cycles

However, instead of major cracks, finer cracks were visibly detected during the compression test due to the partial breakage of PVA fibers under thermal curing, resulting in a weakened bond between the EGC matrix and the PVA fibers. On the other hand, the specimens reinforced with PP fibers experienced severe fragmentation and exhibited brittle properties when exposed to high temperatures. This is due to the complete melting of PP fiber at a temperature of 160 °C. This change in failure mode from ductile to brittle properties is in agreement with the literature that applied PP fibers in their studies [33, 36].

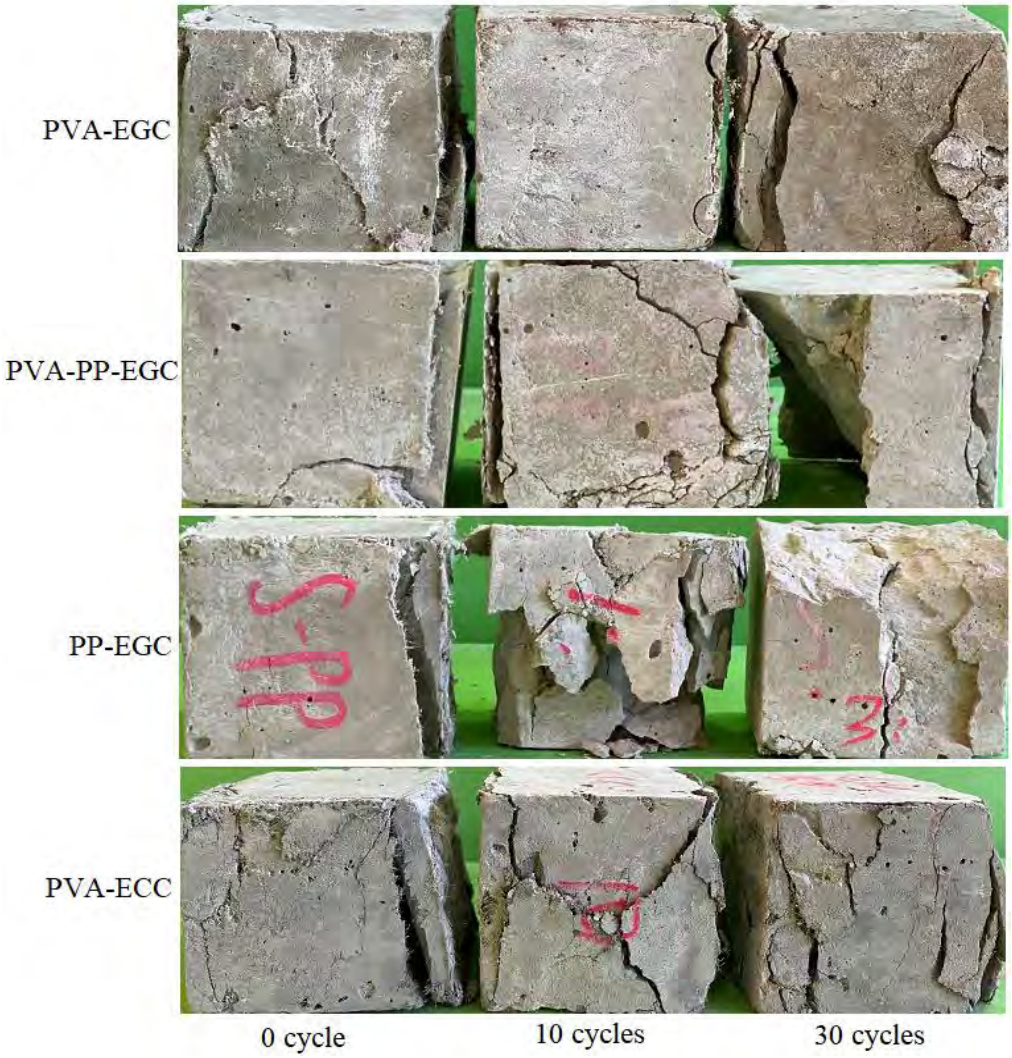
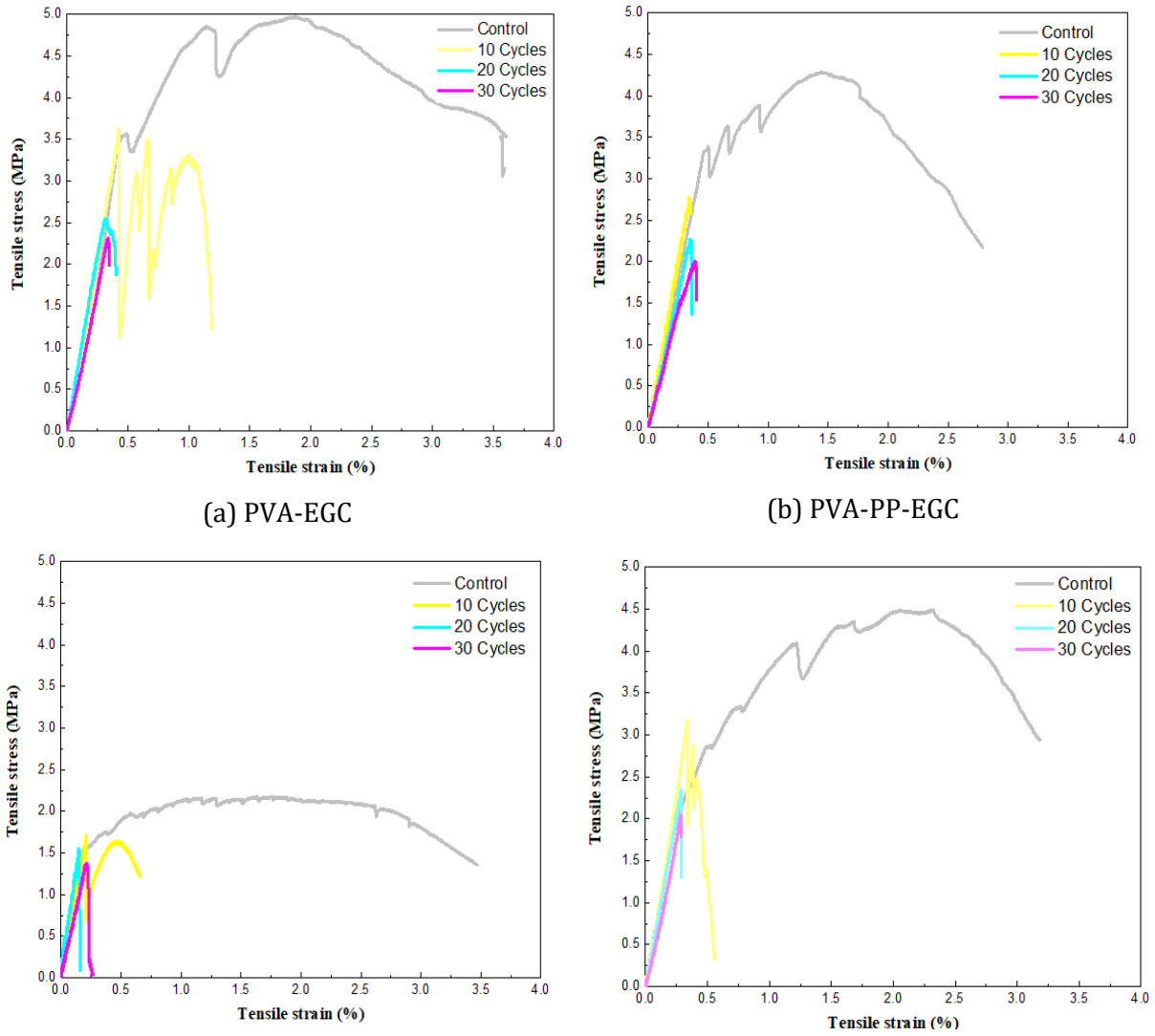


Fig. 9. The failure shape of green LW-ECC and LW-EGC specimens at compression test under different thermal cycles

3.3 Tensile Test

Direct tensile tests were conducted to examine the stress-strain and tensile strength responses of the LW-ECC and LW-EGC composites under heating and cooling cycles, as presented in Fig. 10. Overall, all specimens showed strain hardening behavior, with crack propagation and narrow crack widths. The ultimate tensile strength of both ECC and EGC composites before thermal curing was significantly higher than the first crack strength. It was observed that at room temperature, the tensile strength of PP-EGC, PVA-PP-EGC, and PVA-EGC composites was 2.17 MPa, 4.28 MPa, and 4.97 MPa, respectively, with strain capacities of 2.09%, 1.43%, and 1.90%.

The results showed that PVA fiber-reinforced specimens exhibited higher tensile stress, but lower tensile ductility compared to specimens reinforced with PP fibers. The tensile stress of PVA-EGC specimens was 229% higher than that of PP-EGC specimens, while the ductility of PP-EGC specimens was 10% higher than that of PVA-EGC specimens. The use of inexpensive polypropylene fibers in LW-EGC composites demonstrated improved strain behavior. However, the tensile strength of PVA-EGC samples was 10 times higher than that of PVA-ECC specimens, while the strain capacity of PVA-EGC specimens was 22% lower than that of PVA-ECC specimens. This increase in tensile ductility of LW-ECC composites was attributed to the incorporation of FA binder, which reduced the bond between the PVA fibers and ECC matrix, resulting in higher ductility and lower fiber bridging strength.



(a) PVA-EGC (b) PVA-PP-EGC

(c) PP-EGC (d) PVA-ECC

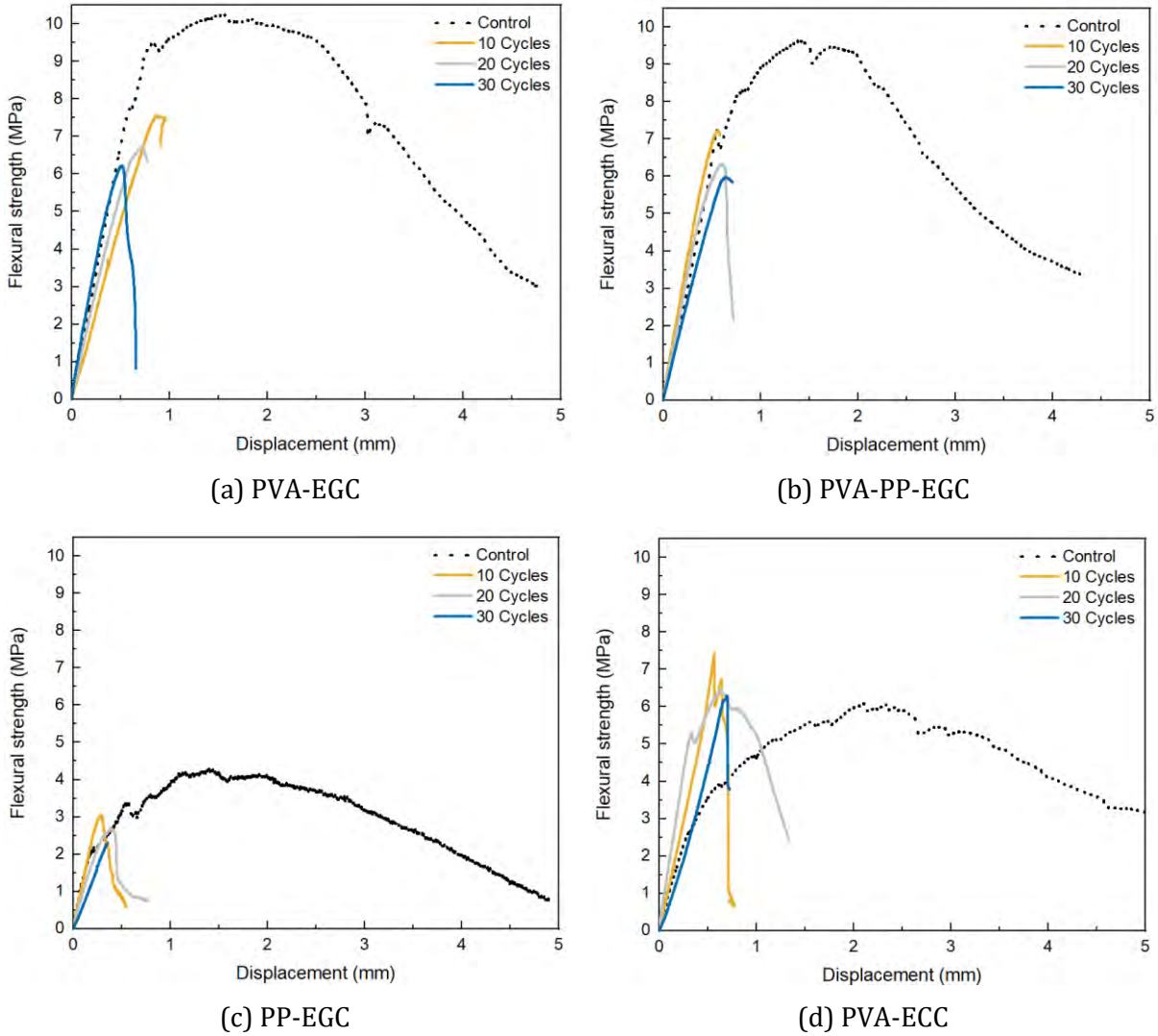
Fig. 10. The tensile stress-strain behavior of LW- ECC and EGC composite before and after undergoing thermal cycles

The effect of thermal cycling on the tensile stress and tensile ductility of green LW-ECC and LW-EGC composites is also presented in Fig. 10. The results exhibited an important decrease in tensile stress and tensile ductility of slag-based LW-EGC composites when subjected to different temperature treatments. The specimens lost their strain-hardening performance and exhibited brittle behavior similar to plain concrete under thermal cycling. Similar behavior has been observed in previous studies. The tensile strength of PVA-EGC specimens decreased by 27%, 49%, and 54% when exposed to 10, 20, and 30 cycles, respectively.

Moreover, specimens reinforced with PVA fibers exhibited a lower decrease in tensile stress and strain compared to specimens reinforced with PP fibers. This can be attributed to the deterioration of PP fibers at 200 °C, as PP fibers typically melt at around 160 °C. In contrast, polyvinyl alcohol fibers have a higher melting point above 200 °C but are considerably damaged, leading to a loss of interlayer bonding between the PVA fibers and the EGC matrix. It is worth noting that specimens reinforced with PP fibers exhibited a brittle property due to the complete melting of PP fibers at high temperatures and lost their strength. This finding aligns with the SEM observations of LW-EGC composites discussed earlier. Therefore, it was determined that the reduction in tensile strength of LW-ECC and EGC specimens under thermal cycling was more prominent than that of compressive strength, as tensile stress and strain were more susceptible to the expansion of microstructural flaws such as crack initiation and void formation during thermal curing.

3.4 Flexural Strength

The Flexural strength-deflection of green LW-ECC and EGC composites after undergoing thermal curing is presented in Fig. 11. EGC specimens reinforced by PVA fibers exhibited better flexural strength (rupture modulus) but lower deflection ability compared to specimens reinforced with PP fibers. Regardless of the fiber type, both LW-ECC and EGC specimens showed deformation-hardening behavior when tested at room temperature. The integration of PVA and PP fibers in the LW-EGC mix contributed to the control and reduction of flaws, as well as improved the interlayer connection between the fibers and cement matrix. The presence of PP and PVA fibers positively affected the deflection ability of LW-EGC composites, facilitating crack control and enhancing tension behavior in the concrete mix. The flexural performance of green LW-EGC samples, irrespective of the fiber type, significantly decreased when subjected to thermal curing at 200 °C, leading to the loss of deformation-hardening behavior. The number and width of cracks decreased with increasing thermal curing. In contrast, LW-ECC composites, with their higher porosity, allowed for steam pressure escape and exhibited fewer internal stresses, resulting in enhanced flexural strength. The flexural strength (modulus rupture) of PVA-EGC specimens decreased by 26.2%, 34.6%, and 39.3% after being subjected to 10, 20, and 30 cycle, respectively.



(a) PVA-EGC (b) PVA-PP-EGC

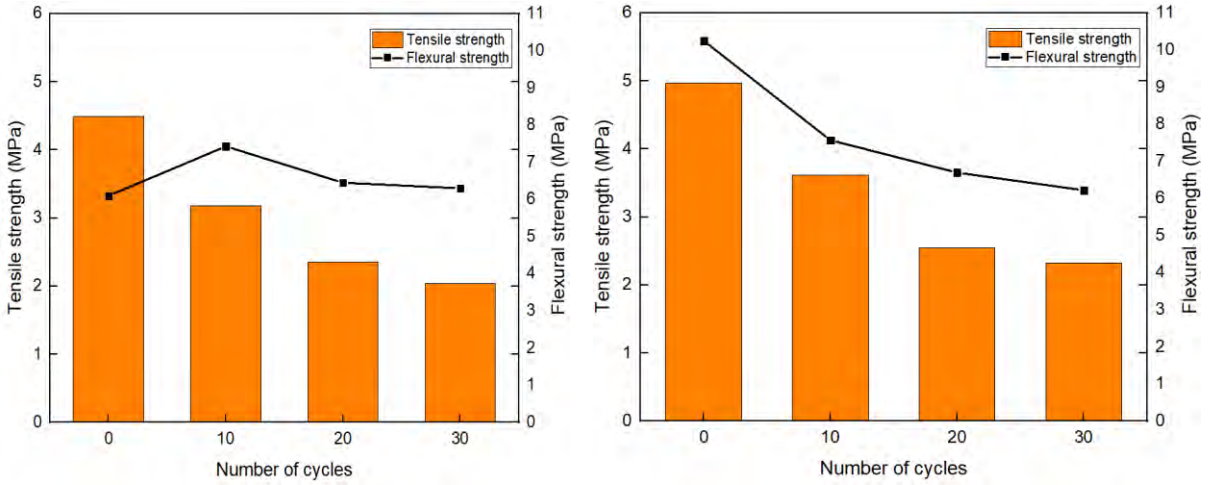
(c) PP-EGC (d) PVA-ECC

Fig. 11. Flexural strength versus deflection curves for LW- EGC and LW- ECC before and after endergoing to thermal cycles

Fig. 11 also illustrates that the residual flexural strength of PVA fiber-reinforced EGC specimens was higher than that of PP fiber-reinforced specimens after undergoing thermal curing. The degradation in flexural strength of green LW-EGC composites under thermal curing resulted in the

loss of deformation-hardening behavior, resembling plain concrete rather than traditional fiber-reinforced concrete. The degradation of fiber-matrix interfacial properties and the increase in matrix toughness contributed to the significant deterioration in flexural properties. In contrast, the flexural strength of LW-ECC specimens significantly improved with thermal curing. The flexural strength of PVA-ECC specimens increased by 21.95%, 5.8%, and 3.3% after 10, 20, and 30 thermal cycles, respectively. Nevertheless, the deflection ability of PVA-ECC specimens progressively decreased with increasing temperature variations, showing lower values compared to specimens treated at room temperature. The deterioration of PVA fibers due to temperature cycling resulted in the degradation of fiber bridging, negatively impacting the bending properties of ECC specimens.

The influence of cooling and heating treatment on the flexural, tensile, and compressive strength of green LW-ECC and EGC composites is shown in Fig. 12. The compressive and flexural strength of green LW-ECC and EGC composites remained relatively stable during thermal processing. However, the behavior of tensile strength exhibited a different trend under thermal curing conditions. This observation highlights the need for further investigation to comprehensively understand the impact of different thermal curing methods and elevated temperatures on the tensile strength of normal weight and LW-EGC composites. The experimental results obtained in this study serve as a fundamental database for understanding the properties of EGC when exposed to cooling and heating curing processes.



(a) PVA-EGC (b) PVA-ECC

Fig. 12. Correlation between tensile strength and flexural strength at different heating-cooling cycles for LW- PVA-ECC and PVA-EGC composites

6. Conclusions and Recommendations

This research investigates the influence of two types of fibers, namely polypropylene and polyvinyl alcohol, on the mechanical behavior of slag-based EGC and ECC subjected to 0, 10, 20, and 30 heating and cooling curing cycles. LW-EGC and ECC have a density ranging from 1790 to 1870 kg/m^3, lower than that of normal-weight geopolymer concrete and normal-weight ECC. Except for the PVA-EGC composite, all the studied samples are classified as lightweight concrete. Experimental tests were conducted before and after temperature treatment, including measurements of residual mechanical performance, scanning electron microscopy, and mass loss, encompassing cyclic and static loading, deflection, failure stages, and stress-strain responses. The main contributions of this paper are as follows:

- The compressive strength of green LW-EGC specimens significantly decreased under various heating and cooling cycles due to the reduced porosity and higher density of the slag-based LW-EGC mixture. Conversely, the compressive strength of LW-ECC specimens substantially improved with increasing temperature cycling due to the enhanced reactivity of FA particles during thermal cycling.

- The addition of PP fiber in the green LW-EGC mix improved the strain properties at room temperature, providing a cost-effective alternative to the relatively expensive PVA fibers for reinforcing EGC or ECC mixtures. Irrespective of the type of composite, the tensile behavior of all the studied specimens significantly deteriorated when subjected to different thermal cycles. This behavior was attributed to the increased sensitivity of the microstructure to the expansion of internal flaws, such as starting of cracks and the development of porous problems, at various temperature curing conditions.
- The flexural properties of green LW-EGC specimens, regardless of the fiber type, were significantly reduced when subjected to various cooling and heating sequences, resulting in the complete loss of deflection-hardening properties. In contrast, the flexural strength of LW-ECC specimens remarkably enhanced under thermal cycling owing to the hydration process and accelerated pozzolanic reactions of FA. However, the deformation capacity gradually decreased due to an increase in thermal cycles, attributed to PVA fibers suffering significant damage, leading to a reduced bond between PVA fibers and the EGC matrix.
- Microstructure analysis revealed that green LW-EGC specimens experienced more severe damage than LW-ECC samples when exposed to various cooling- heating cycles. This was attributed to the higher number and porosity of ECC's microstructure, which decreased the effect of thermal treatment on the microstructure of ECC. Additionally, PVA fibers did not completely melt under thermal cycling at 200 °C, unlike PP fibers, which softened completely and disappeared during temperature curing. The microstructure of the LW-EGC specimens showed evident defects such as small cracks and a high number of capillary voids, likely due to the PP fibers leaving behind minor cracks in the EGC mixture. These defects might adversely affect the remaining mechanical behavior of LW-EGC specimens.

Future research should consider expanding the scope to other fiber types, such as steel, glass, or basalt fibers, which may offer improved high-temperature performance or other benefits. Also, extending the temperature range beyond 200°C to simulate more extreme environments like fire resistance, is crucial in many construction applications. The study could be enhanced by simulating more varied real-world conditions, such as the effects of freeze-thaw cycles or exposure to chemicals like saltwater or acids. This would give a better idea of how SEGC would perform in diverse environments. A more extended analysis of the long-term durability of SEGC is recommended, including creep, fatigue, and shrinkage characteristics under various environmental conditions. Given the sustainability angle of the research, a lifecycle assessment (LCA) could provide a more comprehensive view of the environmental impact of SEGC and ECC, comparing their carbon footprints over their entire lifespan.

References

[1] Farhan KZ, Johari MAM, Demirboğa R. Impact of fiber reinforcements on properties of geopolymer composites: A review. J Build Eng. 2021;44:102628. https://doi.org/10.1016/j.jobe.2021.102628

[2] Alcan HG, Bayrak B, Öz A, Çelebi O, Kaplan G, Aydın AC. Synergetic effect of fibers on geopolymers: Cost-effective and sustainable perspective. Constr Build Mater. 2024;414:135059. https://doi.org/10.1016/j.conbuildmat.2024.135059

[3] Abdalla JA, Hawileh RA, Bahurudeen A, Jyothsna G, Sofi A, Shanmugam V, et al. A comprehensive review on the use of natural fibers in cement/geopolymer concrete: A step towards sustainability. Case Stud Constr Mater. 2023;22:e02244. https://doi.org/10.1016/j.cscm.2023.e02244

[4] Wasim M, Ngo TD, Law D. A state-of-the-art review on the durability of geopolymer concrete for sustainable structures and infrastructure. Constr Build Mater. 2021;291:123381. https://doi.org/10.1016/j.conbuildmat.2021.123381

[5] Duan P, Yan C, Zhou W, Ren D. Fresh properties, compressive strength and microstructure of fly ash geopolymer paste blended with iron ore tailing under thermal cycle. Constr Build Mater. 2016;118:76-88. https://doi.org/10.1016/j.conbuildmat.2016.05.059

[6] Duan P, Yan C, Zhou W. Compressive strength and microstructure of fly ash-based geopolymer blended with silica fume under thermal cycle. Cem Concr Compos. 2017;78:108-19. https://doi.org/10.1016/j.cemconcomp.2017.01.009

[7] Humur G, Çevik A. Effects of hybrid fibers and nanosilica on mechanical and durability properties of lightweight engineered geopolymer composites subjected to cyclic loading and heating-cooling cycles. Constr Build Mater. 2022;326:126846. https://doi.org/10.1016/j.conbuildmat.2022.126846

[8] Lin Z, Xu W, Wang W, Zhang J, Wang H, Wang R. Experimental study on hydraulic and macro-mechanical property of a mortar under heating and cooling treatment. J Adv Concr Technol. 2016;14:261-70. https://doi.org/10.3151/jact.14.261
[9] An M, Huang H, Wang Y, Zhao G. Effect of thermal cycling on the properties of high-performance concrete: Microstructure and mechanism. Constr Build Mater. 2020;243:118310. https://doi.org/10.1016/j.conbuildmat.2020.118310
[10] Das D, Gołąbiewska A, Rout PK. Geopolymer bricks: The next generation of construction materials for sustainable environment. Constr Build Mater. 2024;445:137876. https://doi.org/10.1016/j.conbuildmat.2024.137876
[11] Chelluri S, Hossiney N. Performance evaluation of ternary blended geopolymer binders comprising of slag, fly ash and brick kiln rice husk ash. Case Stud Constr Mater. 2024;20:e02918. https://doi.org/10.1016/j.cscm.2024.e02918
[12] Debnath K, Das D, Rout PK. Effect of mechanical milling of fly ash powder on compressive strength of geopolymer. Mater Today Proc. 2022;68:242-9. https://doi.org/10.1016/j.matpr.2022.08.321
[13] Alanazi H, Hu J, Kim YR. Effect of slag, silica fume, and metakaolin on properties and performance of alkali-activated fly ash cured at ambient temperature. Constr Build Mater. 2019;197:747-56. https://doi.org/10.1016/j.conbuildmat.2018.11.172
[14] Sbahieh S, McKay G, Al-Ghamdi SG. Comprehensive analysis of geopolymer materials: Properties, environmental impacts, and applications. Materials. 2023;16:7363. https://doi.org/10.3390/ma16237363
[15] Wang F, Ma J, Ding Y, Yu J, Yu K. Engineered geopolymer composite (EGC) with ultra-low fiber content of 0.2%. Constr Build Mater. 2024;411:134626. https://doi.org/10.1016/j.conbuildmat.2023.134626
[16] Subramaniam DN, Sathiparan N. Comparative study of fly ash and rice husk ash as cement replacement in pervious concrete: Mechanical characteristics and sustainability analysis. Int J Pavement Eng. 2023;24:2075867. https://doi.org/10.1080/10298436.2022.2075867
[17] Elmessalami N, El Refai A, Abed F. Fiber-reinforced polymers bars for compression reinforcement: A promising alternative to steel bars. Constr Build Mater. 2019;209:725-37. https://doi.org/10.1016/j.conbuildmat.2019.03.105
[18] Ling Y, Wang K, Li W, Shi G, Lu P. Effect of slag on the mechanical properties and bond strength of fly ash-based engineered geopolymer composites. Compos Part B Eng. 2019;164:747-57. https://doi.org/10.1016/j.compositesb.2019.01.092
[19] Humur G, Çevik A. Mechanical characterization of lightweight engineered geopolymer composites exposed to elevated temperatures. Ceram Int. 2022;48:13634-50. https://doi.org/10.1016/j.ceramint.2022.01.243
[20] ASTM. ASTM C109/C109M-02: Standard test method for compressive strength of hydraulic cement mortar. West Conshohocken, PA, USA: ASTM International; 2002.
[21] Bhat PS, Chang V, Li M. Effect of elevated temperature on strain-hardening engineered cementitious composites. Constr Build Mater. 2014;69:370-80. https://doi.org/10.1016/j.conbuildmat.2014.07.052
[22] Rokugo K. Recommendations for design and construction of high performance fiber reinforced cement composites with multiple fine cracks (HPFRCC). Tokyo, Japan: Japan Society of Civil Engineers, Concrete Committee; 2008.
[23] Şahmaran M, Lachemi M, Hossain KM, Li VC. Internal curing of engineered cementitious composites for prevention of early age autogenous shrinkage cracking. Cem Concr Res. 2009;39:893-901. https://doi.org/10.1016/j.cemconres.2009.07.006
[24] Li Y, Li W, Deng D, Wang K, Duan WH. Reinforcement effects of polyvinyl alcohol and polypropylene fibers on flexural behaviors of sulfoaluminate cement matrices. Cem Concr Compos. 2018;88:139-49. https://doi.org/10.1016/j.cemconcomp.2018.02.004
[25] Lin J-X, Song Y, Xie Z-H, Guo Y-C, Yuan B, Zeng J-J, et al. Static and dynamic mechanical behavior of engineered cementitious composites with PP and PVA fibers. J Build Eng. 2020;29:101097. https://doi.org/10.1016/j.jobe.2019.101097
[26] Aygörmez Y, Canpolat O, Al-Mashhadani MM, Uysal M. Elevated temperature, freezing-thawing and wetting-drying effects on polypropylene fiber reinforced metakaolin-based geopolymer composites. Constr Build Mater. 2020;235:117502. https://doi.org/10.1016/j.conbuildmat.2019.117502
[27] Şahmaran M, Lachemi M, Li VC. Assessing mechanical properties and microstructure of fire-damaged engineered cementitious composites. ACI Mater J. 2010;107. https://doi.org/10.14359/51663759
[28] Zhou X, Li Z. A constitutive model for fiber-reinforced extrudable fresh cementitious paste. Comput Concr. 2011;8:371-88. https://doi.org/10.12989/cac.2011.8.4.371
[29] ACI Committee. Guide for selecting proportions for high-strength concrete using Portland cement and other cementitious materials. Farmington Hills, MI: ACI Committee; 2008.
[30] Nath S, Kumar S. Influence of iron-making slags on strength and microstructure of fly ash geopolymer. Constr Build Mater. 2013;38:924-30. https://doi.org/10.1016/j.conbuildmat.2012.09.070

[31] Nath S, Kumar S. Influence of granulated silico-manganese slag on compressive strength and microstructure of ambient cured alkali-activated fly ash binder. Waste Biomass Valorization. 2019;10:2045-55. https://doi.org/10.1007/s12649-018-0213-1

[32] Fang G, Ho WK, Tu W, Zhang M. Workability and mechanical properties of alkali-activated fly ash-slag concrete cured at ambient temperature. Constr Build Mater. 2018;172:476-87. https://doi.org/10.1016/j.conbuildmat.2018.04.008

[33] Mohammedameen A, Gülşan ME, Alzeebaree R, Çevik A, Niş A. Mechanical and durability performance of FRP-confined and unconfined strain-hardening cementitious composites exposed to sulfate attack. Constr Build Mater. 2019;207:158-73. https://doi.org/10.1016/j.conbuildmat.2019.02.108

[34] Gülşan ME, Mohammedameen A, Şahmaran M, Niş A, Alzeebaree R, Çevik A. Effects of sulphuric acid on mechanical and durability properties of ECC confined by FRP fabrics. Adv Concr Constr. 2018;6:199.

[35] Irshidat MR, Al-Nuaimi N, Rabie M. Hybrid effect of carbon nanotubes and polypropylene microfibers on fire resistance, thermal characteristics and microstructure of cementitious composites. Constr Build Mater. 2021;266:121154. https://doi.org/10.1016/j.conbuildmat.2020.121154

Blank Page

Research on Engineering Structures & Materials
www.jresm.org

Research Article

Mechanical and rheological performance of plastic concrete: Investigation of several properties

Mohammad Sadegh Shahidzadeh [*,a], Mahbobeh Mirzaie Aliabadi [b], Hamid Mansouri Far [c], Amir Hossein Derakhshan Nezhad [d]

Department of Civil Engineering, Technical and Engineering Faculty, Behbahan Khatam Alanbia University of Technology, Behbahan, Iran

Article Info

Article History:

Received 02 Sep 2024

Accepted 28 Nov 2024

Keywords:

Plastic concrete;
Slump test;
Mixing design;
Carbon based materials

Abstract

Incorporating carbon-based materials, particularly carbon nanotubes (CNTs), into the initial composition of plastic concrete has demonstrated potential in enhancing properties such as particle cohesion and resistance to corrosive environments. This study investigates the influence of CNTs on the mechanical and durability characteristics of concrete through 24 distinct mix designs, all maintaining a constant water-to-cement ratio of 0.5. The CNT content varied at levels of 5%, 10%, 15%, and 20% by weight of cement. For each mix, six cylindrical specimens (15 × 30 cm) and three cubic specimens (15 × 15 × 15 cm) were prepared for evaluating compressive strength, permeability, and modulus of elasticity. The experimental results indicate that under a fixed water-to-cement ratio, increasing the cement content significantly raises the viscosity of the concrete mixture, often resulting in a slurry-like consistency. Conversely, an increase in bentonite content at a fixed water-to-cement ratio enhanced fluidity, thereby increasing the slump of fresh concrete. However, this fluidity caused segregation of aggregate particles during placement into molds, adversely affecting compressive strength. Furthermore, for designs containing 30 kg of bentonite, the water absorption and particle segregation rates increased with a higher cement content. In contrast, as the bentonite content increased from 30 kg to 60 kg, water absorption at the concrete surface and particle segregation decreased, suggesting improved homogeneity and resistance to moisture penetration. These findings provide insights into optimizing the composition of plastic concrete containing CNTs and bentonite for enhanced performance in structural applications.

© 2025 MIM Research Group. All rights reserved.

1. Introduction

From a long time until now, one of the major challenges for the advancement of the dam industry has been the issue of water escaping from the sides and foundations of dams [1]. So that the foundations and flanks of dams have always been among the places that have been allocated the largest amount of geotechnical research [2-4]. Due to the importance of this issue, examining the characteristics of the permeability of the lower layers of the foundation and the sides of the dam has been included in most of this research [5]. Since there is always an underground flow of water under the bed of the lower layers of the construction site of the dam, therefore, with the increase in the height of the water behind the dams, the pore water pressure in the lower layer of the dam increases, which itself causes destruction [6-8], washing Inefficiency, the lower layers of the dam become blocked [9]. Also, the conducted research shows that the increase in pore water pressure in the lower layer of the dam causes soil flotation in the heel of the dams [10-12]. To prevent water

*Corresponding author: shahidzadeh@bkatu.ac.ir
[a]orcid.org/0000-0001-5910-7724; [b]orcid.org/0000-0002-9594-0489; [c]orcid.org/0009-0004-8061-8675; [d]orcid.org/0009-0008-0994-8590
DOI: http://dx.doi.org/10.17515/resm2024.430me0902rs

penetration and reduce seepage behind dams, there are various methods [13], one of these methods is digging a trench behind the dam and filling it with plastic concrete materials [14-16]. In plastic concrete, in addition to the primary materials available in ordinary concrete such as cement, stone materials and water, a type of clay called bentonite is also used, to which ordinary clay, pozzolans, etc [17,18] may also be added [19]. Also, more water-cement ratios are used in plastic concrete [20]. In addition to high deformability and low permeability, plastic concrete has a shear resistance proportional to the applied pressure [21]. The high ratio of water to cement as well as the presence of bentonite in plastic concrete has caused this concrete to have different properties than normal concrete, among these properties we can mention its low strength and high plasticity [22-24]. In addition to having high ductility and low resistance, plastic concrete has low permeability, which sometimes we can minimize this permeability by increasing the concentration of bentonite slurry [25-27]. Plastic concrete is mainly used in hydraulic structures such as dams, and retaining walls [28]. These structures need materials that can minimize water leakage and at the same time have the ability to withstand changes in water pressure and relative soil movements [29]. The high plasticity of this concrete allows the structure to change its shape against volume changes and relative movements between the soil and the structure without causing large cracks or fractures [30]. In retaining walls and underground structures, plastic concrete is used as a protective layer against non-uniform soil deformations and lateral pressures [31]. Plastic concrete in these applications can withstand non-uniform settlements and dynamic pressures caused by earthquake vibrations or heavy machinery due to its high ability to absorb energy and plastic deformation [32]. In areas affected by strong vibrations or mechanical vibrations, plastic concrete acts as an energy absorbing material. The internal structure of this concrete due to the presence of clay particles; Like bentonite, it can absorb and dissipate vibration energy, which reduces local stresses and prevents premature failures in the structure [33-35]. Plastic concrete has high viscosity and significant plastic deformation. This behavior is caused by the use of clay materials; It is like bentonite which strengthens the matrix structure of cement and reduces the speed of free flow of water in concrete. Compared to normal concrete, the constituent ratios in plastic concrete are completely different. About 80% of the composition of ordinary concrete is sand [36]. The amount of cement is on average between 12% and 14% and the amount of water is between 6% and 8%. But these proportions in plastic concrete are such that sand is about 65-75% (average 10% less), cement about 5-10%, bentonite slurry (combination of water, and bentonite) about 20-25%. is Due to this amount of combination ratios, plastic concrete has high fluidity and has less resistance than normal concrete. Therefore, the main ingredients of plastic concrete are water, sand, cement and bentonite, which are briefly mentioned below. Among the most important properties of plastic concrete that are studied more, we can mention permeability, modulus of elasticity, compressive strength, durability and abrasion resistance, ductility and efficiency [37]. One of the most important features that plastic concretes should have is that they show good durability in normal and corrosive environmental conditions [38]. The durability of plastic concrete means its resistance and waterproofness in non-corrosive and aggressive (corrosive) environments, which is achieved by proper concrete mixing design. For watertight wall structures, the concept of appropriate abrasion resistance should be compared to the concept of permeability, as this concept is expressed as the resistance of concrete materials to percolation under hydraulic gradient [39]. By conducting experiments, it has been found that the resistance to wear depends on the compressive strength, the amount of air, the granulation of materials, slump, etc [40]. Plastic concrete offers notable advantages over conventional concrete, including reduced permeability, increased flexibility, and enhanced workability. Economically, it also proves to be more cost-effective compared to ordinary concrete. Studies conducted by Pashang Pisheh et al. (2018) and Kazemi et al. (2016) on the properties of plastic concrete used in dam sealing curtains revealed that increasing the cement content improves both compressive strength and the modulus of elasticity. Conversely, these properties decrease as the proportion of bentonite increases. These findings were derived from analyzing various compositions of plastic concrete materials. In 2024, Derakhshan Nezhad et al. investigated the mechanical performance of self-compacting concrete (SCC) enhanced with palm fibers at dosages of 0%, 0.5%, 1%, 1.5%, and 2% by cement weight. Their experimental results demonstrated that incorporating palm fibers significantly improved tensile strength at 7 and 28 days of curing. Specifically, the increases in tensile strength for SCC containing 0.5%, 1%, 1.5%, and

2% palm fibers were 16.37%, 34.27%, 56.39%, and 82.24% at 7 days, and 13.56%, 27.61%, 46.96%, and 67.6% at 28 days, respectively, compared to plain SCC without fibers.

The importance of using plastic concrete in the discussion of concrete structure and technology is as follows; Plastic concrete is capable of exhibiting controlled plastic behavior that allows the structure to withstand excessive loads to temporarily deform without breaking. This feature is very important for areas with high vibration and lowest dynamics such as earthquakes, because ordinary concrete in similar conditions may become brittle and irreparable. In environments with thermal variations or web text loadings, cracking is a common material in conventional concrete. But plastic concrete, due to its low modulus of elasticity and non-linear behavior, greatly reduces this type of cracking. This feature is one of the most important in dams and marine structures that are exposed to constant pressure and temperature changes. Due to its good density and chemical resistance, plastic concrete is suitable for use in chemical storage tanks, and underground structures in leak-sensitive areas. These features help reduce environmental risks and increase the lifespan of structures. The low modulus of elasticity in plastic concrete makes it more difficult to compress. This allows for controllable deformations in bulk structures and results from transmission. The creep behavior of plastic concrete is one of its main advantages. Plastic concrete can change long-term and static paths in the form of creep, which prevents the creation of high internal stresses in the structure. Plastic concrete is ideal in earthquake and explosion resistant structures due to its controllable plastic behavior and energy absorption during deformation. This prevents vandalism and creates security. The composition of plastic concrete is designed in such a way that it is viscous. This feature prevents the separation of particles and makes the concrete stable in different stages of construction and processing. This feature is special in tall and bulky structures that require high stability and uniform filling. Plastic concrete is such that under low stresses, it shows elastic behavior, but high loading should enter the plastic state. This characteristic gives those concrete changes its shape when critical stresses occur and absorbs energy and prevents cracks from spreading and digging. Plastic concrete typically provides a longer, more controlled setting time to reduce initial stresses and prevent early cracking. This feature is very important in bulky structures such as dams and tunnels where the risk of early cracks is high. In this research, the fresh properties of plastic concrete were investigated through slump test and hardened plastic concrete test through modulus of elasticity, compressive strength and tensile strength.

2. Sample Mixing and Processing Plan

In this study, 24 distinct concrete mix designs were developed and executed. For each mix design, six cylindrical specimens measuring 30×15 cm and three cubic specimens measuring 15×15×15 cm were prepared to evaluate the tensile and compressive strength at 28 days. The detailed mix design configurations are presented in Table 1. The research employed three distinct cement quantities and two bentonite dosages. Due to the inherently fluid nature of plastic concrete, a fixed water-to-cement (W/C) ratio of 0.5 was adopted across all mix designs. once at night. This process was meticulously followed to maintain consistent hydration and achieve reliable mechanical property results for plastic concrete.

Table 1. Plastic concrete mixing plan [35]

Naming each design	W/C	Carbon)%(	Bentonite)Kg/m^3)	Cement)Kg/m^3)	Gravel)Kg/m^3)	Water)Kg/m^3)	Sand)Kg/m^3)
PC-1	0.5	5	30	100	1000	250	500
PC-2	0.5	10	30	100	1000	250	500
PC-3	0.5	15	30	100	1000	250	500
PC-4	0.5	20	30	100	1000	250	500
PC-5	0.5	5	30	150	1000	250	500
PC-6	0.5	10	30	150	1000	250	500
PC-7	0.5	15	30	150	1000	250	500
PC-8	0.5	20	30	150	1000	250	500

PC-9	0.5	5	30	200	1000	250	500
PC-10	0.5	10	30	200	1000	250	500
PC-11	0.5	15	30	200	1000	250	500
PC-12	0.5	20	30	200	1000	250	500
PC-13	0.5	0	60	100	1000	250	500
PC-14	0.5	5	60	100	1000	250	500
PC-15	0.5	10	60	100	1000	250	500
PC-16	0.5	15	60	100	1000	250	500
PC-17	0.5	20	60	100	1000	250	500
PC-18	0.5	5	60	150	1000	250	500
PC-19	0.5	10	60	150	1000	250	500
PC-20	0.5	15	60	150	1000	250	500
PC-21	0.5	20	60	150	1000	250	500
PC-22	0.5	5	60	200	1000	250	500
PC-23	0.5	10	60	200	1000	250	500
PC-24	0.5	20	60	200	1000	250	500

The primary objective of utilizing plastic concrete is to enhance its modulus of softness for specific applications. Consequently, the mix design with the maximum W/C ratio was selected as the baseline configuration to achieve optimal performance. The curing of the specimens in this research followed wet environmental conditions. After demolding, the specimens were wrapped in hemp cloth and placed in a controlled environment within the concrete research laboratory, maintained at an average temperature of 25°C. To preserve the moisture of the hemp covering and ensure adequate curing, the specimens were thoroughly moistened twice daily—once during the day and

2.1. Materials Used in Plastic Concrete

2.1.1. Cement

In this study, Type 5 Portland cement produced by Behbehan Cement Factory was employed. The cement's physical and chemical properties are presented in the table below, in compliance with the ASTM C150 [41] standard (see Table 2).

Table 2. Chemical and Physical Properties of Type 5 Portland Cement

Feature	SiO_2	Al_2O_3	Fe_2O_3	MgO	CaO	SO_3	K_2O	Insoluble residue	Specific weight (kg/m^3)
Percentage	21.18	4.96	5.04	1.40	62.4	2.12	0.57	0.74	3050

2.1.2. Aggregates

Fine-grained aggregates (washed sand) and coarse aggregates of broken type with granulation of residue on sieve 8 and residue on sieve 16 have been used in the mixing plan. The material of these aggregates is limestone, and they were supplied from Behbahan mines, and their physical characteristics and granularity are given in Table 3, which is in accordance with the ASTM C33 standard [42].

Table 3. Physical characteristics of aggregates

Water absorption percentage	)kg/m^3(specific weight	Aggregate type
0.85	2200	Coarse grain
0.65	1900	Fine grain

2.1.3. Water

In order to make the samples, the consumption (urban) water of Behbahan city was used, which conforms to the requirements of ASTM C 94 [43] (according to Table 4).

Table 4. Characteristics of drinking water

Chloride ion concentration	PH	Temperature (°C)
50	6	20

2.1.4. Bentonite

Bentonite produced in Avin Bentonite Company was used to make the samples, the specifications and values of each of them are given in Table 5.

Table 5. Characteristics of bentonite components

Feature	SiO_2	Al_2O_3	Fe_2O_3	MgO	CaO	TiO_2	K_2O	Na_2O	Specific weight (kg/m^3)
Percentage	69.8	11.88	1.3	1.42	8.17	0.2	0.47	4.88	2105

2.1.5. Carbon

The carbon produced in Gerd Asia Company has been used for mixing in the mixing plan. According to the manufacturer's announcement, this product does not contain harmful elements for the environment and is suitable for the southern regions of the country that have relatively corrosive soil (according to Table 6).

Table 6. Characteristics of carbon components

Feature	Sulfur	Carbon
Percentage	1.6%	98.4%

3.Steps of Plastic Concrete Mixing Plan

The bentonite needed for each series of samples is soaked in 70% of the water of the mixing plan 24 hours before making the samples, and every 4 to 6 hours, it is mixed with a rod for 5 minutes in the container until it is well mixed. Dissolve in water ASTM C595 [44] (according to Figure 1).



Fig. 1. Adding water to bentonite and preparation for making concrete



Fig. 2. A sample of sand in order to measure the moisture content of the materials

To prepare the mix design, the moisture content of the aggregates was determined by oven-drying the samples to a constant weight. Based on the measured moisture content, the mix proportions for the concrete were adjusted to ensure the aggregates were in a saturated surface dry (SSD) condition. Figure 2 illustrates the moisture level of the aggregate samples subjected to this process. For sample preparation, sand was initially introduced into the mixer, followed by gravel. The aggregates were mixed for approximately two minutes to ensure homogeneity. Cement was then gradually added to the mixer, allowing it to integrate thoroughly with the aggregates. Before

introducing water and bentonite, the mixture was manually stirred using a rod to achieve preliminary uniformity. The water and bentonite were then slowly poured into the mixer while it was in operation. In the final step, carbon was carefully added to the mix to prevent clumping and ensure even dispersion. The angle of the mixer's stirrer significantly influenced the uniform distribution of the aggregates, directly affecting the homogeneity of the concrete. Due to variations in the flow rate of concrete across different mixtures, adjustments were made to the stirrer angle to optimize the mixing process and achieve a consistent and evenly blended concrete mix.



(a) (b)

Fig 3. (a) Adding water, bentonite and carbon to concrete and (b) molding samples with concrete

The method of making, and the time of composition and mixing were tried as much as possible to be done in the same way for all the current research projects. The arrangements considered in the research include the same operators performing the tests, making concrete in a short time, the same sand, the same moisture content of the materials, and the same mixing time of the concrete in the mixer are some of these factors.

4. Slump Test Results and Appearance Characteristics of The Samples

The slump test results conducted during the preparation of each series are presented in Table 7. This study demonstrated that at a constant water-to-cement (w/c) ratio, increasing the cement content significantly raises the viscosity of the concrete, transforming it into a slurry-like consistency. Conversely, an increase in bentonite content at a fixed w/c ratio enhanced the fluidity of the mix, leading to a corresponding increase in the slump of the fresh concrete. When comparing the results of carbon-free plastic concrete at a cement dosage of 100 kg/m^3, the inclusion of carbon was found to reduce the slump, whereas at higher cement contents, its influence was comparable to that observed under carbon-free conditions. The increased fluidity of the concrete mix occasionally resulted in segregation of the aggregate components during placement into the sampling molds. This segregation effect is likely to negatively impact the compressive strength of the concrete as specified in ASTM C143 [45].

Figure 4 illustrates representative slump measurements obtained during the experiments conducted in this study. Farajpour [10], in his research on plastic concrete without carbon, observed that slump effectiveness and slump loss were more pronounced compared to plastic concrete containing carbon. He attributed this to the lower adhesion between cement particles and aggregates in the absence of carbon. Similarly, Rafiq [40] investigated the slump behavior of plastic concrete with and without carbon and found that the addition of carbon significantly reduced the slump. This reduction was linked to the surface characteristics and strong water-absorbing properties of carbon, which decrease the amount of free water in the mixture.

Table 7. Slump measurement results of samples of this research

Naming each design	W/C	(%)Carbon	Bentonite (Kg/m^3)	Cement (Kg/m^3)	Water (Kg/m^3)	(cm) Slump
PC-1	0.5	5	30	100	250	19.5
PC-2	0.5	10	30	100	250	19
PC-3	0.5	15	30	100	250	22
PC-4	0.5	20	30	100	250	17
PC-5	0.5	5	30	150	250	slurry
PC-6	0.5	10	30	150	250	25
PC-7	0.5	15	30	150	250	slurry
PC-8	0.5	20	30	150	250	slurry
PC-9	0.5	5	30	200	250	slurry
PC-10	0.5	10	30	200	250	slurry
PC-11	0.5	15	30	200	250	slurry
PC-12	0.5	20	30	200	250	slurry
PC-13	0.5	5	60	100	250	24
PC-14	0.5	10	60	100	250	25
PC-15	0.5	15	60	100	250	24.5
PC-16	0.5	20	60	100	250	25
PC-17	0.5	5	60	150	250	25
PC-18	0.5	10	60	150	250	21.5
PC-19	0.5	15	60	150	250	26.5
PC-20	0.5	20	60	150	250	27
PC-21	0.5	5	60	200	250	slurry
PC-22	0.5	10	60	200	250	29
PC-23	0.5	15	60	200	250	28.5
PC-24	0.5	20	60	200	250	slurry

Carbon additives, by partially absorbing the mixing water, limit the lubricating effect within the concrete, resulting in a stiffer mixture with reduced slump. The incorporation of carbon with a high specific surface area amplifies this effect, as the larger surface area enhances water absorption and subsequently reduces fluidity. Conversely, plastic concrete without carbon admixtures demonstrated higher slump values, indicating superior fluidity and workability in its fresh state. This increased slump is attributed to the unrestricted movement of water throughout the mixture in the absence of carbon, allowing for greater flowability and easier handling.



Fig 4. Slump test: (a) flowability of plastic concrete with carbon, (b) height difference of plastic concrete with slump, (c) determination of slump of plastic concrete with carbon and (d) efficiency and fluidity of plastic concrete with carbon on a flat plate

Table 8. Measured Weight of Fresh Concrete and Observational Insights During Sample Preparation

Naming each design	(%) Carbon	Minimum weight of fresh concrete is 2 (kg)	Weight of the most fresh concrete is 2 (kg)	segregation of aggregates	surface bleeding
PC-1	5	5.730	5.810	Average	Average
PC-2	10	5.9	5.960	Average	Average
PC-3	15	5.740	5.770	Average	Low
PC-4	20	5.890	5.920	Average	Average
PC-5	5	5.770	5.850	A lot	Intense
PC-6	10	5.850	5.920	Very Little	Intense
PC-7	15	5.820	5.870	A lot	Intense
PC-8	20	5.610	5.680	A lot	Intense
PC-9	5	5.590	5.598	A lot	Intense
PC-10	10	5.880	5.920	A lot	Intense
PC-11	15	5.855	5.870	A lot	Intense
PC-12	20	4.950	5.370	A lot	Intense
PC-13	5	5.815	5.830	Average	Average
PC-14	10	5.840	5.880	Weak	Have not
PC-15	15	5.680	5.750	Average	low
PC-16	20	5.560	5.660	Average	low
PC-17	5	5.680	5.710	Very Little	low
PC-18	10	5.590	5.620	Very Little	Average
PC-19	15	5.470	5.690	Very Weak	low
PC-20	20	5.570	5.610	Very Weak	low
PC-21	5	5.670	5.790	Too much	Intense
PC-22	10	5.550	5.560	Very Weak	Low
PC-23	15	5.760	5.8	Very Weak	Low
PC-24	20	5.520	5.610	Too much	Intense

These properties are particularly advantageous for concrete mixtures requiring enhanced workability. The addition of carbon may improve the compressive strength of hardened concrete; however, the reduction in slump and increased stiffness of fresh concrete necessitate the optimization of the water-cement ratio, along with the use of superplasticizing admixtures, to achieve a balanced performance between fresh and hardened properties of plastic concrete. In this study, the weight of fresh concrete was measured using two identical containers, as shown in Table 8. The table also includes other characteristics, such as surface water absorption and grain separation during the molding of the samples. Based on the results presented in Table 8, it is observed that increasing the cement content in mixtures with 30 kg of bentonite leads to higher water absorption and increased grain separation. Notably, the addition of carbon does not influence these characteristics. On the contrary, increasing the bentonite content from 30 to 60 kg reduces the surface water absorption and minimizes grain separation.

5. Appearance of Concrete After Initial Setting

The incorporation of bentonite in the concrete mixture significantly delays the setting time of the samples, resulting in a later setting period. During sample preparation, due to the soft nature of the concrete after 48 hours, the setting time was extended to 72 hours, as per ASTM C1602 [46]. Moreover, in the designs exhibiting significant slump, a sharp decrease in concrete level was observed. The drop in the surface level of fresh concrete is directly correlated with the amount of slurry present in the mixture.

6. Choosing Optimal Conditions for Processing Samples

In similar conditions for processing plastic concrete samples, based on ASTM C31 standard [47], the method of wetting the surface with coating was chosen and the resistance of concrete in wet coating conditions increases according to the standard and research precedent in this field, and from this processing method used for the samples of the present research.

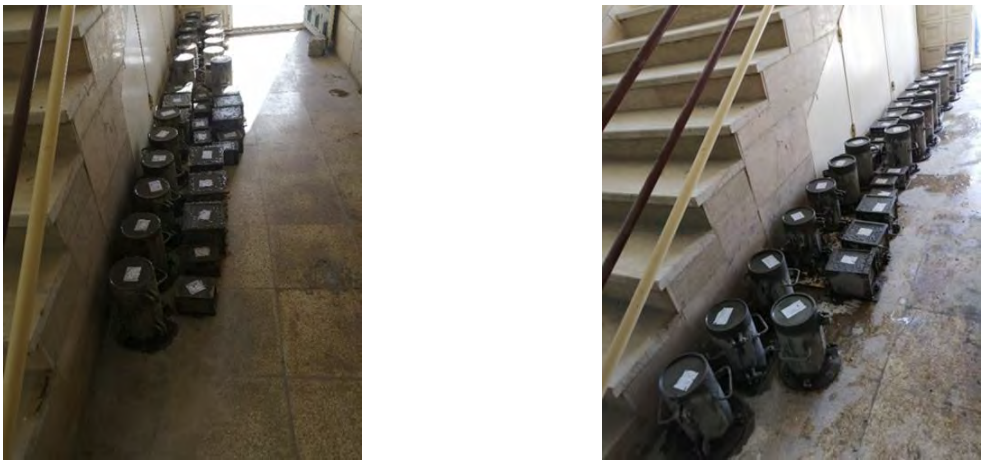


Fig. 7. (a) Fresh concrete in a cylindrical mold, (b) Putting fresh concrete in the mold



Fig. 8. Processing samples with a wet cover in the concrete laboratory

The samples of the present research were kept at room temperature after being placed in the molds to protect them from wind conditions and temperature changes during the time of placement in the sample molds (according to Figure 7). The duration of placing the samples was 24 hours ASTM C31 [47]. After being separated from the mold with wet coating, the samples were processed in the concrete laboratory, which has a wet environment, and a part of it is shown in Figure 8.

7. Failure of Samples

The compressive strength of both cylindrical and cubic concrete samples was evaluated in accordance with the standard PART116: BS1881, with a 15 cm diameter for cylindrical samples and 15 cm dimensions for cubic samples, after 28 days of curing, as specified by ASTM C39 [48]. To calculate the elastic modulus for various concrete designs, the Universal testing machine was employed, with the compressive strength measurements serving as the basis, as shown in Figure 9, following ASTM C78 [49]. In the modulus of elasticity and compressive strength tests using the Universal testing device, it was observed that for plastic concrete incorporating carbon, the combination of carbon particles within the cement matrix induces slight deviations in the initial linear stress-strain curve. These deviations are attributed to phenomena such as interparticle sliding and deformation mechanisms occurring at the nanoscale. Carbon particles play a critical role in the uniform distribution of stress across the sample. Their high strength contributes to a more even stress distribution, preventing localized stress concentrations, which in turn enhances the modulus of elasticity. This effect can be further analyzed through microscopic examination of strain and fracture mechanics. In the plastic deformation region, increased loading leads to the propagation and bridging of microscopic cracks within the concrete matrix. However, in samples containing carbon, the carbon particles act as inhibitors of crack growth. This retarding effect is

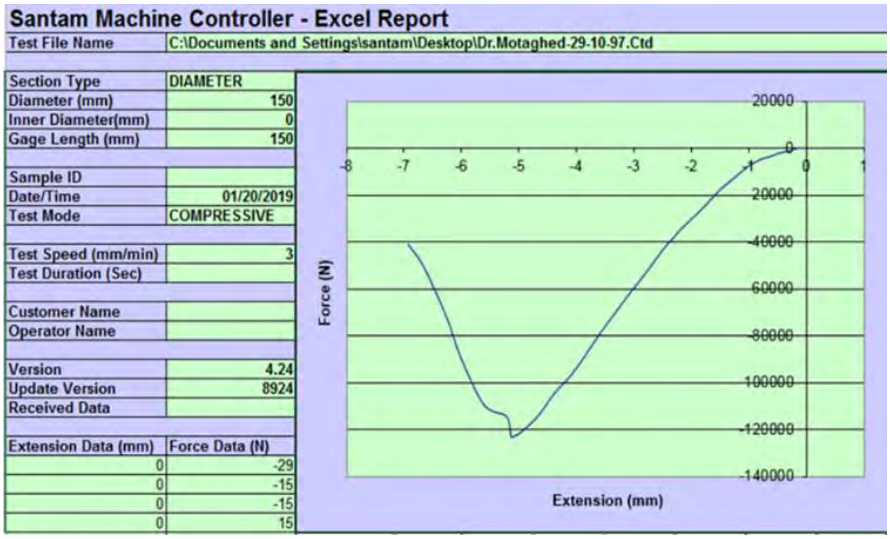
due to the high resistance of carbon particles and their ability to absorb fracture energy, thereby enhancing the toughness of the concrete through energy-dissipation mechanisms.



Fig. 9. Example under universal device

Plastic concrete with carbon has a greater tendency to fail in shear paths than a completely vertical and brittle failure. Due to the fact that carbon can be distributed homogeneously or in the form of small groups (agglomerates) in concrete, the place of crack growth in this concrete will be different. In plastic concretes, it is possible for cracks to accumulate around these particles or interparticle contact surfaces. In plastic concrete with carbon, the failure behavior is heterogeneous due to the presence of carbon particles; In the sense that the failure proceeds in a more localized and controlled manner. As the loading increases, it can be observed that the finer cracks spread throughout the specimen and connect to each other, and eventually total failure occurs. This process leads to a type of pseudo-plastic behavior in concrete failure, which is called pseudo-ductile failure. The final strength of plastic concrete with carbon is related to the nanoscale and microscopic effects of carbon particles in the cement matrix. In tests, these materials using a universal device can show characteristics such as higher compressive strength and gradual changes in fracture. In this way, plastic concrete containing carbon has less tendency to brittle failure and instead, it faces discontinuous and gradual failure, which is caused by better adhesion of particles and reduction of stress concentration.

For a more accurate evaluation, it is particularly important to use a universal device to record strain-stress changes at high levels and electron microscope images to examine the cracked areas. Also, tools such as digital image analysis (Digital Image Correlation) can accurately show surface strain distribution. In the Universal testing device, both the stress-strain diagram and force-displacement curve are generated simultaneously. Using the output data from this device, the maximum stress and strain values are calculated, as illustrated in Figure 9. The Universal device produces a curve representing the variations in force and displacement, an example of which for a cylindrical sample is shown in Figure 10, following ASTM C39 [48]. For evaluating the permeability of plastic concrete, cubic specimens with dimensions of 15×15×15 cm were used. This test is essential to assess the concrete's resistance to water, ions, sulfates, and its overall durability, which is crucial for its long-term performance under environmental exposure, as per ASTM C78 [49]. Permeability is a critical factor in the durability of concrete, influencing its resistance to progressive degradation due to water penetration, particularly when exposed to aggressive gases or dissolved minerals. The permeability of concrete, including its susceptibility to water infiltration and corrosion caused by carbonation, is one of the key determinants of concrete's durability. In this study, permeability tests were conducted on both cubic and cylindrical specimens subjected to 5 bar hydrostatic pressure, in accordance with established standards. Environmental conditions, including air pressure and temperature, were maintained at 25°C during the 72-hour testing period. The permeability coefficient was then calculated, as depicted in Figure 11.



Santam Machine Controller - Excel Report

Test File Name	C:\Documents and Settings\santam\Desktop\Dr.Motaghed-29-10-97.Ctd
Section Type	DIAMETER
Diameter (mm)	150
Inner Diameter(mm)	0
Gage Length (mm)	150
Sample ID	
Date/Time	01/20/2019
Test Mode	COMPRESSIVE
Test Speed (mm/min)	3
Test Duration (Sec)	
Customer Name	
Operator Name	
Version	4.24
Update Version	8924
Received Data	

Extension Data (mm)	Force Data (N)
0	-29
0	-15
0	-15
0	15

Fig. 10. The output diagram of the sample in the universal device



Fig. 11. Concrete permeability device

8. Summary, and Analysis of Data

Carbon-based materials, including carbon nanoparticles, carbon nanotubes (CNTs), and graphene, significantly influence the mechanical properties of plastic concrete. These materials enhance concrete performance due to their exceptional characteristics, such as high strength, elevated Young's modulus, and superior thermal and electrical conductivity. The experimental findings demonstrated that the plastic concrete produced in this study is approximately 15 times softer than conventional concrete. Furthermore, an increase in the bentonite content within the plastic concrete mixture resulted in a higher softening modulus. Additionally, as the water-to-cement ratio increased, a reduction in the concrete's resistance was observed, accompanied by an increase in the modulus of concrete softening. This softening modulus is a critical parameter, particularly with respect to the permeability of plastic concrete. The data corresponding to a water-to-cement ratio of 0.5, which was consistently applied in this research, are presented in Table 9. The analysis of compressive strength reveals that plastic concretes exhibit heterogeneous distributions of carbon particles, with variations in their density and dispersion. Carbon particles, owing to their intrinsic strength and stiffness, are capable of resisting local deformations; however, this resistance is contingent upon both the dispersion of the particles and the bond formation between the carbon particles and the cement matrix. For samples demonstrating higher compressive strength (e.g., PC-14 and PC-17), it is likely that a stronger interface bond between the carbon particles and the cement matrix is formed, resulting in a more uniform distribution of carbon particles throughout the matrix, which consequently enhances compressive strength.

Table 9. Results of failure of cylindrical concrete samples

Mixing plan	Compressive strength (MPa)	Displacement equivalent to maximum force (mm)	Displacement corresponds to 0.45 max (mm)
PC-1	2.718	3.85	1.48
PC-2	3.121	3.63	1.72
PC-3	2.639	5.6	3.56
PC-4	3.301	5.1	2.7
PC-5	2.519	3.22	1.41
PC-6	1.586	2.6	1.16
PC-7	2.418	3.48	1.33
PC-8	2.492	2.86	2.62
PC-9	3.107	3.33	1.36
PC-10	1.843	5.8	2.7
PC-11	2.270	4.8	1.45
PC-12	3.108	4.51	1.97
PC-13	3.592	6.47	3.63
PC-14	3.980	4.89	2.3
PC-15	1.901	4.81	0.26
PC-16	3.927	4.56	2.47
PC-17	3.839	8.41	4.66
PC-18	2.842	3.15	1.27
PC-19	2.263	3.81	1.77
PC-20	2.183	2.63	1.18
PC-21	2.266	3.42	1.01
PC-22	2.394	2.9	1.1
PC-23	2.328	4.03	1.39
PC-24	1.922	2.45	0.96

The transition zones between the carbon particles and the cement matrix are particularly susceptible to stress concentration. In samples exhibiting greater softness and mobility (such as PC-17), these regions effectively withstand higher stresses without failure, owing to the improved distribution and uniform transfer of stress between the carbon and cement phases. The larger displacements observed at maximum force indicate a softer behavior and a more gradual failure of the concrete, a phenomenon attributed to the energy-absorbing properties of the carbon particles and their contribution to increased flexibility in the fracture zone. For samples such as PC-13 and PC-17, which exhibit higher equivalent displacements, it can be inferred that the incorporation of carbon particles in the concrete improves its plastic deformation capacity, thereby reducing stress concentrations and intensities at the failure point. This behavior in concretes that have a soft failure behavior is usually associated with small and controlled failures in the entire structure, and therefore they do not suffer brittle failure. In plastic concretes, softness can vary due to density, size and shape of carbon particles. For specimens with lower displacements, such as PC-6 and PC-20, the carbon particles may not be effectively distributed and stress concentration at certain points leads to rapid and brittle failure. In this case, the fracture area is limited and brittle. Displacement values equivalent to 0.45 times the maximum force indicate the tolerance of the sample in initial deformations. Samples such as PC-17 and PC-13, which have higher displacements, show greater flexibility against initial stresses and can absorb more energy in the inelastic region. This behavior somehow has the property of increasing the resistance to crack propagation, which is also known as "property of preventing crack propagation". More stainability in this area most likely indicates more effective connection between carbon particles and reduction of stress concentration along the matrix.

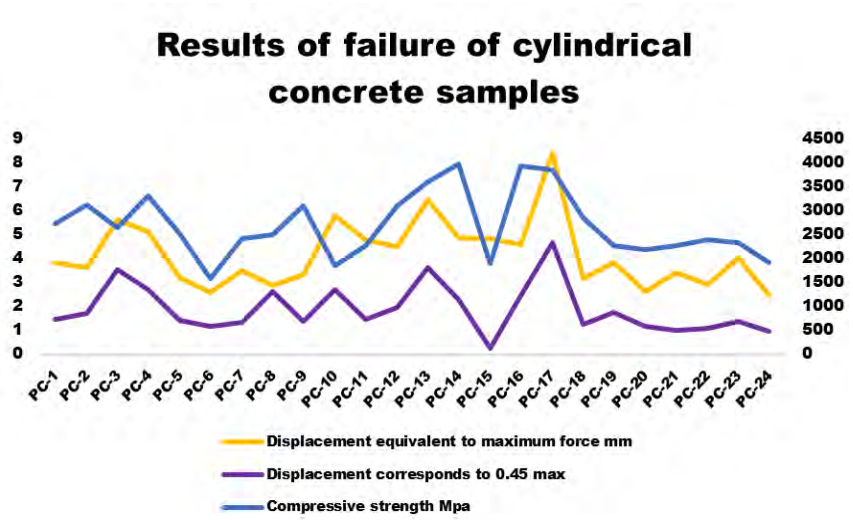


Fig. 12. Compressive strength results obtained from the failure of cylindrical plastic concrete samples

Table 10. Results of failure modulus of elasticity of cylindrical concrete samples

Mixing plan	Maximum force 0.45max (kg)	Ultimate modulus of elasticity (kg)
PC-1	21600	292447
PC-2	24800	404574
PC-3	20977	249576
PC-4	26235	254694
PC-5	20024	295834
PC-6	12607	400095
PC-7	19216	315452
PC-8	19805	335240
PC-9	24692	363154
PC-10	14647	317753
PC-11	18037	336409
PC-12	24705	213198
PC-13	28546	210993
PC-14	31632	291872
PC-15	15111	824787
PC-16	31208	214794
PC-17	30513	196486
PC-18	22586	424147
PC-19	17984	303940
PC-20	17375	407902
PC-21	18011	303160
PC-22	19030	230839
PC-23	18501	255709
PC-24	15276	288558

In these samples, the matrix structure acts with carbon distribution to make microscopic cracks more dispersed and crack propagation more controlled in the early stages of loading. Samples such as PC-17 and PC-13, which have higher ductility, have a better distribution of carbon particles in the cement structure and the ability to absorb energy, more effectively distributing stresses throughout the sample. In this situation, instead of sudden failure, a controlled and gradual failure occurs, which is a valuable feature in earthquake-resistant building applications. Samples with lower displacement and ductility (such as PC-6 and PC-20) behave more brittlely against loading. In these samples, stress concentration at certain points is probably due to non-uniform distribution

of carbon particles, which leads to rapid and inefficient failure. This brittle behavior in concrete is usually associated with severe and sudden failures, which can be dangerous for structures. According to the obtained data, it can be concluded that the optimal composition and distribution of carbon particles in the cement matrix can have a significant effect on the softness and final strength of concrete. To achieve optimal mechanical behavior, using methods such as optimization of composition ratios, and advanced carbon dispersion processes can help reduce stress concentration and increase concrete strength.

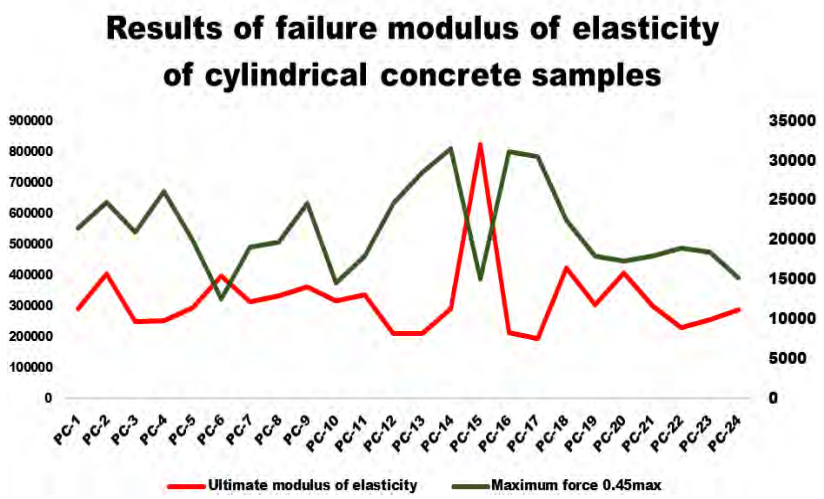


Fig. 13. Results of modulus of elasticity obtained from the failure of cylindrical plastic concrete samples

The analysis of the data presented in Table 10 indicates a direct relationship between the final modulus of elasticity and the force equivalent to 0.45 times the maximum force in carbon-reinforced concrete samples, with the samples' softness and failure behavior. For samples exhibiting a high modulus of elasticity, such as PC-15 and PC-18, significant elastic resistance is observed. This resistance correlates with an increased load-bearing capacity, which helps prevent stress concentration and sudden crack formation. These samples demonstrate enhanced energy absorption due to their higher softness under load, leading to a gradual and controlled failure behavior. This suggests a more effective distribution of carbon particles and a stronger bond between the carbon phase and the cement matrix. In contrast, samples with lower values of elastic modulus, such as PC-13 and PC-17, exhibit a greater tendency toward brittle failure. This behavior can likely be attributed to an uneven distribution of carbon particles or insufficient bonding between the carbon particles and the matrix, which increases stress concentration at specific points and reduces the overall elastic capacity of the samples. For instance, samples PC-12 and PC-13, which exhibit lower ultimate modulus values, likely suffer from poor dispersion of carbon particles. Consequently, stress concentrations in localized regions promote faster failure. Additionally, samples with high equivalent forces, such as PC-15, which reaches 824,787 kg, show greater flexibility and are capable of withstanding larger elastic deformations. This enhanced behavior is likely due to the uniform dispersion of carbon particles in the cement matrix, which contributes to the formation of a continuous structure in the transition zone. In these samples, stress is more uniformly distributed across the material, leading to a gradual failure rather than an abrupt fracture. Samples exhibiting higher values of modulus of elasticity and equivalent force demonstrate softer properties, which correlate with better resistance to dynamic and cyclic loading conditions. To optimize the mechanical performance of carbon-reinforced concrete, controlling the distribution of carbon particles and enhancing the bond between the carbon phase and the cement matrix is essential. This approach helps reduce stress concentrations, improving both the softness and strength of the concrete.

Table 11. Compressive strength failure results of cubic plastic concrete samples

Mixing plan	Compressive strength (MPa)	Displacement equivalent to maximum force (mm)	Displacement corresponds to 0.45 max (mm)
PC-1	2.78	6.19	2.43
PC-2	3.74	5.75	2.93
PC-3	3	4.33	1.69
PC-4	4	3.73	1.22
PC-5	3.74	3.16	1.02
PC-6	2.98	8.28	3.9
PC-7	2.85	4.59	1.84
PC-8	2.87	9.3	5.57
PC-9	2.88	6.57	3.03
PC-10	2.71	7.38	4.16
PC-11	3	5.04	2.14
PC-12	3.46	3.1	1.04
PC-13	4.31	4.45	1.75
PC-14	5.22	4.07	1.98
PC-15	1.52	3.62	1.38
PC-16	1.46	3.05	1
PC-17	3.42	4.22	1.45
PC-18	3.75	4.85	1.97
PC-19	2.98	3.6	1.15
PC-20	2.8	3.9	1.28
PC-21	2.46	5.09	1.16
PC-22	2.83	3.55	1.23
PC-23	2.17	3.3	1.27
PC-24	2.2	3.35	0.82

Samples with high compressive strength such as PC-14 (5.22 MPa), and PC-13 (4.31 MPa) are much harder and more resistant due to stronger connection, and better distribution of carbon particles within the cement matrix. These samples with less equivalent displacement at maximum force (4.07 mm and 4.45 mm, respectively), show a more quasi-elastic behavior and show a greater ability to resist compressive loads. In this way, the carbon particles in these samples act as reinforcing elements and by improving the connection in the transition zone (ITZ), they increase the hardness and reduce the stress concentration. Samples with higher displacement (such as PC-8 with 9.3 mm displacement and PC-10 with 7.38 mm displacement) exhibit more softness and have a softer recoil behavior, which could be due to a more uniform distribution of carbon particles. Such a distribution allows the cement matrix to absorb and release energy more effectively, enabling gradual failure. This behavior, which is also known as pseudo-plastic or pseudo-ductile behavior, helps to increase the durability and flexibility of the structure, especially under dynamic loading conditions. Some samples, such as PC-5 and PC-16, have a lower displacement at the time of reaching the maximum force and at a displacement equivalent to 0.45 of the maximum force, which indicates a decrease in ductility and brittle behavior at failure. This behavior probably occurs due to the irregular density or defects in the distribution of carbon particles, which leads to stress concentration in certain areas and leads to rapid and uncontrollable failure. In these samples, the inefficient connection between the carbon particles and the cement matrix causes a decrease in cohesion and, as a result, a decrease in resistance to compressive loads. Samples with higher displacements at the moment of failure, such as PC-6 and PC-8, show pseudo-ductile behavior and higher deformation capacity. This soft and discontinuous behavior is due to the optimal presence of carbon particles and the creation of an efficient energy absorption system in the fracture zone. This phenomenon is linked to a reduction in stress concentration and an enhancement in stress transfer between the carbon particles and the cement matrix, allowing the samples to undergo more deformation prior to ultimate failure.

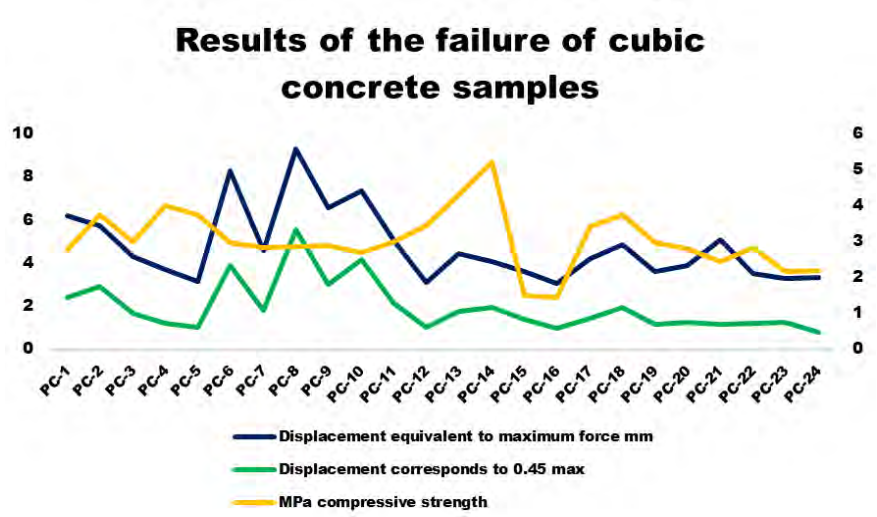


Fig. 14. Compressive strength failure results of cubic plastic concrete samples

Table 12. Results of the failure of cubic concrete samples

Mixing plan	Ultimate modulus of elasticity (kg)	Maximum force 0.45max (kg)
PC-1	1260519	28166
PC-2	1478937	37869
PC-3	1538480	34499
PC-4	3393060	41577
PC-5	3718902	37916
PC-6	923670	30181
PC-7	1227798	28973
PC-8	401759	29036
PC-9	928118	29109
PC-10	475064	27433
PC-11	938395	30426
PC-12	3170617	35068
PC-13	2911800	43677
PC-14	2878082	52729
PC-15	1072357	15435
PC-16	1627213	14792
PC-17	1771179	34618
PC-18	1459237	38028
PC-19	2167131	30208
PC-20	1614400	28374
PC-21	2417842	24911
PC-22	1539571	28692
PC-23	1935622	21944
PC-24	2070789	22328

The optimal distribution and density of carbon particles are critical factors in enhancing the mechanical properties of plastic concrete. In samples with well-distributed carbon particles and a strong bond between the carbon phase and the cement matrix, high compressive strength and pseudo-ductile behavior are achieved. This leads to a substantial improvement in the durability of the structure, particularly in its resistance to sudden and dynamic loading conditions. Conversely, samples with poor distribution and low density of carbon particles exhibit a tendency for brittle and abrupt failure, representing structural vulnerabilities from an engineering perspective.

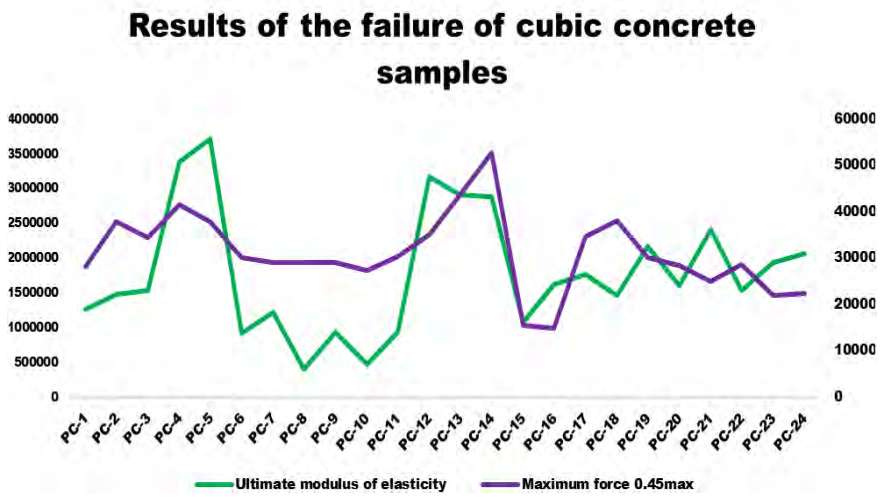


Fig. 15. Results obtained from the failure of cubic plastic concrete samples

The PC-4 and PC-5 samples, exhibiting the highest breaking forces (41,577 kg and 37,916 kg, respectively) and higher moduli of elasticity (3,393,060 kg and 3,718,902 kg, respectively), demonstrate exceptional performance under compressive loads. This performance reflects a well-balanced combination of material properties and an optimized concrete mix design. In contrast, the PC-15 and PC-16 samples, with the lowest breaking forces (15,435 kg and 14,792 kg, respectively) and moduli of elasticity (1,072,357 kg and 1,627,213 kg, respectively), display brittle and softer behaviors. These samples may exhibit brittle failure under load due to the non-uniform distribution of carbon particles and instability in the transition zones (ITZ). The lack of an effective bond between the carbon particles and the cement matrix causes localized stress concentrations, leading to rapid and abrupt failure. In contrast, specimens with a well-balanced mix design, such as PC-12 and PC-13, which possess moderate values for both the modulus of elasticity and breaking force (3,170,617 kg and 2,911,800 kg, respectively), exhibit an optimal balance between softness and strength. Due to the appropriate distribution of carbon particles and a strong bond with the cement matrix, these samples exhibit enhanced energy absorption capacity and can withstand higher stresses without experiencing sudden failure. The ITZ regions between the carbon particles and the cement matrix play a critical role in resisting local deformations and load variations. When these regions are properly designed with a more uniform distribution of carbon particles, the concrete demonstrates improved resistance to stress concentration and deformation. In the PC-4 and PC-5 samples, it is likely that the ITZ zones possess superior mechanical properties, contributing to the overall improved performance of the concrete under compressive loads. Energy absorption and failure behavior are closely linked to both softness and modulus of elasticity. Samples with higher moduli of elasticity generally exhibit better elastic behavior, offering greater resistance to compressive loads. This enhanced behavior allows microscopic cracks to propagate more evenly under load, preventing rapid failure. Conversely, samples with lower moduli of elasticity, such as PC-10 and PC-8, tend to fail more quickly due to insufficient energy absorption and localized stress concentrations. The data also indicate that increasing the carbon content from 5% to 10% (as seen in PC-1 and PC-2) leads to a notable increase in the modulus of elasticity (from 277.1 to 304.14 GPa). This improvement can be attributed to enhanced cohesion between the concrete grains and the carbon particles, resulting in superior mechanical properties. However, with a further increase in carbon content to 15% (in PC-3), the modulus of elasticity decreases to 200.65 GPa, possibly due to the saturation point being reached, which may disrupt the cohesion and negatively impact the overall mechanical properties. The observed reduction in the modulus of elasticity suggests that excessive incorporation of carbon into the concrete mix may adversely affect the structural integrity of the material. This negative impact is likely due to the over-accumulation of carbon particles, leading to discontinuities and weak points within the cement matrix.

Table 13. Average Values of the Elastic Modulus for the Cylindrical Samples in the Current Study

Mixing plan	(%) Carbon	(Kg) Bentonite	(Kg) cement	(cm) Slump	Modulus of elasticity (GPa)
PC-1	5	30	100	19.5	277.1
PC-2	10	30	100	19	304.14
PC-3	15	30	100	22	200.65
PC-4	20	30	100	17	229.1
PC-5	5	30	150	slurry	193
PC-6	10	30	150	25	201.28
PC-7	15	30	150	slurry	232.31
PC-8	20	30	150	slurry	306.94
PC-9	5	30	200	slurry	333.71
PC-10	10	30	200	slurry	196.52
PC-11	15	30	200	slurry	186.93
PC-12	20	30	200	slurry	213.19
PC-13	5	60	100	24	210
PC-14	10	60	100	25	202.28
PC-15	15	60	100	24.5	108.16
PC-16	20	60	100	25	138.21
PC-17	5	60	150	25	143.93
PC-18	10	60	150	21.5	157.14
PC-19	15	60	150	26.5	230.81
PC-20	20	60	150	27	226.96
PC-21	5	60	200	slurry	237.35
PC-22	10	60	200	29	234.97
PC-23	15	60	200	28.5	236.60
PC-24	20	60	200	slurry	278.6

Bentonite, as a modifier, can significantly influence the mechanical properties of concrete. When 30 kg of bentonite was added to the mix, as in samples PC-1 and PC-2, the modulus of elasticity was enhanced. For instance, sample PC-9, containing 20% carbon and 20 kg of bentonite, exhibited a modulus of elasticity of 333.71 GPa, highlighting the beneficial role of bentonite in improving cohesion and strengthening the overall mechanical properties of the concrete. The softness of the concrete mix has a direct impact on its mechanical behavior. Concrete in the "slurry" state, such as PC-10 and PC-15, tends to exhibit lower modulus of elasticity values (e.g., 108.16 GPa), suggesting that an increase in softness creates more space between particles, thereby reducing the material's resistance to applied loads. These findings emphasize the importance of mix design in achieving desired mechanical properties. For example, PC-8, which contains 20 kg of bentonite and 5% carbon, demonstrates a higher modulus of elasticity (306.94 GPa), suggesting that optimizing material proportions can yield a notable improvement in concrete performance. In terms of permeability, samples with higher carbon content (e.g., PC-8 and PC-9) typically exhibited increased permeability. This may result from the non-uniform dispersion of carbon particles within the matrix, as well as the creation of voids and pore channels within the concrete structure. Conversely, samples with lower carbon content (such as PC-1 and PC-2) demonstrated reduced permeability, indicating a more uniform particle distribution and smaller, fewer pore spaces. Variations in the proportion of cement and bentonite in different mix designs can substantially affect the permeability. In the case of PC-5, the permeability was significantly elevated, likely due to the higher proportion of bentonite in the mix. As a water-absorbing material, bentonite influences the pore structure, and under increased load, the concrete's micro and macrostructure may undergo changes, leading to a rise in permeability.

Table 14. Permeability results of carbon-based plastic concrete

Mixing plan	Permeability (mm)
PC-1	4.8
PC-2	4.6
PC-3	5.1
PC-4	4.2
PC-5	10
PC-6	6
PC-7	10.2
PC-8	10.7
PC-9	11.2
PC-10	10.6
PC-11	10.2
PC-12	11.3
PC-13	6
PC-14	6.1
PC-15	5.9
PC-16	6.1
PC-17	6.2
PC-18	5.2
PC-19	7.5
PC-20	8
PC-21	11.2
PC-22	9
PC-23	8.3
PC-24	11

High-permeability samples (such as PC-12 and PC-21) are likely to have a weaker structure that increases the permeability of water and other fluids. The results show that there is an inverse relationship between softness and permeability. Samples that show higher displacement in compression tests (such as PC-8) usually have higher permeability. This means that when concrete is able to withstand more changes, its structure is likely to become more vulnerable to liquid penetration. Samples with less softness (such as PC-1) show better results in reducing permeability, which indicates greater strength and uniformity in the concrete matrix.

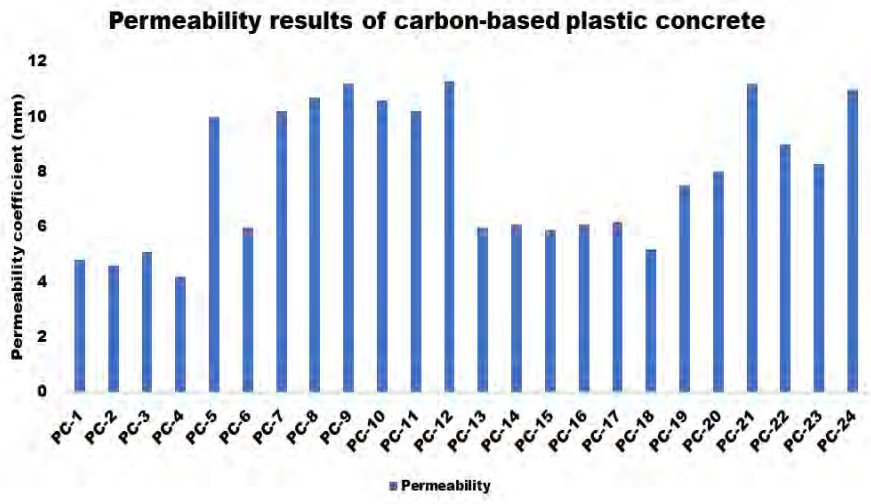


Fig. 16. Carbon-based plastic concrete permeability test results

9. Conclusion

This study investigates the impact of carbon as an additive on the properties of plastic concrete. Out of 24 mix designs, a fixed water-to-cement ratio of 0.5 was maintained, while varying the carbon content at 5%, 10%, 15%, and 20%. The results indicate that incorporating carbon into the plastic concrete mixture enhances its mechanical properties, particularly the adhesion between concrete particles, thereby improving its overall strength. By increasing the amount of cement for designs with 30 kg of bentonite, the amount of water absorption and separation of grains increases, and adding carbon for this part has no effect on these characteristics. On the other hand, by increasing the amount of bentonite from 30 to 60 kg, the level of water absorption on the concrete surface and the separation of grains decreases.

- Increasing the water-to-cement ratio enhances the fluidity of plastic concrete, similar to what is observed in conventional concrete. However, the increase in flow rate of plastic concrete is more pronounced compared to standard concrete due to the inclusion of bentonite.
- The addition of carbon to plastic concrete notably reduces its permeability. This reduction is attributed to the improvement in the microstructure and nanostructure of the concrete, which strengthens the network of cement hydrates.
- A thorough analysis of the test results reveals significant differences in the mechanical behavior of cylindrical and cubic plastic concrete samples under varying loads, particularly in terms of compressive strength, modulus of elasticity, and permeability. These differences are largely influenced by the proportions of carbon and bentonite within the mix.
- The compressive strength of cylindrical samples showed the highest value in sample PC-14 (3.98 MPa) and the lowest in sample PC-6 (1.586 MPa). This variation indicates that the changes in the mixture's components, particularly the carbon and bentonite content, have a considerable impact on strength. The observed percentage differences in compressive strength between cylindrical samples highlight the effective role of composite materials and varying percentages of additives in improving concrete's performance for specific applications.
- Displacement equivalent to the maximum force and displacement at 0.45 times the maximum force: The results show that the PC-17 sample exhibited the highest displacement at maximum force (8.41 mm), while the PC-6 sample showed the lowest (2.6 mm). These results underscore the impact of high carbon and bentonite content on the flexibility of concrete, enhancing its ability to withstand larger displacements.
- Ultimate modulus of elasticity: The highest modulus of elasticity was recorded in sample PC-15 (824,787 kg), while the lowest was in sample PC-12 (213,198 kg). This substantial difference in modulus values suggests significant structural and mechanical changes in the concrete under applied pressure. These variations affect the concrete's hardness and flexural strength, making the modulus of elasticity a crucial parameter in structural analysis and the design of specialized concrete applications.
- Compressive strength of cubic samples: Similar to the cylindrical samples, the cubic samples demonstrated varying behavior. The highest compressive strength (5.22 MPa) was found in sample PC-14, while the lowest value (1.52 MPa) was in sample PC-15. This indicates notable discrepancies in the distribution of force and strength across the cubic samples.
- Permeability of samples: The highest permeability was observed in sample PC-12 (11.3), and the lowest in sample PC-4 (4.2). The increase in permeability in certain samples is attributed to the structural characteristics and high carbon and bentonite content in the mixtures. These findings are critical for assessing the durability of concrete against environmental factors and for designing concrete for specific structures. Lower permeability generally correlates with improved resistance to environmental degradation and extended service life of the concrete.

The results derived from comparing the mechanical and physical properties of various plastic concrete samples demonstrate that an optimal combination of concrete mixture components, particularly the proportions of carbon and bentonite, significantly influences the material's strength, modulus of elasticity, and permeability. This study provides valuable insights for selecting the most suitable concrete mix, especially for designing structures that demand high strength and long-term durability. It serves as a reference for improving the performance of concrete in specialized applications where enhanced mechanical properties and environmental resistance are essential.

Table 15. Summary of Compressive Strength, Modulus of Elasticity, and Permeability Results for Cylindrical and Cubic Samples

Feature	Highest amount	Lowest amount
(Based on the findings presented in Table 9)		
Compressive strength of cylinder samples	PC-14 3.98 MPa	PC-6 1.586 MPa
Displacement equivalent to maximum force	PC-17 8.41 mm	PC-6 2.6 mm
Displacement corresponding to 0.45 max	PC-17 4.66 mm	PC-15 0.26 mm
(Based on the findings presented in Table 10)		
Ultimate modulus of elasticity of the cylindrical sample	PC-15 824787 kg	PC-12 213198 kg
Maximum force (0.45max)	PC-14 31632 kg	PC-6 12607 kg
(According to the results of Table 11)		
Compressive strength of cubic samples	PC-14 5.22 MPa	PC-15 1.52 MPa
Displacement equivalent to maximum force	PC-8 9.3 mm	PC-4 3.73 mm
Displacement corresponding to 0.45 max	PC-8 5.57 mm	PC-16 1 mm
(According to the results of Table 12)		
Ultimate modulus of elasticity of the cubic sample	PC-4 339306 kg	PC-10 475064 kg
Maximum force (0.45max)	PC-14 52729 kg	PC-15 15435 kg
(According to the results of Table 14)		
Permeability of cubic samples	PC-12 11.3	PC-4 4.2

References

[1] Mirzaie Aliabadi, M., Derakhshan Nezhad, A. H., Shahidzadeh, M. S., Dadpur, A. Date palm fibers to improve tensile strength in self-compacting concrete with silica fume. Civil Engineering Infrastructures Journal, 2024; . doi: 10.22059/ceij.2024.368987.1988.

[2] Asghari pari, S. A., Derakhshan nezhad, A. H., mirzaie Aliabadi, M. Investigating the effect of rust and iron shavings on the mechanical properties of self-compacting concrete. Journal of Structural and Construction Engineering, 2024; doi: 10.22065/jsce.2024.441467.3355.

[3] Derakhshan Nezhad, A. H., mirzaie Aliabadi, M., Shahidzade, M. S., Dadpour, A. Investigating the effect of date palm fibers on the mechanical properties of self-compacting concrete. Journal of Structural and Construction Engineering, 2024; doi: 10.22065/jsce.2024.441194.3351.

[4] Mirzaie Aliabadi, M., derakhshan nezhad, A. H., Mousavi Abdullah nezhad, S. A., Hitavi, A. Investigating the effect of heat transfer from the mold on the mechanical properties of self-compacting concrete with. Journal of Structural and Construction Engineering, 2024; 11(5): doi: 10.22065/jsce.2023.403066.3155.

[5] Derakhshan Nezhad, A. H., Mirzaie Aliabadi, M., Shahidzadeh, M. S. Laboratory investigation of the effect of plastic packaging belt fibers and iron oxide on the mechanical properties of self-compacting concrete. Amirkabir Journal of Civil Engineering, 2024; 56(5): 517-550. doi: 10.22060/ceej.2024.23070.8099.

[6] Mirzaie Aliabadi, M., Shahidzadeh, M. S., Piran shahi, H., Rashidi Fard, H., Derakhshan Nezhad, A. H. Comparison of the effect of crushed cement block and construction waste on fresh and hardened

properties of self-compacting concrete. Journal of Concrete Structures and Materials, 2024; 9(1): 1-19. doi: 10.30478/jcsm.2024.448781.1365.
[7] mirzaie Aliabadi, M., derakhshan nezhad, A. H. Laboratory investigation of the effect of recycled polyethylene terephthalate fibers on the mechanical properties of self-compacting concrete. Journal of Structural and Construction Engineering, 2024; 11(8): -. doi: 10.22065/jsce.2024.428815.3293.
[8] Rahimi Behod A. Investigating the optimal mixing plan of plastic concrete (based on the data of the Tabriz metro workshop) [master's thesis]. University of Tabriz; 2015.
[9] Reza Mohajeri Borj Qala, Ajam A. Investigation of the ratio of water to cement on the permeability of plastic concrete of dams' watertight walls. Proceedings of the Second National Conference on New Findings in Civil Engineering; 15-16 Azar 1391; Najaf Abad, Iran.
[10] Farajpour Z, Ghanbari T. Investigating plastic concrete waterproof walls of Silweh dam. Proceedings of the First International Conference on Impermeable Concrete for Drinking Water Storage Tanks; June 2019; Gilan, Iran.
[11] Fathi Naz M. Investigation of the effect of bentonite content and lateral pressure of soil on the properties of plastic concrete waterproofing wall [master's thesis]. Amirkabir University of Technology; 2018.
[12] Kiarostami R. Investigating the effect of magnetic water on the properties of fresh and hardened plastic concrete for use in dams' waterproof curtain [master's thesis]. Khatam Al Anbia Behbahan University of Technology; 2017.
[13] Namdar A. Natural minerals mixture for enhancing concrete compressive strength. Frattura ed Integrità Strutturale. 2012;22:26-30. https://doi.org/10.3221/IGF-ESIS.22.04
[14] Zhang P, Guan Q, Li Q. Mechanical properties of plastic concrete containing bentonite. Research Journal of Applied Sciences, Engineering and Technology. 2013;5(4):1317-1322. https://doi.org/10.19026/rjaset.5.4867
[15] ASTM C469. Standard Test Method for Static Modulus of Elasticity and Poisson's Ratio of Concrete in Compression. ASTM International; 2012.
[16] ICOLD (International Commission on Large Dams). Filling materials for watertight cutoff walls. Bulletin No. 51. Paris: ICOLD; 1985.
[17] Kazemian S, Ghareh S, Torkanloo L. Investigation of plastic concrete bentonite changes on its physical properties. Procedia Engineering. 2016;145:1080-1087. https://doi.org/10.1016/j.proeng.2016.04.140
[18] Mahboubi AT, Ajorloo AT. Experimental studies of the mechanical behavior of plastic concrete in triaxial composition. Cement and Concrete Research. 2005;35:412-419. https://doi.org/10.1016/j.cemconres.2004.09.011
[19] Pashang Pisheh Y, Mir Mohammad Hosseini M. Experimental investigation of mechanical behavior of plastic concrete in cutoff walls. Journal of Materials in Civil Engineering. 2018;31(1):04018355. https://doi.org/10.1061/(ASCE)MT.1943-5533.0002544
[20] Qiszheng W, Qingyon W, Jialiu P. Mechanical properties of plastic concrete and nonlinear structural analysis of plastic concrete cut-off wall. Journal of Computational Mechanics in Structural. 1992;273-285.
[21] Xanthakos W. MC Grow-Hill Book Company. New York; 1979.
[22] Zhang Y, Yin QZ. Carbon and other light element contents in the Earth's core based on first-principles molecular dynamics. Proceedings of the National Academy of Sciences USA. 2012;109:19579-19583. https://doi.org/10.1073/pnas.1203826109
[23] Allègre CJ, Poirier JP, Humler E, Hofmann AW. The chemical composition of the Earth. Earth and Planetary Science Letters. 1995;134:515-526. https://doi.org/10.1016/0012-821X(95)00123-T
[24] Pace NR. The universal nature of biochemistry. Proceedings of the National Academy of Sciences USA. 2001;98:805-808. https://doi.org/10.1073/pnas.98.3.805
[25] Stehlik M, Hermankova V, Vitek L. Journal of Civil Engineering and Management. 2015;21:177-184. https://doi.org/10.3846/13923730.2013.802721
[26] Holcapek O, Kotatkova K, Reiterman P. Advances in Civil Engineering. 2018:1-10. https://doi.org/10.1155/2018/3251523
[27] Foldyna J, Foldyna V, Zelenak M. Procedia Engineering. 2016;149:94-99. https://doi.org/10.1016/j.proeng.2016.06.643
[28] Jarolim T, Labaj M, Hela R, Michnova K. Advances in Materials Science and Engineering. 2016:1-6. https://doi.org/10.1155/2016/7508904
[29] Mirzaei Aliabadi M, Derakhshan Nezhad AH. Concrete structure quality control with Schmidt hammer method. Proceedings of the 5th International Conference and 6th National Conference on Civil Engineering, Architecture, Art and Urban Design; 2023.
[30] Mirzaei Aliabadi M, Derakhshan Nezhad AH. Health monitoring of concrete structure using ultrasonic. Proceedings of the 7th International Conference on Research in Science and Engineering and the 4th International Congress on Civil Engineering, Architecture and Urban Planning of Asia; 2023.

[31] Shahid Zadeh MS, Derakhshan Nezhad AH, Mirzaie Aliabadi M. Analyzing and examining the impact of various fiber types on the mechanical and functional characteristics of UHPC. Journal Research on Engineering Structures and Materials. 2024:1-26. http://dx.doi.org/10.17515/resm2024.367me0725rs.
[32] Yin W, Li X, Sun T, Wang J, Chen Y, Yan G. Experimental investigation on the mechanical and rheological properties of high-performance concrete (HPC) incorporating sinking bead. Construction and Building Materials. 2020;243:118293. https://doi.org/10.1016/j.conbuildmat.2020.118293
[33] Qaidi S, Al-Kamaki Y, Hakeem I, Dulaimi AF, Özkılıç Y, Sabri M, Sergeev V. Investigation of the physical-mechanical properties and durability of high-strength concrete with recycled PET as a partial replacement for fine aggregates. Frontiers in Materials. 2023;10. https://doi.org/10.3389/fmats.2023.1101146
[34] Zumba E, Velasco N, Melendres Medina EM, Buñay J, Estrada Brito NA. Correction: Forecasting the rheological state properties of self-compacting concrete mixes using the response surface methodology technique for sustainable structural concreting. PLOS ONE. 2024;19(7):e0307891. https://doi.org/10.1371/journal.pone.0307891
[35] Faraj RH, Hama Ali HF, Sherwani AFH, Hassan BR, Karim H. Use of recycled plastic in self-compacting concrete: A comprehensive review on fresh and mechanical properties. Journal of Building Engineering. 2020;30:101283. https://doi.org/10.1016/j.jobe.2020.101283
[36] Mohammed A, Rafiq S, Mahmood W, Noaman R, AL-Darkazali H, Ghafor K, Qadir W. Microstructure characterizations, thermal properties, yield stress, plastic viscosity, and compression strength of cement paste modified with nanosilica. Journal of Materials Research and Technology. 2020;9(5):10941-10956. https://doi.org/10.1016/j.jmrt.2020.07.083
[37] ASTM International. ASTM C150/C150M. Standard Specification for Portland Cement. 2012.
[38] ASTM International. ASTM C33. Standard Specification for Concrete Aggregates. 2003.
[39] ASTM International. ASTM C94. Standard Specification for Ready-Mixed Concrete. 2009.
[40] ASTM International. ASTM C595. Standard Specification for Blended Hydraulic Cements. 2022.
[41] ASTM International. ASTM C143/C143M. Standard Test Method for Slump of Hydraulic-Cement Concrete. 2021.
[42] ASTM International. ASTM C1602/C1602M. Standard Specification for Mixing Water Used in the Production of Hydraulic Cement Concrete. 2021.
[43] ASTM International. ASTM C31/C31M. Standard Practice for Making and Curing Concrete Test Specimens in the Field. 2021.
[44] ASTM International. ASTM C39/C39M. Standard Test Method for Compressive Strength of Cylindrical Concrete Specimens. 2021.
[45] ASTM International. ASTM C78/C78M. Standard Test Method for Flexural Strength of Concrete (Using Simple Beam with Third-Point Loading). 2021.
[45] ASTM International. (2021). ASTM C143/C143M - Standard Test Method for Slump of Hydraulic-Cement Concrete.
[46] ASTM International. (2021). ASTM C1602/C1602M - Standard Specification for Mixing Water Used in the Production of Hydraulic Cement Concrete.
[47] ASTM International. (2021). ASTM C31/C31M - Standard Practice for Making and Curing Concrete Test Specimens in the Fiel
[48]ASTM International. (2021). ASTM C39/C39M - Standard Test Method for Compressive Strength of Cylindrical Concrete Specimens.
[49] ASTM International. (2021). ASTM C78/C78M - Standard Test Method for Flexural Strength of Concrete (Using Simple Beam with Third-Point Loading).

Blank Page

Research on Engineering Structures & Materials
www.jresm.org

Research Article

Experimental investigation on the effect of varied injection timings in a CRDI diesel engine driven by a biodiesel-diesel blend

Sudarsanam Mark [1,2,a], Jayaprabakar Jayaraman [*,1,b]

[1]*Dept. of Mechanical Engineering, Sathyabama Institute of Science and Technology, Chennai, India*
[2]*Dept. of Mechanical Engineering, VEMU Institute of Technology, Chittoor, India*

Article Info

Article History:

Received 04 Sep 2024
Accepted 08 Dec 2024

Keywords:

Diesel engine;
Emission;
Performance;
Biodiesel;
Waste cooking oil;
Injection timing

Abstract

The issues with handling high viscosity biodiesel include noise and lack of smoothness in regular diesel engines. The use of Common Rail Direct Injection (CRDI) technology has the potential to significantly remove or reduce difficulties associated with biodiesel handling. In this study, the use of blends comprising waste cooking oil biodiesel was investigated in a CRDI diesel engine with injection timings ranging from 24° to 21° bTDC. For a diesel engine, injection timing is a critical element that influences engine performance, emissions, and durability. This study is the first to try combining the CRDI approach with varying injection timings for waste cooking oil biodiesel blends. The impact of varying injection timing has been assessed for blends of waste cooking oil (WCO) biodiesel fuels, specifically B20 (20% WCO+80% Diesel), and the results were compared to those of baseline mineral diesel fuel. During the experimental assessments, B20 demonstrated optimal performance at retarded injection timing of 22° bTDC (RT22), surpassing the standard injection timing of 23° bTDC. The optimum outcome revealed a 3.78% increase in Brake Thermal Efficiency for B20+RT22, accompanied by a 7.74% decrease in CO and a 3.15% reduction in NO_x emissions. Appropriate injection timing settings led to significant enhancements in both emissions and performance for WCO blends compared to the diesel fuel and standard injection timing. Moreover, this approach holds promise as a potential long-term solution to address the challenge of waste cooking oil disposal.

© 2025 MIM Research Group. All rights reserved.

1. Introduction

The escalating energy consumption attributed to rapid urbanization and industrialization has raised concerns about the depletion of fossil fuels and the detrimental emissions produced by engines, along with the management of waste cooking oil biodiesel (WCO). Despite extensive prior research on potential alternative fuels, there has been a recent shift towards investigating the conversion of waste into fuel. The main sources of waste cooking oil in India are the residential and commercial food sectors. The disposal of WCO contributes to a significant environmental hazard, and as of now, no effective method has been universally adopted for its management. Hence, the need for a feasible alternative fuel for Compression Ignition (CI) engines [1,2]. Among various energy alternatives explored, the adaptation of WCO into liquid fuel has gained substantial attention. CI engines have gained popularity owing to their commendable thermal efficiency. However, they release substantial amounts of nitrogen oxides (NO_x), carbon monoxide (CO), hydrocarbon (HC), and smoke, posing environmental and health concerns. Stringent emission regulations have been implemented in response to these issues [3]. Additionally, the escalating demand for energy and the generation of waste contributes to the depletion of natural resources,

*Corresponding author: jayaprabakar.mech@sathyabama.ac.in
[a]orcid.org/0009-0003-3013-9812; [b]orcid.org/0000-0003-3290-5771
DOI: http://dx.doi.org/10.17515/resm2024.433ma0904rs

exacerbating the diminishing petroleum reserves [4-7]. The use of biodiesel in CI engines significantly reduces the consumption of fossil fuels [8]. However, a primary drawback of biodiesel is its high viscosity, which can result in incomplete combustion during the premixed combustion stage, ultimately leading to lower brake thermal efficiency (BTE) [9]. Sonachalam et al. [10] analysed the effect of varying dual-fuel mode along with varying injection timing (IT) on the emissions and performance of a diesel engine. Experimental results revealed that the optimal configuration, the brake specific fuel consumption (BSFC) decreased by 7.3%, while BTE increased by 1.6% compared to mineral diesel. Emission wise, a 12.5%, 25.6% and 7.5% reductions in HC, CO and smoke respectively. Sonachalam et al. [11-12] have also investigated multi-walled carbon nanotubes, renowned for their high surface area and unique properties. These blends were subsequently tested in a diesel engine to assess their performance, emissions, and combustion characteristics. The implementation of advanced combustion technologies and optimization of fuel quantity significantly reduces traditional fossil fuel consumption and lowers emission levels.

Datla et al. [13] studied the engine performance with varying start of main IT by consuming neem oil biodiesel-diesel as fuel in variable geometry turbocharger stationary engine. Transesterification was done to convert raw neem oil to neem oil biodiesel. NB20 (20% Neem biodiesel + 80% diesel) was chosen for investigation. Injection cylinder pressure of 800 bar and 1700 rpm was maintained. The start of IT was varied between 2° and 10° before top dead centre (bTDC). HRR, engine cylinder pressure is higher for mineral diesel compared to NB20 fuel blend at altered IT. Exhaust NO_x emission for NB20 reduced. BSFC and BTE showed better improvement and were close to diesel. Finally, 10° bTDC start of main IT showed an improved 13% of BTE and reduced 21% of BSFC with a reduction in 7.5% of CO_2 emission. Jiaqiang et al. [14] evaluated fish oil as a fuel in a stationary diesel engine. Simulation and experimental methods were used to investigate the influence of fuel IT and fuel injection pressure operating with fish oil and its blends. Raw fish oil is transesterified to produce biodiesel. Various blends ranging from B10 to B50 were utilized for analysis. As the biodiesel concentration increases, NOx emissions rise while soot, HC, and CO emissions decrease. The study was further carried out by increasing fuel IT. It was perceived that BTE increased and emissions like CO, HC, smoke, etc. reduced with the advancement of IT. Fish oil biodiesel was compatible with engine usage and enhanced outputs were noted on varying IT. Zhang et al. [15] experimented with a dual fueling operation in an engine with diesel and Ethylene Glycol (EG) with EG energy ratios of 0%, 10%, and 15% named EG0, EG10, and EG15 respectively. Port IT and direct IT modification strategies were used for performance improvement. Results showed a rise in maximum cylinder pressure and maximum heat release rate (HRR) along with a rise of 19.45% BTE is observed for advanced injection direct IT and increasing EG ratios. Emissions like CO_2, HC, NO_x, and soot are reduced with an increase in CO emissions. Advanced direct injection timing along with a suitable EG energy ratio decreased particulate matter (PM).

Karthic et al. [16] experimented with a diesel engine to investigate the combustion, performance, and emission parameters of Syzygiumcumini oil biodiesel as sole fuel by varying IT. A stationary laboratory water-cooled direct injection (DI) 1500 rpm diesel engine was employed for this work. Various blends B30, B70, and B100 were tested and compared. These fuels were subjected to injection pressures between 200 bar and 260 bar and IT of 21° to 25° bTDC. Net result output was compared with base fuel diesel. B30 fueled with 240 bar showed a 17.85% increase in BTE. On advancement of fuel IT with an increase of injection pressure, emissions of HC and CO were 46.15% and 15.9% less than usual injection timing and injection pressure. The smoke was reduced and an increase of NO_x was noted. B30 with 240 bar injection pressure and 25° bTDC advancing IT was better to operate in the engine. Wei et al. [17] experimented with a 4-cylinder diesel engine with 0%, 10% and 30% of 2,5-dimethylfuran (DMF). Improvement in combustion characteristics, and reduced NO_x and PM for different fuel IT was noted. Particulate size distribution, particulate number, and mass concentration were also measured and improved. The addition of DMF increased the delay period and reduced BSFC. Maximum in-cylinder pressure was obtained for 10% DMF. The accumulation mode of fuel is reduced but nucleation mode increases which has negative health effect on human body. Geometric mean diameter declined with DMF concentration because of an increase in nucleation mode and varying IT have a momentous effect on engine outputs. How et al. [18] experimented with unmodified medium-duty diesel engine using biodiesel blends of B20

and B50. Emission reduction and combustion enhancement strategies were implemented by altering IT and split injection of fuel inside cylinder. A remarkable reduction in NO_x less than 100 ppm is obtained and less smoke for retarded injection timing and multiple injection timing for blends B20 and B50 are obtained. Emissions like HC, CO, CO_2, and PM decreased for both B20 and B50 with retarded IT and multiple injections reducing emissions more than individual operations. Thus combined effect of the two injection strategies reduced emissions and improved the performance of biodiesel than diesel.

Many international research has been conducted on the performance and emissions of DI diesel engines using different types of biodiesel derived from animal fat and non-edible vegetable oil. However, little research has been done on the performance of CRDI diesel engines. There have only been a few studies that examine the efficiency, emissions, and combustion behavior of WCO biodiesel blends in CRDI engines [19]. This study aims to analyze the engine performance and emissions of biodiesel derived from used WCO tested at varied IT. One of the biggest challenges in industrial biodiesel production is determining the ideal engine conditions for running efficient, eco-friendly blends. CRDI engines use a high-pressure fuel rail to accurately distribute high viscosity biodiesel fuel into the combustion chamber, resulting in increased fuel efficiency and lower usage. CRDI engines run quieter and smoother with biodiesel blends because of the timing flexibility. Controlled injection decreases stress on engine components, resulting in durability and reliability. In a diesel engine, injection timing is a significant factor influencing engine performance, emissions, and durability. This might be the first study to combine the CRDI technique with different IT for WCO biodiesel blends. Over the past three decades, researchers have extensively investigated the use of alternate fuels. Additionally, studies on engine modification have been conducted. However, there is a need for further exploration of investigation on alternate fuels and suitable engine modification to achieve anticipated performance and minimize emissions. Limited work has been conducted on the utilization of WCO blended fuel in CI engines and its influence on engine characteristics of emissions and performance. Therefore, in this work, a single-cylinder CRDI diesel engine was employed to examine the influence of injection timing on both engine performance and exhaust emissions when utilizing WCO-diesel blended fuel.

2. Materials and methods

2.1 Fuel Blend Preparation

In this research, WCO involved utilizing a method known as splash blending, which includes adding fuels a specified amount to a vessel and stirring the mix for 5 min. Various testing fuels were obtained, which containing 90%, 80% & 70% of diesel, and 10%, 20% & 30% of WCO, and then compared with mineral diesel. Throughout the research, B20 (WCO 20% + Diesel 80%) blends, were taken into consideration based on aforementioned literature. It's noteworthy that compared to diesel, WCO exhibits higher viscosity, thus increase in the proportion of WCO in the test fuel could potentially lead to critical issues such as separation of phase owing to density differences and abridged performance parameters [20]. Therefore, to mitigate these concerns, the proportion of WCO in the assessment fuels was capped at 20%. Table 1 provides a summary of the physicochemical properties of the test fuels.

Table 1. Properties of test fuels

Property	Diesel	WCO	B20	ASTM method
Kinematic viscosity (cSt)	2.8	2.62	2.24	D-445
Density (kg/m^3)	846	831	838	D-1298
Flashpoint (°C)	67	46	52	D-93
Cetane number	52	48	45	D-613
Heating value (kJ/kg)	44200	42630	43160	D-240

2.2 Experimental Setup

The current study employed a CRDI diesel engine for conducting tests. CRDI engines employ a high-pressure fuel rail to accurately distribute high viscosity biodiesel fuel into the combustion chamber,

resulting in increased fuel efficiency and lower usage. Direct Injection is a fuel delivery technology that employs a mechanical pump to feed gasoline into the engine's ignition chamber. DI engines provide less power than CRDI engines. CRDI engines run quieter and smoother with biodiesel blends because of the timing flexibility. Controlled injection decreases stress on engine components, resulting in longevity and dependability. The increased refinement results in smoother running and reduced wear and tear on the engine's body. As a result, CRDI engines can claim superior long-term longevity over direct injection. CRDI emits less pollutants than standard diesel engines, however it still produces certain dangerous compounds. The test engine specifications are detailed in Table 2, and Fig. 1 shows the engine setup. The IT was varied from 24° to 21° bTDC, maintaining 600 bar of injection pressure at loads from 25% to 100%, with B20 blends.

Table 2. Engine specifications

Particulars	Specifications
Type	Kirloskar – 4S CRDI diesel engine
Number of cylinders	One
Compression ratio	17.5:1
Standard injection timing	23°bTDC
Bore	87.5 mm
Stroke	110 mm
Power	3.7 kW
Injection pressure	600 bar
Speed	1500 rpm

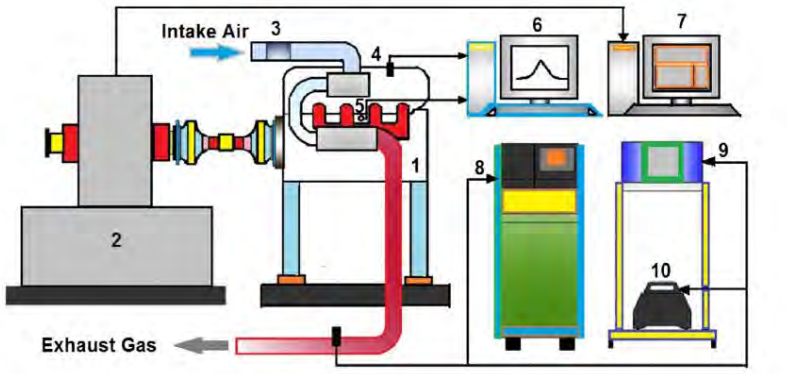


Fig. 1. Engine setup layout

2.3 Modification in Injection Timing

The standard IT was attuned by employing the number of shims inside the fuel pump. The fuel IT could be altered by either increasing or decreasing the number of shims in the fuel pump. Upon the initial assembly of the engine, 3 shims were already fitted in the injection pump. To achieve retarded IT, a shim (0.3 mm thick) was added, while advanced IT was achieved by taking away the shim. Every shim, equivalent to 1° crank angle (CA), could provide either advancement or retardation, depending on the shims existing in the fuel pump. The IT was physically attuned after each change to the shims, whether they were added or removed. These alterations to the fuel IT had significant effects on the engine. Advanced IT leads to a more pronounced enhancement in mixture turbulence, facilitating quicker and immediate combustion. This adjustment also results in a prolonged ignition delay, contributing to decreased temperature and pressure. Retarded IT

caused delayed engine combustion, slower combustion rate, shortened ignition delay period, and heightened temperature and pressure.

3. Results and Discussion

Through minimal engine adjustments, WCO exhibits the prospective to reduce emissions. In CI engines, IT significantly influences both emissions and performance. The initial tests on WCO were conducted at the standard injection timing (ST) set at 23° bTDC to establish baseline values. Test findings indicated that NO_x emissions produced at the ST of WCO exceeded those generated by diesel fuel. Four variable IT settings (ranging from 24° bTDC to 21° bTDC) were implemented at different engine loadings from 25% to 100%. Advanced IT revealed inferior results for WCO blend fuels compared to ST. Conversely, retarded injection timing (RT) exhibited improved results for WCO blends. Some insights were also derived from existing literature, emphasizing the focus on RT in the current research work. The ST for diesel engine is 23° bTDC. This IT is suitable for diesel fuel, but biofuel whose viscosity is higher and has higher oxygen and therefore leads to higher NO_x. At RT of 22° bTDC and 21° bTDC, it is found to exhibit lowered NO_x emissions. So, the Research is focused more on RT till 21° bTDC. Beyond that, the performance reduces because of drop in engine cylinder temperatures. Advancing an engine's IT causes the injection process to begin earlier than the manufacturer's parameters. In contrast, retarding occurs when adjustments are made to cause the fuel to release later than expected. Although retarding is less common than advancing, it can resolve a lag or smoking issue in a biodiesel engine. It can also help with performance and fuel efficiency issues. The present study used one advanced IT of 24° bTDC and RT of 22° bTDC and 21° bTDC in order to assess the influence on both sides, in addition to the ST of 23° bTDC as specified by the engine manufacturer. It is also crucial to conduct investigation at full load. During the optimization of IT, the speed was held steady at 1500 rpm, and fuel pressure was maintained at consistently at 600 bar. The present research is conducted with standard IT of 23° bTDC, retarded IT of 22° bTDC, 21° bTDC and advanced IT of 24° bTDC.

3.1 Performance Characteristics

Fig. 2 displays the variations of BTE for B20 at different IT with engine load. The maximum BTE is 32.31% reported for B20+RT22 at full load condition. In retarded IT of 22° bTDC, the B20 blends performance is increased by 3.78%, while more retardation IT of 21° bTDC was found to drop in BTE by 5.27% at 100% engine load condition owing to variations in ignition delay period within the combustion chamber. BTE increases with the retardation in IT were already reported by Jaichandar et al. [21]; Agarwal et al. [22].

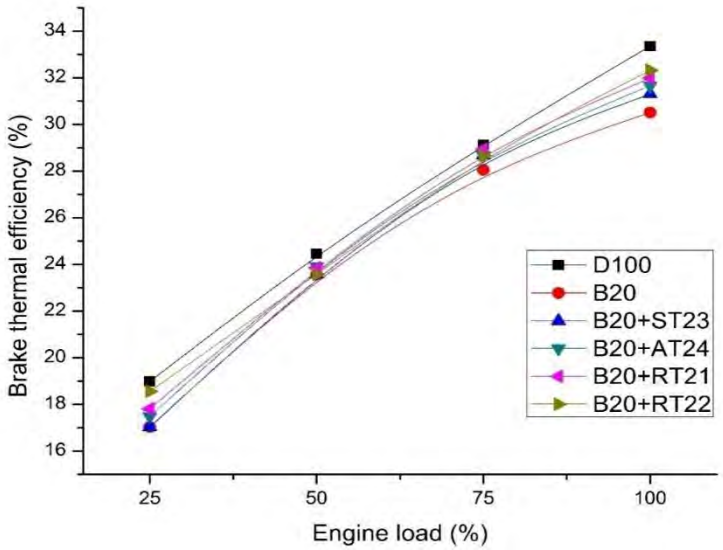


Fig. 2. BTE vs Engine load

This shows the efficiency of the B20 blend at retarded RT. This could be probably the standard IT of 23° bTDC favoring only diesel fuel combustion, but not the oxygenated blends. While retarding IT, the injection of fuel begins very late after the TDC which could have provided sufficient residence time for the formation of the air-fuel mixture thereby ensuring the O_2 utilization in B20 blend followed by higher BTE. Advancing the IT of 24° bTDC was found to reduce the BTE of 1.13% very marginally concerning B20+ST23. BTE trend is always lesser due to reduced cylinder temperature prevailing at lower loads where the occurrence of combustion is very early with respect to TDC diminishing the output power via losses of pumping.

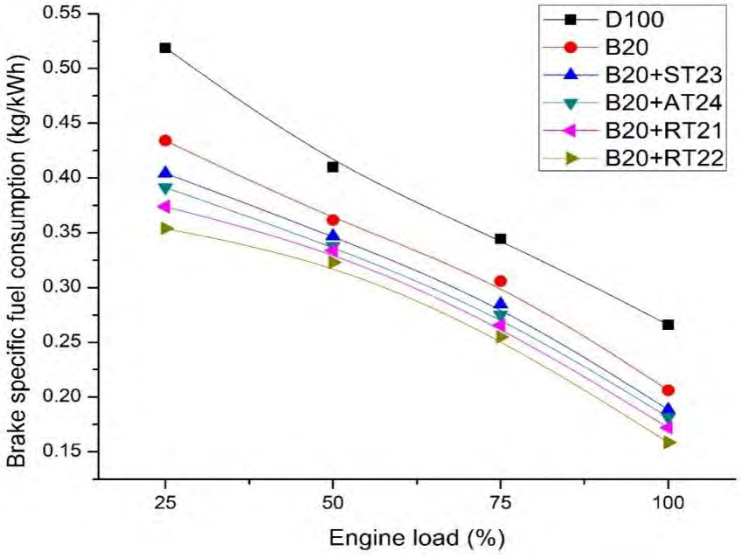


Fig. 3. BSFC vs Engine load

Fig. 3 displays the variation of BSFC for B20 at different IT with engine load. It can be perceived that maximum BSFC is for B20 blend throughout the load condition which is evidence of poor mixture formation and abundant fuel congregation in the zone of combustion followed by higher energy required to maintain constant engine speed of 1500 rpm. At full load, the BSFC of B20+AT24 and B20+RT21 were higher than B20+ST23 by about 3.68% and 8.70% respectively, while the least fuel consumption of 158 g/kWh is recorded for B20+RT22. However, retarding injection timing further to about 21° bTDC named as B20+RT21 which is not lower the BSFC further, and in contrast, it is increased. These BSFC reductions for retard injection timing were on par with the outcomes of Mani & Nagarajan [23], and Agarwal et al. [22] who indicated that optimum fuel injection timing required for biofuel blends will favoring the combustion efficiency.

3.2 Emission Characteristics

Fig. 4 displays the fluctuation of CO emissions for B20 at different IT with engine load. D100 possess the highest CO emissions among other oxygenated blends owing to the lack of O_2 in mineral diesel which makes the blend unable to sustain oxidation. Whereas with B20, the CO emissions are reduced substantially indicating significant improvement in combustion. Retarding the injection timing of 22° bTDC along with B20 results in lowering CO emissions in comparison with the B20 blend at engine loads of 25%, 50%, 75%, and 100% by about 42.01%, 86.74%, 33.04% and 60.2% respectively. Lowered CO emissions with retardation in IT were on par with the research findings of Mani & Nagarajan [21], and Agarwal et al. [22]. It is found that further retardation from 22° bTDC to 21° bTDC is not effective and found to increase CO emissions as found in similar studies of Sayin et al. [25] and Ganapathy et al. [26]. Also, advanced timings of 24° bTDC are found to increase the CO emissions by about 35.63% in comparison with B20+ST23 as a result of poor rate of oxidation and existence of more rich fuel zones in the bowl especially at varied timings of 21° bTDC, and 24° bTDC causing hindrance in the oxidation of CO to CO_2 followed by higher CO emissions.

Fig. 5 displays the variation of HC emissions for B20 at different IT with respect to load. It can be found that diesel fuel displays the highest HC emissions throughout the load condition. The HC emission profile of B20 is very low compared with diesel fuel. With injection timing retardation,

the HC emissions were found to lower significantly, especially with B20+RT22 at 25%, 50%, 75%, and 100% load conditions which possess HC emissions of 0.065, 0.0525, 0.056, and 0.04 g/kWh respectively. Similar reductions in HC emissions with IT retardation are found in some literature [21-22]. Whereas, some literature also proved to increase the HC with injection timing retardation such as Hwang et al. [24]. Further, fuel injection timings of 24° bTDC and 21° bTDC were found to increase the HC emission signifying the insufficient residence time for preparation of mixture and more possibility of formation of fuel-rich zones thereby resulting in high HC emissions.

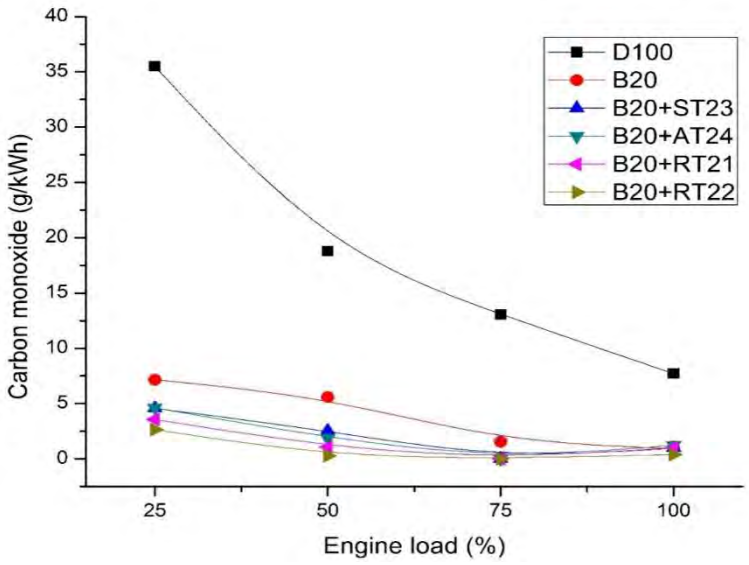


Fig. 4. CO emission vs Engine load

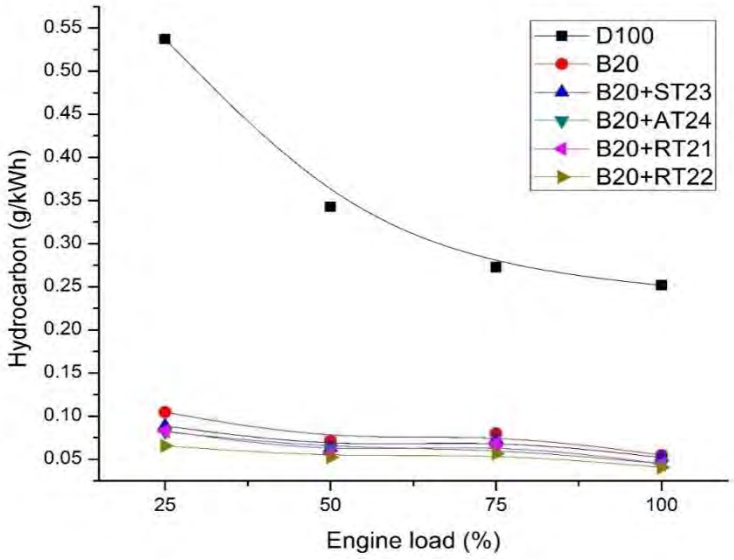


Fig. 5. HC emission vs Engine load

Fig. 6 portrays the variation of NO_x emission for B20 at different IT with respect to load. The prime reason for the variation of NO_x emissions is characterized by higher burning rate, excess O_2 content, and improved adiabatic flame temperature at which O_2 and N_2 tend to form NO emissions. It can be seen that B20 blends tend to liberate more NO_x emissions in comparison with mineral diesel blends indicating an increase in combustion rate along with higher in-cylinder temperatures. It is found that the NO_x emissions of B20+RT21 and B20+RT22 were higher at about 5.06% and 6.25% respectively at 100% load. This can be perhaps due to an improvement in residence time of fuel accumulation followed by higher adiabatic flame temperature and thereby overall improvement in O_2 and N_2 reacting in the air followed by higher NO_x emissions. Further retardation in IT 21° bTDC drops the NO_x emission subsequently as seen in some similar research by Mani & Nagarajan [21]

and Sayin et al. [25]. When the fuel injection timing is advanced to 24° bTDC for B20, there is a marginal NO_x emission improvement in comparison with B20+ST23 such a marginal improvement and NO_x emission is attributed to B20 blends earlier start of combustion concerning TDC thereby causing improved cylinder pressure, HRR and adiabatic flame temperature along with higher NO_x emissions. These results are on par with the results of Hwang et al. [24], Ganapathy et al. [26] and Sayin et al. [25].

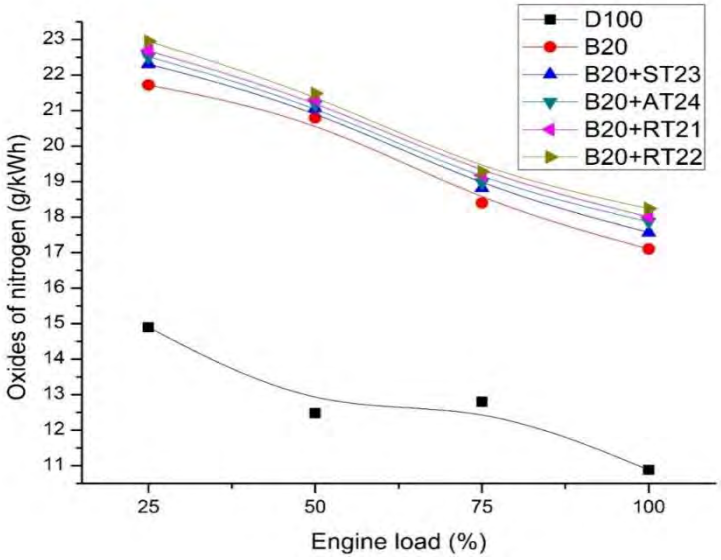


Fig. 6. NO_x emission vs Engine load

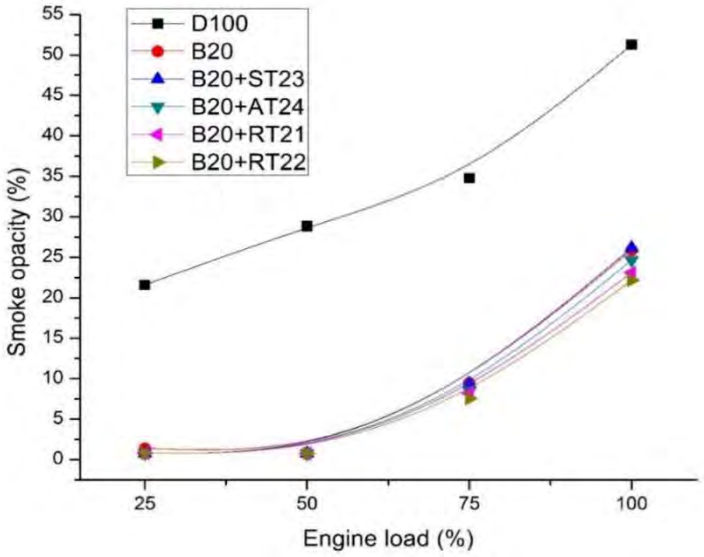


Fig. 7. Smoke opacity vs Engine load

Fig. 7 depicts the fluctuation of smoke for B20 at different IT concerning load. The fluctuation in smoke opacity is on par with the NO_x-smoke trade of characteristics. Lowermost profile of smoke emission is found for B20+RT22 of about 0.79%, 0.77%, 7.5%, and 22.17% at engine loads of 25% - 100% respectively compared to B20. This can be ascribed to the presence of higher residence time for accumulation of test fuel leading to improvement in in-cylinder pressure and HRR, excellent spray characteristics followed by lowered fuel-rich zones, and thereby reduced smoke. Further, when the IT is advanced, more chances of soot oxidation are there due to higher cylinder temperatures leading to evaporation in B20 blend, thereby improving in combustion rate and reducing smoke. These are on par with the research findings of Gnanasekaran et al. [27] and Sayin et al. [25]. When the fuel injection timing is retarded, the smoke increases which is on par with characteristics of NO_x-smoke trade-off. B20+ST23 possesses higher smoke opacity than B20+RT21

and B20+RT22 about 23.1% and 22.17% respectively. Lowered smoke opacity with retardation in injection timing is alike with the findings of Mani & Nagarajan [23].

4. Conclusion

The increasing demand for fossil fuels and the prevailing geopolitical situation have raised significant global concerns. As a result, there is an increasing need for alternative fuels for IC engines. By making slight adjustments to fueling systems, this biodiesel can potentially be transformed into an alternative fossil fuel. In this research, a Common Rail Direct Injection diesel engine was operated at different injection timings using waste cooking oil blends with mineral diesel. The study aimed to assess the impact of injection timing variations, including advanced, standard, and retarded settings, on both engine emissions and performance. The outcomes indicated that changes in injection timing had a substantial influence on the performance and emission characteristics. The blend B20+RT22 was found to have improved brake thermal efficiency along with the lowered brake specific fuel consumption owing to retarded injection timing of fuel yielding proper residence time for fuel-air mixture formation leading to higher combustion efficiency and improved performance. Also the blend B20+RT22 has 60.2% lowered CO, 18.8% lowered HC, and slightly higher NO_x emissions by 6.25% as a result of advancing injection timing. Overall, it is perceived that the B20+RT22 is found to be superior in terms of improved performance, and minimized emissions. The current study has a limitation on the biodiesel concentration of 20%. Hence higher biodiesel concentration blends are need to be assessed. By adopting appropriate injection timing settings led to significant enhancements in both emissions and performance for waste cooking oil blends compared to the diesel fuel and standard injection timing. Moreover, this approach holds promise as a potential long-term solution to address the challenge of waste cooking oil disposal. Further, studies on the effect of Nano additives in waste cooking oil biodiesel blended fuel on CI engine performance are also need to be investigated. In future, Influence of Silicon Catalytic Reduction and the use of Exhaust Gas Recirculation on a waste cooking oil biodiesel engine could also be explored for effective NO_x reduction.

Abbreviations

ASTM	- American Society of Testing and Measurement	EG	- Ethylene Glycol
AT24	- 24° bTDC advanced injection timing	HC	- Hydrocarbon
B20	- 20% biodiesel + 80% diesel	HRR	- Heat Release Rate
BSFC	- Brake Specific Fuel Consumption	IT	- Injection Timing
bTDC	- before Top Dead Centre	NO_x	- Oxides of nitrogen
BTE	- Brake Thermal Efficiency	O_2	- Oxygen
CA	- Crank Angle	PM	- Particulate Matter
CI	- Compression Ignition	RT21	- 21° bTDC retarded injection timing
CO	- Carbon monoxide	RT22	- 22° bTDC retarded injection timing
CRDI	- Common Rail Direct Injection	ST23	- 23° bTDC standard injection timing
D100	- Diesel	TDC	- Top Dead Centre
DMF	- Dimethylfuran	WCO	- Waste Cooking Oil

Acknowledgement

The authors acknowledge that there are no external funding/grants received for this research work.

References

[1] Appavu P, Madhavan VR, Venu H, Jayaraman J. Experimental investigation of an unmodified diesel engine operated with ternary fuel. Biofuels. 2019;12(10):1183-9. https://doi.org/10.1080/17597269.2019.1600454

[2] Kannan R, Ramalingam S, Sampath S, Nedunchezhiyan M, Dillikannan D, Jayabal R. Optimization and synthesis process of biodiesel production from coconut oil using central composite rotatable design of response surface methodology. Proceedings of the Institution of Mechanical Engineers, Part E: Journal of Process Mechanical Engineering. 2024. https://doi.org/10.1177/09544089241230251

[3] Jayabal R, Soundararajan G, Kumar RA, Choubey G, Devarajan Y, Raja T, et al. Study of the effects of bio-silica nanoparticle additives on the performance, combustion, and emission characteristics of biodiesel produced from waste fat. Scientific Reports. 2023;13(1). https://doi.org/10.1038/s41598-023-46140-w

[4] Jayaprabakar J, Karthikeyan A. Analysis on the Performance, Combustion and Emission Characteristicsof a CI Engine Fuelled with Algae Biodiesel. Applied Mechanics and Materials. 2014;591:33-7. https://doi.org/10.4028/www.scientific.net/AMM.591.33

[5] Jayaraman J, Basha SMM, Anil PPSV, Mariadhas A, Joy N, Appavu P. Influence of liquid additives on waste cooking oil biodiesel-isopropanol blend operated in CI engine. Materials Today: Proceedings. 2021;44:3595-600. https://doi.org/10.1016/j.matpr.2020.09.489

[6] Jayabal R, Lionus Leo GM, Chrispin Das M, Sekar S, Arivazhagan S. Impact of ammonia energy fraction on improving thermal efficiency and emissions of ammonia/biodiesel in dual fuel diesel engine. Process Safety and Environmental Protection. 2024;188:1398-410. https://doi.org/10.1016/j.psep.2024.06.016

[7] Jayabal R. Effect of hydrogen/sapota seed biodiesel as an alternative fuel in a diesel engine using dual-fuel mode. Process Safety and Environmental Protection. 2024;183:890-900. https://doi.org/10.1016/j.psep.2024.01.046

[8] Jayabal R. Optimization and impact of modified operating parameters of a diesel engine emissions characteristic utilizing waste fat biodiesel/di-tert-butyl peroxide blend. Process Safety and Environmental Protection. 2024;186:694-705. https://doi.org/10.1016/j.psep.2024.04.019

[9] Sonachalam M, Jayaprakash R, Manieniyan V, Raghavendra Rao PS, Vinodhini G, Sharma M, Teku K, Warimani M, Hasan SM, Yunus Khan TM, Abdul SS, Keerthi S. Performance analysis of dual-fuel engines using acetylene and microalgae biodiesel: The role of fuel injection timing. Case Studies in Thermal Engineering. 2024;64:105370. https://doi.org/10.1016/j.csite.2024.105370

[10] Sonachalam M, Jayaprakash R, Manieniyan V, Srinivasa Murthy .M., Johar MGM, Sivaprakasam S, Warimani M, Nithin K, Ali M, Majed A, Saiful I, Muhammad IA. Impact of injection pressure on a dual-fuel engine using acetylene gas and microalgae blends of chlorella protothecoides. Case Studies in Thermal Engineering. 2024;60:104653. https://doi.org/10.1016/j.csite.2024.104653

[11] Sonachalam M, Manieniyan V, Senthilkumar R, K RM, Warimani M, Kumar R, Ankit K, Yunus Khan TM, Naif A. Experimental investigation of performance, emission, and combustion characteristics of a diesel engine using blends of waste cooking oil-ethanol biodiesel with MWCNT nanoparticles. Case Studies in Thermal Engineering. 2024;61:105094. https://doi.org/10.1016/j.csite.2024.105094

[12] Sonachalam M, Manieniyan V, Senthilkumar R. Optimization on manifold injection in DI diesel engine fuelled with acetylene. Proceedings of the Institution of Mechanical Engineers, Part A: Journal of Power and Energy. 2024;238(7):1213-27. https://doi.org/10.1177/09576509241264441

[13] Datla R, Puli RK, Velayudhan Parvathy C, Varuvel EG. Effect of start of main injection timing on performance, emission, and combustion characteristics of a VGT CI engine fueled with neem biodiesel. Environmental Science and Pollution Research. 2020;28(10):11942-53. https://doi.org/10.1007/s11356-020-08231-3

[14] Jiaqiang E, Pham M, Deng Y, Nguyen T, Duy V, Le D, Wei Z, Qingguo P, and Zhiqing Z. Effects of injection timing and injection pressure on performance and exhaust emissions of a common rail diesel engine fueled by various concentrations of fish-oil biodiesel blends. Energy. 2018;149:979-89. https://doi.org/10.1016/j.energy.2018.02.053

[15] Zhang P, He J, Chen H, Zhao X, Geng L. Improved combustion and emission characteristics of ethylene glycol/diesel dual-fuel engine by port injection timing and direct injection timing. Fuel Processing Technology. 2020;199:106289. https://doi.org/10.1016/j.fuproc.2019.106289

[16] Karthic SV, Senthil Kumar M, Nataraj G, Pradeep P. An assessment on injection pressure and timing to reduce emissions on diesel engine powered by renewable fuel. Journal of Cleaner Production. 2020;255:120186. https://doi.org/10.1016/j.jclepro.2020.120186

[17] Wei M, Li S, Liu J, Guo G, Sun Z, Xiao H. Effects of injection timing on combustion and emissions in a diesel engine fueled with 2,5-dimethylfuran-diesel blends. Fuel. 2017;192:208-17. https://doi.org/10.1016/j.fuel.2016.11.084

[18] How HG, Masjuki HH, Kalam MA, Teoh YH. Influence of injection timing and split injection strategies on performance, emissions, and combustion characteristics of diesel engine fueled with biodiesel blended fuels. Fuel. 2018;213:106-14. https://doi.org/10.1016/j.fuel.2017.10.102
[19] Mohanrajhu N, Sekar S, Jayabal R, Sureshkumar R. Screening nano additives for favorable NOx/smoke emissions trade-off in a CRDI diesel engine fueled by industry leather waste fat biodiesel blend. Process Safety and Environmental Protection. 2024;187:332-42. https://doi.org/10.1016/j.psep.2024.04.115
[20] Ayodhya AS, Lamani VT, Bedar P, Kumar GN. Effect of exhaust gas recirculation on a CRDI engine fueled with waste plastic oil blend. Fuel. 2018;227:394-400. https://doi.org/10.1016/j.fuel.2018.04.128
[21] Jaichandar S, Senthil Kumar P, Annamalai K. Combined effect of injection timing and combustion chamber geometry on the performance of a biodiesel fueled diesel engine. Energy. 2012;47(1):388-94. https://doi.org/10.1016/j.energy.2012.09.059
[22] Agarwal AK, Srivastava DK, Dhar A, Maurya RK, Shukla PC, Singh AP. Effect of fuel injection timing and pressure on combustion, emissions and performance characteristics of a single cylinder diesel engine. Fuel. 2013;111:374-83. https://doi.org/10.1016/j.fuel.2013.03.016
[23] Mani M, Nagarajan G. Influence of injection timing on performance, emission and combustion characteristics of a DI diesel engine running on waste plastic oil. Energy. 2009;34(10):1617-23. https://doi.org/10.1016/j.energy.2009.07.010
[24] Hwang J, Qi D, Jung Y, Bae C. Effect of injection parameters on the combustion and emission characteristics in a common-rail direct injection diesel engine fueled with waste cooking oil biodiesel. Renewable Energy. 2014;63:9-17. https://doi.org/10.1016/j.renene.2013.08.051
[25] Sayin C, Ilhan M, Canakci M, Gumus M. Effect of injection timing on the exhaust emissions of a diesel engine using diesel-methanol blends. Renewable Energy. 2009;34(5):1261-9. https://doi.org/10.1016/j.renene.2008.10.010
[26] Ganapathy T, Gakkhar RP, Murugesan K. Influence of injection timing on performance, combustion and emission characteristics of Jatropha biodiesel engine. Applied Energy. 2011;88(12):4376-86. https://doi.org/10.1016/j.apenergy.2011.05.016
[27] Gnanasekaran S, Saravanan N, Ilangkumaran M. Influence of injection timing on performance, emission and combustion characteristics of a DI diesel engine running on fish oil biodiesel. Energy. 2016;116:1218-29. https://doi.org/10.1016/j.energy.2016.10.039

Blank Page

Research on Engineering Structures & Materials
www.jresm.org
MIM Research Group

Research Article

Data-driven prediction of mechanical properties in friction stir processed Al6061-Alumina composite using enhanced machine learning models

Satish Saini [1,a], Neeraj Sharma [*,2,b], Ranjeev Kumar Chopra [3,c], Monika Mehra [4,d], Ravi Kumar [5,e], Sushil Bhardwaj [3,f], Dinesh Kumar [6,g]

[1]*ECE Department, RIMT University, Punjab, India*
[2]*Dept. of Information Technology, VPPCOE& VA, Sion, Mumbai, India*
[3]*School of Computing, RIMT University, Punjab, India*
[4]*ECE Department, Chandigarh University, Punjab, India*
[5]*Department of Physics and Electronics, Hansraj College, University of Delhi, India*
[6]*Dept. of Mechanical Eng., Maharishi Markandeshwar (Deemed to be University) Mullana, India*

Article Info

Article History:

Received 07 Sep 2024
Accepted 01 Dec 2024

Keywords:

Friction stir processing;
Al-6061 alloy;
Alumina;
Mechanical properties;
Special relativity search;
Long short-term memory

Abstract

This study explores friction stir processing (FSP) of Al-6061 aluminum alloy reinforced with alumina nanoparticles, analyzing the effects of processing parameters—including transverse speed, rotational speed, and number of passes—on ultimate tensile strength, yield strength, natural frequencies, and damping ratios. Using a CNC milling machine, FSP was conducted at rotational speeds of 900, 1100, 1300, and 1500 rpm, with traverse speeds of 10, 15, and 20 mm/min. An advanced machine learning model, SRS-optimized long short-term memory (LSTME), was utilized to predict the properties of the processed material, achieving high R^2 values of 0.911 for ultimate strength, 0.951 for yield strength, 0.953 for natural frequency, and 0.985 for damping ratio. Key findings indicate that FSP improves damping characteristics and mechanical properties, with maximum damping effectiveness observed at 900 rpm across all passes. Alumina nanoparticles enhanced damping capabilities, while increased rotational speeds promoted grain refinement, resulting in a stronger, more deformation-resistant material. The LSTME model outperformed other machine learning approaches, reaching R^2 values between 0.965 and 0.993 in training and 0.911 to 0.987 in testing. These results demonstrate the efficacy of combining FSP with machine learning to optimize material properties for high-performance applications.

© 2025MIM Research Group. All rights reserved.

1. Introduction

Drilling The advancement of composite materials has been crucial in enhancing several engineering disciplines because of its distinctive capacity to amalgamate qualities from diverse materials, yielding components that are stronger, lighter, and more resilient. Initially, composites were fundamental amalgamations created to satisfy basic structural requirements [1]. With technological improvements, composites have developed to include various matrix and reinforcing materials, resulting in high-performance composites appropriate for aerospace, automotive, and marine applications [2]. The use of composites has markedly increased, rendering these materials

*Corresponding author: kumar.d041789@gmail.com
[a]orcid.org/0000-0002-9194-3068:[b]orcid.org/0009-0007-5244-4868; [c]orcid.org/0009-0002-2929-4148; [d]orcid.org/0000-0008-4331-5033; [e]orcid.org/0000-0002-9112-3473; [f]orcid.org/0000-0001-5184-3866; [g]orcid.org/0000-0003-1885-2431
DOI: http://dx.doi.org/10.17515/resm2024.438me0907rs

indispensable in sectors that need lightweight and high-strength characteristics [3]. Aluminum-based composites have gained prominence owing to their superior strength-to-weight ratio, corrosion resistance, and thermal characteristics. Al-6061, a widely used aluminum alloy, is recognized for its adaptability in structural applications. Al-6061 composites, when augmented with ceramic particles or fibers, are appropriate for high-stress applications in automotive, aerospace, and industrial equipment, where durability and performance are paramount [4]. Traditional techniques for producing metal matrix composites (MMCs) include casting, powder metallurgy, and extrusion. These technologies are well-established; nonetheless, they often need elevated temperatures, and protracted procedures, and may encounter challenges in attaining uniform reinforcement distribution. Casting is economical and prevalent; yet, it may result in complications with reinforcement distribution owing to density disparities between the matrix and reinforcement phases [5]. To address the constraints of conventional techniques, innovative manufacturing methods, such as Friction Stir Processing (FSP), have been developed. FSP is a solid-state method that improves mechanical qualities by producing a precise microstructure without melting the material. Friction Stir Processing (FSP) enables meticulous regulation of the distribution of reinforcement particles inside the Al-6061 composite matrix [6]. This procedure generates a homogenous composite with superior mechanical characteristics and higher wear resistance by the application of targeted frictional heat and plastic deformation.

The advancement of composite materials has transformed engineering by presenting alternatives to conventional metals and alloys, delivering a distinctive amalgamation of qualities from both the matrix and reinforcement components [7]. Initially, composites were basic amalgamations of materials intended to fulfill certain structural or functional requirements. Technological breakthroughs have led to the evolution of composites, facilitating the creation of high-strength, lightweight, and durable materials [8]. This progress has catalyzed extensive acceptance across sectors, particularly in applications where weight reduction and superior mechanical strength are critical. Composites are used in several sectors, including aircraft, automotive, sports equipment, and medical devices. They are progressively preferred over traditional materials because of their superior mechanical qualities, corrosion resistance, and capacity for customization [9]. These materials are designed to provide superior performance while minimizing component weight, a characteristic that is especially advantageous in transportation sectors focused on fuel economy and emissions reduction. Aluminum composites have established a unique role within metal matrix composites (MMCs). Although MMCs may use diverse matrices such as titanium, magnesium, and copper, aluminum-based composites are mostly favored owing to aluminum's low density, superior corrosion resistance, and advantageous cost-to-performance ratio [10]. Titanium-based composites provide elevated strength and thermal resistance; yet, they are associated with increased prices and density [11]. Magnesium composites have lightweight properties but are deficient in mechanical strength compared to aluminum [12]. Aluminum composites provide a harmonious combination of strength, weight, and cost, making them a flexible option across several sectors. Aluminum composites are extensively used in industries where weight and durability are essential considerations [13]. In the aerospace sector, they are used in structural components such as wings and fuselage sections [14]. Aluminum composites are used in vehicle production for engine components, wheels, and brake systems, enhancing fuel economy and performance [15]. Aluminum composites are advantageous for the maritime and electronics sectors because to their corrosion resistance and thermal stability, rendering them suitable for components subjected to severe conditions or necessitating efficient heat dissipation [16].

Al-6061 is a highly flexible and extensively used aluminum alloy, esteemed for its superior mechanical qualities, weldability, and resistance to corrosion. Al-6061, categorized under the 6xxx family of aluminum alloys, is mostly alloyed with magnesium and silicon, resulting in a distinctive amalgamation of strength, toughness, and favorable machinability. This alloy is used in diverse industrial applications, including aerospace and automotive components, as well as structural elements in construction, owing to its capacity for facile forming, welding, and heat treatment to improve its mechanical characteristics [17]. Al-6061 is used in components such as frames, pipelines, maritime fittings, and recreational equipment, where strength, lightweight properties, and durability are critical [18]. The Al-2024 alloy, belonging to the 2xxx class, is mostly alloyed with

copper, imparting it remarkable strength and fatigue resistance [19]. The Al-7075 alloy is recognized for its remarkable strength; it is an aluminum-zinc alloy that almost matches the strength of some steels while being much lighter. Although Al-7075 exhibits worse corrosion resistance compared to Al-6061, it is often used in applications demanding optimal strength with lowest weight [20]. The Al-5052 alloy is part of the 5xxx family, recognized for its superior corrosion resistance, especially in marine settings, attributed to its elevated magnesium concentration [21]. Al-3003, a widely used aluminum alloy, is alloyed with manganese, offering moderate strength and superior corrosion resistance [22]. Al-6063, like to Al-6061, belongs to the 6xxx class but is mostly selected for its enhanced extrudability and visual appeal. It is often used for architectural and decorative purposes, including window frames, door frames, and metal furnishings. Despite possessing inferior strength compared to Al-6061, Al-6063's superior corrosion resistance and exceptional anodizing characteristics make it appropriate for outdoor and ornamental uses. Every aluminum alloy provides a unique equilibrium of characteristics, including strength, corrosion resistance, formability, and machinability, making aluminum alloys essential in contemporary industries. Al-6061 is widely preferred for its varied performance; nevertheless, other alloys such as Al-2024, Al-7075, Al-5052, Al-3003, and Al-6063 are also essential in specific applications within the aerospace, marine, automotive, and architectural industries.

The investigation used a CNC milling machine to examine the influence of processing factors, including feed rate, number of passes, and rotational speed, on critical material characteristics such as ultimate strength, yield strength, natural frequencies, and damping ratios of the samples [23]. These qualities are essential for evaluating material performance in applications necessitating mechanical robustness and dynamic stability. Conventional modeling techniques often fail to accurately represent the intricate, nonlinear relationships among these factors, particularly when forecasting dynamic attributes such as natural frequencies and damping ratios [24]. To address these issues, an advanced machine learning approach called SRS-optimized Long Short-Term Memory with Embedded Learning (LSTME) was used. The SRS-optimized LSTME model is explicitly designed to process sequential data, making it suitable for capturing the complex temporal patterns and relationships intrinsic to CNC milling operations [25]. This method integrates the capabilities of Long Short-Term Memory (LSTM) networks, recognized for their proficiency in managing time-series data, with Special Relativity Search (SRS) optimization. The SRS component emphasizes frequency-domain analysis, enabling the model to enhance its comprehension and prediction of reactions associated with the material's dynamic behavior, including natural frequency and damping ratio. The integrated learning capacity of LSTME allows the model to learn and adapt in real-time with the introduction of new data, hence improving its accuracy and resilience [26]. The implementation of the SRS-optimized LSTME model commences with a training phase, using previous data from CNC milling trials to elucidate the correlations between processing parameters and material attributes. During the SRS optimization phase, the model focuses on the spectral attributes that most profoundly affect dynamic responses. Upon training, the model can precisely forecast ultimate and yield strengths, together with dynamic characteristics such as natural frequencies and damping ratios, derived from fresh CNC milling inputs. The model's performance is meticulously verified against experimental data, using accuracy measures such as mean absolute error (MAE), root mean square error (RMSE), and R-squared (R^2) values to assess its prediction dependability. The benefits of using SRS-optimized LSTME in this setting are substantial [27]. By including both temporal and spectral attributes of the CNC milling process, the model attains superior prediction accuracy and adaptively modifies to fluctuating milling settings, making it more adaptable than conventional machine learning techniques [28]. This methodology enables producers to forecast the mechanical and dynamic characteristics of milled samples, so considerably reducing the need for comprehensive experimental testing, resulting in time and cost savings. Moreover, the model's real-time predictive capabilities allows immediate process modifications, so assuring uniform product quality. In conclusion, SRS-optimized LSTME offers a comprehensive solution for comprehending and refining CNC milling parameters, allowing businesses to attain specified material characteristics and improved process regulation. In this work, Aluminium alloy 6061 (Al-6061) was used as the matrix material for metal matrix composites (MMCs), with alumina (Al_2O_3) serving as the reinforcing component [29]. Al-6061/Alumina MMCs provide an advantageous amalgamation of lightweight, high strength, and

wear resistance, rendering them appropriate for diverse applications across various sectors. These composites improve mechanical qualities, including strength, stiffness, wear resistance, and corrosion resistance, which are essential for rigorous operating settings. Furthermore, by adjusting the volume percentage and dimensions of alumina reinforcement particles, the composite's density may be decreased relative to steel, making it an optimal choice for lightweight applications. To enhance these qualities, we used sophisticated machine learning techniques to forecast the optimal processing parameters for Friction Stir Processing (FSP) of Al-6061 alloy augmented with alumina nanoparticles. Our aim was to use machine learning to determine the ideal FSP conditions that improve the mechanical performance and longevity of the composite [30]. This novel methodology offers a data-driven resolution to enhance the efficiency and efficacy of the FSP process, resulting in advanced Al-6061/alumina nanocomposites designed for high-performance applications. During the investigation, we examined the mechanical characteristics and dynamic reactions of the treated materials under different FSP settings. Employing advanced machine learning methods, namely a refined Long Short-Term Memory with Embedded Learning (LSTME) model augmented by Spectral Response Surface (SRS) optimization, we precisely predicted the mechanical properties of the samples. The LSTME-SRS model was meticulously assessed against three other machine-learning algorithms to measure its predicted accuracy and overall performance. This extensive modelling methodology has shown significant promise for improving FSP parameters, hence aiding in the creation of high-performance Al-6061/Alumina MMCs appropriate for lightweight and durable applications. In this work, Aluminum alloy 6061 (Al-6061) was used as the matrix material for metal matrix composites (MMCs), with alumina (Al_2O_3) serving as the reinforcing component [31]. Al-6061/Alumina MMCs provide an advantageous amalgamation of lightweight, high strength, and wear resistance, rendering them appropriate for diverse applications across various sectors. These composites improve mechanical qualities, including strength, stiffness, wear resistance, and corrosion resistance, which are essential for rigorous operating conditions. Furthermore, by adjusting the volume percentage and dimensions of alumina reinforcement particles, the composite's density may be decreased relative to steel, making it an optimal choice for lightweight applications. To enhance these qualities, we used sophisticated machine learning techniques to forecast the optimal processing parameters for Friction Stir Processing (FSP) of Al-6061 alloy augmented with alumina nanoparticles [32]. The aim of the study is to use machine learning to determine the ideal FSP conditions that improve the mechanical performance and longevity of the composite. This novel methodology offers a data-driven resolution to enhance the efficiency and efficacy of the FSP process, resulting in enhanced Al-6061/alumina nanocomposites designed for high-performance applications. During the investigation, we examined the mechanical characteristics and dynamic reactions of the treated materials under several FSP settings. Employing advanced machine learning methods, namely a refined Long Short-Term Memory with Embedded Learning (LSTME) model augmented by Spectral Response Surface (SRS) optimization, we precisely predicted the mechanical properties of the samples. The LSTME-SRS model was meticulously assessed in comparison to three other machine-learning algorithms to determine its predicted accuracy and overall efficacy. This extensive modeling methodology has shown significant promise for improving FSP parameters, hence aiding in the creation of high-performance Al-6061/Alumina MMCs appropriate for lightweight and durable applications.

2. Materials and Method

2.1 Matrix and Reinforcement

The base of the structure was a sheet of Al-6061 aluminum alloy, which had a thickness of 4 mm. The Al_2O_3 nanoparticle was used as reinforcement.

Table 1. Composition of Al-6061 alloy

Elements	Al	Mg	Si	Fe	Cu	Cr	Mn
Wt.%	98.00	0.797	0.51	0.257	0.219	0.157	0.043

Table 1 displays the outcomes of the chemical analysis performed on the aluminum alloy and the FSP tool using a spectroscopic analyzer. The transmission electron microscopy (TEM) analysis revealed that the reinforcing particles exhibited a high level of purity, measuring at 99.9 percent, and had an average size of 16±5.6 nm as shown in Figure 1.

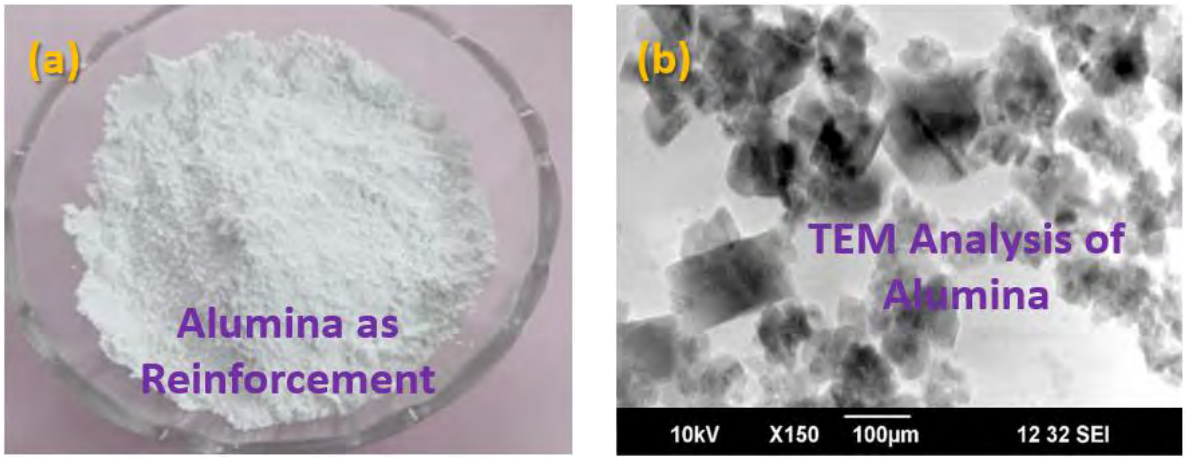


Fig.1. (a) Al_2O_3 powder in typical form and (b) TEM Analysis of Al_2O_3 nanoparticles

2.2 Composite Fabrication Method

Friction Stir Processing (FSP) is a solid-state joining method aimed at improving the microstructure and characteristics of materials, especially metals such as aluminum. The procedure starts with the production of an aluminum sheet, which is precisely machined to form longitudinal grooves that will subsequently contain the reinforcing particles.

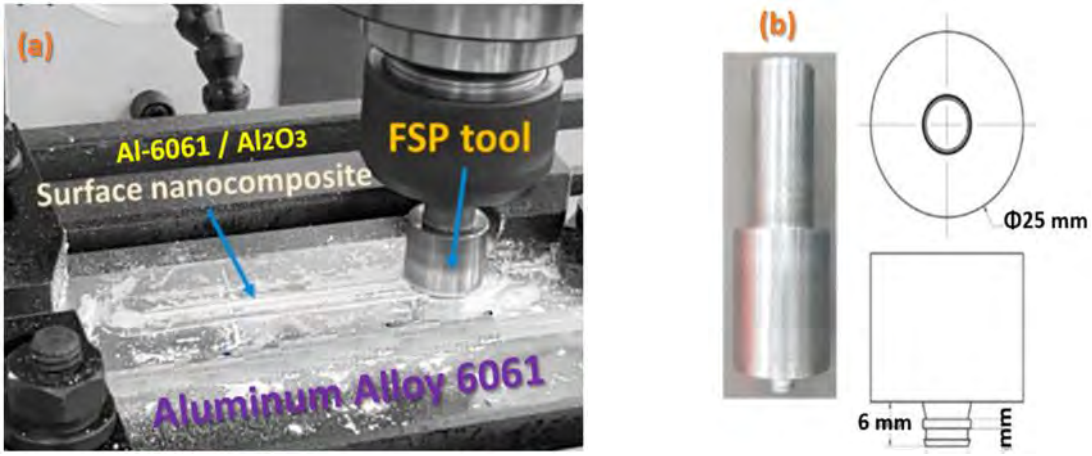


Fig. 2. (a) Tool specifications and (b) FSP processing on Base Alloy

For this particular FSP procedure, a tool with a tapered square form is used to provide excellent contact with the aluminum matrix during processing. A CNC milling machine is configured with the selected tool, which is then brought into contact with the prepared aluminum sheet. The tool rotates at varying rates of 900, 1120, 1400, and 1800 revolutions per minute while traversing the sheet at speeds of 10, 15, and 20 millimeters per minute. The interplay of rotational and translational motion produces frictional heat and mechanical deformation, facilitating the effective alteration of the microstructure in the treated areas. In accordance with the FSP procedure, surface flaws are rectified by grinding with silicon carbide paper, using grit sizes ranging from 450 to 2200. This stage is essential for attaining a polished surface, following which the ground samples are rinsed with water to remove any abrasive residues or metallic particles.

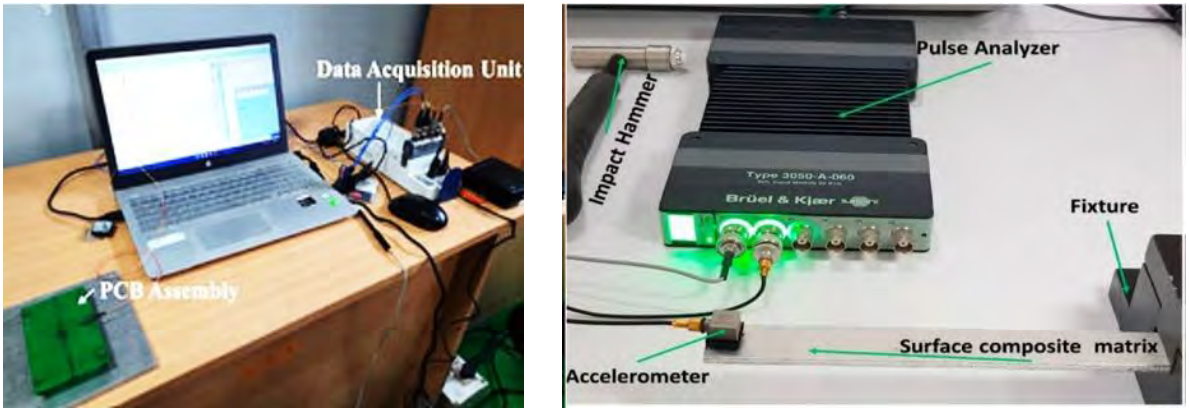


Fig. 3. Free impact vibration 3050 Pulse analyzer

The samples are subjected to an etching process using a solution of hydrofluoric acid, nitric acid, and filtered water at room temperature to improve surface quality and expose microstructural characteristics. The etching procedure is essential for elucidating the microstructure and macrostructure of the treated materials. The samples are examined until the requisite surface quality is achieved, guaranteeing comprehensive cleaning prior to analysis. Flat dog bone-shaped samples are extracted from the middle of the treated zone for mechanical property assessment, in compliance with ASTM requirements. The samples, constructed with precise dimensions, are subjected to tensile testing using a Universal Testing Machine (UTM) with a maximum load capacity of 100 kN, in compliance with ASTM B557 standards. The natural frequency and damping factor of the composite surface are evaluated by free vibration analysis. Accelerometers are affixed to the samples to assess their vibrational response over time, using a pulse data analyzer and an impact hammer. Multiple repetitions of the free vibration tests are conducted to assure precision, using a modal analysis tool to compute the Frequency Response Function (FRF), damping ratio, and fundamental frequencies of the material. This thorough method not only improves the comprehension of the aluminum-alumina composite but also offers insights into its long-term performance and stability under operating settings.

2.3 Special Relativity Search Optimized Long Short-Term Memory Modelling

The Special Relativity Search Modelling Approach is a computational methodology designed to analyze and predict the behavior of systems in high-velocity scenarios, where the principles of special relativity become significant. The process begins with defining the physical system under investigation and identifying the key parameters that influence its behavior, such as rotational speed, number of passes, and transverse speed in friction stir processing.

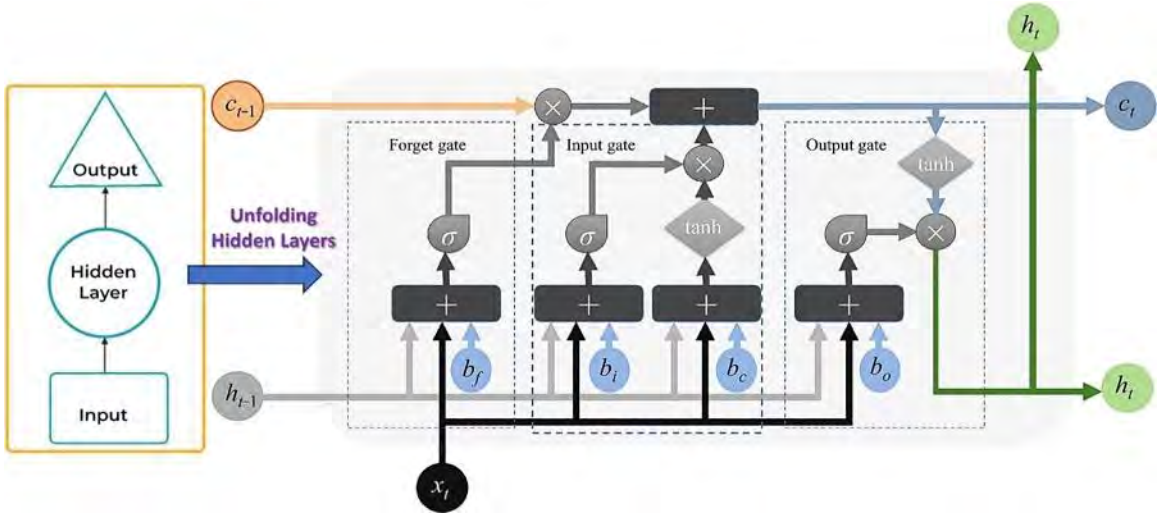


Fig. 4. Systematic View of LSTME Network

SRS modelling approach incorporates several key components that facilitate the analysis and prediction of phenomena in high-velocity scenarios governed by the principles of special relativity. Here are the essential components of the SRS approach:

2.3.1 Relativistic Equations

The foundation of the SRS approach is built upon the equations of special relativity, such as the Lorentz transformations. These equations describe how measurements of time, length, and velocity are affected for observers in different inertial frames, allowing for accurate modeling of relativistic effects.

2.3.2. Parameter Identification:

Clearly defining and identifying the key parameters that influence the behavior of the system under investigation is crucial. This includes variables such as velocity, energy, momentum, and mass, which must be considered to understand how they interact within a relativistic framework.

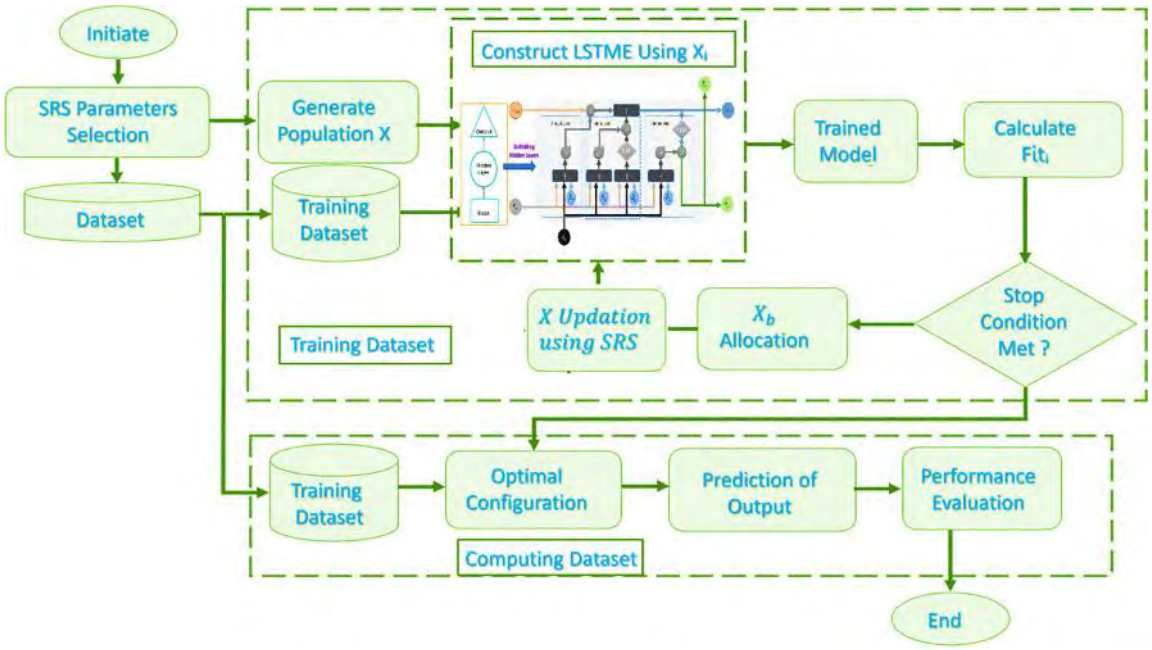


Fig. 5. Special Relativity Search-based LSTME Network Model

2.3.3 Data Collection

Gathering data relevant to the system being modeled is a critical component. This may involve experimental measurements or numerical simulations that reflect the system's behavior at relativistic speeds. The quality and comprehensiveness of this data are vital for model accuracy.

2.3.4 Model Development:

In the SRS approach, a computational model is developed to represent the relationships between input parameters and output behaviors based on the principles of special relativity. This model can utilize techniques from statistics, machine learning, or traditional numerical methods to approximate the system's response.

2.3.5 Optimization Techniques

The SRS approach employs optimization algorithms to explore the parameter space effectively. By systematically varying input parameters, the model identifies optimal conditions that maximize or minimize desired outcomes, such as efficiency or performance in relativistic contexts.

2.3.6 Simulation and Analysis:

Once the model is established, simulations are conducted to predict system behavior under various scenarios. This allows for the examination of how relativistic effects, such as time dilation and length contraction, influence the outputs.

2.3.7 Validation

A critical step in the SRS approach involves validating the model's predictions against independent experimental results or established theoretical benchmarks. This ensures that the model accurately captures the dynamics of the relativistic system.

3. Results and Discussions

The study's findings, depicted in Figures 6-8, clearly establish a direct correlation between the FSP Parameters and damping ratio. Nevertheless, the capacity to diminish vibrations can be improved at a particular optimal rotational velocity.

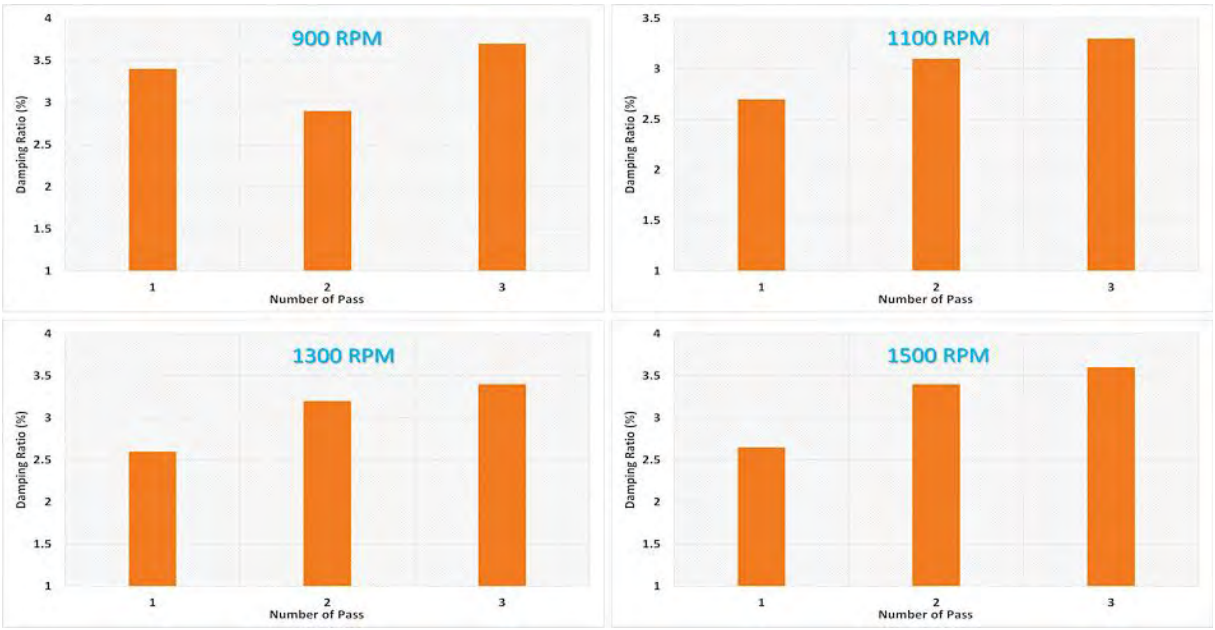


Fig. 6. Damping capacity of the samples at a traverse speed of 10 mm/min.

The data illustrates the influence of rotational speed (RPM) and the number of passes on the damping ratio of an aluminum alloy processed through friction stir processing (FSP) at a consistent traverse speed of 10 mm/min. At 1000 RPM, the damping ratio increases as the number of passes rises, reaching 3.68% after three passes. Similarly, at 1200 RPM, the damping ratio improves with additional passes, peaking at 3.43% with three passes. However, an interesting trend emerges at 1400 RPM, where the highest damping ratio of 4.62% occurs at two passes, suggesting an optimal setting for vibration reduction at this speed. In contrast, at 1600 RPM, the damping ratio fluctuates less significantly, increasing modestly with more passes but not reaching the levels observed at 1400 RPM. Overall, the findings indicate that both RPM and the number of passes play critical roles in determining the damping ratio, with an optimal combination observed at 1400 RPM and two passes [33]–[35].

The data at a traverse speed of 15 mm/min shows the impact of varying rotational speeds (RPM) and the number of passes on the damping ratio. At 1000 RPM, the damping ratio increases significantly with the second pass, reaching a peak of 4.74%, before slightly decreasing to 3.86% with the third pass. This indicates an optimal damping performance at two passes. At 1200 RPM, the damping ratio gradually improves with additional passes, increasing from 2.72% after the first pass to 3.27% after the third pass. For 1400 RPM, the damping ratio initially dips to 3.34% at two passes but rises to 4.43% at three passes, suggesting enhanced vibration reduction with increased processing passes at this speed. However, at 1600 RPM, the damping ratio does not follow a

consistent trend; it begins at 3.09% for the first pass, drops to 2.41% at two passes, and rises to 3.37% at three passes.

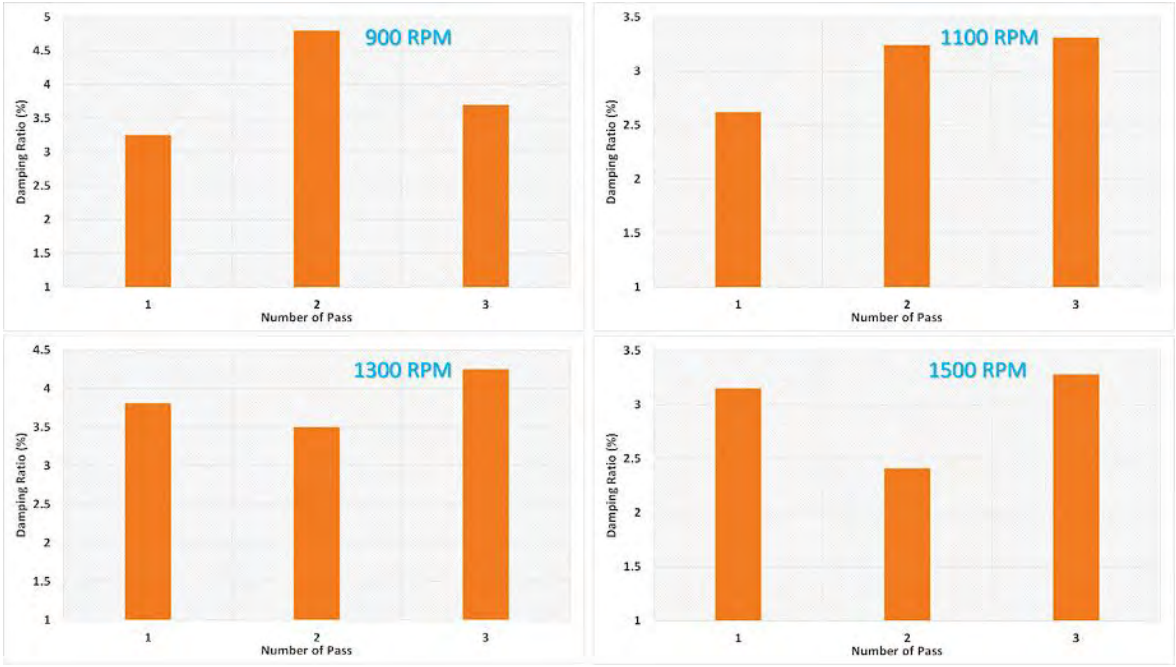


Fig. 7. Sample's damping ratio at 15 mm/min traverse speed

The data at a traverse speed of 20 mm/min reveals how rotational speed (RPM) and the number of passes affect the damping ratio. At 1000 RPM, the damping ratio increases significantly with two passes, reaching 4.48%, before slightly decreasing to 3.02% with the third pass. This suggests an optimal damping effect with two passes at this speed. For 1200 RPM, the damping ratio is initially high at 3.47% for the first pass and reaches a maximum of 3.59% at two passes before dropping to 2.97% at the third pass. At 1400 RPM, there is a notable decrease from 3.11% after the first pass to 2.39% at two passes, with a slight recovery to 2.76% after the third pass.

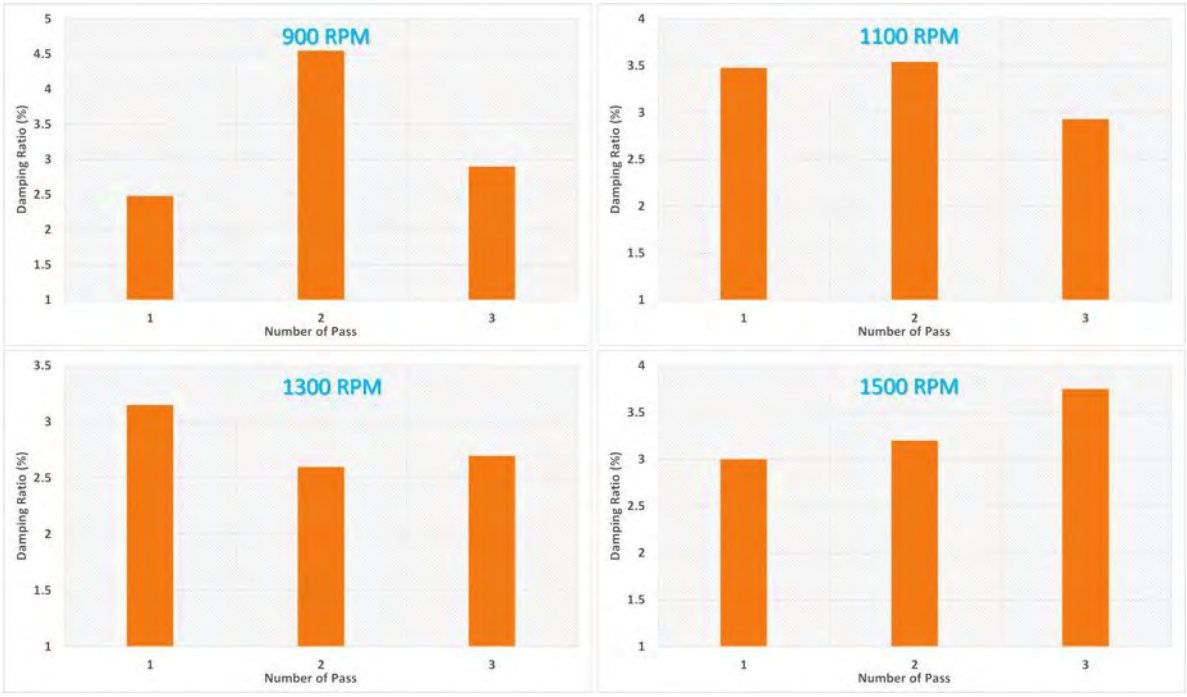


Fig. 8. Damping capacity of the samples at a traverse speed of 20 mm/min.

Meanwhile, at 1600 RPM, the damping ratio gradually increases from 3.05% at one pass to 3.74% at three passes, indicating improved damping properties with more passes at higher speeds. Overall, these results show that both RPM and the number of passes influence the damping performance, with the best performance observed at 1000 RPM with two passes and at 1600 RPM with three passes under a traverse speed of 20 mm/min.

The samples' natural frequency drops according to the increase in the number of passes. The instrument's recurring agitation causes the disintegration of material particles, leading to a loss in stiffness and the subsequent generation of this phenomenon. On the other hand, increasing the number of passes leads to samples that have a greater damping ratio. The agitating movement enhances the grain structure, hence augmenting the presence of imperfections and enhancing its efficacy in catching and absorbing vibrations. Similarly, when the number of passes grows, the sample loss factor also increases. The reason for the increase in frictional losses is due to the presence of a more precise grain structure. The loss factor, on the other hand, quantifies the amount of energy that is converted into heat during vibration. Also, the retained modulus of samples drops with increasing pass count. Deterioration of the grain structure, which results in reduced elasticity, is a likely cause. If we increase the number of passes, we get a similar trend in the samples' loss modulus. The fundamental rationale for this occurrence is provided by the loss modulus, which measures the energy dissipation that occurs during vibration; materials with finer grain patterns show bigger levels of frictional losses.

Table 2. Significant process parameters of the FSP Process [36-38]

Rotational Speed	Number of Passes	Transverse Speed	Damping Ratio (ζ)	Loss Factor	Shear Modulus
1100 rpm	3	20 mm/min	2.98	0.058	26.12 MPa
900 rpm	3	15 mm/min	3.57	0.072	25.91 MPa

Table 2 provides a concise overview of the variations in the dynamic characteristics of the samples at various RPMs. Rotational speed plays a crucial role in determining the heat generation and plastic deformation during the Friction Stir Processing (FSP) process. At a higher rotational speed of 1100 rpm, the damping ratio is lower (2.98%) compared to 3.57% at 900 rpm. This reduction in damping ratio at higher speeds can be attributed to the increased thermal input, which may result in finer grain structures but potentially reduces the material's ability to dissipate energy. The loss factor, which represents the material's capacity to absorb vibrational energy, is also lower at 1100 rpm (0.058) than at 900 rpm (0.072), indicating that slower rotational speeds may enhance energy dissipation. In both cases, three passes were used. Multiple passes generally improve the homogeneity of the processed zone and help in refining the microstructure further. A refined and homogeneous microstructure often leads to improved mechanical properties, such as better damping characteristics and enhanced shear modulus. Thus, conducting multiple passes ensures a more uniform material structure, leading to consistent mechanical property results across different speeds. The transverse or traverse speed, which represents the tool's movement along the workpiece, influences the heat input and material flow characteristics. A slower traverse speed (15 mm/min) allows for more heat accumulation, potentially resulting in a softer, more ductile material, as seen with the higher damping ratio (3.57%) and loss factor (0.072) at this speed. In contrast, a faster traverse speed (20 mm/min) reduces the heat input per unit length, leading to a relatively lower damping ratio (2.98%) and loss factor (0.058). This difference is because the lower heat input at higher traverse speeds tends to produce a stiffer material structure, slightly decreasing its ability to dissipate vibrational energy. The shear modulus values are relatively close for both conditions (26.12 MPa at 1100 rpm and 25.91 MPa at 900 rpm), though a slight increase is observed at the higher speed of 1100 rpm. This suggests that the stiffer material structure obtained at higher rotational and transverse speeds may slightly enhance the shear modulus. However, the difference is not substantial, indicating that the FSP process has a limited but positive impact on shear modulus at these parameter settings.

3.1 Mechanical Properties

In friction stir surface processing (FSP), the primary mechanism that strengthens the material is grain refinement. By using a rotating tool to generate heat and mechanical deformation, FSP produces a fine, uniform grain structure, which directly impacts the mechanical properties of the material. Initially, the Al-6061 alloy has a relatively coarse grain structure, with an average grain size of about 142 μm and an aspect ratio of 32.3%. Grain size and aspect ratio are key factors in determining the mechanical behavior of metals: smaller, more equiaxed (rounded) grains generally improve strength and ductility. After three passes of FSP, the grain size is reduced to just 12.92 μm, and the aspect ratio increases to 91.8%, indicating that the grains are now more uniform and compact. This fine-grained structure enhances the material's mechanical performance by creating more grain boundaries, which act as barriers to dislocation movement (dislocations are defects in the crystal structure that lead to deformation).

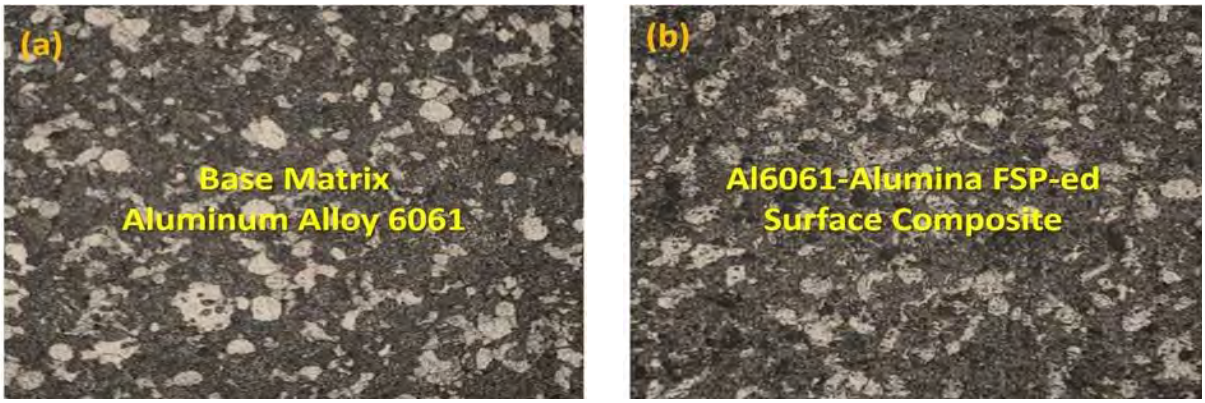


Fig. 9. Optical microscope analysis (a) Base Alloy and (b) FSP-ed Composite

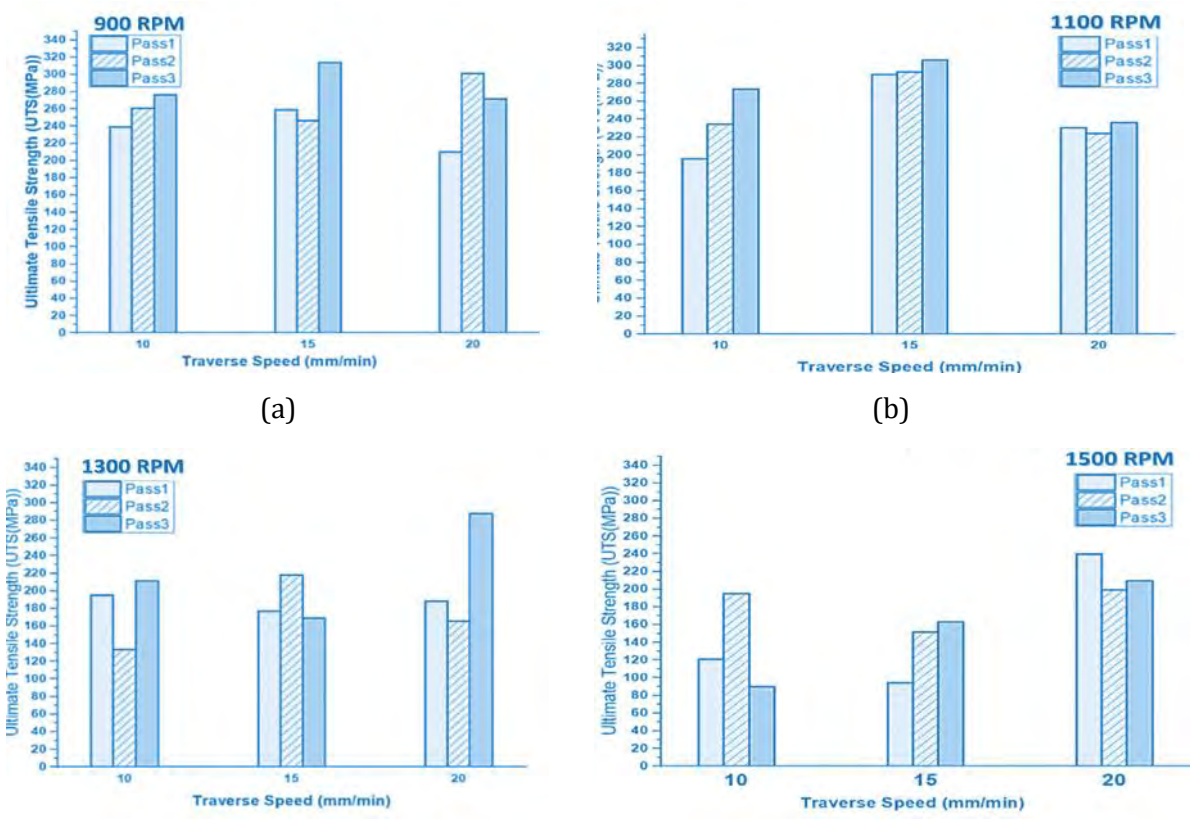


Fig. 10. Tensile Strength of the specimens at different RPM (a) 900 RPM, (b) 1100 RPM, (c) 1300 RPM and (d) 1500 RPM

The microstructure images in Figure 9 confirm this refinement, showing that FSP successfully produces a finer grain structure. This refined microstructure has a direct impact on the material's ultimate tensile strength (UTS) and yield strength (YS). The findings suggest that as the rotational speed of the FSP tool increases, more heat is generated, which facilitates dynamic recrystallization—a process where the grains are continuously broken down and reformed into smaller grains. The combination of heat and mechanical action at higher speeds accelerates this process, leading to a more uniform microstructure and, consequently, stronger material properties. Higher rotational speeds not only refine the grain structure but also improve the material's resistance to deformation, enhancing its yield strength. A finer microstructure limits dislocation motion and requires greater force to initiate plastic deformation, thereby increasing yield strength. This makes the material stronger and more durable, as it can withstand greater forces before it starts to deform. In summary, the increased rotational speeds in FSP contribute to a more refined grain structure, which strengthens the material by impeding dislocation movement, enhancing both UTS and YS.

The observed decrease in yield strength (YS) and ultimate tensile strength (UTS) with an increasing number of FSP passes can be understood in terms of the effects of excessive grain refinement and heat input. In FSP, each pass of the tool applies heat and mechanical agitation to the material, breaking down grains and refining the microstructure. However, after a certain point, too many passes can lead to over-processing of the material. With repeated agitation, the grains can become excessively fragmented, which may lead to the formation of ultra-fine or even amorphous regions that lack the cohesive crystal structure needed to maintain high strength. In a finely grained microstructure, dislocations (defects within the crystal lattice) have a harder time moving, which generally improves strength. However, if the grains become too small or disordered, the material may lose its ability to effectively carry loads due to compromised grain boundaries, which weakens its structural integrity and leads to a reduction in YS and UTS. Similarly, reducing the feed rate (i.e., slowing down the tool's movement across the surface) increases the duration of heat exposure per unit area. This slower rate of travel means that heat dissipates more slowly, allowing for prolonged thermal exposure. When the material remains hot for too long, it can cause excessive grain growth or even coarsening in some cases, leading to a reduction in strength. Prolonged heating also reduces the effectiveness of grain boundary strengthening, as it allows grains to relax or reorient in ways that make them less resistant to deformation [39]–[41].

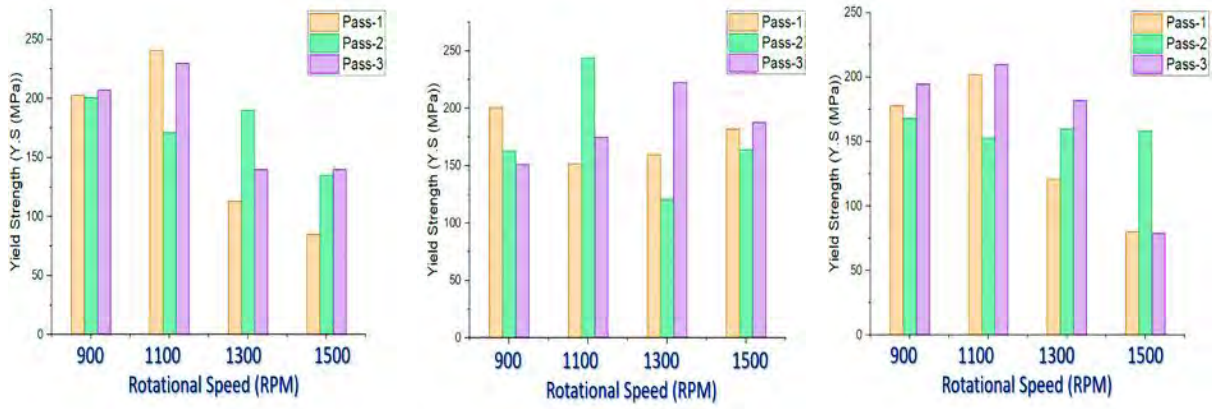


Fig. 11. Yield Strength of the specimens at different RPM and no. of pass

3.2 Predicted Results

The research effort focuses on employing four distinct machine-learning models to predict specific features of processed data, including Ultimate Tensile Strength (UTS), Yield Strength (YS), natural frequency, and damping ratio.

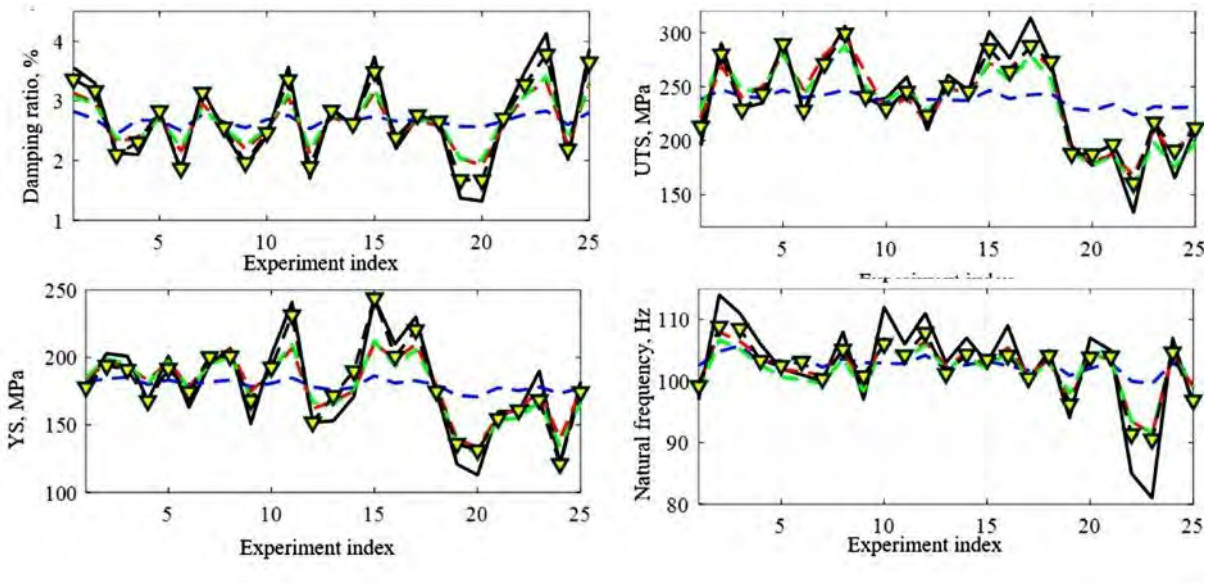


Fig. 12. Training process of experimental and predicted data

The first model is an independent Long Short-Term Memory (LSTM) model, which learns to make predictions based solely on the input data without any additional optimization techniques. The following three models build upon the LSTM framework by incorporating various optimization approaches. These optimized models include LSTME-FHO, which enhances the LSTM with the Firefly Algorithm, LSTME-SRS that utilizes Particle Swarm Optimization, and LSTME-DMOA, which applies the Differential Multi-Objective Algorithm for optimization.

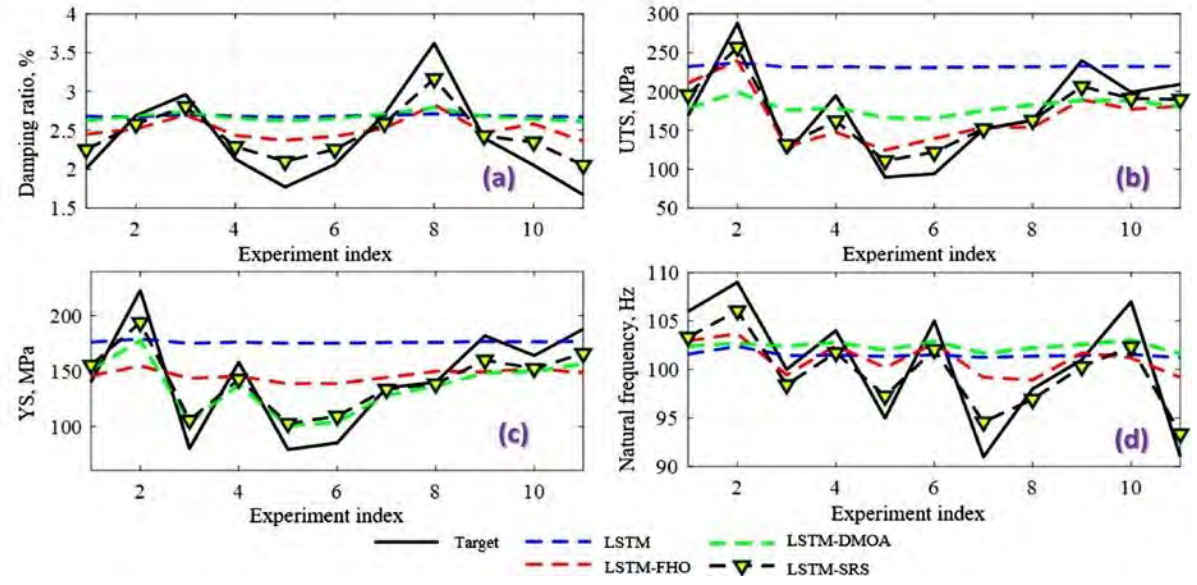


Fig. 13. Testing process of experimental and predicted data

To evaluate the models' performance, empirical data is divided into two parts: 70% of the data is allocated for training the models, allowing them to learn patterns and adjust their parameters, while the remaining 30% is reserved for testing, which assesses how well the trained models can predict outcomes for unseen data. The effectiveness of each model is measured using three accuracy metrics: Root Mean Square Error (RMSE), which quantifies the difference between predicted and actual values; Coefficient of Determination (R^2), reflecting the proportion of variance in the dependent variable explained by the independent variables; and Mean Absolute Error (MAE), which indicates the average absolute differences between predictions and actual values. Through this research, the aim is to enhance prediction accuracy for important engineering characteristics by exploring the capabilities of various machine-learning models and their optimization technique.

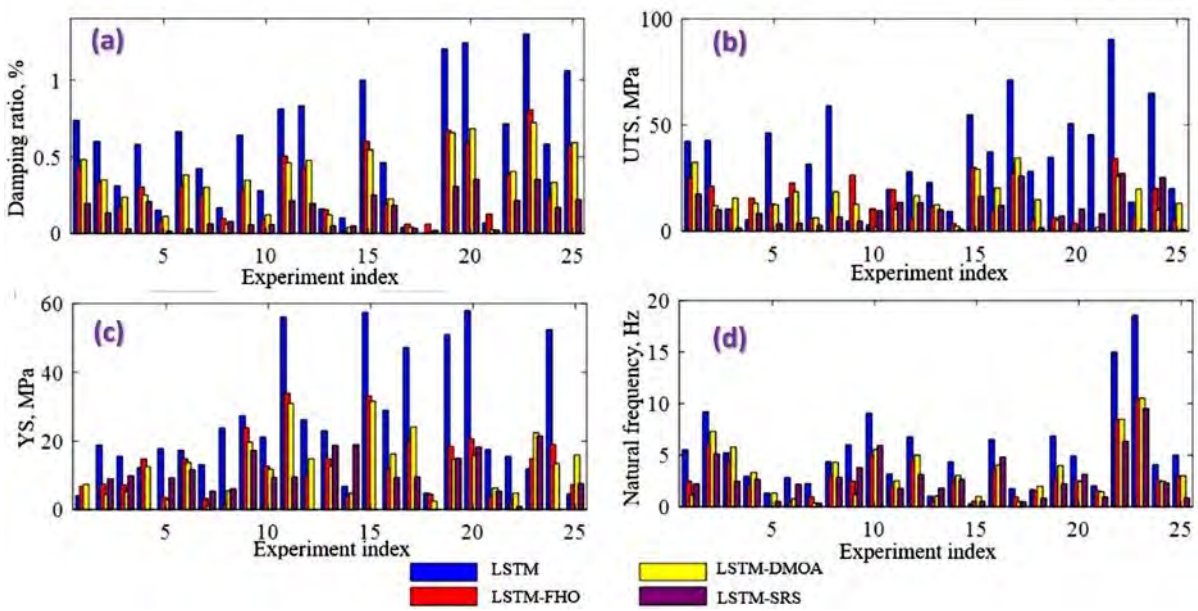


Fig. 14. Training processing error of experimental and predicted data

The findings of the research demonstrate a strong correlation between the experimentally acquired data and the predicted outcomes generated by the machine learning models. Among the models tested, the LSTME-SRS model outperformed all others, indicating its effectiveness in making accurate predictions. It was followed closely by the LSTME-DMOA and LSTME-FHO models, which also showed commendable performance. In contrast, the independent LSTM model consistently exhibited the least alignment with the experimental data during both the training and testing phases, indicating its limitations in capturing the underlying patterns in the data. Furthermore, an analysis of absolute errors revealed that the LSTME-SRS model maintained the lowest error across all characteristics examined, reinforcing its superior predictive power. This consistent performance supports the earlier findings of strong correlation. Additionally, when comparing the absolute errors of the LSTME-SRS model with those of the LSTM model, it was noted that the errors produced by the LSTME-DMOA and LSTME-FHO models were relatively small, although they did not surpass the accuracy of the LSTME-SRS.

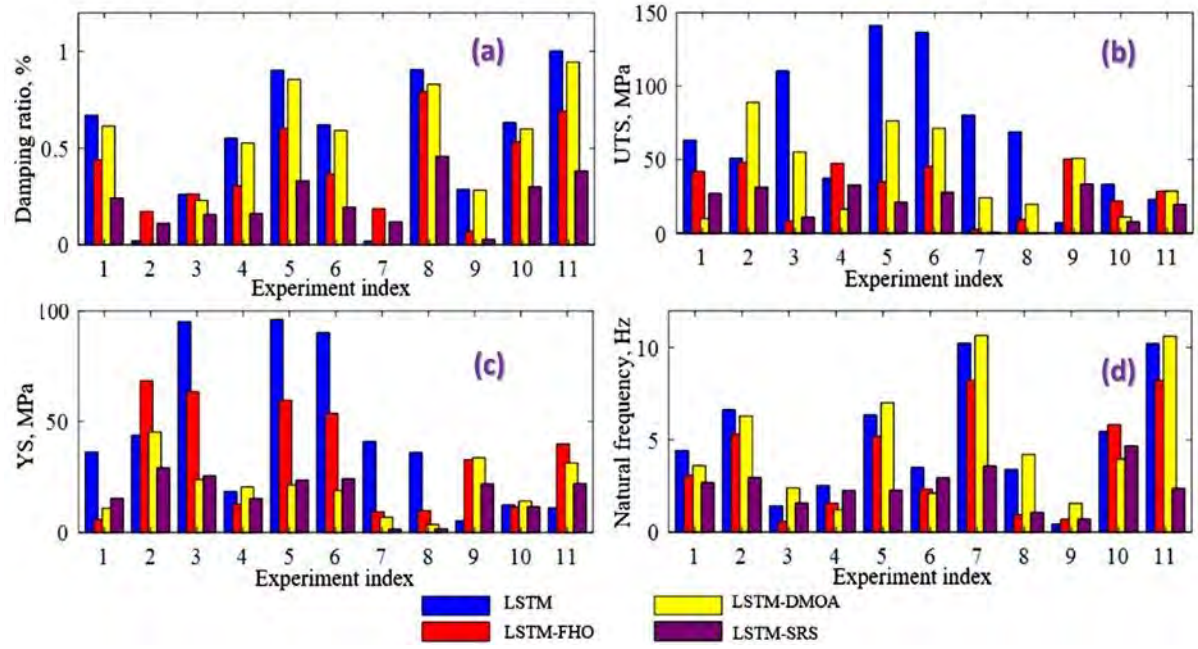


Fig. 15. Testing processing error of experimental and predicted data

Overall, these results highlight the efficacy of optimization techniques in enhancing the predictive capabilities of LSTM models, particularly the advantages offered by the LSTME-SRS approach. The LSTME-SRS algorithm exhibits exceptional efficacy in accurately predicting various attributes of processed data, as evidenced by its ability to generate minimal absolute error in predictions. The results of this study indicate that LSTME-SRS consistently outperforms the other models in terms of predictive accuracy, highlighting its capability to effectively anticipate the features of the processed data.

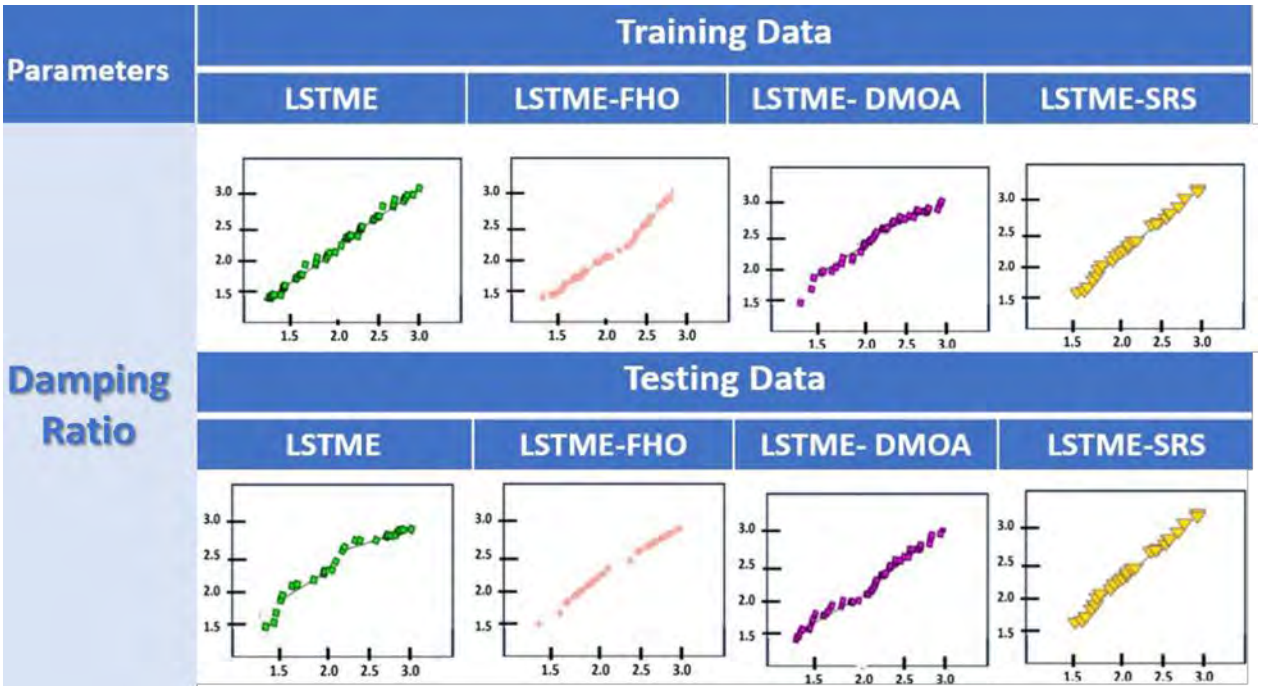


Fig. 16. QQ plots for damping ratio during training and testing of data

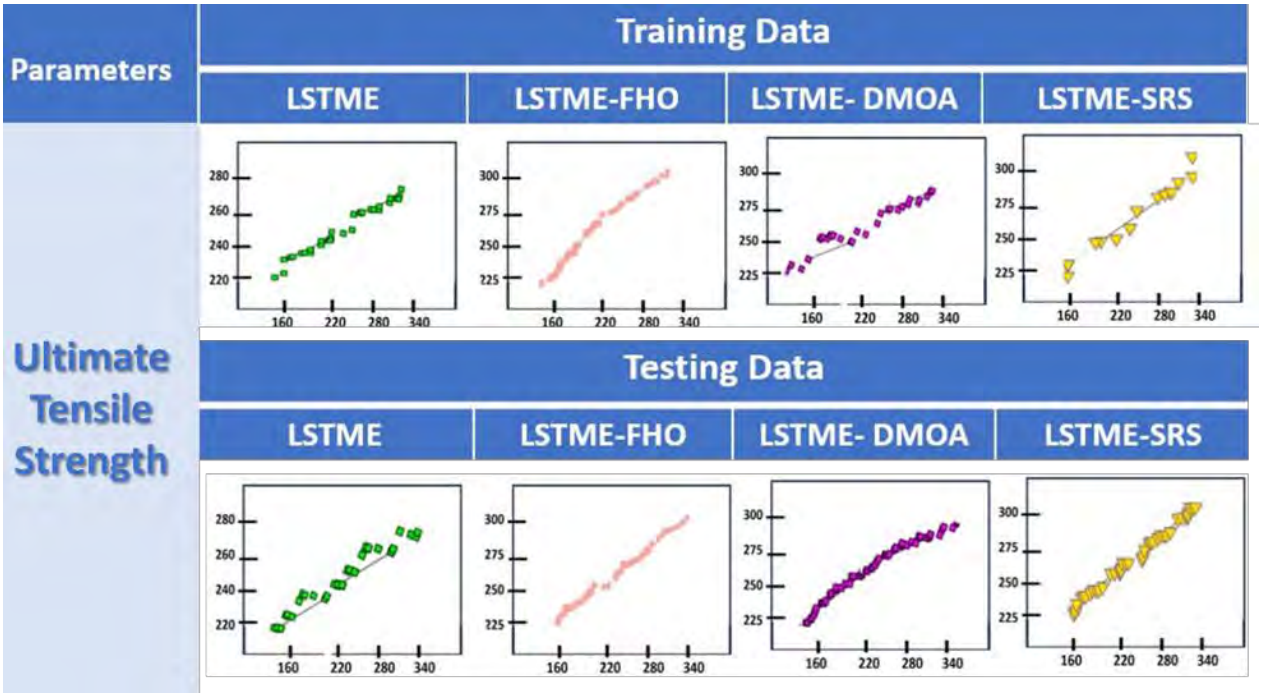


Fig.17. QQ plots for ultimate tensile strength during training and testing of data

When comparing the QQ (Quantile-Quantile) plots illustrated in Figures 16-19, it becomes apparent that there is a stronger correlation between the predicted and actual data for the LSTME-DMOA

and LSTME-FHO models when assessed against the LSTME-SRS model. This suggests that while LSTME-SRS remains the top performer, the LSTME-DMOA and LSTME-FHO models also establish a relatively robust relationship with the experimental data. The QQ plots provide a visual representation of how closely the predicted values align with the actual values, reinforcing the findings that LSTME-SRS is superior in accuracy, but indicating that the other two models still maintain meaningful predictive capabilities.

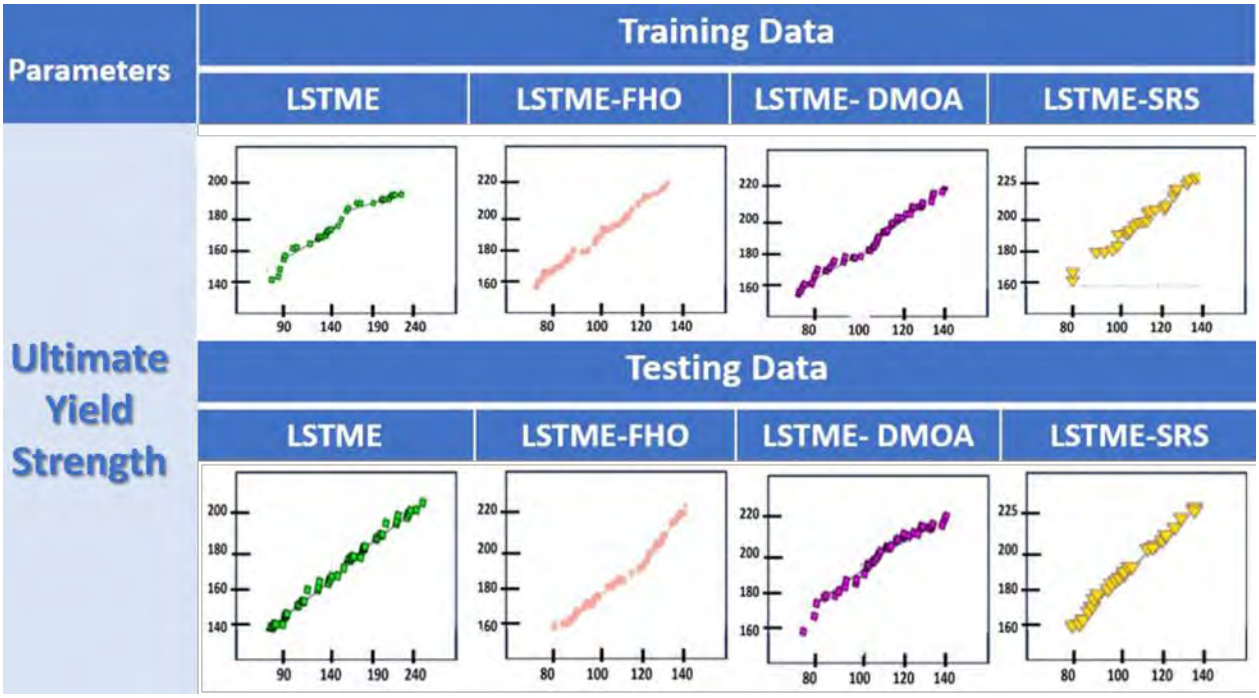


Fig. 18: QQ plots for ultimate yield strength during training and testing of data

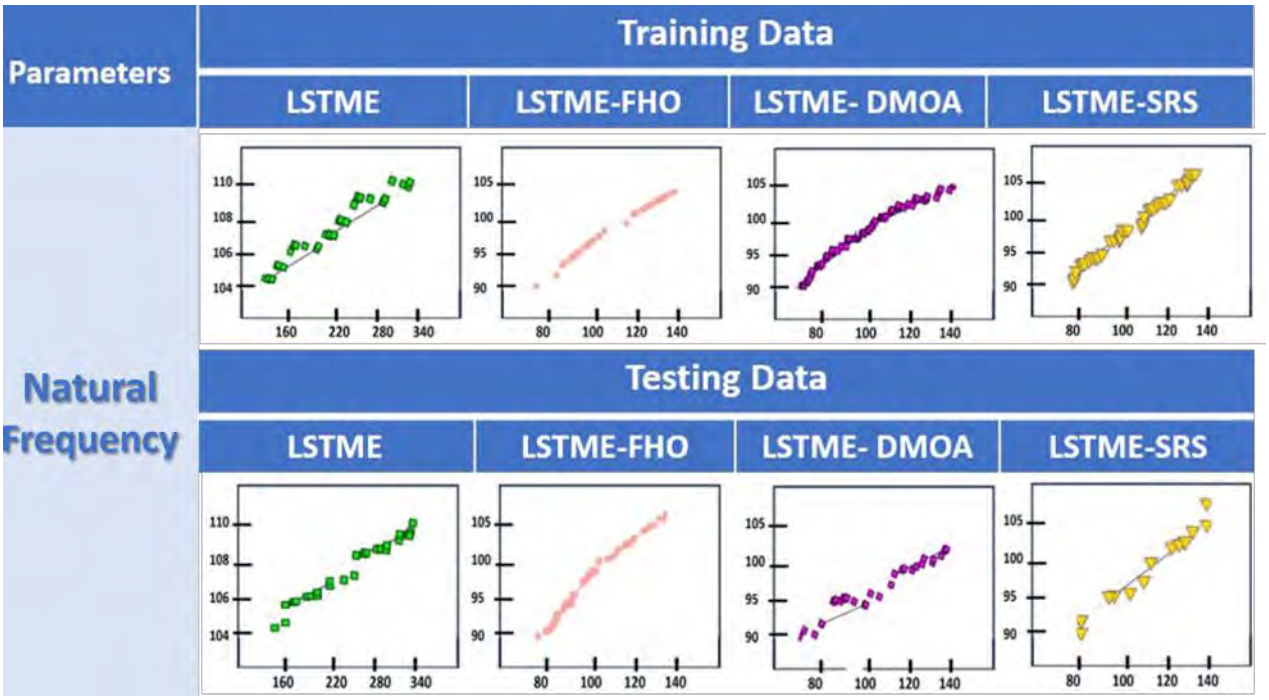


Fig. 19. QQ plots for natural frequency during training and testing of data

The predictive accuracy of the LSTME-SRS model is evidenced by the close proximity of its predicted outcomes—represented in yellow—to the diagonal lines on the plot, which typically signify ideal predictions where the predicted values match the actual experimental results

perfectly. In contrast, the predictions generated by the independent LSTM model, depicted in a light green, show a greater deviation from these diagonal lines, highlighting its poorer performance and accuracy. This noticeable disparity in prediction accuracy further reinforces the conclusion that the LSTME-SRS model significantly outperforms the independent LSTM, LSTME-FHO, and LSTME-DMOA models. The assessment of model performance through various metrics—such as the coefficient of determination (R^2), mean absolute error (MAE), and root mean square error (RMSE)—further substantiates the findings. These metrics quantitatively confirm that LSTME-SRS consistently yields higher accuracy, characterized by lower error values and a stronger fit to the experimental data, distinguishing it as the most reliable model among those tested[1], [42], [43].

Table 3 presents the results in a concise format for your convenience. The provided data highlights the performance metrics of four machine learning models—LSTME-SRS, LSTME-FHO, LSTME-DMOA, and the independent LSTM model—across four different predictive tasks: damping ratio (ζ), natural frequency, ultimate tensile strength (UTS), and yield strength (YS). The metrics evaluated include the coefficient of determination (R^2), root mean square error (RMSE), and mean absolute error (MAE) for both training and testing datasets. For the damping ratio, the LSTME-SRS model achieved an impressive R^2 value of 0.992 during training, indicating a strong fit to the data, and maintained a high R^2 of 0.985 during testing. Its RMSE and MAE values were also the lowest among all models, demonstrating superior predictive accuracy. The LSTME-DMOA model followed closely with an R^2 of 0.999 in training, although its RMSE and MAE were slightly higher, indicating some discrepancy in predictions. The LSTME-FHO model, while still effective, showed lower performance, particularly in testing with an R^2 of 0.823, highlighting its limitations in capturing the damping ratio accurately. In stark contrast, the independent LSTM model exhibited the weakest performance, with the lowest R^2 values and highest error metrics across both training and testing phases.

Table 3. Machine-learning model and performance measures

Properties	Models	Training Data			Testing Data		
		R^2	RMSE	MAE	R^2	RMSE	MAE
Damping ratio (ζ)	LSTME-SRS	0.992	0.172	0.138	0.985	0.258	0.227
	LSTME-FHO	0.988	0.374	0.307	0.823	0.459	0.405
	LSTME-DMOA	0.999	0.387	0.316	0.977	0.589	0.499
	LSTME	0.746	0.688	0.564	0.724	0.629	0.5336
Natural Frequency (Hz)	LSTME-SRS	0.977	2.803	2.221	0.952	2.684	2.463
	LSTME-FHO	0.964	5.756	4.456	0.710	4.692	3.805
	LSTME-DMOA	0.923	5.582	4.413	0.845	5.846	4.876
	LSTME	0.668	6.674	5.234	0.541	5.837	4.959
Ultimate Tensile Strength (MPa)	LSTME-SRS	0.964	12.384	9.687	0.911	22.706	19.277
	LSTME-FHO	0.899	16.783	1.392	0.704	65.103	30.723
	LSTME-DMOA	0.895	17.003	14.367	0.885	49.306	41.109
	LSTME	0.788	40.766	34.120	0.721	80.692	68.359
Yield Strength (MPa)	LSTME-SRS	0.966	10.824	8.497	0.953	19.583	17.439
	LSTME-FHO	0.902	15.367	12.518	0.756	40.784	33.336
	LSTME-DMOA	0.943	15.062	12.573	0.934	24.016	20.947
	LSTME	0.882	30.660	25.271	0.861	55.020	44.185

In predicting natural frequency, the LSTME-SRS model again led the pack with an R^2 of 0.977 during training and 0.952 in testing, along with relatively low RMSE and MAE values. The LSTME-FHO and LSTME-DMOA models performed adequately but had noticeably higher errors, indicating a greater challenge in accurately predicting this characteristic compared to the damping ratio. The independent LSTM model struggled here as well, with a low R^2 of 0.541 in testing. When assessing ultimate tensile strength, the LSTME-SRS model continued to perform strongly with an R^2 of 0.964 in training, although the RMSE and MAE were considerably higher than in previous metrics, suggesting the inherent complexity of this prediction task. The LSTME-FHO and LSTME-DMOA models showed significant errors during testing, especially the LSTME-FHO, which had an RMSE of

65.103, indicating a poor fit for UTS predictions. Again, the independent LSTM model showed the least effectiveness, reflected in its high error metrics. Lastly, for yield strength, the LSTME-SRS model again outperformed the others with an R^2 of 0.966 in training and 0.953 in testing, coupled with lower RMSE and MAE values, affirming its reliability. The LSTME-DMOA model also performed well, though it showed a slight increase in error metrics compared to its training performance. The independent LSTM model's performance remained consistently poor across all tasks. Overall, the results clearly indicate that the LSTME-SRS model is the most effective among the models tested, achieving high R^2 values and low error metrics across various characteristics. The integration of optimization techniques in models like LSTME-FHO and LSTME-DMOA enhances predictive accuracy compared to the independent LSTM model, yet they still fall short of the performance demonstrated by LSTME-SRS, particularly in more complex prediction tasks like ultimate tensile strength and yield strength.

4. Conclusions

The study introduces a novel approach to predicting the mechanical properties of aluminum alloys processed through friction stir processing (FSP) by employing a Special Relativity Search Optimized Long Short-Term Memory (LSTME-SRS) model. This study employed a CNC milling machine to conduct friction stir processing on Al-6061 aluminum alloy, utilizing aluminum oxide nanoparticles as reinforcements. The incorporation of alumina nanoparticles and controlled adjustments to FSP parameters, such as rotational speed and the number of passes, significantly impacted the material's damping capacity, yield strength, and tensile strength. Using a machine learning approach, specifically the SRS-optimized LSTME model, provided highly accurate predictions of these properties, which validated the experimental findings and highlighted the effectiveness of the optimization. The following conclusions were mentioned as follows:

- The highest damping capability was achieved with a rotational speed of 900 rpm and a traverse speed of 15 mm/min, where the damping ratio (ζ) reached 3.57, and the loss factor was 0.072.
- This optimal condition allowed the material to absorb and mitigate vibrations more effectively, largely due to a fine and evenly dispersed grain structure, enhanced by alumina nanoparticle reinforcement.
- Higher rotational speeds led to increased thermal energy, which refined the grain structure and made the material stronger yet less rigid.
- The shear modulus decreased to 25.91 MPa at 900 rpm and further dropped at higher rotational speeds, indicating a balance between strength and flexibility as rotational speed increased.
- Increased rotational speeds improved yield strength (YS) and ultimate tensile strength (UTS). The optimized LSTME model achieved R^2 values of 0.953 for YS and 0.911 for UTS, demonstrating a strong correlation between speed and material strength. This improvement results from grain refinement, which increased resistance to deformation.
- The SRS-optimized LSTME model excelled in prediction accuracy, outperforming other models with R^2 values between 0.911 and 0.992 for UTS, YS, natural frequency, and damping ratio.
- The SRS optimization reduced the root mean square error (RMSE) and mean absolute error (MAE) by up to 71.86% and 71.61%, respectively. This demonstrates the model's robustness in forecasting material properties effectively.
- More friction-stir processing passes led to a reduction in natural frequency and stiffness, while increasing the damping ratio and loss modulus. With more passes, energy dissipation during vibrations increased, as reflected by a rise in the loss modulus, which indicates more effective damping capability. Each pass further refined the grain structure, enhancing the presence of microscopic imperfections that improved vibration absorption.
- With increased RPM, there was a noted rise in damping capacity, as the refined grain structure introduced by higher rotational speeds enabled the material to better absorb and dissipate energy. The data suggest that higher thermal energy generation during FSP aids grain breakdown, yielding a finely tuned microstructure ideal for high damping applications.

- The friction-stir processing led to significant grain refinement, reducing the average grain size from an initial 142 μm to 12.92 μm after three FSP passes, and increasing the aspect ratio from 32.3% to 91.8%. This transformation in microstructure substantially improved the material's strength and deformation resistance.

5. Applications

- Al-6061/alumina composites are suitable for airplane frames, fuselage structures, and engine parts due to their lightweight and high strength. The LSTME-SRS model predicts and optimizes mechanical parameters, improving performance and fuel economy.
- Advanced composites increase vehicle performance by decreasing weight and preserving strength and durability. Structural components, chassis sections, and body panels may benefit from improved damping for ride comfort and noise reduction.
- High-performance sporting equipment including bicycle frames, golf clubs, and tennis rackets used advanced composites. Composites' lightweight and enhanced mechanical qualities help shock absorption and vibration damping.
- Construction companies use the study's findings to create lightweight, robust materials for buildings, bridges, and other infrastructure. Processing parameters enhance mechanical properties for safer and more efficient designs.
- Al-6061/alumina composites are suited for maritime applications such as boat hulls and harsh environment components because of their corrosion resistance and mechanical strength. These materials are optimized for marine durability and performance using predictive modeling.
- Aluminum composites' biocompatibility and mechanical qualities are used to make medical devices and implants. Predicting and controlling material qualities may improve surgical equipment and prostheses.
- Manufacturing processes may use the LSTME-SRS model to anticipate and optimize FSP parameters in real time. This boosts manufacturing efficiency, eliminates waste, and increases product quality.

6. Future Perspective

- The LSTME-SRS model can be applied to other metal matrix composites (MMCs) and materials besides Al-6061. This demonstrates the model's versatility across numerous material systems, perhaps leading to practical applications.
- Real-time industrial process input may increase predictive model accuracy and adaptability. This connectivity would allow real-time processing setting changes during FSP, improving material properties and production efficiency.
- Tool geometry, cooling methods, and post-processing treatments may affect composite mechanical properties in future study. Understanding these components may enhance material performance.
- Long-term studies on treated materials' durability and fatigue resistance in various environments would provide light on their practical performance. This may help assess the durability and reliability of composite components.
- Hybrid reinforcing systems that combine alumina with nanoparticles or fibers may improve composite mechanical properties. To increase performance, research may focus on reinforcement interactions.
- Machine learning advances may improve LSTME-SRS predictions. Novel algorithms and hybrid models may enhance material quality and processing predictions.

References

[1] Subramani N, Haridass R, Pramodh S, Anand AP, Manikandan N. Mechanical strength analysis of Al6061 & Al2024 based metal matrix composite prepared through stir casting method. Mater Today Proc. 2021;47:4513-7. https://doi.org/10.1016/j.matpr.2021.05.417

[2] Subburaj A, Marcel A, Antony M, Decruz J. Mechanical characterization and micro-structural analysis on AA2024 hybrid composites reinforced with WC and graphene nanoparticles. Trans Indian Inst Met. 2022;75(7):1721-30. https://doi.org/10.1007/s12666-021-02488-z

[3] Kumar D, Singh S, Angra S. Morphology and corrosion behavior of stir-cast Al6061-CeO2 nanocomposite immersed in NaCl and H2SO4 solutions. Evergreen J Carbon Resour Sci Green Asia Strategy. 2023;10(1):94-104. https://doi.org/10.5109/6781054

[4] Kumar D, Kumar R, Thakur L. A review on environment-friendly and lightweight magnesium-based metal matrix composites and alloys. Mater Today Proc. 2020;xxxx. https://doi.org/10.1016/j.matpr.2020.07.424

[5] Yang X, Zhang Y, Huang J, Liu J, Chen J, Li T. Interfacial microstructure evolution and mechanical properties of carbon fiber reinforced Al-matrix composites fabricated by a pressureless infiltration process. Mater Sci Eng A. 2024;891:145968. https://doi.org/10.1016/j.msea.2023.145968

[6] Raja R, et al. Development of Al-Mg2Si alloy hybrid surface composites by friction stir processing: Mechanical, wear, and microstructure evaluation. Materials. 2023;16:4131. https://doi.org/10.3390/ma16114131

[7] Khan MM, Nisar M. Effect of in situ TiC reinforcement and applied load on the high-stress abrasive wear behaviour of zinc-aluminum alloy. Wear. 2022;488-9:204082. https://doi.org/10.1016/j.wear.2021.204082

[8] Ramezani NM, Davoodi B. Evaluating the influence of various friction stir processing strategies on surface integrity of hybrid nanocomposite Al6061. Sci Rep. 2024;xxxx:1-15.

[9] Aydin F. Effect of solid waste materials on properties of magnesium matrix composites: A systematic review. J Magnes Alloys. 2022;xxxx. https://doi.org/10.1016/j.jma.2022.09.005

[10] Konovalova V. The effect of temperature on the corrosion rate of iron-carbon alloys. Mater Today Proc. 2021;38:1326-9. https://doi.org/10.1016/j.matpr.2020.08.094

[11] Saravanan C, et al. Investigation on the mechanical, tribological, morphological and machinability behavior of stir-casted Al/SiC/Mo reinforced MMCs. Mater Today Proc. 2020;21:1-10.

[12] Devanathan C, Babu AS. Friction stir welding of metal matrix composite using coated tool. Procedia Mater Sci. 2014;6:1470-5. https://doi.org/10.1016/j.mspro.2014.07.126

[13] Sharma AK, Bhandari R, Aherwar A, Rimašauskiene R. Matrix materials used in composites: A comprehensive study. Mater Today Proc. 2020;21:1559-62. https://doi.org/10.1016/j.matpr.2019.11.086

[14] Ahmed MR, Moosa A, Ramazani SA, Kubba FA. Synergetic effects of graphene and nonfunctionalized carbon nanotubes hybrid reinforced epoxy matrix on mechanical, thermal and wettability properties of nanocomposites. Am J Mater Sci. 2017;7(1):1-11.

[15] Venkateswarlu K, Ramakrishna K. Recent advances in phase change materials for thermal energy storage: A review. J Braz Soc Mech Sci Eng. 2022;44(1):1-17. https://doi.org/10.1007/s40430-021-03308-7

[16] Kumar S, Kumar A, Vanitha C. Corrosion behaviour of Al7075/TiC composites processed through friction stir processing. Mater Today Proc. 2019;15:21-9. https://doi.org/10.1016/j.matpr.2019.05.019

[17] Reddy PS, Kesavan R, Ramnath BV. Investigation of mechanical properties of aluminium 6061-silicon carbide, boron carbide metal matrix composite. Silicon. 2018;10(2):495-502. https://doi.org/10.1007/s12633-016-9479-8

[18] Kumar D, Singh S, Angra S. Synergistic effects of graphene and ceria nanoparticulates on microstructure and mechanical behavior of stir-cast hybrid aluminum composite. Trans Indian Inst Met. 2024;xxxx:1-15. https://doi.org/10.1007/s12666-024-03368-y

[19] Zheng T, Wang L, Liu J. Corrosion inhibition of levofloxacin and Ce(NO3)3 for AA2024-T4 in 3.5% NaCl. Mater Today Proc. 2020;2782(3):xxxx. https://doi.org/10.1080/1478422X.2019.1681152

[20] Rana H, Badheka V. Influence of friction stir processing conditions on the manufacturing of Al-Mg-Zn-Cu alloy/boron carbide surface composite. J Mater Process Technol. 2018;255:795-807. https://doi.org/10.1016/j.jmatprotec.2018.01.020

[21] Rajkumar V, Venkateshkannan M, Sadeesh P, Arivazhagan N. Studies on effect of tool design and welding parameters on the friction stir welding of dissimilar aluminium alloys AA 5052 - AA 6061. Procedia Eng. 2014;75:93-7. https://doi.org/10.1016/j.proeng.2013.11.019

[22] Ador SH, Kabir S, Ahmed F, Ahmad F, Adil S. Effects of minimum quantity lubrication (MQL) on surface roughness in milling Al Alloy 383/ADC 12 using nano hybrid cutting fluid. 2022;9(4):xxxx. https://doi.org/10.5109/6625790

[23] Sadiq TO, et al. Effect of different machining parameters on surface roughness of aluminium alloys based on Si and Mg content. J Braz Soc Mech Sci Eng. 2019;41(10):1-11. https://doi.org/10.1007/s40430-019-1948-8
[24] Bhatt RJ, Raval HK. Investigation on flow forming process using Taguchi-based grey relational analysis (GRA) through experiments and finite element analysis (FEA). J Braz Soc Mech Sci Eng. 2018;40(11):1-24. https://doi.org/10.1007/s40430-018-1456-2
[25] Hasan MS, Kordijazi A, Rohatgi PK, Nosonovsky M. Application of triboinformatics approach in tribological studies of aluminum alloys and aluminum-graphite metal matrix composites. Miner Met Mater Ser. 2022;1:41-51. https://doi.org/10.1007/978-3-030-92567-3_3
[26] Hasan MS, Wong T, Rohatgi PK, Nosonovsky M. Analysis of the friction and wear of graphene reinforced aluminum metal matrix composites using machine learning models. Tribol Int. 2022;170:107527. https://doi.org/10.1016/j.triboint.2022.107527
[27] Mahajan L, Bhagat S. Machine learning approaches for predicting compressive strength of concrete with fly ash admixture. Res Eng Struct Mater. 2022;xx:1-27.
[28] Prasad KA, John MRS. Optimization of external roller burnishing process on magnesium silicon carbide metal matrix composite using response surface methodology. J Braz Soc Mech Sci Eng. 2021;43(7):1-12. https://doi.org/10.1007/s40430-021-03069-3
[29] Bourkhani RD, Eivani AR, Nateghi HR. Through-thickness inhomogeneity in microstructure and tensile properties and tribological performance of friction stir processed AA1050-Al2O3 nanocomposite. Compos Part B. 2019;174:107061. https://doi.org/10.1016/j.compositesb.2019.107061
[30] Lorenzo-Martin MC, Ajayi OO. Surface layer modification of 6061 Al alloy by friction stir processing and second phase hard particles for improved friction and wear performance. J Tribol. 2014;136(4):1-6. https://doi.org/10.1115/1.4027860
[31] Vedabouriswaran G, Aravindan S. Development and characterization studies on magnesium alloy (RZ 5) surface metal matrix composites through friction stir processing. J Magnes Alloys. 2018;6(2):145-63. https://doi.org/10.1016/j.jma.2018.03.001
[32] Pelevin IA, et al. Selective laser melting of Al-based matrix composites with Al2O3 reinforcement: Features and advantages. 2021;1-18. https://doi.org/10.3390/ma14102648
[33] Aqida SN, Ghazali MI, Hashim J. Effect of porosity on mechanical properties of metal matrix composite: An overview. J Teknol. 2012;40:17-32. https://doi.org/10.11113/jt.v40.395
[34] Casati R, Vedani M. Metal matrix composites reinforced by nanoparticles: A review. 2014;65-83. https://doi.org/10.3390/met4010065
[35] Rajak DK, Pagar DD, Menezes PL, Linul E. Fiber-reinforced polymer composites: Manufacturing, properties, and applications. Polymers. 2019;11(10):xxxx. https://doi.org/10.3390/polym11101667
[36] Kaya N, Çetinkaya C, Karakoç H, Ada H. Effect of process parameters of Al5083/SiC surface composites fabricated by FSP on microstructure, mechanical properties and wear behaviors. Mater Chem Phys. 2024;315:128991. https://doi.org/10.1016/j.matchemphys.2024.128991
[37] Maqbool A, Lone NF, Ahmad T, Khan NZ, Siddiquee AN. Effect of hybrid reinforcement and number of passes on microstructure, mechanical and corrosion behavior of WE43 Mg alloy based metal matrix composite. J Manuf Process. 2023;89:170-81. https://doi.org/10.1016/j.jmapro.2023.01.070
[38] Kumar D, Kumar P. Microstructural, microhardness and electrical conductivity analysis of AD31T alloy processed by friction stir processing. 2024;xxxx. https://doi.org/10.1108/MMMS-01-2024-0025
[39] Romashkina A, Khovaiko M, Nemov A. Modelling of composite materials with thermoplastic matrices, carbon fibres, and nanoparticles. 2022;49(1):182-92.
[40] Kumar D, Singh S, Angra S. Effect of reinforcements on mechanical and tribological behavior of magnesium-based composites: A review. 2022;50(3):439-58.
[41] Kumar D, Angra S, Singh S. High-temperature dry sliding wear behavior of hybrid aluminum composite reinforced with ceria and graphene nanoparticles. Eng Fail Anal. 2023;151:107426. https://doi.org/10.1016/j.engfailanal.2023.107426
[42] Okafor CE, Okafor EJ, Ikebudu KO. Evaluation of machine learning methods in predicting optimum tensile strength of microwave post-cured composite tailored for weight-sensitiv e applications. Eng Sci Technol Int J. 2022;25:100985. https://doi.org/10.1016/j.jestch.2021.04.004
[43] Mahanta S, Chandrasekaran M, Samanta S, Arunachalam RM. EDM investigation of Al7075 alloy reinforced with B4C and fly ash nanoparticles and parametric optimization for sustainable production. J Braz Soc Mech Sci Eng. 2018;40(5):1-17. https://doi.org/10.1007/s40430-018-1191-8

Blank Page

Research on Engineering Structures & Materials
www.jresm.org

Research Article

Design and construction of full octagonal transducer-based low-cost dynamometer for measuring cutting forces during turning process

Agus Susanto [1,*,a], Budi Setiyana [2,b], Rifky Ismail [2,c], Risma Alfiyani [1,d]

[1]*Lab. of Precision Engineering, Faculty of Engineering, State Polytechnic of Madiun, Indonesia*
[2]*Department of Mechanical Engineering, Faculty of Engineering, Diponegoro University, Indonesia*

Article Info

Article History:

Received 14 Sep 2024

Accepted 22 Dec 2024

Keywords:

Full octagonal ring-shaped transducer;
Dynamometer;
Cutting forces;
Calibrations;
Machining tests

Abstract

This research focuses on developing a low-cost dynamometer based on a novel transducer, full octagonal ring, which was used to a sensing element of cutting forces in turning process. Various evaluations were performed which aiming to produce accurate dynamometer. Static analysis showed that proposed transducer was capable of withstanding normal load of 224 N and tangential load of 388 N with stress, strain, and deflection of 233 MPa, 9.9 × 10-4, and 8.5 × 10-2 mm, respectively. The dynamic aspect indicated that the natural frequency of developed dynamometer could stabilize at 3.85 kHz with stiffness constant, k, damping ratio, ζ, and damping coefficient, c, of 18.5 × 10-6 N/m, 1.04%, 16 N-s/m. The calibration tests showed that the dynamometer sensitivity for normal force was 78.1 mV/N with cross sensitivity and linearity error values of 10.2% and 0.63%. The sensitivity for tangential force was 85.7 mV/N with cross sensitivity and linearity errors of 8.98% and 3.7%. The performance evaluation of dynamometer through machining tests proved that measured cutting forces matched well to the simulation ones. The spectrum frequencies also revealed characteristics of turning process. These results show that the developed dynamometer in this study was valid used for measuring cutting forces.

© 2025 MIM Research Group. All rights reserved.

1. Introduction

The machining process is a sequential and systematic stage to transform raw materials into products that have functions in a mechanical system. This process is a chain of manufacturing processes that are widely used in industry, wheatear drilling, milling, sawing, grinding, broaching, shaping, and turning processes. From the various types of machining processes, turning is a cutting process that is almost certainly applied to manufacture a product in many industries [1], wheatear it is for processing automotive components [2], aircraft [3], railways [4,5], HDPE-100 pipe [6], and others [7]. The interaction of the cutting-tool and the workpiece during turning process produces cutting forces that induce vibration, deformation, raising cutting temperature, and accelerate tool wear during machining process [8–10]. The cutting forces, therefore, has direct implications for the success of the machining process.

When it is possible to measure the cutting forces during the machining accurately and interpret them correctly, then the machining process can be optimized, tool wear might be monitored in real time, and even cutting errors can be minimized [11,12]. Cutting forces during turning process are generally measured using a piezoelectric-based commercial table dynamometer, which are installed on the machine's tool-post [13–15]. Zheng et al. [14] clamped Kistler 9257 table

*Corresponding author: agus_eng.dept@pnm.ac.id
[a]orcid.org/0000-0001-9588-8484; [b]orcid.org/0000-0003-1498-0735; [c]orcid.org/0000-0003-0445-3405; [d]orcid.org/0009-0002-8586-6083
DOI: http://dx.doi.org/10.17515/resm2024.448st0814rs

dynamometer on the tool-post of CA6240 lathe machine for measuring forces during Titanium alloy machining. Fodor et al. [16] measured the cutting forces on dried orthogonal turning Aluminum alloy of AL2024-T351 using a Kistler 9129 dynamometer. A six-component table dynamometer was also used to acquire the cutting forces in hard turning of chrome molybdenum 42CrMo24-type alloy by [17]. However, the price of piezoelectric-based dynamometers, which reaches thousands of dollars, is not seen as cheap by some campus academics, researchers, and industrial operators to implement a machining process monitoring system through observation of cutting forces. Moreover, disassembling-assembling the lathe's tool-post first to install the table dynamometer is a bit of a tedious job. To overcome this problem, researchers have actually proposed low-cost-based dynamometers. You et al. [18] developed cutting forces measurement tool based on strain gauges by applying the transducer model of two perpendicular octagonal rings (TPOR). Their developed dynamometer had sensitivity of 0.32 mV/N and natural frequency of 771 Hz, and it had been applied for measuring the cutting forces during AISI 1045 and Aluminum alloy turning process. However, they used commercial data acquisition that had not been included in production costs in the development of dynamometers. Uquillas et al. [19,20] developed a force measuring tool by utilizing strain gauges with wireless transmission technology.

Rizal et al. [21,22] focused on designing and manufacturing the dynamometers based on both octagonal ring and cross beam transducer models. They claimed that their developed dynamometer had a dynamic response of about 766 Hz, sensitivity of 3.13–172.4 mV/N, 0.87% in cross-sensitivity error, and appropriate for acquiring cutting forces about 3 kN. Korkut [23], Yaldiz et al. [24,25] developed instrument for measuring cutting forces based on the octagonal ring. They implemented it in either turning or milling processes. The eight-shaped rings transducer-based dynamometer was developed for measuring milling forces [26]. Various transducer models were applied as an essential element composing dynamometer, including circular ring [27], diaphragm type [28], elastic body [29], bending beam [30,31], hexagonal ring [32], square ring [33], octagonal-elliptical ring [34–38], and two extended octagonal rings [39].

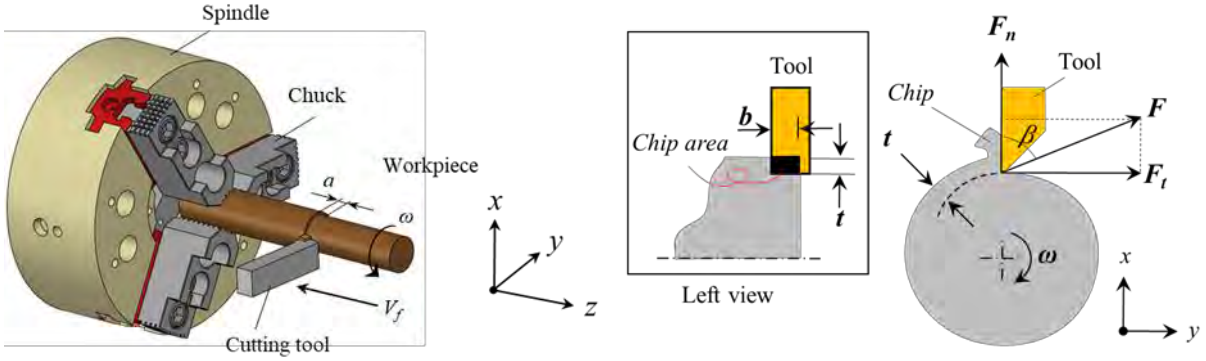
Based on those studies, one of the important components of composing a dynamometer is the transducer. It was used as a sensing element for measuring cutting forces during machining. The design of the transducers that has an inner circular shape, such as octagonal ring transducers [22–25,34–38,40], circular rings [27], and the eight-shaped (ES) [26], has a shortcoming in the sensor installation. Those transducers caused the strain gauge installed on the inside of transducer to experience initial compression, even when the load had not been applied. This clearly effects on the accuracy of cutting forces measurements. Therefore, an alternative transducer design needs to be studied, that can be worked to sense cutting forces in turning process precisely.

This study focuses on designing, analyzing, and fabrication of low-cost dynamometer based on proposed novel transducer, namely full octagonal ring-shaped transducer. Various evaluations were performed which aiming to produce accurate and reliable dynamometer, which cover static and dynamic analysis, and calibration tests. Following, machining tests were conducted to evaluate the performance of the developed dynamometer for acquiring cutting forces during turning process. In the following sections, cutting forces model in turning operation is first explained in Section 2. The materials and methods are following discussing in Section 3. The results and discussions of the study are described in Section 4, which include static and dynamic analysis of transducer, configuration of the developed dynamometer and its calibrations, evaluating the performance of the developed dynamometer through various machining tests.

2. Cutting Forces Model During Turning Process

Turning process is applied to cylindrical workpiece for producing parts that are basically round in shape, either external or internal shapes [41]. In orthogonal turning process, a workpiece is cut using a cutting tool with the angle of cutting-edge perpendicular to the cutting direction as shown in Fig. 1. From Fig. 1(a), the rotating workpiece with the rotational speed of ω (rpm) is cut by a sharp cutting tool that moves translationally along the cutting length with axial cutting depth of a (mm) and feeding speed of V_f (mm/min.). During machining, the cutting forces are generated that

cause plastic deformation on the workpiece material and producing in chips. These cutting forces acting in turning process are shown in Fig. 1(b).



(a) (b)

Fig. 1. Cutting process in turning (a) Turning process and its machining parameters and (b) Cutting forces generated during turning process

Based on Fig. 1(b), the cutting force, F (N), acting during turning process is proportional to the specific cutting force, Ks (N/mm^2), multiplied by cross-sectional area of chip, A_C (mm^2), which is formulated as [42]s;

$$F = A_c \,.\, K_s \tag{1}$$

The cutting force can then be decomposed into normal, F_n, and tangential, F_t, force components by cutting force angle, β. They are calculated as follows;

$$F_t = Ks \,.\, b \,.\, a \,.\, sin\,\beta \tag{2}$$

$$F_n = Ks \,.\, b \,.\, a \,.\, cos\,\beta \tag{3}$$

where b is chip thickness.

3. Methods

3.1. Developed Transducer

The method used in this study was a development and construction model that aims to produce an accurate, precise, and reliable dynamometer when used for measuring cutting forces in turning process. The development of dynamometers focused on the transducer which is one of the urgent components of composing a dynamometer that functions as a sensing element of cutting forces. This study proposed a full octagonal shaped ring transducer model as displayed in Fig. 2(a) in developing dynamometer. The material of this component was steel with dimensions of width, thickness, and ring radius of 15 mm, 3 mm, and 13.5 mm, respectively. It is seen that the transducer is different from the octagonal-elliptical ring-shaped transducers used by [21,23–26,36], and others [35,38]. Those old transducer models caused the sensor attached to the transducer's inner surface having pre-compressive, even when the forces had not been applied as shown in Fig. 2(b). This obviously affected the accuracy and reliability of the cutting forces measurement. On the other hand, the proposed transducer in this study does not cause pre-compressive in sensor as shown in Fig. 2(c), so that the precision of the measurement of the cutting force – in the initial assumption – is more guaranteed. Various evaluations were performed which aiming to produce accurate dynamometer, namely; (1) static analysis, (2) dynamical test, transducer and dynamometer calibrations, and machining tests.

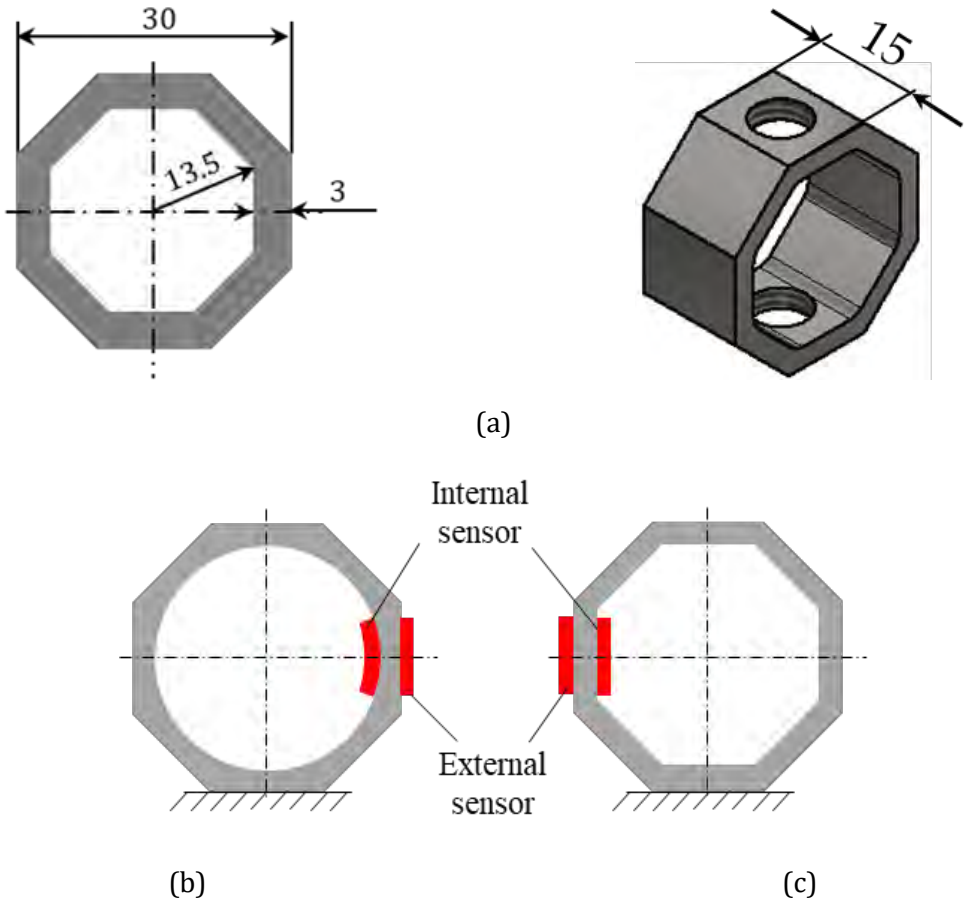


Fig. 2. Transducer model used in dynamometer: (a) isometric view of developed transducer and its dimension, (b) pre-compressive effect on the sensor using old transducer, (c) no pre-compressive effect on the sensor using proposed transducer model

3.2 Static Analysis Based on The Finite Element Method (FEM)

Static analysis based on the finite element method (FEM) is performed to evaluate the strength of the developed transducer structure against the applied loads. Fig. 3 displays the meshing in FEM environment. Type meshing of 3D Hexahedrons with 91015 nodes and 59671 elements was used in the calculation. Five types of meshing independence tests including skewness index, element quality parameters, orthogonal quality, aspect ratio, and parallel deviation were conducted to determine the meshing quality. The results showed that the meshing was verified to be able to proceed to the next analysis step.

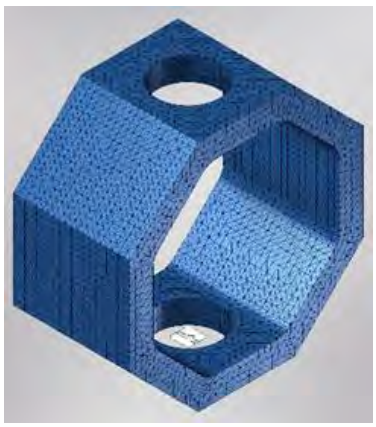


Fig. 3. Meshing of developed transducer in FEM environment

3.3. Test of Dynamical Characteristic of Transducer

During turning process, the cutting forces are not in a static situation, but also dynamic [8]. Therefore, it is also important to consider the system response to dynamic loads. And, the component of dynamometer that is most susceptible to dynamic problems is the transducer. In this case, the dynamic response of the dynamometer structure is influenced by the forced frequency of the spindle rotation. During machining process, the natural frequency and forced frequency must be very different from each other. This will ensure that the cutting force obtained will not be affected by dynamic phenomena caused by the construction of the dynamometer.

For identifying the dynamical behavior of transducer, the test – well-known as hammering tests – was carried out. Fig. 4 shows the experimental hammering test along with the instruments needed in the tests. It is seen that the transducer is excited by an Dytran 5800B3 electrical hammer, so that the structure vibrates. The transient external force of the excitation was measured by a piezotronics embedded in the hammer tip and the vibration response was quantified by an Dytran 3413A2 less-mass accelerometer attached to the structure. Those instruments had been activated by an Omega power supply. Both impulse forces and vibration responses were then acquired by a data storage oscilloscope, GW Instek, where the data can be checked by a software-interfaced personal computer. To ensure the data were based on correct assumptions, a certain amount of collecting data, 3-5 times the replication were collected which were then averaged.

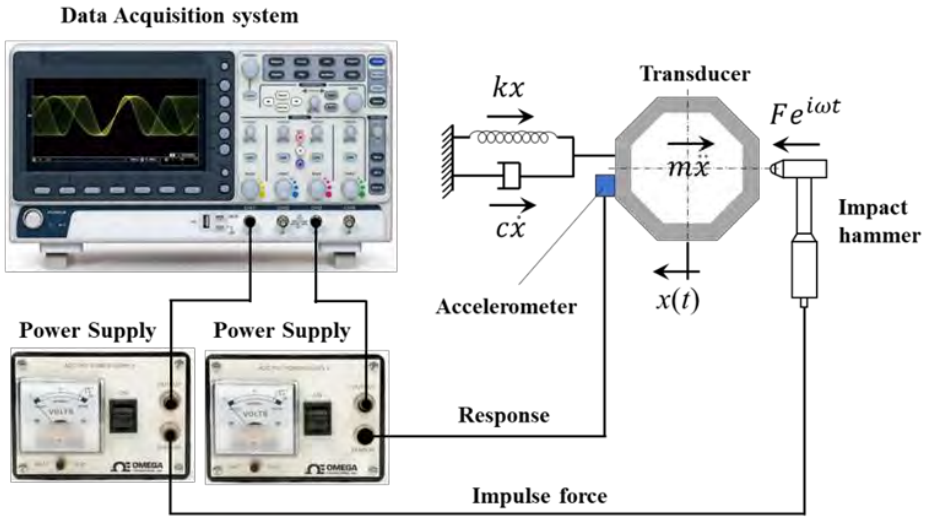


Fig. 4. Schematic diagram of hammering test

Based on the single degree of vibration model shown in Fig. 4, the vibration equation can be written by summing inertial, damping, stiffness and external forces as follows:

$$m\ddot{x} + c\dot{x} + kx = Fe^{i\omega t} \tag{4}$$

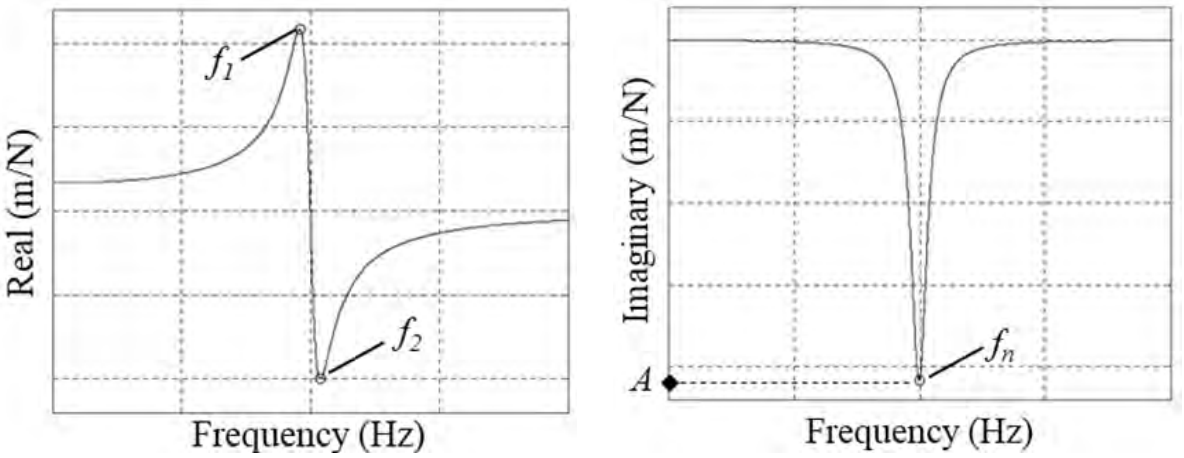
where *m, c,* and *k* are dynamic modal parameters of mass (kg), stiffness constant (N/m), and damping coefficient (N-s/m), respectively. $Fe^{i\omega t}$ is the transient impulse force in function of frequency (ω, Hz), with $i = \sqrt{-1}$ is an imaginary value. While, $x = Xe^{i\omega t}$ is the deflection of transducer due to being hit by hammer and it can be derived into velocity and acceleration, which are $\dot{x} = i\omega Xe^{i\omega t}$ and $\ddot{x} = -\omega^2 Xe^{i\omega t}$. By substituting these deriving variables into Eq. (4) and eliminating the exponential numbers, the frequency response function (FRF) is obtained in the form of;

$$\frac{X}{F} = \frac{1}{-\omega^2 m + i\omega c + k} \tag{5}$$

Equation (5) can be decomposed into a pair of the real and imaginary parts of the FRF, namely:

$$\left.\begin{aligned}\mathrm{Re}\left(G(f)\right)&=\frac{\left(1-r^2\right)}{k\left(\left(1-r^2\right)^2+\left(2\zeta r\right)^2\right)}\\ \mathrm{Im}\left(G(f)\right)&=\frac{-2\zeta f}{k\left(\left(1-r^2\right)^2+\left(2\zeta r\right)^2\right)}\end{aligned}\right\} \tag{6}$$

Where ζ is the damping ratio and the ratio between frequency function to the natural frequency is shown by $r=\omega/\omega_n$. Furthermore, the equations of the real and imaginary parts of the FRF formulated in Eq. (6) can be depicted in Fig. 5.



(a) (b)

Fig. 5. A pair of FRF parts that are "measured" from testing (a) Real part and (b) Imaginary part

It can be seen that each peak is identified with small circles in both figures, namely f_n, f_1, and f_2 (Hz) and A (m/N). They are indispensable for extracting dynamic modal parameters of transducer. Following are four steps to extract them;

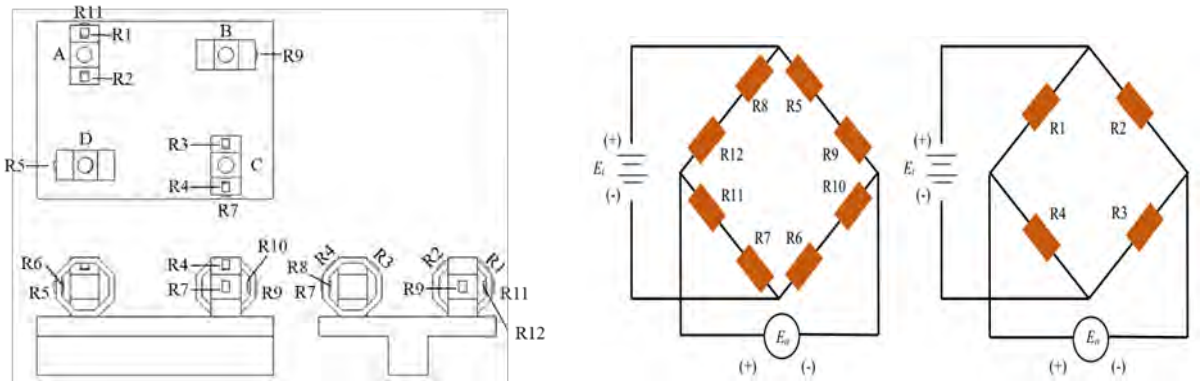
- Find a damping ratio ζ (%) by $\zeta=\dfrac{f_2-f_1}{2f_n}$
- Find the constant stiffness k (N/m) through $k=-\dfrac{1}{2A\zeta}$.
- Convert the natural frequency fn (Hz) to ω_n (radian/s) by multiplying 2π to get compatible units and use $\omega_n=\sqrt{\dfrac{k}{m}}$ to calculate the modal mass m (kg).
- Finally, calculate $c=2\zeta\sqrt{km}$ to determine the damping coefficient c (N-s/m).

3.4 Dynamometer Configures and Data Acquisition System

The configuration and orientation of the transducer on the developed dynamometer is shown in Fig. 5. It can be seen that the sensors of strain gauges that are attached to the transducer with a certain configuration and orientation to produce the shape of the dynamometer as shown in Fig. 6(a). The configuration and orientation of the transducer were intended for measuring normal (F_n) and tangential (F_t) cutting forces during the turning process as discussed in Section 2. For each measurement of the force component, the strain gauges are assembled based on Wheatstone bridges as seen in Fig. 6(b).

To measure the tangential force, transducers A and B in Fig. 6(a) are attached to a series of strain gauges whose arrangement is shown in Fig. 6(b-right). It can be seen that there are four strain gauges (R1, R2, R3 and R4) that are connected based on the Wheatstone bridge. R1 and R3 are

attached on the outer surface of the transducer at an angle of 45° to the vertical plane that would be subjected to tensile stress. R2 and R4 are attached on the outer surface of the transducer at an angle of 45° to the vertical plane so that they would be subjected to compressive stress. For measuring normal force (F_n), transducers A, B, C and D in Fig. 6(b) are attached with eight strain gauges which the arrangements are shown in Fig. 5(b-left). R5, R7, R9 and R11 are attached on the outer surface of the transducers at an angle of 90° to the vertical plane that would be subjected to tensile stress. R6, R8, R10 and R12 are attached on the inner surface of the transducer with the perpendicular angle to the vertical plane that would be subjected to compressive stress. The strain gauges used were BF(BA)350-3AA with dimensions of 7.44 × 4.4 mm and a gauge factor was 2.0-2.2.

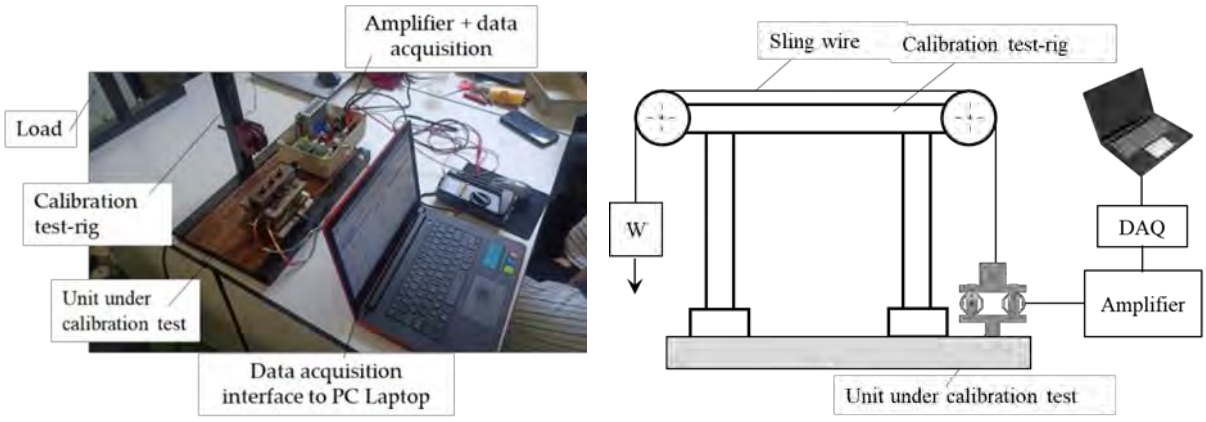


(a) (b)

Fig. 6. Configuration and orientation transducer on developed dynamometer (a) Arrangement strain gauges that attached on transducer and (b) Wheatstone bridges-based order strain gauges for measure: (left) normal force, and (right) tangential force

3.5 Calibration Tests

To determine the characteristics of transducers and dynamometers due to the applied loads, calibration tests were conducted. The experimental set-up and schematic diagram for both the individual transducer and dynamometer are shown in Fig. 7. Fig. 7(a) shows the experimental set-up and the instruments required in the calibration. It can be seen that the instruments needed for the calibration test include; units tested either dynamometer or transducer, calibration test-rig, wire sling, load, data acquisition system, and PC laptop.



(a) (b)

Fig. 7. Experimental set-up and schematic diagram for calibration tests (a) Instruments required for calibration tests and (b) Schematic diagrams of calibration tests; individual transducer or constructed dynamometer

Fig. 7(b) shows a schematic diagram of the calibration on the unit under test, either an individual transducer or constructed dynamometer. In the calibration of the individual transducer, the structure was subjected to a load that ranged from 0 to 60 N with a step addition of 10 N, where the load was connected by a sling wire. The loading was intended to evaluate the sensing of transducer to the given loads, both the outer part and the inner part of transducer (see Fig. 2). In addition, calibration due to cross-load effect was also observed to evaluate the transducer response due to cross-load, both the normal response due to the tangential load, and the tangential response due to the normal load. In the calibration of a constructed dynamometer, the tests were performed on two orientations of the force component; F_n and F_t, with gradual loading until reaching 100 N with a load interval of 10 N. To ensure the consistency of the output results, the tests were repeated 3 times. The results of the calibration test were then used to evaluate cross-sensitivity and linearity errors. In addition, a linear equation was also obtained based on this calibration.

3.6 Machining Tests

The next tests were conducted for evaluating the performance of the developed dynamometer in measuring the cutting forces. Dry machining was carried out on the ANNYANG conventional lathe machine. The experimental set-up of the cutting process is shown in Fig. 8. Based on Fig. 8(a), a 1045 carbon steel workpiece with 25 mm in diameter and a length of 100 mm is clamped on the machine spindle. Tool holder of DASAN MWLNR (20 × 20 mm) with insert cutting tool of tungsten carbide (WNMG0804) is clamped on a developed dynamometer by M8 bolts and it was mounted on the tool-post of machine. The installation of the developed dynamometer was easy to use than measuring the cutting force using a piezoelectric-based table dynamometer as it had been commonly used [14,43]. This is because, the installation of dynamometer did not need to disassemble-assemble the tool-post of machine.

Cutting forces measurement are carried out based on the schematic diagram as shown in Fig. 8(b). The machining process is performed at a constant cutting depth (a) of 0.2 mm, and a constant feed rate (f_r) of 0.06 mm/rev., and varying spindle rotational speed, ω, namely 160, 320, and 450 rpm. These machining parameters were similar to those used by other researchers when testing the dynamometers they developed [14,22,40].

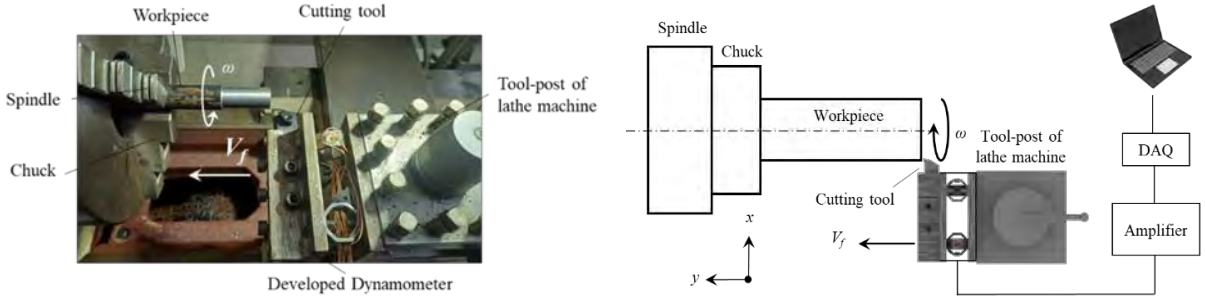


Fig. 8. Cutting tests conducted for developed performance evaluation (a) experimental set-up and (b) schematic diagram of the cutting test

4. Results and Discussions

4.1. Static And Dynamic Analysis of The Transducer

Static analysis based on the finite element method (FEM) is performed to evaluate the strength of the structure against the applied load. Fig. 9 displays the condition of the full octagonal shaped ring transducer which is subjected to normal force (F_n) and tangential force (F_t) of 224 N and 388 N evaluated based on FEM. Those conditions display distribution of stresses, strains, deflections, and safety factors.

Based on Fig. 9(a), the forces cause the transducer to having stress over the entire area with stress distribution ranging from 0.5 – 233 MPa as shown on the color bar. The part of the transducer that

is most having stresses when the forces were applied is indicated by red. Fig. 9(b) shows the strain distribution experienced by the transducer with a maximum strain of 9.9×10^{-4}. This maximum strain is relatively small which indicates that this transducer was quite rigid. The deflection is also fairly small, namely 8.541×10^{-2} mm as shown in Fig. 9(c). The transducer is rigidly designed to keep the turning forced frequency away from the natural frequency of developed dynamometer, so that the transducer was not going through damage due to the loads. Fig. 9(d) shows the safety factor analysis of the transducer which indicate that the transducer is still in a good condition to be used with the given loads. This is because the maximum stress that occurs had not reached the yield strength of the transducer material, 250 MPa.

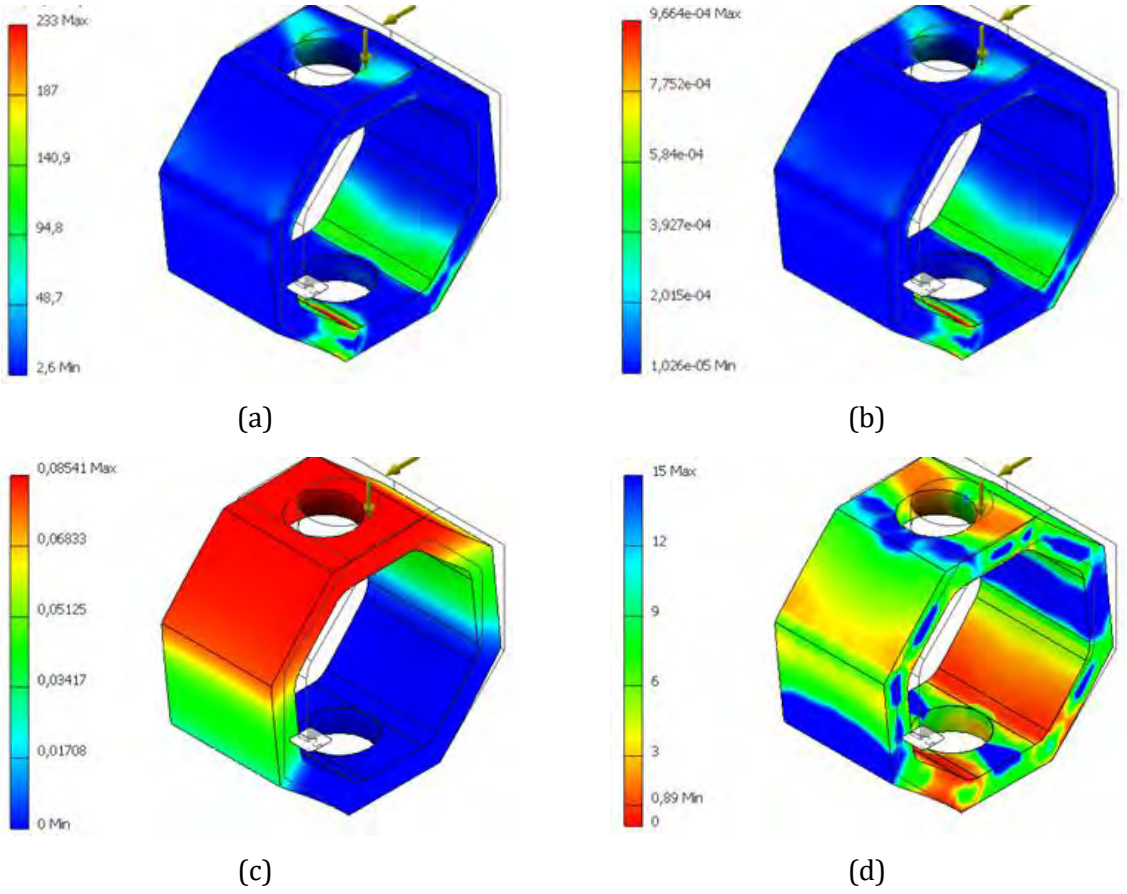
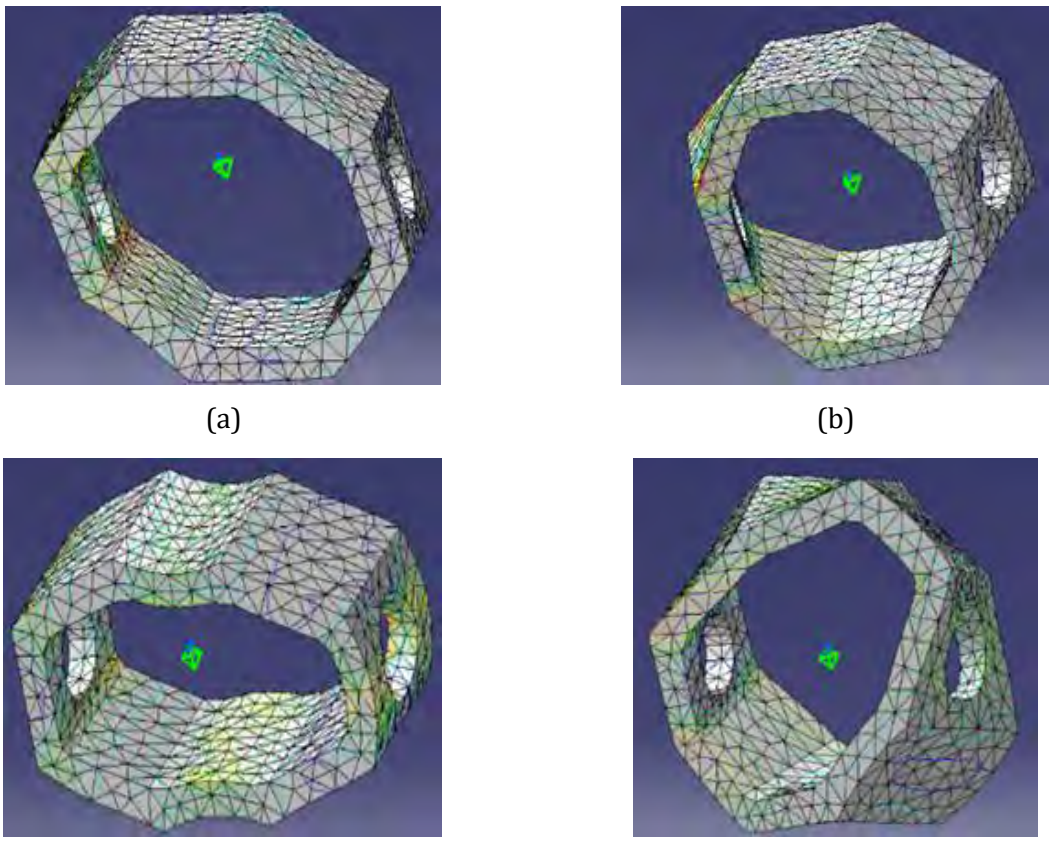


Fig. 9. Distribution of stresses, strains, displacements, and safety factors experienced the surface of the developed transducer when subjected by normal and tangential forces (a) Stress distribution (MPa), (b) Strain distribution, (c) Displacement distribution (mm) and (d) Safety factor distribution

The dynamic analysis based on the FEM are shown in Fig. 10, which shows the first four vibration modes experienced by the transducer due to the normal force and tangential force applied to the transducer. Fig. 10(a) shows the first vibration mode with a natural frequency of 3.85 kHz. It can be seen that the transducer is deformed, but still maintain its shape. Figs. 10(b) – 9(d) show the second to fourth vibration modes with frequencies of 6.41, 14.1 and 20 kHz, respectively. At these frequencies, the transducer undergoes a deformation due to dynamic loads and does not hold its initial shape. So, it is quite risky to use the developed dynamometer at those frequencies.

Fig. 11 displays raw data in the time domain data obtained by impact tests. They are the impulse force and vibration response which are shown in Figs. 11(a) and 11(b), respectively. It is seen that when the transducer was excited with a force of 1 N by hammer, the damped free vibration was given by structure. The oscillation decays over time and the vibration finally vanished. Those time domain data were then transformed into a frequency response function (FRF) to determine dynamic modal parameters of transducer in receiving dynamic loads. Fig. 12 is an FRFs consisting of the real and the imaginary parts of FRF. By utilizing these two graphs, the dynamic modal

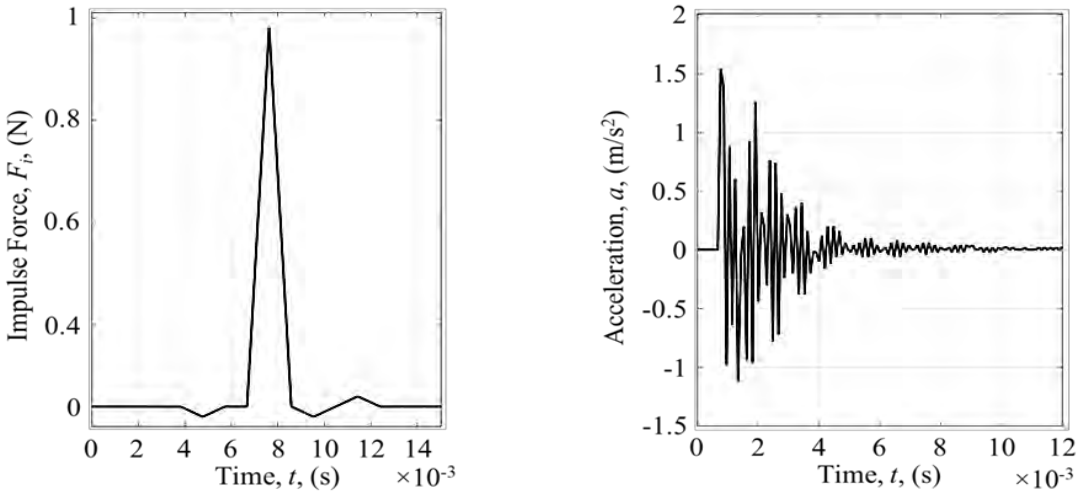
parameters of transducer can be extracted based on the explanation in Section 3.2, as well as have been applied to mechanical structures in general, whether in precision table grinding [44], lathes [45], milling [46], drilling [47], and automotive vehicles [48]. The results of the extraction of dynamic modal parameters, which including mass (m), damping coefficient (c), stiffness (k), damping ratio (ζ), and natural frequency (f_n) are tabulated in Table 1. These results are valid with simulation results based on FEM in previous discussion.



(a) (b)

(c) (d)

Fig. 10. The first four vibration modes of the transducer under the of applied forces (a) 1st mode, (b) 2nd mode, (c) 3rd mode and (d) 4th mode



(a) (b)

Fig. 11. Time domain data measured by impact test (a) Impulse force and (b) Vibration response

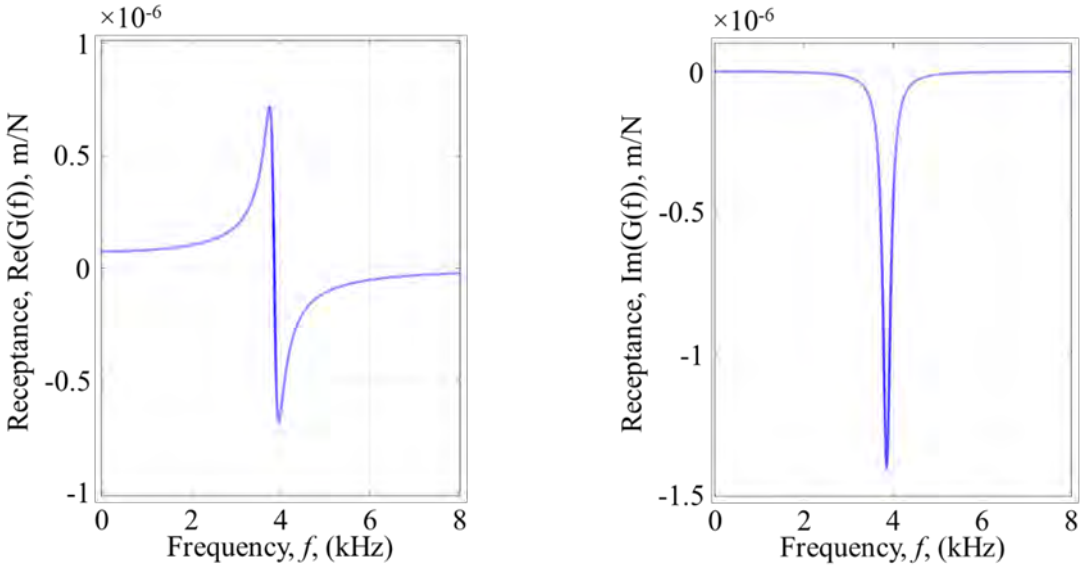


Fig. 12. Frequency response function (FRF) associated to raw time-domain data (a) Real part of FRF and (b) Imaginary part of FRF

Table 1. Parameter modal dynamic of transducer

Dynamic Parameters	Value
Mass (m)	32 g
Damping coefficient (c)	16 N-s/m
Stiffness (k)	18,5 x 10^{-6} N/m
Frequency (f_n)	3,85 kHz
Damping ratio (ζ)	1,04%

4.2 Calibration of Transducer

Calibration on individual transducer aims to evaluate the transducer through the response given by the transducer due to the load applied to it. Fig. 13 shows the output results during calibration tests. Fig. 13(a) shows the transducer calibration for normal response and Fig. 13(b) shows the transducer calibration in tangential response. Both Figs 13(a) and 13(b) show three data due to the load applied to the transducer through the experiment described in Fig. 7. The black and red graphs are responses sensed by sensors attached to the outer transducer and inner transducer, respectively, (see Fig. 2). The blue graph is the calibration of the transducer due to the cross-load effect which used to evaluate the transducer response in normal direction due to the application of tangential directional loads.

It can be seen that the normal load calibration for the external sensor above shows an upward trend with respect to the given load, while the normal load calibration for the inner sensor shows a downward trend. This shows that the measurement of normal loading using a developed transducer worked well. In addition, the blue graph indicates that the transducer is not affected by the cross-load effect, both the normal directional response due to tangential loading and the tangential directional response due to normal loading. This shows that the developed transducer measures the cutting force independently and was not affected by the directional loading.

In calibration test of the normal direction transducer**,** the regression equation was $y_n = 0{,}1425\text{x} - 0{,}0514$. Meanwhile, the root mean square error (RMSE) [49] for the data was 3.2%, and the mean absolute error (MAE) [13,16,49,50] was 2.4%. On the other hand, the regression equation of the transducer calibration resulted for the tangential direction of data was $y_t = 0{,}1379\text{x} - 0{,}0197$. The RMSE for the data was 2.5%. Meanwhile, the MAE for these three data was 2.1%. Those lower the RMSE and MAE indicated that calibration tests show the better the model performs.

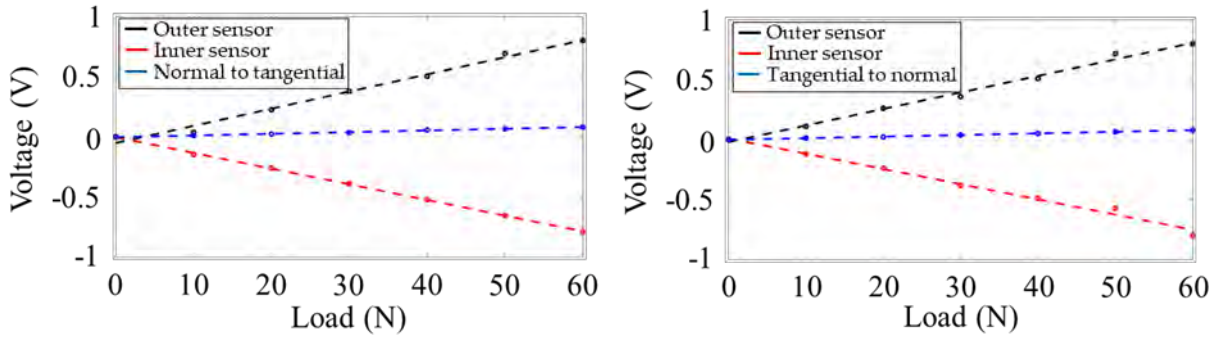


Fig. 13. The transducer calibration (a) normal, (b) tangential responses

4.3 Design and Construction of Low-Cost Dynamometer Based on Full Octagonal Transducer

Fig. 14 displays a construction of low-cost dynamometer based on a full octagonal shaped ring and the important other instrument to measure cutting forces in turning process. The configuration of the strain gauge installation on the transducer of dynamometer along with the necessary fittings is presented in Fig. 14(a). Besides, Fig. 14(b) is a prototype of developed dynamometer. The overall cost of producing these dynamometers is about 70% cheaper than the commercial piezoelectric dynamometers widely used by previous researchers [13,16,50].

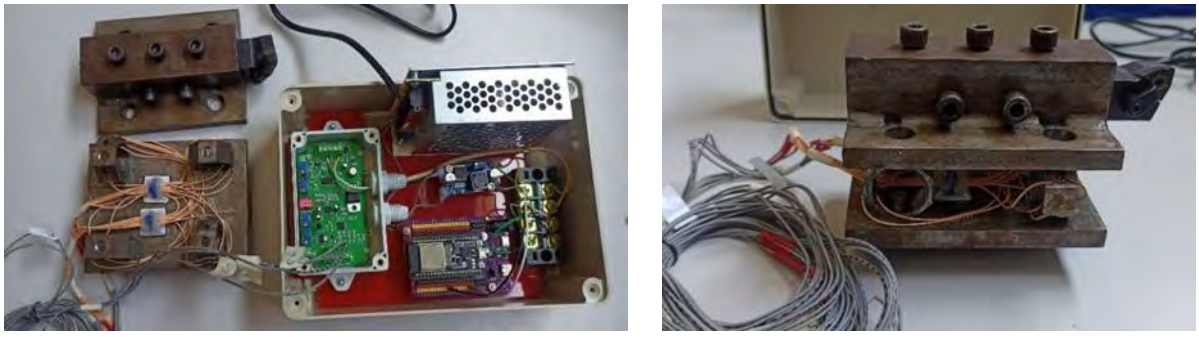


Fig. 14. Construction low-cost dynamometer base on full octagonal shaped ring and the essential components (a) Installation strain gauge on transducer and the data acquisition and (b) Prototype of developed dynamometer

This developed dynamometer consisted of upper and lower plates with dimensions of 120 × 90 × 10 mm. The bottom plate was used to a handle to which the tool-post was attached. The top plate was used as a place for the cutting tool. Four transducers attached strain gauges with a wiring system were placed between the bottom and the top plates, which are then fastened by M8 nuts. Besides, other instruments in the developed dynamometer include a 24V power supply, step down, amplifier and ESP 32 acquisition data. This part was usually ignored in the development of low-cost dynamometers as shown in previous results [18,21,22].

4.3 Dynamometer Calibration

The dynamometer calibration results are shown in Fig. 15 where Fig. 15(a) is the dynamometer calibration for normal force, and Fig. 15(b) is for tangential force due to the loading applied. It can be seen that there are two graphs in each figure. The black curve is a dynamometer response due to direct load, namely; (a) normal force calibration due to normal load, and (b) tangential force calibration due to tangential load. Meanwhile, the red graph is a dynamometer response due to the cross-load effect, namely; (a) normal force calibration due to tangential loads, and (b) tangential force calibration due to normal loads.

Both black curves, both normal and tangential force calibrations, indicate an uptrend. The calibration sensitivity of the dynamometer to normal force was 78.1 mV/N. The linear regression equation of the test was $y_n = 0{,}0781\text{x} + 0{,}014$, which RSME was 2.9%, and the MAE was 2.1%. Meanwhile, the calibration sensitivity of the dynamometer to the tangential force was 85.7 mV/N with a linear regression from data of $y_t = 0{,}0784\text{x} - 0{,}0209$, which RMSE of 3.2% and MAE of 2.7%.

The cross effect of tangential load on the normal force for dynamometer calibration shows slight upward trend with a maximum error of 10.2%, so that the cross effect of tangential tool does not interfere with the normal force measurement on the dynamometer. From three tests, a regression equation was obtained, namely $y_{nct} = 0{,}0014x - 0{,}0018$, and they had RMSE of 0.17%, and MAE of 0.14%. Meanwhile, the cross effect of normal load on tangential force calibration was also insignificant and did not interfere to the measurement results with a maximum error of 8.98%. The regression of the test was $y_{tcn} = 0{,}0029x - 0{,}0097$. RMSE was 0.47%, and MAE was 0.37%.

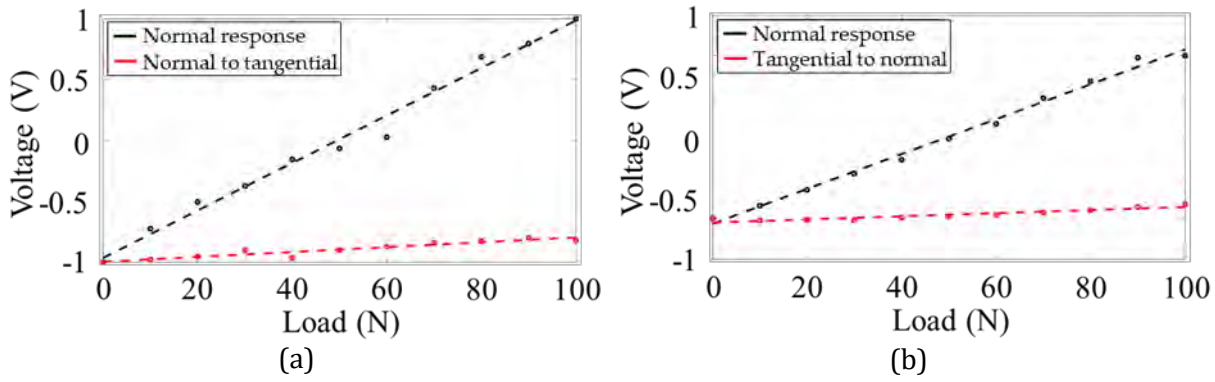


Fig. 15. Dynamometer calibrations (a) normal response, (b) tangential response due to the load application

The calibration was then used to evaluate linearity errors when a maximum load of about 100 N was applied to the dynamometer. It was found that the linearity error in normal force was 0.63% and for linearity error in tangential force was 3.7%. This means that the developed dynamometer was acceptable for measuring cutting forces in turning process.

4.4 Machining Tests

Machining tests are carried out to evaluate the cutting force measurement in turning process using a developed dynamometer. Fig. 16 shows cutting forces measured using developed dynamometer based on the variation in spindle rotational speed. Figs. 16(a), 16(b) and 16(c) show the cutting forces associated with spindle rotational speed of 160 rpm, 320 rpm, and 450 rpm, respectively. In addition of normal and tangential forces, resultant forces are also seen that were calculated by $F = \sqrt{F_t^2 + F_n^2}$. It is seen that the quantity of the cutting forces is similar. This indicated that variations in spindle rotation speed did not affect the quantity of cutting force, but they affected the cutting time; the greater the spindle rotation speed, the faster the machining process, and vice versa. This is because the quantity of the cutting force was affected by the axial depth of cut [42,51]. For all cutting experiments, it was seen that the normal force had a smaller quantity than the other cutting force.

From the figures, it is seen that the cutting forces fluctuate. These fluctuations were strongly influenced by the dynamic cutting process during contacted between the cutting-tool and the workpiece, noise from surrounding environment, namely from material factors and machine conditions [8,9]. Some theories such as Hamilton's principle need to be considered to ensure this phenomenon and considering the importance of static and dynamic analysis in structural design [52]. On the other hand, those cutting force trends had a good agreement with previous studies which used commercial dynamometers such as in [16,17,30]. In order to confirm above deduction and to evaluate the measurement results, cutting forces measured by the cutting tests were compared with calculated cutting forces, which the equations have been described in Section 2. The

comparison between the measured cutting forces to the simulation one is shown in Figs. 17, 18, and 19. Random noise has been added to the simulation, while considering other conditions are in the same as the conditions of machining tests. The specific cutting force, *Ks*, of 2600 N/mm^2 for 1045 carbon steel was applied in the simulation [53]. Based on the figures, the cutting forces obtained through experimental tests comparing to the simulation results show well agreement.

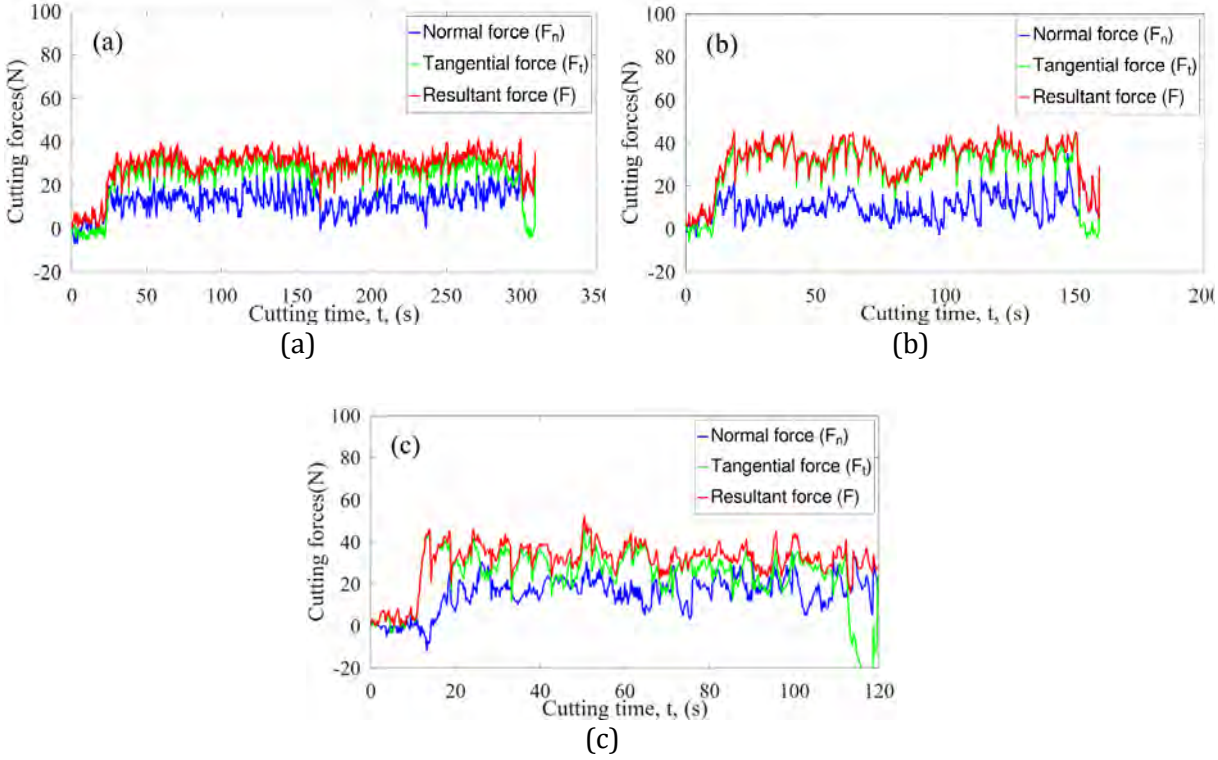


Fig. 16. Cutting forces measured by machining tests using developed dynamometer with the spindle rotation speed; (a) 160 rpm, (b) 320 rpm, and (c) 450 rpm

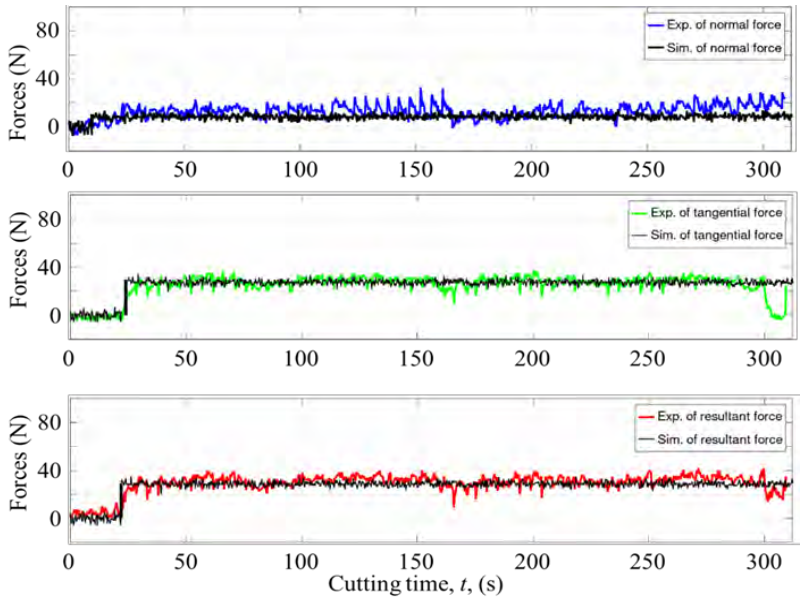


Fig. 17. Comparison of cutting force obtained by machining tests to the simulations for spindle rotation speed of 160 rpm

Fig. 17 shows cutting forces comparison between the measured to the simulation for spindle rotational speed of 160 rpm. Figs. 17(a), 17(b) and 17(c) represent the normal, tangential, and resultant cutting forces, respectively. It can be seen that the cutting time required to machine about

50 mm in cutting length is 313 seconds. The cutting force in the first 15 seconds is still close to zero, which indicates there was no cutting process occurred. When the cutting process has started until the end of the operation, the cutting forces are steady with certain quantity.

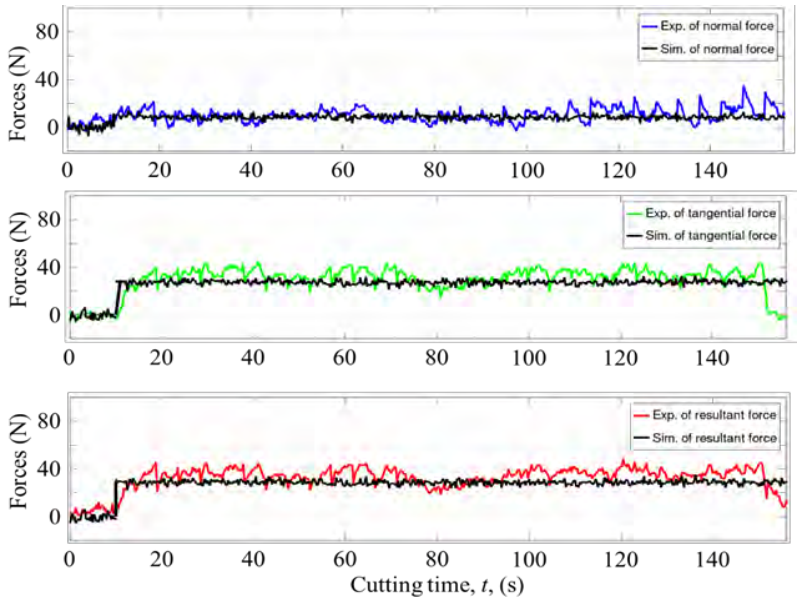


Fig. 18. Comparison of cutting force obtained by machining tests to the simulations for spindle rotation speed of 320 rpm

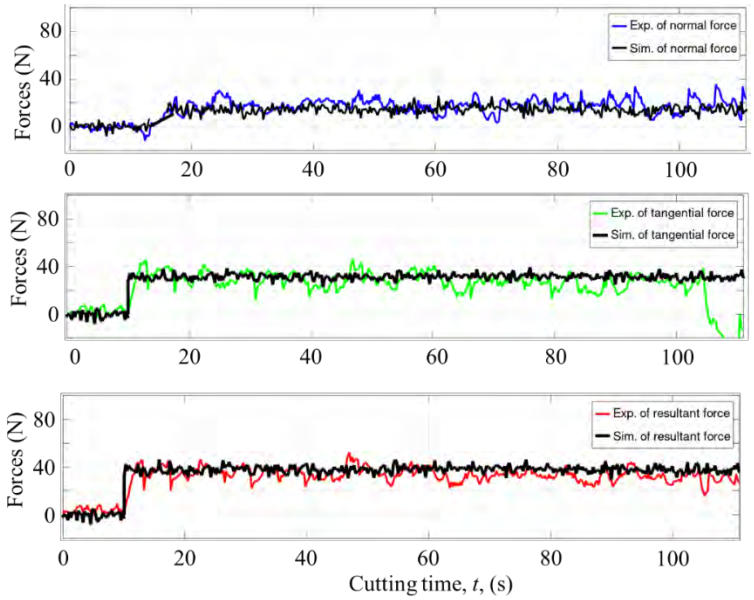


Fig. 19. Comparison of cutting force obtained by machining tests to the simulations for spindle rotation speed of 450 rpm

Fig. 18 displays cutting forces comparison for experiment with simulation one in spindle rotational speed of 320 rpm. With the same cutting length, the cutting time is twice as fast, which is 156 seconds. Fig. 19 is a comparison of the measured cutting forces to the simulation in a spindle rotational speed of 450 rpm. It is seen that the cutting time is faster than the other two, which is 111 seconds. To find out the effect of spindle speeds on the attributes of turning process, it was necessary to transform the cutting forces obtained in machining tests displayed in Fig. 16 to the frequency spectrum to observe the frequency characteristics of cutting. This is because the spindle rotational speed almost certainly affects the frequency content of the cutting process in machining process. The frequency spectrum calculated by fast Fourier transform (FTT) are shown in Fig. 20.

Those Figs. 20(a), 20(b) and 20(c) are frequency spectrum that correspond to cutting force of (a) 160 rpm, (b) 320 rpm, and (c) 450 rpm, respectively.

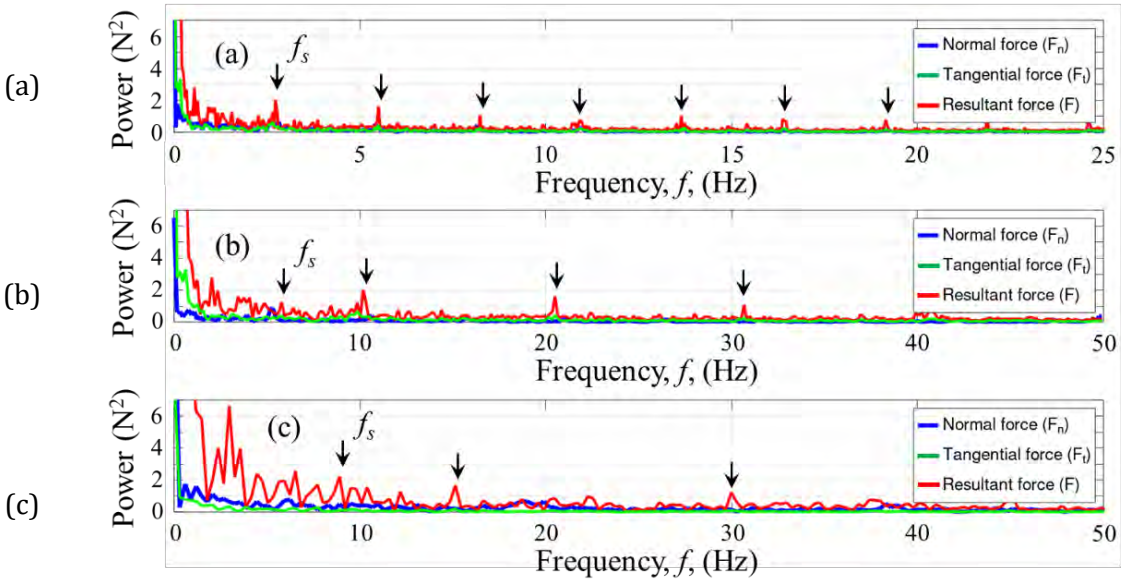


Fig. 20. The frequency spectrum of cutting forces measured during machining tests corresponding to; (a) 160 rpm, (b) 320 rpm, and (c) 450 rpm

The spectrum above shows the frequency content of the cutting forces, the normal, tangential, and resultant of cutting forces which are visualized with the colour of each graph. Based on each frequency spectrum above, there are various frequencies that are observed. They are spindle rotation frequency, f_s, and its harmonic frequencies marked by the arrow. Both the spindle and harmonic frequencies were characteristic frequencies which were a consequence of the machining process. Harmonic frequency was calculated by multiplication of f_s by integer numbers.

Based on the frequency spectrum in Fig. 20(a), the spindle frequency is 2.7 Hz. It was associated to spindle rotation speed of 160 rpm. This frequency is followed by its harmonic frequencies, namely 5.4, 8.1, 10.8, Hz and so on. From Fig. 20(b), it is found spindle rotational frequency of 5.4 Hz, which associated to spindle rotational speed of 320 rpm, and followed by its harmonic frequencies, namely 10.6 and 21.2 Hz. Frequency spectrum in Fig. 20(c) displays spindle rotational frequency of 7.5 Hz, which associated to spindle rotational speed of 450 rpm, and its harmonic frequencies at 15 and 30 Hz. All of these characteristic frequencies were typically forced vibration. These spectrum frequency results indicated that the developed dynamometer perform well. It was because the dynamometer revealed the characteristic frequencies during turning process.

5. Conclusions

This study discusses the low-cost dynamometer developed for measuring cutting forces during turning process. Owing to the transducer is one of the main components that is used to as a sensing element of cutting forces, a novel full-octagonal ring- shaped transducer was proposed to overcome the weaknesses of the inner circular ring-based transducer which has been introduced previously. Various evaluations were performed which aiming to produce accurate and reliable dynamometer, which cover static analysis by Finite Element Method (FEM), dynamic analysis by impact tests, and calibration tests. Finally, machining tests were conducted for varying the performance of the developed dynamometer. Based on the results and discussions, several important points are drawn as follows;

- Static analysis showed that the proposed transducer was capable of withstanding normal load of 224 N and tangential load of 388 N with stress, strain, and deflection of 233 MPa, 9.9 × 10^{-4}, and 8.5 × 10^{-2} mm, respectively. The transducer was also safe to use as indicated by the distribution of safety factors.

- The dynamic aspect indicated that the natural frequency of developed dynamometer could stabilize at 3.85 kHz with stiffness constant, k, damping ratio, ζ, and damping coefficient, c, of 18.5×10^{-6} N/m, 1.04%, 16 N-s/m, respectively.
- The calibration tests revealed that the sensitivity, cross sensitivity, and linearity errors for normal force were 78.1 mV/N, 10.2%, and 0.63%. Meanwhile, for tangential force was 85.7 mV/N in sensitivity with cross sensitivity and linearity errors were 8.98% and 3.7%, respectively.
- The cutting forces obtained during machining tests showed good agreement with the simulation-based cutting forces. It means that developed dynamometer was accurate for measuring cutting forces during turning process.
- The characteristic frequencies of cutting processes which were explored by fast Fourier transform showed that the developed dynamometer was valid used for measuring cutting forces in turning process. The frequency of rotational spindle and its harmonics appeared in the spectrum frequency.

Acknowledgment

Authors sincerely thank you to Diponegoro University which has funded this research during Postdoctoral Grant in World Class University Program.

References

[1] Gasagara A, Jin W, Uwimbabazi A. Stability analysis for a single-point cutting tool deflection in turning operation. Advances in Mechanical Engineering. 2019;11(6):1-14. https://doi.org/10.1177/1687814019853188
[2] Wang SM, Chen YS, Lee CY, Yeh CC, Wang CC. Methods of in-process on-machine auto-inspection of dimensional error and auto-compensation of tool wear for precision turning. Applied Sciences. 2016;6(5). https://doi.org/10.3390/app6040107
[3] Shi D, Gindy NN. Development of an online machining process monitoring system: Application in hard turning. Sensors and Actuators A: Physical. 2007;135(2):405-14. https://doi.org/10.1016/j.sna.2006.08.011
[4] Coromant S. Railway turning: Railway turning: Re-turning and new wheel turning. Sandvik Coromant. 2022.
[5] Industry KR. Technical Information Korloy: Railway Industry. Korloy. 2022;
[6] Mammeri S, Chaoui K, Bouacha K. Manufacturing of testing specimens from tough HDPE-100 pipe: Turning parameters optimization. Research on Engineering Structures & Materials. 2024;10(2):513-36.
[7] Lukács J, Horváth R. Comprehensive Investigations of Cutting with Round Insert: Introduction of a Predictive Force Model with Verification. Metals. 2022;12(2). https://doi.org/10.3390/met12020257
[8] Susanto A, Liu CH, Yamada K, Hwang YR, Tanaka R, Sekiya K. Application of Hilbert-Huang transform for vibration signal analysis in end-milling. Precision Engineering. 2018;53:263-77. https://doi.org/10.1016/j.precisioneng.2018.04.008
[9] Susanto A, Liu C-H, Yamada K, Hwang Y-R, Tanaka R, Sekiya K. Milling Process Monitoring Based on Vibration Analysis Using Hilbert-Huang Transform. Int. J. of Automation and Technology. 2018;12(5):688-98. https://doi.org/10.20965/ijat.2018.p0688
[10] Susanto A, Yamada K, Tanaka R, Handoko YA, Subhan MF. Chatter identification in turning process based on vibration analysis using Hilbert- Huang transform. Journal of Mechanical Engineering and Science. 2020;14(2):6856-68. https://doi.org/10.15282/jmes.14.2.2020.25.0537
[11] Kim JH, Chang HK, Han DC, Jang DY, Oh SI. Cutting force estimation by measuring spindle displacement in milling process. CIRP Ann - Manuf Technol. 2005;54(1):67-70. https://doi.org/10.1016/S0007-8506(07)60051-1
[12] Lauro CH, Brandão LC, Baldo D, Reis RA, Davim JP. Monitoring and processing signal applied in machining processes - A review. Measurement. 2014;58:73-86. https://doi.org/10.1016/j.measurement.2014.08.035
[13] Stein JL, Huh K. Monitoring cutting forces in turning: A model-based approach. Journal of Manufacturing Science and Engineering. 2002;124(1):26-31. https://doi.org/10.1115/1.1432666
[14] Zheng Q, Yang C, Zhang S, Hu Y. Simulation and experimental research on cutting force of turning titanium alloy. MATEC Web Conf. 2015;31:4-8. https://doi.org/10.1051/matecconf/20153103013
[15] Krajcoviech S, Holubjak J, Richtarik M, Czánová T. Identification of process Prime A turning when machining steel C56E2 and monitoring of cutting forces. Transp Res Procedia. 2021;55:605-12. https://doi.org/10.1016/j.trpro.2021.07.027

[16] Fodor G, Sykora HT, Bachrathy D. Stochastic modeling of the cutting force in turning processes. Int J Adv Manuf Technol. 2020;111(1-2):213-26. https://doi.org/10.1007/s00170-020-05877-8
[17] Cahuc O, Gerard A, Bisu C, Ispas C. A force torsor analysis for a turning process in the presence of selfexcited vibrations. Appl Mech Mater. 2011;62:135-46. https://doi.org/10.4028/www.scientific.net/AMM.62.135
[18] You Z, Yulong Z, Taobo G. Application of a strain gauge cutting force sensor in machining process monitoring. 2019 14th IEEE Int Conf Electron Meas Instruments, ICEMI 2019. 2019;891-7. https://doi.org/10.1109/ICEMI46757.2019.9101849
[19] Reyes-Uquillas DA, Yeh SS. Tool holder sensor design for measuring the cutting force in CNC turning machines. IEEE/ASME Int Conf Adv Intell Mechatronics, AIM. 2015;2015-Augus:1218-23. https://doi.org/10.1109/AIM.2015.7222705
[20] Reyes-Uquillas DA, Hsiao T. Wireless tool holder sensor design for cutting force measurement applied to chatter detection. IEEE Reg 10 Annu Int Conf Proceedings/TENCON. 2017;1845-8. https://doi.org/10.1109/TENCON.2016.7848340
[21] Rizal M, Ghani JA, Husni, Husaini. Design and construction of a strain gauge-based dynamometer for a 3-axis cutting force measurement in turning process. J Mech Eng Sci. 2018;12(4):4072-87. https://doi.org/10.15282/jmes.12.4.2018.07.0353
[22] Rizal M, Ghani JA, Mubarak AZ. Design and Development of a Tri-Axial Turning Dynamometer Utilizing Cross-Beam Type Force Transducer for Fine-Turning Cutting Force Measurement. Sensors. 2022;22(22). https://doi.org/10.3390/s22228751
[23] Korkut I. A dynamometer design and its construction for milling operation. Mater Des. 2003;24(8):631-7. https://doi.org/10.1016/S0261-3069(03)00122-5
[24] Yaldiz S, Ünsaçar F. Design, development and testing of a turning dynamometer for cutting force measurement. Mater Des. 2006;27(10):839-46. https://doi.org/10.1016/j.matdes.2005.04.001
[25] Yaldiz S, Ünsaçar F, Sağlam H, Işik H. Design, development and testing of a four-component milling dynamometer for the measurement of cutting force and torque. Mech Syst Signal Process. 2007;21(3):1499-511. https://doi.org/10.1016/j.ymssp.2006.06.005
[26] Mohanraj T, Deepesh T, Dhinesh R, Jayaprakash S, Sai Krishna S. Design and analysis of a strain gauge based eight-shaped elliptical ring dynamometer for milling force measurement. Proc Inst Mech Eng Part C J Mech Eng Sci. 2021;235(17):3125-34. https://doi.org/10.1177/0954406220967681
[27] Kumar H, Sharma C, Kumar A, Arora PK, Kumar S. Design, development and metrological characterization of a low capacity precision industrial force transducer. ISA Trans. 2015;58:659-66. https://doi.org/10.1016/j.isatra.2015.07.011
[28] Kumar R, Pant BD, Maji S. Development and Characterization of a Diaphragm-Shaped Force Transducer for Static Force Measurement. Mapan - J Metrol Soc India. 2017;32(3):167-74. https://doi.org/10.1007/s12647-017-0207-7
[29] Liu M, Zhang Z, Zhou Z, Peng S, Tan Y. A new method based on Fiber Bragg grating sensor for the milling force measurement. Mechatronics. 2015;31:22-9. https://doi.org/10.1016/j.mechatronics.2015.03.007
[30] Şeker U, Kurt A, Çiftçi I. Design and construction of dynamometer for measurement of cutting forces during machining with linear motion. Mater Des. 2002;23(4):355-60. https://doi.org/10.1016/S0261-3069(02)00013-4
[31] Xie Z, Lu Y, Li J. Development and testing of an integrated smart tool holder for four-component cutting force measurement. Mechanical System Signal Processing. 2017;93:225-40. https://doi.org/10.1016/j.ymssp.2017.01.038
[32] Kumar H, Pardeep, Kaushik M, Kumar A. Development and Characterization of a Modified Ring Shaped Force Transducer. Mapan - J Metrol Soc India. 2015;30(1):37-47. https://doi.org/10.1007/s12647-014-0118-9
[33] Kumar H, Sharma C, Kumar A. The development and characterization of a square ring shaped force transducer. Meas Sci Technol. 2013;24(9). https://doi.org/10.1088/0957-0233/24/9/095007
[34] Kroencke M, Hull ML. A method for designing multiload component dynamometers incorporating octagonal strain rings. Exp Mech. 1989;29(2):195-204. https://doi.org/10.1007/BF02321375
[35] Dandage R V, Bhatwadekar SG, Bhagwat MM. Design , Development and Testing of a Four Component Milling Tool Dynamometer. Int J Appl Eng Technol. 2012;2(1):45-50.
[36] Soliman E. Performance analysis of octal rings as mechanical force transducers. Alexandria Eng J [Internet]. 2015;54(2):155-62. https://doi.org/10.1016/j.aej.2015.01.004
[37] Uddin MS, Songyi D. On the design and analysis of an octagonal-ellipse ring based cutting force measuring transducer. Meas J Int Meas Confed. 2016;90:168-77. https://doi.org/10.1016/j.measurement.2016.04.055
[38] Pathri BP, Garg AK, Unune DR, Mali HS, Dhami SS, Nagar R. Design and Fabrication of a Strain Gauge Type 3-axis Milling Tool Dynamometer. Int J Mater Form Mach Process. 2016;3(2):1-15. https://doi.org/10.4018/IJMFMP.2016070101

[39] Ammar AA, Jallouli M, Bouaziz Z. Design and development of a dynamometer for the simulation of the cutting forces in milling. Int J Autom Control. 2011;5(1):44-60. https://doi.org/10.1504/IJAAC.2011.037379
[40] Rizal M, Ghani JA, Nuawi MZ, Haron CHC. Development and testing of an integrated rotating dynamometer on tool holder for milling process. Mech Syst Signal Process. 2015;52-53(1):559-76. https://doi.org/10.1016/j.ymssp.2014.07.017
[41] Kalpakjian S, Schmid SR. Manufacturing Engineering and Technology. Prentice Hall International, Singapore. New Jersey: Prentice Hall Singapore; 2001.
[42] Tony L. Schmitz, Smith KS. Machining Dynamics: Frequency Response to Improved Productivity. Vol. 1, Springer. 2008. 1-303 p.
[43] Amigo FJ, Urbikain G, López de Lacalle LN, Pereira O, Fernández-Lucio P, Fernández-Valdivielso A. Prediction of cutting forces including tool wear in high-feed turning of Nimonic® C-263 superalloy: A geometric distortion-based model. Meas J Int Meas Confed. 2023;211(December 2022). https://doi.org/10.1016/j.measurement.2023.112580
[44] Cha KC, Wang N, Liao JY. Stability analysis for the crankshaft grinding machine subjected to a variable-position worktable. Int J Adv Manuf Technol. 2013;67(1-4):501-16. https://doi.org/10.1007/s00170-012-4501-9
[45] Zaeh MF, Kleinwort R, Fagerer P, Altintas Y. Automatic tuning of active vibration control systems using inertial actuators. CIRP Ann - Manuf Technol. 2017;66(1):365-8. https://doi.org/10.1016/j.cirp.2017.04.051
[46] Azka M, Yamada K, Huda M Al, Tanaka R, Sekiya K. Influence of Tool Posture and Position on Stability in Milling with Parallel Kinematic Machine Tool. Int. J. Precis Eng Manuf [Internet]. 2020;21(12):2359-73. https://doi.org/10.1007/s12541-020-00416-7
[47] Mehrabadi IM, Nouri M, Madoliat R. Investigating chatter vibration in deep drilling, including process damping and the gyroscopic effect. Int J Mach Tools Manuf. 2009;49(2):939-946. https://doi.org/10.1016/j.ijmachtools.2009.06.009
[48] Jing W, Hong Z, Gang X, Erbing W, Xiang L. Operational modal analysis for automobile. In: Lecture Notes in Electrical Engineering. 2012. p. 525-32. https://doi.org/10.1007/978-3-642-27311-7_70
[49] Li X, Luan F, Wu Y. A comparative assessment of six machine learning models for prediction of bending force in hot strip rolling process. Metals (Basel). 2020;10(5). https://doi.org/10.3390/met10050685
[50] Sadílek M, Dubský J, Sadílková Z, Poruba Z. Cutting forces during turning with variable depth of cut. Perspect Sci. 2016;7:357-63. https://doi.org/10.1016/j.pisc.2015.11.055
[51] Altintas Y. Manufacturing Automation: Metal Cutting Mechanics, Machine Tool Vibrations, and CNC Design. Cambridge University Press Cambridge, New York. Cambridge University Press Cambridge, New York; 2012. 1-365. https://doi.org/10.1017/CBO9780511843723
[52] Hadji L, Plevris V, Madan R, Ait Atmane H. Multi-Directional Functionally Graded Sandwich Plates: Buckling and Free Vibration Analysis with Refined Plate Models under Various Boundary Conditions. Computation. 2024;12(4). https://doi.org/10.3390/computation12040065
[53] Tlusty G. Manufacturing Processes and Equipment. New Jersey: Practice-Hall; 2020.

Blank Page

Research on Engineering Structures & Materials
www.jresm.org

Research Article

Physical and mechanical characteristics of lightweight POFA geopolymer concrete with timber clinker aggregate

Muhammad Nura Isa [1,a], Hanizam Awang [*,2,b], Tan Ying Yi [2,c]

[1]*Faculty of Environmental Technology, Abubakar Tafawa Balewa University, Nigeria*
[2]*School of Housing, Building and Planning, Universiti Sains Malaysia, Malaysia*

Article Info

Article History:

Received 20 Sep 2024

Accepted 19 Nov 2024

Keywords:

Wood ash lye;
POFA;
GGBS;
Timber clinker;
Geopolymer concrete;
Sustainable building materials

Abstract

The construction industry is seeking sustainable alternatives to traditional Portland cement-based concrete due to its environmental impact. Geopolymer concrete, using industrial byproducts as binders, offers a solution by reducing emissions and improving durability. However, challenges such as costly activators and energy-intensive curing processes limit its adoption. This research investigates the properties of wood ash (WA) lye activated blended geopolymer concrete incorporating sustainable timber clinker aggregate (TCA). A fixed liquid-to-binder ratio of 0.5 and an alkaline activator ratio of 3.0 were used in the mix design. The study focused on replacing conventional coarse aggregates with TCA to enhance sustainability. Key analyses included physical, mechanical, durability, environmental and cost efficiency assessments. Results showed that the replacement of natural granite with TCA led to reduction in the density of the concrete from 2063.13kg/m^3 to 1805.66kg/m^3 for 0% and 100% TCA, respectively. Strength also decreased as TCA content rose, attributed to lower density. Water absorption increased with TCA content, though all samples stayed within the 10% absorption limit set by BS882: 1992. Notably, the TCA60 specimen met ASTM C330 (2009) requirements for structural lightweight aggregate concrete. The development of wood ash lye activated lightweight binary blended geopolymer concrete incorporating timber clinker aggregate represents a potentially groundbreaking advancement in sustainable construction materials.

© 2025 MIM Research Group. All rights reserved.

1. Introduction

The construction industry is in the midst of a paradigm shift as it seeks innovative, sustainable, and environmentally responsible building materials. Traditional Portland cement-based concrete, while tried and tested, poses considerable environmental challenges due to its high carbon footprint and substantial consumption of finite natural resources [1]. To address these concerns, researchers and industry experts are increasingly turning to geopolymer concrete, a sustainable alternative that provides multiple benefits, such as lower greenhouse gas emissions and improved durability.

Geopolymer concrete represents a revolutionary approach to conventional concrete. It substitutes Portland cement with a geopolymer binder, typically derived from industrial byproducts like fly ash, slag, or metakaolin, which serve as the primary source of the reactive alumina-silica components [2]. The geopolymerization process entails dissolving these materials in an alkaline solution, leading to the formation of a three-dimensional network of silicate and aluminate species, creating a binder similar to traditional Portland cement but with distinct environmental benefits [3]. Geopolymer concrete has gained prominence in recent years due to its sustainability advantages. It notably reduces carbon emissions as the production of the geopolymer binder

*Corresponding author: hanizam@usm.my
[a]orcid.org/0000-0003-4812-2210; [b]orcid.org/0000-0003-1070-9534; [c]orcid.org/0009-0001-1178-8396
DOI: http://dx.doi.org/10.17515/resm2024.451me0920rs

requires less energy and generates fewer greenhouse gases than Portland cement. Furthermore, geopolymer concrete displays exceptional resistance to various forms of deterioration, including chemical attacks, alkali-silica reactions, and sulfate attacks, making it an attractive choice as normal weight and lightweight concrete for enduring and resilient construction projects [4]. Recognizing the environmental concerns linked with conventional lightweight concrete, researchers have turned to geopolymer technology to develop lightweight geopolymer concrete. By replacing Portland cement with a geopolymer binder, it becomes possible to create lightweight concrete with significantly reduced carbon emissions and a lower environmental footprint.

Extensive study has been conducted on geopolymer concrete as a possible substitute for traditional Portland cement concrete. However, despite its promising advantages, the adoption of geopolymer technology is primarily limited to laboratory settings and has not been widely implemented in the field. This limitation is mainly due to challenges such as the use of chemical activators and the need for energy-intensive oven curing. To address these challenges, researchers have explored the use of agricultural and industrial by-products like palm oil fuel ash (POFA), wood ash (WA), and ground granulated blast furnace slag (GGBS) in the production of geopolymer concrete.

POFA is derived from burning the residue of the oil extraction process from fresh palm fruits, which is typically discarded in open fields, leading to environmental and health issues. In Malaysia, it is estimated that about 10 million tons of POFA are produced annually [5]. However, most studies have focused on activating POFA-based geopolymers using sodium hydroxide (NaOH) or potassium hydroxide (KOH), which raises production costs [6,7,8]. It is imperative to examine the use of more economical substitutes, such as WA lye, a strong alkaline solution, as a replacement for the expensive chemical activators often employed in the production of geopolymer concrete. Another sustainability issue facing in the concrete sector is the depletion of natural resources, which poses a significant environmental concern. The ongoing extraction of naturally existing rocks for coarse aggregates may ultimately result in their exhaustion [9]. To address this issue, many researchers have turned their attention to using waste materials like palm oil clinker aggregate (POCA), recycled concrete aggregate (RCA), timber clinker aggregate (TCA), and palm oil shell (POS) as alternatives in concrete production. Among these, TCA has begun to gain attention as a supplementary material to replace natural aggregates in concrete manufacturing.

Integrating TCA into lightweight geopolymer concrete offers a novel and innovative method for improving its properties. Timber clinker is a material produced through the thermal treatment of wood waste, including wood chips and sawdust. This clinkering process subjects wood waste to high temperatures in the absence of oxygen, leading to the formation of high-strength, porous, and lightweight aggregates. Incorporating TCA into geopolymer concrete offers several potential benefits. Firstly, it allows for the use of abundant wood waste materials, which are typically underutilized in the construction industry. This promotes the recycling and repurposing of wood waste, reducing the environmental impact associated with its disposal. Additionally, TCA are known for their low thermal conductivity, making them an ideal choice for enhancing the thermal insulation properties of lightweight geopolymer concrete. Furthermore, the porous structure of TCA has the potential to improve the lightweight properties of the concrete, which can be particularly advantageous in applications where weight reduction is critical.

According to a previous study by Chai et al. [10], concrete incorporating TCA demonstrated high compressive strength, reduced void content, and lower water permeability. Additionally, adding TCA improved the durability of concrete, with a maximum replacement level of up to 20%. Utilizing timber clinker aggregates not only enhances concrete performance but also promotes sustainability by recycling wood waste. Meanwhile, there is limited study on the application of TCA as a replacement for natural aggregate in geopolymer concrete. As such, it is still lack of comprehensive understanding on the effect of TCA on the physical and mechanical properties of geopolymer concrete. Therefore, this study aims to evaluate the potential of TCA as a partial replacement for natural aggregate in geopolymer concrete. Additionally, the effectiveness of WA lye in activating POFA geopolymer concrete is also being study. By adopting geopolymer technology and incorporating TCA and WA lye as activator, this research highlights a commitment to reducing the environmental impact of construction materials. It explores the transformation of

wood waste into high-strength aggregates, providing an innovative solution for recycling abundant wood waste. This approach aligns with circular economy principles, emphasizing efficient resource use and waste minimization.

2. Materials and Methods

2.1. POFA

The research utilized POFA sourced from an oil mill located in Nibong Tebal, Pulau Pinang, Malaysia. This POFA is a byproduct resulting from the combustion of materials like husk and shells, which are burned to generate steam for use in a turbine engine for electricity generation, as reported by Salam et al. [11]. The factory's report indicated that the end product was incinerated within a temperature range of 400 to 500℃. The collected POFA was subjected to oven drying at 105 ± 5℃ for a duration of 24 hours. Following this, it was passed through a 300μm sieve and then milled using a ball mill for 2 hours, resulting in an ash with a particle size of approximately 80% passing through a 45μm sieve. This meet the requirements specified in ASTM C618 [12], and the specific gravity of the POFA was determined to be 2.40. The Blaine fineness test was conducted to determine the specific surface area in accordance with BS EN 196-6 (2010), and POFA was found to have a Blaine surface area of 4433.7 cm^2/g. The chemical composition of the POFA utilized in the study is presented in Table 1.

2.2. GGBS

In this research, GGBS was used as the high-calcium binding agent. The GGBS used was sourced from MDC Sdn. Bhd. in Kedah, Malaysia, and it had a specific gravity of 2.80. The chemical composition of the GGBS employed in the study can be found in Table 1.

2.3. Alkaline Activator

WA lye, derived from waste wood ash, a byproduct of wood industry operations, is an abundant and environmentally friendly alternative. It offers a 100% cost-effective solution while posing fewer health risks to humans compared to NaOH. In this study, WA lye with a high pH level of 13.16, was utilized alongside sodium silicate as an alkaline activator in the geopolymer concrete production process. The chemical composition of the WA used is detailed in Table 1. The total SiO_2, Al_2O_3, and Fe_2O_3 content is 62.21%; hence, the untreated POFA is classified as class C pozzolana by ASTM C618 [12]. In addition, the XRF study reveals that GGBS constitutes 32.79% of CaO. Additionally, it was discovered that the WA utilized contained a significant amount of K_2O. Fig. 1 shows the XRD patterns of WA, POFA, and GGBS.

Table 1. Chemical composition of POFA, GGBS and WA

Oxide compounds	Composition (%)		
	WA	POFA	GGBS
MgO	8.24	5.02	6.38
Al2O3	3.01	3.27	14.62
SiO_2	12.06	54.98	30.35
SO3	2.55	4.09	-
Cl	0.04	1.78	-
K2O	10.15	9.50	0.38
CaO	55.01	10.77	32.79
Cr_2O_3	0.02	-	-
MnO	1.29	0.14	0.45
Fe2O3	2.92	3.96	0.35
ZnO	0.03	-	-
SrO	0.11	-	-
AS2O3	0.01	-	-
CuO	0.02	-	-
Rb2O	0.01	-	-
NiO	0.02	-	-

Na2O	0.14	0.40	0.27
P_2O5	4.01	5.64	0.01
Ga_2O_3	0.01	-	-
Y2O3	0.01	-	-
ZrO2	0.01	-	-
TiO_2	-	0.19	0.57
BaO	0.04	-	-
LOI	-	5.66	-

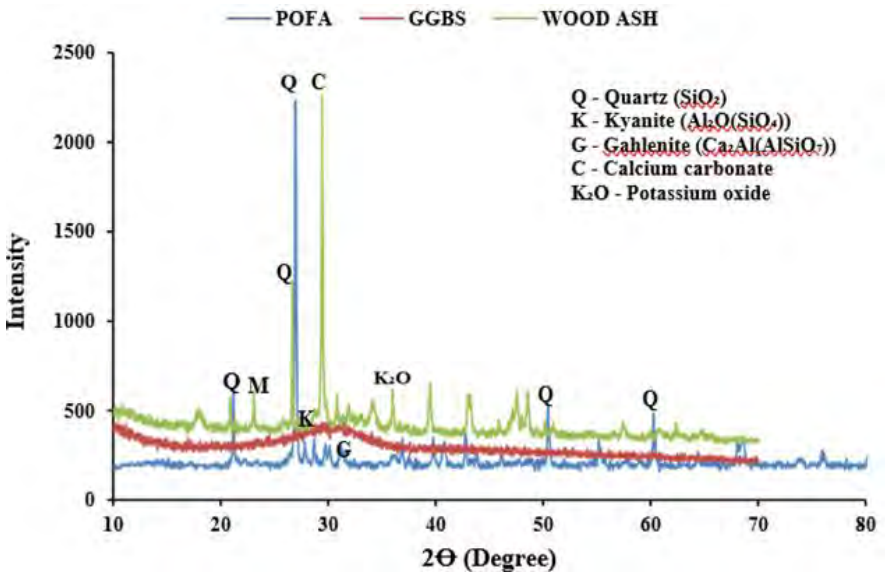


Fig. 1. XRD patterns of POFA, WA and GGBS

2.4. Aggregate

2.4.1 Fine Aggregate

The research employed fine aggregate sourced from local suppliers, which was river sand. This sand underwent sieving through a 4.75mm sieve and possesses a specific gravity of 2.63. The sand was subjected to sieve analysis in accordance with ASTM C136 [13], and Fig. 2 provides a visual representation of the sieve analysis results. The cumulative percentage passing of the river sand was compared to ASTM C33 [14] and found to be within the specified finer and coarser limits for fine aggregate as shown in Table 2.

Table 2. Sieve analysis of river sand

Sieve size	ASTM C33	Percent Passing
10mm	100	100
4.75mm	95 – 100	100
2.36nm	80 – 100	84.1
1.18nm	50 – 85	51.7
600µm	25 – 60	20.8
300µm	5 - 30	7.40
150µm	0 - 10	1.60
75µm	-	0.34
Pan	-	0

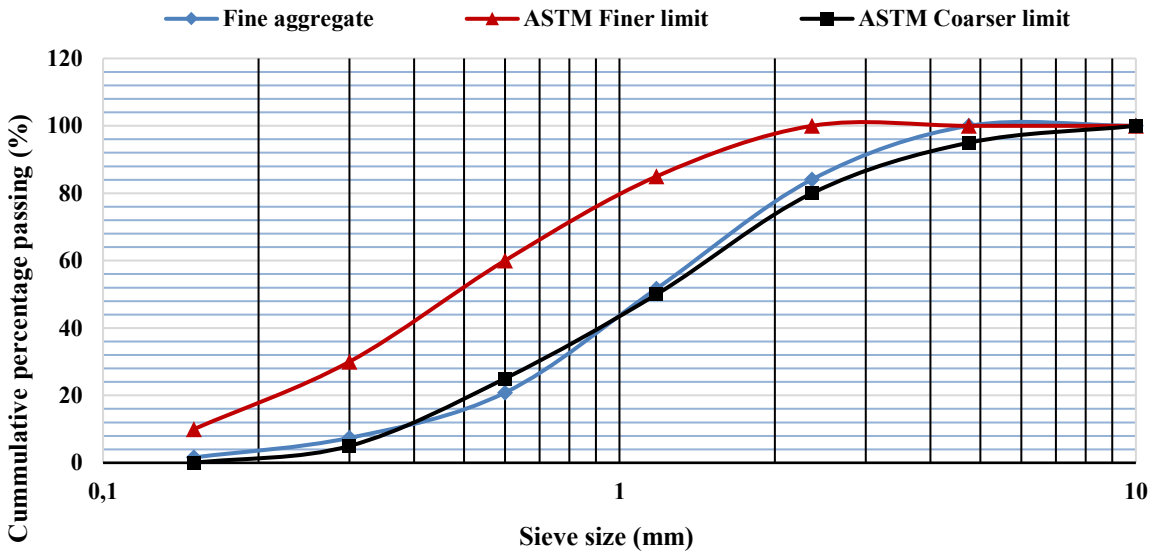


Fig. 2. Sieve analysis of river sand

2.4.2 Natural aggregate

The study utilized coarse aggregate sourced from local suppliers, consisting of 12mm diameter crushed granite. This aggregate exhibited fundamental attributes of an excellent coarse aggregate, including low porosity, strong crushing resistance, and minimal water absorption. Table 3 summarizes the physical characteristics of this crushed granite aggregate, while Fig. 3 presents the sieve analysis graph for the crushed granite.

2.4.3 Timber clinker aggregate (TCA)

TCA is another outcome of burning wood in boilers for the purpose of generating electricity. Typically, it appears as chunky clinkers and is frequently discarded in landfills. These clinkers are crushed to achieve the preferred size of 12mm, which is then used as coarse aggregate (as depicted in Fig. 4). The physical characteristics of this TCA, encompassing factors like specific gravity, aggregate crushing value, and water absorption, are detailed in Table 3. Furthermore, Fig. 3 illustrates the sieve analysis results for the TCA employed in this research.

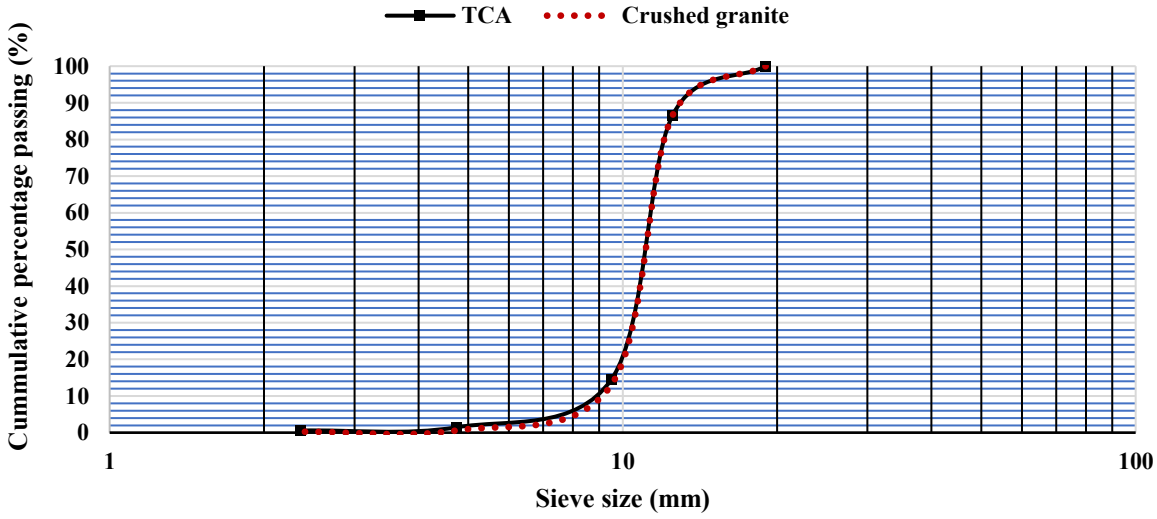


Fig. 3. Sieve analysis graph of natural granite and TCA

Table 3. Physical properties of coarse aggregates

Properties	Crushed Granite	Timber Clinker	Standards
Specific Gravity	2.64	2.10	IS 383: 1970
Water Absorption	0.81%	2.31%	BS 882: 1992
Aggregate Crushing Value	19%	22%	BS 882: 1992

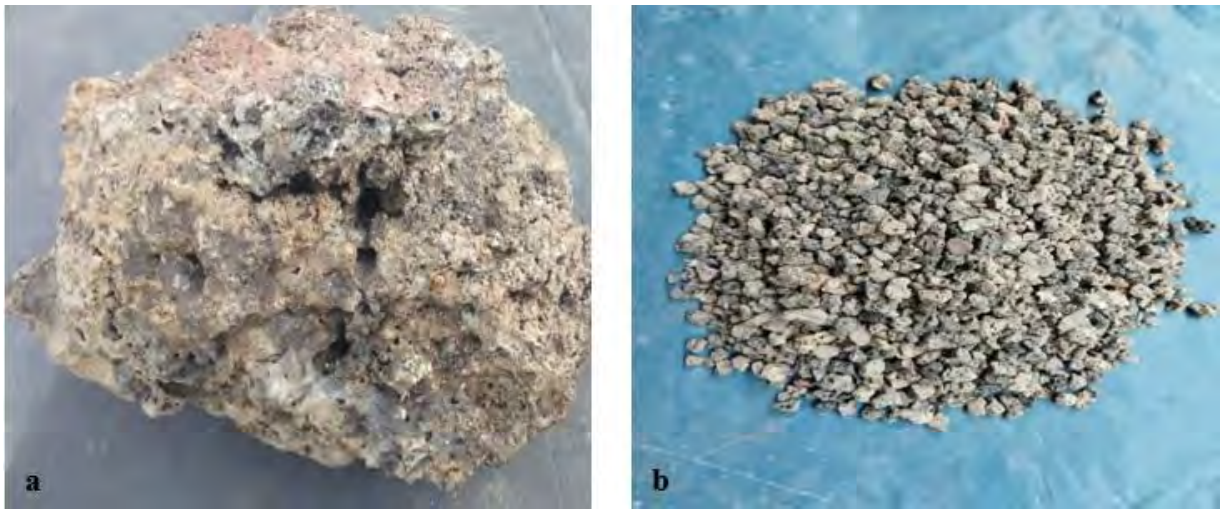


Fig. 4. (a) Timber clinker chunk (b) Crushed timber clinker aggreate (12mm)

2.5. Preparation and Curing of Specimen

The alkaline activator in this study was created by combining water and sieved WA at a specific ratio of 1:2. This mixture was left undisturbed for several days until it reached a pH of 13.16. The authors employed a liquid-to-binder (L/B) ratio of 0.5 and an alkaline activator ratio (AAR) of 3.0, based on findings from their earlier research. Cube size of 100 x 100 x 100mm were produced and subjected to compression tests at various time intervals (3, 7, 14, 28, 56, and 180 days). Additionally, cylindrical specimens measuring 100 x 200mm for split tensile strength tests and 100 x 100 x 500mm beams for flexural strength tests were produced. The workability of the fresh geopolymer concrete was assessed through a slump test.

Table 4. Geopolymer concrete mix proportion

TCA Content (%)	POFA (kg/m³)	GGBS (kg/m³)	Sand (kg/m³)	Natural Gravel (kg/m³)	TCA (kg/m³)	Lye (kg/m³)	Na_2SiO_3 (kg/m³)
0	315.00	135.00	756.70	888.30	0.00	56.25	168.75
20	311.59	133.54	494.78	710.64	135.50	55.64	166.90
40	311.59	133.54	494.78	532.98	271.01	55.64	166.90
60	311.59	133.54	494.78	355.32	406.51	55.64	166.90
80	311.59	133.54	494.78	177.66	542.02	55.64	166.90
100	311.59	133.54	494.78	0.00	677.52	55.64	166.90

The specific mix proportions for the binary blended lightweight geopolymer concrete with TCA can be found in Table 4. An epicyclic mixer, conforming to ASTM C305 [15] was employed to prepare the geopolymer concrete mix. Initially, POFA and GGBS were dry mixed for about 3 minutes to achieve a uniform consistency. Next, the alkaline activator was added, and the mixture was stirred for an additional 6 minutes to form a three-dimensional geopolymer network. Following this, aggregates were added and mixing continued for another 5 minutes. The prepared mixture was then poured into molds and vibrated to ensure proper compaction. The specimens were wrapped in plastic to prevent moisture loss and left to set for 24 hours before demolding. After demolding, the specimens are cured at ambient conditions, maintaining a temperature of 25°C ± 5°C and a relative humidity of 75% ± 5%.

2.6. Testing Methods

2.6.1. Slump Test

The workability of the geopolymer concrete was evaluated using the conventional slump test in accordance with ASTM C143 [16]. The test involved filling a metal cone with concrete in three layers, with each layer tamped 25 times using a metal rod as shown in fig. 5. After filling, the cone was carefully lifted, and the slump was measured as the distance from the top of the slumped concrete to the top of the inverted cone.



Fig. 5. Slump test



Fig. 6. Compressive Strength Test

2.6.2. Compressive Strength

The compressive strength test was performed using a GOTECH GT-7001-BS300 machine with a capacity of 3000 kN, in accordance with BS EN 12390-3 [17] as shown in Fig. 6. The compressive strength of the mortar was tested at 3, 7, 14, 28, 56, and 180 days.

2.6.3. Flexural and Tensile Strength

For concrete prisms of size 100 x 100 x 500mm, the flexural strength test was conducted according to ASTM C293 [18] using ELE universal testing machine as shown in Fig. 7.



Fig. 7. Flexural Strength Test



Fig. 8. Tensile Strength Test

The tensile strength test for lightweight geopolymer concrete was conducted using cylindrical specimens with a diameter of 100mm and height of 200mm, following ASTM C496 [19]. The test was performed on a GOTECH GT-7001-BS300 machine with a 3000kN capacity, in accordance with BS EN 12390-3 [20] (Fig. 8). The tensile strength was measured at 3, 7, 14, 28, 56, and 180 days.

2.6.4. Ultrasonic Pulse Velocity (UPV) Test

The ultrasonic pulse velocity (UPV) test, a non-destructive test, was conducted on 100mm x 100mm x 100mm concrete cubes before the compressive strength tests at 3, 7, 28, 56, and 180 days. This test followed the MS EN 12504-4 [21] standard, using the Proceq Tico ultrasonic instrument as shown in Fig. 9.



Fig. 9. UPV Test



Fig. 10. Water Absorption Test

2.6.5. Water Absorption

The water absorption test was performed on cylindrical specimens measuring 75 mm in diameter and 100 mm in length, following ASTM C642 [22], as illustrated in Fig. 10. The water absorption percentage was determined by subtracting the oven-dry weight of the sample from its saturated weight, dividing this difference by the oven-dry weight, and multiplying by 100.

2.6.6. Drying Shrinkage

The drying shrinkage measurement was carried out according to ASTM C157 [23] as shown in Fig. 11. The drying shrinkage test was conducted at intervals of 3, 7, 14, 28, 56, 90, 180, and 270 days to track changes in specimen length over time.



Fig. 11. Drying Shrinkage Test



Fig. 12. Sulphate Resistance Test

2.6.7. Sulphate Resistance

Sulphate resistance test is conducted following ASTM C1012-04 [24]. Concrete cubes measuring 100mm x 100mm x 100mm were produced and cured at ambient temperature for 28 days before being exposed to a 5% magnesium sulfate ($MgSO_4$) solution for up to 180 days (Fig. 12). The solution was prepared by dissolving 1000g of $MgSO_4$ in 10 liters of water to achieve the desired concentration, with the solution changed monthly. Durability was assessed by monitoring mass change and residual compressive strength at intervals of 0, 28, 56, and 180 days of immersion. The compressive strength of the immersed specimens was compared to control specimens cured at ambient temperature for the same duration.

3. Results and Discussions

3.1. Workability

The workability of the geopolymer concrete was assessed by measuring the slump, and the outcomes are depicted in Fig. 13. An observable decrease in the slump height was noted as the content of TCA increased within the mixture. This phenomenon can likely be attributed to the superior water absorption capacity of TCA in comparison to conventional aggregates, as corroborated by the research of [25], which compares palm oil clinker aggregate (POCA) with conventional aggregates, noting higher water absorption of POFA that reduces slump height. This suggests that mixtures with higher TCA content tend to absorb more of the alkaline solution compared to control mixes with lower TCA content. The highest slump measurement of 115mm was achieved in the TCA0 mix, while subsequent increments of 20% TCA content resulted in an approximately 18% reduction in the slump height, with the lowest value of 43mm attained by the TCA100 mix.

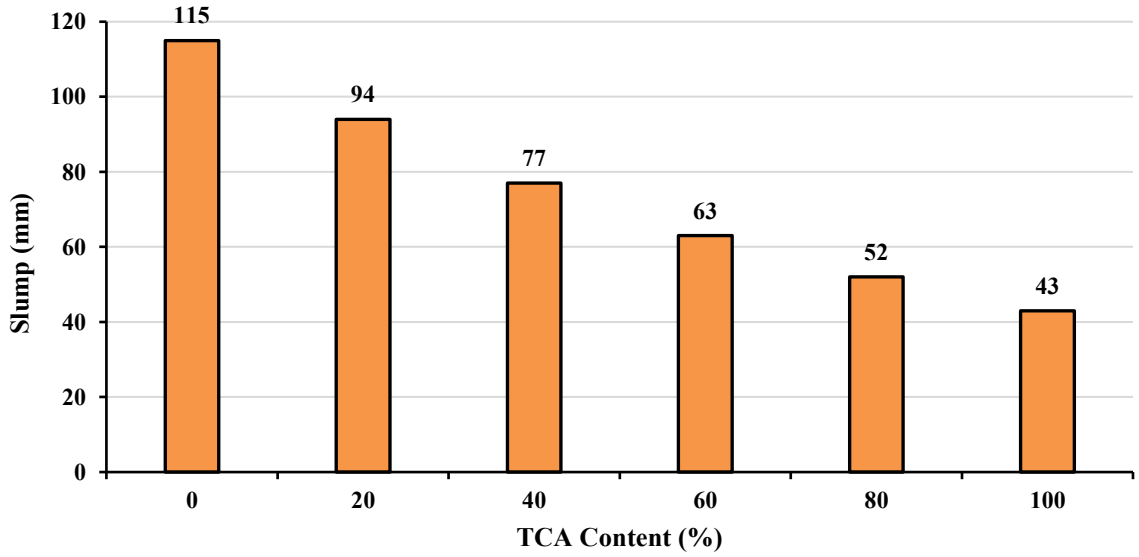


Fig. 13. Workability result of binary blended POFA:GGBS geopolymer concrete incorporating TCA

In this experimental research, to prevent any dilution effects against the WA lye, additional water or superplasticizers were intentionally not utilized. Unlike Ordinary Portland Cement (OPC) concrete, where superplasticizers can notably enhance material performance, their use in geopolymer binders typically has minimal to no discernible impact. This is due to the tendency of the alkaline solution to degrade the superplasticizer and diminish its effectiveness, as noted in the literature [26]. Notably, in lightweight geopolymer concrete, it was observed that the alkaline solution tends to enhance the workability of the mixture [25]. This observation was reaffirmed in this research, where a moderate to high workability was achieved without the need for extra water or superplasticizers.

Another contributing factor affecting the workability of the geopolymer concrete is the shape of the TCA, which is angular and rough in contrast to natural aggregates. Rehman et al. [26] reported that using rounded aggregates in concrete results in a higher slump. However, in this research, the angular shape of the aggregate appeared to create a frictional effect that hindered particle movement, consequently reducing the flowability of the concrete. Similar findings were also documented by Rehman et al. [27].

3.2. Density

The 28-day density of geopolymer concrete containing TCA is depicted in Fig. 14 below. According to ASTM C330 [28] structural lightweight concrete typically falls within the density range of 1440 - 1840 kg/m^3 when 100% lightweight aggregate is used. The density of lightweight concrete is influenced by the unit weight of the aggregate, as affirmed by Malkawi et al. [25], owing to their higher proportion in the concrete mix. The bulk density of the TCA employed in this experimental study is lower than that of natural aggregates, which implies an expected reduction in the concrete density when TCA partially replaces natural aggregates.

The analysis of the experimental results shows a consistent reduction in the density of the geopolymer concrete with the addition of TCA. The 28-day density of specimens with normal aggregates measured at 2063.13 kg/m^3, followed by the 20% TCA specimens with a density of 1960.97 kg/m^3, indicating an approximate 4.95% reduction in density. The specimens featuring 100% TCA recorded a density of 1805.66 kg/m^3, marking an approximate 12.48% reduction in density when compared to the control specimens. Notably, it is worth mentioning that specimens with 100% TCA content fall within the range specified by ASTM C330 [28] for structural lightweight concrete, making them suitable for various structural lightweight concrete applications.

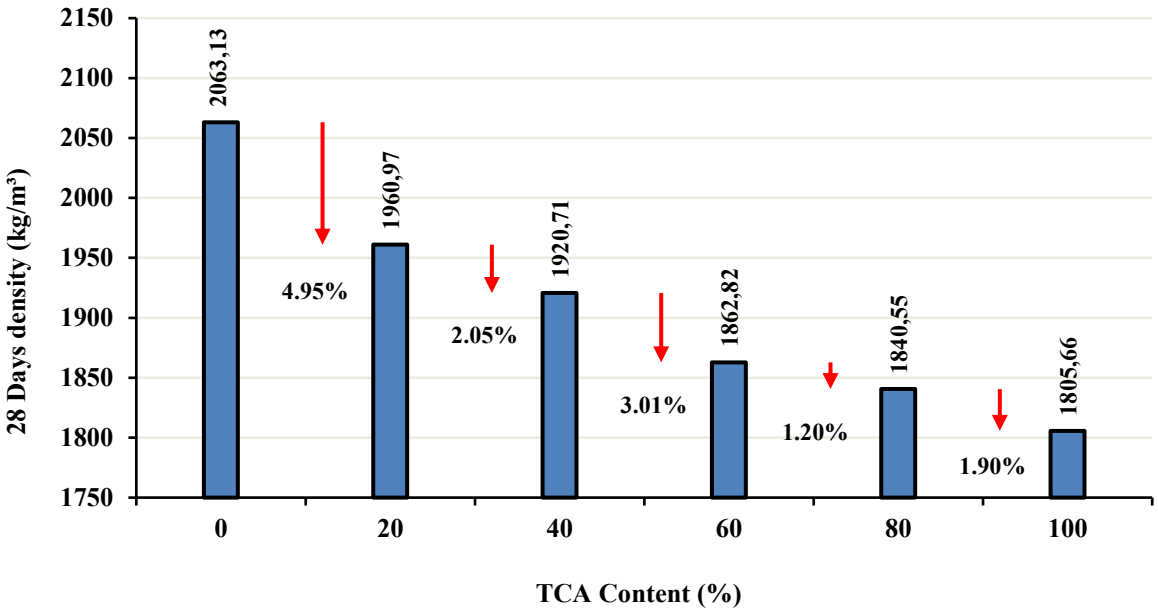


Fig. 14. Average density of binary blended POFA: GGBS geopolymer concrete incorporating TCA at 28 days

3.3. Compressive Strength

Fig. 15 shows the compressive strength results of POFA geopolymer concrete incorporating TCA at different replacement percentages for natural aggregate. A noticeable trend emerges, where the substitution of natural aggregate with TCA leads to both a reduction in density and a decline in the concrete's compressive strength. This outcome can likely be attributed to the relatively lower strength and bulk density of lightweight aggregates compared to their natural counterparts; a finding that is consistent with the research conducted by Malkawi et al. [25]. Given the gradual development of strength in geopolymer concrete cured under ambient conditions, the early

strength measurements were only around 50% of the 28-day strengths. However, these concrete mixes continue to gain strength as the curing period progresses.

Analyzing the test results, it becomes evident that the control specimen achieved the highest strength of 28.78 MPa at 3 days, while a consistent reduction in strength is observed in the TCA specimens, with reductions of 20.74%, 32.59%, 42.84%, 48.75%, and 57.61% for 20%, 40%, 60%, 80%, and 100% TCA content, respectively. After 28 days of ambient curing, the control specimen retained approximately 88.40% of its 180-day strength, a trend also observed in the remaining TCA specimens, which attained approximately 88% to 90% of their 180-day strength at 28 days. This sustained strength development over the curing period is possibly attributed to the water absorbed by the porous TCA, which is subsequently released, triggering the hydration reaction [27].

Chai et al. [10] conducted a study on the effects of TCA in concrete, showing that incorporating TCA up to a 20% replacement level improved the durability and compressive strength, while higher TCA contents negatively impacted compressive strength. This indicates that moderate levels of TCA can balance strength and sustainability, but excessive replacement reduces workability and strength due to high water absorption. This is also proven by the study of Malkawi et al. [25], which explored the use of palm oil clinker aggregate (POCA), another lightweight aggregate, in geopolymer concrete, observing that increasing POCA content reduced density and compressive strength. Similar to TCA, the lightweight nature and porosity of POCA contributed to a decline in strength, but it also provided advantages in terms of lower thermal conductivity and reduced overall concrete weight.

Furthermore, it was observed that the loss of strength was more pronounced at higher levels of TCA replacement. This could be attributed to the reduced workability of the specimens, making them somewhat challenging to compact. Malkawi et al. [25] reported that a higher content of lightweight aggregates resulted in the absorption of the alkaline solution in the mixture, which, in turn, left some of the binder particles unreacted. This factor may also contribute to the reduction in strength of geopolymer concrete when incorporating TCA in comparison to specimens using natural aggregates.

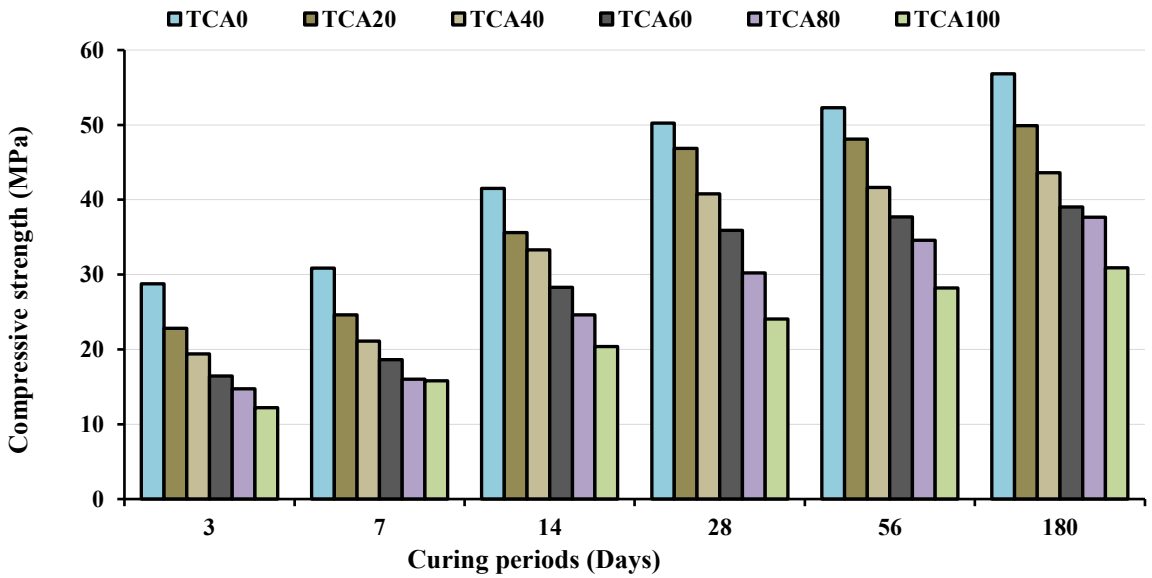


Fig. 15. Compressive strength of binary blended POFA:GGBS geopolymer concrete incorporating TCA

The compressive strength of lightweight geopolymer concrete is closely related to its density. Generally, higher-density concrete exhibits greater compressive strength. Fig. 16 illustrates the relationship between the density at 28 days and the corresponding compressive strength at the same curing age. The addition of TCA in the geopolymer concrete reduced its density, which in turn lowered the compressive strength.

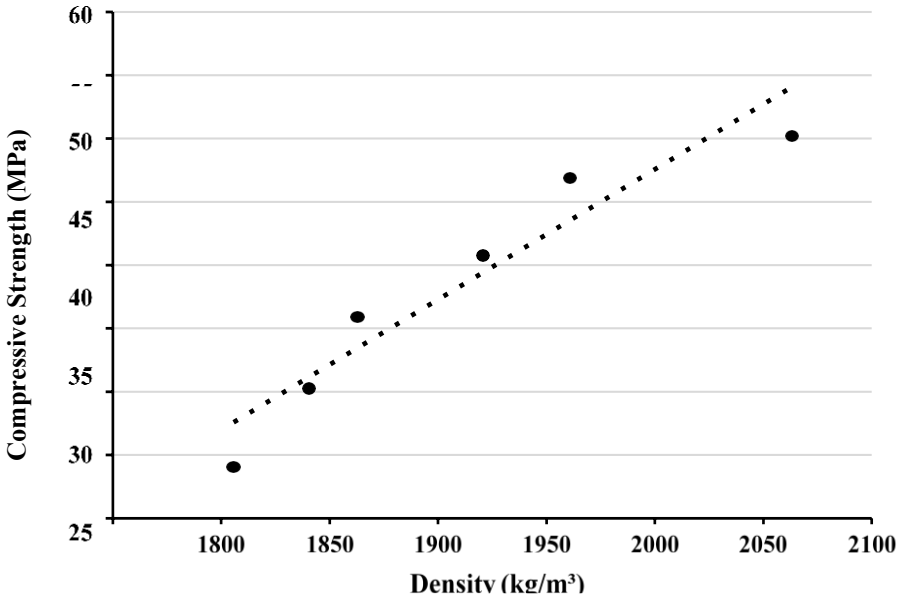


Fig. 16. Relationship between compressive strength and density at 28 days of curing

3.4. Flexural and Tensile Strength

The flexural strength of different replacements of TCA in binary blended POFA: GGBS geopolymer concrete was tested at 3, 7, 14, 28, 56, and 180 days, respectively. Referring to the test result (Fig. 17), the flexural strength of the geopolymer concrete decreases with increasing percentages of TCA in the mixture. The percentage reduction in the flexural strength at 28 days as compared to the control sample were 2.94, 5.48, 8.61, 16.83, and 25.44% for 20, 40, 60, 80, and 100% TCA, respectively. Malkawi et al. [25] reported that failure in tension generally occurs due to the breakdown of binder-aggregate bond. This was observed to create the presence of voids in the concrete which caused stresses concentration and let to cracks propagation. In this experimental study, the presence of voids was noticed in concrete with TCA content as shown in Fig. 18, this explains the reduction in the flexural strength of the TCA concrete specimens. Moreover, it was reported that the lower crushing value of lightweight aggregates (LWA) has very little or no impact on concrete's flexural strength [25]. This was due to fact that the compression zone in concrete beam specimen have an insignificant effect on bending failure [29].

Referring to the results of the tensile strength in this study (Fig. 19), the inclusion of TCA in the concrete reduced the strength of concrete. A tensile strength of 3.92MPa was attained by the control specimens at 28 days, a subsequent decrease in the concrete's strength was recorded for 20, 40, 60, 80, and 100% TCA concretes with approximately 3.74, 3.63, 3.31, 2.67, and 2.54MPa, respectively. The decline in the split tensile strength may be due to the porous nature of TCA which results in higher water absorption compared to control specimens [20]. This finding was also noted in this study where the specimens with TCA possessed higher water absorption compared to control specimens. Also, the voids presence in the concrete as shown in Fig. 18 contributed to the stresses concentration which hastened the development of cracks in the concrete. As opposed to compression strength, where the matrix and aggregate support one another as a result of the compressive pressures, the aggregates and matrix are separated apart under the action of tensile forces [27]. It was also reported that lightweight aggregate utilization in concrete usually led to a high reduction in the split tensile strength and elastic modulus compared to compressive strength [31]. It is worth mentioning that all lightweight geopolymer concretes produced with TCA in this study meets the 28 days minimum tensile strength requirement of 2.0MPa [28]. Hence TCA can effectively be utilized as an aggregate in structural lightweight concrete.

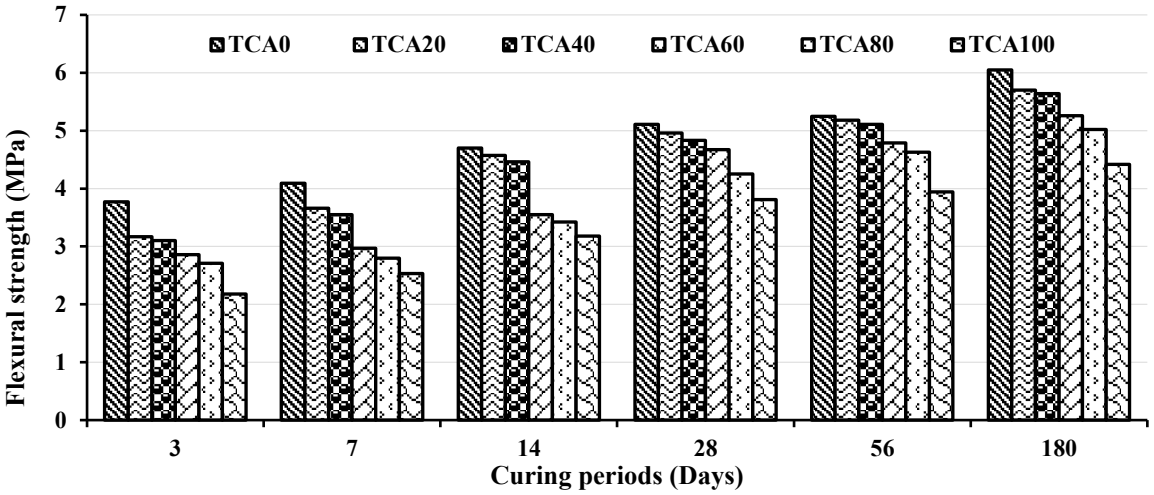


Fig. 17. Flexural strength of binary blended POFA: GGBS geopolymer concrete incorporating TCA

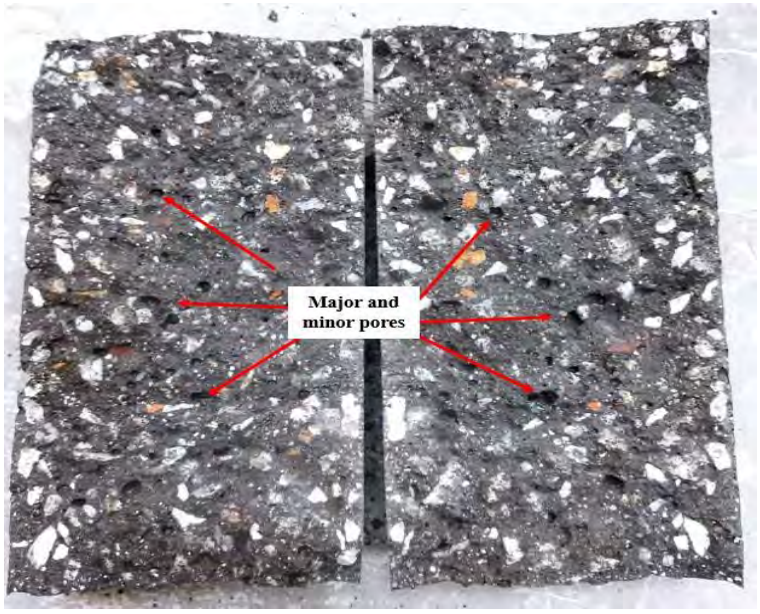


Fig. 18. TCA specimen with arrows showing pores in concrete

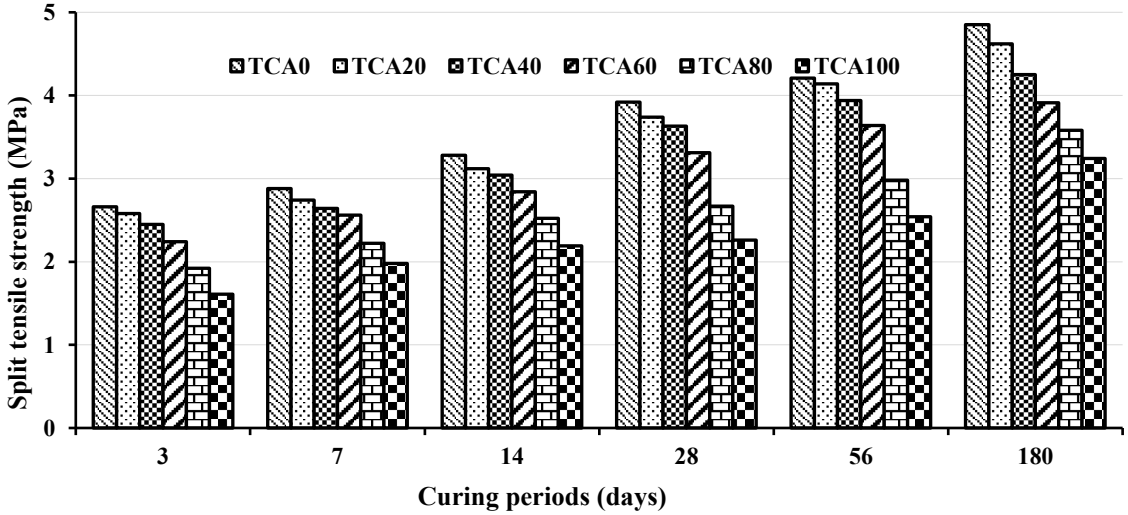


Fig. 19. Split tensile strength of binary blended POFA: GGBS geopolymer concrete incorporating TCA

3.5. Ultrasonic Pulse Velocity

Quality of concrete and its internal structure like micro pores, homogeneity, and cracks can be assessed using UPV non-destructive test. This test relates concrete's quality to ultrasonic pulse speed dispersed through the concrete from one transmitter to the other. The higher of the pulse's speed indicates the quality of the concrete and vice versa. UPV test was carried out in this experimental study at 7, 28, 56, and 180 days, respectively.

The UPV test results of the binary blended POFA: GGBS geopolymer concrete incorporating TCA are illustrated in Fig. 20 below. It can clearly be observed that the inclusion of TCA in the concrete decreased the UPV readings, this was already anticipated because TCA inclusion creates more pores in the concrete as compared to control specimens. It was established that the increase in the number of micro pores in concrete reduced the speed of the pulse which results in low readings. However, for all the samples tested, the UPV increased gradually as the curing period increases, indicating a gradual refinement in the micropore structures of the concrete with the increase in the curing duration. The reduction in the micro pores may be due to the ongoing geopolymerization reaction creating extra C-A-S-H gel which solidifies the concrete over time.

Referring to the test results presented, the control specimen exhibited the highest UPV readings of 3930, 4135, 4170, and 4504 m/s at 7, 28, 56, and 180 days, respectively. These were 26.77, 27.09, 25.90, and 29.51% compared to 100% TCA specimens. It is worth mentioning that all the concrete specimens tested fall within the category of medium – excellent concretes [32].

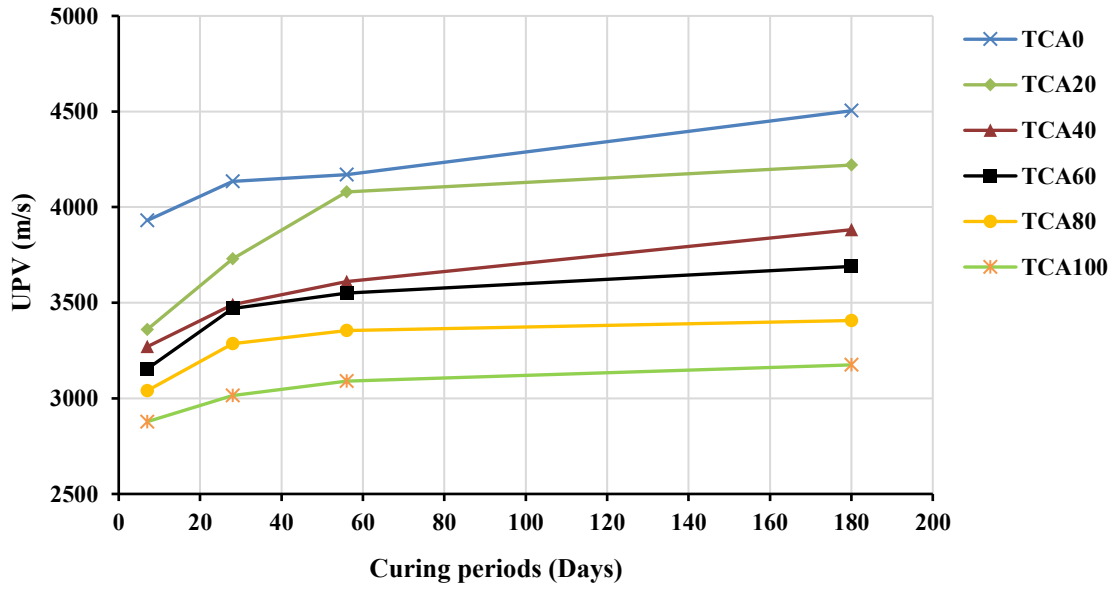


Fig. 20. Effect of TCA inclusion on UPV

3.6. Water Absorption

Water absorption in concrete is an indication of pore volume within the specimen. According to BS 1881 [33], a maximum water absorption of 10% is acceptable for various construction applications, including structural elements, minor structural elements, and non-structural elements. In this phase of the study, the water absorption was taken as an average of three specimens at 3, 7, 14, 28, 56, and 180 days. Fig. 21 displays the average results for various percentages of TCA inclusion in the concrete as a partial replacement for coarse aggregate. The addition of TCA to the concrete results in higher water absorption, which aligns with expectations given its porous nature. Ahmad et al. [34] also reported that the elevated water absorption in lightweight concrete is mainly governed by the porosity of the lightweight aggregates. Other researchers have reported similar findings, indicating that lightweight concrete typically exhibits higher water absorption compared to normal weight concrete [35, 36].

Referring back to the result of this study, it was observed that the water absorption of all the specimens decreases with the prolong curing period which was possibly due to the gradual refinement of the micro pores in the concrete as a result of continuous geopolymerization process over time. However, the observed trend in water absorption aligns with the typical pattern reported in the literature, where the absorption rate increases with the proportion of lightweight aggregate in the concrete. The 28-day water absorption for the control concrete (TCA0) was measured at 4.59%. With the addition of TCA at replacement levels of 20%, 40%, 60%, 80%, and 100%, the water absorption values increased to 5.02%, 5.38%, 5.75%, 6.02%, and 6.52%, respectively. These results are consistent with previous studies on POFA geopolymer concrete with natural aggregates, which typically show water absorption rates below 10%, remaining within the acceptable limits specified by standards such as BS882:1992 [37]. In summary, it is notable that all tested specimens stayed below the 10% maximum water absorption limit set by BS 882:1992, indicating compliance with standard requirements for water absorption.

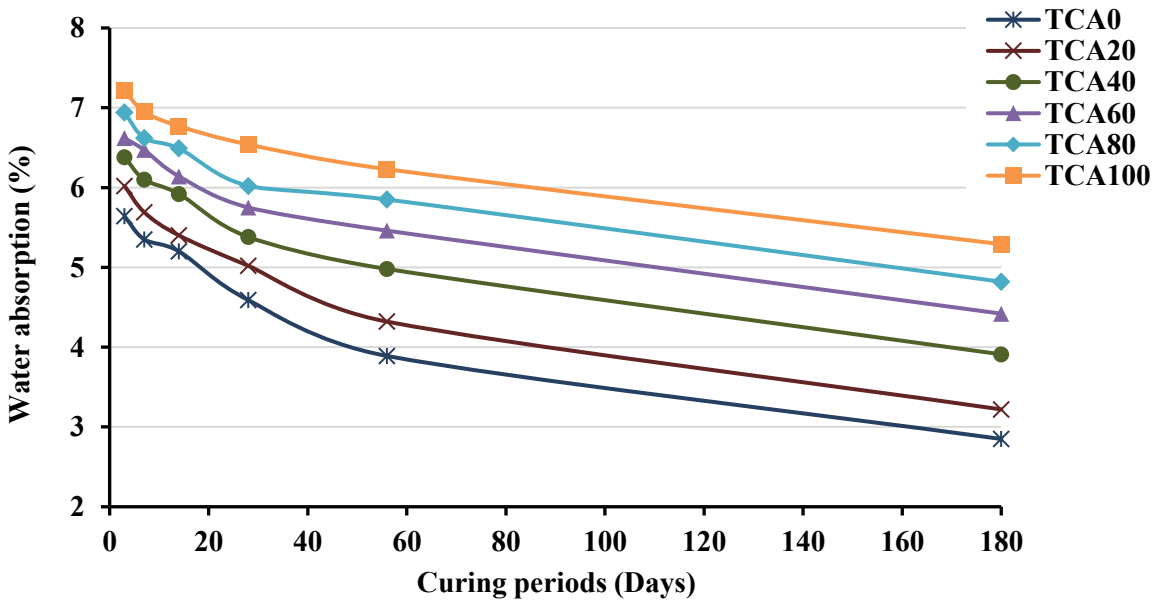


Fig. 21. Effect of TCA inclusion on water absorption

3.7. Drying Shrinkage

The drying shrinkage was calculated as the average of two beams, with changes in length recorded over a period of 270 days, as shown in Fig. 22. Based on the drying shrinkage results from this study, it was observed that increasing the TCA content in the mixture resulted in higher water absorption and porosity, which in turn caused greater drying shrinkage in the concrete compared to those with normal aggregates. Furthermore, the drying shrinkage at early age was more pronounced at up to 56 days for all the specimens. At a prolong drying period, the drying shrinkage observed was nearly horizontal line which shows a very low increase in the drying shrinkage probably due to the fact that the specimens at this age are mostly dried. It was observed that the drying shrinkage increased with the increase in TCA content due to the porous nature of the TCA which tend to absorb the mixing alkaline solution and also the drying shrinkage decreased over time for all specimens. Relating the drying shrinkage with porosity and water absorption it was noticed that specimens with high porosity and water absorption exhibit the highest drying shrinkage.

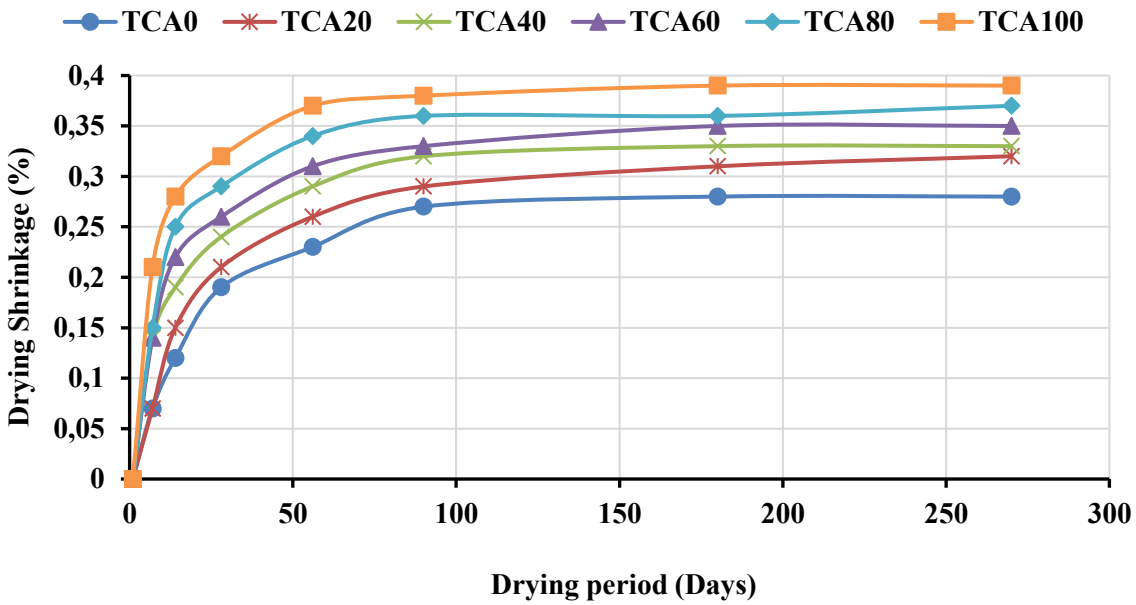


Fig. 22. Effect of TCA inclusion on drying shrinkage

3.8. Resistance to Sulphate Attack

Concrete is increasingly utilized across diverse applications and challenging environments. In such conditions, conventional concrete may not always meet the required standards of quality or durability throughout its lifespan. Sulphate attack led to ordinary concrete deterioration due to the removal of hydration products forming ettringite and gypsum which led to the expansion of the concrete and transformation of C-S-H to magnesium sulphate hydrates (M-S-H), this causes strength reduction [38]. Patil et al. [39] reported that geopolymer concretes greatly resist sulphate attack, it shows no sign [38] of compressive strength degradation, mass, length change, and physical appearance. In this study, the POFA: GGBS lightweight geopolymer concrete resistance to aggressive environment was assessed in terms of sulphate resistance. The specimens subjected to the $MgSO_4$ solution were assessed for weight loss over the immersion period of 0, 28, 56, and 180 days, respectively. Similarly, the compression strength of these specimens was determined and compared to the strength of the specimens subjected to ambient curing at 28, 56, and 180 days, respectively.

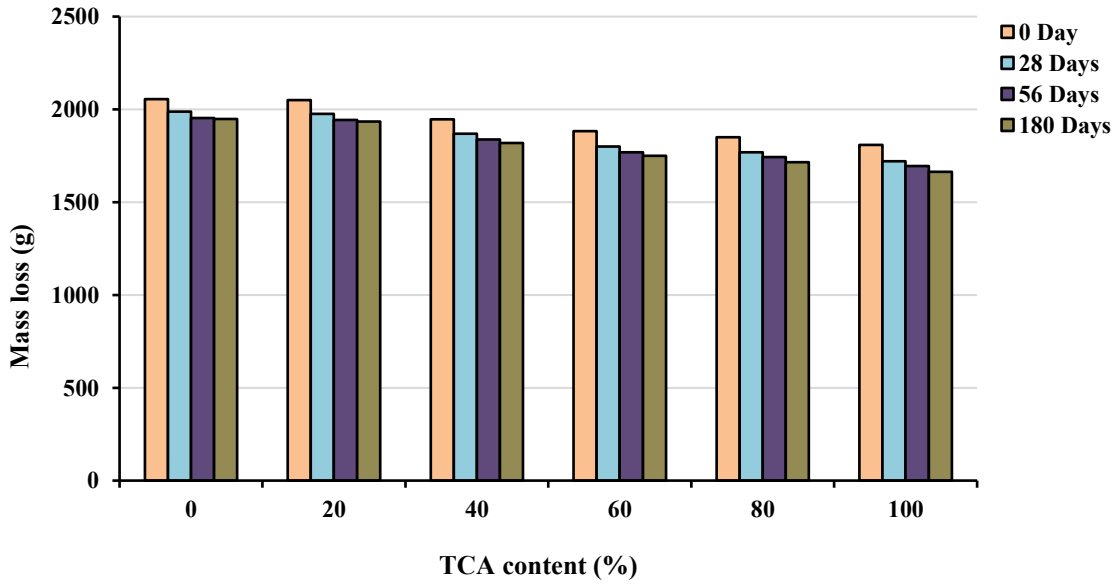


Fig. 23. Mass loss of specimens subjected to $MgSO_4$ solution up to 180 days

The visual test of the lightweight POFA: GGBS geopolymer concrete specimens subjected to $MgSO_4$ solution was carried out at 28, 56, and 180 days, respectively. It was noted that no sign of deterioration appeared on the concrete specimens at all the testing periods. This finding was also confirmed by Kabir et al. [40]. The weight reduction of all the specimens subjected to $MgSO_4$ solution with the increase in immersion period was examined and presented in Fig. 23 below. Compared to specimens' weight at 28 days, the weight loss at 180 days were 1.95, 2.09, 2.6, 2.80, 3.08, and 3.34% for 0, 20, 40, 60, 80, and 100% TCA, respectively. In general, it was observed that the mass of all the tested specimens reduced with the increase in the immersion period. Similarly, weight loss was in line with the water absorption test result, that is the highest weight loss was recorded for specimens with highest content of TCA. This was probably due to voids presence in the specimens with the high TCA content which makes it easier for the sulphate ions to penetrate the concrete compared to less void's concretes.

Table 5. Strength development and percentage reduction of concretes subjected to $MgSO_4$

TCA Content (%)	28 Days comp. strength (MPa)			56 Days comp. strength (MPa)			180 Days comp. strength (MPa)		
	Control	$MgSO_4$	% Loss	Control	$MgSO_4$	% Loss	Control	$MgSO_4$	% Loss
TCA0	52.31	51.36	1.82	53.82	51.90	3.57	56.44	54.30	3.79
TCA20	48.10	47.05	2.18	48.90	47.10	3.68	49.28	48.08	2.44
TCA40	41.63	40.82	1.95	42.88	41.28	3.73	44.21	42.79	3.21
TCA60	37.70	36.81	2.36	38.62	37.24	3.57	40.05	38.78	3.17
TCA80	34.58	33.62	2.78	34.92	34.18	2.12	37.52	36.43	2.91
TCA100	28.21	27.45	2.69	29.31	28.22	3.72	31.10	30.18	2.96

Table 5 presents the development in strength and the percentage reduction in strength of the POFA: GGBS lightweight geopolymer concretes. The impact of the $MgSO_4$ solution on the compressive strength of concrete was assessed by comparing the results of specimens exposed to the sulphate solution with those of the control specimens. At 28 days of immersion, the average strength loss was between 1.8 – 2.8% for all the specimens. However, at 180 days, the strength loss rose to 2.4 – 3.8% for all concrete specimens probably due to long term immersion. The lesser percentage of strength reduction in the geopolymer concretes was attributed to the ability of the geopolymer concretes to resist sulphate attack compared to OPC concretes.

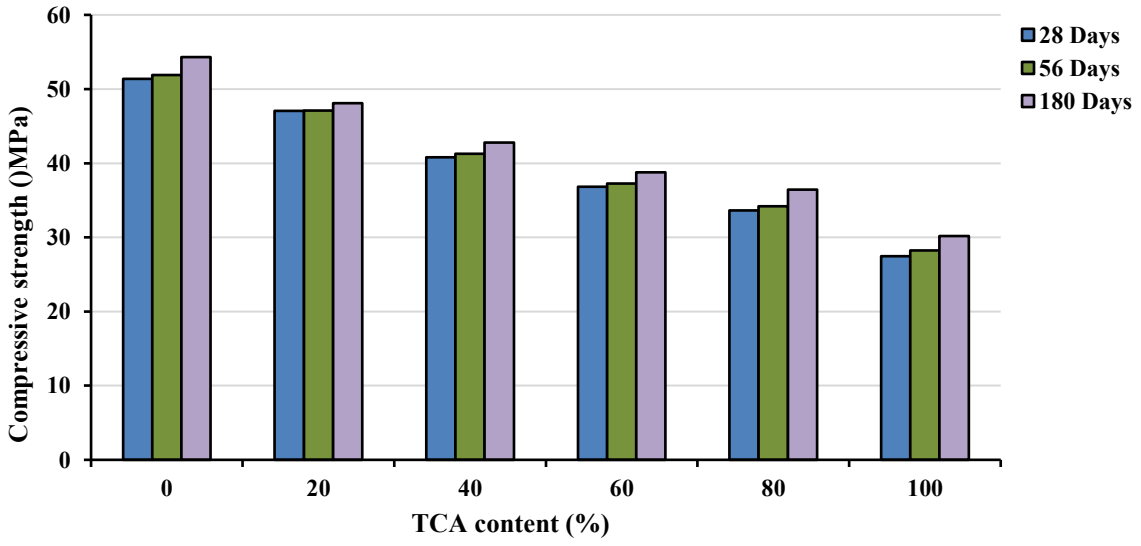


Fig. 24. Compressive strength of specimens subjected to $MgSO_4$ solution up to 180 days

As indicated in Fig. 24, the strength of the specimens before immersion in the sulphate solution was observed to increase with the duration of immersion. This strength development may be attributed to the sufficient geopolymerization over the prolong period. Similar findings were reported by other researchers where the strength of concretes subjected to sulphate solution increases with increase in the duration of immersion [41, 42].

3.9. Sustainability WA Lye Activated Lightweight Geopolymer Concrete

This study has successfully developed a friendly ambient cured geopolymer concrete activated with WA lye incorporating TCA as a promising alternative to conventional geopolymer concrete activated with NaOH. However, in order to achieve this concrete's extensive application as a sustainable construction material, it is important to investigate its environmental and economic efficiency. The environmental efficiency of concrete was conducted using the method of CO_2 Life Cycle Assessment (LCA) of concrete according to ISO 14040 [43]. LCA is an evaluation technique which takes into consideration the consequences and benefits from both upstream and downstream uses of a material across its lifetime [43].

3.9.1 Environmental Efficiency

The environmental efficiency of WA lye activated geopolymer concrete is evaluated through determining the CO_2 emission of the materials. The CO_2 factors of 0.027, 0.014, 0.041, 1.425, and 0.78 kg CO_2-eq/kg for GGBS, sand, gravel, NaOH, and Na_2SiO_3 were adopted from previous studies [44]. The given mass of 8M NaOH in 1 litre of water is 320g, this was used in the analysis due to the fact that the WA lye produced successfully compete with 8M NaOH. The CO_2 emission of POFA, WA, and TCA were ignored because they are waste materials. The embodied CO_2 index (CI) of the geopolymer concrete was calculated by dividing the 28 days compressive strength by the total CO_2 emission of the non-waste materials. The CO_2 emission of both the concretes were presented in Table 6. It was noted that the CO_2 emission of normal weight geopolymer concrete activated with 8M NaOH (NWGC) was almost 25.32% higher than that of the LWGC, this was credited to the total and partial replacement of both NaOH and natural gravel by WA lye and TCA, respectively.

Moreover, the CI of both NWGC and LWGC were determined as 0.23 and 0.23, respectively as presented in Table 7. It was observed that the eco-efficiency of both geopolymer concretes were similar, this was due to the fact that the compressive strength of the NWGC activated with NaOH is higher than that of the LWGC activated with WA lye. Sandanayake et al. [44] and Yang et al. [45] also observed similar findings, they reported that the use of geopolymer/alkali activated concretes contributes to CO_2 emission reduction in comparison to conventional concretes.

Table 6. CO_2 emission of cubic meter of NWGC and LWGC

Concrete type	28 Days comp. strength (MPa)					Total ($kgCO_2$-eq/m^3)
	GGBS	Sand	Gravels	NaOH	Na_2SiO_3	
NWGC	3.65	10.59	36.42	25.65	131.63	207.94
LWGC	3.61	6.93	14.57	-	130.18	155.29

Table 7. Embodied CO_2 index of NWGC and LWGC

Concrete type	28 days compressive strength	Total carbon emission ($kgCO_2$-eq/m^3)	Embodied CO_2 index
NWGC	48.85	207.94	0.23
LWGC	35.93	155.29	0.23

3.9.2 Cost Efficiency

In addition to environmental impact, the cost efficiency of LWGC and NWGC plays a vital role in assessing the overall sustainability of these materials, as the affordability of raw components greatly affects their feasibility for widespread use. The cost of independent constituents of the LWGC incorporating was estimated as shown in Table 8. The prices of the materials were based on

the current market price in Malaysia and does not include transportation cost. The prices of the individual constituents are RM0.240, RM0.036, RM0.041, RM5 and RM58/kg, for GGBS, sand, gravel, Na_2SiO_3, and NaOH respectively. The cost of NWGC activated with 8M NaOH was also calculated for comparison purpose. The cost efficiency is determined by dividing the 28 days compressive strength by the cubic meter total cost. Similarly, all the cost of POFA, WA, and TCA were not considered because they are waste materials. Total costs of both NWGC and LWGC were RM1983.81 and RM898.93, respectively, indicating a cost reduction of about 54.69% which was attributed to the complete and partial replacement of NaOH and natural gravel, respectively. The 28 days compressive strength of both the LWGC and NWGC were 35.93 and 48.85MPa, respectively. Thus, the cost efficiency of NWGC was 0.02, while that of LWGC was 0.04. This lower cost efficiency of NWGC indicates that it is more expensive than LWGC. With a lower cost-to-strength ratio, LWGC is more cost-effective per unit of strength compared to NWGC. Although NWGC has a higher compressive strength, its higher cost makes it less efficient overall.

Table 8. Cost of cubic meter of NWGC and LWGC

Concrete type	Materials cost (RM/m^3)					Total (RM/m^3)
	GGBS	Sand	Gravels	NaOH	Na_2SiO_3	
NWGC	32.40	27.24	36.42	1044	843.75	1983.81
LWGC	32.05	17.81	14.57	-	834.50	898.93

4. Conclusions

This study investigates on the performance of WA lye activated POFA geopolymer concrete incorporating TCA as partial replacement for natural aggregates, with the aim of evaluating the mechanical properties, durability and environmental impact. The concluding remarks from the results are as follows:

- The incorporation of TCA into WA lye activated geopolymer concrete led to lower compressive, flexural, and splitting tensile strengths compared to the control specimens. This reduction in strength can be attributed to the decrease in density caused by the porous nature of TCA. The addition of TCA in the geopolymer concrete reduced its density, which in turn lowered the compressive strength.
- The integration of TCA in the WA lye activated geopolymer concrete increases the water absorption and the drying shrinkage of the concrete which were credited to the porous nature of the TCA. However, the water absorption was below the maximum limit specified by BS882: 1992.
- The durability of the TCA-incorporated geopolymer concrete was assessed by immersing specimens in $MgSO_4$ solution and comparing the strength results with control specimens. After 28 and 180 days of immersion, TCA-incorporated geopolymer concrete exhibited a relatively low strength loss, ranging between 1.8 – 2.8% at 28 days and 2.4 – 3.8% at 180 days. This demonstrates the geopolymer concrete enhanced resistance to sulfate attack compared to conventional OPC concrete, which typically experiences much higher strength loss under similar conditions. The lower strength loss in sulfate-rich environments is especially important for infrastructure exposed to harsh conditions, like sewage systems and marine structures, where OPC concrete is susceptible to early degradation.
- The incorporation of TCA in geopolymer concrete not only enhances the environmental profile but also contributes to cost-effectiveness. By utilizing TCA, it will be reduced with need for natural aggregate, make it an attractive alternative to traditional concrete for sustainable construction. Optimum replacement of TCA in geopolymer concrete can be further study to achieved an effective balance between the strength and sustainability.

In conclusion, the results of this study highlight the potential of TCA as a viable partial replacement for natural aggregates in geopolymer concrete, offering significant benefits in terms of mechanical properties, durability, and cost-efficiency. The ability of geopolymer concrete incorporating TCA to withstand sulfate attack, with its reduced environmental footprint and cost-effectiveness, offering a promising sustainable building material for the future. These findings not only expand the

existing knowledge on geopolymer concrete but also encourage its wider adoption in the construction industry as an eco-friendly and durable alternative to traditional concrete.

Acknowledgement

The authors gratefully acknowledge the Ministry of Higher Education, Malaysia for providing financial support to this research through the Fundamental Research Grant Scheme Grant Ref. No. FRGS/1/2022/TK01/USM/02/2.

References

[1] Kaptan K, Cunha S, Aguiar J. A Review: Construction and Demolition Waste as a Novel Source for CO2 Reduction in Portland Cement Production for Concrete. Sustainability (Switzerland), 2024; 16: 585. https://doi.org/10.3390/su16020585
[2] Davidovits J. Geopolymer cement: A review. Geopolymer Science and Technics, 2013; 1-11. https://doi.org/10.1520/STP156620120106
[3] Davidovits J. Geopolymer: Chemistry and applications. (5th ed.) Institut Géopolymère, 2020.
[4] Alaneme GU, Olonade KA, Esenogho E. (2023). Eco-friendly agro-waste based geopolymer-concrete: a systematic review. Discover Materials, 2023; 3(14). https://doi.org/10.1007/s43939-023-00052-8
[5] Hamada, Hussein M, Jokhio GA, Yahaya FM, Humada AM, Gul Y. The present state of the use of palm oil fuel ash (POFA) in concrete. Construction and Building Materials, 2018; 175: 26-40. https://doi.org/10.1016/j.conbuildmat.2018.03.227
[6] Tudin DZA, Rizalman, AN, Astah H. Performance of Palm Oil Fuel Ash and Rice Husk Ash Based Geopolymer Mortar. E3S Web of Conferences, 2018; 65: 02011. https://doi.org/10.1051/e3sconf/20186502011
[7] Kubba Z, Fahim Huseien G, Sa ARM, Shah KW, Asaad MA, Ismail M, Tahir, MM, Mirza J. Impact of curing temperatures and alkaline activators on compressive strength and porosity of ternary blended geopolymer mortars. Case Studies in Construction Materials, 2018; 9: e00205. https://doi.org/10.1016/j.cscm.2018.e00205
[8] Monita O, Lora MT, Edy S. Properties of Palm Oil Fuel Ash (POFA) Geopolymer Mortar Cured at Ambient Temperature. MATEC Web of Conferences, January, 2017: 0-7.
[9] Zawawi MZAA, Muthusamy K, Majeed APPA, Musa RM, Budiea AMA. Mechanical properties of oil palm waste lightweight aggregate concrete with fly ash as fine aggregate replacement. Journal of Building Engineering, 2020; 27: 100924. https://doi.org/10.1016/j.jobe.2019.100924
[10] Chai TJ, Sidek AB, Chow TK, Noor NM. Strength Properties of 10 Milimeters Timber Clinker Aggregate Concrete, 2017; 29(3): 333-344.
[11] Salam MA, Safiuddin M, Jumaat MZ. Durability indicators for sustainable self-consolidating high-strength concrete incorporating palm oil fuel ash. Sustainability (Switzerland), 2018; 10(7): 2345. https://doi.org/10.3390/su10072345
[12] ASTM C618. Standard Specification for Coal Fly Ash and Raw or Calcined Natural Pozzolan for Use. Annual Book of ASTM Standards, C, 2010: 3-6
[13] ASTM C136. Standard Test Method for Sieve Analysis of Fine and Coarse Aggregates. ASTM Standard Book, 2019: 3-7.
[14] ASTM C33. Standard Specification for Concrete Aggregates. Annual Book of ASTM Standards, ASTM International, 2003.
[15] ASTM C305. Standard Practice for Mechanical Mixing of Hydraulic Cement Pastes and Mortars of Plastic Consistency. ASTM International, 16(Reapproved), 2022: 1-5.
[16] ASTM C143. Standard test method for slump of hydraulic-cement concrete. ASTM, ASTM International, 2010.
[17] BS EN 12390-3. Testing hardened concrete. Compressive strength of test specimens, 2009.
[18] ASTM C293. Standard Test Method for Flexural Strength of Concrete (Using simple beam with center-point loading). ASTM, ASTM International, 2016.
[19] ASTM C496. Standard Test Method for Splitting Tensile Strength for Clindrical Concrete Specimens. ASTM, ASTM International, 2017
[20] BS EN 12390-3. Testing Hardened Concrete: Compressive strength of test specimens, 2009.
[21] MS EN 12504-4. Testing Concrete in Structures - Part 4: Determination of Ultrasonic Pulse Velocity. ASTM, ASTM International, 2013.
[22] ASTM C642. Standard Test Method for Density, Absorption, and Voids in Hardened Concrete. ASTM, ASTM International, 2013.

[23] ASTM C157. Standard Test Method for Length Change of Hardened Hydraulic-Cement Mortar. ASTM International, 2009: 1-7.
[24] ASTM C1012-04. Standard Test Method for Length Change of Hydraulic-Cement Mortars Exposed to a Sulfate Solution. ASTM International, 2004: 1-6.
[25] Malkawi AB, Habib M, Alzubi Y, Aladwan J. Engineering properties of lightweight geopolymer concrete using Palm Oil Clinker aggregate. International Journal of GEOMATE, 2020; 18(65): 132-139. https://doi.org/10.21660/2020.65.89948
[26] Malkawi AB, Nuruddin MF, Fauzi A, Almattarneh H, Mohammed BS. Effects of Alkaline Solution on Properties of the HCFA Geopolymer Mortars. Procedia Engineering, 2016; 148: 710-717. https://doi.org/10.1016/j.proeng.2016.06.581
[27] Rehman MU, Rashid K, Zafar I, Alqahtani FK, Khan MI. Formulation and characterization of geopolymer and conventional lightweight green concrete by incorporating synthetic lightweight aggregate. Journal of Building Engineering, 2020; 31: 101363. https://doi.org/10.1016/j.jobe.2020.101363
[28] ASTM C330. Standard Specification for Lightweight Aggregates for Structural Concrete. ASTM International, 2009.
[29] Al-Akhras NM, Jamal Shannag M, Malkawi AB. Evaluation of shear-deficient lightweight RC beams retrofitted with adhesively bonded CFRP sheets. European Journal of Environmental and Civil Engineering, 2016; 20(8): 899-913. https://doi.org/10.1080/19648189.2015.1084383
[30] Puthussery JV, Kumar R, Garg A. Evaluation of recycled concrete aggregates for their suitability in construction activities: An experimental study. Waste Management, 2017; 60: 270-276. https://doi.org/10.1016/j.wasman.2016.06.008
[31] Kockal NU, Ozturan T. Strength and elastic properties of structural lightweight concretes. Materials and Design, 2011; 32(4): 2396-2403. https://doi.org/10.1016/j.matdes.2010.12.053
[32] Saint-pierre F, Philibert A, Giroux B, Rivard P. Concrete Quality Designation based on Ultrasonic Pulse Velocity. Construction and Building Materials, 2016; 125: 1022-1027. https://doi.org/10.1016/j.conbuildmat.2016.08.158
[33] BS 1881-122. Method for Determination of Water Absorption. BSI Standard Publication, 2011.
[34] Ahmad MR, Chen B. Experimental research on the performance of lightweight concrete containing foam and expanded clay aggregate. Composites Part B: Engineering, 2019; 171: 46-60. https://doi.org/10.1016/j.compositesb.2019.04.025
[35] Tang P, Brouwers HJH. The durability and environmental properties of self-compacting concrete incorporating cold bonded lightweight aggregates produced from combined industrial solid wastes. Construction and Building Materials, 2018; 167: 271-285. https://doi.org/10.1016/j.conbuildmat.2018.02.035
[36] Wang J, Zheng K, Cui N, Cheng X, Ren K, Hou P, Feng L, Zhou Z, Xie N. Green and durable lightweight aggregate concrete: The role of waste and recycled materials. Materials, 2020; 13(13): 1-26. https://doi.org/10.3390/ma13133041
[37] BS 882:1992. Specification for Aggregates from Natural Sources for Concrete, 2002.
[38] Mostofinejad D, Hosseini SM, Nosouhian F, Ozbakkaloglu T, Nader Tehrani B. Durability of concrete containing recycled concrete coarse and fine aggregates and milled waste glass in magnesium sulfate environment. Journal of Building Engineering, 2020; 29: 101182. https://doi.org/10.1016/j.jobe.2020.101182
[39] Patil SV, Karikatti VB, Chitawadagi M. Granulated Blast-Furnace Slag (GGBS) based Geopolymer Concrete - Review. International Journal of Advanced Science and Engineering, 2018; 5(1): 789-885. https://doi.org/10.29294/IJASE.5.1.2018.789-885
[40] Kabir SMA, Alengaram UJ, Jumaat MZ, Yusoff S, Sharmin A, Bashar II. Performance evaluation and some durability characteristics of environmental friendly palm oil clinker based geopolymer concrete. Journal of Cleaner Production, 2017; 161(10): 477-492. https://doi.org/10.1016/j.jclepro.2017.05.002
[41] Ariffin MAM, Bhutta MAR, Hussin MW, Mohd Tahir M, Aziah N. Sulfuric acid resistance of blended ash geopolymer concrete. Construction and Building Materials, 2013; 43: 80-86. https://doi.org/10.1016/j.conbuildmat.2013.01.018
[42] Bhutta MAR, Hussin WM, Azreen M, Tahir MM. Sulphate Resistance of Geopolymer Concrete Prepared from Blended Waste Fuel Ash. Journal of Materials in Civil Engineering, 2014; 26(11): 1-6. https://doi.org/10.1061/(ASCE)MT.1943-5533.0001030
[43] ISO 14040. Environment management - Life cycle assessment - Principles and framework. International Standard, 2006.
[44] Sandanayake M, Gunasekara C, Law D, Zhang G, Setunge S. Greenhouse gas emissions of different fly ash based geopolymer concretes in building construction. Journal of Cleaner Production, 2018; 204: 399-408. https://doi.org/10.1016/j.jclepro.2018.08.311
[45] Yang KH, Song JK, Song KI. Assessment of CO2 reduction of alkali-activated concrete. Journal of Cleaner Production, 2013; 39: 265-272. https://doi.org/10.1016/j.jclepro.2012.08.001

Blank Page

Research on Engineering Structures & Materials
www.jresm.org
Research Group

Research Article

Melting and solidification of a PCM in a bottom-heated/cooled cavity with and without metal fins

Giulia Martino [1,a], Claudia Naldi [*,1,b], Cesare Biserni [1,c], Sylvie Lorente [2,d]

[1]*Department of Industrial Engineering, University of Bologna, via Risorgimento 2, 40136 Bologna, Italy*
[2]*Mechanical Engineering Department, Villanova University, 800 Lancaster Ave., Villanova, PA 19085, USA*

Article Info

Article history:

Received 19 Sep 2024
Accepted 21 Dec 2024

Keywords:

Phase change materials;
Melting;
Solidification;
Metal fins;
Numerical study

Abstract

In this research, a numerical investigation is conducted using COMSOL Multiphysics to examine both melting and solidification of the PCM lauric acid, placed in a vertical rectangular enclosure. The system is subjected to bottom heating and cooling, with or without metallic fins. The study focuses on evaluating the effect of the presence of metallic inclusion on the speed of the phase transition front and the consequent duration of the melting and solidification processes. The presented findings are the average liquid fraction over time, location of the phase change front, and temperature distribution within the cavity. The obtained outcomes highlight how different heat transfer processes, conductive and convective, are involved at various time instants during the PCM charging and discharging phases, as well as the heat transfer improvement yielded by the presence of metallic fins, which reduces the time needed for melting (solidification) by about 75% (86%). In addition, solid drops falling is observed when the horizontal melt layers spreading from the fin tops come in contact.

© 2025 MIM Research Group. All rights reserved.

1. Preface

Nowadays, the continuously growing energy request makes it essential to optimize the use of sustainable energy solutions. In this context, thermal energy storage (TES) systems are crucial, as they allow the link between energy generation and consumption. Indeed, in applications characterized by non-programmable energy generation, such as solar thermal systems, the adoption of appropriate storage tanks is essential for storing heat and releasing it once needed [1].

PCMs (phase change materials), have shown great potential for use in thermal energy storage systems in order to enhance the heat capacity by utilizing the latent heat of fusion during the phase transition between solid and liquid states [2,3]. Nevertheless, one of the main disadvantages of the PCMs is their low values of thermal conductivity, which inhibit the heat transfer within the material, slowing down the storage and release of heat. To overcome this disadvantage, many techniques have been proposed in the literature, such as the optimization of the PCM allocation in relation to the source of heat [4], or the coupling of PCMs with metal oxide nanoparticles [5], graphene [6], high-porosity open-cell metal foams [7], or metallic fins [8-11], to accelerate the PCM melting and solidification.

Regarding latent thermal energy storage (LTES) systems, bottom-heated LTES have been widely studied in different works [12-18]. In particular, Feng et al. [14] modeled the melting process of ice-copper nanoparticle mixtures using a new lattice Boltzmann method. Their results showed that the addition of nanoparticles of copper to the phase

*Corresponding author: claudia.naldi2@unibo.it
[a] orcid.org/0009-0004-7423-0121; [b] orcid.org/0000-0003-4126-8153; [c] orcid.org/0000-0003-0081-2036; [d] orcid.org/0000-0002-5817-9686
DOI: http://dx.doi.org/10.17515/resm2024.456ma0919rs

change material accelerates the melting process and improves heat transfer. Similarly, a numerical investigation on a phase change material inserted in a bottom-heated square cavity during melting was performed by Gong and Mujumdar [15]. The authors used the finite element method Streamline Upwind/Petrov Galerkin, and their results revealed that a variation in the Rayleigh number leads to different flow patterns within the system. Moreover, Fteiti and Nasrallah [16] numerically studied the melting of a pure PCM in a rectangular enclosure heated/cooled from the bottom and from the top, respectively. They observed that the aspect ratio of the enclosure affects the duration of the process. In particular, if the aspect ratio is reduced, the melting process takes place faster. Parsazadeh and Duan [17] investigated the melting from the bottom of coconut oil, used as a PCM. The geometry studied is a cavity with a rectangular shape in which the PCM is confined. Their outcomes showed that the melting process takes place with two different mechanisms, depending on the Rayleigh number. In particular, the beginning of the process, characterized by small Rayleigh numbers, is dominated by heat conduction, whereas natural convection characterized by the formation of Rayleigh-Bénard cells is the heat transfer mechanism when the Rayleigh number exceeds the critical value. Also, Kousksou et al. [18] conducted a numeric analysis on the melting of gallium, inserted in a rectangular enclosure heated from a horizontal wavy surface, driven by convection. Their analysis focused on how the amplitude of the wavy bottom affects heat transfer during melting. They found that the number of Rayleigh-Bénard rolls is significantly influenced by the liquid layer height.

In this paper, a rectangular enclosure filled with a PCM, i.e. lauric acid, is numerically studied. The cavity is heated or cooled from the bottom side, whilst the other walls are adiabatic, and can include three metal fins placed from below. A specific geometry has been selected in this study in order to show the effects of the fins inclusion in a vertical enclosure, where the fins do not reach the cavity top, heated/cooled from the bottom. The behavior of the PCM during both melting and solidification is studied in order to evidence the impact of the metallic fins on the heat transfer mechanisms, duration of the melting/solidification processes, and slope of the liquid fraction trend.

2. Methods

2.1. Geometrical Configuration and Material Properties

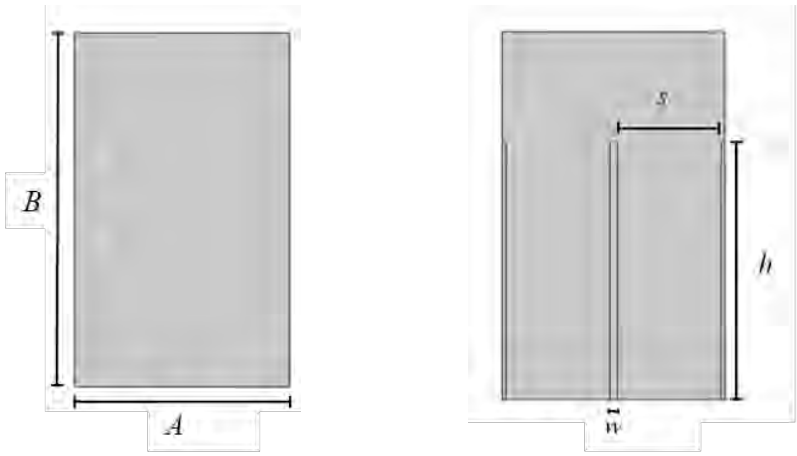
A rectangular cavity with length A = 3 cm and height B = 5 cm is selected for the numerical analysis (see Fig. 1a). The enclosure contains the PCM lauric acid. Table 1 reports the main material properties.

Table 1. Lauric acid properties [19]

	Solid state	Liquid state
Temperature, T [K]	316.65	321.35
Density, ρ [kg/m^3]	940	940
Heat conductivity, λ [W/(m·K)]	0.16	0.14
Specific heat capacity, c_p [J/(kg·K)]	2180	2390
Dynamic viscosity, μ [Pa·s]		0.008
Thermal expansion coefficient, β [1/K]	0.0008	
Latent heat of fusion, L [J/kg]	187210	

The melting temperature range of the considered PCM is ΔT_m = 4.7 K. The melting of the material starts at T_m = 316.65 K, while solidification starts at T_s = 321.35 K. Two distinct scenarios are examined: only the PCM is present in the cavity; also 3 aluminum fins (λ_{fins} =

237 W/(m·K), ρ_{fins} = 2700 kg/m^3, c_{pfins} = 897 J/(kg·K)) are included. The fins are attached to the cavity bottom and shorter than the enclosure (see Fig. 1b). The width and height of the fins are respectively w = 0.1 cm and h = 3.5 cm, while the spacing between fins is s = 1.4 cm. It is important to note that the fins located in correspondence of the cavity lateral sides have a width halved with respect to that of the central fin, to minimize the boundary influence.



(a) (b)

Fig. 1. Studied geometry: vertical enclosure without (a), or with (b) fins

2.2. Numerical Method

To simulate the melting and solidification processes of lauric acid, contained within the cavity, with and without fins, the top and lateral surfaces of the enclosure are considered adiabatic, whereas the bottom wall is maintained at a fixed temperature. In particular, throughout melting, the cavity is bottom-heated at T_H, which is determined as the sum of the melting temperature T_m, and a constant value ΔT_p, that is equal to 37.35 K:

$$T_H = T_m + \Delta T_p \tag{1}$$

In this case, an initial temperature equal to T_m is assumed for the entire domain, ensuring that the lauric acid is in the solid phase. Similarly, the solidification process is conducted by setting the bottom side of the cavity at a fixed temperature value equal to T_C, defined as the difference between the solidification temperature T_s, and the constant value ΔT_p:

$$T_C = T_s - \Delta T_p \tag{2}$$

For the solidification process, the initial temperature is T_s in the whole domain, ensuring that the lauric acid is in the liquid phase. Furthermore, the phase change material in the liquid state is considered incompressible, the flow is assumed to be laminar (Boussinesq approximation is adopted), PCM and metallic inclusions exhibit isotropic properties. The governing equations consist of the conservation of mass, momentum, and energy:

$$\nabla \cdot \vec{v} = 0 \tag{3}$$

$$\rho \frac{\partial \vec{v}}{\partial \tau} + \rho\left(\vec{v} \cdot \nabla\right)\vec{v} = -\nabla p + \mu \nabla^2 \vec{v} + \rho \vec{g} - \vec{g}\beta\rho\left(T - T_m\right)\theta \tag{4}$$

$$\frac{\partial T}{\partial \tau}+\left(\vec{v}\cdot\nabla\right)T=\frac{\lambda}{\rho c_{p,m}}\nabla^2 T \tag{5}$$

where $\vec{v}$ is the velocity vector, p is pressure, $\vec{g}$ is the gravity acceleration vector, τ is time, θ is the PCM local liquid fraction, and $c_{p,m}$ is the modified specific heat capacity. In particular, the latter is defined in agreement with the apparent heat capacity method as follows [20]:

$$c_{p,m}=c_p \text{ if } T<T_m \text{ or } T>T_s \text{ (solid and liquid state)} \tag{6}$$

$$c_{p,m}=c_p+\frac{L}{\Delta T_m} \text{ if } T_m<T<T_s \text{ (mushy region)} \tag{7}$$

where L is the PCM latent heat of fusion. Furthermore, θ is a dimensionless parameter that quantifies the fraction of liquid present. In detail, θ assumes the following values:

$$\theta=0 \text{ if } T<T_m \text{ (solid state)} \tag{8}$$

$$\theta=\frac{T-T_m}{\Delta T_m} \text{ if } T_m<T<T_s \text{ (mushy region)} \tag{9}$$

$$\theta=1 \text{ if } T>T_s \text{ (liquid state)} \tag{10}$$

In the case with the aluminum fins attached to the cavity bottom, heat transfer through the fins is due to conduction:

$$\rho_{fins} c_{p,fins}\frac{\partial T}{\partial \tau}=\lambda_{fins}\nabla^2 T \tag{11}$$

The boundary conditions regarding the melting and solidification processes are reported in Eqs. (12)-(14) and Eqs. (12)-(13), (15), respectively. The initial conditions for the melting process are expressed by Eqs. (16)-(17), whereas those for the solidification one by Eqs. (16), (18):

$$\vec{v}(0,y,\tau)=\vec{v}(A,y,\tau)=\vec{v}(x,0,\tau)=\vec{v}(x,B,\tau)=0 \tag{12}$$

$$\left.\frac{\partial T}{\partial x}\right|_{x=0}=\left.\frac{\partial T}{\partial x}\right|_{x=A}=\left.\frac{\partial T}{\partial y}\right|_{y=B}=0 \tag{13}$$

$$T(x,0,\tau)=T_H \tag{14}$$

$$T(x,0,\tau)=T_C \tag{15}$$

$$\vec{v}(x,y,0)=0 \tag{16}$$

$$T(x,y,0)=T_m \tag{17}$$

$$T(x,y,0)=T_s \tag{18}$$

The equations were solved using the finite element software COMSOL Multiphysics.

2.3. Mesh Sensitivity Analysis

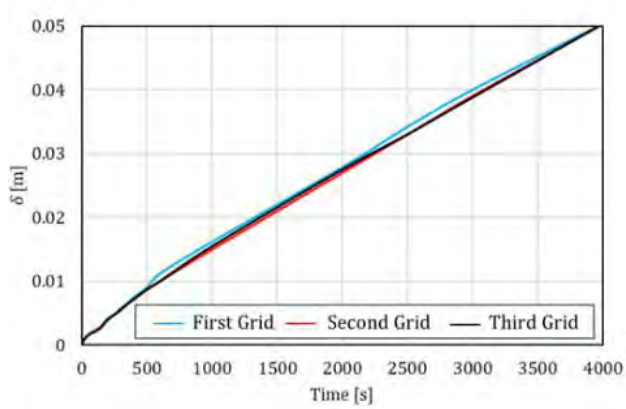
An unstructured grid with triangles as elements is used for the discretization of the domain. Along the walls and the fins, a boundary layer mesh is included, to optimize the grid for laminar flow. To verify the independence of the results from the grid, three distinct

meshes are considered. The average liquid fraction values over time for the PCM melting in the cases with and without fins, obtained with the three grids, are compared by considering maximum absolute error and root mean square error (RMSE), as shown in Table 2.

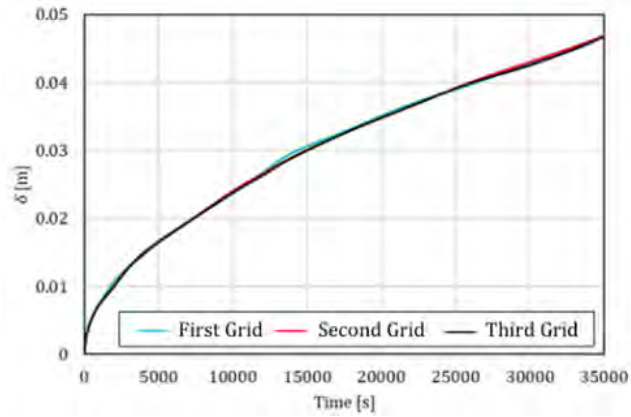
Table 2. Results of the mesh sensitivity analysis: average liquid fraction errors

Grid	Cavity without fins			Cavity with three fins		
	Element count	Maximum absolute error	RMSE	Element count	Maximum absolute error	RMSE
First Grid	5742	0.0213	0.0120	6117	0.1012	0.0109
Second Grid	5970	0.0096	0.0044	7601	0.0168	0.0013
Third Grid	6378	-	-	8412	-	-

In addition, the height of the phase change front as a function of time, evaluated in the middle of the cavity without fins with the three different meshes, is compared for both the melting (see Fig. 2a) and solidification (see Fig. 2b) processes.



(a)



(b)

Fig. 2. Results of the mesh sensitivity analysis: melting (a) and solidification (b) front height as a function of time in the middle of the cavity without fins

Due to the very low values of the errors, in terms of average liquid fraction, obtained by the Second Grid (see Table 2) and to the negligible difference between the phase change front position obtained with the Second Grid with respect to the Third Grid (see Fig. 2), the mesh with 5970 elements is adopted.

2.4. Model Validation

The model used in this study is validated against the results presented by Shokouhmand and Kamkari [21] for the melting process, and against the results presented by Kiyak et al. [22] for the solidification process. Shokouhmand and Kamkari [21] studied experimentally the temperature distribution and the progression of the melting front of lauric acid contained in a vertical rectangular heat storage with one-side heating. In particular, they performed many experimental runs by heating the right wall at various constant temperature values, providing benchmark data to validate numerical codes.

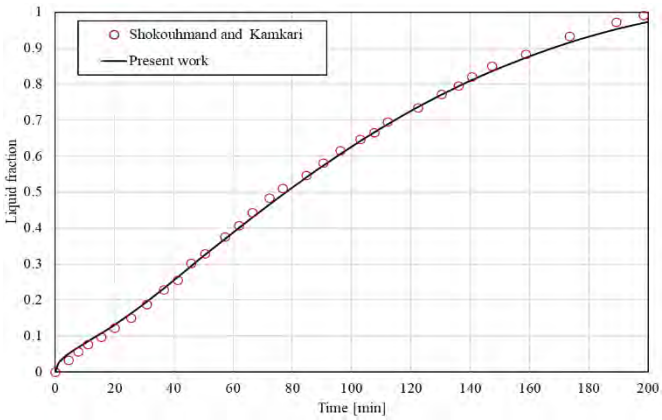


Fig. 3. Average liquid fraction of lauric acid over time, results by Shokouhmand and Kamkari [21] and by the present model

The average liquid fraction trend obtained with the proposed method and that yielded by the experiment of Shokouhmand and Kamkari in the case of a constant wall temperature equal to 70 °C is shown in Fig. 3. Moreover, the melting front position at some instants yielded by the proposed method and by the experiment of Shokouhmand and Kamkari [21] is compared in Fig. 4. A good agreement is observed between the results of this work and those obtained in Ref. [21]. The maximum absolute error in the average liquid fraction values is 0.0206 and the RMSE is 0.0114, while the maximum discrepancy between the melting front position obtained by this model and by Shokouhmand and Kamkari [21] is 0.0027 m.

Kiyak et al. [22] numerically studied the performance of thermal energy storage units filled with PCM. The investigation was assessed for the melting and solidification processes of the PCM RT42, considering the influences of the heater and cooler positions (bottom, top, and side) and the impact of the geometry shape (square and circular). Fig. 5 shows the average liquid fraction trend obtained by this model with that yielded by Kiyak et al. [22] in the case of cooling of RT42 confined within a square cavity cooled from the bottom. A good agreement can be found between the results of this study and those reported in Ref. [22]: the maximum absolute error in the average liquid fraction is 0.0175, and the RMSE is 0.0112. Furthermore, Fig. 6 compares the solidification front position within the square cavity at different time instants, as determined by the proposed method and by Kiyak et al. [22]. A good agreement can be observed: the maximum difference between the solidification front height obtained by this model and that of Ref. [22] is equal to 0.0020 m.

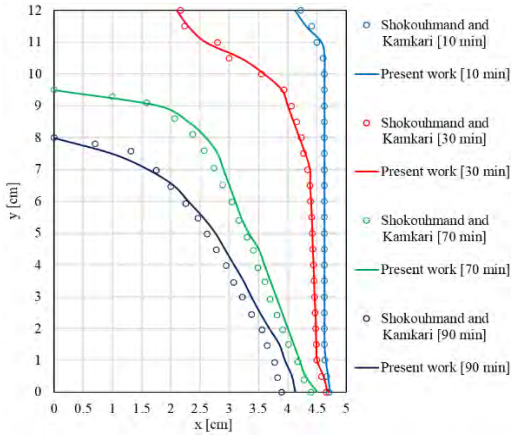


Fig. 4. Melting front evolution at different times, results by Shokouhmand and Kamkari [21] and by the present model

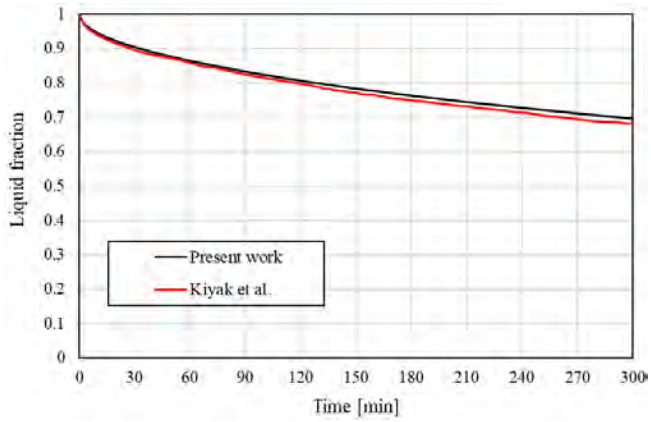


Fig. 5. Average liquid fraction of RT42 over time, results by Kiyak et al. [22] and by the present model

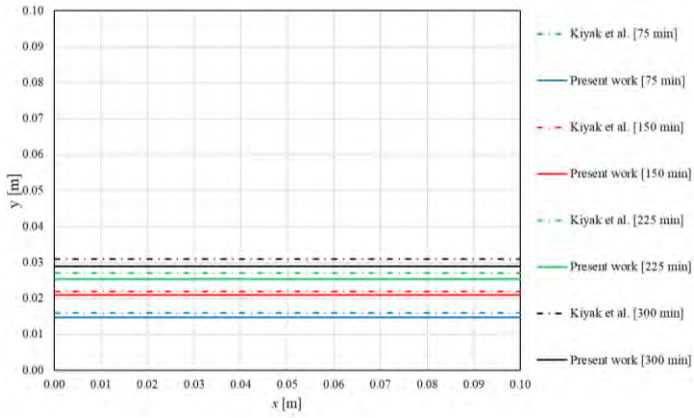


Fig. 6. Solidification front evolution at different times, results by Kiyak et al. [22]and by the present model

3. Results and Discussion

The average liquid fraction values, obtained for the PCM melting and solidification in the cavity with and without fins, are shown as a function of time in Figs. 7-8. It is noticeable how the use of metal fins leads to a significant reduction in the time required to conclude the melting process of lauric acid (average liquid fraction of 1 in Fig. 7), because they enhance the phase change by conveying heat from the bottom to the top of the cavity. Specifically, the melting time is about 4458 s for the cavity without fins, while it is only about 1095 s in the case with fins, which means a reduction of about 75%.

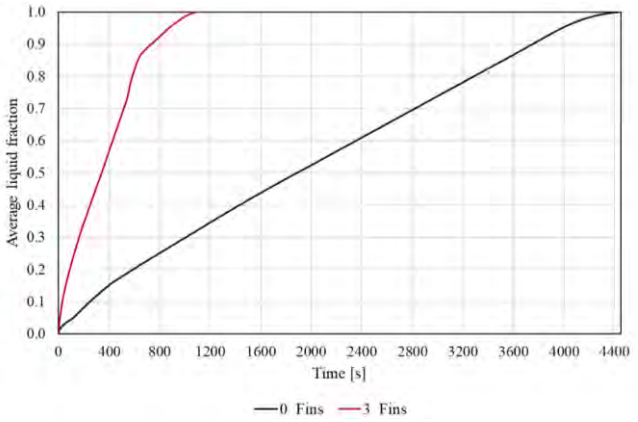


Fig. 7. Average liquid fraction for the lauric acid melting, cavity with/without fins

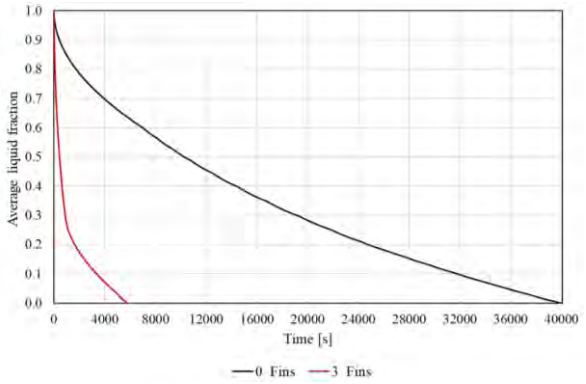


Fig. 8. Average liquid fraction for the lauric acid solidification, cavity with/without fins

The use of fins allows a significant reduction in the solidification time as well, as evident by comparing the red and black curves in Fig. 8. In particular, a reduction in the solidification time of about 86% is observed: from 40075 s in the absence of fins to 5793 s when 3 fins are added (average liquid fraction equal to 0 in Fig. 8).

It is worth noting that the PCM solidification is significantly longer than the melting. The formation of convective cells, in fact, accelerates the melting. The solidification process, on the other hand, is governed by the conductive regime only (bottom-cooled enclosure), resulting in much longer times needed to finish the transition from liquid to solid. More in detail, the PCM melting process is initially dominated by thermal conduction, whereas, subsequently, Rayleigh–Bénard cells begin to develop, triggering a shift in the heat transfer mechanism from a conductive regime to a natural convective one [23].

Fig. 9 shows the time sequence of temperature distribution and streamlines in the case of melting without fins: at the beginning (τ = 50 s in Fig. 9) the melting front is planar (conductive regime), but when the convective regime turns out to be more effective to transfer heat from the enclosure bottom, Rayleigh–Bénard cells begin to develop (τ = 135 s in Fig. 9), then the rolls become bigger and less numerous (τ= 800 s in Fig. 9).

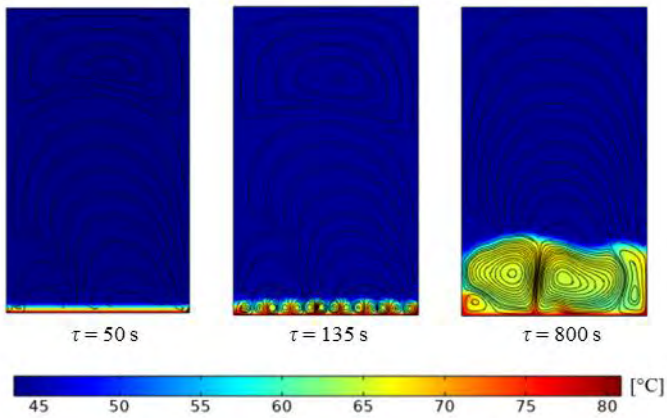


Fig. 9. Progression of lauric acid melting without fins: τ = 50 s (conductive regime), τ = 135 s (transition from conduction to convection), τ = 800 s (convective regime)

Fig. 10 shows the liquid layer thickness δ over time during the melting process in the cavity without fins, evaluated at the enclosure center. It is evident how the evolution of δ follows two different trends: during the initial part of the process, δ is proportional to $\tau^{0.5}$, then to τ, in agreement with the theoretical results [23]. Moreover, the transition between conduction to the convection is highlighted in Fig. 10 by the inflection on the curve, which matches the theoretical analysis predictions: τ = 134.92 s and δ = 0.0019 m (see the black lines in Fig. 7).

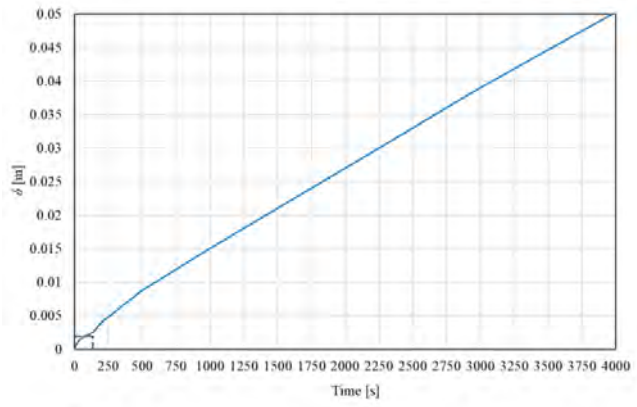


Fig. 10. Liquid layer thickness versus time; cavity without fins

Fig. 11 shows the progression of lauric acid melting in the presence of fins. In this case, the melting process occurs simultaneously from the cavity bottom and from the fins, which are heated up to the temperature T_H very soon. After a brief phase where the PCM is heated by conduction from the fins and from the bottom wall, Rayleigh–Bénard cells develop in the bottom space between two adjacent fins, as well as convective cells along the fins (see Fig. 11, left). As the heating process continues, the cells formed along the fins tend to enlarge

at the fin top and to merge, generating drops of solid material at the center between consecutive fins (see Fig. 11, middle). The convective cells exhibit a descending liquid movement at the boundary with the solid phase, so that the shear forces drive the solid drop downward to the cavity base, where the solid material completes its melting (note that the density of the material in both phases is the same). Additionally, convective cells also develop from the fins top, and combine with the vertical cells developed along the fins (that now fill the entire spacing between fins, see Fig. 11, right). These new rolls help melt the PCM located at the enclosure top, which is not reached by the metallic fins. Indeed, the melting of the material above the fins is slower, as highlighted by the decreased slope of the final part of the red curve in Fig. 7.

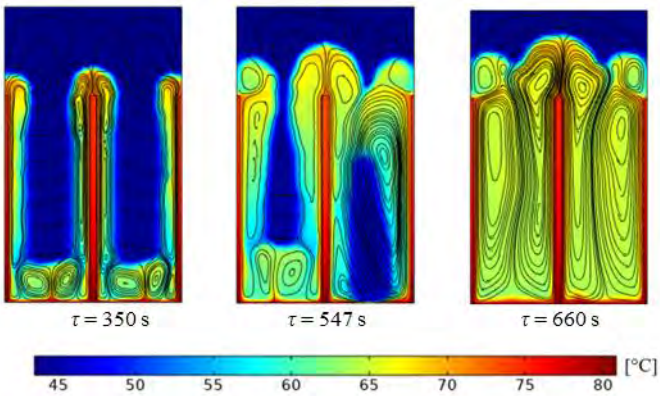


Fig. 11. Progression of lauric acid melting with fins: τ = 350 s (rolls formation), τ =547 s (solid drops falling), τ = 660 s (cells merged)

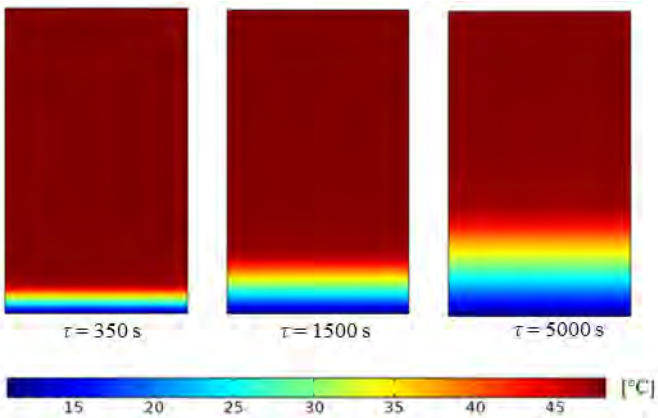


Fig. 12. Progression of lauric acid solidification without fins

Figs. 12-13 show the progression of the solidification of lauric acid in the absence/presence of fins, respectively. It is evident that in this case, the conditions for the formation of convective cells are not present. Therefore, the solidification process occurs solely through the conduction regime, in agreement with the literature [24]. As a result, the solidification times are much longer than the melting ones (by about 5-9 times). However, the inclusion of fins accelerates the PCM solidification (compare temperature distributions at corresponding time instants in Figs. 12-13), but when the phase transition front arrives at the upper part of the fins, the process slows down, as captured by the slope change in the red curve of Fig. 8. Fig. 14 shows the vertical position δ' of the phase change

front versus time in the case of solidification in the cavity without fins, evaluated at the enclosure center. The time evolution of δ' is proportional to $\tau^{0.5}$, without any change in the curve slope, consistently with the conduction-dominated regime of the phase change.

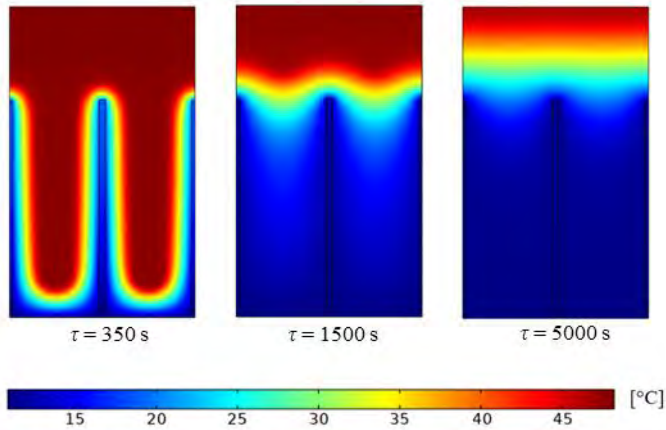


Fig. 13. Progression of lauric acid solidification with fins

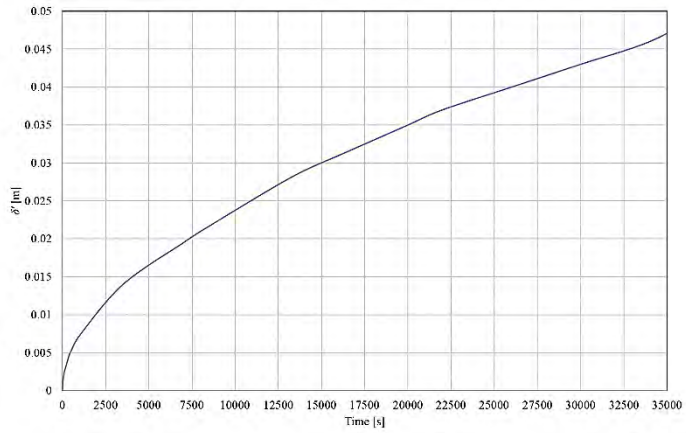


Fig. 14. Solid layer thickness versus time; cavity without fins

4. Conclusions

In this paper, a computational study is performed on the phase transition from solid to liquid, and vice versa, of lauric acid used as PCM. The material is confined within a rectangular cavity, with and without metallic fins, and is heated or cooled from the bottom, while the other walls of the enclosure are adiabatic.

The performance of the system during both melting and solidification is numerically analyzed in order to highlight the influence of the presence of the metallic fins on the heat transfer typology (namely, conduction or convection), speed of the phase change front, and duration of the melting/solidification process in a vertical rectangular enclosure with fixed geometry and temperature values of the bottom side. The governing equations are solved through the commercial software COMSOL Multiphysics and both mesh sensitivity analysis and validation of the model against literature results have been performed.

The obtained results evidence how, without fins, the melting of the PCM takes place due to a combination of an initial conductive regime, and a subsequent convective regime with the development of Rayleigh–Bénard cells. Specifically, when convection is more efficient in the heat transfer from the enclosure bottom with respect to conduction, convective cells start to develop, enhancing the PCM melting. In contrast, the solidification process occurs only through thermal conduction, with consequent longer times to complete the phase change.

If metal fins are attached to the bottom side of the enclosure, also convective cells develop vertically along the fins during the melting process. Then solid drops are created, due to the progression of the melting front spreading in the horizontal direction from the upper part of the fins. The shear forces due to the convective rolls push the solid drops toward the cavity bottom, where they end up melting. In addition, convective cells develop from the fins top and combine with the cells along the fins, enhancing the fusion of lauric acid located at the enclosure top, which is not reached by the metallic fins. The presence of high-conductivity inserts can reduce the duration of melting and solidification processes respectively by 75% and 86%.

Acknowledgement

The authors acknowledge that this study is supported by the National Recovery and Resilience Plan (NRRP), Mission 4 Component 2 Investment 1.3 - "Creazione di “Partenariati estesi alle università, ai centri di ricerca, alle aziende per il finanziamento di progetti di ricerca di base”" of Italian Ministry of University and Research funded by the European Union – NextGenerationEU; Project code PE0000021, “Network 4 Energy Sustainable Transition (NEST)", Spoke 5 (Energy Conversion), CUP J33C22002890007, and by the the Emilia-Romagna Regional Development Fund PR-FESR 2021-2027 Program under the project SACER – Sviluppo e integrazione di Accumuli innovativi nelle Comunità Energetiche Rinnovabili, CUP J47G22000760003.

References

[1] Ali HM, Rehman T, Arıcı M, Said Z, Durakovi'c B, Mohammed HI, Kumarj R, Rathod MK, Buyukdagli O, Teggarl M. Advances in thermal energy storage: Fundamentals and applications. Progress in Energy and Combustion Science, 2024; 100: 101109. https://doi.org/10.1016/j.pecs.2023.101109

[2] Sharma A, Tyagi VV, Chen CR, Buddhi D. Review on thermal energy storage with phase change materials and applications. Renewable and Sustainable Energy Reviews, 2009; 13: 318-345. https://doi.org/10.1016/j.rser.2007.10.005

[3] Tao YB, He Y. A review of phase change material and performance enhancement method for latent heat storage system. Renewable and Sustainable Energy Reviews, 2018; 93: 245-259. https://doi.org/10.1016/j.rser.2018.05.028

[4] Lorente S, Bejan A, Niu JL. Phase change heat storage in an enclosure with vertical pipe in the center. International Journal of Heat and Mass Transfer, 2014; 72: 329-335. https://doi.org/10.1016/j.ijheatmasstransfer.2014.01.021

[5] Khan Z, Khan ZA, Sewell P. Heat transfer evaluation of metal oxides based nano PCMs for latent heat storage system application. International Journal of Heat and Mass Transfer, 2019; 144: 118619. https://doi.org/10.1016/j.ijheatmasstransfer.2019.118619

[6] Kant K, Shukla A, Sharma A, Biwole PH. Heat transfer study of phase change materials with graphene nano particle for thermal energy storage. Solar Energy, 2017; 146: 453-463. https://doi.org/10.1016/j.solener.2017.03.013

[7] Cui W, Si T, Li X, Li X, Lu L, Ma T, Wang Q. Heat transfer enhancement of phase change materials embedded with metal foam for thermal energy storage: A review. Renewable

and Sustainable Energy Reviews, 2022; 169: 112912. https://doi.org/10.1016/j.rser.2022.112912
[8] Al-Omari SAB, Qureshi ZA, Elnajjar E, Mahmoud F. A heat sink integrating fins within high thermal conductivity phase change material to cool high heat-flux heat sources. International Journal of Thermal Sciences, 2022; 172: 107190. https://doi.org/10.1016/j.ijthermalsci.2021.107190
[9] Acir A, Canlı ME. Investigation of fin application effects on melting time in a latent thermal energy storage system with phase change material (PCM). Applied Thermal Engineering, 2018; 144: 1071-1080. https://doi.org/10.1016/j.applthermaleng.2018.09.013
[10] Shukla A, Kant K, Biwole PH, Pitchumani R, Sharma A. Melting and solidification of a phase change material with constructal tree-shaped fins for thermal energy storage. Journal of Energy Storage, 2022; 53: 105158. https://doi.org/10.1016/j.est.2022.105158
[11] Kirincic M, Trp A, Lenic K, Torbarina F. Numerical analysis of the influence of geometry parameters on charging and discharging performance of shell-and-tube latent thermal energy storage with longitudinal fins. Applied Thermal Engineering, 2024; 236: 121385. https://doi.org/10.1016/j.applthermaleng.2023.121385
[12] Yanga XH, Tana SC, Dinga YJ, Wanga L, Liua J, Zhoua YX. Experimental and numerical investigation of low melting point metal based PCM heat sink with internal fins. International Communications in Heat and Mass Transfer, 2017; 87: 118-124. https://doi.org/10.1016/j.icheatmasstransfer.2017.07.001
[13] Satbhai O, Roy S. Criteria for the onset of convection in the phase-change Rayleigh-Bénard system with moving melting-boundary. Physics of Fluids, 2020; 32: 064107. https://doi.org/10.1063/5.0004979
[14] Feng Y, Li H, Li L, Bu L, Wang T. Numerical investigation on the melting of nanoparticle-enhanced phase change materials (NEPCM) in a bottom-heated rectangular cavity using lattice Boltzmann method. International Journal of Heat and Mass Transfer, 2015; 81: 415-425. https://doi.org/10.1016/j.ijheatmasstransfer.2014.10.048
[15] Gong ZX, Mujumdar AS. Flow and heat transfer in convection-dominated melting in a rectangular cavity heated from below. International Journal of Heat and Mass Transfer, 1998; 41: 2573-2580. https://doi.org/10.1016/S0017-9310(97)00374-8
[16] Fteiti M, Nasrallah SB. Numerical study of interaction between the fluid structure and the moving interface during the melting from below in a rectangular closed enclosure. Computational Mechanics, 2005; 35: 161-169. https://doi.org/10.1007/s00466-004-0597-6
[17] Parsazadeh M, Duan X. Numerical and experimental investigation of phase change heat transfer in the presence of Rayleigh-Benard convection. ASME Journal of Heat and Mass Transfer, 2020; 142: 062401. https://doi.org/10.1115/1.4046537
[18] Kousksou T, Mahdaoui M, Ahmed A, Msaad AA. Melting over a wavy surface in a rectangular cavity heated from below, Energy, 2014; 64: 212-219. https://doi.org/10.1016/j.energy.2013.11.033
[19] Zhang X, Lorente S, Wemhoff AP. Modeling the thermal energy storage capability of a phase change material confined in a rectangular cavity. International Communications in Heat and Mass Transfer, 2021; 126: 105367. https://doi.org/10.1016/j.icheatmasstransfer.2021.105367
[20] Naldi C, Dongellini M, Morini GL. The evaluation of the effective thermal conductivity of metal-foam loaded phase change materials. Journal of Energy Storage, 2022; 51: 104450. https://doi.org/10.1016/j.est.2022.104450
[21] Shokouhmand H, Kamkari B. Experimental investigation on melting heat transfer characteristics of lauric acid in a rectangular thermal storage unit. Experimental

Thermal and Fluid Science, 2013; 50: 201-212. https://doi.org/10.1016/j.expthermflusci.2013.06.010

[22] Kiyak B, Oztop H. F, Biswas N, Selimefendigil F. Effects of geometrical configurations on melting and solidification processes in phase change materials. Applied Thermal Engineering, 2025; 258: 124726. https://doi.org/10.1016/j.applthermaleng.2024.124726

[23] Naldi C, Martino G, Dongellini M, Lorente S. Rayleigh-Bénard type PCM melting and solid drops. International Journal of Heat and Mass Transfer, 2024; 218: 124767. https://doi.org/10.1016/j.ijheatmasstransfer.2023.124767

[24] Stritih U. An experimental study of enhanced heat transfer in rectangular PCM thermal storage. International Journal of Heat and Mass Transfer, 2004; 47: 2841-2847. https://doi.org/10.1016/j.ijheatmasstransfer.2004.02.001

Research on Engineering Structures & Materials
www.jresm.org

Research Article

Experimental and numerical investigation of solid and hollow recycled aggregate concrete beams subjected to torsion

Nilesh Masne [*,1, a], Akshay Pawar [2,b]

[1]*Department of Civil Engineering, GES R.H.Sapat College of Engineering Management Studies & Research Nashik (MS), 422005, India*
[2]*Department of Applied Sciences and Humanities, SVKM's College of Engineering, Shirpur (MS), 425405, India*

Article Info

Article History:

Received 20 Sep 2024
Accepted 05 Dec 2024

Keywords:

Abaqus;
Hollow beam;
Recycled aggregate;
Concrete;
Solid Beam;
Torsion

Abstract

To attain sustainable development there is an increasing need of appropriate substitute materials of concrete ingredients such as coarse aggregates. The main aspiration of this effort is to produce the concrete using recycled concrete aggregates derived from construction and demolition (C&D) waste. As such, the use of recycled aggregate concrete (RAC) in structural elements becomes absolutely essential. A series of solid and hollow RAC beams were tested experimentally and simulated under torsional load to compared with natural aggregate concrete (NAC) beams. All tested solid and hollow beams of size, 150 mm wide x 250 mm depth x 1800 mm length with 50 mm x 150 mm opening for hollow beam, which composed of recycled concrete aggregate with replacement ratios of 0%, 50%, and 100%. The torsional capacity of hollow beams was found only lower by 5.49 %, 6.69 % and 8.67 % than the experimental solid beams in test results. The simulation results yielded similar trends, with reductions of 7.52%, 7.90%, and 8.26% in the torsional capacity of hollow beams compared to solid beams. The observed torsional parameter of beams such as crack pattern, torsional ability and twisting angle were found comparable with FE analysis. The findings of this study reveal that RAC beams, whether solid or hollow, possess sufficient torsional capacity and structural integrity, as good as to that of NAC beams. This suggests that RAC can be effectively utilized in structural applications subjected to torsional loads.

© 2025 MIM Research Group. All rights reserved.

1. Introduction

Torsion is the one main structural action in ultimate limit state method and it is the subject of scientific research studies since long time. In 21st century many engineering structures are subjected to torsion because of structural geometry and unbalance loading. Eccentric box girders, curved beams and spiral staircases are some different structures subjected to torsion and the behaviour of these structures dominate due to torsion. Till date, pure torsion is an active research area on traditional reinforced concrete material with recycled concrete aggregate concretes. In accordance with its mix-proportion and cement content, the RAC might have an excellent compressive and tensile strength. There is a compelling need for the civil engineering profession to concentrate on the research, development, and application of innovative materials for modern infrastructure [1-3]. RAC is becoming crucial in structural applications. [4-5]. The RAC attracted a lot of researchers in the last two decades to investigate its performance under different load action such as shear and flexural loading. Fatifazl et al. [6] and Kang et al. [7] found that existing flexural theory applies to reinforced recycled concrete beams, with minimal changes in flexural behavior. A similar tendency was found when recycled concrete compared with conventional concrete in

*Corresponding author: nilesh.masne@ges-coengg.org
[a]orcid.org/0000-0003-2146-910X; [b]orcid.org/0000-0003-4902-2182
DOI: http://dx.doi.org/10.17515/resm2024.457me0920rs

service, yielding and ultimate state results in flexure [8]. The substitution of recycled concrete aggregate in structural concrete has a minor change on the shear parameter [9-10]. Infrequent research work on hollow recycled concrete aggregate concrete beam in torsion has been found in the literature. Some important investigations exist on the failure pattern as well as overall torsional behaviour of hollow beams with NAC and other type of concretes. Hollow concrete sections are gaining popularity in the construction of offshore structures, towers, buildings, and bridges, particularly for accommodating mechanical pipelines and electrical services. The hollow concrete beams reduce structure weight, which affects transport, handling, and erection costs [11]. The hollow beam crack at lower torque than solid beam and ultimate strengths were same for both beams with same strength, size, and reinforcement [12-13]. Torsion causes solid and hollow beams to collapse with 10 % below design loads [14]. Torsional shear stress flows around the section's periphery, peaking at the outside fiber and decreasing away from the surface [15]. The solid and hollow beams responded similarly in shear and torsion [16]. The comparison of experimental results with various code provisions was done and found that the ACI 318-02 code was gave good predictions for the ultimate torsion of hollow beams in pure torsion [17]. The solid and hollow beams of equal size and reinforcement collapse under the equal stress in pure torsion [18–19]. The torsional ductility gets more challenging with increasing concrete strength in hollow beams [20-21]. The hollow RC member cracking torque values are lower than solid member values [22]. The opening size affects the hollow beam capacity under torsion, flexure, and cyclic loading in the EFM analysis [23]. Recent studies have explored the torsional behavior of solid RAC beams, revealing satisfactory torsional performance comparable to NAC solid beams [24-27]. These findings suggest the potential suitability of RAC for structural concrete applications. Untreated coarse recycled concrete aggregate is limited to 40% in concrete grades up to M30, while treated coarse recycled concrete aggregate can be used as a full replacement. This was ascribed to the enhancement in the interfacial transition zone (ITZ) [28]. Self-sensing concrete made from recycled aggregate is more effective at stress-sensing than existing structural health monitoring approaches. This novel material could revolutionize SHM by monitoring structures in real time, improving safety and maintenance [29]. Sustainable construction relies on waste materials in concrete to conserve the environment and improve concrete qualities. To obtain required concrete characteristics and performance, coarse aggregate replacement percentage must be carefully considered [30-33]. The economic feasibility of new civil engineering material as compared to available material is very important in the view of future demand [34]. In order to evaluate whether RAC can be useful for structural use or not, many civil engineers and the researchers has been extensively studied the types of loading tests of solid RAC beams. To the author's knowledge, there is a noticeable lack of experimental and numerical investigations in the existing literature on the structural behavior of hollow RAC beams under torsion. In an effort to address this gap the objective were finalized; the investigation of various properties of recycled aggregate concrete, assess code provisions for torsion, and validate through beam tests and FEA simulation. This study aims to promote the safe and effective use of recycled concrete aggregate in concrete beams.

2. Experimental Materials and Test Setup

2.1. Materials

This investigation utilized OPC 53-grade cement had specific gravity 3.14, fineness 3080 cm^2/g, and 55.5 MPa compressive strength that adhered to the specifications outlined in IS:12269 [35]. Fine Aggregates (FA) of nominal maximum size 4.75mm, fineness modulus = 2.80, water absorption 3.50%, specific gravity 2.65, and Natural Coarse Aggregates (NCA) fineness modulus = 6.70, maximum nominal size 20 mm, specific gravity 2.65, Impact test value 18.18% and crushing value 21.21% meeting the requirements of IS: 383 [36] were used in this study. In compliance with IS: 456 [37], for concreting and curing purposes tap water was used. A chemical admixture meeting the requirements of IS: 9103 [38] was employed to attain the required workability of the concrete. TMT deformed steel bars having average yield strength 515 MPa were used as beam reinforcement and tested as per the practice suggested in IS: 1608 [39]. Concrete cylinders (150 mm x 300 mm) were prepared using steel molds for the purpose of conducting tensile and compressive strength tests.

2.2. Recycled Concrete Aggregates

Rapid urbanization and infrastructural development are consuming natural resources rapidly. Reusing and recycling recycled concrete aggregate was necessary because to rising demand for natural aggregates [40-41]. Construction waste from building and demolition processes must be reduced. In this study, recycled concrete aggregate was sourced from waste concrete panels obtained from demolished reinforced concrete structures [42-43]. Fig.1 showed flow chart of the C&D waste process plant, because the actual photography of plant was not permitted.

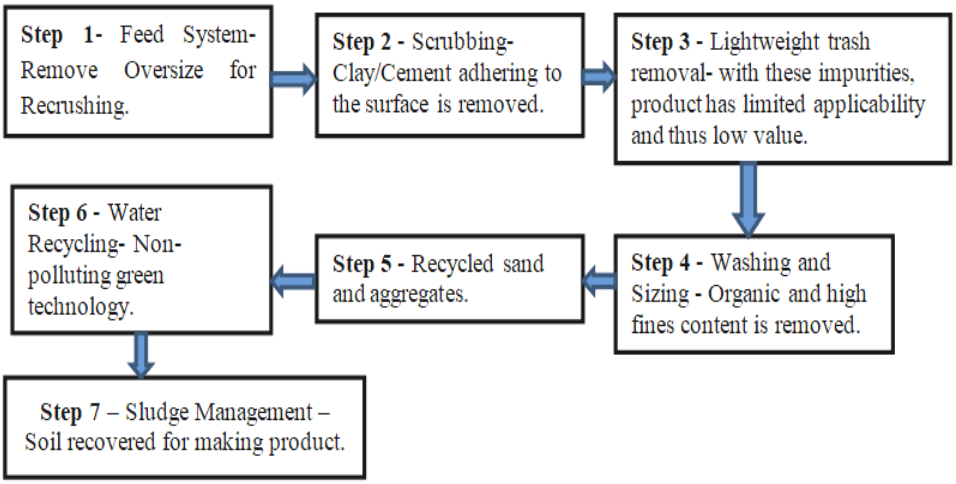
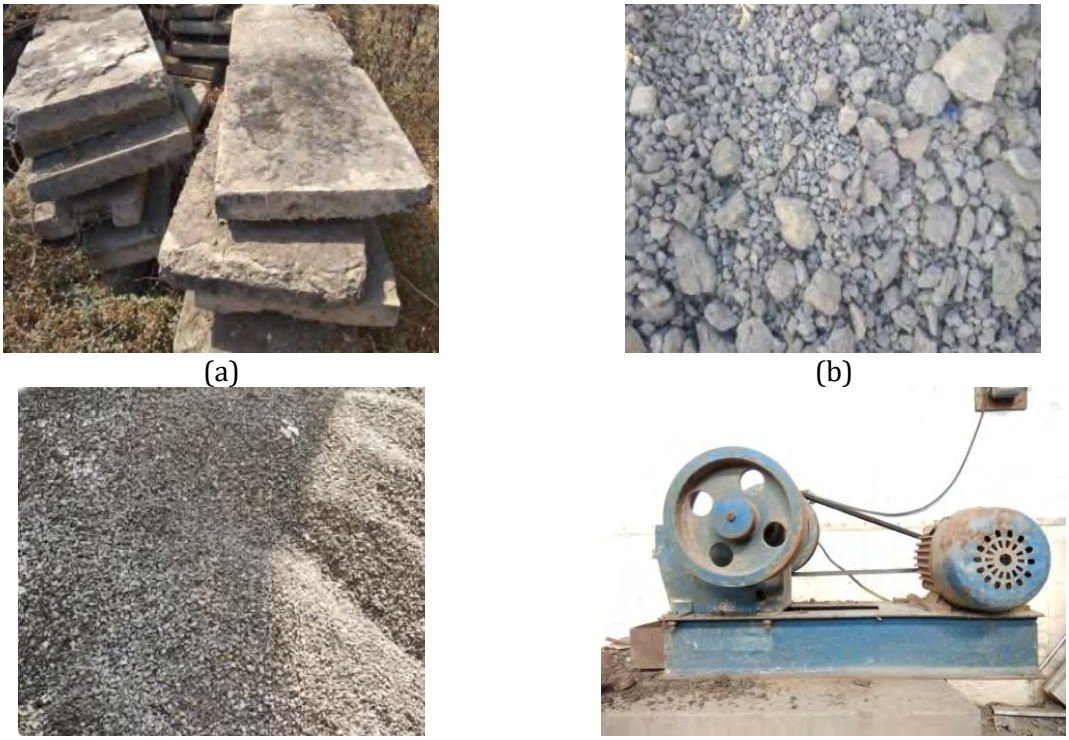


Fig. 1. Flowchart of Processing plant

Fig. 2a showed the concrete panels at the C&D waste center to crush in to required range using a processing plant machine shown in Fig. 2b. After the complete processing on waste concrete lumps, recycled concrete aggregate were transported to working lab for further testing and use shown in Fig.2 (c) and grinding machine shown in Fig. 2 (d) was also used to converts concrete waste into aggregates. The recycled concrete aggregates were categorized into four size fractions (16-20 mm, 12.5-16 mm, 10-12.5 mm, 4.75-10 mm) and stored separately. The recycled coarse aggregate fractions were manually blended to match the grading curve of natural coarse aggregate, conforming to the specifications outlined in IS 383 [36].

Table 1. Coarse Aggregates Properties

Properties	Maximum Size (mm)	Moisture Content (%)	Fineness Modulus	Bulk density (kg/m^3)	Specific gravity	Water absorption (%)	Impact value (%)	Crushing value (%)
Natural Coarse Aggregate	20	0.55	6.66	1530	2.64	0.55	18.58	20.16
Recycled Concrete Aggregate	20	2.31	6.32	1420	2.43	3.59	20.88	22.72

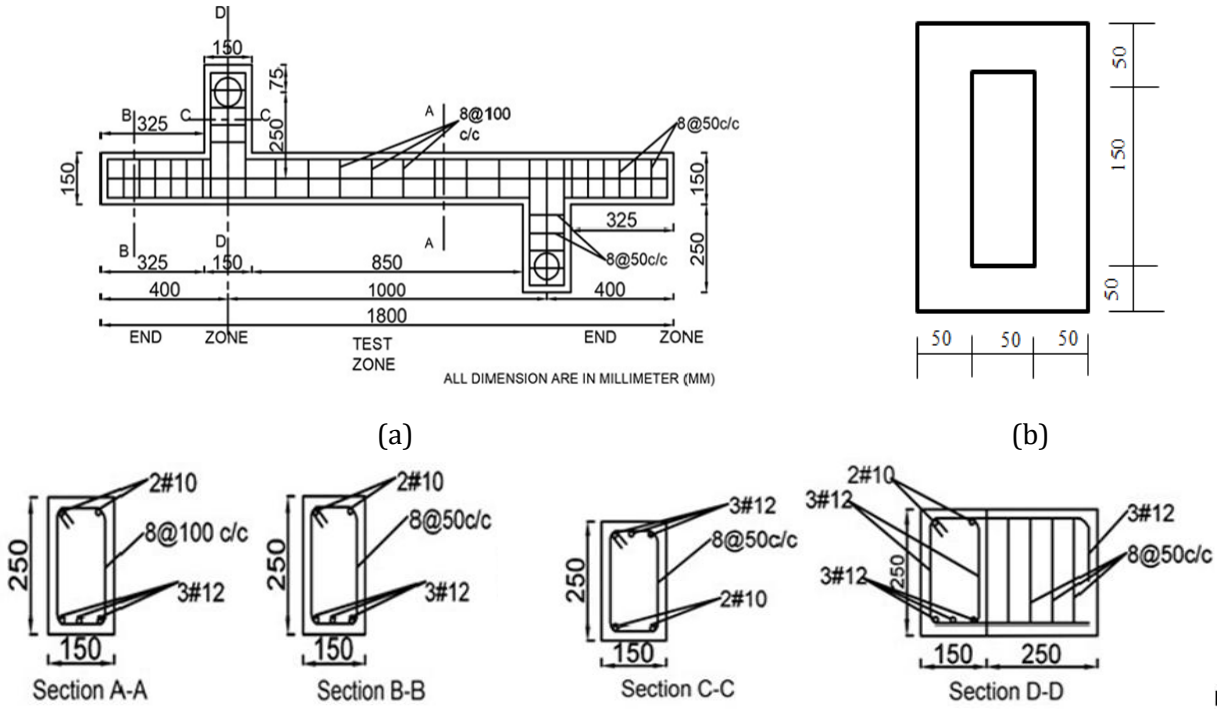


(a) (b) (c) (d)

Fig. 2. (a) Waste concrete panels (b) Crushed concrete lumps (c) Recycled concrete aggregates (d) Grinding machine

2.3. Details of Solid and Hollow Beam Specimens

Three pairs (two each) solid and hollow beams with 0%, 50%, and 100% recycled concrete aggregate beams were cast and tested. The beams measured in length 1800 mm, width 150 mm, and depth 250 mm, with standardized reinforcement, with longitudinal top and bottom reinforcement of 3ø12 and 2ø10 respectively.



(a) (b) (c) (d)

Fig. 3. Reinforcement Detailing for Solid and Hollow Beams

8mmø @100mm c/c closed stirrups was provided in the test zone. 250 mm x 150 mm Lever arm was provided for applying torque with reinforcement shown in Fig.3 (a). Hollow beams featured a 50mm x 150mm core, surrounded by a 50mm peripheral wall thickness, as illustrated in Fig. 3(b). To cast these beams, 150mm x 250mm end plates with 50mm x 150mm openings were employed. Plywood sheets wrapped with cardboard were inserted to form openings along the beam's length. After 24 hours, the hollow beams were demolded, and the plywood sheets were carefully removed to maintain the wall thickness, which significantly affects the torque and twist values of the hollow beams. The section A-A taken in the test region and section B-B taken in the end zone as shown in the Fig. 3 (c). The section C-C and section D-D taken in the lever arm zone as shown in the Fig.3 (d).

2.4. Concrete Proportioning

A concrete mix design conforming to M30 grade was developed according to IS: 10262 [44], employing the absolute volume method. Recycled concrete aggregate was in the SSD state to maintain constant free water and workability. The volume replacement method was employed, considering the specific gravity difference between natural coarse aggregate and recycled concrete aggregate. Three series of mixtures were prepared as mention in Table 2. The concrete mixtures were named as follows: "M" indicated the mixture, and "R" represented the alternate % of natural coarse aggregate with recycled concrete aggregate.

Table 2. Concrete mix proportion (1 m^3) in Kg

Mix	Cement	Water	Sand	Natural Coarse Aggregate	Recycled Concrete Aggregate
M-R00	380	180	680	1160	000
M-R50	380	180	675	567	552
M-R100	380	180	620	000	1130

2.5. Batching, Mixing and Casting of Concrete Beams

Concrete mixing was performed in the lab in a tilting-drum mixer. Weighed and bagged materials were mixed in a specific sequence. The mixing process involved moistening coarse aggregates with 1/3 of the entire water, followed by addition of 1/3 of the cement. The residual fine aggregates, cement and water, were added, and the mixture was blended thoroughly. The mixed concrete was then transported, poured into molds, compacted, and finished before the initial setting time. The interior surfaces of the molds were coated with shutter oil. For hollow beam casting, 150 x 250 mm end plates with 50 x 150 mm openings and 50 mm peripheral wall thickness were used. Plywood plates wrapped with cardboard were inserted to create openings along the beam's length shown in Fig. 4a. After 24 hours, the plywood plates were carefully removed shown in Fig. 4b, and the cardboard was removed by sprinkling water. The concrete was compacted using a needle vibrator as shown in Fig. 4c. The beam specimens were demolded after 24 hours, then wrapped in gunny bags and cured on a clean, level laboratory floor.



(a)



(b)



(c)

Fig. 4. Casting of beams

2.6. Instrumentation and Test Setup

A custom setup for test was planned to apply torsion to the beam specimen. As revealed in Fig. 5, the beam was placed on roller supports, allowing its ends to rotate, extend, and contract freely. The strategic placement of roller supports at both ends prevented longitudinal compression, ensuring that the beam was subjected to torsion only.

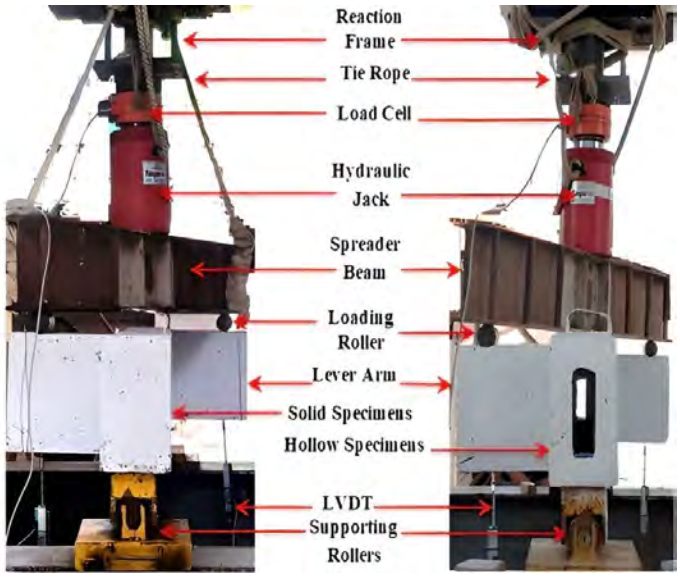


Fig. 5. Solid and hollow beam torsion test setup

Torsion was applied to a 850 mm free span, within an effective range of 1000mm. Vertical deformations were recorded by two LVDTs positioned beneath the soffit of two lever arms. The load sensor and LVDT were connected to a data acquisition system. All the beams were subjected to progressive loading at its center, using a 1000kN hydraulic jack, with incremental load increments until failure.

3. Results and Discussion

3.1Fresh Concrete Slump

The inferior slump values of RAC mixes, compared to NAC mixes, can be attributed to the irregular shape and lower specific gravity of recycled concrete aggregate relative to natural coarse aggregate. The recycled concrete aggregate has an older recycled concrete aggregate-cement bond that is different from the new cement bond. This makes it harder for RAC to flow. To get the right slump for RAC, super plasticizer must be used in RAC, just like it is needed for recycled concrete aggregate, which has an odd shape. So, adding super plasticizer to RAC made it similar to NAC in that it was

easy to work with and compacted well. Consequently, the addition of super plasticizer to RAC allowed RAC to attain comparable workability and compaction to that of NAC. All mixes were planned to slump in the S3 slump class (100-150 mm).

3.2 Density of Concrete

The density of RAC decreased linearly with increasing replacement ratios of natural coarse aggregate to recycled concrete aggregate, yielding lower densities compared to NAC. Table 3 shows that RAC mixes containing 50% and 100% RCA had densities 1.92% and 3.75% lower, respectively, than NAC. This trend is attributed to the direct relationship between concrete density and the density of its constituent particles.

3.3. Mechanical Properties of Concrete

To evaluate the compressive and tensile strength of each mix, cylinders of 150 mm x 300 mm were made according to IS: 516 [45] and IS: 5816 [46]. The beams were given the following names in Table 3: (1) the solid and hollow beams marked by SB and HB. (2) R shows the % of replacement of recycled concrete aggregate.

Table 3. Measured properties of concrete

Beam Id	Density (Kg/m^3)	Compressive Strength (MPa)	Tensile Strength (MPa)
SB-R00	2400	37.55	4.11
HB-R00	2400	37.45	4.11
SB-R50	2354	36.85	3.98
HB-R50	2354	36.82	3.97
SB-R100	2310	32.33	3.15
HB-R100	2310	32.36	3.11

The types of failure did not show any significant variations. The NAC and RAC had approximately equal ultimate compressive strength for each pair of beams as shown in Table 3. The 50% and 100 % recycled concrete aggregate mixes were lower than natural coarse aggregate i.e.1.6 % and 5.1 % respectively. The equivalent strength of concrete mixes may be justified by the particle shape, their adherence to the paste of cement and caliber of concrete. Compared to natural coarse aggregate concrete, the tensile strength reductions of 3.41% and 14.63% were observed for 50% and 100% recycled concrete aggregate concrete, respectively. The strong attachment between the cement paste and recycled aggregate, facilitated by the aggregate's rough and porous texture, may contribute to this reduction. The tensile strength was influenced more by the recycled concrete aggregate's quality rather of their amount [47]. It is abundantly evident that if the recycled aggregates are employed in the SSD state, replacing natural aggregates by recycled aggregates at whatever percentage leads only in a minor difference in concrete slump. The concrete mix achieved the desired compressive strength (30 MPa) at 28-day. Although moisture conditions of the coarse aggregates affected compressive strength, replacing natural aggregate with recycled aggregate proved beneficial. Importantly, this substitution did not significantly impact the concrete's workability, compressive strength, or tensile strength.

3.4. Effect of Recycled Concrete Aggregate on Cracking Behaviour of Solid and Hollow Beams

This analysis included the examination of propagation with failure patterns of cracks. The test revealed that the tensile cracking about all faces of the RAC and NAC beams. There were no visible fractures in any of the beams as the torque was progressively increased at the start of the test. Fig. 6 illustrates the cracking and failure patterns of RAC beams with varying replacement ratios. The results indicate a positive correlation between the replacement ratio and the number of cracks, with an increase in cracks as the replacement ratio increased. Diagonal cracks appeared on both wider and shorter faces, simultaneously. As torque increased, cracks on the larger faces shifted

towards the shorter faces, at right angles to the longitudinal beam's axis. Identified cracks joined with original 45-degree cracks on shorter faces, resulting in S-shaped curves. The results show that recycled concrete aggregate in solid and hollow beams promotes numerous cracks and stress redeployment subsequent to original cracking. Key findings include are (1) RAC beams developed multiple diagonal cracks after the first crack. (2) Cracks and twist angles increased with torque. (3) A notable diagonal break occurred at 45-48 degrees from the beam axis. (4)RCA increased the diagonal crack angle in solid and hollow beams. (5) The test results showed that hollow beams exhibited cracking and failure at marginally lower loads compared to solid beams. This suggests that the concrete core in solid beams plays a beneficial role in enhancing the cracking load.

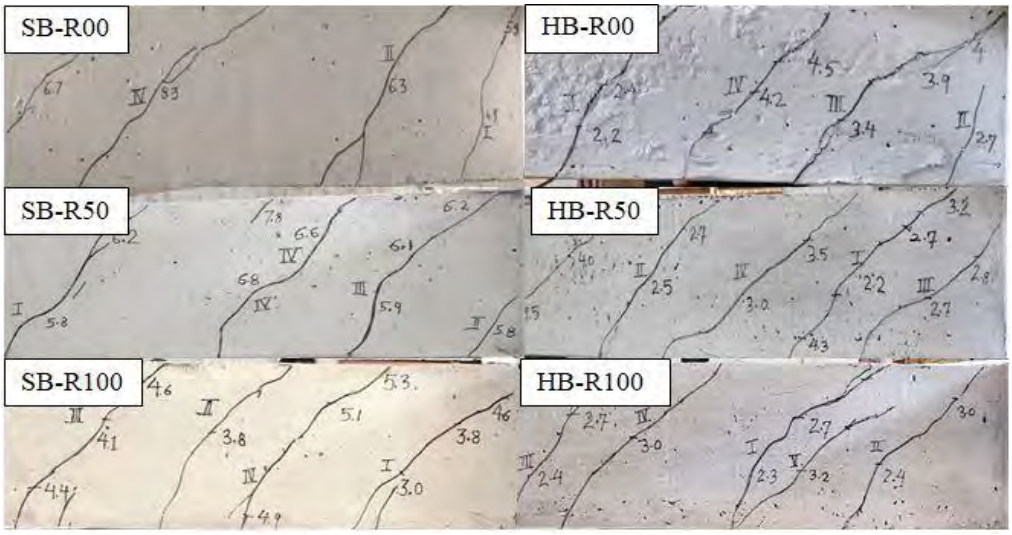


Fig. 6. Cracks pattern in test region of solid and hollow beams

3.5. Effect of Recycled Concrete Aggregate on Torque and Twist angle

The hollow RAC beams exhibited lower cracking resistance and maximum rotational force compared to solid NAC beams, which showed minimal damage. Table 4 indicates that as the proportion of recycled concrete aggregate in the beam increased, the torsional strength decreased, while the angle of twist increased.

Table 4. Measured torque and twist angle

Beam ID	Cracking State		Ultimate State	
	T_{cr} (kN.m)	θ_{cr} (rad/m)	T_u (kN.m)	θ_u (rad/m)
SB-R00	3.68	0.003	11.10	0.027
HB-R00	3.11	0.003	10.51	0.028
SB-R50	3.40	0.003	10.44	0.027
HB-R50	2.87	0.003	9.76	0.029
SB-R100	2.89	0.004	9.82	0.031
HB-R100	2.71	0.006	8.97	0.033

The torsional capacity of the beams was only reduced by 5.49% and angle of twist was increases by 3.70% for HB-R00. The torsional capacity of the beams was only reduced by 6.69% and angle of twist was increases by 6.89 % for HB-R50. The torsional capacity of the beams was only reduced by 8.67% and angle of twist was increases by 9.09% for HB-R100 at ultimate state as compared to that of SB-R00, SB-R50 and SB-R100 beams. Both beams had about the equivalent force resistance capacity, but solid beams had a little more. The strength of hollow beams was identical to that found in the solid beams. The concrete core's absence was the lone deviation. Both series points lie on the same curve, indicating that similar reinforcing levels resulted in nearly equal torsion ultimate strengths. The results suggest that the concrete core does not provide a significant contribution to the ultimate torsional strength of a solid beam, and the torque was not caused by the concrete core's resistance as is generally believed. It will help figure out what changes need to be made to

the current standards and how to use RAC solid and hollow beams for building structures. The lesser modulus of elasticity of RAC compare to NAC results in increased twist angles, especially with higher recycled concrete aggregate ratios under different stress conditions. Nevertheless, hollow RAC beams exhibit acceptable behavior, albeit slightly inferior, compared to solid RAC beams at all loading stages in torsion.

3.6. Effect of Recycled Concrete Aggregate on Torque-Twist Relationship

It can be understood from Fig.7 the hollow beams perform nearly well with solid beams in test results. The fact that both series points are on the same curve suggests that equivalent torsion ultimate strengths were produced by comparable levels of reinforcing. As a result, it appears that the concrete core did not increase a solid beam's final torsional strength, and contrary to popular belief, the torque was not brought on by the resistance of the concrete core.

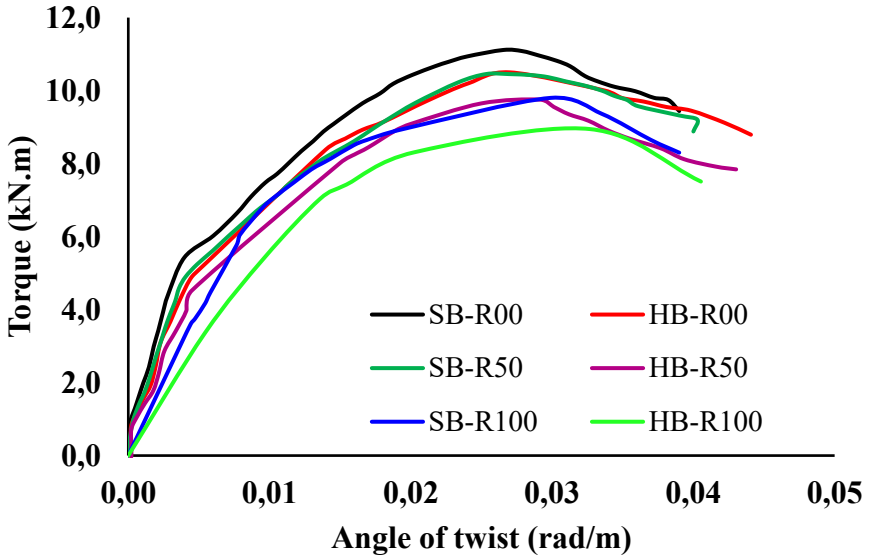


Fig. 7. Measured Torque-Twist curves for all tested beams

For the solid beam, the peak torsional moment was 11.10kN.m, for the hollow beam it was 10.51kN.m, and for the solid beam it was 9.76kN.m. The peak torsional moment for the solid beam was 10.44kN.m. The measured twist angles for solid and hollow beams were 0.027rad/m, 0.027rad/m, 0.031 rad/m and 0.028rad/m, 0.029rad/m, 0.033rad/m, respectively for 0%, 50%, and 100% replacement of recycled concrete aggregate. The final torque and angle of twist was not affected to a great extent because of the replacement ratio of recycled concrete aggregate. However, the consequence was not big adequate to stop using recycled concrete aggregate in RAC beams for pure torsion in solid and hollow beams. Form the achieved results, the torsional behaviour, angle of twist and crack pattern at every state loading with the failure mode of varying % of RAC in solid and hollow beams it can be committed that the application of RAC in structural use under torsion is feasible with prior care.

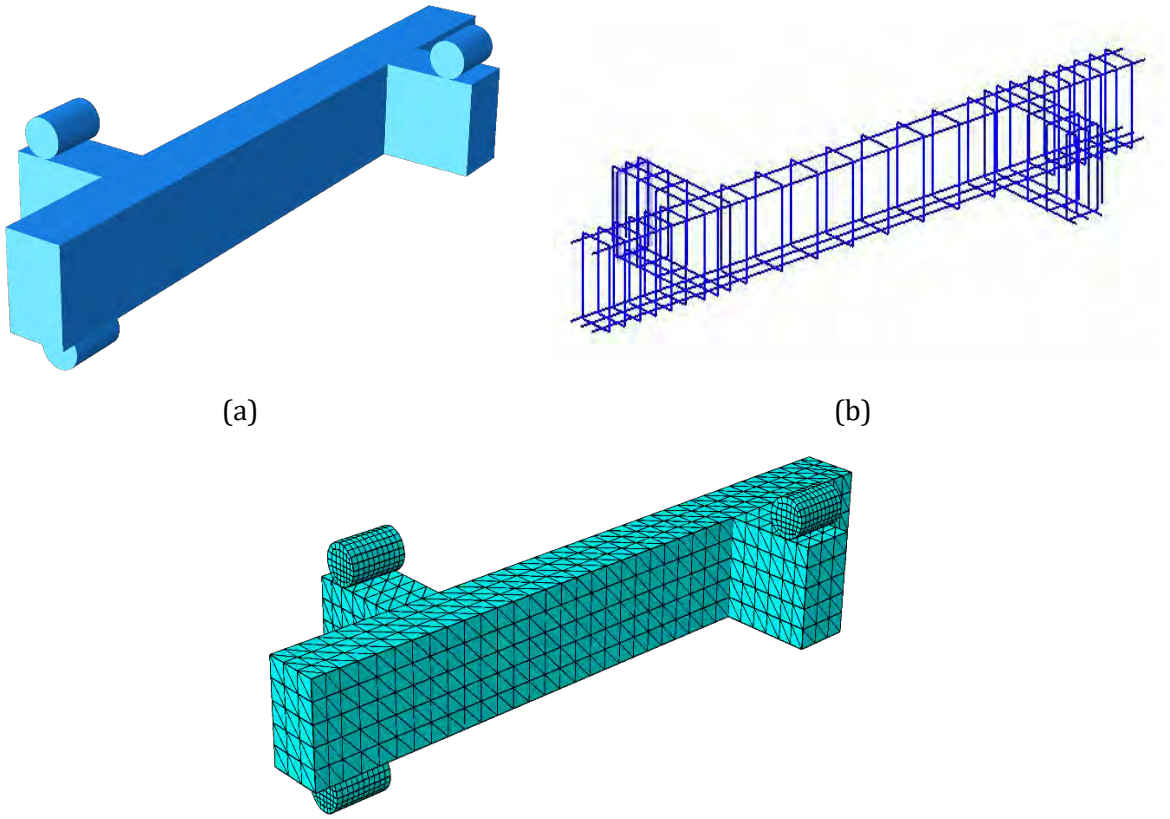
4. Validation of Laboratory Tested Beams by Finite Element Method

The increasing use of finite element analysis to simulate the complicated structural issues ABAQUS, ATENA-3D, ANSYS, LS-Dyna and some other software are available. These FE software's help to analyses the structural concrete element under the variety of loading such as flexure, shear and torsion. The accuracy of FE model based on compatibility of non-linear method and adopted materials model. This study simulated hollow and solid beams with coarse RCA subjected to torsion using ABAQUS FEA software. The simple object method was used to create geometry in ABAQUS. The brittle-cracking model was adapted as a material model, which yield better results of concrete. Simple Rankine yield criterion was employed to perceive accurate crack initiations and propagations on the beams, which allows the crack closing and reopening. The top of the beam was loaded via displacement-controlled method to match the spreader beam center deformation rate.

The rigid steel roller support was vertically constrained and modeled by a line of contact boundary condition. Monitoring stations were set at the spreader beam top and lever arm soffit to record load and deformation.

4.1. Geometrical Definition and Meshing

A three-dimensional geometrical model of the beam specimens shown in Fig.(a) was developed in ABAQUS utilizing the built-in modeling tools and element library. The Fig. 8 (b) shown longitudinal and transverse directions reinforcement, modeled as truss elements (T3D2) based on experimental details. The reinforcement consisted of 12 mm diameter for bottom steel, 10 mm diameter bars for top reinforcement and 8 mm diameter bars for web reinforcement. Web reinforcement was spaced 100 mm apart to achieve the desired torsion response. ABAQUS effectively modeled curved parts, such as steel rollers, using precise contact shown in Figs. 8 (a) and 8(c). The model employed 25 mm; eight-noded, hexahedral (brick) elements with incompatible modes (C3D8I) to prevent overly rigid behavior under bending. The steel rebars were replicated using 10 mm-sized 3D linear truss (T3D2) elements.



(a) (b)

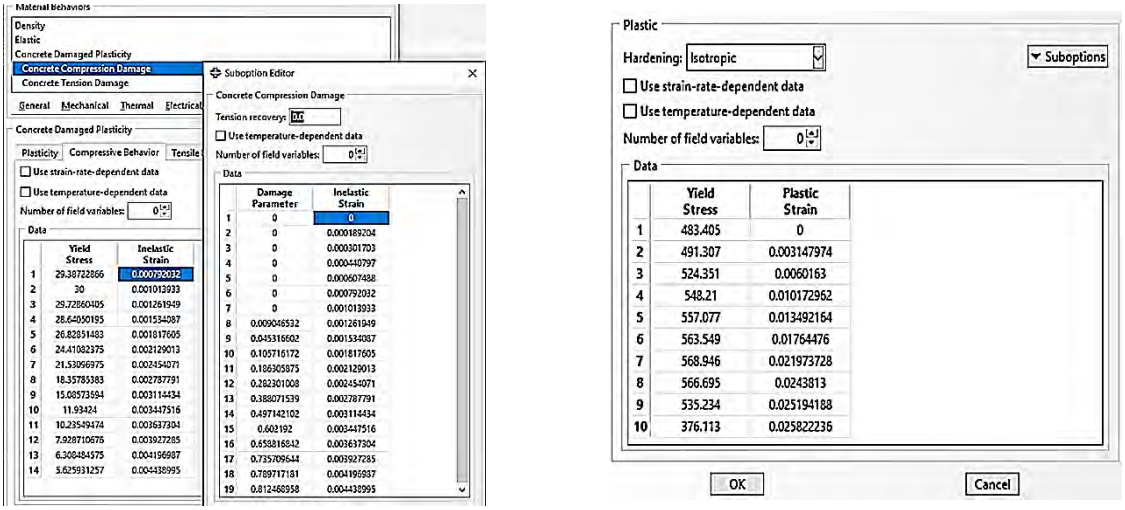
(c)

Fig. 8. Geometrical modelling and meshed beams

4.2. Material Models

For various materials and applications, ABAQUS provides a range of material models. ABAQUS also allows users to create custom material models, a valuable feature when working with unconventional materials. While predefined models suffice for standard concrete structures, they cannot accurately simulate concretes containing alternative ingredients like silica fume, fly ash, or recycled aggregates. To address this limitation, the constitutive model published by Suryawanshi et al. [48] was employed to capture the non-linear performance of NAC and RAC. The simple stress-strain relationship is defined by Eq. 1.

$$\bar{\sigma} = a(\bar{\varepsilon}) + b(\bar{\varepsilon})^2 + c(\bar{\varepsilon})^3 + d(\bar{\varepsilon})^4 \quad (1)$$



(a) (b)

Fig.9. Input parameter - Stress-strain relations for concrete and reinforcement

Figure 9 (a) shows the window for user-defined material definition using stress-strain data of compression test and inelastic strain damage factors. The Concrete Damage Plasticity model can be characterized using tensile test stress-strain data in conjunction with the associated material damage parameters. According to Earij et al. [49], ABAQUS has adopted appropriate values for input parameters like dilation angle, eccentricity, and viscosity parameters from existing literature. Concrete's compressive and tensile behaviors, as well as its elastic and plastic qualities, are examples of additional material input characteristics. Concrete's non-linear stress-strain behavior must be taken into account when predicting material damage using the damage coefficient. ABAQUS also permits users to incorporate the actual nonlinear stress-strain behavior of steel, thereby enabling more precise simulations compared to idealize elastic-plastic models. The dialogue window appears in Fig.9 (b) after entering stress-strain values. Note that ABAQUS only accepts inelastic strain and stress values. Differentiating total strain and elastic strain yields inelastic strain.

4.3. Cracking Behaviour of Solid and Hollow RAC Beams

In ABAQUS, the bands of principal tensile strain generated during the loading. Tensile strain bands with precise color to represents definite magnitude of strain that can compare with actual crack pattern observed during test. During loading, the crack pattern (principal tensile strain band) was monitored in both beams.

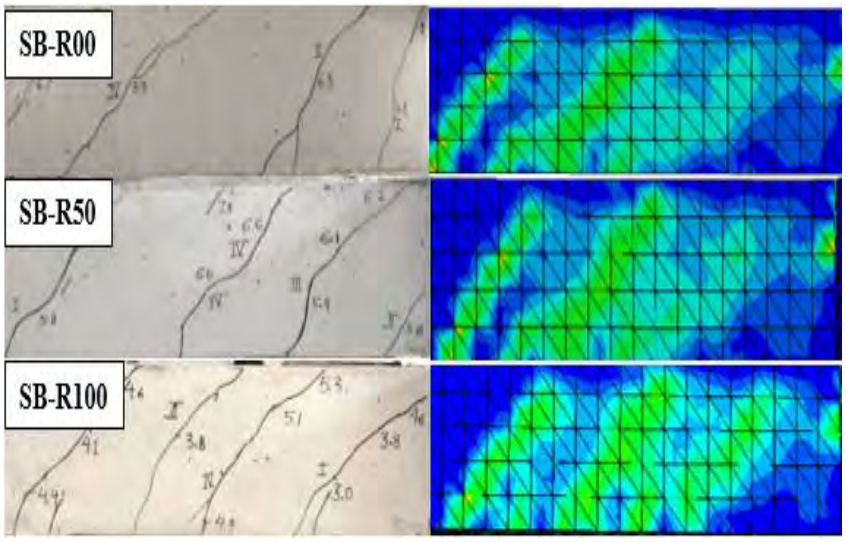


Fig. 9. Comparative crack pattern of solid beams

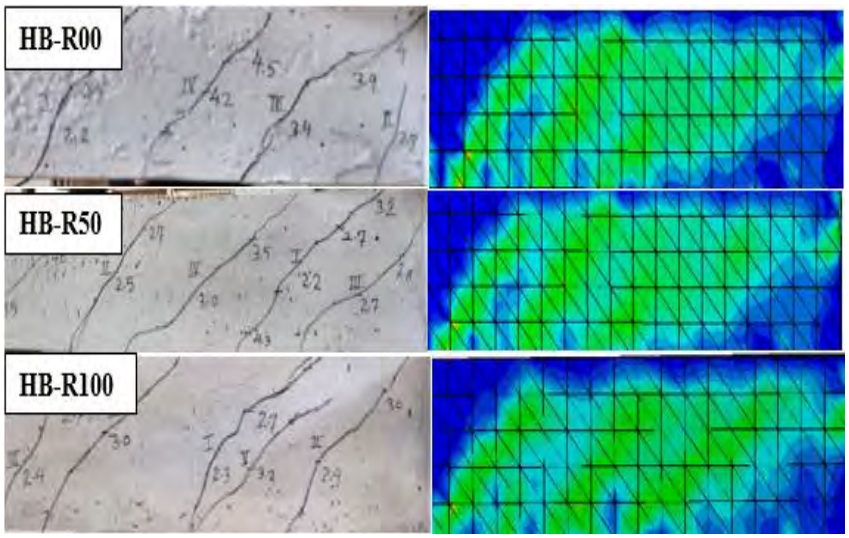


Fig. 10. Comparative crack pattern of Hollow beams

The first diagonal crack appeared at the same depth as observed experimentally. As the load increased, the diagonal crack pattern propagated to other faces of the beams, with additional crack bands forming. Figs. 9 and 10 shows that the crack patterns, characterized by principal tensile strain, were comparable in both solid and hollow beams, regardless of the recycled concrete aggregate content. The development of tensile strain bands, characterized by distinct colors indicating particular strain magnitudes, can be correlated with the actual crack patterns found in experimental settings. Figure 9 and 10 illustrates the relationship of fracture pattern in beams with varying substitution amounts of recycled concrete aggregate, alongside the primary tensile strain patterns simulated by ABAQUS. Notably, the major tensile strains patterns produced by ABAQUS and experimental were align with each other. Fig. 10 displays the identical cracking patterns produced by ABAQUS analysis along with cracking patterns that were obtained from experiment. The cracking pattern in all solid and hollow beams with varying percentages of recycled concrete aggregate was identical. All solid beam specimens shown the first crack was almost at somewhat higher torsion than the hollow beam. However, as the percentage of recycled aggregates replacing natural aggregates rise, the peak load falls in both results for all beams. This suggests that RAC-beam and NAC-beam behave similarly in both the tests. The beam containing recycled concrete aggregate 50% and 100% found more cracks than NAC beam in both the test. Hollow beams showed wider crack than the solid beam in experiment test and FEM analysis.

4.4. Torque-Twist Capacity RAC Beams at Ultimate State

All the solid and hollow beam were tested in load frame experimentally and the tested beam validated through finite element software ABAQUS. The load and deformation data were recorded continuously and transform into Torque-Twist form for more analysis. The twisting angle along with torsional ability of all the beams at ultimate state was compared with ABAQUS analysis. Table 5 shows torsional capacity of solid beams somewhat more than hollow beam in both studies. As the % of RCA increase torsional capacity decreases in both the methods.

Table 5. Observed and simulated torsional moment of RAC beam

Beam Id	Ultimate Torsional Moment Measured (kN.m)	Ultimate Torsional Moment ABAQUS (kN.m)	Angle of twist Measured (rad/m)	Angle of twist ABAQUS (rad/m)
SB-R00	11.10	11.70	0.027	0.028
HB-R00	10.51	10.82	0.028	0.031
SB-R50	10.44	10.75	0.027	0.030
HB-R50	9.76	9.90	0.029	0.033
SB-R100	9.82	9.92	0.031	0.032
HB-R100	8.97	9.10	0.033	0.035

The ultimate torsional capacity of experimentally tested solid beams SB-R00, SB-R50 and SB-R100 was decreased by 5.12%, 2.88% and 1% than the numerical torsional value. The ultimate torsional capacity of experimentally tested hollow beam HB-R00, HB-R50 and HB-R100 was decreased by 2.86%, 1.14% and 1% than the numerical torsional value. The torsional ability of hollow beams was found lower by 7.52 %, 7.90 % and 8.26 % than the solid beams in simulation results. From the test results in the both method it was seen that the torsional capacity of ABAQUS software was found nearly close to experimental values at the definitive state for all the beams.

4.5. Torque-Twist Behaviour of RAC Beams

The experimental and numerical results showed similar behavior for hollow and solid beams before and after the peak. However, the ABAQUS simulation yielded a slightly larger area under the torque-twist curve compared to the experimental curve, as illustrated in Fig. 11. The ABAQUS investigation shows a comparable trend of reduced resistance capability of torque and increasing twisting angle at higher replacement levels. This could be due to a decrease concrete modulus of elasticity, which corresponds to a greater extent of natural coarse aggregate substitution.

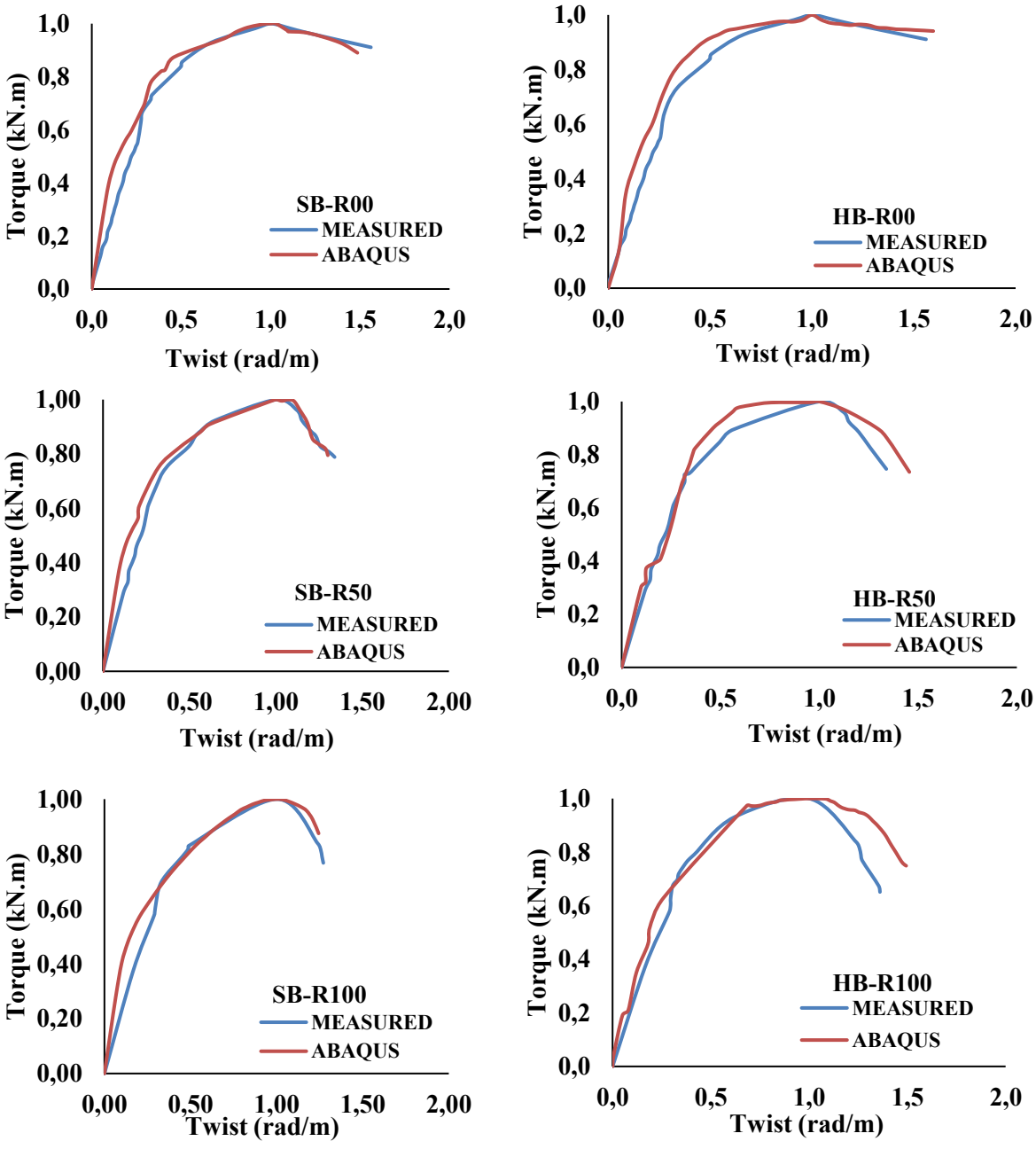


Fig. 11. Comparative torque-twist performance of solid and hollow beam

Fig. 11 displays the torque-twist relationships established by ABAQUS software. The specimens responded virtually linearly after cracking until the tension bar yielded. Following this, each specimen showed nonlinear behavior until reaching its failure load. Enough rotation of the plastic hinge causes high stress in the specimens' compression zone, leading to crushing failure. The experimental torque-twist curves for all solid and hollow beam specimens compared in Fig. 11. Both analyses showed similar torque-twist tendencies. The presence of two interfacial transition zones (ITZs) in RAC beams reduced their cracking stress and stiffness compared to natural NAC beams, which have only one ITZ. This is attributed to the lower modulus of elasticity of RAC.

The torque-twist behavior of solid beam showed somewhat higher torque at cracking state and same at the ultimate state than hollow beams. The experimentally tested 50% and 100% recycled concrete aggregate hollow beam showed lower torque-twist behavior with the comparison of simulation during ultimate to failure state as shown in Fig.11 (HB-R50 and HB-R100). Increasing the replacement level of recycled concrete aggregate reduces the area under the torque-twist curve. Furthermore, the incorporation of recycled concrete aggregate in concrete leads to a more gradual post-peak decline in the torque-twist curves, highlighting the increased weakness of RAC compared to NAC.

5. Conclusions

A numerical investigation was conducted to examine the impact of recycled concrete aggregate on the torsional behavior of reinforced concrete beams, with validation provided by experimental results. The primary findings are outlined below:

- To achieve satisfactory workability, the addition of super plasticizer was found suitable and the concrete density of RAC beam was not affected considerably as compare to NAC.
- The tensile and compressive strength with 0% and 50% recycled concrete aggregate of concrete were found decrease by 3.16% and 1.86% respectively. However, the RAC with 100% recycled concrete aggregate of tensile and compressive strength w.r.t. NAC found decrease by 23.35% and 13.82%. Because of the breakdown of the aggregate-cement paste bond inferior results of RAC was found as compare to NAC.
- Both experimental and numerical results showed similar crack initiation and propagation patterns in solid and hollow beams. Upon reaching maximum torsion, a dominant crack in the test zone expanded significantly, leading to tensile failure of the beams in both experimental and numerical methods.
- Similar diagonal cracks were observed in hollow and solid beam and the beam containing recycled concrete aggregate found more cracks than NAC beam in both the test. Hollow beams showed wider crack than the solid beam in test and FEM analysis.
- The experimental torque of the all hollow beams was found decreased than solid beam by 5.31%, 6.51% and 8.05% at ultimate state with the increased twisting angle and % of recycled concrete aggregate in comparison to solid beams. The twist angle of the beam was increased for HB-R00 by 3.70%, for HB-R50 by 6.89% and for HB-R100 by 9.09% at ultimate state as compare with SB-R00, SB-R50 and SB-R100 beams.
- Increasing the proportion of recycled concrete aggregate (RCA) reduces the area under the torque-twist curve. Moreover, RCA inclusion leads to a more pronounced reduction in the post-peak gradient of the torque-twist curve, indicating increased brittleness in RAC compared to NAC.
- The inclusion of recycled concrete aggregate in structural concrete leads to a reduce in the area under the torque-twist curve as the replacement level increases. Furthermore, the utilize of recycled concrete aggregate reduces the post-peak gradients of the torque-twist curve, highlighting the increased brittleness of RAC compare to NAC.

- The ultimate torsional capacity of experimentally tested solid beams SB-R00, SB-R50 and SB-R100 was decreased by 5.12%, 2.88% and 1% than the numerical torque. The ultimate torsional capacity of experimentally tested hollow beam HB-R00, HB-R50 and HB-R100 was decreased by 2.86%, 1.14% and 1% than the numerical torque. The torque-twist characteristic revealed that, ABAQUS simulation results were significantly closer to experimental results at all the parameters. This indicates that the significance of sound characterize material definition in expressions of calculated stress-strain relation of yield of numerical simulation.
- The torque-twist behaviour of solid beam showed somewhat higher torque at cracking state and same at the ultimate state than hollow beams. The experimentally tested 50% and 100% recycled concrete aggregate hollow beam showed lower torque-twist behaviour with the comparison of simulation during ultimate to failure state.

According to the findings, additional research is necessary in order to reach an agreement regarding its torsional performance of RAC beams.

References

[1] Patare SA, Bhirud YL. Effect of displacement control gain on the shape of functionally graded piezoelectric beam using a simple beam theory. Asian J Civ. Eng. 2022; 23:887–905. https://doi.org/10.1007/s42107-022-00463-7

[2] Nataraja MC, Bhat G, Manoj M, Mallya S. Investigation on concrete with crushed vitrified tiles as coarse aggregates. J Build Path and Rehabil. 2022;7: 103 https://doi.org/10.1007/s41024-022-00245-3

[3] Manthene SL, Boddepalli KR. Effect of tile aggregate and flyash on durability and mechanical properties of self-compacting concrete. J Build Rehab. 2022; 7, 68 https://doi.org/10.1007/s41024-022-00209-7

[4] Pawar AJ, Suryawanshi SR. Comprehensive Analysis of Stress-strain Relationships for Recycled Aggregate Concrete. Inter J Eng, Transactions B: Applications. 2022; 35(11): 1184-1191. http://dx.doi.org/10.5829/ije.2022.35.11b.05

[5] Masne N, Suryawanshi S. Effect of replacement ratio on the torsional behaviour of recycled aggregate concrete beams. Inter J Eng, Transactions A: Basics. 2023; 36 (04): 659-668. https://doi.org/10.5829/ije.2023.36.04a.06

[6] Fathifazl G, Razaqpur AG, Isgor OB, Abbas A, Fournier B, Foo S. Flexural performance of steel-reinforced recycled concrete beams. ACI St J. 2009; 106 (6): 858-867. https://doi.org/10.14359/51663187

[7] Kang THK, Kim W, Kwak YK, Hong SG. Flexural testing of reinforced concrete beams with recycled concrete aggregates. ACI St J. 2014; 111 (3):607-616. https://doi.org/10.14359/51686622

[8] Seara-Paza S, González-Fonteboab B, Martínez-Abellab F, Eiras-Lópezb J. Flexural performance of reinforced concrete beams made with recycled concrete coarse aggregate. Eng St. 2018; 156:32–45. https://doi.org/10.1016/j.engstruct.2017.11.015

[9] Rahal KN, Alrefaei YT. Shear strength of recycled aggregate concrete beams containing stirrups. Cons and Build Mat. 2018; 191:866–876. https://doi.org/10.1016/j.conbuildmat.2018.10.023

[10] Albostami AS, Al-Hamd Rwayda KS, Alzabeebee S. Shear strength assessment of reinforced recycled aggregate concrete beams without stirrups using soft computing techniques. J Build Path Rehabili.2018;8:98 https://doi.org/10.1007/s41024-023-00343-w

[11] Alshimmeri AJH, Al-Maliki HNG. Structural Behaviour of Reinforced Concrete Hollow Beams under Partial Uniformly Distributed Load. J Eng. 2014; 20 (7): 130-145.

[12] Hsu TTC. Torsion of structural concrete behaviour of reinforced concrete rectangular members torsion of structural concrete pure torsion-reinforced sections. ACI, 1968; Paper SP 18-10, Detroid, 261-306.

[13] Lampert P, Thurlimann BT. Ultimate Strength and Design of Reinforced Concrete Beams in Torsion and Bending. Intern Asso for Bridge and Structural Eng. 1971; 31(1):107-131.

[14] Bhatt P, Ebireri JO. Direct design of beams for combined bending and torsion. Stavebnicky Casopis, Building J (Bratislava). 1989; 37 (4):249–263.

[15] Collins MP, Mitchell D. Pre-stressed concrete structures. Prentice Hall Inc.1991, Englewood Cliffs, NJ.

[16] Fouad E, Ghoneim M, Issa M, Shaheen H. Combined shear and torsion in normal and high strength concrete beams Experimental Study. J Eng App Sci. 2000; 47(6): 1059–1078.

[17] Bernardo L, Lopes S, Oliveira L. Torsion in reinforced high-strength concrete hollow beams. INCOS, 2003; 5:277-286.

[18] Bernardo LFA, Lopes SMR. Behaviour of concrete beams under torsion: NSC plain and hollow beams. Mat and St. 2008; 41:1143–1167. http://dx.doi.org/10.1617/s11527-007-9315

[19] Alnuaimi AS, Al-Jabri KS,Hago A. Comparison between solid and hollow reinforced concrete beams. Mat and St. 2008; 41:269-281. http://dx.doi.org/10.1617/s11527-007-9237-x

[20] Lopes SMR, Bernardo LFA. Cracking and failure mode in HSC hollow beams under torsion. Cons and Buil Mat. 2014; 51: 163–178. http://dx.doi.org/10.1016/j.conbuildmat.2013.10.062
[21] Lopes SMR, Bernardo LFA. Twist behaviour of high-strength concrete hollow beams _Formation of plastic hinges along the length. Eng St. 2009; 31: 138-149. http://dx.doi.org/10.1016/j.engstruct.2008.08.003
[22] Jeng CH, Chao M, Peng SF. Constitutive relationships of concrete for hollow RC members in pure torsion. Mag Con Res. 2014; 66 (17):896–912.
[23] Jabbar S, Hejazi F, Mahmod HM. Effect of an Opening on Reinforced Concrete Hollow Beam Web Under Torsional, Flexural, and Cyclic Loadings. Lat Amer J Sol and St. 2016; 13:1576-1595. https://doi.org/10.1590/1679-782512629
[24] Fu JL, Liu BK, Ma JW, Zhou H. Experimental study on seismic behaviour of recycled aggregate concrete torsion beams with Abaqus Ad Mat Res. 2015; 1079-1080: 220-225. https://doi.org/10.4028/www.scientific.net/AMR.1079-1080.220
[25] Wang X, Liu B, Zhang C. Seismic behaviour of recycled aggregate concrete beams under cyclic torsion. Con and Build Mat. 2016; 129:193–203. http://dx.doi.org/10.1016/j.conbuildmat.2016.10.101
[26] Sarsam KF, Salih N, Hussein M. Assessment of reinforced recycling aggregate concrete beams under torsional moment. Intl J Eng & Tech. 2016; 7 (4.20): 623-628. http://dx.doi.org/10.14419/ijet.v7i4.20.27403
[27] Masne N, Suryawanshi S. Numerical and Experimental Investigation of Recycled Aggregate Concrete Beams Subjected to Pure Torsion. Int J Eng Transactions A: Basics. 2022; 35 (10): 1123-1132. http://dx.doi.org/10.5829/ije.2022.35.10a.14
[28] Ojha PN, Kaura P, Singh B. Studies on mechanical performance of treated and non-treated coarse recycled concrete aggregate and its performance in concrete-an Indian case study. Res. Eng. Struct. Mater. 2024; 10(1): 341-362. : http://dx.doi.org/10.17515/resm2023.53me0728rs
[29] Kumar CA, Reddy PN, Kulkarni AP. Self-sensing concrete with recycled coarse aggregates and multi-walled carbon nanotubes: A sustainable and effective method. Res. Eng. Struct. Mater. 2024; 10(1): 41-56. http://dx.doi.org/10.17515/resm2023.773ma0520
[30] Belmouhoub A, Abdelouahed A, Noui A. Experimental and factorial design of the mechanical and physical properties of concrete containing waste rubber powder. Res. Eng. Struct. Mater. 2024; 10(2): 461-480. http://dx.doi.org/10.17515/resm2023.54me0810rs
[31] Poonam, Singh VP. Response surface methodology use in optimization of concrete properties using blast furnace slag aggregate and recycled concrete sand. Res. Eng. Struct. Mater. 2024; 10(1): 111-133.DOI: http://dx.doi.org/10.17515/resm2023.788me0614
[32] Masne N, Suryawanshi S. Effect of waste water curing and elevated temperature on recycled concrete aggregates from construction and demolition waste. Iranian (Iranica) Journal of Energy & Environment – Peer review Journal. 2023; 4(2): 152-158. https://doi.org/10.5829/IJEE.2023.14.02.07
[33] Masne N, Suryawanshi S. An Investigation of the Mechanical Properties of Recycled Aggregate Concrete with Silica Fume. Sustainable Building Materials and Construction, Lecture Notes in Civil Engineering, Springer, 2022; 222: 379-387. https://doi.org/10.1007/978-981-16-8496-8_47
[34] Hussein Talab Nhabih, Mohammad R. K. M. Al-Badkubi, A. A. El-barbary, Marwa Marza Salman. Recycling harmful plastic waste to produce a fiber equivalent to carbon fiber reinforced polymer for reinforcement and rehabilitation of structural members. Curved and Layered Structures. 2024; 11: 20240003. https://doi.org/10.1515/cls-2024-0003
[35] IS: 12269. Ordinary Portland cement 53 grade-specifications. Bureau of Indian Standards, 2013 New Delhi, India.
[36] IS: 383 Specification for coarse and fine aggregates from natural sources for concrete. Bureau of Indian Standards, 2016, New Delhi, India.
[37] IS: 456. Indian standard plain and reinforced concrete code of practice. Bureau of Indian Standards, 2016, New Delhi, India.
[38] IS: 9103. Concrete Admixtures Specification. Bureau of Indian Standards, 1999, New Delhi, India.
[39] IS: 1608-1. Metallic Materials Tensile Testing Part 1. Bureau of Indian Standards, 2018, New Delhi, India.
[40] Rama M, Shanthi VM. Study on Strength, Permeability and Micro-structure of Pervious Concrete Blended with Metakaolin. Jord J Civ Eng. 2023; 17 (1): https://doi.org/10.14525/JJCE.v17i1.02
[41] Stephen AA, Jeffrey M. Predictive Models for Evaluation of Compressive and Split Tensile Strengths of Recycled Aggregate Concrete Containing Lathe Waste Steel Fiber. Jord J Civ Eng, 2020; 14(4): 598-607.
[42] Jai KL, Sharma DK, Choudhary R, Bhargava S. Impact of Waste Iron Slag on Mechanical and Durability Properties of Concrete. Jord J of Civ Eng, 2023; 17 (1): 45-57. https://doi.org/10.14525/JJCE.v17i1.05
[43] Padmapriya R, Sudarsan JS, Nithiyanantham S. Formation of high strength concrete through sustainable waste materials as a partial replacement of cement. J Build Path Rehab. 2022; 7:86. https://doi.org/10.1007/s41024-022-00228-4
[44] IS: 10262. Concrete mix proportioning-Guidelines. Bureau of Indian Standards, 2009, New Delhi, India.

[45] IS: 516. Method of tests for strength of concrete. Bureau of Indian Standards, 2004 New Delhi, India.
[46] IS: 5816. Method of tests for strength of concrete. Bureau of Indian Standards, 2004, New Delhi, India.
[47] Masne N, Suryawanshi S. Evaluation of Ductility Ratio of Recycled Aggregate Concrete Beams Under Torsion. Recent Developments in Structural Engineering, 4: SEC 2023. Lecture Notes in Civil Engineering, 2024; 549:495-503. Springer, Singapore. https://doi.org/10.1007/978-981-97-6603-1_47
[48] Suryawanshi S, Singh B, Bhargava P. Equation for stress–strain relationship of recycled aggregate concrete in axial compression. Magaz Con Res. 2018; 163-171. https://doi.org/10.1680/jmacr.16.00108
[49] Earij A, Alfano G, Cashell K, Zhou X. Nonlinear three–dimensional finite–element modelling of reinforced– concrete beams: Computational challenges and experimental validation. Engin Fail Analy. 2017; 82: 92- 115. https://doi.org/https://doi.org/10.1016/j.engfailanal.2017.08.02

Blank Page

Research on Engineering Structures & Materials
www.jresm.org

Research Article

Mechanical properties of hybrid banana fibre, rice husk, and eggshell reinforced epoxy composite

Adeolu A. Adediran [1,2,a], Oluwasogo L. Ogundipe [*,1,b], Timothy Adeniyi Adekanye [1,c], Isaiah C. Okolie [1,d], Bradley E. Ihimekpen [1,e], Olajide A. Aogo [3,f], Bamidele T. Ogunsemi [1,g], Peter P. Ikubanni [1,h]

[1]*Dept. of Mechanical Engineering, College of Engineering, Landmark University, Omu-Aran, Nigeria*
[2]*Department of Mechanical Engineering Science, University of Johannesburg, South Africa*
[3]*SCL Academy, Consulting, Training, and Research Firm, Abuja, Nigeria*

Article Info

Article History:

Received 20 Sep 2024

Accepted 01 Dec 2024

Keywords:

Rice husks;
Egg shells;
Banana fibres;
Polymer;
Mechanical properties;
Composite

Abstract

The hybridization of natural fibres improves composite development by compensating the drawbacks of single fibre reinforcement in a polymer matrix. This study examined the influence of rice husks, eggshells, and banana fibres on the mechanical properties of an epoxy polymer composite with the aim of developing a sustainable composite material with improved mechanical properties from agricultural wastes. The composites were developed from varied proportions of banana fibre (BF) and eggshell (ES) with constant rice husks (RH) in an epoxy polymer matrix; 5:20:20, 10:15:20, 15:10:20, and 20:5:20 respectively. The BF and RH were treated with 5% NaOH before its usage as a reinforcement. The mechanical properties; flexural, tensile, and impact strength of the cured samples were investigated and the test results revealed that hybridized BF/ES/RH enhanced the mechanical properties of the epoxy polymer matrix composite. The best flexural, tensile, and impact strength was obtained at composition 15:10:20 BF/ES/RH. The flexural, tensile, impact strength, flexural modulus, and tensile modulus ranged from 3.66 to 25.06 MPa, 11.35 to 17.42 MPa, 14.98 to 28.61 J/mm^2, 133.80 to 850.75 MPa, and 469.18 to 1872.09 MPa respectively. The composite exhibited 64.7%, 9.3%, and 39.84% improvements in flexural, tensile, and impact strength, respectively, over the control sample. The BF, ES, and RH contribute to the composite's tensile strength, impact resistance, and rigidity respectively. The result showed that the composite is suitable for various applications in engineering such as car door panels due to its improved mechanical strength while causing a reduction of waste circulation in the environment.

© 2025 MIM Research Group. All rights reserved.

1. Introduction

Research on composites is growing rapidly due to the rising demand for environmentally friendly materials with improved properties Raju *et al.* and Jain *et al.* [1,2]. Traditionally, composites have been produced via the use of carbon or glass fibres (synthetic) for reinforcement in a polymer matrix. Synthetic fibres like glass fibres have good mechanical properties such as increased tensile, flexural, and impact strength but they pose health risks during processing or disposal, introduce pollution into the environment, lack sustainability, and cause an overall increase in production cost Mahir *et al.* [3]. Now, there is an increment in opposition to the use of synthetic fibres due to their negative effects on the ecosystem. Finding alternative methods that are eco-friendly and

*Corresponding author: ogundipe.oluwasogo@lmu.edu.ng
[a]orcid.org/0000-0001-9457-1071; [b]orcid.org/0009-0001-4630-2253; [c]orcid.org/0000-0002-7581-8785; [d]orcid.org/0009-0007-2306-679X; [e]orcid.org/0009-0009-0274-1850; [f]orcid.org/0000-0003-0582-8715; [g]orcid.org/0000-0003-3266-9924; [h]orcid.org/0000-0002-2710-1130
DOI: http://dx.doi.org/10.17515/resm2024.458me0920rs

sustainable for polymeric composites development is therefore necessary. As a result, the emphasis has turned to the use of natural fibres for composite production due to their advantages such as availability, affordability, environmental friendliness Arjmandi *et al*. [4], recyclability, renewability, and biodegradability Bisht & Gope [5].

Natural fibres and fillers are plant and animal base which are mostly agricultural wastes. The plant-based natural fibres including jute, sisal, banana fibre, coir, rice husk, and so on, can be obtained from different parts of the plant. The animal-based natural fibres or fillers include eggshells, feathers, hair (wool), bone, etc. The wastes obtained from plants and animals can be utilized as a reinforcing material for composite production that is light in weight, cost-effective, sustainable Adediran *et al*. [6], nonabrasive, nonhazardous, and biodegradable Alkaron *et al*. [7]. In light of waste usage for composite development, rice husks (RH), eggshells (ES), and banana fibre (BF) are used in an epoxy polymer matrix to improve the epoxy matrix polymer matrix. Rice husk is mostly used as a reinforcing material due to its abrasiveness [8] and stiffness Ogundipe *et al*. [9]. Bisht and Gope investigated the impact of rice husk reinforcement loading on the bio composite's ability to withstand fracture, using epoxy resin filler loadings 10 to 40% by weight. The study revealed an increase in fracture toughness from 1.072 to 2.876 MPa√mm as the filler loading rises from 10 to 20% RH Bisht & Gope [10] which is in support of Premnath & Nivedhitha [11] Studies.

Eggshell as a filler material has been used instead of the commercial $CaCO_3$ fillers because they contain 95% $CaCO_3$. Its use in composite formation improves the properties of the composite [12-14]. Petrasek and Muller investigated the use of eggshell particles as reinforcement in an epoxy matrix with 10, 20, 30, and 40% weight. The properties of the pure epoxy matrix were improved with a 22% increase in the tensile strength at 10% eggshell reinforcement Petrasek & Muller [15]. Banana fibre is used as reinforcement in composite production due to its high tensile strength [16] and good surface adhesion [17] with epoxy resins. Ramesh *et al*. developed a composite using banana fibres as reinforcing material with an epoxy matrix. The composite materials of 50:50 banana fibre and epoxy resin gave better properties of 112.58 MPa tensile, 76.53 MPa flexural, and 9.48 Joules impact energy [18].

According to Sahoo *et al*. [19], composite obtained from reinforced natural fibres such as banana fibre hybrid produces better material properties when subjected to physical (ultraviolent, corona, etc.) [20], chemical (alkalinity, acetylation, etc.) [21] and biological treatments Birniwa *et al*. [22]. Fibre treatment for better properties was affirmed by [23] for it increases the surface roughness of the fibres and promotes adhesion capability with the polymer matrix. Composite materials produced from treated fibres are used by different industries such as the automotive vehicle interiors - front and rear door lining, foot mats, etc. Mohammed *et al*. [24] construction industry such as the manufacture of particle boards and roofing sheets [1] aerospace industry (flaps, aircraft wings, ice protection panels covering the fuselage, etc.).

There are different studies on the utilization of BF and RH Deepan *et al*. [25], BF and ES Ganesan *et al*. [26], RH and ES Lokesh *et al*. [27] for composite development but there are limited studies on the combination of the three reinforcing materials. Eggshell is a good reinforcing material because it causes an increase in the strength of the material due to its higher concentration of calcium carbonates and surface area Ganesan *et al*. [26]. Rice husk is a lightweight material with good refractory properties due to its high silica content [5] while banana fibre has a higher tensile strength which RH and ES are deficient Deepan *et al*. [25]. Epoxy is a thermoset polymer used as a matrix for reinforcement because of its high tensile strength, temperature-resistant capability, and effective wetting of natural fibres for proper adhesion [12,22]. According to [28,29], hybridization of the fibres improves the mechanical properties of the composite compared to the utilization of single fibres, therefore, this study aims to study the mechanical properties of banana fibre, rice husks, and eggshells as reinforcing material for composite production useful for the production of the interior components of an automobile such as door panels and dashboard.

2. Materials and Method

The materials used for this study were; epoxy, hardener, banana fibre, rice husk, and eggshells. They were locally sourced i.e., the rice husk was obtained from a rice mill, eggshells from the

Landmark University Cafeteria, and banana fibre from Opeyemi farm; all in Omu-Aran, Kwara State, Nigeria. The epoxy and hardener of density 1.169 g/cm^3 and 1.0195 g/cm^3 respectively were obtained at Lagos from Tony International Enterprise, Ojota, Lagos.

2.1 Material Properties

The physical properties of rice husk, eggshell, and banana fibre are shown in Table 1, the chemical properties are illustrated in Table 2, and Table 3 shows the mechanical properties of the fibres.

Table 1. Physical properties of rice husk, eggshell, and banana fibre

Fibre/filler	Particle size/ fibre length	Density g/cm^3	Specific surface area (m^2/g)	Porosity (%)
Rice husk	125 μm	1.12	1.45	87
Eggshell	75 μm	2.42	2.61	60
Banana fibre	4 mm	0.91	-	-

Table 2. Chemical properties of rice husk, eggshell, and banana fibre

Fibre/filler	Elemental composition
Rice husk	C (39.02%), O (28.73%), Si (16.23%), Rb (16.02%)
Eggshell	Ca (47.15%), O (34.52%), C (13.14%), Sb (2.52%), I (1.44%), and Mg (1.23%)
Banana fibre	C (37.05%), O (36.60%), Al (12.28%), Ca (7.90%), Si (3.09%), and K (3.08%)

Table 3. Mechanical properties of the fibres

Fibres	Tensile strength (MPa)	Young modulus (GPa)	References
Banana fibre	400 – 650	25 - 36	[30]
Rice husk	25 to 75	2.5 to 3.7	[31]

2.2 Material Preparation

2.2.1 Rice Husk Preparation

The rice husks obtained from the rice mill were washed with distilled water to remove impurities and contaminants and then dried in the sun for 3 days. The rice husk sample was thereafter ball-milled to obtain smaller rice husk particles. The screened rice husk particles of 125 µm particle size [32] were used. The rice husks were oven-dried at 40 – 60°C for a full day to get rid of the inherent moisture content [33]. After that, the dried fibres were treated with 5% NaOH for 4 hours to remove the foreign matter that can prevent the effective combination of the fibres in the epoxy polymer matrix [20]. Then, the fibres were washed to remove the alkalinity solution and dried at 60°C for 10 hours to obtain moisture-free fibres. Figures 1 (a), and (b) show the obtained rice husks and the treated milled rice husks.

2.2.2 Banana Fibre Extraction and Preparation

Banana fibre was extracted from the pseudo-stem of banana trees through water and mechanical retting. The stem was cut and separated into strips. The banana strips were then soaked in water for 6 hours to reduce the lignin content, soften it and make the fibre extraction easy. The strips were removed from the water after 6 hours and placed on a smooth, clean, and hard surface for the fibre extraction using a knife. A knife was used to remove the gum, wax, and remaining lignin contents to obtain the banana fibre content [34]. The banana fibres obtained were cut into 40 mm lengths with scissors [35] oven-dried at 40 – 60°C for a full day to get rid of the inherent moisture content [33]. The dried banana fibres were then treated with 5% NaOH to remove impurities and non-cellulosic material that can hinder the adhesion of the fibres with the polymer matrix [20]. Then, the fibres were washed to remove the alkalinity solution and dried at 60°C for 10 hours to

obtain moisture-free fibres. Figures 1 (c), (d), (e), and (f) show the banana stem, stripped banana stem, extracted banana fibre, and chopped treated banana fibre respectively.



Fig.1. (a) rice husk, (b) milled treated rice husk (c) banana stem, (d) stripped banana stem, (e) extracted BF, and (f) chopped treated BF

2.2.3 Eggshell Preparation

The eggshell waste was soaked in water for 24 hours and washed severally to remove the organic residue and membrane secretion [36]. The washed eggshells were sun-dried for three days and then ball-milled to obtain eggshell powder. The eggshell powder was collected and stored in an air-tight container. Figures 2 (a) and (b) show the dried chicken eggshell and the milled eggshells.



(a) (b)

Fig. 2. (a) dried chicken eggshells and (b) milled chicken eggshell

2.3 Method

The polymer composite was developed using an open mould hand lay-up method and the experiment was carried out under laboratory room temperature (20 – 25℃) and 40 - 60% humidity. The epoxy resin was mixed with the hardener in a ratio of 2:1 to obtain the matrix. The eggshell (ES), rice husk (RH), and banana fibre (BF) at different proportions as shown in Table 4 were then mixed for each test to form a homogenous mixture. The selection of the materials with fibre contents was based on previous research. Thereafter, the mould was placed properly on a polythene bag and taped with a cellotape to enable the stability of the various moulds. A petroleum gel was used as a lubricant to lubricate the mould before pouring the mixture inside the mould. The uniform mixtures were poured into tensile, flexural, and impact moulds as shown in Figure 3 (a), (b), and (c) respectively. The polymer matrix was cured at room temperature for a full day before its removal from the mould [37] as illustrated in Figure 3 (d), (e), and (f) respectively. The cured samples were subjected to tensile, flexural, and impact tests, and the fractured samples are shown in Figure 5 (a), (b), and (c).

Table 4. Composite composition

Samples	Sample designation	BF (%)	ES (%)	RH (%)	EPOXY (%)
A	$BF_5ES_{20}RH_{20}$	5	20	20	55
B	$BF_{10}ES_{15}RH_{20}$	10	15	20	55
C	$BF_{15}ES_{10}RH_{20}$	15	10	20	55
D	$BF_{20}ES_5RH_{20}$	20	5	20	55
Control	$BF_0ES_0RH_0$	0	0	0	100

ES: Eggshell, RH: Rice husk, BF: Banana fibre



(a) (b) (c)



(d) (e) (f)

Fig. 3. (a) tensile mould, (b) flexural mould, (c) impact mould, (d) cured tensile samples, (e) cured flexural sample, and (f) cured impact samples

The epoxy polymer composite without reinforcement was produced as a control. The epoxy polymer matrix was then reinforced with the various fibres at different mixing ratios as shown in Table 4, and then compared with the Control. The different material composition was used to obtain an improved epoxy natural fibre-reinforced composite [38].

2.4 Mechanical Test on Composite Samples

2.4.1 Tensile Test

The composite material sample was produced according to Tensile (ASTM D3039-17) standards [17,39] with a gauge length of 55 mm, width of 14 mm, and thickness of 3 mm as shown in Figure 3 (a). The tensile strength was done using an Instron-3369 Universal Testing Machine (UTM) as shown in Figure 4, with 50 kN applied load at 5 mm/min crosshead speed. The test was done in triplicates and the average was reported. Figure 3 (a) and (d) refer to the ASTM standard mould for the production of the composites for tensile test and cured composite respectively. The tensile fractured sample is shown in Figure 5 (a)

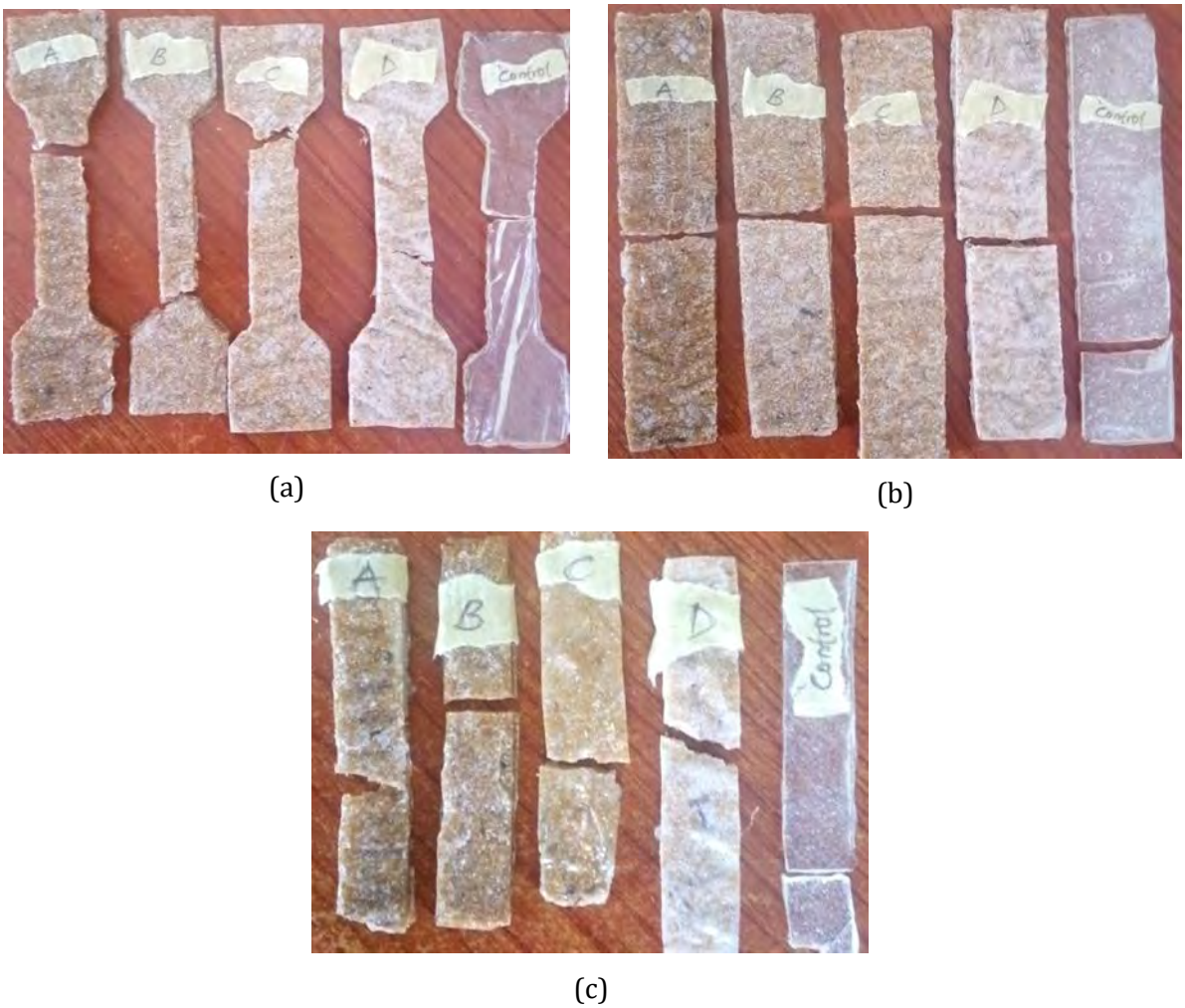


Fig. 4. Universal testing machine (Instron-3369)

2.4.2 Flexural Test

The material's ability to bear bending applied forces that are perpendicular to the object's longitudinal axis is referred to as its flexural strength. A 3-point flexural bending test was conducted for the flexural samples using ASTM D790-17 standards [40] with dimensions 127 mm × 24 mm × 3 mm as shown in Figure 3 (b). The crosshead position was used to calculate the specimen deflection. The Universal Testing Machine utilized, has a consistent rate of crosshead

motion throughout the entire range and the load measurement systems error wasn't greater than 1% of the maximum load that was anticipated. The test was done in triplicates and the average value for the flexural strength and displacement were reported. Figure 3 (b) and (e) show the flexural mould and the cured composite. The flexural fractured samples are shown in Figure 5 (b).



(a) (b)

(c)

Fig. 5. (a) fractured tensile samples, (b) fractured flexural samples, and (c) fractured impact samples

2.4.3 Impact Test

The impact test was carried out according to impact (ASTM D256-23e1) standards with the application of an impact testing machine. The samples were prepared with mould size 65 x 12 x 3 mm as shown in Figure 3 (c) and the cured samples as shown in Figure 3 (f). A V-groove was cut on the longer side of the sample at a depth of 2.5 mm and a distance of 31.73 mm to initiate cracks as the load was applied on the sample that was horizontally placed on the impact testing machine support. The V-notch sample faced outward and aligned to ensure a hammer struck the sample's center. The hammer was released, causing the sample to fracture. The impact strength for each composite sample was carried out and an average energy absorbed result for the samples was recorded after the conduction of three (3) measurements [11]. The fractured sample is shown in Figure 5(c).

2.4.4 Morphological Examination of Composite Sample

The morphological test investigation revealed the interfacial interaction of banana fibres, rice husks, eggshells, and epoxy resin. The unfractured and fractured samples were examined using a scanning electron microscope (SEM). The samples were layered with a small coating of gold to

allow sample conductivity with minimum electrostatic charges. The photographs of the samples were taken to understand the morphological properties of the polymer composite.

3. Results and Discussion

The mechanical properties of the produced epoxy polymer composite obtained from reinforced rice husks, banana fibre, and eggshells were evaluated and the average value of each test was used.

3.1 Tensile Test Result of Produced Samples

3.1.1 Load and Displacement of Tensile Samples

Figure 6 shows the graph of tensile load versus displacement. There was an increase in displacement of all the samples from their original position when the load was continuously applied. A continuous increase was observed from the origin until a point when the load was constant but with increased displacement; the samples exhibited behaviour that is associated with Hooke's law. Sample C shows a higher load-bearing capacity compared to Sample A, B, D, and control because it was able to withstand much deformation of 895 N load before it fractures. The slope is the steepest; indicating that it can bear more load before it fails.

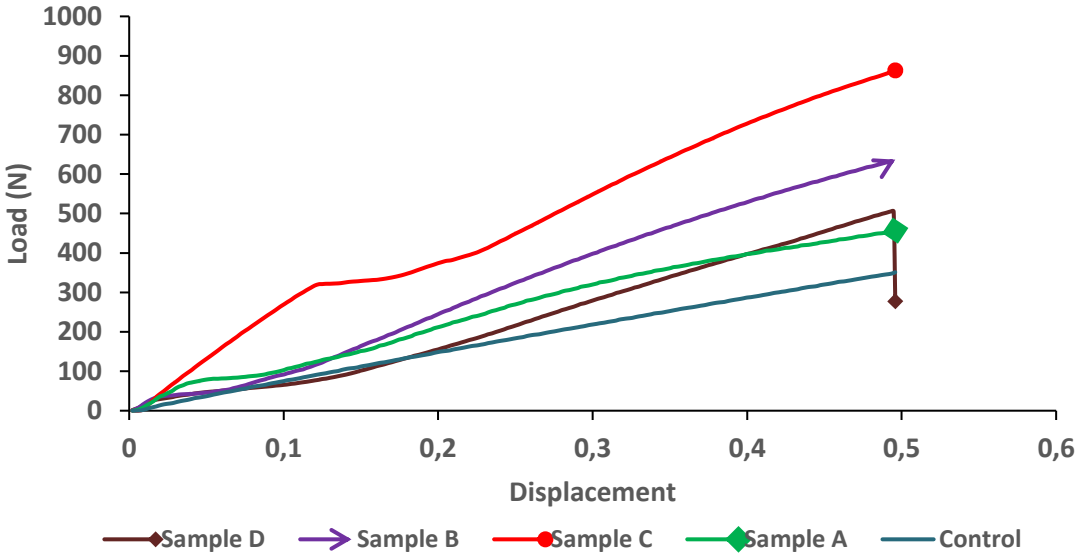


Fig. 6. Load vs displacement graph of tensile samples

An increase in the displacement of all the samples from their original position when the load was continuously applied was due to the strengthening of the matrix by the increase in the BF content. The reinforcing material in sample C was evenly dispersed in the epoxy matrix with better wettability as shown in Figure 13 (c) which leads to good interfacial bonding of the fibres with the matrix. A composite with good interfacial bonding will support more loads before it fractures [38]. As the banana fibre increased by more than 15%, agglomeration occurred, causing a reduction in the interfacial bonding in Sample D; making the material fail with the application of lesser loads compared to Sample C. Figure 6 shows that reinforcement of the epoxy matrix improves the properties of the composite; Sample C is better than the control sample which agrees with the studies of Oladele *et al*. and Amir *et al*. [37,40].

3.1.2 Tensile Strength

The tensile strength result according to Figure 7, shows that the epoxy polymer matrix, Control was improved when compared with the reinforced composites. Sample C of 15% BF, 20% RH, and 10% ES composition has the highest tensile strength with a 6.3% increase as compared with the pure matrix. The tensile strength of the composite increases with an increase in the banana fibre content from 5 to 15% and begins to decline after 15% banana fibre in the composite. The decline in the tensile after the 15% increment in banana fibre was due to the agglomeration of the fibres in the

matrix. The interfacial bonding between the fibre and the matrix worsens with an increase in BF after 15% fibre loading. Also, irregularly shaped fibres decrease the strength of the composites due to the inability of the filler to enhance the stress transferred from the polymer matrix [5]. As the eggshell powder content begins to reduce with an increased banana fibre, the tensile strength increases. The findings from the current studies agree with previous studies by Panchal *et al.* and Fan [41,42]. The result shows that there is a limit at which better tensile strength can be obtained when hybridized with rice husks and eggshells are used as filler in polymer composite production. Therefore, with every increase in the BF% wt., there was an increase in the tensile strength according to [43]. The maximum tensile strength obtained from the hybridized sample is greater than the singular RH-reinforced composite as reported by [44].

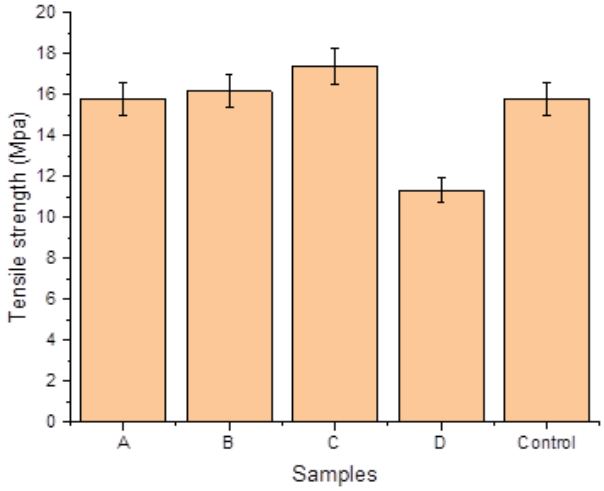


Fig. 7. Tensile strength of BF/RH/ES reinforced polymer matrix composite

3.1.3 Tensile Modulus

Figure 8 shows the tensile modulus of different samples; A, B, C, D, and Control. The tensile modulus signifies material stiffness which indicates how much such material can deform under stress application.

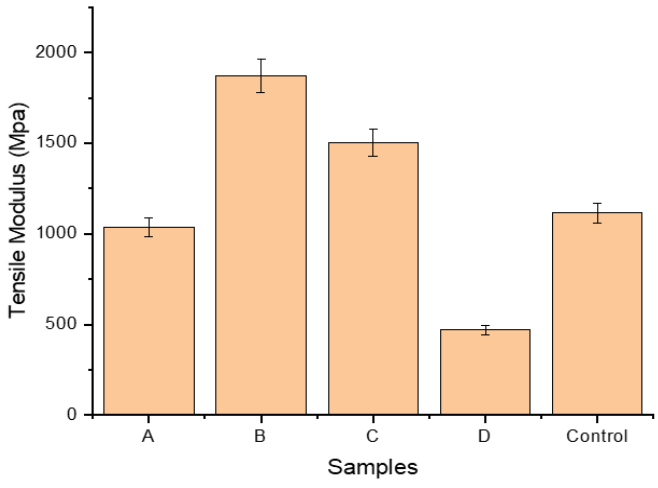


Fig. 8. Tensile modulus of BF/RH/ES reinforced polymer matrix composite

Sample B has the highest tensile modulus; making it the stiffest composite sample among all the samples. It is 40.45% better than the pure epoxy polymer matrix. Sample D is the least stiff composite due to its lower tensile modulus value. The tensile modulus of the composite increased from 5 to 10% Banana fibre and began to decrease after 10% BF as shown in Figure 8 due to agglomeration of the fibres which is in line with the findings reported by [17]. The behavior of increase in tensile modulus in Sample B was because of the fibre content increase without void

formation which leads to the transfer of more load from the matrix to the filler. The decreases in the interfacial bonding due to the agglomeration of the fibre lead to poor adhesion between the filler and matrix which causes slippage and a decrease in the stiffness of the composite as observed in Sample D [5]. The tensile modulus of the composite developed from the hybrid reinforced BF/RH/ES yields better results than a single reinforced composite as reported by Bisht and Gope [5].

3.2. Flexural Test Result of Produced Samples

3.2.1 Load and Displacement of Flexural Samples

Figure 9 shows the load and displacement of the flexural samples. For every increase in load, there was an increase in displacement. Sample C exhibited higher displacement at a higher load compared with other samples. It was able to withstand 37 N of load before it fractured. The control sample was unable to withstand more than 12 N of load before it failed. Sample A has the lowest displacement when subjected to a load of 5.2 N. The control sample was able to withstand 11.5 N before it began to deform. However, it fails faster compared with the reinforced Sample C composite. This suggests that reinforcing the epoxy polymer matrix increases the flexural properties of the composite as shown in Thiagamani *et al.* study [45].

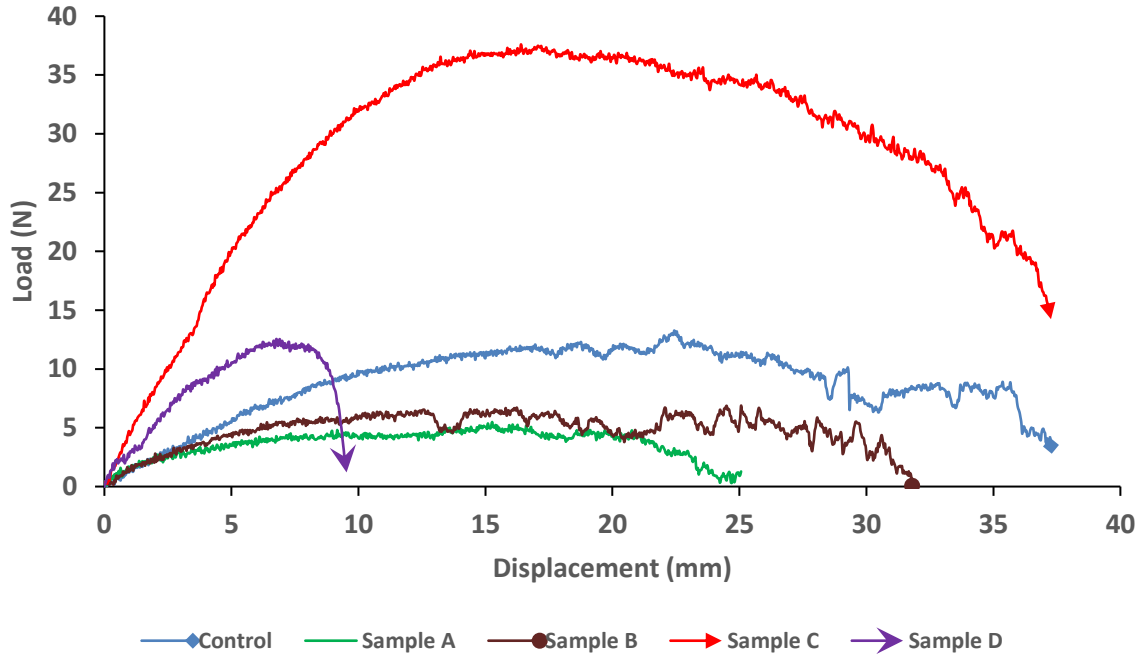


Fig. 9. Load vs displacement of flexural samples

3.2.2 Flexural Strength

Figure 10 shows different composite sample compositions for flexural strength and sample C has the highest value. There was an increase in the flexural strength with an increase in BF content from 5 to 15%. The ES content influenced the flexural strength of the composite. As the ES decreases with a simultaneous increase in the BF, the flexural strength increases until 10% ES and 15% BF when the maximum tensile strength was obtained for the produced samples. A decrease in the flexural strength was observed when the BF content increased by more than 15% in the composition. The maximum flexural strength of the reinforced composite is 64.7% better than the Control (pure polymer matrix composite). Reinforcing the epoxy polymer matrix with BF, RH, and ES significantly improves the flexural strength which conforms to the findings reported by [40].

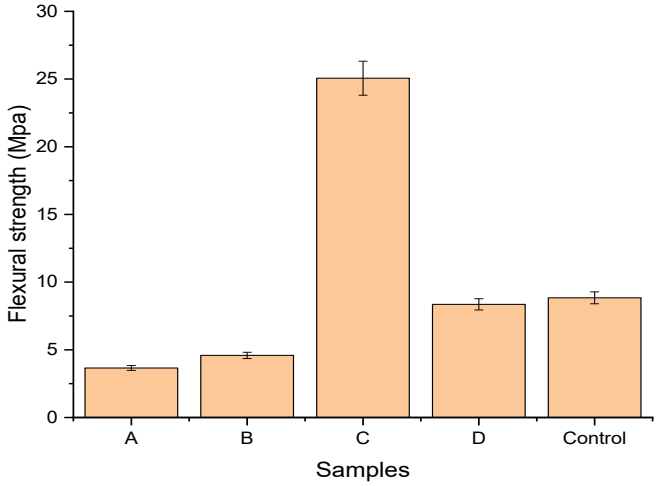


Fig. 10. Flexural strength of BF/RH/ES reinforced polymer matrix composite

3.2.3 Flexural Modulus of Produced Samples

Figure 11 shows the flexural modulus of different composite samples; A, B, C, D, and Control. The flexural modulus describes the ability of materials to resist deformation under load when subjected to bending. This property helps to understand structural applications of materials where flexure and bending are of concern e.g. panels and different structural components.

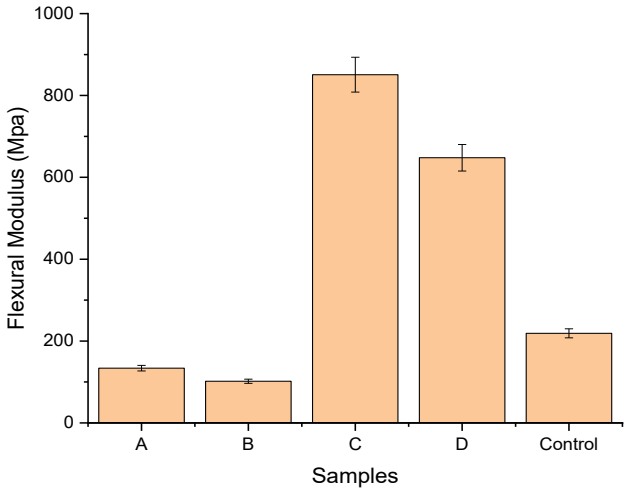


Fig. 11. Flexural modulus of BF/RH/ES reinforced polymer matrix composite

Sample C has the highest flexural modulus compared to other samples with the lowest error bar which indicates reliability and consistency of the result. The high flexural strength value of Sample C indicates high resistance to bending forces, thus, making it excellent for applications that require significant stiffness and rigidity. The high flexural modulus of Sample C was attributed to the presence of BF/RH/ES used as reinforcement that enhances the composite stiffness. The lower flexural modulus in Sample A and B is due to material composition difference, and degree of cross-linking in the polymer matrix [41].

3.3 Impact Strength of the Produced Samples

Impact testing investigates the resilience of the material and its capacity to absorb during a high-velocity impact. The outcome from this evaluation indicates the impact strength of the epoxy matrix composite samples. Figure 12 shows different samples of the composite made from different combinations. It was observed that the impact value increases with the % w.t of the reinforcement addition. Sample C has the best impact value compared to the control due to the increase in the %

wt. of the reinforcement. Progressively from 5% BF, the impact strength increases to 15% BF and begins to decline after the 15% BF, the study agrees with Amir *et al*. [40].

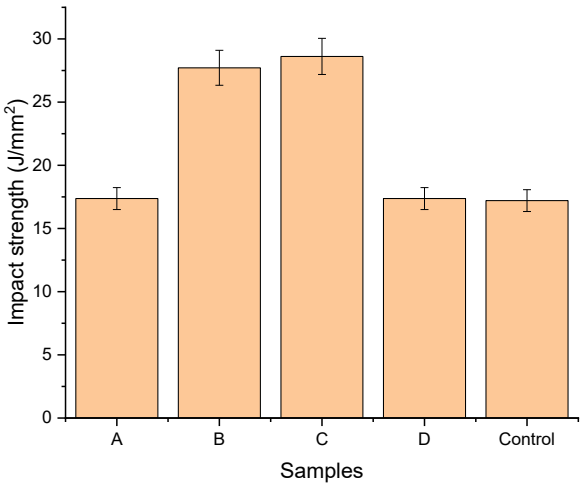
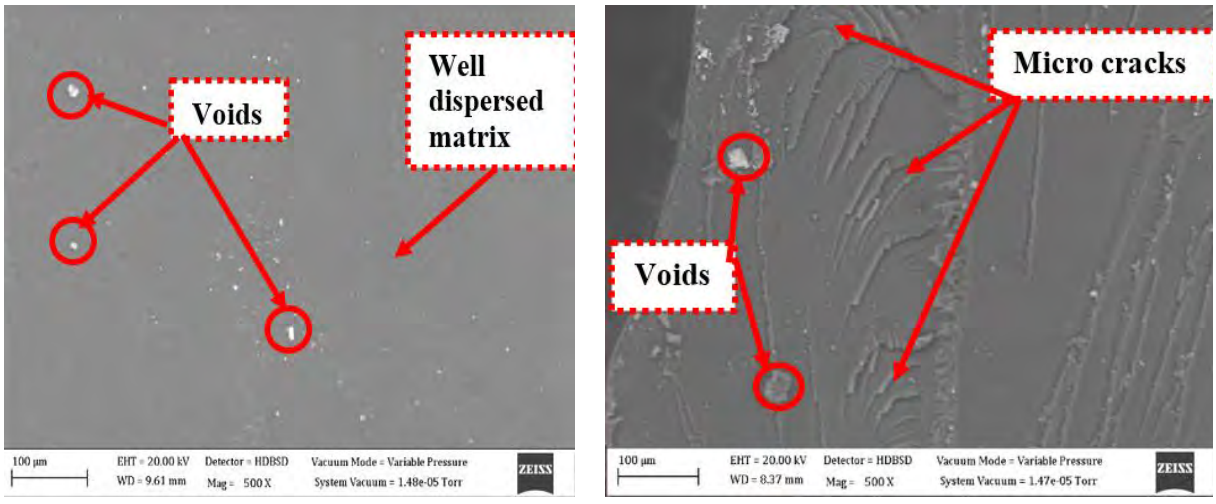


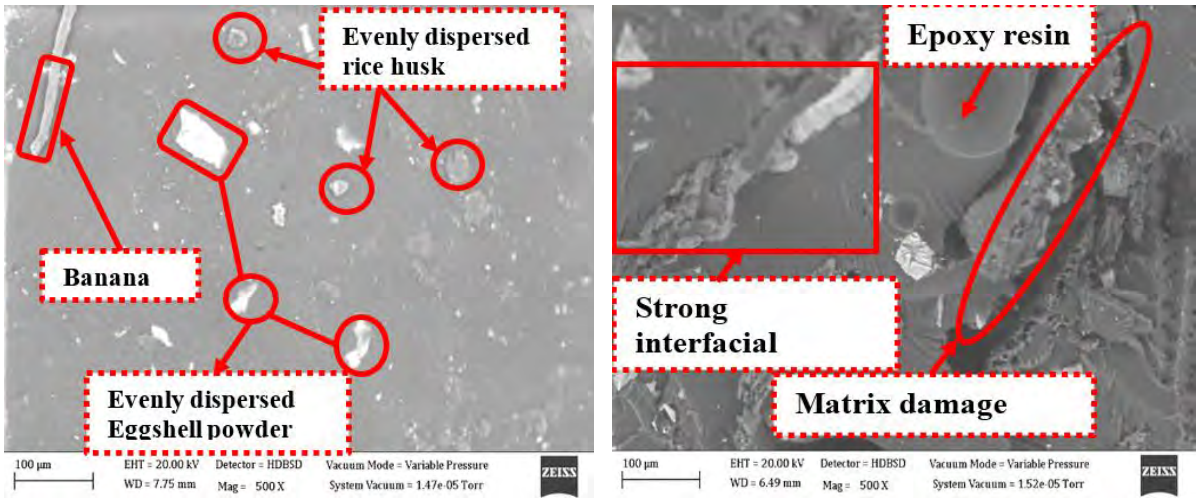
Fig.12: Impact strength of BF/RH/ES reinforced polymer matrix composite

3.4. Morphological Examination of Unfractured and Fractured Samples

Figure 13 shows the Scanning Electron Morphology (SEM) for the control and the best sample of the produced composite. Figure 13 (a) and (b) show a uniformly dispersed epoxy matrix and fractured surface of the control sample. The voids promote the micro cracking as shown in Fig. 13 (b). Figure 13 (c) shows that the rice husk and the banana fibre were evenly dispersed. There is no agglomeration of the fibre that reduces its mechanical strength which is why it was the best composite sample produced. Figure 13 (d) shows the fractured sample in which the eggshell, rice husk, and banana fibre were evenly distributed. The treatment of the fibre causes surface roughness of the fibre to promote strong interfacial bonding. A better distribution of fibres or filler in the matrix aids interfacial bonding that causes an increase in the mechanical properties of the composite Oladele *et al*. [37].



(a) (b)



(c) (d)

Fig.13. (a) SEM image of the Control sample before fracture, (b) fractured surface of the Control sample, (c) Sem image of Sample C before fracture, and (d) Sample C fractured surface

4. Comparison of Previous Studies with the Current Studies

Table 5. Mechanical properties comparative table of previous studies and the current studies on the utilization of Rice husk, Eggshell, and Banana fibre as reinforcement for composite development

Ref.	Natural fibre types	Fibre/ filler ratio	Proportion of best sample	Matrix type	Method of production	Tensile strength (MPa)	Flexural Strength (MPa)	Impact strength (J/mm^2)
[46]	BF	10, 20, 30, 40, 50	30	Epoxy	Hand lay-up	65.6	38.1	2.8
[47]	BF	0, 5, 10, 15, 20	20	Polyester	Vacuum moulding	15.40	31.67	6.87
[48]	BF	5, 10, 15, 20	15	Polyester	Hand lay-up	19.9	66.8	6.08
[49]	ES	20, 40, 50, 70, 80	20	Polyester	Hand lay-up	22.20	52.97	0.4152
[50]	ES	0.5, 5, 10	10	Epoxy		22.80	-	-
[51]	RH	2.5, 5, 7.5, 10, 12.5 & 15	5	Epoxy	Hand lay up	16.67	28.21	4.91
[52]	RH	10, 15, 20	10	Epoxy	Solution casting	66.5	-	-
[53]	BF & ES	20:2.5, 25:2.5, 30:2.5	25:2.5	Epoxy	Compression moulding	31.21	33.69	2.84
Current Studies	BF, ES, & RH	45	15:10:20	Epoxy	Hand lay-up	17.42	25.06	28.61

It is evident from Table 5, that single reinforcement of fibres does not possess the required mechanical properties needed for automobile applications such as the door panel, bumper, or dashboard where materials that absorb more energy before failure are needed. Developing composite material with higher impact strength without compromising the flexural and tensile properties is very key in automobile applications. Although the tensile and flexural strength of the previous studies with the use of RH, ES, and BF as reinforcement is greater than the current studies, their impact strength is very low. The tensile and flexural strength of the current study is within the acceptable standards for automobile applications. Therefore, more study is needed for the formation of composite with higher impact, flexural, and tensile strength in the automobile industry to reduce the rate of automobile parts destruction during a collision.

5. Conclusion

The mechanical properties of a hybridized BF, RH, and ES as reinforcement in an epoxy polymer matrix were studied. The cured samples were subjected to mechanical tests and the findings promote the composite usage for automotive and construction applications. The outcome of the results for the study are as follows:

- The hybridization of the BF, ES, and RH affects the flexural strength of the composite. There was an increase in flexural strength as the banana fibre increased until it reached 15% and decreased after 15% BF. The maximum flexural strength for the sample was 25.06 MPa which is 64.7% better than the pure matrix. The flexural strength of the reinforced samples increased due to the increase in BF in the composite.
- The tensile strength of the pure epoxy matrix was enhanced by 9.3%. The highest tensile strength among all the samples was Sample C which indicates the best composite that is resistance to the tensile forces. This suggests that the material composition 15:10:20 of BF, ES, and RH respectively is the most suitable composite for applications of high tensile strength. An increase in the BF was proportional to the tensile strength increase. The increase in fibre content in the matrix results in agglomeration which leads to the propagation of cracks in the composite and in-turns causes matrix damage. The strong interfacial bonding causes an increase in the tensile strength. The maximum tensile strength for the composite samples was 17.42 MPa which is better than the pure epoxy polymer matrix.
- The impact properties of the composite samples increased with an increase in BF. It ranged from 14.98 to 28.61 J/mm^2. Sample C showed a very impressive impact response which was 39.84% better than the pure epoxy matrix. This means the composite has the best impact value compared to the control and can be used where resistance to fracture and high energy absorption is essential. In comparison with the previous studies, as illustrated in Table 5, the present study has a better impact strength which is a significant property for an automobile application (door panel, dashboard, and bumper). It helps to minimize losses, especially during collisions or accidents.
- The produced samples can be grouped according to the area of application using the mechanical test results. Sample A & B will be good at making boat parts, Sample C will have good applications in automobile and construction industries such as door panel lining, bumper, and so on due to its high impact strength and Sample D will be good at making the helmet dues to high impact response and flexural strength.

6. Recommendations

Elaborate studies are needed to be carried out on BF/RH/ES hybrid composite and different properties to be investigated such as tribological, flame-retardant, durability tests, etc as the properties would be relevant for automotive and construction applications. Different methods of production of polymer composite such as injection moulding, etc. should also be encouraged. In addition, different agricultural wastes should be hybridized to obtain better mechanical material properties to reduce environmental pollution. Also, an analytical study for fibre contribution with an analytical model to quantify the effect of each fibre on the composite is recommended for further studies.

Acknowledgment

The authors acknowledged Landmark University, Omu-Aran for the provision of an enabling environment for this research work and the technologist in charge of the laboratory used; Engr. Joan Akintunde for her support during the experimental work.

References

[1] Raju GU, Kumarappa S, Gaitonde VN. Mechanical and physical characterization of agricultural waste reinforced polymer composites. J Mater Environ Sci. 2012;3(5):907-16.
[2] Jain N, Somvanshi KS, Gope PC, Singh VK. Mechanical characterization and machining performance evaluation of rice husk/epoxy: an agricultural waste-based composite material. J Mech Behav Mater. 2019;28(1):29-38. https://doi.org/10.1515/jmbm-2019-0005
[3] Mahir FI, Keya KN, Sarker B, Nahiun KM, Khan RA. A brief review on the natural fibre used as a replacement of synthetic fibre in polymer composites. Mater Eng Res. 2019;1(2):88-99. https://doi.org/10.25082/MER.2019.02.007
[4] Arjmandi R, Hassan A, Majeed K, Zakaria Z. Rice husk filled polymer composites. Int J Polym Sci. 2015;2015:1-10. https://doi.org/10.1155/2015/501471
[5] Bisht N, Gope C. Mechanical properties of rice husk flour reinforced epoxy bio-composite. J Eng Res Appl. 2015;5(5):66-71.
[6] Adediran AA, Akinwande AA, Balogun OA, Olasoju OS, Adesina OS. Experimental evaluation of bamboo fibre/particulate coconut shell hybrid PVC composite. Sci Rep. 2021;11(1):5465. https://doi.org/10.1038/s41598-021-85038-3
[7] Alkaron WA, Hamad SF, Sabri MM. Studying the fabrication and characterization of polymer composites reinforced with waste eggshell powder. Adv Polym Technol. 2023;2023:1-11. https://doi.org/10.1155/2023/7640478
[8] Bisht N, Gope PC. Effect of alkali treatment on mechanical properties of rice husk flour reinforced epoxy bio-composite. Mater Today Proc. 2018;5(1):14089-96. https://doi.org/10.1016/j.matpr.2018.10.228
[9] Ogundipe O, Adetunla A, Igbinosa O, Ikumapayi O. A cost-effective ceramic filter for water purification in developing nations. In: 2023 International Conference on Science, Engineering and Business for Sustainable Development Goals (SEB-SDG); 2023 Apr 1-5; IEEE. p. 1-5. https://doi.org/10.1109/SEB-SDG57117.2023.10124576
[10] Bisht N, Gope PC. Effect of rice husk (treated/untreated) and rice husk ash on fracture toughness of epoxy bio-composite. J Mech Behav Mater. 2020;29(1):177-85. https://doi.org/10.1515/jmbm-2020-0018
[11] Premnath AA, Nivedhitha R. Effect of rice husk filler on hardness and impact strength of basalt fibre epoxy polymer composite. Mater Its Charact. 2022;1(2):90-5. https://doi.org/10.46632/mc/1/2/4
[12] Shah AH, Zhang Y, Xu X, Dayo AQ, Li X, Wang S, et al. Reinforcement of stearic acid treated eggshell particles in epoxy thermosets: structural, thermal, and mechanical characterization. Materials. 2018;11(10):1-15. https://doi.org/10.3390/ma11101872
[13] Mohan TP, Kanny K. Thermal, mechanical, and physical properties of nano eggshell particle-filled epoxy nanocomposites. J Compos Mater. 2018;52(29):3989-4000. https://doi.org/10.1177/0021998318773445
[14] Ogundipe OL, Adediran AA, Ikubanni PP, Adekanye TA, Ajisegiri ES, Ikumapayi OM, et al. Influence of eggshell addition on the properties of natural fibre-reinforced epoxy composite-a mini-review. In: 2024 International Conference on Science, Engineering and Business for Driving Sustainable Development Goals (SEB4SDG); 2024 Apr 1-7; IEEE. p. 1-7. https://doi.org/10.1109/SEB4SDG60871.2024.10629942
[15] Petrasek S, Muller M. Polymeric particle composites based on filler from hen eggshells. Eng Rural Dev. 2017;16:175-80. https://doi.org/10.22616/ERDev2017.16.N034
[16] Sapuan SM, Leenie A, Harimi M, Beng YK. Mechanical properties of woven banana fibre reinforced epoxy composites. Mater Des. 2006;27(8):689-93. https://doi.org/10.1016/j.matdes.2004.12.016
[17] Srinivasan T, Suresh G, Santhoshpriya K, Chidambaram CT, Vijayakumar KR, Munaf AA. Experimental analysis on mechanical properties of banana fibre/epoxy (particulate) reinforced composite. Mater Today Proc. 2021;45:1285-9. https://doi.org/10.1016/j.matpr.2020.05.103
[18] Ramesh M, Sri Ananda Atreya T, Aswin US, Eashwar H, Deepa C. Processing and mechanical property evaluation of banana fibre reinforced polymer composites. Procedia Eng. 2014;97:563-72. https://doi.org/10.1016/j.proeng.2014.12.284
[19] Sahoo M, Gopinathan R, Kumar KP, Rani JJA, Pradhan R, Parida L. Study on the influence of stacking pattern on mechanical behaviour of banana/snake grass fibres hybrid epoxy composite. Mater Today Proc. 2022;2022:1-8. https://doi.org/10.1016/j.matpr.2022.08.185

[20] Ho MP, Wang H, Lee JH, Ho CK, Lau KT, Leng J, et al. Critical factors on manufacturing processes of natural fibre composites. Compos B Eng. 2012;43(8):3549-62. https://doi.org/10.1016/j.compositesb.2011.10.001
[21] Ravi M, Dubey RR, Shome A, Guha S, Anil Kumar C. Effect of surface treatment on natural fibres composite. IOP Conf Ser Mater Sci Eng. 2018;376(1):1-8. https://doi.org/10.1088/1757-899X/376/1/012053
[22] Birniwa AH, Abdullahi SS, Ali M, Mohammad REA, Jagaba AH, Amran M, et al. Recent trends in treatment and fabrication of plant-based fibre-reinforced epoxy composite: a review. J Compos Sci. 2023;7(3):1-20. https://doi.org/10.3390/jcs7030120
[23] Samanth M, Subrahmanya Bhat K. Conventional and unconventional chemical treatment methods of natural fibres for sustainable biocomposites. In Sustainable Chemistry for Climate Action. 2023; 3. https://doi.org/10.1016/j.scca.2023.100034
[24] Mohammed L, Ansari MNM, Pua G, Jawaid M, Islam MS. A review on natural fibre reinforced polymer composite and its applications. Int J Polym Sci. 2015;2015:1-15. https://doi.org/10.1155/2015/243947
[25] Deepan S, Jeyakumar R, Mohankumar V, Manojkumar A. Influence of rice husk fillers on mechanical properties of banana/epoxy natural fibre hybrid composites. Mater Today Proc. 2023;74:575-80. https://doi.org/10.1016/j.matpr.2022.09.459
[26] Ganesan V, Chohan JS, Subburaj GS, Panneerselvam H, Nagabhushanam KY, Venkatesan MK, et al. Experimental analysis of mechanical properties of banana fibre/eggshell powder-reinforced hybrid epoxy composite. Eng Proc. 2024;61(1):18. https://doi.org/10.3390/engproc2024061018
[27] Lokesh KS, Kumar KS, Keerthan N, Revanth R, Sandeep S, Lakkundi SB, et al. Experimental analysis of the rice husk and eggshell powder-based natural fibre composite. J Inst Eng India Ser D. 2023;1-8. https://doi.org/10.1007/s40033-023-00557-9
[28] Dashtizadeh Z, Abdan K, Jawaid M, Khan MA, Behmanesh M, Dashtizadeh M, et al. Mechanical and thermal properties of natural fibre based hybrid composites: a review. Pertanika J Sci Technol. 2017;25(4):1-10.
[29] Ahmed A, Hameed AM, Abdullaha SA. Improve mechanical properties of epoxy composite material by enhancing it with natural fibres hybridization. AIP Conf Proc. 2024;3002(1):1-8. https://doi.org/10.1063/5.0208085
[30] Akubueze EU, Nwaeche FC, Muniru OS, Ezeanyanaso CS, Nwaze IO, Nwauzor GO, et al. Hybrid thermosetting composite of kenaf/banana fibres for utilisation in a passenger car bumper. J Mater Sci Res Rev. 2019;2(4):474-9.
[31] Kengkhetkit N, Wongpreedee T. Physical and mechanical properties of natural rubber composites filled with rice husk and rice straw. Creat Sci. 2021;13(3):86-95.
[32] Nandiyanto ABD, Fatimah S, Ragadhita R, Husaeni DN. Particle size and pore size of rice husk ash on the resin-based brake pads performance: experiments and bibliometric literature review. J Eng Sci Technol. 2022;17(6):4065-81.
[33] Prakash KB, Fageehi YA, Saminathan R, Manoj Kumar P, Saravanakumar S, Subbiah R, et al. Influence of fibre volume and fibre length on thermal and flexural properties of a hybrid natural polymer composite prepared with banana stem, pineapple leaf, and S-glass. Adv Mater Sci Eng. 2021;2021:6329400. https://doi.org/10.1155/2021/6329400
[34] Ernest EM, Peter AC. Application of selected chemical modification agents on banana fibre for enhanced composite production. Cleaner Mater. 2022;5:100131. https://doi.org/10.1016/j.clema.2022.100131
[35] Alam SS, Munshi MR, Shufian A, Haque MM, Haque MR, Hasan M, et al. Influence of alkalisation and eggshell particles on mechanical, thermal, and physical properties of rattan-bamboo fibre reinforced hybrid polyester laminated composite. Adv Mater Process Technol. 2024;10(2):329-48. https://doi.org/10.1080/2374068X.2022.2157079
[36] Skórczewska K, Lewandowski K, Szewczykowski P, Wilczewski S, Szulc J, Stopa P, et al. Waste eggshells as a natural filler for the poly(vinyl chloride) composites. Polymers. 2022;14(20):1-20. https://doi.org/10.3390/polym14204372
[37] Oladele IO, Makinde-Isola BA, Adediran AA, Oladejo MO, Owa AF, Olayanju TMA. Mechanical and wear behaviour of pulverised poultry eggshell/sisal fibre hybrid reinforced epoxy composites. Mater Res Express. 2020;7(4):1-10. https://doi.org/10.1088/2053-1591/ab8585
[38] Daramola OO, Akinwande AA, Adediran AA, Balogun OA, Olajide JL, Adedoyin KJ, et al. Optimization of the mechanical properties of polyester/coconut shell ash (CSA) composite for lightweight engineering applications. Sci Rep. 2023;13(1):1066. https://doi.org/10.1038/s41598-022-26632-x
[39] Adediran AA, Akinwande AA, Balogun OA, Bello OS, Akinbowale MK, Adesina OS, et al. Mechanical and optimization studies of polypropylene hybrid biocomposites. Sci Rep. 2022;12(1):2468. https://doi.org/10.1038/s41598-022-06304-6

[40] Amir N, Abidin KAZ, Shiri FBM. Effects of fibre configuration on mechanical properties of banana fibre/PP/MAPP natural fibre reinforced polymer composite. Procedia Eng. 2017;184:573-80. https://doi.org/10.1016/j.proeng.2017.04.140
[41] Panchal M, Raghavendra G, Reddy AR, Omprakash M, Ojha S. Experimental investigation of mechanical and erosion behavior of eggshell nanoparticulate epoxy biocomposite. Polym Polym Compos. 2021;29(7):897-908. https://doi.org/10.1177/0967391120943454
[42] Fan Y. Study on preparation and application of banana fibre-based composites. J Phys Conf Ser. 2023;2539(1):1-10. https://doi.org/10.1088/1742-6596/2539/1/012093
[43] Patel BY, Patel HK. Retting of banana pseudostem fibre using Bacillus strains to get excellent mechanical properties as biomaterial in textile & fibre industry. Heliyon. 2022;8(9):e09902. https://doi.org/10.1016/j.heliyon.2022.e10652
[44] Olaitan AJ, Terhemen A, King G, Oluwatoyin O. Comparative assessment of mechanical properties of groundnut shell and rice husk reinforced epoxy composites. Am J Mech Eng. 2017;5(3):76-86.
[45] Thiagamani SMK, Pulikkalparambil H, Siengchin S, Ilyas RA, Krishnasamy S, Muthukumar C, et al. Mechanical, absorption, and swelling properties of jute/kenaf/banana reinforced epoxy hybrid composites: influence of various stacking sequences. Polym Compos. 2022;43(11):8297-307. https://doi.org/10.1002/pc.26999
[46] Gairola SP, Tyagi YK, Gangil B, Sharma A. Fabrication and mechanical property evaluation of non-woven banana fibre epoxy-based polymer composite. Mater Today Proc. 2021;44:3990-6. https://doi.org/10.1016/j.matpr.2020.10.103
[47] Ernest EM, Peter AC. Application of selected chemical modification agents on banana fibre for enhanced composite production. Cleaner Mater. 2022;5:100131. https://doi.org/10.1016/j.clema.2022.100131
[48] Ezeh EM, Onukwuli OD. Physicochemical characterization of cow horn ash and its effect as filler material on the mechanical property of polyester-banana fibre composite. World J Eng. 2020;17(6):823-9. https://doi.org/10.1108/WJE-08-2020-0351
[49] Khashi'Ie NS, Hamzah K. Mechanical properties of jute fiber polyester hybrid composite filled with eggshell. Semarak Eng J. 2024;6(1):20-8.
[50] Souza JWL, Jaques NG, Popp M, Kolbe J, Fook MVL, Wellen RMR. Optimization of epoxy resin: an investigation of eggshell as a synergic filler. Materials. 2019;12(9):1489. https://doi.org/10.3390/ma12091489
[51] Olaitan, A. J., Terhemen, A., King, G., & Oluwatoyin, O. Comparative assessment of mechanical properties of groundnut shell and rice husk reinforced epoxy composites. Am. J. Mech. Eng. 2017 5(3), 76-86.
[52] Jain N, Somvanshi KS, Gope PC, Singh VK. Mechanical characterization and machining performance evaluation of rice husk/epoxy: an agricultural waste-based composite material. J Mech Behav Mater. 2019;28(1):29-38. https://doi.org/10.1515/jmbm-2019-0005
[53] Ganesan V, Chohan JS, Subburaj GS, Panneerselvam H, Nagabhushanam KY, Venkatesan MK, et al. Experimental analysis of mechanical properties of banana fibre/eggshell powder-reinforced hybrid epoxy composite. Eng Proc. 2024;61(1):18. https://doi.org/10.3390/engproc2024061018

Blank Page

Research on Engineering Structures & Materials
www.jresm.org

Research Article

Using sewage sludge ash as a replacement for cement in mortar applications

Ahmed Amine Meraghni [*,a], Abderrezak Khellou [b], Saïd Abani [c]

Laboratory of Exploitation and Valorization of Natural Resources in Arid Zones, Kasdi Merbah University Ouargla, Faculty of Applied Sciences, Route de Ghardaia BP.511, 30 000 Ouargla, Algeria

Article Info

Article History:

Received 20 Sep 2024

Accepted 03 Jan 2025

Keywords:

Sewage sludge ash;
Mortar;
Sustainable construction materials;
Pozzolanic activity;
Waste management

Abstract

In the quest for sustainable construction practices, integrating waste materials into the construction sector has gained significant attention. Sewage sludge ash (SSA) is a very attractive resource since it is readily available in large quantities and has the potential to provide significant environmental advantages. The present study, this study investigates the feasibility of utilizing supplementary cementitious materials (such as SSA) as a portion alternative to cement in mortar, aiming to reduce the environmental burden of sewage waste and enhance mortar properties. Experiments incorporated integrated SSA at 0% (control), 15%, 25%, 50%, and 75% of cement's weight. Characteristics of mortar were evaluated at 7, 28, 60, and 90 days, evaluating mechanical characteristics such as flexural and compressive strengths, as well as physical attributes including water absorption, dry bulk density, and apparent porosity. The findings revealed that SSA inclusion significantly influenced the physical and mechanical characteristics of the mortar. 28-day compressive strength of the mortar sample reached 31 MPa when 25% of the cement was substituted with SSA. In comparison, the control sample exhibited a compressive strength of 42.25 MPa, indicating that up to 25% substitution is feasible and meets standard norms. SSA inclusion decreased dry bulk densities, increased water absorption, and improved porosity. Thus, this study demonstrates the performance of using SSA as an environmentally friendly substance and economical cement alternative in sustainable construction materials.

© 2025 MIM Research Group. All rights reserved.

1. Introduction

Sewage sludge is a byproduct that is initiated as a result of the techniques used in treating and cleansing wastewater which presents considerable difficulties when it comes to disposal within areas with high population. The accumulation of substantial quantities of sewage sludge at treatment facilities and the constrained disposal options heightens environmental concerns. Traditionally, landfilling has served as the primary method for sewage sludge disposal [1,2]. Nevertheless, the increasing amount of sewage sludge requires the investigation of viable alternative solutions. New strategy includes using sewage sludge ash (SSA) in concrete where it functions as a partial replacement for cement or filler by relying on its physicochemical properties [3,4]. This strategy doesn't only mitigate the dilemma of disposal but also reduces the environmental footprint associated with conventional landfilling and agricultural applications which are prone to contaminating soil and water bodies. By embedding SSA within building materials, the management of its burgeoning production can be optimized, presenting a forward-thinking solution to the sewage sludge disposal quandary.

*Corresponding author: meraghni.ahmedamine@univ-ouargla.dz
[a]orcid.org/0009-0008-5815-2329; [b]orcid.org/0009-0007-2585-5493; [c]orcid.org/0009-0002-2306-2514
DOI: http://dx.doi.org/10.17515/resm2025-459ma0920rs
Res. Eng. Struct. Mat. Vol. 11 Iss. 5 (2025) 2211-2229

Regarding decreasing of volume, burning sewage sludge is a very efficient approach. This process can reduce the volume of sludge to 95% or even more with significantly mitigating the levels of heavy metals and organic pollutants contained within the sludge [5-8]. The resulted product, known as sewage sludge ash (SSA), harbors diverse applications which are primarily used as an additive in the manufacturing of mortar and concrete, thereby, it replaces a portion of the cement. This application of SSA has attracted considerable global interest through spotlighting its potential as a sustainable solution in the construction sector.Cement is crucial in the manufacturing of concrete since it directly affects its mechanical and thermal properties [9,10]. Producing one ton of cement releases a considerable amount of CO_2 that contributes to 7% of the total global CO_2 emissions [11-13]. Over the last several decades, many experiments have been carried out to create sustainable concrete by substituting a portion of Ordinary Portland Cement (OPC) with other materials [14,15]. Collectively, these facts clearly highlight the potential benefits of substituting cement with SSA, both in terms of addressing sewage sludge disposal and reducing cement production which in turn would lead to a decrease of CO_2 emissions [16].

Furthermore, the variances in SSA's mineral composition, attributable to geographic differences, significantly affect the fundamental characteristics of mortar, for instance, compressive and flexural strength, workability, and durability. These disparities underscore the necessity for meticulous evaluation of SSA's applicability as a construction material to ensure that its integration preserves or enhances the desired characteristics of the final product. Hence, localized research and development endeavors are imperative to refine the usage of SSA in concrete formulations, accounting for the unique attributes of SSA derived from various locations.

The density of concrete that incorporates SSA likely varies based on the incineration temperature, leading to fluctuations in its density [17,18]. A significant amount of sewage sludge is produced in Algeria, a quantity that continues to increase, with projections reaching four hundred thousand tons per year by 2025 [19]. Given its composition of organic substances and harmful heavy metals, it presents a worldwide concern [20]. Yet, with advancements in industrial techniques related to pozzolanic activities, integrating SSA and its constituents – including SiO_2, AL_2O_3, Fe_2O_3, CaO, MgO, P_2O_5 – which result from the burning of sewage sludge, has emerged as a strategy to curb CO_2 emissions (Roughly 900 kilograms per metric tons of cement.) and minimize their ecological footprint [21,22].

In 1999, Monzó et al [23] conducted a study. The investigation revealed that substituting cement with either 15% or 30% SSA had little impact on the compressive strength of cement mortar when exposed to a temperature of 40°.Include a grace period that spans from 3 to 28 days. In 2003, Pan et al [24] made a discovery that changing the size of particles in mortar mixes containing SSA could improve their effectiveness. Their investigation concluded that the length of time spent grinding the SSA particles did not have a notable impact on the compressive strength of the mortar. In a 2007 investigation, In a study conducted by Cyr et al [4], it was discovered that replacing cement with 25% and 50% SSA led to a primary decline in the compressive strength of the cement mortars. However, after a long period of time, this change greatly enhanced the compressive strength. Garcés et al [25] Performed a study to assess the appropriateness of utilizing SSA with different types of cement. The study determined that CEM II/B-M (V-LL) 42.5R cement is the most suitable option for using SSA. Moreover, it has been demonstrated that a substitution rate of 10% yields the most substantial improvement in compressive strength. Moreover, the employment of superplasticizers was acknowledged as a technique to mitigate the adverse consequences of SSA on the workability. The research conducted by Chang et al [26].Examined the chemistry makeup of SSA and its use in concrete blends. the findings Indicated that the inclusion of SSA led to a decrease in both the workability and compressive strength of the mortar. Lynn et al concluded that SSA can be successfully incorporated into concrete as either fine aggregates or fillers, mostly due to its particle morphology. The particles, distinguished by their irregular morphology, were found to have a size range that falls between fine sand and silt, as determined by their percent [27].

Studies have shown that adding 8% by weight of SSA to ultra-high strength concrete (UHPC) has a negative impact on its ductility and hampers the initial hydration process of the cement [28]. However, subsequent phases of the curing process exhibited improvements in pozzolanic reactions

[28]. The utilization of SSA led to alterations to the pore structure of UHPC, resulting in an increase in the overall pore volume and a decrease in the volume of bigger pores [28]. Xia et al. conducted economic and environmental assessments which indicated that the inclusion of SSA in UHPC might lead to substantial cost reductions and a reduction in impact on the environment [28]. The addition of SSA into the mixture yielded in a marginal decrease in the flexural strength and workability of UHPC, as evidenced by compressive strength tests conducted at 7 and 28 days. The experiments showed a progressive improvement in compressive strength with a 10% replacement of supplementary cementitious materials (SCMs) [29]. Furthermore, the SSA was found to lead to increase levels of autogenous and drying shrinkage [29]. The additional SSA to mortar improved its ability to withstand compression and decrease its rate of water absorption. The most favorable outcomes were observed when using 10% SSA to boost compressive strength and between 5% and 10% SSA to lower water absorption rates [30]. Higher SSA concentrations in the binder increased the drying shrinkage in the blocks. Overall, the literature suggests that SSA improves mortar performance and extends concrete setting time [31,32]. Therefore, this study seeks to fill the substantial research void thorough examination of the influence of Sewage Sludge Ash (SSA) derived from an Algerian desert location on mortar properties. By focusing on a specific source which is Touggourt City in Algeria, this research Aims to understand the intricate relationship between SSA composition and mortar performance. The study not only contribute to existing knowledge but also offers practical insights for developing robust and region-specific strategies for incorporating SSA into mortar mixes. The collection of sewage sludge was carried out in a sewage treatment facility situated in the same city and subjected to detailed analysis. The dehydrated sludge underwent incineration and pulverization before being used as a substitute for a portion of cement in mortar compositions by employing five different ratios of SSA (0%, 15%, 25%, 50%, and 75%).

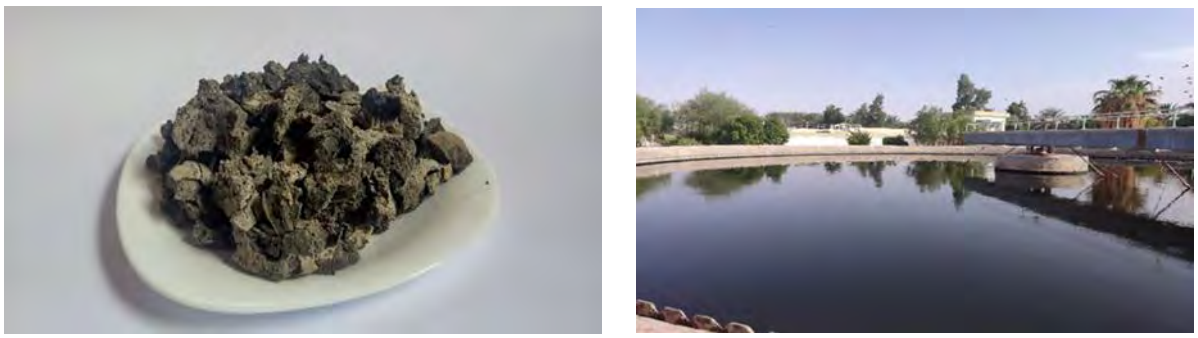
Several experiments were performed on these specimens so as to examine their physical and chemical characteristics. The included tasks in this study encompassed the analysis of the elemental and crystalline content of the SSA, as well as the assessment of its pozzolanic activity in mortar. Further evaluations are included which are testing the specimens' workability, durability, flexural strength, and compressive strength.

2. Materials and Experimental Methodology

2.1. Materials

2.1.1 Ash SSA

The dry sewage sludge, obtained as the final output of the purification process, was gathered from a metropolitan wastewater facility located in Touggourt City, as shown in Figure 1. After the drying process, the stones and impurities were removed. Due to the normally elevated levels of organic matter in sludge obtained from urban sewage treatment plants, the dewatered sludge was subjected to incineration at a temperature of 850°C to reduce its organic content and prevent any potential negative effects.



(a) (b)

Fig. 1. Plant for treating wastewater :(a) dry sewage sludge and (b) activated sludge

As a consequence of this process, sewage sludge ash (SSA) was generated, as depicted in Figure 2. In order to utilize SSA as an additive in mortar, additional processing of the ash was required. The furnace-produced ash had larger particle sizes. Therefore, we thoroughly crushed it with a hammer to reduce its particle size and then sieved it through a 0.08 mm sieve to ensure uniformity and readiness for use in mortar formulations.



Fig. 2. Sewage Sludge Ash (SSA)

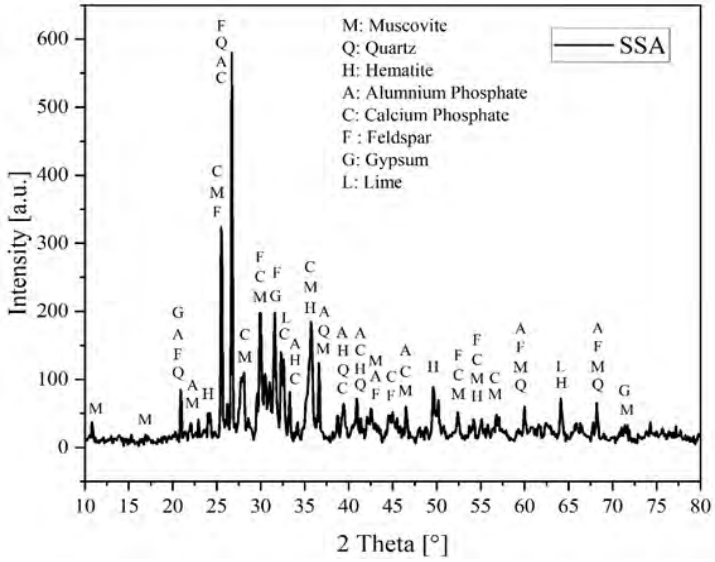


Fig. 3. XRD analysis of Sewage Sludge Ash SSA

The X-ray diffraction (XRD) pattern of the sewage sludge ash (SSA) sample, as depicted in Figure 3, provides a comprehensive overview of its major mineral phases. Notably, the analysis identifies significant peaks corresponding to Quartz, muscovite, Hematite, Aluminum Phosphate, and calcium Phosphate, indicating the prevalence of these crystalline constituents. Additionally, smaller fractions of Feldspar, Gypsum, and Lime are discernible in the pattern, contributing to the overall diversity of the mineral composition.

2.1.2 Sand

The standardized CEN sand (ISO standardized sand) is a natural sand, particularly siliceous in its finest fractions. It is characterized by its clean, isometric, and rounded grains, ensuring uniformity and minimal variability in size and shape. This sand undergoes a meticulous drying, sieving, and preparation process in a modern workshop that adheres to the highest standards of quality and consistency, thus meeting the specific requirements set forth by NF EN 196-1 [33]. The physical properties of this sand, including its grain size distribution, density, and moisture content, are rigorously controlled to ensure optimal performance in its applications. Table 1 and Figure 4 illustrate the physical properties and The distribution of particle sizes curve of the CEN standardized sand. the utilized sand not only guarantees the structural integrity of the materials

produced with it but also enhances the reproducibility of test results in cement and mortar research.

Table 1. Comprehensive material properties of construction-grade sand [34]

Real Density	2.64 t/m3	Alumina Content (Al_2O_3)	0.25 %
Apparent Density	1.62 t/m3	Iron Content (Fe_2O_3)	0.06 %
Fineness Modulus	26<> 2.7	Phosphorus Pentoxide Content (P_2O_5)	0.00 %
Loss on Ignition at 950°C	0.16 %	Titanium Dioxide Content (TiO_2)	0.02 %
Water Absorption	0.20 %	Silica Content (SiO_2)	98.69 %
Water Content	<0.2	Chloride Ion Content (Cl^-)	<50ppm

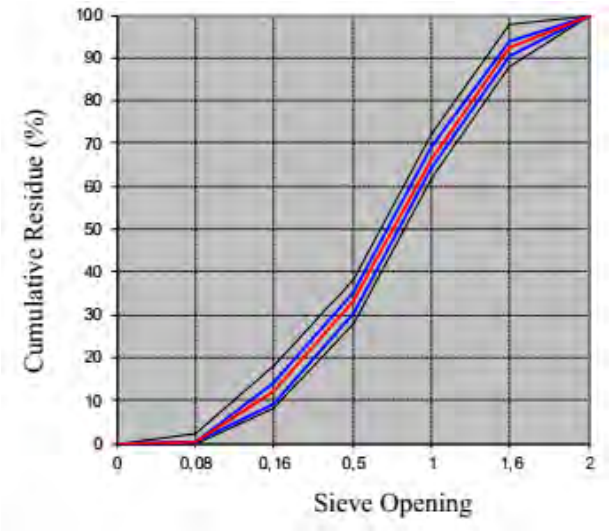


Fig. 4. Particle Size Distribution Curve for Sand Analysis [34]

2.1.3 Cement

All the specimens in this research were crafted using Type I Ordinary Portland Cement (OPC). This complies with EN 197-1 [35] and NA 442 [36]; Tables 2 and 3 provide the chemical and mineral analysis as well as the physical qualities of the cement used.

Table 2. Analysis of the chemical and mineral characteristics of Portland cement [37]

Loss on ignition (%)(NA5042)	0. 5 to 3%
Sulfate (SO_3) (%)	1. 8 to 3
Magnesium oxide MgO (%)	1. 2 to 3
Chloride (Cl^-) (NA5042) (%)	0. 01 to 0.05
C_3A rate	<3. 0 %

Table 3. The findings of the analysis on the physical characteristics [37]

Normal consistency (%)	25 to 28
Blaine technique measures the fineness (cm^2/g)(NA231)	3200 to 3800
28-day shrinkage (µm/m)	< 1000
Enlargement (mm)	≤ 2
Hydration heat	<270 j/g
Start of setting at 20 (min)	>60
End of setting at 20 (min)	240 to 400

2.2 Experimental Methodology

2.2.1 Proportional Blending Of Components and Preparation of Samples

In order to assess the sustainability and efficacy of sludge ash powder as an alternative to traditional cement, our experiment began with the precise blending of sand and sludge ash powder for two minutes to ensure a homogeneous dry mixture. This step was significant for achieving a consistent base before introducing any liquid components. Subsequently, water and 'Sika' - a super plasticizer - was added to the dry mix within a mechanical mixer. This process was carefully monitored to ensure a gradual and uniform combination of the materials, continuing until a consistent and homogenous mixture was achieved. This methodological approach aimed at not only for examining the structural benefits of substituting cement with sludge ash powder but also to explore the environmental advantages with particular emphasis on achieving a vital uniform mixture for ensuring the structural integrity and sustainability of the concoction.

Before employing SSA as a fragmentary replacement for cement, its pozzolanic activity needs to be assessed. To achieve this, samples with varied SSA contents were compared to a control sample (A0) without sludge. Consequently, five mixture configurations were examined to determine the mechanical strength of prismatic 4x4x16 cm mortar samples in accordance with NF EN 196-1 standards [33]. Each configuration consisted of six samples to ensure statistical relevance and accuracy. The specifics of these mixtures are outlined in Table 4.

Table 4. A mortar test piece recipe containing the SSA-specified substitution ratio (in%)

Mixtures	Cement (g)	SSA (g)	Sand (g)	Substitution ratio (%)
A0	450	0	1350	**0%**
A15	382.5	67.5	1350	**15%**
A25	337.5	112.5	1350	**25%**
A50	225	225	1350	**50%**
A75	112.5	337.5	1350	**75%**



Fig. 5. Prepared mortar samples with different SSA substitution ratios

2.3 Procedure for the Experiment

2.3.1 Flexural Strength

Flexural strength is generally assessed by flexural tensile tests. They are produced on prismatic specimens 4x4x16 cm, resting on two supports and subjected to a single concentrated load applied to the middle. This configuration develops a bending stress in the specimen, allowing its flexural strength to be measured indirectly. Our investigation centered on prismatic mortar specimens measuring 4x4x16 cm, with each batch designed to incorporate SSA at varying replacement ratios: A0 as a control and A15, A25, A50, and A75 representing different percentages of the cement's weight. In order to ensure the dependability and consistency of the outcomes, four distinct studies were created for every level of substitution. The experiment was conducted at different curing periods of 7, 28, 60, and 90 days. This setup is not only allowed for a direct assessment of the specimen's response under bending stress but also provided valuable insights into its flexibility and breakpoint, and offering a comprehensive view of its mechanical behaviors by including resistance to bending and flexural forces. These measurements are pivotal for determining the

durability and structural integrity of enhanced concrete with SSA for echoing our objective to confirm SSA's viability as a sustainable and efficacious alternative to conventional cement in mortar.



Fig. 6. Assessment of mechanical properties: a focus on flexural strength testing

2.3.2 Compressive Strength

The compressive strength was calculated by testing specimens which are taken from the original pavers after conducting the tensile strength tests which resulted in each specimen being split into two halves. For each replacement ratio (A0, A15, A25, A50, and A75), four halves were selected to undergo compressive strength testing. These tests were conducted at specific period of 7, 28, 60, and 90 days to monitor the development of strength over time.

During the compressive strength test, the force was applied to the samples via square steel plates with a width of 40 mm. The compressive strength was concluded through dividing the force at the moment of failure by the surface area over which the load was applied. The result for each replacement ratio at each curing period was taken as the average of four measurements. This method ensured the reliability and reproducibility of the results that provide comprehensive insights into the performance and structural integrity of mortar samples incorporating SSA.



Fig. 7. Evaluating mechanical properties: focus on compressive strength testing

3. Results and Discussion

3.1 SSA Test Results

3.1.1 XRD

The X-ray diffraction (XRD) analysis results for the mortar sample A0 (without SSA) are visually represented in Figure 8 that offering crucial insights into the material's mineral composition. Peaks in the spectrum reveal the prevalence of quartz and calcium-bearing minerals, which is serving as key indicators of the primary mineral phases within the mortar. Specifically, the identified peaks point towards the presence of quartz, dicalcite silicate, tricalcium silicate, tricalcium aluminate, and tetracalcium aluminoferrite are dominant constituents in the mortat structure. Notably, the distinctive peaks corresponding to calcium-bearing minerals are attributed to the cementitious components, whereas the manifestation of quartz peaks is ascribed to the sand fraction of the mortar mixture.

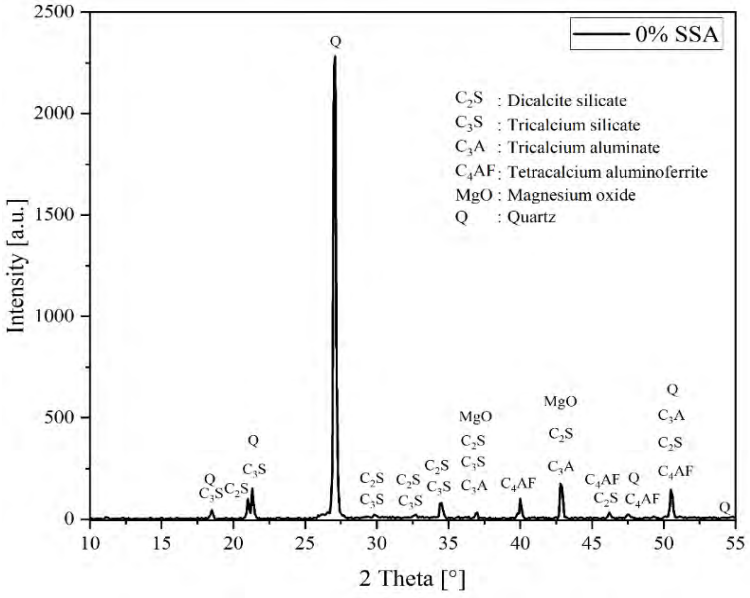


Fig. 8. XRD analysis of mortar powder without SSA (A 0)

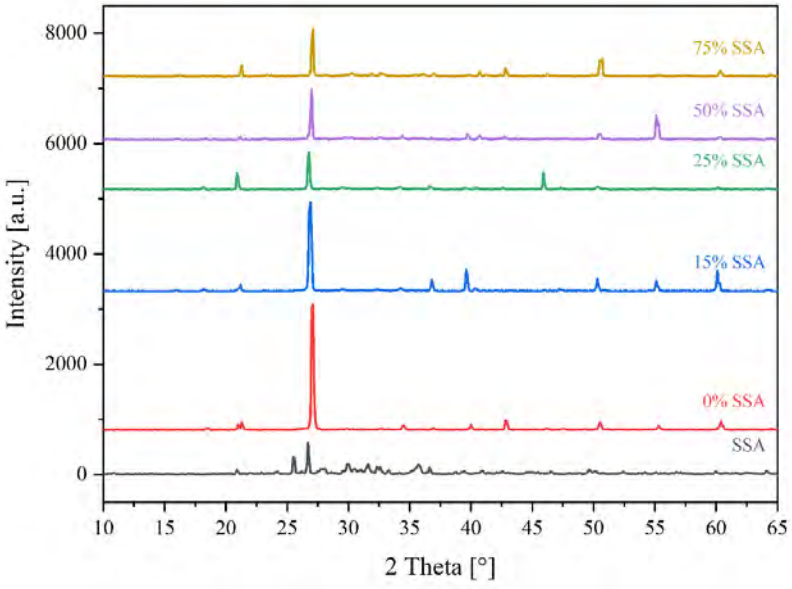


Fig. 9. XRD Analysis of mortar samples with varying SSA content

In Figure 9, the XRD analysis of mortar samples, incorporating different proportions of Sewage Sludge Ash (SSA) as a substitute for cement, is presented. the stacked XRD patterns provide a visual representation facilitating a direct comparison of the mineral phases. Notably, a discernible trend emerges as the proportion of (SSA) rises, revealing a consistent decrease in peak intensity. This diminishing intensity aligns with the inherently lower intensity of SSA peaks compared to the more pronounced peaks observed in samples without SSA. Moreover, the comparative analysis unveils the emergence of specific peaks corresponding to SSA phases within the mortar samples. This observation strongly suggests the successful incorporation of SSA into the mortar matrix.

3.1.2 The Fourier Transform Infrared (FTIR) Spectra

The Fourier Transform Infrared (FTIR) analysis was conducted on Sewage Sludge Ash (SSA) samples subjected to thermal treatment at 850°C to assess the chemical modifications induced by the combustion process. The analysis included both the initial SSA sample, labeled "Before" to denote its state prior to burning, and subsequent mortar samples that incorporated the thermally treated SSA in varying proportions as a cement substitute. The FTIR spectrum of the "Before" sample exhibited characteristic absorption peaks at wavenumbers 3309, 2922.23, 2847.68, 1655, 1514, 1417.78, 1012.31, and 454 cm^{-1}. These peaks correspond to specific functional groups, revealing the existence of hydroxyl (O-H) and aliphatic (C-H) stretching, carbonyl (C=O) stretching, (N-H) and (C-H) bending, as well as mineral oxides like Si-O-Si stretching vibrations. This spectral analysis not only underscores the chemical complexity of the SSA before thermal treatment but also sets a baseline for comparing the alterations in functional groups and bonding configurations post-combustion when SSA is integrated into the mortar samples.

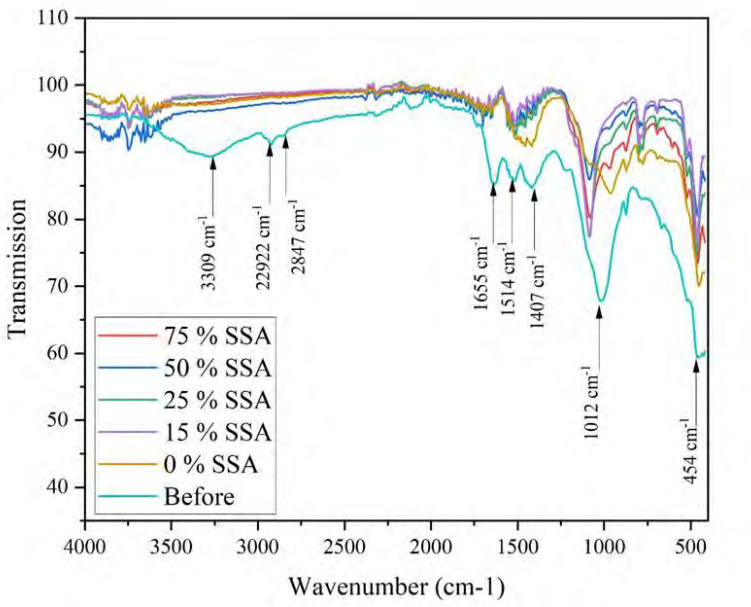


Fig. 10. The Fourier Transform Infrared (FTIR) analysis was conducted on Sewage Sludge Ash and Various Mortar Samples Incorporating Different Proportions of SSA

Following thermal treatment, several peaks, including those at 3309, 2922, 2847.68, 1655, and 1012.31 cm^{-1}, disappeared in the spectra of mortar samples with varying SSA content. This disappearance suggests the effective removal or alteration of specific organic functional groups due to the thermal treatment, aligning with its purpose of eliminating organic matter from the mortar samples. The remaining peaks in the post-treatment spectra indicate the modified composition of SSA in the mortar matrix. The FTIR analysis, therefore, not only delineates the functional groups in the initial SSA sample but also reveals the impact of thermal treatment on the functional group composition in mortar samples incorporating SSA as a cement substitute.

3.2 Mortar Test Results

3.2.1 Workability Test

Before mortar hardens, it is placed in molds. The process of placing should be efficient to save time and avoid deformations resulting from pouring, which are difficult to rectify later. Mortar is considered more workable if the process of pouring it into molds is easier. Therefore, this experiment aimed to measure the flow of mortar using a flow table test, infer from this test about the quality of the mortar, assess its workability, and determine the appropriate water ratio for acceptable workability.



Fig. 11. Flow table apparatus and mortar spread

To attain satisfactory workability, additional water becomes essential when SSA is used to replace cement at proportions of 25%, 50%, and 75%. When comparing mix design A0 with mix design A75, it is evident that the workability of mix design A75 diminishes even with a 20% increase in water content. To maintain workability at this high level of SSA substitution, we incorporated a plasticizer, specifically Sika, which significantly improved the mortar's workability. The flow table test results are summarized in Table 5.

Previous studies support the conclusion that increasing the SSA replacement ratio significantly impacts mortar workability, as the increased SSA content decreases fluidity due to its porous nature and irregular particle morphology [26,39–41].

Table 5. Mix design and flow table results

Mix Design	Plasticizer (Sika)	E/C	Water (gr)	Average Spread Diameter (mm)
A0	No	0.5	225	167
A15	No	0.55	247.5	175
A25	No	0.55	247.5	157
A50	No	0.6	270	165
A75	No	0.6	270	132
A75	Yes	0.6	270	155

The flow table test results demonstrated that for mix design A0, the average spread diameter was 167 mm. For mix design A75, without the plasticizer, the average spread diameter decreased to 132 mm despite the additional water. However, with the inclusion of Sika, the spread diameter for mix design A75 improved to 155 mm, indicating a significant enhancement in workability.

Research by Guo et al. [39] and Chang et al. [26] reinforces this observation, noting that the integration of SSA in concrete tends to lead to a decrease in workability.

3.2.2 Alteration of Physical Appearance

The first alteration seen after the implementation of SSA was evident in the physical characteristics of the specimens. Figure 12 displays five mortar specimens with varying sludge ash levels. It is obvious that samples containing a greater proportion of SSA present a beige color.



Fig. 12. Specimen appearance changes following SSA addition

3.2.3 Bulk Density

Figure 13 illustrates that incorporating sewage sludge ash (SSA) as a substitute for a portion of cement results in a decrease in the overall density of mortar. The decrease in size can be ascribed to the low mass of SSA particles. The employed cement in this experiment has a determined bulk density of 1429.88 kg/m^3, but the bulk density of SSA was found to be 824.65 kg/m^3.

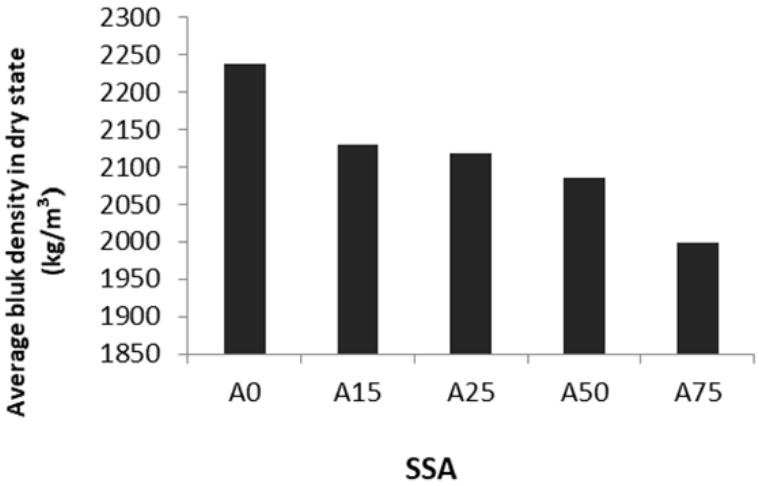


Fig. 13. Bulk density of the combinations that were tested

In specimens A15 and A75, the bulk density is reduced by 4.83% and 10.68%, respectively, compared to specimen A0. The results suggest that when the proportion of SSA rises, the bulk density of the mortar falls. This is because SSA has a lesser density than cement that is resulting in a lighter mixture overall. This discovery highlights the potential of using SSA as a sustainable and lightweight alternative in mortar formulations which can help reduce the overall weight of construction materials while maintaining adequate structural properties.

These results are influential as they show that incorporating SSA can lead to the production of lighter construction materials without compromising structural integrity. This diminution in weight can be particularly advantageous in various construction applications where minimizing weight is critical.

3.2.4 Water Absorption

Figure 14 summarizes the water absorption rates of the various mortar specimens. The data clearly indicates an upward trend with water absorption rates increasing as the percentage of SSA substitution rises. Precisely, the absorption rate starts at approximately 0.45% for the A0 specimens and reaches approximately 1.43% for the A75 specimens. The rise in water absorption may be ascribed to the intrinsic characteristics of SSA which tend to enhance the porosity of the mortar matrix. As more SSA is incorporated into the mix, the overall density of the mixture decreases that resulting in higher water absorption rates. This observation aligns with the previously discussed trends in bulk density, and further emphasizing the impact of SSA on the physical properties of the mortar.

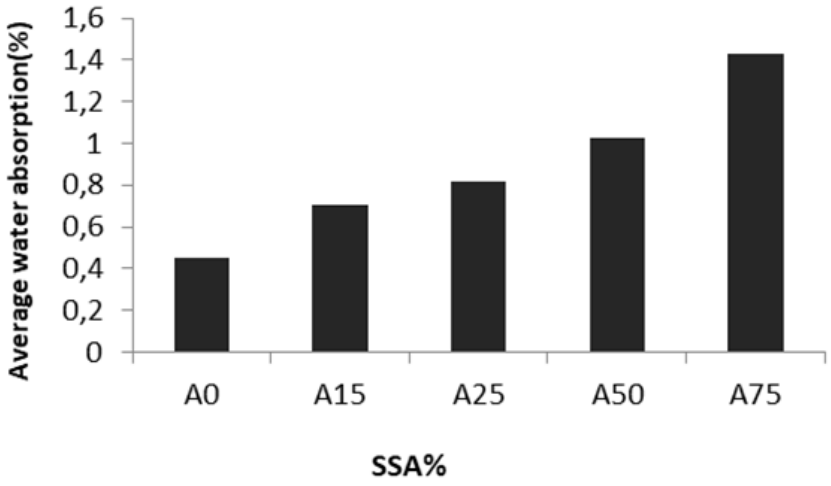


Fig. 14. Absorption of Water by the Tested Combinations

Prior studies have demonstrated that mixing SSA into mortar increases water absorption and demand. This arises from SSA's porous microstructure and irregular morphology, which leads to water adsorption upon the exterior of SSA particles. Consequently, There is less free water in the mortar [43]. Additionally, the rough surface of SSA increases the resistance between particles, impacting fluidity and increasing the need for water [44]. These factors, combined with the lower density of SSA compared to cement, explain the increase in water absorption as the SSA content increases. These results are significant as they underscore the importance of carefully evaluating water absorption rates when designing mortar mixtures containing SSA. Thus, increased water absorption can affect the durability and longevity of the mortar by making it crucial to balance the benefits of using SSA with its impact on water absorption.

3.2.5 Ultrasonic Pulse Velocity

The ultrasonic pulse velocity (UPV) test is a nondestructive technique employed to assess the soundness and excellence of mortar materials. This method entails the measurement of the duration. It takes an ultrasonic pulse to travel through the material, and gives valuable insights into the material's density, porosity, and microstructure. Mainly in this study, the UPV test was managed to enrich the data on density, porosity, and microstructure that is obtained from other tests. The results, as illustrated in Figure 15, indicate a fall in ultrasonic pulse velocity with the partial substitution of cement by SSA. This decrease in UPV can be attributed to the risen porosity and reduced density of the mortar mixtures containing SSA.

The findings from the UPV test show the impact of SSA on the material integrity of the mortar. As SSA content increases, the ultrasonic pulse velocity decreases that indicates probable changes in the material's internal structure. This insight is crucial for comprehending the impact of SSA on the durability and mechanical characteristics of mortars mixtures.

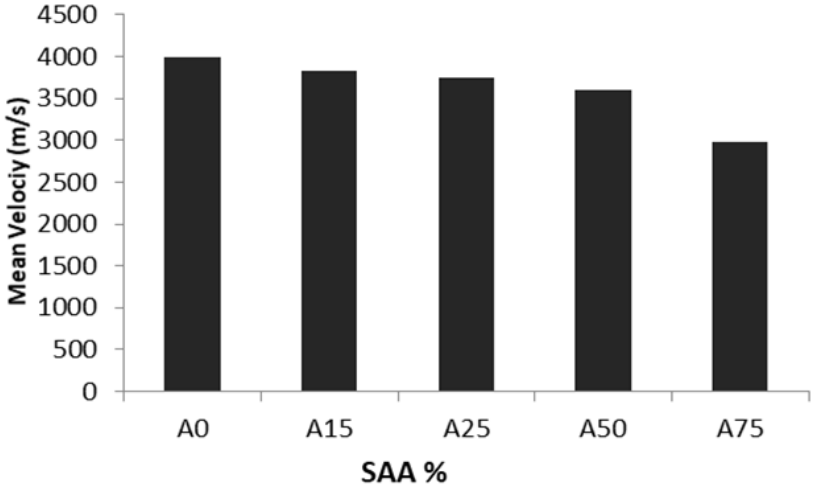


Fig. 15. Measurement of ultrasonic pulse velocity in tested mixes



Fig. 16. Ultrasonic pulse velocity measurement in mortar specime

3.2.6 Flexural Strength

The study aimed at examining the impact of varying quantities of sewage sludge ash (SSA) which affects the flexural strength of mortar samples when employed as a partial alternative to cement. Figure 17 depicts the differences in flexural strength throughout different curing durations. As the curing period advanced, the flexural strength of the mortar enhanced to indicate that the inclusion of SSA did not impede the hardening process within the studied substitution range. However, specimens with A15, A25, A50, and A75 substitution exhibited a reduction in flexural strength compared to the control specimens (A0) without SSA. The flexural strength showed a linear decrease with increasing SSA substitution. There are two possible explanations that may be given to account for this observation:

- Firstly, an excessive amount of water was used to provide the necessary texture for producing a practical mortar mixture. The presence of excessive moisture heightened the flexibility and the susceptibility to collapse of the mortar while diminishing its cohesiveness. Hence, an excessive amount of water and insufficient cement would lead to a less robust and less long-lasting mortar.
- The second theory is that the ash's hydraulic capabilities were inferior to those of cement, perhaps owing to its CaO component. Ash, although being pozzolanic, has a lime content (CaO) of less than 10%. Furthermore, the pozzolanic glassy silica and alumina in the ash require a cementing agent, such as hydrated lime or Portland cement, and water to undergo a reaction and generate cementitious compounds.

The results correspond with prior studies showing that mortar's flexural strength after 28 days with SSA is often less than cement mortar's. Specifically, as shown in several sources, an increased replacement ratio of SSA correlates with decreased flexural strength [4,25,39,41,45–49]. However, it is essential to mention that some researchers have found that at lower replacement ratios, the flexural resistance of SSA mortar may surpass that of cement mortar because of SSA's significant water absorption and filling capabilities. The ideal ratio of water to cement decreases due to SSA's heightened water absorption characteristics, which offsets the cement dilution effect [50]. Nonetheless, significant reductions in flexural strength occur when the SSA replacement rate exceeds 30%, primarily attributable to the minimal reactivity of SSA [45].

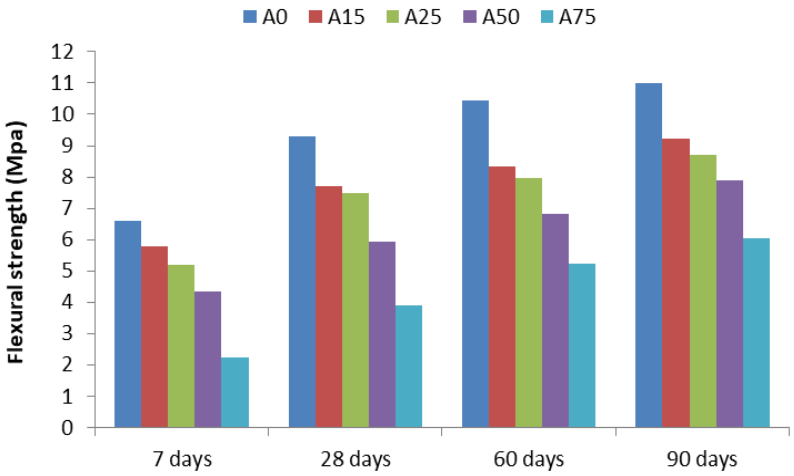


Fig. 17. Flexural strength of mortar specimens with varying levels of changed SSA content was measured over a period of 7to 90 days

3.2.7 Compressive Strength

The study evaluated the compressive strength of mortar samples to analyze the effects of including sewage sludge ash (SSA) as a substitute for cement. Figure 18 presents the compressive strength results over different curing periods. The data indicate a reduction in compressive strength for all specimens with SSA substitution at 7, 28, 60, and 90 days.

Our study aims to explore the impact of pozzolan on the initial compressive strength of mortar during the curing process, notably between 7 to 28 days. Previous research has highlighted this time frame as a period with notable variations in compressive strength. [4,40]. The pozzolanic activity index, which measures the effectiveness of SSA in maintaining compressive strength, is another crucial aspect. This index is the ratio of the compressive strength of SSA-substituted specimens to the reference specimen (A0). Higher values indicate better performance. Table 6 shows the calculated pozzolanic activity index for each curing period.

Furthermore, the chemical interaction between SSA and cement during hydration is essential. SSA which is rich in pozzolanic materials like alumina and silica, undergoes a chemical reaction with calcium hydroxide to generate more calcium silicate hydrate (C-S-H). However, the lower lime content in SSA can slow down the creation of C-S-H, which partly explains the reduced early compressive strength. Moreover, the increased porosity resulting from SSA substitution may weaken the interfacial transition zones (ITZ) between the aggregate and cement matrix, further reducing the overall compressive strength.

The decrease in compressive strength observed in SSA-substituted mortar samples is consistent with findings from previous studies, which report a decrease in strength due to the lower reactivity of SSA and increased porosity caused by its irregular shape and high-water absorption characteristics [26,45,52–55]. Additionally, SSA's lower CaO content can delay hydration and decrease the creation of hydration products such as C-S-H, further affecting early strength [23,56].

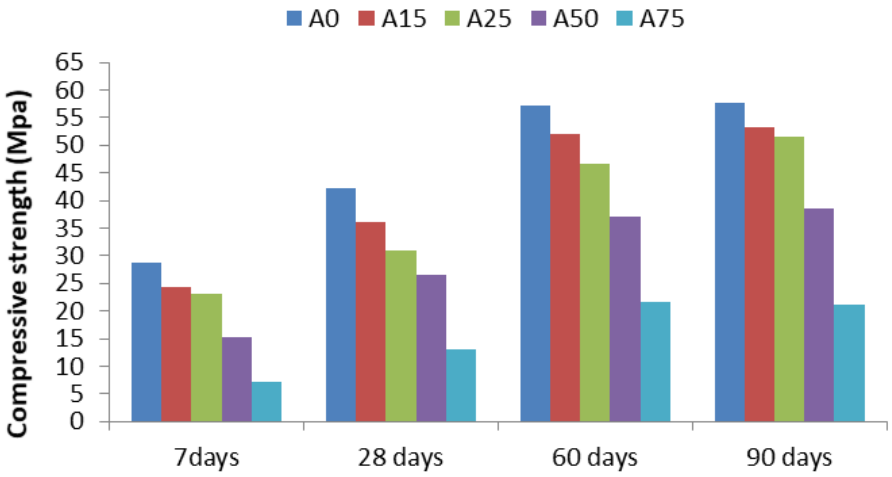


Fig. 18. Compressive strength of mortars specimens with different amounts of changed SSA content measured over a period of 7 to 90 days

Table 6. Pozzolanic activity index of mortars at various ages

	A15	A25	A50	A75
7 days	84.9%	80.8%	52.9%	24.9%
28 days	85.2%	73.4%	62.9%	30.6%
60 days	91%	81.7%	65%	38%
90 days	92.4%	89.6%	66.8%	36.7%

The pozzolanic activity index shows a decreasing trend with higher SSA content aligning with the noticed reduction in compressive strength. These results underscore the need to optimize SSA content in mortar mixtures to balance environmental benefits with mechanical performance. The chemical interactions and increased porosity due to SSA substitution highlight the complex nature of using SSA in cementitious materials and the importance of comprehensive analysis to ensure structural integrity.

3.2.8 Understanding the Pozzolanic Activity of SSA

The pozzolanic activity of SSA was assessed by comparing the compressive strengths at 28 days to those at 7 days for mortar samples with variety of concentrations of SSA. According to the data shown in Table 7, the ratio demonstrates a direct correlation with higher amounts of SSA. The findings suggest that the amorphous structures seen in SSA serve as a pozzolan over extended durations, hence enhancing the strength of the mortar samples.

Table 7. Compressive strength ratios in various SSA contents from 28 days 7 days

Mix Design	Relative Strengths (Compressive, 28-day to 7-day)
A0	1.472125
A15	1.476923
A25	1.336207
A50	1.752883
A75	1.807692

These results highlight the long-term pozzolanic reactivity of SSA contributing to the continued strength development of mortar. Over time, the amorphous silica and alumina in SSA undergo a

reaction with calcium hydroxide. This leads to the creation of more calcium silicate hydrate (C-S-H). This technique ultimately improves the compressive strength of the mortar.

4. Conclusion

This research explored the potential use of sewage sludge ash (SSA) as a partial substitute for cement in mortar applications. The study focused on analyzing the physical and mechanical properties of mortar when varying amounts of SSA were introduced. The findings showed that the inclusion of SSA resulted in several key changes in the properties of the mortar.

The addition of SSA led to a decrease in slump measurements, which suggests that the workability of the mortar could be affected, necessitating adjustments in water content or the use of plasticizers to maintain the desired consistency. Furthermore, the increase in SSA content altered the color of the mortar specimens, which may be a consideration for aesthetic purposes in certain construction applications.

From a mechanical standpoint, the introduction of SSA caused a reduction in the mortar's flexural strength, with a 5% increase in SSA content leading to a 4.83% decrease in 28-day flexural strength. This indicates that while SSA can be used as a sustainable alternative to a portion of the cement, it does impact the strength of the mortar, requiring careful balance in mix design to ensure structural integrity.

The study also observed that SSA contributed to an increase in water absorption and a reduction in bulk density and ultrasonic pulse velocity (UPV) of the mortar. These findings suggest that SSA may be beneficial in applications where lighter weight and enhanced thermal properties are desired, though at the cost of some mechanical strength.

While the research provides valuable insights into the use of SSA in mortar, further studies are needed to fully understand its long-term effects on mortar durability and performance under various environmental conditions. Future research should also investigate the optimization of SSA content in mortar mixes to maximize both environmental and structural benefits. Considering the impact of SSA on physical and chemical properties such as compressive strength, density, and porosity, it is crucial to select substitution ratios to ensure satisfactory performance standards carefully. The presence of SSA affects the workability, water absorption, flexural strength, and compressive strength of mortars due to its porous nature and irregular particle morphology. Although these characteristics can decrease mechanical strength, the pozzolanic properties of SSA can enhance durability over time, offering potential advantages in certain circumstances. To balance these benefits and limitations in mechanical performance, it is advisable to use moderate substitution ratios, preferably below 25%, and utilize chemical admixtures to maintain workability and structural integrity.

This research proves that using SSA in mortar production at replacement ratios below 25% can be a sustainable and viable option. This method sheds light on the benefits and obstacles of utilizing SSA, promoting additional studies to comprehend its potential in the construction industry fully. It is essential to fine-tune the mixture compositions to strike a perfect harmony between sustainability and effectiveness. Moreover, upcoming research should explore using ternary blended materials and geopolymers as alternative sustainable choices, which could provide substantial environmental advantages and help overcome some of the difficulties linked with substituting SSA.

Acknowledgement

We would like to express our sincere gratitude to Saïd Abani for his guidance as our supervisor and to Abderrezak Khellou for his assistance as our assistant supervisor. Special thanks to Mohamed Manni for his valuable help in understanding the experiments, and to Mohammed Laid Tedjani for his support with the DRX study. We also acknowledge the financial support and facilities provided by the Laboratoire: Exploitation et valorisation des ressources naturelles en zones arides at Université Kasdi Merbah Ouargla, which was instrumental in conducting this research.

References

[1] Kelessidis A, Stasinakis AS. Comparative study of the methods used for treatment and final disposal of sewage sludge in European countries. Waste Manag. 2012;32(6):1186-95. https://doi.org/10.1016/j.wasman.2012.01.012

[2] Lin DF, Luo HL, Cheng JF, Zhuang ML. Strengthening tiles manufactured with sewage sludge ash replacement by adding micro carbon powder. Mater Struct Constr. 2016;49(9):3559-67. https://doi.org/10.1617/s11527-015-0739-7

[3] Cong X, Lu S, Gao Y, Yao Y, Elchalakani M, Shi X. Effects of microwave, thermomechanical and chemical treatments of sewage sludge ash on its early-age behavior as supplementary cementitious material. J Clean Prod . 2020;258:120647. https://doi.org/10.1016/j.jclepro.2020.120647

[4] Cyr M, Coutand M, Clastres P. Technological and environmental behavior of sewage sludge ash (SSA) in cement-based materials. Cem Concr Res. 2007;37(8):1278-89. https://doi.org/10.1016/j.cemconres.2007.04.003

[5] Alvarez JI, Veiga R, Martínez-Ramírez S, Secco M, Faria P, Maravelaki PN, et al. RILEM TC 277-LHS report: a review on the mechanisms of setting and hardening of lime-based binding systems. Mater Struct Constr. 2021;54(2). https://doi.org/10.1617/s11527-021-01648-3

[6] Hanein T, Thienel KC, Zunino F, Marsh ATM, Maier M, Wang B, et al. Clay calcination technology: state-of-the-art review by the RILEM TC 282-CCL. Mater Struct Constr. 2022;55(1). https://doi.org/10.1617/s11527-021-01807-6

[7] Lundin M, Olofsson M, Pettersson GJ, Zetterlund H. Environmental and economic assessment of sewage sludge handling options. Resour Conserv Recycl. 2004;41(4):255-78. https://doi.org/10.1016/j.resconrec.2003.10.006

[8] Cieślik BM, Namieśnik J, Konieczka P. Review of sewage sludge management: Standards, regulations and analytical methods. J Clean Prod. 2015;90:1-15. https://doi.org/10.1016/j.jclepro.2014.11.031

[9] Kioumarsi M, Azarhomayun F, Haji M, Shekarchi M. Effect of shrinkage reducing admixture on drying shrinkage of concrete with different W/C ratios. Materials (Basel). 2020 Dec 2;13(24):1-16. https://doi.org/10.3390/ma13245721

[10] Kioumarsi M, Dabiri H, Kandiri A, Farhangi V. Compressive strength of concrete containing furnace blast slag; optimized machine learning-based models. Clean Eng Technol. 2023;13:100604. https://doi.org/10.1016/j.clet.2023.100604

[11] Azarhomayun F, Haji M, Kioumarsi M, Shekarchi M. Effect of calcium stearate and aluminum powder on free and restrained drying shrinkage, crack characteristic and mechanical properties of concrete. Cem Concr Compos. 2022;125:104276. https://doi.org/10.1016/j.cemconcomp.2021.104276

[12] Benhelal E, Zahedi G, Shamsaei E, Bahadori A. Global strategies and potentials to curb CO2 emissions in cement industry. J Clean Prod. 2013;51:142-61. https://doi.org/10.1016/j.jclepro.2012.10.049

[13] Herisson J, Guéguen-Minerbe M, van Hullebusch ED, Chaussadent T. Influence of the binder on the behaviour of mortars exposed to H2S in sewer networks: a long-term durability study. Mater Struct Constr. 2017;50(1). https://doi.org/10.1617/s11527-016-0919-0

[14] Dabiri H, Sharbatdar MK, Kavyani A, Baghdadi M. The Influence of Replacing Sand with Waste Glass Particle on the Physical and Mechanical Parameters of Concrete. Civ Eng J. 2018;4(7):1646. https://doi.org/10.28991/cej-03091101

[15] Kandiri A, Sartipi F, Kioumarsi M. Predicting compressive strength of concrete containing recycled aggregate using modified ann with different optimization algorithms. Appl Sci. 2021;11(2):1-19. https://doi.org/10.3390/app11020485

[16] Farahzadi L, Kioumarsi M. Application of machine learning initiatives and intelligent perspectives for CO2 emissions reduction in construction. J Clean Prod. 2023;384:135504. https://doi.org/10.1016/j.jclepro.2022.135504

[17] Nakic D, Vouk D, Serdar M, Cheeseman CR. Use of MID-MIX® treated sewage sludge in cement mortars and concrete. Eur J Environ Civ Eng. 2020;24(10):1483-98. https://doi.org/10.1080/19648189.2018.1474383

[18] Krishta David T, Karan Nair S. Compressive Strength of Concrete with Sewage Sludge Ash (SSA). IOP Conf Ser Mater Sci Eng. 2018;371(1). https://doi.org/10.1088/1757-899X/371/1/012009

[19] Office National des Assainissement (ONA). 2019.

[20] Valls S, Yagüe A, Vázquez E, Mariscal C. Physical and mechanical properties of concrete with added dry sludge from a sewage treatment plant. Cem Concr Res. 2004;34(12):2203-8. https://doi.org/10.1016/j.cemconres.2004.02.004

[21] Istuque DB, Soriano L, Akasaki JL, Melges JLP, Borrachero M V., Monzó J, et al. Effect of sewage sludge ash on mechanical and microstructural properties of geopolymers based on metakaolin. Constr Build Mater. 2019;203:95-103. https://doi.org/10.1016/j.conbuildmat.2019.01.093

[22] Tutur N, Dahalan NH, Rosseli SR, Johari MA. Rice husk ash and sewage sludge ash as sustainable replacement material for concrete. J Phys Conf Ser. 2019;1349(1). https://doi.org/10.1088/1742-6596/1349/1/012092
[23] Monzó J, Payá J, Borrachero M V, Peris-Mora E. Mechanical behavior of mortars containing sewage sludge ash (SSA) and Portland cements with different tricalcium aluminate content. Cem Concr Res. 1999;29(1):87-94. https://doi.org/10.1016/S0008-8846(98)00177-X
[24] Pan SC, Tseng DH, Lee CC, Lee C. Influence of the fineness of sewage sludge ash on the mortar properties. Cem Concr Res. 2003 Nov 1;33(11):1749-54. https://doi.org/10.1016/S0008-8846(03)00165-0
[25] Garcés P, Pérez Carrión M, García-Alcocel E, Payá J, Monzó J, Borrachero M V. Mechanical and physical properties of cement blended with sewage sludge ash. Waste Manag. 2008 Dec;28(12):2495-502. https://doi.org/10.1016/j.wasman.2008.02.019
[26] Chang FC, Lin JD, Tsai CC, Wang KS. Study on cement mortar and concrete made with sewage sludge ash. Water Sci Technol. 2010;62(7):1689-93. https://doi.org/10.2166/wst.2010.459
[27] Lynn CJ, Dhir RK, Ghataora GS, West RP. Sewage sludge ash characteristics and potential for use in concrete. Constr Build Mater. 2015;98:767-79. https://doi.org/10.1016/j.conbuildmat.2015.08.122
[28] Xia Y, Liu M, Zhao Y, Chi X, Lu Z, Tang K, et al. Utilization of sewage sludge ash in ultra-high performance concrete (UHPC): Microstructure and life-cycle assessment. J Environ Manage. 2023 Jan 15;326:116690. https://doi.org/10.1016/j.jenvman.2022.116690
[29] Gu C, Ji Y, Yao J, Yang Y, Liu J, Ni T, et al. Feasibility of recycling sewage sludge ash in ultra-high performance concrete: Volume deformation, microstructure and ecological evaluation. Constr Build Mater. 2022 Feb 7;318:125823. https://doi.org/10.1016/j.conbuildmat.2021.125823
[30] Nurul Nazierah MY, Kartini K, Hamidah MS, Nuraini T. Compressive strength and water absorption of sewage sludge ash (SSA) mortar. InCIEC 2015: Proceedings of the International Civil and Infrastructure Engineering Conference. Springer Singapore, 2016. https://doi.org/10.1007/978-981-10-0155-0_19
[31] Kourd AAE. Properties of concrete incorporating natural and crushed stone very fine sand. Mater J. 1989;86(4):417-24. https://doi.org/10.14359/2201
[32] Pinarli V. Sustainable Waste Management-Studies on the use of sewage sludge ash in the construction industry as concrete material. In: Sustainable Construction: Use of Incinerator Ash. Thomas Telford Publishing; 2000. p. 415-25.
[33] NF EN 196-1. Methods of testing cement. Part 1: determination of strength. CEN; 2006.
[34] Berlier J baptiste. Contrôles de production Certificat de conformité Sable Normalisé CEN , EN 196 - 1. 1910;1910.
[35] European Committee for Standardization. EN 197-1: Cement - Part 1: Composition, Specifications and Conformity Criteria for Common Cements. CEN; 2022.
[36] European Committee for Standardization. NA 442 v: Guidelines for the application of EN 1990 in the context of national regulations. CEN; 2013.
[37] INACEM. Ciment Portland. 2013;1-2.
[38] NF EN 1015-3. NF EN 1015-3Methods of test for mortar for masonry - Part 3: Determination of consistence of fresh mortar (by flow table). 2004.
[39] Chen Z, Poon CS. Comparative studies on the effects of sewage sludge ash and fly ash on cement hydration and properties of cement mortars. Constr Build Mater. 2017 Nov 15;154:791-803. https://doi.org/10.1016/j.conbuildmat.2017.08.003
[40] Aadraoui M, Elbaghdadi M, Rais J, Barakat A, Ennaji W, Karroum LA, et al. Effect of incineration of sewage sludge on the evolution of physicochemical characterization and mineralogical properties. J Mater Environ Sci. 2017;8(8):2800-6.
[41] Vouk D, Serdar M, Vučinić AA. Use of incinerated sewage sludge ash in cement mortars: Case study in Croatia. Teh Vjesn. 2017 Feb 1;24(1):43-51. https://doi.org/10.17559/TV-20150901095705
[42] Guo S, Dong R, Chang Z, Xie Y, Chen G, Long G. Performance and microstructure of sustainable cementitious materials mixed by municipal sewage sludge ash, slag, and fly ash. Constr Build Mater. 2023 Feb 27;367:130028. https://doi.org/10.1016/j.conbuildmat.2022.130028
[43] Monzó J, Paya J, Borrachero M V., Córcoles A. Use of sewage sludge ash(SSA)-cement admixtures in mortars. Cem Concr Res. 1996 Sep 1;26(9):1389-98. https://doi.org/10.1016/0008-8846(96)00119-6
[44] Lynn CJ, Dhir RK, Ghataora GS, West RP. Sewage sludge ash characteristics and potential for use in concrete. Constr Build Mater. 2015;98:767-79. https://doi.org/10.1016/j.conbuildmat.2015.08.122
[45] Li JS, Guo MZ, Xue Q, Poon CS. Recycling of incinerated sewage sludge ash and cathode ray tube funnel glass in cement mortars. J Clean Prod. 2017 May 20;152:142-9. https://doi.org/10.1016/j.jclepro.2017.03.116
[46] da Cunha Oliveira JV, Chagas LSVB, de Andrade Meira FFD, Carneiro AMP, de Melo Neto AA. Study of the Potential of Adhesion to the Substrate of Masonry and Tensile in the Flexion in Mortars of Coating with Gray of the Sewage Sludge. Mater Sci Forum . 2020 Oct;1012:256-61. https://doi.org/10.4028/www.scientific.net/MSF.1012.256

[47] Pinarli V, Emre NK. Constructive sludge management - reutilization of municipal sewage sludge in Portland cement mortars. Environ Technol . 1994 Sep 1;15(9):833-41. https://doi.org/10.1080/09593339409385490
[48] Nakic D, Vouk D, Serdar M, Cheeseman CR. Use of MID-MIX® treated sewage sludge in cement mortars and concrete. Eur J Environ Civ Eng. 2020 Aug 23;24(10):1483-98. https://doi.org/10.1080/19648189.2018.1474383
[49] Vouk D, Nakic D, Stirmer N, Cheeseman C. Influence of combustion temperature on the performance of sewage sludge ash as a supplementary cementitious material. J Mater Cycles Waste Manag. 2018;20(3):1458-67. https://doi.org/10.1007/s10163-018-0707-8
[50] Pan SC, Tseng DH, Lee C. Use of sewage sludge ash as fine aggregate and pozzolan in portland cement mortar. J Solid Waste Technol Manag. 2002 Aug 1;28:121-30.
[51] Boshoff WP, Combrinck R. Modelling the severity of plastic shrinkage cracking in concrete. Cem Concr Res. 2013;48:34-9. https://doi.org/10.1016/j.cemconres.2013.02.003
[52] Kappel A, Ottosen LM, Kirkelund GM. Colour, compressive strength and workability of mortars with an iron rich sewage sludge ash. Constr Build Mater. 2017 Dec 30;157:1199-205. https://doi.org/10.1016/j.conbuildmat.2017.09.157
[53] Lin DF, Lin KL, Chang WC, Luo HL, Cai MQ. Improvements of nano-SiO2 on sludge/fly ash mortar. Waste Manag. 2008 Jan 1;28(6):1081-7. https://doi.org/10.1016/j.wasman.2007.03.023
[54] Rahman MM, Khan MMR, Uddin MT, Islam MA. Textile Effluent Treatment Plant Sludge: Characterization and Utilization in Building Materials. Arab J Sci Eng. 2017;42(4):1435-42. https://doi.org/10.1007/s13369-016-2298-9
[55] Pan SC, Lin CC, Tseng DH. Reusing sewage sludge ash as adsorbent for copper removal from wastewater. Resour Conserv Recycl. 2003 Aug 1;39(1):79-90. https://doi.org/10.1016/S0921-3449(02)00122-2
[56] Federico LM, Chidiac SE. Waste glass as a supplementary cementitious material in concrete-critical review of treatment methods. Cem Concr Compos. 2009;31(8):606-10. https://doi.org/10.1016/j.cemconcomp.2009.02.001

Blank Page

Research on Engineering Structures & Materials
www.jresm.org

Research Article

Variable tube geometry micro channel heat exchanger (MCHX) using analytical and CFD analysis

Ram A[a], P D Jeya Kumar *[,b], Prince Arockia Doss [c]

Dept. of Mechanical Eng., B.S. Abdur Rahman Crescent Institute of Science and Technology, India

Article Info

Article History:

Received 05 Oct 2024

Accepted 29 Jan 2025

Keywords:

Variable geometry;
Calorie meter;
Heat transfer coefficient;
Analytical calculation;
CFD

Abstract

The aim of this study is to improve condenser performance by incorporating unique tubes and shapes that control the volume of refrigerant. Analytical calculations were performed to determine hydraulic diameters for various tubes and port shapes. The heat and pressure drop across the condenser were estimated using the calculated hydraulic diameters. The refrigerant pressure drop correlation was chosen based on its advantages, and the findings were compared to experimental data (component calorimeter results). For the first time, two-phase density was calculated analytically, and its impact on heat transfer was investigated. The analytical results were compared to CFD simulation and experimental data. The findings demonstrated that an analytical method may be employed in the early stages of design during the development of automotive cooling units and that it could then be correlated with experimental data. This will eliminate the cost of developing prototype parts and shorten the lead time to market.

© 2025 MIM Research Group. All rights reserved.

1. Introduction

A compact heat exchanger is a common piece of equipment used to effectively transfer heat between fluids. It is differentiated by laminar flow, small flow passageways, large heat transfer coefficients, and a high heat transfer area to volume ratio. The goal of compact heat exchangers is to reduce the size of the heat exchanger installation. They are designed to have a high area density, or a large area of heat transfer surface per heat exchanger volume. Plate and frame, plate-fin, spiral, ceramic, welded plate, brazed plate, and printed circuit are some examples of compact heat exchanger designs. Although there is little literature on the installation of small heat exchangers in the aluminium industry, efforts are being made to reduce installation sizes.

The heating, ventilation and air conditioning (HVAC) sectors have recently been interested in smaller heat exchangers, which are utilized in residential, commercial, and automobile air conditioning systems. The compact heat exchanger is a device used in air conditioner evaporators, car radiators & condensers, electronic cooling devices, charge air coolers, and cryogenic exchangers. Various enhanced surfaces have been created to increase heat transfer performance while reducing the size and weight of heat exchangers. Plain, wavy, offset, perforated, pin, and louvered fins are examples of common fin geometries. In a small automobile condenser, complicated geometries are often configured in a crossflow configuration with a louvered fin shape. Thermal resistance often dominates the airside of small heat exchangers, making about 80% of the overall thermal resistance, since the surface area for heat transfer on the air side is much bigger than the refrigerant side. Therefore, any enhancement in airside heat transfer enhances the heat exchanger's total performance. A thorough examination of how operating parameters affect air-side pressure drop and heat transfer in MCHX under wet surface conditions was presented by Srisomba et al. [1]. The important variables affecting heat transfer performance were emphasized

*Corresponding author: pdjeyakumar@crescent.education
[a]orcid.org/ 0000-0002-7358-0304; [b]orcid.org/ 0000-0003-0298-9468; [c]orcid.org/ 0009-0003-6833-3936
DOI: http://dx.doi.org/10.17515/resm2025-472an1005rs

and suggested correlations between pressure drop and heat transfer coefficient were presented. Kolepaka et al. [2] focused on comparing heat transfer rates between unidirectional parallel flow and bidirectional counterflow arrangements in heat exchangers. The study involved computational fluid dynamics (CFD) analysis and thermal analysis for various fluids (such as hot water, R134A, R22, and R600A) and different heat exchanger materials (aluminium and copper). The results indicate that counterflow exhibits higher heat transfer coefficients but lower heat transfer rates compared to parallel flow. Furthermore, the highest heat flux is achieved in a counterflow heat exchanger when using R600A as the refrigerant and copper as the material. Kabar et al. [3] studied a two-dimensional steady-state heat transfer problem in two parallel-plate microchannel heat sinks.

S. Singh and Kukreja [4] focused on the experimental calculation of the condensation heat transfer coefficient (HTC) in micro-fin tubes with different helix angles (15° and 18°). The experiments were carried out using refrigerant R-410A at various mass fluxes, vapor qualities, and saturation temperatures. The results show that the average heat transfer coefficients in micro-fin tubes were 1.15-1.47 times larger than those in smooth tubes. With an average variation of 5.71%, the generated correlation is in line with the experimental results. The results advance our knowledge and design of heat exchangers and offer important new insights on condensation heat transfer in micro fin tubes. Louver-directed flows, on the other hand, occurred when airflow is parallel to louvers at high Reynolds numbers.

The phenomenon was further validated by Achaichia and Cowell [5]. Chang and Wang [6] investigated and validated correlations for louvered fins using experimental results of heat transfer characteristics of various louver fin shapes. The parallel branching of R-134a and R-410A upward flow into mini-channel tubes from a circular header for the mass flux from 92 to 277 kg/m^{2}s was studied by Kim and Bullard [7]. A parallel-flow heat exchanger with a two-pass configuration was the subject of an R-410A flow distribution study conducted by Kim [8]. For an input quality of 0.3 and a mass flux ranging from 50 kg/m^{2}s to 70 kg/m^{2}s, tubes were heated to maintain the test section outlet superheat at 5°C.

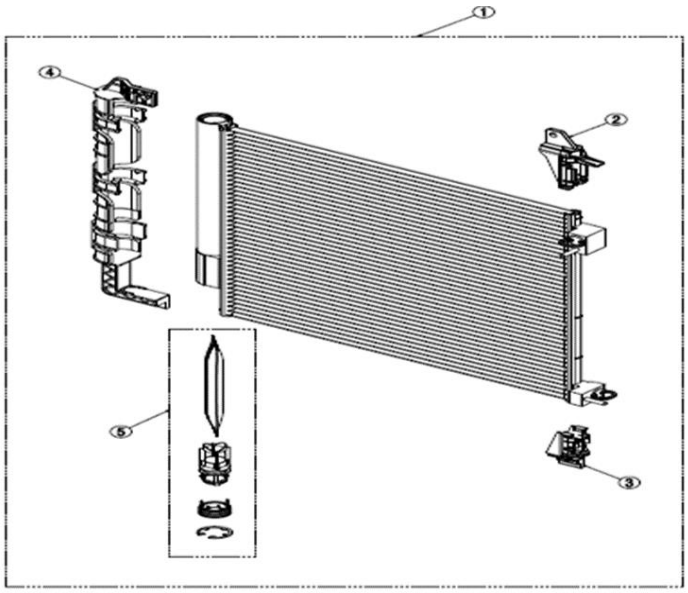
A Mathematical model for a parallel flow condenser that takes the dispersion of refrigerant flow was proposed by Liang et al. [9]. Investigations were conducted on the effects of aspect ratio, mass flow, and pass arrangement on pressure drop, heat transfer, and flow distribution. It has been discovered that altering the aspect ratio or pass arrangement has a greater impact on heat capacity than on pressure drop and flow distribution. Automotive heat exchangers were studied experimentally and through simulation, and a distributed parameter model was created and verified using coil designer software. According to research, condensers with shorter louvered fins may hold 3–8.6% more heat than those with longer fins [10]. To shorten the study time, numerical studies of the louvered fin array have been conducted extensively recently. A model based on finite volume was introduced by Panda et al. [11] to study microchannel heat exchangers with changeable tube and fin shapes. It was believed that the refrigerant flow into the tubes was distributed equally, and the suggested design's advantages included improved material usage and heat exchanger performance. These correlations did, however, significantly deviate from actual results because of disparate experimental and data reduction techniques.

This study's primary goal is to determine how various tube geometries affect pressure drop and heat rejection using analytical and computational fluid dynamics methods. According to reports, a number of improved surfaces were investigated to enhance air-side heat transfer capabilities while lowering the weight and size of the heat exchangers. These surfaces include simple, wavy, offset, perforated, pin, and louvered fins. Characterizing the frictional pressure loss in two-phase flow is an important factor to take into account when designing condenser/evaporator operations for air conditioning and refrigeration applications. As a first step, the two-phase density was determined analytically, and the consequences of heat transfer on the refrigerant side were investigated. With the increasing requirement to minimize the overall refrigerant charge in refrigeration systems, many heat exchanger tubes now have hydraulic diameters less than 1.2 mm. Despite this tendency, there has been little investigation on the modelling of two-phase pressure loss in micro-channels

of small diameters. As a result, this study intends to fill this gap by comparing research data to current correlations, which primarily apply to greater diameters (Di > 5 mm) and small tubes.

2. Model of Automotive Condenser (Heat Exchanger)

The radiator where the gaseous refrigerant loses heat and transforms back into a liquid is called the air-conditioning condenser, and it is placed between the engine-cooling radiator and the car's grille. The interior is cooled by the liquid refrigerant as it passes through the dashboard's evaporator. An automotive condenser is constituted of tubes, inlet and outlet manifolds and fins. Partitions within the condenser's manifolds will guide the refrigerant flow along a predetermined direction. The overall contact surface area between the tube and the refrigerant increases when an efficient route arrangement is created. By giving the cooling medium (air) a wide surface area, the fins will assist heat to be forced into convection mode released from refrigerant through the connecting tubes. For the condenser to function, this heat rejection is essential. Fig. 1 depicts a condenser model.

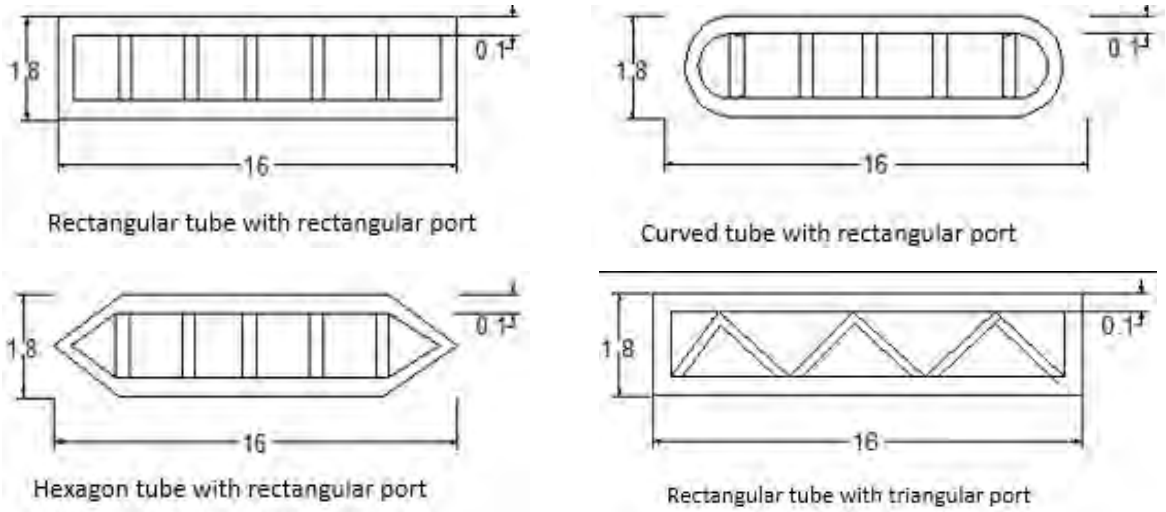


05	DRYER BAG ASSEMBLY + RETAINING RING 5.1 DRYER BAG 5.2 FILTER 5.3 KOMO PLUG ASSEMBLY 5.4 RETAINING RING
04	KOMO SIDE PASTIC FRAME
03	CLASSICAL SIDE PLASTIC FRAME BOTTOM
02	CLASSICAL SIDE PLASTIC TOP FRAME
01	CONDENSER CPL/ASSY
SR. NO.	DESCRIPTION

Fig. 1. Condenser model

3. Tube Hydraulic Diameter Calculation

The geometrical sections of the tube considered in the study are oval, hexagonal, and rectangular, with rectangular and triangular ports for each section as shown in Fig. 2.



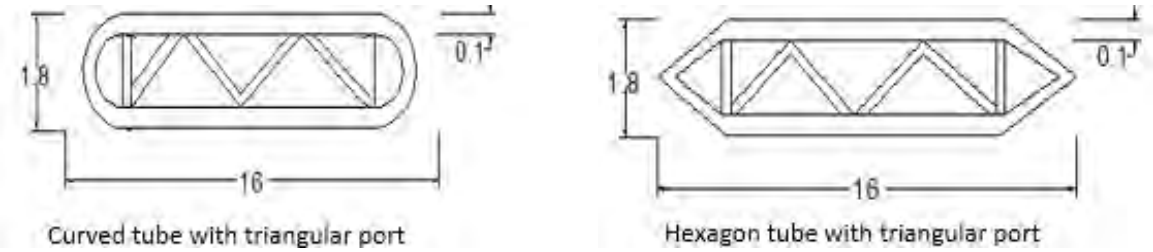


Fig. 2. Various Novel condenser tube and port shapes

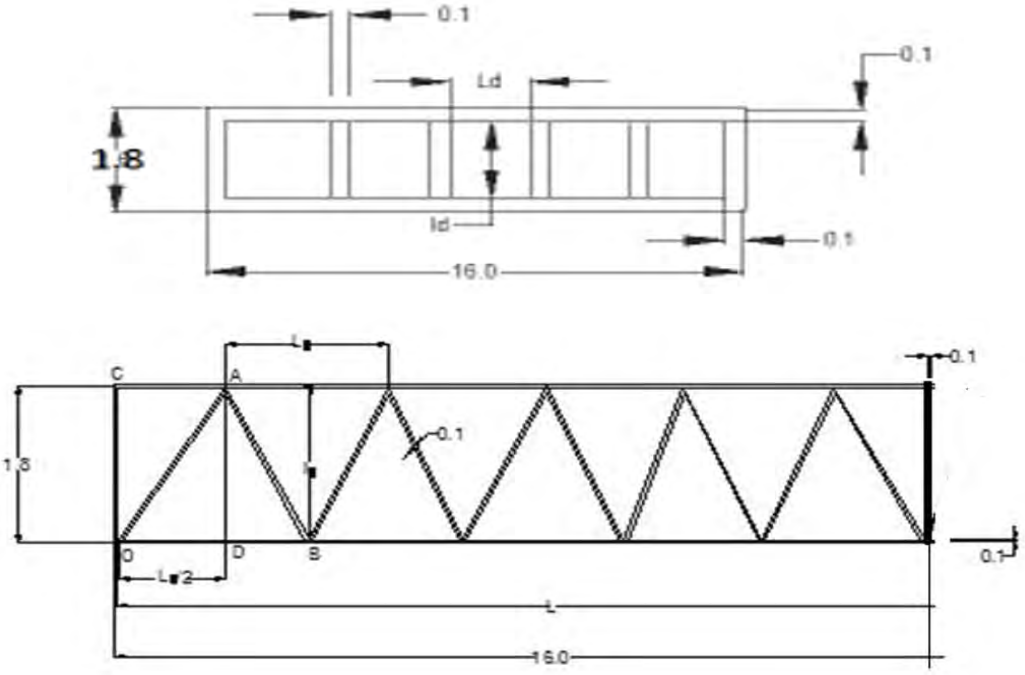


Fig. 3. Rectangular section with rectangular ports and triangular ports

Geometrical properties such as hydraulic diameter, aspect ratio, and perimeter are determined for the considered geometrical sections using mathematical techniques [12]. For evaporators, condensers, and heating and cooling coils under all operating conditions, a comprehensive general-purpose modelling tool for air/refrigerant heat exchangers has been created. Examples of Rectangular section with rectangular and triangular ports are shown in Fig. 3. As per Fig. 3,

- L = 15.8 mm (overall length in mm)
- l_d = 1.5 mm (height of the rectangle in mm)
- l'_d = 1.8 mm (outer height of the triangle in mm)
- L_d = triangle base length in mm
- l = triangle side length in mm

$$r_d = \frac{L_d}{l_d} \tag{1}$$

Aspect ratio

- θ = Base angle of iso lateral triangle
- N = Total number of Triangle (except semi end triangle)

$$n = \frac{N}{2}$$ = number of triangles in one side direction (2)

$$P_{w1} = \left(3 \times N \big/ \tan\theta\right) \times \left(\frac{1}{\cos\theta} + 1\right) \quad (3)$$

$$P_{w2} = \left(\frac{L_d}{2} + l + l_d\right) \quad (4)$$

Perimeter of end triangle

$$P'_w = 1.5\left[\frac{2}{\tan\theta} \times \left(\frac{1}{\cos\theta} + 1\right) \times (N+1) + 2\right] \quad (5)$$

P_w=Fluid flow surface area per unit length, D_h = hydraulic diameter

$$D_{h1} = \left(4 \times A \big/ P_{w1}\right) \quad (6)$$

$$D_{h2} = \left(4 \times A \big/ P_{w2}\right) \quad (7)$$

Where, A = Frontal Area of fluid flow passage in 'mm2

The expressions for aspect ratio & perimeter for variable geometry are derived based on the geometry and shape of the tube & ports. Based on these expressions, the hydraulic diameters for each tube shape were calculated [13]. The effects of the roughness parameters on heat transfer and friction characteristics were systematically investigated in a dimpled tube. The geometrical parameters are deduced from the basic dimensioning details from the tube geometry, the shape differences are captured using hydraulic diameter and the perimeters [6].

Table 1. Tube Hydraulic diameter for variable geometry

Sections	Aspect ratio (r_d)	Perimeter P_w in mm	Hydraulic Diameter D_h in mm
Rectangular tube with rectangular ports	$r_d = \frac{9.9375}{n} - 0.062$	$P_w = 3.2(1 + r_d)$	$D_h = \frac{3.2 \times r_d}{(1 + r_d)}$
Hexagon tube with rectangular ports	$r_d = \frac{8.8125}{n} - 0.062$	$P_w = 3.2(1 + r_d)$	$D_h = \frac{3.2 \times r_d}{(1 + r_d)}$
Oval tube with rectangular ports	$r_d = \frac{8.8125}{n} - 0.062$	$P_w = 3.2(1 + r_d)$	$D_h = \frac{3.2 \times r_d}{(1 + r_d)}$
Rectangular tube with rectangular ports	$r_d = \left(\frac{2}{\tan\theta}\right)$	$P_{w1} = \left(3 \times N \big/ \tan\theta\right) \times \left(\frac{1}{\cos\theta} + 1\right)$	$D_{h1} = \left(4 \times A \big/ P_{w1}\right)$
Hexagon tube with rectangular ports	$r_d = \left(\frac{2}{\tan\alpha}\right)$	$P_w = \frac{3}{\tan\alpha}\left[1 + \frac{1}{\cos\alpha}\right]$	$D_h = \frac{4 \times A}{P_w}$
Oval tube with rectangular ports	$r_d = \left(\frac{2}{\tan\alpha}\right)$	$P_{w1} = 1.97485 + \frac{1.5}{\sin\alpha}$	$D_h = \left(\frac{4 \times A}{P_w}\right)$

3.1 Two Phase Pressure Drop Correlations

As shown in equations 8, 9, and 10, a number of the two-phase pressure drop correlations are based on the separated flow model created by Lockhart and Martinelli (1949), Friedel (1979), and Chisholm (1967) [14, 15 and16]. Notably, the present study marks the first instance of conducting analytical calculations for two-phase refrigerant flow in micro-channels of this scale. The comparison of these correlations with the data obtained from the study will contribute to a more comprehensive understanding of two-phase pressure drop characteristics in small-diameter extruded aluminium micro-channels.

- Lockhart Martinelli Correlation

$$\left(\frac{dp}{dz}\right)=\varphi_L\left(\frac{dp_F}{dz}\right)_L$$
$$\varphi_L=1+\frac{C}{X}+\frac{1}{X^2},\ \varphi_G=1+CX+X^2 \tag{8}$$

- Friedel Correlation

$$\left(\frac{dp}{dz}\right)=\varphi_{LO}\left(\frac{dp_F}{dz}\right)_{LO}$$
$$\varphi_{LO}=E+\frac{3.24\times F\times H}{Fr^{0.045}\times we^{0.035}} \tag{9}$$

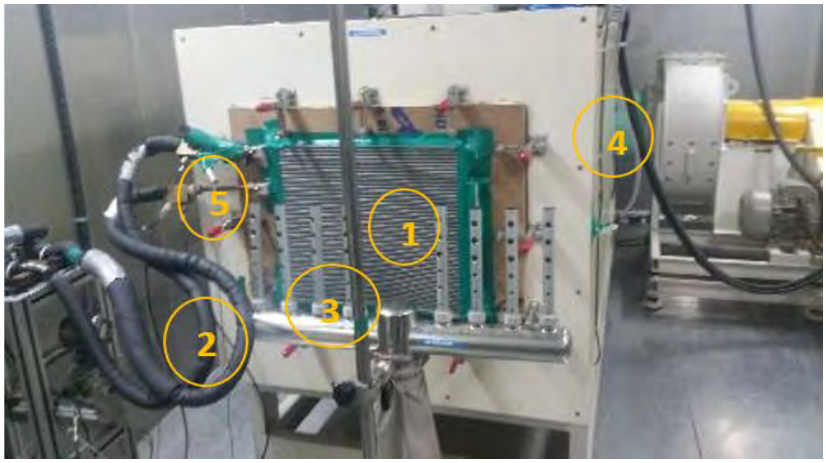
- Chisholm Correlation

$$\left(\frac{dp}{dz}\right)=\varphi_{LO}\left(\frac{dp_F}{dz}\right)_{LO}$$
$$\varphi_L=1+(Y^2-1)*\left\{Bx^{\left(\frac{2-n}{n}\right)}(1-x)^{\left(\frac{2-n}{2}\right)}+x^{2-n}\right\} \tag{10}$$

In a related study by Liang Ye, Ming Wei Tong, and Xin Zeng [17], the heat transfer performances of parallel flow (PF) and multi-parallel pass condensers were investigated at air velocities of 2.5 m/s and 4.5 m/s. The results clearly indicate that the overall heat transfer of the Multi Parallel Pass (MPP) condenser exhibited a higher performance, surpassing the parallel flow condenser by 10% for an automotive application. These findings underscore the potential advantages of the multi-parallel pass configuration in enhancing heat transfer efficiency in the context of automotive condenser applications. In another study [18], a visualization experiment has been carried out to study the effect of the header and channels' orientations on the phase distribution of two-phase flow in three parallel micro-channels. The pressure drops properties of R134a within multiport micro-channels on several refrigerants, including R236ea (low pressure) and R410A, have been experimentally studied [19].

4. Experimental and Analytical Results

The experiment involved the base configuration of an oval tube shape with a rectangular port in the condenser calorimeter, as depicted in Figure 4. The test rig is designed for assessing the performance of a heat exchanger. The setup includes provisions for supplying high-pressure air to the cold side of the test unit, consisting of a blower, dampers, and necessary instruments. The test rig also incorporates a water inlet system, with refrigerant supplied through the tube (hot) side of the test unit. During the experiments, the mass flow rate of the refrigerant was adjusted using a flow control valve, ranging from 3 to 7 kg per minute (kg/m). Simultaneously, the air velocity is controlled by adjusting the damper position, ranging from 2 to 10 meters per second (m/s). Measurements of refrigerant outlet temperature, air inlet and outlet temperatures, and pressure drops across the air and sides of the refrigerant are recorded for different mass flow rates. Based on these measurements, the performance of the heat exchanger is estimated, and results are plotted graphically.



[1]Condenser
[2]Refrigerant Pipe
[3]Air flow sensors
[4]Wind duct
[5]Refrigerant sensor

Fig. 4. Experimental setup of condenser calorimeter

The temperature measurements of the air-steam mixture are conducted using T-type thermocouple meshes inserted from the top and bottom surfaces of the test section. These meshes consist of multiple thermocouples with an average span-wise interval of 40 mm. Air velocity is measured with a portable anemometer, and the air pressure drop across the heat exchanger is measured using calibrated pressure transducers. The setup also includes pre-calibrated thermocouples to measure refrigerant, inlet, and outlet temperatures, as well as a flow meter to measure the refrigerant volume flow rate. Data acquisition is facilitated through a data acquisition system. To minimize heat loss, all components and pipes are insulated with a 10 mm thick glass wool layer. The experimental setup enables comprehensive data collection, allowing for accurate evaluation and analysis of the heat exchanger's performance.

5. Uncertainty Analysis

Uncertainty in experimental results is inevitable due to various factors such as instrument precision, environmental influences, and measurement methods. Identifying and quantifying these uncertainties helps in assessing the reliability of the findings.

- Thermocouple has a certain degree of accuracy (±1°C, for example), which affects temperature measurements on both the air and refrigerant sides.
- Refrigerant flow rate measurement depends on the flow meter’s accuracy.
- Ambient temperature fluctuations can slightly affect the heat loss or gain, despite the insulation, thus impacting measured temperatures.
- If thermocouples aren't precisely positioned, it can lead to spatial inaccuracies.
- The accuracy of the air velocity measurement depends on how well-calibrated the anemometer is.

The overall uncertainty is influenced by the variability between several experimental runs (repeatability) and possible variations when the experiment is repeated using different setups or operators (reproducibility), particularly if specific conditions or adjustments cannot be replicated exactly each time. Test carried out at an authorized component calorimeter lab in Germany with a high reliability level of the data output. Table 2 displays the experimental findings for the samples with an average input pressure of 16.2 bar (abs), superheat temperature of 25 °C, sub cool temperature of 5 °C, and air temperature of 35 °C. The experimental data was collected using a component calorimeter, and the corresponding results are presented graphically in Figure 5. This experimental setup allowed for the measurement and analysis of specific performance parameters or characteristics, and the graphical representation in Figure 5 serves as a visual depiction of the outcomes derived from the experimentation in the component calorimeter.

Table 2. Experimental results showing multiple samples

Air velocity (m/s)	Parameter	Sample 1	Sample 2	Sample 3	Sample Average
8	Average Heat Rejection kW	20.81	21.37	21.18	21.12
	Air velocity m/s	7.98	7.99	7.99	7.98
	Airside pressure Drop Pa	344.60	350.74	350.68	348.67
	Average Pressure bar	15.94	15.9	16.03	15.96
	Refrigerant side Pressure Drop mbar	2405.75	2352.58	2465.79	2408.04
	Refrigerant Mass flow kg/min	6.71	6.85	6.82	6.79
5	Average Heat Rejection kW	17.56	17.79	17.68	17.67
	Air velocity m/s	5.04	5.05	5.02	5.04
	Airside pressure Drop Pa	167.14	169.64	168.4	168.39
	Average Pressure bar	16.31	16.32	16.32	16.32
	Refrigerant side Pressure Drop mbar	1877.68	1757.96	1921.08	1852.24
	Refrigerant Mass flow kg/min	5.77	5.81	5.79	5.79
2	Average Heat Rejection kW	9.72	9.84	9.67	9.74
	Air velocity m/s	2.05	2.03	2.03	2.03
	Airside pressure Drop Pa	41.32	40.84	41.22	41.13
	Average Pressure bar	16.25	16.28	16.29	16.27
	Refrigerant side Pressure Drop mbar	682.29	657.34	655.89	665.18
	Refrigerant Mass flow kg/min	3.23	3.27	3.21	3.24

Fig. 6 compares experimental and Friedel correlation results, demonstrating good agreement. This suggests the Friedel correlation accurately predicts the phenomenon under study, indicating its usefulness in understanding and predicting system behavior. Additionally, the pressure drop through the condenser for oval-shaped tubes is calculated using these correlations in an analytical technique, and the results correlate with the analytical method as seen in Figures 6, 7, and 8. The results obtained from the Lockhart Martinelli correlations show slight deviations when compared to the experimental results. The Chisholm correlation results exhibit greater deviations in comparison to the experimental results as well as the results obtained from the Friedel and Lockhart Martinelli correlations.

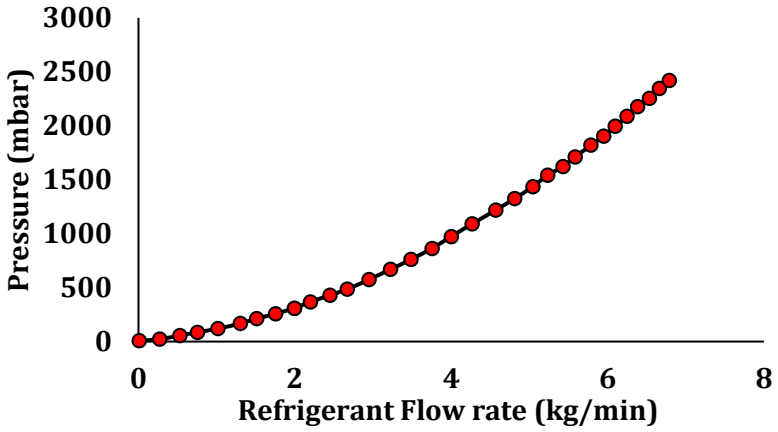


Fig. 5. Experimental refrigerant side pressure drop

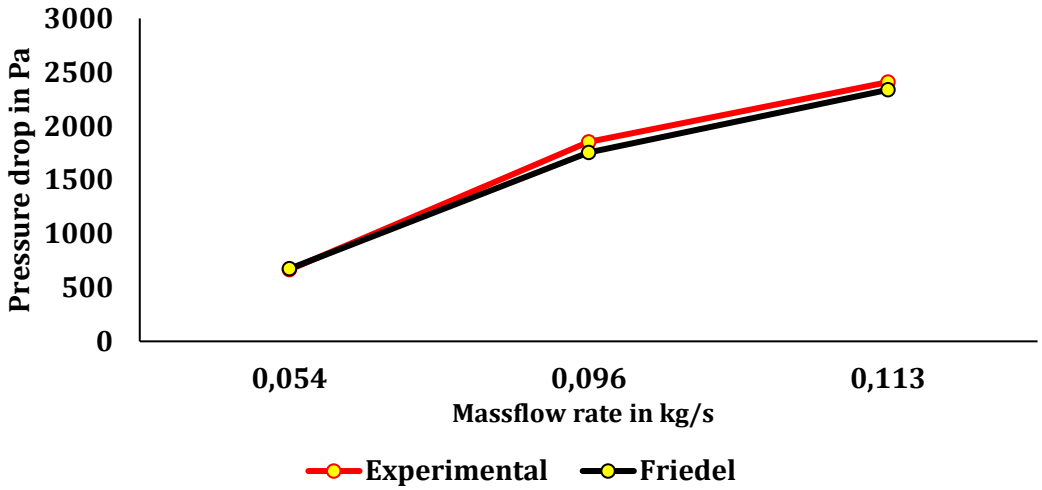


Fig. 6. Friedel correlation vs Experimental

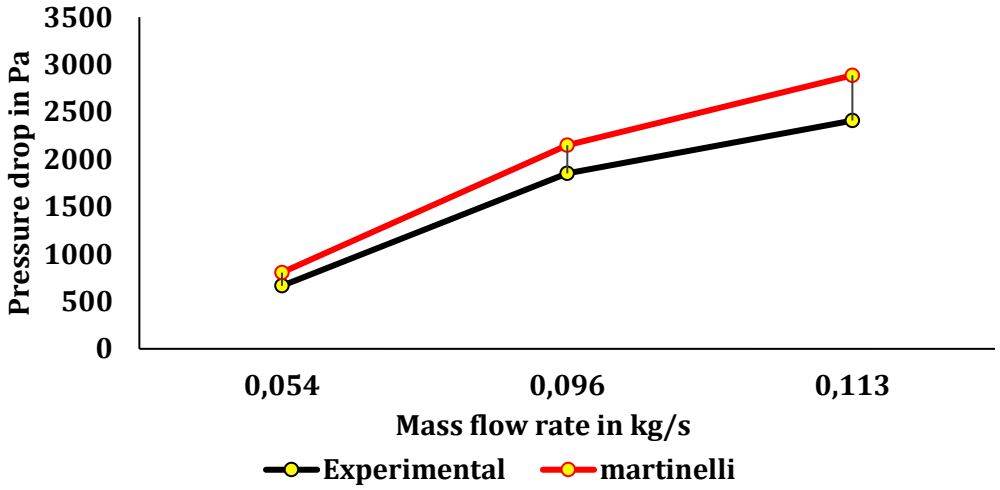


Fig. 7. Experimental vs Lockhart Martinelli

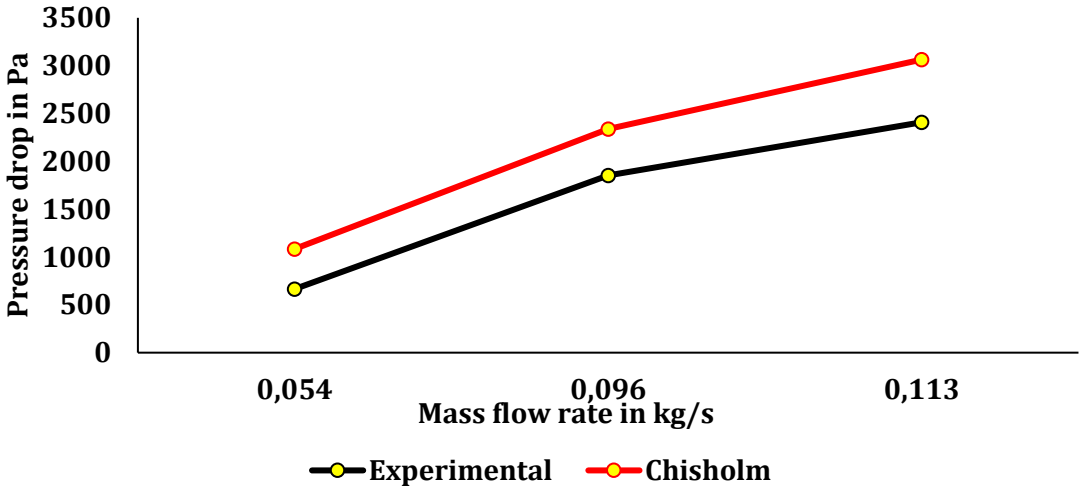


Fig. 8. Experimental vs Chisholm correlation

Table 3. Pressure drops between Analytical data and Experimental data

Ref. Mass flow rate kg/s	Pressure Drop in mbar (Oval-Rec Section)- Correlations			
	Friedel	Lockhart & Martinelli	Chisholm	Experimental Result
0.054	708	855	1140	665
0.096	1842	2282	2464	1852
0.113	2455	3063	3227	2408

Table 3 shows the pressure drop of the Friedel correlation for different refrigerant flow rates (kg/s) that were closer to the experimental results of pressure drop. So, the Friedel correlation was considered for the analytical calculation for different tube and port shapes.

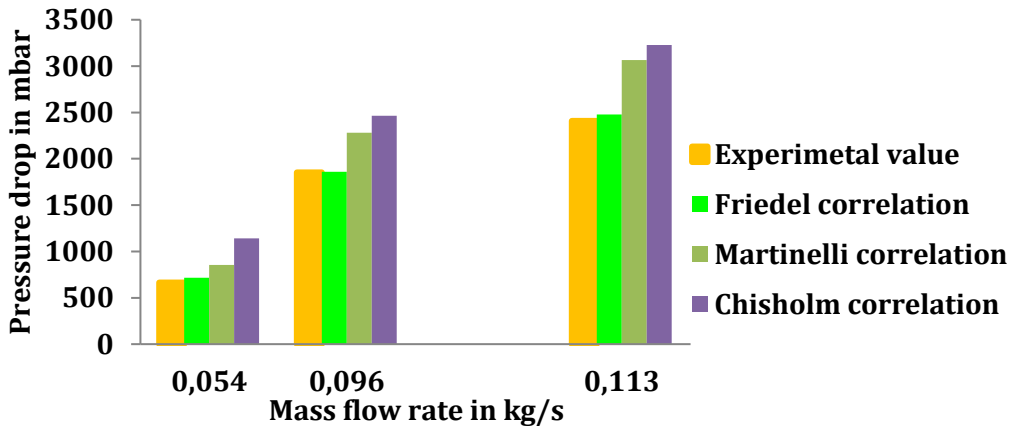


Fig. 9. Summary of correlation data vs Experimental Data

Table 4. Analytical results of variable geometry Pressure drop (Refrigerant side)

Ref. Mass flow rate kg/s	Pressure Drop in mbar using Friedel Correlations					
	Rec-Rec	Oval-Rec	Hex-Rec	Rec-tri	Oval-tri	Hex-tri
0.054	674	708	774	832	920	1207
0.096	1753	1 842	201 5	2164	2394	4421
0.113	2337	2455	2685	2885	3190	5889

The results show that the refrigerant pressure drop for the rectangular port was lesser compared to other tubes and port shapes. Later, with the help of refrigerant pressure drop, the heat rejection for various tube & port shapes was calculated as shown in Table 5. The results show that the tube with a hexagon shape has a better heat transfer coefficient, but the refrigerant side pressure drop is very high.

Table 5. Analytical results of variable geometry Heat transfer co-efficient (Refrigerant side)

Refrigerant Side Heat Transfer Co-efficient (W/m^{2K})						
Refrigerant Mass flow rate (Kg/s)	Rec-Rec	Oval-Rec	Hex-Rec	Rec-tri	Oval-tri	Hex-tri
0.054	2330	2345	2418	2405	2494	3024
0.096	3605	3611	3723	3701	3840	4269
0.113	4102	4118	4246	4221	4379	4869

Further, CFD analysis was made to understand the behavior of heat transfer coefficient and pressure drop for different tube shapes. Using the obtained theoretical correlations, the pressure drops and heat transfer coefficient for various geometrical shapes at different flow rate conditions are calculated. These obtained results are compared with the numerical results. The chosen rectangular tube with rectangular ports as a benchmark analytical result is compared with experimental and numerical results. With the same agreement, analytical and numerical results for the other cases are also compared. The numerical results of heat rejection on the refrigerant side are compared with the experimental results as shown in Table 6. The lesser error percentage revealed that there is good agreement between the analytical and experimental values of heat rejection.

Table 6. Comparison between analytical and experimental Heat rejection (Refrigerant side)

Mass flow rate kg/s	Inlet temp °C	Inlet Enthalpy kJ/kg	Out Temp °C	outlet Enthalpy kJ/kg	Heat rejection (analytical) kJ	Heat rejection (experimental) kJ
0.054	83	460	43	260	10.8	9.72
0.096	83	460	44	262.43	18.9	17.56
0.113	83	460	49	270.07	21.4	20.81

6. CFD Simulation

The numerical approach is the best approach to analyse the two-phase flow behaviour of the refrigerant as a full-scale model. Bensafi, Borg, and Parent [20] studied the computational model of detail design of plate & fin tube heat exchangers for various refrigerant mixtures of R32, R1, 25 & R134a. Ansys-Fluent utilizes a finite volume approach to simulate fluid flow, employing a RANS k-epsilon model. The volume fraction represents the occupied space of each phase in the simulation domain, assuming that each cell is filled with one phase and not empty or a vacuum. The conservation equations for mass and momentum are applied separately to each phase. Heat transfer and energy equations are not considered in this model, and there is no phase change or interphase mass and momentum transfer. The interaction between phases requires additional closure models such as Interaction Length Scale, Interaction Area Density, Drag & Lift Force, etc. These models and parameters are essential for capturing the forces exerted by the phases on each other. Through a detailed examination of heat conduction in solids and a transient 1D analysis, a numerical model [21] of the fluid dynamic and thermal behaviour of condensers and evaporators has been created. The conservation equations (momentum, continuity, energy, and vapor species) are given in Equations 11, 12, 13, and 14, respectively.

- Momentum equation:

$$V_p \frac{\partial \overline{\rho v}}{\partial t} + \dot{m}_{g,e^s} v_{g,e^s} + \dot{m}_{1,e^s} v_{1,e^s} - \dot{m}_{g,w^s} v_{g,w^s} + \dot{m}_{1,w^s} v_{1,w} = (p_P - p_E)A - \bar{\tau}_w P \Delta z - mg \sin\theta \quad (11)$$

- Continuity equation:

$$V_p \frac{\partial \overline{\rho_p}}{\partial t} + \dot{m}_e - \dot{m}_w = 0 \quad (12)$$

- Energy equation:

$$\frac{\partial \check{\rho}_P \bar{e}_P}{\partial t} A\Delta z + \dot{m}_P^s e_e - \dot{m}_W^s e_W = \bar{\dot{q}}_P P \Delta z + \frac{\partial \bar{P}_P}{\partial t} A\Delta z \quad (13)$$

- Vapor species equation:

$$\frac{\partial(\rho \omega_v)}{\partial t} + \nabla(\rho \omega_v \overline{w}) = \nabla(\rho D_e \bar{\nabla} \omega_v) + S_v = 0 \quad (14)$$

The distribution is greatly impacted by the pressure drop that occurs during phase shift in the microchannel tubes used in the suggested system. User-defined functions are to estimate the pressure decrease. Heat transfer models are not used, and associated characteristics are not simulated, despite the fact that heat transfer for phase change within the tubes and consequently influences the pressure drop. Rather, the user-defined pressure drops calculations assume heat flux value as constant for heat transmission in the tubes. For the single- and two-phase superheated areas, different equations are used to calculate the pressure decrease. The tube's intake condition and the percentage of the tube that is occupied by the two-phase region—known as the Length Ratio (LR) and calculated—determine the pressure drop. The Blasius correlation and the Darcy-Weisbach equation are applied to single-phase pressure decrease. A homogeneous formulation with the Smoothed Muller-Steinhagen & Heck friction factor correlation is used to compute the pressure drop for two phase flows. The formulation treats both phases as a homogeneous mixture, though they were one phase with identical velocities. Assuming a homogeneous two-phase mixture, density and viscosity are computed using the Reynolds number. Fig. 10 shows the computational domain.

6.1 Input Parameters for Simulation

There is very little variation in the data above 3 million, which is thought to be the ideal mesh count for this inquiry. Reference pressure is taken as 2408 mbar from the experimental results. A hybrid mesh (hex-dominated mesh) of base mesh size of 1.2 mm with 5 layers is chosen for the simulation. Based on the standard correlation, results are calculated as a rough estimation, and at the same time, numerical results are helped to validate the geometry optimization in an accurate manner. Initially the experimental results are validated with the numerical result; based on this numerical result accuracy, further geometry optimization study was made.

- Refrigerant Properties

Specific heat (Cp)	:1.1604 kJ/kgK
Thermal Conductivity (k)	:0.0182 W/mK
Absolute Viscosity (P)	:1.411e-5 kg/ms
Density (ρ)	:69.589 kg/m^3

- Aluminium material Properties

Density (ρ)	:2719 kg/m^3
Specific heat (Cp)	:0.871 kJ/kg K
Thermal Conductivity (k)	:202.4 W/mK

Normally, analytical study is preferred to compare the experimental results with a moderate accuracy level. For high accuracy and for complex shape & visualization, numerical results are employed. In the numerical analysis of two-phase flow behaviour within the heat exchanger, certain assumptions are typically made to simplify the complex flow and heat transfer dynamics. Those are,

- Flow is often assumed to be steady, meaning that variables like pressure, temperature, and velocity do not change with time. However, the real systems experience transient behaviour, especially during startup or shutdown, so assuming steady-state can overlook fluctuations in temperature and flow rate.
- Flow and temperature across the tube cross-section or at inlets are assumed to be uniform; however, in reality, flow and temperature profiles vary across the tube diameter, especially due to boundary layer development and turbulence.
- Gravitational forces and buoyancy effects are often ignored, especially in horizontal or small-scale models, assuming they have minimal impact.
- Two-phase flow analysis often simplifies phase transitions, assuming smooth transitions between liquid and vapor phases or using an idealized model.

Table 7. Boundary condition for CFD simulation

Refrigerant Inlet Temp	Tr,i	83.4 °C
Refrigerant Pressure	Pr,i	16.2 bar
Mass Flow rate	mref	0.054 kg/s
Air Inlet Temp	Ta,i	35 °C
Convective heat transfer coefficient	(h)	325 w/m^{2}K

The input boundary conditions are specified in Table 7; the mass flow inlet is maintained as constant at the inlet, and pressure outlet boundary conditions are used as outlet boundary conditions. Convective heat transfer coefficient used as a constant wall boundary on the tube outer surface. The surrounding conditions are maintained as atmospheric conditions (35 °C and 1 ATM). The boundary condition for the condenser was considered for the CFD simulation as shown in Fig. 11. The cross section of various tubes was analysed in CFD to understand the temperature and pressure contours across the length for different pass structures.

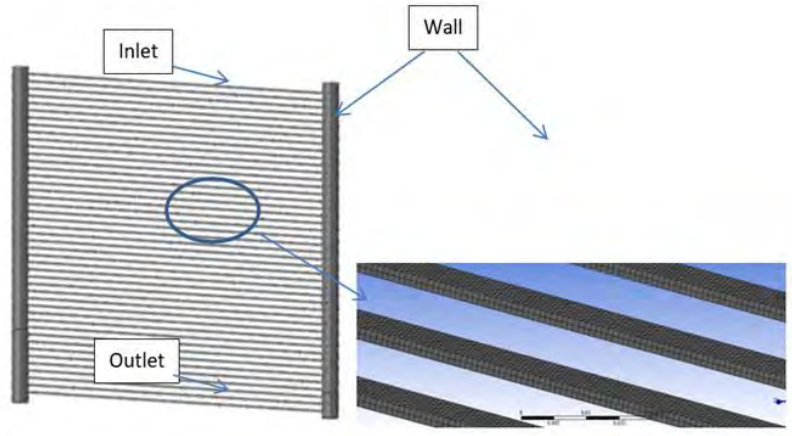


Fig. 10. Computational Domains

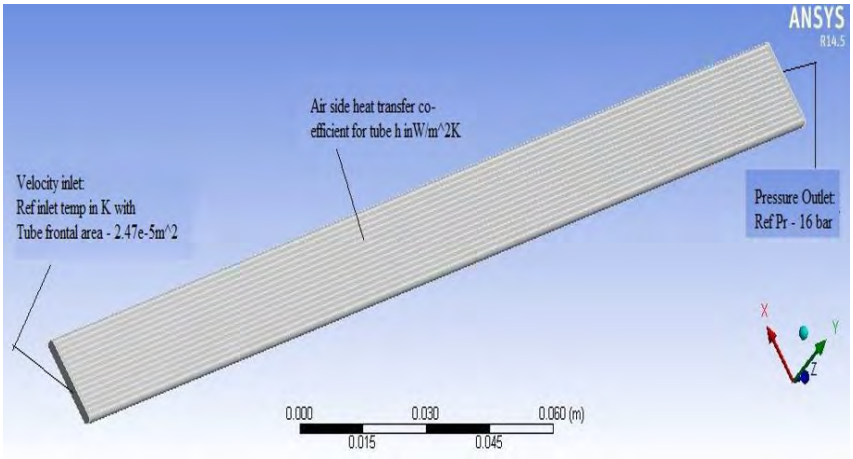


Fig. 11. Boundary condition used in oval shape tube

Numerical analysis of the two-phase refrigerant flow is the best approach to analyse the two-phase flow behaviour of the refrigerant; ANSYS-Fluent is used as a numerical solver. Figs. 12 & 13 show the temperature contour for the oval-shaped tube varies from pass-1 to pass-4, and the temperature drops from 74°C to 48°C at the outlet of the condenser, respectively. Due to the flow of the refrigerant, the heat to the atmosphere is rejected. Full model simulation was carried out to understand the behaviour of two-phase flow in refrigerant tubes in contact with the frontal airflow, which rejects the heat into the atmosphere. The heat is absorbed by the evaporator due to cabin heat load to attain the thermal equilibrium.

Table 8. Mesh independent study

Mesh Count in (million)	Pressure Drop mbar	Result Variation in %
1.5	2650	9.2
2.0	2580	6.67
2.5	2523	4.78
3.0	2494	3.57
3.5	2491	3.46

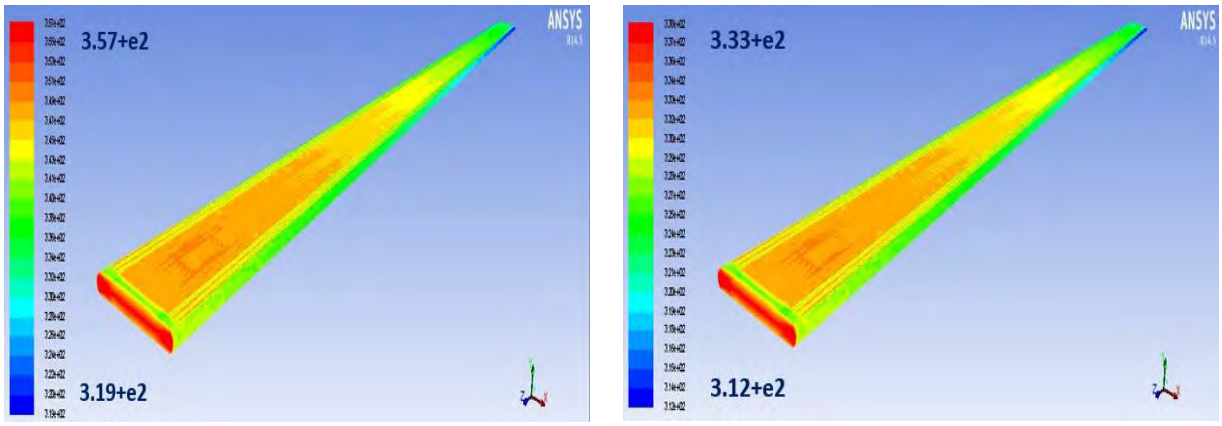


Fig. 12. CFD simulation of pass 1 and 2

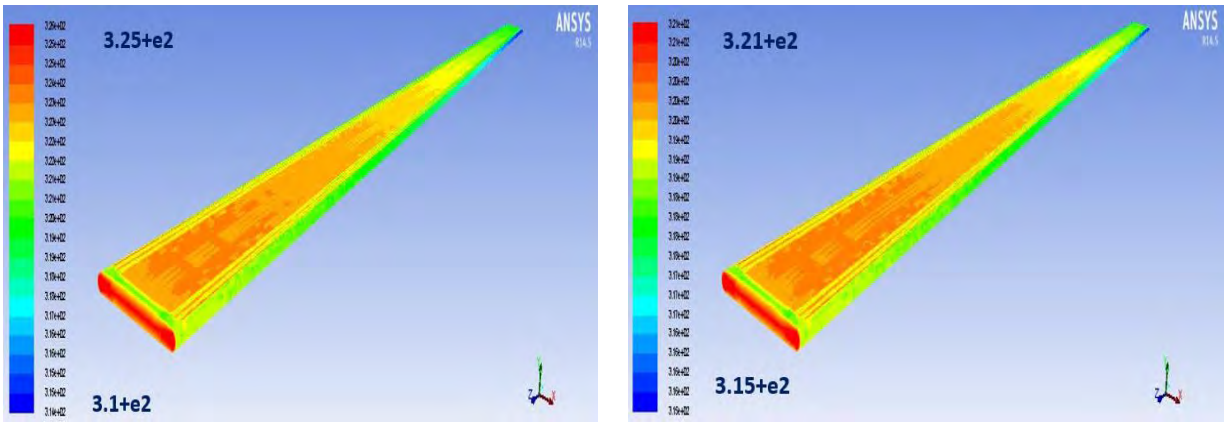


Fig. 13. CFD simulation of pass 3and 4

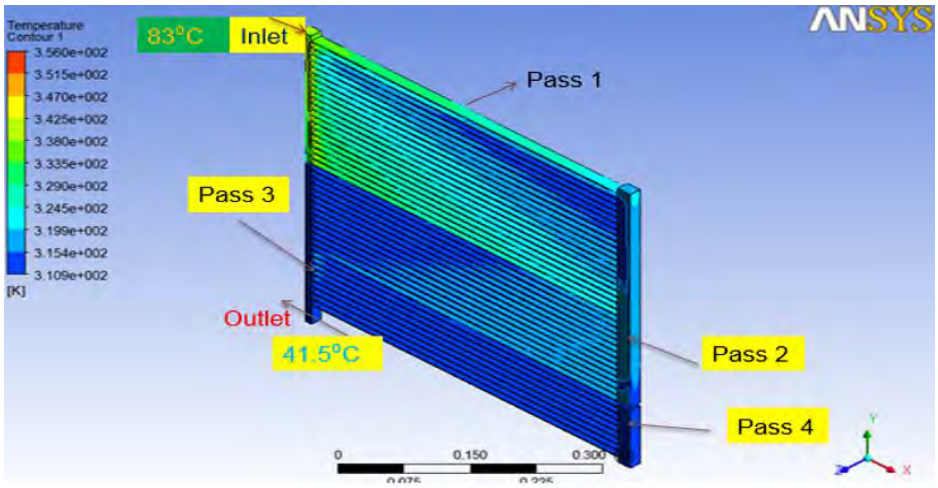


Fig. 14. CFD of condenser model with temperature contour

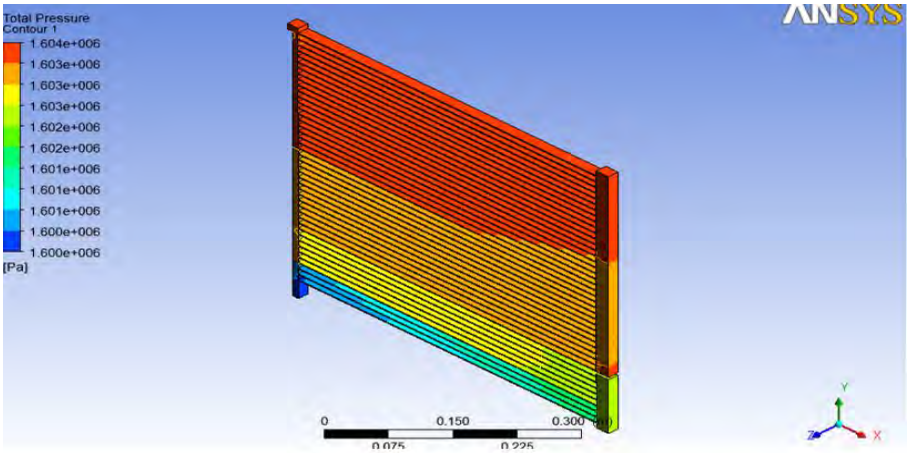


Fig. 15. CFD of condenser model with pressure contour

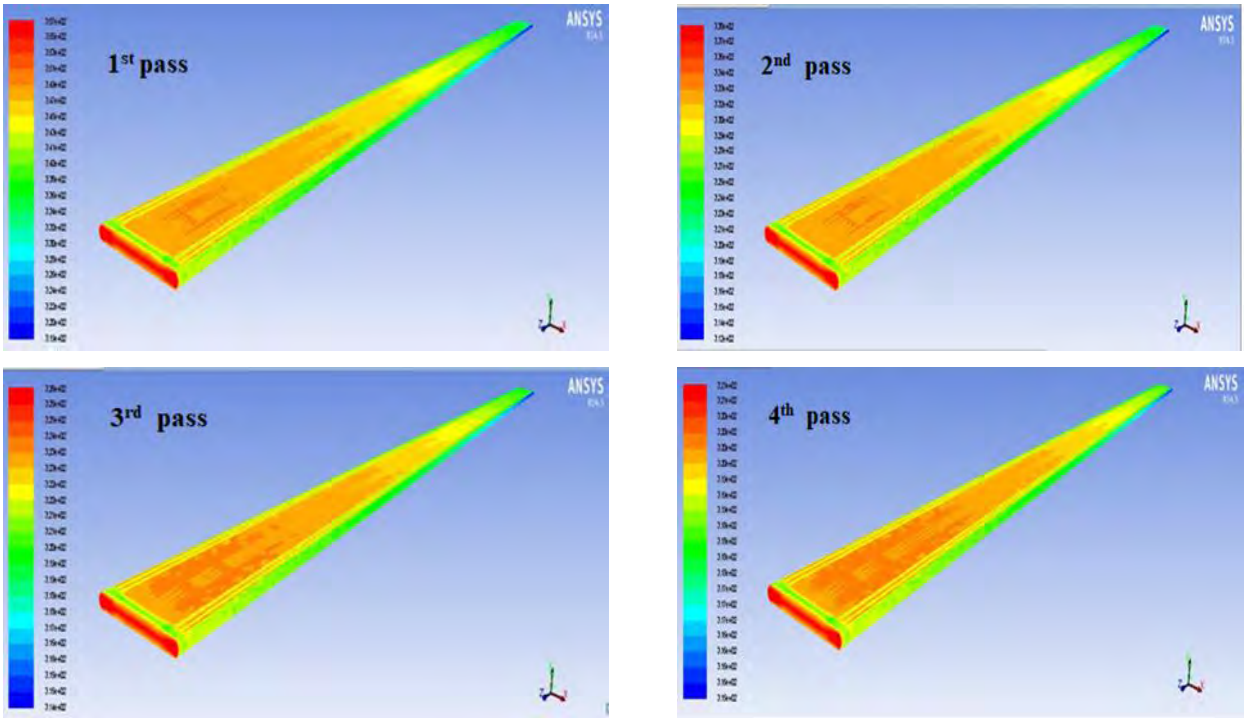
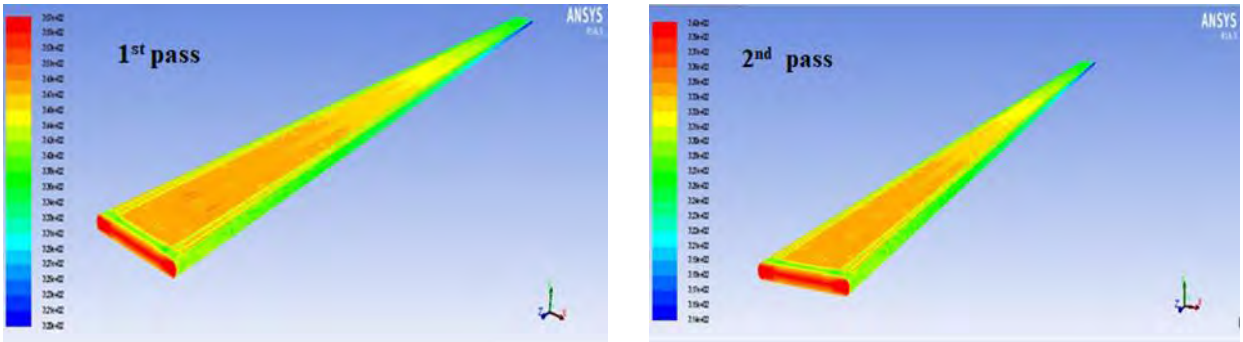


Fig. 16. Oval tube temperature contour at 2 m/s



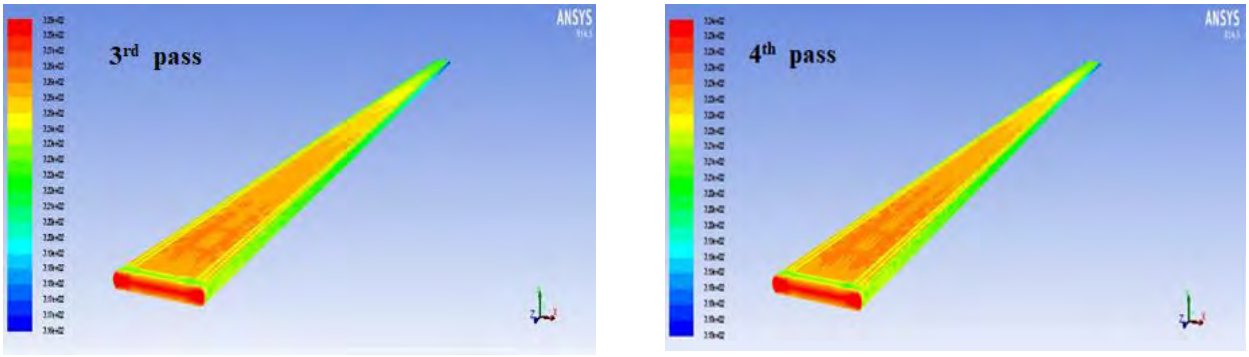


Fig. 17. Oval tube temperature contour at 5 m/s

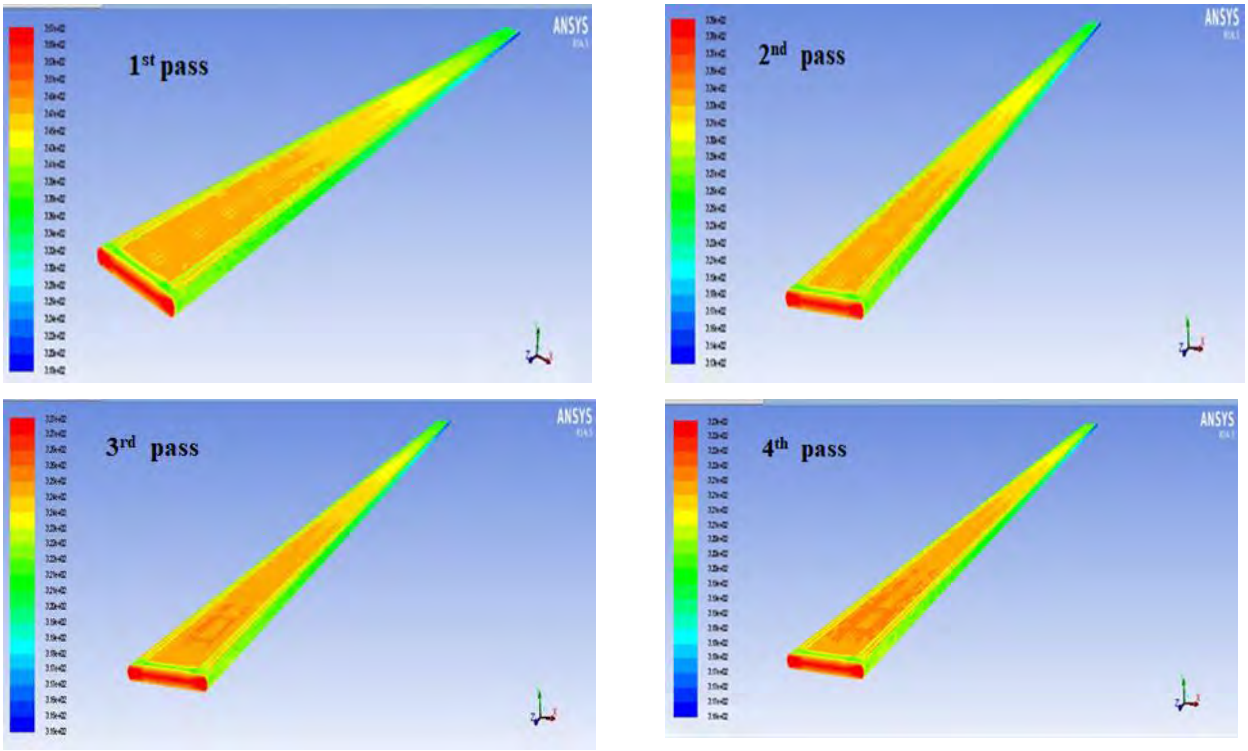
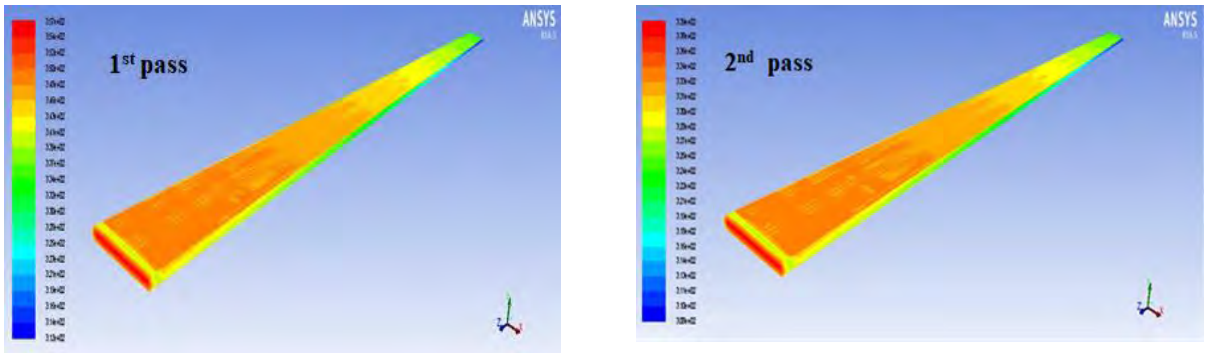


Fig. 18. Oval tube temperature contour at 8 m/s



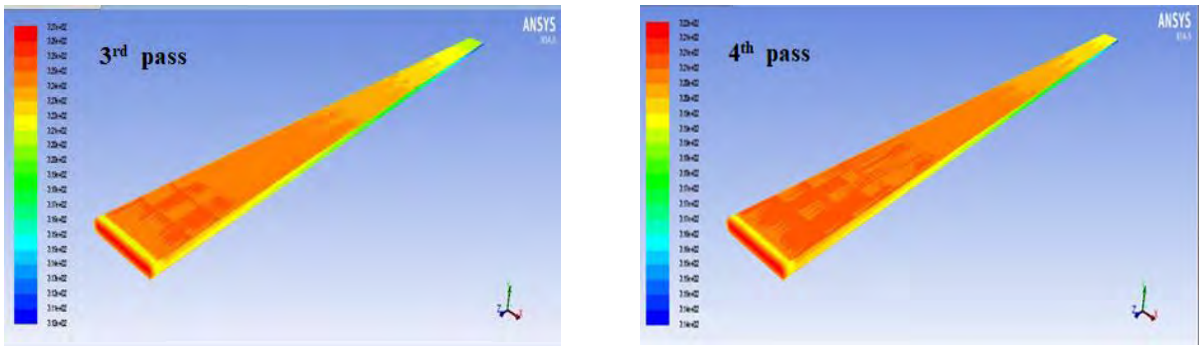


Fig. 19. Hexa tube temperature contour at 2 m/s

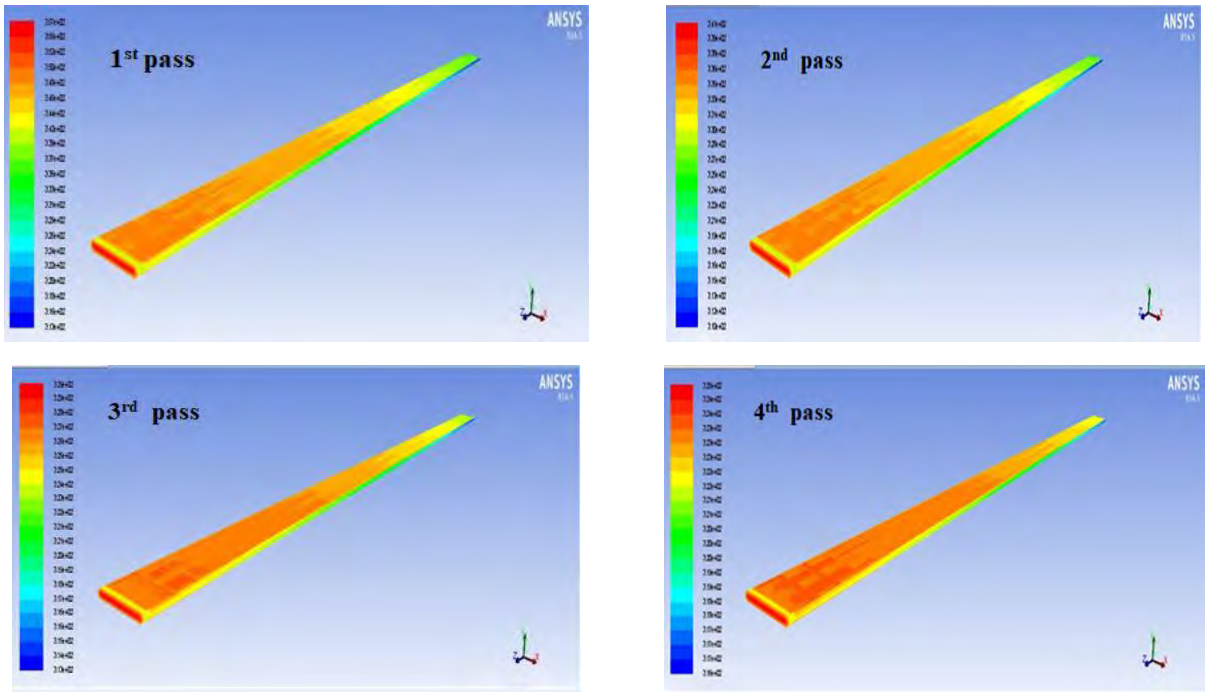
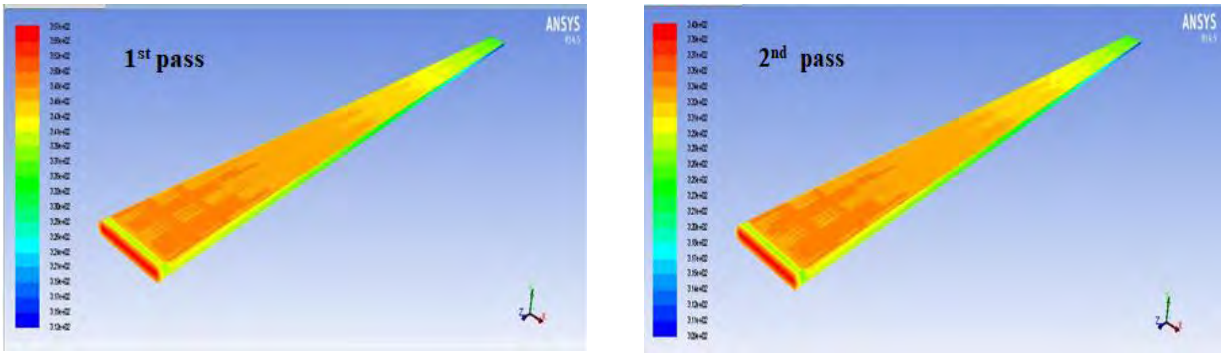


Fig. 20. Hexa tube temperature contour at 5 m/s



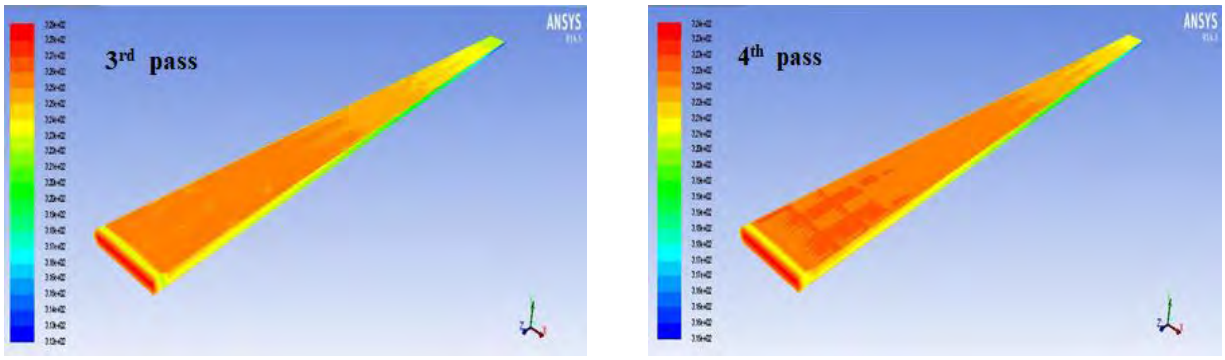


Fig. 21. Hexa tube temperature contour at 8 m/s

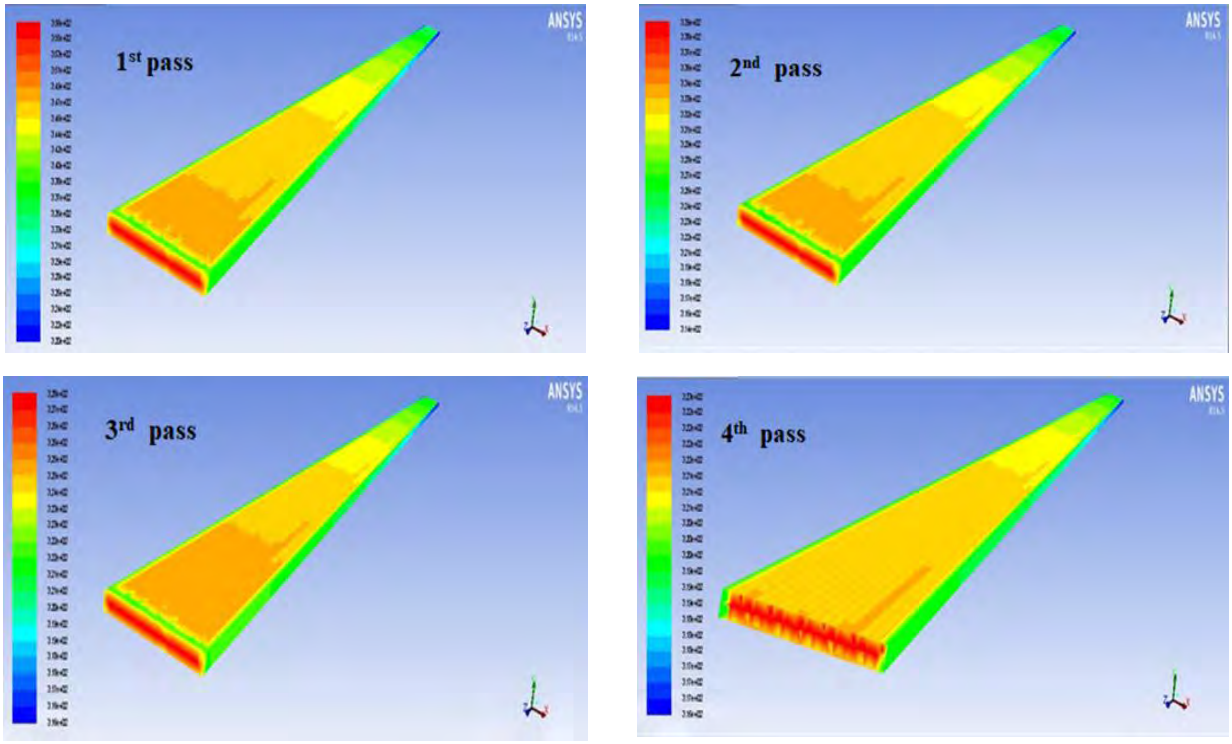
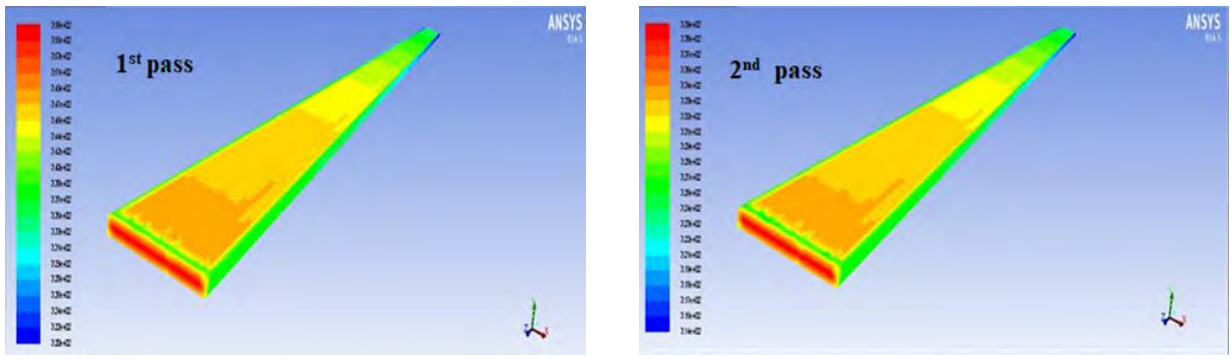


Fig. 22. Rectangular tube temperature contour at 2 m/s



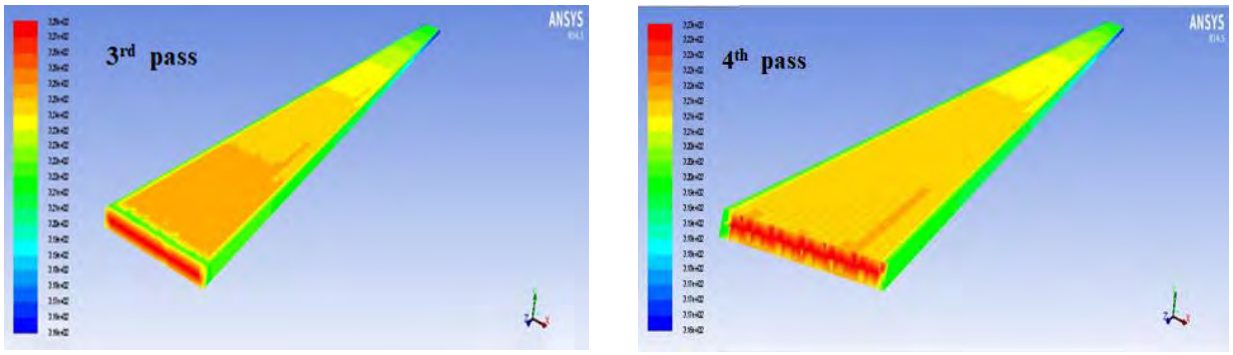


Fig. 23. Rectangular tube temperature contour at 5 m/s

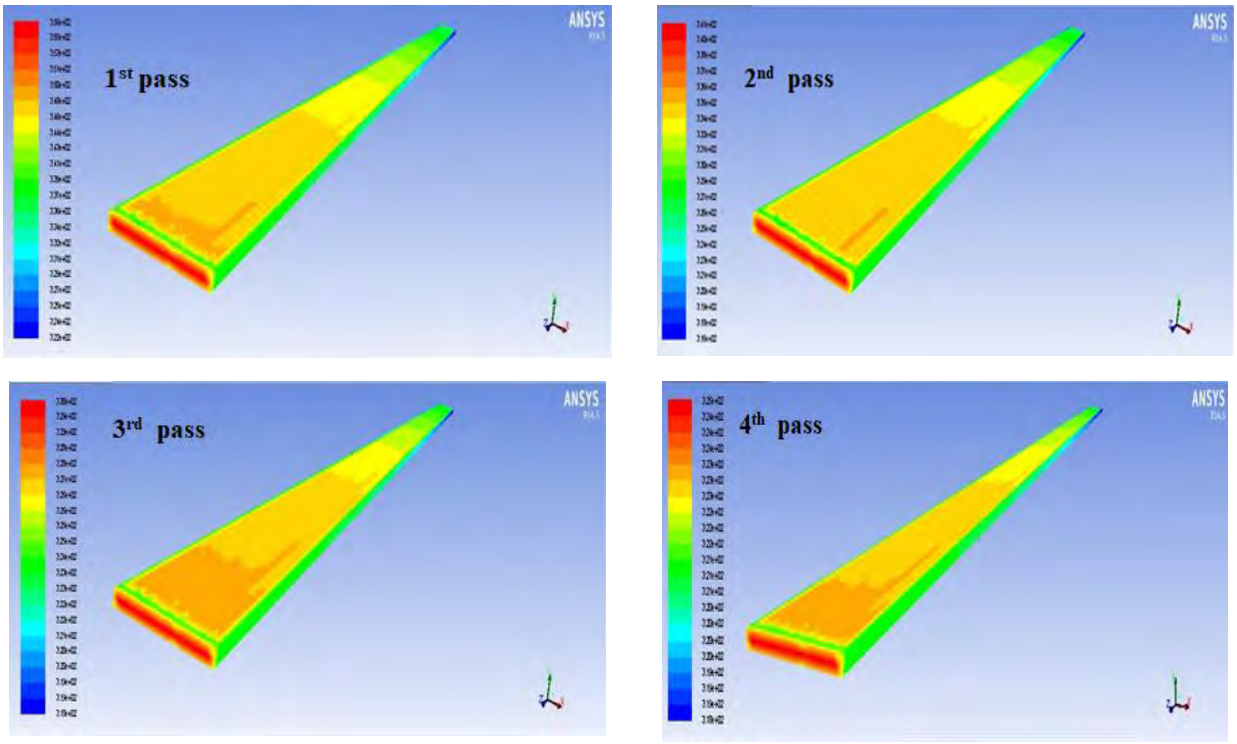


Fig. 24. Rectangular tube temperature contour at 8 m/s

Figures 14 and 15 show overall pressure and temperature distribution across the condenser for two-phase flow of refrigerant. The figures 16-24 show the CFD simulation being carried out for hexagon, oval, and rectangle shapes at the air velocities of 2 m/s, 5 m/s, and 8 m/s, respectively. The CFD simulation considered two-phase refrigerant flow for a 4-pass condenser configuration. This simulation helps to compare the results with the experimental & analytical study.

Table 9 presents the comparison of refrigerant outlet temperature based on CFD and analytical calculations. Table 10 summarizes the pressure drop from CFD and experiments. Numerical results were compared with experimental ones for pressure drop; it gives good agreement in the error percentage as shown in Table 10. Table 9 shows 5 to 16% variation in the outlet refrigerant temperature between CFD & experimental results. But Table 10 shows 3 to 10% variation in the pressure drop between CFD & experimental results. The result shows some acceptable error percentage between experimental and CFD results.

Table 9. Comparison of Refrigerant Outlet Temperature of CFD & Analytical calculation.

Air flow (m/s)	Pass	Oval Tube Profile			Hexagonal Tube Profile			Rectangular Tube Profile		
		Refrigerant outlet Temperature in °C								
		CFD analysis	Experimental	% deviation	CFD analysis	Experimental	% deviation	CFD analysis	Experimental	% deviation
2	1	65	68.4	5.1	65.9	67.9	3.0	66.3	68.4	3.0
	2	52.7	59.6	11.6	54	58.9	8.4	54.6	59.5	8.3
	3	48	56.3	14.8	48.7	55.6	12.4	49.8	56.2	11.5
	4	46	54.8	16.1	46.7	54.2	13.8	47.7	54.8	13.0
5	1	66.7	69.5	4.0	67.4	69.0	2.3	67.9	69.4	2.2
	2	55.2	60.7	9.1	56.3	60.0	6.2	57	60.6	5.9
	3	50.7	57.3	11.6	51.6	56.6	8.9	52.4	57.3	8.5
	4	48.7	55.9	12.9	49.5	55.2	10.4	50.3	55.8	9.9
8	1	66.1	68.6	3.7	66.8	68.2	2.1	67.4	68.6	1.7
	2	54.3	57.6	5.7	55.4	57.3	3.3	56.3	57.6	2.2
	3	49.7	52.4	5.3	50.7	52.3	3.2	51.6	52.4	1.6
	4	47.7	50.3	5.2	48.6	50.2	3.3	49.5	50.3	1.6

Table 10. Summary of pressure drop variation from CFD and Experiments

Ref. Mass flow rate (Kg/s)	Outlet temp (°C)	Pressure drops (mbar)	
		Experimental	CFD
0.054	44	708	730
0.096	43.5	1842	1959
0.113	43.5	2455	2674

7. Conclusion

The aim of this study is to improve condenser performance by incorporating unique tubes and shapes that control the volume of refrigerant. As per the aim, the study on different condenser tube shapes is made, and the summary of major findings is as follows:

- Of all the correlations, the refrigerant side Friedel correlation fits with experimental data the best, with differences of less than ±10%. Therefore, for analytical calculations for the varied tube geometries, Friedel correlation was employed.
- To comprehend the discrepancy between the CFD values and experimental ones of pressure loss and temperature across the tube, a CFD simulation was later run for various tube forms and ports.
- Further comparison of the CFD findings with the actual data revealed that, for various mass flow rates of the refrigerant, the variance ranged from 3 to 10%.
- Based on the extensive work done on the analytical calculation by using various correlations, it helped to understand the impact of variable tube geometry in the design phase of the product development in the automotive application.
- The rectangular model offers low heat transfer coefficient values in addition to low pressure drops.
- The hexagon model has a larger heat transfer coefficient and a higher pressure drop.
- Hexagon with rectangular port configuration is more suitable than other shapes such as rectangular & oval tubes.

Overall, the findings demonstrated that the analytical technique could be used in the first stage of product development in the automobile industry and that it could subsequently be connected with experimental data. This will shorten the lead time to market and avoid the expense of developing prototype parts. By lowering the size and effectiveness of the mobile air conditioner, a two-phase variable fin shape helps to increase the condenser's efficiency, which in turn lessens the total load on the compressor and, ultimately, increases the vehicle's fuel efficiency.

Nomenclature

- m - Mass flow
- m_{flux} - mass flux
- x - Vapor quality
- ρ_l & ρ_g - Liquid and Vapor density
- ρ_H - Homogeneous density
- D_h - Hydraulic diameter
- Re_L & Re_G - Reynold's number of liquid and Vapor
- Re_f - Reynold's number of the film
- F_{Lo} & F_{Go} - Friction factor of the liquid and Vapor
- μ_l - Dynamic viscosity of liquid
- μ_g - Dynamic viscosity of vapor
- $(\frac{dp}{dz})\,\mathrm{Lo}$ - Frictional pressure drop
- Fr, We, E, F, H - dimension less numbers
- ϕ_L^2 - multiplication factor for pressure drop
- τ - shear stress(wall)
- δ^+ and T_d^+ - Dimensionless parameter
- Pr_L - Prandel number
- h_r - Refrigerant side heat transfer coefficient in
- A_f - tube frontal flow area

References

[1] Srisomba R, Asirvatham L, Mahian O, Dalkiliç A, Awad M, Wongwises S. Air-side performance of a micro-channel heat exchanger in wet surace conditions. Thermal Science. 2017;21(1). https://doi.org/10.2298/TSCI150906227S

[2] Sridhar K, Bicha K. Comparative Analysis of Parallel and Counter Flow Heat Exchangers. International Journal of Scientific Engineering and Technology Research. 2017 Feb;6(4):638-44.

[3] Kabar Y, Rebay M, Kadja M, Padet C. Numerical Resolution of Conjugate Heat Transfer Problem in Parallelplate Micro-Channel. InCONV-09. Proceedings of International Symposium on Convective Heat and Mass Transfer in Sustainable Energy 2009. Begel House Inc. https://doi.org/10.1615/ICHMT.2009.CONV.280

[4] Singh S, Kukreja R. Experimental heat transfer coefficient during condensation of R-410A in horizontal micro-fin tubes. InJournal of Physics: Conference Series 2019 Jul 1 (Vol. 1240, No. 1, p. 012052). IOP Publishing. https://doi.org/10.1088/1742-6596/1240/1/012052

[5] Achaichia A, Cowell TA. Heat transfer and pressure drop characteristics of flat tube and louvered plate fin surfaces. Experimental Thermal and Fluid Science. 1988 Apr 1;1(2):147-57. https://doi.org/10.1016/0894-1777(88)90032-5

[6] Chang YJ, Wang CC. A generalized heat transfer correlation for Iouver fin geometry. International Journal of heat and mass transfer. 1997 Feb 1;40(3):533-44. https://doi.org/10.1016/0017-9310(96)00116-0

[7] Kim MH, Bullard CW. Air-side thermal hydraulic performance of multi-louvered fin aluminum heat exchangers. International journal of refrigeration. 2002 May 1;25(3):390-400. https://doi.org/10.1016/S0140-7007(01)00025-1

[8] Kim NH. Single-phase pressure drop and heat transfer measurements of turbulent flow inside helically dimpled tubes. Journal of Enhanced Heat Transfer. 2015;22(4). https://doi.org/10.1615/JEnhHeatTransf.2016016494

[9] Liang YY, Liu CC, Li CZ, Chen JP. Experimental and simulation study on the air side thermal hydraulic performance of automotive heat exchangers. Applied Thermal Engineering. 2015 Aug 5;87:305-15. https://doi.org/10.1016/j.applthermaleng.2015.05.018
[10] Wijayanta AT, Miyazaki T, Koyama S. Liquid-vapor phase distribution in horizontal headers with upward minichannel-branching conduits. Experimental Thermal and Fluid Science. 2016 Sep 1;76:264-74. https://doi.org/10.1016/j.expthermflusci.2016.03.021
[11] Panda K, Hirokawa T, Huang L. Design study of microchannel heat exchanger headers using experimentally validated multiphase flow CFD simulation. Applied Thermal Engineering. 2020 Sep 1;178:115585. https://doi.org/10.1016/j.applthermaleng.2020.115585
[12] Jiang H, Aute V, Radermacher R. CoilDesigner: a general-purpose simulation and design tool for air-to-refrigerant heat exchangers. International Journal of Refrigeration. 2006 Jun 1;29(4):601-10. https://doi.org/10.1016/j.ijrefrig.2005.09.019
[13] Yang L, Du X, Yang Y. Improvement of thermal performance for air-cooled condensers by using flow guiding device. Journal of Enhanced Heat Transfer. 2012;19(1). https://doi.org/10.1615/JEnhHeatTransf.2011002707
[14] Lockhart, W. R. (1949). Proposed correlation of data for isothermal two-phase, two-component flow in pipes. Chemical engineering progress, 45(1), 39-48.
[15] Friedel, L. (1979). Improved friction pressure drop correlations for horizontal and vertical two-phase pipe flow. In European two-phase group meeting, Ispra, Italy.
[16] Chisholm, D. (1967). A theoretical basis for the Lockhart-Martinelli correlation for two-phase flow. International Journal of Heat and Mass Transfer, 10(12), 1767-1778. https://doi.org/10.1016/0017-9310(67)90047-6
[17] LiangYe MW, Zeng X. Design and analysis of multi Parallel Pass Condensers'. International Journal of Refrigeration. 2009;32. https://doi.org/10.1016/j.ijrefrig.2009.01.012
[18] Liu Y, Sun W, Wu W, Wang S. Gas-liquid two-phase flow distribution in parallel micro-channels with different header and channels' orientations. International Journal of Heat and Mass Transfer. 2017 Sep 1;112:767-78. https://doi.org/10.1016/j.ijheatmasstransfer.2017.05.029
[19] Cavallini A, Del Col D, Doretti L, Matkovic M, Rossetto L, Zilio C. Two-phase frictional pressure gradient of R236ea, R134a and R410A inside multi-port mini-channels. Experimental Thermal and Fluid Science. 2005 Aug 1;29(7):861-70. https://doi.org/10.1016/j.expthermflusci.2005.03.012
[20] Bensafi A, Borg S, Parent D. CYRANO: a computational model for the detailed design of plate-fin-and-tube heat exchangers using pure and mixed refrigerants. International Journal of Refrigeration. 1997 May 1;20(3):218-28. https://doi.org/10.1016/S0140-7007(96)00052-7
[21] Valladares OG, Perez-Segarra CD, Rigola J. Numerical simulation of double pipe condensers and evaporators. International Journal of Refrigeration. 2004;27:656-70. https://doi.org/10.1016/j.ijrefrig.2004.01.006

Research on Engineering Structures & Materials
www.jresm.org
Research Group

Research Article

Flow of non-Newtonian fluids in self-similar networks across different scales

Antonio F. Miguel [*,1,2,a]

[1]*Complex Flow Systems Lab, University of Evora, Portugal*
[2]*Institute of Earth Sciences, the branch of Evora, Portugal*

Article Info

Article history:

Received 05 Oct 2024
Accepted 01 Jan 2025

Keywords:

Flow systems;
Scale-invariance;
Self-similarity;
Prefractal dimension;
Flow resistance;
Non-newtonian fluids

Abstract

Several natural and manufactured flow systems exhibit scale-invariance or self-similarity, despite appearing to be disordered. This study focuses on the laminar flow of non-Newtonian fluids through self-similar systems of tubes with porous walls (intrinsic permeability much less than 10^{-4} m^2). Two arrangements of tubes are discussed: a dendritic flow structure and a bundle of tubes. The size of these arrangements is described as a function of structural parameters for both straight and tortuous tubes, and the flow resistance is obtained as a function of structural parameters and fluid properties. Among other findings, it is shown that the prefractal dimension of dendritic networks for maximum flow access is dependent on the size constraint chosen to design the network. Results also show that as the prefractal dimensions of diameters and lengths rise, so does the overall size of the dendritic network and tube bundle system. In contrast, it is observed that the flow resistance diminishes as the prefractal dimension for diameters increases, whereas for tortuous tubes the flow resistance increases as the prefractal dimension for lengths increases. The approaches presented in this paper have numerous potential applications, including fluxes in biological systems, microfluidic media, and hydrology.

© 2025 MIM Research Group. All rights reserved.

1. Introduction

Fluid flow through complex networks of pores/tubes is common both in man-made and natural systems [1-3]. Fluid properties and the geometry through which the fluid circulates are crucial to establish the characteristics of the flow [3]. Therefore, diffusion coefficients and viscosities are properties of ample practical interest as well as the internal shape and structure of flow sites and their connectivity between them. In systems with specific geometries, the Euclidean dimension is insufficient to properly represent the system, hence the concept of prefractal was established [4-7]. Thus, for systems that have statistical self-similarity across a variety of scales, a measure of the complexity of the lengths/times that characterize these systems is obtained based on the so-called prefractal dimension. Prefractals are characterized by power laws with non-integer or integer exponents [4,5]. These scale-invariant systems are ubiquitous in nature and feature diverse man-made systems.

From a fundamental perspective, fluid flow in permeable media raises interesting challenges, particularly concerning the prefractal geometry of open space. Several attempts have been made to explain how the prefractal features of media affect fluid flow [7-10]. These attempts can be divided into two categories: one related to the flow represented by conventional flow equations through a prefractal open space, and the other

*Corresponding author: afm@uevora.pt
[a] orcid.org/0000-0001-6287-2056
DOI: http://dx.doi.org/10.17515/resm2025-474ma1005rs

to the flow network related to a continuum flow driven by nonconventional (prefractal) flow equations. A comprehensive review of the recent development of prefractal design of flow systems is provided by Babadagli [11].

This paper is based on the methodology presented in the articles of Miguel et al. [12,13] and presents analytical models for two different configurations: one composed of a self-similar dendritic network of porous tubes, and the other composed of a self-similar arrangement of porous tubes embedded in a porous material (intrinsic permeability less than 10^{-4} m^2), whose dimensions follow scaling laws. Our study considers non-Newtonian fluid flows and relies on the power law approach (Ostwald de Waele fluid) to estimate the variations in the fluid viscosity due to the applied shear rate. Power-law fluids are used in a variety of applications, including biological flow systems, microfluidic media, and engineering systems.

2. Theory

2.1. Fluid Flow Through a Tube with Porous Wall

Consider a time-independent laminar flow, axisymmetric through a cylindrical tube with rigid and impervious wall. According to Navier-Stokes equations, the flow of a Newtonian fluid is given by;

$$\frac{dp/dz}{\mu Q} = -\frac{8s_f}{D^4} \tag{1}$$

which is known as the Hagen–Poiseuille equation. Here Q is the volumetric flow rate, s_f is a shape factor ($16/\pi$), D is the diameter, z is a space variable, p is the pressure, and μ is the dynamic viscosity.

Now consider that the tube's wall is made of pores and has constant intrinsic permeability. Assuming that the exterior pressure is considered constant (i.e., a reference pressure $p_{ext} = 0$), the permeation flow is not constant due to the tube's inner pressure. Differentiating Eq. (1) yields;

$$\frac{dQ}{dz} = -\frac{D^4}{8\mu s_f}\frac{d^2p}{dz^2} \tag{2}$$

As the Darcy law governs the creeping fluid flow through the wall, the fluid flow variation along the tube is given by;

$$\frac{dQ}{dz} = \frac{dQ_p}{dz} = -\pi D\frac{k}{\mu}\frac{p}{l} \tag{3}$$

where k is the intrinsic permeability and l is the wall thickness. Substitution of Eq. (3) into Eq. (2) yields;

$$\frac{d^2p}{dz^2} - \frac{8\pi s_f k}{D^3 l}p = 0 \tag{4}$$

which has a solution of the form $p(z)= a_1\exp(-bz)+a_2 \exp(bz)$, where a_1, a_2 and b are constants [14]. Middleman [15] and Vassilieff [16] noticed that the pressure with respect to the axial position experiences a slight curve. Since the properties of the fluid and the geometric characteristics of the tube are constant, both the above solution or a parabolic pressure solution of type $p(z)=c_1+c_2\, z+c_3z^2$ can be applied [15]. Accounting for the

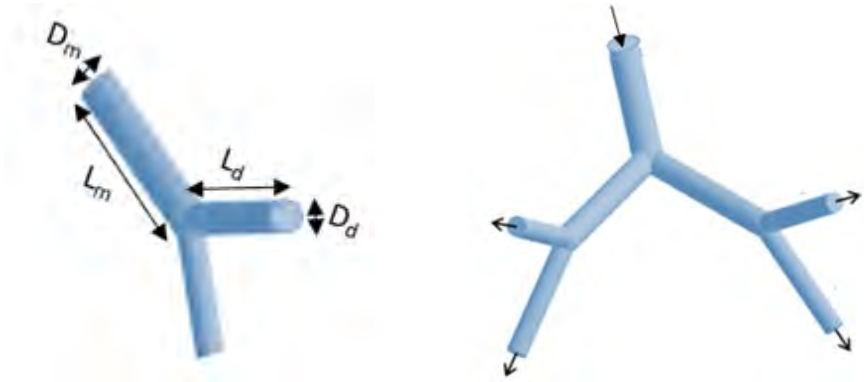
continuity equation, and that $dp/dz=8s_f\mu Q_{in}/D^4$ and at inlet the pressure is p_{in}, the pressure variation along the length of the tube can be written as;

$$p(z)-p_{in}=\frac{8s_f\mu Q_{in}}{\rho D^4}z\left[1+\frac{3k}{2Q_{in}}\left(\frac{p_{in}\rho D^4-64\mu LQ_{in}}{3D^3-64\mu kL^2}\right)z\right] \tag{5}$$

The pressure difference between the outlet and the inlet of the tube is;

$$p_L-p_{in}=\frac{8s_f\mu LQ_{in}}{\rho D^4}\left[1+\frac{3Lk}{2Q_{in}}\left(\frac{p_{in}\rho D^4-64\mu LQ_{in}}{3D^3-64\mu kL^2}\right)\right] \tag{6}$$

Note that the Hagen-Poiseuille equation is obtained when the intrinsic permeability of the tube walls is zero.



(a) (b)

Fig. 1. The base system consists of a tube that splits into two tubes (a) to form a network of dendritic tubes (b)

2.2. Flow through Bifurcated Tubes of a Newtonian Fluid

Consider a symmetric configuration composed of a tube that bifurcates into two daughter tubes (Fig. 1a). Defining the flow resistance as the ratio between fluid flow and pressure difference, the total flow resistance of the configuration of tubes is [6];

$$R=R_m+\frac{1}{2}R_d \tag{7}$$

with;

$$R_m=\frac{s_f\mu L_m}{D_m^4}\left[1+\frac{3L_mk}{2Q_{in}}\left(\frac{p_{in}\rho D_m^4-64\mu L_mQ_{in}}{3D_m^3-64\mu kL_m^2}\right)\right] \tag{8}$$

$$R_d=\frac{s_f\mu L_d}{D_d^4}\left\{1+\frac{3L_dk}{(Q_{in}-Q_k)}\left[\frac{p_{in,d}\rho D_d^4-32\mu L_d(Q_{in}-Q_k)}{3D_d^3-64\mu kL_d^2}\right]\right\} \tag{9}$$

where the subscripts m and d mean parent and daughter tubes, respectively. The total size of this bifurcated system is given by;

$$S = s_s D_m^w L_m + 2 s_s D_d^w L_d \tag{10}$$

where w takes a value of 1 or 2 for the lateral area and volume, respectively, and s_s is a shape factor equal to π for the lateral area and to $\pi/4$ for the volume. Consider that this bifurcated flow system is repeated over multiple spatial scales (Fig. 1b). Since self-similarity is a characterizing property, two crucial characteristics of the flow network are observed: the bifurcation of tubes and the decrease in the diameter of tubes (and cross-sectional area) from one level to the next in the tree. This can be approached by;

$$D_j = \alpha^j D_0 \qquad j = 1, 2, \ldots n \tag{11}$$

where the scaling factor for diameters or magnification factor α (a constant for the dendritic network) can be related to the number of bifurcating tubes n and the prefractal dimension d_f according to;

$$\alpha = c_o n^{-\frac{1}{d_f}} \tag{12}$$

where c_o is a constant. This power-law relationship ensures that the design of the tubes appears the same across different length scales of observation. A measure of the change of n can be obtained by differentiating Eq. (11) with respect to D_j;

$$\frac{dn}{n} = -d_f \frac{dD_j}{jD_j} \tag{13}$$

This result shows that n and D_j vary in opposite ways, that is, when one of them increases the other decreases. As a result, a self-similar dendritic network of tubes is composed of a few large-diameter tubes and many small-diameter tubes.

The diameter of the tubes that comprise each bifurcation level is related to the flow resistance. For a minimum flow resistance under space constraint, the following relationship must be verified [6];

$$\frac{\partial R}{\partial D_m}\frac{\partial D_m}{\partial D_d} + \frac{\partial R}{\partial D_d} = 0 \tag{14}$$

with the $\partial D_m/\partial D_d$ obtained from the space constraint given by Eq. (10). According to Eqs. (7), (10), and (14), the relationship between daughter and parent diameters for minimum flow resistance is given by;

$$\frac{D_d}{D_m} = \left\{ \frac{\left[28672(\mu k L_m^2)^2 - 3552 \mu k L_m^2 D_m^3 + 36 D_m^6 + \frac{27\rho}{2Q_{in}} \mathrm{p}_{in} L_m k D_m^7 \right]^{\frac{1}{2}} \left(64 \mu k L_d^2 - 3 D_d^3 \right)}{\left[40960(\mu k L_d^2)^2 - 3552 \mu k L_d^2 D_d^3 + 36 D_d^6 + 27\rho (Q_{in} - Q_k)^{-1} \mathrm{p}_{in,d} L_d k D_d^7 \right]^{\frac{1}{2}} \left(64 \mu k L_m^2 - 3 D_m^3 \right)} \right\}^{\frac{2}{4+w}} 2^{-\frac{2}{4+w}} \tag{15}$$

Eq. (14) is implicit and needs to be solved iteratively. For $k<10^{-4}$ m^2, the previous equation's k-dependent terms are significantly less than the other terms and can be ignored (refer to the results of section 3.1). Then, the previous equation can be expressed as;

$$\frac{D_d}{D_m} = 2^{-\frac{2}{4+w}} \tag{16}$$

Using a similar process and replacing D by L in Eq. (14), the optimal length ratio (i.e., length ratio for minimum flow resistance) is given by;

$$\frac{L_d}{L_m} = 2^{-\frac{1+w}{4+w}} \tag{17}$$

2.3. Flow through Bifurcated Tubes of a non-Newtonian Fluid

Because of its effectiveness and simplicity, we use the Hagen-Poiseuille equation (laminar flow) and a power law to account for variations in fluid viscosity caused by the applied shear rate. The Ostwald de Waele power law is a well-known model because a wide variety of problems were solved based on this approach. For $k<<10^{-4}$ m^2, the flow resistance of a single tube can be obtained as;

$$R = \frac{2^{3\chi+4}\left(\frac{3\chi+1}{4\chi}\right)^{\chi} KL}{\pi^{\chi} D^{3\chi+1}} Q^{\chi-1} \tag{18}$$

where Q is the volumetric flow rate, K is the consistency of fluid, and χ is the fluid behavior index ($\chi<1$ the fluid is named pseudoplastic or shear thinning, $\chi>1$ the fluid is called dilatant or shear thickening, and for $\chi=1$ the Newtonian fluid is obtained).

The resistance of a system composed of a parent tube that branches into 2 symmetric daughter tubes is;

$$R = \left(\frac{3\chi+1}{4\chi}\right)^{\chi} \frac{KQ^{\chi-1}}{\pi^{\chi}} \left[\frac{2^{3\chi+4} L_m}{D_m^{3\chi+1}} + \frac{2^{2\chi+4} L_d}{D_d^{3\chi+1}} \right] \tag{19}$$

Using a methodology akin to that described in the preceding section, the optimal size ratios for a tube that splits into two tubes (Fig. 1a) are;

$$\frac{D_d}{D_m} = 2^{\frac{-(\chi+1)}{3\chi+w+1}} \tag{20}$$

$$\frac{L_d}{L_m} = 2^{\frac{3\chi^2-3\chi-2}{3\chi+w+1}} \tag{21}$$

Note that when $\chi=1$ the allometric relations for Newtonian fluids (Eqs. 16 and 17) are obtained.

2.3.1 Geometric Characteristics for Minimum Flow Resistance and Prefractal Dimension

The ratio of diameters and lengths for the least resistance of fluid flow under surface area and volume constraints is illustrated by the allometric Eqs. (20) and (21). Eqs. (11), (12), (20) and (21) provide the following definition of the prefractal dimension;

$$d_{fD} = \frac{3\chi+w+1}{\chi+1} \tag{22}$$

$$d_{fL} = \frac{3\chi + w + 1}{2 + 3\chi - 3\chi^2} \tag{23}$$

According to these equations, both the prefractal dimension for diameters (d_{fD}) and lengths (d_{fL}) depend on the constraints of the system and the fluid behavior index. For example, d_{fD} for a Newtonian fluid is 2.5 or 3.0, depending on whether the constraint is the tube's lateral area or volume, respectively.

The total size and the total resistance of the bifurcated system of tubes (Eqs. 10 and 19, Fig. 1a) can be written in terms of prefractal dimensions as;

$$S = s_s D_m^w L_m \left(1 + 2^{1 - \frac{w}{d_{fD}} - \frac{1}{d_{fL}}} \right) \tag{24}$$

$$R = \frac{KQ^{\chi-1}}{\pi^{\chi}} \frac{L_m}{D_m^{3\chi+1}} \left(\frac{3\chi + 1}{4\chi} \right)^{\chi} \left(1 + 2^{3\chi + 4 + \frac{3\chi+1}{d_{fD}} - \frac{1}{d_{fL}}} \right) \tag{25}$$

For example, for a network composed of j-levels of bifurcated tubes (Fig. 1b), the total size of tubes is given by;

$$S = \sum_{i=0}^{j} s_s 2^i D_i^w L_i = s_s D_0^w L_0 \frac{1 - \left[2 \frac{L_1}{L_0} \left(\frac{D_1}{D_0} \right)^w \right]^{j+1}}{1 - \left[2 \frac{L_1}{L_0} \left(\frac{D_1}{D_0} \right)^w \right]} = s_s D_0^w L_0 \frac{1 - \left(2^{1 - \frac{w}{d_{fD}} - \frac{1}{df_L}} \right)^{j+1}}{1 - 2^{1 - \frac{w}{d_{fD}} - \frac{1}{df_L}}} \tag{26}$$

where d_{fD} and d_{fL} are given by Eqs. (22) and (23), respectively.

2.4. Fluid Flow Through Self-Similar Arrangement of Tubes

Consider a system composed of tubes with varied cross-sectional diameters (Fig. 2). Let L be the length of the material which has a self-similar distribution of tubes with diameters ranging from minimum diameters D_{min} and maximum diameters D_{max} (i.e., $D_{min} \leq D \leq D_{max}$ and $D_{min} <<< D_{max}$). Using an approach similar to those shown in the previous section (Eq. 11 and 12), we can write [4,12,13];

$$D = \beta D_{\max} \tag{27}$$

with the scaling factor for diameters given by;

$$\beta = N(\geq D)^{-\frac{1}{d_{fD}}} \tag{28}$$

where N is the number of tubes having a diameter equal to or greater than D. Differentiating this equation yields;

$$\frac{dN(\geq D)}{N(\geq D)} = -d_{fD} \frac{dD}{D_{\max}} \tag{29}$$

This equation, like Eq. (13), shows that the number of tubes in the flow system reduces as the diameter increases. As a consequence, a self-similar arrangement of tubes consists of many small-diameter tubes and a small number of larger-diameter tubes [4].

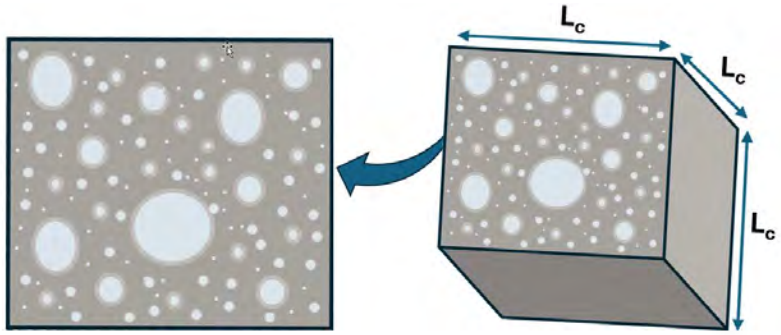


Fig. 2. Self-similar arrangement of tubes that are independent of one another

2.4.1 Size and Fluid Flow Resistance of An Arrangement of Straight Tubes

Consider that the arrangement of tubes in the Fig. 2 is composed of straight-length tubes. Taking into account Eqs. (27) to (29), the total volume of the tubes is given by;

$$S = \int_{D_{\min}}^{D_{\max}} s_s D^2 L_c (dN(\geq D)) = \int_{D_{\min}}^{D_{\max}} s_s L_c d_{fD} D_{\max}^{d_{fD}-1} D^{2-d_{fD}} dD \tag{30}$$

Integrating the previous equation yields;

$$S = \frac{s_s L_c d_{fD} D_{\max}^2}{3-d_{fD}} \left[1 - \left(\frac{D_{\min}}{D_{\max}} \right)^{3-d_{fD}} \right] \tag{31}$$

Using a similar process, for k<<10^{-4} m^2 the total flow resistance of the arrangement of tubes is given by;

$$Q = \int_{D_{\min}}^{D_{\max}} - \frac{c_\chi \Delta p^{\frac{1}{\chi}} d_{fD} D_{\max}^{d_{fD}-1} D^{\frac{\chi(3-d_{fD})+1}{\chi}}}{L_c^{\frac{1}{\chi}}} dD \tag{32}$$

and the flow resistance is;

$$R = \frac{Q^{\chi-1} L_c}{\left\{ \frac{\chi c_\chi d_{fD}}{\chi(4-d_{fD})+1} D_{\max}^{3+\frac{1}{\chi}} \left[1 - \left(\frac{D_{\min}}{D_{\max}} \right)^{4-d_{fD}+\frac{1}{\chi}} \right] \right\}^\chi} = \frac{c_R L_c \, \mathrm{Re}_{MR}^{\frac{\chi-1}{2-\chi}} D_{\max}^{\frac{(4-3\chi)(\chi-1)}{2-\chi}}}{\left\{ \frac{\chi c_\chi d_{fD}}{\chi(4-d_{fD})+1} D_{\max}^{3+\frac{1}{\chi}} \left[1 - \left(\frac{D_{\min}}{D_{\max}} \right)^{4-d_{fD}+\frac{1}{\chi}} \right] \right\}^\chi} \tag{33}$$

with;

$$c_R = \frac{\pi^{\chi-1} \left(\frac{3\chi+1}{4\chi} \right)^{\frac{\chi(\chi-1)}{2-\chi}} K^{\frac{\chi-1}{2-\chi}}}{2^{\frac{2(4-3\chi)(\chi-1)}{2-\chi}} \rho^{\frac{\chi-1}{2-\chi}}} \tag{34}$$

$$\mathrm{Re}_{MR}=\frac{2^{2(4-3\chi)}\rho Q^{2-\chi}}{\pi^{2-\chi}D_{\max}^{4-3\chi}\left(\frac{3\chi+1}{4\chi}\right)^{\chi}K} \tag{35}$$

where Re_{MR} is the Metzner–Reed Reynolds number, and S and R are the total size of the tubes and the total resistance of the tubes, respectively.

2.4.2 Size and Fluid Flow Resistance of An Arrangement of Tortuous Tubes

Tortuous describes the sinuosity of the tube in space, and tortuosity can be defined as the ratio of tube curve length over the line distance between the two ends. Consider that the tubes' length is tortuous rather than straight ($L\geq L_c$). Tube diameters satisfy Eqs. (27) and (28), whereas the following scaling equations describe tube lengths that follow self-similarity [13];

$$L=\theta L_c \tag{36}$$

with the scaling factor given by;

$$\theta=\left(\frac{D}{L_c}\right)^{1-d_{fL}} \tag{37}$$

where d_{fL} is the prefractal dimension of the tortuous tubes. In this case, the total volume of the tortuous tubes is given by;

$$S=\int_{D_{\min}}^{D_{\max}}s_s L_c^{d_{fL}}d_{fD}D_{\max}^{d_{fD}-1}D^{3-d_{fD}-d_{fL}}dD \tag{38}$$

After integration, the above equation yields;

$$S=\frac{s_s L_c^{d_{fL}}d_{fD}D_{\max}^{3-d_{fL}}}{4-d_{fD}-d_{fL}}\left[1-\left(\frac{D_{\min}}{D_{\max}}\right)^{4-d_{fD}-d_{fL}}\right] \tag{39}$$

The resistance can be obtained in the same manner as described in the preceding section. Assuming that the intrinsic permeability is much less than 10^{-4} m^2;

$$Q=\int_{D_{\min}}^{D_{\max}}-\frac{c_\chi\Delta p^{\frac{1}{\chi}}d_{fD}D_{\max}^{d_{fD}-1}D^{\frac{\chi(3-d_{fD})+d_{fL}}{\chi}}}{L_c^{\frac{d_{fL}}{\chi}}}dD \tag{40}$$

and the total flow resistance is;

$$R=\frac{Q^{\chi-1}L_c}{\left\{\frac{\chi c_\chi d_{fD}}{\chi\left(4-d_{fD}\right)+d_{fL}}D_{\max}^{3+\frac{d_{fL}}{\chi}}\left[1-\left(\frac{D_{\min}}{D_{\max}}\right)^{4-d_{fD}+\frac{d_{fL}}{\chi}}\right]\right\}^{\chi}}=\frac{c_R L_c\,\mathrm{Re}_{MR}^{\frac{\chi-1}{2-\chi}}D_{\max}^{\frac{(4-3\chi)(\chi-1)}{2-\chi}}}{\left\{\frac{\chi c_\chi d_{fD}}{\chi\left(4-d_{fD}\right)+d_{fL}}D_{\max}^{3+\frac{d_{fL}}{\chi}}\left[1-\left(\frac{D_{\min}}{D_{\max}}\right)^{4-d_{fD}+\frac{d_{fL}}{\chi}}\right]\right\}^{\chi}} \tag{41}$$

It should be noted that for tubes of non-tortuous length, the prefractal dimension d_{fL} is 1, and Eqs. (31) and (33) are obtained again.

3. Results and Discussion

3.1. Fluid Flow in Porous Wall Bifurcated Tubes Designed with Minimum Flow Resistance

Fig. 3 illustrates how the ratio of the daughter tube to the parent-daughter tube diameters (Fig. 1a), for minimum flow resistance, varies with the k, w, and L_d/L_m. Regardless of the intrinsic permeability of the walls and the ratio between the lengths of the daughter tubes and the parent tube, we may conclude that D_d/D_m depends on w which represents the type of space constraint imposed on the system. Additionally, for an intrinsic permeability of less than 10^{-4} m^2, D_d/D_m remains independent of L_d/L_m. Then, the ratio of diameters that is only dependent on the constraint w is given by $D_d/D_m=2^{-2/4+w}$ (for k<10-4 m2). Additionally, it should be mentioned that for volume constraint (w=2) the ratio of the diameters D_d/D_m is larger than for lateral area constraint (w=1).

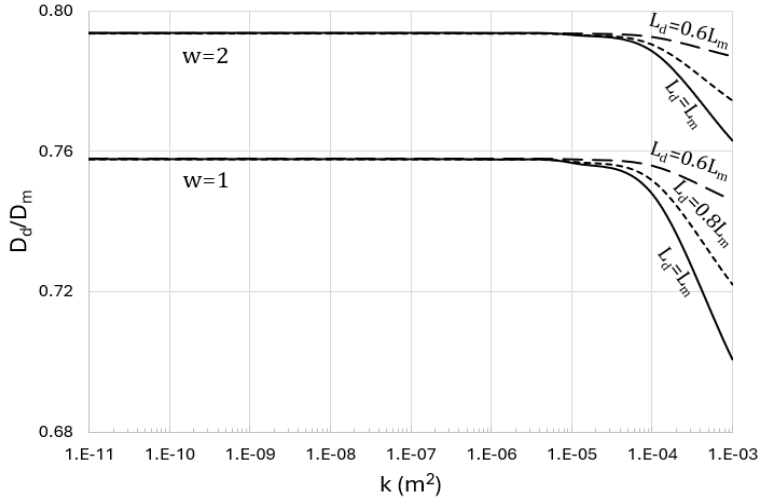


Fig. 3. Optimal ratio between the diameters of daughter and parent tubes versus the intrinsic permeability of porous wall (Eq. 15)

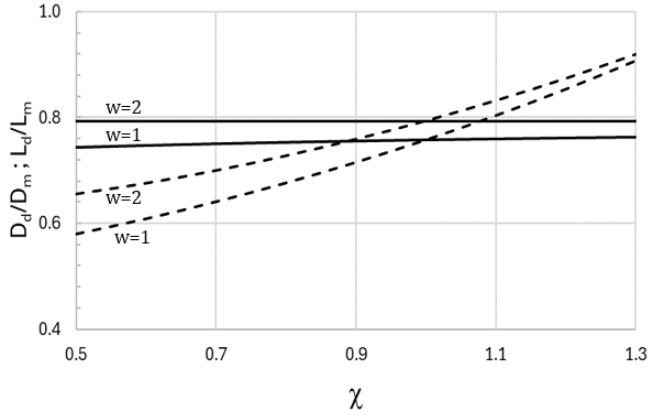


Fig. 4. Ratios between the diameters of daughter and parent tubes D_d/D_m (—, Eq. 20) and between the lengths of daughter and parent tubes L_d/L_m (---, Eq. 21) versus fluid behavior index χ and the geometric constraint w

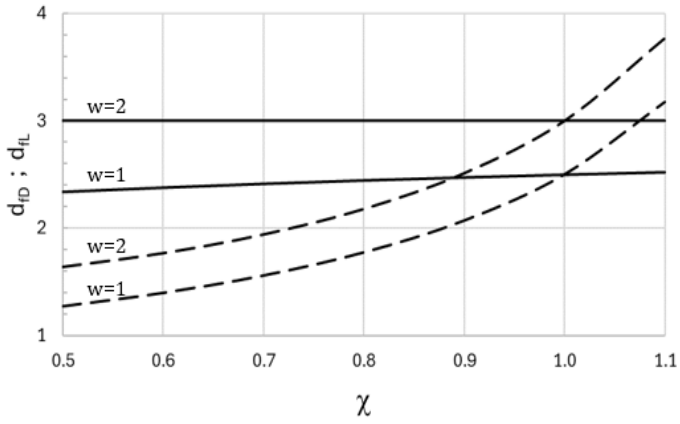


Fig. 5. Prefractal dimension for diameters d_{fD} (—, Eq. 22) and lengths d_{fL} (---, Eq. 23) versus fluid behavior index χ and the geometric constraint w

For branching systems designed with minimum flow resistance, Figs. 4 and 5 depict the variation of the size ratios and the prefractal dimensions with respect to the fluid behavior index χ and the geometric factor w. Fig. 4 indicates that the diameter and length ratios are greater for volume constraint than lateral area constraint. Besides, the length ratio grows with the fluid behavior index, but the diameter ratio remains relatively constant. The same tendency of variation with w and χ recorded for the size ratios occurs for the prefractal dimensions d_{fD} and d_{fL} (Fig. 5).

3.2. Fluid Flow Through a Dendritic Network of Tubes

Consider now the design's base unit for dendritic flow networks, which consists of a parent tube that bifurcates into two daughter tubes. Figs. 6 and 7 show the dimensionless total size (Eq. 24) and the dimensionless total flow resistance (Eq. 25). Fig. 6 indicates that increasing the prefractal dimension for diameters or the prefractal dimension for lengths increases the network's overall size.

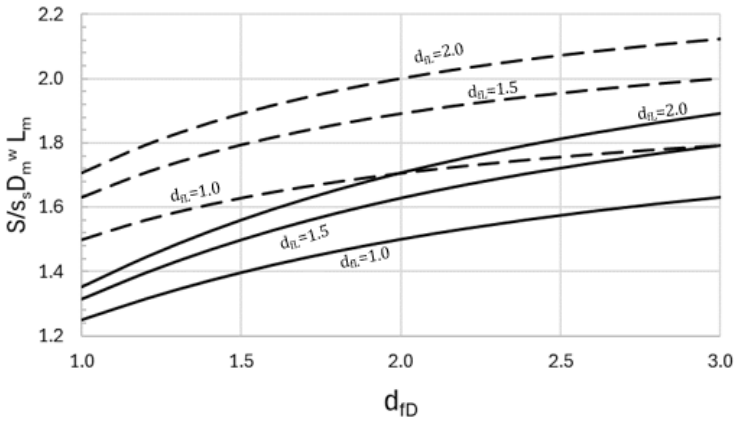


Fig. 6. Dimensionless total size of network versus the prefractal dimensions (d_{fD} and d_{fL}) and the geometric constraints (w=1 (---) and w=2 (–))

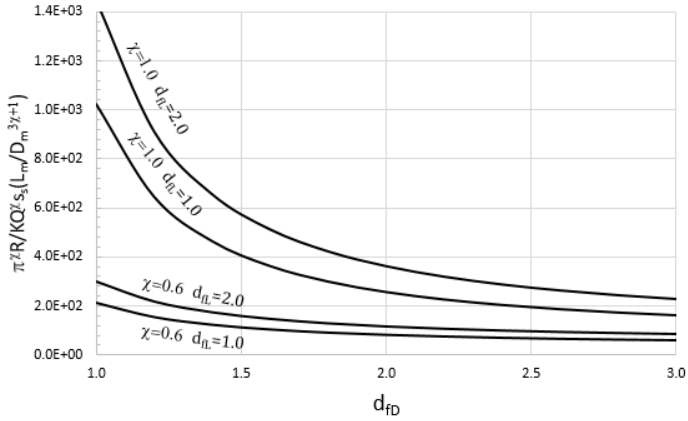


Fig. 7. Dimensionless total flow resistance of network versus the prefractal dimensions (d_{fD} and d_{fL}) and the fluid behavior index χ.

The system size is larger when the constraint is the lateral area. However, the dimensionless total flow resistance decreases as the prefractal dimension for diameters increases, and it increases as the prefractal dimension for lengths increases (Fig. 7). An increase in the fluid behavior index also increases dimensionless resistance.

3.3. Fluid Flow Fluid Through Self-Similar Arrangement of Tubes

For the system depicted in Fig. 2, Eqs. (39) and (41) are plotted in Figs. 8 and 9. The dimensionless total size of tubes increases as the prefractal dimensions (d_{fD} and d_{fL}) increase. It is also worth noting that only when the tube diameter's fractal dimension exceeds two does the d_{fL} become significant. Regarding the dimensionless flow resistance of the system of tubes, the increase in prefractal dimensions (df_D or df_L) raises the total dimensionless resistance. Furthermore, the dimensionless resistance to flow increases for fluids with a higher fluid behavior index.

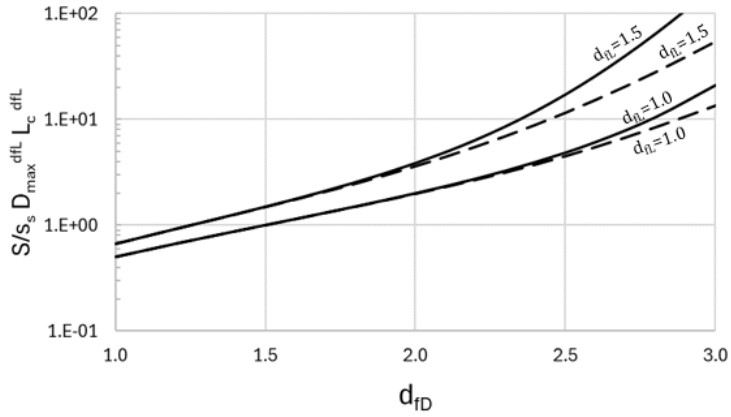


Fig. 8. Dimensionless total size of tubes versus the prefractal dimensions (d_{fD} and d_{fL}) and the geometric constraints (w=1 (---) and w=2 (–))

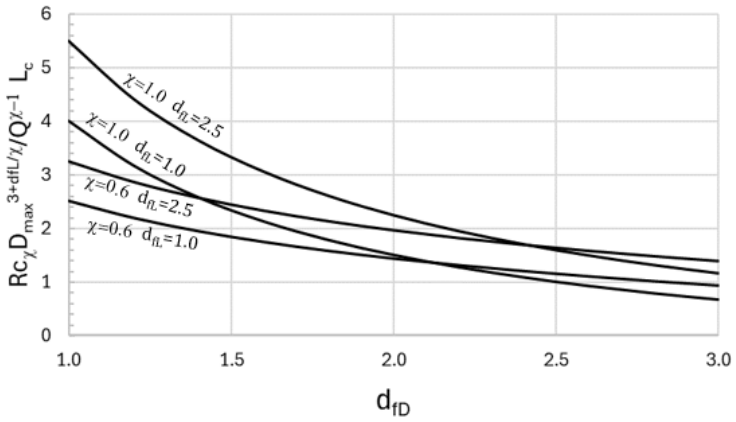


Fig. 9. Dimensionless total flow resistance of tubes versus the prefractal dimensions (d_{fD} and d_{fL}) and the fluid behavior index χ.

Variations in the prefractal dimension of biological systems are often linked to changes in the way they operate. The above figures may be useful in understanding why changes in the prefractal dimension of biological systems may be connected with changes in the system's operation.

The prevalence of osteoporosis, for example, is related to an increase in prefractal dimension [17]. Healthy bones have a prefractal dimension of about 2.60, while severe osteoporosis has a prefractal value of around 2.95. This means that a larger prefractal dimension results in a larger size of empty spaces (Figs. 6 and 8). Thus, as the prefractal dimension rises, the open space expands, which may contribute to a decrease in structural strength, but it's not the only issue. The ability to produce blood cells is also compromised (less material, more open gaps), which is also a major concern.

Understanding other conditions can be aided by a similar perception based on Figs. 6 and 8. Cardiomyopathy is a condition affecting the cardiac muscle (myocardial). In this case, the muscle walls of the heart chambers are gradually wearing down in terms of structure and function. It is connected with an increase in prefractal dimension [18] and causes difficulty in blood pumping by the heart, resulting in extended intervals between beats (heart failure). It is also important to note that a full understanding of the concept of prefractal dimension and its determination may be useful for distinguishing hypertrophic cardiomyopathy from an athlete's heart, as echocardiography and cardiac magnetic resonance fail to discriminate between the two in some circumstances [19].

Emphysema is characterized by a reduction in prefractal dimension [20]. Figs. 7 and 9 show that when the prefractal dimension decreases, the resistance to fluid flow increases. In other words, under the same pressure, the airflow is reduced, resulting in shortness of breath and fatigue. Low peribronchial emphysema with a prefractal dimension of about 2.7 is associated with increased mortality risk [20], which corresponds to an increase in flow resistance of more than 10% (Fig. 7).

4. Conclusions

Length scale-invariance property characterize many natural and manufactured flow systems. The evaluation of their size and flow resistance is significant and of importance in multi-disciplinary fields. The prefractal theory is appropriated to obtain important insights into the design of these systems. Here, we consider flows of power-law fluids

(Ostwald-de Waele fluid) through porous tubes, and two different flow systems characterized by length scale invariance properties are investigated. First, the highest porosity limit of the walls of porous tubes that can be regarded as having an insignificant impact on the optimal ratio between the sizes of daughter and parent tubes is investigated. Then, a system consisting of Y-shaped tubes – a dendritic flow network - is analyzed. This flow system is characterized by a scaling law between the diameters of the parent tube and the daughter tubes, and the magnification factor of this law is related to the prefractal dimension. Taking as a goal the maximum fluid transport (i.e., minimum flow resistance), and assuming the space occupied by the network is a constant, the value of the prefractal dimension is determined. Expressions for the total size of a network composed of several levels of bifurcating tubes and for its flow resistance can be obtained.

In addition, a system composed of a bundle of tubes is studied. Tubes with tortuous lengths are assumed to exhibit self-similar properties that are scale-independent and statistically consistent at all levels. Thus, power laws are used to characterize the distribution of diameters and lengths. Expressions for the total size and flow resistance are derived in terms of prefractal dimensions.

In summary, these models, which account for the fluid properties and structural characteristics observed in these self-similarity systems, may shed light on an understanding of a variety of flow systems, including hydrology, microfluidic media, and biological systems. The variation in the prefractal dimension that systems can exhibit with the use and with certain illnesses is especially intriguing. A few cases of biological systems are briefly examined.

Acknowledgment

This work was partially supported by funding awarded by FCT - Foundation for Science and Technology, I.P., Projects UIDB/04683/2020 and UIDP/04683/2020.

References

[1] Harush U, Barzel B. Dynamic patterns of information flow in complex networks, Nature Communications 2017; 8: 2181. https://doi.org/10.1038/s41467-017-01916-3

[2] Chen S, Miguel AF, Aydin M. Constructal design in the cooling and hydraulic performance of tube heat sinks. International Communications in Heat and Mass Transfer 2021; 129: 105668. https://doi.org/10.1016/j.icheatmasstransfer.2021.105668

[3] Miguel AF, Rocha LAO. Tree-shaped flow networks fundamentals, in: Tree Shaped Fluid Flow and Heat Transfer, Springer, New York, 2018; 9-34. https://doi.org/10.1007/978-3-319-73260-2_2

[4] Mandelbrot BB. The Fractal Geometry of Nature, W. H. Freeman and co, San Francisco, 1982.

[5] Falconer K. Fractal Geometry: Mathematical Foundations and Applications, John Wiley & Sons, Hoboken, 2004. https://doi.org/10.1002/0470013850

[6] Miguel AF. Low dissipative configuration in flow networks subject to constraints, Physica D 2024; 467: 134269. https://doi.org/10.1016/j.physd.2024.134269

[7] Miguel AF. A constructal view of prefractal dendritic flow networks using an exergy analysis, International Journal of Exergy 2021; 36: 56 - 75. https://doi.org/10.1504/IJEX.2021.10040964

[8] Mourzenko VV, Thovert JF, Adler PM. Macroscopic permeability of three-dimensional fracture networks with power-laws size distribution, Physical Review E 2004; 69: 066307. https://doi.org/10.1103/PhysRevE.69.066307

[9] Balankin AS. The topological Hausdorff dimension and transport properties of Sierpinski carpets, Physics Letters A 2017; 381: 2801-2808. https://doi.org/10.1016/j.physleta.2017.06.049
[10] Sahu AK, Roy A. Clustering, connectivity and flow responses of deterministic fractal-fracture networks, Advances in Geosciences 2020; 54: 149-156. https://doi.org/10.5194/adgeo-54-149-2020
[11] Babadagli T. Unravelling transport in complex natural fractures with fractal geometry: a comprehensive review and new insights, Journal of Hydrology 2020; 587: 124937. https://doi.org/10.1016/j.jhydrol.2020.124937
[12] Miguel AF, Rosa R, Silva AM. Fractal geometry description of the permeability of a natural fissured rock. Proceedings of 9th International Congress on Deterioration and Conservation of Stone, Elsevier Science BV, 2000; 1: 595-560. https://doi.org/10.1016/B978-044450517-0/50145-8
[13] Miguel AF. Permeability of fractal porous materials composed of different combinations of capillary tubes, International Journal of Hydromechatronics 2020; 3: 199-212. https://doi.org/10.1504/IJHM.2020.107783
[14] Miguel AF. Fluid flow in a porous tree-shaped network: optimal design and extension of Hess-Murray's law, Physica A 2015; 423: 61-71. https://doi.org/10.1016/j.physa.2014.12.025
[15] Middleman S. An Introduction to Fluid Dynamics: Principles of Analysis and Design, Wiley, New York, 1997
[16] Vassilieff CS. An elliptic filtration variation on Poiseuille-type laminar solutions of Navier-Stokes equations, Journal of Membrane Science 1994; 91: 153-161. https://doi.org/10.1016/0376-7388(94)00030-1
[17] Harrar K, Hamami L. The fractal dimension correlated to the bone mineral density, Transactions on Signal Processing 2008; 4: 110-126
[18] Captur G, Karperien AL, Hughes AD, Francis DP, Moon JC. The fractal heart - embracing mathematics in the cardiology clinic, Nature Reviews Cardiology 2017; 14: 56-64. https://doi.org/10.1038/nrcardio.2016.161
[19] Vilades D, Garcia-Moll X, Gomez-Llorente M, Pujadas S, Ferrero-Gregori A, Doñate T, Mirabet S, Leta R, Pons-Lladó G, Carreras F, Cinca J. Differentiation of athlete's heart and hypertrophic cardiomyopathy by the fractal dimension of left ventricular trabeculae, International Journal of Cardiology 2021; 330: 232-237. https://doi.org/10.1016/j.ijcard.2021.02.042
[20] Bodduluri S, Puliyakote ASK, Gerard SE, Reinhardt JM, Hoffman EA, Newell Jr. JD, Nath HP, Han MK, Washko GR, Estépar RSJ, Dransfield MT, Bhatt SP. Airway fractal dimension predicts respiratory morbidity and mortality in COPD, Journal of Clinical Investigation 2018; 128: 5374-5382. https://doi.org/10.1172/JCI120693

Research on Engineering Structures & Materials
www.jresm.org

Research Article

Performance assessment of ternary blended fiber-reinforced recycled aggregate concrete

V. Gayathri [1,a], C. Govardhan [*,1,b], S. Sruthi [2,c], Nabarun Dey [3,d]

[1]*Dept. of Civil Eng., Kumaraguru College of Technology, Coimbatore, Tamil Nadu-641049, India*
[2]*Chaitanya Bharathi Institute of Technology, Andhra Pradesh-516360, India*
[3]*Dept. of Civil Eng., Adamas University, Barasat, Kolkata- 700126, India*

Article Info

Article History:

Received 18 Oct 2024

Accepted 29 Jan 2025

Keywords:

Recycled concrete aggregate;
Alccofine;
Fiber reinforced ternary blends;
Response surface methodology;
Sorptivity

Abstract

Amid growing environmental concerns and the urgent need for sustainable construction practices, recycled concrete aggregates (RCA) have garnered significant attention. This research explores the enhancement of recycled aggregate concrete (RAC) performance while increasing the substitution level of RCA. The study investigates the mechanical and durability properties of M30-grade RAC, incorporating various combinations of OPC, PPC, Alccofine, manufactured sand, natural aggregates, and recycled coarse aggregates across 27 mixes. The results reveal that the mix containing 80% RCA with PPC, 10% Alccofine, and 0.50% glass fiber achieved a compressive strength of 39.74 MPa, surpassing the target strength. The flexural strength for this mix was 3.89 MPa, exceeding the requirements for low-volume road applications. The performance of RAC improved significantly in binary, ternary, and fiber-reinforced ternary blends, with fiber-reinforced ternary blends demonstrating superior performance and sustainability benefits. The durability of RAC was found to be improved with the inclusion of Alccofine and glass fibers. Alccofine showed superior improvement in durability properties such as chloride penetration, Sorptivity, and drying shrinkage. Compressive strength results were validated using response surface methodology (RSM). These findings highlight the viability of fiber-reinforced ternary blends for applications like pavements, which demand large quantities of aggregates. The study underscores the potential of recycling construction waste, reducing the carbon footprint, and advancing sustainable construction practices, paving the way for a greener future in the industry.

© 2025 MIM Research Group. All rights reserved.

1. Introduction

The urgency of sustainable development in the construction sector is paramount. It is crucial to create buildings and infrastructure that are environmentally responsible and resource-efficient throughout their lifecycle. This includes using sustainable materials, designing for energy efficiency, and incorporating renewable energy sources to reduce carbon footprint and environmental impact. It also involves practices that minimize waste, conserve water, and improve indoor environmental quality, which promotes healthier living and working conditions. Every raw material used in concrete will considerably impact nature and raise concerns about sustainability issues [1]. Sustainable development balances economic growth, environmental stewardship, and social well-being, ensuring that construction activities contribute positively to present and future generations. The significance of this topic cannot be overstated, as it shapes the future of our built environment and the well-being of our society.

*Corresponding author: govardhan.20phd@kct.ac.in
[a]orcid.org/0000-0002-7838-3481; [b]orcid.org/0009-0003-1617-4291; [c]orcid.org/0000-0002-4102-7977;
[d]orcid.org/0000-0002-9551-8210
DOI: http://dx.doi.org/10.17515/resm2025-491ma1018rs

Using Ordinary Portland Cement (OPC) in construction has numerous challenges. OPC production has a significant environmental impact due to high carbon dioxide emissions, contributing to global warming. The process is energy-intensive and heavily relies on fossil fuels, causing further ecological degradation. Furthermore, it depletes natural resources like limestone and clay [2]. OPC structures are susceptible to chemical attacks, and their production demands large amounts of water, posing issues in water-scarce regions. Exploring alternative materials and sustainable practices to address these issues is crucial, and using natural coarse aggregates in construction activities poses various challenges. These include the depletion of natural resources due to extensive mining and quarrying, leading to habitat destruction and ecological imbalance. The extraction and transportation processes are energy-intensive, contributing to greenhouse gas emissions and air pollution. Moreover, using natural coarse aggregates can lead to significant land degradation. As the availability of high-quality natural aggregates diminishes, there is a growing need to explore sustainable alternatives such as recycled or alternative aggregates to reduce environmental impact and ensure the sustainability of construction practices. Based on the above concerns, the current research is focused on utilizing materials that will reduce the problems associated with the degradation of the environment. For this purpose, Portland pozzolana cement (PPC), Manufactured sand (M-sand), and recycled concrete aggregates (RCA) were chosen. PPC incorporates fly ash, reducing the clinker content in cement production, which lowers carbon dioxide emissions, promotes the utilization of industrial waste like fly ash, enhances durability, and improves energy efficiency. Similarly, M-sand, produced by crushing stones or rocks, eliminates the need for riverbed mining, thereby protecting natural ecosystems. Additionally, M-sand is often produced locally, which reduces transportation requirements and further decreases carbon emissions.

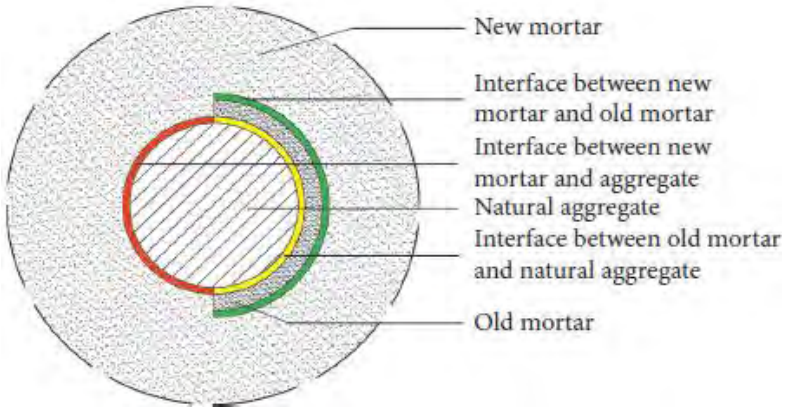


Fig. 1. Microstructure and scanning electron microscope (SEM) image of recycled concrete showing old and new mortars with ITZs [7]

As the RCA possesses inferior properties to NCA, its usage is mostly limited to non-structural applications. Water absorption (WA) of RCA is one such significant factor that affects the performance of recycled aggregate concrete (RAC) [3]. The mechanical behavior of RAC is found to be inferior to conventional concrete as RCA contains a layer of old mortar; it results in the formation of additional ITZ (Interfacial Transition Zone), absorbs more water during mixing, increases porosity, and results in the generation of micro-cracks [4,5]. The Interfacial Transition Zone (ITZ), or aggregate-paste interface [6,7], consists of calcium hydroxide, calcium silicate hydrate, and ettringite, with a higher water-to-cement (w/c) ratio than the mortar, making it porous and weak [8,9]. This weakness reduces the macro-mechanical properties of concrete. Recycled coarse aggregate (RCA) introduces two ITZs: (a) the old ITZ from residual mortar and (b) the new ITZ formed during mixing, as shown in Fig. 1. Pedro et al. observed the declining nature of the performance of workability and density of RAC with increasing levels of RCA [10]. Saha and Rajasekaran investigated the mechanical behavior of RAC, and they observed that an increase in the substitution level of RCA content led to a decrease in the performance of the RAC [11]. The behavior of RAC in durability parameters was also found to be inferior to that of conventional concrete [12,13].

For structural and non-structural applications of RCA, different nations published guidelines stating the amount of RCA (limitations of RCA in RAC) that can be used for a particular application up to a specific concrete grade. Indian Standards IS-383-2016 [14] limits the RCA to 25%, 20% (up to M20), and 100% (up to M15) for plain, reinforced, and lean concrete applications, respectively. The current research aimed at maximizing the utilization of RCA and applying it to higher grades of concrete. For this purpose, in the current study, Portland Pozzolana cement (PPC) is obtained by intergrinding the Portland clinker with gypsum in combination with fly ash, which is an industrial waste from thermal power plants possessing cementitious properties is used as a complete replacement and compared their properties. Alccofine C-1203, which comes under the category of Supplementary cementitious materials (SCM), is partially replaced for the binding material, and glass fibers were used, resulting in the fiber-reinforced ternary concrete matrix.

2. Research Significance

The research on fiber-reinforced concrete blends using recycled concrete aggregates (RCA), PPC, Alccofine, and glass fibers holds significant importance in advancing sustainable construction. By incorporating RCA, the study promotes waste recycling and reduces dependence on natural aggregates, addressing resource depletion and environmental degradation. The use of PPC and Alccofine enhances the sustainability and durability of the blends by lowering clinker content, reducing carbon emissions, and improving material performance. Glass fibers further reinforce the blends, enhancing tensile and flexural strength, crack resistance, and overall durability, making them suitable for demanding applications such as pavements and low-volume roads. These innovative blends demonstrate cost-effectiveness by utilizing industrial by-products and minimizing maintenance needs.

The study aims to enhance the mechanical and durability properties of RAC. It examines key parameters such as compressive strength, flexural strength, modulus of elasticity, drying shrinkage, chloride ion diffusion resistance, and sorptivity. This research contributes to developing eco-friendly construction materials, supporting the circular economy, and reducing the carbon footprint, paving the way for a greener, more sustainable future in the construction industry.

3. Methodology

Ordinary Portland Cement (OPC) of 53grade and Portland Pozzolana cement (PPC) confirming to IS:12269 [15] and IS:1489 [16] are used as binding agents. Alccofine (AL) C-1203 is used as a Supplementary cementitious material (SCM) as a partial substitute to the binding agent (PPC), forming a ternary blend. The trial studies are conducted to determine the optimum dosage of alccofine by conducting compressive strength on concrete, and it is found that a 10% substitution of alccofine yields optimum strength. for the current study, 10% of Alccofine is chosen as a replacement for the binding material. Table 1 shows the oxide compositions of the cementitious materials used. Alccofine is used as an SCM due to its calcium oxide, silica, and aluminum oxide content. Manufactured sand (M Sand) serves as a fine aggregate (FA) with a specific gravity of 2.68 and 1% water absorption. Crushed granite of 20mm nominal size is used as a natural coarse aggregate (NCA) with a specific gravity of 2.79 and water absorption of 0.50%, and recycled concrete aggregate (RCA) is substituted at different levels of NCA. The test results of the aggregates' physical properties and gradation analysis satisfy the codal requirements of IS:2386-Part I & III [17,18] and IS:383-2016. The gradation analysis of fine aggregate meets the Zone-II specifications, and the gradation analysis for the aggregates is shown in Fig. 2. The RCA is obtained from Hyderabad's construction and demolition waste (C&D) recycling plant. However, the physical properties of RCA exhibit inferior properties compared to the NCA, such as higher water absorption, crushing, and abrasion values. RCA's specific gravity and water absorption are 2.64 and 3.54%, respectively. The RCA is cleaned with water to remove the dust particles and soaked in water for 24 hours so that the RCA reaches an SSD state. When used in concrete, it reduces the absorption of mixing water. RCA is brought to be a saturated surface dry condition (SSD) by ensuring no water remains on the aggregate surface before it is used in the concreting. To achieve the desired workability, maintaining a uniform slump of 50±5 mm, a super-plasticizer named

conplast SP-430 was used. By using SP at the rate of 1% by the weight of cement, reduces the water content by 23% which is observed from the trial studies.

Table 1. Oxide composition and physical properties of binders

	Al_2O_3	SiO_2	MgO	CaO	Fe_2O_3	SO_3	Na_2O	K_2O	LOI	Specific gravity
Alccofine	24.57	37.53	5.23	29.46	0.92	0.18	0.032	0.61	0.58	2.86
OPC	6.2	21.20	1.26	62.05	4.75	0.67	0.13	0.34	2.01	3.14
PPC	11.04	36.40	1.0	42.29	4.68	2.1	0.18	0.4	2.66	3.08

Table 2. Classification and notations of the mixes

Series	Notation	Expansion of Notation
Unary mixes	A0	Concrete consisting of OPC and 100% NCA
	A1	Concrete consisting of OPC, 80% NCA, and 20% RCA
	A2	Concrete consisting of OPC, 60% NCA, and 40% RCA
	A3	Concrete consisting of OPC, 40% NCA, and 60% RCA
	A4	Concrete consisting of OPC, 20% NCA, and 80% RCA
	A5	Concrete consisting of OPC, 0% NCA, and 100% RCA
Binary blended mixes	B0	Concrete consisting of PPC and 100% NCA
	B1	Concrete consisting of PPC, 80% NCA, and 20% RCA
	B2	Concrete consisting of PPC, 60% NCA, and 40% RCA
	B3	Concrete consisting of PPC, 40% NCA, and 60% RCA
	B4	Concrete consisting of PPC, 20% NCA, and 80% RCA
	B5	Concrete consisting of PPC, 0% NCA, and 100% RCA
Ternary blended mixes	C0	Concrete consisting of PPC, Alccofine 10%, and 100% NCA
	C1	Concrete consisting of PPC, Alccofine 10%, 80% NCA, and 20% RCA
	C2	Concrete consisting of PPC, Alccofine 10%, 60% NCA, and 40% RCA
	C3	Concrete consisting of PPC, Alccofine 10%, 40% NCA, and 60% RCA
	C4	Concrete consisting of PPC, Alccofine 10%, 20% NCA, and 80% RCA
	C5	Concrete consisting of PPC, Alccofine 10%, 0% NCA, and 100% RCA
Fiber-reinforced ternary blended mixes	D1	Concrete consisting of PPC, Alccofine 10%, 40% NCA, 60% RCA, and glass fiber 0.25%
	D2	Concrete consisting of PPC, Alccofine 10%, 40% NCA, 60% RCA, and glass fiber 0.50%
	D3	Concrete consisting of PPC, Alccofine 10%, 40% NCA, 60% RCA, and glass fiber 0.75%
	E1	Concrete consisting of PPC, Alccofine 10%, 20% NCA, 80% RCA, and glass fiber 0.25%
	E2	Concrete consisting of PPC, Alccofine 10%, 20% NCA, 80% RCA, and glass fiber 0.50%
	E3	Concrete consisting of PPC, Alccofine 10%, 20% NCA, 80% RCA, and glass fiber 0.75%
	F1	Concrete consisting of PPC, Alccofine 10%, 0% NCA, 100% RCA, and glass fiber 0.25%
	F2	Concrete consisting of PPC, Alccofine 10%, 0% NCA, 100% RCA, and glass fiber 0.50%
	F3	Concrete consisting of PPC, Alccofine 10%, 0% NCA, 100% RCA, and glass fiber 0.75%

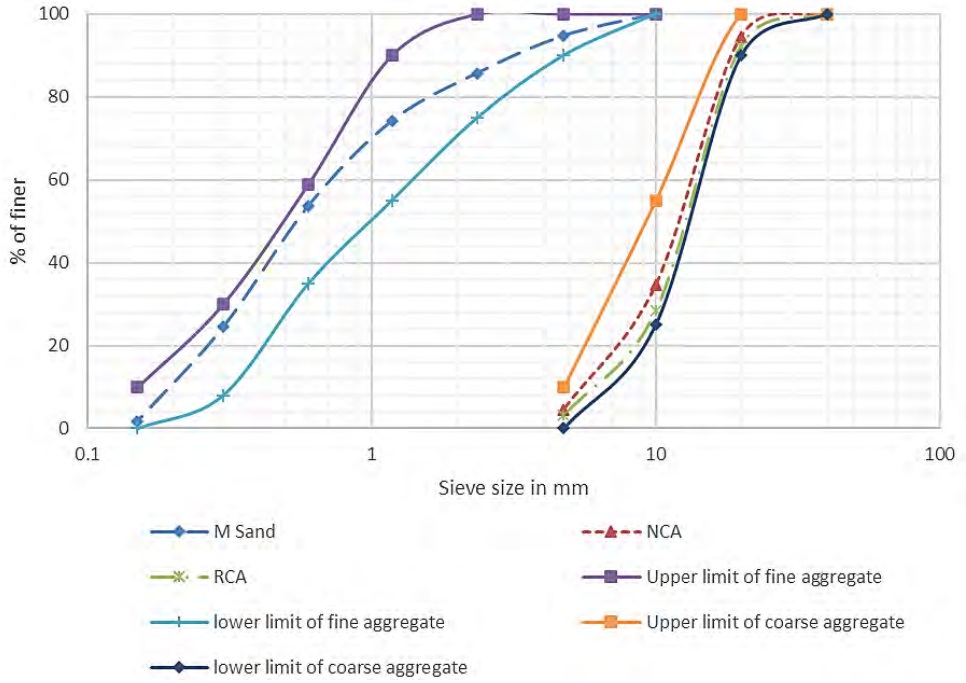


Fig. 2. Gradation analysis of aggregates

Table 3. Mix proportions for 1 m^3 of concrete

Mix ID	Cement (kg)	M sand (kg)	NCA (kg)	RCA (kg)	Alccofine (kg)	Glass fibers (%)	Water (kg)	Slump (mm)	SP (%)
A0	376	676	1256	0	0	0	170	51	0.65
A1	376	676	1005	231	0	0	170	50	0.69
A2	376	676	754	462	0	0	170	49	0.75
A3	376	676	502	692	0	0	170	47	0.83
A4	376	676	251	923	0	0	170	45	0.89
A5	376	676	0	1154	0	0	170	45	0.96
B0	376	676	1256	0	0	0	170	53	0.59
B1	376	676	1005	231	0	0	170	52	0.61
B2	376	676	754	462	0	0	170	51	0.67
B3	376	676	502	692	0	0	170	50	0.76
B4	376	676	251	923	0	0	170	48	0.82
B5	376	676	0	1154	0	0	170	47	0.89
C0	338.4	676	1256	0	37.6	0	170	55	0.48
C1	338.4	676	1005	231	37.6	0	170	54	0.50
C2	338.4	676	754	462	37.6	0	170	52	0.56
C3	338.4	676	502	692	37.6	0	170	52	0.66
C4	338.4	676	251	923	37.6	0	170	50	0.72
C5	338.4	676	0	1154	37.6	0	170	49	0.79
D1	338.4	676	502	692	37.6	0.25	170	53	0.79
D2	338.4	676	502	692	37.6	0.50	170	51	0.92
D3	338.4	676	502	692	37.6	0.75	170	49	1.09
E1	338.4	676	251	923	37.6	0.25	170	51	0.92
E2	338.4	676	251	923	37.6	0.50	170	49	1.12
E3	338.4	676	251	923	37.6	0.75	170	48	1.33
F1	338.4	676	0	1154	37.6	0.25	170	50	1.14
F2	338.4	676	0	1154	37.6	0.50	170	48	1.36
F3	338.4	676	0	1154	37.6	0.75	170	45	1.55

Glass fibers (GF) of 12mm length were used, forming fiber-reinforced ternary blended concrete. The raw materials used in the current study are shown in Fig. 3. The guidelines for the mix design M30 (target strength is 38.25 MPa) are followed as per the IS:10262-2019 [19]. In all the mixes, the water-cement ratio and fine aggregate quantity are maintained as a constant. The variables were NCA (0%, 20%, 40%, 60%, 80%, and 100%), RCA (0%, 20%, 40%, 60%, 80%, and 100%), and glass fibers (0.25%, 0.50%, and 0.75%). Twenty-seven mixes were cast and tested to evaluate the performance of concrete. The 27 mixes were split into four series, as shown in Table 2, and the details of the mix proportions are shown in Table 3.

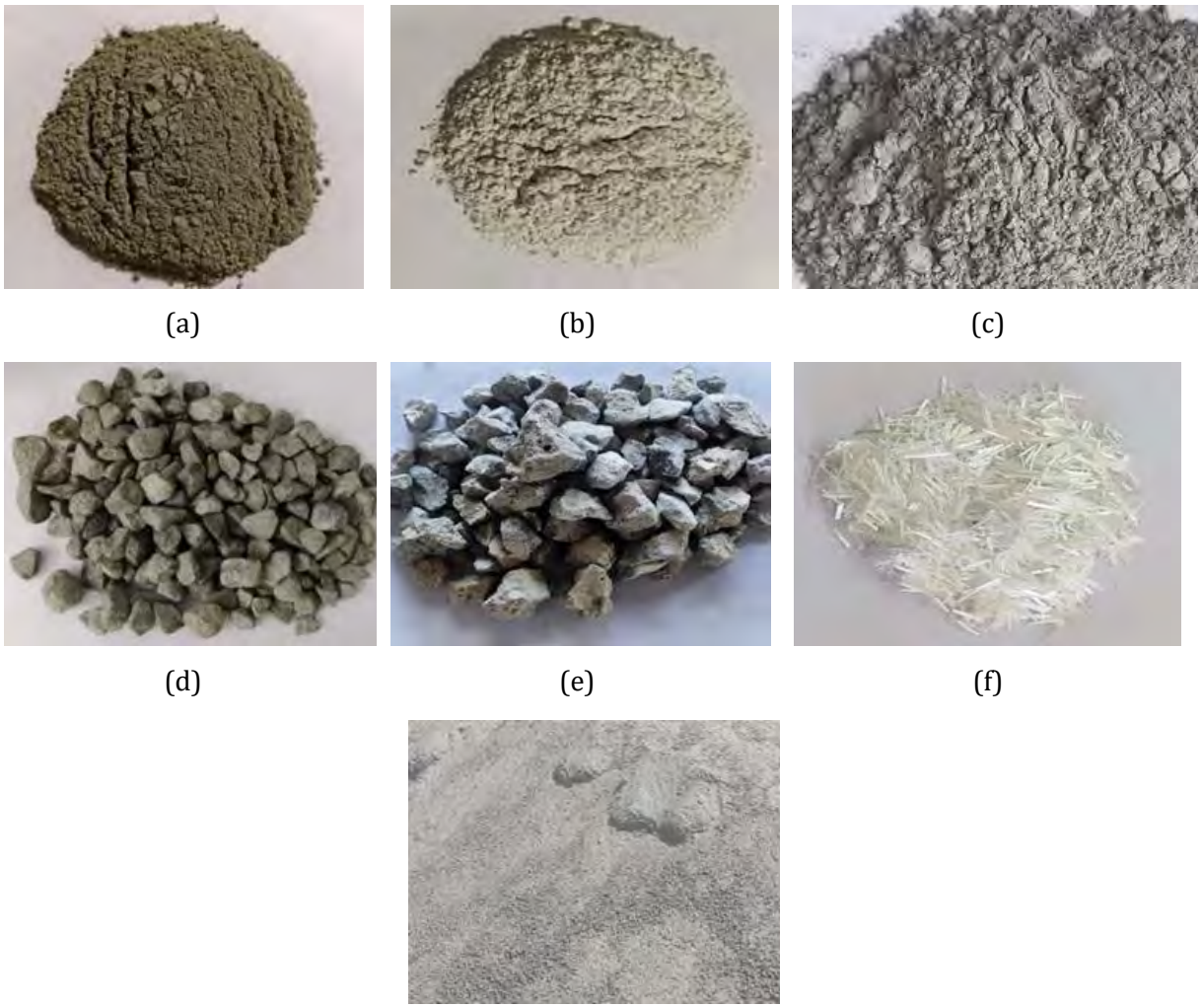
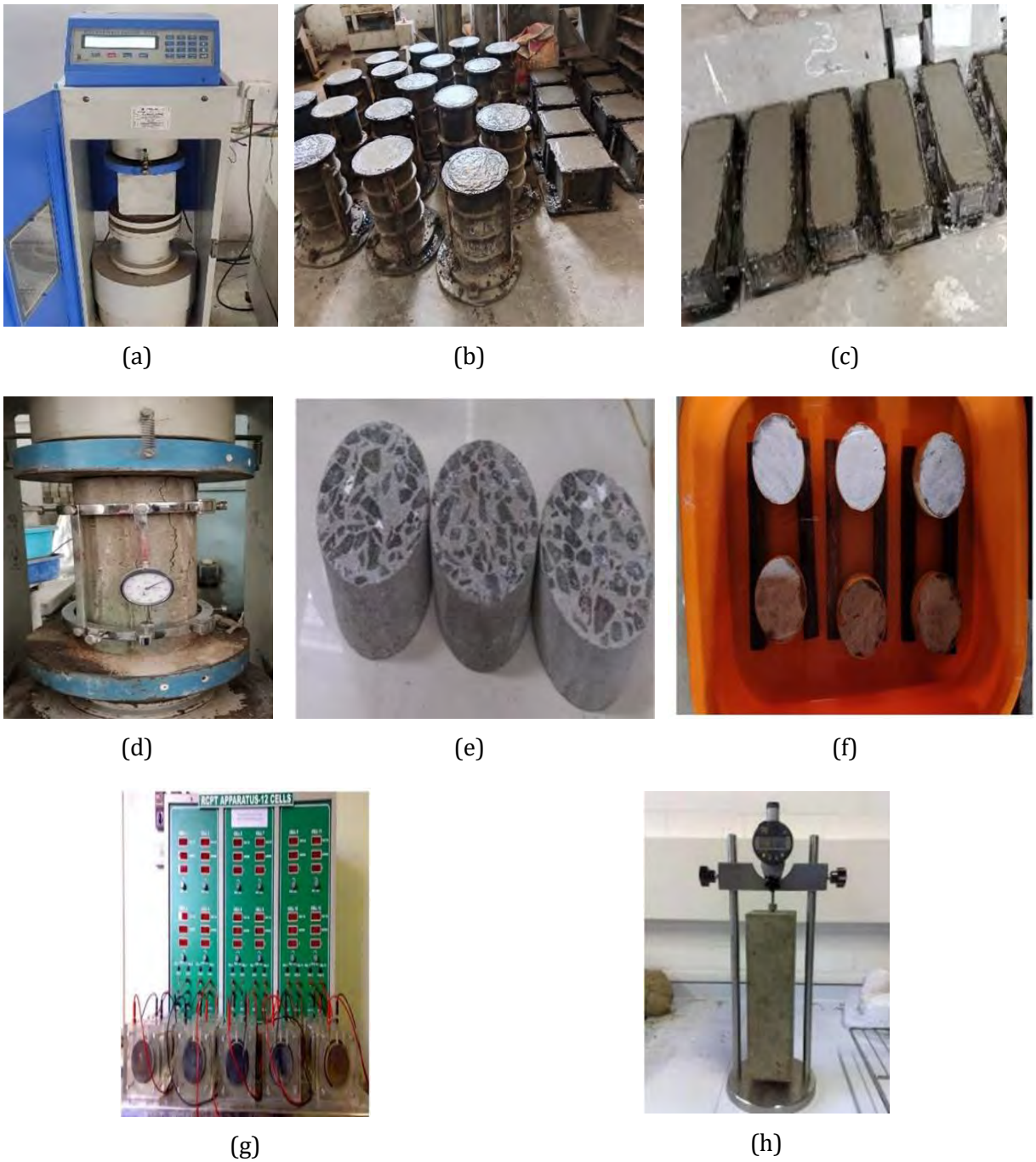


Fig. 3. Raw materials employed in the study: (a) OPC, (b) Alccofine, (c) PPC, (d) NCA, (e) RCA, (f) Glass fibers, (g) M-sand

4. Details of The Experiments Performed

As per IS:516-1959 [20], cube specimens of 150 mm size and prism of 500 mm X 100 mm X 100 mm size were cast to evaluate the behavior of concrete in compression and flexure, respectively, after 28 days of curing. Three specimens were cast for each mix, and the average of the three sample results was considered. Three cylinders of 150 mm diameter with 300 mm height were cast for every mix to evaluate concrete's Modulus of Elasticity (MOE) at 28 days. The durability properties of concrete, such as rapid chloride penetration test (RCPT), sorptivity, and drying shrinkage, were performed as per ASTM C-1202 [21], ASTM C-1585-04 [22], and IS:516- part 6 [23], respectively. Disc specimens 50 mm thick with 100mm diameter are used for RCPT and sorptivity. Test on concrete by RCPT helps evaluate the penetration resistance of concrete against the movement of

chloride ions, and the charge passed is noted down at regular intervals. The sorptivity test evaluates the ability of concrete to resist water ingress through capillary action. To occur the capillary action, the specimens are placed in the water so that the bottom of the specimen is placed at a certain height, and the water level is maintained at a height of 5mm from the bottom. The circumferential surface of the specimens used for sorptivity is sealed with a water-proofer so that the water enters the concrete from its bottom only. The weights of the specimens are noted down at respective time intervals. Executing a drying shrinkage test helps in noting the contraction behavior of concrete that occurs due to the loss of moisture when exposed to the environment. For this purpose, 300 mm X 75 mm X 75 mm size specimens were used and tested after 90 days. The test setup and sample cast are shown in Fig. 4.



(a) (b) (c)

(d) (e) (f)

(g) (h)

Fig. 4. (a) Compressive strength test set up, (b) Cube and cylindrical specimens, (c) Prism specimens, (d) Test set up for MOE, (e) Disc-shaped specimens for RCPT and sorptivity, (f) Sorptivity test set up, (g) RCPT test set up, and (h) Test set up for drying shrinkage

5. Results and Discussions

5.1 Compressive Strength

5.1.1 Effect of RCA on CS in Unary Mixes

Fig. 5 shows the variations in the outcomes of the compressive strength. The compressive strength (CS) of concrete exhibits a declining nature with an increase in the substitution level of RCA. The decrease in strength increases as the replacement level of RCA rises. The strength is reduced by 8.72% to 16.34% compared to the traditional unary mix at different levels of RCA. The reduction in strength is attributed to the inferior properties of RCA, such as higher water absorption and the inferior quality of old mortar on the surface of RCA. The decline in the strength is also due to the formation of multiple ITZs in the RAC matrix [24]. In the work by Babar Ali et al., the CS is reduced by 18% when NCA was completely replaced by RCA [25]. In the work by Job Thomas et al., the CS decreases by 11-19% when 100% RCA was used [26].

5.1.2 Effect of Binary Blends, Ternary Blends, and Glass Fiber in CS of RAC

In the case of binary blends, the CS was reduced by 9.26% to 18.13% compared to the traditional binary mix. However, in the case of binary blends, the CS was enhanced by 1.37% to 3.59% when compared to the respective unary mixes. The increase in CS is due to the pozzolanic nature of PPC, which consists of fly ash particles. This resulted in the formation of additional C-S-H gel, which is denser and more stable than the primary hydration products. The newly formed C-S-H fills micro-pores and voids within the cement matrix, effectively reducing porosity and enhancing packing density.

In the case of ternary blended mixes, Alccofine, an SCM, has ultra-fine particles that fill the micro-pores and voids, forming a dense concrete matrix. Alccofine reacts with the leftover CH produced during the hydration of cement, resulting in the C-S-H gel formation, which resulted in strength gain at all ages of curing. The fine particles of Alccofine improved the bond between the aggregates and the cement paste and reduced the formation of micro-cracks, enhancing concrete performance. The enhancement in strength was observed to be 5.88%- 9.62% when compared to the respective binary mixes. In ternary blend mixes, the strength of the mix C3(60%RCA) was found to be 38.67MPa, which is higher than that of the required target strength.

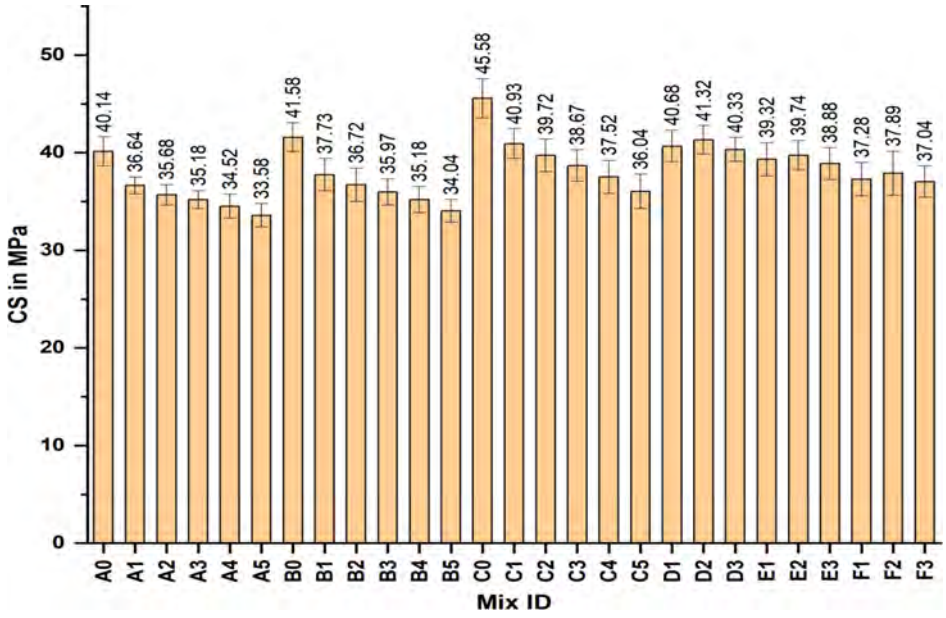


Fig. 5. Variations in Compressive strength outcomes after 28 days

The fibers are uniformly distributed in fiber-reinforced concrete mixes at lower dosages (0.25% and 0.50%). This helped to control the micro-cracks by preventing the cracks from propagating and widening, resulting in a strength gain. However, the dispersion is not uniform at higher fiber

dosages due to the balling effect that creates voids, reducing the strength and other concrete performances. The presence of fiber enhanced the performance of fiber-reinforced concrete by 2.77% to 6.85% when compared to the respective ternary mixes. The percentage of change in the CS is shown in Fig. 6, and the typical failures of the specimen are shown in Fig.7.

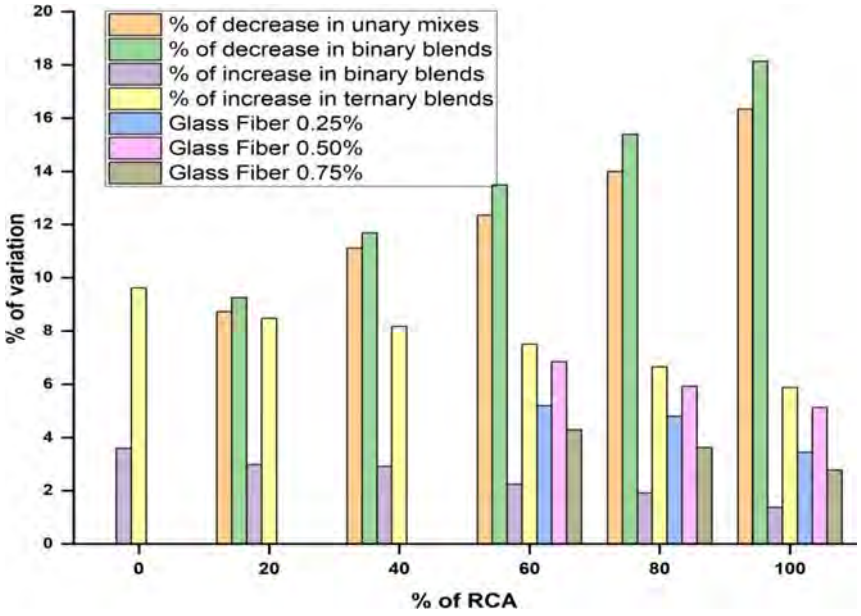


Fig. 6. Variations in Compressive strength outcomes after 28 days

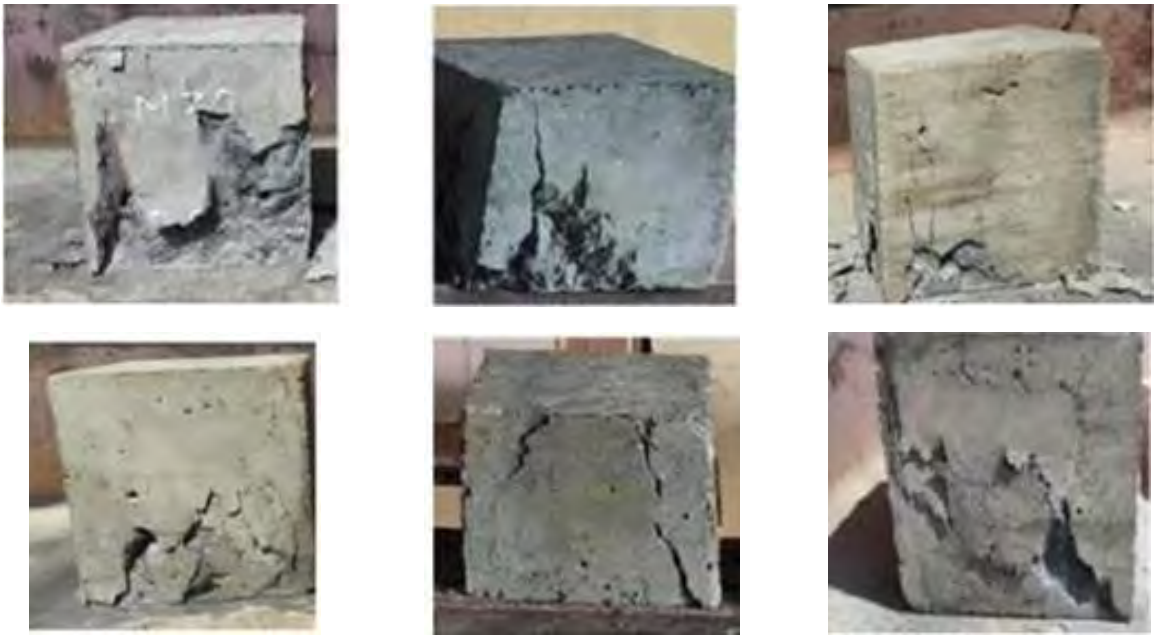


Fig. 7. Failure patterns in cubical specimens

5.2 Flexural Strength

Flexural strength is another crucial mechanical property of concrete, as it measures the material's ability to resist bending or cracking under applied loads. Figure 8 shows the variation of flexural test outcomes. The FS of the concrete with 100% NCA (A0) is 4.18 MPa, and it is reduced to 3.08 when 100% RCA (A5) is used, which shows a decline in strength of 26.32%. The reduction in strength is due to the newly formed ITZ between the RCA and the cement matrix. This newly formed ITZ is weaker than the ITZ formed between the NCA and the cement matrix. This newly formed weaker ITZ contributes to the reduced flexural strength and crack propagation under loading.

From Fig. 8, it can be seen that the optimum strength values are observed in fiber-reinforced blends and then followed by ternary, binary, and unary blends. Mixes with higher levels of RCA exhibited poorer performance, and the relationship between the RCA levels and flexural strength is inversely proportional, which means that the higher the RCA, the lower the strength. In ternary mixes, due to the combined action of PPC and Alccofine, the strength was enhanced due to the fine nature of the materials, which resulted in the improved packing density of the concrete matrix. Mixes with glass fibers have shown the highest strength improvement among all the series. The FS was enhanced by 6.81% to 12.97% for mixes with glass fibers. Typical failures in flexure are shown in Fig. 9. For concrete to be used in rural road applications, the minimum flexural strength should be 3.8 MPa per IRC: SP:62-2014 [27]. Achieving the minimum flexural strength in concrete is essential for rural road applications, as it significantly influences the pavement's structural performance and durability. In rural areas, where maintenance resources are often limited, ensuring sufficient flexural strength minimizes the risk of cracking, deformation, and premature failure. In the present study, flexural strength was found to be 3.89 MPa for the mix E2 (80% RCA), which can be used safely for rural road pavement applications as it satisfies the minimum strength requirement.

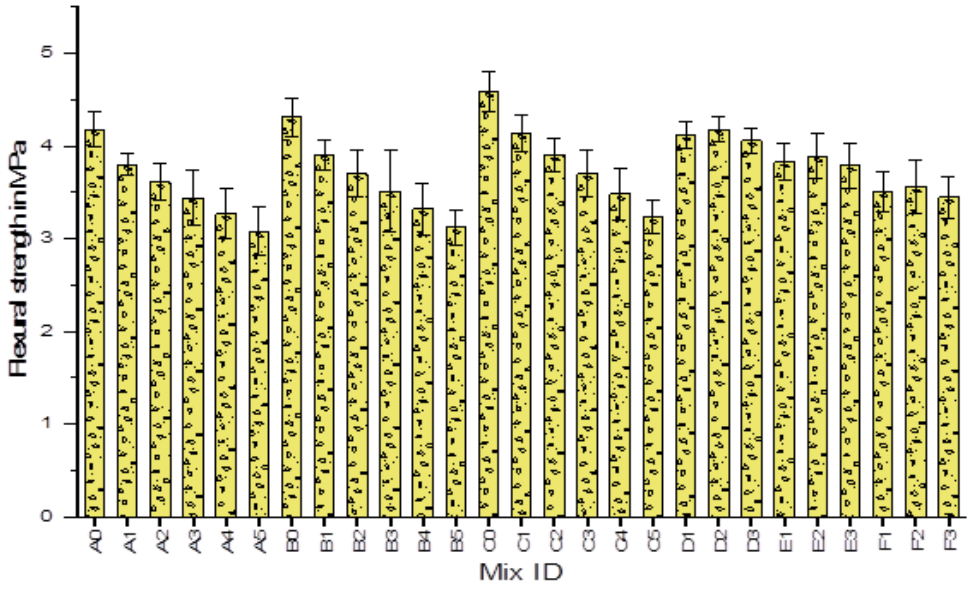


Fig. 8. Test outcomes of flexural strength



Fig. 9. Typical failures of prisms under flexure

5.3 Modulus of Elasticity

The modulus of elasticity is one of the essential mechanical parameters as it represents the compactness and stiffness of the concrete. The elastic modulus after 28 days with different levels of RCA, Alccofine, and glass fibers is investigated in the present study, and its outcomes and variations are shown in Fig. 10 and 11. Fig. 10 shows that the performance of RAC in MOE declined with the rise in the substitution level of RCA in all the series. The MOE for the concrete with 100%

NCA (A0) is 33.82 MPa, and 27.34 MPa (A5) when 100% RCA is used, which shows the MOE is reduced by 19.16%. The decline in the performance of MOE is due to the weaker bond between the cement paste and RCA. The MOE of concrete decreases with an increase in the level of RCA due to the existence of residual mortar, which has lower stiffness and strength, reducing the overall stiffness of the concrete when RCA content increases. In the mixes with PPC, i.e., binary blend series, the MOE with 100% NCA is 34.68 MPa (B0) and 27.73 MPa (B5) when 100% RCA is used. Comparing the outcomes of binary mixes with unary blends, the MOE is enhanced by 1.43% - 2.54% at different levels of RCA. This increase in strength is due to the pozzolanic nature of PPC, which helps maintain the integrity of the concrete matrix by reducing the cracking and shrinkage parameters. In ternary blends, the Alccofine improved the particle packing density, and due to its finer particle size, it enhanced the bond between the aggregates and the cement paste, and MOE was found to be between 36.42 MPa(C1) to 28.64 MPa(C5), which resulted in an improvement of 3.28%-5.02% when compared to binary blends. The variations in the percentage of strength gain or decline are shown in Fig. 11. Fiber-reinforced mixes exhibited superior performance as the presence of glass fibers helps reduce shrinkage, minimizes the risk of cracking, and improves the ductility of concrete, making it withstand deformation without cracking.

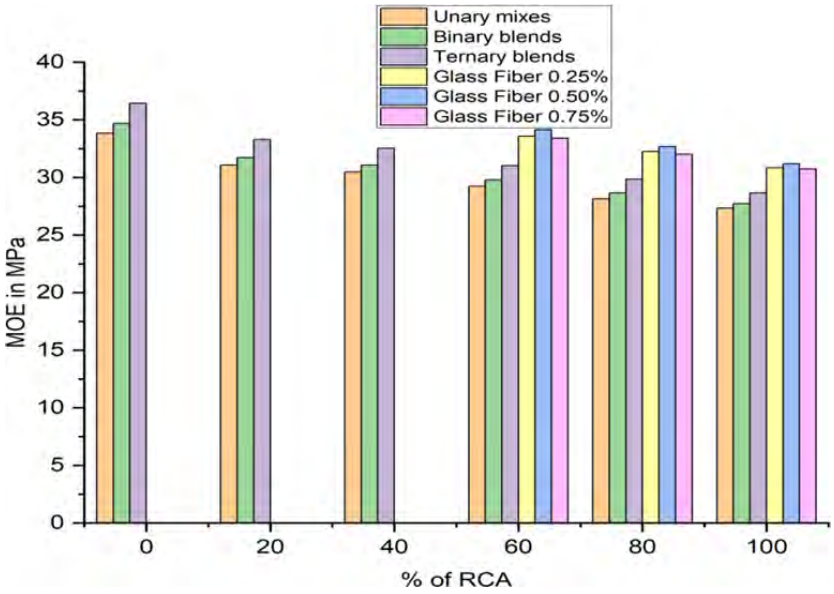


Fig. 10. Modulus of elasticity outcomes after 28 days

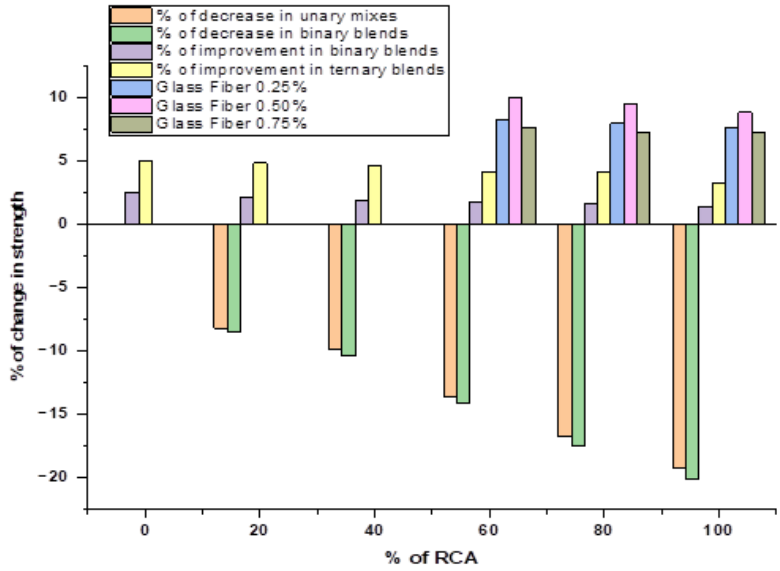


Fig. 11. Variation in modulus of elasticity

5.4 Rapid Chloride Penetration Test

Rapid chloride penetration test helps determine the concrete matrix's efficacy in impeding the ingress of chloride ions. The charge passed in coulombs is 1822 for the concrete mix having 100% NCA (A0), and the charge passed is increased to 2266 coulombs for the RAC having 100% RCA (A5), which shows the decline in the performance by 24.37%. From Fig. 12, an increase in the percentage of RCA in RAC typically results in higher chloride ion permeability. This is due to micro-cracks on the residual mortar on the surface of RCA, which acts as an additional channel for chloride ions to penetrate, increasing the permeability of RCA in RAC. Also, due to the porous nature of RCA, which increased permeability, leading to the faster passage of chloride ions, the concrete is less resistant to the passage of chloride ions. A similar pattern of outcomes was observed in the work carried out by other researchers [4,28]. In the binary mixes, the charge passed is 1692 coulombs for the mix having 100% NCA (B0) and 2176 coulombs for the RAC mix having 100%RCA (B5). However, the penetration resistance was enhanced in binary and ternary mixes due to the C-S-H gel formation, which improved the concrete impermeability by densifying the microstructure and by refining the pore structure due to the micro-filling ability and pozzolanic reactivity, respectively and the variation is shown in Fig. 12.

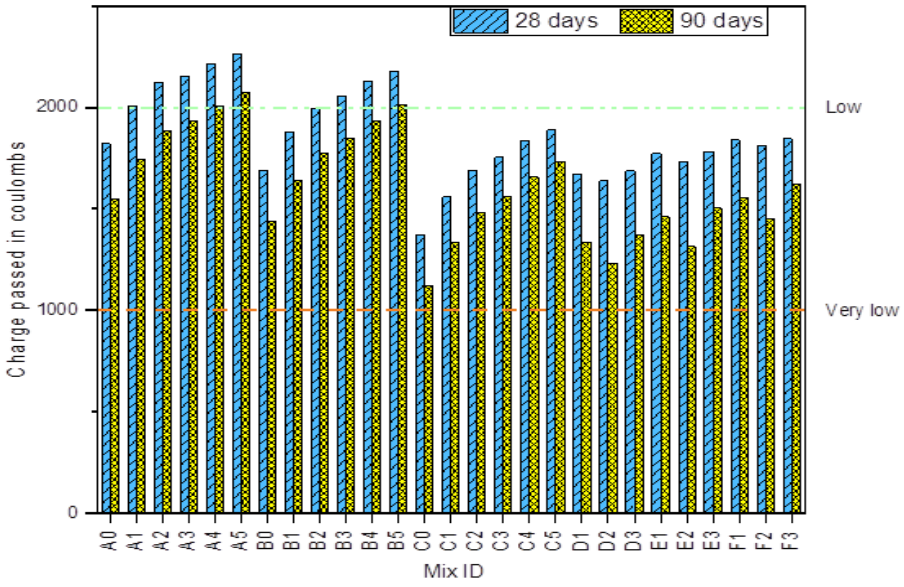


Fig. 12. Variations in RCPT

In binary blends, the charge passed is 1692 coulombs for mix B0 (100% NCA) and 2176 coulombs for mix B5 (100%RCA). This shows that in binary mixes, the penetration resistance is improved by 3.97% to 7.14% compared to the unary mixes. The improvement is due to the pozzolanic reactivity of PPC. In ternary blends, the charge passed is 1374 coulombs for mix C0 (100% NCA) and 1888 coulombs for mix C5 (100% RCA). The test results of the ternary mixes show that the chloride penetration resistance of RAC improved by 13.24% to 18.79% compared with the binary mixes. For fiber-reinforced ternary blends, the resistance was further enhanced. However, for the 90-day curing period, the charge passed through the concrete matrix was further reduced in all the mixes compared to 28 days. In unary and binary blends, at low RCA, the RCPT falls into the low category; as RCA increases, the RCPT shifts to the moderate category. In the case of ternary and fiber-reinforced ternary mixes, RCPT is in the low category region for both samples of different ages. Table 4 shows the classification of chloride ion permeability based on ASTM-C-1202. Based on the ASTM classification mentioned in Table 4, the RCPT outcomes shown in Fig. 12 say that the RCPT is in the range of moderate and low chloride ion penetrability for the unary and binary mixes. The charge passed for different ages of curing samples in the ternary and fiber-reinforced mixes lies in the low chloride ion permeability category.

Table 4. Classification of chloride ion penetrability based on ASTM – C – 1202

Charge passed in coulombs	>4000	2000 – 4000	1000 – 2000	100 – 1000	<100
Chloride ion penetrability	High	Moderate	Low	Very low	Negligible

5.5 Sorptivity

Sorptivity is one of the essential durability parameters of concrete, and the concrete matrix's resistance against water penetration in uni-directional is evaluated. Like the other concrete parameters, the sorptivity exhibited poorer behavior with the increasing level of RCA. The sorptivity of concrete increased with an increase in RCA in all the series. Similar observations were found in the work done by other researchers [29-31]. The variation in the test outcomes is shown in Fig. 13. From Fig. 13, it can be seen that for 28 days results in unary, binary, and ternary blends, the sorptivity ranged from 0.154 mm/min$^{1/2}$ to 0.218 mm/min$^{1/2}$, 0.141 mm/min$^{1/2}$ to 0.209 mm/min$^{1/2}$ and 0.118 mm/min$^{1/2}$ to 0.194 mm/min$^{1/2}$ respectively.

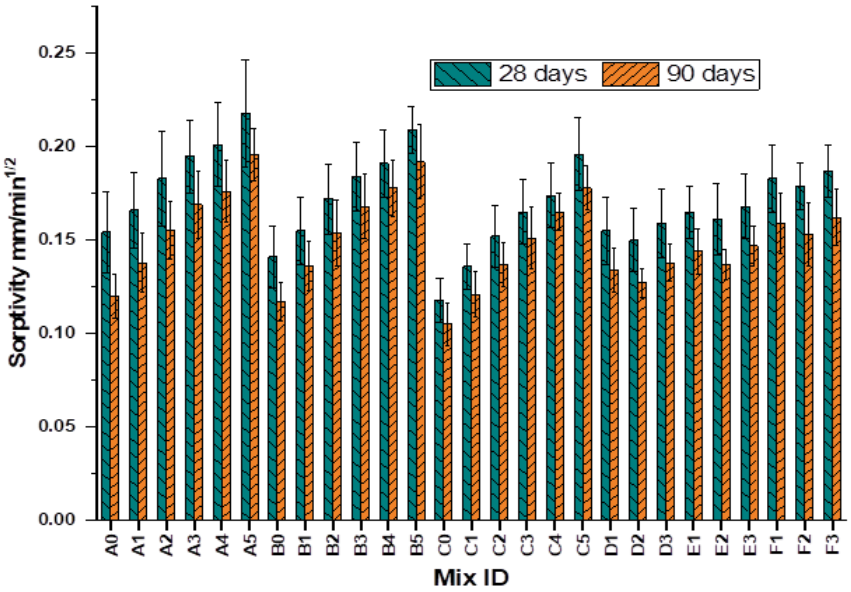


Fig. 13. Variations in Sorptivity

The performance dropped by 41.56% for 100% RCA (A5) compared to the unary conventional mix after 28 days. However, in the binary blends and ternary blends, the resistance of the concrete matrix was enhanced by 4.13% - 8.44% and 7.18% to 16.31% when compared with the unary and binary blends, respectively, after 28 days curing period. In fiber-reinforced ternary mixes, up to the optimum dosage of fibers, the resistance of the concrete matrix was enhanced, but beyond that, the matrix's resistance dropped. The classification of concrete acceptance criteria based on sorptivity is given in Table 5. From Fig. 13, it can be seen that the acceptance criteria were acceptable for ternary and fiber-reinforced ternary blends. Still, for unary and binary blends, it is between acceptable and poor for test results with 28 days of curing samples. The test results of 90 days of samples showed acceptable criteria for all the mixes shown in Fig. 13.

Table 5. Acceptance criteria for sorptivity

Criteria	Very good	Acceptable	Poor
Sorptivity (mm/min$^{1/2}$)	< 0.1	0.10 – 0.20	> 0.20

5.6 Drying Shrinkage

Drying shrinkage is another critical parameter of concrete, which causes an increase in tensile stress, which may result in cracking, external deflection, and internal warping[32]. Various factors, such as the water-cement ratio, the binder's content, and the aggregate type, influence the drying shrinkage behavior [33].

5.6.1 Effect of RCA on Drying Shrinkage

Fig. 14 shows the variations in outcomes of drying shrinkage. In the unary mix series, the drying shrinkage was found to be 250 micro-strains for mix A0 (0%RCA), and it was 908 micro-strains for 100% RCA (A5), which is 3.63 times higher than the conventional mix (A0). The drying shrinkage was found to be increased with an increase in the replacement level of RCA. A similar pattern of increasing outcomes is observed in the work carried out by [34]. Micro-cracks and voids on the outer surface of RCA are prone to moisture loss, leading to higher drying shrinkage in concrete.

5.6.2 Effect of PPC, Alccofine, and Glass Fibers on Drying Shrinkage

Drying shrinkage for 100% RCA (mix A5) in the unary series is 908 micro-strains, and it was reduced to 863 micro-strains for 100% RCA (mix B5) in the binary series, which showed a reduction of 4.95%. The inclusion of PPC led to the additional C-S-H gel formation, which reduced the amount of free lime that helped minimize the potential for developing micro-cracks, reducing the shrinkage of concrete. As the heat of hydration is lower in PPC than in OPC, it reduces the risk of thermal shrinkage and cracking. Alccofine, an ultra-fine material with high pozzolanic reactivity, refines the micro-structure of concrete, reducing the permeability and resulting in lower shrinkage strains. The drying shrinkage strain in ternary mixes for the mix C5 (100% RCA) is found to be 752 micro-strains, which is reduced by 12.86% compared with the binary mix (B5). Due to the crack-arresting capability of glass fibers, fiber-reinforced ternary blends exhibited lower strain values than ternary blends.

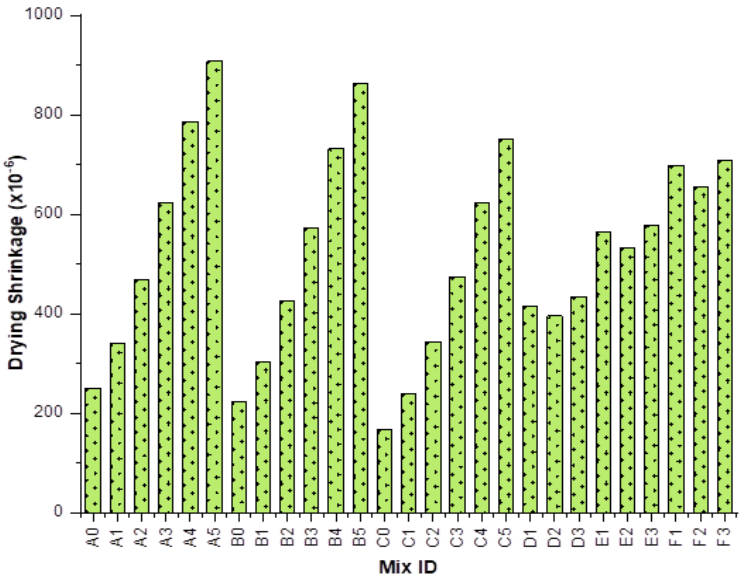


Fig. 14. Outcomes of drying shrinkage

6. Response Surface Methodology (RSM)

Response Surface Methodology (RSM) is a statistical and mathematical tool for modeling and optimizing processes. This technique focuses on understanding the complex relationships between multiple input variables and a single response variable, typically an output parameter [35]. RSM plays a vital role in process optimization and improvement by identifying key input variables influencing the response, Modeling the relationship between input and output variables, and predicting optimal input combinations for desired outcomes. By utilizing experimental data, RSM

fits regression models and creates response surfaces, enabling the identification of optimal conditions. This approach provides predictive mathematical models that simplify the analysis of how variations in one factor affect others. A crucial component of RSM is the Design of Experiments (DoE), which enables efficient and systematic testing of input variables.

Initially developed for physical experiments, RSM and DoE strategies are widely applied in numerical investigations, offering valuable insights into complex systems. RSM integrates with Design of Experiments (DoE) to systematically plan experiments and minimize the number of trials while maximizing information. RSM offers visual tools like contour and surface plots to interpret results and understand relationships between factors easily. RSM's Key benefits are enhanced process understanding, improved output variable optimization, reduced experimentation costs, and increased efficiency in numerical investigations.

In the current research, Alccofine, RCA, and GF were input variables in percentages for generating the RSM model. Surface plots for the compressive and flexural strength are shown in Fig. 14 and 15, whereas contour plots are shown in Fig. 16 and 17, respectively.

6.1 Inference from Surface Plots of CS and FS

Surface plots help visualize the relationship between multiple variables and how different factors affect strength. Fig. 15 shows the surface plot outcomes for the compressive strength. From Fig. 15, it can be concluded that the CS increased with an increase in the alccofine dosage and with the glass fibers up to its optimum dosage. The decline in the outcomes of CS is observed with an increase in levels of RCA.

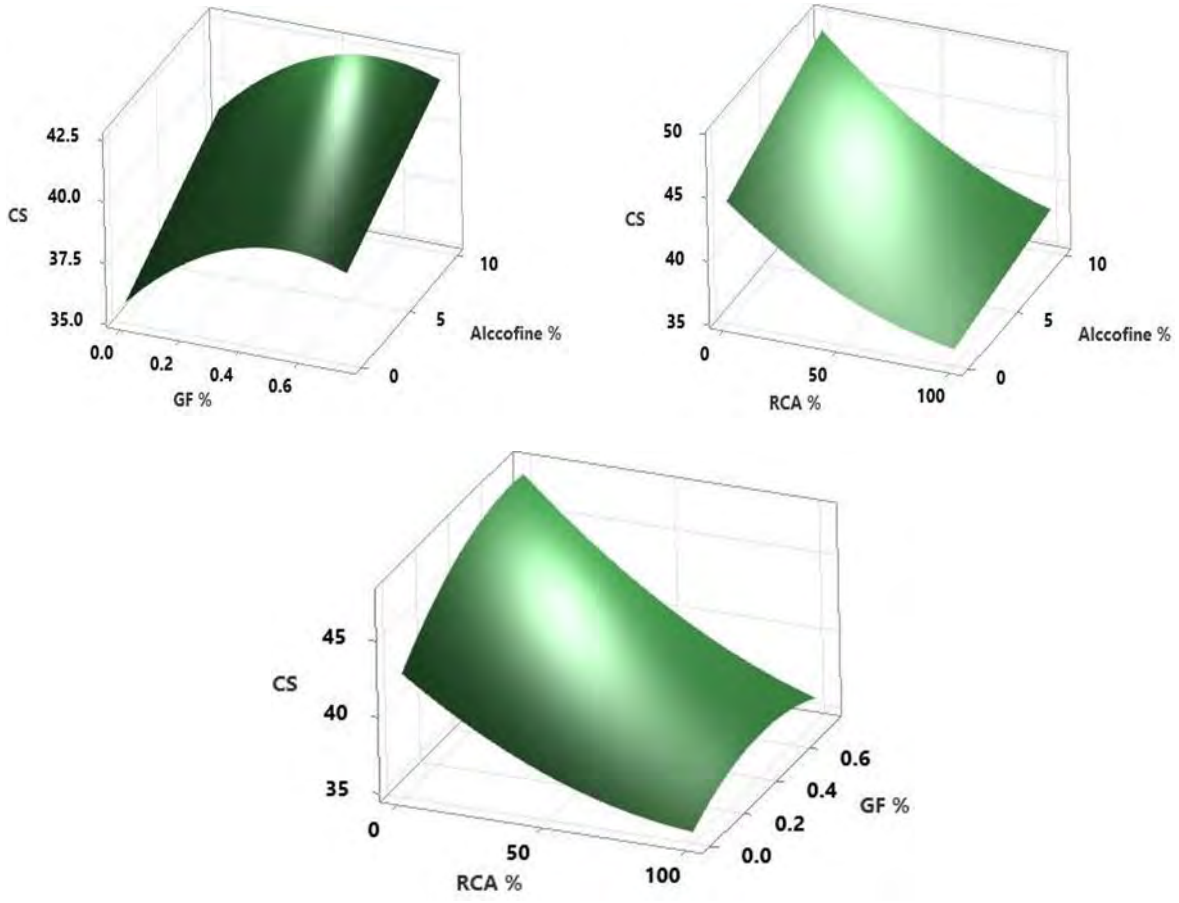


Fig. 15. Surface plots among the variables for CS

Fig. 16 shows the variations in flexural strength using surface plots. From Fig. 16, it can be seen that the lower the levels of RCA, the better the performance of concrete in flexure. The inclusion of alccofine and glass fibers enhanced the flexural behavior of concrete. However, the optimum

performance in flexure is observed with the optimum dosage of glass fiber. The response surface regression equations 1 and 2 for the compressive and flexural strength are given.

The following equations are generated using Minitab, a statistical software. The steps involved in generating these equations are as follows. Open Minitab. Enter the input variables in the worksheet. Go to the menu bar, click on the Stat tab, then select DOE, followed by the response surface option. Then, select the analyze response surface design option. Select the continuous factors and the responses, and then click ok. Then, select the required parameters and click ok. The outputs are displayed in the worksheet, and the plots with regression data will be displayed in the output datasheet.

$$Compressive\ strength = 40.275 - 0.1212\ RCA + 15.25\ GF + 0.4571\ Alccofine + 0.000599\ RCA*RCA - 11.33\ GF*GF - 0.0578\ RCA*GF - 0.00249\ RCA*Alccofine \quad (1)$$

$$Flexural\ strength = 4.1996 + 0.03461\ Alccofine - 0.01486\ RCA + 2.510\ GF + 0.000040\ RCA*RCA - 1.931\ GF*GF - 0.000213\ Alccofine*RCA - 0.00819\ RCA*GF \quad (2)$$

For the CS, the R^2, MSE, and RMSE were 95.10%, 0.358692, and 0.598909, respectively. For the FS, the R^2, MSE, and RMSE were found to be 98.25%, 0.002466, and 0.04966, respectively.

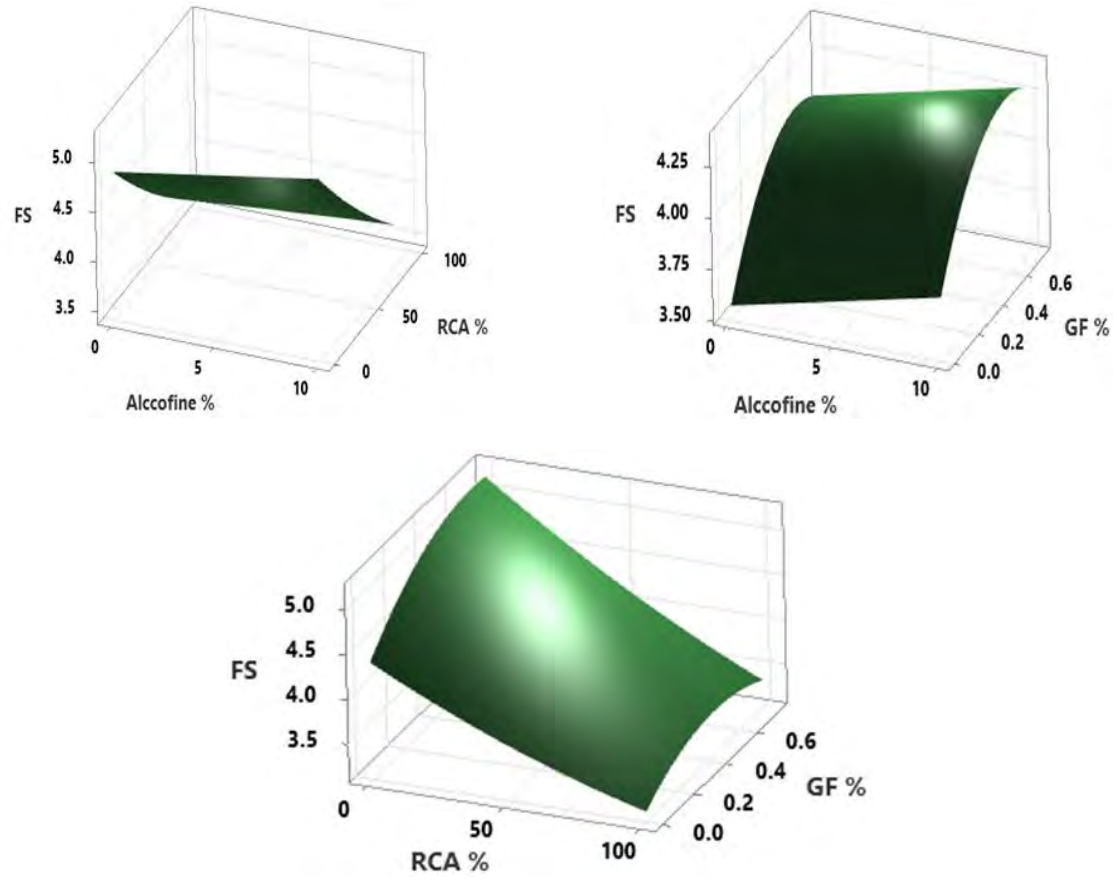


Fig. 16. Surface plots among the variables for FS

6.2 Inference from Contour Plots of CS and FS

Contour plots visually represent the relationship between multiple variables and their impact on a response, which can be a strength or durability parameter. Fig. 17 shows the contour plots for compressive strength. In Fig. 17, from the GF% vs RCA% plot, compressive strength decreases as RCA% increases at higher GF levels. In the Alccofine% vs RCA% plot, strength improves with higher Alccofine% for all RCA levels. Areas with higher CS (e.g., green regions) indicate the combinations

of variables that yield better compressive strength. These regions are critical for optimizing the mix design.

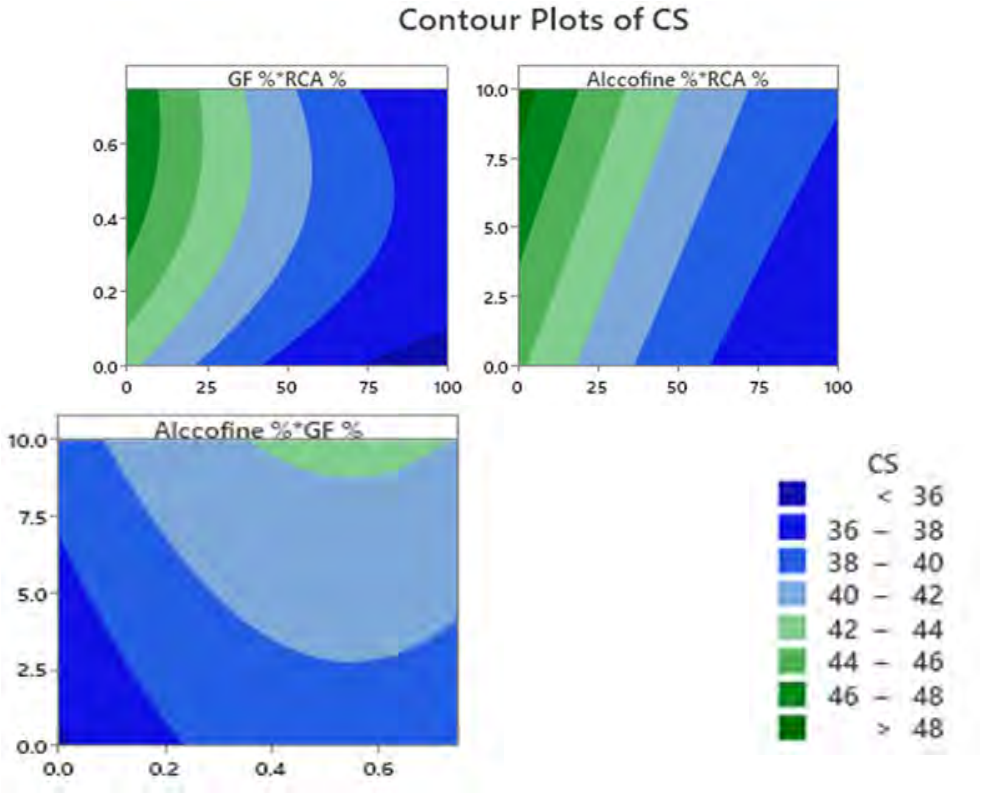
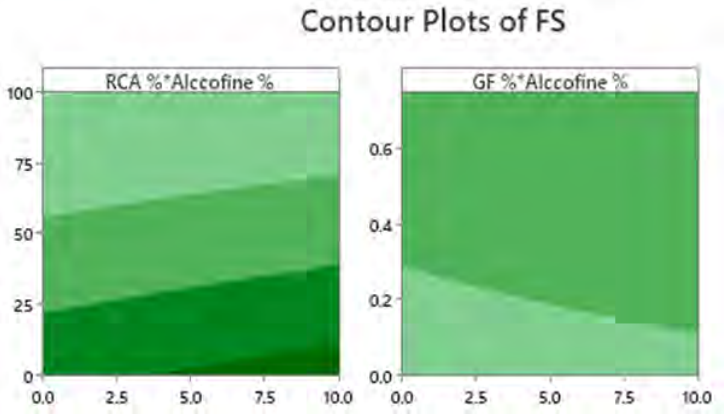


Fig. 17. Contour plots among the variables for CS

Fig. 18 shows the contour plot for the flexural strength. In the RCA (%) vs Alccofine(%) plot, flexural strength increases with higher Alccofine (%), as indicated by the darker green regions. Higher levels of RCA% slightly reduce FS, but this reduction is mitigated at high Alccofine percentages. In the GF (%) vs Alccofine (%) plot, FS improves significantly with increasing Alccofine%, regardless of GF levels. In the GF% vs NCA% plot, FS decreases with increasing RCA% for all GF levels, as indicated by the lighter regions toward the right. Higher GF% helps counterbalance the adverse effects of RCA%, as FS improves slightly in darker green zones at high GF levels. A combination of high GF% and low RCA% yields the highest FS, showing that GF can enhance the interfacial properties in RCA mixes. The surface and contour plots illustrate the relationships between key variables, offering valuable insights for optimizing concrete mix proportions. These visualizations enable designers to determine the ideal balance of materials required to achieve targeted performance characteristics, such as enhanced durability, strength, and water resistance.



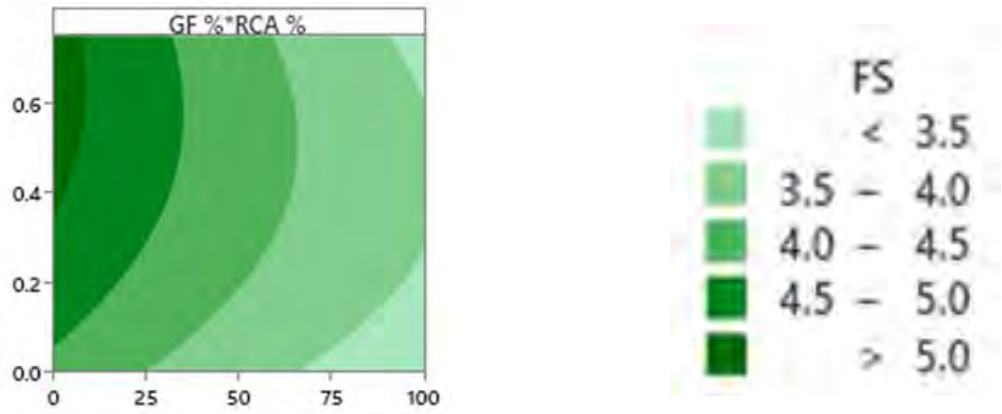


Fig. 18. Contour plots among the variables for FS

7. Microstructural Observations

Microstructural observations for the present study are carried out using scanning electron microscopy (SEM). SEM analysis is performed on the A0, A1, B1, and C1 mixes to understand the concrete matrix's micromorphology. These high-resolution images reveal each specimen's microstructure and surface morphology at a microscopic level.

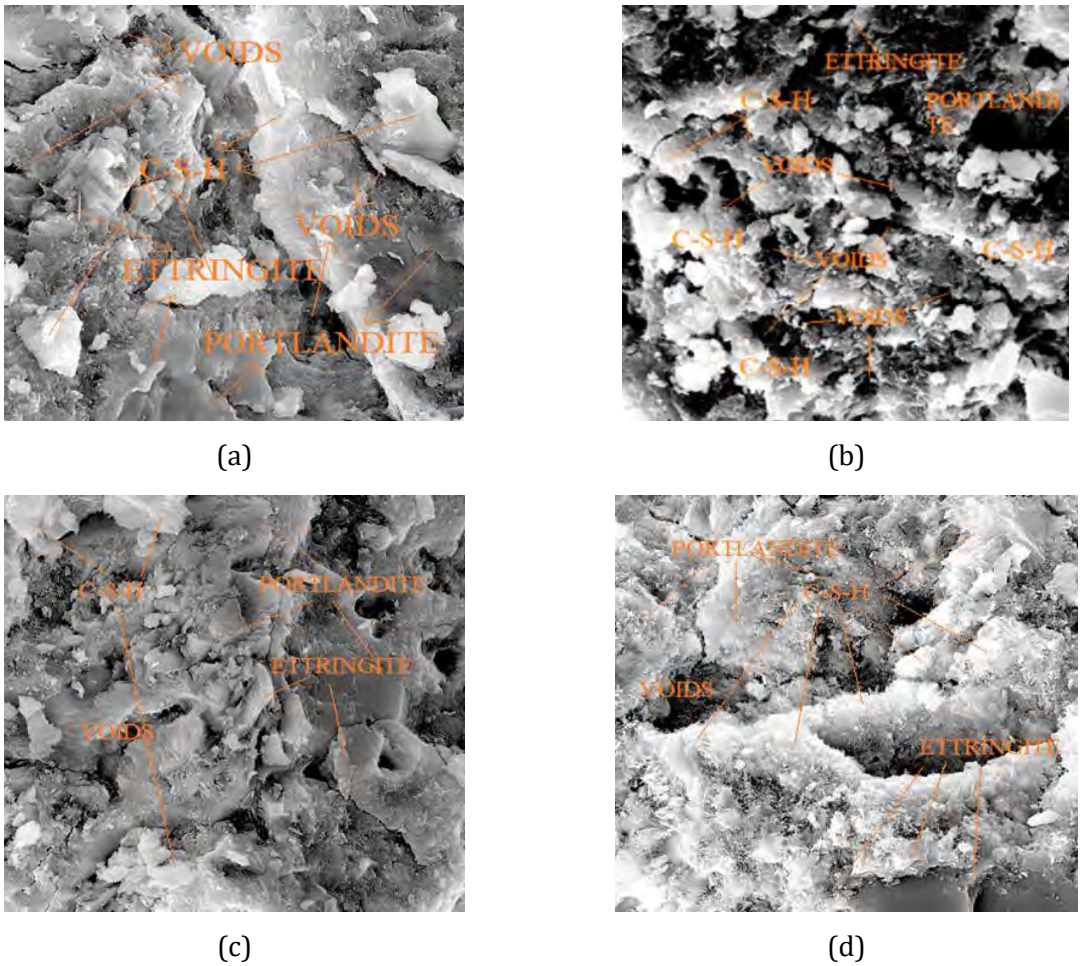


Fig. 19. SEM images (a) A0 mix, (b) A1 mix, (c) B1 mix , and (d) C1 mix

The SEM image of mix A0, representing conventional concrete, reveals a flaky and fragmented structure, as shown in Fig. 19(a). In mix A1, voids resulting from including RCA are evident, as depicted in Fig. 19(b). For mix B1, additional C-S-H gel formations are observed, filling the voids and contributing to strength enhancement, as shown in Fig. 19(c). In mix C1, the ultra-fine particles

of Alccofine effectively fill the voids, leading to dense C-S-H gel formations and a compact microstructure, as seen in Fig. 19(d). This dense microstructure in mix C1 significantly improves strength compared to the other mixes.

8. Conclusions

- The test results of the coarse aggregate indicate that RCA shows inferior performance compared with NCA. This is due to the existence of old mortar on the surface of the aggregates.
- Compared to OPC, mixes with PPC test outcomes exhibit better performance. Adding RCA lowers the compressive strength performance by 16.34% and 18.13% in series one and two, respectively. The partial substitution of Alccofine in RAC leads to remarkable enhancements in its properties. Consequently, incorporating Alccofine yields a maximum compressive strength augmentation of 9.62%. Incorporating glass fibers in RAC improves its behavior, with optimal benefits achieved at a fiber dosage of 0.50%. The compressive strength results achieve the target strength with an even 80% RCA level. As the desired target strength is achieved with 80% of RCA in the mix E2, it can be used for structural applications.
- The flexural strength test results show that fiber-reinforced ternary blends exhibit optimal behavior. Glass fiber inclusions result in higher strength gain in flexural behavior than concrete compression behavior. Mix E1 and E2 test results surpass rural road applications' minimum flexural strength requirements. Improved RAC can be used for low-volume rural road applications, reducing reliance on natural aggregates.
- The modulus of elasticity of concrete decreases with increased RCA replacement. The MOE lowers by 19.16% and 20.04%, respectively, for series one and two with 100% RCA. Glass fibers contribute to a higher strength gain in MOE.
- PPC exhibits minor improvements in all the mechanical properties of concrete. However, replacing PPC will help reduce construction costs and carbon footprint. At the same time, Alccofine and glass fibers exhibited a considerable strength gain. The performance of RAC improves as it transitions from unary to fiber-reinforced ternary blends.
- The test results of RCPT indicate that the charge passed in coulombs is directly proportional to the amount of RCA at all ages of curing. Binary and ternary blends exhibit superior performance in restricting the passage of chloride ions. The chloride ion permeability improves from moderate to low at all curing ages. Concrete with low RCPT values can be used in constructing pavements near coastal areas and in constructing basements to enhance the structure's lifespan.
- Similar to the RCPT results, the sorptivity outcomes also exhibit a proportional relationship with the amount of RCA. The test results reveal that the sorptivity performance of concrete improves from poor to acceptable levels. Since the sorptivity values fall within the acceptable range, the material is suitable for use in structures subjected to moderate environmental stresses, ensuring durability and reducing maintenance costs.
- Drying shrinkage outcomes indicate that the shrinkage strain with 100% RCA is 3.69 and 3.83 times higher than the conventional mix results. The drying shrinkage performance was improved by adding alccofine and glass fibers.
- Fiber-reinforced ternary blends offer notable economic and scalability benefits in construction by improving material efficiency and performance. Combining supplementary cementitious materials like Alccofine with Portland cement and reinforcing fibers reduces reliance on expensive, carbon-intensive cement, cutting costs and lowering CO_2 emissions. These blends enhance strength, durability, and crack resistance, extending structural lifespan and reducing maintenance expenses.

9. Future Work

Future studies could focus on evaluating freeze-thaw cycles, assessing carbonation depth, analyzing structural behavior, and conducting fatigue tests to provide a more comprehensive understanding.

Abbreviations

RCA – Recycled Concrete Aggregate/Recycled Coarse Aggregate
RAC – Recycled Aggregate Concrete
CS – Compressive Strength
FS – Flexural Strength
MOE – Modulus of Elasticity
GF – Glass Fiber
C&D waste – Construction and demolition waste
SCM - Supplementary Cementitious Material
OPC – Ordinary Portland Cement
PPC – Portland Pozzolana Cement
RCPT – Rapid Chloride Penetration Test
C-S-H – Calcium – Silicate – Hydrate
ITZ – Interfacial Transition Zone
WA – Water Absorption
SP – Super-Plasticizer

References

[1] Rajesh K.S, Samanta A. K, and Singha Roy D.K. An Experimental Study on the Compressive Strength of Alccofine with Silica Fume Based Concrete. Applied Mechanics and Materials. 2016;857:36-40. https://doi.org/10.4028/www.scientific.net/AMM.857.36
[2] Ozbakkaloglu. T, Gu. L, and Gholampour. A. Short-Term Mechanical Properties of Concrete Containing Recycled Polypropylene Coarse Aggregates under Ambient and Elevated Temperature. Journal of Materials in Civil Engineering. 2017;29(10):1-10. https://doi.org/10.1061/(ASCE)MT.1943-5533.0002046
[3] Joseph. M, Boehme. L, Sierens. Z, and Vandewalle. L. Water absorption variability of recycled concrete aggregates. Magazine of Concrete Research. 2015;67(11):592-97. https://doi.org/10.1680/macr.14.00210
[4] Thomas. J, Thaickavil. N. N, and Wilson. P. M. Strength and durability of concrete containing recycled concrete aggregates. Journal of Building Engineering. 2018;19:349-65. https://doi.org/10.1016/j.jobe.2018.05.007
[5] Tufekci. M. M and Cakir. O. An Investigation on Mechanical and Physical Properties of Recycled Coarse Aggregate (RCA) Concrete with GGBFS. International Journal of Civil Engineering. 2017;15(4):549-63. https://doi.org/10.1007/s40999-017-0167-x
[6] Gonzalez. B, Seara-Paz. S, De Brito. J, Gonzalez-Taboada. I, Martinez-Abella. F, and Vasco-Silva. R. Recycled concrete with coarse recycled aggregate. An overview and analysis. 2018;68(330);1-29. https://doi.org/10.3989/mc.2018.13317
[7] Xu. F, Tian. B, and Xu. G. Influence of the ITZ thickness on the damage performance of recycled concrete. Advances in Materials Science and Engineering. 2021;2021:1-8. https://doi.org/10.1155/2021/6643956
[8] Diamond. S and Huang. J. The ITZ in concrete-a different view based on image analysis and SEM observations. Cement & Concrete Composites. 2001;23:179-88. https://doi.org/10.1016/S0958-9465(00)00065-2
[9] Scrivener. K. L, Lyon. A. K. C, and Laugesen. F. P. The Interfacial Transition Zone (ITZ) Between Cement Paste and Aggregate in Concrete. Interface Science. 2004;12:411-21. https://doi.org/10.1023/B:INTS.0000042339.92990.4c
[10] Pedro. D, De Brito. J, and Evangelista. L. Influence of the use of recycled concrete aggregates from different sources on structural concrete. Construction and Building Materials. 2014;71:141-51. https://doi.org/10.1016/j.conbuildmat.2014.08.030
[11] Saha. S and Rajasekaran. C. Mechanical properties of recycled aggregate concrete produced with Portland Pozzolana Cement. Advances in Concrete Construction. 2016;4(1):27-35. https://doi.org/10.12989/acc.2016.4.1.027
[12] Kisku. N, Joshi. H, Ansari. M, Panda. S. K, Nayak. S, and Dutta. S. C. A critical review and assessment for usage of recycled aggregate as sustainable construction material. Construction and Building Materials. 2017;131:721-40. https://doi.org/10.1016/j.conbuildmat.2016.11.029
[13] Silva. R. V, De Brito. J, Neves. R, and Dhir. R. Prediction of chloride ion penetration of recycled aggregate concrete. Materials Research. 2015;18(2):427-40. https://doi.org/10.1590/1516-1439.000214
[14] IS 383-2016. Coarse and Fine Aggregate for Concrete-Specification.
[15] IS 12269:2013. Ordinary Portland cement, 53 Grade-Specification.
[16] IS 1489 (Part 1): 2015. Portland Pozzolana Cement-Specification.

[17] IS 2386-1 (1963). Methods of Test for Aggregates for Concrete. Part I: Particle Size and Shape.
[18] IS 2386-3 (1963). Methods of test for aggregates for concrete. Part 3: Specific gravity, density, voids, absorption, and bulking.
[19] IS 10262:2019. Concrete mix Proportioning - Guidelines.
[20] IS 516 (Part 1/Sec 1): 2021. Hardened Concrete-Methods of Test.
[21] ASTM C 1202. Standard Test Method for Electrical Indication of Concrete's Ability to Resist Chloride Ion Penetration.
[22] ASTM C 1585-04. Standard Test Method for Measurement of Rate of Absorption of Water by Hydraulic-Cement Concretes.
[23] IS 516 (Part 6): 2020. Hardened Concrete - Methods of Test.
[24] Ojha. P. N, Kaura. P, and Singh. B. Studies on mechanical performance of treated and non-treated coarse recycled concrete aggregate and its performance in concrete-an Indian case study. Research on Engineering Structures and Materials. 2024;10(1):341-62.
[25] Ali. B, Qureshi. L. A., and Khan. S. U. Flexural behavior of glass fiber-reinforced recycled aggregate concrete and its impact on the cost and carbon footprint of concrete pavement. Construction Building Materials. 2020;262:1-15. https://doi.org/10.1016/j.conbuildmat.2020.120820
[26] Thomas. J, Thaickavil. N.N, and Wilson. P.M. Strength and durability of concrete containing recycled concrete aggregates. Journal of Building Engineering. 2018;19:349-65. https://doi.org/10.1016/j.jobe.2018.05.007
[27] IRC: SP: 62-2014. Guidelines For Design and Construction of Cement Concrete Pavements For Low Volume Roads.
[28] Chundupalle. S, Seeri. N, Veera. S. R, and Nelluri. V. R. Strength and Durability Characteristics of Self-Compacting Concrete (SCC) With Recycled Aggregate and Manufactured Sand. Acta Polytechnica CTU Proceedings. Czech Technical University in Prague, 92-97,2022. https://doi.org/10.14311/APP.2022.33.0092
[29] Babu. V. S, Mullick. A. K, Jain. K. K, and Singh. P. K. Strength and durability characteristics of high-strength concrete with recycled aggregate-influence of processing. Journal of Sustainable Cement-Based Materials. 2014;4(1):54-71. https://doi.org/10.1080/21650373.2014.976777
[30] Muduli. R and Mukharjee. B. B. Performance assessment of concrete incorporating recycled coarse aggregates and metakaolin: A systematic approach. Construction and Building Materials. 2020;233:1-22. https://doi.org/10.1016/j.conbuildmat.2019.117223
[31] Jimenez. L. F and Moreno. E. I. Durability Indicators in High Absorption Recycled Aggregate Concrete. Advances in Materials Science and Engineering. 2015;2015:1-8. https://doi.org/10.1155/2015/505423
[32] Xiao. J, Lu. D, and Ying. J. Durability of recycled aggregate concrete: An overview. Journal of Advanced Concrete Technology. 2013;11:347-59. https://doi.org/10.3151/jact.11.347
[33] Aamar Danish and Mohammad Ali Mosaberpanah. A review on recycled concrete aggregate (RCA) characteristics to promote RCA utilization in developing sustainable recycled aggregate concrete (RAC). Taylor & Francis. 2022;26(9):6505-39. https://doi.org/10.1080/19648189.2021.1946721
[34] Cong Kou. S, Poon. C. S, and Chan. D. Influence of Fly Ash as Cement Replacement on the Properties of Recycled Aggregate Concrete. Journal of Materials in Civil Engineering. 2007;19:709-17. https://doi.org/10.1061/(ASCE)0899-1561(2007)19:9(709)
[35] Chinnusamy. B. S and Venkataraman. G. A comparative analysis of high-performance concrete: evaluation of strength and durability parameters with alternate fine aggregates and alccofine through response surface methodology model. Revista Materia. 2024;29(3). https://doi.org/10.1590/1517-7076-rmat-2024-0021

Blank Page

Research on Engineering Structures & Materials
www.jresm.org

Research Article

Enhancing concrete mechanical properties using nano-silica, calcined clay, and glass fibers optimized by response surface methodology

Ashish Attari [*,a], Balwinder Lallotra [b]

Department of Civil Engineering, Chandigarh University, Mohali, India

Article Info

Article History:

Received 18 Oct 2024

Accepted 17 Jan 2025

Keywords:

Calcined clay;
Glass fibers;
Mechanical properties;
Nano-silica;
Response surface methodology

Abstract

This study investigates the combined effects of nano-silica, calcined clay, and glass fibers on the mechanical properties of normal-grade concrete (M30), with a primary aim to utilize industrial waste materials and improve concrete performance while promoting environmental sustainability. Response Surface Methodology (RSM) was employed to optimize material proportions and evaluate their impact. The experimental design incorporated nano-silica (0– 10%), calcined clay (0–30%), and glass fibers (0–2%), corresponded to the minimum and maximum values in the range. A total of 120 specimens were tested to assess compressive strength, flexural strength, rebound hammer values, and ultrasonic pulse velocity (UPV). The optimized mix predicted compressive strength of 49.41 MPa, flexural strength of 9.05 MPa, rebound hammer value of 62 MPa, and UPV of 5445 m/s. Validation tests demonstrated observed compressive strength of 46.55 MPa, flexural strength of 8.05 MPa, rebound hammer value of 60 MPa, and UPV of 4890 m/s, with errors of 5.79%, 11.00%, 3.22%, and 10.19%, respectively. Analysis of variance (ANOVA), a statistical method for determining the significance of factors on observed outcomes, indicated that nano-silica had the most substantial impact on all performance metrics. The models showed high reliability, with R^2 values of 0.9653 for compressive strength, 0.9268 for flexural strength, 0.9266 for rebound hammer, and 0.8894 for UPV. The study demonstrates the potential of incorporating waste materials like calcined clay and nano-silica into concrete to enhance its mechanical properties and reduce environmental impact. This approach aligns with sustainable construction practices by lowering reliance on traditional cement, reducing carbon emissions, and promoting the reuse of industrial by products. The findings support the development of cost-effective, durable, and eco-friendly infrastructure, addressing the dual objectives of improved performance and environmental sustainability.

© 2025 MIM Research Group. All rights reserved.

1. Introduction

The utilization of advanced materials in concrete has become increasingly significant in modern construction, as researchers and engineers seek to enhance the structural integrity and durability of concrete compositions. Among these materials, glass fibres and nano-silica have attracted considerable scholarly interest due to their capacity to improve the mechanical properties and longevity of concrete. Glass fibres, noted for their high tensile strength and resistance to corrosion, offer a more effective alternative to traditional reinforcement materials such as steel. When incorporated into concrete, glass fibres can substantially enhance its tensile and flexural strength, thereby increasing its overall robustness.

*Corresponding author: 21mce1411@cuchd.in
[a]orcid.org/0000-0002-1813-3683; [b]orcid.org/0009-0008-1527-2734
DOI: http://dx.doi.org/10.17515/resm2025-492me1018rs

Similarly, nano-silica has emerged as a critical material in enhancing the microstructure and mechanical properties of concrete. By reducing porosity and increasing the density of the cement matrix, nano-silica contributes to the overall strength and durability of the concrete. This enhancement is particularly advantageous in applications where concrete must endure challenging environmental conditions, such as in large-scale infrastructure projects[1]. The integration of calcined clay, particularly kaolinitic clay, as a supplementary cementitious material (SCM) in concrete has gained considerable attention due to its pozzolanic properties, which significantly improve the mechanical durability and performance of concrete structures [Ng and Engelsen 2018]. Calcined clay is produced by thermally treating clay at temperatures between 600°C and 900°C, leading to the dehydroxylation of clay minerals and the formation of reactive amorphous silica and alumina. This transformation is crucial as it allows calcined clay to react with calcium hydroxide produced during the hydration of Portland cement, resulting in the formation of calcium silicate hydrates (C-S-H), which are essential for concrete strength and durability [2-3].

Several studies have shown that the pozzolanic activity of calcined clay is influenced by various factors, such as the type of clay, calcination temperature, and fineness of the material. For instance, higher calcination temperatures have been found to increase the reactivity of kaolinitic clays, enhancing their effectiveness as SCMs. The pozzolanic reaction not only improves the mechanical strength of concrete but also enhances its durability by refining the pore structure, reducing porosity, and increasing density, which is particularly beneficial in environments where concrete is exposed to aggressive chemicals and moisture [4].

Research has also demonstrated that the inclusion of calcined clay can lead to significant improvements in compressive strength and durability. Additionally, calcined clay has been shown to accelerate hydration kinetics, particularly in high pH environments, promoting the dissolution of clay particles and stimulating pozzolanic reactions. This acceleration can lead to faster strength development, making calcined clay an attractive option for projects requiring shorter construction timelines. Moreover, from a sustainability perspective, the use of calcined clay reduces the carbon footprint associated with cement production by partially substituting Portland cement, thereby decreasing the amount of clinker required, which is important due to the high greenhouse gas emissions from cement manufacturing [5-6].

The incorporation of nano-silica into concrete has emerged as a major advancement in materials science, especially in enhancing the mechanical and durability properties of cementitious materials. Nano-silica, with its extremely small particle size and high surface area, plays a critical role in refining the microstructure of concrete, leading to improved performance. Its inclusion reduces porosity and enhances the density of the cement matrix, both of which are essential for the durability and longevity of concrete structures. Wu and Khayat [2017] demonstrated that adding just 1% nano-silica reduced the porosity of ultra-high strength concrete by 29% after one day and 19% after 28 days. This reduction in porosity correlates directly with improved resistance to environmental factors such as moisture and chemical attacks, ultimately enhancing the overall durability of concrete [7-8].

Nano-silica's pozzolanic properties significantly contribute to improving the strength of concrete. This improvement is largely attributed to the filler effect of nano-silica, which refines the pore structure and promotes the formation of additional calcium silicate hydrates (C-S-H) during hydration, thereby enhancing the mechanical properties of concrete [9].

In addition to its mechanical benefits, nano-silica enhances the resistance of concrete to carbonation, which is a key factor in the long-term degradation of concrete structures. Alqamish and Al-Tamimi [2021] reported that incorporating nano-silica into concrete formulations improved carbonation resistance, thus extending the lifespan of concrete in environments exposed to carbon dioxide[10]. This improvement in carbonation resistance is particularly important for maintaining structural integrity in various applications. Furthermore, the rheological properties of concrete mixtures are positively influenced by the addition of nano-silica. Alvansazyazdi [2023] found that nano-silica in shotcrete improved its strength and impermeability, optimizing the interfacial structure of the cementitious materials, which is crucial for applications such as tunnels and underground constructions [11].

The interfacial transition zone (ITZ) between aggregates and cement paste is another area where nano-silica proves beneficial. Babalu and Sunil [2019] showed that the incorporation of nano-silica enhances the pore structure and improves the ITZ, often a weak point in concrete[Babalu* and Sunil 2019]. This refinement leads to stronger adhesion between aggregates and the cement paste, resulting in improved overall strength and durability [12]. Additionally, nano-silica has been linked to a reduction in shrinkage rates in concrete. Nano-silica in high-volume fly ash concrete significantly improved durability, including reduced water absorption and shrinkage, which are critical for minimizing cracking and ensuring the long-term stability of concrete structures [13].

Research indicates that the optimal dosage of nano-silica is critical; while a 1% addition by weight of cement has been shown to maximize strength, higher concentrations can adversely affect workability and strength [14]. Specifically, concentrations exceeding 3% may lead to a reduction in compressive strength due to the lumping phenomenon, which negatively impacts the mixture's workability [15]. This underscores the importance of carefully balancing the amount of nano-silica used in concrete formulations to achieve desired mechanical properties without compromising workability. The pozzolanic reaction of nano-silica with calcium hydroxide during hydration produces additional calcium silicate hydrate (C-S-H) gel, which is responsible for the strength of concrete [16]. This reaction not only enhances the mechanical properties but also reduces the porosity of the concrete, leading to improved durability [17]. Studies have shown that incorporating nano-silica can increase compressive strength by up to 21% and tensile strength by 44% compared to control specimens without nano-silica [18].

The incorporation of glass fibers into concrete has gained significant attention in recent years due to their capacity to enhance both the mechanical properties and durability of concrete structures. A key advantage of glass fibers is their ability to improve both tensile and flexural strength in concrete mixtures. For instance, the addition of glass fibers to peach shell lightweight concrete led to a substantial increase in compressive strength, attributed to improved bonding at the interface between the fibers and the cement paste [19].

Extensive research has been conducted to assess the mechanical properties of glass fiber reinforced concrete (GFRC). The flexural modulus of elasticity showed minimal variation across different fiber volume fractions, the overall mechanical performance of GFRC was notably enhanced [Tahir et al. 2023]. The incorporation of glass fibers improves ductility and resistance to crack failure, thereby enhancing the structural integrity of concrete [Fenu, Forni, and Cadoni 2016]. Additionally, the durability of GFRC is a crucial aspect, with Yıldırım and Özhan (2023) reporting that alkali-resistant glass fibers significantly mitigate deterioration in alkaline conditions, thereby extending the longevity of concrete compositions [20].

Furthermore, glass fibers play a vital role in reducing fracture propagation, which is essential for maintaining the structural integrity of concrete under external forces. Zaid et al. (2021) emphasized that glass fibers act as bridges between fissures, preventing them from merging and thus preserving the integrity of the concrete [21]. The successful integration of glass fibers into various concrete formulations, including geopolymer concrete, has also been documented. Adding glass fibers to geopolymer mixtures significantly improved flexural strength [22].

The objective of this research is to examine the collective impacts of these substances on the mechanical characteristics of concrete through the application of Response Surface Methodology (RSM) for optimization. RSM is a powerful statistical method that makes it possible to assess and optimize several factors at once, giving researchers new information about how calcined clay, nano-silica, and glass fibres interact. Through a methodical examination of these materials' effects on important mechanical attributes like compressive strength and flexural strength, this study aims to create an ideal concrete mix design that optimizes performance while preserving material economy. The study's conclusions will benefit the larger field of sustainable building materials by providing a thorough understanding of the efficient integration of these cutting-edge ingredients into concrete formulas.

2. Experimental methodology

2.1 Materials

The materials used in this study were carefully selected to enhance the mechanical properties and sustainability of the concrete mix. Ordinary Portland Cement (OPC) 43 Grade, with a specific gravity of 3.14 and a fineness of 4.0%, served as the primary binder as per Indian standard. Nano-silica, characterized by a particle size of 20-50 nm and a specific gravity of 2.33, was incorporated as a partial cement replacement. Its ultrafine particles contributed significantly to improving the microstructure of the concrete by filling voids and increasing density, thereby enhancing compressive strength and durability. Natural river sand, conforming to Zone III specifications, was used as the fine aggregate, with a specific gravity of 2.65 and a fineness modulus of 2.75. To further enhance durability, calcined kaolinite clay, with a specific gravity of 2.60, was used as a sand substitute. Calcined clay acted as a pozzolanic material, reacting with calcium hydroxide to form additional cementitious compounds, thereby improving the concrete's long-term strength and resistance to chemical attack.

Glass fibers, with a diameter of 25 microns, a length of 15 cm, and a specific gravity of 2.68, were added to enhance flexural performance. These fibers effectively bridged microcracks, reducing crack propagation and improving the concrete's resistance to bending and tension forces. Crushed angular coarse aggregates, with a nominal size of 20 mm and a specific gravity of 2.71, were used as the primary coarse aggregate to provide bulk and strength. Portable water with a specific gravity of 1.0 was used for the mixing process to ensure proper hydration and workability. Additionally, a Sikaplast superplasticizer was added at a dosage of 1% to improve workability and ensure uniform distribution of the mix components. The combination of these advanced materials—nano-silica, calcined clay, and glass fibers—demonstrates their collective ability to enhance the performance, durability, and sustainability of concrete and the Figure 1 shows materials used in this study.



(a) (b) (c)

Fig. 1. Materials used in this study (a) Nano silica (b) Calcinated clay and (c) Glass fiber

2.2 Mix Design

The study investigates the effects of varying replacement levels of nano-silica, calcined clay, and glass fibers on the mechanical properties and durability of concrete as per IS10262:2019 (BIS 2019). Nano-silica was used as a partial cement replacement at levels of 0%, 3%, 5%, 7%, and 10% by weight of cement. Calcined clay was substituted for sand at levels of 0%, 10%, 20%, 25%, and 30% by weight of sand. Additionally, glass fibers were added to the concrete mix at levels of 0%, 0.5%, 1.0%, 1.5%, and 2.0% of the total concrete volume. These varied levels were selected to systematically evaluate the impact of each material on the overall performance of the concrete, aiming to identify the optimal combination for enhancing both strength and durability.

The Design of experiment (DoE) software was selected to fully consider the experimental aspect. Preliminary tests were initially conducted to define the main parameters and related limits, both

lower and upper. The factors and levels to be used in the DoE were defined based on these tests, as described in Table 1. The control features of the experiment correspond with the literature.

Table 1. Factor level

Material	Range (min-max)	Neutral (0)	Low (-1)	High (+1)
Nano-Silica	0-10	5	0	10
Calcined Clay	0-30	15	0	30
Glass Fiber	0-2	1	0	2

In this response surface methodology (RSM), a central composite design (CCD) was applied to optimize the experimental conditions. Three continuous variables were used: Nano-Silica (0% to 10%), Calcined Clay (0% to 30%), and Glass Fiber (0% to 2%). The CCD involved low (-1), central (0), and high (+1) levels for each variable, with center points included to ensure accurate estimation of curvature. The experimental design was randomized to minimize bias, and multiple replicates were conducted at the center point for improving the reliability of the model and the precision of the response predictions. The experimental matrix is presented in Table 2. In this study, the water content was fixed at 181 kg/m^3, and a gallium-based superplasticizer was included at a dosage of 1% by weight of cement for the mix.

Table 2. Experimental matrix

Mix	Nano-Silica (%)	Calcined Clay (%)	Glass Fiber (%)	Nano-Silica (kg/m^3)	Cement (kg/m^3)	Calcined Clay (kg/m^3)	sand (kg/m^3)	Coarse aggregate (kg/m^3)
CM	0	0	0	0.00	422.30	0.00	671.10	1098.5
C1	5	15	0	21.12	401.19	100.67	570.44	1098.5
C2	5	0	1	21.12	401.19	0.00	671.10	1098.5
C3	0	30	2	0.00	422.30	201.33	469.77	1098.5
C4	5	15	1	21.12	401.19	100.67	570.44	1098.5
C5	5	15	1	21.12	401.19	100.67	570.44	1098.5
C6	10	0	2	42.23	380.07	0.00	671.10	1098.5
C7	5	30	2	21.12	401.19	201.33	469.77	1098.5
C8	5	0	1	21.12	401.19	0.00	671.10	1098.5
C9	5	15	0	21.12	401.19	100.67	570.44	1098.5
C10	0	30	2	0.00	422.30	201.33	469.77	1098.5
C11	5	30	1	21.12	401.19	201.33	469.77	1098.5
C12	5	0	2	21.12	401.19	0.00	671.10	1098.5
C13	0	30	2	0.00	422.30	201.33	469.77	1098.5
C14	5	0	2	21.12	401.19	0.00	671.10	1098.5
C15	10	0	2	42.23	380.07	0.00	671.10	1098.5
C16	0	0	1	0.00	422.30	0.00	671.10	1098.5
C17	5	15	1	21.12	401.19	100.67	570.44	1098.5
C18	5	15	0	21.12	401.19	100.67	570.44	1098.5
C19	10	15	2	42.23	380.07	100.67	570.44	1098.5
C20	0	0	1	0.00	422.30	0.00	671.10	1098.5

Table 2 experimental matrix with results outlines the effects of varying proportions of nano-silica, calcined clay, and glass fibers on concrete properties for M30grade concrete. Mixes with nano-silica (e.g., C4) showed improved compressive strength and flexural performance due to enhanced microstructure. Calcined clay significantly boosted results, with mixes like C10 (30% calcined clay) achieving the highest compressive strength (41.3 MPa) and flexural strength (6.4 MPa), attributed

to its pozzolanic activity. Glass fibers enhanced flexural properties by bridging microcracks, as seen in mixes like C6 (10% nano-silica, 2% glass fibers). Overall, combinations of these materials improved durability, strength, and uniformity.

2.3 Experimental Setup

2.3.1 Compressive Strength

This test was conducted in accordance with IS 516 (Part 1/Sec 1):2021, which provides the procedure for determining the compressive strength of concrete. Cube specimens measuring 150 mm × 150 mm × 150 mm were tested after 28 days of water curing using a compression testing machine to assess their strength. The specific results are shown in Table 3 and Figure 2.

2.3.2 Flexural Strength

The flexural strength test was carried out as per IS 516 (Part 1/Sec 1):2021. This standard outlines the method for determining the flexural strength of concrete by applying loads to beam specimens measuring 100 mm × 100 mm × 500 mm until failure.

2.3.3 Rebound Hammer

The rebound hammer test was performed according to IS 516 (Part 5/Sec 4):2020. This non-destructive test assesses the surface hardness of concrete and estimates its compressive strength based on the rebound values measured from the hammer. Cube specimens measuring 150 mm × 150 mm × 150 mm were used for this test.

2.3.4 UPV Test

The Ultrasonic Pulse Velocity (UPV) test was conducted following IS 516 (Part 5/Sec 1):2018. This test measures the velocity of ultrasonic pulses passing through concrete to evaluate its quality, uniformity, and potential defects. Cube specimens measuring 150 mm × 150 mm × 150 mm were used for this test.

Table 3. Mix and their results of specific properties

Mix	R1: Compressive Strength (MPa)	R2: Flexural Strength (MPa)	R3: Rebound Hammer (MPa)	R 4: UPV Test (m/s)
CM	39.4	5.07	36	3500
C1	39.5	5.7	37	3400
C2	40	6	38	3500
C3	39.3	5.85	36	3250
C4	40.05	6.02	37	3550
C5	40.05	6.02	37	3550
C6	40.7	6.3	39	3620
C7	41	6.25	38	3650
C8	40.05	6.02	37	3600
C9	40.05	6.02	37	3600
C10	41.3	6.4	41	3740
C11	40.5	6	38	3600
C12	39.3	5.75	36	3250
C13	40.8	6.35	40	3700
C14	40.05	6.02	37	3600
C15	38.5	5.5	34	3250
C16	38.7	5.6	34	3200
C17	38.75	5.6	35	3300
C18	40.1	6.05	37	3600

C19	40.2	6.05	36	3600
C20	38.9	5.7	35	3250

After 28 days of water curing, the compressive strength of the concrete mixes was evaluated using both cube compressive strength and rebound hammer tests as shown in figure 3. The cube compressive strength ranged from 38.5 MPa to 41.3 MPa, with the highest value observed in Mix C10 (41.3 MPa), containing 30% calcined clay and 2% glass fiber, likely due to the pozzolanic reaction of calcined clay enhancing the concrete matrix and the glass fibers improving crack resistance. Similarly, the rebound hammer test, which measures surface hardness, showed a range of 34 MPa to 41 MPa, with Mix C10 again exhibiting the highest value of 41 MPa. A strong correlation (R^2 = 0.8452) was observed between the two testing methods, confirming their consistency. Mixes with higher calcined clay and glass fiber content showed better strength performance, as calcined clay increases long-term strength through continued hydration. In contrast, mixes with 10% nano-silica, such as C15, exhibited relatively lower strength values, possibly due to the fine particle size of nano-silica leading to poor dispersion or incompatibility with other materials, which may affect overall strength development.



(a)



(b)



(c)



(d)

Fig. 2. Testing setup (a) CS testing, (b) FS Testing, (c) RH testing, and (d) UPV testing

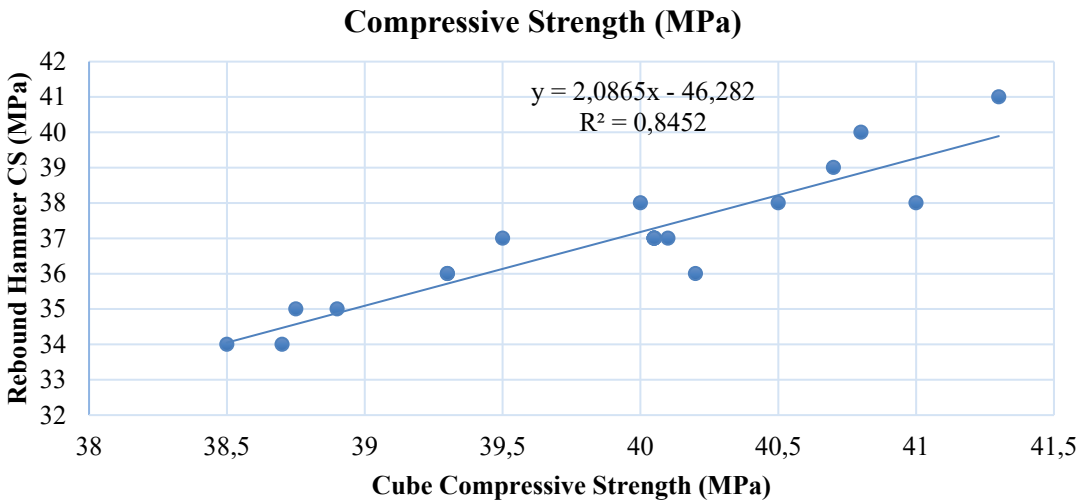


Fig. 3. Compressive strength analysis

The strength development in cementitious materials is primarily influenced by the hydration process of cement and the pozzolanic reactions of supplementary cementitious materials (SCMs) like nano-silica. While nano-silica can enhance the formation of calcium silicate hydrates (C-S-H), which contribute to strength, the aforementioned issues of dispersion and compatibility can hinder these reactions, leading to suboptimal strength outcomes (Neves, Nunes, and Monteiro 2020).

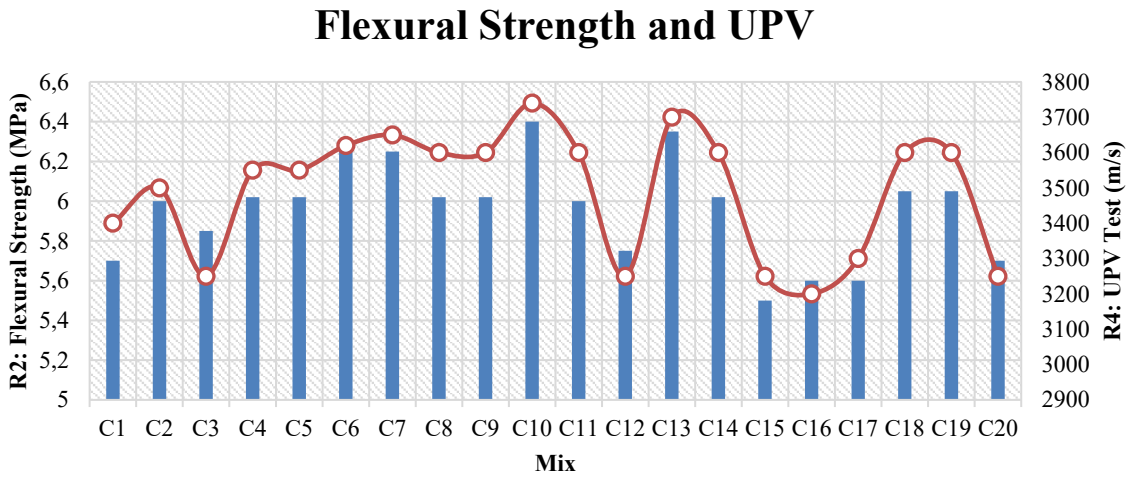


Fig. 4. Flexural Strength and UPV analysis

After 28 days of water curing, the flexural strength (R2) and ultrasonic pulse velocity (UPV) test (R4) results of the concrete mixes were recorded as shown figure 4. The flexural strength concrete when subjected to bending, ranged from 5.5 MPa to 6.4 MPa, with the highest value observed in Mix C10 (6.4 MPa), containing 30% calcined clay and 2% glass fiber. The presence of calcined clay and glass fibers likely contributed to better load distribution and crack resistance. Mix C6 (10% nano-silica and 2% glass fiber) also showed high flexural strength (6.3 MPa), indicating the positive role of nano-silica in improving the tensile capacity of the concrete matrix. Conversely, the lowest flexural strength (5.5 MPa) was seen in Mix C15 (10% nano-silica and 2% glass fiber), possibly due to suboptimal dispersion of nano-silica or its interaction with other components. However, the effects of nano-silica on flexural strength are dosage-dependent. Studies have identified an optimal range for nano-silica content, typically around 1% to 3% by weight of cement, where significant improvements in flexural strength are observed. Exceeding this optimal range can lead to negative outcomes. For example, it has been reported that when the nano-silica content surpasses 3%, the flexural strength may decrease due to issues such as particle agglomeration, which adversely affects the workability and uniformity of the concrete (Kara and Durmuş 2019). This phenomenon

highlights the importance of careful dosage optimization to harness the benefits of nano-silica without compromising the material's performance [23].

The trivial differences in flexural strength observed in this study can be attributed to the limited fiber content (0%–2%) and the nano-silica dosage not exceeding 10%. Research indicates that higher fiber content typically enhances flexural strength due to improved crack bridging and energy absorption. For instance, Pang et al. (2018) found that increasing fiber content beyond 2% significantly improved flexural performance, suggesting that the current study's limited fiber reinforcement may have constrained flexural strength gains [24]. Furthermore, while nano-silica is known to enhance concrete's microstructure and overall strength, its effects on flexural strength can be minimal at lower dosages. Alvansazyazdi et al. (2023) demonstrated that while nano-silica significantly improved compressive strength, the enhancements in flexural strength were marginal when the dosage was kept below 10%. This aligns with the findings of the current study, indicating that the limited dosage may not have been sufficient to elicit substantial flexural improvements [25].

The UPV test, which measures the velocity of an ultrasonic pulse through concrete to assess its quality and uniformity, revealed velocities ranging from 3200 m/s to 3740 m/s. The highest velocity was recorded in Mix C10 (3740 m/s), again highlighting the effectiveness of calcined clay and glass fibers in creating a dense and uniform concrete matrix. The lowest UPV result (3200 m/s) was found in Mix C16 (no nano-silica, calcined clay, or glass fiber), indicating less compactness and internal consistency. Overall, mixes with calcined clay and glass fiber exhibited better results in both flexural strength and UPV tests, suggesting improved durability and structural integrity.

2.4 RSM Analyses

The Response Surface Methodology (RSM) analysis was carried out to evaluate the influence of three key factors, Nano-Silica (A), Calcined Clay (B), and Glass Fiber (C) on the performance of concrete materials as shown in table 4. The analysis focused on four key responses: compressive strength, flexural strength, rebound hammer test, and ultrasonic pulse velocity (UPV) test. The ANOVA results demonstrated that all three factors had a significant impact on the material properties, with Nano-Silica having the most substantial effect across all tests. High R^2 values and adequate precision indicate the models' strong predictive capabilities, though further refinements may be necessary in some areas to address any lack of fit.

Table 4. Response surface models and analysis of variance (ANOVA)

Response	Source	Sum of Squares	df	F-value	p-value	Significance
Compressive Strength	Model	11.04	3	148.2	< 0.0001	Significant
	A-Nano-Silica	9.8	1	394.63	< 0.0001	
	B-Calcined Clay	0.841	1	33.86	< 0.0001	
	C-Glass Fiber	0.4	1	16.11	0.001	
Flexural Strength	Model	1.23	3	67.49	< 0.0001	Significant
	A-Nano-Silica	1.06	1	174.23	< 0.0001	
	B-Calcined Clay	0.081	1	13.36	0.0021	
	C-Glass Fiber	0.0903	1	14.89	0.0014	

Rebound Hammer Test	Model	65.6	3	67.28	< 0.0001	Significant
	A-Nano-Silica	57.6	1	177.23	< 0.0001	
	B-Calcined Clay	6.4	1	19.69	0.0004	
	C-Glass Fiber	1.6	1	4.92	0.0413	
UPV Test	Model	5.93E+05	3	42.9	< 0.0001	Significant
	A-Nano-Silica	5.52E+05	1	119.81	< 0.0001	
	B-Calcined Clay	25000	1	5.42	0.0333	
	C-Glass Fiber	16000	1	3.47	0.0809	

Table 4 presents the results of an ANOVA analysis performed to assess the impact of three factors like, Nano-Silica, Calcined Clay, and Glass Fiber on the compressive strength, flexural strength, rebound hammer test, and ultrasonic pulse velocity (UPV) of materials. The analysis reveals that all three factors significantly influence material performance across most tests, with Nano-Silica consistently showing the highest effect. Notably, the significant p-values (<0.05) for model terms indicate strong predictive power, while significant lack of fit in some cases suggests room for model improvement. These findings underscore the importance of optimizing material compositions for enhanced structural properties.

The ANOVA analysis in Table 3 confirms that Nano-Silica has the most significant impact on compressive strength, flexural strength, rebound hammer test, and UPV values, consistent with prior studies that highlight the microstructural refinement provided by Nano-Silica, leading to enhanced strength and durability. For instance, earlier research by [26] also demonstrated that Nano-Silica contributes to higher compressive strength due to improved pozzolanic activity and densification of the cement matrix. Similarly, Calcined Clay's pozzolanic properties align with findings in [27] , where its partial replacement enhanced durability and long-term strength.

Glass fibers, while less influential than Nano-Silica and Calcined Clay, significantly improved tensile and flexural properties, consistent with [28], who observed enhanced crack resistance due to fiber reinforcement. The high F-values and low p-values in this study are in agreement with previous models' fit statistics, further validating the reliability and robustness of the response surface methodology employed. Comparing these results with the literature supports the conclusion that the optimized mix composition achieves superior structural performance, emphasizing the importance of tailored material combinations in concrete engineering.

In table 5 ANOVA analysis was conducted on four key material performance metrics: compressive strength, flexural strength, rebound hammer test, and ultrasonic pulse velocity (UPV). Significant model terms were identified across all responses, with Nano-Silica, Calcined Clay, and Glass Fiber showing substantial effects on material strength. Adeq Precision values (>21 for all metrics) surpass the threshold of 4.0 commonly used in response surface methodology, corroborating the strong signal-to-noise ratio observed in similar optimization studies [29].

Despite these strengths, the detected lack of fit in some cases mirrors findings [30], who attributed such discrepancies to complex interactions between material components. This underscores the need for further refinement of the model, as noted in studies addressing nonlinear effects of advanced materials in concrete (Althoey et al. 2023). By comparing these results, the study demonstrates consistency with established benchmarks while identifying areas for further enhancement to advance structural performance optimization. The equation 1 to 4 shows the the

response (Compressive Strength, Flexural Strength, Rebound Hammer Test, UPV Test) as dependent variables, with A, B, and C being the factors contributing to each response.

Table 5. Model validation

Response	Compressive Strength	Flexural Strength	Rebound Hammer Test	UPV Test
Std. Dev.	0.1576	0.0779	0.5701	67.8924
R^2	0.9653	0.9268	0.9266	0.8894
Adjusted R^2	0.9587	0.913	0.9128	0.8687
Mean	39.9125	5.975	37.6	3480
C.V. %	0.3948	1.3031	1.5162	1.9509
Predicted R^2	0.9457	0.8831	0.8938	0.8323
Adeq Precision	41.999	29.293	28.241	21.408

- Compressive Strength Equation:

$$Compressive\ Strength = 39.9125 + 0.99A + 0.29B + 0.20C \quad (1)$$

- Flexural Strength Equation:

$$Flexural\ Strength = 5.975 + 0.325A + 0.090B + 0.095C \quad (2)$$

- Rebound Hammer Test Equation:

$$Rebound\ Hammer\ Test = 37.6 + 2.4A + 0.8B + 0.4C \quad (3)$$

- UPV Test Equation:

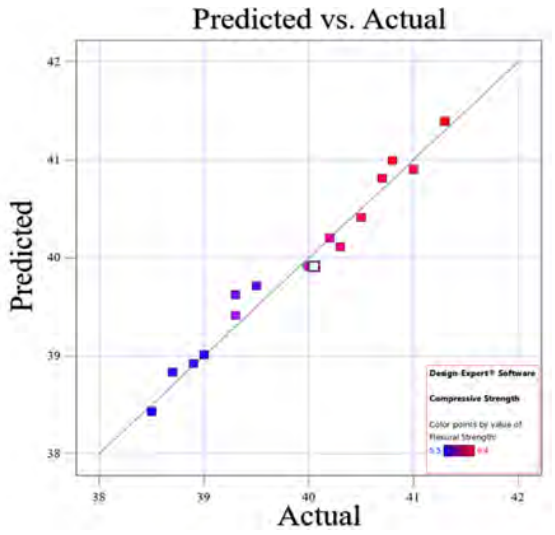
$$UPV\ Test = 3480 + 235A + 50B + 40C \quad (4)$$

These equations describe the relationships between the response variables (Compressive Strength, Flexural Strength, Rebound Hammer Test, and UPV Test) and the factors A, B, and C. This figure 5(a) shows the predicted versus actual compressive strength values. The actual values range from 38 to 42, while the predicted values range from approximately 38 to 42 as well. The close alignment of data points with the diagonal line indicates that the predictive model performs well across this range. Figure 5b shows a 3D surface plot illustrating the effect of varying percentages of calcined clay (0% to 24%) and nano silica (0% to 10%) on compressive strength, which ranges between 38.5 MPa and 41.5 MPa. The plot indicates the interactive influence of these two factors on compressive strength, with the surface highlighting how different combinations affect the overall strength values.

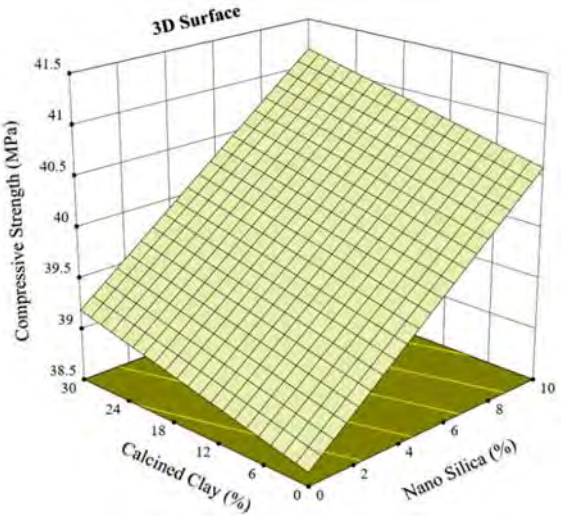
In Figure 5(c), the predicted vs. actual values for flexural strength exhibit a strong correlation, with actual values ranging from 5.4 to 6.6 MPa and predictions closely aligning along the diagonal line. Similar precision was reported in [31], where predictive models using Nano-Silica and Calcined Clay also demonstrated strong alignment, achieving flexural strength values within a comparable range. The influence of Nano-Silica and Calcined Clay on flexural strength, as depicted in Figure 5(d), aligns with earlier studies, such as [32], where these materials were shown to synergistically enhance flexural strength due to improved microstructure and pozzolanic activity.

In Figure 6(e), the predicted vs. actual values for the Rebound Hammer Test reveal accurate predictions across the observed range of 34 to 42 MPa. This mirrors findings from [33], which highlighted similar improvements in compressive strength with Nano-Silica and Calcined Clay integration. The accuracy of the predictive model, indicated by the close alignment of data points, is consistent with earlier works that employed quadratic models for concrete property predictions.

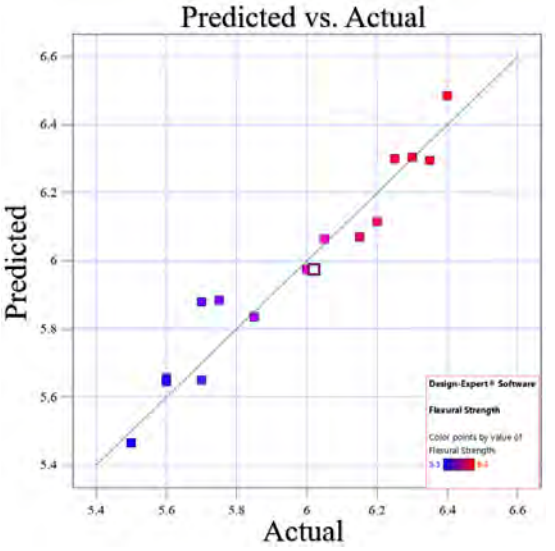
The 3D surface plot in Figure 6(f) demonstrates the combined effects of Nano-Silica and Calcined Clay on the Rebound Hammer Test results, with compressive strength ranging from 34 to 41 MPa.


Predicted vs. Actual
Predicted
Actual
Design-Expert® Software
Compressive Strength
Color points by value of
Flexural Strength:

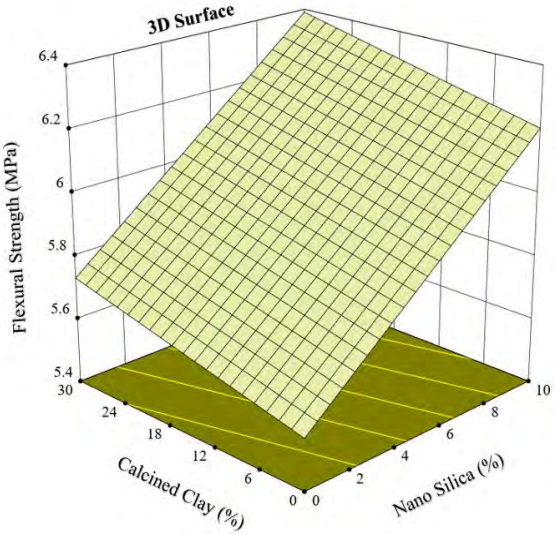
(a)


3D Surface
Compressive Strength (MPa)
Calcined Clay (%)
Nano Silica (%)

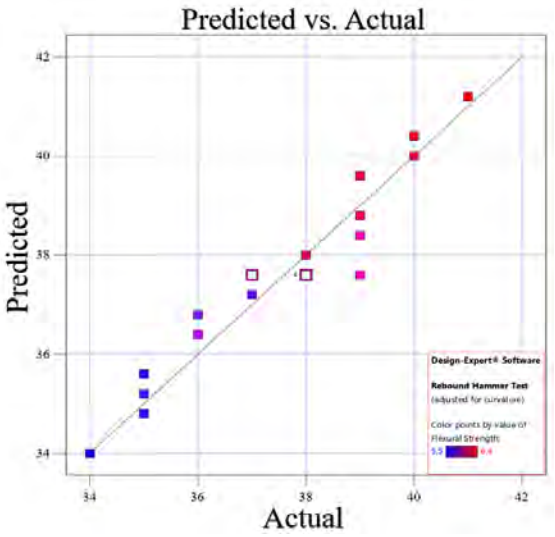
(b)


Predicted vs. Actual
Predicted
Actual
Design-Expert® Software
Flexural Strength
Color points by value of
Flexural Strength:

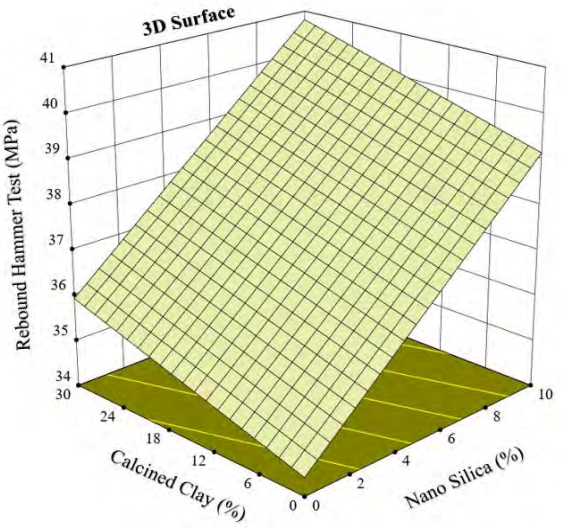
(c)


3D Surface
Flexural Strength (MPa)
Calcined Clay (%)
Nano Silica (%)

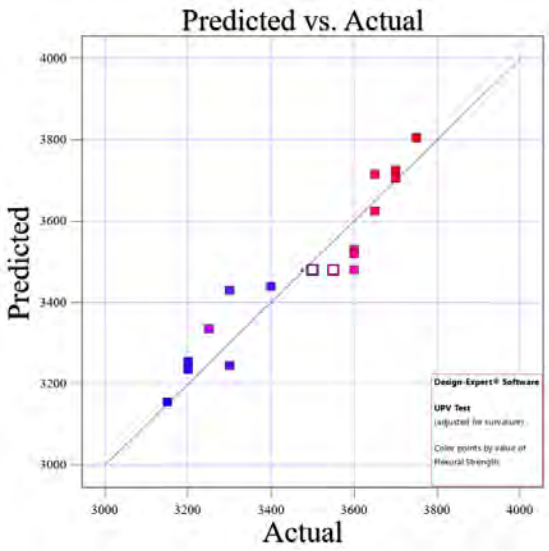
(d)


Predicted vs. Actual
Predicted
Actual
Design-Expert® Software
Rebound Hammer Test
(adjusted for curvature)
Color points by value of
Flexural Strength:

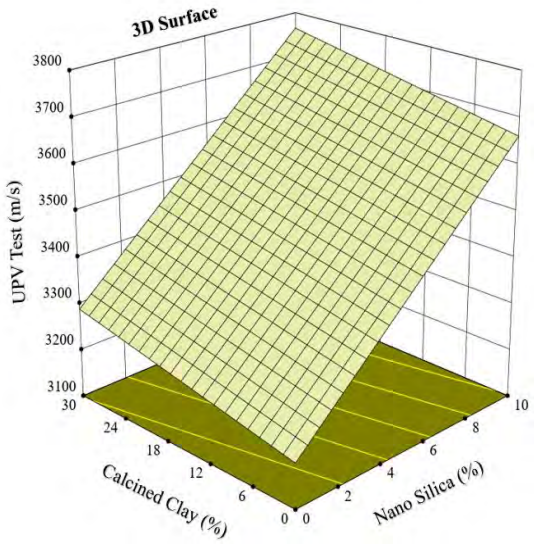
(e)


3D Surface
Rebound Hammer Test (MPa)
Calcined Clay (%)
Nano Silica (%)

(f)



(g)



(h)

Fig. 5. Predicted vs Actual and 3D surface analysis (a) Actual vs predicted CS, (b) 3D Surface analysis of CS, (c) Actual vs predicted FS, (d) 3D Surface analysis of FS, (e) Actual vs predicted RH, (f) 3D Surface analysis of RH, (g) Actual vs predicted UPV, and (h) 3D Surface analysis of UPV

Previous research, such as [34], similarly observed that increasing Nano-Silica and Calcined Clay proportions led to higher compressive strength due to refined pore structure and enhanced matrix densification. These comparisons validate the findings of the present study, reinforcing that the observed relationships and predictive accuracy are consistent with established research while highlighting the combined role of Nano-Silica and Calcined Clay in optimizing material performance.

Figure 7(g) shows the predicted versus actual values for the UPV (Ultrasonic Pulse Velocity) Test, where the actual values range from 3000 to 4000 m/s, and the predicted values also range similarly. The data points, mostly aligned with the diagonal line, indicate a good correlation between the predicted and actual values, demonstrating the model's accuracy for the UPV test results. Figure 7(h) is a 3D surface plot that illustrates the influence of calcined clay (0% to 24%) and nano silica (0% to 10%) on the UPV test results, with the velocity ranging between 3100 m/s and 3800 m/s. The surface represents how the combination of these two factors affects the ultrasonic pulse velocity in the material.

2.5 Confirmation Analysis

Table 6 compares the predicted and observed values for Compressive Strength, Flexural Strength, Rebound Hammer Test, and UPV Test. The predicted compressive strength (49.41 MPa) slightly overestimates the observed value (46.55 MPa) with a 5.79% error. Flexural strength shows an 11% error, with predicted (9.05 MPa) higher than observed (8.05 MPa). The rebound hammer test has a minor error of 3.23%, while the UPV test shows a 10.19% error. Overall, the predicted values closely align with the observed results, confirming the accuracy of the response models.

Table 6. Confirmation analysis

Response	Predicted	Observed	Error (%)
Compressive Strength (MPa)	49.41	46.55	-5.79
Flexural Strength (MPa)	9.045	8.05	-11.00
Rebound Hammer Test (MPa)	62	60	-3.22
UPV Test (m/s)	5445	4890	-10.19

3. Results

3.1 Compressive Strength

The optimized concrete mix, incorporating 5% nano-silica, 15% calcined clay, and 1% glass fiber, achieved a compressive strength of 49.41 MPa, closely aligned with the observed value of 46.55 MPa. This result reflects a high-strength concrete mix suitable for structural applications. The compressive strength ranged from 38 MPa to 42 MPa, with the optimized mix achieving a maximum of 41.3 MPa, closely predicted by the model (R^2 = 0.9653).

3.2 Flexural Strength

The mix demonstrated excellent tensile properties with a predicted flexural strength of 9.05 MPa, while the observed value was 8.05 MPa, indicating a significant improvement in the material's ability to resist bending forces. Flexural strength values spanned from 5.4 MPa to 6.6 MPa, with the highest recorded at 6.4 MPa, supported by a robust predictive model (R^2 = 0.9268).

3.3 Rebound Hammer Test

The optimized mix exhibited a predicted rebound hammer value of 62 MPa, with an observed value of 60 MPa, showing the concrete's surface hardness and strength retention over time. Rebound Hammer Test results showed compressive strength between 34 MPa and 42 MPa, with the model exhibiting strong reliability (R^2 = 0.9266).

3.4 Ultrasonic Pulse Velocity (UPV)

The UPV test results demonstrated the concrete's uniformity and quality, with a predicted value of 5445 m/s and an observed value of 4890 m/s, indicating a dense and durable concrete structure. Ultrasonic Pulse Velocity (UPV) values ranged from 3200 m/s to 3740 m/s, with the highest velocity observed in Mix C10, indicating a dense and uniform matrix (R^2 = 0.8894).

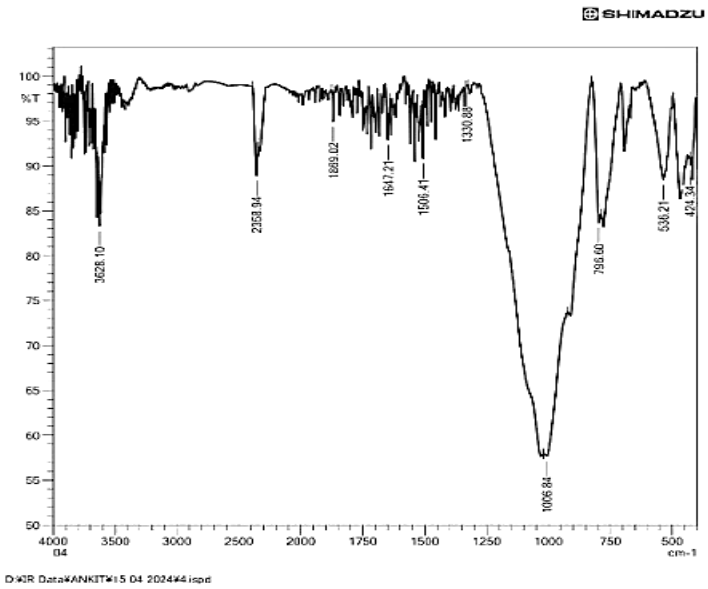
3.5 ANOVA Results

The analysis revealed that nano-silica had the most substantial influence on all mechanical properties, followed by calcined clay and glass fibers. The high R^2 values (e.g., 0.9653 for compressive strength and 0.9268 for flexural strength) confirm the robustness and predictive capability of the response models.

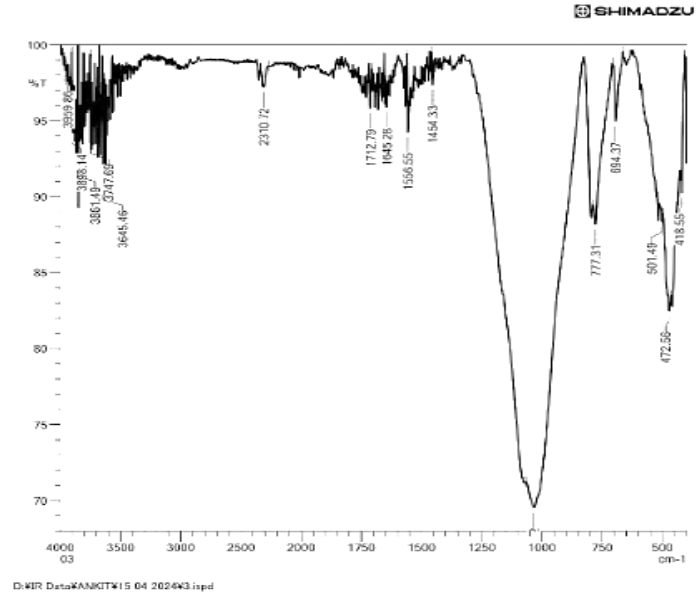
The numerical results validate the significant contribution of Nano-Silica, Calcined Clay, and Glass Fibers. Nano-Silica emerged as the most impactful factor across all responses, enhancing compressive strength by up to 2.4 MPa and flexural strength by up to 0.325 MPa per unit increase. Calcined Clay improved strength and durability, contributing up to 0.29 MPa in compressive strength and 0.090 MPa in flexural strength per unit increase. Glass Fibers enhanced flexural strength by 0.095 MPa and reduced crack propagation, improving overall tensile performance.

3.6 Fourier Transform Infrared Spectroscopy (FTIR)

Fourier Transform Infrared Spectroscopy (FTIR) is a key technique for analyzing the crystal structure of clay minerals by identifying functional groups and molecular bonds. It works by detecting the absorption of specific infrared wavelengths, which correspond to different functional groups or bonds. As infrared light passes through the sample, the transmitted light is captured, generating a spectrum that reveals chemical information. This method helps in characterizing the molecular composition and structure of both raw and calcined clay samples. The FTIR patterns of these samples are shown in Figure 6.



(a)



(b)

Fig. 6. FTIR analysis of clay samples (a) Raw clay sample and (b) Calcinated clay sample

4. Conclusion

This study demonstrates significant improvements in concrete's mechanical properties through the optimized incorporation of nano-silica, calcined clay, and glass fibers. Using Response Surface Methodology (RSM), the optimal mix was identified as 5% nano-silica, 15% calcined clay, and 1% glass fiber. The optimized concrete achieved a compressive strength of 49.41 MPa, closely aligned with the observed value of 46.55 MPa, highlighting its suitability for high-strength structural applications. The flexural strength improved significantly, with a predicted value of 9.05 MPa and an observed value of 8.05 MPa, showcasing its enhanced resistance to tensile and bending forces. The mix also displayed excellent surface hardness and durability, as evidenced by the rebound hammer test, with a predicted value of 62 MPa and an observed value of 60 MPa. The ultrasonic pulse velocity (UPV) results further confirmed the concrete's uniformity and density, with predicted and observed values of 5445 m/s and 4890 m/s, respectively. These findings underline the material's durability and long-term performance. Nano-silica emerged as the most influential

component, significantly improving the microstructure by filling voids in the cement matrix, thereby increasing density and strength. Calcined clay provided pozzolanic activity, enhancing durability and chemical resistance. Glass fibers contributed to improved flexural strength by bridging microcracks and preventing crack propagation. Statistical validation using ANOVA revealed high R^2 values, such as 0.9653 for compressive strength, confirming the accuracy and robustness of the predictive models. Minimal error margins, ranging from 3.22% to 11.00%, further validated the reliability of the results. This study highlights the potential of combining nano-silica, calcined clay, and glass fibers to create high-performance, sustainable concrete. The findings offer a pathway for developing eco-friendly, durable, and structurally reliable materials, meeting modern construction demands while contributing to environmental sustainability.

In conclusion, this research successfully demonstrates the synergistic benefits of combining nano-silica, calcined clay, and glass fibers in concrete. The optimized mix achieved significant improvements in compressive strength, flexural strength, surface hardness, and uniformity, with predicted values closely matching observed results. The statistical analysis validated the models' accuracy, underscoring the role of nano-silica as the most influential factor. These findings lay a strong foundation for future innovations in sustainable building materials, offering a pathway toward eco-friendly, durable, and high-performance concrete solutions that meet the demands of modern construction. By addressing both structural integrity and environmental sustainability, this study contributes significantly to the advancement of contemporary construction practices.

Acknowledgement

The authors thank the staff of department of civil engineering Chandigarh University Mohali, India.

References

[1] Abreu G, Silva F, Peixoto C, Fischer G, Toledo Filho RD. Mechanical properties and microstructure of high-performance concrete containing stabilized nano-silica. Matéria (Rio de Janeiro). 2017;22(2). https://doi.org/10.1590/s1517-707620170002.0156

[2] Akonda M, Kandola BK, Horrocks AR. Effect of alkali and ultraviolet aging on physical, thermal, and mechanical properties of fibers for potential use as reinforcing elements in glass/silicate composites. Polym Adv Technol. 2011;23(11):1454-63. https://doi.org/10.1002/pat.2067

[3] Alqamish HH, Al-Tamimi AK. Development and evaluation of nano-silica sustainable concrete. Appl Sci. 2021;11(7):3041. https://doi.org/10.3390/app11073041

[4] Althoey F, Ansari WS, Sufian M, Deifalla AF. Advancements in low-carbon concrete as a construction material for the sustainable built environment. Dev Built Environ. 2023;16:100284. https://doi.org/10.1016/j.dibe.2023.100284

[5] Alvansazyazdi M. Evaluating the influence of hydrophobic nano-silica on cement mixtures for corrosion-resistant concrete in green building and sustainable urban development. Sustainability. 2023;15(21):15311. https://doi.org/10.3390/su152115311

[6] Ayati B, Newport DJ, Wong HS, Cheeseman CR. Low-carbon cements: potential for low-grade calcined clays to form supplementary cementitious materials. Clean Mater. 2022;5:100099. https://doi.org/10.1016/j.clema.2022.100099

[7] Babalu R, Sunil P. Chemical resistance of nano silica added concrete. Int J Innov Technol Explor Eng. 2019;8(12):3472-6. https://doi.org/10.35940/ijitee.L2607.1081219

[8] Banerjee P. Effects of glass fibre on the strength and properties of concrete. E3S Web Conf. 2023;405:3003. https://doi.org/10.1051/e3sconf/202340503003

[9] Bheel N, Shaikh FN, Jamaluddin N, Kumar A. A comprehensive study on the impact of nano-silica and ground granulated blast furnace slag on high strength concrete characteristics: RSM modeling and optimization. Structures. 2024;62:106160. https://doi.org/10.1016/j.istruc.2024.106160

[10] Bureau of Indian Standards (BIS). IS 10262:2019, Indian standard, concrete mix proportioning - guidelines (second revision). 2019.

[11] Fahmy MA, El-Hassan MMA, Kamh GME, Bashandy AA. Investigation of using nano-silica, silica fume and fly ash in high strength concrete. Eng Res J. 2020;43(3):211-21. https://doi.org/10.21608/erjm.2020.95144

[12] Farajzadehha S, Mahdikhani M, Moayed RZ, Farajzadehha S. Experimental study of permeability and elastic modulus of plastic concrete containing nano silica. Struct Concr. 2020;23(1):521-32. https://doi.org/10.1002/suco.202000551
[13] Fenu L, Forni D, Cadoni E. Dynamic behaviour of cement mortars reinforced with glass and basalt fibres. Compos Part B Eng. 2016;92:142-50. https://doi.org/10.1016/j.compositesb.2016.02.035
[14] Guo D, Guo M, Zhou Y, Zhu Z. Use of nano-silica to improve the performance of LC3-UHPC: mechanical behavior and microstructural characteristics. Constr Build Mater. 2024;411:134280. https://doi.org/10.1016/j.conbuildmat.2023.134280
[15] Hamada HM, Abed F, Al-Sadoon ZA, Alashkar A. Enhancing pozzolanic activity of fly ash via dry and wet milling: a comparative study for sustainable construction material enhancement. J CO2 Util. 2024;83:102811. https://doi.org/10.1016/j.jcou.2024.102811
[16] Jekel C, Haftka R, Venter G, Venter M. Lack-of-fit tests to indicate material model improvement or experimental data noise reduction. 2018. https://doi.org/10.2514/6.2018-1664
[17] Kara İB, Durmuş ÖF. Effect of nano silica on cement mortars containing micro silica. Challenge J Concr Res Lett. 2019;10(2):42. https://doi.org/10.20528/cjcrl.2019.02.003
[18] Motalea EA, Debaiky AS, Taha MR. The effect of nano-micro silica mixture on the shear strength of reinforced concrete beams. J Eng Res. 2021;0(0):0. https://doi.org/10.21608/erjeng.2021.109550.1042
[19] Nasr MS, Salih SI, Hassan MS. Pozzolanic activity and compressive strength of concrete incorporated nano/micro silica. Eng Technol J. 2016;34(3):483-96. https://doi.org/10.30684/etj.34.3A.5
[20] Neves MC, Nunes LM, Monteiro JP. Evaluation of GRACE data for water resource management in Iberia: a case study of groundwater storage monitoring in the Algarve region. J Hydrol Reg Stud. 2020;32:July. https://doi.org/10.1016/j.ejrh.2020.100734
[21] Ng S, Engelsen CJ. Construction and demolition wastes. In: Siddique R, Cachim PB, editors. Waste and supplementary cementitious materials in concrete. Woodhead Publishing; 2018. p. 229-55. https://doi.org/10.1016/B978-0-08-102156-9.00008-0
[22] Ngo VT, Lam TQK, Dung TM, Nguyen TA. Nano concrete aggregation with steel fibers: a problem to enhance the tensile strength of concrete. E3S Web Conf. 2019;135:3001. https://doi.org/10.1051/e3sconf/201913503001
[23] Nigam M, Verma M. Effect of nano-silica on the fresh and mechanical properties of conventional concrete. Forces Mech. 2023;10:100165. https://doi.org/10.1016/j.finmec.2022.100165
[24] Ojha SK, Biswal BK, Rath SS, Mohapatra S, Panda S, Sahoo SK, et al. Response surface methodology based optimization and scale-up production of amylase from a novel bacterial strain, Bacillus aryabhattai KIIT BE-1. Biotechnol Rep. 2020;27:e00506. https://doi.org/10.1016/j.btre.2020.e00506
[25] Pang B, Zhang Y, Liu G, She W. Interface properties of nanosilica-modified waterborne epoxy cement repairing system. ACS Appl Mater Interfaces. 2018. https://doi.org/10.1021/acsami.8b04092
[26] Praveen Kumar VV, Dey S. Study on strength and durability characteristics of nano-silica based blended concrete. Hybrid Adv. 2023;2:100011. https://doi.org/10.1016/j.hybadv.2022.100011
[27] Rostamiyan Y, Golestani-Fard F, Ebrahimi-Nejad S. Experimental and optimizing flexural strength of epoxy-based nanocomposite: effect of using nano silica and nano clay by using response surface design methodology. Mater Des. 2015;69. https://doi.org/10.1016/j.matdes.2014.11.062
[28] Sapiai N, Roslan SA, Ishak MR, Sapuan SM, Ahmad I, Rahman NA, et al. Tensile and flexural properties of silica nanoparticles modified unidirectional kenaf and hybrid glass/kenaf epoxy composites. Polymers. 2020;12(11). https://doi.org/10.3390/polym12112733
[29] Siddiqui NA, Sham M, Tang BZ, Munir A, Kim J. Tensile strength of glass fibres with carbon nanotube–epoxy nanocomposite coating. Composites Part A: Applied Science and Manufacturing. 2009 Oct;40(10):1606-14. https://doi.org/10.1016/j.compositesa.2009.07.005

[30] Sridhar J, Vivek D, Jegatheeswaran D. Mechanical and flexural behavior of high performance concrete containing nano silica. Int J Eng Adv Technol. 2019;9(2):2017-23. https://doi.org/10.35940/ijeat.B3164.129219
[31] Stefanini L, Ansari D, Walkley B, Provis JL. Characterisation of calcined waste clays from kaolinite extraction in alkali-activated GGBFS blends. Mater Today Commun. 2024;38:107777. https://doi.org/10.1016/j.mtcomm.2023.107777
[32] Sundaramoorthy M, Rathod D. Behaviour of hybrid fibre in RC column with basalt and E-glass fibre under axial loading. J Eng Res. 2022.
[33] Swetha A, Suguna K, Raghunath PN. Strength and durability studies on steel fiber reinforced ternary blended concrete containing nano silica and zeolite. Civ Eng Archit. 2022;10(6):2306-21. https://doi.org/10.13189/cea.2022.100606
[34] Tahir H, et al. Optimisation of mechanical characteristics of alkali-resistant glass fibre concrete towards sustainable construction. Sustainability. 2023;15(14):11147. https://doi.org/10.3390/su151411147
[35] Tironi A, Trezza MA, Scian AN, Irassar EF. Thermal analysis to assess pozzolanic activity of calcined kaolinitic clays. J Therm Anal Calorim. 2014;117(2):547-56. https://doi.org/10.1007/s10973-014-3816-1
[36] Wu Z, Shi C, Khayat KH. Influence of silica fume content on microstructure development and bond to steel fiber in ultra-high strength cement-based materials (UHSC). Cem Concr Compos. 2016;71:97-109. https://doi.org/10.1016/j.cemconcomp.2016.05.005
[37] Zaid O, et al. A step towards sustainable glass fiber reinforced concrete utilizing silica fume and waste coconut shell aggregate. Sci Rep. 2021. https://doi.org/10.1038/s41598-021-92228-6

Research on Engineering Structures & Materials
www.jresm.org

Research Article

Assessment of the harmfulness of corrosion defects in a pressurized pipeline with a single corrosion defect using FEA and ANN

Yassine El Kiri [a], Laidi Zahiri [b], Khalifa Mansouri [c], Zakaria Mighouar [d]

Laboratory of Modelling and Simulation of Intelligent Industrial Systems (M2S2I), ENSET, Hassan II University of Casablanca, Morocco

Article Info

Article History:

Received 26 Oct 2024

Accepted 06 Feb 2025

Keywords:

Pipeline;
Defect;
Corrosion;
Burst pressure;
Finite element method;
Artificial neural network

Abstract

External corrosion is a significant issue that can lead to ruptures in long-distance liquid transportation facilities such as pipelines. Highlighting the need for regular monitoring of their condition, which can compromise their integrity and safety. Three types of external corrosion defects were studied since it is necessary in some to prioritize interventions when multiple defects appear simultaneously on different sections considering burst pressure of the structure. These pressures were determined using numerical simulations in SolidWorks, based on models validated by previous experimental results. An artificial neural network was developed to quickly predict burst pressures, optimizing the network's topology through detailed analysis and thus avoiding the need for complex finite element analyses in the future. The results indicate that the defect having parabolic shape is generally the most detrimental to the structure, although the circumferential defect may be more damaging in certain cases. Additionally, the depth of the defect is a crucial parameter compared to geometric characteristics, emphasizing the importance of continuous monitoring to prevent corrosion risks.

© 2025 MIM Research Group. All rights reserved.

1. Introduction

The transportation of liquid and gaseous hydrocarbons has now become crucial due to the increase in volumes of products used and consumed, emphasizing the need to use large-scale and economically viable means of transportation, notably pipelines [1]. In this context, the installation of pipeline networks has evolved to offer great flexibility in transportation and adaptation to the requirements of the transported products [2]. Pipelines represent the primary means of transportation for oil, gas, water, and various petroleum products [3]. However, their aging, impacts with foreign bodies, as well as exposure to a corrosive environment, can lead to the occurrence of various defects such as cracks, dents, notches, and corrosion [4-8].

According to systematic statistics from the European Gas Pipeline Incident Data Group (EGIG) on incident frequencies concerning gas pipelines, it is evident that incidents related to corrosion and external interferences in these infrastructures represent significant portions to be considered, as shown in Fig. 1 [9]. This highlights the importance of conducting scientific research to counter leaks or explosions resulting from these anomalies.

Corrosion results from the aggressiveness of the soil, environment, and transported products. Over time, it can lead to an increase in roughness, thereby causing a decrease in thickness and mechanical strength of pipelines [10]. Therefore, monitoring and tracking the condition of

*Corresponding author: yassine.elkiri-etu@etu.univh2c.ma
[a]orcid.org/ 0000-0002-8089-8273; [b]orcid.org/ 0000-0003-2685-6088; [c]orcid.org/ 0000-0003-2242-0973; [d]orcid.org/ 0000-0002-0716-8231
DOI: http://dx.doi.org/10.17515/resm2025-502ml1026rs

pipelines remain essential operations for planning maintenance interventions to avoid unexpected fluid transport shutdowns due to leaks or explosions [11-13]. Corrosion of mechanical components in operation poses a significant obstacle in design, as its impacts are observed at various stages, ranging from mining extraction to the design, manufacturing, usage, reuse, and recycling phases [14]. When a component undergoes corrosion, whether it experiences generalized or localized corrosion, it undergoes geometric modifications and alters its surface condition, as shown in Fig. 2. Furthermore, the formation of localized corrosion zones creates areas of high stress concentration, thereby becoming preferential sites for crack initiation and propagation [15].

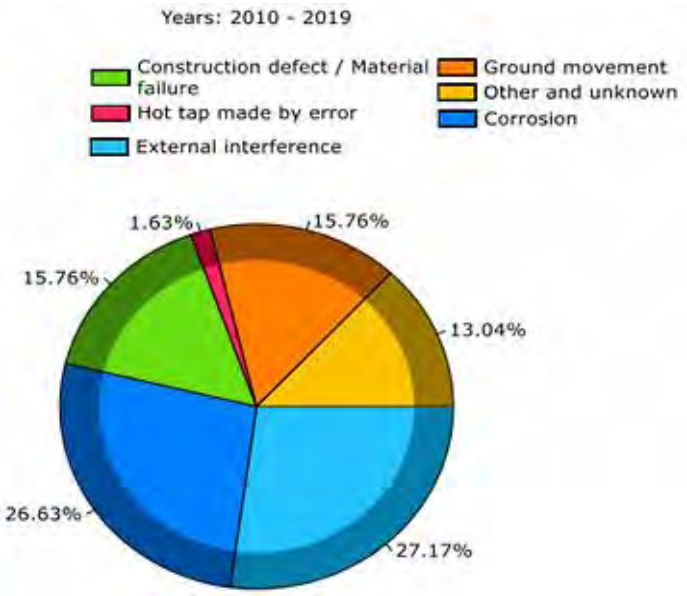


Fig. 1. Distribution of gas pipeline incidents (2010-2019), 11th EGIG-report [9]

Corrosion results from the aggressiveness of the soil, environment, and transported products. Over time, it can lead to an increase in roughness, thereby causing a decrease in thickness and mechanical strength of pipelines [10]. Therefore, monitoring and tracking the condition of pipelines remain essential operations for planning maintenance interventions to avoid unexpected fluid transport shutdowns due to leaks or explosions [11-13]. Corrosion of mechanical components in operation poses a significant obstacle in design, as its impacts are observed at various stages, ranging from mining extraction to the design, manufacturing, usage, reuse, and recycling phases [14]. When a component undergoes corrosion, whether it experiences generalized or localized corrosion, it undergoes geometric modifications and alters its surface condition, as shown in Fig. 2. Furthermore, the formation of localized corrosion zones creates areas of high stress concentration, thereby becoming preferential sites for crack initiation and propagation [15].



Fig. 2. An excavated gas pipeline subject to external corrosion [16]

In the oil and gas industry, numerous assessment standards are utilized to evaluate the residual strength of corroded pipelines. Among these, standards such as ASME B31G [17], Modified B31G [18], RSTRENG [19], PCORRC [20] and DNV RP-F101 [21]. are widely practiced for pipeline

inspection and maintenance, ensuring their proper functioning. However, most of these standards focus solely on assessing corroded pipelines [22].

Some studies have utilized finite element analysis (FEA) results to develop analytical solutions that can be implemented as quickly as standards and codes while preserving the accuracy of the finite element method [23-25]. Studies [23] have analyzed the residual strength of a pipeline exhibiting a circumferential corrosion groove under internal pressure, employing seven equations that incorporate the length and depth of the defect. The results obtained demonstrated satisfactory agreement with finite element analyses (FEA), exhibiting errors below 5%. It is noteworthy that the corrosion defect modeled in references [22, 23] was idealized as rectangular, this configuration being frequently adopted for assessing the corrosion-induced rupture of pipelines [21, 26].

Commonly employed standards for assessing the burst pressure of corroded pipelines exhibit limitations, particularly when dealing with complex and non-idealized loading configurations. These limitations result in conservative estimates, frequently being oversized. To address these inadequacies, recent studies have explored the application of artificial intelligence (AI) techniques, specifically through the development of an artificial neural network (ANN) model. This model, trained on a synthetic dataset generated using the finite element method (FEM), aims to accurately reproduce FEM results while overcoming the restrictions of traditional standards and avoiding the need for volumetric FEM analyses [22,27].

Several research works have successfully developed neural networks capable of predicting the burst pressure of a corroded pipeline based on finite element analysis (FEA) results [28-31]. This advancement encourages us to also apply artificial neural networks (ANN) in evaluating the harmfulness of three types of corrosion defects.

Despite research conducted on pipeline defects, a gap is observed in the evaluation of the harmfulness of certain defects present in pipelines, notably the most damaging corrosion form depending on the applied external load. To address this gap, our study specifically focuses on evaluating the degree of harmfulness of the three common forms of corrosion: rectangular, parabolic, and circumferential, using the results of the artificial neural network (ANN).

The analysis will enable a classification of the severity of the three considered types of corrosion defects, through the application of standardized formulations within the field. The evaluation will be based on the ASME B31G code [17] for parabolic-shaped defects [18], the DNV-RP-F101 code [21] for rectangular-shaped defects, and equations derived from prior research [23] for circumferential-shaped defects. A comparison of the results obtained using the neural network approach for these three types of corrosion defects will be conducted. An overview of some research works on corrosion defects in pressurized pipelines, using FEA and ANN to evaluate burst pressure, as shown in Table 1.

Table 1. Recent prior research on pressurized pipelines affected by corrosion

References	Type of defect	Loading	Methods
Michael Lo et al.[22] (2022)	Rectangular	Internal pressure with axial compressive stress	FEA/ANN
Arumugam et al. [23] (2020)	Circumferential	Internal pressure	FEA
Arumugam et al. [32] (2020)	Rectangular	Internal pressure with axial compressive stress	FEA
Xu et al. [33] (2017)	Rectangular circumferential in interaction	Internal pressure	FEA/ANN
Kumar et al. [34] (2022)	Circumferential interaction	Internal pressure with axial compressive stress	FEA/ANN

These research works illustrate the growing importance of integrating advanced numerical modeling techniques such as FEA and ANN in assessing the safety and reliability of pressurized

pipelines. These approaches enhance understanding of the factors influencing pipeline strength and enable more informed decisions regarding maintenance and operation.

2. Materials and Methods

This article proposes a two-step approach to assess the stability of corroded and pressurized pipelines. In the first step, the finite element method (FEA) is used to validate three numerical models representing different types of external corrosion on the pipeline. The aim of this step is to establish numerical models of these corroded pipelines to predict the internal pressure required to avoid bursting near the defect zones. This prediction is based on stress field analysis according to the Von Mises criterion, which is commonly used to assess plastic deformation in materials. The length and depth of defects are the key geometric parameters in evaluating burst pressure. To quantify their influence on this pressure, a parametric analysis is conducted by varying these magnitudes, thereby generating a structured database. This dataset, characterized by the diversity of defect geometries and their associated burst pressures, will serve as the foundation for the development of a new predictive numerical equation. This equation will be developed through artificial neural network (ANN) learning, a machine learning technique recognized for its ability to model complex relationships between variables.

Once the burst pressure prediction is made using the artificial neural network, we proceed to evaluate the harmfulness of the three identified defect types. This evaluation aims to analyze the impact of these defects on the normal operation of the pipeline. Furthermore, it aims to deduce the geometric parameter that most rapidly influences burst, which could prioritize inspections and repairs based on this parameter.

In summary, the proposed approach combines numerical analysis techniques, modeling by artificial neural networks, and harmfulness assessment to evaluate the stability of corroded and pressurized pipelines, as well as to identify critical defects requiring particular attention.

2.1 Numerical Model

The assumption that the corrosion defect adopts a rectangular shape was chosen because this approach is widely used for assessing pipeline corrosion and has been validated by several researchers, thus providing fairly accurate predictions of burst pressure [35-39]. To reduce computation time without compromising result accuracy, a reduced-size model was employed in this study [40]. This model consists of a symmetric quarter-pipe, as illustrated in Fig. 3, to faithfully represent the actual geometry of the pipeline. Additionally, the pipe was specified with a length of 2,000 mm to avoid any influence of end conditions on the corrosion defect zones during finite element analysis.

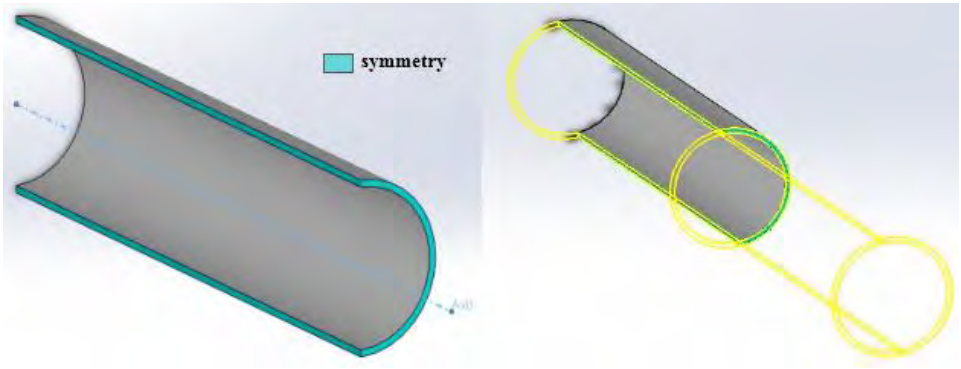


Fig. 3. API 5L X65 quarter-pipe model

The 3D modeling software SolidWorks was used to create the models. Since this study focuses on single corrosion defects (rectangular, parabolic, and circumferential) with symmetric geometries, only a quarter of the pipe was modeled to accurately represent the conduit's real geometry. Furthermore, the pipelines were modeled with a length of 1,000 mm, corresponding to half the length of the model.

2.2 Mechanical and Geometric Properties of the Numerical Model

The numerical model developed in SolidWorks involves digitally modeling a section of a corroded pipeline subjected to internal pressure. We will study the quality of the API 5L X65 steel pipe. The mechanical properties of this grade are presented in Table 2. This numerical module aims to replace analytical expressions that evaluate burst pressure based on the form of corrosion defect. The geometric dimensions for the numerical pipeline model can be found in Table 3.

Table 2. Mechanical properties of steel tube API 5L X65 [41]

Mechanical properties	Values
Modulus of Elasticity, E	210 GPa
Poisson's ratio, ϑ	0,3
Yield Strength, σ_y	464 MPa
Ultimate tensile strength, σ_u	563 MPa
True ultimate tensile strength, σ_{uts}	629 MPa

Table 3. Geometric properties of the pipeline

Geometric properties	Values
Pipe outside diameter, D (mm)	250
Length of pipe, L (mm)	2000
Wall thickness, t (mm)	10

2.3 Model Validation

Finite element (FE) modeling of irregular defects or local instabilities requires a careful and iterative approach. Mesh refinement, appropriate selection of boundary conditions, and validation against experimental data are essential to obtain reliable predictions, particularly for the determination of burst pressure. The validation of the finite element analysis (FEA) model was conducted by comparing simulation results with experimental data obtained by Lo et al. [22]. who performed burst tests on two specimens, designated LD and LF. To evaluate the influence of spatial discretization parameters and boundary conditions, a sensitivity analysis was carried out. This study examined three mesh generation methodologies (standard, curvature-based, and curvature-based with conformal mesh transitions) as well as two boundary condition configurations:

- Case 1: A planar support on one face, combined with a longitudinal edge fixed support.
- Case 2: Only a longitudinal edge fixed support.

The comparative analysis of numerical results for different combinations of mesh and boundary conditions revealed a significant influence of these parameters on burst pressure prediction. The results of this sensitivity study are summarized in Table 4. For both specimens studied, the comparison of burst pressures predicted by FEA and experimental values demonstrated satisfactory agreement, with a relative error of less than 10% for a curvature-based mesh with Case 1 boundary conditions, thus providing a more realistic numerical model.

The validation of the numerical model was supported by a second comparative analysis. The theoretical burst pressure of the intact pipe, calculated using Eq (1) [42], was compared to the FEA-estimated burst pressure of the intact pipe, revealing an error of 2.37% (Table 5). This slight discrepancy can be attributed to several sources of uncertainty, including:

- The idealization of the defect geometry.
- The choices of discretization parameters (finite elements, element size).
- Inherent errors in numerical calculation methods.

These small errors confirm the appropriate choice of mesh parameters and boundary conditions.

$$P_i = \frac{\sigma_{uts}.t}{r_i} \quad (1)$$

Table 4. Failure pressure from burst tests compared with failure pressure predicted in FEA

Specimen	Failure pressure from burst tests [22]	Boundary conditions	Mesh (Mesh generator)	Failure pressure from FEA (MPA)	Relative error (%)
LD	19.80 MPa	Planar support and Fixed support	Standard mesh	32,62	64,74
			Curvature-based mesh	20,78	4,95
			Blanded Curvature-based mesh	24,51	23,78
		Fixed support	Standard mesh	36,12	82,42
			Curvature-based mesh	29,48	48,89
			Blanded Curvature-based mesh	25,35	28,03
LF	15.00 MPa	Planar support and Fixed support	Standard mesh	26,05	73,67
			Curvature-based mesh	15,89	5,94
			Blanded Curvature-based mesh	20,45	36,34
		Fixed support	Standard mesh	29,5	96,67
			Curvature-based mesh	23,17	54,47
			Blanded Curvature-based mesh	21,71	44,74

Table 5. Comparison between theoretical and numerical intact pressure

Theoretical burst pressure	Numerical burst pressure	Relative error
54.7 MPa	56 MPa	2,37 %

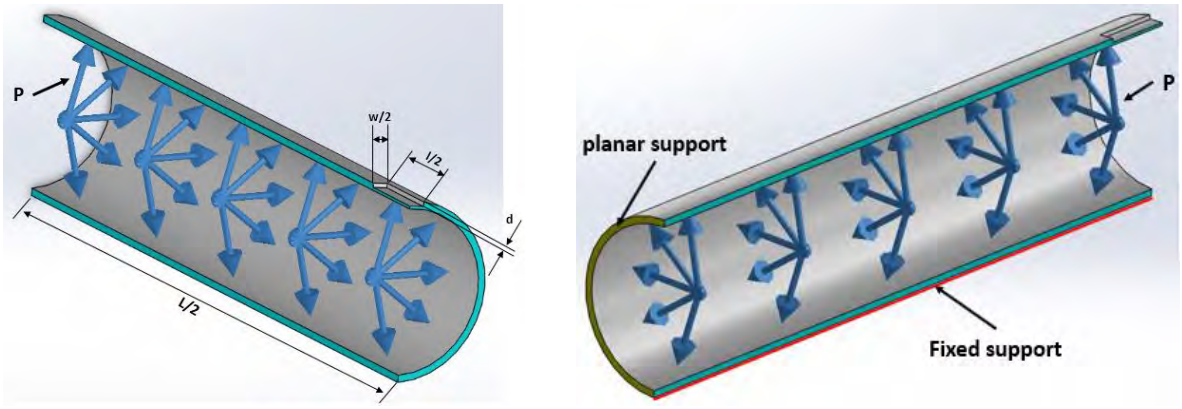
2.4 Meshing and Boundary Conditions

2.4.1 Rectangular Defect

Fig. 4 depicts the rectangular defect located at the center of the studied pipe. For symmetry reasons, only a quarter of the defect has been represented. The geometric characteristics of the defect are schematically shown in the same figure. Pressure has been applied to the internal section of the pipe, while two boundary conditions have been imposed: a planar support on the yellow facet and a fixed boundary condition on the bottom red line (Fig. 4). The quality and accuracy of the computational results are highly dependent on the characteristics of the mesh used. Therefore, the essential parameters defining the mesh are clearly presented in Table 6, allowing for a complete understanding of the discretization strategy employed.

Table 6. Mesh parameters

Mesh type	Rectangular defect volume mesh	Parabolic defect volume mesh	Circumferential defect volume mesh
Mesh generator used		Curvature-based mesh	
Jacobian points for high-quality mesh	At the nodes	16 Points	At the nodes
Maximum element size	35,3 mm	25,186 mm	30,056 mm
Minimum element size	35 mm	24,745 mm	17,68 mm
Mesh quality		Draft	
Total number of nodes	788	1818	1035
Total number of elements	2123	5165	2824
Maximum aspect ratio	10,245	4,911	18,236
% of elements with aspect ratio < 3	36,3	95,4	60,1
% of elements with aspect ratio > 10	0,094	0	0,46

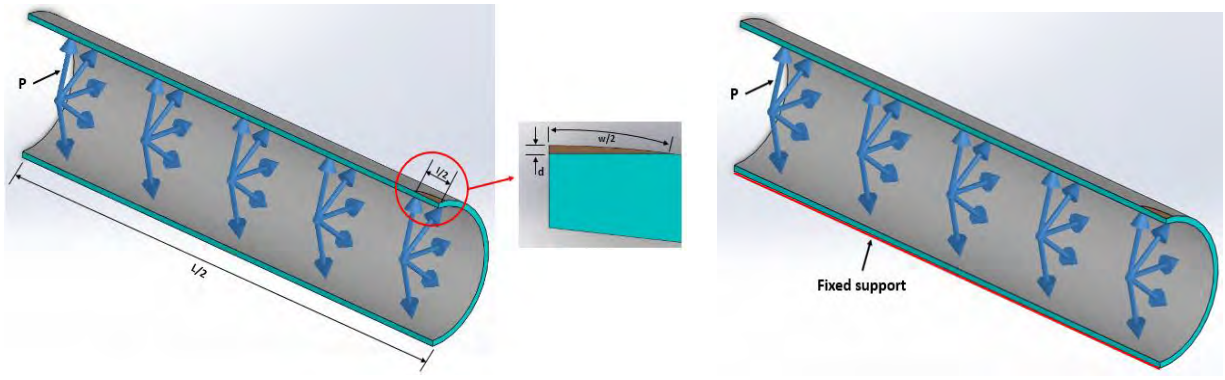


(a) (b)

Fig. 4. (a) Geometric characteristics of the rectangular defect, (b)boundary conditions and loading

2.4.2 Parabolic Defect

Fig. 5 illustrates the parabolic defect localized at the center of the examined pipeline. Given the symmetry of the pipe, only a quarter section of the defect is represented. The geometric characteristics of the defect are schematically shown in the same figure.



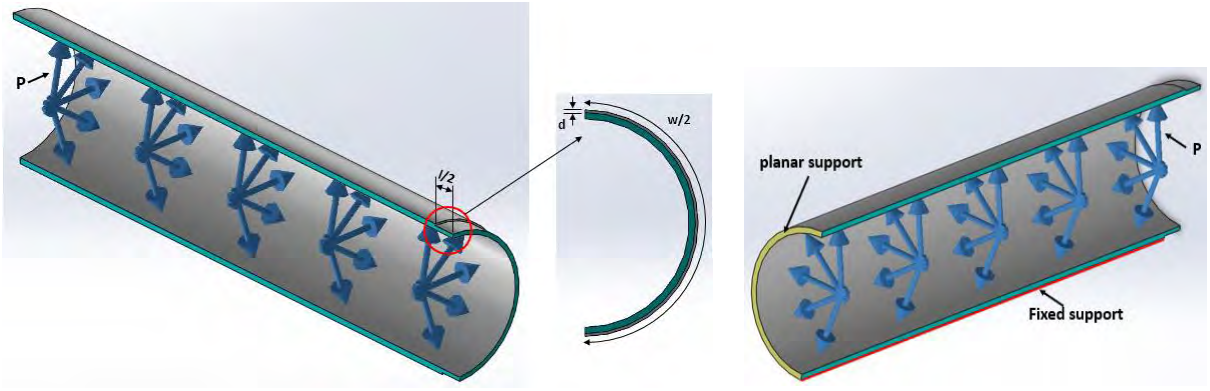
(a) (b)

Fig. 5. Geometric characteristics of the parabolic defect (a), boundary conditions and loading (b)

Pressure has been applied to the internal section of the pipe, while a fixed boundary condition is imposed on the bottom red line, as shown in Fig. 5. The mesh parameters are represented in Table 6.

2.4.3 Circumferential Defect

Fig. 6 depicts a circumferential defect localized at the center of the examined pipeline. Due to the pipe's symmetry, only a quarter section representing the defect is visible. The geometric characteristics of this defect are schematically shown in the same figure. Pressure has been applied to the internal section of the pipe. Two boundary conditions have been defined: a planar support on the yellow facet and a fixed boundary condition on the bottom red line, as shown in Fig. 6. The mesh parameters are represented in Table 6.



(a) (b)

Fig. 6. (a) Geometric characteristics of the circumferential defect, (b) boundary conditions and loading

2.5 Geometric Parameters of the Study

In this study, we examined the length and depth of a corrosion defect as key variables in determining the burst pressure of a pipeline. These parameters are specified in Table 7, with the defect length ranging from 40 to 220 mm in increments of 20 mm, and the depth ranging from 1 to 6 mm in increments of 1 mm. Fig. 7 and 8 illustrate the shapes of three types of defects.

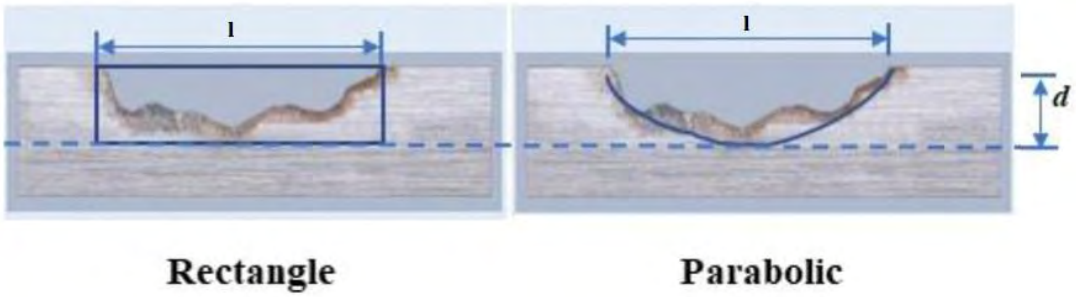


Fig. 7. Geometric dimension of a rectangular and parabolic corrosion defect on pipes [43]

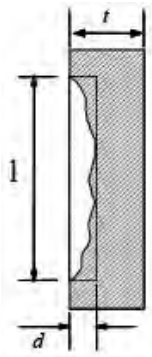


Fig. 8. Geometric dimension of a circumferential corrosion defect [44]

The defect width, denoted as "w," was not considered in this analysis as its impact on the rupture resistance of a corroded pipeline subjected to internal pressure is deemed negligible [17,21,32,23]. Using the parameters listed in Table 7, the burst pressures obtained via the Finite Element Method (FEM) were used to create a training dataset for the Artificial Neural Network (ANN). The geometric dimensions required for the FEA parametric study are detailed in Table 7.

Table 7. Geometric defect parameters

Defect depth, d (mm)		1-2-3-4-5-6
Defect length, l (mm)		40-60-80-100-120-140-160-180-200-220
Defect width, w (mm)	- rectangular defect	20°
	- parabolic defect	20°
	- circumferential defect	$\pi.250$

2.6 Burst Condition

Various criteria have been proposed in previous studies to predict the burst pressure of pipelines with corrosion defects [45]. However, the Finite Element Analysis (FEA) method in SolidWorks cannot anticipate local instability, such as necking, which often leads to final burst. Therefore, accurately predicting the burst pressure of a corroded pipeline using FEA is challenging unless an appropriate rupture criterion is well defined during the simulation, as highlighted by several previous studies [46]. When the effective von Mises stress reaches σ_{uts} throughout the wall, the corresponding internal pressure can be defined as the burst pressure. Predicting burst pressure based on σ_{uts} provides more accurate results, as the failure mechanism is controlled by plastic collapse, notably due to the high toughness of the material under study [47].

In this article, the rupture criterion for the corroded pipeline is based on the local stress in the defect area. Burst occurs when the local stress in this area exceeds the ultimate tensile strength. We applied the Von Mises theory in SolidWorks to analyze stress distribution in the corroded pipe. Cylindrical coordinates are used in the numerical model to detail the three stress components present in the pipe, namely: axial, radial, and circumferential stress, which define the effective Von Mises stress in cylindrical coordinates [48], as shown in Eq (2).

$$\sigma_e = \sqrt{\frac{1}{2}[(\sigma_h - \sigma_r)^2 + (\sigma_h - \sigma_l)^2 + (\sigma_r - \sigma_l)^2]} \tag{2}$$

2.7 Burst Pressure Using the Theoretical Approach, $P_{f,ana}$

This paper presents a study of three common methods for evaluating the burst pressure of pressurized pipelines: the DNV code for longitudinal rectangular defects, ASME B31G for parabolic defects, and the equations from reference [23] for circumferential defects. Both ASME B31G and the equations from [23] incorporate defect geometry into their calculations.

- DNV-RP-F101 code [21]

$$P_{f,ana} = \frac{2.t.\sigma_y.(1-\frac{d}{t})}{(D-t).(1-\frac{d}{t.Q})} \quad \text{With} \quad Q = \sqrt{1+0.31.(\frac{l}{\sqrt{D.t}})^2} \tag{3}$$

- ASME B31G code [17]

$$P_{f,ana} = \frac{2.1,1.\sigma_y.t}{D}.\frac{(1-0,66.(d/t)}{(1-\frac{0,66(\frac{d}{t})}{M_F})} \quad \text{if} \quad \sqrt{0.8.\left(\frac{D}{t}\right).(\frac{l}{D})^2} \leq 4 \tag{4}$$

With $M_F = \sqrt{1+0,8.\left(\frac{l}{D}\right)^2.(\frac{D}{t})}$

- Equations developed by Arumugam et al. [23]

$$P_{f,ana} = P_i.(1 - 3{,}738.\left(\frac{d}{t}\right)^{1{,}785}.\left(\frac{l}{D}\right)^{1{,}094} \quad \text{if} \quad \frac{d}{t} \le 0{,}4 \text{ and } \frac{l}{D} \le 0{,}4 \tag{5}$$

$$P_{f,ana} = P_i.(1 - 1{,}362.\left(\frac{d}{t}\right)^{1{,}431}.\left(\frac{l}{D}\right)^{0{,}333} \quad \text{if} \quad \frac{d}{t} \le 0{,}4 \text{ and } 0{,}4 < \frac{l}{D} \le 0{,}8 \tag{6}$$

$$P_{f,ana} = P_i.(1 - 1{,}127.\left(\frac{d}{t}\right)^{1{,}280}.\left(\frac{l}{D}\right)^{0{,}176} \quad \text{if} \quad \frac{d}{t} \le 0{,}4 \text{ and } 0{,}8 < \frac{l}{D} \le 1{,}2 \tag{7}$$

$$P_{f,ana} = P_i.(1 - 1{,}714.\left(\frac{d}{t}\right)^{1{,}627}.\left(\frac{l}{D}\right)^{0{,}536} \quad \text{if} \quad 0{,}4 < \frac{d}{t} \le 0{,}8 \text{ and } 0{,}1 < \frac{l}{D} \le 0{,}4 \tag{8}$$

$$P_{f,ana} = P_i.(1 - 1{,}058.\left(\frac{d}{t}\right)^{1{,}248}.\left(\frac{l}{D}\right)^{0{,}120} \quad \text{if} \quad 0{,}4 < \frac{d}{t} \le 0{,}8 \text{ and } 0{,}4 < \frac{l}{D} \le 0{,}8 \tag{9}$$

$$P_{f,ana} = P_i.(1 - 0{,}999.\left(\frac{d}{t}\right)^{1{,}129}.\left(\frac{l}{D}\right)^{0{,}039} \quad \text{if} \quad 0{,}4 < \frac{d}{t} \le 0{,}8 \text{ and } 0{,}8 < \frac{l}{D} \le 1{,}2 \tag{10}$$

2.7 Comparative Analysis of Theoretical and Numerical Burst Pressures

The determination of burst pressure is conditioned by the defect geometry. We progressively modified this geometry by adjusting the defect length (denoted as "l") and depth (denoted as "d"), while maintaining its width at a value of 20° for the rectangular and parabolic defects and π.D for the circumferential defect. These adjustments were made to closely approximate the actual geometry of corrosion defects. The burst pressures calculated by the DNV method, the ASME B31G code, and the equations of Arumugam et al. were normalized with respect to the intact pressure. The theoretical pressures in Fig. 9 were determined by varying the geometric parameters of the defects, as illustrated in Table 8. For each type of defect, we studied 60 specimens obtained by combining six variations of the d/t ratio with ten variations of the l/D ratio.

Table 8. Geometric parameters of the three types of defects

l/D	0,16-0,24-0,32-0,4-0,48-0,56-0,64-0,72-0,8-0,88
$l/\sqrt{Dt}$	0,8-1,2-1,6-2-2,4-2,8-3,2-3,6-4-4,4
d/t	0,1-0,2-0,3-0,4-0,5-0,6

The analysis of the numerical models in SolidWorks demonstrated a satisfactory correlation with the three methods deployed, as evidenced by the relative error values ranging from -6.24% to 8.29% for the circumferential defect, -5.42% to 7.75% for the parabolic defect, and -9.95% to 7.45% for the rectangular defect, as shown in Fig. 10. These error margins, all below 10%, indicate that this numerical approach is capable of predicting the burst pressure of a corroded pipe with geometric parameters within the studied range, thereby validating our numerical model.

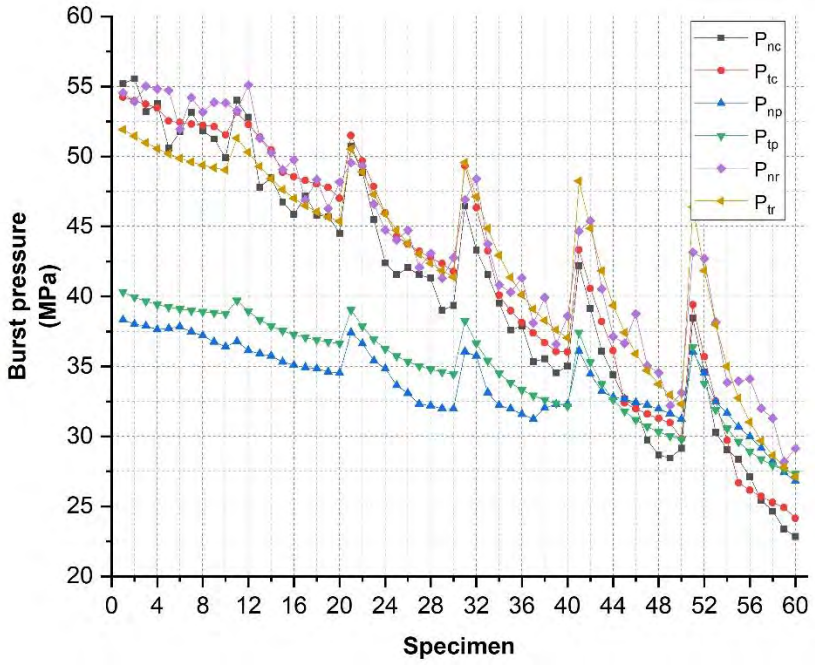


Fig. 9. Evolution of theoretical and numerical burst pressure

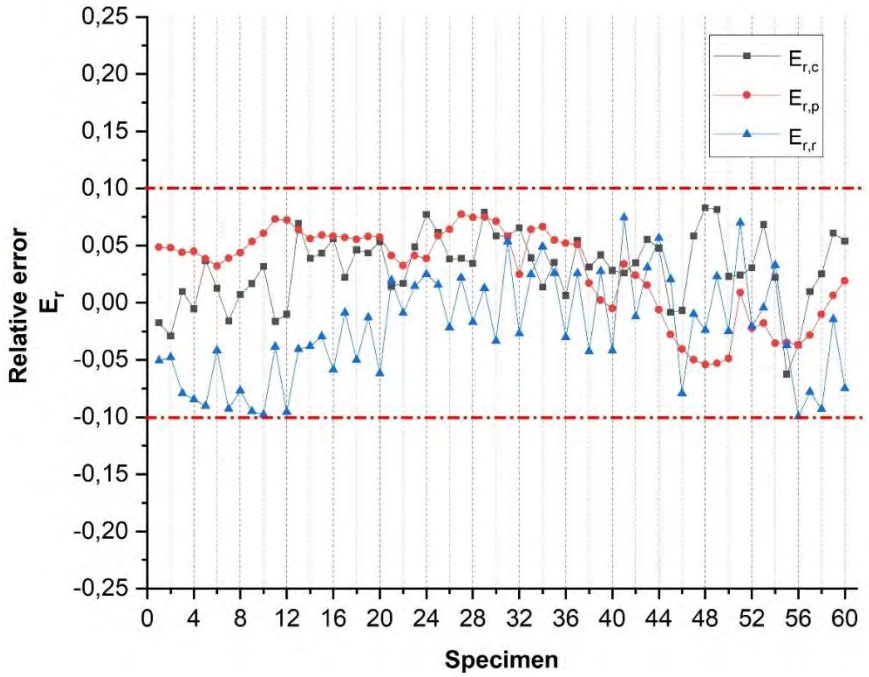


Fig. 10. Relative error between theoretical and numerical pressure of the three defects

2.8 Burst Pressure Prediction Using an Artificial Neural Network

2.8.1. Flowchart for Determining the Optimal Neural Network Topology

Using artificial intelligence in scientific domains has become an alternative approach to numerical simulation, facilitating the prediction of outcomes for complex problems through mathematical equations based on the principle of machine learning from pre-established results (dataset). The structure of the artificial neural network will be developed using Matlab R19a software, with a dataset distributed as follows: 70%, 80%, and 90% for training, and 30%, 20%, and 10% for testing. This data comes from a model validated through numerical simulation in SolidWorks software.

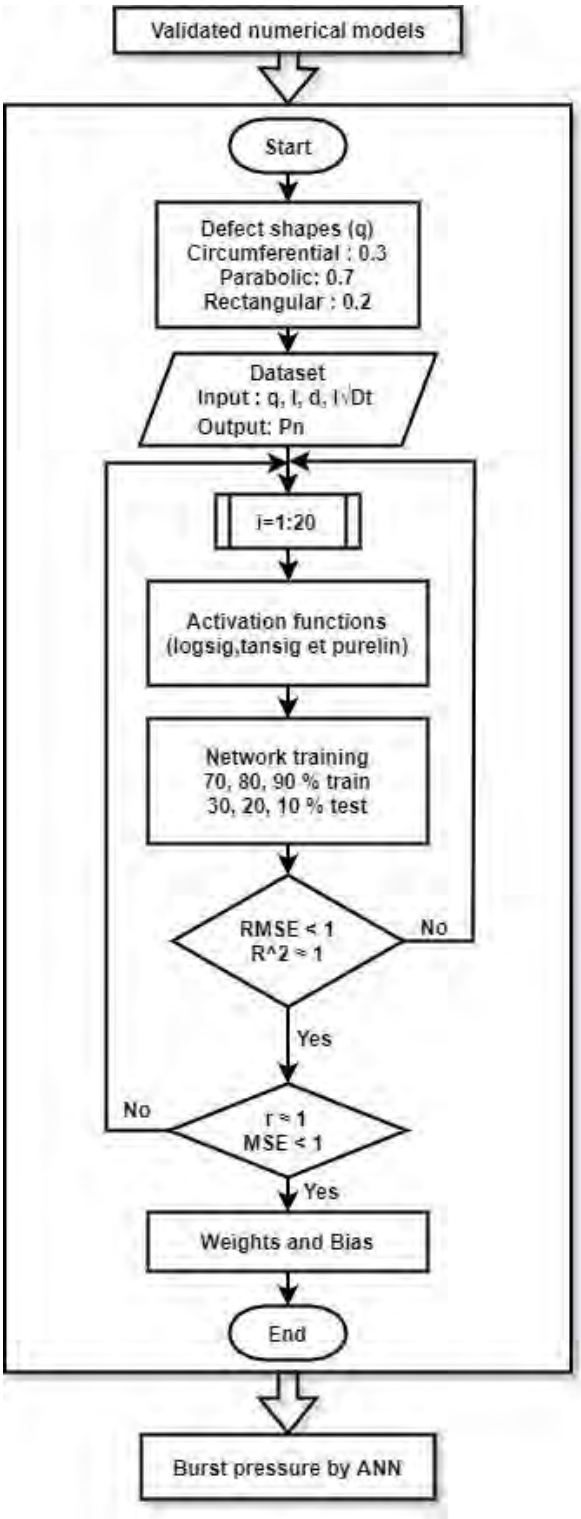


Fig. 11. Flowchart of the steps for optimal neural network selection

We will select a neural network with a single hidden layer, evaluated based on two metrics: a root mean square error (RMSE) below 1 and a coefficient of determination (R^2) close to 1. A loop testing 1 to 20 neurons in the hidden layer was carried out to determine the optimal number of neurons needed to achieve the desired accuracy. Various configurations of the three most commonly used activation functions in machine learning (tansig, logsig, and purelin) were tested, along with different dataset splits between training and testing.

Using Matlab R19a, the structure will be validated according to two complementary metrics: a correlation coefficient (r) close to 1 and a mean square error (MSE) below 1 (Fig.11). The weights

and biases obtained from the selected neural network enable highly accurate prediction of the burst pressure of a pressurized pipeline with a circumferential, parabolic, or rectangular corrosion defect.

2.8.2 Burst Pressure Prediction

Through the use of artificial neural networks, we developed a structure in Matlab R19a to predict the burst pressure of a pressurized pipeline with rectangular, parabolic, and circumferential corrosion defects. The objective was to develop a single hidden layer neural network capable of providing highly accurate results. To achieve this, we explored various configurations, varying the number of neurons in the hidden layer from 1 to 20 using a for loop (for i=1:20), as well as different activation functions (purelin, logsig and tansig) [50], These functions are most suitable in the linear regression problem [22, 33, 34]. Random weights were assigned to the network input for each type of defect, denoted as q, namely: 0.3 for circumferential, 0.7 for parabolic, and 0.2 for rectangular. The network was trained using gradient backpropagation, adjusting the weights and biases of each neuron to minimize the error between the predictions and the actual data [49]. Given the relatively small size of the numerical dataset, with approximately 180 samples, an analysis of the effect of data distribution on prediction accuracy was conducted. The dataset was divided into two portions according to three different ratios: 70%, 80%, and 90% for training, and 30%, 20%, and 10% for testing. To ensure prediction accuracy, we opted for 1000 training epochs, with a maximum of 500 validation failures to refine the learning phase. At each iteration, a combination of activation functions among purelin, logsig, and tansig was selected. At the end of execution, we evaluated the model's performance using four metrics: root mean square error (RMSE) Eq (11), mean squared error (MSE) Eq (12) [51], coefficient of determination (R^2) Eq (13) and correlation coefficient (r) Eq (14) [52].

- Expression of activation functions [50]

Sigmoid	Hyperbolic tangent	Lineair
$f(n) = \frac{1}{1+e^{-n}}$	$f(n) = \frac{2}{1+e^{-2n}} - 1$	$f(n) = n$

- Expression of root mean squared error (RMSE) and mean squared error (MSE) [51]

$$RMSE = \sqrt{\frac{1}{m}\sum_{i=1}^{m}(y_i - \hat{y}_i)^2} \tag{11}$$

$$MSE = \frac{1}{m}\sum_{i=1}^{m}(y_i - \hat{y}_i)^2 \tag{12}$$

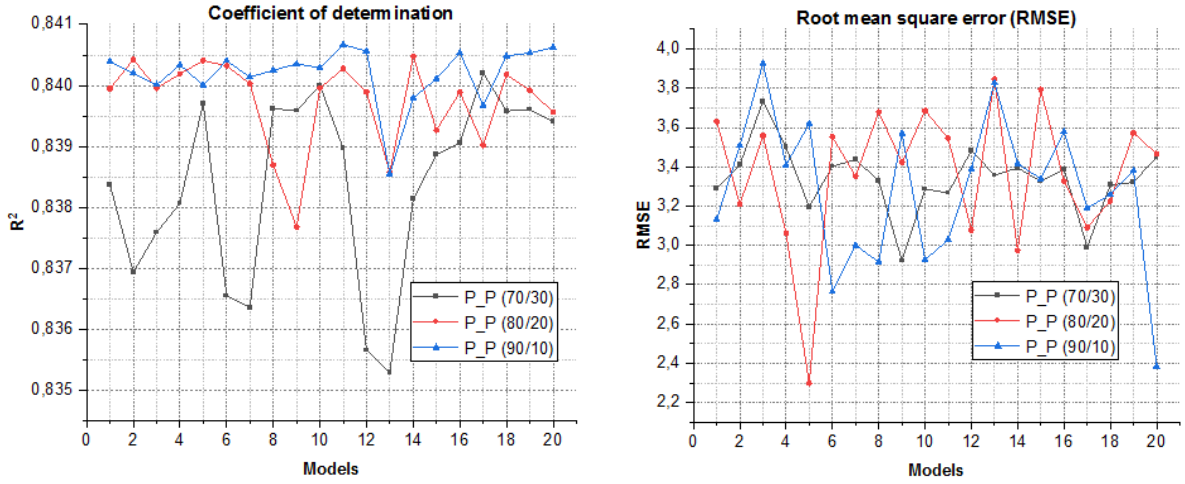
- Expression of coefficient of determination (R^2 or R-squared) and correlation coefficient (r) [52]

$$R^2 = 1 - \frac{\sum_{i=1}^{m}(y_i - \hat{y}_i)^2}{\sum_{i=1}^{m}(y_i - \bar{y})^2} \tag{13}$$

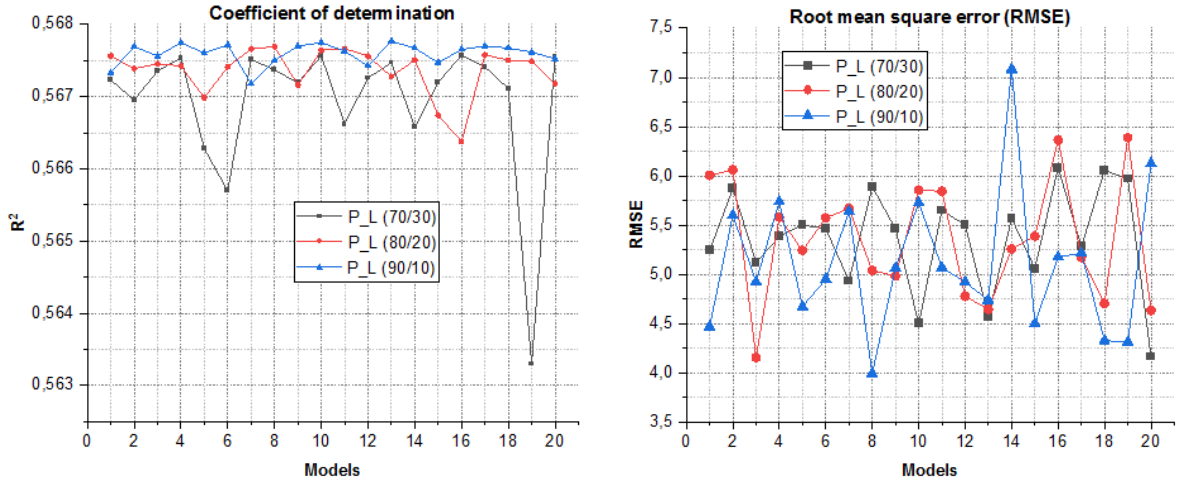
$$r = \frac{\sum_{i=1}^{m}(y_i - \bar{y}) * \left(\hat{y}_i - {\sum_{i=1}^{m}\hat{y}_i}/{m}\right)}{\sqrt{\sum_{i=1}^{m}(y_i - \bar{y})^2 . (\hat{y}_i - {\sum_{i=1}^{m}\hat{y}_i}/{m})^2}} \tag{14}$$

Fig. 12, 13, and 14 present the R^2 and RMSE metrics for various configurations of activation functions between the hidden layer and the output layer, as well as the data ratio for the training and testing phases, covering the 20 models examined to assess the relevance of the chosen model. In Fig. 12, the exploration begins with the use of the purelin activation function for the hidden layer

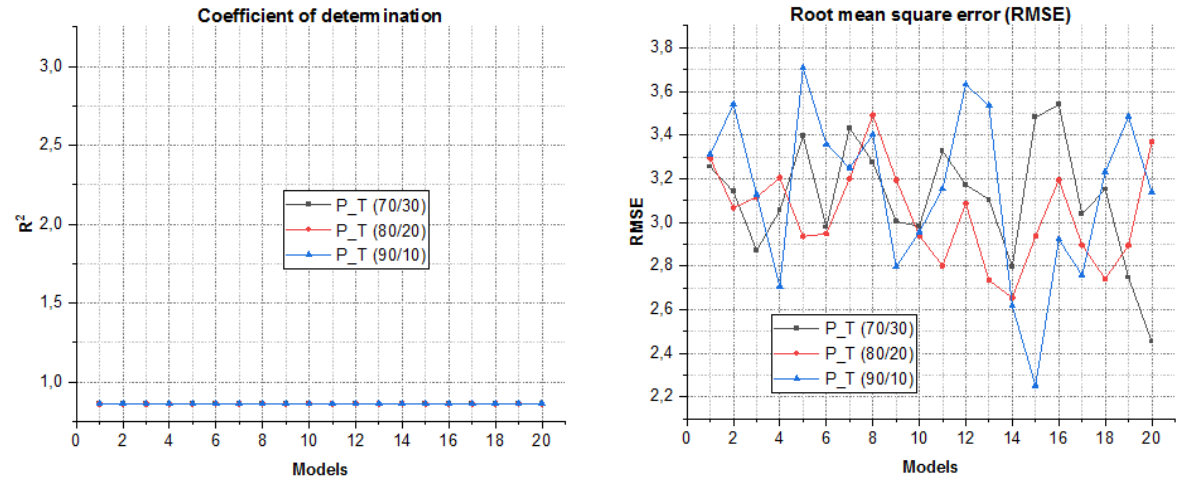
and three activation function options for the output layer. The analysis of this figure reveals an inability to achieve the desired accuracy in all three cases, indicated by a coefficient of determination far from 1 and significant fluctuations in RMSE between the training and test sets.



(a)



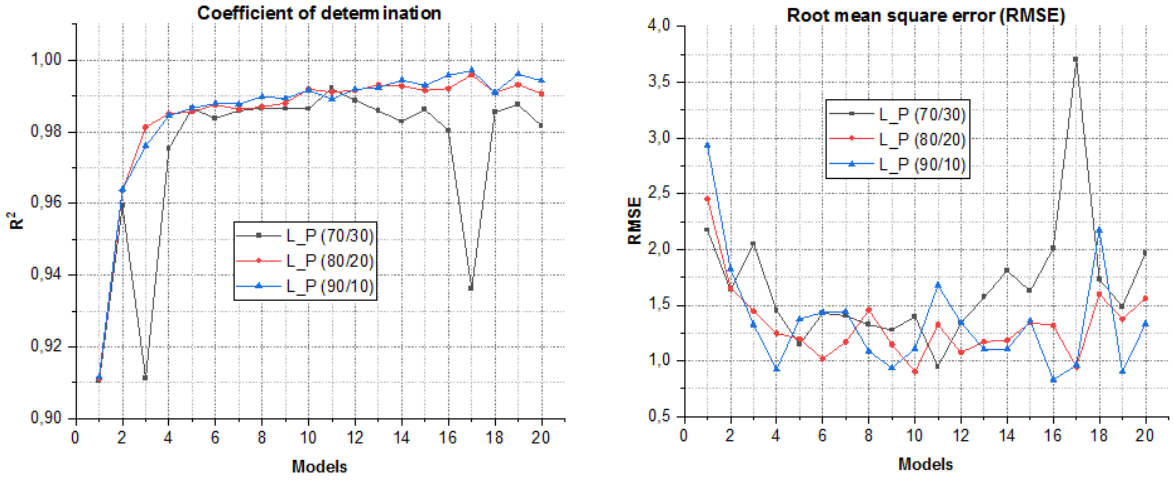
(b)



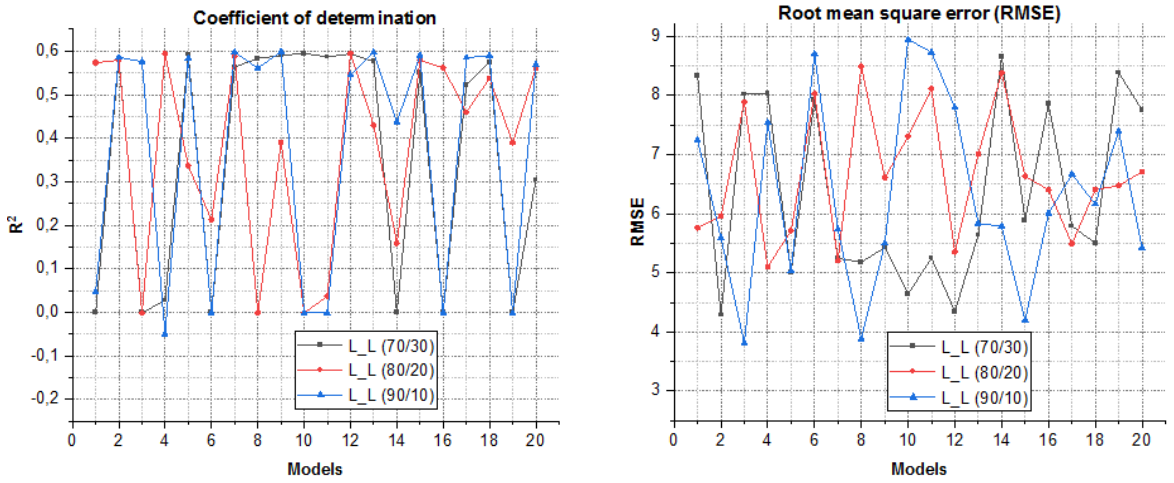
(c)

Fig. 12. Performance of 20 models evaluated by R^2 and RMSE metrics as a function of activation; (a) purelin-purelin, (b) purelin-logsig and (c) purelin-tansig

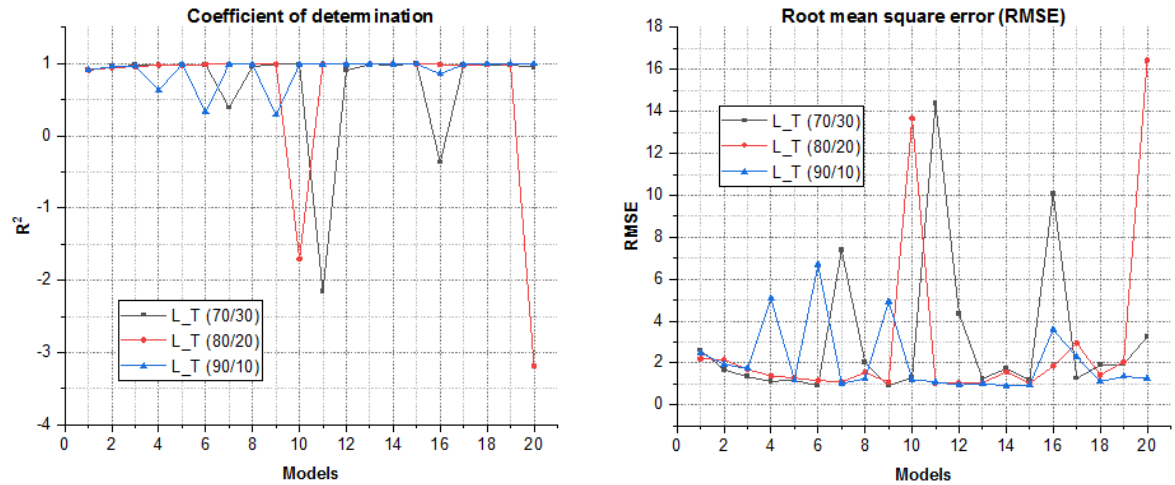
In contrast, in Fig. 13, an improvement is observed, where the RMSE values for training and testing become closer and decrease in cases a and c, suggesting an enhancement in learning. Additionally, a gradual improvement in the coefficient of determination is noted, particularly in case c with the use of the tansig function in the output layer.



(a)



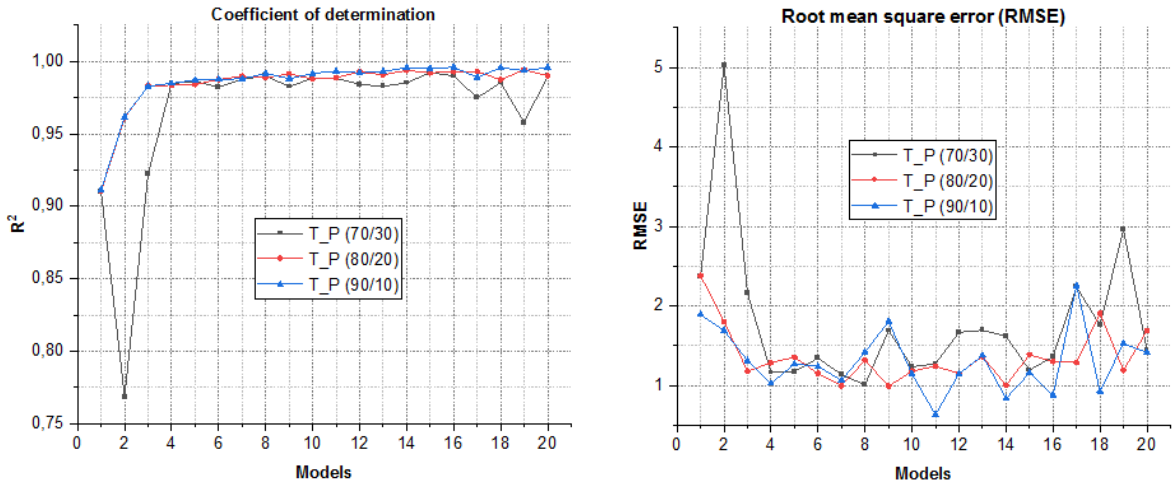
(b)



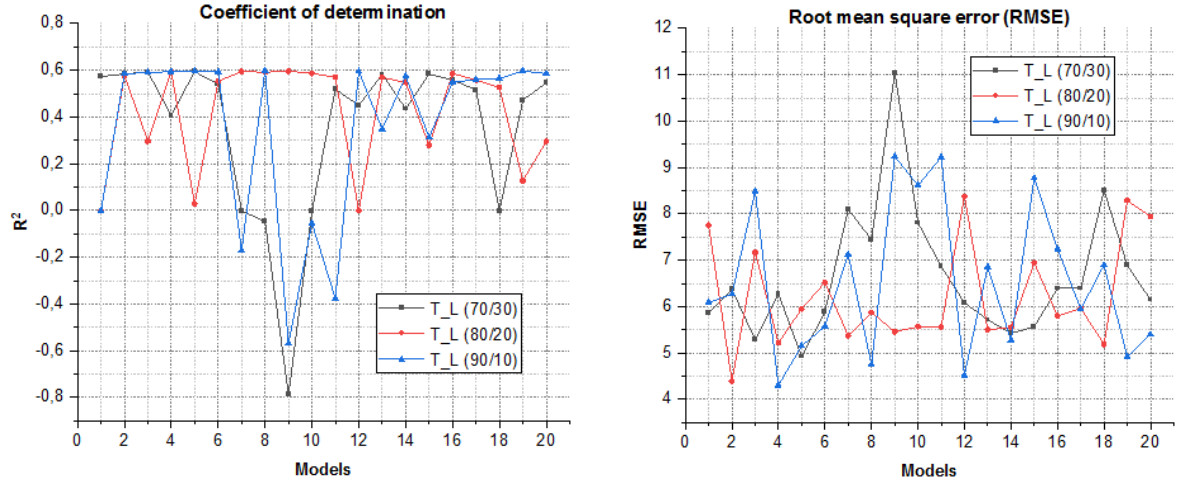
(c)

Fig. 13. Performance of 20 models evaluated by R2 and RMSE metrics as a function of activation; (a) logsig-purelin, (b) logsig-logsig and (c) logsig-tansig

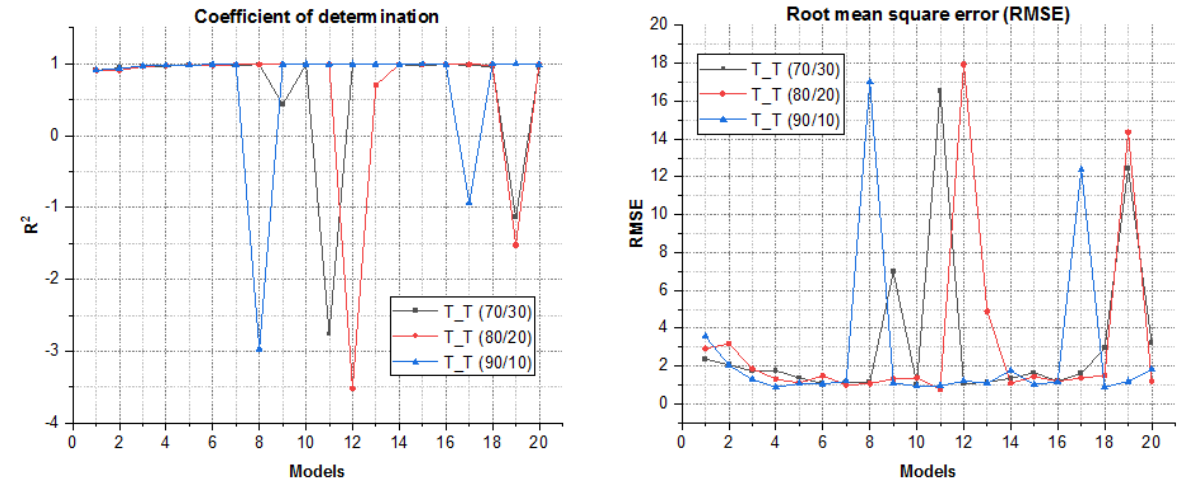
This suggests an effective adaptation of the logsig activation function to the single hidden layer network with the backpropagation algorithm. Regarding Fig. 14, the RMSE values for training and testing also converge and start to decrease, except for some models exhibiting poor performance, likely due to improper learning.



(a)



(b)



(c)

Fig. 14. Performance of 20 models evaluated by R2 and RMSE metrics as a function of activation;(a) tansig-purelin, (b) tansig-logsig and (c) tansig-tansig

The R^2 trends also begin to improve, especially in cases a and c, which approach the target, except for some samples that can be explained by an inadequate number of neurons for the activation functions and learning algorithm used.

The analysis of Figures 12, 13, and 14 demonstrates that the model providing the highest predictive accuracy, with minimal error, incorporates the *tansig* activation function in the hidden layer and *purelin* in the output layer. More specifically, Model 11 in case (a) of Fig.14. shows an RMSE value of 0.23 with a 90/10 data split (90% for training and 10% for testing). This result, among the lowest observed in all the models analyzed, testifies to an optimal performance thanks to this combination of activation functions. In addition, this RMSE value, remains lower than 1, indicating a high precision prediction on the entire dataset. This observation is reinforced by the metric of the coefficient of determination R^2, which reaches 0.992, thus approaching very close to 1. This value suggests that the model's predictions almost perfectly match the target values, indicating near-linear behavior. The overall analysis highlights the significant impact of activation functions and the data split ratio between training and testing on the neural network's performance, without requiring changes to other operational parameters.

To confirm the choice of model 11, we evaluated it using two additional metrics: the mean squared error (MSE) of testing and the correlation coefficient. Fig. 15. illustrates the training MSE, calculated by Matlab. This metric quantifies the arithmetic mean of the squares of the differences between the model predictions and the observed values. An MSE close to zero indicates that the model's predictions are very close to the actual values, reflecting high accuracy. The analysis of Fig. 15. reveals a training MSE of 0.467 over a total of 1000 epochs for the selected architecture. The MSE decreases rapidly as the artificial neural network (ANN) progresses in its learning. The two MSE curves coincide from the first epoch, suggesting an optimal match between the choice of activation functions, the data split ratio, and the backpropagation algorithm used. Consequently, this network is capable of providing accurate predictions regarding burst pressure.

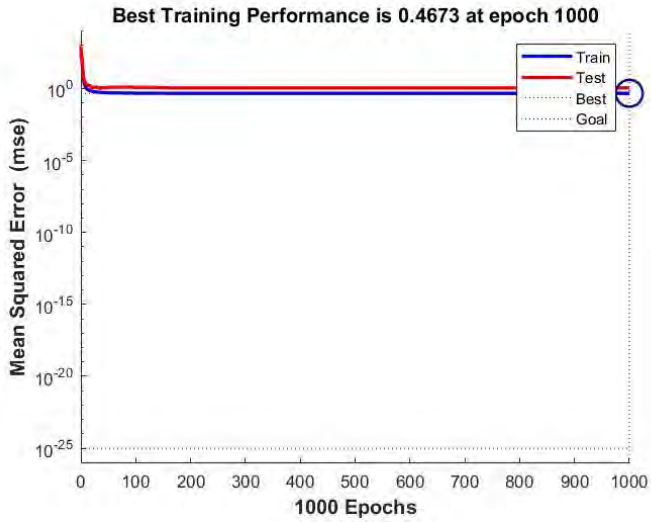


Fig. 15. MSE training

Fig. 16. generated using Matlab R2019a, provides details on the performance of the linear regression for the selected model. The correlation coefficient r measures the accuracy of predictions from a linear regression and ranges between 0 and 1. An r value close to 1 indicates an optimal fit of the model's predictions to the observed data, signifying an almost perfect correlation. Conversely, a value close to zero indicates a low correlation, suggesting that the model does not accurately reflect the data trends.

The correlation coefficient is crucial for forecasting future events using an established model, as it indicates how well past results can be used to predict future outcomes. According to the observations in Fig. 16. the r coefficient remains close to 1 throughout the evaluations, confirming the efficiency and relevance of the chosen model. This suggests not only that the model is well-

fitted but also that it is capable of providing reliable and accurate predictions, an essential aspect for any future deployment of the model in practical applications.

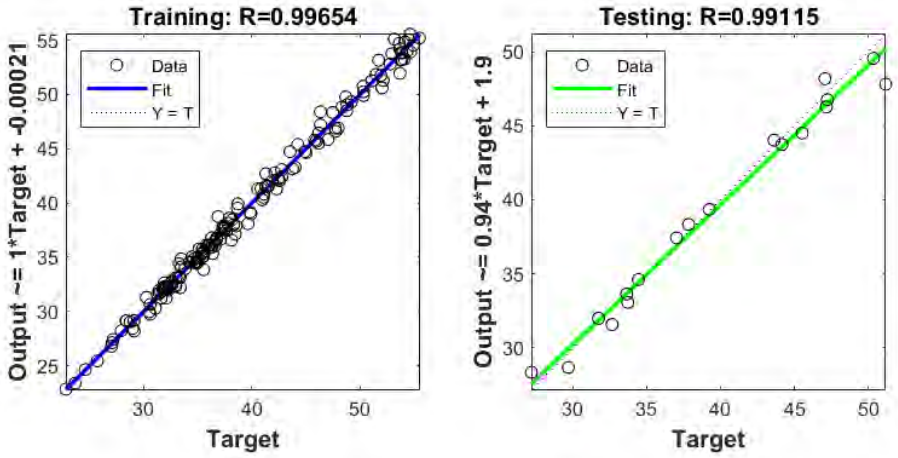


Fig. 16. Correlation coefficient

3. Results and Discussion

3.1. Topology of The Chosen Neural Network

In our study, we adopted a neural network model with a single hidden layer, as demonstrated in Fig. 17. The number of neurons in the input layer is equivalent to the number of variables in our dataset, which is 4, while the output layer consists of a single neuron representing the target variable of our dataset. The choice of 11 neurons for the hidden layer was justified by analyzing metrics such as RMSE, the coefficient of determination (R^2), the training MSE, and the correlation coefficient (r). This decision was made after multiple iterations exploring different configurations, from 1 to 20 neurons. Given the nature of our problem, which pertains to regression, we opted to use backpropagation trained with the Levenberg-Marquardt algorithm (ML) [53].

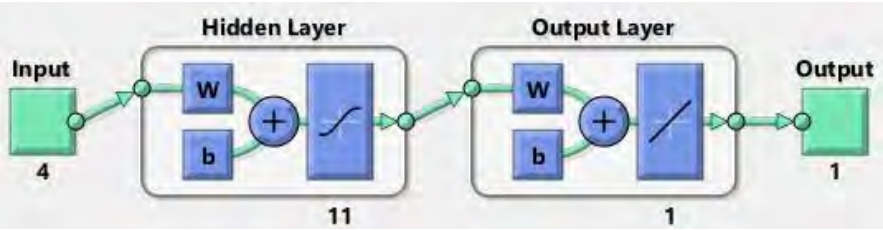


Fig. 17. The topology of the network under study

- Mathematical equation for the hidden layer

$$\begin{pmatrix} h_1 \\ h_2 \\ h_3 \\ h_4 \\ h_5 \\ h_6 \\ h_7 \\ h_8 \\ h_9 \\ h_{10} \\ h_{11} \end{pmatrix} = \begin{pmatrix} 0{,}241 & -1{,}230 & -0{,}583 & 1{,}765 \\ -8{,}605 & 0{,}540 & -8{,}864 & -1{,}954 \\ -6{,}304 & 0{,}887 & -0{,}109 & -0{,}046 \\ 0{,}461 & 2{,}649 & 1{,}789 & 4{,}073 \\ 16{,}749 & -0{,}271 & -0{,}091 & 1{,}292 \\ -0{,}078 & -0{,}461 & -3{,}111 & 0{,}907 \\ -40{,}564 & -25{,}244 & -81{,}911 & -24{,}195 \\ -0{,}087 & 0{,}043 & -3{,}177 & 0{,}406 \\ 1{,}272 & -1{,}067 & 0{,}165 & 1{,}624 \\ 0{,}142 & 17{,}184 & -0{,}504 & 18{,}631 \\ 2{,}047 & -0{,}359 & -0{,}737 & 0{,}232 \end{pmatrix} \begin{pmatrix} q \\ l \\ d \\ l/\sqrt{Dt} \end{pmatrix} + \begin{pmatrix} -0{,}619 \\ 12{,}752 \\ 6{,}104 \\ 3{,}442 \\ 8{,}111 \\ -1{,}437 \\ -35{,}484 \\ -1{,}468 \\ 1{,}097 \\ 3{,}818 \\ 1{,}240 \end{pmatrix} \quad (15)$$

- Equation for predicting burst pressure P_p using the selected neural network

$$P_p = f\left((1{,}503\ \ -0{,}109\ \ -0{,}967\ \ -0{,}083\ \ -0{,}891\ \ -11{,}433\ \ -0{,}030\ \ 11{,}106\ \ -1{,}215\ \ 0{,}057\ \ 0{,}579)\begin{pmatrix} f(h_1)\\ f(h_2)\\ f(h_3)\\ f(h_4)\\ f(h_5)\\ f(h_6)\\ f(h_7)\\ f(h_8)\\ f(h_9)\\ f(h_{10})\\ f(h_{11}) \end{pmatrix} + 1{,}423\right) \quad (16)$$

3.2. Differences Between FEA and ANN Burst Pressure Values

Fig. 18. compares burst pressure trends obtained from finite element analysis (P_n) with predictions from a neural network (P_p) for circumferential, parabolic, and rectangular defects. The close agreement between the curves generated by both methods, for each defect type, confirms the judicious selection of activation functions, network structure, and hidden layer neuron counts in the neural network model. The figure further permits the assessment of relative error between finite element simulation results and neural network predictions. This error is observed to be between 0% and 7% for circumferential defects, 0% and 4% for parabolic defects, and 0% and 5% for rectangular defects. These variations, although apparent, do not detract from the reliability of the model, as evidenced by consistently low error rates.

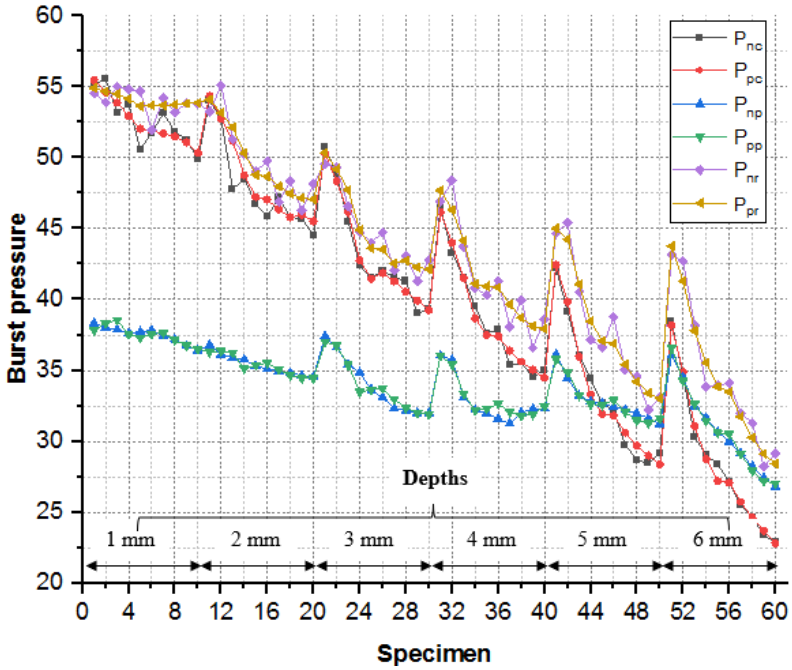


Fig. 18. Burst pressure evolution of simulation and neural network

Fig. 19. evaluates the performance of the neural network model against simulations, by presenting the distribution of relative errors (in %) for circumferential, parabolic, and rectangular defects, within a ±3σ range. The standard deviations observed for these defects are, respectively, 1.86, 1.19, and 2.23, indicating a low dispersion of errors. The entirety of the probability distributions lies within the ±3σ range, thus validating the selected neural network topology and its ability to meet the defined accuracy metrics. The application of the 3σ rule indicates that 99.73% of the errors are within the respective intervals of ±5.58%, ±3.57%, and ±6.69%, for the circumferential, parabolic, and rectangular defects. These reduced standard deviations confirm a low dispersion of errors, this robustness being attributable to the network topology and a judicious optimization of its parameters, as evidenced by the low maximal level of relative errors. These conclusions confirm that the adopted modeling method is appropriate for estimating burst pressure in the studied context.

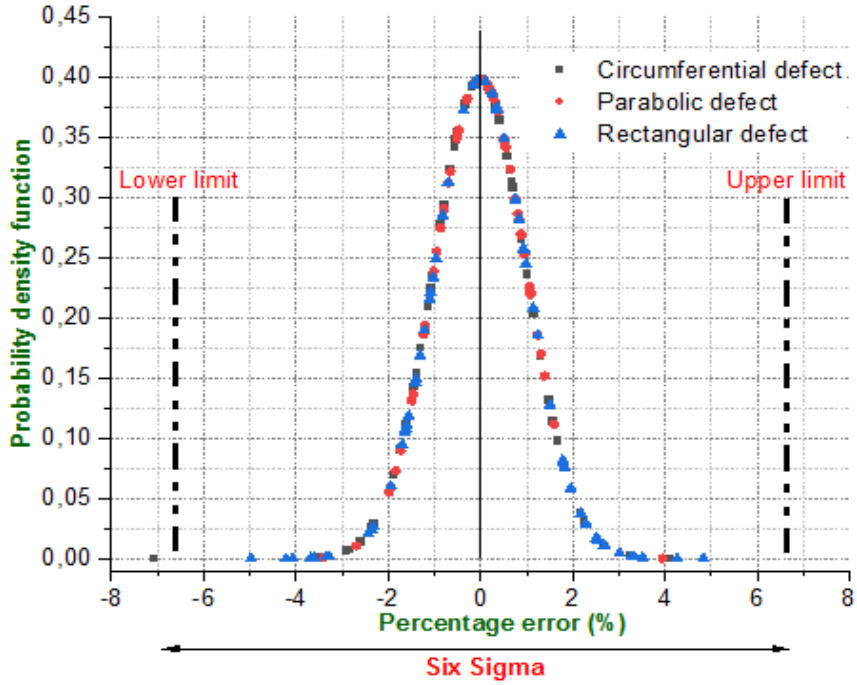


Fig. 19. Reduced normal distribution of the relative error between P_n and P_p

3.3. Discussion of the Harmfulness of The Three Corrosion Defects and Also the Geometrical Parameter Influencing Burst Pressure

Fig. 18. demonstrates a consistent decrease in burst pressure with increasing corrosion defect geometry across all three defect types. Initially, the burst pressure reduction is similar for rectangular and circumferential defects up to a depth of 4 mm; beyond this depth, the circumferential defect shows a more significant decrease, registering approximately 6 MPa lower. Given comparable defect dimensions, our results show that, generally, a parabolic defect remains more impactful than the other types. The figure also shows that at 5 mm depth and lengths of 120 and 220 mm, burst pressures for parabolic and circumferential defects become comparable. Furthermore, at 220 mm length and 5 mm depth, burst pressures for all three defects converge. Increasing defect depth, along with length, shows a progressive decrease in burst pressure, indicating a significant influence of defect depth on burst pressure. Cross-sectional analysis reveals that, with the exception of specific length ranges (160-220 mm at 5 mm depth and 80-220 mm at 6 mm depth) where the circumferential defect is most critical, the parabolic defect is consistently the most detrimental.

3.4. Recommendations and Limitations

The integration of artificial intelligence (AI) presents a paradigm shift from traditional, dataset-reliant methodologies, offering enhanced decision-making capabilities within the industrial sector. This study leverages AI to provide actionable insights for pipeline maintenance, specifically by accurately predicting burst pressures associated with rectangular, parabolic, and circumferential corrosion defects. Furthermore, the research proposes a prioritized intervention sequence for scenarios involving the simultaneous presence of these three distinct defect types across 2000 mm sections of pressurized pipelines. The developed neural network facilitates rapid burst pressure predictions, utilizing mathematical formulations (Eq (15) and (16)) within a mobile application, eliminating the need for computationally intensive finite element analysis in volumetric modeling software. However, this research acknowledges limitations regarding its broad applicability. Variations in pipeline materials and their associated Young's modulus may introduce inaccuracies in predictions. Moreover, the modeling of defects as ideal geometries necessitates expert interpretation when addressing real-world corrosion configurations.

4. Conclusions

This study investigates the impact of corrosion defects (parabolic, circumferential, longitudinal) on the rupture of pressurized pipelines, utilizing numerical simulations (SolidWorks validated by experimental data) to determine burst pressures.

Key Findings:

- Rectangular and circumferential defects exhibit a similar decrease in burst pressure up to a depth of 4 mm. Beyond this, the circumferential defect experiences a pressure drop approximately 6 MPa greater than the rectangular defect, warranting prioritized intervention.
- The parabolic defect is generally the most critical, except for certain length/depth combinations (160-220 mm at 5 mm, 80-220 mm at 6 mm) where the circumferential defect becomes the most detrimental.
- Similar burst pressures are observed for parabolic and circumferential defects at lengths of 120 mm and 220 mm (5 mm depth). At 220 mm/5 mm, all three defect types show nearly identical burst pressures.
- Burst pressure progressively decreases with increasing defect depth, with depth being the dominant parameter.

Neural Network Optimization:

The neural network topology was optimized through the analysis of metrics (RMSE, R^2, r, MSE) and by varying the training data distribution (70%, 80%, 90%) and test data distribution (30%, 20%, 10%) over 20 iterations. The final configuration, chosen for its optimal performance (RMSE and MSE < 1, R^2 and r ≈ 1), consists of 11 neurons in the hidden layer (hyperbolic tangent activation functions) and a linear output layer. This neural network accurately predicts burst pressures, as validated by the metrics, and advantageously replaces the computationally intensive Finite Element Analysis (FEA).

Future Directions:

This study aims to expand its scope by exploring other types of defects present in pressurized pipelines, analyzing their stress fields using advanced numerical simulations, and employing artificial intelligence techniques to formulate relevant recommendations for the industry. In the future, it would be beneficial to investigate the impact of stress corrosion cracking, which is a major factor in pipeline degradation. Furthermore, integrating real-time inspection data into the predictive model would enable the development of predictive maintenance systems capable of anticipating ruptures and optimizing interventions.

Nomenclature

DNV	DNV-RP-F101 corrosion assessment method	σ_u	Ultimate tensile strength
ANN	Artificial neural network	σ_{uts}	True ultimate tensile strength
FEA	Finite element analysis	E	Modulus of Elasticity
σ_c	Axial compressive stress	ϑ	Poisson's ratio
σ_y	Yield stress	D	Pipe outside diameter
σ_e	Effective von Mises stress	L	Length of pipe
σ_h	Hoop stress	t	Wall thickness
σ_r	Radial stress	d	Defect depth
σ_l	Axial/Longitudinal stress	l	Defect length
w	Defect width	r_i	Inside radius
3D	Three dimensional	MF	Folias factor
Q	Geometric correction factor	RMSE	Root Mean Squared Error
R^2	Coefficient of determination	r	Correlation coefficient
MSE	Mean squared error	q	Type of defects
P_p	Burst pressure via ANN	P_n	burst pressure via FEA

P_{tr}	Theorical burst pressure of rectangular defect	P_{tp}	Theorical burst pressure of parabolic defect
P_{tc}	Theorical burst pressure of circumferential defect	P_{nr}	Numerical burst pressure of rectangular defect
P_{pr}	Predicted burst pressure of rectangular defect	P_{np}	Numerical burst pressure of parabolic defect
P_{pp}	Predicted burst pressure of parabolic defect	P_{nc}	Numerical burst pressure of circumferential defect
P_{pc}	Predicted burst pressure of circumferential defect	Er,p	Relative error in the case of a parabolic defect
Er,c	Relative error for circumferential defects	h	Neuron output from hidden layer
Er,r	Relative error for rectangular defects	P_i	Failure pressure of intact pipe
n	Pre-activation	m	Number of samples
$\bar{y}$	Average targets value	$\hat{y}$	Predicted value
y	Target value		

References

[1] Zhang J, Liang Z, Han CJ. Effects of ellipsoidal corrosion defects on failure pressure of corroded pipelines based on finite element analysis. Int J Electrochem Sci. 2015;10(6):5036-47. https://doi.org/10.1016/S1452-3981(23)06684-1

[2] El Kiri Y, Mighouar Z, Zahiri L, Mansouri K, El Ouardi S, Chaiti H. Predicting the failure of plain dent pipeline subjected to cyclic loads using an artificial neural network. In: 2023 7th IEEE Congress on Information Science and Technology (CiSt); 2023; 179-86. https://doi.org/10.1109/CiSt56084.2023.10409983

[3] Li H, Huang K, Zeng Q, Sun C. Residual Strength Assessment and Residual Life Prediction of Corroded Pipelines: A Decade Review; 2022;15(3): 726. https://doi.org/10.3390/en15030726

[4] Mighouar Z, Khatib H, Zahiri L, Mansouri K. Comparison of the most harmful defects present in a steel pipe that can cause fatigue failure. IOP Conf Ser Mater Sci Eng. 2021;1126(1):012007. https://doi.org/10.1088/1757-899X/1126/1/012007

[5] Zakaria M, Zahiri L, Khatib H, Mansouri K. Effect of Water Hammer on Pipes Containing a Crack Defect; 2018.

[6] Zahiri L, Mighouar Z, Khatib H, Mansouri K, Salhi B. Fatigue Life Analysis of Dented Pipes Subjected to Internal Pressure.

[7] Zahiri L, El Houssine Ech-Chhibat M, Jammoukh M, Mighouar Z, Mansouri K. Numerical Modeling and Comparison of Defects Present in a Metal Pipe Under Internal Pressure. Solid State Technol. 2020;63(6):12821-32.

[8] Wang R, Kania R. IPC2016-64098; 2017. p. 1-7.

[9] Ireland GN, et al. Gas pipeline incidents 11; 2019.

[10] Fekete G, Varga L. The effect of the width to length ratios of corrosion defects on the burst pressures of transmission pipelines. Eng Fail Anal. 2012;21:21-30. https://doi.org/10.1016/j.engfailanal.2011.12.002

[11] Parvizsedghy L, Senouci A, Zayed T, Mirahadi SF, El-Abbasy MS. Condition-based maintenance decision support system for oil and gas pipelines. Struct Infrastruct Eng. 2015;11(10):1323-37. https://doi.org/10.1080/15732479.2014.964266

[12] Zakikhani K, Nasiri F, Zayed T. A review of failure prediction models for oil and gas pipelines. J Pipeline Syst Eng Pract. 2020;11(1):03119001. https://doi.org/10.1061/(ASCE)PS.1949-1204.0000407

[13] Razvarz S, Jafari R, Gegov A. A review on different pipeline defect detection techniques. In: Flow Modeling and Control of Pipeline Systems: A Formal Systems Approach; 2021; 25-57. https://doi.org/10.1007/978-3-030-59246-2_2

[14] Milošev I, Scully JR. Challenges for the Corrosion Science, Engineering, and Technology Community as a Consequence of Growing Demand and Consumption of Materials: A Sustainability Issue. Corrosion. 2023;79(9):988-96. https://doi.org/10.5006/4428

[15] Zahiri L, Khatib H, Ech-Chhibat ME. Fatigue-Corrosion Defect in a Metal Pipe Under Internal. 2020;

[16] Valor A, Caleyo F, Hallen JM. RISK16-8 744; 2016.

[17] American Society of Mechanical Engineers. Manual for Determining the Remaining Strength of Corroded Pipelines: A Supplement to ASME B31 Code for Pressure Piping: an American National Standard. American Society of Mechanical Engineers; 2012.
[18] Kiefner JF, Vieth PH. New method corrects criterion for evaluating corroded pipe. Oil Gas J. 1990;88(32).
[19] Wang LB. Development of Software for Residual Strength Evaluation and Residual Life Prediction of Corroded Pipelines. Xi'an Shiyou University, Xi'an, China; 2014.
[20] Stephens DR, Leis BN. Development of an alternative criterion for residual strength of corrosion defects in moderate-to high-toughness pipe. In: International Pipeline Conference; 2000. p. V002T06A012. https://doi.org/10.1115/IPC2000-192
[21] Det Norske Veritas. Corroded Pipelines. DNV; 2006.
[22] Lo M, Karuppanan S, Ovinis M. ANN-and FEA-based assessment equation for a corroded pipeline with a single corrosion defect. J Mar Sci Eng. 2022;10(4):476. https://doi.org/10.3390/jmse10040476
[23] Arumugam T, Karuppanan S, Ovinis M. Residual strength analysis of pipeline with circumferential groove corrosion subjected to internal pressure. Mater Today Proc. 2020;29(November 2018):88-93. https://doi.org/10.1016/j.matpr.2020.05.699
[24] Zahiri L, Khatib H, Ech-Chhibat ME. Fatigue-Corrosion Defect in a Metal Pipe Under Internal. 2020;8(10).
[25] Mighouar Z, Zahiri L, Khatib H, Mansouri K. Damage Accumulation Model for Cracked Pipes Subjected to Water Hammer. 2020;5(4):523-30. https://doi.org/10.25046/aj050462
[26] Cronin DS. Assessment of corrosion defects in pipelines. 2000.
[27] Su Y, Li J, Yu B, Zhao Y, Yao J. Fast and accurate prediction of failure pressure of oil and gas defective pipelines using the deep learning model. Reliab Eng Syst Saf. 2021;216(May). https://doi.org/10.1016/j.ress.2021.108016
[28] El Kiri YE, Zahiri L, Mansouri K, Mighouar Z. Prediction of the rupture pressure of a corroded pipeline by ANN. 2023;00031. https://doi.org/10.1051/e3sconf/202346900031
[29] Devi S, Kumar V, Karuppanan S, Ovinis M. An Empirical Equation for Failure Pressure Prediction of High Toughness Pipeline with Interacting Corrosion Defects Subjected to Combined Loadings Based on Artificial Neural Network. 2021.
[30] Kumar SDV, Karuppanan S, Ovinis M. Failure pressure prediction of high toughness pipeline with a single corrosion defect subjected to combined loadings using artificial neural network (ANN). Metals (Basel). 2021;11(2):373. https://doi.org/10.3390/met11020373
[31] Ren M, Zhang Y, Fan M, Xiao Z. Numerical Simulation and ANN Prediction of Crack Problems within Corrosion Defects. 2024. https://doi.org/10.3390/ma17133237
[32] Arumugam T, Karuppanan S, Ovinis M. Finite element analyses of corroded pipeline with single defect subjected to internal pressure and axial compressive stress. Mar Struct. 2020;72:102746. https://doi.org/10.1016/j.marstruc.2020.102746
[33] Xu W, Bao C, Choung J, Lee J. Corroded pipeline failure analysis using artificial neural network. Adv Eng Softw. 2017;0:1-12. https://doi.org/10.1016/j.advengsoft.2017.05.006
[34] Devi S, Kumar V, Karuppanan S, Ovinis M. Artificial Neural Network-Based Failure Pressure Prediction of API 5L X80 Pipeline with Circumferentially Aligned Interacting Corrosion Defects Subjected to Combined Loadings. 2022.
[35] Netto TA, Ferraz US, Estefen SF. The effect of corrosion defects on the burst pressure of pipelines. 2005;61:1185-204. https://doi.org/10.1016/j.jcsr.2005.02.010
[36] Chen Y, Wang W, Li X, Bai Y, Chen B, Li L. Ultimate load capacity of offshore pipeline with arbitrary shape corrosion defects. China Ocean Eng. 2015;29:241-52. https://doi.org/10.1007/s13344-015-0017-z
[37] Chen Z, Zhu W, Di Q, Wang W. Burst pressure analysis of pipes with geometric eccentricity and small thickness-to-diameter ratio. J Pet Sci Eng. 2015;127:452-8. https://doi.org/10.1016/j.petrol.2015.01.043
[38] Cronin DS, Pick RJ. Prediction of the failure pressure for complex corrosion defects. Int J Press Vessel Pip. 2002;79(4):279-87. https://doi.org/10.1016/S0308-0161(02)00020-0
[39] Wang YL, Li CM, Chang RR, Huang HR. State evaluation of a corroded pipeline. J Mar Eng Technol. 2016;15(2):88-96. https://doi.org/10.1080/20464177.2016.1224615
[40] Belachew CT, Che Ismail M, Karuppanan S. Strength assessment of corroded pipelines-Finite element simulations and parametric studies. Int J Struct Stab Dyn. 2017;17(07):1750069. https://doi.org/10.1142/S0219455417500699
[41] Baek J, Kim Y, Kim W, Koo J, Seok C. Load bearing capacity of API X65 pipe with dent defect under internal pressure and in-plane bending. Mater Sci Eng A. 2012;540:70-82. https://doi.org/10.1016/j.msea.2012.01.078
[42] Amaya-Gómez R, Sánchez-Silva M, Bastidas-Arteaga E, Schoefs F, Munoz F. Reliability assessments of corroded pipelines based on internal pressure-A review. Eng Fail Anal. 2019;98:190-214. https://doi.org/10.1016/j.engfailanal.2019.01.064

[43] Amandi KU, Diemuodeke EO, Briggs TA. Model for remaining strength estimation of a corroded pipeline with interacting defects for oil and gas operations. Cogent Eng. 2019;6(1):1663682. https://doi.org/10.1080/23311916.2019.1663682
[44] DNV CP. Recommended Practice DNV-RP-F101. Oslo, Norway: DNV; 2017.
[45] Batte AD, Fu B, Kirkwood MG, Vu D. New methods for determining the remaining strength of corroded pipelines. In: Proceedings of the international conference on offshore mechanics and arctic engineering; 1997. p. 221-8.
[46] Belachew CT, Ismail MC, Karuppanan S. Burst strength analysis of corroded pipelines by finite element method. J Appl Sci. 2011;11(10):1845-50. https://doi.org/10.3923/jas.2011.1845.1850
[47] Choi JB, Goo BK, Kim JC, Kim YJ, Kim WS. Development of limit load solutions for corroded gas pipelines. Int J Press Vessel Pip. 2003;80:121-8. https://doi.org/10.1016/S0308-0161(03)00005-X
[48] Wang YH, Wang GZ, Tu ST, Xuan FZ. In-plane and out-of-plane constraint characterization of different constraint parameters for semi-elliptical surface cracks in pipes. Eng Fract Mech. 2020;235:107161. https://doi.org/10.1016/j.engfracmech.2020.107161
[49] Bai B, Zhang J, Wu X, Zhu GW, Li X. Reliability prediction-based improved dynamic weight particle swarm optimization and back propagation neural network in engineering systems. Expert Syst Appl. 2021;177:114952. https://doi.org/10.1016/j.eswa.2021.114952
[50] Laabid Z, Moumen A, Mansouri K, Siadat A. Numerical study of the speed's response of the various intelligent models using the tansig, logsig and purelin activation functions in different layers of artificial neural network. IAES Int J Artif Intell. 2023;12(1):155. https://doi.org/10.11591/ijai.v12.i1.pp155-161
[51] Chicco D, Warrens MJ, Jurman G. The coefficient of determination R-squared is more informative than SMAPE, MAE, MAPE, MSE and RMSE in regression analysis evaluation. PeerJ Comput Sci. 2021;7:e623. https://doi.org/10.7717/peerj-cs.623
[52] Rodríguez Sánchez A, Salmerón Gómez R, García C. The coefficient of determination in the ridge regression. Commun Stat Comput. 2022;51(1):201-19. https://doi.org/10.1080/03610918.2019.1649421
[53] Sapna S, Tamilarasi A, Kumar MP. Backpropagation learning algorithm based on Levenberg Marquardt Algorithm. Comput Sci Inf Technol (CSIT). 2012;2:393-8. https://doi.org/10.5121/csit.2012.2438

Research on Engineering Structures & Materials
www.jresm.org

Research Article

Performance optimization of a horizontal axis wind turbine simulator under the effects of blade's pitch angle variation

Abdulhamid Hamdan Al-Hinai [*,a], Karu Clement Varaprasad [b], V. Vinod Kumar [c]

Department of Mechanical and Mechatronic Engineering, Sohar University, Sohar, Oman

Article Info

Article History:

Received 28 Oct 2024

Accepted 05 Dec 2024

Keywords:

Blade pitch angle;
Power output;
Rotational speed;
Vibration level;
Wind turbine

Abstract

The optimization of wind turbine performance is a critical issue for enhancing energy conversion efficiency. This study investigates the effects of blade pitch angles and Variable Frequency Drive settings on the performance of a wind turbine system using the Spectra Quest wind turbine simulator. Employing a Taguchi design of experiments with a full factorial approach, a total of 81 experimental tests are conducted to analyze the influence of three blade pitch angles (0°, 10°, and 20°) combined with three distinct Variable Frequency Drive settings (12, 15, and 18) on shaft rotational speed, power output, and vibration levels. Using Taguchi's response analysis and analysis of variance, this research identifies Variable Frequency Drive as the most influential factor on turbine performance metrics. Regression modelling further elucidates the complex relationships between the operational parameters and performance outcomes. The results reveal significant interactions between the input parameters and demonstrate that lower blade pitch angles in conjunction with higher Variable Frequency Drive settings maximize both shaft rotational speed (171 rpm) and power output (24.102 W), maintaining acceptable vibration levels. The best pitch angle input parameters are found to be β1=0o, β2=0o and β3=0o with a VFD setting of 18. A notable increase in air resistance at higher pitch angles corroborates the findings of previous studies, highlighting the need for optimal parameter settings to enhance turbine efficiency.

© 2025 MIM Research Group. All rights reserved.

1. Introduction

The increasing reliance at renewable power sources marked a significant transition in worldwide strength strategies aimed toward mitigating weather change and lowering dependence on fossil fuels. Among numerous renewable technologies, wind energy has emerged as one of the maximum promising solutions due to its sustainability, low environmental impact, and potential for scalability. The international installed wind energy capability has grown drastically in recent years, accomplishing 837 GW throughout 31 nations in 2021 [1]. This expansion has caused considerable CO2 emission reductions, with projections signifying wind power should account for over 30% of the worldwide energy era via mid-century [2]. The industry has visible technological improvements, such as larger turbines and accelerated efficiencies [3]. By 2017, wind strength had turned out to be the second-largest form of power technology in Europe [4]. Despite demanding situations, projections endorse international wind power capacity may want to attain 5800 GW by 2050 [5].

The outcomes of blade pitch angles and rotor speeds on wind turbine performance have been considerably studied using simulations and experimental techniques [6]. Research showed that varying pitch angles and angular velocities significantly affect turbine overall performance parameters which include power output, torque, and performance [7]. For a horizontal-axis wind

*Corresponding author: abdulhamidalhinai@gmail.com
[a]orcid.org/0009-0005-5354-2895; [b]orcid.org/0000-0002-8182-804X; [c]orcid.org/0000-0001-5420-4584
DOI: http://dx.doi.org/10.17515/resm2024.505st1028rs

turbine, optimal pitch angles exist for maximum energy technology at given wind velocities [8]. In Darrieus-type turbines, a small negative valued fixed pitch angle could improve performance, although variable-pitch blades can enhance starting torque and efficiency at lower tip speed ratios [9][10]. Experimental studies on a horizontal wind turbine with NACA 6412 airfoils at low wind speeds revealed that an 8° pitch angle produced higher electrical power and total efficiency [11]. Multiple studies employed Taguchi-based design of experiments to analyze the effects of various parameters on turbine efficiency [12]. Wind speed and blade number also significantly impact turbine performance, with optimal results observed at higher wind speeds and 5-blade configurations [13]. The Taguchi method, sometimes combined with Grey Relational Analysis, proved effective for both parameter and tolerance design optimization [14]. Tittus and Diaz (2020) analyzed a turbine performance for different blade tip sizes and twist angles and found that drag and lift coefficients had less significance compared to other parameters [15]. Bossanyi (2003) proposed individual blade pitch control as a method for significant load reduction in pitch-regulated turbines [16]. Firman Aryanto et al. (2013) investigated the impact of wind speed and blade number variations on horizontal-axis wind turbine performance, concluding that the best efficiency was achieved with 5 blades at 4 m/s wind speed [13]. Labib, A.M., et al. (2020) examined the effect of blade angle variation on the aerodynamic performance of a horizontal axis wind turbine using computational simulation and experimental validation [17]. Gumilar, L. et al. (2020) revealed that increasing the pitch angle of a horizontal-axis wind turbine decreases the maximum power produced [18]. These findings highlighted the importance of optimizing blade pitch angles and rotor speeds to enhance wind turbine performance across various designs and operating conditions [19].

The value of this study lies in its systematic investigation of ways varying blade pitch angles and VFD settings have an impact on vital performance measures, particularly shaft rotational speed, energy output, and vibration levels. By addressing this subject matter, the interplay of these parameters and their implications for wind turbine design and operation may be explored. The primary objectives of this study are to: 1) analyze the outcomes of different blade pitch angles and VFD settings on the performance of a wind turbine system, 2) offer an in-depth statistical evaluation of the records through Taguchi's response evaluation and regression modelling techniques, and 3) optimize the operational parameters to maximize strength output at the same time as minimizing vibration problems.

This article is structured as follows: section 2 discusses the methods and materials employed, detailing the experimental design, data collection process, and analytical techniques used. Section 3 highlights the results and discussion including the experimental measurements and their analysis, Taguchi design response analysis, analysis of variance (ANOVA) from regression modelling and finally optimization using Grey Relational Analysis of best-fit responses with optimal parameter settings [20][21]. Finally, section 4 summarizes the conclusions with key contributions of this research work, suggests practical implications, and outlines directions for future research in the domain of wind energy optimization.

2. Methods and Materials

2.1 Experimental Set-Up

This section outlined the methodology employed in this research. The WTS model used in this research study was the Spectra Quest (SQ) type that used a Vibra Quest (VQ) simulation software and data acquisition system, shown in Fig.s 1 and 2. The SQ WTS weights 222.7 kg, has a centerline height of 2.369 m, a sweeping blade diameter of 3.3 m, and base measurements of 2.991 m × 2.438 m. On the rotational shaft, a tachometer and an accelerometer were installed to detect the vibration level and rotational speed in one direction of vibrational excitation, respectively.



Fig. 1. SQ WTS

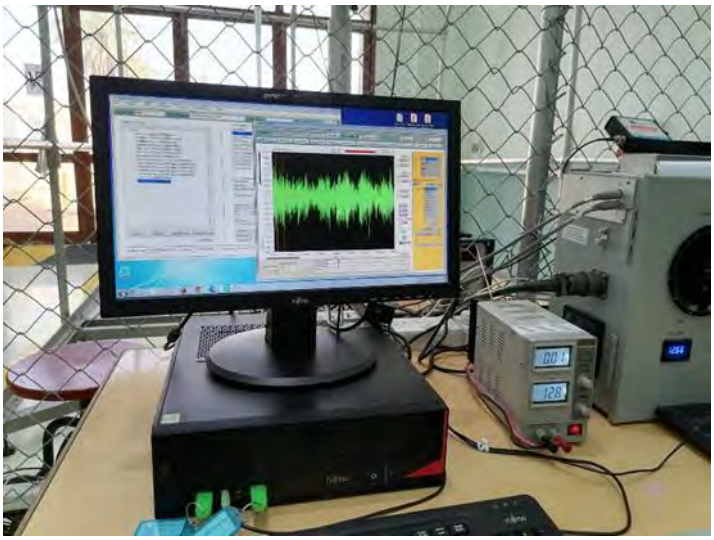


Fig. 2. VQ analysis software

2.2 Taguchi Design of Experiment

The analysis was predicated on four critical input parameters:

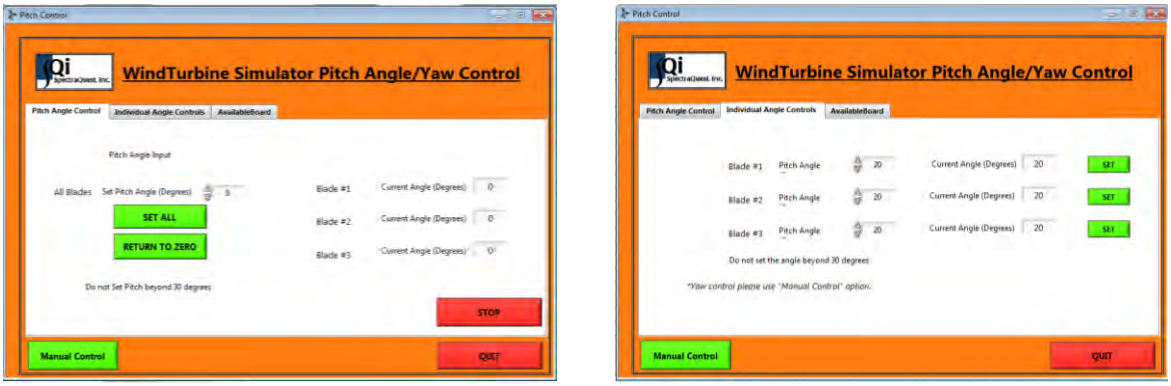
- The pitch angles of the three blades were varied systematically. Each pitch angle was selected from three distinct levels to examine the effects of adjustment.
- The variable frequency drive (VFD) controlled the rotational speed of the turbine shaft. Three different VFD settings were utilized to create varied operational conditions. The running conditions emphasized that the turbine would operate under varying shaft rotational speeds due to input parameters.

Studying pitch angles from 0° to 30° strikes a balance between capturing meaningful aerodynamic and structural behavior and avoiding overly complex or unrealistic scenarios. This range is particularly relevant for applications involving lift, drag, energy capture, and load control. This confirms practical visions for engineering design and analysis. The Taguchi design of experiments DoE with a full factorial approach was used to plan the experimental work. There are four input parameters, β1, β2, β3 and VFD. Taguchi design of experiments with a full factorial approach was used to plan the experimental works. The Experimental layout was based on L_{81} (3^4) orthogonal array. To design the Experimental layout based on this L_{81} (3^4) orthogonal array, three levels were required for each input parameter. The determining pitch angle variations were 0^o, 10^o and 20^o, which were selected within the pitch angle range, with equal increments in between. The four input parameters each had three levels are shown in Table 1. The responses were the shaft rotational speed, vibration level and power output.

The blade angles were changed using pitch control software, shown in Fig. 3. The initial setting was when $\beta1=0^o$, $\beta2=0^o$ and $\beta3=0^o$. Both the initial and maximum settings of the angles are shown in Fig. 3. The Variable Frequency Drive (VFD) was set for three levelling values; 12, 15 and 18, as shown in Fig. 4.

Table 1. Experimental input parameters and their levels

Factor	Name	Levels		
β1	Blade 1 Pitch Angle	0^o	10^o	20^o
β2	Blade 2 Pitch Angle	0^o	10^o	20^o
β3	Blade 3 Pitch Angle	0^o	10^o	20^o
VFD	Variable Frequency Drive	12	15	18



(a) (b)

Fig. 3. Setting of blade angles (a) Initial setting and (b) maximum setting)



(a) (b) (c)

Fig. 4. VFD settings (a) 12, (b) 15 and (c) 18

2.3 Experimental testing of the WTS as per DoE

This involved a systematic change of the pitch angle of each blade, starting first with 0º pitch angle for all three blades, setting the VFD to 12 and performing the experiment. The shaft rotational speed, vibration level and power output were measured and recorded using a mounted tachometer, accelerometer and a 3-phase field-controlled alternator, respectively. Then, the VFD setting was changed to 15 then 18, and the experiment was performed again for each VFD setting. After that, the pitch angles were changed as per the design of experiment and the experimental work was performed for 81 tests.

2.4 Results Analysis

The results of 81 experiments were analyzed to investigate the effects of changing pitch angles on the shaft rotational speed, vibration level and power output. The Vibra Quest software generated the vibration waveform reports in MS Excel format. At higher angles, the air resistance was expected to play a negative role on rotational speed and power output. Simultaneously and at certain combinations of pitch angles, the wind turbine was expected to undergo a balancing scenario at which the vibration level decreased within the same setting of VFD.

2.5 Regression Modelling:

The regression modelling for the three responses was performed using Minitab software to develop the best fit regression models, considering the R-squared values for each response.

2.5 Optimization

The multi-responses of this research work were optimized using Grey Relational Analysis. For the shaft rotational speed and power output, the higher-the-better criterion was used. While, for vibration level, the lower-the-better criterion was used. The normalization of the original sequence of each response was calculated as follows:

For higher-the-better criterion:

$$Y_{ij} = \frac{X_{ij} - min(X_{ij})}{max(X_{ij}) - min(X_{ij})} \quad (1)$$

For lower-the-better criterion:

$$Y_{ij} = \frac{max(X_{ij}) - X_{ij}}{max(X_{ij}) - min(X_{ij})} \quad (2)$$

where x_{ij} is the measured response, $min(x_{ij})$ is the minimum of x_{ij} and $max(x_{ij})$ is the maximum of x_{ij}, i is the response variables and j is the experiment number. The Deviation Sequence (distinguishing coefficient) Δ_{ij} was calculated as follows:

$$\Delta_{ij} = max(Y_{ij}) - Y_{ij} \quad (3)$$

where $max(Y_{ij})$ is the expected sequence, Y_{ij} is the comparability sequence and Δ_{ij} is the deviation sequence of $max(Y_{ij})$ and Y_{ij}. The grey relational coefficient ξ_{ij} was calculated as follows:

$$\xi_{ij} = \frac{min(\Delta_{ij}) + \zeta \times max(\Delta_{ij})}{\Delta_{ij} + \zeta \times max(\Delta_{ij})} \quad (4)$$

where ζ is the differentiating coefficient, $0 \leq \zeta \leq 1$, and 0.5 is the widely accepted value. The grey relational grade GRG (γ_j) for each experiment was computed as follows, for n number of responses:

$$\gamma_j = \frac{\sum_{i=1}^{n} \xi_{ij}}{n} \quad (5)$$

If larger γ_j is obtained, then the equivalent set of process parameters is nearer to the most favorable optimal setting.

3. Results and Discussion

The results of the experimental tests using the Spectra Quest Wind Turbine Simulator (SQ WTS) are presented in this section. This detailed the effects of varying the pitch angles of the blades under different settings of Variable Frequency Drive (VFD) on shaft rotational speed, power output, and vibration levels.

3.1 Experimental Overview

A total of 81 experiments were conducted based on the Taguchi design of experiments approach using a full factorial design with $L_{81}(3^4)$ orthogonal array. Each experiment was systematically designed to assess the impact of the three blade pitch angles' combinations (0°, 10°, and 20° for each of the three blades) and three Variable Frequency Drive (VFD) settings (12, 15, and 18). Table 2 shows the measured responses of the experimental work.

Table 2. Measured responses from experimental tests

Exp	Input Parameters				Measured responses		
	β1 (°)	β2 (°)	β3 (°)	VFD	Rot. Spd. (rpm)	Power Output (W)	Vibration Level (m/s²)
1	0	0	0	12	112	10.730	6.274
2	0	0	0	15	141	17.430	10.106
3	0	0	0	18	171	24.102	10.326
4	0	0	10	12	111	10.643	6.943
5	0	0	10	15	139	16.898	11.238

Table 2 (continued)

Exp	Input Parameters				Measured responses		
	β1 (°)	β2 (°)	β3 (°)	VFD	Rot. Spd. (rpm)	Power Output (W)	Vibration Level (m/s²)
6	0	0	10	18	168	23.868	10.849
7	0	0	20	12	107	10.237	7.486
8	0	0	20	15	134	16.014	10.239
9	0	0	20	18	157	21.164	10.411
10	0	10	0	12	110	10.701	7.400
11	0	10	0	15	139	17.290	11.402
12	0	10	0	18	167	23.868	10.760
13	0	10	10	12	109	10.382	7.352
14	0	10	10	15	137	16.558	11.181
15	0	10	10	18	164	22.610	10.354
16	0	10	20	12	106	9.688	8.013
17	0	10	20	15	131	15.015	9.925
18	0	10	20	18	153	20.498	10.859
19	0	20	0	12	107	10.411	8.005
20	0	20	0	15	135	16.218	11.316
21	0	20	0	18	159	22.192	10.966
22	0	20	10	12	107	10.121	7.308
23	0	20	10	15	132	15.844	10.204
24	0	20	10	18	155	20.905	10.396
25	0	20	20	12	103	9.380	8.424
26	0	20	20	15	126	14.652	8.952
27	0	20	20	18	143	17.955	11.675
28	10	0	0	12	110	10.701	7.712
29	10	0	0	15	139	17.325	12.348
30	10	0	0	18	166	23.907	10.925
31	10	0	10	12	108	10.614	7.795
32	10	0	10	15	136	16.660	12.325
33	10	0	10	18	162	23.028	11.423
34	10	0	20	12	105	10.295	6.774
35	10	0	20	15	133	15.576	7.052
36	10	0	20	18	155	21.090	10.072
37	10	10	0	12	109	10.701	10.528
38	10	10	0	15	137	16.762	7.474
39	10	10	0	18	163	23.400	12.156
40	10	10	10	12	108	10.498	10.750
41	10	10	10	15	135	16.422	7.739
42	10	10	10	18	159	22.306	11.469
43	10	10	20	12	105	10.092	10.872
44	10	10	20	15	129	15.180	8.217
45	10	10	20	18	150	20.424	9.910
46	10	20	0	12	106	10.353	11.462
47	10	20	0	15	132	15.980	8.174
48	10	20	0	18	153	20.831	10.679
49	10	20	10	12	105	10.237	11.416
50	10	20	10	15	130	15.312	8.378
51	10	20	10	18	152	22.572	10.309

Table 2 (continued)

Exp	Input Parameters				Measured responses		
	β1 (°)	β2 (°)	β3 (°)	VFD	Rot. Spd. (rpm)	Power Output (W)	Vibration Level (m/s²)
52	10	20	20	12	103	9.240	7.490
53	10	20	20	15	128	14.080	7.599
54	10	20	20	18	143	17.710	10.287
55	20	0	0	12	108	10.440	6.916
56	20	0	0	15	137	16.558	10.124
57	20	0	0	18	162	22.534	9.982
58	20	0	10	12	107	10.237	7.081
59	20	0	10	15	134	15.444	9.469
60	20	0	10	18	157	20.905	9.675
61	20	0	20	12	104	9.660	8.354
62	20	0	20	15	128	14.652	8.630
63	20	0	20	18	146	18.720	11.268
64	20	10	0	12	106	10.034	7.744
65	20	10	0	15	133	15.378	9.940
66	20	10	0	18	156	20.646	10.647
67	20	10	10	12	105	9.520	7.942
68	20	10	10	15	130	14.916	9.354
69	20	10	10	18	152	20.128	10.513
70	20	10	20	12	101	9.184	8.862
71	20	10	20	15	124	13.760	8.772
72	20	10	20	18	140	17.535	12.254
73	20	20	0	12	103	9.296	8.976
74	20	20	0	15	127	14.718	8.951
75	20	20	0	18	147	19.152	10.863
76	20	20	10	12	102	9.100	8.739
77	20	20	10	15	125	13.952	8.912
78	20	20	10	18	142	17.920	12.414
79	20	20	20	12	99	8.505	9.561
80	20	20	20	15	119	12.524	8.593
81	20	20	20	18	133	15.411	10.496

3.2 Shaft Rotational Speed

The collected experimental results showed varied shaft rotational speeds based on different combinations of input parameters. Fig. 5 shows the graph of shaft rotational speed versus the VFD setting for each combination of blade pitch angles (legend β1+β2+β3). For each VFD setting, the rotational speed varied as a result of air resistance on the blade, mostly with higher pitch angles. From the initial blades' angle settings (input parameters) to the final blades' angle settings (input parameters), the rotational speed varied from 99 rpm to 112 rpm at VFD = 12. For VFD = 15, the rotational speed changed from 119 rpm to 141 rpm. While, for VFD = 18, the rotational speed altered from 133 rpm to 171 rpm. The maximum pitch angle settings (20°) marked a decrease in rotational speed. This confirmed the hypothesis that increased blade angle contributes to higher air resistance [22].

3.3 Power Output

The power output results reflected similarly the interdependencies of the blade angles and VFD settings, as shown in Fig. 6. This power output was proportionally related to the shaft rotational speed connected to the power alternator by the gearbox. For the angle adjustments of the first blades (input parameters) and the last blades (input parameters), if VFD = 12, the power output

varied from 8.505 W to 10.730 W, if VFD = 15, the power output varied from 12.524 W to 17.430 W, and when VFD = 18, the power output varied from 15.411 W to 24.102 W. An inverse relationship was noted at the maximum blade angle settings (20°), which resulted in reduced power outputs due to increased drag [17].

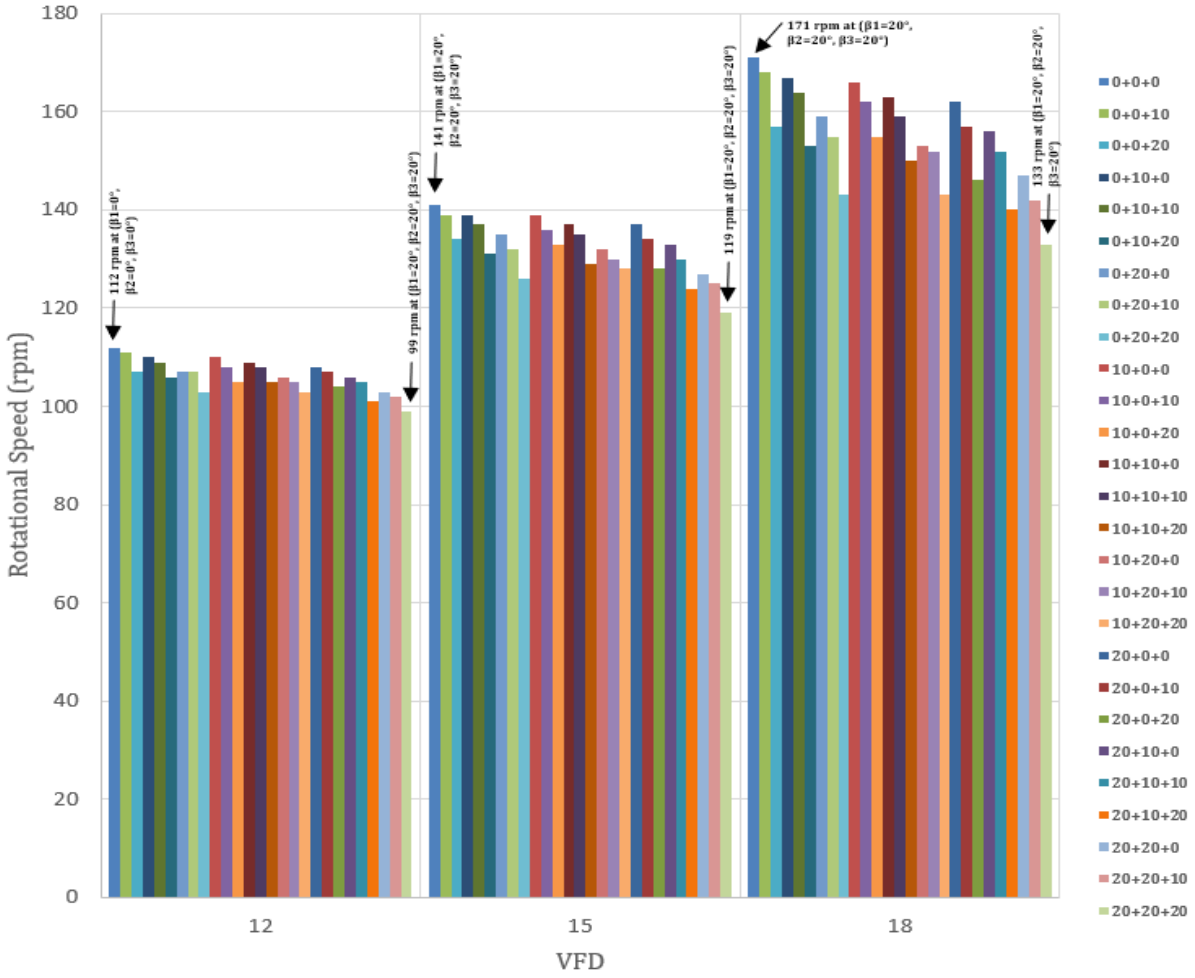


Fig. 5. Variation of shaft rotational speed against the VFD setting (legend β1+β2+β3)

3.4 Vibration Level

The measurements of the vibration levels, as illustrated in Fig. 7, revealed that combinations of higher pitch angles often led to increased vibration levels. However, some specific combinations of pitch angles and VFD settings led to a balancing effect. For example, in VFD = 12, the pitch angle combinations of (experiment 34) showed a vibration level of (6.77 m/s2) and (experiment 55) showed a vibration level of (6.92 m/s2). These two combinations showed lower vibration levels just above the initial reading of (experiment 1) which was (6.27 m/s2). The same for VFD = 15, the pitch angle combinations of (experiment 35), (experiment 38) and (experiment 53) showed much lower vibration levels of (7.05 m/s2), (7.47 m/s2) and (7.60 m/s2) respectively. This is compared to the initial reading of (experiment 1) which was (10.11 m/s2). For VFD=18, the pitch angle combinations of (experiment 60), (experiment 45) and (experiment 36) showed much lower vibration levels of (9.68 m/s2), (9.91 m/s2) and (10.07 m/s2) respectively. This is compared to the initial reading of (experiment 1) which was (10.33 m/s2). To some extent, the wind turbine system underwent balancing scenarios at these combinations of pitch angles [23].

3.5 Taguchi Response Analysis

Taguchi's response analysis focused on optimizing performance metrics through the design of experiments and the minimization of variability. The experimental investigations of blade angle variations on wind turbine systems were analyzed using Taguchi's response analysis, as responses

for means and signal-to-noise ratios. The influence of selected input process parameters on various performance measures like the shaft rotational speed, power output and vibration level are detailed.

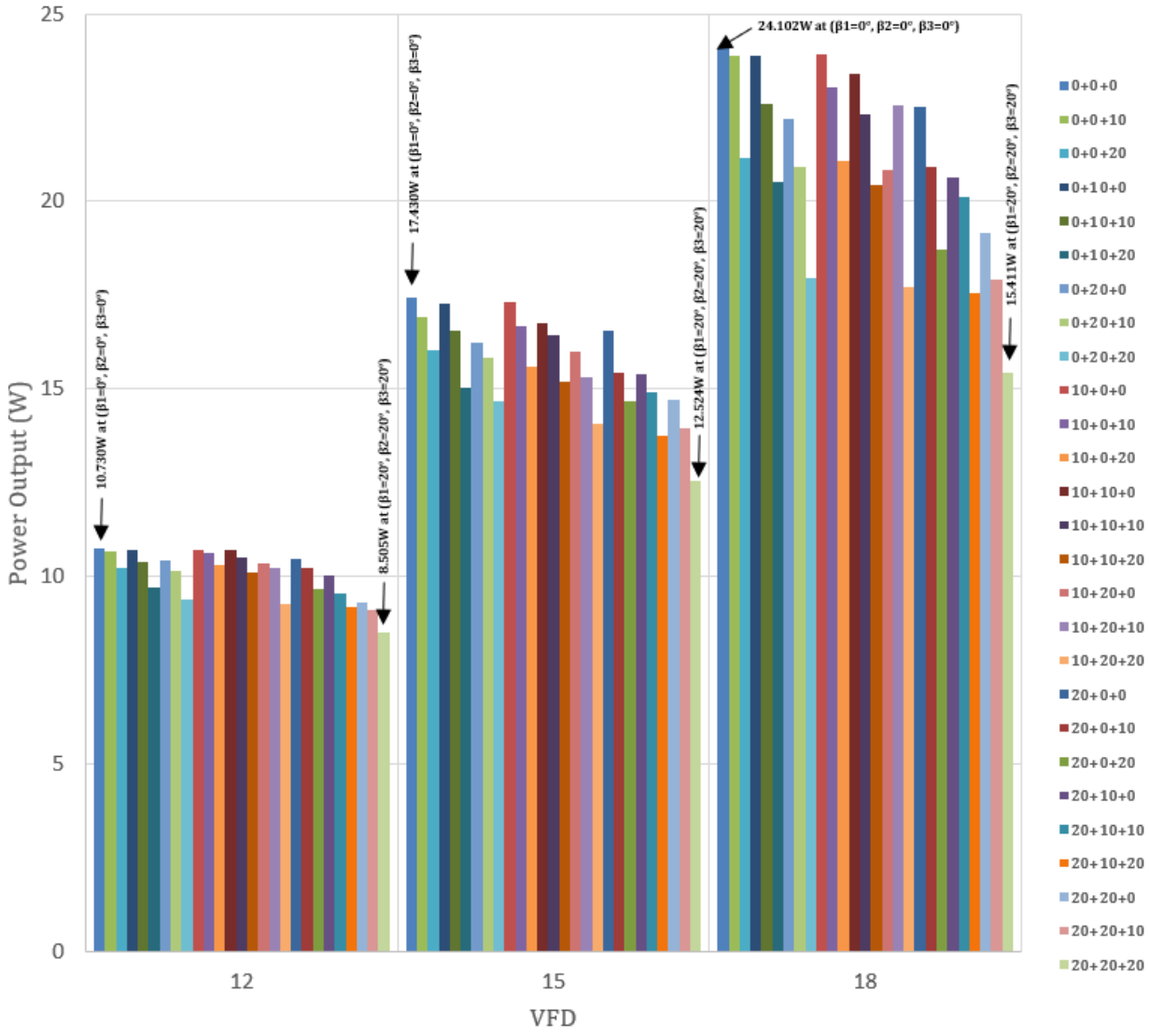


Fig. 6. Variation of power output against the VFD setting (legend β1+β2+β3)

3.5.1 Taguchi's Response Analysis for The Shaft Rotational Speed

In this case, the process parameters β1, β2, β3 and VFD were analyzed for their effects on the shaft rotational speed. In Table 3, the Mean and Signal to Noise Ratios values illustrated how changes in each factor impact the system's performance. Considering the higher-the-better criterion, the best possible set of process parameters observed from the analysis was β1-1, β2-1, β3-1 and VFD-3, which means (β1=0°, β2=0°, β3=0° and VFD=18). The response graphs for the rotational speed of both Means and Signal to Noise Ratios are shown in Fig. 8.

Table 3. Response table for the shaft rotational speed

Level	Means				Signal to Noise Ratios			
	β1	β2	β3	VFD	β1	β2	β3	VFD
1	134.2	134.7	134.6	106.1	42.44	42.47	42.46	40.51
2	131.9	131.8	132.3	132.2	42.30	42.29	42.32	42.42
3	126.9	126.5	126.1	154.6	41.97	41.95	41.92	43.77
Delta	7.3	8.2	8.5	48.5	0.47	0.52	0.54	3.26
Rank	4	3	2	1	4	3	2	1

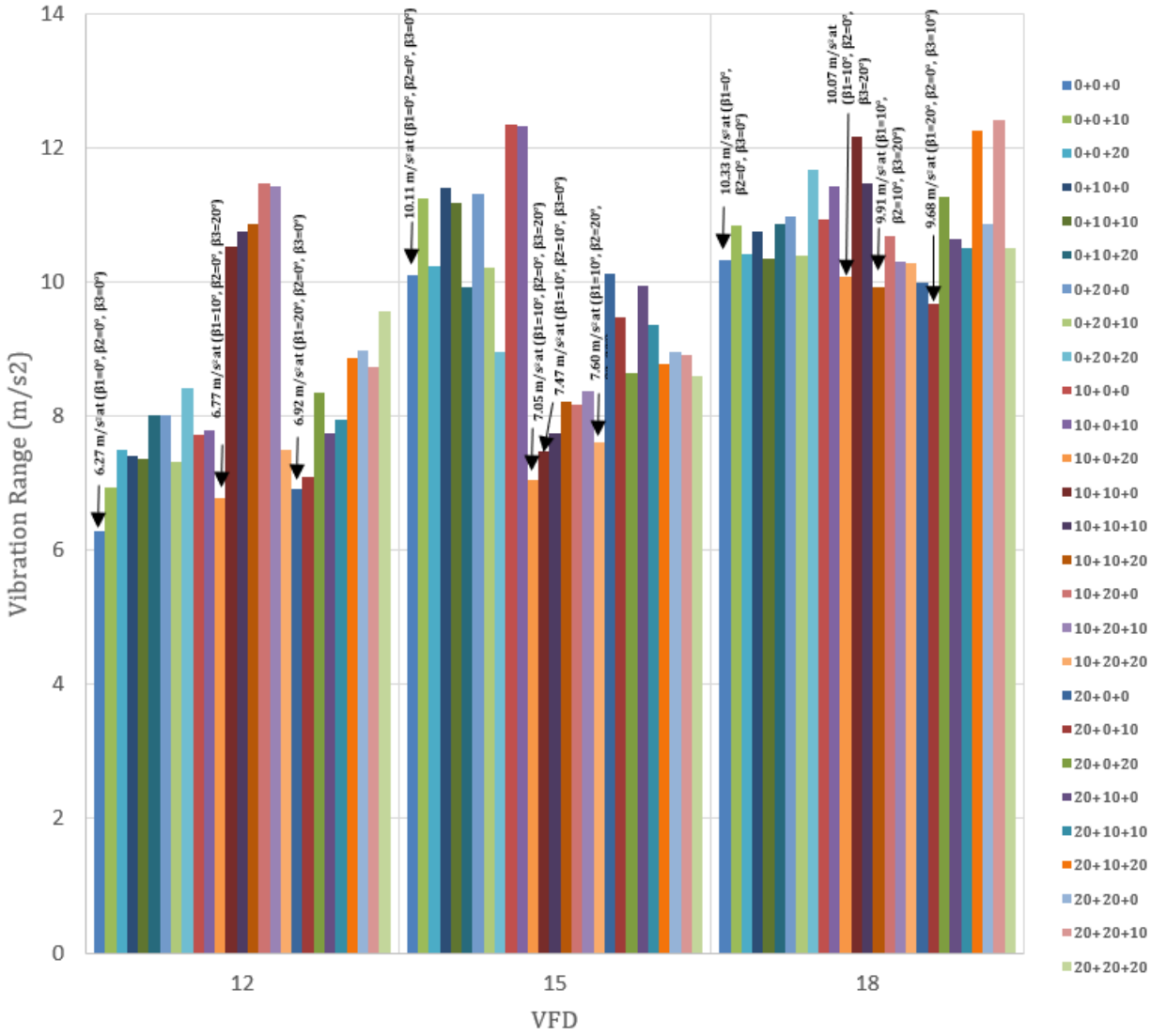
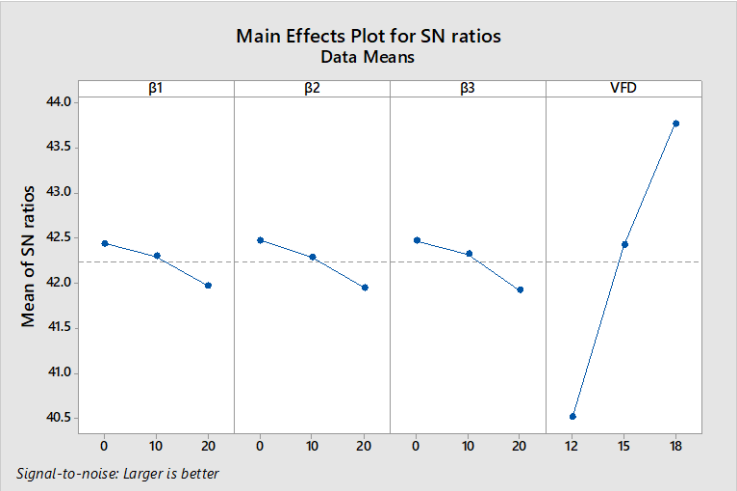


Fig. 7. Vibration levels across different settings (legend β1+β2+β3)



(a)



(b)

Fig. 8. Response graphs for the shaft rotational speed: (a) Means, 8b) Signal to Noise Ratios

3.5.2 Influence of Process Parameters on The Shaft Rotational Speed

Looking at the rankings in Table 4, VFD had the most significant impact on the rotational speed with the highest Delta values (48.5 for Means and 3.26 for S/N Ratios). This indicated that the shaft rotational speed was most sensitive to changes in the VFD settings. The pitch angles β3, β2, and β1 followed in descending order of influence, with β3 showing a slightly higher impact than β2 and β1.

3.5.3 Taguchi's Response Analysis for The Power Output

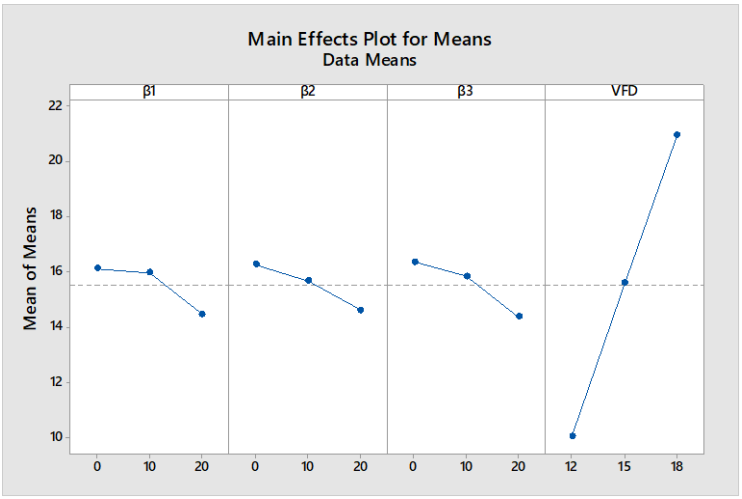
In this instance, the impact of the process parameters β1, β2, β3, and VFD on the power output was examined. Table 5 shows how variations in each factor affect the system's performance through the Mean and Signal to Noise Ratios values. The analysis revealed that the optimal set of process parameters, based on the higher-the-better criterion, was β1-1, β2-1, β3-1, and VFD-3, similar to the shaft rotational speed response with β1=0°, β2=0°, β3=0°, and VFD=18. Fig. 9 displays the response graphs for the rotating speed of Means and Signal to Noise Ratios.

Table 4. Response table for the power output

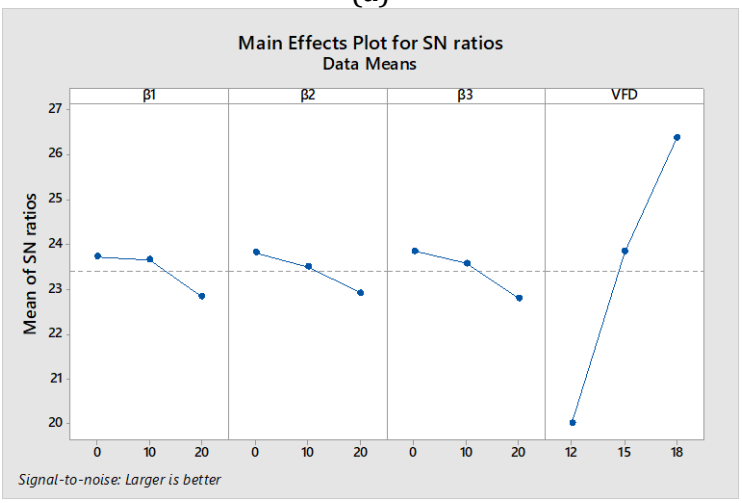
Level	Means				Signal to Noise Ratios			
	β1	β2	β3	VFD	β1	β2	β3	VFD
1	16.12	16.28	16.36	10.04	23.72	23.81	23.85	20.02
2	15.97	15.69	15.84	15.60	23.66	23.49	23.57	23.83
3	14.48	14.61	14.38	20.94	22.84	22.91	22.80	26.37
Delta	1.65	1.66	1.98	10.90	0.89	0.90	1.05	6.35
Rank	4	3	2	1	4	3	2	1

3.5.4 Influence of Process Parameters on The Power Output

When examining the influence of each parameter on power output, VFD had the most substantial impact, with the highest Delta values of 10.90 for Means and 6.35 for S/N Ratios. This indicated that the power output was also highly sensitive to changes in the VFD setting. The pitch angles β3, β2, and β1 follow in descending order of influence. The rankings confirmed that VFD was the most critical factor in optimizing power output. The pitch angles had a comparatively smaller, but still significant, impact. The consistency in the optimal parameter settings for both power output and shaft rotational speed underscored the interconnected nature of these performance metrics within the system.



(a)



(b)

Fig. 9. Response graphs for power output: (a) Means, (b) Signal to Noise Ratios

3.5.5 Taguchi's Response Analysis for The Vibration Level

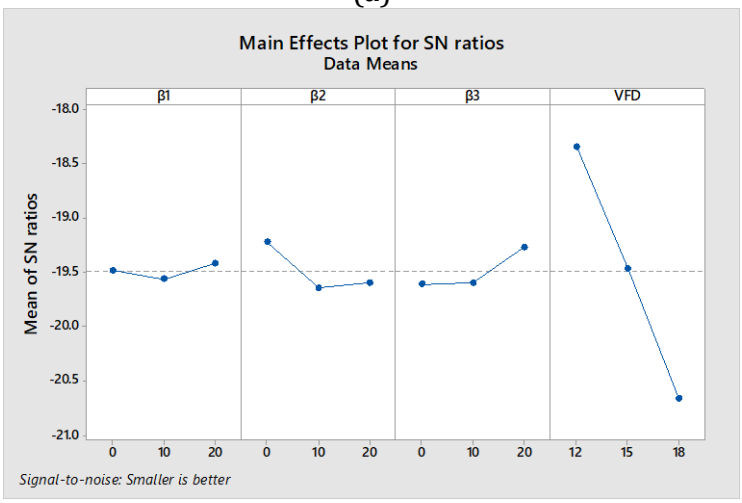
In the third case, the impact of process parameters β1, β2, β3, and VFD on the vibration level was examined. Table 5 displays how variations in each factor affect the system's performance in terms of Mean and Signal to Noise Ratio values. The analysis revealed that the optimal set of process parameters, based on the lower-the-better criterion, was β1-3, β2-1, β3-3, and VFD-1, (β1=20°, β2=0°, β3=20°, and VFD=12). Fig. 10 displays the response graphs for the rotating speed of Means and Signal to Noise Ratios.

Table 5. Response table for vibration level

Level	Means				Signal to Noise Ratios			
	β1	β2	β3	VFD	β1	β2	β3	VFD
1	9.569	9.326	9.709	8.377	-19.48	-19.22	-19.61	-18.34
2	9.679	9.718	9.686	9.504	-19.56	-19.64	-19.59	-19.46
3	9.446	9.650	9.298	10.812	-19.42	-19.60	-19.26	-20.66
Delta	0.234	0.392	0.411	2.435	0.14	0.42	0.34	2.32
Rank	4	3	2	1	4	2	3	1



(a)



(b)

Fig. 10. Response graphs for vibration level (a) Means, (b) Signal to Noise Ratios

3.5.6 Influence of Process Parameters on The Vibration Level

When assessing the impact of each parameter on vibration levels, the VFD setting had again the most significant influence. It indicated the highest Delta values of 2.435 for Means and 2.32 for S/N Ratios. The vibration level is highly sensitive to changes in VFD also. The pitch angle β3 showed a slightly higher impact on vibration levels compared to β2 and β1. This ranking emphasized that the blade pitch angles played a significant role, particularly β3.

3.6 Analysis of Variance for Measured Performance

The analysis of variance (ANOVA) for the measured performance in wind turbine showed the significance of the input parameters on the system's responses. ANOVA was used on the performance measures at 95% confidence level and was computed using Minitab statistical software. In this context, ANOVA revealed that VFD was the more dominant factor influencing system responses. Due to balancing scenarios at which the rotational speed was affected, the P-values of the blade pitch angles input parameters were higher than 0.05, but still they created influence as shown in Fig. 7. Table 6 shows this analysis.

3.7 Regression Modelling Results

In this section, a regression analysis was conducted to quantify the relationship between input parameters (predictors) and system responses. Two types of regression models were developed to determine the best model fit for wind turbine performance, namely; linear model and full quadratic model. Minitab software was used in the regression analysis. Table 7 shows the input variables of

each model. The R-squared values of the developed models were compared to determine the best-fit model, as shown in Table 8.

Table 6. Analysis of variance (ANOVA) analysis

Response	Source	DF	Adj SS	Adj MS	F-Value	P-Value
Shaft rotational speed (rpm)	β1	2	743.4	371.7	44.15	0.000
	β2	2	929.0	464.5	55.17	0.000
	β3	2	1043.9	521.9	62.00	0.000
	VFD	2	31791.6	15895.8	1888.15	0.000
	Error	72	606.1	8.4		
	Total	80	35114.0			
Power output (W)	β1	2	44.92	22.460	35.51	0.000
	β2	2	38.31	19.155	30.28	0.000
	β3	2	56.79	28.396	44.89	0.000
	VFD	2	1605.03	802.515	1268.66	0.000
	Error	72	45.54	0.633		
	Total	80	1790.60			
Vibration level (m/s^2)	β1	2	0.737	0.3684	0.22	0.801
	β2	2	2.372	1.1858	0.72	0.492
	β3	2	2.885	1.4425	0.87	0.423
	VFD	2	80.220	40.1102	24.20	0.000
	Error	72	119.320	1.6572		
	Total	80	205.534			

Table 7. Regression models input parameters

Regression model	Input variables
Linear	Linear: β1, β2, β3 and VFD
Full quadratic (Linear + Squared + Interaction)	Linear: β1, β2, β3 and VFD Squared: $β1^2$, $β2^2$, $β3^2$ and VFD^2 Interaction: (β1×β2), (β2×β3), (β3×β1), (β1×VFD), (β2×VFD), (β3×VFD)

Table 8. R^2 values of various developed regression models

Regression model	R^2 values (%)		
	Rotational speed (rpm)	Power output (W)	Vibration level (m/s^2)
Linear	97.76	96.71	40.86
Full quadratic (Linear + Squared + Interaction)	99.72	99.33	44.89

From the developed regression models shown in Table 10, the full quadratic model showed the best fit. The regression equations for the responses are:

$$\textit{Rotational Speed} = -56.71 + 0.854\,\beta1 + 0.957\,\beta2 + 1.144\,\beta3 + 16.330\,VFD - 0.01333\,\beta1^2 - 0.01167\,\beta2^2 - 0.01889\,\beta3^2 - 0.2037\,VFD^2 - 0.00361\,\beta1x\beta2 + 0.00139\,\beta2x\beta3 - 0.00111\,\beta3x\beta1 - 0.06019\,\beta1xVFD - 0.07407\,\beta2xVFD - 0.07963\,\beta3xVFD$$

$$\text{Power Output} = -20.59 + 0.3165\,\beta1 + 0.2354\,\beta2 + 0.3254\,\beta3 + 2.722\,VFD - 0.00674\,\beta1^2 - 0.00241\,\beta2^2 - 0.00469\,\beta3^2 - 0.0120\,VFD^2 - 0.001434\,\beta1x\beta2 - 0.000938\,\beta2x\beta3 - 0.000129\,\beta3x\beta1 - 0.01657\,\beta1xVFD - 0.01644\,\beta2xVFD - 0.02133\,\beta3xVFD$$

$$\text{Vibration Level} = 3.03 + 0.088\,\beta1 + 0.239\,\beta2 + 0.025\,\beta3 + 0.28\,VFD - 0.00172\,\beta1^2 - 0.00230\,\beta2^2 - 0.00183\,\beta3^2 + 0.0101\,VFD^2 + 0.00073\,\beta1x\beta2 - 0.00052\,\beta2x\beta3 + 0.00089\,\beta3x\beta1 - 0.00505\,\beta1xVFD - 0.01194\,\beta2xVFD - 0.00082\,\beta3xVFD$$

3.8 Performance Optimization

This section optimized the performance of the wind turbine system by balancing the system output responses. The optimization process utilized Grey Relational Analysis (GRA) in conjunction with a full factorial design in Minitab software. The optimization process resulted in defining the optimal settings of process parameters. The GRA focused on two primary criteria: maximizing the shaft rotational speed and power output (higher-the-better), and minimizing the vibration level (Lower-the-better). By applying these criteria, a Grey Relational Grade (GRG) was computed for each experimental test. Table 9 shows the calculated GRCs and GRG values, and ranking.

Table 9. Calculated GRCs and GRG values, and ranking

Exp.	Dependent Variables (Responses)			Grey Relation Coefficients			GRG	Rank
	Rot. Speed	Vibration Level	Power Output	Rot. Speed	Vibration Level	Power Output		
1	112	6.274	10.730	0.379	1.000	0.368	0.582	22
2	141	10.106	17.430	0.545	0.445	0.539	0.510	35
3	**171**	**10.326**	**24.102**	**1.000**	**0.431**	**1.000**	**0.810**	**1**
4	111	6.943	10.643	0.375	0.821	0.367	0.521	29
5	139	11.238	16.898	0.529	0.382	0.520	0.477	48
6	**168**	**10.849**	**23.868**	**0.923**	**0.402**	**0.971**	**0.765**	**2**
7	107	7.486	10.237	0.360	0.717	0.360	0.479	47
8	134	10.239	16.014	0.493	0.436	0.491	0.473	51
9	157	10.411	21.164	0.720	0.426	0.726	0.624	13
10	110	7.400	10.701	0.371	0.732	0.368	0.490	39
11	139	11.402	17.290	0.529	0.375	0.534	0.479	46
12	**167**	**10.760**	**23.868**	**0.900**	**0.406**	**0.971**	**0.759**	**3**
13	109	7.352	10.382	0.367	0.740	0.362	0.490	40
14	137	11.181	16.558	0.514	0.385	0.508	0.469	57
15	164	10.354	22.610	0.837	0.429	0.839	0.702	5
16	106	8.013	9.688	0.356	0.638	0.351	0.449	70
17	131	9.925	15.015	0.474	0.457	0.462	0.464	62
18	153	10.859	20.498	0.667	0.401	0.684	0.584	20
19	107	8.005	10.411	0.360	0.639	0.363	0.454	67
20	135	11.316	16.218	0.500	0.378	0.497	0.459	66
21	159	10.966	22.192	0.750	0.396	0.803	0.650	9
22	107	7.308	10.121	0.360	0.748	0.358	0.489	42
23	132	10.204	15.844	0.480	0.439	0.486	0.468	59
24	155	10.396	20.905	0.692	0.427	0.709	0.609	15
25	103	8.424	9.380	0.346	0.588	0.346	0.427	72
26	126	8.952	14.652	0.444	0.534	0.452	0.477	49
27	143	11.675	17.955	0.563	0.362	0.559	0.495	37
28	110	7.712	10.701	0.371	0.681	0.368	0.473	52
29	139	12.348	17.325	0.529	0.336	0.535	0.467	60
30	166	10.925	23.907	0.878	0.398	0.976	0.750	4
31	108	7.795	10.614	0.364	0.669	0.366	0.466	61

Table 9 (continued)

Exp	Dependent Variables (Responses)			Grey Relation Coefficients			GRG	Rank
	Rot. Speed	Vibration Level	Power Output	Rot. Speed	Vibration Level	Power Output		
32	136	12.325	16.660	0.507	0.337	0.512	0.452	68
33	162	11.423	23.028	0.800	0.374	0.879	0.684	8
34	105	6.774	10.295	0.353	0.860	0.361	0.525	28
35	133	7.052	15.576	0.486	0.798	0.478	0.587	19
36	155	10.072	21.090	0.692	0.447	0.721	0.620	14
37	109	10.528	10.701	0.367	0.419	0.368	0.385	76
38	137	7.474	16.762	0.514	0.719	0.515	0.583	21
39	163	12.156	23.400	0.818	0.343	0.917	0.693	7
40	108	10.750	10.498	0.364	0.407	0.364	0.378	78
41	135	7.739	16.422	0.500	0.677	0.504	0.560	24
42	159	11.469	22.306	0.750	0.371	0.813	0.645	10
43	105	10.872	10.092	0.353	0.400	0.358	0.370	79
44	129	8.217	15.180	0.462	0.612	0.466	0.513	33
45	150	9.910	20.424	0.632	0.458	0.680	0.590	18
46	106	11.462	10.353	0.356	0.372	0.362	0.363	80
47	132	8.174	15.980	0.480	0.618	0.490	0.529	27
48	153	10.679	20.831	0.667	0.411	0.705	0.594	17
49	105	11.416	10.237	0.353	0.374	0.360	0.362	81
50	130	8.378	15.312	0.468	0.593	0.470	0.510	34
51	152	10.309	22.572	0.655	0.432	0.836	0.641	11
52	103	7.490	9.240	0.346	0.716	0.344	0.469	58
53	128	7.599	14.080	0.456	0.699	0.438	0.531	26
54	143	10.287	17.710	0.563	0.433	0.550	0.515	32
55	108	6.916	10.440	0.364	0.827	0.363	0.518	31
56	137	10.124	16.558	0.514	0.444	0.508	0.489	41
57	162	9.982	22.534	0.800	0.453	0.833	0.695	6
58	107	7.081	10.237	0.360	0.792	0.360	0.504	36
59	134	9.469	15.444	0.493	0.490	0.474	0.486	43
60	157	9.675	20.905	0.720	0.474	0.709	0.635	12
61	104	8.354	9.660	0.350	0.596	0.351	0.432	71
62	128	8.630	14.652	0.456	0.566	0.452	0.491	38
63	146	11.268	18.720	0.590	0.381	0.592	0.521	30
64	106	7.744	10.034	0.356	0.676	0.357	0.463	63
65	133	9.940	15.378	0.486	0.456	0.472	0.471	55
66	156	10.647	20.646	0.706	0.412	0.693	0.604	16
67	105	7.942	9.520	0.353	0.648	0.348	0.450	69
68	130	9.354	14.916	0.468	0.499	0.459	0.475	50
69	152	10.513	20.128	0.655	0.420	0.662	0.579	23
70	101	8.862	9.184	0.340	0.543	0.343	0.409	74
71	124	8.772	13.760	0.434	0.551	0.430	0.472	54
72	140	12.254	17.535	0.537	0.339	0.543	0.473	53
73	103	8.976	9.296	0.346	0.532	0.345	0.408	75
74	127	8.951	14.718	0.450	0.534	0.454	0.479	45
75	147	10.863	19.152	0.600	0.401	0.612	0.538	25
76	102	8.739	9.100	0.343	0.555	0.342	0.413	73
77	125	8.912	13.952	0.439	0.538	0.434	0.470	56

Table 9 (continued)

Exp	Dependent Variables (Responses)			Grey Relation Coefficients			GRG	Rank
	Rot. Speed	Vibration Level	Power Output	Rot. Speed	Vibration Level	Power Output		
78	142	12.414	17.920	0.554	0.333	0.558	0.482	44
79	99	9.561	8.505	0.333	0.483	0.333	0.383	77
80	119	8.593	12.524	0.409	0.570	0.402	0.460	64
81	133	10.496	15.411	0.486	0.421	0.473	0.460	65

The GRG combined the GRCs into a single performance score. Test 3 showed the highest GRG (0.810), making it the top rank, which means β1=0°, β2=0°, β3=0° and VFD=18. This indicated the best overall performance. With higher GRG achieved, test 3 was the best balance between power output and vibration control, making it a more optimal scenario. The optimal setting for system performance is shown in Table 10. The regression equation for GRG is:

$$GRG = 0.933 + 0.00757\,\beta1 + 0.00034\,\beta2 + 0.01168\,\beta3 - 0.0928\,VFD - 0.000111\,\beta1^2 + 0.000032\,\beta2^2 - 0.000070\,\beta3^2 + 0.00466\,VFD^2 + 0.000011\,\beta1x\beta2 + 0.000079\,\beta2x\beta3 + 0.000044\,\beta3x\beta1 - 0.000566\,\beta1xVFD - 0.000361\,\beta2xVFD - 0.000941\,\beta3xVFD$$

Table 10. Optimal setting for system performance analysis

	Optimal setting
Parameters and levels	β1=0°, β2=0°, β3=0° and VFD=18
Shaft rotational speed (rpm)	171
Power output (W)	24.102
Vibration level (m/s²)	10.326
Grey Relational Grade	0.810

4. Conclusion

This study conducted a comprehensive investigation into the impact of varying blade pitch angles and Variable Frequency Drive (VFD) settings on the performance characteristics of a wind turbine system. Using the Spectra Quest Wind Turbine Simulator (SQ WTS), a systematic experimental approach, grounded in Taguchi's method, was implemented to evaluate the influence of these variables on critical metrics, including shaft rotational speed, power output, and vibration levels. A total of 81 experiments were designed to capture the interactions between different pitch angles and VFD settings, revealing that these factors significantly influence the operational efficiency of wind turbines.

The results highlighted that an optimal combination of lower blade pitch angles (0°) and higher VFD settings (18) achieved the best performance, with a peak shaft rotational speed of 171 rpm and a maximum power output of 24.102 W, while maintaining vibration levels within acceptable limits. Conversely, increasing blade pitch angles introduced higher air resistance, negatively impacting rotational speed and power output. Some specific combinations of pitch angles, however, demonstrated a unique balancing effect, reducing vibration while maintaining satisfactory power levels, suggesting potential avenues for refining wind turbine design to optimize performance.

Furthermore, the main two regression models developed highlighted the critical role of VFD settings in enhancing system performance. This demonstrated that it is the most significant predictor for rotational speed and power output. Analysis of Variance (ANOVA) confirmed these findings, with VFD showing a dominant influence over system responses compared to blade pitch angles, which still contributed to performance variation. Mostly, in the balancing scenarios.

The optimization process employing Grey Relational Analysis (GRA) technique identified the optimal operating condition that maximized power output while minimizing vibration. This underscored the potential for future operational guidelines in wind turbine design and management. These insights not only contributed to the foundational knowledge of wind turbine

performance dynamics, but also served as a basis for future research targeting improved efficiency and sustainability in wind energy technology.

Acknowledgement

The authors are thankful to the Faculty of Engineering at Sohar University for their guidance and cooperation.

References

[1] Long Y, Chen Y, Xu C, Li Z, Liu Y, Wang H. The role of global installed wind energy in mitigating CO2 emission and temperature rising. Journal of Clean Production. 2023;423(138778):138778. https://doi.org/10.1016/j.jclepro.2023.138778
[2] Anderson CL, Cardell JB. Wind Power Uncertainty and Power System Performance. Engineering. 2013;05(10):41-51. https://doi.org/10.4236/eng.2013.510A007
[3] Arshad M, O'Kelly B. Global status of wind power generation: theory, practice, and challenges. International Journal of Green Energy. 2019;16(14):1073-90. https://doi.org/10.1080/15435075.2019.1597369
[4] Croce A, Cacciola S, Riboldi CED, Sartori L. The science of making torque from wind (TORQUE 2018). Journal of Physics: Conference Series. 2018; 1037:011001. https://doi.org/10.1088/1742-6596/1037/1/011001
[5] Wiser R, Jenni K, Seel J, Baker E, Hand M, Lantz E, et al. Expert elicitation survey on future wind energy costs. Nat Energy. 2016;1(10). https://doi.org/10.1038/nenergy.2016.135
[6] Ishugah TF, Li Y, Wang RZ, Kiplagat JK. Advances in wind energy resource exploitation in urban environment: A review. Renewable and Sustainable Energy Reviews. 2014; 37:613-26. https://doi.org/10.1016/j.rser.2014.05.053
[7] Roul R, Kumar A. Effect of blade pitch angle on the aerodynamic characteristics of a twisted blade horizontal axis wind turbine based on numerical simulations. International Journal of Power Electronics and Drive Systems (IJPEDS) . 2021;12(1):511. https://doi.org/10.11591/ijpeds.v12.i1.pp511-519
[8] Sawant M, Thakare S, Rao AP, Feijóo-Lorenzo AE, Bokde ND. A review on state-of-the-art reviews in wind-turbine- and wind-farm-related topics. Energies. 2021;14(8):2041. https://doi.org/10.3390/en14082041
[9] Sagharichi A, Maghrebi MJ, ArabGolarcheh A. Variable pitch blades: An approach for improving performance of Darrieus wind turbine. Journal of Renewable and Sustainable Energy. 2016;8(5). https://doi.org/10.1063/1.4964310
[10] Chen Y, Li H, Jin K, Song Q. Wind farm layout optimization using genetic algorithm with different hub height wind turbines. Energy Conversion and Managemen. 2013; 70:56-65. https://doi.org/10.1016/j.enconman.2013.02.007
[11] Experimental study of the effect of blade pitch angle on the wind turbine performance at low wind speed condition. International Jounral of Smart Grid and Clean Energy. 2019;627-32. https://doi.org/10.12720/sgce.8.5.627-632
[12] Hu Y, Rao SS. Robust design of horizontal axis wind turbines using Taguchi method. Journal of Mechanical Design. N Y. 2011;133(11). https://doi.org/10.1115/1.4004989
[13] Aryanto F, Mara M, Nuarsa M. Pengaruh Kecepatan Angin Dan Variasi Jumlah Sudu Terhadap Unjuk Kerja Turbin Angin Poros Horizontal. Din Tek Mesin. 2013;3(1). https://doi.org/10.29303/d.v3i1.88
[14] Kaushik V, Shankar RN, Rashid NIH, Khope P. Implementation of Taguchi method for designing a robust wind turbine. Transdisciplinary Journal of Engineering and Science. 2022;13. https://doi.org/10.22545/2022/00216
[15] Tittus P, Diaz PM. Horizontal axis wind turbine modelling and data analysis by multilinear regression. Mechanical Science. 2020;11(2):447-64. https://doi.org/10.5194/ms-11-447-2020
[16] Bossanyi EA. Individual blade pitch control for load reduction. Wind Energy. 2003;6(2):119-28. https://doi.org/10.1002/we.76
[17] Maher Labib A, Abdel Gawad AF, Nasseif MM. Effect of blade angle on aerodynamic performance of Archimedes spiral wind turbine. Journal of Advanced Research in Fluid Mechanics and Thermal Sciences. 2020;78(1):122-36. https://doi.org/10.37934/arfmts.78.1.122136
[18] Gumilar L, Afandi AN, Sias QA, Nugroho WS, Sholeh M, Gunawan A. Comparative study: Pitch angle variation for making power curve and search maximum power of horizontal axis wind turbine. In: AIP Conference Proceedings. AIP Publishing; 2020. p. 030005. https://doi.org/10.1063/5.0000898
[19] Méndez C, Bicer Y. Qatar's wind energy potential with associated financial and environmental benefits for the natural gas industry. Energies. 2019;12(17):3329. https://doi.org/10.3390/en12173329
[20] Samuel BO, Sumaila M, Dan-Asabe B. Multi-objective optimization and modeling of a natural fiber hybrid reinforced composite (P x G y E z) for wind turbine blade development using grey relational analysis and

regression analysis. Mechanics of Advanced Materials and Structures. 2024;31(3):640-58. https://doi.org/10.1080/15376494.2022.2118404
[21] Schütt M. Wind turbines and property values: A meta-regression analysis. . Environmental and Resource Economics. 2024;87(1):1-43. https://doi.org/10.1007/s10640-023-00809-y
[22] Jeon S-T, Cho J-P. Effect of pitch angle and blade length on an axial flow fan performance. Journal of the Korea Academia-Industrial Cooperation Society, 2013;14(7):3170-623. https://doi.org/10.5762/KAIS.2013.14.7.3170
[23] Tang J, Dai K, Luo Y, Bezabeh MA, Ding Z. Integrated control strategy for the vibration mitigation of wind turbines based on pitch angle control and TMDI systems. Engineering Structures. 2024;303(117529):117529 https://doi.org/10.1016/j.engstruct.2024.117529

Blank Page

Research on Engineering Structures & Materials
www.jresm.org

Research Article

Investigation of CFRP strengthening efficiency experimentally and analytically on reinforced concrete beams

Kadir Sengun [*,1,a], Guray Arslan [2,b]

[1]*Department of Civil Engineering, Istanbul Aydin University, Istanbul, Türkiye*
[2]*Department of Civil Engineering, Yildiz Technical University, Istanbul, Türkiye*

Article Info

Article History:

Received 19 Nov 2024
Accepted 22 Jan 2025

Keywords:

U-wrapping;
Strengthening;
Reinforced concrete beam;
Shear span to effective depth ratios;
CFRP;
side bonding;
Shear strength

Abstract

The influence of stirrups, shear span to effective depth ratio, FRP strengthening configuration, and strip width to spacing ratio over the experimental performance of the CFRP-strengthened beams and the estimation accuracy of a total of eleven analytical expressions were evaluated in this study. The main findings obtained in the experimental investigation were as follows. CFRP Strengthening enhanced the load-carrying capacities in all series by an average of 44% with regard to the reference specimens. The use of CFRP for strengthening beams enhanced the maximum deflection and ductility of RC beams across all series. The reduction in stiffness owing to the shear cracks occurring diagonally was more apparent in the reference beams without strengthening. There was no significant difference in the failure loads and CFRP contribution to the strength of both side-bonded and U-wrapped beams when CFRP debonding controlled the failure of the specimens. The failure loads of the strengthened beams and CFRP contribution to strength occur lower as a/d increased. The shear contribution of CFRP was found to be lower in beams with stirrups compared to those without. The investigated equations had more reliable and consistent predictions in beams without stirrups in comparison to the beams with stirrups in both side-bonded and U-wrapped beams. The predictions of the ACI 440.2R, Fib-TG 9.3, CNR-DT200, and CSA-S806 yielded highly inconsistent and unconservative results when the stirrups ratio (ρw) is greater than 0.003.

© 2025 MIM Research Group. All rights reserved.

1. Introduction

Strengthening of deteriorated reinforced concrete (RC) structures with insufficient strength and performance is a critical issue for civil engineers nowadays. Various techniques and methods have been applied to strengthen the deteriorated structures up to now. Strengthening structures with composite materials like Fiber-reinforced polymer (FRP), has been a promising and increasingly common practice. The superior properties of FRP such as corrosion resistance, high strength to weight ratio, and easy of installation, have set it an option to conventional strengthening methods. As the use of FRP in strengthening applications has become widespread in the last two decades, the researchers have paid their attention to the examination of FRP strengthening efficiency. Analytical [1-17] and experimental studies [18-66,88-92] were performed to examine the parameters effective on the performance, behaviour and FRP shear contribution. Chen & Teng [1-2]; Khalifa & Nanni [3]; Triantafillou [4] performed an analytical study on the FRP strengthened beams in shear and proposed equations depending on the effective strains or stresses to predict the contribution of FRP to shear strength. The statistical assessment of the prediction consistency of the equations proposed in the literature to predict FRP shear contribution was carried out by some researchers [67-70]. The behaviour of RC beams strengthened by FRP in a way to enhance the flexural and shear strength were investigated experimentally by a limited number of researchers [47, 50, 53, 61]. The

*Corresponding author: kadirsengun@aydin.edu.tr
[a]orcid.org/0000-0002-4893-0093; [b]orcid.org/0000-0001-5004-8617
DOI: http://dx.doi.org/10.17515/resm2025-538me1119rs
Res. Eng. Struct. Mat. Vol. 11 Iss. 5 (2025) 2351-2379

effect of some parameters such as stirrups [22-23,25] and the shear span to effective depth ratio (*a/d*) [33-36] on the experimental behaviour of FRP strengthened specimens in shear has been studied experimentally by various researchers. Grande et al. [18], Bousselham & Chaallal [23], and Khalifa et al. [41] stated that the FRP shear contribution is lower in beams with stirrups compared to the beams without stirrups. Jayaprakash et al. [27], Li & Leung [33], and Khalifa et al. [35] expressed that the *a/d* possessed a considerable influence on the shear contribution of FRP. Another important parameter is the shear strip width to spacing ratio (w_f/s_f) influencing the behaviour and performance as stated by many researchers [27,46,49,57]. The impact of the various strengthening FRP configurations on the strengthened beams in shear was experimentally investigated by Leung et al. [45] and Diagana et al. [46].

The previous studies have identified several parameters significantly impact the behaviour of FRP strengthened beams, such as a/d, existing stirrups, w_f/s_f, and strengthening configuration. However, it is not well understood how these parameters specifically affect the behaviour of FRP strengthened beams. In addition, most of the experimental studies were carried out on member strengthened with FRP in either flexure or shear. Therefore, it is necessary to evaluate the effect of these parameters on the beams strengthened in both flexure and shear at the same time. Furthermore, many popular models currently in use, proposed by specifications and researchers for U-wrapped and Side-bonded, do not consider these important variables. This lack of consideration poses safety risks for members designed using these models. Therefore, it is necessary to analytically investigate the extent to which these variables influence the calculation of FRP contribution to shear force in order to determine the accuracy of these models. Previous studies have not investigated the effect of these variables on the proposed relations; rather, they have focused on overall assessing the accuracy of the models' predictions. By determining which model consistently provides more reliable predictions in different situations, it is anticipated that more consistent and dependable designs can be achieved.

Within the scope of this study, RC beams with various properties such as two different stirrups spacings (S0 and S20) and three different a/d (a/d=2.5,3.5, and 4.5) were strengthened by CFRP in three strengthening configurations (The U-wrapping, completely wrapping and side-bonding) and tested to investigate the impact of certain parameter such as a/d, stirrups, FRP strengthening configuration, and w_f/s_f under three-point bending tests with the aim of contribution to previous findings. Experimental findings of the tested specimens were examined from the point of the load-carrying capacity, stiffness, ductility, failure modes, and strains of the reinforcement. In addition to the experimental study, the accuracy of the eleven prediction models proposed by researchers and specifications to obtain the FRP contribution to the shear strength in U-wrapped and side-bonded beams were evaluated using the experimental findings of a total of 259 FRP-strengthened beams in shear, which were previously tested by various researchers. The impact of parameters such as stirrups and a/d on the precision of the equations was assessed. In the analytical study, the equation proposed by Sengun & Arslan [88] for calculating the FRP shear contribution in fully wrapped beams was also considered to investigate the feasibility of calculating the FRP shear contribution in U-wrapped and side-bonded beams.

1.1 Research Significance

In the present study, the behaviour of U-wrapped and side-bonded beams was investigated in greater detail and comparatively through experimental analysis. The true novelty of this research lies in examining the extent to which critical parameters, previously shown to be experimentally effective but not considered in analytical models, influence the accuracy of these models. This was achieved using a database of 259 beams. To the best of the authors' knowledge, few studies explicitly explore the impact of these parameters.

2. Experimental Program

The three-point bending test was carried out on RC test specimens with two different stirrups spacing (s=0 and ,200 mm), three different *a/d* (2.5,3.5, and 4.5), and three different strengthening configurations (Completely Wrapped, U-Wrapped, Side Bonded) to observe FRP strengthening efficiency.

2.1 Features of Test Specimens and Materials

Sixteen RC beams, whose geometric dimensions and reinforcement details were introduced in Fig. 1, were tested. The specimens were separated into four different series based on various *a/d* and stirrup spacing as given in Table 2 so as to make the experimental results easier to interpret and compare. The experimental findings of the reference beams in each series were taken from the study carried out by Sengun & Arslan [88]. The concrete compressive strength was obtained as 43 MPa by compression test on the cube samples with 150 mm side dimensions taken during concrete casting. Two 18 mm steel rebars (2Ø18) were used as tensile reinforcements in all specimens. In the series of K2.5S20 and K3.5S20 (Fig. 1a), 2Ø12 steel bars were placed as compression reinforcements at the top of the beams. The stirrups (Ø8) spaced with 200 mm across the entire beam span in the series of K2.5S20 and K3.5S20 were utilized as shear reinforcements. The mechanical properties of both tensile and shear reinforcements were presented in Table 1.

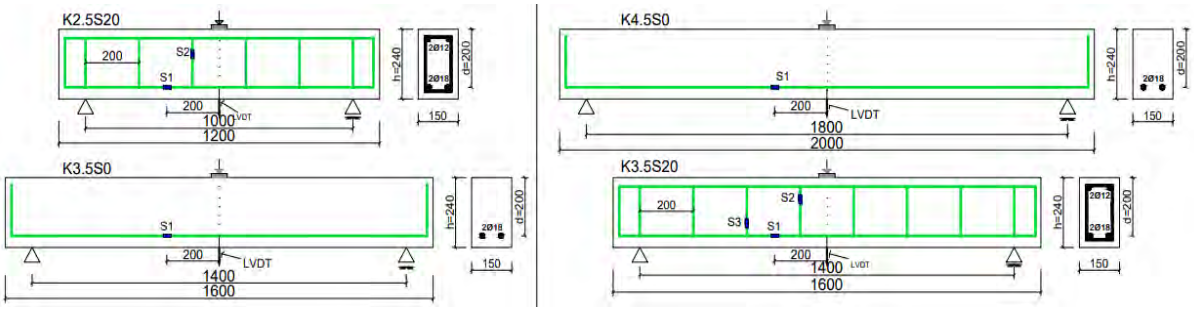
Table 1. Properties of the materials

Materials		Yield strength (MPa)	Tensile strength (MPa)	Modulus of elasticity (GPa)	Thickness(mm)
Steel	D=18 mm	502	654	200	-
	D=12 mm	506	662	200	-
	D=8 mm	610	788	200	-
FRP	CFRP	-	4400	255	0.34

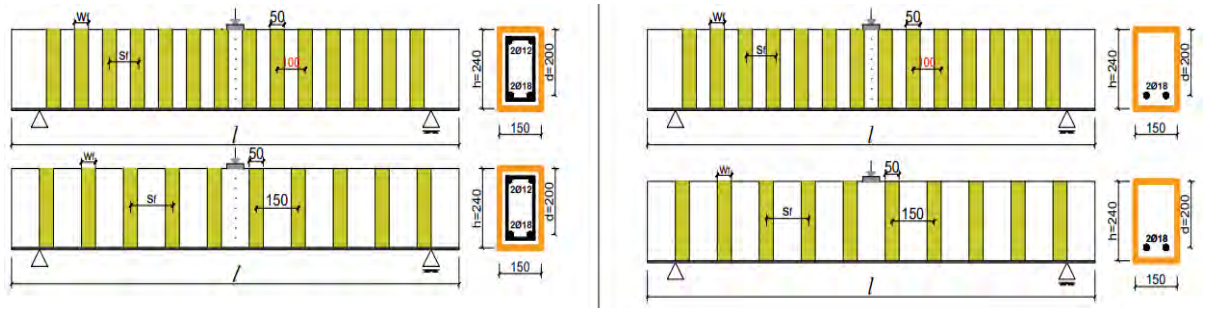
Epoxy obtained by mixing two materials such as hardener and resin in the proportions recommended by the manufacturer was used for bonding CFRP to the beam surface. The mechanical properties of unidirectional CFRP given by the manufacturer were presented in Table 1.

2.2 The Details of The Strengthening Schemes

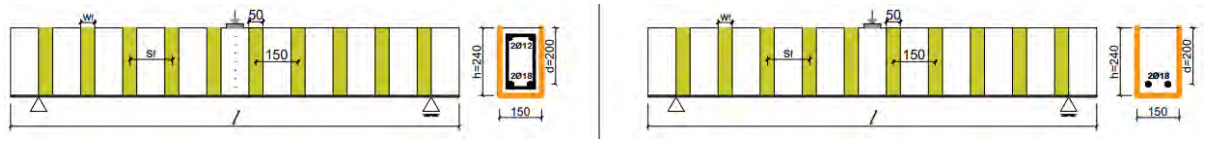
Various configurations, including complete wrapping, U-wrapping, and side bonding, were implemented on the tested beams. In each series, one beam was kept as a reference without CFRP strengthening. The experimental results for these reference beams were sourced from the research conducted by Sengun & Arslan [88]. U-wrapping configurations in shear strengthening as given in Fig. 1c was performed in one-beams of all series tested. In addition, strengthening of the one beam of the K4.5S0, K3.5S20, and K3.5S0 series was conducted by side-bonding CFRP configuration in only shear as given in Fig. 1d. The remaining beams were strengthened for both flexure and shear using CFRP. For shear strengthening, the beams were completely wrapped with CFRP as illustrated in Fig. 1b. To enhance flexural strength, a 150 mm wide CFRP sheet, consisting of two layers, was affixed to the bottom surface of the completely wrapped beams. Additionally, discrete CFRP strips, positioned perpendicular to the beam axis, were applied to all tested beams for shear strengthening. The numerical details of the CFRP strengthening were given in Table 2.



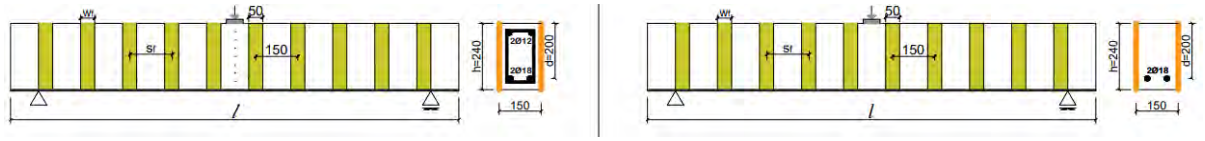
(a)



(b) Completely Wrapped



(c) U-Wrapped



(d) Side-Bonded

Fig. 1. (a) Geometry and test setup of the test beams; (b), (c), (d) Strengthening configurations

The meanings of the numbers and letters utilized in the denotation of the tested beams given in Table 2 were as follows.

Table 2. Properties of FRP strengthening on tested beam

Series	Specimen	FRP	l (mm)	w_f (mm)	n_f	s_f (mm)	n_s	s_n (mm)	ρ_f	w_f/s_f
K3.5S0	K3.5S0-R [88]	-	1600	-	-	-	-	-	-	-
	K3.5S0-C-5-2K	CFRP	1600	50	2	100	2	50	0.0045	0.5
	K3.5S0-C-10-2K		1600			150	2	100	0.003	0.33
	K3.5S0-C-10-U		1600		-	150	1	100	0.0015	0.33
	K3.5S0-C-10-S		1600			150	1	100	0.0015	0.33
K4.5S0	K4.5S0-R [88]	-	2000	-	-	-	-	-	-	-
	K4.5S0-C-10-U	CFRP	2000	50	-	150	1	100	0.0015	0.33
	K4.5S0-C-10-S		2000			150	1	100	0.0015	0.33
K3.5S20	K3.5S20-R [88]	-	1600	-	-	-	-	-	-	-
	K3.5S20-C-5-2K	CFRP	1600	50	2	100	2	50	0.0045	0.5
	K3.5S20-C-10-2K		1600			150	2	100	0.003	0.33
	K3.5S20-C-10-U		1600		-	150	1	100	0.0015	0.33
	K3.5S20-C-10-S		1600			150	1	100	0.0015	0.33
K2.5S20	K2.5S20-R [88]	-	1200	-	-	-	-	-	-	-
	K2.5S20-C-5-2K	CFRP	1200	50	2	100	1	50	0.0045	0.5
	K2.5S20-C-10-U		1200		-	150	1	100	0.0015	0.33

n_s: The number of CFRP layers used for shear strengthening; ***n_f*** **:** Flexural strengthening; ***w_f:*** CFRP shear strips width; ***s_n:*** the net (clear) distance between two adjacent strips, ***w_f/s_f, ρ_f:*** CFRP reinforcement ratios (used at shear strengthening; ***s_f:*** center to center distance of the two adjacent strips; ***l:*** the length of the beam

KaaSbb-c-dd-ee

- "aa" takes the values of 2.5, 3.5, and 4.5 and represents the a/d.
- "bb" refers to the stirrup spacing (in cm). "0" was used for beams without stirrups. "20" demonstrates the beams with stirrups (center-to-center distance is 20 cm).

- "c" expresses the FRP type used in strengthening. "C" indicates the CFRP.
- "dd" refers to the clear distance between CFRP shear strips (in cm) (s_n).
- "ee" was used to show strengthening configurations. "2K" refers to the strengthened beams with completely wrapped two layers of CFRP in shear and two layers of CFRP in flexure. "U" and "S" indicates the strengthened beams with U wrapped and side-bonded CFRP in only shear, respectively.

2.3 Test Setting and Instrumentation

An experimental investigation was performed utilizing a displacement-controlled three-point bending test with point loading at mid-span. A computer-controlled data acquisition system was employed to capture experimental data, including applied loads, strains on longitudinal and shear reinforcements, and vertical deflections at mid-span. Vertical deflections of all tested beams were measured using linear variable displacement transducers (LVDTs) positioned at mid-span, as depicted in Fig. 1a. Strain gauges were installed on the tensile reinforcements of all specimens at the locations marked S1 in Fig. 1a to measure strains and assess the influence of flexural strengthening on the strain behavior of the longitudinal reinforcement. To evaluate the impact of CFRP shear strengthening on stirrup strains, two strain gauges were affixed at the positions marked S2 and S3 in Fig. 1a, considering potential shear crack locations in the K3.5S20 and K2.5S20 series. In the K2.5S20 series, strain gauges (S2 and S3) were attached to both legs of the third stirrups.

3. Results and Discussions

The overall performance and experimental results of the beams were evaluated in terms of strength, ductility, reinforcement strains, and stiffness using load-deflection curves (Fig. 2) and test results (Table 3). The effects of variables such as shear span to effective depth ratios (a/d), stirrups, strip width to spacing ratio (w_f/s_f), and CFRP strengthening configurations on failure modes, failure load, strain behavior, and cracking patterns were also examined in detail in the subsequent sections.

3.1 The General Behavior of The Tested Specimens

The general behavior of the tested beams was evaluated by means of the load-deflection curves and the test results without considering any specific effect of the investigated parameters.

3.1.1. Strength, Ductility, Stiffness, And Strains

CFRP strengthening enhanced the load-carrying capacities in all series by an average of 44% with regard to the reference specimens due to the contribution of FRP to strength. Based on the ductility index and the area under the load-deflection curves (A) in Table 3, the use of CFRP for strengthening beams enhanced the maximum deflection and ductility of RC beams across all series when compared to reference beams by preventing the propagation and widening of cracks. The CFRP shear strips functioned as anchorage, preventing the complete debonding of CFRP applied for flexural strengthening during the experiments. Additionally, the initial stiffness of CFRP-strengthened beams was generally higher than that of the reference beams in each series. Besides, the reduction in stiffness owing to the shear cracks occurring diagonally was more apparent in the reference beams in comparison to the strengthened beams as seen in the load-deflection curves since the strength of compression struts was enhanced by the confinement effect of CFRP strengthening and CFRP prevented the crack width. It could be concluded considering the load values at which stirrups started to actively contribute to the shear strength that strengthening RC beams with CFRP in shear improved the first diagonal cracking load in the K3.5S20 and K2.5S20 series. The highest strains occurring on the tensile reinforcement were greater on the FRP-strengthened beams due to the higher failure loads and ductility capacities than the reference beams (Table 3). The tensile reinforcement on the reference specimens in K3.5S0 and K4.5S0 series did not yield due to the shear failure mode occurring suddenly (Fig. 3). The horizontal red dashed line ($\varepsilon_{y,longidutional}$, $\varepsilon_{y,stirrups}$) in Fig.3 indicates the yield strain of tensile reinforcement and stirrups, respectively. The longitudinal reinforcement on all the strengthened beams yielded except for

beam K4.5S0-C-10-S before the failure occurred. The flexural strengthening by CFRP postponed the yielding of the tensile reinforcement and slowed the flexural cracks to be widen.

Table 3. Experimental results

Series	Specimens	P_n (kN)	Increase at P_n	δ_u (mm)	δ_y (mm)	δ_u/δ_y	A (kNmm)	ε_1 (S1)	ε_2 (S2)	ε_3 (S3)
	K3.5S20-R [88]	133.07	-	11.82	6.16	1.92	1054.43	0.0056	0.0015	0.0019
	K3.5S20-C-5-2K	198.59	49%	56.26	3.60	15.63	8660.79	0.0096	0.0030	0.0023
K3.5S20	K3.5S20-C-10-2K	199.45	50%	14.28	4.24	3.37	1842.31	0.0107	0.0014	0.0030
	K3.5S20-C-10-U	150.25	13%	13.98	3.82	3.66	1469.19	0.0117	0.0015	0.0023
	K3.5S20-C-10-S	149.72	13%	36.48	15.58	2.34	4406.70	0.0033	0.0023	0.0036
	K2.5S20-R [88]	165.17	-	8.06	5.80	1.39	866.35	0.0025	0.0009	-
K2.5S20	K2.5S20-C-5-2K	294.53	78%	12.86	3.62	3.55	2296.32	0.0208	0.0009	-
	K2.5S20-C-10-U	195.04	18%	10.12	2.48	4.08	1757.45	0.0047	0.0027	-
	K3.5S0-R [88]	99.13	-	6.00	-	-	336.38	0.0021	-	-
	K3.5S0-C-5-2K	194.71	96%	93.74	15.26	6.14	16134.90	0.0029	-	-
K3.5S0	K3.5S0-C-10-2K	174.50	76%	82.20	-	-	12570.07	-	-	-
	K3.5S0-C-10-U	138.86	40%	11.84	4.78	2.48	1068.41	0.0143	-	-
	K3.5S0-C-10-S	142.25	43%	18.72	2.56	7.31	2158.71	0.0079	-	-
	K4.5S0-R [88]	85.45	-	7.06	-	-	330.58	0.0024	-	-
K4.5S0	K4.5S0-C-10-U	105.40	23%	13.32	5.62	2.37	936.73	0.0036	-	-
	K4.5S0-C-10-S	109.56	28%	12.64	-	-	922.54	0.0018	-	-

P_n: Maximum load
δ_u: Maximum deflection
δ_y: Deflection at yielding point
A: Area under the load-deflection curves
ε_1: Maximum strain on the longitudinal reinforcement
ε_2,ε_3: Maximum strain on the stirrups

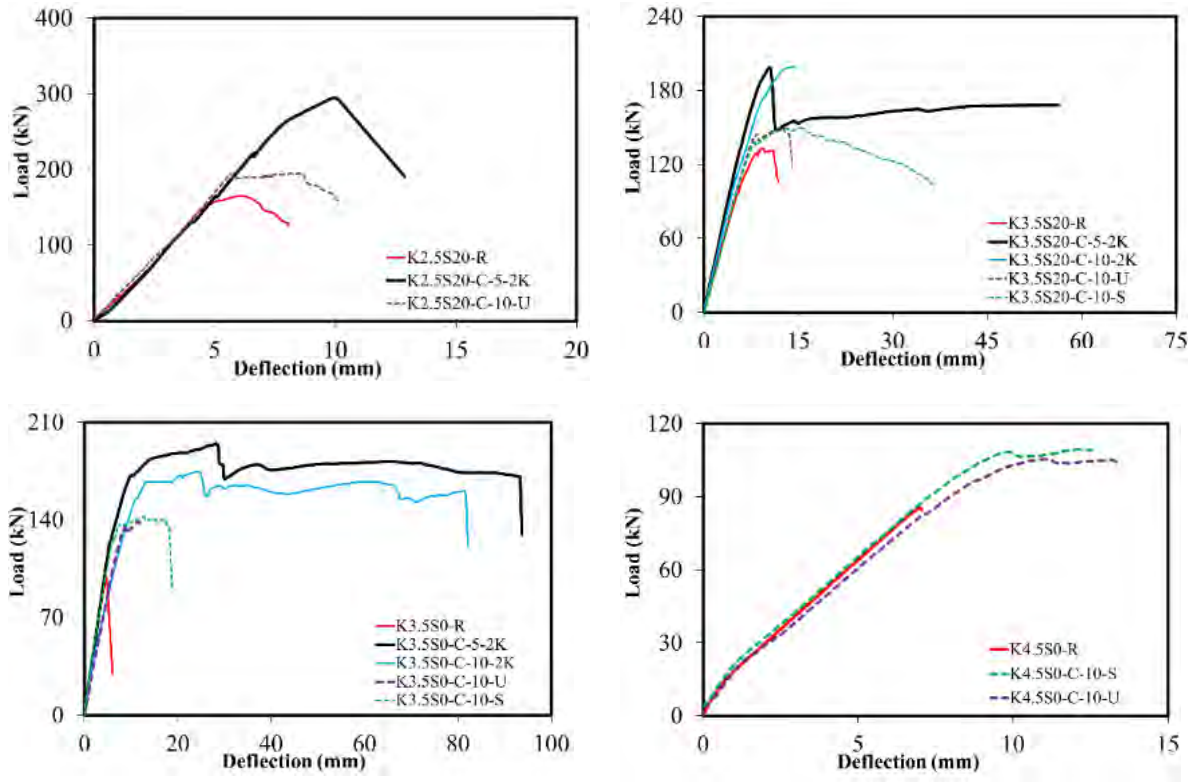


Fig. 2. Load-deflection curves of the tested beams

Due to the wider shear cracks at the intersection points with the third stirrup (ε_3), the third stirrup experienced greater strains compared to the fourth stirrup (ε_2) in the K3.5S20 series, as shown in Fig. 3. Because the strains in the stirrups remained minimal until the formation of shear cracks, the

contribution of the stirrups to the shear strength was limited. After the shear cracks formed, the strains on the stirrups increased and the stirrups actively contributed to the shear strength. The loads were distributed between CFRP and stirrups in the strengthened beams, resulting in strain values on the third stirrup (ε_3) of the strengthened beams in K3.5S20 series that were less than the reference specimens (K3.5S20-R) at the same load levels. As a result of the sudden collapse of U-wrapped and side-bonded beams in the K2.5S20 and K3.5S20 series due to the debonding of CFRP shear strips, it was observed that the stirrups (S2 and S3) except for the third stirrups of K3.5S20-C-10-S did not yield before the fracture occurred. Therefore, it could be concluded that it is not suitable to assume that stirrups intersecting the shear cracks yielded as accepted in the specifications to calculate the stirrups' contribution to shear strength, when shear failure with CFRP debonding in the U-wrapping and side bonding configurations occurred. The experimental study indicated that the performance of the strengthened beams related to, ductility, deflection, and load-carrying capacities were dependent on the parameters such as FRP strengthening configurations, a/d, stirrups, and w_f/s_f. The influence of investigated variables on performance and behavior were examined separately in the subsequent sections.

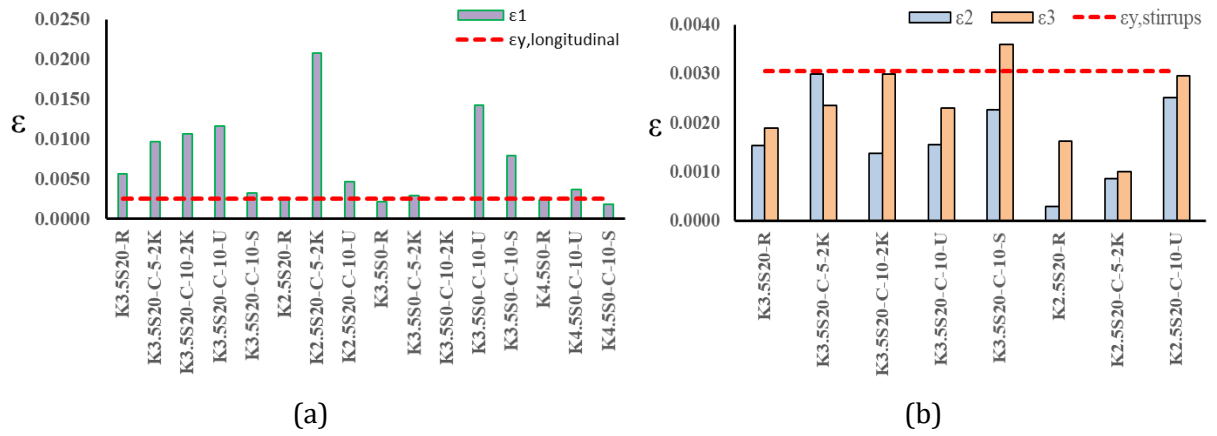


Fig. 3. The highest strains on the reinforcements a) Longitudinal reinforcements, b) Stirrups

3.1.2 Failure Modes and Cracking Structures

The brittle shear failure due to the shear cracks in the shear spans of the reference beams occurred as noticed in Fig. 4. As the *a/d* increased, the flexural cracks at the middle region were more apparent in the reference (K2.5S20-R, K3.5S20-R) beams with stirrups due to the higher effect of bending moments around mid-span with higher a/d. The shear cracks occurring in the reference beams without stirrups (K3.5S0-R, K4.5S0-R) were more noticeable than in the reference specimens including stirrups (K2.5S20-R, K3.5S20-R). K3.5S20-C-5-2K, K3.5S20-C-10-2K, and K2.5S20-C-5-2K failed abruptly in consequence of the CFRP rupture bonded to the bottom of these beams in flexural strengthening as seen in Fig. 4. The shear strengthening with CFRP applied to these beams limited the development of the shear cracks and retarded their propagation compared to the reference beams. K3.5S0-C-10-2K and K3.5S0-C-5-2K had a flexural failure with concrete crushing occurring under the load application point (Fig. 4). The shear cracks were less obvious on these beams than the flexural cracks due to the failure types of concrete crushing and the presence of stirrups. In addition, the flexural cracks width on K3.5S0-C-10-2K and K3.5S0-C-5-2K was wider in comparison to the reference beams, and the beams failing with the rupture of CFRP used in flexural strengthening. The side-bonded and U-wrapped beams in each series experienced shear failure due to the debonding of CFRP shear strips intersecting with diagonal shear cracks. The failure modes and cracking patterns of the U-wrapped and side-bonded beams differed from those of the reference beams and the beams strengthened in both flexure and shear with complete wrapping (Fig. 4) since the characteristic of debonding failure, suddenly occurring, is completely different from the rupture failure of FRP. This observation suggests that stirrups limit the width of shear cracks, that FRP strengthening can alter failure modes compared to reference beams, and that the configuration of FRP strengthening significantly influences failure modes and cracking patterns.

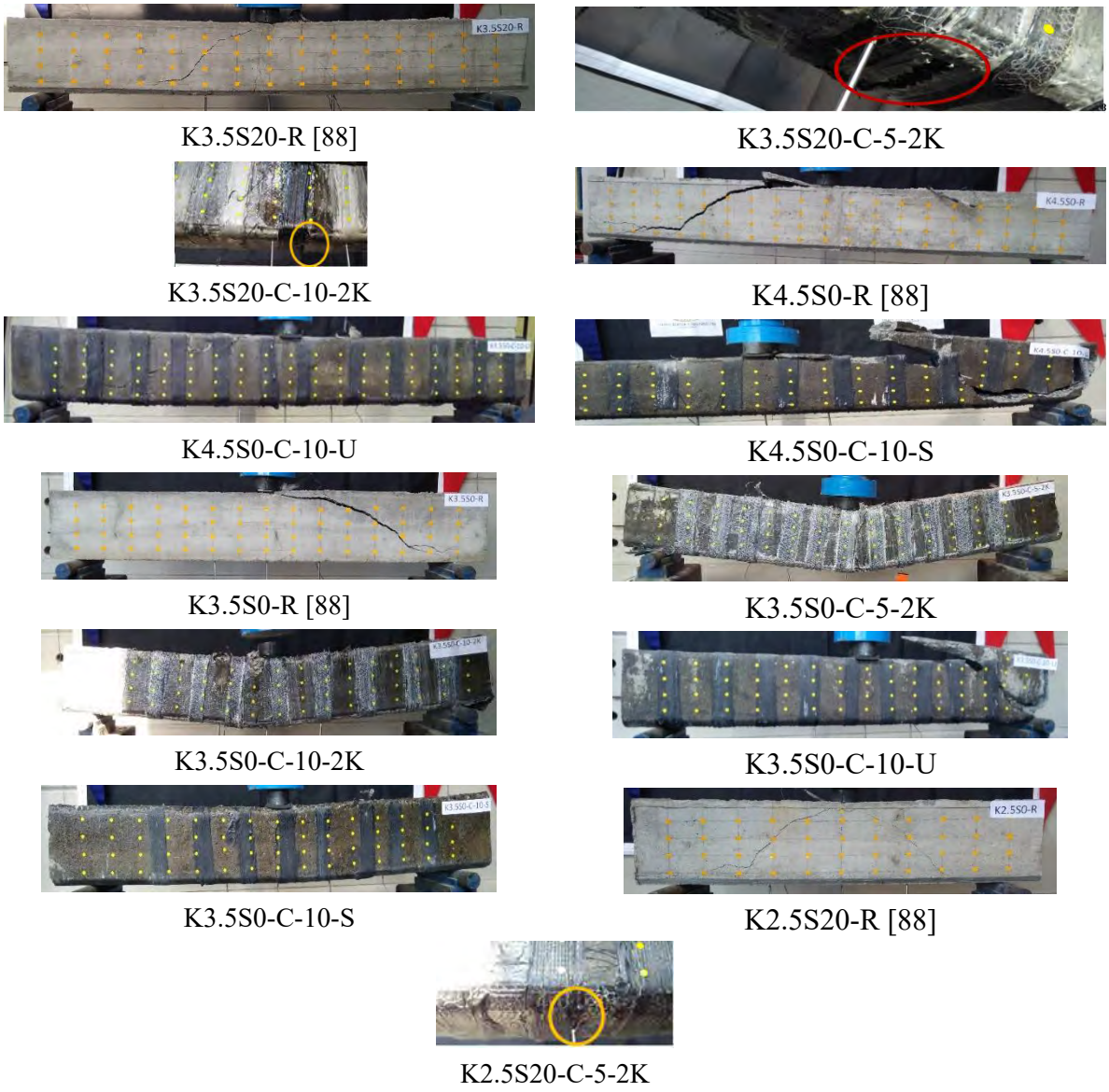


Fig. 4. The condition of the tested beams after the experiment

3.2 Investigated Parameters

3.2.1 Shear Span to Effective Depth Ratios (a/d)

Providing that the RC beams possessed the same geometric dimensions and CFRP reinforcement ratio in shear (ρ_f), the failure loads of the strengthened beams and CFRP contribution to strength became lower in all series as *a/d* increased as seen in Fig. 5. In this study, the load carrying capacity of the beams and the FRP contribution to the shear strength were found to be higher in beams with a/d equal to 2.5. Similar findings were also reported by Li & Leung [33]. Li & Leung [33] stated that the highest contribution of FRP to the shear strength in U-wrapped beams was obtained at values of a/d between 2 and 2.5. However, contrary to the results obtained in this study, Khalifa & Nanni [3] and Bousselham & Chaallal [23] have stated that the contribution of FRP to the shear strength increases as the a/d ratio increases. In addition, as the *a/d* increased, the initial stiffness of the tested specimens decreased since the slender beams effect started to govern the behavior of the beams. The deflection capacities of the U-wrapped beams and completely wrapped in shear improved contrary to the side bonded beam as *a/d* increased. The ductility on U-wrapped and side-bonded beams decreased as *a/d* increased as seen in load-deflection curves given in Fig. 2. The increase in the initial stiffness occurred due to the FRP strengthening compared to reference beams in each series was higher for all strengthening configurations as *a/d* increased. Therefore, it could be concluded that the *a/d* possessed significant impacts the performance and behavior of the

strengthened beams differently based on the CFRP strengthening configurations. The maximum strains on longitudinal reinforcement of the reference beams become higher as the *a/d* ratio increases. The strain values on stirrups of U-wrapped beams declined as the *a/d* ratio enhanced contrary to completely wrapped beams.

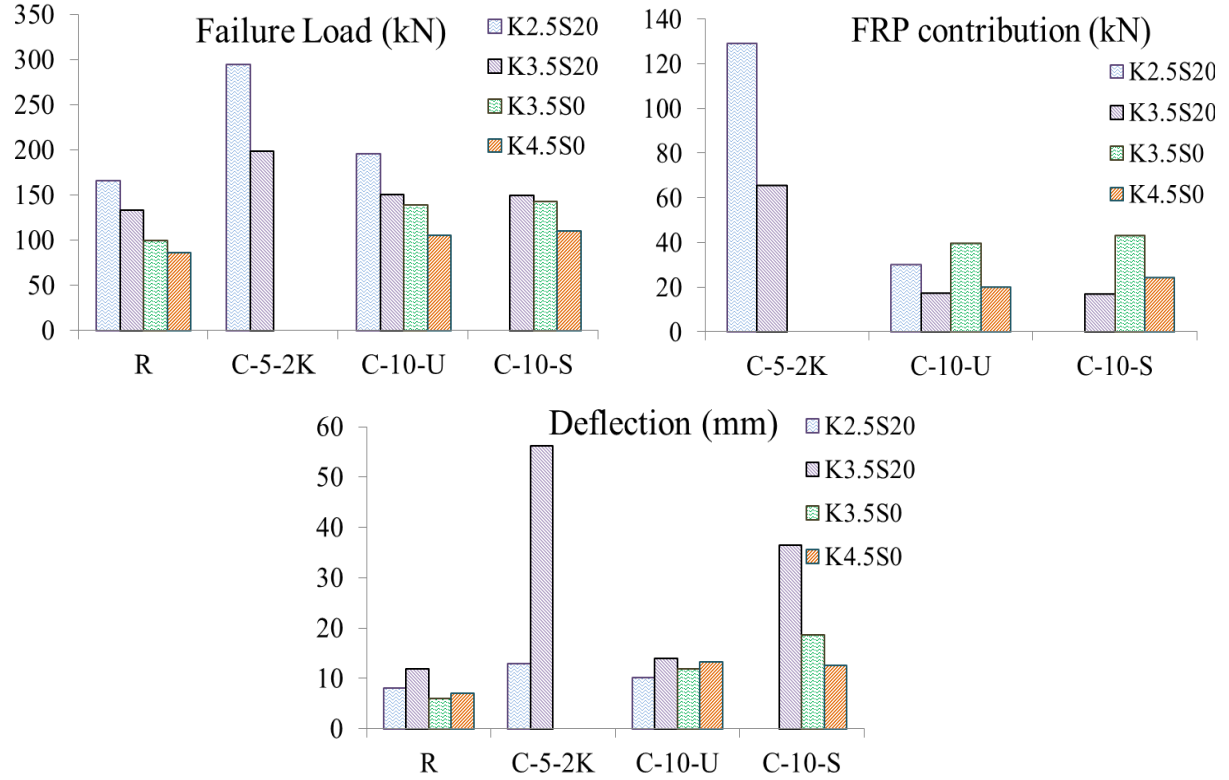


Fig. 5. The effect of a/d on the behavior of tested beams

3.2.2 The Effect of Stirrups

Given that the RC beams had identical geometric dimensions, CFRP reinforcement ratios in shear (ρ_f), and a/d ratios, the strengthened specimens with stirrups exhibited higher failure loads compared to those without stirrups, due to the additional strength provided by the stirrups. The presence of stirrups altered the crack pattern and limited crack widths, resulting in reduced strain values in the CFRP. Therefore, the shear contribution of CFRP was less in beams including stirrups compared to beams without stirrups. Based on this experimental result, it can be evaluated that there could be a possible interaction between the stirrups and CFRP negatively influence the shear contribution of each other. The ductility and deflection capacities in the U-wrapped and side-bonded beams improved as the stirrup ratio increased on account of the confinement effect of stirrups on concrete causing higher failure strains. The beams in K3.5S20 series (K3.5S20-C-5-2K, K3.5S20-C-10-2K) collapsed suddenly due to the rupture of CFRP used in flexure; therefore, the deflection and ductility capacities of these beams become lower compared to the counterpart in K3.5S0 series as demonstrated in Fig. 6. Therefore, it could be evaluated that the presence of the stirrups affects the deflection and ductility behavior of the tested specimens differently based on the CFRP strengthening schemes. As the stirrup ratios increased, the highest-recorded strain on the tensile reinforcement of the side-bonded and U-wrapped beams decreased compared to completely wrapped beams.

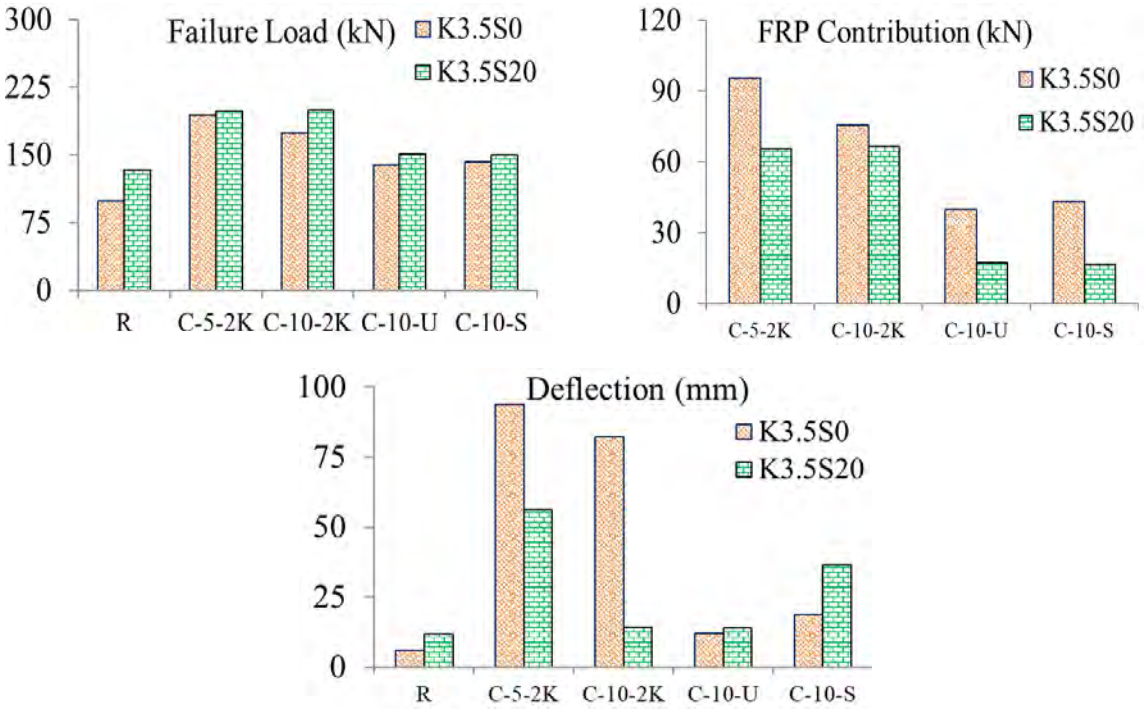


Fig. 6. The effect of stirrups ratios

3.2.3 The Strip Width to Spacing Ratios (w_f/s_f)

The w_f/s_f affected the outcome of the experimental results of tested beams differently depending on whether the beams have stirrups in the shear span. As w_f/s_f enhanced, the CFRP contribution to strength and load-carrying capacity obtained greater on beams without stirrups (K3.5S0 series) since the narrower spacing between CFRP strips was more successful at catching flexural/shear cracks and limiting their expansion.

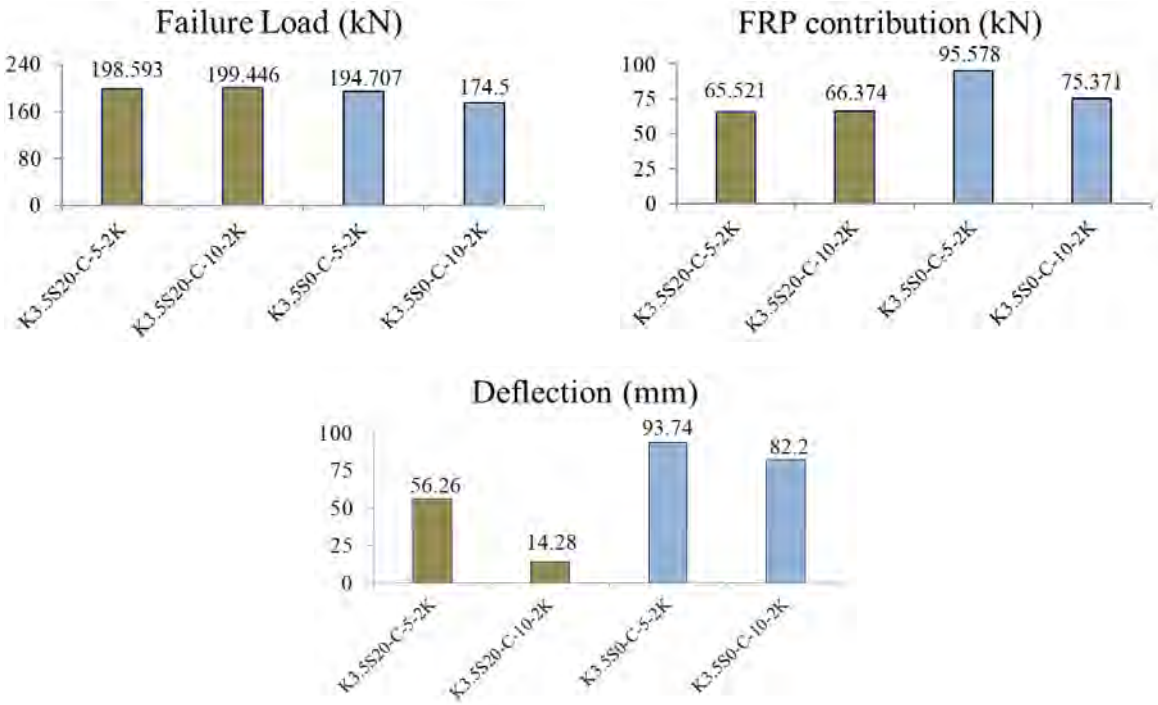


Fig. 7. wf/sf effect on the strengthened beams

However, as w_f/s_f decreased there was no considerable change in the CFRP contribution and load-carrying capacity for beams with stirrups since the beams (K3.5S20-C-10-2K and K3.5S20-C-5-2K)

suddenly failed in flexure and the number and also the width of the diagonal cracks was limited due to the existing stirrups on beams as seen in Figs. 4 and 7. Furthermore, the ductility and deflection capacities of the strengthened specimens decreased as w_f/s_f decreased. The development in the initial stiffness compared to reference beams become lower as w_f/s_f decreases in K3.5S0 and K3.5S20 series. Similarly, Jayaprakash et al. [27] indicated the enhancement of stiffness by increasing in w_f/s_f.

3.2.4 Strengthening Configurations

The failure loads and CFRP contribution in beams strengthened for both flexure and shear were higher than those with U-wrapping and side-bonding CFRP configurations in shear, as shown in Fig. 2 and Table 3. When CFRP debonding dictated the failure modes, there was no significant difference in load-carrying capacity and CFRP contribution between the side-bonding and U-wrapping configurations. This can be explained as follows. Since the FRP debonding occurred at lower strain values as a result of the cracks formed, the contribution of FRP, the failure loads, in short, the strengthening efficiency of FRP was found to be limited in both U-wrapped and side-bonded beams. The ductility and deflection capacities of beams strengthened with complete wrapping in both flexure and shear were superior to those of side-bonded and U-wrapped beams in shear. This is attributable to the higher capacity of completely wrapped FRP at catching occurred cracks. In the K3.5S0 and K3.5S20 series, unlike the K4.5S0 series, side-bonded beams exhibited higher deflection and ductility capacities compared to U-wrapped beams. CFRP strengthening in both flexure and shear resulted in a greater increase in initial stiffness than in side-bonded and U-wrapped beams in shear relative to the reference beams due to the higher confinement effect on concrete. While side-bonded beams in the K4.5S0 series showed a larger increase in initial stiffness compared to U-wrapped beams, U-wrapped beams in the K3.5S20 series displayed a higher increase in initial stiffness than side-bonded beams. Thus, CFRP strengthening enhanced initial stiffness differently based on the strengthening configuration.

4. Analytical Study

This study examined the impact of key experimental parameters, such as a/d ratio and stirrups, on the prediction accuracy of equations proposed by specifications (ACI 440.2R [84], Fib-TG 9.3 [85], CNR-DT200 [86], and CSA-S806 [87]) and various researchers (Chen and Teng [1-2], Khalifa & Nanni [3], Triantafillou [4], Bukhari et al. [10], Khalifa et al. [15], Mofidi & Chaallal [16]) for calculating the FRP shear contribution in both U-wrapped and side-bonded beams. The study utilized data from 259 beams collected from the literature, including the specimens tested in this research (Leung et al. [45], Taerwe et al. [71], Diagana et al. [46], Grande et al.[18], Khalifa [41], Khalifa & Nanni [72], Khalifa & Nanni [3], Panda et al. [48], Panda et al. [73], Pellegrino & Modena [6], Pellegrino & Modena [11], Bousselham & Chaallal [23], Bousselham & Chaallal [22], Sundarraja et al. [57], Lee et al. [90], Baggio et al. [54], Abass & Hassan [25], Benzeguir et al. [37], Ozden et al.[56], Li & Leung [36], Sato et al. [74], Wu et al. [75], Tan & Ye [76], Feng & Chen [77], Allam & Ebeido [42], Rizzo & De Lorenzis [78], Mofidi & Chaallal [79], Micelli et al. [80], Adhikary & Mutsuyoshi [43], Bousselham & Chaallal [34], Mostofinejad et al. [44], Panigrahi et al. [91], Sato el al. [81], Panda et al. [8], Pellegrino & Modena [7], Damnoo & Kumar [21], Chaallal et al. [30], Bukhari et al. [10], Li et al. [39], Saafan [61], Triantafillou [4], Uji [82], Antonopoulos [83]). The compatibility of the equation previously proposed by Sengun & Arslan [88] for the calculation of FRP shear contribution in the FRP-strengthened beams in the form of completely wrapping was also investigated within the analytical study to examine whether it might be used in beams strengthened by CFRP of U-wrapping and side-bonding configurations. The influence of a/d and stirrups on the statistical performance of the proposed equations was evaluated separately for both side-bonded (96 beams) and U-wrapped (163 beams) beams in shear. The necessary variables to calculate FRP shear contribution in each equation were taken from the database provided by Li & Leung [36] and original research papers. The collected database contained the CFRP/GFRP strengthened beams with/without stirrups. The database included rectangular and T-sections FRP-strengthened beams in shear were included in the collected beams. The analytical evaluation of the predictions obtained by the equations was performed as follows. The effect of a/d on estimation accuracy of the strengthened beams by U-wrapping and side-bonding was evaluated in three

different *a/d* ranges (*a/d<2.5, 2.5≤a/d<3.5, a/d≥3.5*). The number of the beams investigated was different for each equation since some of them were valid for only certain cases. The FRP contribution ($V_{f,exp}$) obtained experimentally was figured out by subtracting the shear strength of reference specimens from the FRP-strengthened specimens. The partial safety factors were excluded from each equation to determine the FRP contribution to shear strength, and were assumed to be one. The ratio of the experimental FRP contribution to the predicted FRP contribution ($V_{f,exp}/V_{f,pre}$) was calculated for each beam using various equations. Statistical measures, including mean values (MV), standard deviation (STD), and coefficient of variation (COV) of these ratios ($V_{f,exp}/V_{f,pre}$), were computed and incorporated into the statistical analysis to evaluate the prediction accuracy of the equations.The FRP shear contribution predicted negatively especially in ACI 440.2R [84] were excluded from the statistical evaluation of the database. Since there were three beams with *a/d* higher than 3.5 (*a/d≥3.5*) in side-bonded beams, no statistical evaluation had been made to evaluate the influence of *a/d* in that range of a*/d* higher than 3.5 (*a/d≥3.5*). The STD and COV are indicators used to assess the accuracy of the equations. The prediction accuracy increases as the COV gets smaller. MV may be used to evaluate whether the predicted FRP contribution is conservative or unconservative. The MV, STD, and COV values of each equation for each strengthening configuration (U-wrapping and side-bonding) according to the investigated parameters (*a/d* and stirrups) were given in Tables 4-9.

4.1 Side Bonded Beams

All equations except for Triantafillou [4], Fib-TG 9.3 [85], Mofidi & Chaallal [16], and Sengun & Arslan [88] had conservative results with the MV greater than one in side-bonded beams. Triantafillou [4] and Sengun & Arslan [88] gave the least conservative results due to the lowest MV values compared to other investigated equations (Table 4). Mofidi & Chaallal [16] gave more consistent and reliable prediction with lower COV compared to other equations. ACI 440.2R [84], CNR-DT200 [86], and CSA-S806 [87] yielded inconsistent predictions with the experimental results owing to the higher COV's. In addition, even though the equation proposed by Sengun & Arslan [88] were derived from test carried out on the completely wrapped beams, it also yielded consistent results with a lower COV in side-bonded beams.

Table 4. Statistical results of all side-bonded beams

Equations	Side-bonded all beams				
	Specimen Number	MV	STD	COV	Conservative (%)
ACI 440.2R [84]	67	1.091	1.081	0.991	33
Triantafillou [4]	95	0.615	0.315	0.513	11
Fib-TG 9.3 [85]	91	0.843	0.478	0.567	36
Khalifa et al. [15]	57	1.681	1.705	1.014	42
Khalifa & Nanni [3]	32	1.347	1.118	0.830	44
Mofidi & Chaallal [16]	90	0.977	0.424	0.434	46
Bukhari et al. [10]	91	1.515	0.907	0.598	66
Chen & Teng [1-2]	88	1.415	0.726	0.513	66
CNR-DT200 [86]	90	2.317	2.618	1.130	64
Sengun & Arslan [88]	96	0.675	0.331	0.490	14
CSA-S806 [87]	96	1.857	2.097	1.129	56

4.1.1 The Effect of The Stirrups

Triantafillou [4] gave the least conservative results in both beams with stirrups and beams without stirrups on account of the lowest MV values compared to other investigated equations (Figs. 8-9 and Table 5). Points above the inclined line indicate that the predictions are unconservative, while points below the inclined line imply that the predictions are conservative in Figs. 8-9. The equations proposed by Chen and Teng [1-2] and Mofidi & Chaallal [16] had more reliable predictions than other examined equations in beams with stirrups due to the better statistical results such as lower

COV's. Mofidi & Chaallal [16], Chen and Teng [1-2], and Sengun & Arslan [88] gave more consistent and reliable predictions with lower COV's than other equations in beams without stirrups. With the exception of Chen and Teng [1-2], Khalifa & Nanni [3], and CNR-DT200 [86], the coefficient of variation (COV) values for the evaluated equations were generally higher in beams with stirrups than in those without. Furthermore, apart from Mofidi & Chaallal [16], beams without stirrups exhibited a higher percentage of conservative results for each equation compared to beams with stirrups. Thus, when considering the mean value (MV), standard deviation (STD), and COV for side-bonded beams, it is evident that the equations examined generally yielded more reliable and consistent predictions in beams without stirrups. This is evidenced by MVs exceeding one, lower COVs, and a higher percentage of conservative results.

Table 5. Statistical findings related to stirrups effect

Equations	Side-bonded beams									
	Beams with stirrups					Beams without stirrups				
	Specimen Number	MV	STD	COV	Conservative (%)	Specimen Number	MV	STD	COV	Conservative (%)
ACI 440.2R [84]	28	0.743	1.022	1.377	14	34	1.212	1.060	0.874	38
Triantafillou [4]	39	0.485	0.272	0.560	3	47	0.682	0.329	0.482	15
Fib-TG 9.3 [85]	40	0.650	0.406	0.624	20	42	0.936	0.492	0.526	40
Khalifa et al. [15]	21	0.726	0.819	1.128	10	31	2.112	1.910	0.904	55
Khalifa & Nanni [3]	12	0.645	0.347	0.537	8	16	1.416	0.973	0.687	56
Mofidi & Chaallal [16]	40	0.922	0.466	0.505	48	42	1.001	0.411	0.411	40
Bukhari et al. [10]	40	1.215	0.864	0.711	48	42	1.707	0.935	0.548	76
Chen & Teng [1-2]	38	0.976	0.429	0.440	42	42	1.716	0.766	0.446	81
CNR-DT200 [86]	40	1.046	0.585	0.559	43	42	3.333	3.380	1.014	79
Sengun & Arslan [88]	40	0.490	0.266	0.544	3	47	0.790	0.330	0.418	21
CSA-S806 [87]	40	1.712	2.023	1.182	40	47	1.951	2.302	1.180	62

4.1.2 The Effect of the a/d

The results of the beams without stirrups (*wost)*, and with stirrups *(wst)* were presented in Fig. 10. Since the equation proposed by Triantafillou [4] delivered predictions resulting in the lowest MV of the ratio of experimental results to predictions for all considered ranges of the *a/d*, it yielded the most unconservative results among the considered equations (Fig. 10 and Table 6).

Table 6. Statistical results in terms of a/d effect

Equations	Side-bonded beams									
	a/d<2.5					2.5≤a/d<3.5				
	Specimen Number	MV	STD	COV	Conservative (%)	Specimen Number	MV	STD	COV	Conservative (%)
ACI 440.2R [84]	18	0.678	0.549	0.810	22	37	1.107	1.134	1.025	30
Triantafillou [4]	17	0.460	0.301	0.654	6	62	0.656	0.305	0.465	11
Fib-TG 9.3 [85]	15	0.591	0.424	0.717	13	60	0.879	0.462	0.526	37
Khalifa et al. [15]	14	1.271	0.984	0.774	43	31	1.564	1.628	1.041	35
Khalifa & Nanni [3]	13	1.420	1.080	0.761	46	12	0.741	0.448	0.605	25
Mofidi & Chaallal [16]	15	0.739	0.482	0.652	27	60	1.057	0.400	0.379	52
Bukhari et al. [10]	15	1.116	0.818	0.733	47	60	1.629	0.931	0.572	72
Chen & Teng [1-2]	13	1.302	0.797	0.612	54	60	1.433	0.714	0.498	68
CNR-DT200 [86]	15	1.233	0.843	0.683	60	60	2.538	3.055	1.204	60
Sengun & Arslan [88]	18	0.604	0.461	0.763	11	62	0.693	0.281	0.405	13
CSA-S806 [87]	18	1.424	1.353	0.950	50	62	2.085	2.416	1.159	56

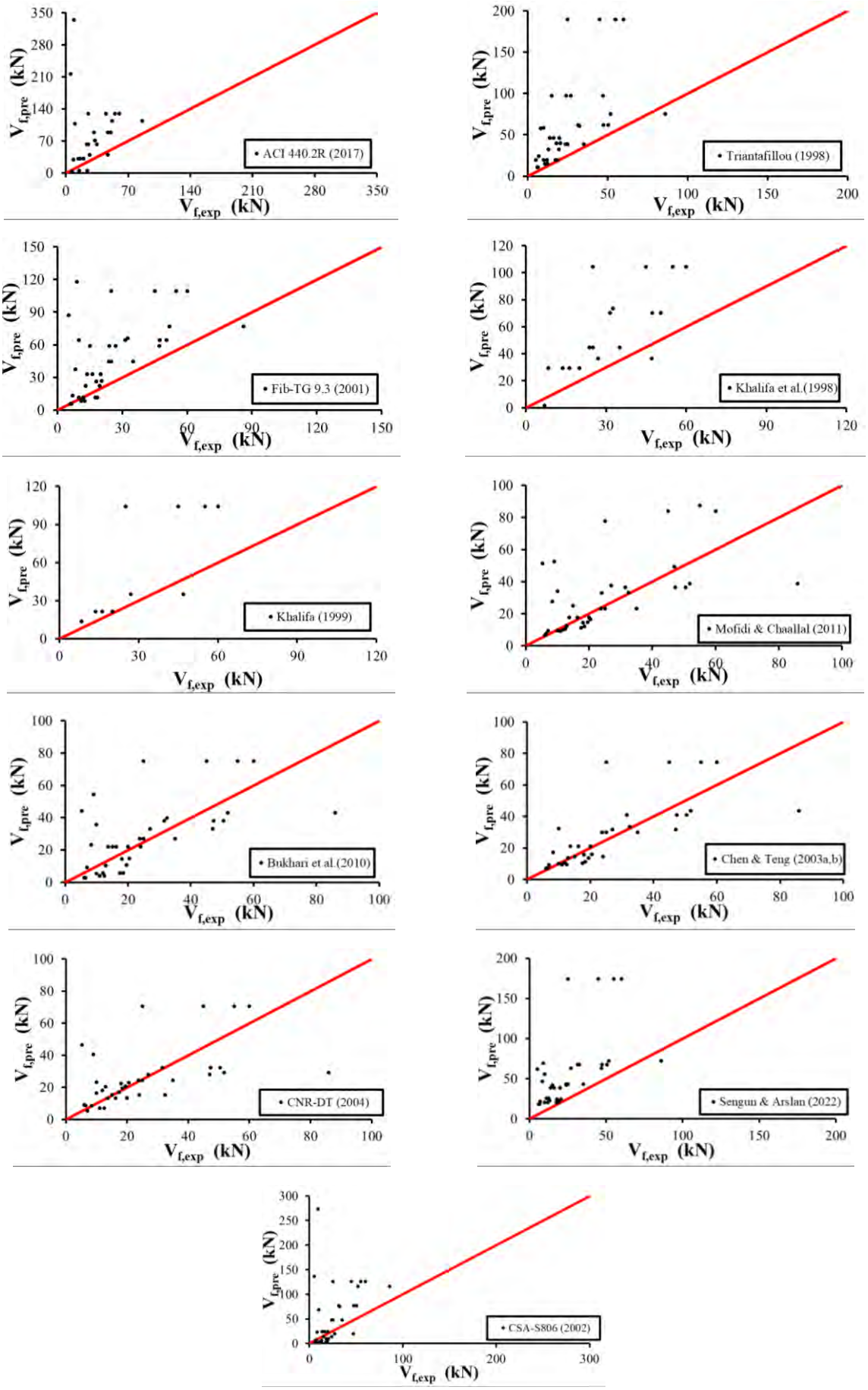


Fig. 8. The distribution of Vf,exp and Vf,pre on side bonded beams with stirrups

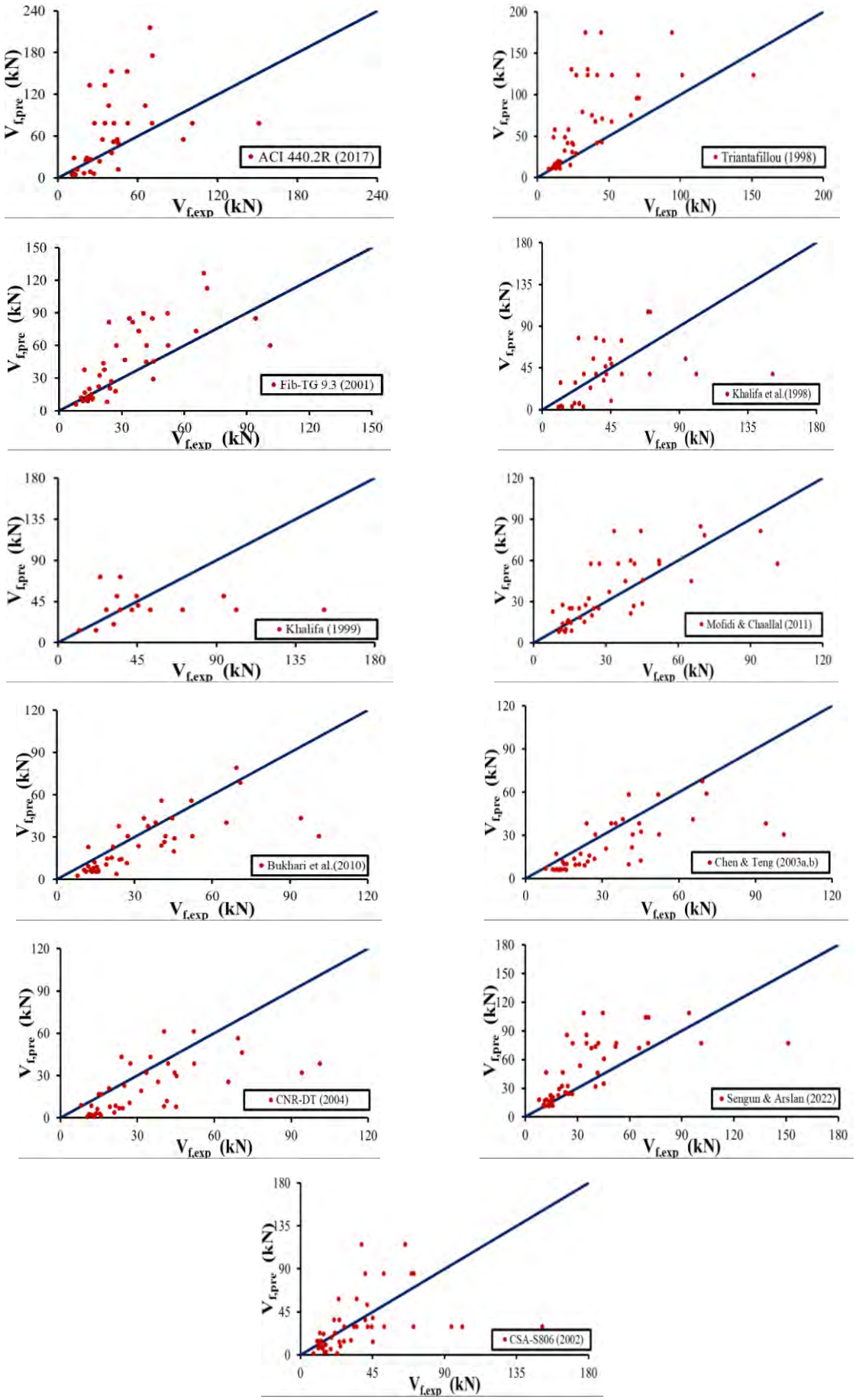
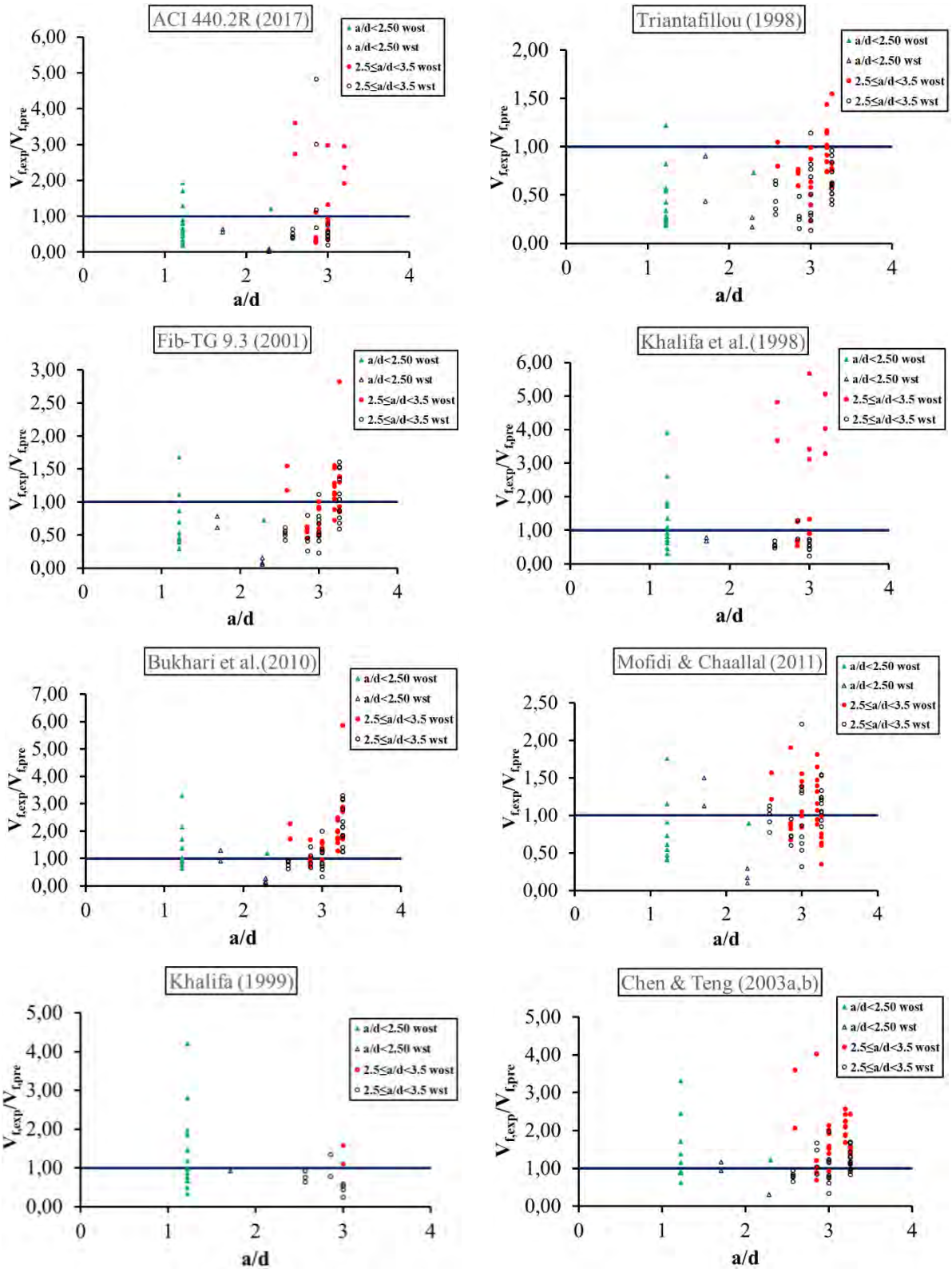


Fig. 9. The distribution of Vf,exp and Vf,pre on side bonded beams without stirrups

Considering the statistical results, the equation of Chen and Teng [1-2] yielded the most consistent predictions for the beams with *a/d* less than 2.5 (*a/d<2.5*), while the equation of Mofidi & Chaallal [16] returned the most reliable results when *a/d* is between 2.5 and 3.5 (*2.5≤a/d<3.5*). Hence, when the values of MV, COV and conservative results percentage were evaluated, it might be expressed that the equations considered in this study generally yielded more consistent predictions for side-bonded beams with *a/d* between 2.5 and 3.5 (*2.5≤a/d<3.5*) compared to those with *a/d* less than 2.5(*a/d<2.5*).



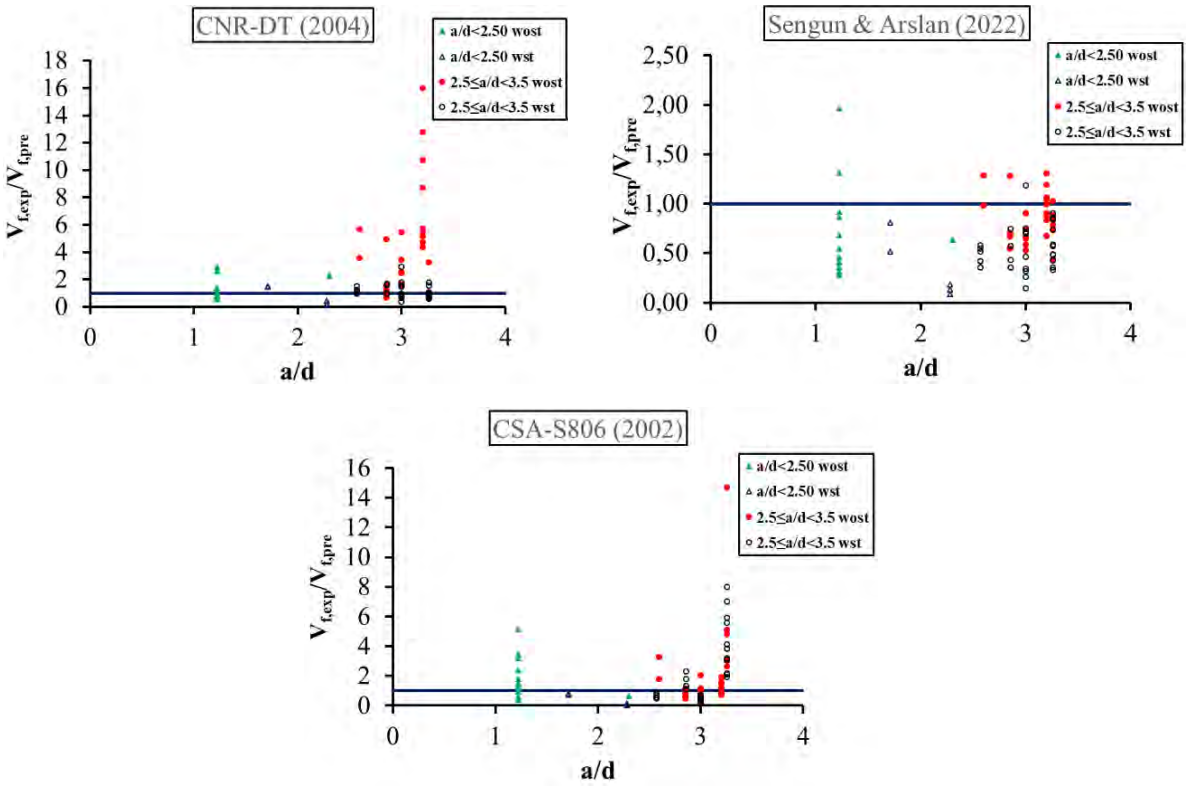


Fig. 10. The distribution of Vf,exp/Vf,pre according to a/d on side-bonded beams

When the results obtained are evaluated collectively, it could be stated that the predictions of the proposed models in side-bonded beams are inconsistent with the experimental results in beams containing stirrups and with a/d ratio less than 2.5 (*a/d<2.5*), and therefore special care should be taken when using these models in such elements.

4.2. U-Wrapped Beams

All equations except for Chen and Teng [1-2], Bukhari et al. [10], Khalifa et al. [15], ACI 440.2R [84], and CSA-S806 [87] gave unconservative results with MV's less than one. Since Triantafillou [4] had the lowest MV, this equation had the most unconservative results among investigated equations. The equations proposed by Sengun & Arslan [88] produced more reliable and consistent predictions due to the lower COV in U-wrapped beams (Table 7).

Table 7. Statistical results of all U-wrapped beams

Equations	U-wrapped all beams				
	Specimen Number	MV	STD	COV	Conservative (%)
ACI 440.2R [84]	157	1.102	0.883	0.802	41
Triantafillou [4]	163	0.598	0.377	0.631	15
Fib-TG 9.3 [85]	163	0.955	0.629	0.658	45
Khalifa et al. [15]	156	1.061	0.835	0.787	42
Khalifa & Nanni [3]	103	0.944	0.720	0.762	39
Mofidi & Chaallal [16]	163	0.947	0.612	0.646	42
Bukhari et al. [10]	163	1.223	1.014	0.829	45
Chen & Teng [1-2]	163	1.354	0.883	0.652	62
CNR-DT200 [86]	163	0.986	0.715	0.725	40
Sengun & Arslan [88]	163	0.693	0.430	0.621	19
CSA-S806 [87]	163	1.037	0.981	0.946	37

4.2.1 The Effect of The Stirrups

Except for Bukhari et al. [10] and Chen and Teng [1-2], the other equations gave unconservative results for the beams with stirrups with MV's less than one. In the beams without stirrups, all the equations other than Triantafillou [4], Mofidi & Chaallal [16], and Sengun & Arslan [88] had conservative results due to having MV's greater than one. The equations proposed by Sengun & Arslan [88] produced more reliable results due to the lower COV in beams with stirrups as seen in Table 8 and Figs. 11-12. Points above the inclined line indicate that the predictions are unconservative, while points below the inclined line imply that the predictions are conservative in Figs. 11-12. Triantafillou [4] and Sengun & Arslan [88] yielded the lower COV's in beams without stirrups. The investigated equations have commonly lower COV's in beams without stirrups with regard to the beams with stirrups. The ratio of the beams having conservative results in beams without stirrups was generally greater than the beam including stirrups. Thus, this result can be obtained for U-wrapped beams that the equations proposed in the calculation of FRP shear contribution have more reliable and consistent results in beams without stirrups.

Furthermore, collected beams contained a total of 102 U-wrapped beams with stirrups ratios (ρ_w) ranging from 0.071 to 0.838%. In beams with stirrups ratio (ρ_w) greater than 0.003, the percentage of unconservative results of ACI 440.2R [84], Fib-TG 9.3 [85], CNR-DT200 [86], and CSA-S806 [87] is 90%, 83%, 90%, and 94%, respectively. The stirrup ratio (ρ_w) is one of the key variables on the FRP contribution and the accuracy of the proposed equations. It could be concluded by means of the distribution of $V_{f,exp}/V_{f,pre}$ and ρ_w as seen in Fig. 13, the predictions of the ACI 440.2R [84], Fib-TG 9.3 [85], CNR-DT200 [86], and CSA-S806 [87] yielded highly inconsistent and unconservative results when the stirrups ratio (ρ_w) is greater than 0.003.

Table 8. Statistical results in terms of stirrups effect

Equations	U-wrapped beams									
	Beams with stirrups					Beams without stirrups				
	Specimen Number	MV	STD	COV	Conservative (%)	Specimen Number	MV	STD	COV	Conservative (%)
ACI 440.2R [84]	98	0.947	0.816	0.862	36	57	1.298	0.867	0.668	47
Triantafillou [4]	102	0.535	0.372	0.695	12	59	0.674	0.326	0.483	17
Fib-TG 9.3 [85]	102	0.848	0.623	0.734	38	59	1.084	0.541	0.499	54
Khalifa et al. [15]	98	0.848	0.633	0.747	36	56	1.393	0.998	0.717	52
Khalifa & Nanni [3]	63	0.770	0.631	0.819	32	38	1.161	0.726	0.626	47
Mofidi & Chaallal [16]	102	0.957	0.687	0.718	43	59	0.909	0.455	0.501	39
Bukhari et al. [10]	102	1.089	1.019	0.935	38	59	1.378	0.886	0.643	54
Chen & Teng [1-2]	102	1.104	0.754	0.683	51	59	1.715	0.879	0.513	80
CNR-DT200 [86]	102	0.914	0.702	0.768	36	59	1.032	0.605	0.586	46
Sengun & Arslan [88]	102	0.538	0.327	0.607	5	59	0.933	0.455	0.488	41
CSA-S806 [87]	102	0.930	1.011	1.086	30	59	1.151	0.829	0.721	46

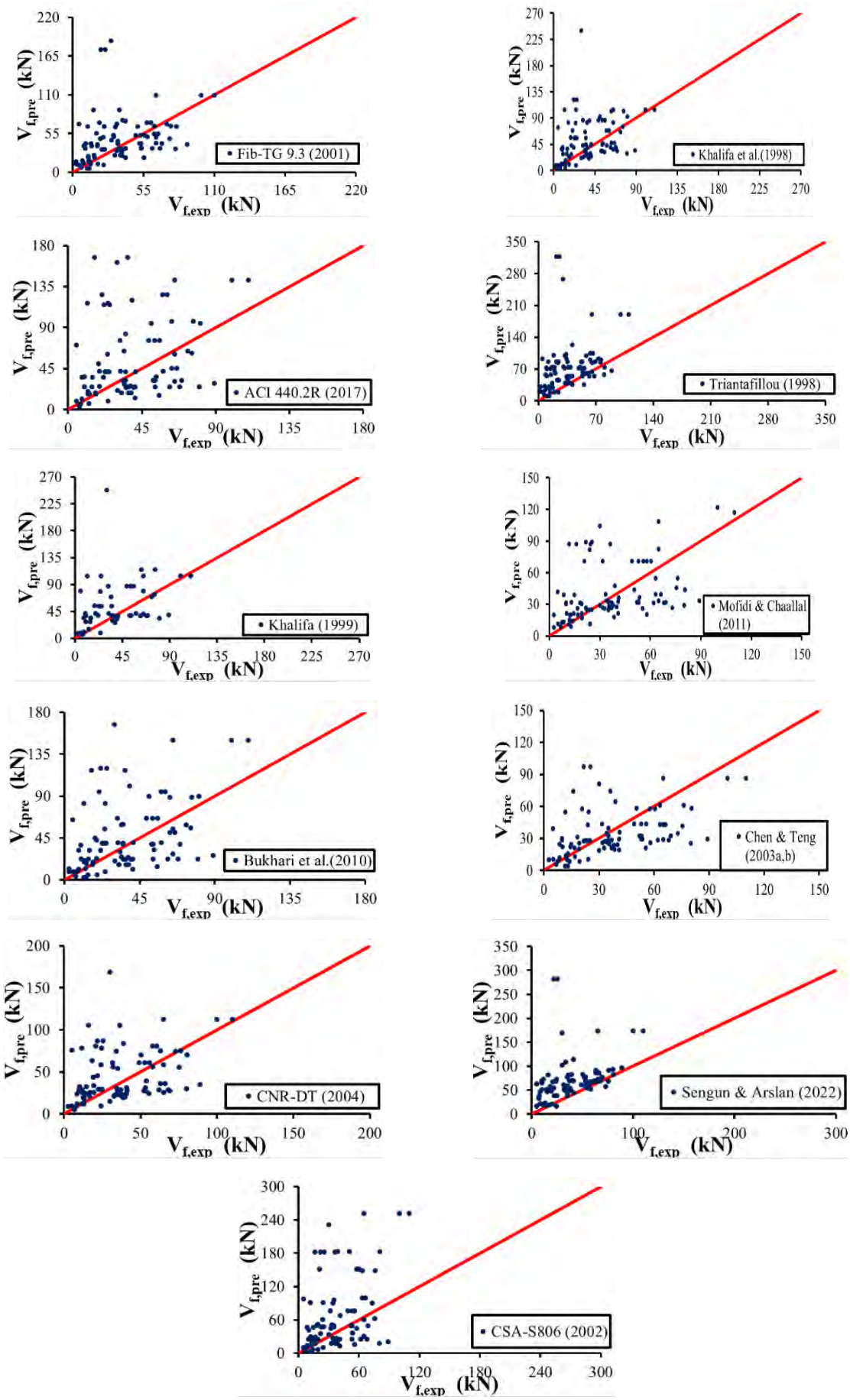


Fig. 11. The distribution of Vf,exp and Vf,pre on U-wrapped beams with stirrups

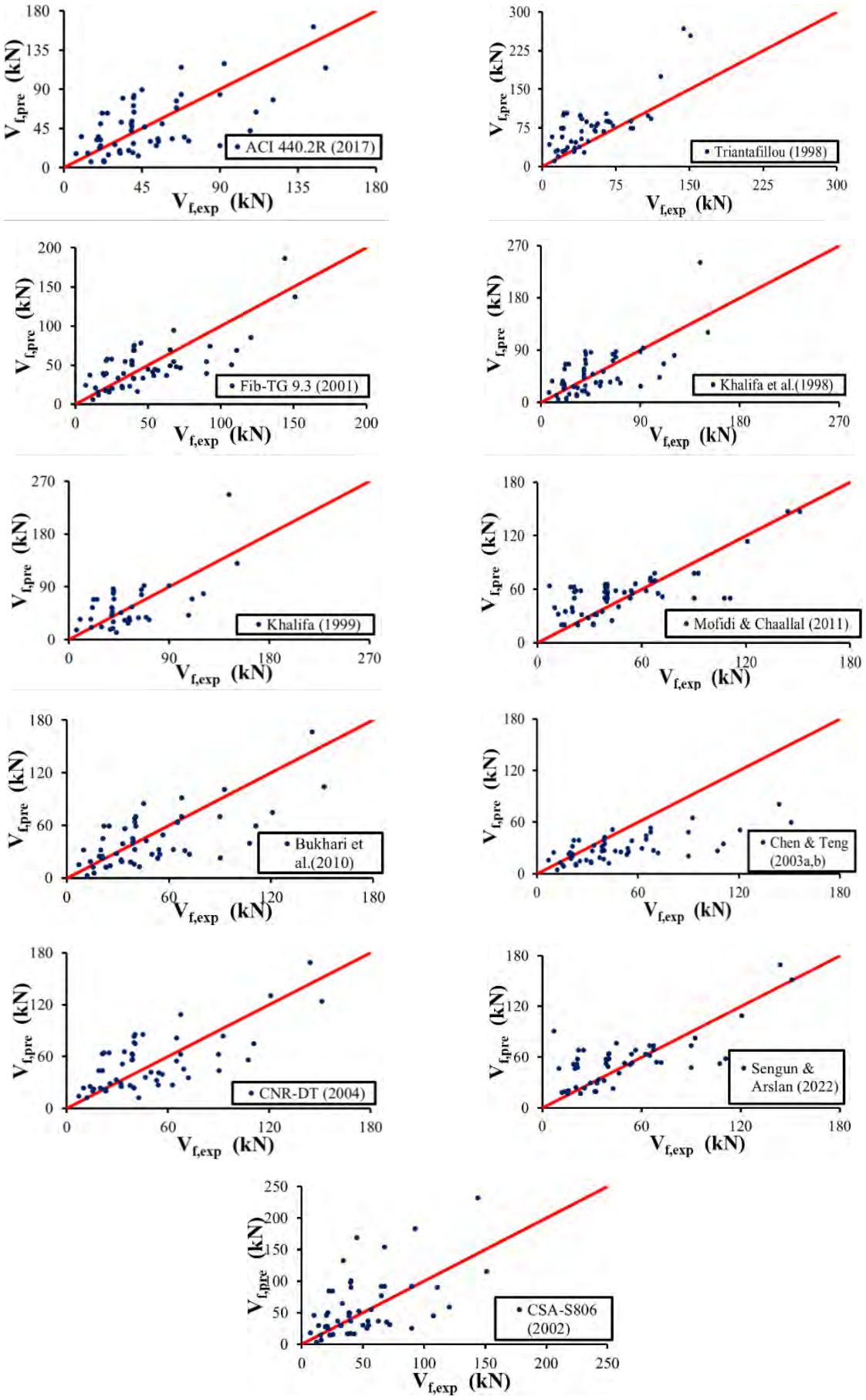


Fig. 12. The distribution of Vf,exp and Vf,pre on U-wrapped beams without stirrups

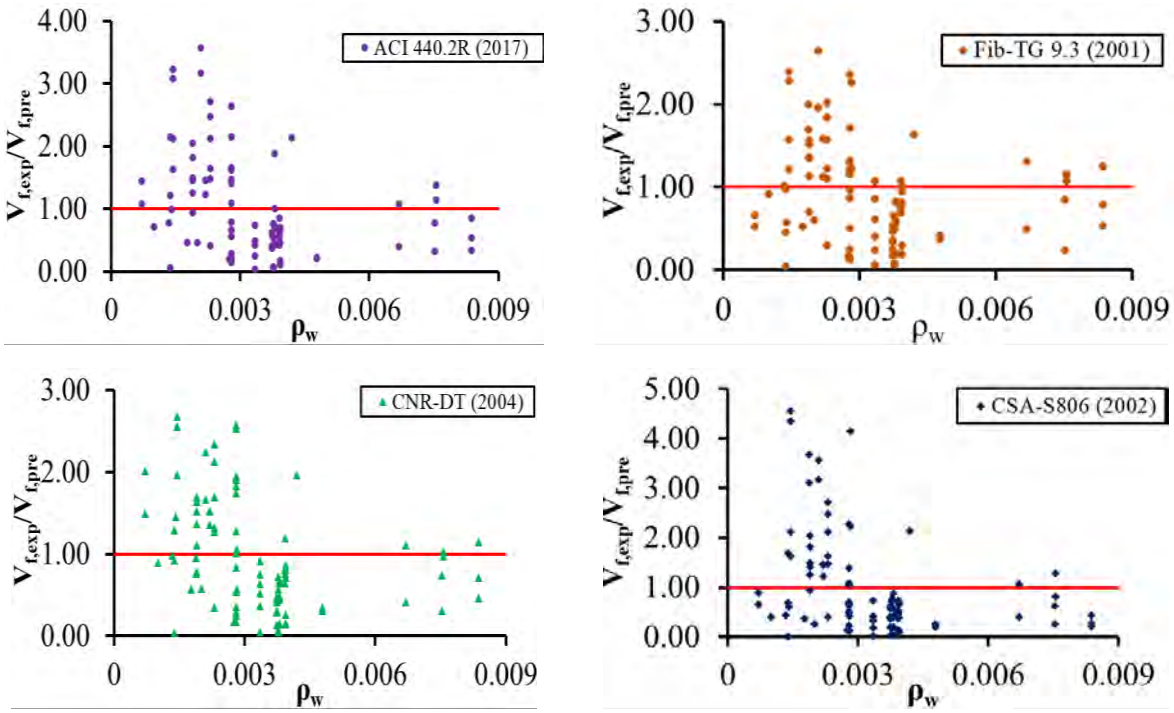


Fig. 13. The distribution of Vf,exp/Vf,pre according to a/d on U-wrapped beams

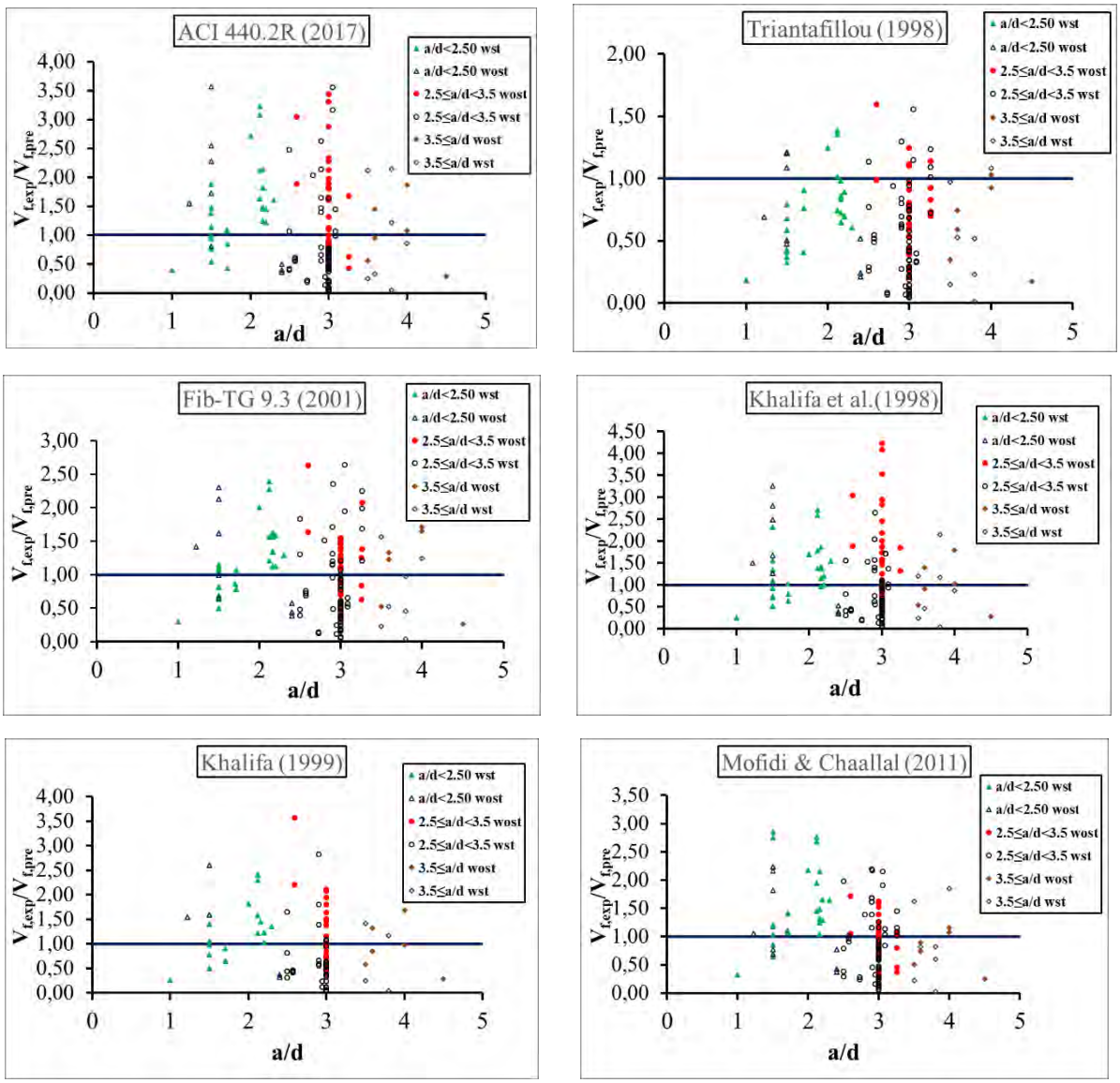
4.2.1 The Effect of a/d

"wost" represents the beams without stirrups, "*wst*" indicates the beams with stirrups in Fig. 14. Since the equation of Triantafillou [4] delivered predictions resulting in the lowest MV of the ratio of experimental results to predictions for all considered ranges of the *a/d*, it produced the most unconservative results among the considered equations (Table 9 and Fig. 14). The equations of Triantafillou [4], Mofidi & Chaallal [16] and Chen and Teng [1-2] yielded more reliable results for the beams with *a/d* less than 2.5 (*a/d<2.5*), between 2.5 and 3.5 (*2.5≤a/d<3.5*), and greater than 3.5 (*a/d≥3.5*), respectively, as they resulted in the lowest COV's.

Table 9. Statistical results in terms of a/d effect

Equations	U-wrapped beams														
	a/d<2.5					2.5≤a/d<3.5					a/d≥3.5				
	Specimen Number	MV	STD	COV	Conservative (%)	Specimen Number	MV	STD	COV	Conservative (%)	Specimen Number	MV	STD	COV	Conservative (%)
ACI 440.2R [84]	36	1.450	0.853	0.589	67	101	0.974	0.849	0.872	32	13	1.008	0.720	0.714	46
Triantafillou [4]	36	0.701	0.340	0.484	19	107	0.561	0.365	0.652	12	13	0.561	0.366	0.653	15
Fib-TG 9.3 [85]	36	1.163	0.587	0.505	61	107	0.876	0.604	0.690	39	13	0.904	0.589	0.652	46
Khalifa et al. [15]	36	1.332	0.772	0.580	67	100	0.979	0.865	0.883	34	13	0.925	0.623	0.673	46
Khalifa & Nanni [3]	23	1.242	0.640	0.515	65	63	0.827	0.724	0.875	30	10	0.857	0.552	0.644	40
Mofidi & Chaallal [16]	36	1.376	0.737	0.536	72	107	0.831	0.511	0.614	35	13	0.815	0.527	0.648	31
Bukhari et al. [10]	36	1.504	0.942	0.626	67	107	1.141	1.021	0.895	38	13	1.002	0.708	0.706	46
Chen & Teng [1-2]	36	1.682	0.967	0.575	78	107	1.264	0.814	0.644	59	13	1.112	0.650	0.585	54
CNR-DT200 [86]	36	1.244	0.706	0.567	58	107	0.864	0.647	0.749	34	13	1.061	0.637	0.601	54
Sengun & Arslan [88]	36	0.811	0.442	0.545	19	107	0.669	0.416	0.622	20	13	0.551	0.385	0.699	8
CSA-S806 [87]	36	1.373	1.079	0.786	58	107	0.937	0.929	0.991	31	13	0.805	0.672	0.834	31

Even though the equation proposed by Sengun & Arslan [88] is valid for the beams completely wrapped with FRP, it returned consistent results for the U-wrapped beams, especially those with *a/d* between 2.5 and 3.5 (*2.5≤a/d<3.5*), with a relatively low COV compared to the other equations. The *a/d* had substantial effect on both the experimental performance and prediction accuracy of the tested U-wrapped beams. All the considered equations except those proposed by Triantafillou [4], Mofidi & Chaallal [16] and Sengun & Arslan [88] produced predictions resulting higher COV's for the beams with *a/d* between 2.5 and 3.5 (*2.5≤a/d<3.5*) compared to the other considered ranges of *a/d*. Hence, their accuracies are lower for this range of *a/d* (*2.5≤a/d<3.5*). In case of the beams with *a/d* between 2.5 and 3.5 (*2.5≤a/d<3.5*), the percentages of the beams with conservative results for most of the considered equations are lower compared to the other considered ranges of *a/d*. In addition, the number of equations resulting in a MV of the ratio of experimental results to predictions less than one in this range of *a/d* (*2.5≤a/d<3.5*) is greater than those for the other considered ranges of *a/d*. The considered equations delivered more inconsistent results for U-wrapped beams, especially for the beams with *a/d* between 2.5 and 3.5 (*2.5≤a/d<3.5*). The *a/d* affects the accuracy of the equations. However, more experimental research is needed to understand better the impact of *a/d* on the FRP shear contribution and the accuracy of the proposed equations.



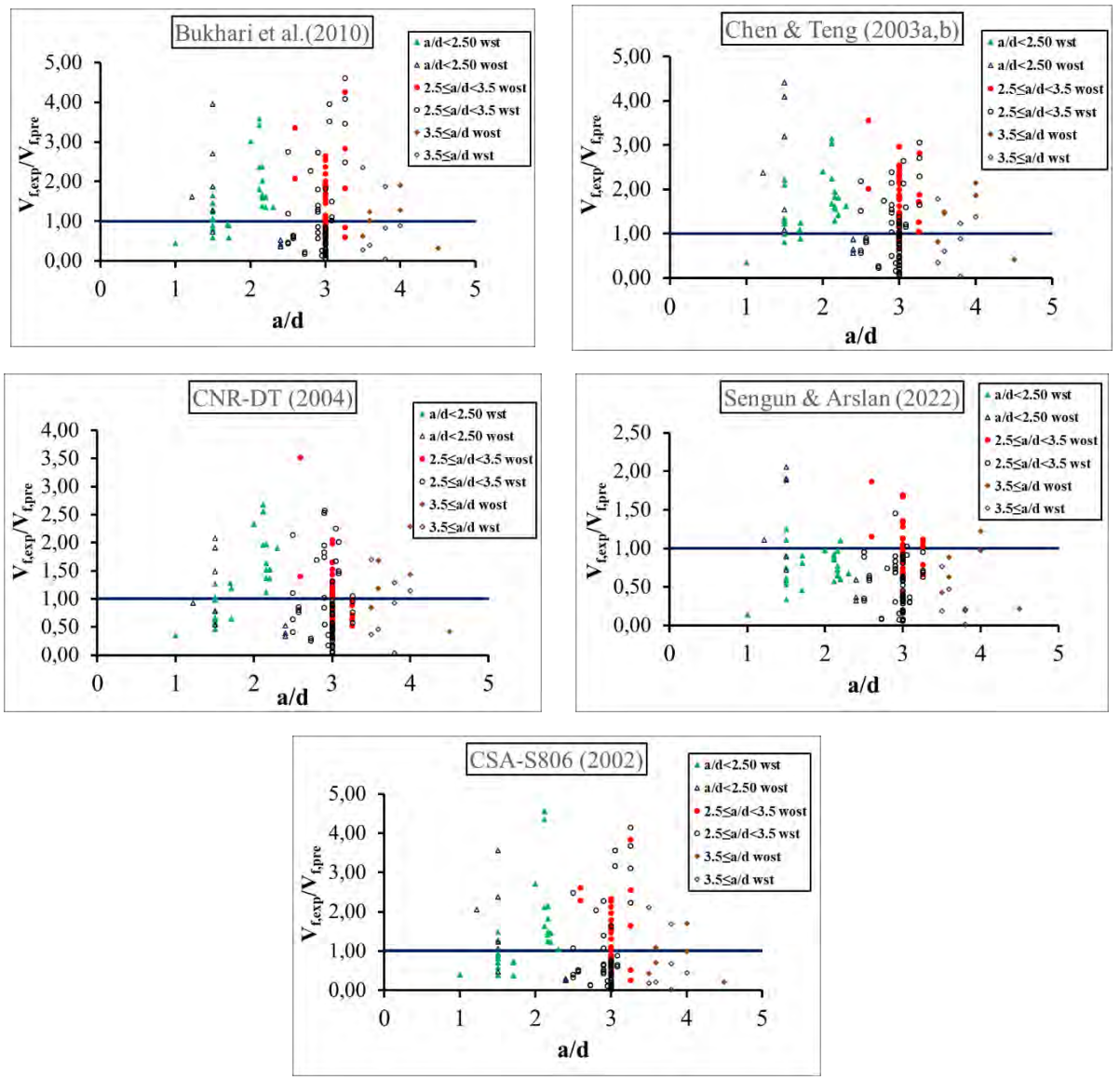


Fig. 14. The distribution of Vf,exp/Vf,pre according to a/d on U-wrapped beams

When the results obtained are evaluated collectively, it could be stated that the predictions of the proposed models in U-wrapped beams are highly inconsistent with the experimental results in beams with stirrups ratio (ρ_w) greater than 0.003 and with a/d between 2.5 and 3.5 (*2.5≤a/d<3.5*). Therefore, more experimental and analytical research are needed to derive analytical expressions including some important parameter such as stirrups and a/d for U-wrapped and side-bonded beams.

5. Conclusions

This study investigated CFRP-strengthened beams through both experimental and analytical methods. The experimental behavior was evaluated based on parameters such as strength, ductility, stiffness, failure modes, and strains. Furthermore, the influence of critical variables, including the a/d ratio and the presence of stirrups, on the experimental behavior of FRP-strengthened beams and the prediction accuracy of commonly used equations for calculating FRP shear contribution were analyzed. The principal findings from these analyses are summarized as follows:

- Strength, deflection, and ductility capacities of the beams were improved by strengthening with CFRP in comprasion to the unstrengthened beams.

- Since CFRP strengthening prevented the expansion and propagation of the cracks, the loss in stiffness subsequent to the diagonal shear cracks was less in the strengthened beams in comparison to the reference beams. In addition, CFRP-strengthening enhanced the load at which the first shear cracks occurred in K3.5S20 and K2.5S20 series compared to the reference beams.
- The yielding of the longitudinal reinforcement was delayed by the flexural strengthening by CFRP and slowed the flexural cracks to be widen. In addition, it could not be suitable to suppose that stirrups intersecting the shear cracks yielded in the case of shear failure in U-wrapping and side-bonding configurations due to the CFRP debonding as accepted in the specifications to figure out the stirrups' contribution to shear strength on CFRP strengthened beams.
- The cracking pattern and failure modes of the strengthened beams, compared to the reference beams, may be influenced by the CFRP strengthening configurations and the a/d ratio.
- As the a/d ratio increased, the failure loads of the strengthened beams and CFRP's contribution to load-carrying capacity decreased across all series. Changing the a/d ratio from 2.5 to 3.5 resulted in an average 25% decrease in strength for the reference beams with stirrups, as well as the completely wrapped and U-wrapped beams. Conversely, when the a/d ratio increased from 3.5 to 4.5, there was an average 20% decrease in the load-carrying capacities of the reference beams without stirrups, as well as the side-bonded and U-wrapped beams.
- The deflection capacities of the strengthened beams in flexure and shear with completely wrapped and the beams with U-wrapped CFRP in shear improved as a/d increased contrary to beams with side-bonded CFRP. It could be concluded that the a/d had substantial effect on the behavior and experimental performance of the strengthened beams differently based on the strengthening configurations.
- The failure loads of the strengthened beams with stirrups were higher than those without stirrups due to the added strength provided by the stirrups. However, the CFRP shear contribution was lower in beams with stirrups compared to those without. This experimental result suggests a potential interaction between the stirrups and CFRP that may negatively affect their individual contributions to shear strength.
- The w_f/s_f influenced the behavior of the strengthened beams differently depending on whether the beams have stirrups in the shear span. As w_f/s_f increased, the load-carrying capacity and CFRP contribution obtained higher on beams having no stirrups (K3.5S0 series) contrary to the beams with stirrups (K3.5S20 series). In beams strengthened with the same configuration of FRP, the reduction of w_f/s_f by increasing the center-to-center distance (s_f) between FRP shear strips resulted in an average of 45% decrease in deflection capacity.
- The CFRP contribution to strength and load-carrying capacity was higher in completely wrapped beams compared to U-wrapped and side-bonded beams in shear. However, if CFRP debonding was the failure mode, there was no significant difference in load-carrying capacity and CFRP contribution between U-wrapped and side-bonded configurations.
- The investigated equations produced more reliable results in beams without stirrups compared to those with stirrups in U-wrapped and side-bonded beams. For U-wrapped beams, the equations provided by Fib-TG 9.3 (2001), CSA-S806 (2002), ACI 440.2R (2017), and CNR-DT200 (2004) for the FRP shear contribution resulted in highly inconsistent and unconservative outcomes when the stirrup ratio exceeded 0.003
- Since Sengun & Arslan (2022) provided more reliable results for U-wrapped beams, their equation may be used to calculate the CFRP contribution in U-wrapped beams. Mofidi & Chaallal (2011) presented more reliable results for side-bonded beams. However, the accuracy of these equations should be verified with additional beams, and if necessary, the proposed equations should be refined.
- a/d affected the accuracy of the equations on both the accuracy of the predictions of the equations was affected by a/d in U-wrapped and side-bonded beams. In side-bonded beams, the investigated equations generally gave more consistent prediction with experimental results when a/d is between 2.5 and 3.5 ($2.5 \leq a/d < 3.5$) compared to the values where a/d is

less than 2.5($a/d<2.5$). The equations had more inconsistent results, especially for the values of a/d between 2.5 and 3.5 ($2.5\leq a/d<3.5$) in U-wrapped beams. Therefore, stirrups ratio and a/d need to be considered in the calculation of FRP shear contribution.

When the findings obtained in the previous and the present study are evaluated, it is concluded that the efficiency of completely-wrapped is superior to other strengthening configurations. Therefore, this configuration should be prioritized for retrofitting applications whenever feasible. In addition to its effect on experimental behavior, the stirrups have been demonstrated to influence the accuracy of prediction models. It is noteworthy that the majority of models do not incorporate this critical parameter explicitly. Consequently, there is a need to develop enhanced design models capable of producing more precise predictions for strengthened beams with stirrups. The integration of machine learning techniques in this field holds promise. Finally, it is observed that the U-wrapped and side-bonded specimens demonstrate similar behavior. The strengthening efficiency is found to be low due to the debonding problem. In these strengthening methods, it is hypothesized that anchors recommended in the literature should be employed to overcome the debonding problem. Additionally, the analytical findings from this study are applicable only to U-wrapped and side-bonded beams with an a/d ratio below 4.5. Further research is needed to determine the applicability of these results to completely-wrapped beams.

Data availability

A comprehensive paper that includes both experimental and analytical study.

References

[1] Chen JF, Teng JG. Shear capacity of FRP-strengthened RC beams: FRP debonding. Constr Build Mater. 2003;17(1):27-41. https://doi.org/10.1016/S0950-0618(02)00091-0

[2] Chen JF, Teng JG. Shear Capacity of Fiber-Reinforced Polymer-Strengthened Reinforced Concrete Beams: Fiber Reinforced Polymer Rupture. J Struct Eng. 2003;129(5):615-625. https://doi.org/10.1061/(ASCE)0733-9445(2003)129:5(615)

[3] Khalifa A, Nanni A. Rehabilitation of rectangular simply supported RC beams with shear deficiencies using CFRP composites. Constr Build Mater. 2002;16(3):135-146. https://doi.org/10.1016/S0950-0618(02)00002-8

[4] Triantafillou TC. Shear strengthening of reinforced concrete beams using epoxy-bonded FRP composites. ACI Struct J. 1998;95:107-115. https://doi.org/10.14359/531

[5] Triantafillou TC, Antonopoulos CP. Design of Concrete Flexural Members Strengthened in Shear with FRP. J Compos Constr. 2000;4(4):198-205. https://doi.org/10.1061/(ASCE)1090-0268(2000)4:4(198)

[6] Pellegrino C, Modena C. An experimentally based analytical model for the shear capacity of FRP-strengthened reinforced concrete beams. Mech Compos Mater. 2008;44(3):231-244. https://doi.org/10.1007/s11029-008-9016-y

[7] Pellegrino C, Modena C. Fiber Reinforced Polymer Shear Strengthening of Reinforced Concrete Beams with Transverse Steel Reinforcement. J Compos Constr. 2002;6(2):104-111. https://doi.org/10.1061/(ASCE)1090-0268(2002)6:2(104)

[8] Panda KC, Bhattacharyya SK, Barai SV. Shear strengthening of RC T-beams with externally side bonded GFRP sheet. J Reinf Plast Compos. 2011;30(13):1139-1154. https://doi.org/10.1177/0731684411417202

[9] Cao SY, Chen JF, Teng JG, Hao Z, Chen J. Debonding in RC Beams Shear Strengthened with Complete FRP Wraps. J Compos Constr. 2005;9(5):417-428. https://doi.org/10.1061/(ASCE)1090-0268(2005)9:5(417)

[10] Bukhari IA, Vollum RL, Ahmad S, Sagaseta J. Shear strengthening of reinforced concrete beams with CFRP. Mag Concr Res. 2010;62(1):65-77. https://doi.org/10.1680/macr.2008.62.1.65

[11] Pellegrino C, Modena C. Fiber-reinforced polymer shear strengthening of reinforced concrete beams: Experimental study and analytical modeling. ACI Struct J. 2006;103(5):720. https://doi.org/10.14359/16924

[12] Adhikary BB, Mutsuyoshi H, Ashraf M. Effective shear strengthening of concrete beams using FRP sheets with bonded anchorage. In: Fibre-Reinforced Polymer Reinforcement for Concrete Structures. 2003:457-466. https://doi.org/10.1142/9789812704863_0042

[13] Ianniruberto U, Imbimbo M. Role of Fiber Reinforced Plastic Sheets in Shear Response of Reinforced Concrete Beams: Experimental and Analytical Results. J Compos Constr. 2004;8(5):415-424. https://doi.org/10.1061/(ASCE)1090-0268(2004)8:5(415)

[14] Mostofinejad D, Tabatabaei Kashani A, Hosseini A. Design model for shear capacity of RC beams strengthened with two-side CFRP wraps based on effective FRP strain concept. Eur J Environ Civ Eng. 2016;20(2):161-179. https://doi.org/10.1080/19648189.2015.1021382
[15] Khalifa A, Gold WJ, Nanni A, MIA AA. Contribution of Externally Bonded FRP to Shear Capacity of RC Flexural Members. J Compos Constr. 1998;2(4):195-202. https://doi.org/10.1061/(ASCE)1090-0268(1998)2:4(195)
[16] Mofidi A, Chaallal O. Shear Strengthening of RC Beams with EB FRP: Influencing Factors and Conceptual Debonding Model. J Compos Constr. 2011;15(1):62-74. https://doi.org/10.1061/(ASCE)CC.1943-5614.0000153
[17] Al-Rousan R. Predicting the Optimum Shear Capacity of Reinforced Concrete Beams Externally Strengthened With CFRP Composites. Procedia Manuf. 2020;44:631-638. https://doi.org/10.1016/j.promfg.2020.02.246
[18] Grande E, Imbimbo M, Rasulo A. Effect of Transverse Steel on the Response of RC Beams Strengthened in Shear by FRP: Experimental Study. J Compos Constr. 2009;13(5):405-414. https://doi.org/10.1061/(ASCE)1090-0268(2009)13:5(405)
[19] Ozturk M, Sengun K, Arslan G. CFRP contribution to load-carrying capacity of retrofitted geopolymer concrete beams. Struct. 2023;48:1391-1402. https://doi.org/10.1016/j.istruc.2023.01.028
[20] Kim G, Sim J, Oh H. Shear strength of strengthened RC beams with FRPs in shear. Constr Build Mater. 2008;22(6):1261-1270. https://doi.org/10.1016/j.conbuildmat.2007.01.021
[21] Damnoo DJ, Kumar S. Experimental study on post repair performance of reinforced concrete beams rehabilitated and strengthened with CFRP sheets. Res J Eng Technol. 2016;7(3):103. https://doi.org/10.5958/2321-581X.2016.00022.2
[22] Bousselham A, Chaallal O. Mechanisms of shear resistance of concrete beams strengthened in shear with externally bonded FRP. J Compos Constr. 2008;12(5):499-512. https://doi.org/10.1061/(ASCE)1090-0268(2008)12:5(499)
[23] Bousselham A, Chaallal O. Effect of transverse steel and shear span on the performance of RC beams strengthened in shear with CFRP. Compos Part B Eng. 2006;37(1):37-46. https://doi.org/10.1016/j.compositesb.2005.05.012
[24] Bencardino F, Spadea G, Swamy RN. The problem of shear in RC beams strengthened with CFRP laminates. Constr Build Mater. 2007;21(11):1997-2006. https://doi.org/10.1016/j.conbuildmat.2006.05.056
[25] Abass AL, Hassan YR. Shear behavior of reinforced concrete wide beams strengthened with CFRP sheet without stirrups. 2019;12(1):19. https://doi.org/10.24237/djes.2019.12110
[26] Benzeguir ZEA, El-Saikaly G, Chaallal O. Influence of size on the behavior of RC T-beams strengthened in shear with externally bonded CFRP.
[27] Jayaprakash J, Abdul Samad AA, Anvar Abbasovich A, Abang Ali AA. Shear capacity of precracked and non-precracked reinforced concrete shear beams with externally bonded bi-directional CFRP strips. Constr Build Mater. 2008;22(6):1148-1165. https://doi.org/10.1016/j.conbuildmat.2007.02.008
[28] Galal K, Mofidi A. Shear strengthening of RC T-beams using mechanically anchored unbonded dry carbon fiber sheets. J Perform Constr Facil. 2010;24(1):31-39. https://doi.org/10.1061/(ASCE)CF.1943-5509.0000067
[29] Carolin A, Täljsten B. Experimental study of strengthening for increased shear bearing capacity. J Compos Constr. 2005;9(6):488-496. https://doi.org/10.1061/(ASCE)1090-0268(2005)9:6(488)
[30] Chaallal O, Nollet MJ, Perraton D. Shear strengthening of RC beams by externally bonded side CFRP strips. J Compos Constr. 1998;2(2):111-113. https://doi.org/10.1061/(ASCE)1090-0268(1998)2:2(111)
[31] Haddad RH, Marji CS. Composite strips with U-shaped CFRP wrap anchor systems for strengthening reinforced concrete beams. Int J Civ Eng. 2019;17(11):1799-1811. https://doi.org/10.1007/s40999-019-00447-w
[32] Teng JG, Chen GM, Chen JF, Rosenboom OA, Lam L. Behavior of RC beams shear strengthened with bonded or unbonded FRP wraps. J Compos Constr. 2009;13(5):394-404. https://doi.org/10.1061/(ASCE)CC.1943-5614.0000040
[33] Li W, Leung CKY. Shear span-depth ratio effect on behavior of RC beam shear strengthened with full-wrapping FRP strip. J Compos Constr. 2016;20(3):04015067. https://doi.org/10.1061/(ASCE)CC.1943-5614.0000627
[34] Bousselham A, Chaallal O. Behavior of reinforced concrete T-beams strengthened in shear with carbon fiber-reinforced polymer-an experimental study. ACI Struct J. 2006;103(3):339. https://doi.org/10.14359/15311
[35] Khalifa A, Belarbi A, Nanni A. Shear performance of RC members strengthened with externally bonded FRP wraps. New Zealand. 2000;9.

[36] Li W, Leung CKY. Effect of shear span-depth ratio on mechanical performance of RC beams strengthened in shear with U-wrapping FRP strips. Compos Struct. 2017;177:141-157. https://doi.org/10.1016/j.compstruct.2017.06.059
[37] Benzeguir ZEA, El-Saikaly G, Chaallal O. Size effect in RC T-beams strengthened in shear with externally bonded CFRP sheets: Experimental study. J Compos Constr. 2019;23(6):04019048. https://doi.org/10.1061/(ASCE)CC.1943-5614.0000975
[38] Benzeguir ZEA, El-Saikaly G, Chaallal O. Size effect of RC T-beams strengthened in shear with externally bonded CFRP L-shaped laminates. J Compos Constr. 2020;24(4):04020031. https://doi.org/10.1061/(ASCE)CC.1943-5614.0001045
[39] Li A, Diagana C, Delmas Y. CRFP contribution to shear capacity of strengthened RC beams. Eng Struct. 2001;23(10):1212-1220. https://doi.org/10.1016/S0141-0296(01)00035-9
[40] Li A, Diagana C, Delmas Y. Shear strengthening effect by bonded composite fabrics on RC beams. Compos Part B Eng. 2002;33(3):225-239. https://doi.org/10.1016/S1359-8368(02)00003-3
[41] Khalifa A, Tumialan G, Nanni A, Belarbi A. Shear strengthening of continuous RC beams using externally bonded CFRP sheets. In: Proc., 4th Int. Symp. on FRP for Reinforcement of Concrete Structures (FRPRCS4); Baltimore, MD: American Concrete Institute; 1999; 995-1008.
[42] Allam SM, Ebeido TI. Retrofitting of RC beams predamaged in shear using CFRP sheets. Alexandria Eng J. 2003;42(1):16.
[43] Adhikary BB, Mutsuyoshi H. Behavior of concrete beams strengthened in shear with carbon-fiber sheets. J Compos Constr. 2004;8(3):258-64. https://doi.org/10.1061/(ASCE)1090-0268(2004)8:3(258)
[44] Mostofinejad D, Hosseini SA, Razavi SB. Influence of different bonding and wrapping techniques on performance of beams strengthened in shear using CFRP reinforcement. Constr Build Mater. 2016;116:310-20. https://doi.org/10.1016/j.conbuildmat.2016.04.113
[45] Leung CKY, Chen Z, Lee S, Ng M, Xu M, Tang J. Effect of size on the failure of geometrically similar concrete beams strengthened in shear with FRP strips. J Compos Constr. 2007;11(5):487-96. https://doi.org/10.1061/(ASCE)1090-0268(2007)11:5(487)
[46] Diagana C, Li A, Gedalia B, Delmas Y. Shear strengthening effectiveness with CFF strips. Eng Struct. 2003;25(4):507-16. https://doi.org/10.1016/S0141-0296(02)00208-0
[47] Mostofinejad D, Tabatabaei Kashani A. Experimental study on effect of EBR and EBROG methods on debonding of FRP sheets used for shear strengthening of RC beams. Compos Part B Eng. 2013;45(1):1704-13. https://doi.org/10.1016/j.compositesb.2012.09.081
[48] Panda KC, Bhattacharyya SK, Barai SV. Effect of transverse steel on the performance of RC T-beams strengthened in shear zone with GFRP sheet. Constr Build Mater. 2013;41:79-90. https://doi.org/10.1016/j.conbuildmat.2012.11.098
[49] Sundarraja MC, Rajamohan S. Strengthening of RC beams in shear using GFRP inclined strips - an experimental study. Constr Build Mater. 2009;23(2):856-64. https://doi.org/10.1016/j.conbuildmat.2008.04.008
[50] Sharkawi AEDM, Etman E. Effect of shear strengthening on the flexural behavior of RC simple beams strengthened externally with FRP laminates. In: Twelfth International Colloquium on Structural and Geotechnical Engineering. Ain Shams University, Faculty of Engineering, Department of Structural Engineering; 2007; 10-12.
[51] Rashidi M, Takhtfirouzeh H. An experimental study on shear and flexural strengthening of concrete beams using GFRP composites. 2018;3(1):7. https://doi.org/10.37516/global.j.civ.eng.2019.0047
[52] Nanda RP, Behera B, Majumder S, Khan HA. RC beam strengthening by glass fibre reinforced polymer. Int J Eng Technol Sci Res. 2018;5:21-6.
[53] Dong J, Wang Q, Guan Z. Structural behaviour of RC beams with external flexural and flexural-shear strengthening by FRP sheets. Compos Part B Eng. 2013;44(1):604-12. https://doi.org/10.1016/j.compositesb.2012.02.018
[54] Baggio D, Soudki K, Noël M. Strengthening of shear critical RC beams with various FRP systems. Constr Build Mater. 2014;66:634-44. https://doi.org/10.1016/j.conbuildmat.2014.05.097
[55] Grace NF, Sayed GA, Soliman AK, Saleh KR. Strengthening reinforced concrete beams using fiber reinforced polymer (FRP) laminates. ACI Struct J. 1999;96(5):865-74. https://doi.org/10.14359/741
[56] Ozden S, Atalay HM, Akpinar E, Erdogan H, Vulaş YZ. Shear strengthening of reinforced concrete T-beams with fully or partially bonded fibre-reinforced polymer composites. Struct Concr. 2014;15(2):229-39. https://doi.org/10.1002/suco.201300031
[57] Sundarraja MC, Rajamohan S, Bhaskar D. Shear strengthening of RC beams using GFRP vertical strips-an experimental study. J Reinf Plast Compos. 2008;27(14):1477-95. https://doi.org/10.1177/0731684407081772
[58] Nanda RP, Behera B. Experimental study of shear-deficient RC beam wrapped with GFRP. Int J Civ Eng. 2020;18(6):655-64. https://doi.org/10.1007/s40999-020-00498-4

[59] Van Cao V, Pham SQ. Comparison of CFRP and GFRP wraps on reducing seismic damage of deficient reinforced concrete structures. Int J Civ Eng. 2019;17(11):1667-81. https://doi.org/10.1007/s40999-019-00429-y
[60] Alacali S, Akkaya HC, Sengun K, Arslan G. Proposal and evaluation of new models for predicting the FRP contribution to shear strength in reinforced concrete beams using gene expression programming. Neural Comput Appl. 2024;36(25):15515-44. https://doi.org/10.1007/s00521-024-09892-8
[61] Saafan MAA. Shear strengthening of reinforced concrete beams using GFRP wraps. Acta Polytech. 2006;46(1). https://doi.org/10.14311/800
[62] Sengun K, Arslan G. Performance of RC beams strengthened in flexure and shear with CFRP and GFRP. Iran J Sci Technol Trans Civ Eng. 2024;48:117-30. https://doi.org/10.1007/s40996-023-01305-5
[63] Hawileh RA, Rasheed HA, Abdalla JA, Al-Tamimi AK. Behavior of reinforced concrete beams strengthened with externally bonded hybrid fiber reinforced polymer systems. Mater Des. 2014;53:972-82. https://doi.org/10.1016/j.matdes.2013.07.087
[64] Keskin RSO, Arslan G, Sengun K. Influence of CFRP on the shear strength of RC and SFRC beams. Constr Build Mater. 2017;153:16-24. https://doi.org/10.1016/j.conbuildmat.2017.06.170
[65] Sengun K, Arslan G. Parameters affecting the behaviour of RC beams strengthened in shear and flexure with various FRP systems. Structures. 2022;40:202-12. https://doi.org/10.1016/j.istruc.2022.04.024
[66] Sengun K, Arslan G. Influence of CFRP on the strength of retrofitted RC beams without stirrups. Sigma J Eng Nat Sci. 2017;35(1):77-85.
[67] Kar S, Biswal KC. Shear strengthening of reinforced concrete T-beams by using fiber-reinforced polymer composites: a data analysis. Arab J Sci Eng. 2020;45(5):4203-34. https://doi.org/10.1007/s13369-020-04412-x
[68] Kotynia R, Oller E, Marí A, Kaszubska M. Efficiency of shear strengthening of RC beams with externally bonded FRP materials - State-of-the-art in the experimental tests. Composite Structures. 2021;18. https://doi.org/10.1016/j.compstruct.2021.113891
[69] Lima JL, Barros JA. Reliability analysis of shear strengthening externally bonded FRP models. Proc Inst Civ Eng Struct Build. 2011;164(1):43-56. https://doi.org/10.1680/stbu.9.00042
[70] Pellegrino C, Vasic M. Assessment of design procedures for the use of externally bonded FRP composites in shear strengthening of reinforced concrete beams. Compos Part B Eng. 2013;45(1):727-41. https://doi.org/10.1016/j.compositesb.2012.07.039
[71] Taerwe L, Khalil H, Matthys S. Behaviour of RC beams strengthened in shear by external CFRP sheets. In: Proc 3rd Int Symp Nonmetallic (FRP) Reinforcement for Concrete Structures. Tokyo: Japan Concrete Institute; 1997. p. 483-90.
[72] Khalifa A, Nanni A. Improving shear capacity of existing RC T-section beams using CFRP composites. Cem Concr Compos. 2000;22(3):165-74. https://doi.org/10.1016/S0958-9465(99)00051-7
[73] Panda KC, Bhattacharyya SK, Barai SV. Shear strengthening effect by bonded GFRP strips and transverse steel on RC T-beams. Struct Eng Mech. 2013;47(1):75-98. https://doi.org/10.12989/sem.2013.47.1.075
[74] Sato Y, Ueda T, Kakuta Y, Ono S. Ultimate shear capacity of reinforced concrete beams with carbon fiber sheet. In: Proc 3rd Symp Non-Metallic (FRP) Reinforcement for Concrete Structures (FRPRCS-3). Sapporo, Japan; 1997; 1: 499-505.
[75] Wu G, An L, Lv ZT. Experimental research on RC beam strengthened in shear with CFRP sheet. J Build Struct. 2000;30(7):16-20, 51. (in Chinese).
[76] Tan Z, Ye LP. Experimental research on shear capacity of RC beam strengthened with externally bonded FRP sheets. China Civ Eng J. 2003;36(11):12-8. (in Chinese).
[77] Feng XS, Chen ZF. Experimental research on shear strengthening of reinforced concrete beams with externally bonded CFRP sheets. Ind Constr. 2004;Supplement:89-93. (in Chinese).
[78] Rizzo A, De Lorenzis L. Behavior and capacity of RC beams strengthened in shear with NSM FRP reinforcement. Constr Build Mater. 2009;23(4):1555-67. https://doi.org/10.1016/j.conbuildmat.2007.08.014
[79] Mofidi A, Chaallal O. Shear strengthening of RC beams with externally bonded FRP composites: Effect of strip-width-to-strip-spacing ratio. J Compos Constr. 2011;15(5):732-42. https://doi.org/10.1061/(ASCE)CC.1943-5614.0000219
[80] Micelli F, Annaiah RH, Nanni A. Strengthening of short shear span reinforced concrete T joists with fiber-reinforced plastic composites. J Compos Constr. 2002;6(4):264-71. https://doi.org/10.1061/(ASCE)1090-0268(2002)6:4(264)
[81] Sato Y, Veda T, Kakuta Y, Tanaka T. Shear reinforcing effect of carbon fiber sheet attached to side of reinforced concrete beams. In: El-Badry MM, editor. Adv Compos Mater Bridges Struct. 1996. p. 621-7.
[82] Uji K. Improving shear capacity of existing reinforced concrete members by applying carbon fiber sheets. Trans Jpn Concr Inst. 1992;14:253-66.
[83] Antonopoulos CP. Shear strengthening of reinforced concrete structures using composite materials [Diploma thesis]. Patras, Greece: University of Patras, Department of Civil Engineering; 2000.

[84] American Concrete Institute. Guide for the design and construction of externally bonded FRP systems for strengthening concrete structures (ACI 440.2R-17). Farmington Hills, MI, USA; 2017.
[85] Fédération internationale du béton. Externally bonded FRP reinforcement for RC structures. Task Group 9.3, Bulletin No. 14. Lausanne, Switzerland; 2001.
[86] CNR-Italian Research Council, Advisory Committee on Technical Recommendations for Construction. Guide for the design and construction of externally bonded FRP systems for strengthening existing structures. Rome, Italy; 2004.
[87] CAN/CSA. Design and construction of building components with fiber-reinforced polymer. S806-02. Canadian Standards Association, Rexdale, Canada; 2002.
[88] Sengun K, Arslan G. Investigation of the parameters affecting the behavior of RC beams strengthened with FRP. Front Struct Civ Eng. 2022. https://doi.org/10.1016/j.istruc.2022.04.024
[89] Guadagnini M, Pilakoutas K, Waldron P. Shear resistance of FRP RC beams: Experimental study. J Compos Constr. 2006;10(6):464-73. https://doi.org/10.1061/(ASCE)1090-0268(2006)10:6(464)
[90] Lee HK, Cheong SH, Ha SK, Lee CG. Behavior and performance of RC T-section deep beams externally strengthened in shear with CFRP sheets. Compos Struct. 2011;93(2):911-22. https://doi.org/10.1016/j.compstruct.2010.07.002
[91] Panigrahi SK, Deb A, Bhattacharyya SK. Modes of failure in shear deficient RC T-beams strengthened with FRP. J Compos Constr. 2016;20(1):04015029. https://doi.org/10.1061/(ASCE)CC.1943-5614.0000586
[92] Akkaya HC, Aydemir C, Arslan G. Evaluation of shear behavior of short-span reinforced concrete deep beams strengthened with fiber reinforced polymer strips. Eng Struct. 2024;299:117145. https://doi.org/10.1016/j.engstruct.2023.117145

Blank Page

Research on Engineering Structures & Materials
www.jresm.org
Research Group

Research Article

Predicting viscosity and yield surfaces for Bingham fluids in a lid-driven cavity employing a deep neural network

Eduardo Henrique Taube Cunegatto [1,a], Flavia Schwarz Franceschini Zinani [*,2,b], Sandro Jose Rigo [1,c]

[1]*Applied Computing Graduate Program, Universidade do Vale do Rio dos Sinos, São Leopoldo, Brazil*
[2]*Institute of Hydraulic Research, Universidade Federal do Rio Grande do Sul, Porto Alegre, Brazil*

Article Info

Article history:

Received 22 Nov 2024
Accepted 20 Jan 2025

Keywords:

Yield stress fluids;
Deep learning;
Computational fluid dynamics;
Artificial neural networks;
Surrogate model;
Lid-driven cavity

Abstract

Computational Fluid Dynamics (CFD) simulation of viscoplastic fluid flows is challenging. It is critical to capture the shape of the yield surfaces that limit yielded and unyielded flow regions. These are highly sensitive to numerical schemes, which usually rely on calculating velocity derivatives and require highly refined computational grids and strict convergence criteria. In this work, CFD and Deep Neural Networks (DNN) were coupled to develop a model to predict yield surface morphologies for the flow of Bingham fluids in a square cavity. Our main goal is to predict the behavior of viscoplastic fluids using a Machine Learning (ML) approach based on CFD results. Design of Experiments techniques were employed in defining the base cases, i.e., combinations of Bingham and Reynolds numbers (Bn and Re) to compose the DNN training data. The DNN predicted the viscosity fields in the problem domain given Bn and Re. These results were postprocessed using masks to create binary images. The chosen architecture was an encoder-decoder since the input and output data had different dimensions. The results of the surrogate model were adequate, giving a Mean Squared Error of 0.0015 for the training data and 0.002 for the testing data. The DNN-predicted images were consistent with those generated from CFD, corroborating the proposed technique as an excellent alternative to be implemented in more complex applications. The combination of CFD and ML is a promising alternative for predicting complex fluid behavior in diverse and challenging scenarios with faster and computationally less expensive resources.

© 2025 MIM Research Group. All rights reserved.

1. Introduction

A class of non-Newtonian fluids, called yield stress or viscoplastic fluids, receives much attention for its broad applicability in engineering. These fluids have the characteristic of presenting yield stress, a minimum stress level required for the material to flow. Below the yield stress, the material behaves as a solid. This non-smooth behavior is a model for the complex behavior of some macromolecular materials. At a specific range of stresses, these materials undergo some molecular configuration changes that cause the drop of their viscosity from a high plateau (solid-like behavior) to a value much lower in the range of a fluid's viscosity [1]. The primary examples of viscoplastic fluids of engineering interest include gels, muds, creams, and molten polymers. Viscoplastic fluids are also referred to as Bingham fluids after the seminal book by E.E. Bingham [2] and the widely employed mathematical model for viscoplastic fluids, the Bingham equation [3].

*Corresponding author: flavia.zinani@ufrgs.br
[a] orcid.org/0000-0002-2692-1479; [b] orcid.org/0000-0001-5402-900X; [c] orcid.org/0000-0001-8140-5621
DOI: http://dx.doi.org/10.17515/resm2025-544ml1122rs

The flow of viscoplastic fluids is usually complex because there may be regions below and above their yield stress along the flow domain. So, the fluid moves with yielded regions (stresses above the yield stress), in which the flow is viscous, and unyielded regions (stresses below the yield stress), in which the movement is the type of rigid body motion, with negligible strain rate. The unyielded regions along the flow usually increase heat and material flow resistance, pressure drop, and pumping power requirements.

The computational modeling of viscoplastic flows using computational fluid dynamics (CFD) has the challenge of capturing the frontiers of the yielded and unyielded regions called yield surfaces. The shape of yield surfaces is sensitive to the fluid's rheology, geometry, and operation conditions. Due to the modeling of the non-smooth material behavior, which depends on local values of stresses, the CFD simulations of viscoplastic flows are computationally intense. They are memory and time-consuming and must rely on finer grids compared to simulations of Newtonian fluid flows under the same conditions.

Numerous works have addressed viscoplastic flows inside lid-driven cavities to test CFD modeling and methods. Like in Newtonian flow, a primary vortex usually occurs in the cavity's center. The shear in such a vortex is so mild that its center usually does not yield. Figure 1 shows a schematic of the flow of a viscoplastic fluid inside a lid-driven cavity, with streamlines and yielded and unyielded regions represented in white and black, respectively.

Some works that employed the lid-driven cavity benchmark with viscoplastic fluids are summarized in the sequence. The work by Frey et al. [4] presented numerical approximations via Galerkin-least-squares-type formulation in a lid-driven cavity, with different ranges of Reynolds and Bingham numbers, providing reliable results for comparing the morphology of yielded and unyielded zones. Dos Santos et al. [5] also studied the lid-driven cavity, employing a regularized viscosity model and providing a parametrical analysis of the problem. The authors discussed the criterion (stress x strain rate) for the yielded and unyielded regions, where they found that using the strain rate provides smoother yield surfaces than those originating from the stress criterion. Syrakos et al. [6] examined the inertia effects of a Bingham fluid in a lid-driven cavity by modifying the viscosity function to employ the regularization of Papanastasiou [7]. By varying the range of both Bingham and Reynolds numbers up to 100 and 5000, respectively, they found that the discretization error increases with the Bingham number due to the discontinuation of the flow around the yielded regions caused by the increase of the truncation error of the regularization. Syrakos et al. [8] investigated a transient version of the lid-driven cavity for Newtonian and Bingham fluids, where a sudden flow stoppage and its effects are analyzed. Such study presents benchmark cases, covering Reynolds and Bingham numbers from 1 to 1000 and 1 to 10, respectively, to be used in further investigations. Kefayati & Huilgol [9] studied the mixed convection in the lid-driven cavity filled with Bingham fluids by solving the model equations via the Lattice Boltzmann Method (LBM). Using such modeling, the authors could find results equivalent to those of more traditional methods, like the finite volume method (FVM). The study also presents an analysis of heat transfer, showing the influence of temperature and of the Prandtl number on flow behavior. Mahmood et al. [10] studied the lid-driven cavity with single and

double lids, also considering Bingham fluids. They found out that, for the double lid, the creation of the unyielded regions happens at the exact center of the cavity, increasing its size as the Bingham number grows. Also, for lower Bingham numbers, the behavior is more symmetric when compared to higher values. Thohura et al. [11] studied Bingham fluids in skewed lid-driven cavities. The study covers skew angles from 45° to 135°, Bingham numbers from 0 to 500, and Reynolds numbers up to 1000, providing benchmark results for the problem. Bui et al. [12] also study skewed cavities, besides square and rectangular ones, focusing on the behavior of Carbopol 940, which was modeled via a combination of Herschel-Bulkley and Papanastasiou models. While keeping the Reynolds number fixed at a value of 0.001, the authors analyzed the effect of the Oldroyd number, ranging from 0 to 50. Ferrari and Franco [13] studied squared cavities, modeling transient viscoplastic flows with the LBM method. Covering a range of Reynolds numbers up to 20000 and Bingham numbers up to 10, the authors analyzed the behavior of the flow until a steady state was reached. The results showed that the time to reach a stationary state increases as the Bingham number grows despite the Reynolds number. Ferrari and Franco [14] expanded their previous study by analyzing the steady and unsteady behavior of a viscoplastic fluid in a cubic cavity, extending the existing dataset. Once again, using the LBM method, the authors found that the three-dimensional approach appears more unstable than the bi-dimensional one, where some aspects of the flow could not be captured. The authors recommend using a Herschel-Bulkley fluid for comparison, as it is easier to compare with real fluids.

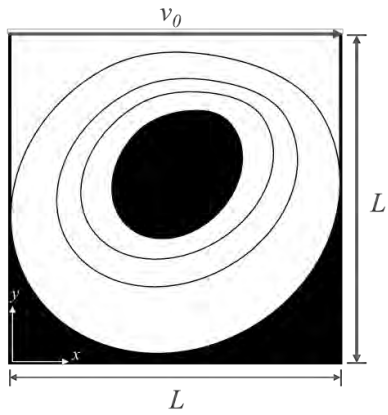


Fig. 1. A representation of viscoplastic fluid flow inside a lid-driven cavity

In recent years, deep neural networks (DNN) have become a versatile and valuable tool for optimizing results in several computational tasks by predicting complex aspects in diverse application contexts. The consistent and relevant results observed through DNN applications generated interest in their use in several fields, such as fluid dynamics. In this context, their use has been highlighted as a valuable method for modeling and predicting many properties and features in many Computational Fluid Dynamics (CFD) applications [15]. It is known that traditional CFD models can be computationally expensive and time-consuming, especially in complex geometries or refined mesh cases. In this context, surrogate models via DNNs have emerged as a promising alternative to accelerate CFD

simulations while maintaining good accuracy [16]. Thus, DNNs are an alternative to help reduce simulations' computational costs using CFD-generated data.

Many numerical methods can provide high-fidelity solutions for viscoplastic flows that may be post-processed to give the morphology of yielded and unyielded regions along the computational domain. If the shape of yield surfaces is the primary interest, such problems could be simplified if only this object of interest is solved, reducing time and computational cost in pre-processing and post-processing. Previous works have explored this concept using machine learning models trained to reproduce and generate CFD-like solutions for many applications. For example, Convolutional Neural Networks (CNN) architectures, coupled with CFD, have been used in heat transfer [17] [18] [19] [20], air/hydrofoil optimization [21] [22], ship designs [23], hemodynamics [24], prediction of porous media [25], performance of solar collectors in [26] and thermal analysis of bearings [27]. Other DNN architectures, such as fully connected with backpropagation, can be found in the works of Kim & Park [28] who applied in indoor airflow prediction, Sang et al. [29] for the prediction of wind load of buildings and Hussain et al. [30], in the modeling of mixed convection in nanofluids. However, regarding viscoplastic flows, the application of DNNs is relatively scarce in the literature. Muravleva et al. [31] used a combination of proper orthogonal decomposition (POD) and a fully connected DNN to build reduced-order models for Bingham flows in ducts. Kumar et al. [32] applied an DNN to simulate the flow of a viscoplastic fluid in a pipe, implementing physical governing equations as the loss function. Similarly, Zhang [33] developed an Augmented Lagrange Method Physics Informed Neural Network (ALM-PINN) to solve steady-state one-dimensional Poiseuille flow and bi-dimensional plane lid-driven cavity for Stokes flow of Bingham fluids. Although the current model is limited to small Bingham numbers, using such architecture, the authors could induce feasible loss functions for the network by formulating them as a linear combination of the mean squared error of the governing equations, providing a mesh-free feature, and developing a versatile network configuration.

Driven by the promising use of machine learning, the current study proposes the use of a DNN, in the form of an encoder-decoder architecture, combined with CFD data, as a surrogate model to predict viscosity contours and yield surfaces for viscoplastic flows inside a lid-driven cavity and different combinations of Bingham and Reynolds numbers. This work also includes the steps to create a custom dataset from CFD simulations, a detailed configuration of the encoder-decoder neural network, and the analysis of the model's performance. As the main objective, this study aims to introduce a versatile approach to studying viscoplastic flows in the lid-driven cavity by applying DNNs. With the excellent accuracy achieved in this work, we expect to establish a foundation for future research in this field and motivate the computational fluid dynamics community to use the capabilities of neural networks, especially when dealing with fluids of complex behavior.

2. Methodology

This section covers all the methods utilized in this work to support the steps taken to achieve the current results and for future use.

2.1. Problem Description

The system under analysis is a bi-dimensional square, representing a cavity filled with a viscoplastic fluid. The flow behavior in such fluids is characterized by the yield stress, the stress level above which the material behaves as a viscous fluid. Below the yield stress, the material would behave as a solid or, as accepted nowadays, as a highly viscous fluid. At unyielded regions, strain rates are negligible.

As presented in Figure 1, the cavity upper lid moves with tangential velocity v0, causing the flow inside the cavity. The remaining edges represent the walls of the cavity, which have length L. Two dimensionless numbers are associated with this physical problem: the Reynolds and Bingham numbers. The Reynolds number (Re) indicates the flow regime and measures the imbalance between inertial and viscous forces. The Bingham number (Bn) measures the fluid's degree of viscoplasticity relative to the system scale. As previously mentioned, Figure 1 is a schematic of the described system, which depicts a representative configuration of yielded and unyielded regions in white and black, respectively.

2.2. Mathematical Modeling

To model the problem, the flow was considered incompressible and in steady state. The balance equations of mass and momentum, Equations (1) and (2), respectively, were used.

$$\nabla \cdot \boldsymbol{v} = 0 \tag{1}$$

$$\rho[(\nabla \cdot \boldsymbol{v})\boldsymbol{v}] = -\nabla P + \nabla \cdot \boldsymbol{\tau} \tag{2}$$

in which $\boldsymbol{v}$ represents the velocity vector, P is the pressure field and ρ is the fluid`s density. In Equation (2), $\boldsymbol{\tau}$ represents the extra stress tensor, mathematically expressed by:

$$\boldsymbol{\tau} = 2\eta(\dot{\gamma})\boldsymbol{D} \tag{3}$$

where $\boldsymbol{D}$ is the strain rate tensor and $\eta(\dot{\gamma})$ represents the viscosity function. In the viscosity function, $\dot{\gamma}$ is the magnitude of the strain rate tensor, which is mathematically represented as:

$$\dot{\gamma} = \sqrt{2tr(\boldsymbol{D} \cdot \boldsymbol{D})} \tag{4}$$

where the *tr* represents the trace operator.

The viscosity function for viscoplastic liquids was modeled using the Bingham model [2], regularized as a bi-viscosity model as follows [34]:

$$\eta(\dot{\gamma}) = \tau_0 \frac{\left(2 - \frac{\dot{\gamma}}{\dot{\gamma}_c}\right)}{\dot{\gamma}_c} + k, \qquad if\ \dot{\gamma} < \dot{\gamma}_c \tag{5}$$

$$\eta(\dot{\gamma}) = \frac{\tau_0}{\dot{\gamma}} + k, \qquad if\ \dot{\gamma} > \dot{\gamma}_c \tag{6}$$

where k is a consistency parameter and τ_0 is the yield stress. The Bingham original model predicts infinite viscosity at stresses lower than τ_0 and the viscosity as in Equation (6) for stresses above τ_0. The present regularized model uses the critical shear rate, $\dot{\gamma}_c$, to give a

continuous stress behavior as a function of the shear rate avoiding infinite viscosity. Below the $\dot{\gamma}_c$, Equation (5) predicts high viscosities, and above $\dot{\gamma}_c$, Equation (6) predicts the same viscosity as the Bingham model. Equations (5) and (6) approximate the original model behavior as $\dot{\gamma}_c$ is lower. So $\dot{\gamma}_c$ must be chosen at a low value to approximate the results expected for the Bingham original model. In this work, the relation $\dot{\gamma}_c/v_0$ was chosen to be always lower than 0.05, because we have detected that the simulation results were insensitive to $\dot{\gamma}_c$for any $\dot{\gamma}_c L/v_0$ lower than 0.05. As previously mentioned, Bingham (Bn) and Reynolds (Re) are the main dimensionless numbers of this problem, which are mathematically given, respectively, by:

$$Bn = \frac{\tau_0 L}{k v_0} \tag{7}$$

$$Re = \frac{\rho L v_0}{k} \tag{8}$$

In this problem, Bn and Re numbers are varied, ranging from 1 to 10 and 1 to 250, respectively.

2.3. Numerical Modeling

The software used to solve the governing equations was ANSYS Fluent 2023R2 [34]. For the pressure-velocity scheme, COUPLED was adopted, and for pressure and momentum interpolation, the second-order model was employed. The convergence criteria for mass and momentum were set to 10^{-10}. The numerical mesh was built by dividing the domain into a grid of 200x200 finite volumes, which was considered by using the works of Neofytou [35], Dos Santos et al. [5] and Kefayati & Huilgol [9] as references, which reported that such configuration provided reliable results regarding the velocity profiles and the morphology of the yielded and unyielded surfaces of the fluid. The boundary conditions set for the problem (see Fig. 1 for reference) are prescribed velocity v_0, at the lid (upper), which is defined by the Re number; the remaining boundaries (left, right and bottom) of the cavity are considered as no-slip walls.

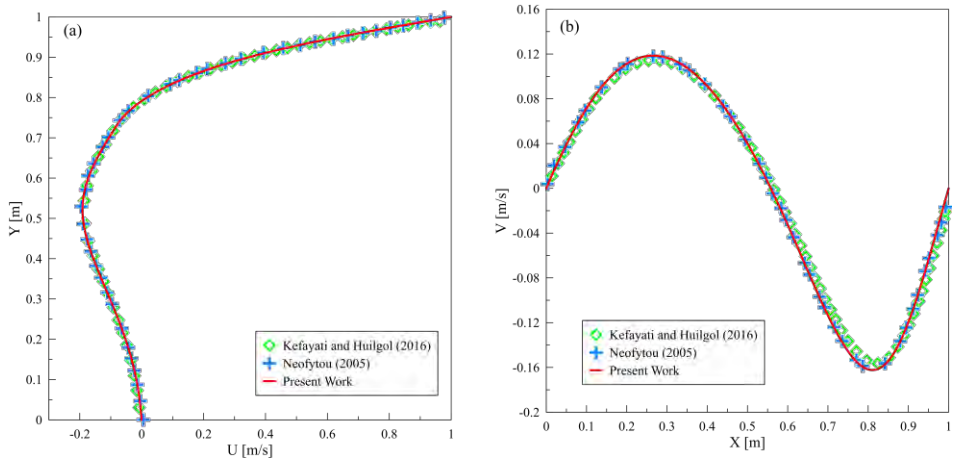


Fig. 2. Velocity profile comparison for model validation: (a) U velocity; (b) V velocity

A verification was performed to ensure that both model and mesh were adequately employed. For this, the u and v velocity profiles along the y and x axis were compared with those from [35] and [9] for Bn = 1 and Re = 100, which are shown in Figure 2. The result shown in Figure 2 shows that both the model and mesh are in accordance with the other studies.

2.4. Design of Experiments for Data Generation

The dataset used to train the artificial neural network was created using Desing of Experiments (DOE) methods with a statistical basis. According to Montgomery & Wiley [36], employing such techniques increases experiment performance and provides high-quality data. Thus, two experimental methods were used to apply the DOE: Central Composite Design (CCD) and Latin Hypercube Sampling (LHS).

The CCD compromises a set of points in the design space, which is defined by the limits of the variables. Those points include 2k factorial model points, where k is the number of factors or variables, axial points, and a central point. As pointed out by Cunegatto et al. [37] and Cunegatto et al. [38], using a CCD provides a general idea of the outputs within the design space. The values for the CCD employed in this work are shown in Table 1 below:

Table 1. Values of the CCD design space.

Variable	Levels				
	Low axial level	Low 2^k value	Central value	High 2^k value	High axial value
Bn	1	2.318	5.5	8.682	10
Re	1	37.465	125.5	213.535	250

For a problem with two variables, such as the one presented here, a Central Composite Design provides nine points. However, as mentioned by Misiulia et al. [39], a surrogate model requires a certain amount of information to understand and capture the relationship between the input and output data. Due to this and based on the suggestion of Yang & Palazzolo [27], the LHS was also employed for the data generation.

According to Stein [40], LHS is a sampling method used to produce input values for function predictions. Since the number of points generated by CCD is fixed, using LHS allows the generation of more sampling points. So, to provide enough data to train the surrogate model, a set of 111 samples was generated using the LHS, resulting in a total of 120 points. Those extra samples were generated considering the points provided by the CCD to avoid overlapping.

2.5. Deep Neural Network (DNN)

The core idea of using artificial neural networks as surrogate models as a predictive tool is to reduce time in preparing and solving traditional CFD models, that is, for subsequent analysis, since it requires the CFD data to learn the patterns. That is, for the algorithm to be able to make reliable predictions, it must learn from some data. Thus, in the current work, CFD data is used to teach the algorithm, and, consequently, the predictions are based on the data used in the learning, much like statistical models that use the available data to make predictions using an equation. In machine learning modeling, it is essential to divide the dataset (collection of CFD results in this case) into training and testing examples; the

first is used to teach the algorithm and the second, which are examples unseen during training, are used to evaluate the model. In the current study, the DNN needs to predict the viscosity contours of the flow inside the lid-driven cavity for a certain combination of Bn and Re numbers, two numerical parameters.

One key characteristic of the current study is that geometry is fixed. For any variable combination, the square cavity remains the same. The only thing that changes is the behavior of the viscosity, which is influenced by the input parameters. Knowing such information is crucial in defining the architecture of the neural network. For example, in the work of Thuerey et al. [21], many geometry configurations are studied, so the DNN must receive the geometry information to predict the desired outcome, which, in their case, is an image. Thus, the architecture employed by the authors was a Convolutional Neural Network (CNN).

As previously mentioned, two numerical parameters define the problem and are used as the input parameters for the neural network. Thus, the DNN should use the information and convert it to the output, which is the viscosity contour. Such a process can be achieved by using an architecture known as encoder-decoder. According to Minaee et al. [41], the encoder-decoder model can learn to map data from input to output using two stages: the encoder, which compresses the input data into a latent-space representation, and the decoder, which uses the latent-space representation to predict the output. The encoder-decoder architecture used in the present work is shown in Figure 3.

The neural network was built in Python computational language by using the TensorFlow [42] and Keras [43] libraries. As shown in Figure 3, each layer in the architecture is labeled as 'Dense', the denomination used in Keras library for fully connected layers, meaning that the neurons in a current layer are connected to the ones in the previous layer. The activation function used in the current work for such layers is the Rectified Linear Unit (ReLU). Also, the values under each layer represent the number of neurons within it. The architecture shows a symmetric behavior about the latent-space layer, as stated by Géron [44], in a way that the encoder gradually reduces the input data to create a compact representation in the latent-space layer. Then, the decoder rebuilt the compact representation, progressively expanding the dimension. The output, also a fully connected layer, is expanded to the size of the desired image, which in this case is 224x224x3, resulting in over 150 thousand neurons that carry the information of the image. Then, the image is recreated by reshaping the output layer into a shape of 224x224 pixels and three-color channels.

As mentioned in Section 2.4, the dataset was built by CFD simulations of the points provided by the DOE methods. Then, the viscosity images were collected and saved into a folder. A data frame containing the input variables, image type, and image directory was created to manipulate the data. Since the original shape of the image differs from 224x224 pixels, the images were resized using the OpenCV library [45].This library was also used to read the images from the folder and transform them into an array with the NumPy library [46].

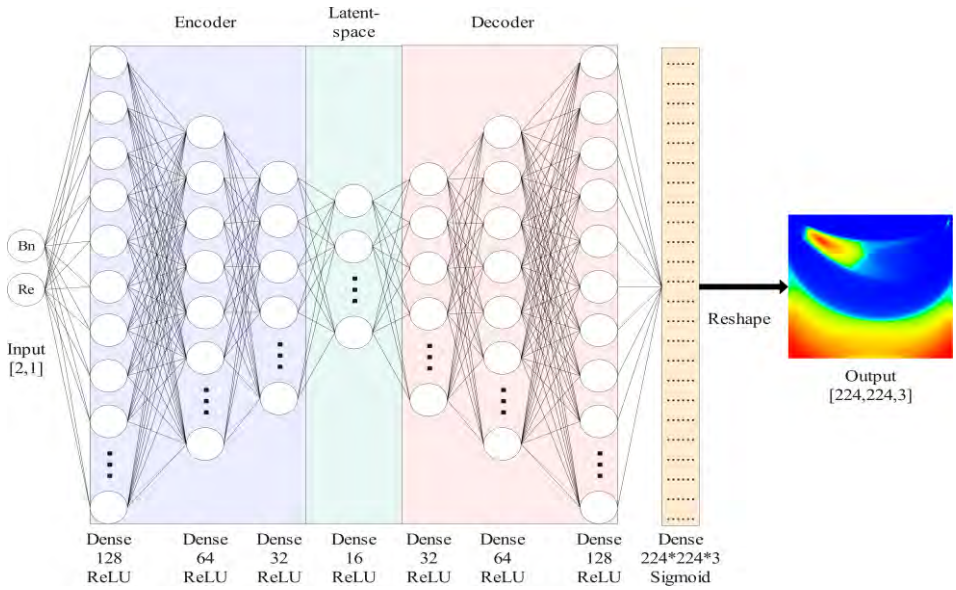


Fig. 3. Encoder-decoder neural network architecture

A crucial part of the data treatment is the data scaling. Machine learning algorithms have issues in their performance when the data have different scales [44]. For example, the Re numbers used in this work vary from 1 to 250, while the Bn number ranges from 1 to 10, which is a great difference between them. So, both input and output data were scaled to perform well. For the input values (Bn and Re), a min-max scaling was used (Eq. (9)), resulting in a range of 0 to 1 for both parameters. As for the output images, the main reason that they were transformed into an array is that each pixel value can be manipulated, allowing its scaling. Since the colors from an image vary from 0 to 255, the scaling was done by dividing each pixel value by 255, resulting in a range of 0 to 1 for the output image. This range was also the reason for using the Sigmoid activation function at the output layer of the neural network since it ranges from 0 to 1.

$$x_i' = \frac{x_i - min\ (x)}{max(x) - min\ (x)} \tag{9}$$

where x_i' is the single scaled variable, x_i is the single variable, min(x) is the minimum value of the variable x and max(x) is its maximum value. In the previous section, some hyperparameters were mentioned, such as the activation functions, the number of layers, and the number of neurons in each layer. However, a few more hyperparameters are needed to provide the complete setup of the employed neural network.

- Train/test split: The dataset was randomly divided to feed the neural network, with 80% used for training and the remaining 20% used for testing.
- Optimizer: The optimizer is an algorithm that helps the neural network adjust its weights to minimize the loss during training. The optimizer chosen in this work is Adam (Adaptive Momentum Estimation). The Adam optimizer has its hyperparameters, the momentum decay and scaling decay, which were set to 0.9 and 0.999, respectively.

- Learning rate: This hyperparameter is related to the optimizer and determines how quickly the weights are adjusted. Since a low value may cause the training process to be slow, and a high value may cause divergence, a tuning was performed, which returned 0.007 as an adequate value.
- Batch size: it defines the number of training samples used in each iteration of weight adjustment. Tuning was also performed, and a value of 8 batches was adopted.
- Number of Epochs: This defines the number of times the training data passes through the neural network during training. One epoch is complete when all the training data, i.e., batches, pass through the neural network once. In this work, 150 epochs were used.

As mentioned above, the optimizer minimizes the loss function when the neural network weights are adjusted during training. The loss function evaluates the neural network's performance, sharing a similar trait as the residuals in CFD, by comparing the predicted values with the CFD data at each epoch. Among the loss functions utilized in machine learning, the Mean Squared Error (MSE) was chosen for this study since the DNN predicts the scalar value of each pixel in the image. The MSE is mathematically expressed by Equation (10):

$$MSE = \frac{1}{N}\sum_{i,j,k=1}^{N}\left(y_{ijk} - \widehat{y_{ijk}}\right)^2 \tag{10}$$

where N represents the total number of pixels, y is the predicted value, $\hat{y}$ is the CFD value, i represents the index of the image length, j is the height index and k is the color channel index.

3. Results

This section thoroughly examines the problem as a physical phenomenon, focusing on the viscosity field and the morphology of yield and unyielded regions along the flow. In the sequence, the performance of the DNN is discussed, where comparisons between predicted and CFD viscosity contours are performed, along with the training metrics. Lastly, we explore using masks to generate the yield surfaces, i.e., the morphology of yielded and unyielded regions, using the predicted viscosity contours as a basis.

3.1. Viscosity and Yield Stress Physics

Before diving into the problem itself, a brief analysis of Re and Bn numbers is performed. The Reynolds number (Eq. (8)) is one of the most important dimensionless numbers in fluid dynamics, as it predicts the behavior of a flow by calculating the ratio between the inertial and viscous forces [47]. As the Reynolds number increases, the influence of the viscous force becomes less significant, which makes it way more challenging to hold the fluid's disturbance, resulting in more momentum in the flow. As observed, the viscosity, i.e., viscous force, is essential in defining a fluid's behavior. This property becomes more complex regarding viscoplastic fluids (Bingham plastics) because it is non-constant and dependent on yield stress. The connection between the viscous force and yield stress is found in the Bingham number (Eq. (7)), representing the ratio between yield and viscous stresses [48]. So, as the Bingham number increases, the stress levels required to yield the

material are higher. Conversely, the decrease in Bn makes the fluid yield more easily, even behaving as Newtonian if Bn = 0. So, by analyzing Equations (7) and (8), it's essential to notice that the only parameters not interchangeable between Bn and Re are τ_0 and ρ, hence why those properties are the ones that define the dimensionless numbers in this work, as mentioned in Section 2.

Returning to the lid-driven cavity problem, Figure 4 presents viscosity contours for different combinations of Re and Bn numbers. Just as a matter of convenience, the viscosity values for each image were scaled from 0 to 1 using the min-max scaling (Eq. (9)), where the red color indicates a very viscous zone, and the blue color indicates a zone with low viscosity. As observed, the main characteristic of the problem is the presence of two distinct viscous regions, which, according to Bui et al. [12], are called the dead zone at the bottom and the moving rigid zone at the upper central region of the cavity. For a low Reynolds number, the viscosity is symmetrically distributed, as the inertial forces are balanced. The moving rigid zone tends to concentrate on the left side for higher Reynolds numbers. In contrast, the dead zone is nearly unaffected by the Reynolds number.

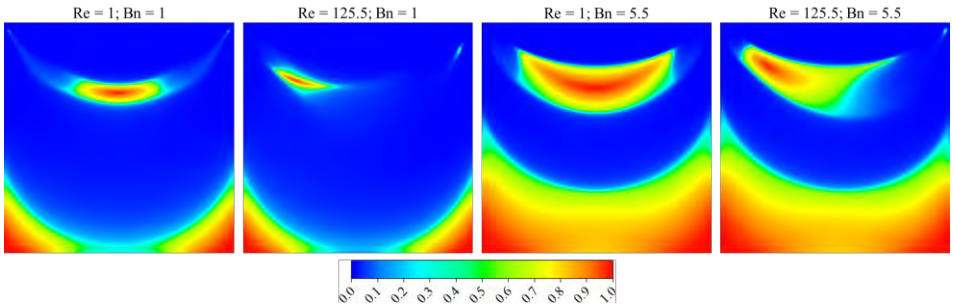


Fig. 4. Dimensionless viscosity contours for different Reynolds and Bingham numbers

Those two regions are developed due to fluid movement inside the cavity, shown in the form of velocity contours in Figure 5. As the fluid flows from left to right, it forms a vortex characterized by unyielded fluid in rigid body motion. The position of the vortex changes as the Reynolds number increases, moving to the right side of the cavity due to the increase in the momentum when the fluid hits the wall, quite the opposite of the moving rigid zone in the viscosity contours. Consequently, the vortex influences the moving rigid zone, which has its formation beside it. However, when considering the Bingham number, the flow becomes slower as the fluid is more rigid, which alters the position and size of the vortex, which is the case for the development of larger moving rigid zones. As for the dead zone, it is formed due to the low movement of the fluid at the bottom of the cavity, as it is far from the motion source (lid). In addition, its size slightly decreases from the augment of Re but increases as Bn grows.

Another important result that can be extracted from viscoplastic flows is its morphology, characterized by the unyielded and yielded regions and the flow aspect when under and above the fluid's yield stress, respectively. Generally, this information is obtained by an iso-surface, using either the critical shear rate for Herschel-Bulkley modeling or the yield stress as a threshold, where the yielded region is white and the unyielded is black. Figure 6 shows the morphology of the cases analyzed in Figures 4 and 5.

In this work, a critical shear rate of 0.05 was used as the input for the Herschel-Bulkley model and, subsequently, as the threshold of the iso-surfaces. This representation is relatable to the viscosity contours, where comparing the unyielded (black) zones with the viscous zones in the viscosity contours is possible. Despite the viscosity contours providing the overview of the property, it does not tell exactly where the fluid yields, hence why the morphology representation is commonly found in the literature, as it precisely shows that information. Due to the similarity between both viscosity contours and morphology, the same analysis regarding the formation of the unyielded zones done previously also applies here, and, in terms of computational vision, the morphology can be characterized as the mask of the viscosity contour.

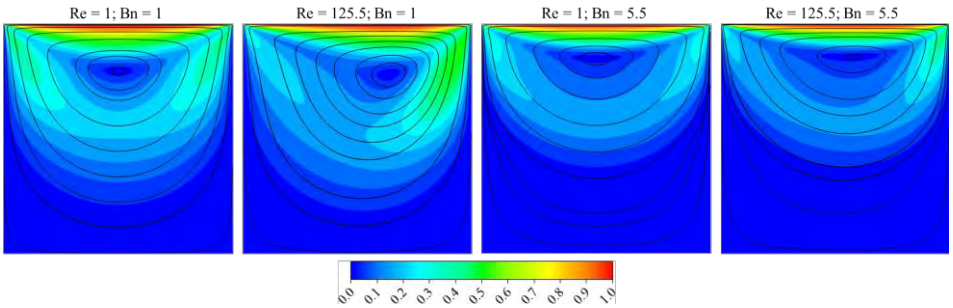


Fig. 5. Dimensionless velocity contours and streamlines for different Reynolds and Bingham numbers

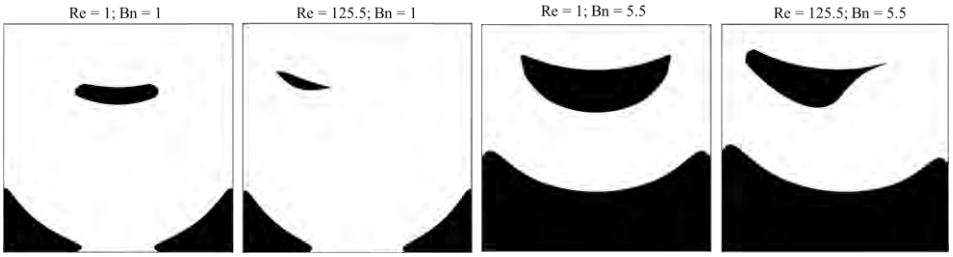


Fig. 6. Morphology of the flow for different Reynolds and Bingham numbers.

3.2. DNN Performance

As mentioned in Section 2, MSE was employed as the loss function and as a measure of the accuracy of the encoder-decoder neural network in predicting the viscosity fields. The MSE quantifies the average squared difference between predicted and CFD values, and a lower MSE means a better alignment between the data.

In the tests performed in this work, the model demonstrated satisfactory MSE values on both training and testing datasets. The MSE reached approximately 0.0015 for the training set, a value good enough to showcase the network's ability to learn and adapt to the training data. As for the testing set, the MSE was around 0.002, indicative of the model's generalization performance to unseen data. Figure 7 illustrates the training and testing loss over epochs during training to represent the neural network's learning progress visually. The x-axis represents the training epochs, while the y-axis depicts the corresponding loss (MSE) values.

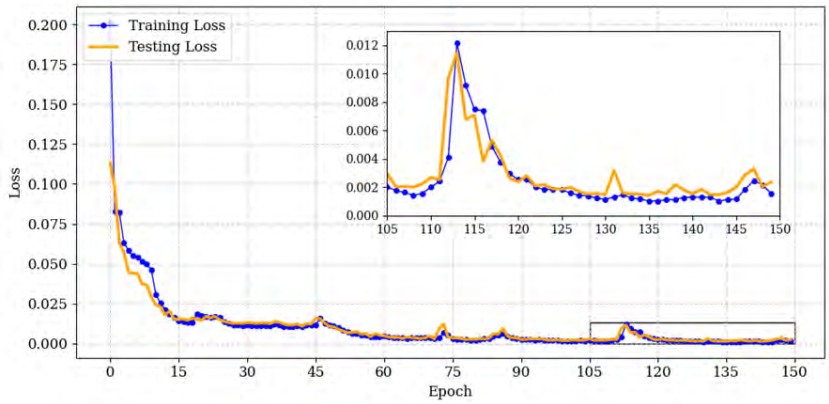


Fig. 7. Training process of the neural network

The training loss curve (blue) demonstrates a steady decrease over the initial epochs, indicative of the model learning from the training data. However, as the training progresses, the loss presents fluctuations, slowing the training a bit, although still decreasing its value. The zoomed section in Figure 7 presents a more detailed examination of the model's performance within a specific range of epochs, from 105 to 150, highlighting the network's behavior during the final training phase. The testing loss curve (orange), which evaluates the model's performance on unseen data, also presents a similar trend, affirming the generalization ability of the deep neural network.

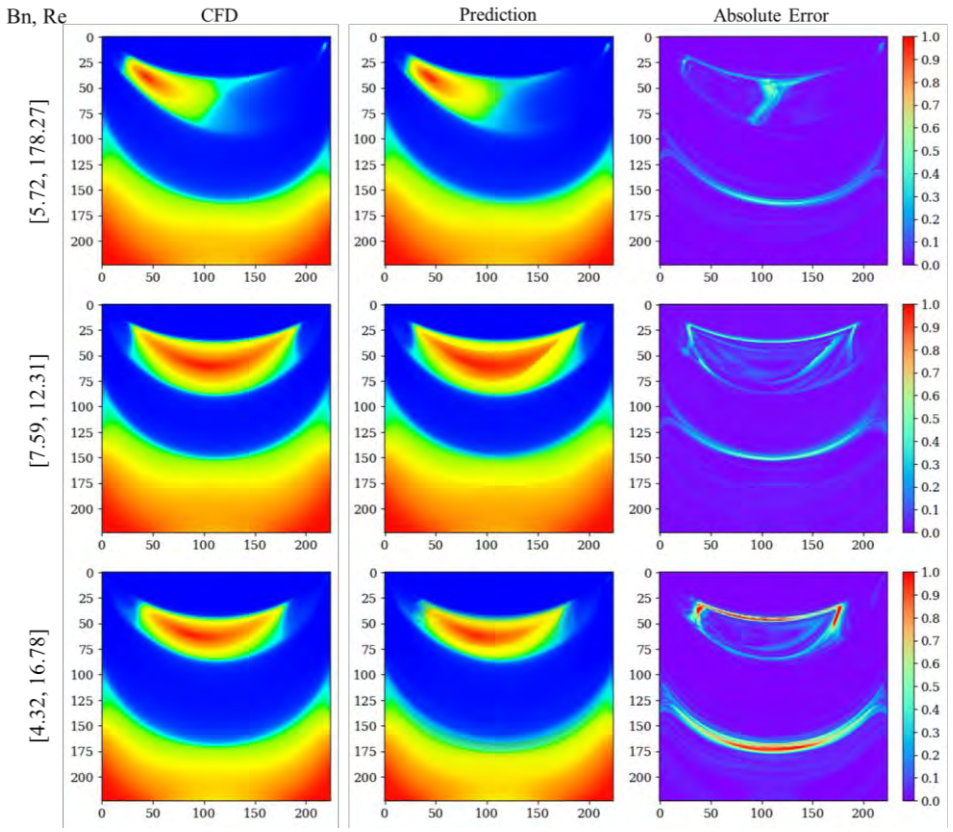
To bring a better understanding of the model's capability to predict the viscosity fields, Figure 8 shows the visual representation of the CFD fields and the corresponding prediction of the viscosity fields (scaled from 0 to 1), alongside with the difference (absolute error) between the images for five different samples of the training set.

Comparing CFD and model viscosity fields can highlight areas of agreement and discrepancy between the predicted and actual values. Simultaneously, the absolute error image portrays the spatial distribution of errors, which is the absolute difference of the pixels, accentuating regions where the model either excels or encounters difficulties. Overall, looking at the images side by side and observing the model's capability to capture and reproduce the actual phenomena is possible, providing reliable predictions.

It is important to emphasize that all the original images were resized to a smaller resolution, from 1600x1600 to 224x224, to provide quicker training for the model and reduce its computational cost. However, the tradeoff for lowering the resolution is losing information from the original image (high resolution). Thus, since the model did not account for the missed information, the predictions presented a higher discrepancy, resulting in differences in the average error plots in Figure 8, especially in the regions where the viscosity gradients are present. Overall, the results obtained by the model are adequate and provide a good overview of the viscosity field behavior for a Bingham fluid flow inside the lid-driven cavity. However, the current setting is limited, as only 120 images were used in the training, and the predictions present some errors in delicate regions, which might influence the pos-processing, especially when the flow morphology is extracted. Another limitation of the current model is that the exact (real) viscosity values for each pixel (node) are not considered, only the color value itself. Still, the morphology

can be extracted from the current results. As mentioned in the last section, the yielded and unyielded regions are affected by the viscosity field behavior, and the prediction errors might propagate into the computational domain. In this section, we use a mask, i.e., a threshold value, to separate regions on an image to capture the shapes of the yielded and unyielded regions. Since the exact values of the strain rate and stress are not present, the creation of the mask relies on defining a color threshold for the predicted viscosity fields.

From the RGB prediction image, the primary reference for the mask is the blue color, which represents a low viscosity in the viscosity fields, indicating a region where the fluid is yielded. So, the task is to find the threshold separating the blue color from the others to create a binarized image (black and white) representing the morphology. So, for this, the blue channel of the predicted viscosity field image serves as the basis for creating the binary mask. A thresholding algorithm was applied, where the intensity of the pixels was tested from 0 to 255, and a pixel intensity of 110 provided the best results. Thus, values over 110 are classified as yielded zones (white), while those below the threshold represent unyielded regions (black). Figure 9 shows the resulting mask, the predicted viscosity field, the CFD data, and the difference between them, considering the same examples in Figure 9.



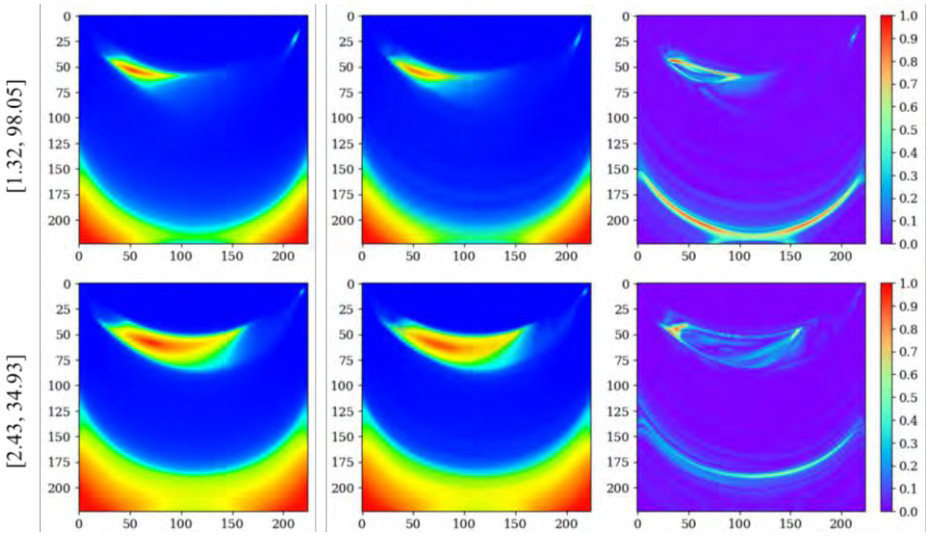


Fig. 8. Viscosity field predictions and absolute error for five testing samples

Based on the results shown in Figure 9, it is possible to confirm that the model predictions are reliable. Still, using masks to identify the yielded and unyielded zones is also adequate. The yielded zones are depicted in white, while the unyielded regions are represented in black. This binary mask offers an intuitive and easily interpretable fluid morphology predicted by the neural network. Also, despite the absolute differences presented in Figure 9, the morphology was not significantly affected, resulting in accurate representations of the real phenomena, as highlighted by the different images. However, a critical piece of information should be considered. Depending on the colors and intensity of the predicted image, the threshold to generate the mask should change. Despite being simple and proven to be a reliable way to reproduce the flow's morphology, it is essential to apply it carefully, as the physical values are not used since the model did not calculate them to generate consistent predictions.

4. Conclusions

In the present study, the lid-driven cavity problem with viscoplastic liquids was revisited by coupling Computational Fluid Dynamics (CFD) results and artificial neural networks to reproduce and predict the shape of yielded/unyielded regions for different Bingham (Bn) and Reynolds (Re) numbers. The dataset was created via Design of Experiments (DOE), where the samples were generated using the Central Composite Design and Latin Hypercube Sampling techniques. Those samples were simulated via CFD, which provided the images of the viscosity fields and the binary images of the flow's morphology for the training and testing of the artificial neural network. The chosen network architecture for the task was an encoder-decoder, which encoded the given Bn and Re and decoded them into the corresponding viscosity field.

Before the network training, the CFD modeling was evaluated, and the comparison with the literature showed enough agreement to provide the data to train the neural network. The training was evaluated by the Mean Squared Error (MSE) metric, which compared the values for each pixel between the predicted and CFD images. A further approach to the

problem was also explored by using the predicted viscosity fields to create binary images representing the flow's morphological behavior. In this approach, the use of masks to separate the yielded and unyielded regions was proposed. This involved the extraction of the adequate color channel and, later, defining a threshold intensity to separate the pixels.

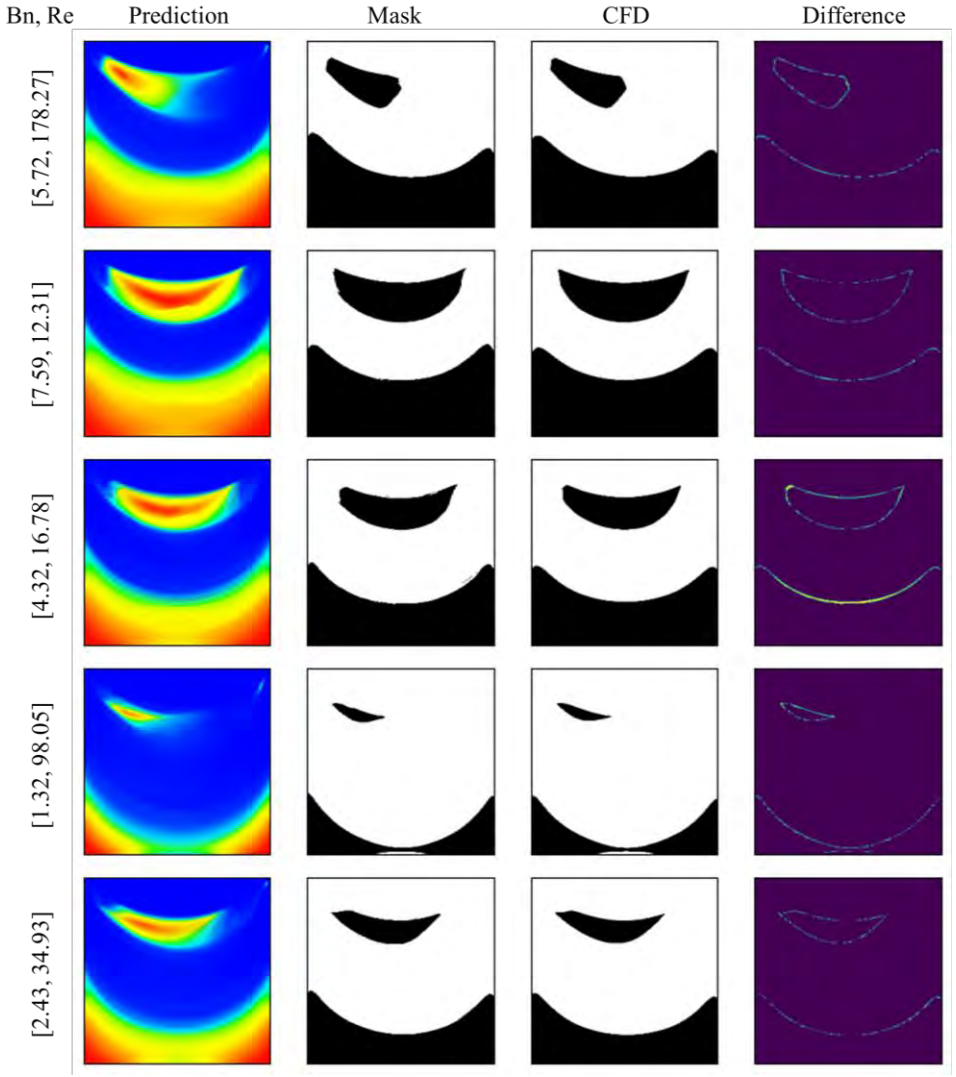


Fig. 9. Generated masks from the predicted viscosity fields for yielded and unyielded regions

As for the results of this study, they provided insights into the effectiveness of an encoder-decoder like neural network architecture in predicting viscosity fields. The quantitative analysis, measured by Mean Squared Error (MSE), showed a robust performance during training and validation, indicating the model's remarkable generalization capability. Such performance resulted in solutions that agreed with the CFD data, providing reliable predictions of viscosity fields for different flow configurations and allowing post-processing to extract the data regarding the flow's morphology. This feature was proposed

by creating binary images from the blue channel of the predicted image, which allowed a clear visual interpretation and highlighted the yielded and unyielded zones of the fluid. These binarized images are interesting in the analysis of viscoplastic flows, as they reveal crucial information about the fluid behavior. Thus, the proposed masks originating from the model's prediction provided a valid alternative for post-processing the results of the current model since the physical values were not considered. Despite the absence of such information, the resulting masks adequately represented the phenomenon, as the differences from the CFD data were minor.

It shall be reinforced that the current model was developed for a specific case test, but could be applied to other flows and geometries, such as flows in contractions and expansions. As observed in this study, the encoder-decoder architecture proved to be a versatile way to model problems with different types of input and output by transforming and associating the information provided by each source. This further opens new perspectives of fluid modeling by coupling intelligent systems with CFD to create fast and reliable solutions for engineering problems.

Acknowledgement

The authors acknowledge the financial support of the Brazilian agencies CAPES, CNPq, and FAPERGS. E.H.T. Cunegatto has a PhD scholarship funded by CAPES (Code 001). F.S.F. Zinani and S.J. Rigo are CNPq grant holders (311444/2021-0 and 305635/2021-2).

References

[1] Souza Mendes PR, Dutra ESS. Viscosity function for yield-stress liquids. Appl Rheol. 2004;14:296–302. https://doi.org/10.1515/arh-2004-0016
[2] Bingham EC. Fluidity and plasticity. New York: McGraw-Hill; 1922.
[3] Chhabra RP, Richardson JF. Non-Newtonian flow and applied rheology. Elsevier; 2008. https://doi.org/10.1016/B978-0-7506-8532-0.X0001-7
[4] Frey S, Silveira FS, Zinani F. Stabilized mixed approximations for inertial viscoplastic fluid flows. Mech Res Commun. 2010;37:145–52. https://doi.org/10.1016/j.mechrescom.2010.01.005
[5] dos Santos DDO, Frey S, Naccache MF, de Souza Mendes PR. Numerical approximations for flow of viscoplastic fluids in a lid-driven cavity. J Nonnewton Fluid Mech. 2011;166:667–79. https://doi.org/10.1016/j.jnnfm.2011.03.004
[6] Syrakos A, Georgiou GC, Alexandrou AN. Performance of the finite volume method in solving regularised Bingham flows: Inertia effects in the lid-driven cavity flow. J Nonnewton Fluid Mech. 2014;208–209:88–107. https://doi.org/10.1016/j.jnnfm.2014.03.004
[7] Papanastasiou TC. Flows of materials with yield. J Rheol (N Y N Y). 1987;31:385–404. https://doi.org/10.1122/1.549926
[8] Syrakos A, Georgiou GC, Alexandrou AN. Cessation of the lid-driven cavity flow of Newtonian and Bingham fluids. Rheol Acta. 2016;55:51–66. https://doi.org/10.1007/s00397-015-0893-4
[9] Kefayati GHR, Huilgol RR. Lattice Boltzmann method for simulation of mixed convection of a Bingham fluid in a lid-driven cavity. Int J Heat Mass Transf. 2016;103:725–43. https://doi.org/10.1016/j.ijheatmasstransfer.2016.07.102
[10] Mahmood R, Kousar N, Yaqub M, Jabeen K. Numerical simulations of the square lid-driven cavity flow of Bingham fluids using nonconforming finite elements coupled with a direct solver. Adv Math Phys. 2017;2017. https://doi.org/10.1155/2017/5210708

[11] Thohura S, Molla MM, Sarker MMA. Bingham fluid flow simulation in a lid-driven skewed cavity using the finite-volume method. Int J Comput Math. 2020;97:1212–33. https://doi.org/10.1080/00207160.2019.1613527
[12] Bui CM, Ho ANT, Nguyen XB. Flow behaviors of polymer solution in a lid-driven cavity. Polymers (Basel). 2022;14. https://doi.org/10.3390/polym14122330
[13] Ferrari MA, Franco AT. Exploring the periodic behavior of the lid-driven cavity flow filled with a Bingham fluid. J Nonnewton Fluid Mech. 2023;316. https://doi.org/10.1016/j.jnnfm.2023.105030
[14] Ferrari MA, Franco AT. The steady and unsteady regimes in a cubic lid-driven cavity with viscoplastic fluid solved with the lattice Boltzmann method. J Nonnewton Fluid Mech. 2024;325. https://doi.org/10.1016/j.jnnfm.2024.105198
[15] Le Clainche S, Ferrer E, Gibson S, Cross E, Parente A, Vinuesa R. Improving aircraft performance using machine learning: A review. Aerosp Sci Technol. 2023;138. https://doi.org/10.1016/j.ast.2023.108354
[16] Calzolari G, Liu W. Deep learning to replace, improve, or aid CFD analysis in built environment applications: A review. Build Environ. 2021;206. https://doi.org/10.1016/j.buildenv.2021.108315
[17] Hemmasian AP, Ogoke F, Akbari P, Malen J, Beuth J, Barati Farimani A. Surrogate modeling of melt pool temperature field using deep learning. Addit Manuf Lett. 2023;5. https://doi.org/10.1016/j.addlet.2023.100123
[18] Peng JZ, Liu X, Aubry N, Chen Z, Wu WT. Data-driven modeling of geometry-adaptive steady heat conduction based on convolutional neural networks. Case Stud Therm Eng. 2021;28. https://doi.org/10.1016/j.csite.2021.101651
[19] Hua Y, Yu CH, Zhao Q, Li MG, Wu WT, Wu P. Surrogate modeling of heat transfers of nanofluids in absorbent tubes with fins based on deep convolutional neural network. Int J Heat Mass Transf. 2023;202. https://doi.org/10.1016/j.ijheatmasstransfer.2022.123736
[20] Hua Y, Wang ZQ, Yuan XY, Bai Li Y, Wu WT, Aubry N. Estimation of steady-state temperature field in multichip modules using deep convolutional neural network. Therm Sci Eng Prog. 2023;40. https://doi.org/10.1016/j.tsep.2023.101755
[21] Thuerey N, Weißenow K, Prantl L, Hu X. Deep learning methods for Reynolds-averaged Navier–Stokes simulations of airfoil flows. AIAA J. 2020;58:25–36. https://doi.org/10.2514/1.J058291.
[22] Li C, Yuan P, Liu Y, Tan J, Si X, Wang S, et al. Fast flow field prediction of hydrofoils based on deep learning. Ocean Eng. 2023;281:114743. https://doi.org/10.1016/j.oceaneng.2023.114743.
[23] Huang L, Pena B, Liu Y, Anderlini E. Machine learning in sustainable ship design and operation: A review. Ocean Eng. 2022;266:112907. https://doi.org/10.1016/j.oceaneng.2022.112907.
[24] Gharleghi R, Sowmya A, Beier S. Transient wall shear stress estimation in coronary bifurcations using convolutional neural networks. Comput Methods Programs Biomed. 2022;225:107013. https://doi.org/10.1016/j.cmpb.2022.107013.
[25] Takbiri S, Kazemi M, Takbiri-Borujeni A, McIlvain J. A deep learning approach to predicting permeability of porous media. J Pet Sci Eng. 2022;211:110069. https://doi.org/10.1016/j.petrol.2021.110069.
[26] Du B, Lund PD, Wang J. Combining CFD and artificial neural network techniques to predict the thermal performance of all-glass straight evacuated tube solar collector. Energy. 2021;220:119713. https://doi.org/10.1016/j.energy.2020.119713.
[27] Yang J, Palazzolo A. Deep convolutional autoencoder augmented CFD thermal analysis of bearings with inter pad groove mixing. Int J Heat Mass Transf. 2022;188:122639. https://doi.org/10.1016/j.ijheatmasstransfer.2022.122639.

[28] Kim MH, Park HJ. Application of artificial neural networks using sequential prediction approach in indoor airflow prediction. J Build Eng. 2023;69:106319. https://doi.org/10.1016/j.jobe.2023.106319.
[29] Sang J, Pan X, Lin T, Liang W, Liu GR. A data-driven artificial neural network model for predicting wind load of buildings using GSM-CFD solver. Eur J Mech B Fluids. 2021;87:24–36. https://doi.org/10.1016/j.euromechflu.2021.01.007.
[30] Hussain SM, Mahat R, Katbar NM, Ullah I, Varun Kumar RS, Prasannakumara BC, et al. Artificial neural network modeling of mixed convection viscoelastic hybrid nanofluid across a circular cylinder with radiation effect: Case study. Case Stud Therm Eng. 2023;50:103487. https://doi.org/10.1016/j.csite.2023.103487.
[31] Muravleva E, Oseledets I, Koroteev D. Application of machine learning to viscoplastic flow modeling. Phys Fluids. 2018;30:5058127. https://doi.org/10.1063/1.5058127.
[32] Kumar A, Ridha S, Narahari M, Ilyas SU. Physics-guided deep neural network to characterize non-Newtonian fluid flow for optimal use of energy resources. Expert Syst Appl. 2021;183:115409. https://doi.org/10.1016/j.eswa.2021.115409.
[33] Zhang J. Physics-informed neural networks for Bingham fluid flow simulation coupled with an augmented Lagrange method. Appl Math. 2023;3:525–51. https://doi.org/10.3390/appliedmath3030028.
[34] ANSYS Fluent Users Guide. 2023.
[35] Neofytou P. A 3rd order upwind finite volume method for generalised Newtonian fluid flows. Adv Eng Softw. 2005;36:664–80. https://doi.org/10.1016/j.advengsoft.2005.03.011.
[36] Montgomery DC. Design and analysis of experiments. 8th ed. Hoboken: Wiley; 2013.
[37] Cunegatto EHT, Gotardo M, Zinani FSF. Numerical analysis of tube arrangements with one, two, and four degrees of freedom for heat transfer with pseudoplastic fluids. Int J Heat Mass Transf. 2023;208:124080. https://doi.org/10.1016/j.ijheatmasstransfer.2023.124080.
[38] Cunegatto EHT, Zinani FSF, Biserni C, Rocha LAO. Constructal design of passive micromixers with multiple obstacles via computational fluid dynamics. Int J Heat Mass Transf. 2023;215:124519. https://doi.org/10.1016/j.ijheatmasstransfer.2023.124519.
[39] Misiulia D, Elsayed K, Andersson AG. Geometry optimization of a deswirler for cyclone separator in terms of pressure drop using CFD and artificial neural network. Sep Purif Technol. 2017;185:10–23. https://doi.org/10.1016/j.seppur.2017.05.025.
[40] Stein M. Large sample properties of simulations using Latin hypercube sampling. Technometrics. 1987;29:143–51. https://doi.org/10.1080/00401706.1987.10488205.
[41] Minaee S, Boykov Y, Porikli F, Plaza A, Kehtarnavaz N, Terzopoulos D. Image segmentation using deep learning: A survey. 2020.
[42] Abadi M, Agarwal A, Barham P, Brevdo E, Chen Z, Citro C, et al. TensorFlow: Large-scale machine learning on heterogeneous distributed systems. 2015.
[43] Chollet F, et al. Keras. 2015.
[44] Géron A. Hands-on machine learning with Scikit-Learn, Keras, and TensorFlow. 2nd ed. Sebastopol: O'Reilly Media; 2019.
[45] Bradski G. The OpenCV library. Dr Dobb's J Softw Tools. 2000.
[46] Harris CR, Millman KJ, van der Walt SJ, Gommers R, Virtanen P, Cournapeau D, et al. Array programming with NumPy. Nature. 2020;585:357–62. https://doi.org/10.1038/s41586-020-2649-2.
[47] Çengel YA, Cimbala JM. Fluid mechanics: Fundamentals and applications. 3rd ed. New York: McGraw-Hill; 2014.
[48] Zamankhan P, Takayama S, Grotberg JB. Steady displacement of long gas bubbles in channels and tubes filled by a Bingham fluid. Phys Rev Fluids. 2018;3:013302. https://doi.org/10.1103/PhysRevFluids.3.013302.

Blank Page

Research on Engineering Structures & Materials
www.jresm.org
Research Group

Research Article

Numerical simulation, constructal design, and systematic search applied to the geometrical evaluation of hat-stiffened plates under bending

Mariana Alvarenga Alves [1,a], Eduarda Machado Rodrigues [2,b], Vinícius Torres Pinto [2,c], Luiz Alberto Oliveira Rocha [1,2,d], Elizaldo Domingues dos Santos [1,2,e], Liércio André Isoldi [*,1,2,f]

[1]*Graduate Program in Computational Modeling (PPGMC), Federal University of Rio Grande - FURG, Brazil*
[2]*Graduate Program in Ocean Engineering (PPGEO), Federal University of Rio Grande - FURG, Brazil*

Article Info

Article history:

Received 29 Nov 2024
Accepted 03 Jan 2025

Keywords:

Stiffened plates;
Finite element method;
Trapezoidal box-girder;
Maximum deflection;
Central deflection

Abstract

Steel plates have wide structural applications in various engineering sectors due to their combination of lightness, efficiency, and high load-bearing capacity. When stiffeners are added to these structures, the deflections can be significantly minimized. In this study, hat-stiffened plates having box-girder stiffeners with a trapezoidal shape, positioned longitudinally along the plate, are considered to evaluate their influence on the maximum and central deflection of the structure. The analyses in this work are carried out using ANSYS Mechanical APDL software, employing a validated and verified computational model developed with the SHELL281 finite element. Starting from a reference plate without stiffeners, the Constructal Design method was applied, allowing to propose different geometric configurations for plates with longitudinal hat-stiffeners, keeping the total steel volume constant. All these cases were simulated numerically and their results were compared through a Systematic Search technique. Among these 100 different cases investigated, the geometric configuration with 1 hat-stiffener of 250 mm in height and 9.53 mm in thickness achieved the best performance, resulting in a reduction of approximately 86% in maximum and central deflections compared to the reference plate. This highlights its effectiveness in minimizing out-of-plane displacements.

© 2025 MIM Research Group. All rights reserved.

1. Introduction

Steel plates with stiffeners are widely used in the naval and offshore industries, aerospace industry, automotive sector, and civil construction [1]. These are versatile structural components that combine lightness and efficiency with high load-bearing capacity [2]. In this context, the computational modeling has assumed an important role in this field, as commercial software like ANSYS, which is based on the Finite Element Method (FEM), enabling highly accurate numerical analysis of real structures.

On the other hand, the Constructal Design method has proven efficient for the geometric evaluation of engineering problems, including structural engineering. Constructal Design is based on the Constructal theory proposed by Adrian Bejan in 1996, which, in turn, is supported by the Constructal Law, stated as: "For a finite-size flow system to persist in time (to live), its configuration must evolve in such a way that provides greater and greater access to the currents that flow through it" [3]. Therefore, this theory suggests that the generation of flow structures, which are observed throughout nature, can be reasoned

[*]Corresponding author: liercioisoldi@furg.br
[a]orcid.org/0009-0003-4630-5782; [b]orcid.org/0009-0002-1470-4271; [c]orcid.org/0000-0002-0977-5086; [d]orcid.org/0000-0003-2409-3152; [e]orcid.org/0000-0003-4566-2350; [f]orcid.org/0000-0002-9337-3169
DOI: http://dx.doi.org/10.17515/resm2025-555st1129rs

through an evolutionary principle of increasing access to flow over time. Its application requires the definition of constraints, degrees of freedom, and performance indicators, aiming not only to achieve superior configurations but also to understand the effect of the degrees of freedom variation over the performance indicator [3]. From Constructal theory, the shape of the system and the architecture of internal flow do not develop randomly but result from the ongoing pursuit of better performance and, therefore, should evolve over time [3-4]. In the analysis of structural engineering, Bejan and Lorente [3] shows that the structures are minimal volume connections through which stresses 'flow' from components to their neighbors, and that optimal use of mechanical support material is achieved when the maximum allowable stresses are uniformly distributed throughout the available material.

Among the studies that associate computational modeling and Constructal Design for the geometric evaluation of stiffened plates subjected to bending, the following can be highlighted: the application of the Constructal Design method combined with a systematic search technique to optimize I-stiffened plates under bending due to uniformly distributed loading, aiming to minimize the central deflection in these structures [5]; the minimization of maximum and central deflections in stiffened plates by varying the heights of I-shaped stiffeners in the transverse and longitudinal directions [6]; the evaluation of the influence of I-shaped stiffeners oriented at 0° and 45° on the minimization of maximum and central deflection by varying the number of transverse and longitudinal stiffeners (which have the same height) [7]; and the geometric analysis of stiffened steel plates to assess the influence of I or T-shaped transverse reinforcements on mechanical behavior in terms of maximum deflection and von Mises stress [8]."

Most studies addressing stiffened plates use rectangular open-section stiffeners (such as I and T-shaped), which are the most traditional types. However, in the present study, an analysis of plates with trapezoidal box-beam-type stiffeners, also known as hat-stiffened plates, will be conducted. Tharian and Nandakumar [9] emphasize that hat stiffeners have numerous advantages compared to open-section stiffeners, mainly due to their high strength-to-weight ratio and torsional rigidity. Considering the analysis of plates with hat-stiffeners, the following works can be highlighted: Tharian and Nandakumar [10] presented a numerical analysis using FEM to quantify the structural advantages of trapezoidal box-beam stiffeners compared to the open-section stiffeners that are typically used; Pal et al. [11] analyzed the maximum deflection and stress of plates with trapezoidal box-beam stiffeners, adopting different boundary conditions for the plates and varying geometries for the stiffeners while maintaining constant volume; Virág and Szirbik [12] conducted a modal analysis of plates with optimized trapezoidal reinforcements to identify any potentially dangerous frequencies and eliminate failure possibilities in the structure; Tharian and Nandakumar [9] presented a study on the application of a super element for the structural analysis of bunkers made from plates with hat-stiffeners; and Filippatos et al. [13] developed a design for composite aircraft components, in which the structure includes a hat-stiffener to evaluate the structural performance of the composite material, as well as its overall impact on sustainability.

In this sense, the present study purposes the geometric evaluation and optimization of simply supported steel plates with trapezoidal hat-stiffeners under the incidence of a uniformly distributed loading. To do so, computational modeling (FEM by means ANSYS Mechanical APDL 2024 R2), Constructal Design method, and Systematic Search technique were employed, aiming to reduce maximum and central deflections of the hat-stiffened plates. A reference plate with no stiffeners is adopted, from which 30% of its volume is transformed into hat-stiffeners. Since it is kept constant its length and width, the hat-stiffened plates are formed by reducing the thickness of the reference plate and incorporating the stiffeners. With this, it was possible to evaluate geometric configurations

of hat-stiffened plates with up to 5 longitudinal stiffeners. The trapezoidal cross section of the box-beam type hat-stiffeners have an angle of 120°. The thickness of the hat-stiffeners varies from 4.75 mm (3/16 in) to 12.7 mm (1/2 in), while its high ranges between 25 mm and 300 mm.

2. Material and Methods

In this study, it was applied the Constructal Design method together with a Systematic Search technique for the evaluation and optimization of the geometric configurations of the hat-stiffened plates. It is worth mentioning that the Constructal Design is not an optimization method, but a geometric evaluation method. However, when associated with an optimization method, such as a Systematic Search, it becomes responsible for generating the search space (composed of possible geometric configurations), and the optimization method identifies the geometry of the system that leads to its best performance [14]. To use Constructal Design, it is necessary to define restrictions (global or local), degrees of freedom (that vary, respecting the restrictions, to generate the geometries), and performance indicators (that must be maximized or minimized, searching the superior performance) [15].

To numerically simulate the mechanical behavior of the reference and hat-stiffened plates, the ANSYS Mechanical APDL software (version 2024 R2) was used, which is based on the FEM. The finite element SHELL281 was adopted both in the plate as in the stiffeners (such as in Nogueira et al. [6], Pinto et al. [7], and Kucharski et al. [8]), being indicated for thin to moderately-thick plate/shell structures. It has eight nodes with 6 degrees of freedom per node: 3 translations (*Ux, Uy, Uz*) and 3 rotations (θx, θy, θz) [16]. The FEM is typically employed in its displacement formulation for structural analysis, where the unknown displacements are obtained by solving a system of algebraic equations [17], which can be represented as;

$$[K]\{U\} = \{F\} \tag{1}$$

where $[K]$ is the global stiffness matrix, $\{U\}$ is the vector of unknown nodal displacements, and $\{F\}$ is the vector of equivalent nodal forces applied to the system. To ensure that the computational model is adequately defined, validation and verifications were carried out, always comparing the results obtained with those in the literature.

2.1. Case Study

As already mentioned, this study is based on the application of the Constructal Design associated to a Systematic Search technique to analyze simply supported rectangular steel plates with trapezoidal box-beam type hat-stiffeners longitudinally positioned, when submitted to a uniformly distributed out-of-plane load. The goal is to minimize the maximum and central deflections of these hat-stiffened plates. To do so, a reference plate (without stiffeners) is adopted, having length a = 2000 mm, width b = 1000 mm, and thickness t_{rp} = 20 mm. From the reference plate a volumetric fraction ϕ = 0.30 [6-8], i.e. 30% of the total steel volume, is transformed into hat-stiffeners. As the values of a and b are kept constants, the thickness of the hat-stiffened plates is t = 14 mm, which when incorporating the stiffeners, maintain the same total volume of material as the reference plate. As in Refs. [6-8], the A-36 steel is employed, having elasticity modulus E = 200 GPa and Poisson's ratio ν = 0.3. The four edges of the plate and the ends of the stiffeners are considered simply supported. The magnitude of the lateral uniformly distributed loading is 10 kPa. In turn, the geometry of the hat-stiffener is defined in agreement with Anej et al. [18] that indicated an angle of 120° as ideal to improve its mechanical strength. In addition, the stiffeners thickness vary: t_s = 4.75 mm (3/16 in); t_s = 6.35 mm (1/4 in); t_s = 8.00 mm (5/16 in); t_s = 9.53 mm (3/8 in); and t_s = 12.7 mm (1/2 in). Likewise, the stiffeners high

assumes a minimal value of 25 mm with maximum values of 300 mm (1 stiffener), 150 mm (2 and 3 stiffeners), 125 mm (4 stiffeners), and 100 mm (5 stiffeners). From the Constructal Design application, it was generated a total of 100 different geometries of hat-stiffened plates that have the same volume of material. Appendix A presents the dimensions of the stiffeners used in each of these analyses, as well as the maximum and central deflection results obtained in each proposed case.

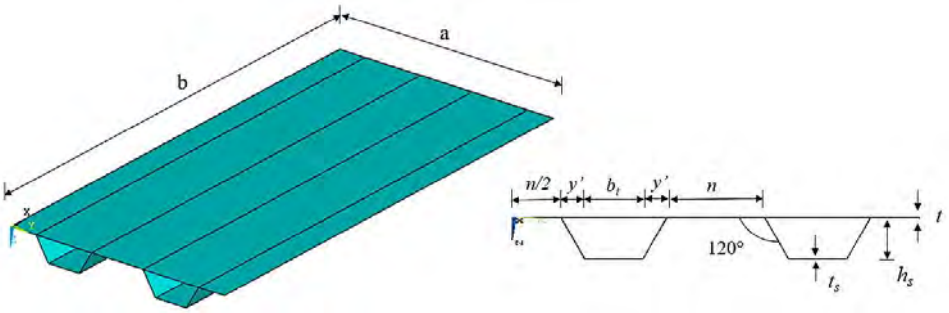


Fig. 1. Schemtaic representation of a hat-stiffened plates with 2 longitudinal stiffeners

Considering a structure composed of multiple hat-stiffened plates, when a plate has only one stiffener, the distance between the stiffener and the plate edge will always be the same on both sides. Starting from two stiffeners, the distance between the stiffener and the plate edge equals half the distance between two stiffeners, as shown in Fig. 1. This is because, when joining multiple plates, the spacing between the stiffeners is always uniform. From Fig. 1, h_s and t_s represent the heightand thickness of the hat-stiffener, respectively; n is the spacing between 2 stiffeners; b_t is the size of the shorter base of the trapezoidal cross-section; and y' is the projection of the stiffener's side onto the y-axis.

3. Results and Discussions

3.1. Computational Model Validation

The computational model validation consisted in the numerical simulation of a stiffened plate experimentally studied by Carrijo et al. [19], as illustrated in Fig. 2.

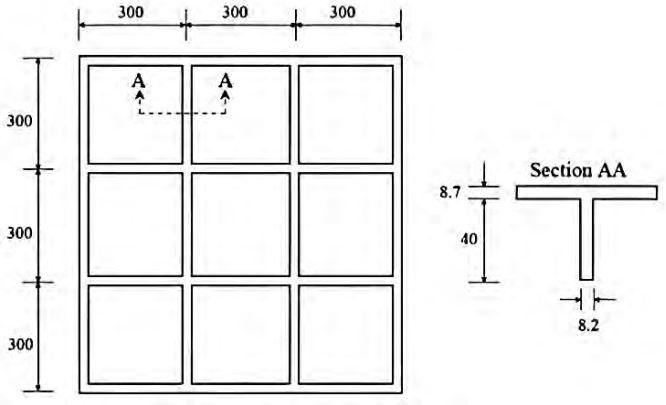


Fig. 2. Geometry of the square plate used in the validation

The square steel plate with eight I-shaped stiffeners equally distributed in both directions across the structure has boundary conditions with all 4 corners simply supported. The

plate was subjected to a uniformly distributed load of 0.96 kPa, and the structure's material has E = 2.5 GPa and ν = 0.36. For this analysis, a converged regular mesh of square SHELL281 finite elements was generated, each with a side length of 2.436 mm. The numerical result obtained for the central deflection was Uz = 6.5075 mm (Fig. 3), while the experimental results from Carrijo et al. [19] is Uz = 6.2200 mm, achieving a relative error of 4.58%, validating the computational model.

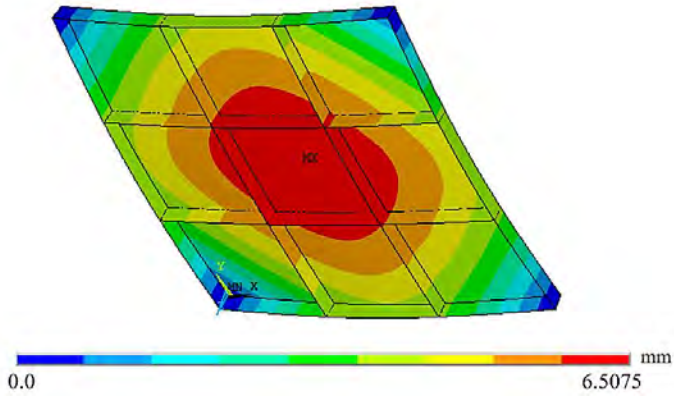


Fig. 3. Displacement distribution for the validation

3.2. Computational Model Verification

First verification was carried out by Tharian and Nandakumar [9], analyzing a rectangular simply supported steel plate with 2 longitudinal hat-stiffeners (Fig. 4). Plate is under an out-of-plane uniformly distributed loading of 10 kPa and has E = 210 GPa and ν = 0.3. For that, the current numerical solution obtained with SHELL281 finite element was compared with those presented by Tharian and Nandakumar [10] with SHELL63 and SHELL93 finite elements.

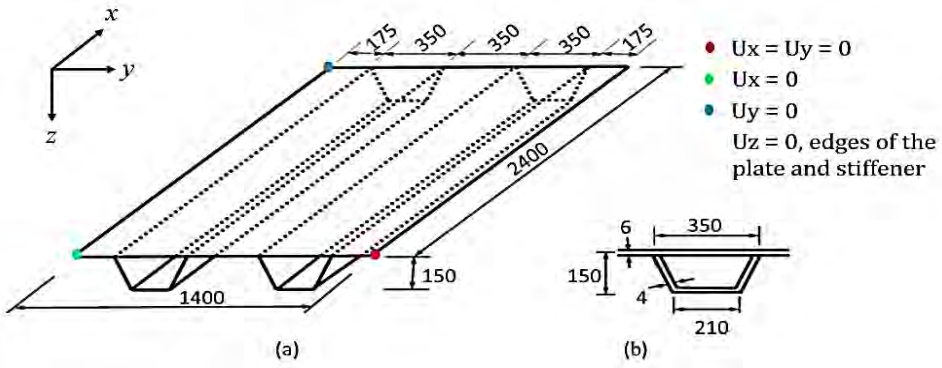


Fig. 4. First verification: (a) hat-stiffened plate dimensions, in mm; and (b) detail of hat-stiffener dimensions, in mm [10]

The spatial discretization was defined through a mesh convergence test, considering square finite elements with 7 different sizes (varying from 5 mm to 150 mm). In Fig. 5 one can note that from mesh with 20 mm (15,600 finite elements) occurs a stabilization for the maximum deflection value. Hence, to guarantee a solution independent of the spatial discretization, it was adopted the mesh with size of 10 mm (60,240 finite elements). A maximum deflection of 0.7295 mm was reached in the present study, while values of

0.7198 mm (SHELL63) and 0.7214 mm (SHELL93) was presented by Tharian and Nandakumar [10].

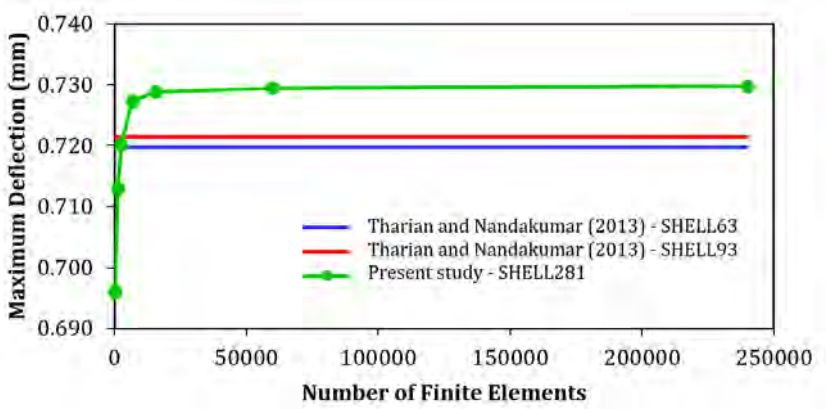


Fig. 5. Mesh convergence test for the first verification

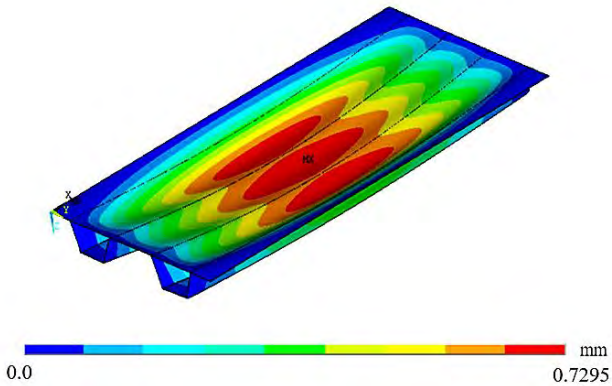


Fig. 6. Displacement distribution for the first verification

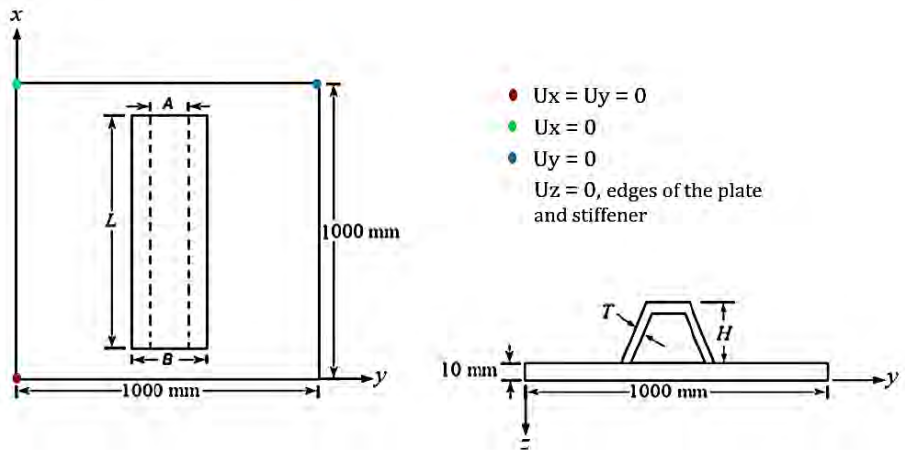


Fig. 7. Hat-stiffened dimensions for the second verification [11]

Therefore, the computational model was verified by relative differences of 1.35% and 1.12%, respectively. Figure 6 depicted the displacement distribution obtained in the

present study, in which it is possible to identify that the maximum structural deflection occurs in the center of the hat-stiffened plate.

Table 1. Hat-stiffener dimensions for the second verification, in mm [11]

Case	Thickness (T)	Shorter Base (A)	Longer Base (B)	Height (H)	Length (L)
1	2	35	60	65	955.90
2	3	35	60	65	637.26
3	4	35	60	65	477.95
4	5	35	60	65	382.36
5	6	35	60	65	318.63
6	2	40	60	65	932.78
7	3	40	60	65	621.86
8	4	40	60	65	466.39
9	5	40	60	65	373.11
10	6	40	60	65	310.93
11	2	40	65	70	878.09
12	3	40	65	70	585.39
13	4	40	65	70	439.04
14	5	40	65	70	351.23
15	6	40	65	70	292.70
16	2	40	60	70	881.92
17	3	40	60	70	587.95
18	4	40	60	70	440.96
19	5	40	60	70	352.77
20	6	40	60	70	293.97
21	2	35	65	65	950.02
22	3	35	65	65	633.35
23	4	35	65	65	475.01
24	5	35	65	65	380.01
25	6	35	65	65	316.67

The second verification was performed with a simply supported square steel plate having a centered hat-stiffener (Fig. 7), earlier investigated by Pal et al. [11]. A uniform distributed loading of 1 kPa is applied perpendicularly to the plate, which in turn has E = 200 GPa and ν = 0.3 as its material mechanical properties. It is important to explain that the hat-stiffener has variable dimensions but keeping constant its total volume of 320,000 mm^3. Table 1 describes the hat-stiffener dimensions for the 25 geometric configurations analyzed. As in the first verification, a mesh convergence test was developed with square finite elements with 7 different sizes (varying from 5 mm to 150 mm) and taken into account the Case of Table 1. In Fig. 8 it is possible to observe a stabilization of the maximum deflection value from the mesh with size of 40 mm (796 finite elements), being chosen for the numerical simulations the mesh with size of 10 mm (11,928 finite elements).

The obtained results for the maximum deflection in the present study (with SHELL281 finite element) for the 25 cases of Table 1 are shown in Table 2 and Fig. 9, in comparison to those obtained by Pal et al. [11] that used SHELL181 and BEAM3 finite elements, respectively, for the plate and stiffener. One can infer in Fig. 9 a good agreement in a qualitative way between the maximum deflection result of the present study and that of Pal et al. [11], for each case. In general, from Table 2, quantitatively an average relative difference of 3.30% was achieved for the 25 cases and maximum relative differences around 5% were identified. Therefore, it is possible to consider that the computational model was proper verified.

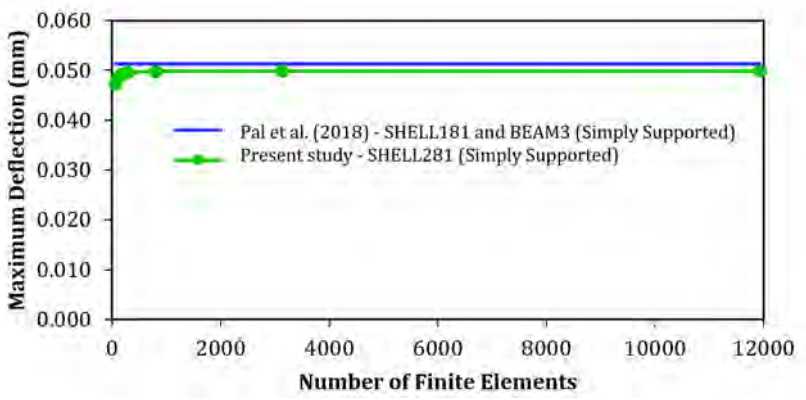


Fig. 8. Mesh convergence test for the second verification

Table 2. Maximum deflection, in mm, for cases of Table 1

Case	Pal *et al.* [11]	Present Study	Relative Difference (%)
1	0.0513	0.0499	-2.73
2	0.0908	0.0936	3.08
3	0.1279	0.1338	4.61
4	0.1506	0.1580	4.91
5	0.1647	0.1732	5.16
6	0.0508	0.0498	-1.97
7	0.0939	0.0970	3.30
8	0.1306	0.1367	4.67
9	0.1527	0.1603	4.98
10	0.1664	0.1750	5.17
11	0.0505	0.0501	-0.79
12	0.1008	0.1046	377
13	0.1365	0.1432	4.91
14	0.1572	0.1653	5.15
15	0.1700	0.1789	5.24
16	0.0503	0.0499	-0.80
17	0.1004	0.1043	3.88
18	0.1364	0.1430	4.84
19	0.1572	0.1653	5.15
20	0.1700	0.1789	5.24
21	0.0514	0.0500	-2.72
22	0.0915	0.0942	2.95
23	0.1284	0.1342	4.52
24	0.1508	0.1583	4.97
25	0.1648	0.1732	5.10

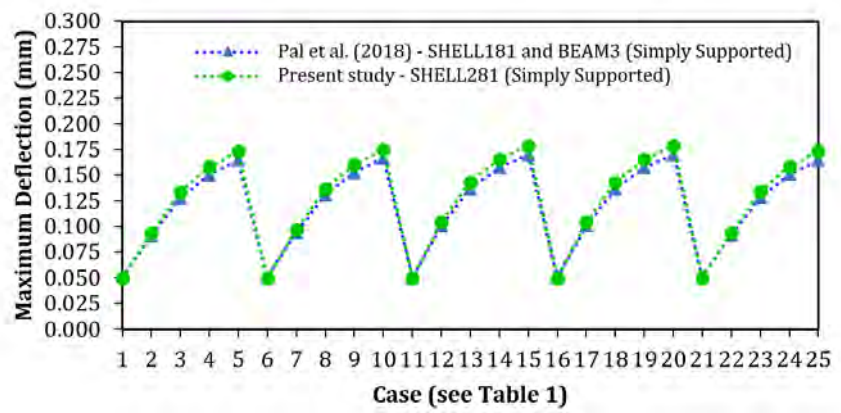


Fig. 9. Maximum deflection for cases of Table 1

3.3 Case Study

As earlier mentioned, all the proposed hat-stiffened plate geometric configurations were derived from the reference plate (with no stiffeners). Based on the structural characteristics outlined in the case study description, it was possible to insert a maximum of five stiffeners in the longitudinal direction of the plate while maintaining the total material volume of the structure constant. The limitation imposed by adopting a 120° angle prevents the addition of more stiffeners, even with variations in height and thickness, without altering the total volume of the structure. As in the validation and verification procedures, it was also necessary here to perform a mesh convergence test considering the structure with the greatest geometric complexity, represented by the plate with 5 stiffeners. Considering the maximum deflection of the hat-stiffened plate, regular meshes formed by square SHELL281 finite elements with 6 different sizes (ranging from 5 to 40 mm) were tested, as shown in Fig. 10.

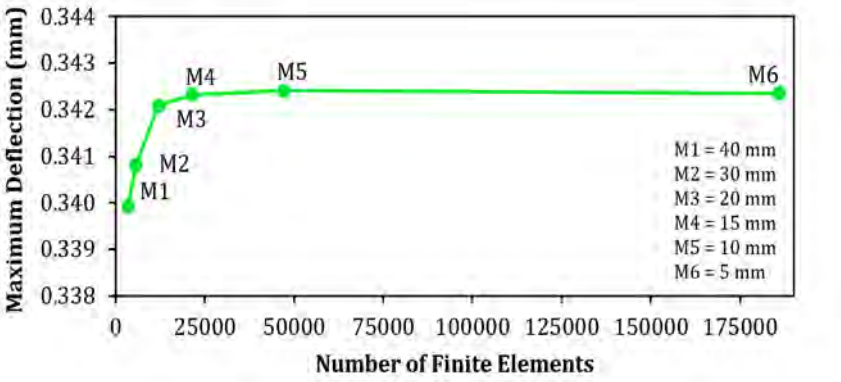


Fig. 10. Convergence test mesh for the case study

It is possible to visualize in Fig. 10 a stabilization of the maximum deflection value from mesh M4. In order to guarantee a mesh-independent solution the mesh M5 (finite elements with a size of 10 mm) was adopted for all numerical simulations of the case study. Therefore, the maximum and central deflections of the reference plate was 0.69758 mm. The main purpose regarding the transformation of 30% of the material volume in hat-stiffeners is to reduce the maximum and central deflections. The results of maximum and

central deflections for the different stiffener height and stiffener thickness of the hat-stiffened plates having 1, 2, 3, 4, and 5 longitudinal hat-stiffeners are plotted, respectively, in Figures 11, 12, 13, 14, and 15.

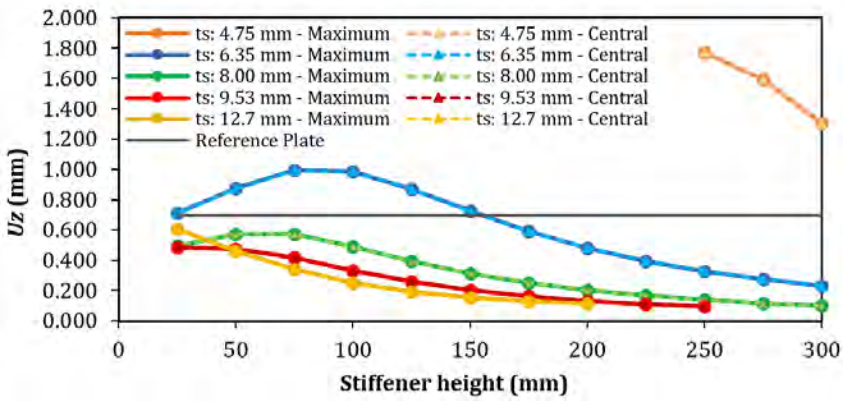


Fig. 11. Results for maximum and central deflections for the plates with 1 hat-stiffener

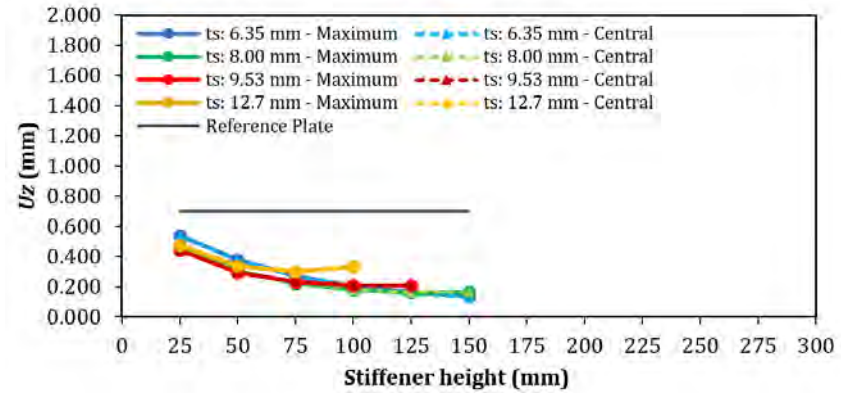


Fig. 12. Results for maximum and central deflections for the plates with 2 hat-stiffeners

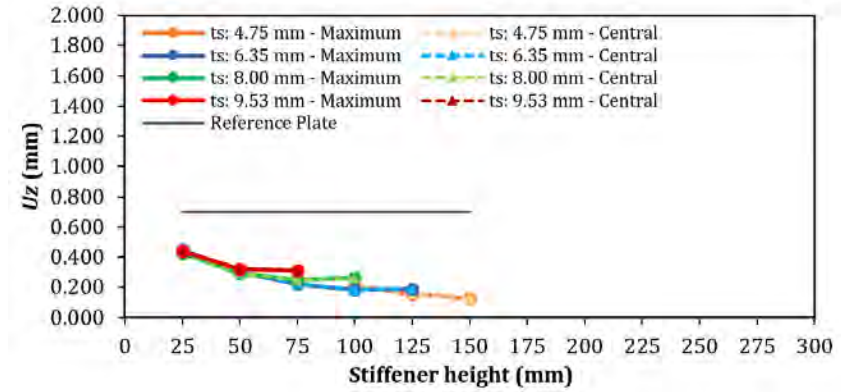


Fig. 13. Results for maximum and central deflections for the plates with 3 hat-stiffeners

Figures 11 to 15 demonstrate that applying Constructal Design to convert 30% of the reference plate into hat-stiffeners effectively reduces out-of-plane displacements. All hat-stiffened plates exhibit maximum and central deflections lower than those of the reference plate. Furthermore, in a general way, from Figs. 11 to 15 it is noticed that the maximum and central deflections coincide for each analyzed case. Moreover, it is also observed that the greater the height of the stiffener, the smaller the resulting displacements, except for the plate with a single hat-stiffener where thicknesses of 6.35 mm and 8.00 mm are used (see Fig. 11). In this case, an initial increase in deflections occurs before they decrease as the height increases.

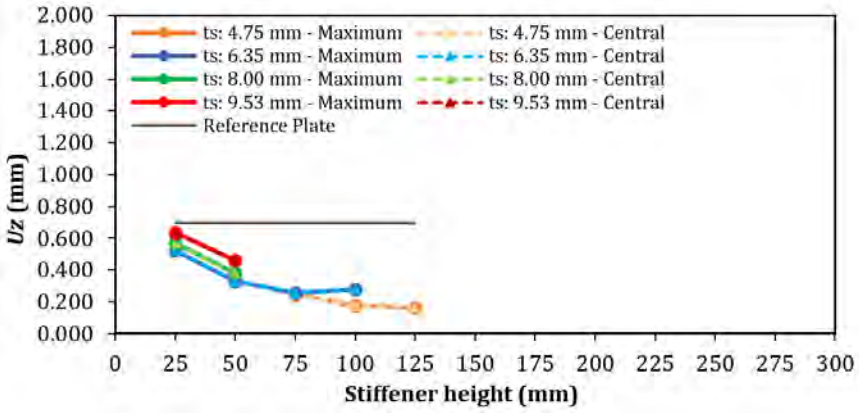


Fig. 14. Results for maximum and central deflections for the plates with 4 hat-stiffeners

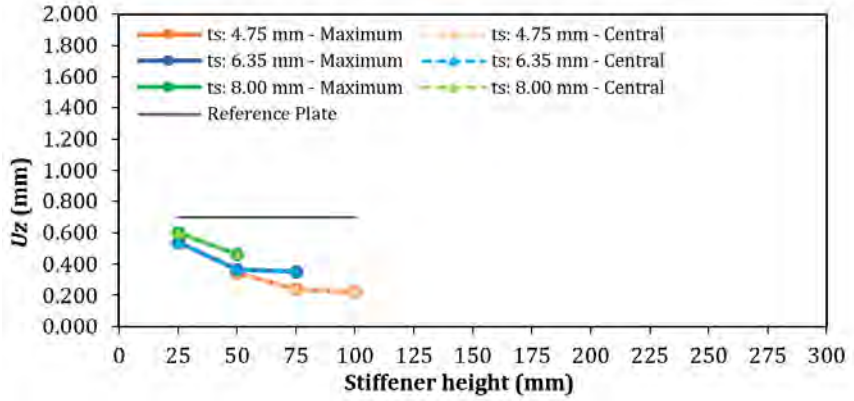


Fig. 15. Results for maximum and central deflections for the plates with 5 hat-stiffeners

For the plates with 1 or 2 hat-stiffeners, the smallest deflections occur at the largest thicknesses. However, for the plates having 3 to 5 hat-stiffeners, the smallest deflections are observed at the smallest thicknesses. As the number of stiffeners increases, the heights and thicknesses become limited because the portion of the plate's material volume converted into stiffeners cannot be fully distributed as the stiffener dimensions change in each proposed geometry.

Table 3 presents the best and worst results according to the number of hat-stiffeners in the longitudinal direction of the plate, as well as the relative difference (RD) in maximum and central deflections compared to the reference plate for these analyzed cases.

Table 3. Best and worst results for the maximum and central deflections according to the number of hat-stiffeners

Number of hat-stiffeners	h_s (mm)	t_s (mm)	U_z^{max} (mm)	$U_z^{central}$ (mm)	RD (%) U_z^{max}	RD (%) $U_z^{central}$
1	250	9.53	0.0958	0.0958	-86.26	-86.26
	250	4.75	1.7735	1.7735	154.23	154.23
2	150	6.35	0.1381	0.1266	-80.20	-81.84
	25	6.35	0.5371	0.5371	-23.01	-23.01
3	150	4.75	0.1244	0.1244	-82.17	-82.17
	25	6.35	0.4497	0.4497	-35.53	-35.53
4	125	4.75	0.1650	0.1650	-76.34	-76.34
	25	9.53	0.6344	0.6345	-9.06	-9.04
5	100	4.75	0.2259	0.2259	-67.61	-67.61
	25	8.00	0.6014	0.6014	-13.79	-13.79

According to Table 3, the worst deflections occur with the smallest stiffener height (25 mm) when the plate has 2 to 5 stiffeners. However, the thickness associated with these results varies: for 1 to 3 stiffeners, the worst deflections happen at the smallest thicknesses, whereas for 4 and 5 stiffeners, the largest deflections occur with the thickest stiffener. For the plate with only 1 stiffener (see Fig. 11), the worst deflection is observed with a height of 250 mm and a thickness of 4.75 mm. This configuration represents the smallest feasible height for this thickness in the proposed geometric arrangement. Moreover, this deflection is, on average, 2.5 times greater than the result for the reference plate, making the use of this thickness unviable. The objective is to minimize maximum and central deflections with the help of stiffeners, thereby increasing the structural rigidity.

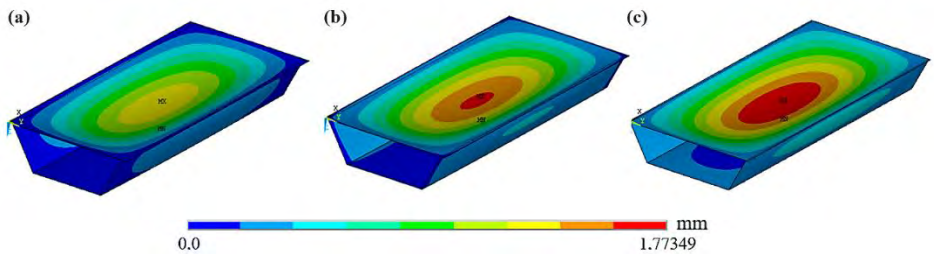


Fig. 16. Displacement distributions of the hat-stiffened plate having 1 stiffener for t_s = 4.75 mm, with: (a) h_s = 300 mm; (b) h_s = 275 mm; and (c) h_s = 250 mm

With only one stiffener on the plate (see Figure 11), 45 analyses were conducted using different geometric arrangements. The maximum stiffener height was 300 mm, and 5 stiffener thicknesses were employed. The only thickness that did not yield satisfactory results was 4.75 mm. For the 3 heights that allowed this thickness, deflection values exceeded 1.3 mm, surpassing the results obtained for the reference plate and making its use not recommended. This can be attributed to the stiffener nearly spanning the entire 1000 mm width of the plate, as shown in Figure 16. For a thickness of 6.35 mm, heights below 150 mm also resulted in displacements exceeding Uz = 0.69758 mm of the reference plate. However, for the other thicknesses, regardless of the adopted height, all results showed deflections lower than the maximum and central deflections of the reference plate. According to Table 3, the smallest maximum and central deflection was 0.0958 mm, achieved with a stiffener height of 250 mm and thickness of 9.53 mm, which is the

maximum height allowed for this thickness. This represents a reduction of 86.26% in maximum and central deflections if compared to the reference plate.

In turn, 21 geometric arrangements were analyzed with two longitudinal stiffeners (see Fig. 12), considering four stiffener thicknesses, with a maximum stiffener height of 150 mm. Among these configurations, the highest and lowest maximum and central deflection results occurred with a thickness of 6.35 mm, being the smallest displacement corresponding to a height of 150 mm and the largest displacement at a height of 25 mm. Regarding the reference plate, the best result achieved reductions of 80.20% and 81.74% in maximum and central deflections, with displacements of 0.1381 mm and 0.1266 mm (see Table 3), respectively. The worst result was 0.5371 mm for both maximum and central deflections. For the 6.35 mm thickness, the maximum and central deflections coincide up to a height of 75 mm. Above this, a slight variation occurs due to the position of the stiffeners, which tend to shift closer to the plate edges as the stiffener height decreases. This is similar to the behavior observed with a single stiffener (see Fig. 16). It is noteworthy that for thicknesses of 12.70 mm, 9.53 mm, and 8.00 mm, there is a slight increase in deflection results at greater heights, where the stiffeners feature very narrow bases. For instance, in the 12.70 mm thickness the stiffeners occupy less than 50% of the plate width, regardless of height, as illustrated in Fig. 17.

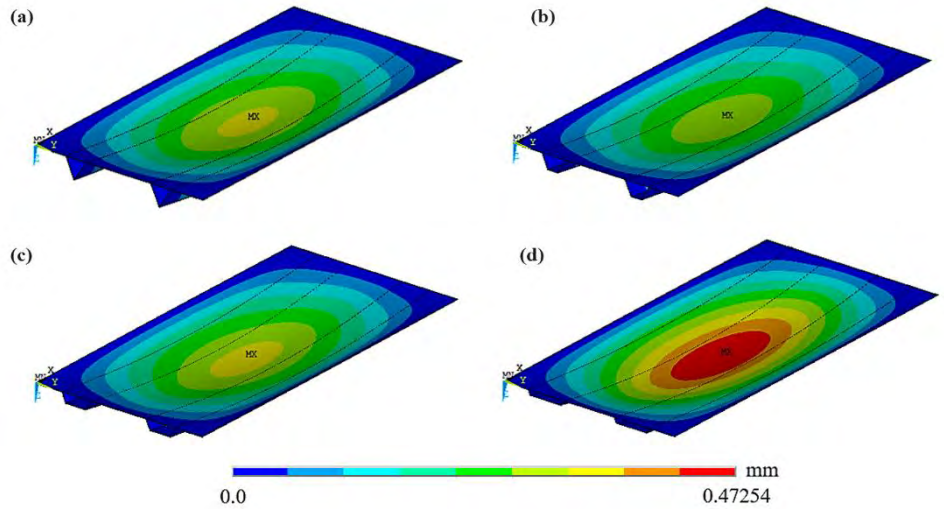


Fig. 17. Displacement distributions of the hat-stiffened plate having 2 stiffener for t_s = 12.70 mm, with: (a) h_s = 100 mm; (b) h_s = 75 mm; (c) h_s = 50 mm; and (d) h_s = 25 mm

In all 15 analyses conducted on the plate with 3 stiffeners (see Fig. 13), the distribution of resulting displacements is similar to that of the reference plate. In this geometric arrangement, the 12.70 mm thickness can no longer be applied, and the available height options are also limited for each analyzed thickness. The maximum height of 150 mm is only achievable with a thickness of 4.75 mm, which also results in the lowest maximum and central deflection of 0.1244 mm, representing an 82.17% reduction compared to the reference plate.

Analyzing the hat-stiffened plate with 4 stiffeners (see Fig. 14), 11 geometric arrangements were studied, considering a minimum thickness of 4.75 mm and a maximum of 9.53 mm. The maximum stiffener height reached 125 mm for the smallest thickness, resulting in the best maximum and central deflection value of 0.1650 mm, which is 4.23 times smaller than the result for the reference plate. On the other hand, the worst displacements occurred at

the smallest height (25 mm) with the largest thickness (9.53 mm), yielding maximum and central deflections of 0.6344 and 0.6345 mm, respectively, still reaching 9% better than the reference plate. Moreover, with 5 hat-stiffeners on the plate (see Fig. 15), the increased number of stiffeners meant that the portion of the reference plate volume converted into stiffeners only allowed for 8 analyses, with 3 stiffener thicknesses and a maximum height of 100 mm. The best results were achieved with a thickness of 4.75 mm, while the worst were observed with a thickness of 8.00 mm. Compared to the reference plate, the smallest displacement showed a reduction of 67.61% in maximum deflection, with maximum and central deflections of *Uz* = 0.2259 mm. The worst result occurred with the smallest stiffener height and thickness, corresponding to 25 mm and 4.75 mm, respectively, yielding maximum and central deflections of *Uz* = 0.6014 mm, about 13.79% lower than the values obtained for the reference plate.

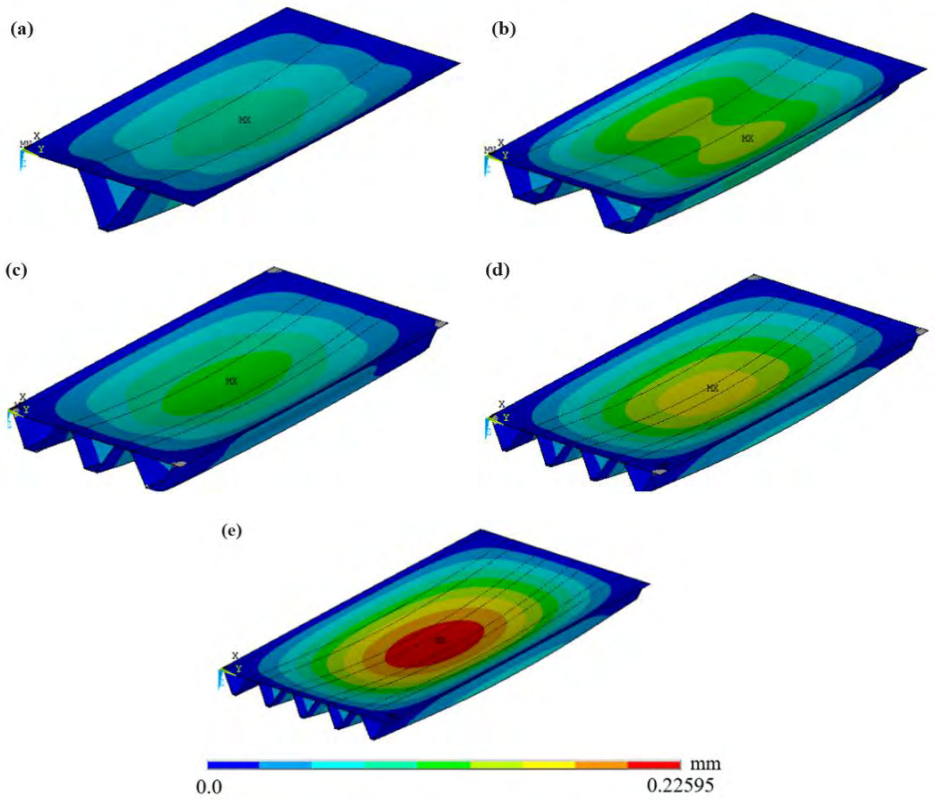


Fig. 18. Displacement distributions with the best result (with minor maximum deflection) for: (a) 1 hat-stiffener; (b) 2 hat-stiffeners; (c) 3 hat-stiffeners; (d) 4 hat-stiffeners; and (e) 5 hat-stiffeners

Figure 18 depicts the displacements distribution for the best result, i.e. with small deflection, for each number of hat-stiffeners investigated (see Figures 11 to 15 and Table 3). It can be observed in Fig. 18 that only in the case with two stiffeners do the maximum and central deflections differ. This occurs because the geometry with 2 hat-stiffeners caused the plate to be divided into two regions with lower maximum displacement, whereas in the other cases, the resulting displacements are concentrated in the central region of the plate (with a similar behavior than reference plate, i.e. having an overall structure deflection). Additionally, the smallest deflection values are observed when the

plate has 1 or 3 hat-stiffeners. In these configurations, there is always a stiffener crossing the central region of the plate, which helps reduce displacements at this point. However, the worst case among those presented in Fig. 18 is the one with five stiffeners, which also includes a central stiffener. Nevertheless, the combination of the stiffeners' height (100 mm) and thickness (4.75 mm) resulted in the poorest mechanical performance among the five best cases with longitudinal stiffeners.

One can also discuss the obtained results in the light of Constructal theory. As earlier mentioned, the Constructal theory is based on the evolution of design over time. When applying Constructal Design, this temporal evolution can be understood as the progression that occurs while maintaining a constant material volume and allowing the degrees of freedom to vary in pursuit of improved performance indicator. Consequently, as material redistribution occurs due to the variation in degrees of freedom, the geometric configuration adapts to achieve superior performance, respecting the defined constraints and proposed search space. Thus, the Constructal principle of the optimal distribution of imperfections is fulfilled, leading to the ideal geometric configuration for the problem under investigation [20]. Specifically, solid mechanic systems can be understood as flow systems in which occurs a flow of stresses [3]. This flow of stresses changes as geometric configurations take different shapes due to variations in the degrees of freedom. From the perspective of Constructal theory and in agreement with Da Silveira et al. [15], the optimal geometry is the one that facilitates the flow of stress, distributes imperfections better, and achieves lower displacements. That said, it can be inferred from Fig. 18 that the optimal global geometry was the one that facilitated the flow of stresses, best distributed the mechanical imperfections, and achieved the smallest displacements.

4. Conclusions

The present study applied the Constructal Design method combined with a Systematic Search technique to analyze trapezoidal box beam hat-stiffeners in the longitudinal direction of a simply supported steel plate. Starting from a non-stiffened reference plate, 100 geometric configurations were proposed and numerically simulated using a FEM computational model, which was properly validated and verified. This approach allowed for a systematic investigation into the influence of the geometry on the mechanical performance of plates with hat-stiffener.

The primary objective of the study was to minimize the structural out-of-plane displacements. Results demonstrated that most of the hat-stiffened plates proposed showed significant improvements in mechanical behavior when compared to the reference plate. For example, the optimized geometric configuration (featuring 1 stiffener with a height of 250 mm and a thickness of 9.53 mm) reduced the maximum and central deflections by approximately 86% if compared to the reference plate. This highlights the potential of strategically designed stiffeners to enhance the stiffness and load-bearing capacity of the structure.

It can also be observed that, maintaining a constant total volume of material, an increase in the number of stiffeners does not necessarily conduct the reduction of the out-of-plane displacements of the structural component. In addition, it is important to highlight the influence of the thickness and height of the stiffeners on the results. As expected, the greater the height of the stiffener, the smaller the resulting deflections in the structure.

The application of Constructal Design allows the evolution of the geometric configuration through the variation of degree of freedoms until the optimized one is defined, i.e., among the proposed geometries that compose the search space, identify the one that facilitates the flow of stresses, best distributed the mechanical imperfections, and reached the smallest displacements.

Future research will expand on these findings by analyzing deflections in plates with trapezoidal box beam hat-stiffeners oriented transversely to the plate. This will help identify the most effective geometric configurations to further enhance structural rigidity and minimize displacements. Additional studies will also consider varying material volume fractions, different aspect ratios between plate dimensions, and the inclusion of von Mises stress as a performance indicator to provide a more comprehensive understanding of the structure's behavior.

Acknowledgement

The authors acknowledge the financial support for conducting this research provided by the Coordination for the Improvement of Higher Education Personnel (CAPES, funding code 001) and the National Council for Scientific and Technological Development (CNPq, grant numbers: 307791/2019-0, 308396/2021-9, and 309648/2021-1).

Appendix A

Tables A1 to A5 present the geometric characterization based on the height and thickness of the stiffener, as well as the maximum and central deflection results, along with the relative percentage differences between these results for each hat-stiffened plate generated through the application of the Constructal Design method and investigated in this study.

Table A1. Plates with 1 longitudinal hat-stiffener

h_s (mm)	t_s (mm)	U_z^{max} (mm)	$U_z^{central}$ (mm)	RD (%)
300	4.75	1.30951	1.30950	−0.001
275	4.75	1.58995	1.59010	0.009
250	4.75	1.77349	1.77350	0.001
300	6.35	0.23210	0.23208	−0.008
275	6.35	0.27515	0.27519	0.015
250	6.35	0.32857	0.32854	−0.009
225	6.35	0.39571	0.39575	0.011
200	6.35	0.48157	0.48153	−0.008
175	6.35	0.59097	0.59102	0.008
150	6.35	0.72568	0.72563	−0.006
125	6.35	0.87134	0.87142	0.010
100	6.35	0.98356	0.98367	0.011
75	6.35	0.99490	0.99488	−0.002
50	6.35	0.87462	0.87474	0.014
25	6.35	0.71122	0.71122	0.000
300	8.00	0.09970	0.09970	0.004
275	8.00	0.11669	0.11666	−0.024
250	8.00	0.13870	0.13871	0.004
225	8.00	0.16708	0.16705	−0.017
200	8.00	0.20354	0.20351	−0.017
175	8.00	0.25087	0.25088	0.005
150	8.00	0.31295	0.31291	−0.014
125	8.00	0.39295	0.39297	0.005
100	8.00	0.48827	0.48822	−0.009
75	8.00	0.57142	0.57146	0.008
50	8.00	0.57404	0.57401	−0.006
25	8.00	0.49597	0.49604	0.015
250	9.53	0.09582	0.09581	−0.010
225	9.53	0.11087	0.11087	−0.003
200	9.53	0.13234	0.13231	−0.023
175	9.53	0.16187	0.16186	−0.003
150	9.53	0.20240	0.20236	−0.018
125	9.53	0.25773	0.25773	0.000

100	9.53	0.33128	0.33123	−0.016
75	9.53	0.41662	0.41663	0.003
50	9.53	0.47598	0.47595	−0.007
25	9.53	0.48389	0.48393	0.008
200	12.7	0.11700	0.11697	−0.022
175	12.7	0.12942	0.12939	−0.025
150	12.7	0.15282	0.15279	−0.022
125	12.7	0.19061	0.19059	−0.009
100	12.7	0.24956	0.24952	−0.016
75	12.7	0.33913	0.33911	−0.004
50	12.7	0.46219	0.46216	−0.007
25	12.7	0.60353	0.60355	0.003

Table A2. Plates with 2 longitudinal hat-stiffeners

h_s (mm)	t_s (mm)	U_z^{max} (mm)	$U_z^{central}$ (mm)	RD (%)
150	6.35	0.13812	0.12665	−8.306
125	6.35	0.16315	0.15477	−5.139
100	6.35	0.20409	0.20027	−1.871
75	6.35	0.27030	0.27026	−0.014
50	6.35	0.37879	0.37880	0.003
25	6.35	0.53705	0.53705	0.000
150	8.00	0.16236	0.16232	−0.024
125	8.00	0.16076	0.16074	−0.015
100	8.00	0.18045	0.18043	−0.013
75	8.00	0.22377	0.22375	−0.009
50	8.00	0.30227	0.30229	0.008
25	8.00	0.45519	0.45518	−0.001
125	9.53	0.20960	0.20959	−0.006
100	9.53	0.20547	0.20546	−0.006
75	9.53	0.23113	0.23111	−0.010
50	9.53	0.29423	0.29426	0.010
25	9.53	0.44266	0.44266	0.001
100	12.7	0.32981	0.32978	−0.009
75	12.7	0.29945	0.29942	−0.009
50	12.7	0.33666	0.33669	0.009
25	12.7	0.47255	0.47254	−0.001

Table A3. Plates with 3 longitudinal hat-stiffeners

h_s (mm)	t_s (mm)	U_z^{max} (mm)	$U_z^{central}$ (mm)	RD (%)
150	4.75	0.12436	0.12437	0.011
125	4.75	0.15318	0.15317	−0.007
100	4.75	0.20518	0.20519	0.006
125	6.35	0.18738	0.18737	−0.005
100	6.35	0.18473	0.18473	−0.002
75	6.35	0.22168	0.22171	0.012
50	6.35	0.30289	0.30289	−0.001
25	6.35	0.44971	0.44975	0.009
100	8.00	0.26199	0.26198	−0.005
75	8.00	0.24723	0.24725	0.010
50	8.00	0.29335	0.29334	−0.002
25	8.00	0.42348	0.42351	0.008
75	9.53	0.31217	0.31219	0.005
50	9.53	0.32200	0.32200	−0.001
25	9.53	0.43755	0.43758	0.006

Table A4. Plates with 4 longitudinal hat-stiffeners

h_s (mm)	t_s (mm)	U_z^{max} (mm)	$U_z^{central}$ (mm)	RD (%)
125	4.75	0.16503	0.16502	–0.005
100	4.75	0.17824	0.17824	0.002
75	4.75	0.24494	0.24495	0.003
100	6.35	0.27831	0.27833	0.006
75	6.35	0.25812	0.25814	0.009
50	6.35	0.33317	0.33317	0.001
25	6.35	0.52355	0.52364	0.017
50	8.00	0.38249	0.38253	0.010
25	8.00	0.56959	0.56959	0.000
50	9.53	0.46197	0.46196	–0.001
25	9.53	0.63441	0.63451	0.016

Table A5: Plates with 5 longitudinal hat-stiffeners

h_s (mm)	t_s (mm)	U_z^{max} (mm)	$U_z^{central}$ (mm)	RD (%)
100	4.75	0.22595	0.22595	0.000
75	4.75	0.23852	0.23855	0.013
50	4.75	0.34241	0.34241	0.001
75	6.35	0.35397	0.35400	0.008
50	6.35	0.36385	0.36385	0.000
25	6.35	0.53978	0.53982	0.007
50	8.00	0.46638	0.46638	0.000
25	8.00	0.60137	0.60140	0.005

References

[1] Szilard R. Theories and Applications of Plate Analysis: Classical Numerical and Engineering Methods. [S.l.]: John Wiley & Sons, 2004: 1-7, ISBN 0-471-42989-9. https://doi.org/10.1002/9780470172872

[2] Ventsel E, Krauthammer T. Thin Plates and Shells - Theory, Analysis and Applications. Marcel Dekker, Inc., 200: 1-4, ISBN 0-824-70575-0.

[3] Bejan A, Lorente S. Design with Constructal Theory. Wiley, Hoboken, 2008: 1-7, ISBN 978-0-471-99816-7.

[4] Reis AH. Constructal Theory: From Engineering to Physics, and How Flow Systems Develop Shape and Structure. Applied Mechanics Reviews. 2006; 59: 269-282. https://doi.org/10.1115/1.2204075

[5] Troina GS, Cunha M, Pinto VT, Rocha LAO, dos Santos ED, Fragassa C, Isoldi LA. Computational Modeling and Constructal Design Theory Applied to the Geometric Optimization of Thin Steel Plates with Stiffeners Subjected to Uniform Transverse Load. MDPI Metals. 2020; 10: 220. https://doi.org/10.3390/met10020220

[6] Nogueira CM, Pinto VT, Rocha LAO, dos Santos ED, Isoldi LA. Numerical simulation and constructal design applied to plates with different heights of transverse and longitudinal stiffeners. Engineering Solid Mechanics. 2021; 9: 221-238. https://doi.org/10.5267/j.esm.2020.12.001

[7] Pinto VT, Cunha M, Martins K, Rocha, LAO, dos Santos ED, Isoldi LA. Bending of stiffened plates considering different stiffeners orientations. Magazine of Civil Engineering. 2021; 103(3): 10310.

[8] Kucharski DMP, Pinto VT, Rocha LAO, dos Santos ED, Fragassa C, Isoldi LA. (2022). Geometric Analysis by Constructal Design of Stiffened Steel Plates under Bending with

Transverse I-shaped or T-shaped Stiffeners. Facta Universitatis, Series: Mechanical Engineering. 2022; 20(3): 617-632. https://doi.org/10.22190/FUME211016070K
[9] Tharian MG, Nandakumar CG. Superelement for Structural Analysis of Steel Bunkers. Proceedings of the 7th Biennial International Conference on Emerging Trends in Engineering, Science & Technology (ICETEST), 2023. https://doi.org/10.2139/ssrn.4512229
[10] Tharian MG, Nandakumar CG. Hat stiffened plates for ship building. International Journal of Applied Engineering Research and Development, IJAERD. 2013; 3: 1-10.
[11] Pal AK, Harry NN, Upadhyay R, Kushwaha YK. (2018). Static Analysis of hat stiffened plate: A parametric study. International Journal of Reasearch in Engineering, Science and Management. 2018; 1: 128-131.
[12] Virág Z, Szirbik S. (2021). Modal Analysis of Optimized Trapezoidal Stiffened Plates under Lateral Pressure and Uniaxial Compression. MDPI Applied Mechanics. 2021; 2: 681-693. https://doi.org/10.3390/applmech2040039
[13] Filippatos A, Markatos D, Tzortzinis G, Abhyankar K, Malefaki S, Gude M, Pantelakis S. (2024). Sustainability-Driven Design of Aircraft Composite Components. MDPI Aeroespace. 2024; 11: 86. https://doi.org/10.3390/aerospace11010086
[14] dos Santos ED, Isoldi LA, Gomes MN, Rocha LAO. The Constructal Design Applied to Renewable Energy Systems. In: Rincón-Mejía, E.; Heras, A. (Org.) Sustainable Energy Technologies, CRC Press - Taylor and Francis, Boca Raton. 2017; 1(1): 63-87.
[15] da Silveira T, Pinto VT, Neufeld JPS, Pavlovic A, Rocha LAO, dos Santos ED, Isoldi LA. Applicability Evidence of Constructal Design in Structural Engineering: Case Study of Biaxial Elasto-Plastic Buckling of Square Steel Plates with Elliptical Cutout. Journal of Applied and Computational Mechanics. 2021; 7(2): 922-934.
[16] ANSYS, Inc. Release 2021 R2 Engineering What's Ahead - Element Reference, 2021.
[17] Vaz LE. Método dos Elementos Finitos em análise de estruturas. Elsevier, Rio de Janeiro, 2011: 37-40, ISBN 978-85-352-3929-4.
[18] Aneja R, Choudharry A, Jain KK, Dave RK. Design and Optimization of Hat Stiffened Plate using Finite Element Method. International Research Journal of Engineering and Technology. 2018; 5: 578-584.
[19] Carrijo EC, Paiva JB, Giogo JS. A numerical and experimental study of stiffened plates in bending. Transactions on Modelling and Simulation. 1999; 21: 12-18.
[20] Bejan, A. The physics of life: the evolution of everything. St. Martin's Press, New York: 2016. ISBN 978-1-250-07882-7.

Blank Page

Research on Engineering Structures & Materials
www.jresm.org
Research Group

Research Article

Numerical analysis of the impact of PCM reservoir width on lithium-ion battery cooling: A constructal design study

Rafael da Silveira Borahel [1,a], Giovani Dambros Telli [2,b], Augusto Antoniolli Bolzoni [2,c], Liércio André Isoldi [1,d], Elizaldo Domingues dos Santos [1,e], Luiz Alberto Oliveira Rocha [*,1,3,4,f]

[1]*School of Engineering, Federal University of Rio Grande, Brazil*
[2]*University of Caxias do Sul, Brazil*
[3]*Graduate Program of Mechanical Engineering (PROMEC), Federal University of Rio Grande do Sul, Brazil*
[4]*Institute of Earth Sciences, Complex Fluid Systems Lab, Portugal*

Article Info

Article history:

Received 02 Dec 2024
Accepted 25 Feb 2025

Keywords:

Constructal design;
Lithium-Ion battery;
Battery cooling;
Thermal runaway

Abstract

The aim of this work is to examine, from the perspective of Constructal Design, the influence of the width (W_{pcm}) of a reservoir filled with PCM (phase change material) on the cooling performance of a Li-ion battery cell under discharge rates of 3C and 5C. The problem is considered two-dimensional and transient. The mathematical model is multiphase, with different characteristics for the solid domain (battery cell) and the fluid domain (PCM reservoir), based on the mass, momentum and energy balance equations. The finite volume method is used to solve the problem numerically, and the grid meshes used in the spatial discretization are subjected to uncertainty analysis. The results show that the use of the PCM reservoir contributes significantly to the cooling of the battery. When the battery discharge occurs at a rate of 5C, there is a 13.1°C reduction in the maximum temperature of the battery (T_{max}).

© 2025 MIM Research Group. All rights reserved.

1. Introduction

Never in history has there been a more urgent need to reassess the impact of our society on the planet, especially with regard to climate change caused by the carbon emissions from our activities. Internal combustion engine vehicles are one of the largest contributors to global pollution, with the transportation sector accounting for approximately 20% of the world's total carbon emissions [1,2]. However, this scenario is about to change as government policies focused on promoting electric vehicles (EVs) gain momentum. In the European Union (EU), for example, only non-CO_2-emitting vehicles, such as EVs, will be permitted to be registered in member countries from 2035 [3]. To achieve this goal, automakers are redoubling their efforts to improve their EVs, with a particular focus on developing the battery packs that will power them.

Lithium-ion (Li-ion) batteries are the best-known power source for electric vehicles due to their high energy and power density, no memory effect, long cycle life, and fast charging capability [4,5]. Despite these advantages, Li-ion batteries require strict thermal control to ensure their performance and safety. In general, very low temperatures increase the battery's internal resistance and polarization, resulting in higher power and energy losses and reduced discharge capacity. On the other hand, very high temperatures accelerate battery degradation, reducing its performance, lifespan and security [6]. According to

*Corresponding author: luizrocha@mecanica.ufrgs.br
[a] orcid.org/0000-0002-8724-132x; [b] orcid.org/0000-0003-1294-0668; [c] orcid.org/0009-0005-7608-6773; [d] orcid.org/0000-0002-9337-3169; [e] orcid.org/0000-0003-4566-2350; [f] orcid.org/0000-0003-2409-3152
DOI: http://dx.doi.org/10.17515/resm2025-557en1202rs

Pesaran [7], the ideal operating temperature for Li-ion batteries is between 25 and 40°C, with the temperature variation within each cell not exceeding 5°C.

Battery thermal management systems (BTMS) are divided into three main categories: active, passive, and hybrid [8]. Passive BTMS based on phase change materials (PCMs) have gained popularity due to their lower complexity, cost and volume; in addition to offering a more uniform battery cooling [9,10]. Srivastava et al. [11] studied the cooling of a cylindrical Li-ion battery surrounded by PCMs. The results obtained show that the use of PCMs is a viable approach to reduce the maximum temperature reached by the battery. Alghassab [12] evaluated the potential of a finned BTMS based on PCM to improve the thermal management of a Li-ion battery. With six copper fins, the authors found an 8°C reduction in battery peak temperature. In both studies, the geometric parameters of the PCM container showed a significant role on the battery cooling. Therefore, adequate thermal control of the battery depends on the correct design of the PCM reservoir, whose geometry can be developed using the Constructal Design Method (CDM).

The CDM has its origins in constructal theory, which supports the idea that the configuration/evolution of any flow system - animated or not - occurs through a physical principle, the constructal law [13,14]. In the constructal realm, the design of the flow system evolves in such way to easily the internal currents, including the engineering systems, where the Constructal Law is applied through the CDM [15]. In engineering, this method has been used to study the geometry of a wide variety of finite-size flow systems [16-19]. It can even be applied to the analysis of the design of passive PCM-based BTMS in Li-ion battery packs, which have a limited volume in EVs. Therefore, the aim of this numerical study is to analyze, using the Constructal Design Method (CDM), the effect of the width of a PCM reservoir (W_{PCM}) on the cooling performance of a Li-ion battery pack discharged at rates of 3C and 5C.

2. Methodology

2.1. Constructal Design Method (CDM)

The geometry of the proposed BTMS was studied using the Constructal Design Method (CDM). The CDM is a method based on constraints (geometric and physical) and objectives (performance indicators), organized in a sequence of well-defined steps [17-20] that are outlined below and illustrated in the flowchart shown in Figure 1.

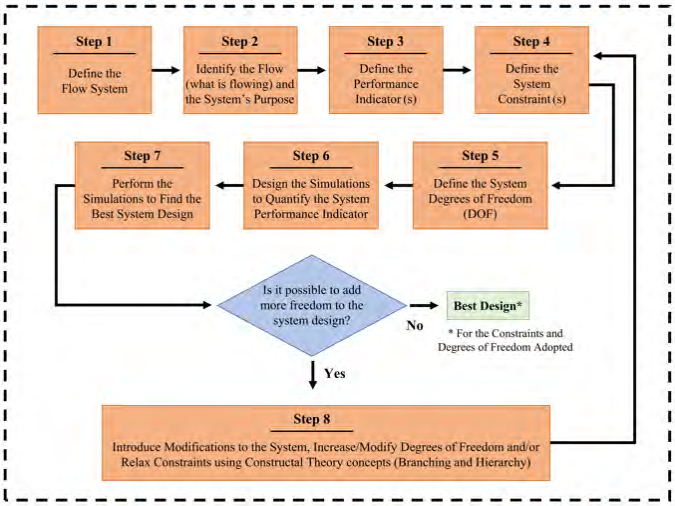


Fig. 1. Flowchart of steps involved in applying the Constructal Design Method (CDM)

- Step 1: Define the Flow System

The system under analysis consists of a Li-ion battery pack [$Li(Ni_1/_3Co_1/_3Mn_1/_3)O_2$] composed of six battery cells connected in a 3s2p configuration by a copper busbar. The battery pack is exposed to ambient air ($T_\infty = 25°C$) and dissipates heat to it by natural convection with a convection heat transfer coefficient (h) equal to 12.8 W/m^2K [21]. The battery cells are 148.8 mm in length (L_{cell}) and 91.6 mm in height (H_{cell}), with a width (W_{cell}) of 26.8 mm. Between each pair of cells, two thermal reservoirs filled with PCM (RT 28HC) are placed, with a thin layer of insulation separating them. The PCM reservoirs are the same length (L_{pcm}) and height (H_{pcm}) as the battery cells, while their width (W_{pcm}) is variable to assess their effects on battery cooling. This analysis is conducted using ϕ, which is defined as the ratio between W_{pcm} and W_{cell}.

The schematic representation of the battery pack analyzed is shown in Fig. 2 (a-c); where Fig. 2 (a) presents the isometric view of the battery pack, Fig. 2 (b) the side view, with the red dashed line delineating the computational domain adopted, which is shown in Fig. 2 (c) with the applied boundary conditions. For clarity, the computational domain consists of a cross-sectional cut of the battery pack, covering (for computational economy) only half of one of the central battery cells and the adjacent PCM reservoir.

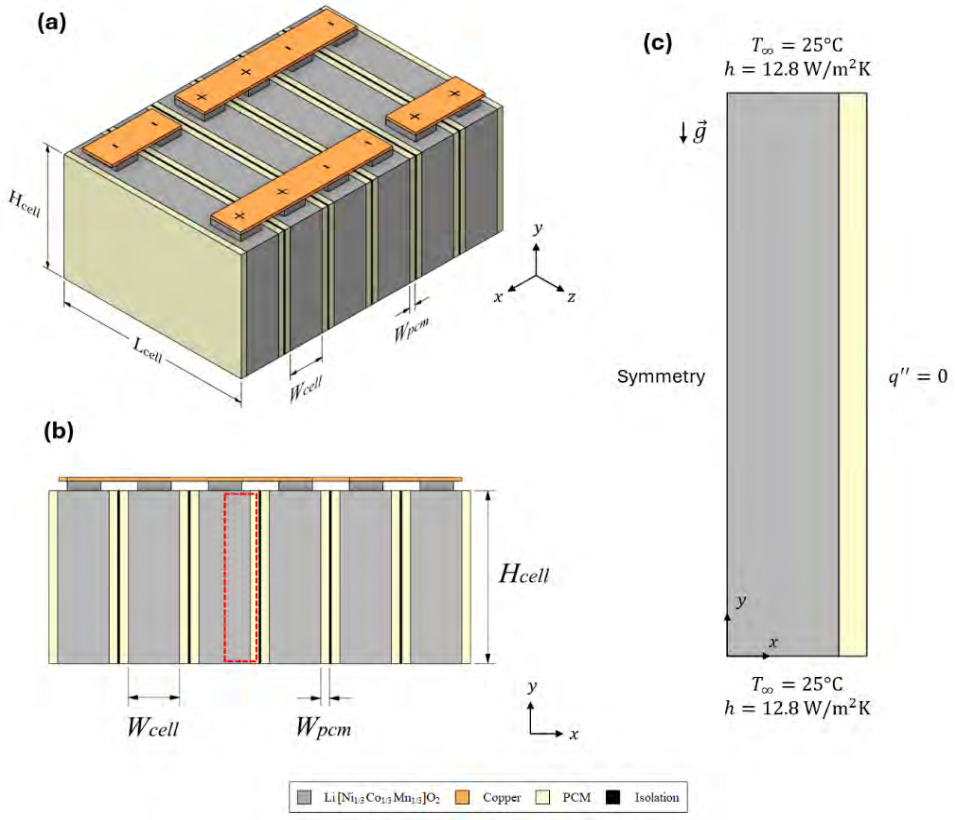


Fig. 2. Schematic representation of the battery pack analyzed, where (a) isometric view, (b) side view and (c) computational domain adopted

The technical specifications and physical properties of the battery cells and the copper busbar are shown in Table 1, while the properties of the PCM (RT 28HC) are shown in

Table 2. Since the thermal conductivity of battery cells (k_{cell}) has an anisotropic behavior, three values are presented for this property, valid for the x, y, and z axes, respectively.

Table 1. Physical properties and technical specifications of the battery cells and busbar.

Physical Properties	Battery Cell [22]	Cooper Busbar [23]
Density (ρ)	2630 (kg/m³)	8978 (kg/m³)
Specific Heat Capacity (c_p)	1100 (J/kg. K)	381 (J/kg. K)
Thermal Conductivity (k)	22.4; 22.4; 1.96 (W/m. K)	387.6 (W/m. K)
Nominal Capacity	37 (Ah)	X – X – X – X – X
Nominal Voltage	3.7 (V)	X – X – X – X – X
Operation Voltage	2.8 – 4.2 (V)	X – X – X – X – X

Table 2. Physical properties of the PCM (RT 28HC)

Physical Properties	RT 28HC [24-25]
Density (ρ)	880 (kg/m³) at 15°C; 770 (kg/m³) at 40°C
Latent Heat (Q_{lat})	250000 (J/kg)
Specific Heat Capacity (c_p)	2000 (J/kg. K)
Thermal Conductivity (k)	0.2 (W/m. K)
Thermal Expansion Coefficient (β)	0.001 (1/K)
Viscosity (μ)	0.0031 (kg/m. s)
Liquidus Temperature (T_L)	29°C
Solidus Temperature (T_S)	27°C

- Step 2: Identify the Flow (*what is flowing*) and the System's Purpose

The purpose of the BTMS evaluated is to promote the cooling of the battery cell. Thus, from the Constructal Theory perspective, the "flow" in this system corresponds to the heat generated by the battery, which is dissipated to the ambient air and the PCM reservoir.

- Step 3: Define the System Performance Indicators

As the purpose of the system is to promote the thermal management of the battery, the performance indicators are the maximum battery temperature (T_{max}) and its temperature difference ($\Delta T_{cell} = T_{max} - T_{min}$) for each instant of time, which reflects the cooling uniformity.

- Step 4: Define the System Constraints

In the proposed problem, the only system constraint is the battery cell volume (V_{cell}), given by:

$$V_{cell} = (L.H.W)_{cell} \tag{1}$$

- Step 5: Define the System Degrees of Freedom (DoF)

The degree of freedom (DoF) admitted for the system is the PCM reservoir width (W_{pcm}), which is expressed in its dimensionless form as:

$$\phi = \frac{W_{pcm}}{W_{cell}} \tag{2}$$

where ϕ is the ratio between the PCM reservoir and battery cell volumes (V_{pcm} and V_{cell}), which in a simplified form gives the width fraction shown in Eq. (2).

- Step 6: Define the Simulations to Quantify the System Performance Indicators

The simulations necessary to evaluate the variations of T_{max} and ΔT_{cell} in response to the system's DoF were designed considering four values to ϕ (0.05, 0.10, 0.15, 0.20) and two battery discharge rates (3C and 5C), resulting in 8 different cases analyzed.

- Step 7: Perform the Simulations to Find the Best System Design

The proposed problem was solved computationally using numerical simulations based on the Finite Volume Method (FVM), performed in the software ANSYS FLUENT 2023 R1.

- Step 8: Introducing Modifications on the System (Increasing DOF/Relaxing Restrictions)

The increase in the system's DoF or the relaxation of its constraints drives the evolution of its design, facilitating the "flow" (the heat generated by the battery) and enhancing the overall system performance. In this work, this step in the application of the CDM was not taken; however, it could be implemented in future works with the purpose of further minimizing the predefined performance indicators (T_{max} and ΔT_{cell}).

2.2. Mathematical Model

The proposed problem is considered two-dimensional and transient. The mathematical model is multiphase, with different characteristics for the solid domain (battery cell) and the fluid domain (PCM reservoir).

2.2.1 Solid Domain (Battery Cell)

The mathematical model implemented for the solid domain (battery cell) consists only of the energy conservation equation [26]:

$$\frac{\partial}{\partial t}\left(\rho c_p T\right) = \nabla(k\nabla T) + \dot{q}''' \tag{3}$$

where t is the time, T is the temperature and $\dot{q}'''$ is the battery volumetric heat generation rate, whose variation with time for the 3C and 5C discharge rates are given by the polynomial equations (3) and (4). These are taken from a previous work [27], that first modeled the battery discharge process, and consequently its heating, using the equivalent circuit model (ECM) [28-29]. The data obtained was then used by the authors to generate the polynomial equations to model the battery heating in terms of $\dot{q}'''$, which proved to be as effective as the ECM, but requiring less computational time [27].

$$\dot{q}'''_{(3C)} = 2.244e^{-14}(t^6) + 1.264e^{-9}(t^5) - 3.677e^{-6}(t^4) + 3.096e^{-3}(t^3) - 1.926t^2 + 471.71t + 34977.73 \tag{4}$$

$$\dot{q}'''_{(5C)} = -1.559e^{-11}(t^6) + 6.683e^{-8}(t^5) - 8.526e^{-5}(t^4) + 0.0482e(t^3) - 13.36t^2 + 1876.77t + 65130.84 \tag{5}$$

2.2.2 Fluid Domain (PCM Reservoir)

The flow of the liquid PCM is considered Newtonian, laminar, and incompressible. The mathematical model implemented in the fluid domain is based on the conservation equations of mass, energy and momentum, supplemented by the enthalpy-porosity method used to model the PCM melting [28].

$$\nabla\left(\rho\vec{V}\right) = 0 \tag{6}$$

$$\frac{\partial(\rho\lambda)}{\partial t} + \nabla\left(\rho\vec{V}\lambda\right) = \nabla(k\nabla T) \tag{7}$$

$$\frac{\partial \rho \vec{V}}{\partial t} + \nabla\left(\rho \vec{V}\vec{V}\right) = -\nabla p + \nabla\left(\mu \nabla \vec{V}\right) + \rho \vec{g} + \vec{S} \tag{8}$$

where $\vec{V}$ is the velocity vector, λ is the total specific enthalpy, p is the pressure, $\vec{g}$ is the gravity acceleration and $\vec{S}$ is the momentum source term, given by:

$$\vec{S} = -A_{(\gamma)}.\vec{V} \tag{9}$$

where $A_{(\gamma)}$ is the porosity function, which is defined by Voller and Prakash [30] as follows:

$$A = \frac{C(1-\gamma)^2}{(\gamma^3 + \omega)} \tag{10}$$

where C is the mushy zone constant, whose value in this study is equal to 10^6 [31]; ω is a small constant (0.001) to avoid division by zero and γ is the PCM liquid fraction, determined by:

$$\gamma = \begin{cases} 0 & if \quad T < T_s \\ \dfrac{T - T_s}{T_l - T_s} & if \quad T_s < T < T_l \\ 1 & if \quad T > T_l \end{cases} \tag{11}$$

Finally, the PCM total specific enthalpy (λ) is the sum of its sensible (λ_{sen}) and latent (λ_{lat}) specific enthalpies:

$$\lambda = \lambda_{sen} + \lambda_{lat} \tag{12}$$

where λ_{sen} and λ_{lat} are defined as follows, respectively:

$$\lambda_{sen} = \lambda_{ref} + \int_{T_{ref}}^{T} c_p dt \tag{13}$$

$$\lambda_{lat} = \begin{cases} 0 & if \quad T < T_s \\ \gamma Q_{lat} & if \quad T_s < T < T_l \\ Q_{lat} & if \quad T > T_l \end{cases} \tag{14}$$

where λ_{ref} is the reference specific enthalpy at a reference temperature (T_{ref}).

2.2.3 Initial and Boundary Conditions

As previously shown in Fig. 2 (c), three different types of boundary conditions were implemented in the computational domain. At the top and bottom walls of the battery cell and the PCM reservoir, heat dissipation by natural convection to the environment was considered, with a convection heat transfer coefficient (h) equal to 12.8 W/m^{2}K and an ambient temperature (T_∞) of 25°C. The symmetry condition was applied to the left wall, while the right wall was considered thermally isolated, assuming a null heat flux ($q'' = 0$). Finally, as an initial condition, the initial temperature (T_i) of the computational domain was assumed equal to 25°C.

2.3. Numerical Model

The proposed problem was solved computationally through numerical simulations in ANSYS Fluent 2023 R1, a computational fluid dynamics (CFD) software based on the FVM. SIMPLE scheme was used to handle the pressure-velocity coupling, *Least Squares Cell-Based* was applied for spatial discretization of gradients, and PRESTO! scheme for pressure. Finally, the *Second Order Upwind* method was used for momentum and energy equations terms. Residuals of 10^{-3} were adopted as the convergence criterion for the continuity and

momentum equations, while 10^{-6} was applied for energy. For the time discretization, three-time steps (0.01s, 0.05s, and 0.1s) were tested and the difference between them for the discharge rate of 5C was analyzed in terms of T_{min} and T_{max} as a function of the battery State of Charge (SoC) for the $\phi = 0.10$ case, as shown in Fig. 3 (a-b).

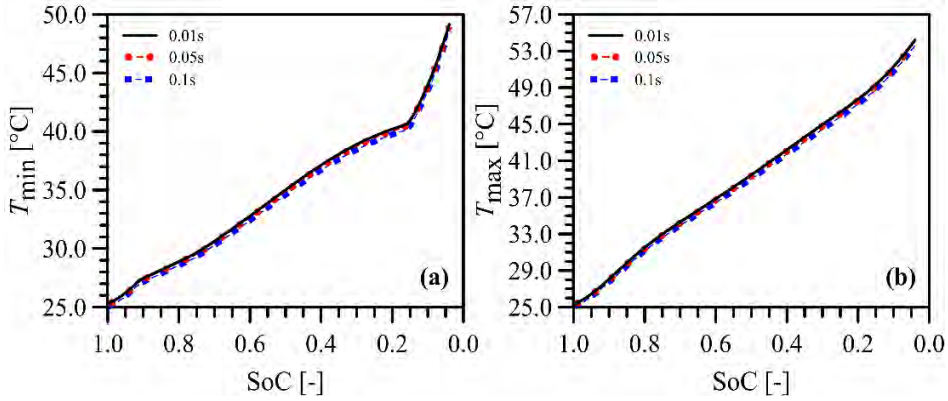


Fig. 3. Minimum and maximum temperatures of the battery as a function of its state of charge (SoC) for the discharge rate of 5C and $\phi = 0.10$, with the three-time steps tested: 0.01s , 0.05s, and 0.1s

As can be seen in Fig. 3 (a-b), the difference between the results obtained with the different time steps is minimal, which indicates that any of the values tested are adequate. In the present work, the intermediate value has been chosen due to the more stable solution obtained with it, which required fewer iterations for the convergence of the equations and, consequently, a shorter computational time. Therefore, a time step of 0.05s was chosen for all simulations, with a maximum of 1000 iterations per time interval, resulting in a computational time of 12 to 48 hours per simulation.

Table 3. Uncertainty between meshes M1 and M2 (GCI_{21}) and M2 and M3 (GCI_{32})

Performance Indicators	GCI_{21}	GCI_{32}
Battery Maximum Temperature (T_{max})	0.03%	0.09%
Battery Difference Temperature (ΔT_{cell})	0.07%	0.12%

The spatial discretization of the computational domain was carried out using structured grid meshes composed of square cells. A higher density of cells was applied along the battery cell/PCM reservoir interface, as well as on all the solid walls of the PCM reservoir, refining the regions where the largest temperature and velocity gradients occur. The mesh uncertainty analysis was conducted using the *Grid Convergence Index* (GCI) method [32-33]. For this purpose, three grid meshes with different numbers of cells (91350, 63945, and 44742 cells; referred to as M1, M2, and M3, respectively) were created and tested in the computational domain. Table 3 shows the uncertainty between meshes M1 and M2 (GCI_{21}), as well as between meshes M2 and M3 (GCI_{32}), for T_{max} and ΔT_{cell} at the end of the battery discharge process (SoC = 0), calculated for the case in which the discharge rate is equal to 5C and $\phi = 0.10$. As can be observed, for both performance indicators analyzed, GCI_{21} and GCI_{32} were found to be below 1%, indicating that the results are not dependent on the meshes. Therefore, the most refined grid mesh – containing 91350 cells – is appropriate for the spatial discretization of the

computational domain; thus, all the other grid meshes were built based on the construction parameters of the respective mesh.

2.4. Model Verification

In order to verify that the mathematical and numerical models implemented are indeed appropriate for the proposed study, initially they were employed to reproduce a similar. study from the literature. The study reproduced for this purpose was the numerical work by Borahel *et al*. [27], which investigated the discharge process of a Li-ion battery pack with the same technical specifications and assembly scheme as the battery studied in this paper. The main difference between the works is the complexity of the models implemented, as Borahel *et al.* [27] evaluate the battery as a whole, in three dimensions, including the electrical effects of discharge through the Equivalent Circuit Model (ECM) [32-33]. Furthermore, in the reference work, the battery is cooled exclusively by natural convection, without the PCM reservoirs between the battery cells, as in the present study.

Fig. 4 (a-b) shows the battery temperature as a function of its State of Charge (SoC) for the discharge rates of 3C and 5C, based on the results reported by Borahel *et al*. [27] and present work; where (a) display the battery average temperature (T_{ave}) and (b) the maximum temperature (T_{max}).

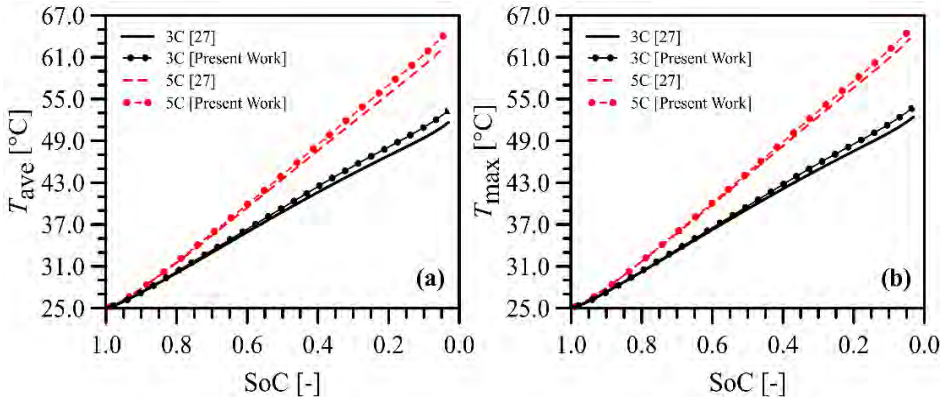


Fig. 4. Average and maximum battery temperatures as a function of State of Charge (SoC) for the discharge rates of 3C and 5C, obtained by Borahel *et al*. [27] and the present work

As can be seen in Fig. 4 (a-b), the results obtained using the mathematical and numerical models implemented in this work are very similar to those reported by Borahel *et al*. [27] for both discharge rates tested. The maximum difference observed between the results in terms of T_{ave} [Fig. 4(a)] was 1.68°C for the 3C discharge rate and 1.74°C for 5C, both found at the end of the discharge process. Regarding T_{max} [Fig. 4(b)], the maximum differences were equals to 1.40°C and 1.32°C for 3C and 5C discharge rates, respectively. Therefore, despite being significantly simpler than the models used by Borahel *et al*. [27], the models implemented in this study were also able to adequately reproduce the heating of the Li-ion battery pack during its discharge. Thus, it can be said that the implemented models are indeed suitable for the proposed study.

3. Results and Discussion

For both discharge rates used (3C and 5C), the cooling of the battery cell and consequently the performance of the BTMS as a function of ϕ was evaluated in terms of T_{max} and ΔT_{cell}.

Figure 5 (a-c) shows (i) T_{max}, (ii) ΔT_{cell} and (iii) γ plotted *versus* SoC for the discharge rates of (a) 3C and (b) 5C.

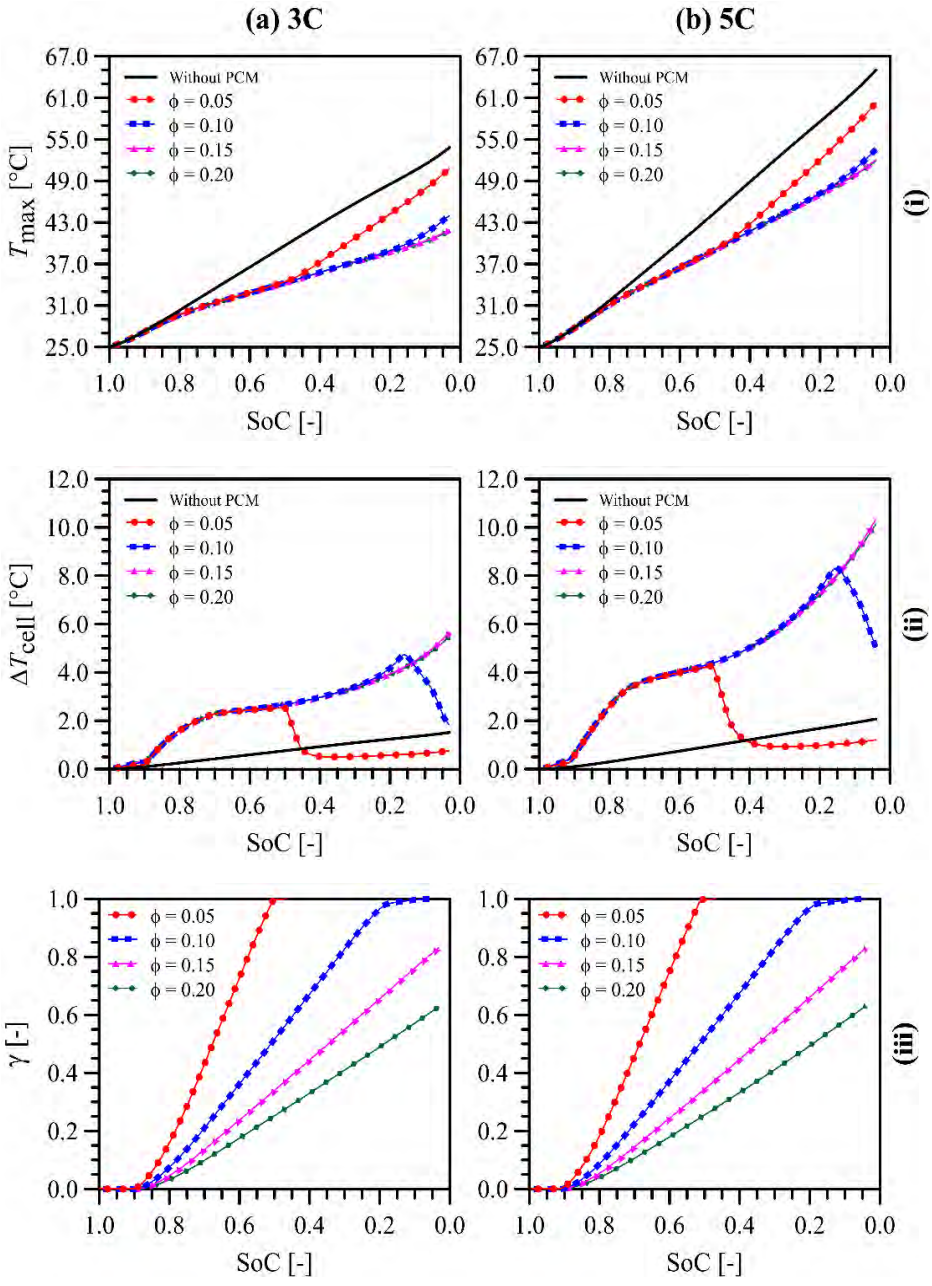


Fig. 5. Curves of (i) T_{max}, (ii) ΔT_{cell} and (iii) γ as a function of SoC for (a) 3C and (b) 5C discharge rates

In this figure, the results of the battery without BTMS are compared with those obtained for the cases with BTMS (with PCM reservoir), where W_{pcm} and, consequently, V_{pcm}, vary with ϕ.As expected, the battery cell heats up throughout the discharge, with the heating

being more pronounced in the 5C case. The highest values of T_{max} are reached at the end of the discharge (SoC ≅ 0), regardless of the presence or absence of the PCM reservoir. At this stage of discharge, T_{max} was 53,8°C for the 3C case without the PCM reservoir [Fig. 5 (a)(i)], followed by 50.8°C for the $\phi = 0.05$ case; 44°C for $\phi = 0.10$; 42°C for $\phi = 0.15$ and 41.8°C for $\phi = 0.20$. For the same cases, but considering the 5C discharge rate [Fig. 5 (b)(i)], T_{max} at SoC ≅ 0 were 65°C; 60.3°C; 53.6°C; 52.1°C and 51.9°C, respectively. Thus, it is clear that the PCM reservoir contributed to the battery cooling, reducing T_{max} by 12°C (53.8°C ⟶ 41.8°C) in the 3C discharge rate cases and by 13.1°C (65°C ⟶ 51.9°C) for 5C. Despite the significant reduction in T_{max}, its maximum values are still above the ideal operating temperature range considered in the present work, which varies between 25°C and 40°C [7]; however, it is still lower than the maximum acceptable temperature (60°C) [34] proposed by some authors and manufacturers. A more detailed analysis of the T_{max} behavior as a function of SoC shows that the battery temperature is not affected by the PCM reservoir in the early stages (SoC ≥ 0.8) of the discharge process. The PCM reservoir only begins to contribute to the battery cooling after SoC = 0.8, when the battery temperature exceeds the PCM melting temperature, initiating the melting process, as shown in Fig. 5 (a-b) (iii). For all ϕ tested, T_{max} showed a very similar behavior until SoC = 0.45. After this moment, T_{max} for the $\phi = 0.05$ case has a more pronounced increase. Since W_{pcm} is reduced for $\phi = 0.05$, the PCM volume (V_{pcm}) and, consequently, the PCM mass are smaller. Thus, the PCM reservoir completes its melting more quickly, in the first half of the battery discharge process (SoC ≅ 0.50), as illustrated in Fig. 5 (a-b) (iii). As a result, the battery cell loses the thermal protection provided by the PCM in the second half of the discharge process, which justifies the increase in T_{max}. For the same reason, a more pronounced heating is observed in the $\phi = 0.10$ case during the final stages of discharge [Fig. 5 (a-b) (i)], as the complete melting of the PCM occurs at SoC ≅ 0.1. On the order hand, V_{pcm} proved to be higher than necessary in the $\phi = 0.15$ and 0.2 cases. Thus, at the end of the discharge process, there is still unmelted PCM in the reservoir [Fig. 5 (a-b) (iii)], which explains the great similarity of T_{max} between these two cases.

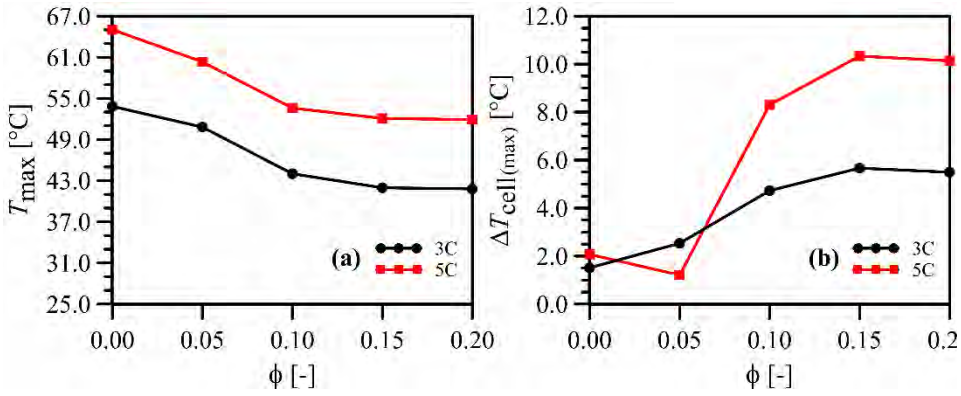


Fig. 6. Curves of (a) T_{max} and (b) $\Delta T_{cell(max)}$ as a function of ϕ for the discharge rates of 3C and 5C

The PCM reservoir, and consequently the ϕ value, also had a significant influence on ΔT_{cell}. This is illustrated in Fig. 5 (a-b)(ii), which presents the variation of ΔT_{cell} as a function of SoC for the battery cell without PCM reservoir, as well as for the cases with reservoir and different ϕ values. For both discharge rates (3C and 5C), the lowest ΔT_{cell} values are associated with the baseline cases (without PCM). When the PCM reservoir is included, there is an increase in ΔT_{cell}, which shows that the cooling it provides is not uniform, especially for the highest values of ϕ. For $\phi = 0.05$ and 0.10, ΔT_{cell} exhibits an increasing

behavior identical to that observed for $\phi = 0.15$ and 0.20. However, after the PCM has melted completely, ΔT_{cell} decreases rapidly, suggesting that the battery cell temperature becomes more uniform as the PCM reservoir ceases to contribute to its cooling. Figure 6 (a-b) provides a more detailed view of the effects of ϕ on the battery cell cooling, showing (a) T_{max} and (b) the maximum cell temperature difference ($\Delta T_{cell(max)}$) as a function of ϕ for the discharge rates of 3C and 5C.

As can be seen in Fig. 6 (a-b), T_{max} and $\Delta T_{cell(max)}$ show opposite behaviors with respect to ϕ. While T_{max} decreases with ϕ for both discharge rates, $\Delta T_{cell(max)}$ increases. This indicates that increasing the PCM volume by ϕ, and therefore its mass, helps to reduce the battery temperature, but the cooling is not homogeneous, as already mentioned. However, ϕ ceases to affect T_{max} and $\Delta T_{cell(max)}$ when its value exceeds 0.1; as evidenced by the nearly constant behavior of these variables for $\phi > 0.1$. This means that it is not necessary to continuously increase the volume of the PCM reservoir to further reduce T_{max} so that its maximum value does not exceed 40°C or to ensure that $\Delta T_{cell(max)}$ does not exceed 5°C. Instead, it requires ensuring that the PCM melts completely at the right time (end of discharge) and that the heat generated by the battery is dissipated homogeneously, which was not achieved for $\phi = 0.15$ and 0.20.

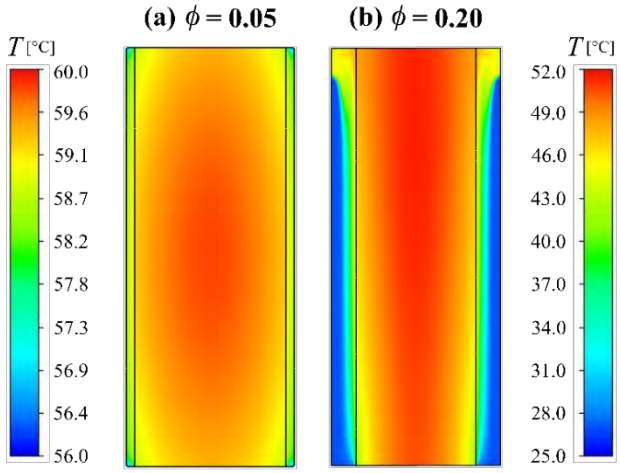


Fig. 7. Temperature contours of the battery cell and the PCM reservoir at the end of the discharge process (SoC ≅ 0) for the 5C rate, where: (a) $\phi = 0.05$ and (b) $\phi = 0.20$

Figure 7 (a-b) presents the temperature contours of the battery cell and the PCM reservoir at the end of the discharge process (SoC ≅ 0) for the 5C rate, considering (a) $\phi = 0.05$ and (b) $\phi = 0.20$. As shown in Fig. 7 (a-b), the highest battery temperatures are concentrated in the center of the cell, regardless of ϕ. The battery temperatures are higher in the case with $\phi = 0.05$ compared to the case with $\phi = 0.20$, as previously indicated by Fig. 5 (b)(i) and 6 (a). Analyzing the PCM reservoir for the case with $\phi = 0.05$ [Fig. 6 (a)], it is clearly visible a homogeneous temperature that varies in a range of values between 58 and 59°C, which is much higher than the PCM melting temperature, 29°C. Therefore, the PCM is entirely liquefied, consistent with what is shown in Fig. 5 (b)(iii). On the other hand, the PCM reservoir for the case with $\phi = 0.20$ [Fig. 7 (b)] shows heterogeneous temperatures, ranging from 25°C to approximately 49°C at its top. The dark blue areas indicate temperatures below the PCM melting temperature, meaning the PCM is still in its solid phase. Thus, the silhouette of the solid layer is clearly visible, being thicker at the base of

the reservoir and gradually thinning towards the top. This shape of the solid PCM layer is closely related to the convection mechanism, which generates an ascending plume of liquid PCM. This liquid PCM accumulates at the top of the reservoir, and due to its higher temperatures, it erodes the solid PCM layer. This accumulation of liquid PCM with higher temperatures at the top of the reservoir is detrimental to the battery cooling, because it reduces the heat dissipation and creates temperature gradients between the top and bottom regions of the battery cell.

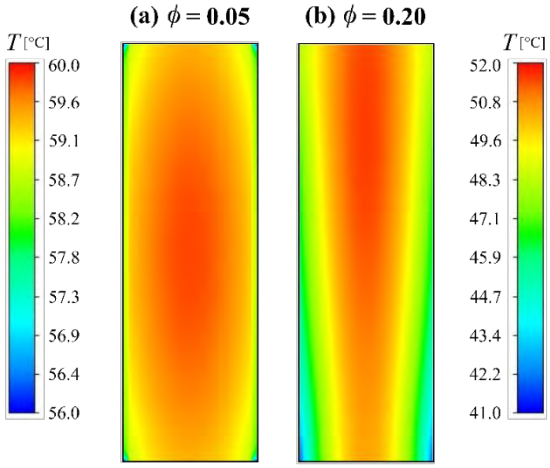


Fig. 8. Temperature contours of the battery cell at the end of its discharge process (SoC ≅ 0) for the 5C rate, with (a) $\phi = 0.05$ and (b) $\phi = 0.20$

A better understanding of how the natural convection of the liquid PCM affects the temperature distribution of the battery cell is provided by Figure 8 (a-b), which shows the temperature contours of the battery at the end of its discharge process (SoC ≅ 0) for the 5C rate, with (a) $\phi = 0.05$ and (b) $\phi = 0.20$. This figure differs from Fig. 7 by focusing exclusively on the battery, without considering the PCM reservoir. This allows a more localized analysis, making the temperature gradients within the battery more evident due to the better adaptation of the contour scale to the battery temperatures. Once again, it can be observed for both cases that the maximum temperatures are located in the central regions of the battery cell. However, the difference between the temperatures at the top and bottom regions of the cell is now clearly evident in the case of $\phi = 0.20$ [Fig. 8 (b)]. Since the hot liquid PCM accumulates at the top region of the reservoir [Fig. 7 (b)], the temperature gradient between this region and the top of the battery is smaller, reducing the heat dissipation from the battery and, consequently, justifying its higher temperatures at the top. On the other hand, the larger amount of solid PCM at the base of the reservoir results in a greater temperature gradient between this region of the reservoir and the lower regions of the battery, promoting the heat transfer and, consequently, mitigating the temperature increase at the base of the battery. Thus, a high temperature gradient is established in the battery cell, which explains the higher $\Delta T_{cell(max)}$ values observed in Fig. 6 (b) for the case under analysis. A possible solution to prevent the accumulation of hot PCM at the top of the reservoir and promote a more uniform temperature in the battery would be to divide the reservoir into several compartments. This could be achieved using fins, which would also help to improve the heat dissipation from the battery.

4. Conclusions

The objective of this study was to evaluate, using the Constructal Design Method (CDM), the influence of the width (W_{pcm}) of a reservoir filled with PCM on the cooling performance of a Li-ion battery pack; composed of six battery cells connected in a 3s2p configuration; discharged at rates of 3C and 5C. In the context of CDM, the constraint of the system was the battery cell volume (V_{pcm}); while the degree of freedom (DoF) was W_{pcm}, which was expressed in dimensionless form by ϕ. The proposed problem was solved computationally through two-dimensional numerical simulations based on the finite volume method (FVM). The mathematical model was multiphase, transient, and based on the conservation equations of mass, energy, and momentum; supplemented by the enthalpy-porosity method to model the PCM melting. Based on the results obtained, the main findings were:

i) The presence of the PCM reservoir, and consequently its width (W_{pcm}), has a strong influence on the battery cooling. At the end of the discharge process (SoC ≅ 0), the maximum temperature (T_{max}) reached by the battery cell was equal to 53.8°C for the 3C case without the PCM reservoir, followed by 50.8°C for the $\phi = 0.05$ case; 44°C for $\phi = 0.10$; 42°C for $\phi = 0.15$ and 41.8°C for $\phi = 0.20$. For the same cases, but considering the 5C discharge rate, T_{max} at SoC ≅ 0 were 65°C; 60.3°C; 53.6°C; 52.1°C and 51.9°C, respectively. In other words, the PCM reservoir contributed to the battery cooling, especially when it had a larger width, represented by ϕ.

ii) In general, T_{max} decreases with ϕ, while the maximum battery cell temperature difference ($\Delta T_{cell(max)}$) increases. However, for values of ϕ greater than 0.15, these variables exhibit an asymptotic behavior, becoming practically constant. Since for $\phi = 0.15$ and 0.20 the volume of the PCM reservoir proved to be larger than necessary, the mass of PCM contained inside it does not melt completely. Thus, the latent heat absorbed by the PCM during its melting becomes practically the same regardless of ϕ, so that T_{max} and $\Delta T_{cell(max)}$ no longer vary as a function of ϕ. Therefore, reducing T_{max} even further and ensuring that $\Delta T_{cell(max)}$ stays below 5°C (the indicated limit) is not done by increasing ϕ. Thus, it can be concluded that the PCM reservoir width (W_{pcm}) significantly contributes to the battery cooling. However, varying this parameter alone is not sufficient to ensure that T_{max} and $\Delta T_{cell(max)}$ remain below the predefined maximum limits considered, which are 40°C and 5°C, respectively. Therefore, solutions that enhance the heat dissipation from the battery and ensure it occurs uniformly are required. One proposed solution, which could be evaluated in future studies, is to divide the PCM reservoir into several partitions using fins. Theoretically, the fins would increase the cooling of the battery and, by dividing the PCM reservoir into several compartments, would prevent the accumulation of molten PCM at high temperatures at the top of the reservoir, thus contributing to the uniform cooling.

Acknowledgement

The authors acknowledge the Brazilian agencies CAPES, CNPq, FAPERGS (Proc. No. 21/2551-0002169-1) and Fundação para a Ciência e Tecnologia, I.P. (doi.org/10.54499/UIDP/04683/2020) for the financial support received. R.S. Borahel has a postdoctoral fellowship funded by FAPERGS. The author G.D. Telli thanks FAPERGS for the financial support (Process: 23/2551-0000802-5). L.A.O. Rocha, L.A. Isoldi and E.D. dos Santos are grant holders of CNPq (Proc. No 307791/2019-0, 309648/2021-1, 308396/ 2021-9).

References

[1] Solaymani S. CO2 emissions patterns in 7 top carbon emitter economies: The case of transport sector. Energy, 2019; 168: 989-1001. https://doi.org/10.1016/j.energy.2018.11.145

[2] Isik M, Sarica K, Ari I. Driving forces of Turkey's transportation sector CO2 emissions: An LMDI approach. Transport Policy, 2020; 97: 210-219. https://doi.org/10.1016/j.tranpol.2020.07.006

[3] Möring-Martínez G, Senzeybek M, Jochem P. Clustering the European Union electric vehicle markets: A scenario analysis until 2035. Transportation Research Part D: Transport and Environment, 2024; 135: 104372. https://doi.org/10.1016/j.trd.2024.104372

[4] Barić D, Grabušić S, Jakara M, Emanović M. Reviewing the cost-benefit analysis and multi-criteria decision-making methods for evaluating the effectiveness of lithium-ion batteries in electric vehicles. Sustainability, 2024; 16(1): 233. https://doi.org/10.3390/su16010233

[5] Saw LH, Poon HM, San Thiam H, Cai Z, Chong WT, Pambudi NA, King YJ. Novel thermal management system using mist cooling for lithium-ion battery packs, Applied Energy. 2018; 223: 146-158. https://doi.org/10.1016/j.apenergy.2018.04.042

[6] Wang Y, Chen X, Li C, Yu Y, Zhou G, Wang C, Zhao W. Temperature prediction of lithium-ion battery based on artificial neural network model. Applied Thermal Engineering, 2023; 228: 120482. https://doi.org/10.1016/j.applthermaleng.2023.120482

[7] Pesaran AA. Battery thermal models for hybrid vehicle simulations. Journal of Power Sources, 2002; 110 (2): 377-382. https://doi.org/10.1016/S0378-7753(02)00200-8

[8] Moaveni A, Siavashi M, Mousavi S. Passive and hybrid battery thermal management system by cooling flow control, employing nano-PCM, fins, and metal foam. Energy, 2024; 288: 129809. https://doi.org/10.1016/j.energy.2023.129809

[9] Li K, Yao X, Li Z, Gao T, Zhang W, Liao Z, Xu C. Thermal management of Li-ion batteries with passive thermal regulators based on composite PCM materials. Journal of Energy Storage, 2024; 89: 111661. https://doi.org/10.1016/j.est.2024.111661

[10] Son YW, Kang D, Kim J. Passive battery thermal management system for an unmanned aerial vehicle using a tetrahedral lattice porous plate. Applied Thermal Engineering, 2023; 225: 120186. https://doi.org/10.1016/j.applthermaleng.2023.120186

[11] Srivastava G, Nandan R, Das MK. Thermal runaway management of Li-ion battery using PCM: A parametric study. Energy Conversion and Management: X, 2022; 16: 100306. https://doi.org/10.1016/j.ecmx.2022.100306

[12] Alghassab MA. Investigating the performance improvement of lithium-ion battery cooling process using copper fins and phase change materials (PCMs). Case Studies in Thermal Engineering, 2024; 59: 104473. https://doi.org/10.1016/j.csite.2024.104473

[13] Bejan A, Lorente S. Constructal theory of generation of configuration in nature and engineering. Journal of Applied Physics, 2006; 100: 1-11. https://doi.org/10.1063/1.2221896

[14] Bejan A, Lorente S. Design with Constructal Theory. John Wiley & Sons Inc, New Jersey, USA, 2008. https://doi.org/10.1002/9780470432709

[15] Bejan A. The Physics of Life: The Evolution of Everything. St. Martin's Press, New York, USA, 2016.

[16] Lorenzini G, Rocha LAO. Constructal design of Y-shaped assembly of fins. International Journal of Heat and Mass Transfer, 2006; 49 (23-24): 4552-4557. https://doi.org/10.1016/j.ijheatmasstransfer.2006.05.019

[17] Borahel RDS, Zinani FSF, Rocha LAO, dos Santos ED, Isoldi LA, Biserni C. Geometric optimization of a rectangular isothermal block inside a lid-driven cavity by means of constructal design. International Communications in Heat and Mass Transfer, 2022; 139: 106499. https://doi.org/10.1016/j.icheatmasstransfer.2022.106499

[18] Cunegatto EHT, Zinani FSF, Biserni C, Rocha LAO. Constructal design of passive micromixers with multiple obstacles via computational fluid dynamics. International Journal of Heat and Mass Transfer, 2023; 215: 124519. https://doi.org/10.1016/j.ijheatmasstransfer.2023.124519
[19] Borahel RDS, Zinani FSF, Isoldi LA, dos Santos ED, Rocha LAO. Analysis of the design of cavities with isothermal blocks under mixed convection. Journal of Applied and Computational Mechanics, 2024.
[20] Cunegatto EHT, Gotardo M, Zinani FSF. Numerical analysis of tube arrangements with one, two, and four degrees of freedom for heat transfer with pseudoplastic fluids. International Journal of Heat and Mass Transfer, 2023; 208: 124080. https://doi.org/10.1016/j.ijheatmasstransfer.2023.124080
[21] Gungor S, Cetkin E, Lorente S. Thermal and electrical characterization of an electric vehicle battery cell, an experimental investigation. Applied Thermal Engineering, 2022; 212: 118530. https://doi.org/10.1016/j.applthermaleng.2022.118530
[22] Yang X, Gao X, Zhang F, Luo W, Duan Y. Experimental study on temperature difference between the interior and surface of Li [Ni1/3Co1/3Mn1/3] O2 prismatic lithium-ion batteries at natural convection and adiabatic condition. Applied Thermal Engineering, 2021; 190: 116746. https://doi.org/10.1016/j.applthermaleng.2021.116746
[23] ANSYS Fluent. Theory Guide. 2023.
[24] Rubitherm Technologies GmbH. Data Sheet RT28HC. 2024.
[25] Hariss M, Gounni A, El Alami M. Impact of innovative fin design on phase change material melting for thermal energy storage system. Applied Thermal Engineering, 2023; 231: 120914. https://doi.org/10.1016/j.applthermaleng.2023.120914
[26] Telli GD, Gungor S, Lorente S. Counterflow canopy-to-canopy and U-turn liquid cooling solutions for battery modules in stationary Battery Energy Storage Systems. Applied Thermal Engineering, 2024; 238: 121997. https://doi.org/10.1016/j.applthermaleng.2023.121997
[27] Borahel RDS, Telli GD, Bolzoni AA, Rocha LAO, dos Santos ED, Isoldi LA. Numerical analysis of the volumetric heating of a lithium-ion battery pack: an alternative approach. Proceedings of the 20th Brazilian Congress of Thermal Sciences and Engineering (ENCIT), Foz do Iguaçu, Brazil, November, 2024.
[28] Chen M, Rincon-Mora GA. Accurate Electrical Battery Model Capable of Predicting Runtime and IV Performance. IEEE Transactions on Energy Conversion, 2006; 21(2): 504-511. https://doi.org/10.1109/TEC.2006.874229
[29] Gungor S, Telli GD, Lorente S. Characterizing Li-ion battery thermal behavior; a methodology when little information is available. International Communications in Heat and Mass Transfer, 2023; 148: 107076. https://doi.org/10.1016/j.icheatmasstransfer.2023.107076
[30] Voller VR, Prakash C. A fixed grid numerical modelling methodology for convection-diffusion mushy region phase-change problems. International Journal of Heat and Mass Transfer, 1987; 30(8): 1709-1719. https://doi.org/10.1016/0017-9310(87)90317-6
[31] Yusuf A, Ballikaya S. Performance analysis of concentrated photovoltaic systems using thermoelectric module with phase change material. Journal of Energy Storage, 2023; 59: 106544. https://doi.org/10.1016/j.est.2022.106544
[32] Roache PJ. Verification and Validation in Computational Science and Engineering, Hermosa, Albuquerque, USA, 1998.
[33] Celik IB, Ghia U, Roache PJ, Freitas CJ, Coleman H, Raad PE. Procedure for estimation and reporting of uncertainty due to discretization in CFD applications. Journal of Fluids Engineering, 2008; 130. https://doi.org/10.1115/1.2960953
[34] Ma S, Jiang M, Tao P, Song C, Wu J, Wang J, Deng T, Shang W. Temperature Effect and Thermal Impact in Lithium-Ion Batteries: A Review, Progress in Natural Science: Materials International, 2018; 28(6): 653-666. https://doi.org/10.1016/j.pnsc.2018.11.002

Blank Page

Research on Engineering Structures & Materials
www.jresm.org

Research Article

Prediction of the flexural capacity of steel fiber reinforced self-compacting concrete beams combining neural networks, the Barcelona test and the gravitational search algorithm

David Cotes-Prieto *[,a], Luis Zapata-Ordúz [b]

Grupo de Investigación en Materiales de Construcción y Estructuras (INME), Universidad Industrial de Santander, Escuela de Ingeniería Civil, Colombia

Article Info

Article History:

Received 08 Dec 2024

Accepted 24 Jan 2025

Keywords:

Steel fiber reinforced self-compacting concrete;
Barcelona test;
Artificial neural networks;
Gravitational search algorithm;
Non-linear finite element analysis

Abstract

Steel fiber reinforced self-compacting concrete (SFRSCC) has improved fresh and hardened state properties compared to conventional concrete. Nonetheless, experimentally validated tools to model its flexural capacity are still required to encourage its massive application in civil infrastructure. This research assessed the maximum bending moment (Mu) of SFRSCC beams in four-point loading using an Artificial Neural Network (ANN). The experimental program considered water-binder ratios (w/b) from 0.40 to 0.60 and steel fiber ratios (%F) from 0.00% to 1.00% in volume. Compressive and tensile behaviors were obtained by combining constitutive models based on uniaxial compression and double-punching Barcelona tests. A modification to the existing Barcelona test constitutive model is proposed to improve post-peak stress prediction. To increase the amount of data needed for proper training of the ANN, non-linear finite element analyses (NLFEAs) were executed through commercial software. NLFEAs were fed using the constitutive relationships from tests. ANN inputs were w/b, and %F, and the output was Mu. Different ANN architectures were evaluated and trained using Momentum Back-Propagation, Particle Swarm Optimization, and Gravitational Search Algorithm (GSA). Results showed that the ANN trained with GSA accurately predicted (R^2=0.99) the Mu.

© 2025 MIM Research Group. All rights reserved.

1. Introduction

Nowadays, concrete is the most used structural material in the construction industry (1). Nonetheless, hardened Conventional Concrete (CC) has low tensile strength, ductility, and tenacity (2,3). Therefore, its use in practice requires incorporating reinforcement to improve its mechanical properties, with steel rebar being the most common choice. Additionally, CC has limited workability in fresh state, so low quality control during casting elements with high rebar ratios can lead to discontinuities due to poor consolidation or undesired reinforcement movements, compromising the structural capacity and durability (4,5).

Hence, to overcome these disadvantages, research attention has been addressed on Steel Fiber Reinforced Self-Compacting Concrete (SFRSCC). SFRSCC improves the CC fresh state properties, allowing it to flow through the formwork mainly by its self-weight with low or no need of vibration. Therefore, higher quality elements are achieved due to the more uniform consolidation during pouring (4–6). Moreover, in hardened state, the addition of steel fibers contributes to control cracking as these markedly improve SFRSCC tensile and strain capacity, compared to CC (2,3,7,8). Consequently, the rebar required can be reduced without compromising strength and ductility (7,9). Despite its benefits, manufacturing SFRSCC requires higher amounts of binder than CC. Hence, its cement consumption is reduced by using supplementary cementitious materials, such as

*Corresponding author: dscotpri@correo.uis.edu.co
[a]orcid.org/0000-0001-7761-1617; [b]orcid.org/0000-0001-8586-602X
DOI: http://dx.doi.org/10.17515/resm2025-569ml1208rs

fly ash, which not only allows SFRSCC to be more cost-effective material but also diminishes its carbon-print (10,11).

The improved characteristics of SFRSCC make it a feasible candidate for wide use in civil infrastructure, which is often subjected to flexure (therefore, tensile stresses and strains). Literature reports show successful implementations of SFRSCC in bending subjected structures, such as buildings, retaining walls, slabs, pipes, and tunnels (3,9,12–15). However, its massive application is scarce in many countries due to the usual need for time and money-consuming laboratory tests to assess its flexural capacity. The main reason behind this is the lack of reliable models and practical tools to predict SFRSCC members hardened state mechanical properties. For instance, in Colombia, the national standard for structural design of buildings (NSR-10) demands intense flexural testing to monitor the cracking strength and post-peak behavior. This standard also lacks on recommendations for theoretically assessing SFRSCC mechanical behavior (16).

Many researchers have published different alternatives to predict the flexural strength of SFRSCC, most based on constitutive modeling of the tensile response along with Non-Linear Finite Element Analysis (NLFEA). Moradi et al. (17) proposed a constitutive model including the post-peak behavior of Steel Fiber Reinforced Concrete (SFRC) based on the results of direct tensile and compressive tests. They successfully implemented the model along with NLFEA to predict the ultimate flexural capacity of beams. Lee et al. (18) modeled the constitutive behavior of SFRC using exponential functions, where the parameters were obtained through bending tests. This model, although functional, still requires the use of expensive laboratory tests. Huo et al. (19) published a stress-strain model that included the orientation effect of the fibers. The inputs of the model were basic material and geometric parameters, easy to obtain with no need for complex testing. The feasibility of the model was proved by accurately predicting the load-displacement curves of beams modeled with NLFEA. Nonetheless, the equations are non-linear and complex, requiring vast knowledge by the practitioner who may use them for applied cases.

An interesting approach to modeling the constitutive behavior of SFRC was presented by Blanco et al. (20). They established simplified equations to assess the tensile behavior of the material based on the results of the Barcelona test. The Barcelona test is a double punching test that captures the tensile response of SFRC with several advantages over the bending and uniaxial tensile tests. It is less time and material-consuming, easier to perform, and its results at different samples of equal dosage exhibit less statistical scatter (20). Nonetheless, the equations underestimated the strength of the material during the post-peak behavior. Moreover, NLFEA may still be required to determine the flexural response of SFRSCC structural elements.

The models previously mentioned may still discourage the implementation of SFRSCC in the industry since they require precise knowledge of constitutive modeling and NLFEA. A more engineering-oriented and user-friendly tool that may be an incentive for the use of SFRSCC is the Artificial Neural Network (ANN). Although training an ANN implies lots of experimental and numerical work, its final usage by a practitioner is straightforward. That is why ANN has been successfully used in civil engineering to predict complex outputs based on simple inputs. Chopra et al. (21) trained an ANN to estimate the compressive strength of concretes varying the curing age and the fly ash content. The investigation yielded R^2>0.80, which indicates good prediction capacity. Hodhoh et al. (22) achieved an ANN capable of predicting SFRC strength properties, such as compressive and impact resistance, based on the dosage of the concrete.

The need for tools that reduce the number of experiments required to predict the flexural capacity of SFRSCC concrete beams is imperative to its massive use in industry. Therefore, this investigation assessed an ANN capable of predicting the flexural strength of SFRSCC concrete beams loaded in the Four Points Bending Test (FPBT). The FPBT was here used as pure bending (no shear force) occurs at the midspan between loads, contrary to other flexural tests such as the Three Point Bending Test (23). Hence, the FPBT is a highly suitable test to achieve a more realistic characterization of the bending moment capacity of SFRSCC beams (23–25).

On the other hand, the input variables for the experiments were the simple parameters water/binder ratio (w/b) and the ratio of hooked-end fibers added by volume ($\%F$). The output was the ultimate bending moment (M_u). The training of the ANN was done by several NLFEAs and

validated with real FPBT. The NLFEA models were fed with constitutive relations calibrated with the results of uniaxial compressive and Barcelona tests. Moreover, a modification was implemented to improve the constitutive model for tensile stress-strain based on the Barcelona test proposed by Blanco et al. (20). The original model was reported by their authors to under-estimate the post-peak stresses of the SFRSCC. In that sense, the change here proposed aimed to face this issue by re-writing the equilibrium equations using the free body diagram of the cracked specimen, contrary to the original set-up of equations which was based on the uncracked configuration. The modification was found to more precisely predict the post-cracking behavior of the material.

2. Materials and Methods

This section describes the experimental campaign performed, constitutive modeling, the NLFEA executed, and the training and validation of the ANN.

2.1 Experimental Campaign

Variables considered for the SFRSCC mixtures were *%F* from 0.00% to 1.00% (0 to 78 kg/m^3) and *w/b* from 0.40 to 0.60. The fibers were hooked-ended and had a tensile strength of 1200 [MPa], length L=60 [mm], diameter d=0.75 [mm], and aspect ratio L/d=80. Ranges of *%F* and *w/b* were chosen due to their common use in Colombia according to local providers. The combinations of *%F* and *w/b* for the mixtures to test were determined using a Central Composite Design (CCD). A CCD is a type of statistical design of experiments that combines the 2^k factorial design, with $2 \cdot k$ axial points and 1 to 5 central points. The 2^k factorial design is an efficient statistical experimental design that allows to evaluate the simultaneous effect of k factors (in this case *%F* and *w/c*) on a response (in this case, the M_u) for a physical phenomenon, by using a minimum number of experimental observations (26). Moreover, the addition of the axial and central points allows fitting the model to a second order response surface. Subsequently, optimization of the factors can be performed (26). Additionally, the use of more than one central point enhances the accuracy of the estimated results on the middle of the experimental domain (26). In addition to the CCD experiments, four control mixtures with no fibers (M 40-00, M 43-00, M 57-00, and M 60-00) were added to evaluate the influences of fibers.

The self-compacting behavior of the mixtures was achieved following the mix design recommendations of Okamura (5), including the use of a super-plasticizer (SP) and a 15% mass replacement of fly ash. The fresh state properties of fluidity and viscosity of the mixtures were considered adequate when the slump-flow test diameter (SFD) was between 520 and 900 [mm], and the T_{500} test time was below 10 [s], according to EFNARC (27). Table 1 shows the mixture proportions and their fresh state control test results. The notation first indicates the *w/b* ratio and, second the *%F*. For each mixture, three batches were manufactured to cast all the specimens described ahead. An exception was considered for the central point M 50-50, where five times more batches (15 batches) were casted. This decision was adopted in order to enhance the statistical accuracy of the results according to the literature (26). Therefore, in the subsequential sections, the number of specimens tested for M 50-50 is always five times the other mixtures. Some of the results of this experimental plan have already been published by the authors (28). The concrete was used to cast cylinders for uniaxial compression tests, Barcelona, and beams for FPBT. Due to limited availability of the test equipment at the university where the experimental campaign was developed, all tests had to be performed at an age of 147 days. Although the typical testing age for structural design purposes according to the standards is 28 days for conventional concretes (up to 56 days for concretes including pozzolanic admixtures), the testing at further ages does not constitutes a major problem from the point of view of the authors as typically, more than 90% of the strength has already developed at these design ages (29). Therefore, the strength obtained testing at 147 days will more likely represents a difference (below 10%) respect to the typical design test ages that does not negatively impact the purposes of this study.

Table 1. Mix proportions and fresh state test results

Mix	w/b	%F	Cement	Fly-ash	Coarse	Fine	SP	SFD	T_{500}
			kg/m³	kg/m³	kg/m³	kg/m³	kg/m³	mm	s
M 40-00	0.40	0.00	526.09	78.91	410.91	958.78	3.39	695.00 (62.85)*	3.31 (2.53)*
M 40-50	0.40	0.50	526.09	78.91	406.90	949.42	2.96	716.67 (21.60)*	3.10 (1.11)*
M 43-00	0.43	0.00	506.74	76.01	410.16	960.79	2.80	673.33 (112.37)*	3.27 (3.21)*
M 43-15	0.43	0.15	506.74	76.01	410.52	956.48	2.10	626.67 (45.02)*	2.43 (0.71)*
M 43-85	0.43	0.85	506.74	76.01	404.43	943.66	2.62	576.67 (49.26)*	6.93 (0.98)*
M 50-00	0.50	0.00	459.13	68.87	412.39	958.38	2.01	575.00 (18.71)*	1.12 (0.21)*
M 50-50	0.50	0.50	459.13	68.87	412.39	958.38	2.01	674.93 (68.85)*	1.28 (0.32)*
M 50-100	0.50	1.00	459.13	68.87	407.24	950.22	2.01	705.00 (133.98)*	1.62 (0.97)*
M 57-00	0.57	0.00	411.18	61.68	426.37	994.84	1.23	556.67 (28.75)*	1.00 (0.00)*
M 57-15	0.57	0.15	411.18	61.68	425.20	992.10	1.23	645.00 (12.25)*	1.00 (0.00)*
M 57-85	0.57	0.85	411.18	61.68	418.45	979.97	1.37	621.67 (123.84)*	2.10 (0.97)*
M 60-00	0.60	0.00	400.00	60.00	424.71	990.99	0.78	556.67 (29.44)*	1.00 (0.00)*
M 60-50	0.60	0.50	400.00	60.00	421.62	980.68	1.29	701.67 (39.71)*	1.00 (0.00)*

*Average (Standard deviation)

2.2 Testing and Methods of Processing Results

2.2.1 Uniaxial Compression Tests

For each mixture, four cylinders of 75x150 [mm] were tested in monotonic load according to ASTM C39 (30). The deformation rate was 1.50 [mm/min] up to an actuator displacement of 6 [mm]. Compressive strength was calculated from the experimental results. Examples of the tested cylinders are presented in Figure 1 and average results of the compressive strength, $f'_{c\,avg}$, are presented in Figure 2. A detailed statistical analysis of the compressive strength is presented in the results section.

2.2.2 Barcelona Tests

Double punching Barcelona Tests were performed in 4 cylinders of 150x150 [mm] for each mixture. The punching effect was achieved by placing two cylindrical steel punches of diameter 37.5 [mm]. The test was performed according to the standard UNE-83515 (31). The deformation rate was monotonic at 0.50 [mm/min] up to an actuator displacement of 6 [mm].

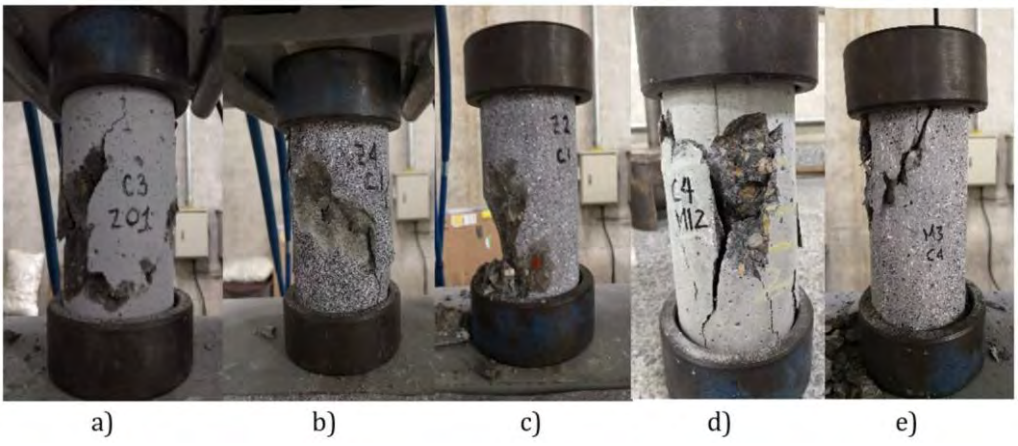


Fig. 1. Compressive strength tested cylinders: a) M 40-00, b) M 60-00, c) M 43-00, d) M 43-10 and e) M 43-85.-

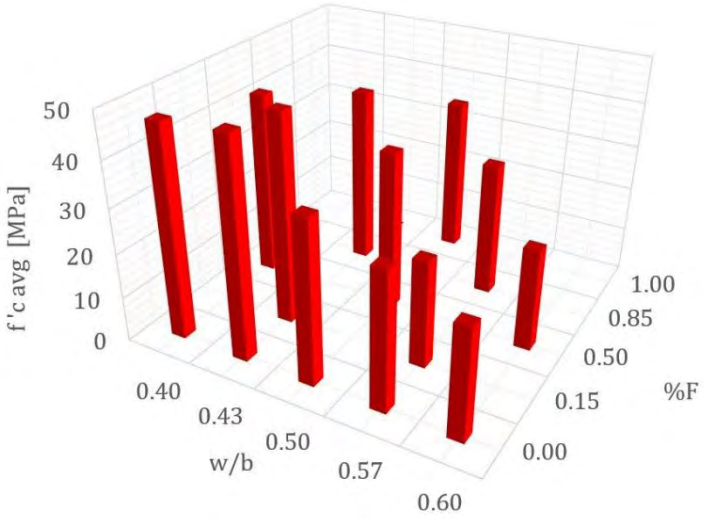


Fig. 2. Average compressive strength as function of w/b and %F

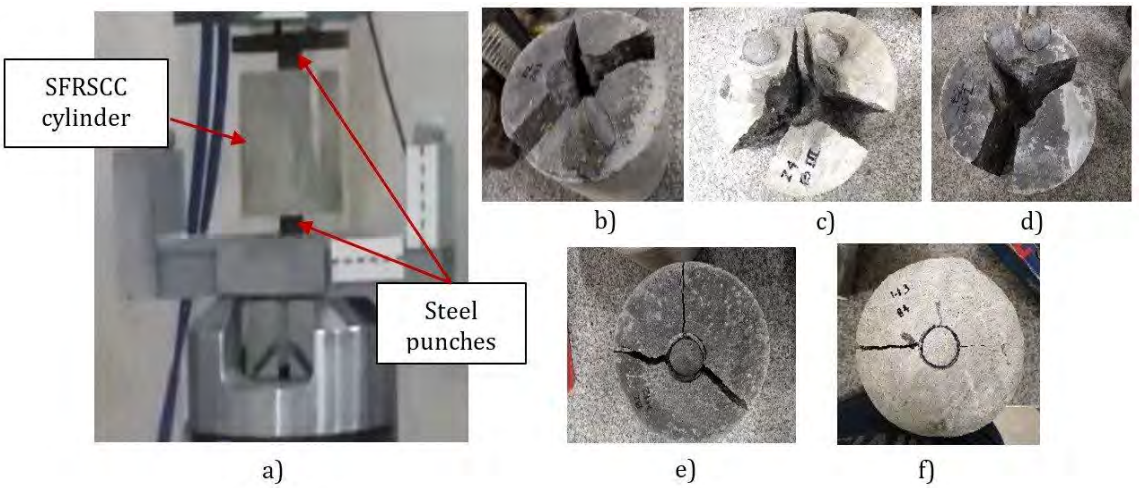


Fig. 3. Barcelona test cylinder: a) Set-up, b) M 40-00, c) M 60-00, d) M 43-00, e) M 43-10 and f) M 43-85

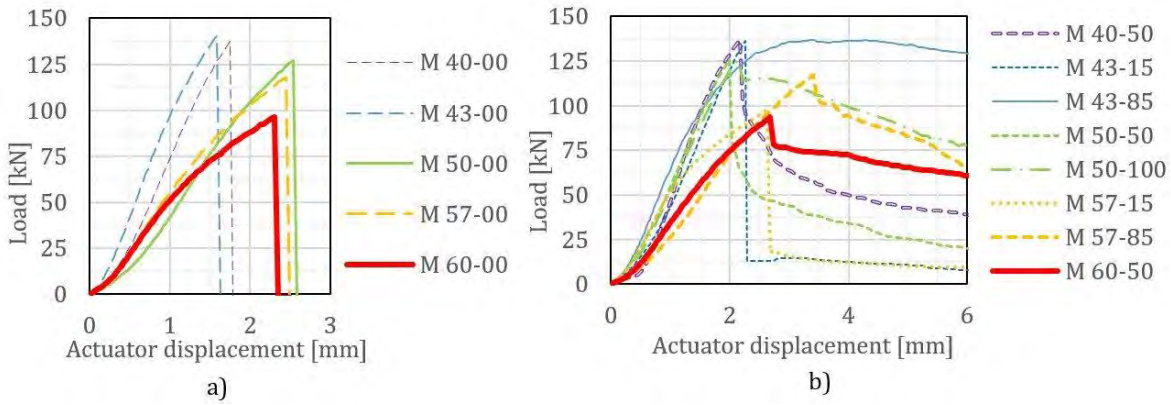


Fig. 4. Load-displacement curves for Barcelona cylinders: a) without fibers, and b) with fibers.

For reference, Figure 3 shows the test set-up and various tested cylinders. Also, examples of the load-actuator displacement curves experimentally obtained are showed in Figure 4. The data from these curves was used as the main input to determine the tensile stress-strain curve of the specimens as described in Section 2.2.6.

2.2.3 Four Points Bending Tests

The FPBTs were performed in four beams of 150x150x500 [mm] for each mixture, following the standards ASTM C1609 and RILEM TC 162-TDF (32,33). Since pure bending occurs at the central length, a notch of depth 22 [mm] and thickness 0.4 [mm] was cropped in the mid-span of the specimens to arouse the cracking there. The free length between supports at testing was 450 [mm], and the separation between loaded points 150 [mm]. Set-up of the test and some examples of beams at the end of the test are shown in Figure 5. Also, examples of the load-actuator displacement curves are presented for every mixture in Figure 6.

During the test, the deformation rate was incremental and varied depending on the actuator displacement: 0.20 [mm/min] from 0 to 1 [mm], 0.25 [mm/min] from 1 to 5 [mm], and 0.70 [mm/min] from 5 to 10 [mm]. As Bernard [29] described, the actuator displacement is not representative of the deflection (flexural deformation) the beam experiences. Therefore, Digital Image Correlation (DIC) was used to measure the mid-span deflection on the beams at each load increment. Details on this procedure can be found in a previous publication by the authors (28). The bending moment at each load was calculated using the equilibrium equations. Finally, the experimental moment-deflection curves were obtained for each tested beam.

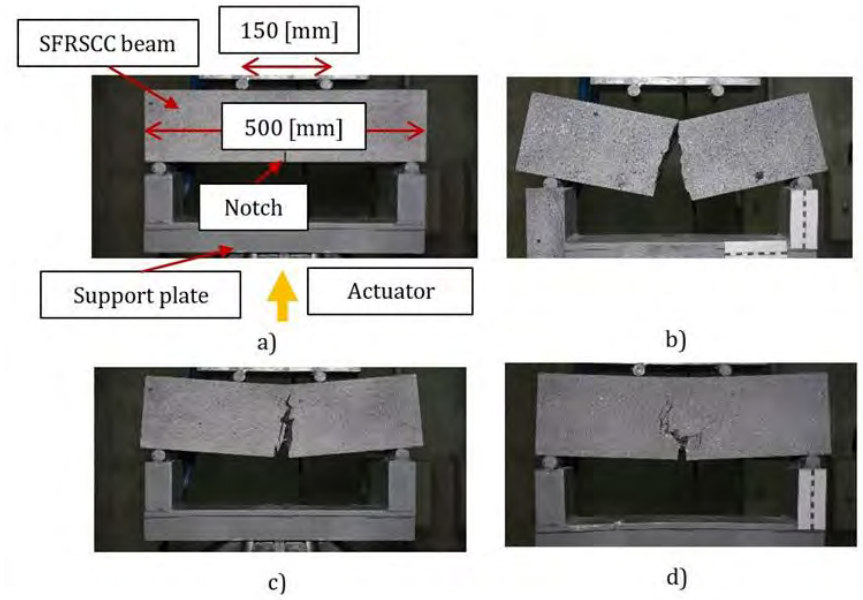


Fig. 5. FPBT beams a) Set-up, b) M 50-00, c) M 50-50, and d) M 50-100

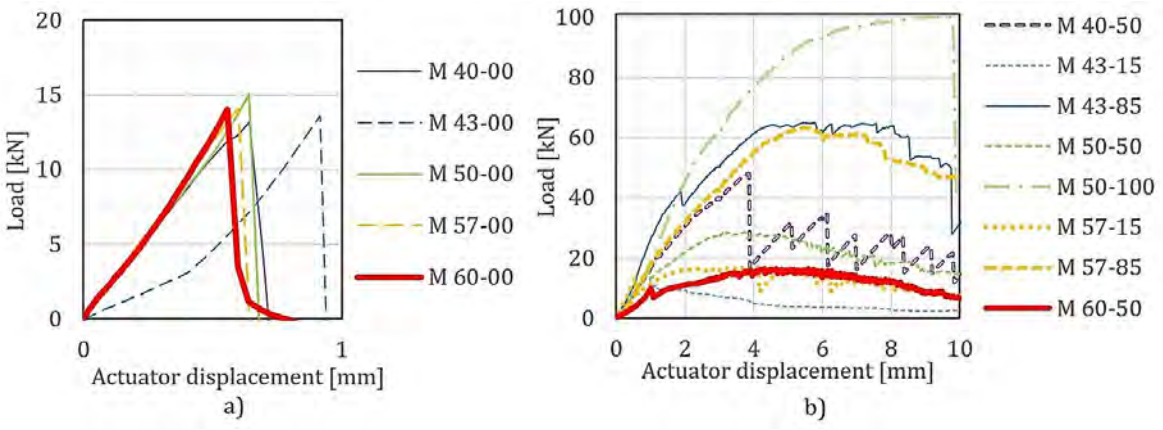


Fig. 6. Load-displacement curves for FPBTs beams: a) without fibers and, b) with fibers

2.2.4 General Aspects on The Implemented Constitutive Models

The constitutive models for the compressive and tensile stress-strain responses of the mixtures were selected based on the literature review. The compression behavior was based on the

equations proposed by Wang et at. (34) and De Oliveira (35). The tensile response was based on the model proposed by Blanco et al. (20), Bortolotti (36) and modifications to these proposed by the authors of this paper.

In all cases, the material was considered homogeneous and isotropic. The shear response was assumed to be linear, and the Poisson ratio was fixed as 0.20. This analysis was performed only for the nine mixtures part of the CCD (M 40-50, M 43-15, M43-85, M 50-00, M 50-50, M 50-100, M 57-15, M 57-86 and M 60-50 in Table 1).

2.2.5 Compressive Stress-Strain Constitutive Relation

The non-linear model implemented here was described by Wang et al. (34) and is presented equation (1). It includes the effect of fibers on compressive strength.

$$f_c = \begin{cases} f_c' \dfrac{\epsilon_c}{\epsilon_c'}\left(\alpha_a + (3-2\alpha_a)\dfrac{\epsilon_c}{\epsilon_c'} + (\alpha_a - 2)\left(\dfrac{\epsilon_c}{\epsilon_c'}\right)^2\right) & \epsilon_c < \epsilon_c' \\ f_c' \dfrac{\epsilon_c}{\epsilon_c'}\left(\dfrac{1}{\alpha_d\left(\frac{\epsilon_c}{\epsilon_c'} - 1\right)^2 + \frac{\epsilon_c}{\epsilon_c'}}\right) & \epsilon_c \geq \epsilon_c' \end{cases} \quad (1)$$

In these equations f_c is the compressive stress in [MPa] evaluated at an axial strain ϵ_c in [mm/mm], and f_c' and ϵ_c' are the compressive strength in [MPa] and its associated axial strain in [mm/mm], respectively. The shape factors α_a and α_d were calculated using the linear relations of equations (2) and (3). These equations were obtained using the empirical values of α_a and α_d published by Wang et al. (34) for $\%F$ (by volume) of 0.00 and 1.00.

$$\alpha_a = 1.5 + 0.2(\%F) \quad (2)$$

$$\alpha_d = 5.4 - 3.9(\%F) \quad (3)$$

The value of f_c' was obtained from the compressive uniaxial tests with the peak load and the cross-sectional area of the cylinder. Since the actuator displacement was not a trustable measure of the axial deformation, ϵ_c' was not determined experimentally. Equation (4), as reported by De Oliveira et al. [31], was used. It was chosen as the materials, types of fibers, and $\%F$ used in their investigation were similar to those used in this work.

$$\epsilon_c' = (0.00048 + 0.0001886(\%F))\ ln(f_c') \quad (4)$$

2.2.6 Tensile Stress-Strain Constitutive Relation

The model used was based on the proposal of Blanco et al. (20). It was chosen as it directly relates the tensile stress and strain of the SFRSCC to the load-actuator displacement curve obtained from the Barcelona test. The model assumes the material follows a linear stress-strain relation up to the peak cracking stress f_r, then captures the residual stresses and their related strain after cracking. This residual behavior is the main contribution of the steel fibers. Blanco et al. (20) reported that their original model underestimates the cracking peak and residual stresses compared to other models validated by international standards. Therefore, two modifications on the calculus of the stresses were proposed here to improve the model:

- The value of f_r in [MPa] was calculated using equation (5) proposed by Bortolotti (36), which is based on the Mohr-Coulomb failure criteria applied to concrete cylinders in double punching.

$$f_r = \frac{P_r}{\pi\left(\frac{d\,h}{2} - \frac{d_c^2}{4\tan(\beta)}\right)} \quad (5)$$

Here, d and h are the diameter and height in [mm] of the SFRSCC cylinder, P_r is the peak load (cylinder cracking load) obtained from the Barcelona test in [N] and d_c and β are the base in [mm]

and inclination angle in [°], of the conical wedge formed by the cylinder cracking, as shown in Figure 7.

The values of P_r and d_c were measured for each cylinder after performing the tests. However, β was not calculable for all tests as the wedge was still harshly attached by the fibers to the fractured specimen. In the cases where β was measured, it was close to 25°, which agrees with the value reported by (20). Therefore, this value was used in the equation.

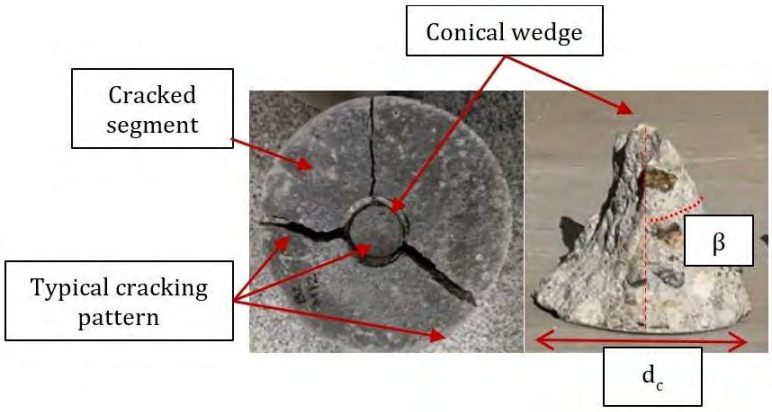


Fig. 7. Typical fracture of a cylinder on Barcelona test

- The equilibrium equations that related the load to the tensile stress in the post-cracking stage were rewritten on a cracked segment of the cylinder (cracked configuration) instead of on a differential element (reference configuration) as initially proposed by Blanco et al. In the opinion of the authors, this approach is more consistent with the actual phenomenon since the cracking of the cylinder is discrete instead of smeared. Therefore, the action of fibers and residual tensile stresses occurs at the cracked surfaces.

For the equilibrium, the same forces considered by Blanco et al. were included, and it was assumed that the cylinder fractured into equal pieces. Figure 8 illustrates the cracked segment for the equilibrium.

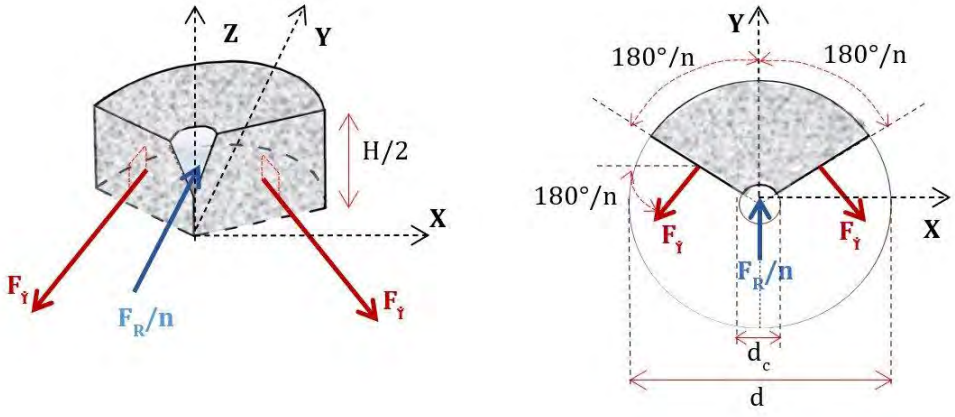


Fig. 8. Free body diagram of the cracked cylinder segment for equilibrium

In this figure, n is the number of cracked segments of the cylinder, which may be different for each test but is usually 2, 3 or 4. F_i are the forces in [N] that act on the XY plane, orthogonal to the cracked surfaces and hold together the segments of the cylinder, mainly due to the action of fibers. F_R is the force in the plane XY resulting from the contact between the wedge and the cracked segment, which is calculated according to (20) using the equation (6).

$$F_R = P\left(\frac{\cos(\beta) - \mu_k sin(\beta)}{sin(\beta) + \mu_k \cos(\beta)}\right) \tag{6}$$

In this equation, P is the actuator load in [N] and μ_k is the kinetic friction coefficient between wedge and segment. Specifically, μ_k represents the ratio between the friction (tangential) and contact (normal) forces that generates in the contact between the conical wedge and the cracked segments of the cylinder during the Barcelona test (see Figure 7). A detailed description of these forces can be found in (20). According to the literature, common assumed values of μ_k used between 0.5 and 1.4 (20,37). In this research, in order to make a more precise estimation of μ_k, its calculation was done using inverse analysis aiming to lower the error between the modeled tensile behavior of the SFRSCC and the actual experimental results. Performing force equilibrium along Y in Figure 8 yields equation (7).

$$-2\ F_i\ sin\left(\frac{180°}{n}\right) + \frac{F_R}{n} = 0 \tag{7}$$

Then, the tensile stress f_t is calculated by replacing (7) and (6), solving F_i and dividing it by the cracking surface. Equation (8) shows this solution.

$$f_t = \frac{P\ \left(\frac{cos(\beta)-\mu_k\ sin(\beta)}{sin(\beta)+\mu_k\ cos(\beta)}\right)}{2\ n\ sin\left(\frac{180°}{n}\right)\left(\frac{d\ h}{4} - \frac{d_c^2}{8\ tan(\beta)}\right)} \tag{8}$$

Notice that the only difference between this equation and the original proposal of Blanco et al. is the expression $n\ sin\left(\frac{180°}{n}\right)$, which corresponds to π in the original equation. If $n \to \infty$ then $n\ sin\left(\frac{180°}{n}\right) \to \pi$, which is the equilibrium on a differential. For n between 2 and 4, this denominator is always lower than π, which results in higher residual stresses, therefore, a more accurate estimation in comparison to the original model.

Strains were calculated following the kinematic equations (9) deduced by Blanco et al. (20). Furthermore, it is worth mentioning that for the post-cracking stage, their equations considered the cracked configuration of the cylinder. Therefore, the proposed approach for deducing the equilibrium equations from the cracked segments is consistent with these original kinematic equations.

$$\epsilon_t = \begin{cases} \dfrac{f_r}{E_c} & at\ cracking \\ \dfrac{n\ U_z}{\pi\ \left(\frac{d}{2}\right)}\ tan(\beta)\ sin\left(\dfrac{180°}{n}\right) & post-cracking \end{cases} \tag{9}$$

Here, ϵ_t is the tensile strain in [mm/mm], U_z is the actuator displacement in [mm], d is the cylinder diameter in [mm], f_r the peak cracking stress in [MPa] and E_c is the elastic modulus of the SFRSCC in [MPa]. The last was assumed as the initial tangent modulus obtained by differentiating the equation (1) according to reference (19).

Equations (5), (8) and (9) were used to determine the tensile stress-strain curve of the SFRSCC. Due to the vast amount of data collected during the Barcelona test, Blanco et al. [20] recommended simplifying the model to a quadrilinear model. Nevertheless, here it was necessary to use a pentalinear model to achieve convergence of the NLFEA, which was further described. The strain points in [mm/mm] considered for the pentalinear stress-strain curve were: (i) $\frac{f_r}{E_c}$, (ii) $\frac{f_r}{E_c} + 0.0005$, (iii) $\epsilon_t = 0.0005$, (iv) $\epsilon_t = 0.0075$ and (v) $\epsilon_t = 0.015$. For these strains the related stresses were calculated. These were respectively noted as f_{t1}, f_{t2}, f_{t3}, f_{t4} and f_{t5}.

2.2.7 Characteristic stress-strain curves

For all the mixtures, four specimens in compression and four in Barcelona double punching were tested. Each specimen had different stress-strain curves, which is expected since there is statistical scatter due to factors such as inherent concrete heterogeneity. Hence, characteristic stress-strain

curves for each mixture were determined by fitting the sample results to the Weibull two-parameter distribution, selected as it has been proven to be adequate to model the statistical variation of ceramic materials such as concrete (38,39). Weibull formula is presented in equation 10, where f_W is the probability density, x is the studied variable, β_W is the scale parameter (similar to mean in normal distribution), λ_W is the shape parameter (similar to standard deviation in normal distributions).

$$f_W = \frac{\lambda_W}{\beta_W}\left(\frac{x}{\beta_W}\right)^{\lambda_W - 1} e^{-\left(\frac{x}{\beta_W}\right)^{\lambda_W}} \tag{10}$$

The Weibull parameters for each mixture (Table 1) were calculated for f_c', f_{t1}, f_{t2}, f_{t3}, f_{t4} and f_{t5} and f_{t5}, using the Maximum Likelihood Method (MLM) through MATLAB R 2020a (40). MLM was implemented as it is a widely used optimization technique which aims to determine the parameters of a probability density function that the maximizes the likelihood that the experimental results belong to the Weibull distribution (38). After fitting the parameters, the goodness of fit of the results was evaluated using the Anderson-Darling test (AD2). The MATLAB script used to calibrate the Weibull parameters and determine the AD2 is presented in the Appendix 1.

2.2.8 Non-Linear Finite Element Analysis

NLFEAs were performed using SAP2000® V.22 (41) to determine the flexural response of beams on FPBT for each mixture. The finite element used was a four-nodes membrane and the material non-linearity was incorporated using multi-linear stress-strain relations based on the characteristic constitutive models calculated as explained in Section 2.2.3. The mesh showed in Figure 9 was determined using convergence analysis, in which a relative error of 0.05% in the peak-load was achieved using 960 elements.

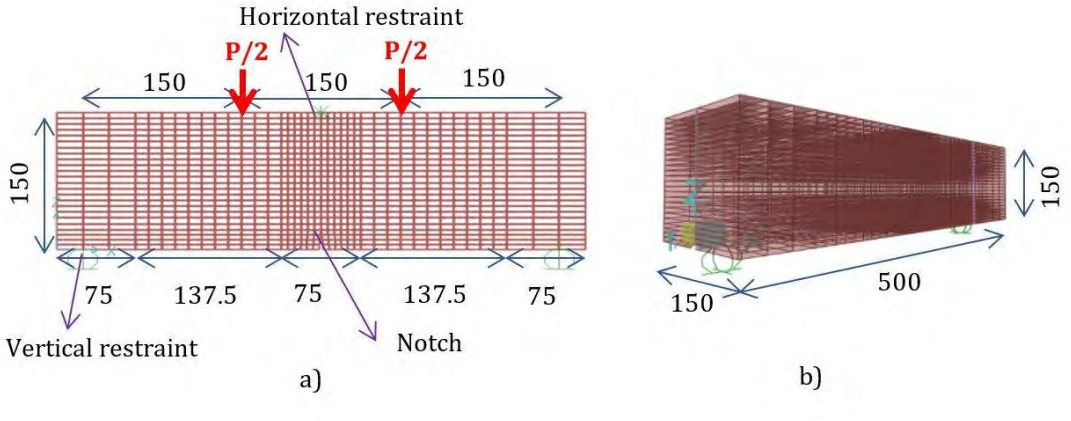


Fig. 9. Finite elements model, a) Front view, b) Extruded view. All distances in [mm]

The analyses were displacement-controlled with 500 steps, up to an objective displacement of 0.25 [mm] at mid-span. SAP2000® uses Newton methods to solve the equilibrium at each step (42). All the analyses were performed on a laptop ASUS N550J with Intel® CoreTMi7 processor, four cores, and 16 [GB] of RAM. The time of the analyses was between 5 and 30 minutes. The parameter μ_k was used to calibrate the NLFEA to the FPBT experimental results by using inverse analysis. This analysis was performed iteratively varying the values of μ_k in the constitutive tensile models, then calculating the numerical maximum bending moment and comparing it to its experimental value. The procedure was continued until the theoretical value was close to the experimental. Obtained μ_k values were between 0.5 and 1.4 as expected, according to (20). The load-deflection curve was obtained from each simulation, and then M_u was determined from equilibrium using the peak load.

2.2.9 Data Set for The Artificial Neural Network

Proper training, calibration, and validation of ANNs, requires several data sets (43). The experimental program only provided 13 data with inputs *w/b* and *%F*, and output M_u, therefore, NLFEA was used to increase the amount of data. This required determining the constitutive model

parameters for different *w/b* and *%F* among the studied ranges. Hence, a Response Surface (RS) based on the 2^k with central and axial points experimental designed used (see Section 2.1), was calculated for each one of the characteristic values f_c', f_{t1}, f_{t2}, f_{t3}, f_{t4}, and f_{t5}. Equations (11) to (16) are the RSs between the constitutive model parameters in [MPa] and the inputs *w/b* and *%F* obtained with Minitab V.16® (44). Moreover, for all these equations R^2>0.89, which indicates good fitness to the experimental data.

$$f_c' = -459.40\left(\frac{w}{b}\right)^2 + 118.80\,(\%F)\left(\frac{w}{b}\right) - 59.30\,(\%F) + 291.20\left(\frac{w}{b}\right) + 7.20 \quad (11)$$

$$f_{t1} = -0.74\,(\%F)^2 - 40.16\left(\frac{w}{b}\right)^2 + 11.17\,(\%F)\left(\frac{w}{b}\right) - 4.80\,(\%F) + 29.59\left(\frac{w}{b}\right) - 1.44 \quad (12)$$

$$f_{t2} = -3.19(\%F)^2 - 59.10\left(\frac{w}{b}\right)^2 + 6.15\,(\%F)\left(\frac{w}{b}\right) + 55.10\left(\frac{w}{b}\right) - 12.65 \quad (13)$$

$$f_{t3} = 0.13(\%F) + 2.98 \quad (14)$$

$$f_{t4} = 1.12\,(\%F)^2 + 1.37\,(\%F) - 2.09\left(\frac{w}{b}\right) + 1.10 \quad (15)$$

$$f_{t5} = 1.73\,(\%F)^2 + 0.35\,(\%F) - 2.38\left(\frac{w}{b}\right) + 1.27 \quad (16)$$

These equations were evaluated for *w/b* from 0.40 to 0.6 in steps of 0.02, and *%F* from 0.00 to 1.00 in steps of 0.10. Then, the constitutive models were used to determine M_u through NLFEA, as described in Section 2.3. A total of 121 simulations were performed, and their results were consequently used to feed the ANN. The process was automatized through a script that allowed to run SAP2000® using MATLAB®, which is presented in Appendix 2.

2.2.10 Artificial Neural Network

The ANN was a multilayered perceptron fully connected with supervised learning. The inputs were *w/b* and *%F*, and the output was the M_u. All its coding was self-made in MATLAB®. A sketch of the architecture of the ANN is presented in Figure 10.

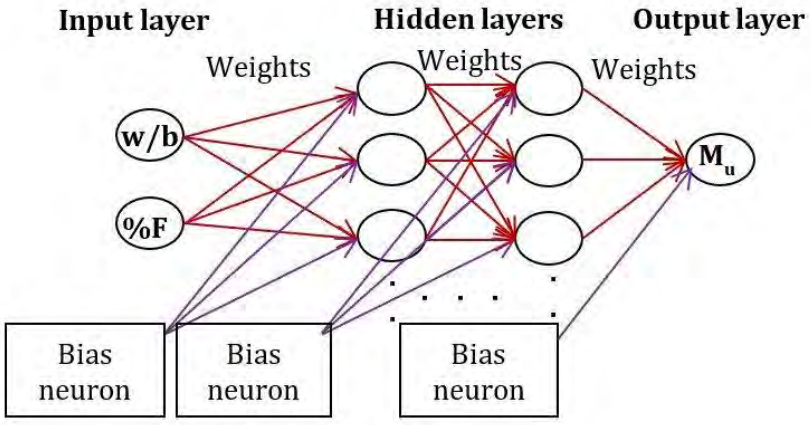


Fig. 10. Architecture of the ANNs

Architectures tested consisted of 1 or 2 Hidden Layers (HL), with 2, 5, 10 or 20 Neurons per Hidden Layer (NHL). For the hidden neurons, the activation function was the hyperbolic tangent, which led to the best results in the preliminary simulations. Moreover, all the input and output data were normalized for the training of the ANN using equation (17), where D_n is the normalized data, D the

original data, and D_{min} and D_{max} the minimum and maximum values of the data before normalization.

$$D_n = \frac{D - D_{min}}{D_{max} - D_{min}} \tag{17}$$

For the assessment of the ANNs, the 121 data were organized in a random permutation according to Ref. (45), then 84 data (≈70%) were used for training, 24 (≈20%) for calibration, and 13 (≈10%) for validation. This division of the data set seeks to avoid the overfitting of the ANN during its training, as described in Ref. (46). The training implied determining the weights (including the bias neurons) to minimize the objective function Mean Squared Error (MSE) presented in equation (18).

$$MSE = \sum_{1}^{N_T} \frac{1}{N_T} (m_{uANN} - m_{uFEM})^2 \tag{18}$$

Where m_{uANN} are the ultimate moments, normalized according to equation (17), predicted by the ANN, m_{uFEM} are the normalized ultimate moments obtained from the NLFEA of Section 2.2.8, and N_T is the number of training data.

Three optimization methods were evaluated for minimizing the MSE: Momentum Back Propagation (MBP), Particle Swarm Optimization (PSO), and Gravitational Search Algorithm (GSA). The calculation of weights for each architecture was performed five times using each algorithm. MBP and PSO are widely used methods that have proven to be successful in similar ANNs training (45,47,48). A detailed description of these algorithms can be found in (46) and (49). Furthermore, GSA is a meta-heuristic optimization method based on the universal gravity law, developed by Rashedi et al. (50) in 2009, which has been reported to achieve superior performance compared to other algorithms of its class, such as PSO or Genetic Algorithms. Moreover, it has proved to be a feasible alternative to solve optimization problems in structural engineering (51). To the best knowledge of the authors, GSA has not been used for ANNs related to SFRSCC. Therefore, its feasibility was explored here.

In the original nomenclature of the GSA, each iteration is referred to as an *age*. Its parameters are the initial gravitational constant G_o, the maximum of iterations age_{max}, the shape factor α, the initial number of agents (candidate solutions) N_{oa}, and the relative error tolerance between iterations e_{min}. GSA pseudo-code is as follows:

- Select G_o, age_{max}, α, N_{oa} and e_{min}.
- Make age=1
- Select random values for the N_{oa} agents. In this case each agent is a vector that contains values for the ANN weights (w_i). This is referred as the position vector of the agent.
- Select random values for the initial velocities of the agents. In this case that refers to the velocity of the weights (Δw_i).
- Evaluate the objective function for each of the agents. In this case that is the MSE.
- Determine the best and worst agents. Here they are the agents with the lower and higher MSE, respectively.
- Determine the mass of each agent M_a using equation (19).

$$M_a = \frac{MSE - MSE_{max}}{MSE_{min} - MSE_{max}} \tag{19}$$

- Calculate the number of effective agents N_a using equation (20). Effective agents refer to the agents with better values for the objective function MSE. Only these will continue in the next ages.

$$N_a = \mathrm{N}_{oa} - \frac{N_{oa}}{age_{max}} age \tag{20}$$

- Calculate the gravitational constant G using equation (21).

$$G = G_o exp^{\alpha \frac{age}{age_{max}}} \quad (21)$$

- Determine the acceleration a_i that acts on each agent. For each *(i)-th* agent, the acceleration that results from its interaction with all the other *(j)-th* agents is calculated using equation (22), where $R_{(i)(j)}$ is the Euclidean distance between the position of agents, ε is a small value to avoid indeterminacy in case both agents have the same position and $rand$ is a random number between 0 and 1.

$$a_i = \frac{1}{M_{a(i)}} \sum_{(j)=1,(j)\neq 1}^{N} [rand\ G \frac{M_{a(i)}\ M_{a(j)}}{R_{(i)(j)} + \varepsilon}(w_i - w_j)]\ ) \quad (22)$$

- Recalculate Δw_i using equation (23).

$$\Delta w_{i\ (age+1)} = rand\ \Delta w_{i\ (age)} + a_{i\ (age)} \quad (23)$$

- Recalculate the position of the agents using equation (24). These are the actualized values of the candidate solutions.

$$w_{i\ (age+1)} = w_{i\ (age)} + \Delta w_{i\ (age+1)} \quad (24)$$

- Recalculate MSE for the new position of the agents.
- Actualize the best agent.
- Calculate the relative error between the actualized best agent and the previous best agent.
- Make age=age+1
- If the relative error<e_{min} and age< age_{max}, repeat steps VI to XVI.

Different values for the parameters of GSA were tested. The results reported utilized $G_o = 1$, $age_{max} = 1000$, $\alpha = 1$, N_{oa} and $e_{min} = 10^{-15}$, which yielded the lowest values of MSE.

3. Results and Discussion

This section presents the detailed results of the experimental compression, Barcelona and Four Point Bending tests. Also, the results of the constitutive modeling, NLFEA calibration and ANN training are presented and discussed.

3.1. Uniaxial Compression and Barcelona Tests

Table 2 presents the average results of the tests for the compressive and Barcelona tests. In the case of the Barcelona test the table includes the cracking peak load and the tenacity (area under the load-actuator displacement curve), which measures the energy dissipation capacity of the SFRSCC in tension.

Table 2. Compression and Barcelona test results

Mix	Compressive strength	Peak load Barcelona	Tenacity Barcelona
	MPa	kN	J
M 40-00	47.31 (0.06)*	130.09 (0.07)*	111.01 (0.12)*
M 40-50	41.90 (0.03)*	132.69 (0.09)*	370.65 (0.08)*
M 43-00	48.53 (0.03)*	149.64 (0.06)*	134.22 (0.17)*
M 43-15	46.99 (0.04)*	135.29 (0.05)*	202.19 (0.16)*
M 43-85	39.99 (0.11)*	115.52 (0.14)*	426.99 (0.12)*
M 50-00	36.37 (0.04)*	119.56 (0.08)*	132.52 (0.17)*
M 50-50	35.81 (0.11)*	123.98 (0.06)*	332.07 (0.09)*
M 50-100	35.10 (0.15)*	117.15 (0.15)*	504.07 (0.23)*
M 57-00	30.82 (0.09)*	112.28 (0.10)*	139.40 (0.18)*
M 57-15	23.96 (0.03)*	91.87 (0.05)*	167.33 (0.10)*
M 57-85	30.17 (0.01)*	119.85 (0.07)*	508.93 (0.31)*
M 60-00	24.67 (0.02)*	96.54 (0.04)*	128.19 (0.12)*

M 60-50	22.87 (0.10)*	91.42 (0.02)*	323.79 (0.17)*

Average (Coefficient of variation)*

As it is expected for concretes, compressive strength decreases as *w/b* increases. However, it should be noted that for most of the *w/b*, the inclusion of fibers reduces the compressive strength between 2% and 18%. This percental decrease is higher for lower values of *w/b* and increases for higher values of *%F*. The same phenomenon has been reported by other researchers (11,52,53) up to decrease values of 25%. The compressive strength decrease might be related to the lost workability of SFRSCC for small values of *w/b* and high values of *%F*, which causes the formation of small voids in the cross sections of specimens during casting. Also, the inclusion of long fibers may generate additional interfacial transition zones by disruption of the binder paste. Both defects promote porous weak zones in the concrete matrix which might increase internal stress concentration during compressive loading, leading to lower compressive capacity.

The peak load Barcelona is a measure of the tensile strength, and it also increases for lower *w/b*, which is expected for concretes (10). Moreover, the inclusion of fibers had a minor effect on the peak load for most of the mixtures, which is well-known as the main contribution of fibers occurs in the post-cracking stage (54). This effect is evidenced in rises of tenacity between 20% and 280% as the *%F* augments. This improvement is related to an increase in ductility since tensile strength is marginally affected. Also, Figure 11 evidences the post-cracking contribution of fibers as the cracking width is markedly reduced for higher *%F*.



a) b) c)

Fig. 11. Compressive and Barcelona test fracture at 6 [mm] actuator displacement for a) M 50-00, M 43-00, b) M 50-50, M 43-15, and c) M 50-100, M 43-85

Coefficients of variation of compressive strength and peak load Barcelona are sharply lower than those of the tenacity. This is evidence of the high statistical scatter existent in SFRSCC mechanical properties that are highly dependent on the fibers. Hence, the use of statistical analysis, as proposed in Section 2.2.3 to characterize the constitutive behavior of SFRSS is imperative. According to the guide ACI-214 (55), coefficients of variation over 0.05 indicate poor agreement of the normal distribution parameters (mean and standard deviation) to the experimental results. Most of these coefficients were higher than this limit, particularly on the tenacity, which is why the Weibull distribution was used to determine the characteristic stress-strain curves, as stated in Section 2.2.3.

3.2 Characteristic Compression Stress-Strain Curves

Fitness of data to the Weibull and Normal distributions to determine the characteristic f_c' are presented in Table 3. P-values of AD^2 considered as null hypothesis that data belong to the distribution. For a significance level of 0.10, it can be seen that all data fit the Weibull distribution, while M 43-15 and M 60-50 do not adjust to the normal distribution. Moreover, characteristic compressive strength obtained from Weibull analysis was in average 3% higher than those of the normal distribution (mean). Similar results have been published in literature and indicate that the mean is still a good indicator of the characteristic f_c' (56).

Using the Weibull f_c' and the equations of Section 2.2.1, stress-strain curves in compression, were determined and presented in Figure 12. The negative sign indicates compression stress and shrinking strain. From these curves it is seen that SFRSCC initial stiffness E_c is inversely related to w/b. Also, the improvement of residual capacity (post-peak) on higher $\%F$ mixes can be noticed as the post-peak stresses on mixes with lower $\%F$ (dashed lines) decrease with a steeper slope than those with higher $\%F$ (solid lines). This behavior explains the control on compressive cracking perceived in Figure 11 for mixes M 43-85 and M 50-100.

Table 3. Goodness of fit analysis for f'c

Mix	Weibull		Normal	
	f'c	P-value	f'c	P-value
	MPa		MPa	
M 40-50	42.46	0.78	41.90	0.27
M 43-15	47.76	0.74	46.99	0.10
M 43-85	41.88	0.77	39.99	0.24
M 50-00	36.89	0.79	36.37	0.14
M 50-50	38.30	0.52	35.81	0.54
M 50-100	37.07	0.98	35.10	0.77
M 57-15	24.24	0.86	23.96	0.36
M 57-85	30.28	0.89	30.17	0.21
M 60-50	23.70	0.38	22.87	0.01

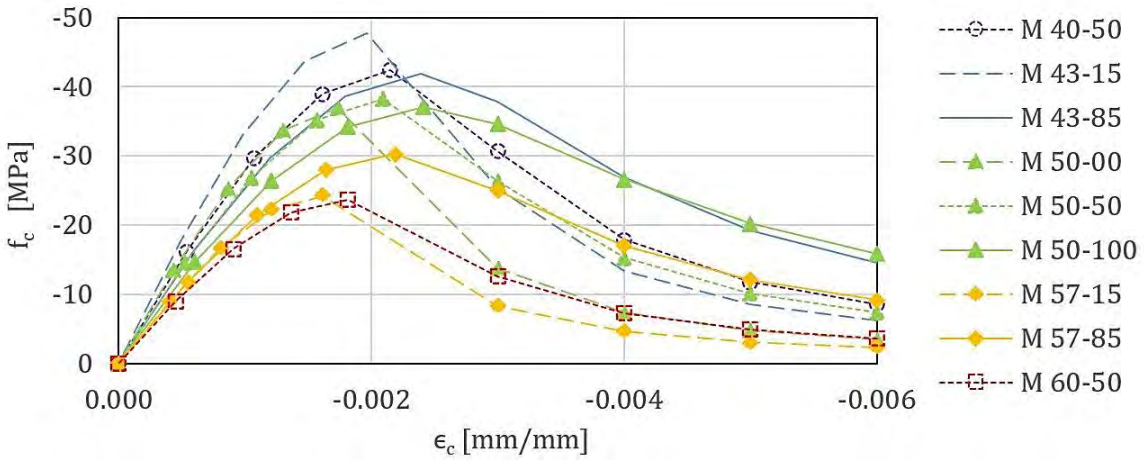


Fig. 12. Compression stress-strain curves

3.3 Characteristic Tensile Stress-Strain Curves

Table 4 presents the five stress parameters for the pentalinear models fitted to Weibull and the μ_k calibrated based on the NLFEA. In this table, the values marked with * did not fulfill the AD² null hypothesis for a significance level of 0.10. These results belong to the M 50-50 for which more experiments were performed, as mentioned in the methodology. Hence, a possible cause of the lack of fitness to Weibull is the blocking effect that might arises from the fact that all the different samples had to be distributed in two different curing chambers with different humidity and temperatures, which could have slightly influenced their strength development (26). Another possible cause of the lack of fitness to Weibull in this case lays in the fact that as it corresponds to the central point, more samples were tested. Hence, according to the statistical theory of the central limit, higher number of samples approximates the observations statistical distribution to a normal distribution (26).

Figure 13 shows the constitutive models calculated using equations of Section 2.2.2. The cracking tensile stresses were, on average, 9.3% of the compressive strength, which is expected for SFRSCC, according to the literature (37). Residual strength (post-peak) increases for higher $\%F$ (solid lines)

due to the more bridging action between cracked segments of the concrete, which will occur for more fiber contents.

Nonetheless, the last post-peak slopes (f_{t4} to f_{t5}) were found to be steeper than those reported by other researchers for stress-strain curves obtained with flexure or direct tensile tests (17,35,57). Therefore, underestimation of the stresses at high strain levels occurs. Although conservative for design purposes, a precise prediction of the mechanical behavior requires more work on the constitutive equations. A possible future modification will be to consider that the area where stress is distributed decreases as the segments separate during the Barcelona test.

Table 4. Parameters for the characteristic tensile stress-strain curves

Mix	f_{t1}	f_{t2}	f_{t3}	f_{t4}	f_{t5}	μ_k
	MPa	MPa	MPa	MPa	MPa	
M 40-50	3.61	2.58	2.31	1.34	1.08	0.55
M 43-15	3.84	0.77	0.76	0.42	0.32	0.60
M 43-85	3.36	2.56	2.48	1.86	1.51	0.80
M 50-00	3.31	0.00	0.00	0.00	0.00	0.60
M 50-50	3.52	2.38	1.69*	1.05*	0.62*	0.55
M 50-100	3.27	3.34	3.30	2.82	2.35	0.55
M 57-15	2.62	0.58	0.32	0.16	0.13	0.60
M 57-85	3.27	2.44	2.36	1.76	1.11	0.95
M 60-50	2.54	1.17	1.07	0.76	0.50	1.00

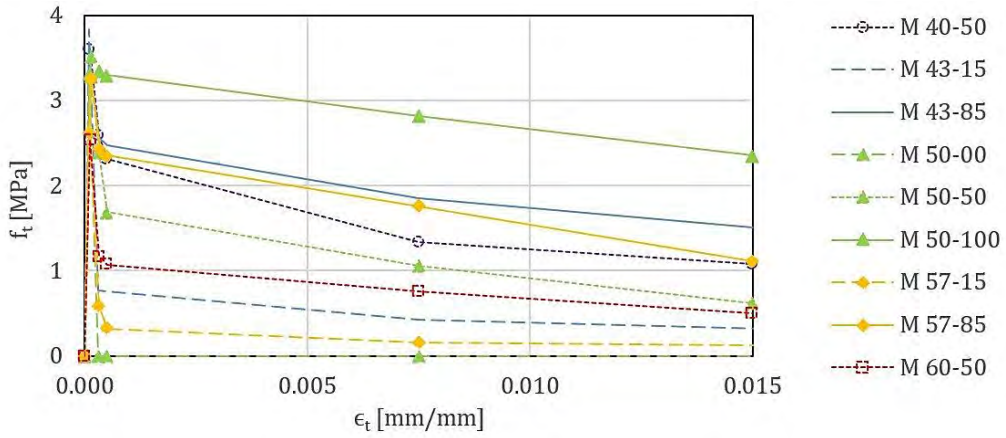


Fig.13. Tensile stress-strain curves

3.4 Experimental and Numerical Flexural Behavior

Figure 14 presents pictures of the FPBT and NLFEA results. The fracture process was captured by the model in an implicit manner through the decrease down to zero of the tensile capacity after the post-peak tensile behavior. There, the bridging effect of fibers is evident as the beam with $\%F$=0.00 completely fractures (Figure 10a), contrary to the beam with fibers added (Figure 10b). The NLFEA exhibits strain concentration occurring at the fractured zone of the beam (Figure 10c) and also satisfactorily simulates the deformed configuration (Figure 10d).

Figure 15 presents the load vs. mid-span deflection curves obtained experimentally and through NLFEA. Due to illumination conditions and the duration time of the experiments, it was only possible to carry out DIC measurements for half of the FPBT (dashed thin lines). For the other half, only the peak load is reported (solid thin lines). The difference between experimental peak loads for beams with equal dosage of SFRSCC evidences the high statistical scatter in the mechanical response, mainly related to the random orientation and position of fibers. Nonetheless, the models had good accuracy to predict the maximum mean loads.

The initial linear portion of the experimental and NLFEA (solid thick lines) curves have a good agreement, however, in some cases (M 40-50, M 43-85 and M 57-85) the experimental results

exhibit a hardening behavior after this linear portion while the NLFEA tend to a softening behavior. This could be explained as described in Section 3.3, since the post linear-elastic behavior is controlled by the tensile constitutive relation, markedly influenced by the fibers. Proposals of other researchers achieve better post-cracking performances, nonetheless their tensile constitutive relationships were directly calibrated from bending tests and did not consider the statistical scatter (35,57).

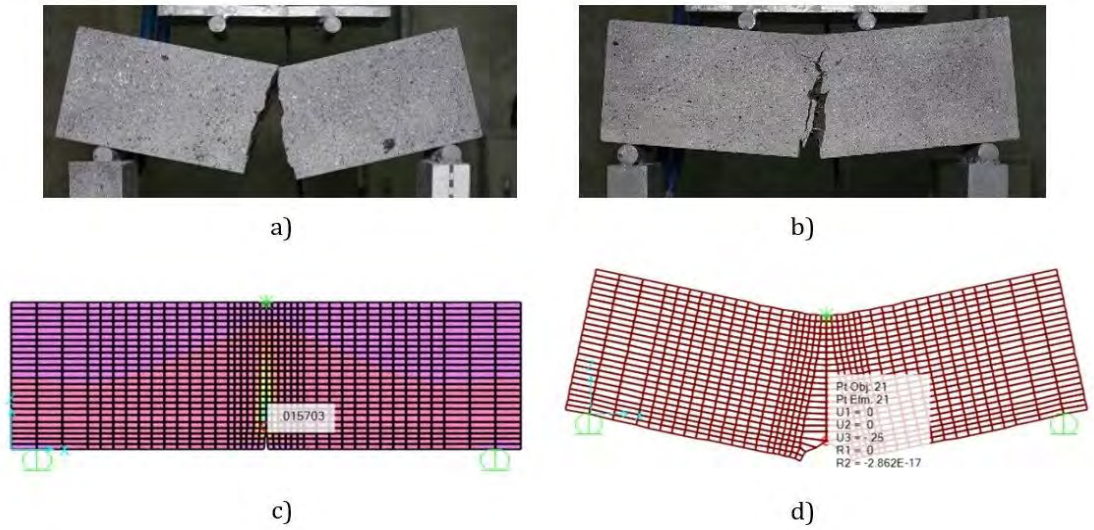
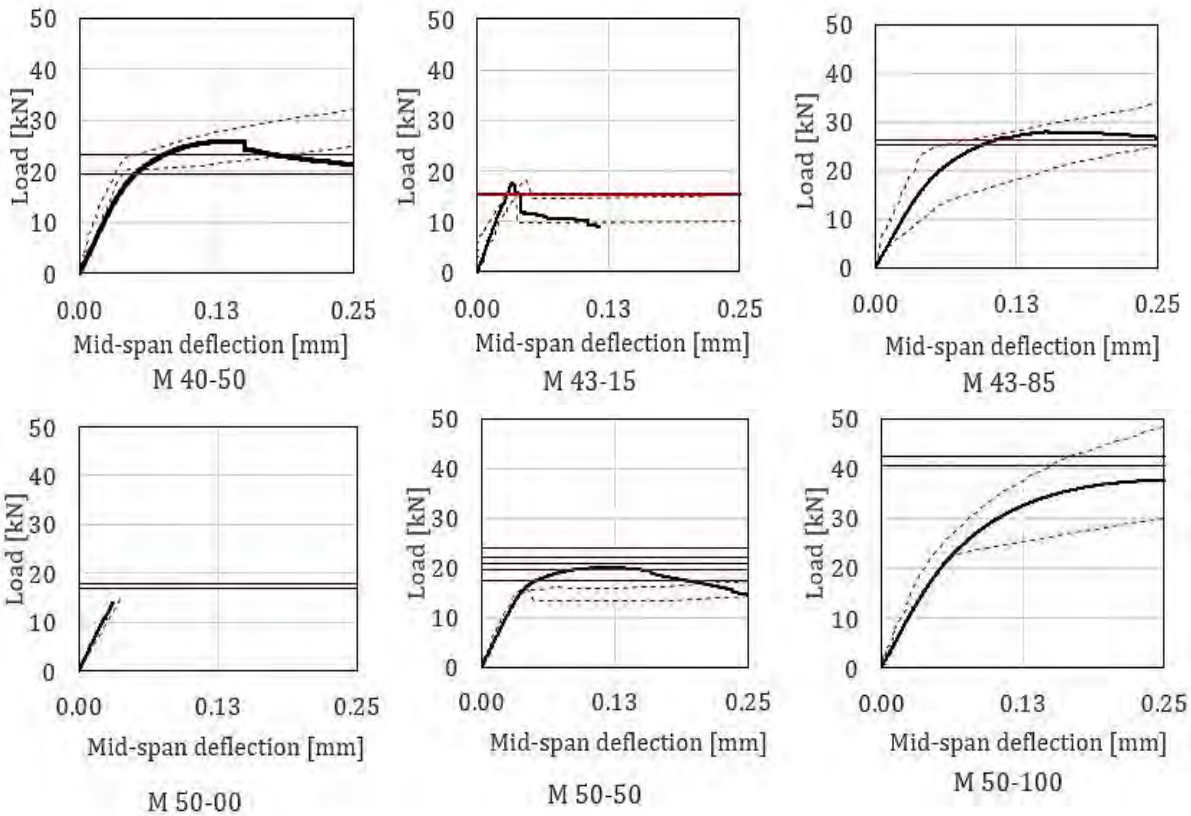


Fig. 14. SFRSCC beams on a) FPBT *%F*=0.00, b) FPBT *%F*=0.50, c) NLFEA strain field and d) NLFEA deformed configuration



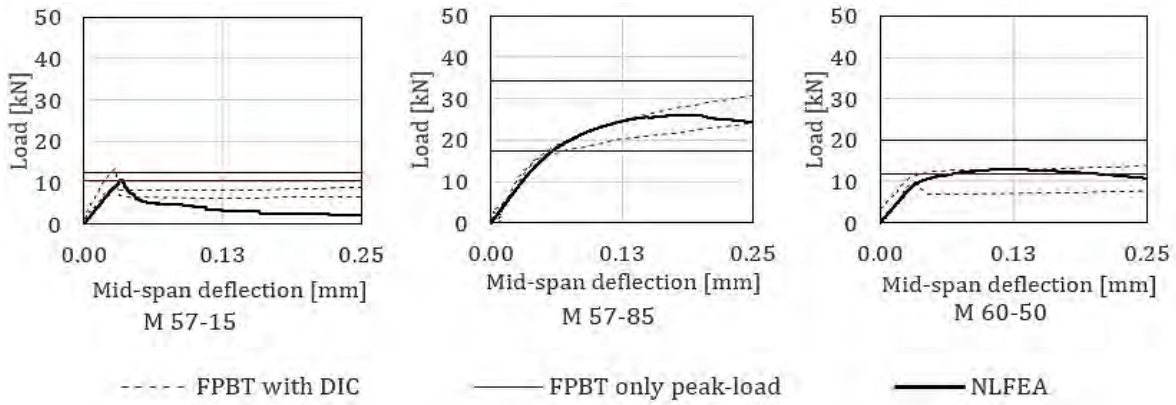


Fig. 15. Load-mid-span deflection curves

Table 5. Maximum bending moments

Mix	M_u - Tests average	M_u - NLFEA	Relative error
	[N-m]	[N-m]	%
M 40-50	1857.93	1945.65	4.72
M 43-15	1245.62	1314.00	5.49
M 43-85	2063.68	2094.75	1.51
M 50-00	1181.11	1050.60	11.05
M 50-50	1492.45	1502.63	0.68
M 50-100	3020.57	2822.78	6.55
M 57-15	856.77	801.45	6.46
M 57-85	1986.93	1950.83	1.82
M 60-50	1037.68	972.08	6.32

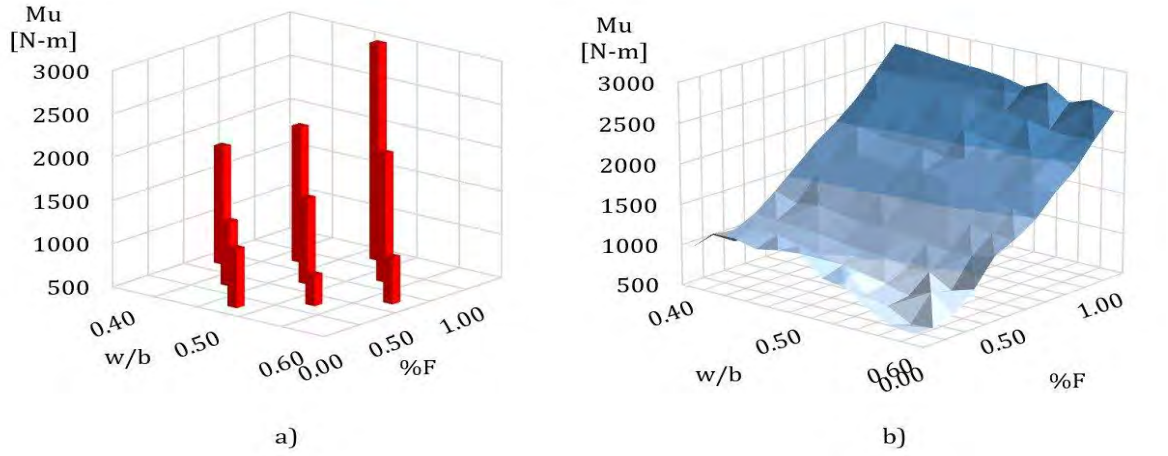


Fig.16. Surface plots of the maximum bending moment vs. *w/b*, *%F* a) Experimental test results, and b) NLFEA results

Table 6. Maximum bending moments for ANN training

N°	w/b	%F	M_u	t	N°	w/b	%F	M_u	t	N°	w/b	%F	M_u	t
			[N-m]	[min]				[N-m]	[min]				[N-m]	[min]
1	0.46	0.40	1265	6	42	0.58	0.80	2024	5	83	0.42	0.90	2464	5
2	0.40	0.20	1050	11	43	0.40	0.90	2475	5	84	0.48	1.00	2661	5
3	0.50	0.30	1039	14	44	0.54	0.00	977	7	85	0.50	0.70	1868	6
4	0.54	0.80	2026	5	45	0.58	0.50	1332	6	86	0.58	0.90	2197	5
5	0.42	1.00	2739	5	46	0.54	0.40	1174	8	87	0.48	0.50	1504	6
6	0.46	0.90	2418	5	47	0.48	0.40	1240	5	88	0.42	0.50	1570	5
7	0.44	1.00	2707	5	48	0.40	0.80	2202	5	89	0.56	0.50	1375	12

8	0.52	1.00	2559	5	49	0.58	0.30	814	8	90	0.58	1.00	2576	11
9	0.48	0.20	997	23	50	0.52	0.90	2331	6	91	0.56	0.90	2220	6
10	0.58	0.20	882	6	51	0.56	0.20	768	7	92	0.54	0.20	846	8
11	0.42	0.30	1141	14	52	0.44	0.30	1129	9	93	0.58	0.00	670	6
12	0.60	0.40	1207	14	53	0.50	0.80	2137	5	94	0.54	0.50	1437	6
13	0.46	0.10	1270	5	54	0.52	0.20	883	14	95	0.46	0.30	1102	11
14	0.52	0.70	1902	5	55	0.52	0.80	2068	6	96	0.54	0.10	808	6
15	0.54	0.30	959	10	56	0.42	0.80	2243	5	97	0.54	1.00	2670	7
16	0.40	0.70	1992	5	57	0.46	0.50	1528	5	98	0.50	0.20	947	6
17	0.50	1.00	2626	5	58	0.44	0.40	1319	9	99	0.58	0.40	1152	10
18	0.40	0.10	1069	7	59	0.56	0.70	1844	5	100	0.50	0.90	2329	5
19	0.40	0.50	1588	5	60	0.58	0.70	1840	6	101	0.48	0.70	1914	5
20	0.44	0.20	1036	20	61	0.58	0.10	582	11	102	0.42	0.00	1240	9
21	0.48	0.10	1203	6	62	0.44	0.70	1944	5	103	0.50	0.10	1134	6
22	0.42	0.40	1272	5	63	0.50	0.60	1743	10	104	0.44	0.00	1243	7
23	0.60	0.30	895	9	64	0.44	0.80	2206	5	105	0.46	1.00	2681	5
24	0.60	0.80	1924	6	65	0.56	0.60	1620	6	106	0.40	0.40	1370	13
25	0.58	0.60	1558	9	66	0.56	1.00	2484	6	107	0.50	0.00	1259	5
26	0.52	0.30	1032	15	67	0.54	0.70	1889	5	108	0.50	0.40	1240	5
27	0.54	0.60	1668	6	68	0.52	0.10	1103	19	109	0.42	0.60	1781	6
28	0.40	0.00	1001	8	69	0.46	0.80	2160	5	110	0.52	0.50	1462	5
29	0.56	0.40	1135	6	70	0.46	0.20	1016	18	111	0.48	0.60	1733	5
30	0.42	0.20	1039	30	71	0.44	0.50	1552	5	112	0.44	0.90	2445	5
31	0.56	0.30	974	6	72	0.50	0.50	1465	5	113	0.48	0.00	1234	7
32	0.40	0.30	1168	15	73	0.60	0.70	1727	6	114	0.60	0.60	1476	6
33	0.42	0.10	1057	30	74	0.42	0.70	2005	5	115	0.48	0.80	2157	6
34	0.48	0.90	2390	7	75	0.52	0.60	1716	5	116	0.44	0.60	1784	5
35	0.46	0.60	1761	6	76	0.52	0.00	1026	5	117	0.60	0.10	605	5
36	0.60	0.50	1325	11	77	0.40	1.00	2754	5	118	0.52	0.40	1219	5
37	0.60	0.90	2222	7	78	0.46	0.00	1179	5	119	0.48	0.30	1060	9
38	0.60	1.00	2490	13	79	0.46	0.70	1924	5	120	0.40	0.60	1816	7
39	0.60	0.00	628	5	80	0.44	0.10	1286	6	121	0.56	0.80	2060	6
40	0.56	0.10	734	28	81	0.54	0.90	2286	6					
41	0.60	0.20	677	24	82	0.56	0.00	806	7					

Using the peak loads, values of M_u were calculated as presented in Table 5. As expected, increasing the $\%F$ augmented the flexural capacity in all cases. Moreover, the predictive capacity of the numerical model is justified as the differences between the experimental and NLFEA bending moments are 5% on average, where better prediction occurs for the cases with fibers addition. With the validated NLFEAs, several simulations for the training of the ANNs were executed, as shown in Table 6. Their results are ordered based on a random permutation as required for assessing the ANNs. The total time of the simulations was 16.26 hours. Average computing time was 8 minutes, with some mixes requiring 30 minutes to achieve convergence.

The fact that only one structural element is modeled remarks the high computational cost needed to model nonlinear behavior of SFRSCC in commercial software. Furthermore, more computing time was required for beams with $\%F$<0.30. This might be caused by the more brittle behavior of these mixtures, which leads to a sudden loss of stiffness after cracking occurs and may slow convergence in the numerical solution (e.g., M 43-15 and M 60-50 in Figure 15). A comparison of the NLFEA data with the experimental bending moments (Table 5) is presented in Figure 16. There it is noticeable how the tendency of the NLFEA models resemblance the experimental resultants and the marked effect that $\%F$ has on the flexural strength.

3.5 Bending Moment Predictions by ANNs

Convergence curves for the best run of each training algorithm for the ANNs with less weights (HL=1, HN=2) and more weights (HL=2, HN=20) are presented in Figure 17. As seen in all these graphs, no divergence occurs between the training and calibration curves, indicating no overfitting of the ANNs, as explained in (46). In general, MBP required more iterations to converge than PSO and GSA. This is explained as only one candidate solution is evaluated per iteration at MBP.

Moreover, PSO performed better at early iterations and converged faster (between 100 and 200 iterations) than GSA (between 400 and 500 iterations). Nonetheless, after these iterations, GSA keep identifying better solutions, which relates to a good exploitation capacity.

PSO successfully located minima in the early stages of the iterations despite the number of the ANNs weights, as the shape of the convergence curve is similar for HL=1, HN=2, and HL=2, HN=20, while MBP and GSA required more iterations to achieve convergence for the ANNs that required calculating more weights (HL=2, HN=20). Nevertheless, GSA achieved the best optimization for six of the eight different architectures of ANNs, as depicted in Table 7.

The MSE presented was calculated, including training, calibration, and validation data. Also, the coefficient of determination R^2 is presented as an additional measure of the fitness of the ANNs predicted bending moments to the NLFEA simulations (Table 6). The only scenarios where the MBP and PSO performed better than GSA were those with a higher number of weights (HL=2, HN=10 and HL=2, HN=20).

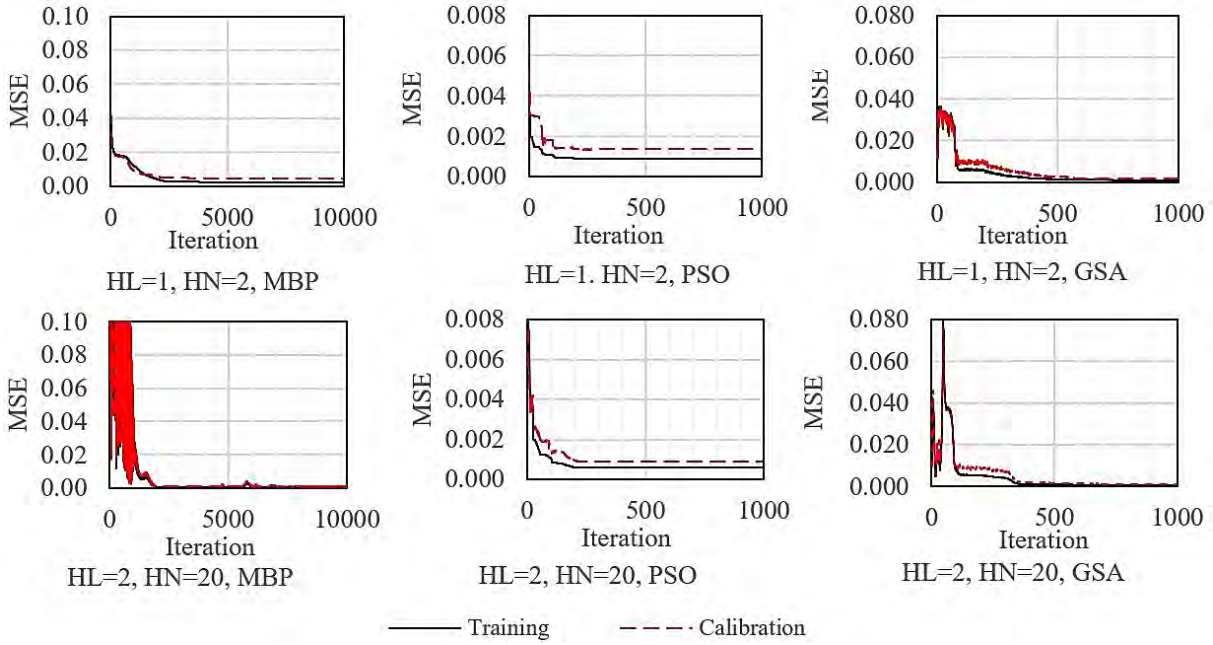


Fig.17. Convergence curves from the training and calibration of the ANN

Table 7. Best ANNs results

HL	HN	Method	Training time [min]	MSE	R^2
1	2	GSA	7.20	1.00E-03	0.9728
1	5	GSA	7.65	4.19E-04	0.9887
1	10	GSA	8.52	3.57E-04	0.9904
1	20	GSA	10.05	5.38E-04	0.9857
2	2	GSA	17.62	6.71E-04	0.9818
2	5	GSA	24.47	4.20E-04	0.9887
2	10	PSO	42.85	3.71E-04	0.9899
2	20	MBP	14.30	5.08E-04	0.9941

The evidence from the convergence curves showed that GSA requires many iterations to achieve its best performance. Hence, a higher number of iterations may allow it to achieve better results for this ANNs architectures. By comparison of MSE and R^2, it was concluded that the ANN architecture that obtained the best predictions of bending moment was HL=1, HN=10, and trained with the GSA. The results of weights for this are presented in Table 8.

Table 8. Weights of the best ANN architecture

Weights between w/b and HL	Weights between %F and HL	Weights between HL and M_u	Biases HL	Bias M_u
0.560	-1.068	-0.770	-0.260	2.509
0.033	-0.514	0.247	0.437	
-0.529	-0.290	0.702	0.049	
-0.033	0.688	0.452	-0.073	
-0.623	0.461	0.821	0.933	
-0.042	0.617	-0.192	0.487	
0.667	1.226	0.424	-0.013	
0.129	0.356	0.687	-1.445	
0.316	0.416	0.703	-1.099	
-0.912	0.823	1.824	-3.384	

Prediction of M_u by means of the ANN are presented in Figure 18a. In general, the tendency of the ANN M_u is close to the experimental and NLFEA results (Figure 16). In addition, Figure 18b presents a contour lines map of the relative error of M_u (in percentage) between the results of the AAN and the NLFEA (Figure 16). There it can be depicted that relative errors are below 5% for most values of w/b and $\%F$, nonetheless for $\%F$<0.30 there are differences up to 20%, which may be improved in future research by using more training data in the assessment of neural networks for low fiber content.

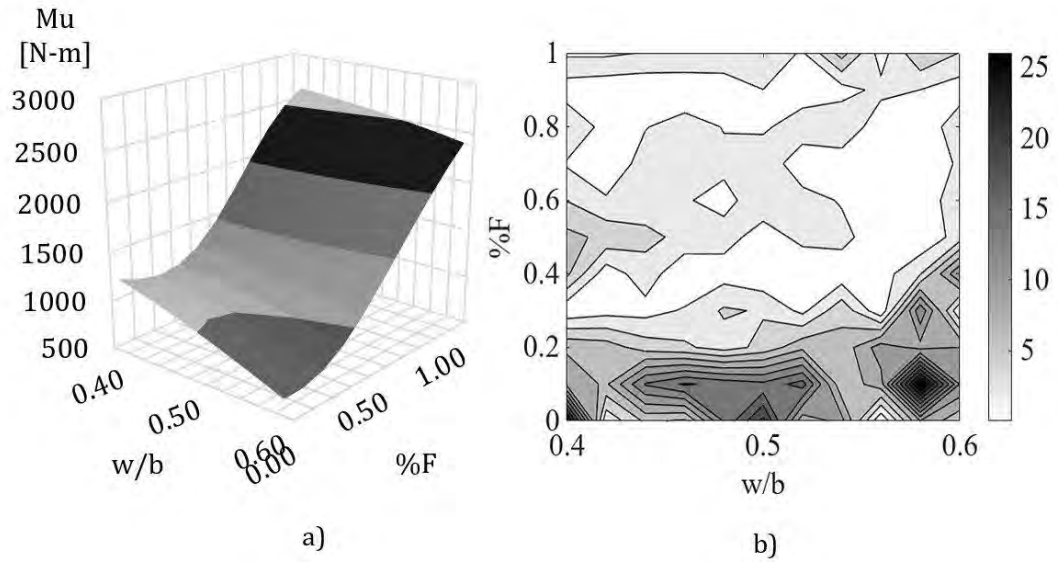


Fig. 18. a) Maximum bending moment with ANN and b) Contour of relative error between ANN and NLFEA results

4. Conclusions

The present research assessed the maximum bending moment of steel fiber reinforced self-compacting concrete beams, integrating uniaxial compression tests, indirect double punching Barcelona tests, four-point bending tests, constitutive modeling, non-linear finite element analysis, and artificial neural networks. The prediction of the flexural resistance was achieved for beams with water-binder ratios from 0.40 to 0.60 and steel hooked-ended fibers content percentages from 0.00% to 1.00% in volume. From the results, the following conclusions are withdrawn:

- Compressive strength can diminish in ranges from 2% to 18% when steel fibers are added, as supported by the uniaxial compression tests. Nonetheless, the post-peak deformation capacity and control of cracking due to compressive loads are improved.

- Tensile cracking strength is not markedly affected by the addition of fibers; however, higher amounts of fibers significantly improve the deformation capacity, strain ductility, and energy dissipation capacity in ranges from 20% to 280%.
- The tensile constitutive model from Barcelona tests presented here is an improvement from the original model. Nonetheless, the model still underestimates the post-peak stress capacity of the material. This is positive in terms of security related to design but is a disadvantage if precise predictions of the material behavior are required.
- The two-parameter Weibull distribution is a proper alternative to assess the characteristic values of mechanical properties of steel fiber self-compacting reinforced concrete since the experimental results had a better fit (in terms of P-values) compared to the normal distribution.
- Non-linear finite element analysis is feasible to predict the flexural capacity of fiber reinforced concrete beams. However, more computing time is required for low quantities of fibers. This might be caused by the abrupt changes in stress and stiffness after the peak load that occurs in brittle materials, which tends to slow the convergence and diminish the accuracy of numerical solutions.
- The gravitational search algorithm is an excellent alternative to train artificial neural networks for predicting the mechanical behavior of fiber concrete, as it reached mean squared errors lower than the classic algorithms, moment back-propagation, and particle swarm optimization.
- Artificial neural networks trained with experimentally calibrated finite element simulations can accurately predict (R^2=0.99) the flexural resistance of beams with fiber reinforced concrete. However, more training data for low values of fibers might be used to improve its overall prediction capacity.

Acknowledgments

This research was financially supported by the Grupo de Investigación en Materiales de Construcción y Estructuras (INME) and the Universidad Industrial de Santander (UIS) in Colombia.

References

[1] Wang L, Zhou H, Zhang J, Wang Z, Zhang L, Nehdi ML. Prediction of concrete strength considering thermal damage using a modified strength-maturity model. Constr Build Mater. 2023 Oct 12;400. https://doi.org/10.1016/j.conbuildmat.2023.132779

[2] Ding Y, Zhang F, Torgal F, Zhang Y. Shear behaviour of steel fibre reinforced self-consolidating concrete beams based on the modified compression field theory. Compos Struct. 2012 Jul;94(8):2440-9. https://doi.org/10.1016/j.compstruct.2012.02.025

[3] Meng G, Gao B, Zhou J, Cao G, Zhang Q. Experimental investigation of the mechanical behavior of the steel fiber reinforced concrete tunnel segment. Constr Build Mater. 2016 Nov 15;126:98-107. https://doi.org/10.1016/j.conbuildmat.2016.09.028

[4] Sonebi M, Cevik A, Grünewald S, Walraven J. Modelling the fresh properties of self-compacting concrete using support vector machine approach. Constr Build Mater. 2016 Mar 1;106:55-64. https://doi.org/10.1016/j.conbuildmat.2015.12.035

[5] Okamura H, Ouchi M. Self-Compacting Concrete. Vol. 1, Journal of Advanced Concrete Technology. 2003. https://doi.org/10.1016/B978-075065686-3/50295-0

[6] El-Dieb AS, Reda Taha MM. Flow characteristics and acceptance criteria of fiber-reinforced self-compacted concrete (FR-SCC). Constr Build Mater. 2012 Feb;27(1):585-96. https://doi.org/10.1016/j.conbuildmat.2011.07.004

[7] Altun F, Haktanir T, Ari K. Effects of steel fiber addition on mechanical properties of concrete and RC beams. Constr Build Mater. 2007 Mar;21(3):654-61. https://doi.org/10.1016/j.conbuildmat.2005.12.006

[8] Batson GB, Birkimer DL, Burnett E, Gray BH, Henry R, Hoff GC, et al. State-of-the-Art Report on Fiber Reinforced Concrete. 1973.

[9] Shakya K, Watanabe K, Matsumoto K, Niwa J. Application of steel fibers in beam-column joints of rigid-framed railway bridges to reduce longitudinal and shear rebars. Constr Build Mater. 2012 Feb;27(1):482-9. https://doi.org/10.1016/j.conbuildmat.2011.07.016

[10] Rai B, Kumar S, Satish K. Influence of Water Binder Ratio and Chemical Admixture on the Properties of Self-Compacting Concrete with composite Cement-Fly Ash binder. Sustainable Structure and Materials [Internet]. 2019;2(1):97-117. Available from: https://doi.org/10.26392/SSM.2019.02.01.097

[11] Gencel O, Brostow W, Datashvili T, Thedford M. Workability and mechanical performance of steel fiber-reinforced self-compacting concrete with fly ash. Compos Interfaces. 2011;18(2):169-84. https://doi.org/10.1163/092764411X567567
[12] Fernandes PAL, Veludo J, Almeida N, Baptista J, Rodrigues H. Study of a self-compacting fiber-reinforced concrete to be applied in the precast industry. Innovative Infrastructure Solutions. 2018 Dec 1;3(1). https://doi.org/10.1007/s41062-018-0136-5
[13] Mohamed N, Soliman AM, Nehdi ML. Mechanical performance of full-scale precast steel fibre-reinforced concrete pipes. Eng Struct. 2015 Feb 1;84:287-99. https://doi.org/10.1016/j.engstruct.2014.11.033
[14] Nematollahi B, Voo YL, Saifulnaz M. R R. Structural behavior of precast Ultra-High Performance Fiber Reinforced Concrete (UHPFRC) cantilever retaining walls: Part II - Full scale experimental testing. KSCE Journal of Civil Engineering. 2014;18(5):1481-95. https://doi.org/10.1007/s12205-014-0412-7
[15] Niwa J, Shakya K, Matsumoto K, Watanabe K. Experimental Study on the Possibility of Using Steel Fiber-Reinforced Concrete to Reduce Conventional Rebars in Beam-Column Joints. Journal of Materials in Civil Engineering. 2012 Dec;24(12):1461-73. https://doi.org/10.1061/(ASCE)MT.1943-5533.0000536
[16] La Comisión Asesora Permanente para el Régimen de Construcciones Sismo Resistentes. Reglamento Colombiano de Construcción Sismo-Resistente (NSR-10). Bogotá; 2010.
[17] Moradi M, Bagherieh AR, Esfahani MR. Constitutive modeling of steel fiber-reinforced concrete. International Journal of Damage Mechanics. 2020 Mar 1;29(3):388-412. https://doi.org/10.1177/1056789519851159
[18] Lee MK, Barr BIG. A four-exponential model to describe the behaviour of fibre reinforced concrete. Vol. 37. https://doi.org/10.1007/BF02481583
[19] Huo L, Bi J, Zhao Y, Wang Z. Constitutive model of steel fiber reinforced concrete by coupling the fiber inclining and spacing effect. Constr Build Mater. 2021 Apr 19;280. https://doi.org/10.1016/j.conbuildmat.2021.122423
[20] Blanco A, Pujadas P, Cavalaro S, De La Fuente A, Aguado A. Constitutive model for fibre reinforced concrete based on the Barcelona test. Cem Concr Compos. 2014;53:327-40. https://doi.org/10.1016/j.cemconcomp.2014.07.017
[21] Chopra P, Sharma RK, Kumar M. Prediction of Compressive Strength of Concrete Using Artificial Neural Network and Genetic Programming. Advances in Materials Science and Engineering. 2016;2016. https://doi.org/10.1155/2016/7648467
[22] Hodhod H, Abdeen MAM. Simulation and prediction for the effect of natural and steel fibers on the performance of concrete using experimental analyses and artificial neural networks numerical modeling. KSCE Journal of Civil Engineering. 2011 Nov;15(8):1373-80. https://doi.org/10.1007/s12205-011-1053-8
[23] Paegle I, Minelli F, Fischer G. Cracking and load-deformation behavior of fiber reinforced concrete: Influence of testing method. Cem Concr Compos. 2016 Oct 1;73:147-63. https://doi.org/10.1016/j.cemconcomp.2016.06.012
[24] Bencardino F. Mechanical parameters and post-cracking behaviour of hpfrc according to three-point and four-point bending test. Advances in Civil Engineering. 2013;2013. https://doi.org/10.1155/2013/179712
[25] Bencardino F, Rizzuti L, Spadea G, Swamy RN. Implications of test methodology on post-cracking and fracture behaviour of Steel Fibre Reinforced Concrete. Compos B Eng. 2013;46:31-8. https://doi.org/10.1016/j.compositesb.2012.10.016
[26] Montgomery D, Runger G. Applied Statistics and Probability for Engineers. Fifth. John Wiley & Sons Inc, editor. Rosewood Drive, Danvers, USA: John Wiley & Sons Inc; 2011.
[27] European Project Gruop. The European Guidelines for Self-Compacting Concrete Specification, Production and Use [Internet]. 2005. Available from: www.efnarc.org
[28] Quiceno Pérez V, Cotes Prieto D, Zapata Orduz LE. Mechanical characterization of self-compacting steel fiber reinforced concrete using digital image correlation. Eng Fract Mech. 2021 Apr 1;246. https://doi.org/10.1016/j.engfracmech.2021.107618
[29] Soutsos M, Hatzitheodorou A, Kanavaris F, Kwasny J. Compressive Strength Estimates of Adiabatically Cured Concretes Using Maturity Methods. Journal of Materials in Civil Engineering. 2019 Jul;31(7). https://doi.org/10.1061/(ASCE)MT.1943-5533.0002757
[30] American Society for Testing Materials. ASTM C39 - Standard Test Method for Compressive Strength of Cylindrical Concrete Specimens [Internet]. 2019. Available from: www.astm.org,
[31] Asociación Española de Normalización y Certificación (AENOR). UNE 83515-Concreto reforzado con fibras. Determinación de la resistencia a fisuración, tenacidad y resistencia residual a tracción. Método Barcelona [Internet]. Madrid; 2010. Available from: www.aenor.es
[32] International Union of Laboratories and Experts in Construction Materials S and S (RILEM). RILEM TC 162-TDF :Test and design methods for steel fibre reinforced concrete. 2000.

[33] American Society for Testing Materials. ASTM C1609 - Standard Test Method for Flexural Performance of Fiber-Reinforced Concrete (Using Beam With Third-Point Loading) [Internet]. Available from: www.astm.org
[34] Wang T, Zhao H, Hao J, Zu J. Research on compressive stress - Strain relationship of fiber reinforced concrete. In: Advanced Materials Research. 2011. p. 384-92. https://doi.org/10.4028/www.scientific.net/AMR.168-170.384
[35] Laranjeira De Oliveira F, Aguado De Cea A. Design-oriented constitutive model for steel fiber reinforced concrete. 2010.
[36] Bortolotti L. Double-Punch Test for Tensile and Compressive Strengths in Concrete. 1988;
[37] International Federation for Structural Concrete (fib). Model code for concrete structures 2010. Berlin: Wilhelm Ernst & Sohn; 2010.
[38] Zapata-Ordúz LE, Portela G, Suárez OM. Weibull statistical analysis of splitting tensile strength of concretes containing class F fly ash, micro/nano-SiO2. Ceram Int. 2014 Jun;40(5):7373-88. https://doi.org/10.1016/j.ceramint.2013.12.083
[39] Deng B, Jiang D, Gong J. Is a three-parameter Weibull function really necessary for the characterization of the statistical variation of the strength of brittle ceramics? J Eur Ceram Soc. 2018 Apr 1;38(4):2234-42. https://doi.org/10.1016/j.jeurceramsoc.2017.10.017
[40] MathWorks. MATLAB R 2020a. MatWorks; 2020.
[41] Computers & Structures (CSI). SAP2000. 2022.
[42] Computers&Structures Inc. CSI Analysis Reference Manual [Internet]. 2016. Available from: www.csiamerica.com
[43] Adhikary BB, Mutsuyoshi H. Prediction of shear strength of steel fiber RC beams using neural networks. Constr Build Mater. 2006 Nov;20(9):801-11. https://doi.org/10.1016/j.conbuildmat.2005.01.047
[44] Minitab LLC. Minitab V.16. 2016.
[45] Açikgenç M, Ulaş M, Alyamaç KE. Using an Artificial Neural Network to Predict Mix Compositions of Steel Fiber-Reinforced Concrete. Arab J Sci Eng. 2015 Feb 1;40(2):407-19. https://doi.org/10.1007/s13369-014-1549-x
[46] Du KL, Swamy MNS. Neural networks and statistical learning. Vol. 9781447155713, Neural Networks and Statistical Learning. Springer-Verlag London Ltd; 2014. 1-824. https://doi.org/10.1007/978-1-4471-5571-3
[47] Mashhadban H, Kutanaei SS, Sayarinejad MA. Prediction and modeling of mechanical properties in fiber reinforced self-compacting concrete using particle swarm optimization algorithm and artificial neural network. Constr Build Mater. 2016 Aug 30;119:277-87. https://doi.org/10.1016/j.conbuildmat.2016.05.034
[48] Awolusi TF, Oke OL, Akinkurolere OO, Sojobi AO, Aluko OG. Performance comparison of neural network training algorithms in the modeling properties of steel fiber reinforced concrete. Heliyon [Internet]. 2018;e01115. https://doi.org/10.1016/j.heliyon.2018.e01115
[49] Kennedy J, Eberhart R. Particle Swarm Optimization. IEEE. 1995;
[50] Rashedi E, Nezamabadi-pour H, Saryazdi S. GSA: A Gravitational Search Algorithm. Inf Sci (N Y). 2009 Jun 13;179(13):2232-48. https://doi.org/10.1016/j.ins.2009.03.004
[51] Khajehzadeh M, Raihan Taha M, El-Shafie A, Eslami M. Optimization of Shallow Foundation Using Gravitational Search Algorithm. Research Journal of Applied Sciences Engineering and Technology [Internet]. 2012;4(9):1124-30. https://www.researchgate.net/publication/230996869
[52] Pająk M, Ponikiewski T. Flexural behavior of self-compacting concrete reinforced with different types of steel fibers. Vol. 47, Construction and Building Materials. 2013. p. 397-408. https://doi.org/10.1016/j.conbuildmat.2013.05.072
[53] Larsen IL, Thorstensen RT. The influence of steel fibres on compressive and tensile strength of ultra high performance concrete: A review. Vol. 256, Construction and Building Materials. Elsevier Ltd; 2020. https://doi.org/10.1016/j.conbuildmat.2020.119459
[54] Molins C, Aguado A, Saludes S. Double punch test to control the energy dissipation in tension of FRC (Barcelona test). Materials and Structures/Materiaux et Constructions. 2009 May;42(4):415-25. https://doi.org/10.1617/s11527-008-9391-9
[55] ACI Committee 214., American Concrete Institute. Guide to evaluation of strength test results of concrete. American Concrete Institute; 2011. 16 p.
[56] Tumidajski PJ, Fiore L, Khodabocus T, Lachemi M, Pari R. Comparison of Weibull and normal distributions for concrete compressive strengths. Canadian Journal of Civil Engineering. 2006 Oct;33(10):1287-92. https://doi.org/10.1139/l06-080
[57] Campione G, Letizia Mangiavillano M. Fibrous reinforced concrete beams in flexure: Experimental investigation, analytical modelling and design considerations. Eng Struct. 2008 Nov;30(11):2970-80. https://doi.org/10.1016/j.engstruct.2008.04.019

Appendix 1

MATLAB script for calibration of the Weibull parameters

```
%1. Barcelona
%2. Compression

for ensayo=2:2

  ini=4;   fin=71;
  fini=int2str(ini);    ffin=int2str(fin);

  switch ensayo
    case 1
      tic()
      aa='barcelona par3.xlsx';
      sesion=xlsread(aa,'DATOS',strcat('B',fini,':','B',ffin));
      zz='Modelos constitutivos corr.xlsx';

      consti=xlsread(aa,'DATOS',strcat('U',fini,':','AD',ffin));
      e1=consti(:,1);   s1=consti(:,2);
      e2=consti(:,3);   s2=consti(:,4);
      e3=consti(:,5);   s3=consti(:,6);
      e4=consti(:,7);    s4=consti(:,8);
      e5=consti(:,9);    s5=consti(:,10);

       cont1=1;
      cont2=1;
      for i=1:4:(fin-ini+1)
        if sesion(i)==1 || sesion(i)==2 || sesion(i)==5 ||...
          sesion(i)==7 || sesion(i)==13
          e11(cont1:cont1+3)=e1(i:i+3);  s11(cont1:cont1+3)=s1(i:i+3);
          e21(cont1:cont1+3)=e2(i:i+3);  s21(cont1:cont1+3)=s2(i:i+3);
          e31(cont1:cont1+3)=e3(i:i+3);  s31(cont1:cont1+3)=s3(i:i+3);
          e41(cont1:cont1+3)=e4(i:i+3);  s41(cont1:cont1+3)=s4(i:i+3);
          e51(cont1:cont1+3)=e5(i:i+3);  s51(cont1:cont1+3)=s5(i:i+3);
          cont1=cont1+4;
        else
          e12(cont2:cont2+3)=e1(i:i+3);  s12(cont2:cont2+3)=s1(i:i+3);
          e22(cont2:cont2+3)=e2(i:i+3);  s22(cont2:cont2+3)=s2(i:i+3);
          e32(cont2:cont2+3)=e3(i:i+3);  s32(cont2:cont2+3)=s3(i:i+3);
          e42(cont2:cont2+3)=e4(i:i+3);  s42(cont2:cont2+3)=s4(i:i+3);
          e52(cont2:cont2+3)=e5(i:i+3);  s52(cont2:cont2+3)=s5(i:i+3);
          cont2=cont2+4;
        end
      end

      s11(s11==0)=0.0000000001;  s21(s21==0)=0.0000000001;
      s31(s31==0)=0.0000000001;  s41(s41==0)=0.0000000001;
      s51(s51==0)=0.0000000001;
      s12(s12==0)=0.0000000001;  s22(s22==0)=0.0000000001;
      s32(s32==0)=0.0000000001;  s42(s42==0)=0.0000000001;
      s52(s52==0)=0.0000000001;

      Wpare11=wblfit(e11);
      dist=makedist('Weibull','A',Wpare11(1),'B',Wpare11(2));
      [ho,PvalueWe11]=adtest(e11,'Distribution',dist);
      Wpars11=wblfit(s11);
      dist=makedist('Weibull','A',Wpars11(1),'B',Wpars11(2));
      [ho,PvalueWs11]=adtest(s11,'Distribution',dist);
      avge11=mean(e11);  stde11=std(e11);
```

```
avgs11=mean(s11);  stds11=std(s11);

Wpare21=wblfit(e21);
dist=makedist('Weibull','A',Wpare21(1),'B',Wpare21(2));
[ho,PvalueWe21]=adtest(e21,'Distribution',dist);
Wpars21=wblfit(s21);
dist=makedist('Weibull','A',Wpars21(1),'B',Wpars21(2));
[ho,PvalueWs21]=adtest(s21,'Distribution',dist);
avge21=mean(e21);  stde21=std(e21);
avgs21=mean(s21);  stds21=std(s21);

Wpare31=wblfit(e31);
dist=makedist('Weibull','A',Wpare31(1),'B',Wpare31(2));
[ho,PvalueWe31]=adtest(e31,'Distribution',dist);
Wpars31=wblfit(s31);
dist=makedist('Weibull','A',Wpars31(1),'B',Wpars31(2));
[ho,PvalueWs31]=adtest(s31,'Distribution',dist);
avge31=mean(e31);  stde31=std(e31);
avgs31=mean(s31);  stds31=std(s31);

Wpare41=wblfit(e41);
dist=makedist('Weibull','A',Wpare41(1),'B',Wpare41(2));
[ho,PvalueWe41]=adtest(e41,'Distribution',dist);
Wpars41=wblfit(s41);
dist=makedist('Weibull','A',Wpars41(1),'B',Wpars41(2));
[ho,PvalueWs41]=adtest(s41,'Distribution',dist);
avge41=mean(e41);  stde41=std(e41);

avgs41=mean(s41);  stds41=std(s41);

Wpare51=wblfit(e51);
dist=makedist('Weibull','A',Wpare51(1),'B',Wpare51(2));
[ho,PvalueWe51]=adtest(e51,'Distribution',dist);
Wpars51=wblfit(s51);
dist=makedist('Weibull','A',Wpars51(1),'B',Wpars51(2));
[ho,PvalueWs51]=adtest(s51,'Distribution',dist);
avge51=mean(e51);  stde51=std(e51);
avgs51=mean(s51);  stds51=std(s51);

cont=0;

for i=1:4:size(s12,2)
   cont=cont+1;
   Wpare12(cont,:)=wblfit(e12(i:i+3));
   dist=makedist('Weibull','A',Wpare12(cont,1),'B',Wpare12(cont,2));
   [ho,PvalueWe12(cont)]=adtest(e12(i:i+3),'Distribution',dist);
   Wpars12(cont,:)=wblfit(s12(i:i+3));
   dist=makedist('Weibull','A',Wpars12(cont,1),'B',Wpars12(cont,2));
   [ho,PvalueWs12(cont)]=adtest(s12(i:i+3),'Distribution',dist);
   avge12(cont)=mean(e12(i:i+3));  stde12(cont)=std(e12(i:i+3));
   avgs12(cont)=mean(s12(i:i+3));  stds12(cont)=std(s12(i:i+3));
   Wpare22(cont,:)=wblfit(e22(i:i+3));
   dist=makedist('Weibull','A',Wpare22(cont,1),'B',Wpare22(cont,2));
   [ho,PvalueWe22(cont)]=adtest(e22(i:i+3),'Distribution',dist);
   Wpars22(cont,:)=wblfit(s22(i:i+3));
   dist=makedist('Weibull','A',Wpars22(cont,1),'B',Wpars22(cont,2));
   [ho,PvalueWs22(cont)]=adtest(s22(i:i+3),'Distribution',dist);
   avge22(cont)=mean(e22(i:i+3));  stde22(cont)=std(e22(i:i+3));
   avgs22(cont)=mean(s22(i:i+3));  stds22(cont)=std(s22(i:i+3));
   Wpare32(cont,:)=wblfit(e32(i:i+3));
   dist=makedist('Weibull','A',Wpare32(cont,1),'B',Wpare32(cont,2));
```

```
    [ho,PvalueWe32(cont)]=adtest(e32(i:i+3),'Distribution',dist);
    Wpars32(cont,:)=wblfit(s32(i:i+3));
    dist=makedist('Weibull','A',Wpars32(cont,1),'B',Wpars32(cont,2));
    [ho,PvalueWs32(cont)]=adtest(s32(i:i+3),'Distribution',dist);
    avge32(cont)=mean(e32(i:i+3));  stde32(cont)=std(e32(i:i+3));
    avgs32(cont)=mean(s32(i:i+3));  stds32(cont)=std(s32(i:i+3));
    Wpare42(cont,:)=wblfit(e42(i:i+3));
    dist=makedist('Weibull','A',Wpare42(cont,1),'B',Wpare42(cont,2));
    [ho,PvalueWe42(cont)]=adtest(e42(i:i+3),'Distribution',dist);
    Wpars42(cont,:)=wblfit(s42(i:i+3));
    dist=makedist('Weibull','A',Wpars42(cont,1),'B',Wpars42(cont,2));
    [ho,PvalueWs42(cont)]=adtest(s42(i:i+3),'Distribution',dist);
    avge42(cont)=mean(e42(i:i+3));
    stde42(cont)=std(e42(i:i+3));
    avgs42(cont)=mean(s42(i:i+3));
    stds42(cont)=std(s42(i:i+3));
    Wpare52(cont,:)=wblfit(e52(i:i+3));
    dist=makedist('Weibull','A',Wpare52(cont,1),'B',Wpare52(cont,2));
    [ho,PvalueWe52(cont)]=adtest(e52(i:i+3),'Distribution',dist);
    Wpars52(cont,:)=wblfit(s52(i:i+3));
    dist=makedist('Weibull','A',Wpars52(cont,1),'B',Wpars52(cont,2));
    [ho,PvalueWs52(cont)]=adtest(s52(i:i+3),'Distribution',dist);
    avge52(cont)=mean(e52(i:i+3));
    stde52(cont)=std(e52(i:i+3));
    avgs52(cont)=mean(s52(i:i+3));
    stds52(cont)=std(s52(i:i+3));
  end
  Wpare1=[Wpare11;Wpare12];  PvalueWe1=[PvalueWe11,PvalueWe12]';
  Wpars1=[Wpars11;Wpars12];  PvalueWs1=[PvalueWs11,PvalueWs12]';
  avge1=[avge11,avge12]';  stde1=[stde11,stde12]';
  avgs1=[avgs11,avgs12]';  stds1=[stds11,stds12]';
  Wpare2=[Wpare21;Wpare22];  PvalueWe2=[PvalueWe21,PvalueWe22]';
  Wpars2=[Wpars21;Wpars22];  PvalueWs2=[PvalueWs21,PvalueWs22]';
  avge2=[avge21,avge22]';  stde2=[stde21,stde22]';
  avgs2=[avgs21,avgs22]';  stds2=[stds21,stds22]';
  Wpare3=[Wpare31;Wpare32];  PvalueWe3=[PvalueWe31,PvalueWe32]';
  Wpars3=[Wpars31;Wpars32];  PvalueWs3=[PvalueWs31,PvalueWs32]';
  avge3=[avge31,avge32]';  stde3=[stde31,stde32]';
  avgs3=[avgs31,avgs32]';  stds3=[stds31,stds32]';
  Wpare4=[Wpare41;Wpare42];  PvalueWe4=[PvalueWe41,PvalueWe42]';
  Wpars4=[Wpars41;Wpars42];  PvalueWs4=[PvalueWs41,PvalueWs42]';
  avge4=[avge41,avge42]';  stde4=[stde41,stde42]';
  avgs4=[avgs41,avgs42]';  stds4=[stds41,stds42]';
  Wpare5=[Wpare51;Wpare52];  PvalueWe5=[PvalueWe51,PvalueWe52]';
  Wpars5=[Wpars51;Wpars52];  PvalueWs5=[PvalueWs51,PvalueWs52]';
  avge5=[avge51,avge52]';  stde5=[stde51,stde52]';
  avgs5=[avgs51,avgs52]';  stds5=[stds51,stds52]';

case 2
  aa='compresion par.xlsx';
  sesion=xlsread(aa,'DATOS',strcat('B',fini,':','B',ffin));
  zz='Modelos Constitutivos.xlsx';
  fc=xlsread(aa,'DATOS',strcat('V',fini,':','V',ffin));
  Ec=xlsread(aa,'DATOS',strcat('AI',fini,':','AI',ffin));%Modulo tangente
  cont1=1;
  cont2=1;
  for i=1:4:(fin-ini+1)
    if sesion(i)==1 || sesion(i)==2 || sesion(i)==5 ||...
        sesion(i)==7 || sesion(i)==13
      fc1(cont1:cont1+3)=fc(i:i+3);
      Ec1(cont1:cont1+3)=Ec(i:i+3);
```

```
            cont1=cont1+4;
          else
            fc2(cont2:cont2+3)=fc(i:i+3);
            Ec2(cont2:cont2+3)=Ec(i:i+3);
            cont2=cont2+4;
          end
        end
        Wpar1=wblfit(fc1);
        dist=makedist('Weibull','A',Wpar1(1),'B',Wpar1(2));
        [ho,pvalue]=adtest(fc1,'Distribution',dist);
        PvalueW1=pvalue;  Wpar1E=wblfit(Ec1);
        dist=makedist('Weibull','A',Wpar1E(1),'B',Wpar1E(2));
        [ho,pvalue]=adtest(Ec1,'Distribution',dist);
        PvalueW1E=pvalue;
        avgfc1=mean(fc1);  stdfc1=std(fc1);
        avgEc1=mean(Ec1);  stdEc1=std(Ec1);

        cont=0;
        for i=1:4:size(fc2,2)
          cont=cont+1;
          param=wblfit(fc2(i:i+3));  Wpar2(cont,:)=param;
          dist=makedist('Weibull','A',Wpar2(cont,1),'B',Wpar2(cont,2));
          [ho,pvalue]=adtest(fc2(i:i+3),'Distribution',dist);
          PvalueW2(cont)=pvalue;
          param=wblfit(Ec2(i:i+3));  Wpar2E(cont,:)=param;
          dist=makedist('Weibull','A',Wpar2E(cont,1),'B',Wpar2E(cont,2));
          [ho,pvalue]=adtest(Ec2(i:i+3),'Distribution',dist);
          PvalueW2E(cont)=pvalue;
          avgfc2(cont)=mean(fc2(i:i+3));  stdfc2(cont)=std(fc2(i:i+3));
          avgEc2(cont)=mean(Ec2(i:i+3));  stdEc2(cont)=std(Ec2(i:i+3));
    end
        Wpar=[Wpar1;Wpar2];  PvalueW=[PvalueW1,PvalueW2]';
        WparE=[Wpar1E;Wpar2E];  PvalueWE=[PvalueW1E,PvalueW2E]';
        avgfc=[avgfc1,avgfc2]';  stdfc=[stdfc1,stdfc2]';
        avgEc=[avgEc1,avgEc2]';  stdEc=[stdEc1,stdEc2]';
      otherwise
  end
end
```

Appendix 2

MATLAB script for automation of SAP2000

```
clear;
clc;
ini=62;  fin=121;
Datosred=zeros(1010,(fin-ini+1)*2);
for i=1:(fin-ini+1)
  %1. Define which SAP to use: already open one (true) o new one (false)
  if i==1
    EnesteSAP=false();
  else
    EnesteSAP=false();
  end
  %2. Specify SAP file route (true) otherwise the last used SAP file route will be used.
  EspecificarSAP=true();

  %3. Specify SAP file route.
  DireccionSAP='C:\Program Files\Computers and Structures\SAP2000 22\SAP2000.exe';

  %4. Specify the route of the API to use.
  DireccionAPIDLL='C:\Program Files\Computers and Structures\SAP2000 22\SAP2000v1.dll';
```

```
  %5. Specify the route of the file where the model is located
  DireccionCarpetaModelo='E:\David\Documentos\Estructuras\MAESTRÍA EN INGENIERÍA CIVIL\Vigas
SFRSCC_SAP\Red neural';
  if ~exist(DireccionCarpetaModelo, 'dir') %If the file exists use it, otherwise create it
    mkdir(DireccionCarpetaModelo);
  end
  NombreModelo=strcat(int2str(ini-1+i),'.sdb'); %Name of the model
  DireccionModelo=strcat(DireccionCarpetaModelo,filesep,NombreModelo); %Text to route
  %6. Create the API assistent.
  a=NET.addAssembly(DireccionAPIDLL);
  asistenteAPI=SAP2000v1.Helper;
  asistenteAPI=NET.explicitCast(asistenteAPI,'SAP2000v1.cHelper');

  %7. Open SAP or use one already open.
  if EnesteSAP
    SapObject=asistenteAPI.GetObject('CSI.SAP2000.API.SapObject');
    SapObject=NET.explicitCast(SapObject,'SAP2000v1.cOAPI');
  else
    if EspecificarSAP
      SapObject=asistenteAPI.CreateObject(DireccionSAP);
    else
      SapObject=asistenteAPI.CreateObjectProgID('CSI.SAP2000.API.SapObject');
    end
    SapObject = NET.explicitCast(SapObject,'SAP2000v1.cOAPI');
    SapObject.ApplicationStart;
  end
  asistenteAPI=0;

  %8.Create SAP model
  SapModel=NET.explicitCast(SapObject.SapModel,'SAP2000v1.cSapModel');
  ret=SapModel.InitializeNewModel;

  %9. Open the SAP model.
  File=NET.explicitCast(SapModel.File,'SAP2000v1.cFile');
  ret=File.OpenFile(DireccionModelo);

  tic()
  %15. Run the SAP model.
  Analyze=NET.explicitCast(SapModel.Analyze,'SAP2000v1.cAnalyze');
  ret=Analyze.RunAnalysis();

  AnalysisResults=NET.explicitCast(SapModel.Results,'SAP2000v1.cAnalysisResults');
  AnalysisResultsSetup=NET.explicitCast(AnalysisResults.Setup,'SAP2000v1.cAnalysisResultsSetup');

  ret=AnalysisResultsSetup.DeselectAllCasesAndCombosForOutput;
  ret=AnalysisResultsSetup.SetCaseSelectedForOutput("FPT-Cracking");
  ret=AnalysisResultsSetup.SetOptionNLStatic(2);

  NumberResults=0;
  Obj=NET.createArray('System.String',1010);
  Elm=NET.createArray('System.String',1010);
  ACase=NET.createArray('System.String',1010);
  StepType=NET.createArray('System.String',1010);
  StepNum=NET.createArray('System.Double',1010);
  U1=NET.createArray('System.Double',1010);  U2=NET.createArray('System.Double',1010);
  U3=NET.createArray('System.Double',1010);  R1=NET.createArray('System.Double',1010);
  R2=NET.createArray('System.Double',1010);  R3=NET.createArray('System.Double',1010);

[ret,NumberResults,Obj,Elm,ACase,StepType,StepNum,U1,U2,U3,R1,R2,R3]=AnalysisResults.JointDispl("21"
,SAP2000v1.eItemTypeElm.ObjectElm,...
```

```
    NumberResults,Obj,Elm,ACase,StepType,StepNum,U1,U2,U3,R1,R2,R3);

  for j=1:NumberResults
    Desplazamiento(j)=U3(j)*-1000;
  end

  NumberResults=0;
  StepType=NET.createArray('System.String',1010);
  StepNum=NET.createArray('System.Double',1010);
  LoadCase=NET.createArray('System.String',1010);
  Fx=NET.createArray('System.Double',1);  Fy=NET.createArray('System.Double',1);
  Fz=NET.createArray('System.Double',1);  Mx=NET.createArray('System.Double',1);
  My=NET.createArray('System.Double',1);  Mz=NET.createArray('System.Double',1);
  gx=0;  gy=0;  gz=0;

[ret,NumberResults,LoadCase,StepType,StepNum,Fx,Fy,Fz,Mx,My,Mz,gx,gy,gz]=AnalysisResults.BaseReact(
NumberResults,LoadCase,StepType,StepNum,...
    Fx,Fy,Fz,Mx,My,Mz,gx,gy,gz);

  for j=1:NumberResults
    Carga(j)=Fz(j);
  end

  NumberResults=0;
  StepType=NET.createArray('System.String',1010);
  StepNum=NET.createArray('System.Double',1010);
  LoadCase=NET.createArray('System.String',1010);
  GD=NET.createArray('System.String',1010);
  DType=NET.createArray('System.String',1);
  Numbdat(i)=NumberResults;

  %17. Close SAP
    ret=SapModel.SetModelIsLocked(false());
    ret=SapObject.ApplicationExit(false());
    File=0;
    PropMaterial=0;  PropFrame=0;
    FrameObj=0;  AreaObj=0;
    PointObj=0;  View=0;
    LoadPatterns=0;  Analyze=0;
    AnalysisResults=0;
    AnalysisResultsSetup=0;
    SapModel=0;  SapObject=0;
    tiempo(2*i-1:2*i)=[toc()/60,0];
    Datosred(1:length(Desplazamiento),2*i-1:2*i)=[Desplazamiento',Carga'];
    clear Desplazamiento Carga
end

xlswrite('Curvas ajustadas final.xlsx',Datosred,'Datos red neural','DT40')
xlswrite('Curvas ajustadas final.xlsx',tiempo,'Datos red neural','DT38')
```

Research on Engineering Structures & Materials
www.jresm.org

Research Article

Removal of cytotoxic tamoxifen from aqueous solutions with hydroxyapatite adsorbent

Serdar Çilenmez [1,a], Yavuz Ergün [*,2,b], İbrahim Bulduk [3,c]

[1]*Graduate School of Education Dept. of Energy and Environmental Sciences, Uşak University, Uşak, Türkiye*
[2]*Dept.of Chemical Eng., Faculty of Engineering and Natural Science, Uşak University, Uşak, Türkiye*
[3]*Dept. of Chemical Eng., Faculty of Engineering, Afyon Kocatepe University, Afyonkarahisar, Türkiye*

Article Info

Article History:

Received 27 Dec 2024
Accepted 25 Feb 2025

Keywords:

Wastewater;
Tamoxifen;
Removal;
Hydroxyapatite;
Adsorption

Abstract

The growing problem of pharmaceutical contamination poses a significant challenge to the protection of water resources. Tamoxifen, a widely used anticarcinogenic drug, is one of the pharmaceutical residues found in wastewater and poses serious environmental risks. In this study, chemically synthesized hydroxyapatite (HAP) was used as an adsorbent to remove tamoxifen from aqueous solutions. The synthesized HAP was thoroughly characterized by BET surface area analysis, SEM-EDX imaging and FTIR spectroscopy. A systematic evaluation of key adsorption parameters was carried out to determine the most effective conditions for tamoxifen removal. Experiments were performed by varying parameters such as initial tamoxifen concentration (20-70 µg/mL), solution pH (2-10), adsorbent dosage (20-50 mg per 50 mL solution), contact time (0-240 min) and temperature (298-318 K). The equilibrium state of the adsorption process was analyzed using Langmuir and Freundlich isotherm models. Pseudo-first and pseudo-second order kinetic models were used to determine the rate of the process. Thermodynamic properties were also calculated to provide information on the nature of the process. A maximum removal efficiency of 90.85% was obtained under optimum conditions of initial concentration 40 µg/mL, adsorbent dosage 40 mg, contact time 180 min and pH 7. Notably, the pseudo-second-order kinetic model (R^2: 0.9997) and the Langmuir isotherm model (R^2: 0.9994) exhibited the closest alignment with the experimental data. Thermodynamic studies have shown that the adsorption was a by itself ($\Delta G<0$), exothermic ($\Delta H<0$) process, accompanied by an increase in system disorder ($\Delta S>0$). Consequently, this research underscores the viability of HAP as an economical and ecologically sound approach for remediating wastewater contaminated with pharmaceuticals.

© 2025 MIM Research Group. All rights reserved.

1. Introduction

Pharmaceutical compounds are chemicals widely used in the prevention, treatment, and diagnosis of diseases. However, through the pharmaceutical industry, hospital wastes, and domestic sewage, these compounds enter water resources and pose significant threats to the environment [1,2]. These chemicals damage the aquatic ecosystem and cause persistent pollution, leading to the development of resistant microorganisms and resistance genes. Moreover, due to their difficult biodegradation, these compounds are easily transported between water, soil, and living organisms and negatively affect human and animal health [3].

Tamoxifen, a powerful antiestrogen, is extensively utilized, particularly in the initial treatment and recurrence of breast cancer. Studies on its environmental effects reveal that this compound can

*Corresponding author: yavuz.ergun@usak.edu.tr
[a]orcid.org/0009-0007-9138-0190; [b]orcid.org/0000-0001-5883-2078; [c]orcid.org/0000-0001-6172-7738
DOI: http://dx.doi.org/10.17515/resm2025-598ma1227rs

negatively impact the reproductive abilities of aquatic organisms. It has been shown to disrupt vitellogenin levels in both female and male species, with generational impacts on their offspring [4]. Tamoxifen has been detected in varying concentrations in hospital wastewater, sewage, and surface waters [5–10], posing significant risks to aquatic ecosystems due to its toxicity, endocrine-disrupting properties, and bioaccumulation potential [11]. These findings highlight the importance of non-biological removal methods as an effective solution to eliminate tamoxifen from aquatic environments and prevent its atmospheric release. Nevertheless, research on the application of non-biological techniques for tamoxifen removal remains limited [12–16]. Therefore, further comprehensive studies are essential to explore alternative approaches for removing this anticancer drug from wastewater.

Pharmaceutical pollutants represent a significant threat to both ecosystems and human health due to their high-water solubility, persistence, and toxic characteristics [17,18]. To address this issue, various treatment methods have been developed, including biodegradation [19], advanced oxidation processes [20], photo-Fenton reactions [21], electro-Fenton systems [22], ozonation, membrane technologies [24], and adsorption techniques [25–27]. Among these, adsorption stands out as a particularly effective option, valued for its simplicity, high efficiency, and cost-effectiveness, especially in the removal of pharmaceutical compounds. In addition to traditional adsorbents like activated carbon, graphene oxide, zeolite, and clay, hydroxyapatite (HAP) has gained attention as an alternative due to its high adsorption capacity and biocompatibility. Adsorption is a versatile and promising technique, relying on the physical or chemical interaction of contaminants with the surface of the adsorbent. Compared to other methods, adsorption not only avoids the production of highly toxic by-products but also offers an efficient, low-cost solution for removing pharmaceutical compounds from wastewater [28–32].

Hydroxyapatite (HAP) has proven to be a highly effective adsorbent due to its unique properties. As a calcium phosphate compound with the chemical formula $Ca_{10}(PO_4)6(OH)_2$. HAP is widely recognized as a primary mineral component of bones and teeth. This remarkable material exhibits excellent biocompatibility, bioactivity, osteoconductivity, affinity, and nontoxicity. Its chemical and structural resemblance to the mineral constituents of human bones and teeth has made it a subject of extensive research over the years [33–37].

HAP's ability to accommodate a wide range of anionic and cationic substituents makes it versatile for various applications. It is commonly utilized in fields such as nanomedicine, drug and gene delivery, ion conduction, catalysis, biosensing, and tissue engineering. HAP can be obtained either synthetically or from natural sources, with numerous synthesis techniques documented in the literature. Synthetic HAP can be produced through a variety of methods, including dry processes (solid-state and mechanochemical synthesis), wet processes (chemical precipitation, hydrolysis, sol-gel, hydrothermal, emulsion, and sonochemical methods), and high-temperature techniques (combustion and pyrolysis) [38]. These diverse approaches enhance HAP's adaptability for specific applications, solidifying its importance across multiple scientific and industrial domains.

In this study, hydroxyapatite (HAP) adsorbents were synthesized using the sol-gel method and subsequently characterized. The potential of HAP for removing tamoxifen from wastewater was systematically evaluated. Adsorption kinetics were analyzed using pseudo-first-order and pseudo-second-order models, while adsorption equilibrium was studied through Langmuir and Freundlich isotherm models. Additionally, thermodynamic parameters were determined at 20, 30, and 40 °C to understand the nature of the adsorption process. To the best of our knowledge, this is the first report on the synthesis of HAP as an adsorbent and its application for the removal of pharmaceutical contaminants from aqueous solutions.

2. Materials and Methods

2.1. Tools, Chemicals and Materials

Tamoxifen levels in aqueous solutions were determined using an Agilent 1260 HPLC system (USA) with a UV detector and Chemstation software. pH measurements were taken with a Mettler-Toledo pH meter (Switzerland) using a glass electrode. All experiments utilized ultrapure water produced

by a Merck-Millipore Milli-Q system (USA), characterized by a conductivity below 0.05 µS/cm and a pH of 6.98, generated through reverse osmosis. Adsorption studies were performed in a WITEG WSB-30 shaking water bath (Germany) to maintain consistent experimental conditions.

Chemicals used included: ammonium phosphate dibasic ($(NH_4)_2HPO_4$, ≥99.0%), calcium nitrate tetrahydrate ($Ca(NO_3)_2{\cdot}4H_2O$, ≥99.0%), sodium hydroxide (NaOH, 98%), hydrochloric acid (HCl, 37%), orthophosphoric acid (H_3PO_4, 85%), and potassium dihydrogen phosphate (KH2PO4, ≥99.0%). All chemicals were procured from Sigma-Aldrich Chemie (Istanbul, Turkey) and used as received. Tamoxifen (CAS No. 10540-29-01, C_26H_29NO, 99%) was purchased from Sigma-Aldrich Chemistry, and tamoxifen tablets (20 mg) were obtained from a local pharmacy in Afyonkarahisar, Turkey. Deionized water was used for all aqueous solutions, with pH adjustments made using HCl and NaOH to achieve the desired experimental conditions.

2.2. Hydroxyapatite (HAP) Synthesis

Natural bone consists of approximately 60 wt% amorphous or crystallized HAP, with a theoretical calcium-to-phosphorus (Ca/P) molar ratio of 1.67. This ratio was carefully considered during the synthesis of HAP via the sol-gel method. The synthesis began by dissolving 8.20 g of calcium nitrate tetrahydrate in 50 mL of ethanol. Simultaneously, 2.38 g of diammonium hydrogen orthophosphate was dissolved in 50 mL of double-distilled water. Both solutions were stirred continuously with a magnetic stirrer at 70 °C for 4 hours to ensure uniformity. After preparation, the solutions were allowed to hydrolyze for 24 hours. Subsequently, the diammonium hydrogen orthophosphate solution was gradually added to the calcium nitrate solution at a rate of 5 mL/min while stirring continuously at 36 °C for 4 hours to facilitate the reaction. The pH of the resulting mixture was adjusted to 7.4 using an ammonia solution.

In this supersaturated melt solution, nucleation occurs as the ions cluster and grow to a valid size. The crystals grow successively to form HAP, ranging in size from a few nanometers to 0.3 µm. Grain growth in solution is dependent on concentration, time and temperature. As the formed HAP particles are covered with pore and film water, drying in an oven at 70 °C for four hours and sintering at 800 °C for one hour causes crystallization and grain growth. The removal of water by sintering causes the formation of heterogeneously grown crystals with a porous interconnected network as a result of the transformation into polycrystalline by the formation of an intergranular neck. The presence of impurities in the solution are factors affecting the formation and growth rate of the nucleus. The final product was stored in a sealed glass jar to preserve its integrity for subsequent adsorption studies.

2.3. Characterization Methods

To analyze the characteristics of the synthesized HAP, several techniques were used. Fourier Transform Infrared Spectroscopy (FTIR, Perkin Elmer) identified the surface functional groups. Brunauer-Emmett-Teller (BET) analysis, performed on a Micromeritics Gemini VII 5.03 system, determined the specific surface area and pore structure. Scanning Electron Microscopy (SEM, Zeiss Sigma 300) revealed the surface morphology, and Energy Dispersive X-ray (EDX) spectroscopy provided elemental composition data.

2.4. Determination of Zero Charge Point (pHpzc) of HAP Adsorbent

The pHpzc of HAP was determined by the salt addition technique. 1 liter of 0.1 M NaCl solution was prepared, and 50 mL volumes were taken into six different volumetric flasks; each of these volumes was transferred to 250 mL bottles. The initial pH value (pHi) of each volume was adjusted stepwise from 2 to 12 using 0.1 M hydrochloric acid (HCl) or 0.1 M sodium hydroxide (NaOH). Then, 0.050 g of HAP was added to each flask, and the mixtures were agitated at 25 °C and 170 rpm for 24 hours. After filtration, the final pH (pHf) of each filtrate was measured. A graph of pHi versus pHf was plotted, and the pHpzc was determined as the intersection point of the two curves [39].

2.5. Batch Adsorption Experiments

This study examined the effectiveness of utilizing HAP adsorbent to remove tamoxifen from aqueous solutions. The first step involved carefully weighing 50 mg of tamoxifen into a 100 mL

beaker, adding 40 mL of ultrapure water, and letting it dissolve. After the solution was moved to a 100 mL volumetric flask, water was added to finish the volume. A stock solution containing 500 mg mL-1 of tamoxifen was made. For five minutes, the stock solution was sonicated in an ultrasonic bath. 50 mL tamoxifen solutions in 250 mL capped Erlenmeyer flasks were used for the adsorption tests. The effects of variables such pH, adsorbent dosage, starting concentration, and temperature on the effectiveness of tamoxifen removal were assessed in adsorption experiments. To achieve the required concentrations for the set of tests, the stock solution was diluted. The solutions were shaken at 170 rpm in a thermostatic water bath after the pH levels had been adjusted and the appropriate quantity of HAP adsorbent had been added. A 0.22 µm membrane syringe filter was used to filter the samples, and an HPLC equipment was used to measure the amount of tamoxifen in the filtrates.

By adjusting pH between 2 and 10 while maintaining constant values for all other parameters, the impact of pH on the effectiveness of tamoxifen elimination was examined. Solutions of 0.1 N HCl or 0.1 N NaOH were used to alter the pH. Next, at the pH that provided the best clearance, the impact of various HAP dosages, ranging from 20 to 50 mg, on adsorption efficiency was assessed. Additionally, while holding other factors constant, the impact of temperature (293–313 K) and starting tamoxifen concentration (20–70 mg L^{-1}) on the removal efficiency was examined. A methodical assessment of the variables influencing adsorption efficiency was made possible by the triplicate execution of each experiment and the reporting of the average results. Equations 1 and 2 were used to determine the quantity of tamoxifen adsorbed per unit mass of HAP at a specific time t (qt) and equilibrium (qe):

$$qt = (Co\text{-}Ct)V/w \tag{1}$$

$$qe = (Co - Ce)V/w \tag{2}$$

Additionally, Equation 3 was used to determine the percentage of adsorbed tamoxifen:

$$Adsorption(\%) = \left(\frac{Co-Ce}{Co}\right)100 \tag{3}$$

Where w (g) is the mass of HAP, V (L) is the volume of the solution, Ce (mg L^{-1}) is the equilibrium concentration, Ct (mg L^{-1}) is the concentration at time t, and C_0 (mg L^{-1}) is the initial concentration [40,41].

2.6. Equilibrium Modeling of Tamoxifen Removal Process

Adsorption isotherms are graphical representations that illustrate the relationship between the concentration of a substance in solution (adsorbate) and the amount of that substance adsorbed onto the surface of a material (adsorbent) at a constant temperature. These isotherms provide valuable insights into the nature of the interactions between the adsorbate and the adsorbent surface. In the context of this study, adsorption isotherms were used to model the interaction between tamoxifen and hydroxyapatite (HAP). By analyzing the equilibrium curves, researchers can understand how much tamoxifen is adsorbed onto the HAP surface at different concentrations, which is crucial for designing efficient adsorption systems. The Langmuir isotherm is a popular model that describes monolayer adsorption, where adsorbate molecules form a single layer on the adsorbent surface. It assumes that adsorption takes place at specific, identical sites on the surface, with each site accommodating only one adsorbate molecule. The linearized form of the Langmuir isotherm is given by Equation 4 [42]. By applying experimental data to this model, key parameters such as the maximum adsorption capacity (qmax) and the equilibrium constant (KL) can be determined. These parameters provide valuable information about the adsorption process and the interaction between tamoxifen and HAP.

$$\frac{Ce}{qe} = \frac{1}{qmKL} + Ce/qm \tag{4}$$

In this formula, qm stands for activated carbon's monolayer adsorption capacity (mg g^{-1}) and KL for the Langmuir adsorption constant (L mg^{-1}). The dimensionless separation factor (RL), which

shows if the adsorption procedure is feasible, can be used to assess the affinity between the adsorbent and the adsorbate. RL is computed using formula 5 as follows:

$$RL = 1/(1 + KLCo) \tag{5}$$

In this context, CoCo denotes the initial concentration of the adsorbate in the solution (mg L^{-1}). The RL value provides insight into the adsorption isotherm: When RL=0, adsorption is irreversible; when 0<RL<1, the isotherm is favorable for adsorption; when RL=1, the isotherm is linear; and when RL>1, the isotherm is unfavorable.

The Freundlich model differs from the Langmuir model in that it assumes the formation of multiple layers of adsorbate molecules on the adsorbent surface rather than a single homogeneous layer. This model is well-suited for describing adsorption on heterogeneous surfaces, where the adsorbent exhibits varying affinities for the adsorbate. The linearized form of the Freundlich isotherm model is represented by Equation 6 [43]:

$$In(qe) = In(KF) + \left(\frac{1}{n}\right) In(Ce) \tag{6}$$

In this equation, KF is the Freundlich constant (L mg^{-1}) and n is a parameter indicating the suitability of the adsorption process. If n > 1, higher concentrations should facilitate adsorbate adsorption on the adsorbent.

2.7. Kinetic Modeling of Tamoxifen Removal Process

The batch adsorption data were interpreted using pseudo-first-order and pseudo-second-order kinetic models and the corresponding kinetic parameters were calculated. The pseudo-first-order model assumes that each molecule of the adsorbate adheres to a specific site on the adsorbent and determines the adsorption rate depending on the sorption capacity of the solid surface. The linear form of this model is expressed as in equation 2.7 below [44,45]:

$$In(qe - qt) = In(qe) - k1t \tag{7}$$

In this equation, $k1$ is the pseudo-first-order rate constant (min^{-1}), and qe and qt indicate the adsorption capacities at equilibrium and at a specific time t (mg g^{-1}), respectively. On the other hand, the pseudo-second-order model explains the adsorption kinetics in relation to the adsorbent's capacity and is expressed by Equation 8.

$$\frac{t}{qt} = \frac{1}{k2qe2} + \left(\frac{1}{qe}\right) t \tag{8}$$

This formula uses t as the elapsed time, k_2 as the pseudo-quadratic model's rate constant (g mg^{-1} min^{-1}), and qe and qt as the adsorption capacities at equilibrium (mg g^{-1}).

2.8. Thermodynamic Modeling of Tamoxifen Removal Process

The spontaneity of the adsorption process and the impact of temperature on adsorption performance were assessed using thermodynamic metrics such as enthalpy (ΔH°), Gibbs free energy (ΔG°), and entropy (ΔS°) variations. Equation 9 [46] was used to determine the Gibbs free energy change (ΔG°):

$$\Delta G° = -RT\ In(Ke) \tag{9}$$

The equilibrium constant, K_e, is defined by equation 2.10, the universal gas constant, R, is 8.314 J mol^{-1} K^{-1}, and T is the absolute temperature (K).

$$Ke = \left(\frac{qe}{Ce}\right) \tag{10}$$

Where Ce and qe are the equilibrium concentrations of tamoxifen in solution (mg L^{-1}) and on the adsorbent (mg g^{-1}), respectively. The relationship between ΔG°, ΔH° and ΔS° is expressed as follows 11:

$$\Delta G° = \Delta H° - T\Delta S° \quad (11)$$

Rearranging this expression leads to a linear equation 2.12 that allows the calculation of thermodynamic parameters:

$$In(Ke) = \left(\frac{\Delta S°}{R}\right) - (\frac{\Delta H°}{RT}) \quad (12)$$

2.9. Quantification of Tamoxifen in Aqueous Solutions

Using a 1260 Infinity LC system (Agilent, USA) and high-performance liquid chromatography (HPLC), the amount of tamoxifen in the solutions was determined. An ODS-3 C18 chromatographic column (250 × 4.6 mm, 5 µm) was used for separation, and a wavelength of 278 nm was used for detection. A mobile phase comprising a 50:50 (v/v) ratio of acetonitrile and 0.01 M KH_2PO_4 solution (pH:2, adjusted with phosphoric acid) was used to conduct the analysis under isocratic conditions. The injection volume was 5 µL, the flow rate was 1.0 mL min^{-1}, and the column temperature was kept at 30 °C.

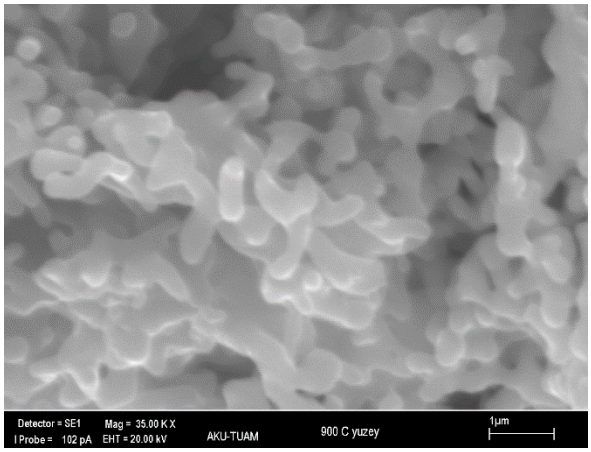
3. Results and Discussion

3.1. Characterization of HAP

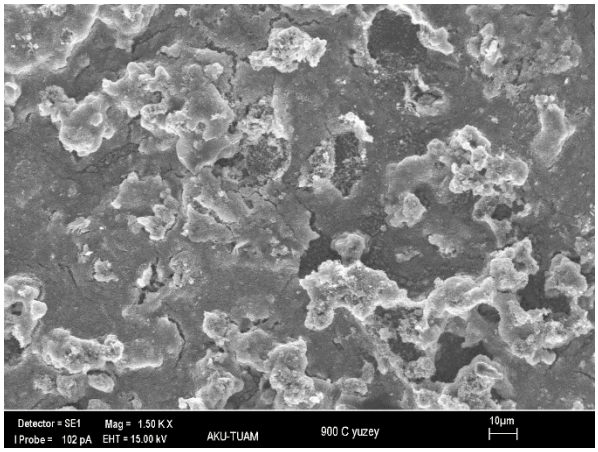
SEM, FTIR, and XRD analyses were used to describe the HAP samples. To examine the surface morphology of HAP, SEM was employed. Figures 1a and 1b display SEM pictures of HAP in the form of polycrystalline bonds. It had a porous structure that varied in size. The results of earlier research on HAP are in line with this extremely porous material [47]. The specific properties, morphology, porosity, pore size, surface area, polarity and stiffness of sol-gel obtained HAPs are largely dependent on the progress of the hydrolysis and condensation reactions and are also influenced by the choice of precursor, water-precursor molar ratio, solvent and co-solvent, pressure, temperature, ageing, drying and sintering conditions.

The structure of HAP was ascertained by FTIR analysis, and the resulting spectrum is shown in Figure 1d. The OH stretching vibrations of the surface P-OH groups were identified as the source of a faint signal at 3670 cm^{-1} in the FTIR spectrum. The stretching vibration of lattice OH ions is identified by a distinct band at 3572 cm^{-1}. The overtone and combination bands of PO_3^{-4} ions are shown by three bands at 2142, 2077, and 1989 cm^{-1}. The OH-O bands of adsorbed water and the HAP of P-O attached to PO_3^{-4} groups are characterized by low-intensity, poorly defined absorption bands in the 1080–1020 cm^{-1} area. Around 600–610 cm^{-1}, there is a distinct peak that is indicative of the O-H vibrational mode. The CO_2^{-3} groups are represented by the bands in the 1380–1580 cm^{-1} range. PO_3^{-4} is responsible for the bands at 900–1300 cm^{-1} [47].

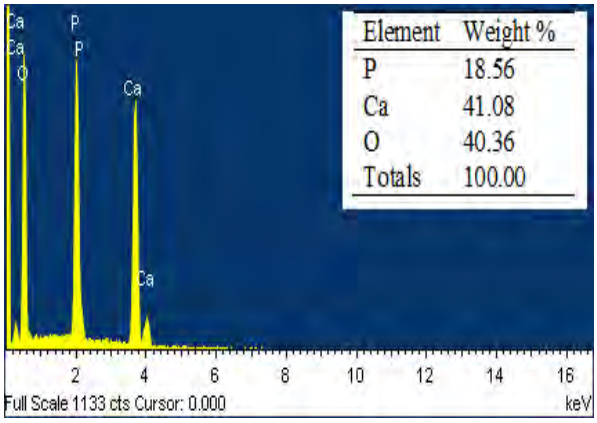
Figure 2a shows the XRD image obtained from HAP samples. As seen intensely in the standard peak of HAP, the approximate 2θ angles of 100%, 63% and 52% peaks vary between ≈ 31-33°. The reflection planes from these angles are distributed in the region between (211) - (300) and (112) respectively. The identified planes were determined by reflection (diffraction) from the lattice parameters of the synthesized HAP samples. Unlike standard HAP, only very little β TCP and trace CaO phases were found. β TCP does not pose any disadvantage in terms of biocompatibility [48]. Nowadays, it has been found that compounds containing calcium phosphate ceramics with a mixture of HA and β TCP give much better results compared to single phase HAP and β TCP [49,50]. The presence of CaO phase may have been formed by the replacement of carbonate groups stabilized in the natural hydroxyl region with OH in the HAP structure [50]. It is seen that the phases obtained from the samples by XRD are very close to the standard phase and the degree of crystallization is quite high with the absence of unwanted phases and the peak intensities obtained are very strong.



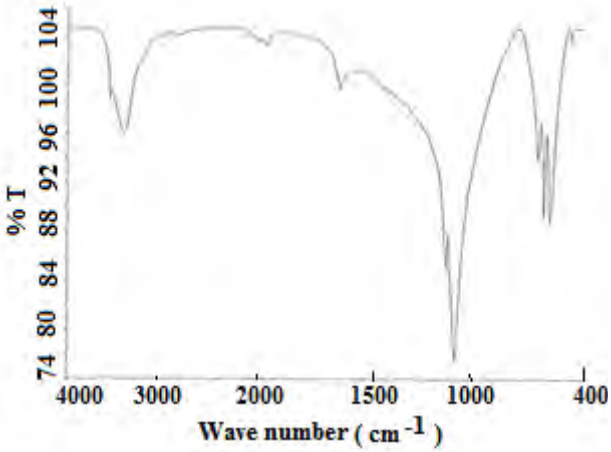
(a)



(b)

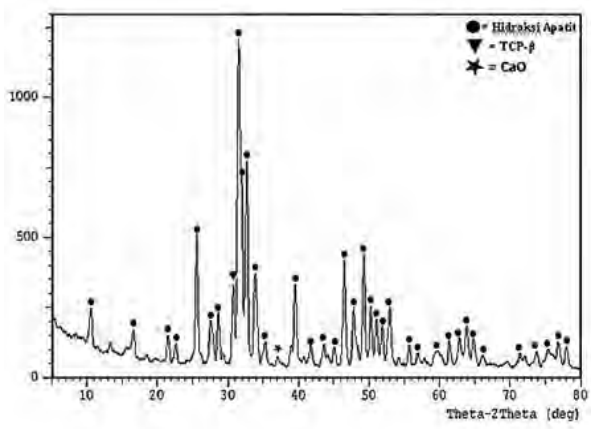


(c)

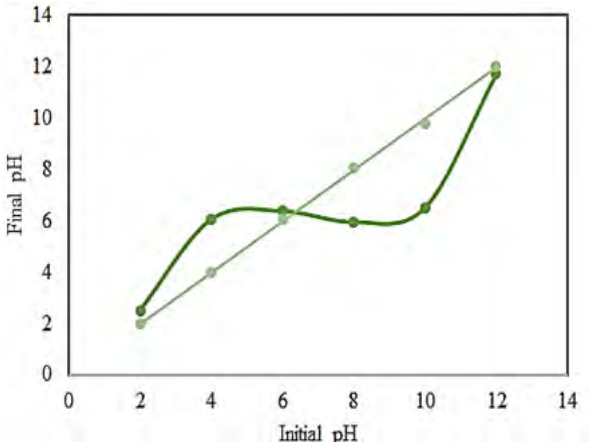


(d)

Fig. 1. (a) and (b) SEM images of HAP at various magnification levels (A: 1 µm, B: 10 µm), (c) EDX image and elemental composition of HAP, and (d) FTIR spectrum of HAP



(a)



(b)

Fig. 2. (a) XRD image of HAPand (b) pHPZC graph

3.2. Determination of pHpzc of HAP

The pHpzc signifies the pH where an adsorbent's surface carries a net neutral charge. This metric is crucial for interpreting electrostatic forces that govern interactions of the adsorbent and adsorbate at varying pH conditions. As depicted in Figure 2b, the pHpzc for HAP is 6.10. Below this pH, the surface of the adsorbent exhibits a positive charge, thereby enhancing its ability to attract

anions. Conversely, at pH levels exceeding the pHpzc, the surface acquires a negative charge, favoring the adsorption of cations [45]. This trend, where the surface charge transitions to negative above pH 6.10, aligns with the behavior observed in activated carbon, which also demonstrates a negative zeta potential under similar conditions.

3.3. Effect of pH on Tamoxifen Removal Efficiency

Five solutions with a concentration of 50 mg L^{-1} and pH values ranging from 2 to 10 were made in order to investigate the impact of pH on adsorption efficiency. Each sample was treated with 40 mg of weighed adsorbent. Following this procedure, the samples were kept in the mixer for three hours at a speed of 170 rpm and an ambient temperature of 25 ^{o}C. The HPLC system was used to evaluate the samples that were collected at the conclusion of the time. Figure 3a presents the findings. Figure 3a in this investigation shows that tamoxifen adsorption rose when solution pH rose to a value of 6. From pH 2 to pH 6, the elimination efficiency rose linearly, from 68.88% to 93.63%. The elimination efficiency then declined as the pH value dropped.

3.4. Effect of Adsorbent Dose on Tamoxifen Removal Efficiency

Six solutions with a concentration of 40 mg L^{-1} and pH 7 were prepared and the effect of the amount of adsorbent used on the efficiency of adsorption has been studied. Different amounts of adsorbents were weighed and added to each solution. The mixtures were shaken on a shaker at 170 rpm stirring speed and 25 °C ambient temperature for 120 min. Two milliliters of solution were drawn into the syringe and filtered into the HPLC vial using a syringe tip filter. Quantification analysis was performed on the HPLC system. Figure 3b shows the change in the adsorption efficiency of the amount of adsorbent with the amount of adsorbent.

Figure 3b illustrates how the clearance efficiency of tamoxifen rises as the dosage amount does. The efficiency in the study, which began with a dose of 20 mg, was 82.90%. At a dose of 40 mg, the removal efficiency increased to about 92.05% by increasing the adsorbent dose. The improvement in removal efficiency can be considered linear up to a dose of 40 mg. The efficiency was determined to be 94.48% in the 50 mg dose study and 95.45% in the 60 mg dose research. The elimination efficiency did not significantly alter after 50 mg, and the graph kept moving horizontally. At 60 mg, the adsorbent dosage achieved 95.45% efficiency. Lastly, a dose of 70 mg produced an efficiency of 95.55%. Although saturation was attained and the efficiency at 50 mg dose was 94.48%, Figure 2b shows that the ideal dose to use the least amount of adsorbent and attain an adsorption efficiency above 90% was 40 mg.

3.5. Effect of Stirring Time on Tamoxifen Removal Efficiency

30 mg of HAP adsorbent was added to tamoxifen solution at an initial concentration of 40 mg L^{-1} with pH 7 at 25 °C, and the mixture was shaken at 170 rpm for 240 minutes in order to examine the impact of stirring duration on adsorption efficiency. An injector was used to sample 1 mL of the solution at predetermined intervals, filter it via a vial equipped with an injector tip filter, and then analyze it in an HPLC system. Figure 3c shows how the adsorption effectiveness changes with stirring time.

Up to 30 minutes, the adsorption efficiency is shown to grow linearly with an increase in stirring time; beyond that, there is a minor increase in removal efficiency between 30 and 60 minutes, after which it becomes almost constant. The efficiency in the 30-minute contact time study was 65.63%. Contact time was 86.48% at 120 minutes, and equilibrium with a yield of 90.85% was established after 180 minutes. Consequently, 180 minutes was determined to be the ideal duration for the subsequent investigation and equilibrium adsorption kinetic modeling. As a consequence, 91.60% efficiency was attained after 240 minutes of equilibrium. These findings led to the conclusion that 180 minutes was the ideal mixing period.

3.6. Effect of Initial Tamoxifen Concentration on Removal Efficiency

Tests were performed at pH 7, temperature 25 °C, stirring period 180 min, adsorbent amount 40 mg in 50 mL, initial concentration 20-70 mg L^{-1}, and to examine the impact of initial concentration on the elimination of tamoxifen. Based on the findings, it was concluded that the starting

concentration affected the adsorption of tamoxifen. The impact of the baseline tamoxifen concentration on the removal level is given in Figure 3d.

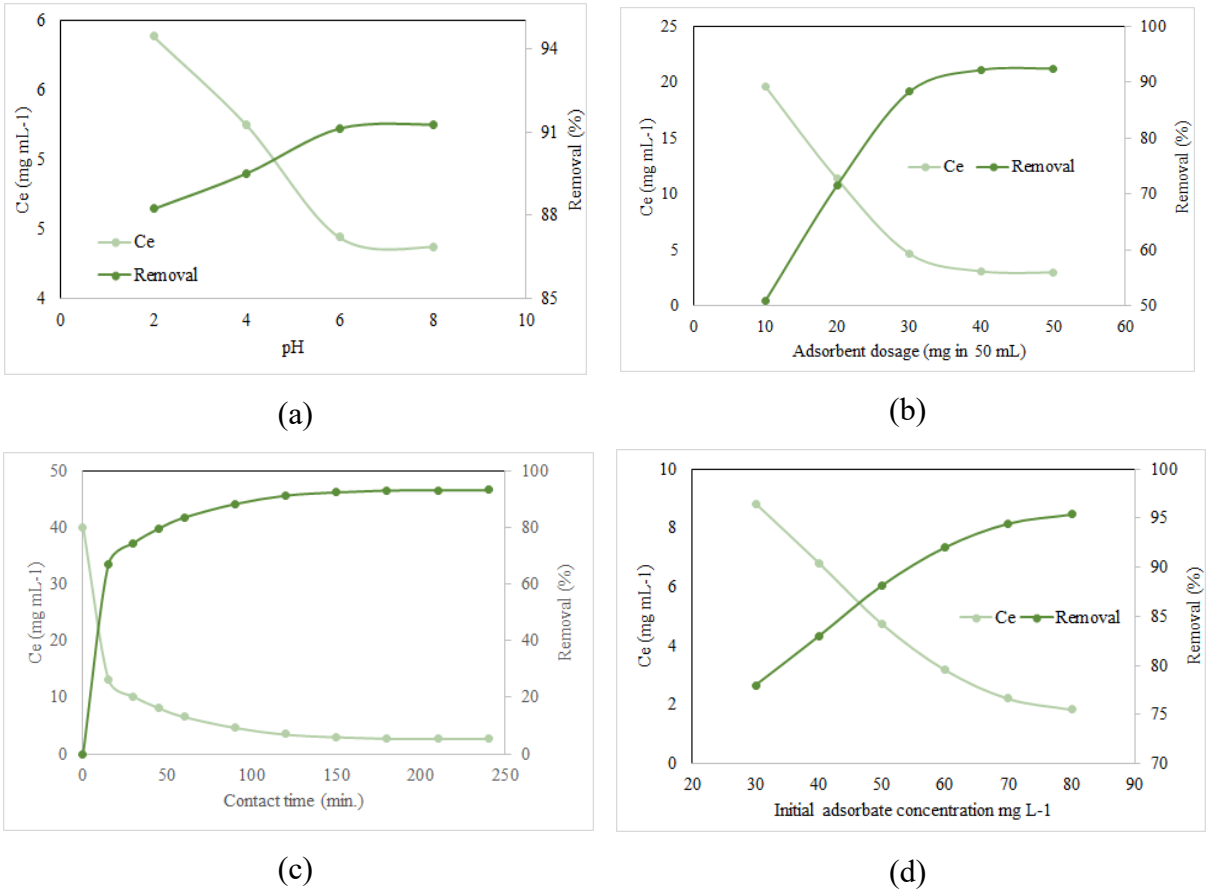


Fig. 3. (a) pH's impact on the effectiveness of tamoxifen elimination, (b) The impact of asorbent dose on the effectiveness of tamoxifen elimination, (c) The impact of stirring duration on the effectiveness of tamoxifen elimination, and (d) The impact of starting concentration on the effectiveness of tamoxifen elimination

The elimination of tamoxifen changes with increasing concentration, as seen in Figure 3D. When the concentration was 20 mg L^{-1}, the clearance efficiency was 82.90%; at 30 mg L^{-1}, it was 88.05%; and at 40 mg L^{-1}, it was 92.05%. In this concentration range, a notable improvement in removal efficiency was noted. At concentrations higher than the initial 40 mg L^{-1} concentration, no discernible improvement in removal efficiency was seen. The elimination efficiency was 94.48% at a concentration of 50 mg L^{-1}, 95.45% at 150 mg L^{-1}, and 95.55% at 70 mg L^{-1}. This is to be expected as tamoxifen retention by the adsorbent diminishes with saturation. These findings led to the conclusion that 40 mg L^{-1} was the ideal starting concentration.

3.7. Effect of Ambient Temperature on Tamoxifen Removal Efficiency

To determine temperature impact on the adsorption process, the temperature was 25 °C, the stirring time was 180 min, the pH of the tamoxifen solution with a volume of 50 mL and an initial concentration of 40 mg L^{-1} was adjusted to 7.00 and 40 mg of adsorbent was added and experiments were carried out. Experimental studies were carried out at 25 °C, 35 °C and 45 °C. The effect of temperature on tamoxifen removal efficiency is presented in Figure 4.

When Figure 4 is examined, it is observed that 90.85% efficiency was achieved at 25 °C. As the temperature increased, the efficiency gradually decreased, dropping to 78.98% at 45 °C. The findings reveal that an increase in temperature reduces adsorption efficiency, indicating that the process is exothermic. Furthermore, it was observed that an increase in temperature negatively affected diffusion within the adsorbent by lowering the solution viscosity. Compared with similar studies in the literature, it was found that the results of this study are consistent with the literature

and that the temperature increase similarly reduced efficiency. In light of all these evaluations, it is concluded that temperature variation affects the adsorption equilibrium capacity.

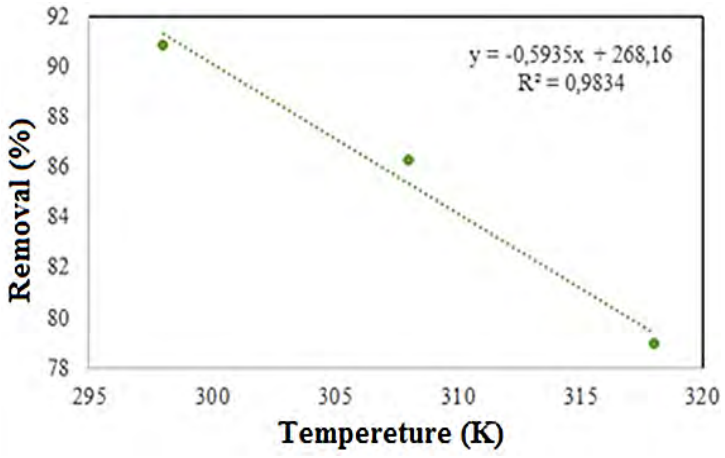


Fig. 4. Effect of temperature on tamoxifen removal efficiency

3.8. Adsorption Thermodynamics

The adsorption process was analyzed thermodynamically by calculating the enthalpy (ΔH), entropy (ΔS), Gibbs free energy change (ΔG), and equilibrium constant (K). Temperature was a critical factor in this study. Using 40 mg of adsorbent and a tamoxifen solution with a concentration of 40 mg L^{-1}, trials were conducted at three temperatures (25 °C, 35 °C, and 45 °C) to investigate the impact of temperature on tamoxifen adsorption. The equilibrium constants (K) were determined for each temperature, and the corresponding ΔG values were derived. The ΔH and ΔS values were calculated using the slope of the linear relationship between 1/T and lnK. The resulting thermodynamic parameters for tamoxifen adsorption are presented in Table 1.

Table 1. Thermodynamic parameters for tamoxifen adsorption

Temperature (K)	ΔG (J mol^{-1})	ΔH (J mol^{-1})	ΔS (J mol^{-1})
298	-70.225	-34.442	107
308	-71.298		
318	-72.371		

The standard free energy change (ΔG) was negative across all temperature conditions, confirming that the adsorption process is spontaneous [47]. As illustrated in Table 2, the free energy change of adsorption becomes less negative with increasing temperature, suggesting that adsorption is more efficient at lower temperatures. In tamoxifen adsorption, higher temperatures reduced the adsorption efficiency. The negative ΔH value indicates that the process is exothermic, and the positive ΔS value points to an increase in system disorder during adsorption.

3.9. Adsorption Isotherms

To elucidate the adsorption mechanism of tamoxifen onto HAP, the experimental results were subjected to analysis using both Langmuir and Freundlich isotherm models. The parameters derived from these models are compiled in Table 2. The accuracy of the models was assessed by their respective correlation coefficients (R^2), revealing that the Langmuir model demonstrated a superior fit to the experimental data. The Langmuir model, which posits a monolayer and uniform adsorption process, proved to be more representative of the observed data. Conversely, the Freundlich model exhibited a poorer fit, reflected in a diminished R^2 value. The strong correlation coefficient (R^2 = 0.9994) obtained from the Langmuir model substantiates the notion that tamoxifen adsorption on HAP occurs as a monolayer, with the adsorbent possessing evenly distributed active sites and consistent binding interactions [48]. The maximum theoretical

adsorption capacity (q_{max}) determined by the Langmuir model serves as a crucial metric for designing methods for efficient adsorption for specific contaminants, and it is closely aligned with the experimentally determined equilibrium capacity values (Table 2). While the Freundlich model yielded comparatively lower R^2 values, the factor affecting heterogeneity (n) exceeded 1, signifying a favorable adsorption process [49]. Nevertheless, due to the diminished agreement between the experimental data and the Freundlich model, a lower R^2 value resulted. Furthermore, the R_L constant, calculated to be 0.1930, indicated a strong adherence to this isotherm, as R_L values within the range of 0 to 1 suggest favorable adsorption. Additionally, the elevated K_L value, which signifies the affinity of tamoxifen for HAP, further reinforces the suitability of the Langmuir isotherm for the data [50].

Table 2. Important parameters of Langmuir and Freundlich isotherm models

Langmuir isotherm model data			Freundlich isotherm model data		
q_{max} (mg g^{-1})	K_L (mgL^{-1})	R^2	K_F (mg g^{-1})	n	R^2
43.48	41.818	0.9994	31.00	5.17	0.7117

3.10. Adsorption Kinetics

To understand the rate of the adsorption process, PFO and PSO kinetic models were employed. The associated set of kinetic parameters and their correlation coefficients are detailed in Table 3. The PFO model implies that adsorption is governed by diffusion through a boundary layer, whereas the PSO model indicates that the main process is chemical adsorption. [51]. Upon examination of the data in the table, it becomes clear that tamoxifen adsorption aligns closer with the PSO model. This is proven by the higher correlation coefficient (R^2 = 0.9997) obtained for the PSO model compared to the PFO model (R^2 = 0.8660). Additionally, the experimentally observed adsorption capacity (qe = 45.80 mg g^{-1}) closely matched the calculated capacity from the PSO model (qe = 47.62 mg g^{-1}), further validating the PSO model's applicability. Consequently, it can be confidently stated that chemical adsorption is the predominant mechanism for tamoxifen adsorption onto the adsorbent surface.

Table 3. Important parameters of the pseudo-first order (PFO) and pseudo-second order (PSO) models

Pseudo-first-order kinetic model data			Pseudo- second-order kinetic model data		
k1 (min -1)	qe (mg g-1)	R2	k2 (g mg-1 min-1)	qe (mg g-1)	R2
0.0282	33.00	0.8660	0.0022	47.62	0.9997

4. Discussion

The results of this study show that hydroxyapatite (HAP) produced by the Sol-gel method can be used as a successful adsorbent for the effective removal of tamoxifen from synthetic wastewater. The optimum conditions obtained (40 µg/mL initial concentration, 25 °C temperature, pH 7, 40 mg HAP dose per 50 mL solution, and 180 min contact time) provided a high efficiency of 90.85% for tamoxifen removal. The high agreement of the measurement values with the Langmuir isotherm model (R^2: 0.9994) indicates that adsorption occurs on monolayer and homogeneous surfaces. This suggests that the HAP surface has a monolayer structure capable of strong interactions with tamoxifen molecules. On the other hand, the fit of the pseudo-second-order kinetic model (R^2: 0.9997) indicates that chemical bonds are at the forefront in the adsorption process and HAP forms specific bonds with tamoxifen molecules. This finding suggests that the chemical properties of HAP may play an important role in the treatment of pharmaceutical compounds.

Thermodynamic analyses showed that the adsorption of tamoxifen on HAP is a by itself ($\Delta G < 0$), exothermic ($\Delta H < 0$) process characterized by entropy increase ($\Delta S > 0$). These results confirm that low temperatures increase tamoxifen removal and that the adsorption has an exothermic nature.

Since exothermic processes are more efficient at low temperatures, this result suggests that HAP can also reduce energy costs in the treatment of wastewater containing tamoxifen. This study makes an important contribution that tamoxifen should be removed with strong adsorbents such as HAPs due to its difficult biodegradation and high toxicity. Conventional methods often result in low efficiency and can produce toxic by-products. The high adsorption capacity, biocompatibility, low cost, and non-toxic nature of HAP make it an environmentally friendly option. In the studies available in the literature, tamoxifen is usually reported to be removed by adsorbents such as activated carbon; however, the high efficiency of HAP demonstrated in this study suggests that HAP may be an important alternative in this field.

In conclusion, the high performance of HAP produced by the Sol-Gel method in tamoxifen removal confirms that this adsorbent offers a potential solution for the removal of pharmaceutical impurities. This study demonstrated that HAP is an effective approach for the treatment of difficult-to-remove pharmaceutical contaminants such as tamoxifen, especially from the pharmaceutical industry and hospital wastewater. In the future, investigating the effects of HAP on other pharmaceutical compounds and environmental pollutants will provide important insights into how this method can be optimized in larger-scale applications. In this context, further studies testing the applicability of HAP in different wastewater matrices could further elucidate the potential of this adsorbent in industrial treatment processes.

References

[1] Lung I, Soran ML, Stegarescu A, Opris O, Gutoiu S, Leostean C, Lazar MD, Kacso I, Silipas TD, Porav AS. Evaluation of CNT-OOH/MnO2/Fe3O4 nanocomposite for ibuprofen and paracetamol removal from aqueous solutions. J Hazard Mater. 2021;403:123528. https://doi.org/10.1016/j.jhazmat.2020.123528

[2] Alothman ZA, Badjah AY, Alharbi OML, Ali I. Copper carboxymethyl cellulose nanoparticles for efficient removal of tetracycline antibiotics in water. Environ Sci Pollut Res Int. 2020;27(32):42960-42968. https://doi.org/10.1007/s11356-020-10189-1

[3] Zandipak R, Sobhanardakani S. Novel mesoporous Fe3O4/SiO2/CTAB-SiO2 as an effective adsorbent for the removal of amoxicillin and tetracycline from water. Clean Technol Environ Policy. 2018;20(4):871-885. https://doi.org/10.1007/s10098-018-1507-5

[4] Li J, Yu G, Pan L, Li C, You F, Xie S, Wang Y, Ma J, Shang X. Study of ciprofloxacin removal by biochar obtained from used tea leaves. J Environ Sci (China). 2018;73:20-30. https://doi.org/10.1016/j.jes.2017.12.024

[5] Sun L, Zha J, Spear AP, Wang Z. Tamoxifen effects on the early life stages and reproduction of Japanese medaka (Oryzias latipes). Environ Toxicol Pharmacol. 2007;24(1):23-29. https://doi.org/10.1016/j.etap.2007.01.003

[6] Roberts PH, Thomas KV. The occurrence of selected pharmaceuticals in wastewater effluent and surface waters of the lower Tyne catchment. Sci Total Environ. 2006;356:143-153. https://doi.org/10.1016/j.scitotenv.2005.04.031

[7] Besse JP, Latour JF, Garric J. Anticancer drugs in surface waters: what can we say about the occurrence and environmental significance of cytotoxic, cytostatic and endocrine therapy drugs? Environ Int. 2012;39(1):73-86. https://doi.org/10.1016/j.envint.2011.10.002

[8] Ashton D, Hilton M, Thomas KV. Investigating the environmental transport of human pharmaceuticals to streams in the United Kingdom. Sci Total Environ. 2004;333:167-184. https://doi.org/10.1016/j.scitotenv.2004.04.062

[9] Ferrando-Climent L, Cruz-Morató C, Marco-Urrea E, Vicent T, Sarrà M, Rodriguez-Mozaz S, Barceló D. Nonconventional biological treatment based on Trametes versicolor for the elimination of recalcitrant anticancer drugs in hospital wastewater. Chemosphere. 2015;136:9-19. https://doi.org/10.1016/j.chemosphere.2015.03.051

[10] Ferrando-Climent L, Rodriguez-Mozaz S, Barceló D. Development of a UPLC-MS/MS method for the determination of 10 anticancer drugs in hospital and urban wastewaters, and its application for the screening of human metabolites assisted by information-dependent acquisition tool (IDA) in sewage samples. Anal Bioanal Chem. 2013;405(19):5937-5952. https://doi.org/10.1007/s00216-013-6794-4

[11] Ferrando-Climent L, Rodriguez-Mozaz S, Barceló D. Incidence of anticancer drugs in an aquatic urban system: from hospital effluents through urban wastewater to the natural environment. Environ Pollut. 2014;193:216-23. https://doi.org/10.1016/j.envpol.2014.07.002

[12] Jean J, Perrodin Y, Pivot C, Trepo D, Perraud M, Droguet J, et al. Identification and prioritization of bioaccumulable pharmaceutical substances discharged in hospital effluents. J Environ Manage. 2012;103:113-21. https://doi.org/10.1016/j.jenvman.2012.03.005

[13] DellaGreca M, Iesce MR, Isidori M, Nardelli A, Previtera L, Rubino M. Phototransformation products of tamoxifen by sunlight in water. Toxicity of the drug and its derivatives on aquatic organisms. Chemosphere. 2007;67(10):1933-9. https://doi.org/10.1016/j.chemosphere.2006.12.001
[14] Chen Z, Park G, Herckes P, Westerhoff P. Physicochemical treatment of three chemotherapy drugs: irinotecan, tamoxifen, and cyclophosphamide. J Adv Oxid Technol. 2008;11(2):254-60. https://doi.org/10.1515/jaots-2008-0209
[15] Zhang J, Chang VWC, Giannis A, Wang JY. Removal of cytostatic drugs from the aquatic environment: a review. Sci Total Environ. 2013;445-6:281-98. https://doi.org/10.1016/j.scitotenv.2012.12.061
[16] Negreira N, Regueiro J, López de Alda M, Barceló D. Transformation of tamoxifen and its major metabolites during water chlorination: identification and in silico toxicity assessment of their disinfection byproducts. Water Res. 2015;85:199-207. https://doi.org/10.1016/j.watres.2015.08.036
[17] Ferrando-Climent L, Gonzalez-Olmos R, Anfruns A, Aymerich I, Corominas L, Barceló D, et al. Elimination study of the chemotherapy drug tamoxifen by different advanced oxidation processes: transformation products and toxicity assessment. Chemosphere. 2017;168:284-92. https://doi.org/10.1016/j.chemosphere.2016.10.057
[18] Zhou Y, He Y, He Y, Liu X, Xu B, Yu J, et al. Analyses of tetracycline adsorption on alkali-acid modified magnetic biochar: site energy distribution consideration. Sci Total Environ. 2019;650:2260-6. https://doi.org/10.1016/j.scitotenv.2018.09.393
[19] Shao S, Hu Y, Cheng J, Chen Y. Biodegradation mechanism of tetracycline (TEC) by strain Klebsiella sp. SQY5 as revealed through products analysis and genomics. Ecotoxicol Environ Saf. 2019;185:109676. https://doi.org/10.1016/j.ecoenv.2019.109676
[20] Li C, Lin H, Armutlulu A, Xie R, Zhang Y, Meng X. Hydroxylamine-assisted catalytic degradation of ciprofloxacin in ferrate/persulfate system. Chem Eng J. 2019;360:612-20. https://doi.org/10.1016/j.cej.2018.11.218
[21] Yi H, Lai C, Huo X, Qin L, Fu Y, Liu S, et al. H_2O_2-free photo-Fenton system for antibiotics degradation in water via the synergism of oxygen-enriched graphitic carbon nitride polymer and nano manganese ferrite. Environ Sci Nano. 2022;9:815-26. https://doi.org/10.1039/D1EN00869B
[22] Shoorangiz M, Nikoo MR, Salari M, Rakhshandehroo GR, Sadegh M. Optimized electro-Fenton process with sacrificial stainless steel anode for degradation/mineralization of ciprofloxacin. Process Saf Environ Prot. 2019;132:340-50. https://doi.org/10.1016/j.psep.2019.10.011
[23] Hassani A, Khataee A, Fathinia M, Karaca S. Photocatalytic ozonation of ciprofloxacin from aqueous solution using TiO_2/MMT nanocomposite: nonlinear modeling and optimization of the process via artificial neural network integrated genetic algorithm. Process Saf Environ Prot. 2018;116:365-76. https://doi.org/10.1016/j.psep.2018.03.013
[24] Palacio DA, Leiton LM, Urbano BF, Rivas BL. Tetracycline removal by polyelectrolyte copolymers in conjunction with ultrafiltration membranes through liquid-phase polymer-based retention. Environ Res. 2020;182:109014. https://doi.org/10.1016/j.envres.2019.109014
[25] Liu J, Zhou B, Zhang H, Ma J, Mu B, Zhang W. A novel biochar modified by chitosan-Fe/S for tetracycline adsorption and studies on-site energy distribution. Bioresour Technol. 2019;294:122152. https://doi.org/10.1016/j.biortech.2019.122152
[26] Dai Y, Zhang K, Meng X, Li J, Guan X, Sun Q, et al. New use for spent coffee ground as an adsorbent for tetracycline removal in water. Chemosphere. 2019;215:163-72. https://doi.org/10.1016/j.chemosphere.2018.09.150
[27] Li MF, Liu YG, Liu SB, Zeng GM, Hu XJ, Tan XF, et al. Performance of magnetic graphene oxide/diethylenetriamine penta acetic acid nanocomposite for the tetracycline and ciprofloxacin adsorption in single and binary systems. J Colloid Interface Sci. 2018;521:150-9. https://doi.org/10.1016/j.jcis.2018.03.003
[28] Chen L, Yuan T, Ni R, Yue Q, Gao B. Multivariate optimization of ciprofloxacin removal by polyvinylpyrrolidone destabilized NZVI/Cu bimetallic particles. Chem Eng J. 2019;365:183-92. https://doi.org/10.1016/j.cej.2019.02.051
[29] Selmi T, Sanchez-Sanchez A, Gadonneix P, Jagiello J, Seffen M, Sammouda H, et al. Tetracycline removal with activated carbons produced by hydrothermal carbonization of Agave americana fibers and mimosa tannin. Ind Crops Prod. 2018;115:146-57. https://doi.org/10.1016/j.indcrop.2018.02.005
[30] Dutta V, Singh P, Shandilya P, Sharma S, Raizada P, Saini AK, et al. Review on advances in photocatalytic water disinfection utilizing graphene and graphene derivatives-based nanocomposites. J Environ Chem Eng. 2019;7:103132. https://doi.org/10.1016/j.jece.2019.103132
[31] de Sousa DNR, Insa S, Mozeto AA, Petrovic M, Chaves TF, Fadini PS. Equilibrium and kinetic studies of the adsorption of antibiotics from aqueous solutions onto powdered zeolites. Chemosphere. 2018;205:137-46. https://doi.org/10.1016/j.chemosphere.2018.04.085

[32] Premarathna KSD, Rajapaksha AU, Adassoriya N, Sarkar B, Sirimuthu NMS, Cooray A, et al. Clay-biochar composites for sorptive removal of tetracycline antibiotic in aqueous media. J Environ Manage. 2019;238:315-22. https://doi.org/10.1016/j.jenvman.2019.02.069
[33] Beiranvand M, Farhadi S, Mohammadi A. Graphene oxide/hydroxyapatite/silver (rGO/HAP/Ag) nanocomposite: synthesis, characterization, catalytic and antibacterial activity. Int J Nano Dimens. 2019;10:180-94.
[34] Xu Y, An L, Chen L, Xu H, Zeng D, Wang G. Controlled hydrothermal synthesis of strontium-substituted hydroxyapatite nanorods and their application as a drug carrier for proteins. Adv Powder Technol. 2018;29:1042-8. https://doi.org/10.1016/j.apt.2018.01.008
[35] Jung KW, Lee SY, Choi JW, Lee YJ. A facile one-pot hydrothermal synthesis of hydroxyapatite/biochar nanocomposites: adsorption behavior and mechanisms for the removal of copper(II) from aqueous media. Chem Eng J. 2019;369:529-41. https://doi.org/10.1016/j.cej.2019.03.102
[36] Kumar GS, Karunakaran G, Girija EK, Kolesnikov E, Van Minh N, Gorshenkov MV, et al. Size and morphology-controlled synthesis of mesoporous hydroxyapatite nanocrystals by microwave-assisted hydrothermal method. Ceram Int. 2018;44:11257-64. https://doi.org/10.1016/j.ceramint.2018.03.170
[37] Syarif DG, Prajitno DH, Kurniawan A, Febrian MB, Lesmana R. Hydrothermally synthesis and characterization of HAP and Zr-doped HAP nanoparticles from bovine bone and zircon for photodynamic therapy. Process Appl Ceram. 2021;15:146-53. https://doi.org/10.2298/PAC2102146S
[38] Sadat-Shojai M, Khorasani M, Dinpanah-Khoshdargi MT. Synthesis methods for nanosized hydroxyapatite with diverse structures. Acta Biomater. 2013;9:7591-621. https://doi.org/10.1016/j.actbio.2013.04.012
[39] Monvisade P, Siriphannon P. Chitosan intercalated montmorillonite: Preparation, characterization and cationic dye adsorption. Appl Clay Sci. 2009;42:427-31. doi:10.1016/j.clay.2008.04.013. https://doi.org/10.1016/j.clay.2008.04.013
[40] Parolo ME, Savini MC, Vallés JM, Baschini MT, Avena MJ. Tetracycline adsorption on montmorillonite: pH and ionic strength effects. Appl Clay Sci. 2008;40:179-86. https://doi.org/10.1016/j.clay.2007.08.003
[41] Arora C, Kumar P, Soni S, Mittal J, Mittal A, Singh B. Efficient removal of malachite green dye from aqueous solution using Curcuma caesia based activated carbon. Desal Water Treat. 2020;195:341-52. https://doi.org/10.5004/dwt.2020.25897
[42] Balarak D, Azarpira H. Rice husk as a biosorbent for antibiotic metronidazole removal: isotherm studies and model validation. Int J ChemTech Res. 2016;9:566-73. https://doi.org/10.21786/bbrc/9.3/32
[43] Balarak D, Azarpira H, Mostafapour FK. Study of the adsorption mechanisms of cephalexin onto Azolla filiculoides. Pharm Chem. 2016;8:114-21.
[44] Rivera-Utrilla J, Gomez-Pacheco CV, Sonchez-Polo M, Lopez-Peoalver JJ. Tetracycline removal from water by adsorption/bioadsorption on activated carbons and sludge-derived adsorbents. Environ Manage. 2013;131:16-24. https://doi.org/10.1016/j.jenvman.2013.09.024
[45] Ji LL, Chen W, Duan L, Zhu DQ. Mechanisms for strong adsorption of tetracycline to carbon nanotubes: a comparative study using activated carbon and graphite as adsorbents. Environ Sci Technol. 2009;43:2322-7. https://doi.org/10.1021/es803268b
[46] Tang Y, Guo H, Xiao L, Yu S, Gao N, Wang Y. Synthesis of reduced graphene oxide/magnetite composites and investigation of their adsorption performance of fluoroquinolone antibiotics. Colloids Surf A. 2013;424:74-80. https://doi.org/10.1016/j.colsurfa.2013.02.030
[47] Abifarin JK, Obada DO, Dauda ET, Dodoo-Arhin D. Experimental data on the characterization of hydroxyapatite synthesized from biowastes. Data Brief. 2019;26:104485. https://doi.org/10.1016/j.dib.2019.104485
[48] Bow SJ, Liou SZC, Chen SY. Structural characterization of room-temperature synthesized nano-sized β-tricalcium phosphate. Biomaterials. 2004;25:3155-61. https://doi.org/10.1016/j.biomaterials.2003.10.046
[49] Kanan S, Ventura JMG, Lemos AF, Barba A, Ferreira JMF. Effect of sodium addition on the preparation of hydroxyapatites and biphasic ceramics. Ceram Int. 2008;34:7-13. https://doi.org/10.1016/j.ceramint.2006.07.007
[50] Manso-Silva MN, Langlet M, Jiménez C, Fernández M, Martínez-Duarta JM. Calcium phosphate coatings prepared by aerosol-gel. J Eur Ceram Soc. 2003;23: pp.243-246. https://doi.org/10.1016/S0955-2219(02)00187-5

Research on Engineering Structures & Materials
www.jresm.org

Research Article

Statistical modeling and optimization of recycled concrete properties enhanced with marble fines using response surface methodology

Tarek Djedid [*,1,4,a], Tahar Zerig [2,b], Messaoud Abbas [3,c], Mohamed Zohaïr Kaab [4,d], Mouloud Belachia [5,6,e]

[1]*LEVRES Laboratory, University of El Oued, 39000, Algeria*
[2]*Laboratory "LGCH", University 8 May 1945, Guelma, Algeria*
[3]*LIAP Laboratory, University of El Oued, PO Box 789, El Oued, Algeria*
[4]*Dept. of Hydraulic and Civil Eng., Faculty of Technology, University of El Oued, 39000, Algeria*
[5]*Dept. of Civil Eng. & Hydraulics, Faculty of Science and Technology, University 8 May 1945 Guelma, Algeria*
[6]*Laboratory LMGHU, University 20 August 1955 Skikda, Algeria*

Article Info

Article History:

Received 08 Mar 2025
Accepted 05 June 2025

Keywords:
Recycled aggregates concrete;
Marble powder fines;
Physical-mechanical characteristics;
Statistical relationships;
Central composite design

Abstract

The reuse of demolished concrete waste is a promising approach for conserving natural resources and protecting the environment. This study investigates the impact of incorporating 0%, 5%, 10%, 15%, and 20% marble fines into recycled aggregate concrete (RAC) using Central Composite Design (CCD) based on the response surface methodology (RSM). The study evaluates multiple physical and mechanical properties to identify the optimal marble fine content. Results show that recycled concrete with 20% marble fines (RC20) exhibits exceptional quality in terms of fineness modulus, enhancing fresh density and reducing slump in the fresh state. Additionally, 10% and 15% marble fines significantly enhance the mechanical properties of hardened RAC. Specifically, RC10 (10% marble fines) increases compressive strength by 13.79% and reduces capillary absorption by 46.75% compared to the control (RC0) after 60 days. The inclusion of 15% marble fines notably improves flexural strength at the same hydration period compared to other formulations. Polynomial correlations, with an R-squared value ≥ 0.98, were established to relate fresh concrete properties (density, slump) and hardened concrete characteristics (porosity, water absorption by immersion) following marble fine addition. The RSM-based CCD model validates an effective approach, yielding optimal compressive strength (35.9 MPa) and flexural strength (4.92 MPa) with a desirability coefficient of approximately 93%, demonstrating the potential of marble fines in enhancing RAC performance.

© 2025 MIM Research Group. All rights reserved.

1. Introduction

The protection of the environment and the conservation of natural resources have become significant socioeconomic concerns. Concrete is the second most widely used building material globally, after water. However, the construction industry faces the challenge of modifying its production and/or application techniques to adopt methods that are in line with sustainable development. In recent years, there has been a considerable increase in the number of constructions in the building sector, which has resulted in an ever-increasing need for raw materials. However, natural deposits of potentially exploitable aggregates are becoming more and

*Corresponding author: tarek-djedid@univ-eloued.dz
[a]orcid.org/0000-0002-1249-156X; [b]orcid.org/0000-0002-6713-4666; [c]orcid.org/0000-0002-7998-9020; [d]orcid.org/ 0000-0003-3572-2890; [e]orcid.org/0000-0001-8800-8119
DOI: http://dx.doi.org/10.17515/resm2025-731ma0308rs

more scarce. Thus, industrialists are facing increasing difficulties in supplying aggregates. Recycling allows for better resource management by recovering wastes and saving traditional natural aggregates. Its environmental and ecological impact is also conditioned by the limitation of deposition areas, the opening of quarries, and the exploitation of alluvial beds [1]. Recycling is further supported by regulations for the creation of new quarries, which are linked to futuristic visions for developing the recycling sector. Numerous experimental studies have demonstrated the feasibility of using cementitious materials based on recycled aggregates, with encouraging results.

Partial or total replacement of traditional aggregates with demolition aggregates leads to concretes with results inferior to ordinary concretes [1]. However, several studies indicate that the use of fines particles from concrete demolition in mortar production improves mechanical properties, and also demonstrates its practical effectiveness in mixing up to 15% fines into mortar formulation [2,3]. These studies also validate the substitution of fine aggregate fractions with a granulometry > 0.6 mm by those of demolition concrete in mortars [2,4]. Other research indicated that the presence of 20% of concrete demolition aggregates, as well as 15% mixed recycled aggregates extracted through demolition and construction waste in mortar showed a better performance [2,5,6]. The inclusion of recycled aggregates in concrete mixes results in a reduction in its mechanical properties versus ordinary concrete [7–10]. In their studies, Kachouh et al. [7,11] examined the impact of full incorporation of recycled concrete aggregates (RCA) on the compressive strength of concrete. Their results indicate that when RCA completely replaces the aggregates, the compressive strength reduces by about 24% compared to that obtained with natural aggregates. Kachouh et al. [7] and Corinaldesi [12] studied the effect of substituting natural fine aggregate with RCA fine aggregate on the mechanical behaviour of concrete. They found that a maximum replacement of 30% achieved the target compressive strength. However, when this replacement was carried out with RCA, the modulus of elasticity showed a reduction of 15% compared with concrete containing natural aggregates. Kachouh et al. [7] and Malešev et al. [13] examined the properties of fresh and hardened concrete using different percentages of RCA replacement (0%, 50% and 100%). The authors concluded that fresh concrete bulk density, wear resistance and elastic modulus decreased as the amount of RCA increased. Interestingly, when RCA obtained by grinding high-strength concrete was used, the compressive strength was not affected compared to concrete using natural aggregates. However, the characteristics of concrete made from RCA were influenced by the source of the RCA used [7,13,14]. Concrete produced with RCA from an unknown source had less compressive and tensile strength than concrete manufactured with RCA from a known source.

Today, the regression method RSM has been observed in the field of cementitious materials in civil engineering to predict and/or optimize their characteristics in the fresh and hardened states [15–20]. However, these methods have been little used in the field of materials recycling, especially recycled concrete, with only a few studies exploiting them [21,22]. The RSM method is a machine learning approach for predicting the impact of independent variables on results. This approach requires the use of a non-linear regression model to determine optimal conditions [23], while minimizing the number of experiments required [24].

This study aims to enhance the properties of concrete composed entirely of recycled materials by incorporating recycled concrete aggregates (RCA) mixed with varying proportions of recycled marble fines (0%, 5%, 10%, 15%, and 20%) as a substitute for recycled fine sand derived from demolished concrete. The impact of this substitution was investigated across multiple parameters, including slump, fresh density, compressive strength, flexural strength, porosity, absorption by immersion, capillary absorption, and the softening coefficient. Furthermore, polynomial regression models, derived from analysis of variance (ANOVA), were developed to correlate the physical performance of fresh and hardened concrete states and to predict the physical characteristics of recycled aggregate concrete (RAC) containing marble fines that have not already been performed. Response Surface Methodology (RSM) optimization was employed to estimate input parameters (percentage of marble fines and hydration duration) and output parameters (compressive and flexural strength).

2. Experimental Procedure

The diagram below illustrates the key stages in an experimental study to assess the properties of ecological concrete incorporating recycled aggregates and marble fines. It details the logical progression from material preparation to analysis using RSM methodology. Each step is represented to clarify the process of research and optimization of mechanical performance. (Fig. 1) presents the flowchart summarizing the production schedule and testing timeline for the different concrete studied.

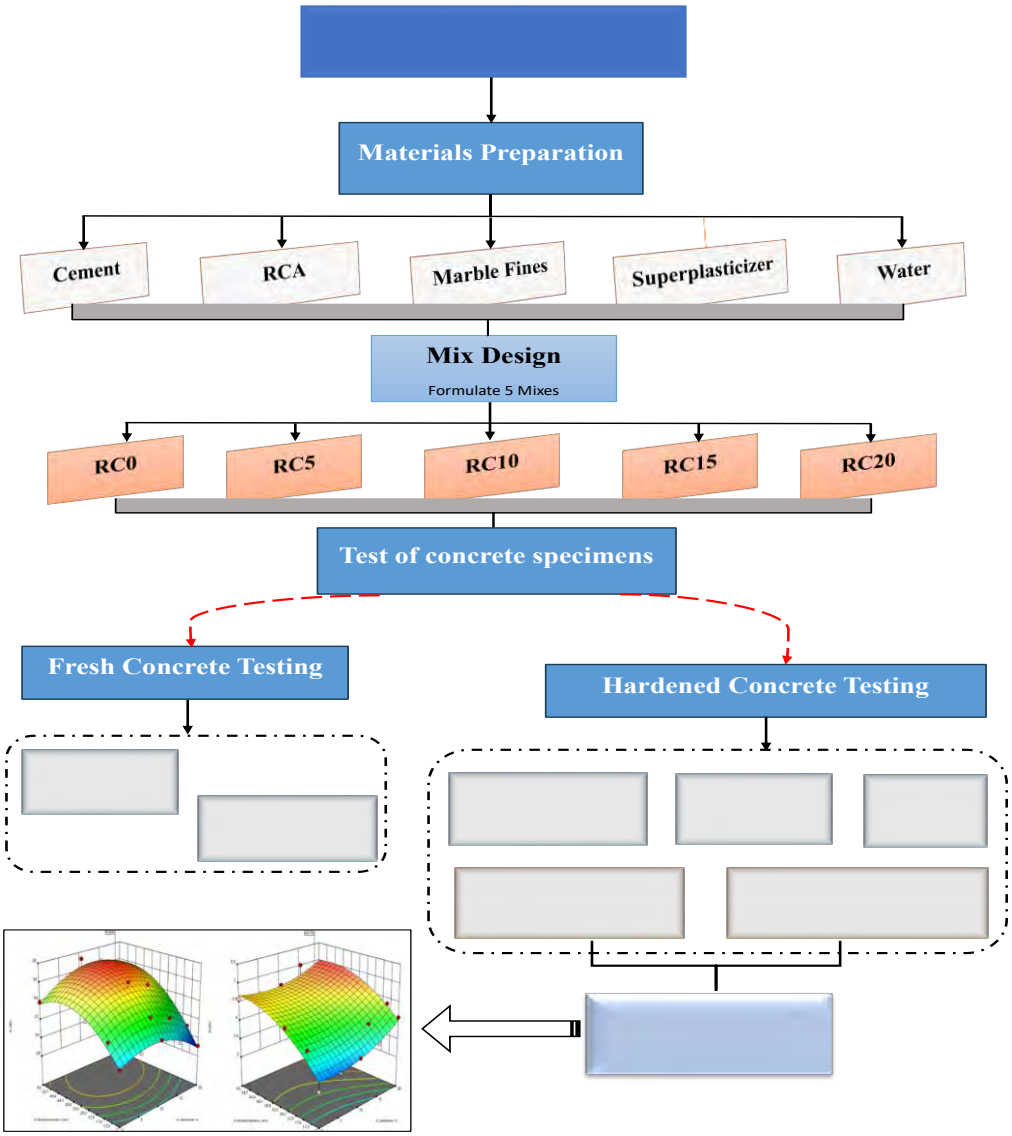


Fig. 1. Flowchart illustrating the research process

2.1. Cement

The type of cement used in this investigation is: CEM II/B-L 42.5N limestone Portland cement manufactured at the SPA BISKRIA CEMENT factory. Table 1 shows the chemical, mineralogical and physical-mechanical properties of this cement.

2.2. Adjuvant (Super Plasticizer)

The admixture used in this study is a light-brown, liquid superplasticizer with high water-reducing properties, enabling the production of high-quality concrete and mortar.

This admixture, marketed under the name MEDAFLOW 145 by GRANITEX, has a density of 1.065 ± 0.015. Its pH is between 5 and 6, its chloride content is less than 1g/L, and its dry extract is 30 ± 1.5%, in compliance with NF EN 934-2 [25] and NA 774 [26] standards. The manufacturer

authorizes a percentage of use ranging from 0.3% to 2.0% of cement weight, i.e., 0.33 to 1.8 liters per 100 kg of cement.

Table 1. Technological properties of cement powder

Chemical composition [% wt]				Bogue composition (%)	
SO_3	Cl^-	MgO	Loss on ignition	C_3S	C_3A
2.4 - 2.8	<0.05	< 3.5	7.5 - 9.5	58 - 66	5.1-7.2
Physical and mechanical properties					
Start of setting [min]				150-200	
End of setting [min]				220-290	
Cement paste consistency [%]				26.5- 28.4	
Hot expansion [mm]				0.0 - 1.0	
28-day compressive strength in [MPa]				42.5- 52.5	
2-day compressive strength in [MPa]				15-25	

2.3. Mixing Water

The water for manufacturing concrete mixes is tap water, which in principle is free from impurities. Its temperature is not controlled during mixing, although the concrete obtained has a temperature of around 20 ± 2°C. However, it complies with the specifications of standard NF P 18-303 [27].

2.4. Aggregates

The aggregates used were extracted from recycled demolished concrete and divided into three classes: sand 0/5 RS, gravel 5/10 and 10/16 RG as shown in Fig 2. The preparation and obtaining of granular classes are done by crushing, screening and sieving.

The granulometric distribution of demolition concrete aggregates with and without marble fines is presented in Fig 3. The chemical and physical-mechanical characteristics of the used aggregates are presented in Table 2 and Table 3 respectively. The fineness modulus values for demolished sand are 3.11, and sand samples graded RS 5%mf, RS 10%mf, RS 15%mf and RS 20%mf are: 2.96, 2.81, 2.65 and 2.50, respectively.

2.5. Marble Fines

The marble fines (m_f) used in this study, come from the marble factory of Chaabani, Bayadha [Algeria] in the form of granules and small pieces, which are ground manually. These properties are presented in Table 2 and Table 3 sequentially.

Table 2. Investigation of various aggregates using XRF spectroscopy

Materials	Chemical composition								
	SiO_2	Al_2O_3	Fe_2O_3	CaO	MgO	SO_3	K_2O	Na_2O	LOI
Marble Powder	0,88	0,37	0,13	51,69	0,94	0,07	0,02	0,09	42,98
Demolished Concrete	21,29	6,13	2,27	52,86	1,75	1,79	0,58	0,98	10,33

LOI: Loss on Ignition

2.6. Experimental detail

According to EN 12350-2 [28], the slump test consists of filling concrete into a truncated sheet metal mold. The concrete was placed in three layers packed with a steel rod of 16mm diameter with a rounded end, at a rate of 25 strokes per layer. The mold was then carefully lifted and the slump was measured. The density of fresh concrete was measured using a watertight and sufficiently rigid container as specified in EN 12350-6 [29]. The concrete was put into the container

and vibrated with a vibrating table, after appropriate levelling. The container and its contents must be weighed to determine the density, which can be obtained using the following Eq (1):

$$D = \frac{(M_2 - M_1)}{V} \quad (1)$$

Where, D - density of fresh concrete, expressed in [g/cm^3]; M_1 - mass of container in grams; M_2 - total mass of container, including concrete, in grams; V - container volume in cubic centimeters.

The compressive strength of the concrete tested was measured by evaluating the applied load leading to crushing by axial compression, in accordance with EN 12390-3 [30], using three 10x10x10 cm cubic specimens per formulation (Fig. 4). The bending test involves breaking a prismatic sample of dimensions 7 x 7 x 28 cm by subjecting it to a flexural moment (Fig. 4), while applying a load according to the advice of the standard NF EN 12390-5 [31]. During the test, the maximum load recorded is noted, and the bending strength is determined by performing the appropriate calculation. A capillary water absorption test was carried out in accordance with ASTM C 642 [32]. As a first step, to get complete drying, samples measuring 7 x 7 x 7 cm were placed in an oven at 70°C until they reached a constant mass such that Δm /day 0.1%. In the next step, all the external faces of the sample were waterproofed with paraffin, except for the face that is in direct contact with water. Then the dry mass was measured and this face was also placed in a basin of water 5 mm thick. The mass of each specimen was subsequently determined at the following times [10, 20, 30, 40, 50, 60, 70, 80, 90] min, 24 h, 48 h and 72 h. Then, for each measurement time t, the capillary absorption coefficient could be defined by the following Eq (2):

$$C_t = \frac{(M_t - M_0)}{A} \quad (2)$$

Where, Ct – absorption coefficient at time t [g/cm^2]; A – sample cross-sectional area [cm^2]; M_t – Mass at time t [g]; M_0 – initial sample mass [g].



Fig. 2. a) Demolished concrete, b) RG 10/16, c) RS 0/5 and d) RG 5/10

The water-accessible porosity test was conducted in accordance with ASTM C 642 [32]. Experimentation proceeds as follows: drying of the sample 10 × 10 × 10 cm in the oven at 70 °C during 24 hours, until a steady mass is reached, in order to evaporate all the water, this mass is noted M_{dry}. The sample was also immersed in water during a period which lasted 24 hours, after removal from the water, the sample was left in the open air for 5 hours, then subjected to weighing. M_{air}, another weighing process of the sample in water was also carried out (hydrostatic weighing) M_{water}. The porosity accessible to water is defined by Eq (3):

$$V_p = \frac{(M_{air} - M_{dry})}{(M_{air} - M_{water})} \; x\,100 \tag{3}$$

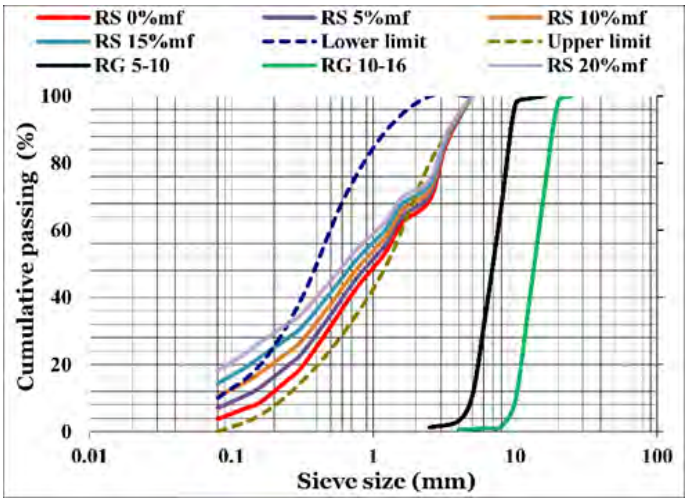


Fig. 3. Particle size analysis of studied aggregates

The test of absorption by immersion is carried out according to a simple method. The specimens of concrete 10 x 10 x 10 cm studied of 60 days of age are weighed after their passage in the oven at 70°C, from where they are withdrawn only after stabilization of their weight [i.e., M_{dry}]. Then they are completely immersed in water 20°C ± 5°C until saturation of the material, then withdrawn and weighed, [i.e., M_{sat}]. The water absorption capacity is expressed as follows Eq (4):

$$A\,\% = \frac{(M_{sat} - M_{dry})}{M_{dry}} \; x100 \tag{4}$$

The immersion absorption value is taken as the average of three specimens of each composition. The softening coefficient is defined as the ratio between the compressive strength of a water-saturated material (R_{sat}) and the compressive strength of the same material in a dry state (R_{dry}). The strengths R_{sat} and the R_{dry} are measured on 10 × 10 × 10 cm cubic specimens at 60 days of age. It is defined by the following Eq (5):

$$k_{sof} = \frac{R_{sat}}{R_{dry}} \tag{5}$$

Where, K_{sof} - softening coefficient; R_{sat} and R_{dry} [in MPa]



Fig. 4. Photographs of the cubic and prismatic samples

Table 3. Technical characteristics of the aggregates used and previous study results

Physical-mechanical characteristics	Results obtained				Results of previous studies			
	RS 0/5	RG		*mf*	RS	RG		
d/D	0/5	,5/10	10/16		0/5	6/20	5/12.5	12.5/20
Absolute density g/cm³	2.38	2.50	2.48	2.70	2.56 [33]	2.28 [33]	1.98 [33]	
Apparent density g/cm³	1.35	1.3**0**	2.29		1.04 [33]	1.14 [33]	1.09 [33]	
Fineness modulus MF	3.11				2.40 [34]			
Flattening coefficient %		6.34					10.10 [34]	
Superficial cleanliness		92.18					97.7[34]	99.00[34]
Sand equivalent (visual) %.	87.27				65.40 [34]			
Sand equivalent (plunger)	88.54							
VB: Methylene Blue	0.17				0.17 [34]			
Water content %	2.56	1.50		1.55	3.13 [34]		0.85 [19]	0.90 [34]
Water Absorption Coefficient %		3.76		0.15	7.09 [34]	11 [35]	6.25[34]	5.36 [34]
Void Index %	80.80							
Porosity %	44.45			0.35				
Compactness %	55.55			99.65				
Los Angeles		34.10				26.00 [1]	38.88[34]	36.20 [34]
Micro-Deval		33.65				31.00 [1]	36.50[34]	38.60 [34]

2.7. Concrete Mix Proportions

Concrete mix design was carried out using the Dreux-Gorisse method [36]. The mixes have been designed to achieve a class C25/30 target strength at 28 days of age in accordance with European standard EN 206-1 [37], and they were produced using a W/C ratio of 0.62 and including a 2% superplasticizer. Five different concrete mixes were formulated and kept after demolding in potable water until the day of crushing, to assess the effect of containing marble fines in various RAC formulations [RC0, RC5, RC10, RC15, and RC20] on the physical and mechanical behavior of eco-concrete with marble fines. The aggregates used in this study were not pre-treated. Table 4 provides detailed information on the mixing proportions for the different concretes produced. Ratings used:

- RC0: 100% recycled concrete aggregate, 0% marble fines;
- RC5: Aggregate concrete 95% RS, 100% RG and 5% marble fines;
- RC10: Aggregate concrete 90% RS, 100% RG and 10% marble fines;
- RC15: Aggregate concrete 85% RS, 100% RG and 15% marble fines;
- RC20: Aggregate concrete 80% RS, 100% RG and 20% marble fines.

Table 4. Proportions of the mixture of different concretes in kg/m³

Designation	Proportions [kg/m³]				
	RC0	RC5	RC10	RC15	RC20
Cement	350	350	350	350	350
Marble fines	0.000	37.065	74.130	111.195	148.260
RS 0/5	741.300	704.235	667.170	630.105	593.040
RG 5/10	338.550	338.550	338.550	338.550	338.550
RG 10/16	570.920	570.920	570.920	570.920	570.920
Mixing water	216.660	216.660	216.660	216.660	216.660
Water/cement ratio [W/C]	0.62	0.62	0.62	0.62	0.62
Super plasticizer	7.00	7.00	7.00	7.00	7.00
Theoretical Density [kg/m³]	2224.43	2224.43	2224.43	2224.43	2224.43

2.8. Mathematical Models Using RSM Methodology

Surface Response Methodology (RSM) is an approach that aims to investigate the relationships between independent variables (input variables) and observed results (output responses) using mathematical and statistical techniques [38]. In this study, the Central Composite Design (CCD) was used to analyze data relating to eco-composites composed of eco-concretes containing marble fines as a partial replacement for recycled sand. Design Expert 13 software was used to implement this design, which comprises 2 factors and 2 responses. A series of 20 experiments was carried out to optimize the compressive and flexural strength values. For the design of a CCD with two extreme levels of factors (+1 and -1), the complete factorial design is represented by 2^k, while the axial points are represented by 2k, where C represents the central points. The number of repetitions of each experiment, carried out to reduce experimental error, is denoted by *n*. The total number of repetitions of the experiment can be calculated as follows Eq (6).

$$N = 2^K + 2K + nC \tag{6}$$

The fundamental principle of Response Surface Methodology (RSM) is to develop regression models to assess the correlations between independent variables and output variables, taking into account the different levels of these variables. In this approach, a second-order polynomial is used to model the relationships between the variables Eq (7).

$$Y = \beta_0 + \sum_{1}^{k} \beta_i X_i + \sum_{1}^{k} \beta_{ij} X_i X_j + \sum_{1}^{k} \beta_{ii} X_i^2 + E \tag{7}$$

β_0, β_i, β_{ii}, and β_{ij} are the model coefficients for the intercept, linear, quadratic, and interaction terms, respectively, and X_i, and X_j variables.

Table 5. Coding and levels for CCD model by RSM

Factors	Levels			
	Coded	Min (-1)	Medium (0)	Max (+1)
Marble fines (%)	A	0	10	20
Hydration duration (days)	B	7	28	60

Table 6. Design properties by RSM

		Input factors		Outputs	
Runs	Code	Marble fines (%)	Hydration duration (days)	Compressive strength (MPa)	Flexural strength (MPa)
1	RC_0	0	7	30.200±1.687	2.820±0.103
2	RC_5	5	7	30.133±1.040	3.290±0.102
3	RC_{10}	10	7	33.867±2.623	3.257±0.554
4	RC_{15}	15	7	28.067±2.344	3.456±0.091
5	RC_{20}	20	7	30.250±1.098	4.216±0.026
6	RC_0	0	14	33.650±0.950	4.450±0.230
7	RC_5	5	14	31.283±0.610	3.487±0.425
8	RC_{10}	10	14	33.963±0.491	3.858±0.351
9	RC_{15}	15	14	31.063±2.054	4.039±0.021
10	RC_{20}	20	14	33.143±2.236	4.417±0.051
11	RC_0	0	28	34.550±2.450	4.500±0.180
12	RC_5	5	28	33.867±2.050	3.827±0.301
13	RC_{10}	10	28	39.100±1.283	3.948±0.099
14	RC_{15}	15	28	35.000±2.639	4.133±0.527
15	RC_{20}	20	28	31.200±2.218	4.593±0.640
16	RC_0	0	60	34.067±0.170	4.220±0.397
17	RC_5	5	60	30.333±2.185	4.447±0.340

18	RC_{10}	10	60	38.767±1.517	4.678±0.225
19	RC_{15}	15	60	38.633±2.288	6.019±0.186
20	RC_{20}	20	60	34.500±0.990	4.186±0.261

Table 5 shows the parameters and their specific percentage levels for marble fines (A) and hydration duration (B) used in the experimental design. The different levels of the factors, in the Design of Experiment methodology, are represented by the codes (−1) and (+1), which correspond respectively to the minimum and maximum values centered around a mean value (0). The aim of the Response Surface Methodology (RSM) method is to propose regression models to assess the impact of factors on compressive and flexural strengths values of eco-concrete. To carry out this study, 20 experiments were carried out. Table 6 presents the detailed experimental design, with the different variables used and their respective levels during the tests. It also shows the experimental results for compressive strength and flexural strength.

3. Experimental Results Analysis and Discussion

3.1. Fresh Concrete Properties

Figure 5 illustrates the results showing how the incorporation rate of marble fines affects the workability of Recycled Aggregate Concrete (RAC) made from demolished aggregates. The mixes are prepared using a constant water-to-cement (W/C) ratio and a percentage of superplasticizer equal to 0.62% and 2%, respectively. The increase in slump is strongly influenced by the presence of marble fines and the reduction in the amount of demolition sand. It is crucial to note that the rate of slump increases in proportion to the percentage of marble fines added. At the same time, the reduction in demolition sand content also contributes to this increase. This relationship is explained by the lower absorption capacity of marble fines compared to recycled concrete aggregates [39,40]. When making concrete with recycled aggregates, a certain difficulty in placing them compared to ordinary concrete has been noted. Indeed, this relationship is attributable to the high-water absorption and high porosity of these aggregates.

Figure 5 also illustrates the variation in concrete density as a function of the rate of incorporation of marble fines in combination with recycled concrete aggregates. It is observed that density increases in proportion to the amount of marble fines present. In fact, marble fines have a higher absolute density than recycled sand [39]. The densities of RC5, RC10, RC15, and RC20 are respectively 1.41%, 3.77%, 4.24%, and 5.18% higher than RC0, then the values of fineness modulus of recycled concretes adjusted with marble fines are advantageous than that of RC0 (as seen in Table 3).

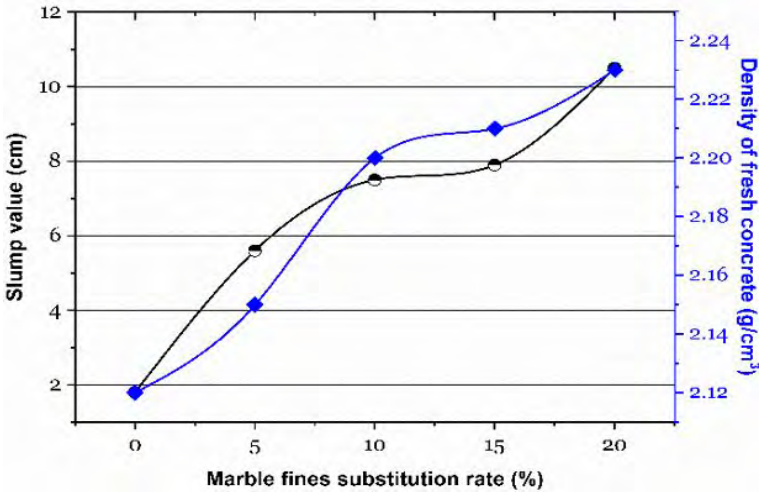


Fig. 5. Effect of marble fines incorporation rate on fresh concrete's workability and density

Finally, the particles of fines fill the voids and improve the density in the fresh state. In this context, it should be noted that RC20 concrete with a fineness modulus of 2.5 has resulted in a decrease in

void volume. Indeed, a good arrangement of the solid grains has been achieved, which finally increases the fresh density [41].

3.2. Hardened State Concrete Properties

3.2.1. Compressive Strength

The compressive strength of each mix was evaluated using three 10×10×10 cm cubic samples at 7, 14, 28, and 60 days after concrete preparation Fig. 6a. The evolution of this strength was determined according to the number of fine marbles, as shown in Fig. 7.

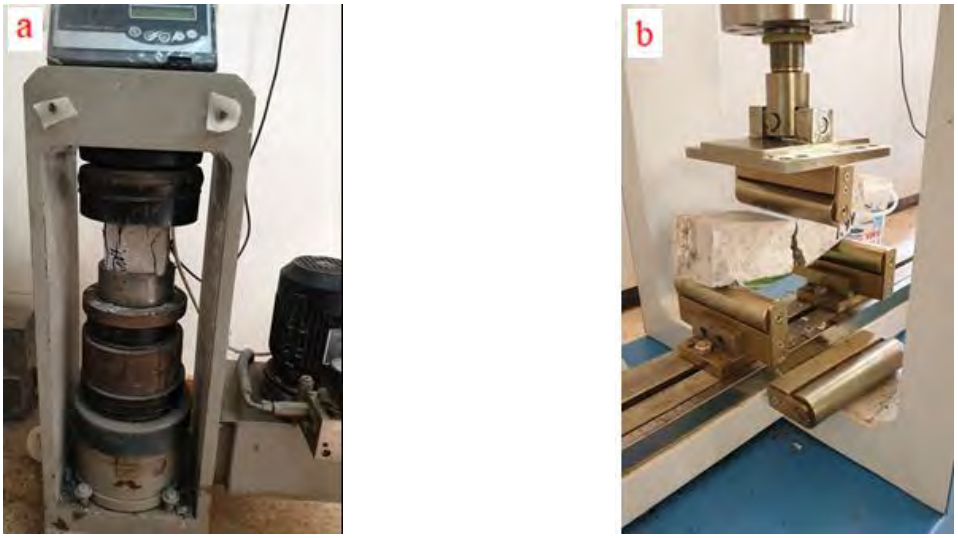


Fig. 6. (a) Compressive strength testing of concrete, (b) Flexural strength testing of concrete

It has been observed that the strength increases gradually over time, reaching its maximum at around 10% and 15% marble fines. The last two percentages increased respectively by 13.17%, 1.30% at 28 days, and 13.79%, 13.38% at 60 days. On the other hand, concrete made with demolition aggregates crushed with 5% and 20% marble fines exhibited lower compressive strength than RC0. This was confirmed by Sadhouari et al [42], who stated that concretes made with crushed sands of different fines content of the order of 0%, 5%, 10%, 15%, and 20% pass through a minimum of 10% to 15% fines with respect to the assessment of occluded air.

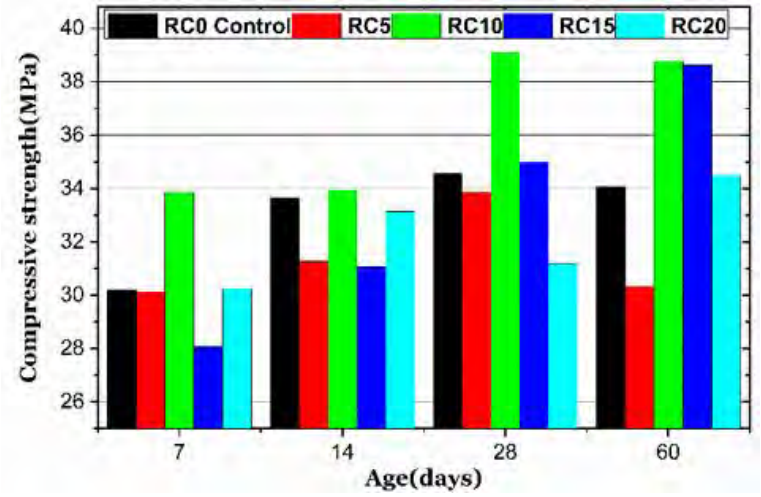


Fig. 7. Compressive strength of different RAC formulations and marble fines

Researchers Berredjem et al [40] found a negative influence of the use of recycled concrete aggregates on the mechanical properties of concrete, such as compressive strength and splitting tensile strength. However, it is important to note that compressive strength is maintained when using class C 25/30. According to Ghorbani et al [43], as the quantity of recycled concrete waste used as a partial substitute for traditional aggregates increases, concrete strength decreases.

Similarly, Kirthika and Singh [44] reported that the optimum rate of river sand substitution by recycled fine aggregate (RFA) was 30%. They observed that at 56 days, concrete made with 30% RFA showed an increase of around 11% in compressive strength, 3.8% in tensile strength, 9.7% in flexural strength, and 4% in modulus of elasticity by comparison with concrete made with river sand. The probable improvement in the mechanical properties of RFA30 is attributable to the high-density structure and lower porosity of RFA-based concrete. In the same way, Benabed et al [45] concluded that when the fines percentage exceeds 15% [in our case RC20 of 18.27%] the strength drops.

3.2.2. Flexural Strength

The Flexural Strength testing was conducted in compliance with NF EN 12390-5 [31]. The average flexural strength of every mixture was evaluated using three prismatic samples measuring 7× 7×28 cm for 7, 14, 28, and 60 days (fig 6b). Fig. 8 shows the variation in flexural strength as a function of marble fines content. The pattern is similar to that observed for compressive strength (Fig.7) Under specified NF EN 206-1 [37], flexural strength values obtained at 60 days for all concrete mixes are significantly higher compared to the flexural strength of RC0 reference concrete for class C 25/30 concretes.

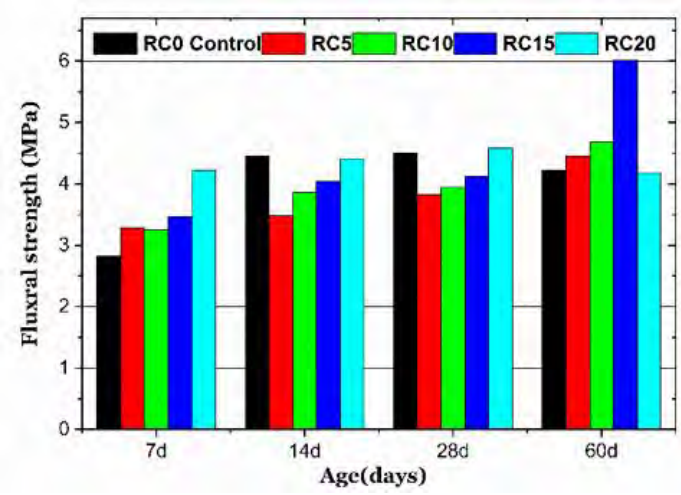


Fig. 8. Flexural strength of different RAC formulations and marble fines

Flexural strength trends are visible up to the final maturity date (60 days), which proves the effectiveness of the existence of marble fines in this type of concrete, except for RC20, which presented a loss of 8.93% at 60 days compared to the 28 days value. It was also found that the values of the maximum breaking force applied in this test are 5.10 KN and 6.55 KN obtained in RC10 and RC15 concrete, respectively, at 60 days. The flexural strength increases during this investigation in all the concretes studied. For the 0% marble fines RC0 concrete, the flexural strength starts with 2.82 MPa at 7 days and reaches the order of 4.50 MPa after 28 days. in RC20 concrete, the flexural strength starts with 4.22 MPa at 7 days and remains almost the same at 28 days. Finally, the optimal substitution rate of marble fines is 10% and 15%. Therefore, we can deduce that the bending strength of concrete made from recycled aggregates and marble fines has been evolving slightly with time. It can be concluded, that the main factors affecting mechanical strength are: cement hydration, fines quality, and relative humidity of the storage environment. This finding was confirmed by Kirthika, and Singh [44].

3.2.3. Capillary Water Absorption Test

Water absorption coefficient is an important predictor of concrete durability. To enable a comparison of the water absorption of samples based on the capillary action of water, it was decided to carry out a capillary water absorption analysis, and to identify the influence of marble fines in the composition based on Recycled Concrete Aggregates (RCA) to the studied mixtures. The kinetics of absorption was studied under normal conditions of laboratory for all types of concretes at 60 days. The results indicated that capillary water absorption was affected by the percentage substitution of marble fines and recycled aggregates of different RAC types, as illustrated in Fig. 9.

In this context, the order of the capillary absorption curves does not necessarily follow the increase in the percentage of marble fines. An optimum level of around 10% effectively clogs the interstitial pores, while limiting the circulation of water inside the specimens due to physical and chemical changes in the concrete matrix [46]. However, above 15%, excessive absorption is observed. This is because the marble fines begin to replace the demolition sand grains, altering the structure of the recycled concrete that the fines were intended to improve [47]. Absorption values showed an increase in all mixtures as time progressed. RC5 and RC10 concrete showed a decrease of 23.38% and 46.75% compared to RC0. This observation is in line with the results reported by Bertrandy and Coquillat [48], who stated that for plastic consistency, the optimum filler content seems to be between 8% and 12% in the crushed sand [in the present study the RC10 fines is about 10.57 %]. Furthermore, Benabed et al [45], concluded that when the percentage of fines exceeds 15% [in this study RC20 of 18.27%] the strength drops. The reason is that the quantity of cement paste is insufficient to envelop all the fine aggregate particles [41]. Other researchers have reported that recycled concrete absorbs more water than concrete containing siliceous aggregates. Olorunsogo et al [49] reported that concrete made from fully recycled aggregates absorbed around 39% more water than concrete made from ordinary aggregates after drying for 28 days.

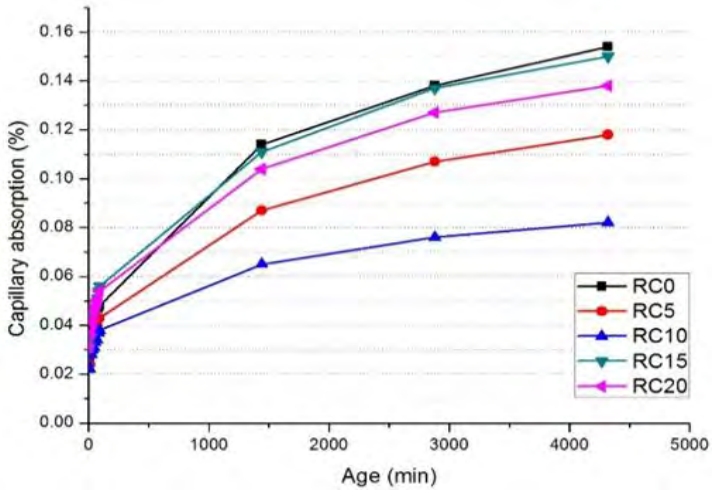


Fig. 9. Capillary water absorption values at 60 days of recycled demolition concrete with and without marble fines as a function of time

3.2.4. Porosity Test and Immersion Water Absorption

Water accessible porosity and water absorption by immersion are two major indicators of the durability of concrete. Indeed, these parameters characterize the ability of the material to let aggressive agents penetrate and circulate, either in liquid or in gas phase. From (Fig. 10) it was found that the porosity of different formulations varied similarly to the absorption by immersion. RC0 has a high porosity compared to RC5, RC10, RC15, and RC20. The RC20 and RC15 concrete samples showed a reduction of 24.47% and 20.88%, successively, compared to the RC0 at 60 days. With regard to water absorption by immersion, the RC20, RC15, and RC10 concretes had percentages of 21.24%, 18.93%, and 16.33%, respectively, which are lower than the RC0 at the last deadline. RC20 concrete has obtained the minimum percentage of porosity and absorption by immersion compared to RC10 and RC15. Its compressive strength is decreased compared to RC10 and RC15 due to the reduced percentage of sand particles in the RC20 sample. These grains, characterized by their angular shapes and rough surfaces, could increase concrete strength by promoting better adhesion between particles [50,51]. It can be concluded that porosity decreases with increasing fines concentration. There-fore, it was found that marble fines clog the pores and provide a good interface between aggregate and paste. In addition, the RC0 reference concrete has acquired high porosity and absorption by immersion, due to the high content of RCA particles, which are characterized by the old cement paste with high porosity [40,43,44]. Omary et al. [52] demonstrated, using the SEM technique, a high-quality interface between the old paste enveloping the natural aggregates present in RA and the new paste. Subsequently, microcracks were detected in the ancient cement paste, probably caused by the process of RA crushing

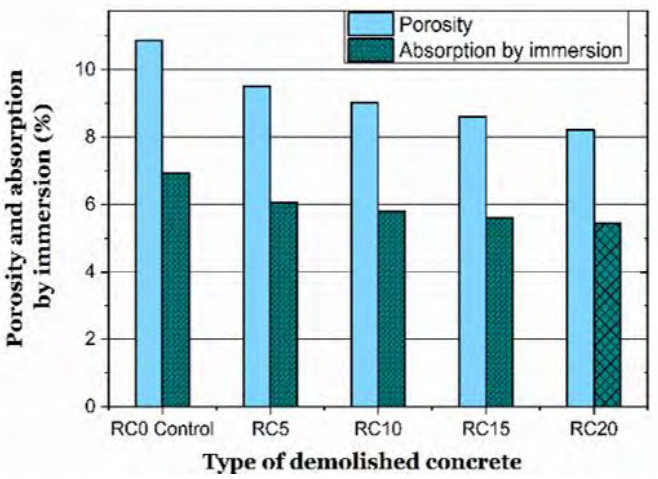


Fig. 10. Variation of porosity and water absorption by immersion as a function of marble fines percentage included in the RAC at 60 days

3.2.5. Softening Coefficient

The values presented in Fig. 11 show that all concrete formulations exhibit a softening coefficient exceeding 0.8. This finding indicates that all the studied samples are resistant to moisture, especially RC10 and RC15. For materials with a softening coefficient equal to or greater than 0.8 are considered to be water resistant especially in areas where moisture is a constant factor [53]. The obtained results for RC10 are consistent with the results of compressive strength and capillary water absorption. This proves how much the incorporation of 10% marble fines has reduced the maximum voids, and offered a better grain arrangement and interface between the grains and the cement paste.

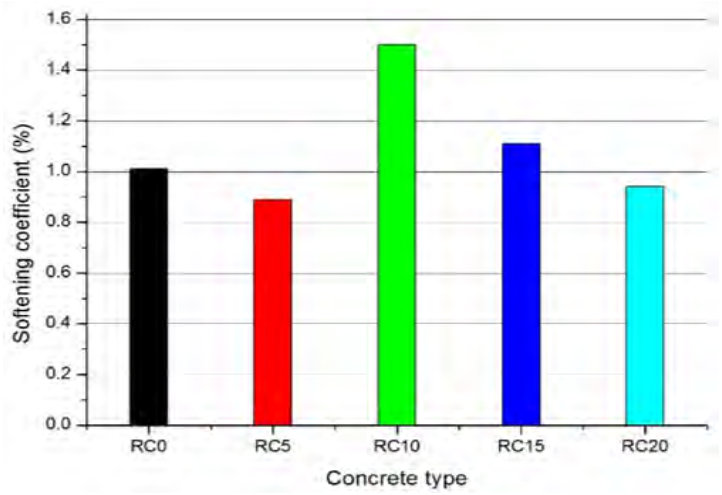


Fig. 11. Softening coefficient at 60 days

Fig. 12 illustrates the condition of cubic concrete specimens (10 × 10 × 10 cm), both dried and saturated, subjected to tests at 60 days to evaluate the softening coefficient, a key indicator of mechanical performance and durability. The dried specimens were tested to determine their compressive strength (R_{dry}), revealing significant cracking and fragmentation, indicative of failure under load. The water-saturated specimens (R_{sat}) exhibited deformations accompanied by scattered debris, highlighting the influence of moisture on compressive strength. The softening coefficient (K_{sof}) was calculated using Eq (5) by comparing the R_{dry} and R_{sat} values to assess the material's durability under varying moisture conditions. These results are critical for applications in water-exposed environments, ensuring long-term structural reliability.



Fig. 12. Specimens after testing for different formulations

3.3. Polynomial Regressions Generated Under the Effect of FM Variation in Concrete Based on Demolished Aggregates and Marble Fines

Several researchers have studied the Recycled Aggregate Concrete (RAC) adjusted with marble fines to find approximate relationships, which have allowed elaborating pseudo-exact expectations of some factors characterizing fresh and hardened concrete properties. The aim is to translate the relationships between the various factors into mathematical equations capable of predicting the RAC's physical-mechanical behavior. It was observed, in the first instance, that when increasing the fines content substituted with the fine aggregate of the fully demolished concrete, the fineness modulus decreases and consequently the fresh density and slump will also be increased [54]. For this purpose, two satisfactory relationships were deduced from the ANOVA analysis of variance, establishing two polynomial correlations between the density and slump of the different formulations as a function of the variation in fineness modulus. The first relationship is characterized by a second-degree equation, as illustrated in Fig. 13, and a correlation coefficient R^2 of 0.953. In addition, a second polynomial relationship of third order is shown in the same graph, matching the slump and the fineness modulus of R^2 equal to 0.984.

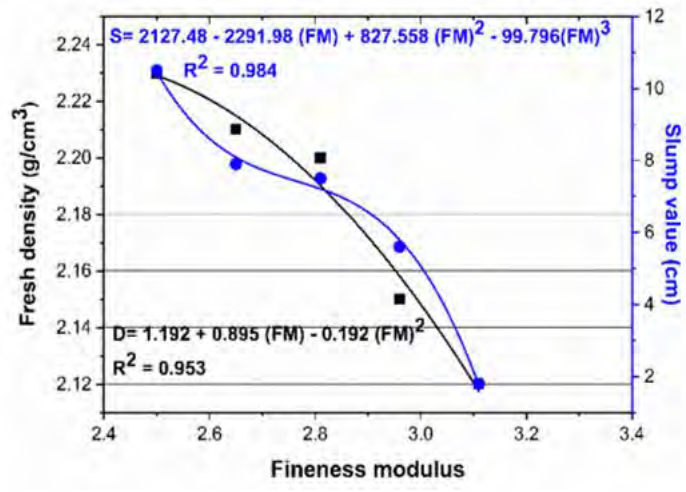


Fig. 13. Relationship between fresh density, slump and fineness modulus of RAC with and without marble fines

Therefore, it can be concluded that when the FM (Fineness Modulus) tends to half the range of the preferred sand of (2.2 – 2.8), the manufactured mix has obtained better fresh state properties of RAC with marble fines. Fig. 14 clearly shows another relationship deduced from the previous results (from Fig. 13) describing a high dependence of a third order linear regression and R^2 equal to 0.999. This approach is likely to be strongly supported in the case where the RAC is modified with a less absorbent material than the demolition RA.

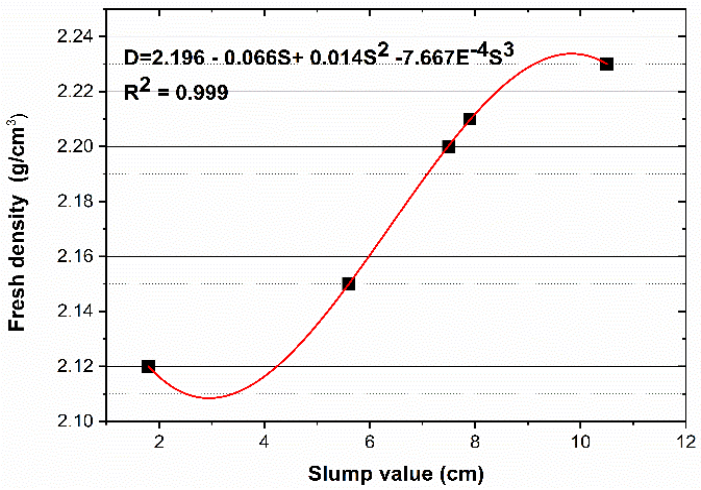


Fig. 14. Relationship between fresh density and slump of RAC with and without marble fines

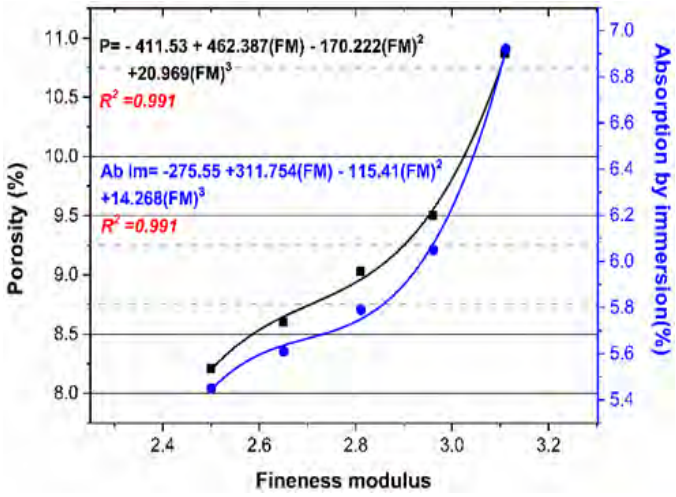


Fig. 15. Relationship between porosity, absorption by immersion and fineness modulus of RAC with and without marble fines

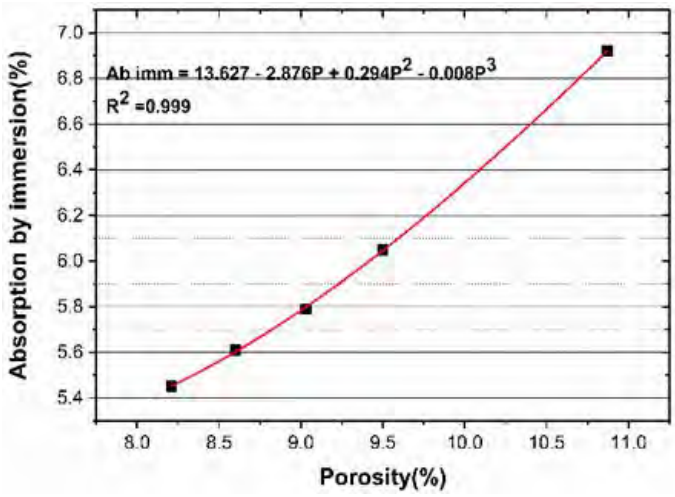


Fig. 16. Relationship between absorption by immersion and porosity of RAC with and without marble fines

Secondly, and concerning the two indicators of liquid transfer (porosity and water absorption by immersion), it was shown that when starting to replace the fine aggregates of the RS with marble fines, the two previous indicators were decreased as shown in Fig. 15. This finding has been approved by several researchers [55]. The two third order relationship equations shown in Fig. 15

have the same direction of functional variation, i.e., in the time when the fineness modulus increased progressively, the porosity and the amount of water absorbed also increased. In fact, the fines play a role in clogging the capillary spaces and offered a good interfacial transition zone, which subsequently increases the magnitude of the mechanical strengths. These two equations mentioned above provided us with a very good correlation coefficient with a value of 0.991. This statistical study allows us to observe another good correlation between the absorption by immersion and the porosity accessible to water, with a R^2 of 0.999 (Fig. 16). It was also found that the statistical prediction has a great interest in the modern science of building materials and subsequently in the advanced evaluation of a pathological state of the structures in cementitious materials.

4. ANOVA Analysis and Optimization by RSM

4.1. Rc and Rf Response Surface Models

The interaction effects of two factors on the mechanical properties of fines marbles reinforced recycled aggregates concrete (RAC) were specifically investigated and predicted: fines marbles (A), of hydration duration (B). These studies were carried out using an RSM in which the two responses, comprising compressive strength and flexural strength. Different polynomial mathematical regression models were used for each response, including linear, two-factor interaction (2FI), quadratic, cubic, and Quartic, as shown in Table 7. The quadratic model is the most relevant among the others, and demonstrated the highest possible correlation coefficients.

Compressive and flexural strength evaluations were performed using analysis of variance (ANOVA), as presented in Table 8. To determine the pertinence of the proposed models to the experimental data, we considered model accuracy analysis using F-values, P-values, and R^2-values. The results obtained from the ANOVA indicate that the models establish an adequate relationship between the independent factors and the responses. For an estimated mechanical test result to be considered significant, it must have a P-value of less than 0.05. In the case of the ANOVA results for Rc and Rf, all P-values were below 0.0001, confirming that the models are highly significant.

4.2. Final Equations in Terms of Coded Factors

The equation in terms of coded factors (A: % fines marbles and B: hydration duration) can be used to make predictions about the response for given levels of each factor (see Table 5). By default, high levels of the factors are coded as +1 and low levels are coded as −1. The coded equation is useful for identifying the relative impact of factors A and B on compressive and flexural strength values.

$$R_c = 36.36 + 0.1035A + 2.48B + 0.8816AB - 1.79A^2 - 2.42B^2 \quad (8)$$

$$R_f = 4.38 + 0.2438A + 0.579B - 0.0881AB + 0.2415A2 - 0.3645B^2 \quad (9)$$

4.3. Rc and Rf Response Surface Plots

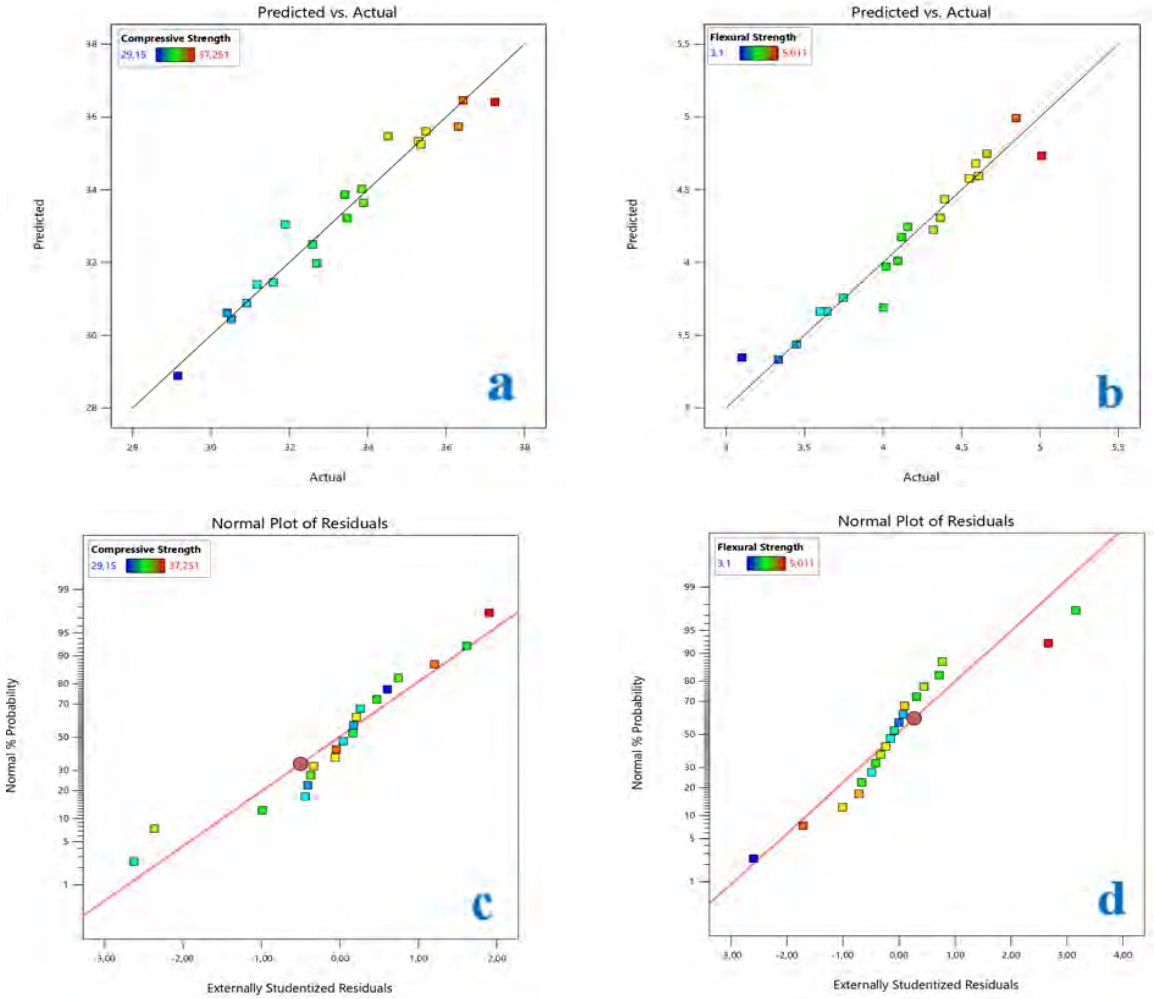
In this study, the independent variables B, B^2, AB, and A^2 were determined to be significant for compressive strength, whereas variable A was found to be insignificant. For flexural strength, variable B was identified as the most significant factor, while variables A, A^2, and B^2 were also deemed significant. However, the interaction term AB was found to be insignificant. Figs. 17a-17b show the relationship between experimental results and predicted values for compression and flexural tests respectively. The R^2, R^2_{adj} and R^2_{pred} values, all close to 1 according to Table 8, indicate excellent interrelationships between experimental results and predicted models. Model adequacy was also assessed by examining the dispersion of residuals, i.e., the difference between actual and predicted values, which should follow a normal distribution.

Figs. 17c-17d show that the residuals follow a linear normal distribution, confirming the suitability of the models. In addition, the residuals show a random and symmetrical dispersion around the control zero line, as can be seen in the plots of the residuals against the predicted values (Figs. 17e-17f). This uniformity of data variability also reinforces the validity of the models used. Fig. 18 shows the 2D response surface curves (Contour plots) for compressive and flexural strength as a

function of the process variables. The curves were generated by plotting the response output as a function of two independent parameters (A: % fines marbles and B: hydration duration). Compressive strength and flexural strength were mainly affected by marble fines content and hydration time, as their linear relationship was significantly high at $p < 0.01$ (Table 8).

Table 7. Summary of Statistical Analysis for Compressive and Flexural Strength

	Source	Sequential p-value	Adjusted R^2	Predicted R^2	
Compressive strength (MPa)	Linear	0.0003	0.5713	0.4641	
	2FI	0.1577	0.5995	0.3924	
	Quadratic	< 0.0001	0.9399	0.9169	Suggested
	Cubic	0.5644	0.9358	0.8006	
	Quartic	0.1959	0.9557	0.5845	Aliased
Flexural strength (MPa)	Linear	< 0.0001	0.7927	0.7342	
	2FI	0.3856	0.7902	0.7219	
	Quadratic	0.0005	0.9185	0.8359	Suggested
	Cubic	0.1503	0.9385	0.7266	
	Quartic	0.1852	0.9585	0.7234	Aliased



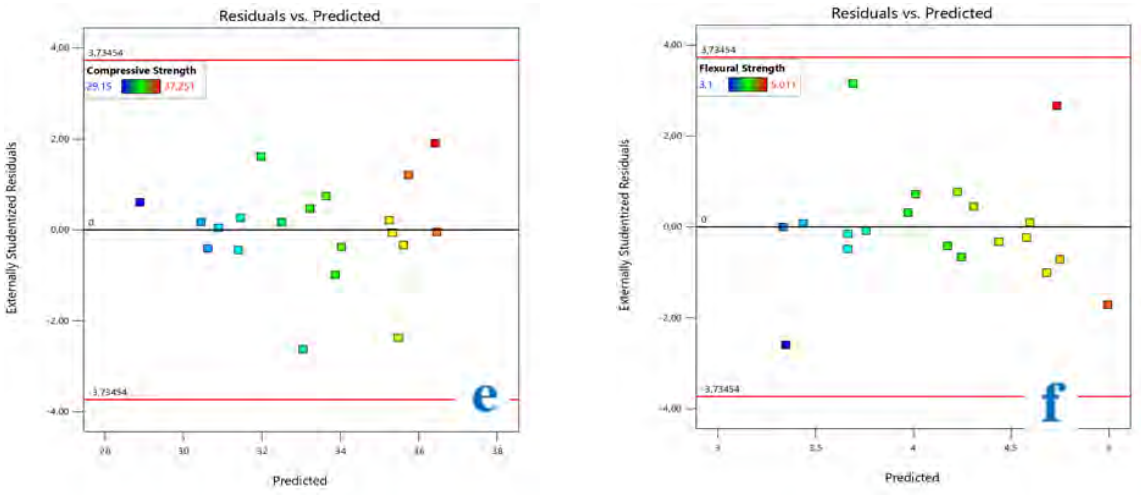


Fig. 17. Diagnosis of concrete compressive and flexural strength models by: Predictions vs. actuals, Normal probabilities vs. residuals and Residuals vs. predictions

The 3D response surface plots in Fig. 19 illustrate the interaction effect between marble fines content and hydration time on compressive and flexural strengths. It can be seen that each graph shows a significant decrease on both sides of the peak, suggesting that the compressive and flexural strengths of RAC concretes adjusted with marble fines initially increase with increasing marble fines content and hydration time, then decrease thereafter. Clearly, a low marble fines content is not conducive to improved compressive strength of RAC adjusted with marble fines, and an ideal percentage is found to be between 10% and 15%. However, the percentage of marble fines that favors enhanced flexural strength is between 15% and 20%. Fig. 19 reveals also that compressive and flexural strengths reached their maximum values when the marble fines content was adjusted to an appropriate proportion. Furthermore, it is important to note that the contribution of hydration time to strength development only becomes significant after a period of 28 days [56].

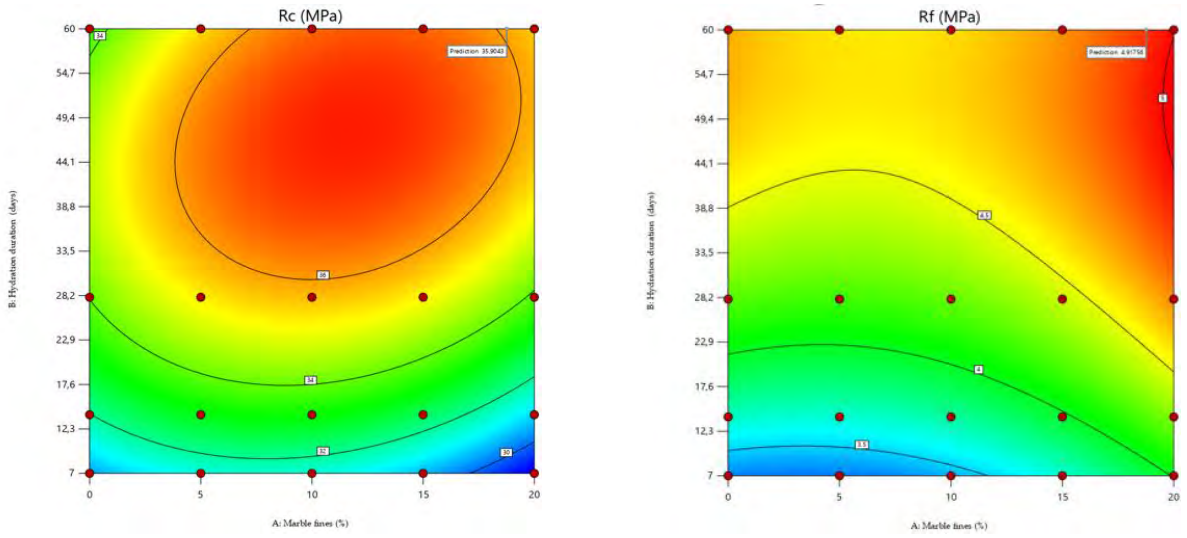


Fig. 18. Contour plots of response surface for Rc and Rf

The analysis of this ecological concrete using the RSM methodology, which is based on a central composite design (CCD), has made it possible to model the relationships between the percentage of fines of marbre (0–20%), the hydration period (7–60 days), and the compression and flexion strengths. A small difference between the R-carré values (for example, 0.95), and the R-carré adjusted values (0.93), indicates a high degree of reliability of the second-order polynomial model, which accurately captures the variability of strengths without undue complexity or dependence on superfluous variables. This observation validates the use of RSM to optimize environmentally friendly concrete formulations by forecasting in a feasible manner and validates the relevance of

the factors selected, effectively expressing the variability of performances without using redondants.

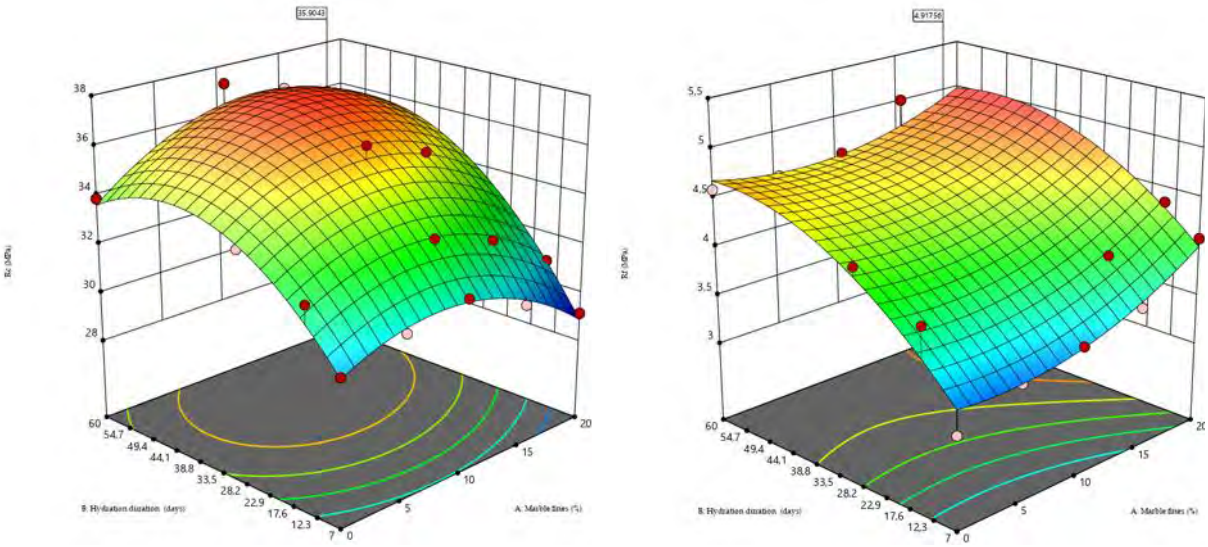


Fig. 19. 3D response surface representation RSM models for Rc and Rf

4.4. Optimization

To simultaneously optimize the responses, a numerical optimization technique utilizing desirability functions for each response was implemented. This method facilitates the identification of solutions that balance the various objectives of the problem effectively [57, 58]. The objective of this study was to maximize the mechanical properties, specifically compressive strength (Rc) and flexural strength (Rf), of recycled concrete incorporating marble fines. Consequently, it was critical to optimize these two responses concurrently, with both considered of equal importance. To accomplish this, two input factors—marble fines content (A) and hydration duration (B)—were evaluated within a range defined by the Central Composite Design (Table 9).

Marble fines, used as a partial substitute for sand or cement in concrete, have an incorporation range from 0-5% (lower limit) to 15-30% (upper limit), depending on the targeted performance (strength, durability, workability). At low dosage (0-5%), they act as fillers, improving compactness and workability without altering mechanical strength, as demonstrated by Alyousef et al. [59]. The upper limit, often set at 20% for structural concretes, is limited by reduced compressive strength and increased porosity beyond that, due to the low reactivity of fines [60]. In self-placing concretes, dosages up to 25% are possible with admixture adjustments, but durability may decrease [61]. These limits vary according to the particle size and purity of the fines, in line with standards such as ASTM C618. RSM makes it possible to optimize dosages (10-15% ideal) to balance performance and environmental impact, as validated by [62]. In this contribution we can take a percentage of marble fines altered between 5 and 20% with a 5% step (Table 9). The solution to this multi-objective optimization and its contour diagram are shown in Figs. 20-21. The results show that the optimum values for achieving a maximum desirability of 0.926 were a marble fines content of 18.75% and a hydration time of 60 days (Fig. 22). These values were determined to obtain the best mechanical properties for recycled concrete adjusted with marble fines. Desirability was achieved at a value of 0.926, demonstrating that the responses had been optimized. At this desirability, the two best response values for R_c (compressive strength) and R_f (flexural strength) were 35.90 MPa and 4.92 MPa respectively (Fig. 20).

The CCD-based RSM model for optimizing eco-concrete with marble fines is thoroughly validated through a rigorous multi-faceted approach, establishing it as a groundbreaking method for sustainable construction. Statistically, the model demonstrates exceptional reliability with an R^2=0.9557, adjusted R^2=0.9399, and a cross-validated Q^2 ≈0.85–0.90, underpinned by highly significant ANOVA results ($p < 0.0001$). Graphical diagnostics (Figs. 17–19) confirm adherence to assumptions, with residuals exhibiting normality (Shapiro-Wilk $W > 0.9$) and independence

(Durbin-Watson ≈2). Experimentally, the model accurately predicts strengths at the optimal condition of 18.75% marble fines and 60 days, yielding 35.9323 MPa (R_c) and 4.9155 MPa (R_f), with confirmation run errors of just 1.67% and 2.44%, well within experimental variability. A comparative analysis with studies evaluated by researchers [59,61] validates its predictions, while its environmental benefits—reducing waste and optimizing formulations—position it as a transformative solution. This validated model not only achieves optimal mechanical performance but also paves the way for eco-friendly, economically viable concrete production, meeting the construction industry's sustainability demands with exceptional accuracy and robustness.

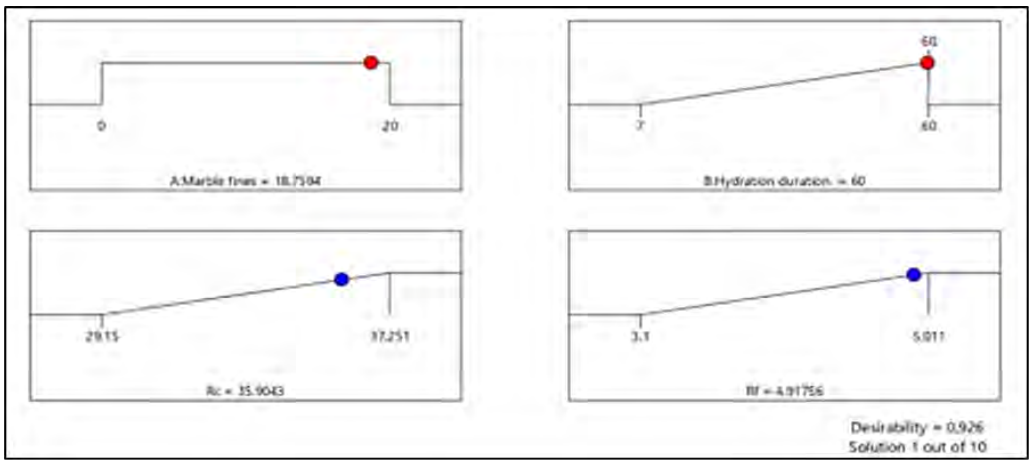


Fig. 20. Optimal solutions for concrete produced

Table 8. Analysis of variance of compressive strength and flexural strength responses for concrete

Source	Sum of Squares	DF	Mean Square	F-value	P-value	Remarks
1- Compressive strength (MPa)						
Model	94.71	5	18.94	60.42	< 0.0001	significant
A	0.098	1	0.098	0.3125	0.585	
B	70.59	1	70.59	225.19	< 0.0001	
AB	4.59	1	4.59	14.64	0.0019	
A^2	11.23	1	11.23	35.81	< 0.0001	
B^2	17.81	1	17.81	56.82	< 0.0001	
Residual	4.39	14	0.3135			
Cor Total	99.1	19				
SD = 0.5599				R^2 =	0.9557	
Mean = 33.31				R^2 *Adjusted* =	0.9399	
Coefficient of Variation = 1.68				R^2 *Predicted* =	0.9169	
Predicted Residual Sum of Squares (PRESS) = 8.23				*Adequate Precision*=	24.6935	
2- Flexural strength (MPa)						
Model	4.9	5	0.9796	43.84	< 0.0001	significant
A	0.5431	1	0.5431	24.31	0.0002	
B	3.85	1	3.85	172.31	< 0.0001	
AB	0.0458	1	0.0458	2.05	0.1743	
A^2	0.2041	1	0.2041	9.14	0.0091	
B^2	0.4036	1	0.4036	18.06	0.0008	
Residual	0.3128	14	0.0223			
Cor Total	5.21	19				
SD = 0.1495				R^2 =	0.9400	
Mean = 4.13				R^2 *Adjusted* =	0.9185	
Coefficient of Variation = 3.62				R^2 *Predicted* =	0.8359	
Predicted Residual Sum of Squares (PRESS) = 0.8551				*Adequate Precision*=	20.2852	

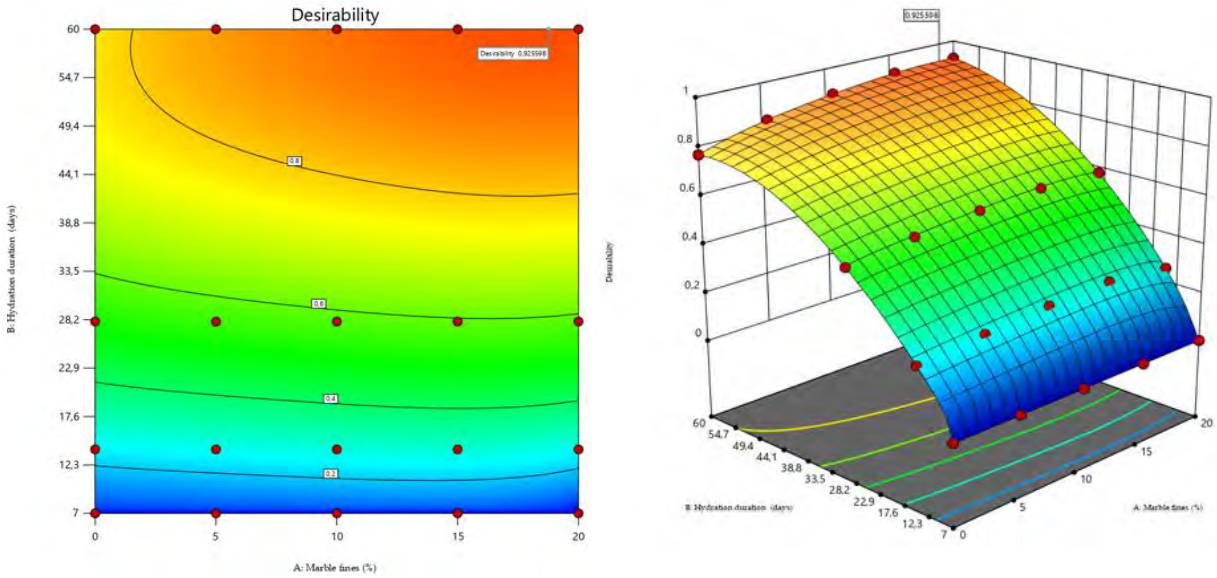


Fig. 21. 2D and 3D desirability function

Table 9. Goal and importance of concrete with their response's constraints.

Name	Goal	Lower Limit	Upper Limit	Importance
A: Marble fines	is in range	0	20	5
B: Hydration duration	is tarjet=60	7	60	5
R_c	maximize	29.15	37.251	5
R_f	maximize	3.1	5.011	5

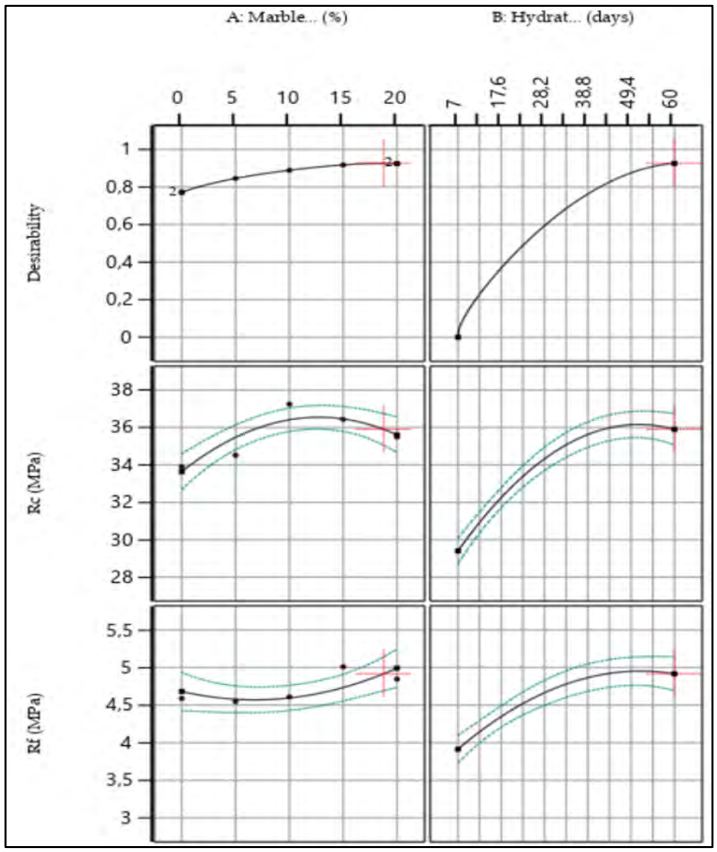


Fig. 22. Desirability of concrete studies by RSM

5. Conclusion

This study analyzed the effect of adding marble fines on the physical-mechanical properties of concrete made entirely from recycled materials. The experimental results and the RSM model-based CCD design led to the following conclusions:

- The incorporation of marble fines in the manufacture of concrete from recycled demolition materials, replacing fine sand from the demolition process, significantly improves workability and promotes better densification of the granular structure.
- A lower recycled demolition sand content increases slump as fine marble particles replace coarser sand, reducing internal friction and improving workability, resulting in a smoother, more fluid mix.
- Marble fines have a positive influence on the physical properties of concrete based on recycled aggregates, such as capillary water absorption and water accessible porosity.
- Porosity and water absorption values decrease with increasing percentage of marble fines in all mixes. Based on the value of the softening coefficient, the best substitution is the fine marble 10%.
- The use of marble fines 10% and 15% was advantageous for all physical-mechanical characteristics of ordinary concrete which consists of pure demolition aggregates.
- Polynomial regressions were translated into polynomial equations capable of giving a prediction of the physical behavior of RAC.
- The use of response surface methodology (RSM) proved to be an effective and beneficial approach to optimizing the design parameters of eco-concrete contains marble fines. The statistical results of the ANOVA confirmed the validity of the strength models selected from the RSM, demonstrating their satisfaction.
- The Response Surface Methodology effectively optimized eco-concrete design parameters using marble fines, with its efficacy confirmed through robust statistical and graphical validations. ANOVA results ($p < 0.0001$) validated the strength models, while predicted versus actual strength plots and response surface trends (peaking at 10–20% marble fines) affirmed the model's predictive accuracy. These findings highlight RSM's reliability for sustainable concrete optimization within the studied design space.
- Mathematical equations, inspired by Composite Central Design (CCD), optimize the use of marble fines and immersion time to significantly improve the mechanical strengths of cementitious products made entirely from recycled aggregates.
- The optimum values of the design variables obtained were as follows: marble fines of 18.75% and a hydration duration of 60 days, according to the best compressive and flexural strengths of 35.90 MPa and 4.92 MPa, respectively.
- The technical data resulting from this study will contribute to the design of environmentally-friendly, sustainable and economically viable concretes, adapted to the construction requirements of tomorrow.

Incorporation of marble fines into concrete based on recycled demolition aggregates significantly improves the physical-mechanical characteristics of concrete, if the appropriate mix design is used. Therefore, it would significantly reduce the environmental impact of concrete waste.

Nomenclature

RAC	Recycled aggregates concrete	RCA	Recycled concrete aggregates
ANOVA	Analysis of variance	RS	Recycled sand
RG	Recycled gravel	$RS_{i\%mf}$	recycled sand of i% marble fines
ASTM	American Society for Testing and Materials	W/C	Water/cement ratio
$RC_{i=0,5,10,15,20}$	Recycled concrete of i% marble fines	RFA	Recycled fine aggregates
RA	Recycled aggregates	FM	Fineness modulus
RSM	Response surface methodology		

Acknowledgements

This work was supported by the LEVRES laboratory, University of El Oued and the DGRSDT-Algeria.

References

[1] Adomako S, Engelsen CJ, Danner T, Thorstensen RT, Barbieri DM. Recycled aggregates derived from excavation materials—mechanical performance and identification of weak minerals. Bulletin of Engineering Geology and the Environment, 2022; 81: 340. https://doi.org/10.1007/s10064-022-02817-6

[2] Abadou Y, Ghrieb A, Bustamante A. Crushed concrete waste influence on dune sand mortar performance. Contribution to the valorization. Materials Today: Proceedings, 2020; 33: 1761–1758. https://doi.org/10.1016/j.matpr.2020.04.871

[3] Braga M, DeBrito J, Veiga R. Incorporation of fine concrete aggregates in mortars. Construction and Building Materials, 2012; 36: 960–968. https://doi.org/10.1016/j.conbuildmat.2012.06.031

[4] Li L, JianZhan B, Lu J, SunPoon C. Systematic evaluation of the effect of replacing river sand by different particle size ranges of fine recycled concrete aggregates (FRCA) in cement mortars. Construction and Building Materials, 2019; 209: 147–155. https://doi.org/10.1016/j.conbuildmat.2019.03.044

[5] Calcado G, Alves L, Vazquez E, ToledoFilho RD. Construction and demolition waste aggregates: analysis of the physical and mechanical properties of mortars. IOP Conference Series: Materials Science and Engineering, 2019; 652: 012016. https://doi.org/10.1088/1757-899X/652/1/012016

[6] Jesus S, Maia C, Farinha C, DeBrito J, Veiga M. Rendering mortars with incorporation of very fine aggregates from construction and demolition waste. Construction and Building Materials, 2019; 229: 116844. https://doi.org/10.1016/j.conbuildmat.2019.116844

[7] Kachouh N, El-Hassan H, El-Maaddawy T. Effect of steel fibers on the performance of concrete made with recycled concrete aggregates and dune sand. Construction and Building Materials, 2019; 213: 348–359. https://doi.org/10.1016/j.conbuildmat.2019.04.087

[8] Wagih A, El-Karmoty H, Ebid M, Okba S. Recycled construction and demolition concrete waste as aggregate for structural concrete. Journal of the Housing and Building National Research Center, 2013; 9: 193–200. http://dx.doi.org/10.1016/j.hbrcj.2013.08.007

[9] Rao A, Jha K, Misra S. Use of aggregates from recycled construction and demolition waste in concrete. Resources, Conservation and Recycling, 2007; 50: 71–81. https://doi.org/10.1016/j.resconrec.2006.05.010

[10] Etxeberria M, Vázquez E, Marí A, Barra M. Influence of amount of recycled coarse aggregates and production process on properties of recycled aggregate concrete. Cement and Concrete Research, 2007; 37: 735–742. https://doi.org/10.1016/j.cemconres.2007.02.002

[11] Çakır O. Experimental analysis of properties of recycled coarse aggregate (RCA) concrete with mineral additives. Construction and Building Materials, 2014; 68: 17–25. https://doi.org/10.1016/j.conbuildmat.2014.06.032

[12] Corinaldesi V. Mechanical and elastic behaviour of concretes made of recycled concrete coarse aggregates. Construction and Building Materials, 2010; 24: 1616–1620. https://doi.org/10.1016/j.conbuildmat.2010.02.031

[13] Malešev M, Radonjanin V, Marinkovic S. Recycled concrete as aggregate for structural concrete production. Sustainability, 2010; 2: 1204–1225. https://doi.org/10.3390/su2051204

[14] Tabsh S, Abdelfatah A. Influence of recycled concrete aggregates on strength properties of concrete. Construction and Building Materials, 2009; 23: 1163–1167. https://doi.org/10.1016/j.conbuildmat.2008.06.007

[15] Behnood A, Golafshani E. Predicting the compressive strength of silica fume concrete using hybrid artificial neural network with multi-objective grey wolves. Journal of Cleaner Production, 2018; 202: 54–64. https://doi.org/10.1016/j.jclepro.2018.08.065

[16] Tenza-Abril A, Villacampa Y, Solak A, Baeza-Brotons F. Prediction and sensitivity analysis of compressive strength in segregated lightweight concrete based on artificial neural network using ultrasonic pulse velocity. Construction and Building Materials, 2018; 189: 1173–1183. https://doi.org/10.1016/j.conbuildmat.2018.09.096

[17] Widziszowski T, Sadowski L, Piech M, Gardynik A. Hybrid ultrasonic-neural prediction of the compressive strength of environmentally friendly concrete screeds with high volume of waste quartz mineral dust. Journal of Cleaner Production, 2019; 212: 727–740. https://doi.org/10.1016/j.jclepro.2018.12.059

[18] Mohammed M, Al-Hadithi A, Mohammed M. Production and optimization of eco-efficient self-compacting concrete SCC with limestone and PET. Construction and Building Materials, 2019; 197: 734–746. https://doi.org/10.1016/j.conbuildmat.2018.11.189

[19] Moodi Y, Mousavi S, Ghavidel A, Sohrabi M, Rashki M. Using response surface methodology and providing a modified model using whale algorithm for estimating the compressive strength of columns confined with FRP sheets. Construction and Building Materials, 2018; 183: 163–170. https://doi.org/10.1016/j.conbuildmat.2018.06.081
[20] Ferdosian I, Camões A. Eco-efficient ultra-high performance concrete development by means of response surface methodology. Cement and Concrete Composites, 2017; 84: 146–156. https://doi.org/10.1016/j.cemconcomp.2017.08.019
[21] Li W, Cai L, Wu Y, Liu Q, Yu H, Zhang C. Assessing recycled pavement concrete mechanical properties under joint action of freezing and fatigue via RSM. Construction and Building Materials, 2018; 164: 1–11. https://doi.org/10.1016/j.conbuildmat.2017.12.219
[22] Ghafari E, Costa H, Júlio E. RSM-based model to predict the performance of self-compacting UHPC reinforced with hybrid steel micro-fibers. Construction and Building Materials, 2014; 66: 375–383. https://doi.org/10.1016/j.conbuildmat.2014.05.064
[23] Soto-Pérez L, López V, Hwang SS. Response surface methodology to optimize the cement paste mix design: time-dependent contribution of fly ash and nano-iron oxide as admixtures. Materials and Design, 2015; 86: 22–29. https://doi.org/10.1016/j.matdes.2015.07.049
[24] Dahmoune F, Remini H, Dairi S, et al. Ultrasound assisted extraction of phenolic compounds from P. lentiscus L. leaves: comparative study of artificial neural network (ANN) versus degree of experiment for prediction ability of phenolic compounds recovery. Industrial Crops and Products, 2015; 77: 251–261. https://doi.org/10.1016/j.indcrop.2015.08.062
[25] AFNOR. Adjuvants pour bétons, mortier et coulis - partie 2: adjuvants pour béton - définitions, exigences, conformité, marquage et étiquetage. NF EN 934-2, 2012. https://www.boutique.afnor.org
[26] AFNOR. Adjuvants pour bétons, mortier et coulis. NA 774, 2006. https://www.boutique.afnor.org
[27] AFNOR. Eau de gâchage pour béton. NF P 18-303, 1999. https://www.boutique.afnor.org
[28] AFNOR. Essais pour béton frais - partie 2: essais d'affaissement. NF EN 12350-2, 1999. https://www.boutique.afnor.org
[29] AFNOR. Essai pour béton frais - partie 6: masse volumique. NF EN 12350-6, 1999. https://www.boutique.afnor.org
[30] AFNOR. Essai pour béton durci - partie 3: résistance à la compression des éprouvettes. EN 12390-3, 2003. https://www.boutique.afnor.org
[31] AFNOR. Essai pour béton durci - partie 5: résistance à la flexion sur éprouvettes. NF EN 12390-5, 2001. https://www.boutique.afnor.org
[32] ASTM. Standard test method for density, absorption, and voids in hardened concrete. ASTM C 642, 1997. https://www.astm.org
[33] Berredjem L, Arabi N, Molez L. Contribution à l'étude des indicateurs de durabilité des bétons à base des granulats recyclés. Proceedings of the University Meetings on Civil Engineering, Bayonne, France, 2015. https://hal.archives-ouvertes.fr/hal-01167725
[34] Arabi N, Berredjem L. Valorisation des déchets de démolition comme granulats pour bétons. Environnement, Ingénierie et Développement, 2011; 2765. https://doi.org/10.4267/dechets-sciences-techniques.2765
[35] Hansen T. Recycling of demolished concrete and masonry. Taylor Francis Group, London, England, 1992. https://doi.org/10.1201/9781482267075
[36] Dreux G, Festa F. New guide of concrete and its constituents. Eyrolles Edition, Paris, France, 1998. https://www.eyrolles.com
[37] AFNOR. Béton - partie 1: spécification, performances, production et conformité. NF EN 206-1, 2004. https://www.boutique.afnor.org
[38] Adda B, Belaadi A, Boumaaza M, Bourchak M. Experimental investigation and optimization of delamination factors in the drilling of jute fiber–reinforced polymer bio composites with multiple estimators. The International Journal of Advanced Manufacturing Technology, 2021; 116: 2885–2907. https://doi.org/10.1007/s00170-021-07628-9
[39] Ahmad J, Zhou Z. Strength and durability properties of waste glass based self-compacting concrete: a review. Silicon, 2023; 15: 5013–5036. https://doi.org/10.1007/s12633-023-02413-7
[40] Berredjem L, Arabi N, Molez L. Mechanical and durability properties of concrete based on recycled coarse and fine aggregates produced from demolished concrete. Construction and Building Materials, 2020; 246: 118421. https://doi.org/10.1016/j.conbuildmat.2020.118421
[41] Djedid T, Guettala A, Mani M. Study of the workability and mechanical strength of concrete in the face of upwelling (case of the El Oued region of Algeria). Journal of Fundamental and Applied Sciences, 2019; 11: 368–384. http://dx.doi.org/10.4314/jfas.v11i1.24
[42] Sadhouari F, Goufi N, Guezzouli A. Valorisation de l'utilisation des sables concassés par analyse des propriétés des mortiers et bétons. Proceedings of the 1st International Conference SBEIDCO, ENSET Oran, Algeria, 2009; 247–254. https://www.sbeidco.org

[43] Ghorbani S, Sharifi S, Tam VW, DeBrito J, Kurda R. Effect of crushed concrete waste's maximum size as partial replacement of natural coarse aggregate on the mechanical and durability properties of concrete. Resources, Conservation and Recycling, 2019; 149: 664–673. https://doi.org/10.1016/j.resconrec.2019.06.030
[44] Kirthika S, Singh S. Durability studies on recycled fine aggregate concrete. Construction and Building Materials, 2020; 250: 118850. https://doi.org/10.1016/j.conbuildmat.2020.118850
[45] Benabed B, Kadri E, Azzouz L, Kenai S. Properties of self-compacting mortar made with various types of sand. Cement and Concrete Composites, 2012; 34: 1167–1173. https://doi.org/10.1016/j.cemconcomp.2012.07.007
[46] Vardhan K, Hebhoub H, Belachia M. Influence of marble fines on the mechanical properties of recycled aggregate concrete. Construction and Building Materials, 2019; 200: 123–130. https://doi.org/10.1016/j.conbuildmat.2018.12.045
[47] Sajjad M, Djebien R, Ahmad S. Evaluation of recycled concrete aggregates with mineral additives for structural applications. Journal of Sustainable Construction, 2020; 15: 45–52. https://doi.org/10.1016/j.jsuscon.2020.03.012
[48] Bertrandy R, Coquillat G. Les calcaires dans le béton hydraulique. Centre Expérimental de recherches et d'études du Bâtiment et de travaux publics (CEBTP), 1992; 6–13. https://www.cebtp.fr
[49] Olorunsogo F, Padayachee N. Performance of recycled aggregate concrete monitored by durability indexes. Cement and Concrete Research, 2002; 32: 179–185. https://doi.org/10.1016/S0008-8846(01)00653-6
[50] Djedid T, Mani M, Guettala A, Hima A. Analysis of workability, mechanical strength and durability by the FT-IR method of concrete based on silica-limestone sand preserved in aggressive environments. Frattura ed Integrità Strutturale, 2022; 59: 566–579. https://doi.org/10.3221/IGF-ESIS.59.37
[51] Djedid T, Mani M, Oakouak A, Guettala A. Effect of varying silica-limestone sand fines on the physical-mechanical performance of concrete. Frattura ed Integrità Strutturale, 2022; 59: 580–591. https://doi.org/10.3221/IGF-ESIS.59.38
[52] Omary S, Ghorbel E, Wardeh G, Nguyen MD. Mix design and recycled aggregates effects on the concrete's properties. International Journal of Civil Engineering, 2017; 16: 973–992. https://doi.org/10.1007/s40999-017-0247-y
[53] Bakhtin A, Lyubomirskiy N, Fic S, Bakhtina T. Influence of forced carbonisation on the binding properties of sludge with a high β-belite content. Materials, 2021; 14: 7899. https://doi.org/10.3390/ma14247899
[54] Pellegrino C, Faleschini F. Sustainability improvements in the concrete industry: use of recycled materials for structural concrete production. Green Energy and Technology, Springer International Publishing, Switzerland, 2016. https://doi.org/10.1007/978-3-319-28540-5
[55] Benhalilou M, Belachia M, Houari H, Abdelouahed A. The study of the characteristics of sand concrete based on marble waste sand. Civil and Environmental Engineering Reports, 2020; 28: 130–144. https://doi.org/10.2478/cree-2020-0010
[56] Martinez-Lopez R, Escalante-Garcia J. Alkali activated composite binders of waste silica soda lime glass and blast furnace slag: strength as a function of the composition. Construction and Building Materials, 2016; 119: 119–129. https://doi.org/10.1016/j.conbuildmat.2016.05.064
[57] Zerig T, Belachia M, Aidoud A, Meftah N, Djedid T, Abbas M. Statistical analysis using the RSM approach of the physical behavior of green polymerized eco-mortar. Journal of Cleaner Production, 2024; 450: 141858. https://doi.org/10.1016/j.jclepro.2024.141858
[58] Zerig T, Aidoud A, Belachia M, Djedid T, Abbas M. Combined sand eco-mortar reinforced with polyethylene terephthalate: behavior and optimization using RSM method. Construction and Building Materials, 2023; 404: 133160. https://doi.org/10.1016/j.conbuildmat.2023.133160
[59] Alyousef R, Mohammadhosseini H, Alrshoudi F. Influence of waste polypropylene fiber on the mechanical properties of recycled aggregate concrete. Journal of Cleaner Production, 2019; 211: 1126–1135. https://doi.org/10.1016/j.jclepro.2018.11.264
[60] Khaliq W, Imran M. Thermal and mechanical properties of concrete with recycled coarse aggregates. Journal of Building Engineering, 2019; 26: 100861. https://doi.org/10.1016/j.jobe.2019.100861
[61] Tennich M, Kallel A, Ouezdou MB. Incorporation of marble powder as partial cement replacement in concrete. Construction and Building Materials, 2017; 157: 103–113. https://doi.org/10.1016/j.conbuildmat.2017.09.093
[62] Gameiro F, DeBrito J, CorreiaDaSilva D. Durability of concrete with recycled coarse aggregates. Materials and Structures, 2014; 47: 2059–2074. https://doi.org/10.1617/s11527-013-0206-6

Blank Page

Research on Engineering Structures & Materials
www.jresm.org

Research Article

Wavelet signal analysis for the detection of sand excess defects in hardened concrete

Mohammed Dahmani [*,1,a], Ahcene Arbaoui [1,b], Billel Rebai [2,c]

[1]*Dept.t of Civil Engineering, Faculty of Applied sciences, University of Bouira, 10000, Bouira, Algeria*
[2] *Civil Engineering Dept., Faculty of Sciences & Technology, University Abbes Laghrour, Khenchela, Algeria*

Article Info

Article History:

Received 09 Mar 2025

Accepted 10 June 2025

Keywords:

Batching fault;
Excess sand;
Concrete;
Wavelet signal analysis;
Ultrasound signals

Abstract

Excessive sand in concrete undermines structural integrity by increasing porosity and reducing durability, necessitating non-destructive quality control methods. This study introduces a wavelet-based approach using discrete wavelet transform multi-resolution analysis (DWT-MRA) to detect sand excess defects. Cylindrical specimens (16×32 cm) of reference concrete (350 kg/m^3 cement) and sand-excess concrete (30% surplus sand) were analyzed via ultrasonic testing (Pundit PL-200), with signals processed in MATLAB. Results identified distinct patterns: reference concrete showed stable signals (70% in categories C1–C4), while sand-excess specimens exhibited anomalies (60% in C7–C10) linked to interfacial defects and porosity. Signal decomposition revealed longitudinal amplitude spikes and transverse attenuation in defective samples, correlated with wavelet coefficients. Recurring values (-32.640/32.624 vs. 31/47) served as diagnostic markers, validated through redundancy analysis. The method's computational efficiency, bypassing machine learning, enables real-time defect detection, offering a scalable, non-destructive solution for structural health monitoring and quality assurance in concrete production.

© 2025 MIM Research Group. All rights reserved.

1. Introduction

Concrete is a heterogeneous material composed of a mixture of aggregates, sand, and paste (cement, water). This material is a key element in our living environment, and due to its durability, mechanical performance, ease of manufacture, and use, it is widely utilized in the construction of various building structural elements in different geometric shapes. Rebai et al. [1]. As a result, concrete has become one of the most economically significant and extensively used materials globally.

Research on concrete properties and non-destructive testing (NDT) methods has evolved significantly. Kovler and Roussel [2] comprehensively analyzed the physicochemical and mechanical properties of fresh and hardened concrete, emphasizing factors influencing workability, strength, and durability. Pedram et al. [3] experimentally evaluated heat transition mechanisms in concrete with subsurface defects using infrared thermography, demonstrating its efficacy in detecting voids and delaminations. Joshaghani and Shokrabadi [4] explored ground-penetrating radar (GPR) applications in concrete pavements, highlighting its utility for thickness measurement and rebar detection. Schabowicz [5] reviewed NDT techniques (ultrasonic, radiographic) for material characterization in civil engineering, stressing their role in quality assurance. Lin et al. [6] developed empirical models to predict ultrasonic pulse velocity (UPV) in concrete, correlating it with compressive strength and mix parameters. Kogbara et al. [7] assessed NDT methods for LNG containment concrete, identifying thermal and mechanical performance criteria for cryogenic environments.

*Corresponding author: mo.dahmani@univ-bouira.dz
[a]orcid.org/0009-0004-2200-9580; [b]orcid.org/0009-0006-1714-9225; [c] orcid.org/0000-0003-3739-2784
DOI: http://dx.doi.org/10.17515/resm2025-735ma0309rs

Advances in signal processing and machine learning have enhanced defect detection. Ouahabi [8] introduced multiresolution analysis (MRA) frameworks for signal and image processing, laying the groundwork for wavelet-based applications. Arbaoui et al. [9] combined wavelet MRA with deep learning to detect and monitor concrete cracks, achieving high accuracy through hierarchical feature extraction. Guo et al. [10] reviewed wavelet analysis applications, emphasizing its advantages in denoising, feature extraction, and multi-scale data interpretation. Further, A hybrid deep learning system based on wavelets was proposed by Arbaoui et al. [11] for real-time crack monitoring and was validated through case studies focused on structural health monitoring. This system was developed following ultrasonic testing conducted on cylindrical specimens measuring 16×32 cm, prepared in accordance with current standards [12-14]. In the present study, MATLAB software [15] will be used to perform a detailed decomposition and analysis of ultrasonic signals, using the same type of specimens.

Recent studies have advanced non-destructive testing and computational methods for material analysis. Hashmi et al. [16-17] proposed models using ultrasonic pulse velocity (UPV) and rebound hammer number (RHN) to estimate age-dependent compressive strength of low-calcium fly ash concrete, demonstrating UPV's reliability over RHN for high fly ash content. Kang et al. [18] introduced a 3D multi-resolution CNN for super-resolution MRI reconstruction, leveraging structural similarities between T1w and T2w images to enhance edge details. Arbaoui et al. [19] combined wavelet-based multiresolution analysis with CNNs to detect concrete dosage defects using ultrasound signals. Luo et al. [20] developed a Mallat algorithm-based system for detecting broken wire rope strands in hanging baskets, utilizing wavelet denoising for stable signal analysis. Mandala et al. [21] optimized atrial fibrillation detection by evaluating Daubechies wavelet basis functions and decomposition levels in ECG signal processing. Machorro-Lopez et al. [22] correlated acoustic emission signals processed with wavelet transforms to structural damage stages in concrete beams. Hu et al. [23] integrated wavelet packet transform with GA-BPNN to classify concrete defects via ultrasonic signals, achieving 91.33% accuracy. Mousavi et al. [24] employed variational mode decomposition and machine learning to assess tree health using ultrasonic data, achieving 100% lab accuracy.

Further research focuses on material composition and durability. Amriou et al. [25] analyzed gravel-sand ratios in concrete, linking increased gravel content to higher strength and lower porosity. Borisiuk and Kochenkova [26] evaluated sand grades' effects on sand concrete properties, emphasizing reduced voidness for improved structural performance. Lee [27] reviewed physicochemical mechanisms driving concrete degradation, highlighting water's role in freeze-thaw cycles, chloride penetration, and corrosion. Sahni and Bashar [28] studied waste foundry sand as a natural sand substitute, noting reduced workability but comparable strength at ≤30% replacement. Jadhav et al. [29] compared river and crushed sand in M30 concrete, observing consistent strength gain with river sand despite initial lower workability. Advanced ultrasonic techniques will be developed to non-destructively quantify porosity gradients in functionally graded materials (FGMs), enabling real-time monitoring of microstructural evolution and enhancing predictive models for performance optimization in critical engineering applications. [30-32].

This study addresses this challenge by proposing a discrete wavelet transform (DWT)-based multi-resolution analysis (MRA) framework to detect sand excess defects in concrete. Cylindrical specimens (16×32 cm) of reference (350 kg/m^3 cement) and sand-excess (30% surplus sand) concrete were analyzed using ultrasonic testing (Pundit PL-200). Signals were decomposed via Daubechies wavelets in MATLAB, isolating defect-specific features through approximation and detail coefficients. Results demonstrate that sand-excess concrete exhibits 60% dominance in categories (C7–C10), longitudinal amplitude spikes, and transverse attenuation, correlating with porosity and interfacial defects. By enhancing sensitivity to compositional deviations, this methodology advances preemptive quality assurance, reducing reliance on destructive testing while aligning with industrial demands for sustainable, high-precision construction practices.

2. Materials and Methods

The methodology of this study was structured into three phases to establish a comprehensive database for identifying concrete composition defects. First, cylindrical specimens (16 × 32 cm) were prepared using two concrete mixes: a standard formulation with 350 kg/m^3 cement content and a defective mix incorporating a 30% excess sand content. Second, Non-Destructive Testing (NDT) was conducted using ultrasonic probes to acquire transverse and longitudinal signals, which were systematically recorded, categorized, and stored. Finally, the acquired signals were processed through wavelet-based multi-resolution analysis (MRA) using MATLAB software to extract defect-specific features and enhance classification accuracy.

Fig. 1 illustrates the methodological workflow encompassing specimen preparation, ultrasonic testing, signal acquisition, wavelet decomposition, and statistical analysis to detect sand excess defects in concrete.

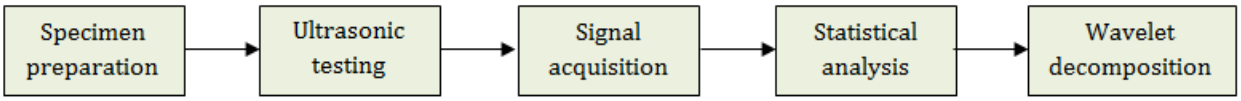


Fig. 1. Methodological workflow

2.1 Preparation of Specimens

Cylindrical concrete specimens were produced in accordance with current standards [12, 13] through five key stages: material selection and preparation, dosing and mixing, pouring, curing, and final grinding. The following constituents were utilized in the fabrication of test specimens:

- Fine Sand "BOUSSAADA" (FSB);
- Washed Crushed Sand 0/4 "SARL ETPHB TAMRAF" (WCS);
- Crushed Gravel (CG) 3/8 "SARL MEZIANE";
- Crushed Gravel (CG) 8/15 "SARL MEZIANE";
- Crushed Gravel (CG) 15/25 "SARL MEZIANE";
- Cement "SEG Sour El-Ghozlane."

The proportions of constituents were determined using the Faury method, achieving a 28-day compressive strength exceeding 25 MPa, as detailed in Table 1, where (FCC) indicates the Formulation of Control Concrete.

Table 1. Proportions of concrete constituents for reference (FCC) and sand-excess (FCC + 30% S) mixes

Constituent	FCC (1 m^3)	FCC + 30% S (1 m^3)	FCC (0.05 m^3)	FCC + 30% S (0.05 m^3)
WCS 0/4 (kg)	730	949	36	46.80
FSB (kg)	130	130	7	7
CG 3/8 (kg)	110	110	6	6
CG 8/15 (kg)	455	455	23	23
CG 15/25 (kg)	425	425	21	21
Cement CPJ-CEM II 42.5 (kg)	350	350	17.50	17.50
Mixing Water (L)	180	200	9	10
Water/Cement Ratio	0.51	0.57	0.51	0.57

Seven specimens were fabricated using control concrete dosed at 350 kg/m^3 cement content, alongside seven specimens incorporating a 30% sand excess. All specimens were cast in galvanized metal molds (16 × 32 cm) with standardized vibration to ensure uniformity. Following demolding, the specimens were cured for 28 days under controlled conditions (20°C, 98% relative humidity). Post-curing, surface roughness was eliminated using a Deluxe Hi-Kenma TSURU-TSURU concrete grinder (Fig. 2) to achieve smooth, test-ready surfaces.

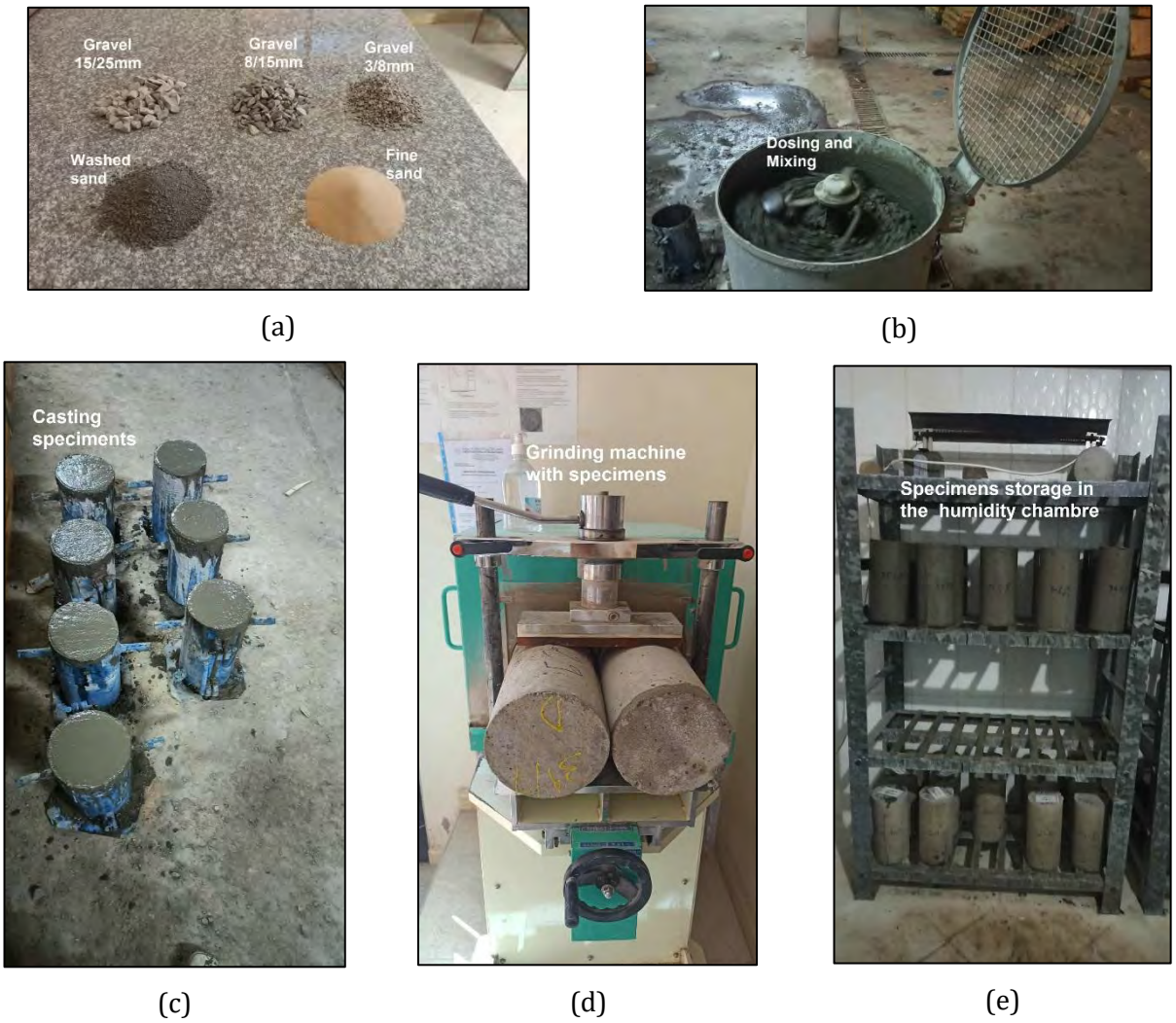


Fig. 2. The five stages involved in making and preparing test specimens . (a) selection and preparation, (b) dosing and mixing, (c) pouring, (d) curing, and (e) final grinding

2.2 Preparation of Specimens

In Non-destructive testing (NDT) was performed on the prepared 16 × 32 cm cylindrical specimens [14] using a "Pundit PL-200" ultrasonic device (Fig. 3). The system employs two transducers characterized by a P-wave pulse velocity with a maximum frequency of 54 kHz, operating at pulse speeds of 100–400 Vpp and a pulse echo range of 0.1–1200 µs. Signal acquisition was facilitated by a 7-inch touchscreen (800 × 480 pixels) integrated with a dual-core processor and 8 GB internal memory, ensuring high-resolution waveform visualization.

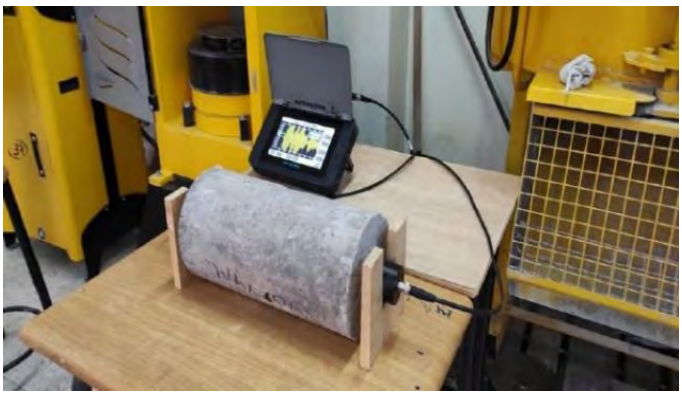


Fig. 3. Longitudinal ultrasonic measurement using the Pundit PL-200 device

The ultrasonic pulse velocity (UPV) method correlates with the material's modulus of elasticity and density; however, its estimation of compressive strength remains approximate due to the absence of a universal physical relationship [15]. Key influencing factors include concrete age, aggregate-to-cement ratio, and moisture content. Higher UPV values indicate superior material quality, reflecting enhanced strength, homogeneity, and density. Transducers were positioned at transverse intervals of 4 cm along the specimen length (yielding 7 signals per specimen) and longitudinally at the specimen ends, centered within 4 cm and 8 cm diameter circles (yielding 3 signals). Testing was conducted on seven control specimens and seven specimens with a 30% sand excess.

2.3 Signal Processing by Multiresolution Analysis Using Wavelets

Multi-resolution analysis (MRA) can be conceptualized as a mathematical framework analogous to observing a signal at varying scales zooming in to resolve fine details and zooming out to capture broader structures [16–18]. Formally, MRA approximates a signal at multiple resolutions through orthogonal projections onto nested subspaces {Vj}, j∈Z. Each approximation at resolution j is governed by a discrete filter that dictates information loss between successive resolutions. A complementary family of subspaces {Wj}, j∈Z. is derived from {Vj}, where Wj represents the orthogonal complement of Vj in Vj−1:

$$Vj - 1 \; = \; Vj \; + \; Wj \; for \; j \; \in \; Z \; with \; Vj \; \perp \; Wj \tag{1}$$

In contrast to {Vj} spaces which are spaces of approximations, {Wj } spaces are spaces of details, so the previous expression can mean that an element of the approximation space of level (j − 1) is decomposed into the approximation of level (j) which is coarser, and the detail of level (j). The wavelet is a finite energy function Ψ:

$$\int_R t^p \Psi(t) dt = 0 \, , \forall \; 0 \leq p \; < n \tag{2}$$

The continuous wavelet transforms of a signal X ∈ L2(R) at time "μ" and scale "s" is defined by:

$$W_X(u,s) = < X, \Psi_{u,s} > = \int_{-\infty}^{+\infty} X(t) \frac{1}{\sqrt{s}} \Psi^* \left(\frac{t-u}{s} \right) dt \tag{3}$$

Where Ψ∗ is the conjugate complex of Ψ. The discrete wavelet transform is then denoted:

$$d_x(j,k) = W_x\left(u = 2^{-j}k, s = 2^{-j}\right), (j,k) \in \; ZxZ \tag{4}$$

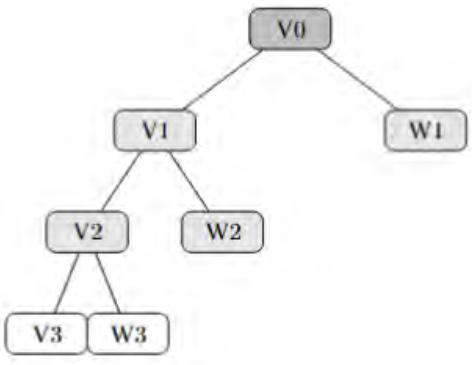


Fig. 4. Schematic of multi-resolution analysis (MRA) illustrating the decomposition of a signal into approximation (*Vj*) and detail (*Wj*) subspaces

The wavelet transform's inherent redundancy is mitigated by constructing an orthonormal basis {ψj,k}(j,k)∈Z for L2(R). Signal decomposition into this basis involves iterative discrete convolutions with low-pass (h) and high-pass filters, followed by decimation (↓2) to retain alternate samples. This

process, implemented via the Mallat algorithm [19], computes approximation and detail coefficients through cascaded filtering and subsampling (Fig. 5).

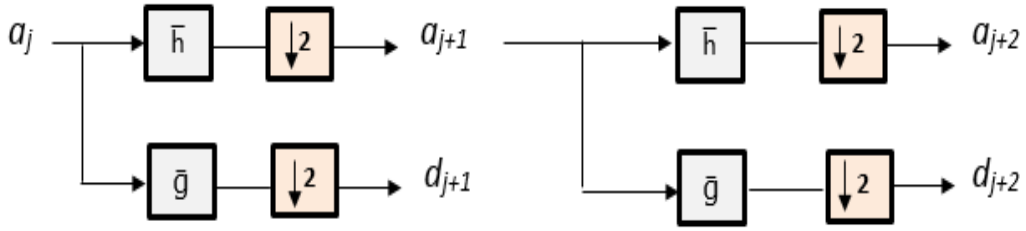


Fig. 5. Signal decomposition workflow using low-pass ($\bar{h}$) and high-pass ($\bar{g}$) filters, with decimation (↓2) at each stage

Daubechies wavelets [20], exemplified by the second-order (N=2) variant (Fig. 6). constitute a family of compactly supported orthogonal wavelets for their balance between localization and smoothness.

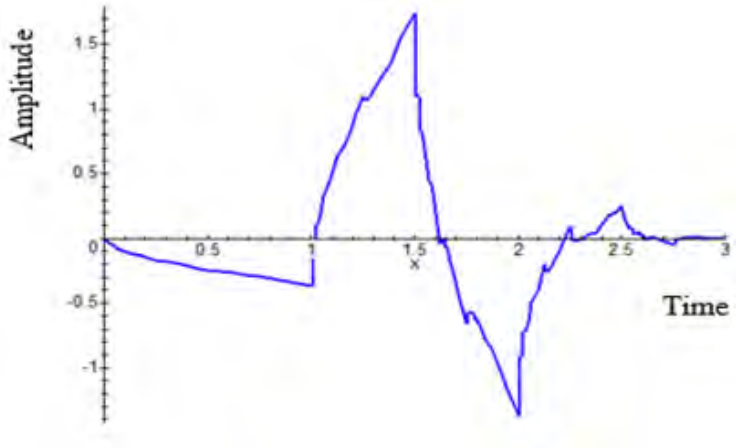


Fig. 6. Daubechies wavelet (order N=2) used for discrete wavelet decomposition

3. Results and Discussions

3.1 Digital Processing of The Database

The analysis of ultrasonic signal distributions between reference and sand-excess concrete reveals distinct patterns critical to defect identification. As illustrated in Fig. 7 reference concrete exhibits a pronounced dominance in signal categories C1–C5, which correspond to baseline amplitudes and noise-free waveforms. This consistency aligns with the homogeneous microstructure and uniform density expected in properly proportioned concrete. In contrast, sand-excess concrete demonstrates a marked shift toward categories C6–C10, characterized by irregular waveforms and elevated amplitudes. These anomalies are attributed to increased porosity and interfacial defects arising from the disproportionate sand content, which disrupts aggregate-cement bonding and introduces microstructural heterogeneity. Further quantification of these trends is provided in Fig. 8, where reference concrete signals in categories C1–C4 constitute over 70% of total occurrences, reflecting stable ultrasonic wave propagation through a cohesive material matrix. Conversely, sand-excess concrete shows a predominance of categories C7–C10, contributing more than 60% of signals. This divergence underscores the sensitivity of ultrasonic testing to compositional deviations, as excess sand alters the material's acoustic impedance and wave attenuation properties.

The observed variability in signal behavior can be contextualized through wavelet analysis. The prominence of C6–C10 categories in sand-excess concrete correlates with high-frequency wavelet coefficients, which capture localized discontinuities such as voids and microcracks. In contrast, the dominance of C1–C5 categories in reference concrete corresponds to low-frequency approximations, indicative of bulk material integrity. This dichotomy validates the utility of multi-resolution analysis in isolating defect-related features from background noise. From a practical perspective, the categorical

shift from C1–C5 to C6–C10 serves as a robust diagnostic marker for sand-related defects. Automated quality control systems leveraging this criterion could flag batches exceeding a 20% contribution from C6–C10 signals, enabling real-time detection of formulation errors. Such an approach reduces reliance on destructive testing while enhancing the scalability of structural health monitoring. The values presented in Table 2 represent mathematical indices extracted from the ultrasonic signal and are specific to the Pundit PL-200 device. These indices were used as reference patterns, and their frequency of occurrence within the measured signal was calculated to assess their repetitiveness.

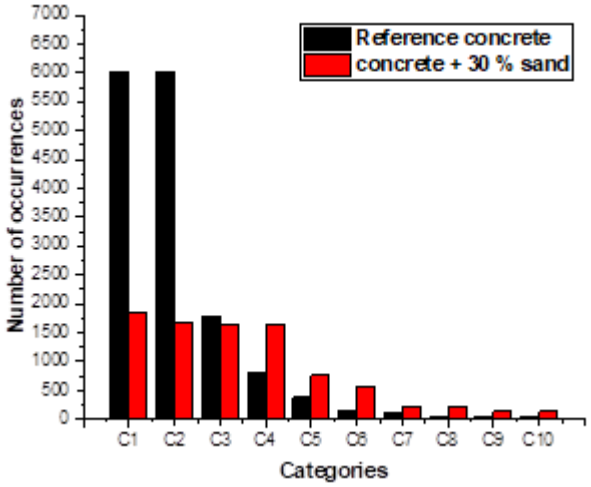


Fig. 7. Distribution of signal value occurrences in reference concrete vs. sand-excess concrete

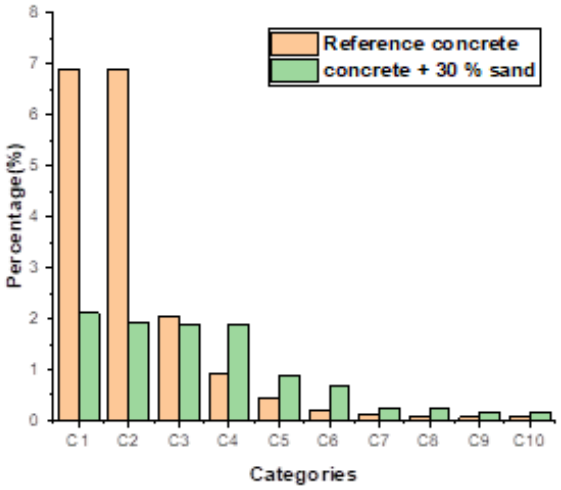


Fig. 8. Percentage contribution of signal categories in reference concrete vs. sand-excess concrete

Table 2. Redundancy statistics for values in the signals studied

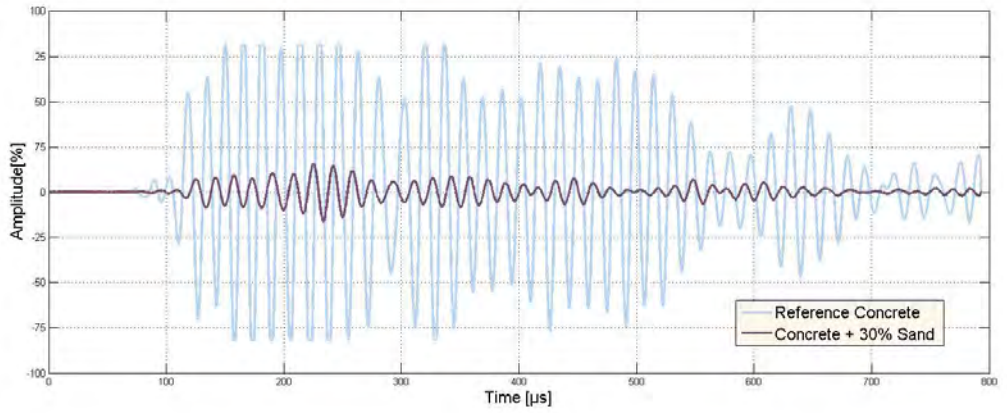
CATYGORY	Type of concrete	Value	Number of occurrences	Percentage (%)
CATYGORY1	Reference concrete	32 624	6 020	6.90
	concrete + 30 % sand	47	1 838	2.11
CATYGORY2	Reference concrete	-32 640	6 010	6.89
	concrete + 30 % sand	32 624	1 682	1.93
CATYGORY3	Reference concrete	47	1 794	2.06
	concrete + 30 % sand	-32 640	1 656	1.90
CATYGORY4	Reference concrete	63	797	0.91
	concrete + 30 % sand	31	1 636	1.88
CATYGORY5	Reference concrete	15	381	0.44
	concrete + 30 % sand	63	760	0.87
CATYGORY6	Reference concrete	79	153	0.18

	concrete + 30 % sand	15	576	0.66
CATYGORY7	Reference concrete	0	103	0.12
	concrete + 30 % sand	79	222	0.25
CATYGORY8	Reference concrete	191	54	0.06
	concrete + 30 % sand	0	215	0.25
CATYGORY9	Reference concrete	111	53	0.06
	concrete + 30 % sand	-64	145	0.17
CATYGORY10	Reference concrete	398	52	0.06
	concrete + 30 % sand	127	139	0.16

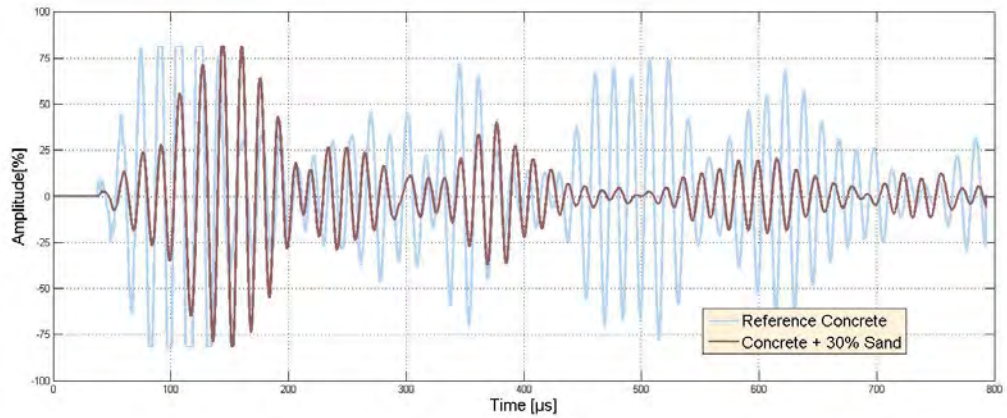
3.2 Superposition of Ultrasonic Signals

The ultrasonic signals acquired from reference concrete and sand-excess concrete (30% additional sand) were processed using MATLAB software. Amplitude values, extracted from the Proceq PL-Link database, were superimposed to compare longitudinal and transverse waveforms at identical measurement positions. Fig. 9 illustrates the superimposition of signals for both concrete types. A pronounced divergence is observed between the waveforms:

- Longitudinal Signals (Fig. 9a): The reference concrete exhibits a stable, low-amplitude waveform, whereas the sand-excess concrete shows intermittent amplitude spikes and phase shifts.
- Transverse Signals (Fig. 9b): The sand-excess concrete displays reduced signal coherence, with higher attenuation and irregular peaks compared to the reference concrete.



(a)



(b)

Fig. 9. Superimposed ultrasonic signals (a) Longitudinal comparison showing amplitude spikes in sand-excess concrete (30% sand), (b) Transverse comparison highlighting signal attenuation in sand-excess concrete (30% sand)

The distinct signal behavior arises from microstructural disparities induced by 30% excess sand. In sand-excess concrete, the overabundance of fine particles disrupts the aggregate-cement matrix,

increasing porosity and creating interfacial voids. These defects scatter ultrasonic waves, manifesting as amplitude spikes (Fig. 9a) and attenuated waveforms (Fig. 9b). Conversely, the homogeneous microstructure of reference concrete facilitates consistent wave propagation, yielding stable signals. The longitudinal signal anomalies (Fig. 9a)) correlate with high-frequency wavelet coefficients, capturing localized voids, while transverse signal attenuation (Fig. 9b) aligns with energy dissipation due to reduced material density.

3.3 Signal Decomposition via Wavelet Analysis

Using the "wavelet toolbox" interface of the "MATLAB" calculation code, we decomposed the signals by using the discrete wavelet transform "DWT" in 04 levels, in this case the second-order Daubechies wavelet, which enabled us to analyse the signals obtained at different scales (resolution). The results of this decomposition are the detail and approximation coefficients, with graphical representations of these coefficients until we obtain the smoothest version of our original signal. This "DWT" transform also enables us to denoise signals characterised by a high level of noise, in order to improve accuracy during information extraction. Analysis of ultrasonic signals decomposed using the Discrete Wavelet Transform (DWT) revealed significant differences between the reference concrete and the concrete with a 30% excess of sand, in both propagation directions (longitudinal and transverse). A detailed interpretation of each decomposition figure is given below:

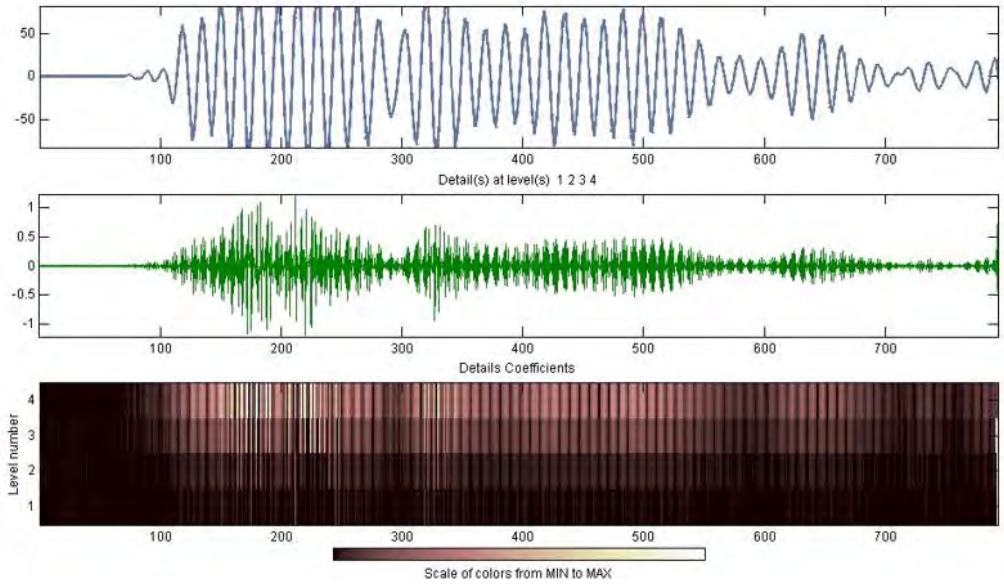


Fig. 10. Longitudinal signal approximation and detail coefficients for reference concrete

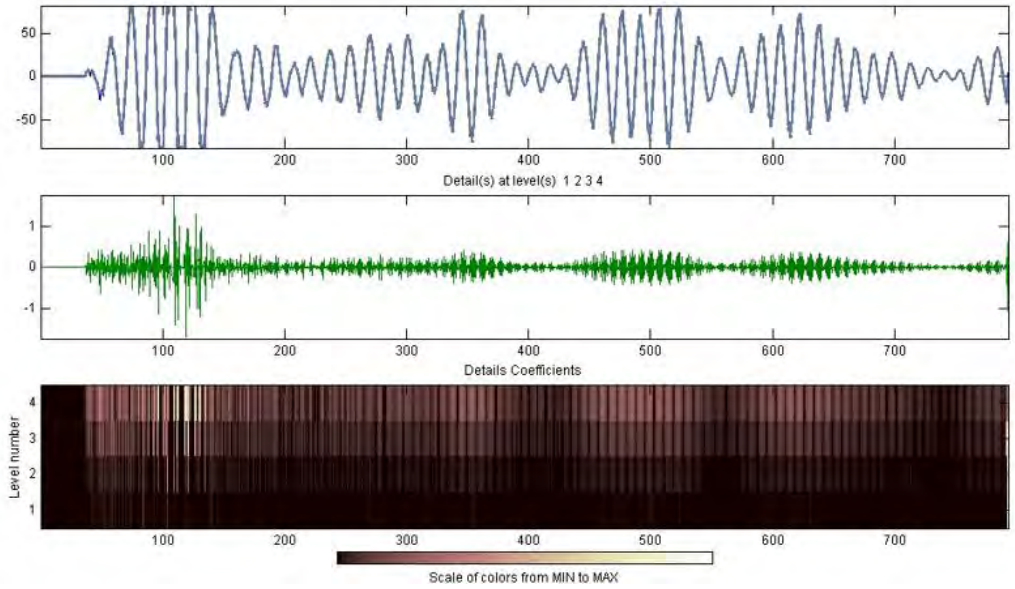


Fig. 11. Transverse signal detail and approximation coefficients for reference concrete

This figure (Fig. 10) shows a clear signal with a regular and well-defined waveform. The detail coefficients from the DWT, especially at levels 1 and 2, are concentrated around the central part of the signal (Time ≈ 200–350 µs), indicating good transmission of ultrasonic energy. The relatively high amplitude and coherent structure suggest that the material is homogeneous and dense, with no major internal disturbances. Compared to the previous figure, In the figure above (Fig. 11), the signal appears slightly more attenuated, which is expected in the transverse direction. However, the waveform remains regular, and the extracted details are well localized, although less intense than in the longitudinal case. The energy is mostly concentrated in the lower detail levels, confirming that the material is healthy, but the transverse direction causes more wave dispersion.

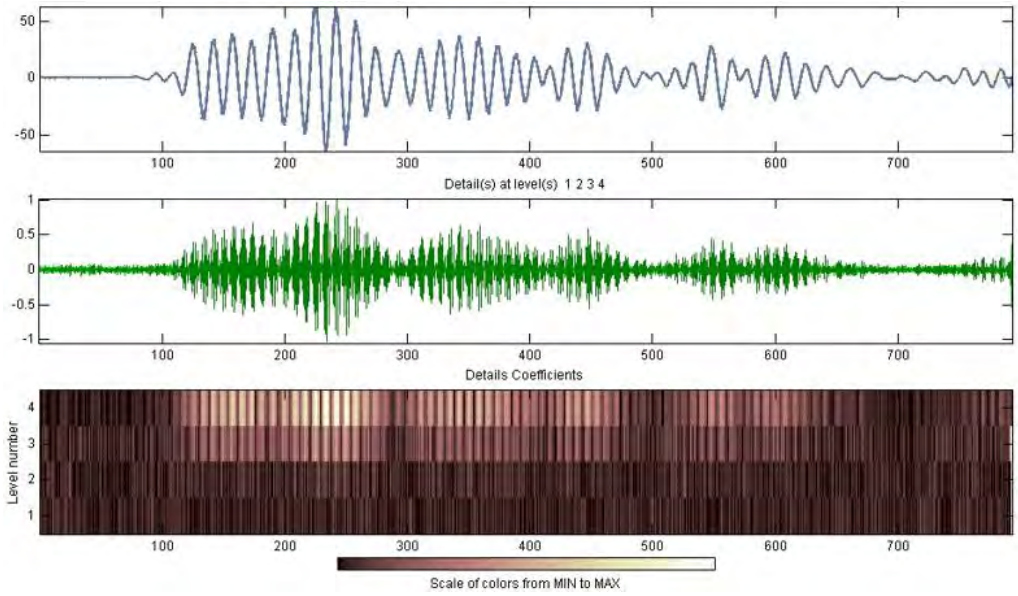


Fig. 12. Longitudinal signal approximation and detail coefficients for sand-excess concrete (30% sand)

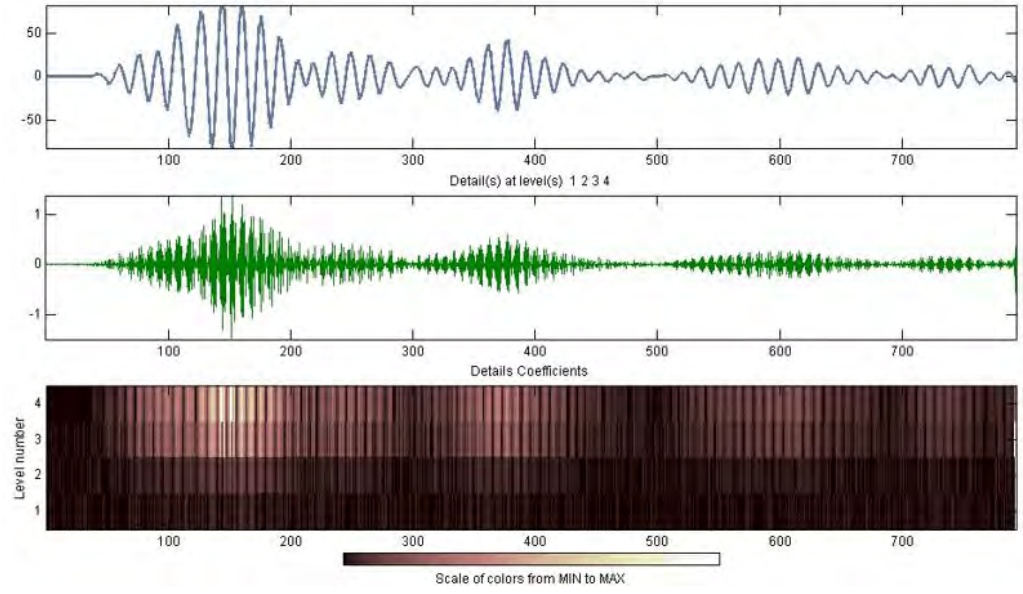


Fig. 13. Transverse signal approximation and detail coefficients for sand-excess concrete (30% sand)

This graphical representation (Fig. 12) shows a noticeable decrease in signal amplitude and a more irregular waveform. The detail coefficients are more spread out, especially from levels 1 to 3. The energy is distributed over a larger portion of the signal, reflecting unstable propagation and the presence of micro-defects. These observations are typical of a heterogeneous concrete, where the excess sand results in poor compaction and multiple interfaces that disturb wave travel.

This illustration (Fig. 13) shows the most pronounced effect of the defect. The signal is strongly attenuated from the beginning, with an asymmetric envelope and lower frequency content. The DWT coefficient distribution shows energy concentrated in a narrow time range (Time ≈ 100–200 μs), followed by a general weakening. This indicates strong energy absorption due to internal heterogeneity and significant scattering. This response is characteristic of a disorganized and porous structure. These observations confirm that excess sand significantly degrades ultrasonic wave transmission, and that this degradation is both visually and quantitatively detectable using the Discrete Wavelet Transform. Each figure clearly demonstrates the ability of this method to reveal the internal structure of concrete, highlighting differences in behavior depending on the propagation direction and the condition of the material.

3.4 Comparative Analysis with Existing Methods

The proposed methodology is contextualized within the broader landscape of wavelet-based signal processing techniques, with key distinctions highlighted against prior studies:

Machorro-Lopez et al. [21] employed continuous wavelet transforms (CWT) with Gaussian wavelets to analyze acoustic emission (AE) signals from concrete beams under flexural loading. Their approach focused on post-processing waveform data to compute wavelet energy (WE) for damage detection, identifying the Gaussian wavelet as optimal for capturing fracture-related features. In contrast, the present study utilizes discrete wavelet transforms (DWT) with Daubechies wavelets, emphasizing compositional defects rather than mechanical damage. By directly comparing decomposition coefficients between reference and sand-excess concrete, this work bypasses the need for energy-based metrics, offering a granular resolution of material heterogeneity.

Hu et al. [22] integrated wavelet packet transforms (WPT) with a hybrid genetic algorithm-backpropagation neural network (GA-BPNN) to classify concrete defects. While their method enhances anomaly detection accuracy through machine learning, it requires extensive training datasets and computational resources. This study, conversely, relies on coefficient-based statistical analysis, enabling defect identification without supervised learning, thus reducing complexity and improving scalability for real-time quality control.

Mousavi et al. [23] applied variational mode decomposition (VMD) to ultrasonic signals from wood samples, targeting physical defects such as voids and decay. Although their work shares a similar non-destructive testing framework, the focus diverges significantly: this research addresses material composition flaws (sand excess) rather than structural voids. The use of DWT here provides a more interpretable decomposition for quantifying constituent-related anomalies, which are less visually apparent than physical discontinuities.

- Methodological Distinction: Unlike CWT/WPT-based studies [21–22], this work leverages DWT's multi-resolution capabilities to isolate compositional defects through coefficient analysis, avoiding reliance on energy thresholds or machine learning.
- Application Scope: Expands ultrasonic testing beyond physical defect detection [23] to diagnose formulation errors, a critical advancement for preemptive quality assurance in concrete production.
- Practical Efficiency: The coefficient-driven approach reduces computational overhead compared to hybrid ML methods [22], aligning with industrial needs for rapid, on-site assessments.

4. Conclusions

This study establishes a wavelet-based framework for non-destructive identification of sand excess defects in concrete, leveraging multi-resolution analysis (MRA) to isolate compositional anomalies. Key findings demonstrate that ultrasonic signal redundancy and distribution patterns serve as robust indicators of material integrity:

- Signal Characterization: The reference concrete exhibited a recurrence of dominant index values (-32, 640, 32, 624), with approximately 70% concentrated within categories C1–C4, indicating a homogeneous microstructure. In contrast, the sand-rich concrete showed repeated values (31, 47), with around 60% falling within categories C7–C10. This distribution is attributed to

increased porosity and interfacial defects resulting from the breakdown of the aggregate–cement bond.

- Wavelet Decomposition: Discrete wavelet transform (DWT) with Daubechies wavelets distinguished defects through approximation coefficients (bulk properties) and detail coefficients (localized voids). Longitudinal signal superimposition revealed amplitude spikes, while transverse analysis highlighted attenuation, correlating with microstructural heterogeneity.
- Methodological Innovation: The coefficient-driven approach eliminates dependency on machine learning, reducing computational complexity and enabling real-time defect detection without extensive training datasets.

Diverging from prior studies focused on physical defects, this work targets formulation errors, advancing ultrasonic testing for preemptive quality control. The integration of MRA enhances sensitivity to subtle compositional deviations, offering a scalable alternative to destructive methods.

Future research should expand the signal database to encompass diverse defect types (aggregate deficiencies, water-cement ratio imbalances) and integrate adaptive algorithms for automated, real-time anomaly classification. Such advancements will further minimize manual intervention, aligning with industrial demands for efficient, high-precision structural.

Acknowledgement

The authors wish to express their gratitude to the team at the LCTP laboratory in Bouira, as well as to the technicians at the Civil Engineering Laboratory of the Faculty of Science and Applied Science at the Akli Mohand Oulhadj University of Bouira, for their support in this study.

References

[1] Rebai B, Benaddi H, Messas T, Salhi M. Evaluation of self-compacting concrete for concrete repair applications. Res. Eng. Struct. Mater., 2025; 11(2): 495-513. http://dx.doi.org/10.17515/resm2024.255st0423rs

[2] Kovler, K., & Roussel, N. (2011). Properties of fresh and hardened concrete. *Cement and Concrete Research*, *41*(7), 775-792. https://doi.org/10.1016/j.cemconres.2011.03.009

[3] Pedram, M., Taylor, S., Hamill, G., Robinson, D., OBrien, E. J., & Uddin, N. (2022). Experimental evaluation of heat transition mechanism in concrete with subsurface defects using infrared thermography. *Construction and Building Materials*, *360*, 129531. https://doi.org/10.1016/j.conbuildmat.2022.129531

[4] Joshaghani, A., & Shokrabadi, M. (2022). Ground penetrating radar (GPR) applications in concrete pavements. *International Journal of Pavement Engineering*, *23*(13), 4504-4531. https://doi.org/10.1080/10298436.2021.1954182

[5] Schabowicz, K. (2019). Non-destructive testing of materials in civil engineering. *Materials*, *12*(19), 3237. https://doi.org/10.3390/ma12193237

[6] Lin, Y., Lai, C. P., & Yen, T. (2003). Prediction of ultrasonic pulse velocity (UPV) in concrete. *Materials Journal*, *100*(1), 21-28. DOI: 10.14359/12459

[7] Kogbara, R. B., Iyengar, S. R., Grasley, Z. C., Masad, E. A., & Zollinger, D. G. (2015). Non-destructive evaluation of concrete mixtures for direct LNG containment. *Materials & Design*, *82*, 260-272. https://doi.org/10.1016/j.matdes.2015.05.084

[8] Ouahabi A. Digital signal and image processing series. Signal and image multiresolution analysis, 1st edition, London John Wiley-ISTE, 2012, ISBN 978-1848212572.

[9] Arbaoui, A., Ouahabi, A., Jacques, S., & Hamiane, M. (2021). Concrete cracks detection and monitoring using deep learning-based multiresolution analysis. *Electronics*, *10*(15), 1772. https://doi.org/10.3390/electronics10151772

[10] Guo, T., Zhang, T., Lim, E., Lopez-Benitez, M., Ma, F., & Yu, L. (2022). A review of wavelet analysis and its applications: Challenges and opportunities. *IEEe Access*, *10*, 58869-58903. https://doi.org/10.1109/ACCESS.2022.3179517

[11] Arbaoui, A., Ouahabi, A., Jacques, S., & Hamiane, M. (2021). Wavelet-based multiresolution analysis coupled with deep learning to efficiently monitor cracks in concrete. *Frattura ed Integrità Strutturale/Fracture and Structural Integrity*, *15*(58), 33-47. https://doi.org/10.3221/IGF-ESIS.58.03

[12] Testing hardened concrete - Part 1: Shape, dimensions and other requirements for test specimens and moulds. Standard EN 12390-1, (October 2001).

[13] Testing Hardened Concrete — Part 2: Making and Curing Specimens for Strength Tests. Standard EN 12390-2, (October 2001).

[14] Testing concrete in structures — Part 4: Determination of ultrasonic pulse velocity. Standard EN 12504-4, (July 2021).
[15] Charbit M, Blanchet G. Digital signal and image processing series. Digital signal and image processing using MATLAB, Volume 1: Fundamentals, 2nd Edition, London John Wiley-ISTE, July 2014, ISBN 978-1-118-99957-8.
[16] Hashmi, A. F., Shariq, M., & Baqi, A. (2022). Age-dependent strength assessment of low calcium fly ash concrete based on ultrasonic pulse velocity and rebound hammer number measurement. *Iranian Journal of Science and Technology, Transactions of Civil Engineering*, *46*(6), 4327-4341. https://doi.org/10.1007/s40996-022-00905-x
[17] OUAHABI A. traité signal et Image. Analyse Multirésolution pour le Signal et l'Image, IC2, Lavoisier Paris, 2012 : 35-46 , ISBN 978-2-7462-2394-3.
[18] Kang, L., Liu, G., Huang, J., & Li, J. (2022). Super-resolution method for MR images based on multi-resolution CNN. *Biomedical Signal Processing and Control*, *72*, 103372. https://doi.org/10.1016/j.bspc.2021.103372
[19] Arbaoui, A., Aribi, C., Boumaiza, M., Mohamadi, S., & Ait Ahmed, F. (2022, May). CNN-Based Concrete Cracks Detection Using Multiresolution Analysis. In *2022 7th International Conference on Image and Signal Processing and their Applications (ISPA)* (pp. 1-5). IEEE. https://doi.org/10.1109/ISPA54004.2022.9786328
[20] Luo, D., Li, Y., Luo, Z., & Han, C. (2023, July). Detection and analysis of hanging basket wire rope broken strands based on Mallat algorithm. In *International Conference on Neural Computing for Advanced Applications* (pp. 518-532). Singapore: Springer Nature Singapore. DOI: https://doi.org/10.1007/978-981-99-5844-3_38
[21] Mandala, S., Pratiwi Wibowo, A. R., Adiwijaya, Suyanto, Zahid, M. S. M., & Rizal, A. (2023). The effects of Daubechies wavelet basis function (DWBF) and decomposition level on the performance of artificial intelligence-based atrial fibrillation (AF) detection based on electrocardiogram (ECG) signals. *Applied Sciences*, *13*(5), 3036. https://doi.org/10.3390/app13053036
[22] Machorro-Lopez, J. M., Hernandez-Figueroa, J. A., Carrion-Viramontes, F. J., Amezquita-Sanchez, J. P., Valtierra-Rodriguez, M., Crespo-Sanchez, S. E., ... & Martinez-Trujano, L. A. (2023). Analysis of acoustic emission signals processed with wavelet transform for structural damage detection in concrete beams. *Mathematics*, *11*(3), 719. https://doi.org/10.3390/math11030719
[23] Hu, T., Zhao, J., Zheng, R., Wang, P., Li, X., & Zhang, Q. (2021). Ultrasonic based concrete defects identification via wavelet packet transform and GA-BP neural network. *PeerJ Computer Science*, *7*, e635. https://doi.org/10.7717/peerj-cs.635
[24] Mousavi, M., Taskhiri, M. S., & Gandomi, A. H. (2023). Standing tree health assessment using contact–ultrasonic testing and machine learning. *Computers and Electronics in Agriculture*, *209*, 107816. https://doi.org/10.1016/j.compag.2023.107816
[25] Amriou, A., et al. (2022). Effect of Gravel Content on Mechanical Performance and Porous Structure of Concrete. *Annales De Chimie-Science Des Materiaux, 46*(1), 19–25. https://doi.org/10.18280/acsm.460103.
[26] Borisiuk, E., & Kochenkova, E. (2022). An Effect of Sands of Different Grades on Structural and Mechanical Properties of Sand Concrete. *Solid State Phenomena, 335*, 151–157. https://doi.org/10.4028/p-8n0znm
[27] Lee, M. (2022). Concrete durability problems: physicochemical and transport mechanisms. *Elsevier eBooks*, 69–107. https://doi.org/10.1016/b978-0-12-824354-1.00003-9
[28] Sahni, H., & Bashar, N. (2024). Mechanical and durability characteristics of concrete utilizing waste foundry sand. *International Journal of Research in Engineering and Innovation, 8*(3), 114–119. https://doi.org/10.36037/ijrei.2024.8303
[29] Jadhav, A., et al. (2024). Influence of river sand and crushed sand on strength gain for M30 concrete. Futuristic Trends in Construction Materials & Civil Engineering Volume 3 Book 4. 2024; 3: 49-59. https://doi.org/10.58532/v3bice4p4ch1
[30] Chitour M, Khadraoui F, Mansouri K, Rebai B, Menasria A, Zemmouri A, Touati S, Boumediri H. A novel high order theory for static bending of functionally graded (FG) beams subjected to various mechanical loads. Res. Eng. Struct. Mater., 2024; 10(4): 1523-1539. http://dx.doi.org/10.17515/resm2024.141me0104rs
[31] Boutrid, A., Rebai, B., Mamen, B., Bouhadra, A., & Tounsi, A. (2024). Combined effect of temperature dependent material properties and boundary conditions on non-linear thermal stability of porous FG beams. *Acta Mechanica*, *235*(5), 2867-2887. https://doi.org/10.1007/s00707-024-03860-y
[32] Messas, T., Rebai, B., Mansouri, K., Chitour, M., Berkia, A., & Litouche, B. (2023). Analyzing vibration behavior of nano FGM (Si3N4/SUS304) plates: impact of homogenization models and nano parameters. J. Nano-Electron. Phys. 15 No 6, 06018 (2023). DOI: https://doi.org/10.21272/jnep.15(6).06018

Blank Page

Research on Engineering Structures & Materials
www.jresm.org

Research Article

Development and validation of an accurate analytical solution for hoop stress distribution in cylindrical functionally graded materials

Jamiatul Akmal [*,1,a], Adam Wisnu Murti [2,b], Asnawi Lubis [1,c], Masdar Helmi [3,d]

[1]*Dept. of Mechanical Eng., Universitas Lampung, Bandar Lampung 35145, Indonesia*
[2]*Dept. of Agricultural Technology, Politeknik Negeri Lampung, Bandar Lampung 35141, Indonesia*
[3]*Dept. of Civil Eng., Universitas Lampung, Bandar Lampung 35145, Indonesia*

Article Info

Article History:

Received 24 Mar 2025

Accepted 29 May 2025

Keywords:

Cylindrical FGM;
Analytical solution;
Stress distribution

Abstract

Functionally graded materials (FGMs) are a type of composite material whose microstructure is not homogeneous, differing at each coordinate position. The development of FGM material technology is an important and strategic effort to meet the needs of an increasingly advanced industry. Theoretically, an important topic that is commonly discussed for mechanical applications is the analytical solution of stress distribution in FGM materials subjected to mechanical loads. Previous studies have proposed a stress distribution solution in cylindrical FGM, but the solution is inaccurate in certain applications. Other studies propose stress distribution solutions, but with different boundary conditions. The present study proposes a new solution different from previous studies and valid for applying to cylindrical FGMs with more general inhomogeneity. The developed solution uses a power function to determine the inhomogeneity constant and applies internal pressure under axisymmetric conditions. The solution proposed in this study was validated through numerical simulations (FEM), and a good agreement is obtained with an error value of less than 2.77%. Moreover, the proposed solution shows good agreement with experimental data from previous studies.

© 2025 MIM Research Group. All rights reserved.

1. Introduction

One of the problems in industrial applications is the difficulty of obtaining products from a homogeneous material that meets all property requirements. For example, it isn't easy to produce pipes that are strong, corrosion-resistant, and heat-resistant at the same time using a homogeneous material. These properties can be obtained by combining the advantages of several different materials into a composite material. Such composite materials can be categorized as functionally graded materials (FGMs), whose microstructure differs at each coordinate position with a specific gradient. Different properties include Young's modulus, shear modulus, and density [1], [2]. FGM materials can be categorized as continuous degradation and layered degradation [3]. Examples of continuous degradation of FGM are bamboo [4] and bone [5], while examples of step degradation FGM are layered composite cylinders [6], [7]. With FGM technology, advantages can be obtained, for example, to reduce the intensity factor on the plane and lateral tensions, to obtain a more even distribution of tension, and to improve thermal performance [8], [9].

The development of FGM material technology includes various fields of study, such as raw materials, production processes, mechanical property analysis, and design methods [3]. FGM materials have been used in various fields of application, for example, in the construction of deep

*Corresponding author: jamiatul.akmal@eng.unila.ac.id
[a]orcid.org/0000-0002-5915-7681; [b]orcid.org/0009-0008-9521-9051; [c]orcid.org/0009-0004-7447-5145;
[d]orcid.org/0000-0001-6781-8948
DOI: http://dx.doi.org/10.17515/resm2025-777an0324rs

offshore oil and gas operations [10, 11], high-pressure vessels [12, 13], heat-resistant and corrosion-resistant pipes for geothermal power plants [14, 15], and reactor tubes in nuclear structures [16]. For the future, it is predicted that FGM materials will be increasingly needed due to technological advances in various industrial fields, but in this article, the discussion is limited to cylindrical structure FGM. Examples of previous studies include the static analysis of FGM cylindrical shells and the effects of stress concentration [17, 18], the vibration and stability of FGM cylindrical shells subjected to external pressures [19, 20], and the nonstationary response of stepped composite cylindrical shells with drop-off plies under moving random loads [21]. Recently, FGM laminated composite cylinders have been researched for the construction of submerged floating tunnel bridges (SFT-Bridges), which require strong, ductile, and corrosion-resistant structures [22-24].

Cylindrical FGM is commonly used in the industrial sector, for example, for pipes and pressure vessels. The properties of the modulus of elasticity are modeled as exponential equations, where the exponent is the degree of inhomogeneity (β). With an exponential equation, the value of the modulus of elasticity can be determined at each coordinate position. The value of the modulus of elasticity is assumed to vary as $E(r) = E_o r^{\beta}$ along the wall thickness. E_o is the stiffness on the outermost surface (r = 1), and β is the empirically determined inhomogeneity constant. An important theme discussed in this study is the equation of stress distribution at each point along the radial axis. Previously, the exact solution had been published by [25], who used mathematical methods to obtain an exact solution for stress distribution in cylinders. The solution was developed from a boundary condition where there was only internal pressure on the inner surface of the cylinder. The article [25] presents the results of radial stress distribution and circumferential stress distribution, as well as the influence of variations in the modulus of elasticity of materials on the distribution of stress.

The problem is that the hoop stress equation proposed by [25] is only valid for β=1, but not for other β values. In addition, the article does not explain in detail the process of developing the equation, making it difficult to understand. Twenty years later, [26] made a new proposal for a stress distribution analytical solution in cylindrical FGM. However, this proposal does not precisely address the existing problems because the solutions developed are based on different boundary conditions. The boundary conditions include: (first) internal pressure applied on the inner surface and tension applied on the outer surface; (second) fixed displacement applied on the inner surface and tension on the outer surface; and (third) internal pressure applied on the inner surface and fixed displacement on the outer surface. Nevertheless, the research in [26] provides a more detailed explanation of the equation development process, making it easier to follow.

This study proposes a new equation for the distribution of hoop stress in cylindrical FGMs with varying inhomogeneity constants (-2 < β < 2). The solution is developed from the boundary conditions: internal pressure is applied on the inner surface, while no pressure or constraint is applied on the outer surface, as done by [25], and it adopts the method proposed by [26]. The stress distribution equation obtained in this study is different from that proposed by [25] and [26]. Furthermore, this solution has been compared with FEM and experimental results, where the experimental study refers to the research conducted by [27]. From the comparative study, it can be seen that the proposed analytical solution shows good agreement with FEM with an error value of less than 2.77%. In addition, this equation was also validated with experiments. This research has been partially presented at a conference [28], and in this article, it is presented in more detail and comprehensively.

2. Model and Analytical Solution

Figure 1 displays the FGM cylinder model with radial coordinates $\bar{r}$ and displacement coordinates $\bar{u}$. R_o represents the outermost radius of the cylinder, and its coordinate is defined in Equation (1).

$$r = \bar{r}/R_o\,, \quad u = \bar{u}/R_o \tag{1}$$

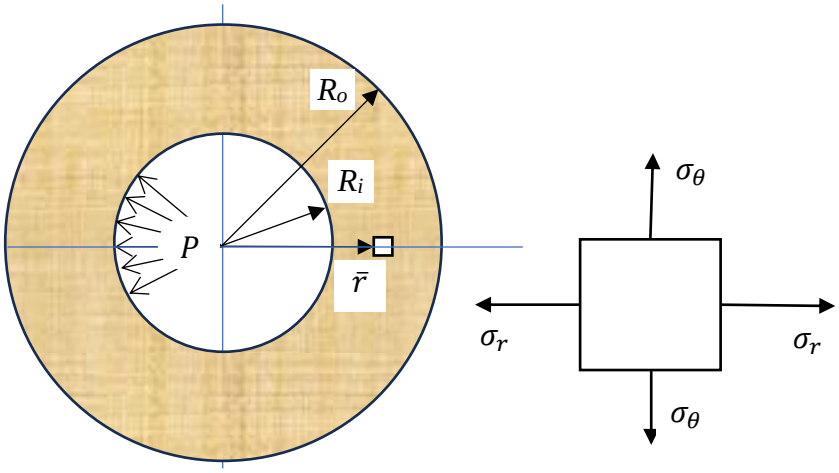


Fig. 1. FGM cylinder cross-section and its coordinate system

Radial strains and hoop strains are analyzed under the plane-strain assumption, so the equilibrium equation is given as shown in Equation (2) [25], [26], [28].

$$\varepsilon_\theta = \varepsilon_\phi = \frac{u}{r} \quad \varepsilon_r = \frac{du}{dr}, \quad \gamma_{r\theta} = \gamma_{r\phi} = \gamma_{\theta\phi} = 0 \tag{2}$$

The material is assumed to be isotropic, with a constant Poisson's ratio and a radially varying Young's modulus. Using the power function, the value of elasticity in radius variation can be seen in Equation (3) [25]. E_o is the value of Young's modulus on the outermost surface ($r/R_o = 1$), and β is the gradient constant of inhomogeneity.

$$E(r) = E_o r^\beta \tag{3}$$

The constitutive equation can be seen in Equation (4) and Equation (5).

$$\sigma_r = C_{11}\varepsilon_r + C_{12}\varepsilon_\theta, \quad \sigma_\theta = C_{12}\varepsilon_r + C_{11}\varepsilon_\theta + C_{12}\varepsilon_\phi \tag{4}$$

Here,

$$C_{11} = c_{11}r^\beta = \left(\frac{E_o(1-v)}{(1+v)(1-2v)}\right)r^\beta, \quad C_{12} = c_{12}r^\beta = \left(\frac{E_o v}{(1+v)(1-2v)}\right)r^\beta \tag{5}$$

The non-trivial equilibrium is Equation (6), and radial displacement is Equation (7).

$$\frac{d\sigma_r}{dr} + \frac{\sigma_r - \sigma_\theta}{r} = 0 \tag{6}$$

$$r^2u'' + (\beta+1)ru' + (v^*\beta - 1)u = 0 \tag{7}$$

The symbol v^* is a simplified form of the Poisson's ratio, where $v^* = v/(1-v)$. Equation (7) can be solved using the second-order Cauchy–Euler equation, assuming the solution as shown in Equation (8). The characteristics of the equation and its roots are given in Equations (9) and (10), respectively.

$$u = r^m, \quad \frac{du}{dr} = mr^{m-1}, \quad \frac{d^2u}{dr^2} = m(m-1)r^{m-2} \tag{8}$$

$$m^2 + \beta m + (v^*\beta - 1) = 0 \tag{9}$$

$$m_1 = \frac{1}{2}\left(-\beta - \sqrt{\beta^2 - 4(v^*\beta - 1)}\right), \qquad m_2 = \frac{1}{2}\left(-\beta + \sqrt{\beta^2 - 4(v^*\beta - 1)}\right) \tag{10}$$

To solve for the variable m, there are three conditions based on the Cauchy-Euler formula. These conditions are as follows [26].

- The values m_1 and m_2 are real and different ($m_1 \neq m_2$); then the solution is as seen in Equation (11).

$$u = Ar^{m_1} + Br^{m_2} \tag{11}$$

- The values m_1 and m_2 are real and equal ($m_1 = m_2 = m$); then the solution is as seen in Equation (12).

$$u = (A + B\,ln\,r)r^m \tag{12}$$

- The values m_1 and m_2 are imaginary ($m_1 = x + yi, m_2 = x - yi$); then the solution is as seen in Equation (13).

$$u = (A\,cos(y\,ln\,r) + B\,sin(y\,ln\,r))r^x \tag{13}$$

Since the material has a Poison value ratio of $0 < v < 0.5$, then $0 < v^* < 1$, and $0 < v^{*2} < 1$. Thus, the value of the square under the root sign in equation (10) is as seen in Equation (14).

$$\Delta = \beta^2 - 4(v^*\beta - 1) = (\beta^2 - 2v^*)^2 + 4(1 - v^{*2}) > 0 \tag{14}$$

The values A and B are parameters that depend on two boundary conditions [25]:

- (1) Boundary condition 1: On the inner surface of the cylinder, internal pressure, P, is applied as seen in Equation (15).
- (2) Boundary condition 2: On the outer surface of the cylinder, no pressure is applied, as seen in Equation (16).

$$\textit{Boundary condition 1: } \sigma_r\left(\frac{R_i}{R_o}\right) = -P$$
$$\varepsilon_r = m_1 A\left(\frac{R_i}{R_o}\right)^{m_2-1} + m_2 B\left(\frac{R_i}{R_o}\right)^{m_2-1}; \quad \varepsilon_\theta = A\left(\frac{R_i}{R_o}\right)^{m_1-1} + B\left(\frac{R_i}{R_o}\right)^{m_2-1} \tag{15}$$

$$\textit{Boundary condition 2: } \sigma_r\left(\frac{R_o}{R_o}\right) = 0$$
$$\varepsilon_r = m_1 A + m_2 B; \qquad \varepsilon_\theta = A + B \tag{16}$$

Parameter A and parameter B can be obtained in the following stages:

- Determine parameter B by eliminating parameter A from boundary condition 1 and boundary condition 2.

From boundary condition 1: Substitute Equation (4) into Equation (15) as seen in Equation (17).

$$\begin{aligned} -P &= C_{11}\varepsilon_r + C_{12}\varepsilon_\theta \\ -P &= \left(\frac{E_o(1-v)}{(1+v)(1-2v)}\right)\left(\frac{R_i}{R_o}\right)^{\beta}\left(m_1 A\left(\frac{R_i}{R_o}\right)^{m_1-1} + m_2 B\left(\frac{R_i}{R_o}\right)^{m_2-1}\right) \\ &\quad + \left(\frac{E_o v}{(1+v)(1-2v)}\right)\left(\frac{R_i}{R_o}\right)^{\beta}\left(A\left(\frac{R_i}{R_o}\right)^{m_1-1} + B\left(\frac{R_i}{R_o}\right)^{m_2-1}\right) \end{aligned} \tag{17}$$

Suppose:

$$X = \left(\frac{E_o(1-v)}{(1+v)(1-2v)}\right), and Y = \left(\frac{E_o v}{(1+v)(1-2v)}\right) \tag{18}$$

Arrange Equation (17) into Equation (19).

$$\begin{aligned} -P &= X\left(\frac{R_i}{R_o}\right)^{\beta} m_1 A\left(\frac{R_i}{R_o}\right)^{m_1-1} + X\left(\frac{R_i}{R_o}\right)^{\beta} m_2 B\left(\frac{R_i}{R_o}\right)^{m_2-1} + Y\left(\frac{R_i}{R_o}\right)^{\beta} A\left(\frac{R_i}{R_o}\right)^{m_1-1} + \\ & Y\left(\frac{R_i}{R_o}\right)^{\beta} B\left(\frac{R_i}{R_o}\right)^{m_2-1} \\ &= \left(X\left(\frac{R_i}{R_o}\right)^{\beta} m_1\left(\frac{R_i}{R_o}\right)^{m_1-1} + Y\left(\frac{R_i}{R_o}\right)^{\beta}\left(\frac{R_i}{R_o}\right)^{m_1-1}\right)A + \left(X\left(\frac{R_i}{R_o}\right)^{\beta} m_2\left(\frac{R_i}{R_o}\right)^{m_2-1} + \right. \\ & \left. Y\left(\frac{R_i}{R_o}\right)^{\beta}\left(\frac{R_i}{R_o}\right)^{m_2-1}\right)B \end{aligned} \tag{19}$$

Parameter A can be obtained as seen in Equation (20).

$$-A = \frac{P\left(\frac{R_i}{R_o}\right)^{1-\beta}(1+v)(1-2v) + (E_o(1-v)m_2 + E_o v)\left(\frac{R_i}{R_o}\right)^{m_2} B}{(E_o(1-v)m_1 + E_o v)\left(\frac{R_i}{R_o}\right)^{m_1}} \tag{20}$$

From the boundary condition 2: Substitute Equation (4) into Equation (16) as seen in Equation (21).

$$0 = C_{11}\varepsilon_r + C_{12}\varepsilon_\theta \tag{21}$$

We obtain Equation (22) by assuming X and Y as written in Equation (18).

$$\begin{aligned} 0 &= Xm_1A + Xm_2B + YA + YB \\ &= (Xm_1 + Y)A + (Xm_2 + Y)B \end{aligned} \tag{22}$$

Parameter A can be obtained as seen in Equation (23).

$$A = \frac{-B(E_o(1-v)m_2 + E_o v)\left(\frac{R_i}{R_o}\right)^{m_1}}{(E_o(1-v)m_1 + E_o v)\left(\frac{R_i}{R_o}\right)^{m_1}} \tag{23}$$

Parameter B can be obtained by eliminating parameter A by adding Equation (20) and Equation (23), as seen in Equation (24).

$$B = \frac{P\left(\frac{R_i}{R_o}\right)^{1-\beta}(1+v)(1-2v)}{E_o\left(\left(\frac{R_i}{R_o}\right)^{m_1} - \left(\frac{R_i}{R_o}\right)^{m_2}\right)(v+(1-v)m_2)} \tag{24}$$

- Determine parameter A by eliminating parameter B from boundary condition 1 and boundary condition 2.

Similar to point (1), from boundary condition 1 and boundary condition 2, parameter B is obtained as seen in Equation (25) and Equation (26), respectively.

$$-B = \frac{P\left(\frac{R_i}{R_o}\right)^{1-\beta}(1+v)(1-2v) + (E_o(1-v)m_1 + E_o v)\left(\frac{R_i}{R_o}\right)^{m_1} A}{(E_o(1-v)m_2 + E_o v)\left(\frac{R_i}{R_o}\right)^{m_2}} \tag{25}$$

$$B = \frac{-A(E_o(1-v)m_1 + E_o v)\left(\frac{R_i}{R_o}\right)^{m_2}}{(E_o(1-v)m_2 + E_o v)\left(\frac{R_i}{R_o}\right)^{m_2}} \tag{26}$$

Parameter A is obtained by eliminating parameter B by adding Equation (25) and Equation (26), as seen in Equation (27).

$$A = -\frac{P\left(\frac{R_i}{R_o}\right)^{1-\beta}(1+v)(1-2v)}{E_o\left(\left(\frac{R_i}{R_o}\right)^{m_1}-\left(\frac{R_i}{R_o}\right)^{m_2}\right)(v+(1-v)m_1)} \quad (27)$$

From Equation (4), radial stress can be determined as shown in Equation (28). By substituting parameter A as defined in Equation (27) and parameter B as defined in Equation (24), the radial stress is obtained as shown in Equation (29).

$$\sigma_r = C_{11}\varepsilon_r + C_{12}\varepsilon_\theta, \\ = \left(\frac{E_o(1-v)}{(1+v)(1-2v)}\right) r^\beta (m_1 A r^{m_1-1} + m_2 B r^{m_2-1}) + \left(\frac{E_o v}{(1+v)(1-2v)}\right) r^\beta (A r^{m_1-1} + B r^{m_2-1}) \quad (28)$$

$$\sigma_r = \frac{P\left(\frac{R_i}{R_o}\right)^{1-\beta}(r^{m_1}-r^{m_2})r^{\beta-1}}{\left(\frac{R_i}{R_o}\right)^{m_1}-\left(\frac{R_i}{R_o}\right)^{m_2}} \quad (29)$$

Similarly, from Equation (4), hoop stress can be determined as seen in Equation (30). By substituting parameter A as written in Equation (27) and parameter B as written in Equation (24), the hoop stress is obtained as seen in Equation (31). The simple form is as written in Equation (32), where χ_1 and χ_2 are as stated by Equation (33).

$$\sigma_\theta = C_{12}\varepsilon_r + C_{11}\varepsilon_\theta \\ = \left(\frac{E_o v}{(1+v)(1-2v)}\right) r^\beta (m_1 A r^{m_1-1} + m_2 B r^{m_2-1}) \\ + \left(\frac{E_o(1-v)}{(1+v)(1-2v)}\right) r^\beta (A r^{m_1-1} + B r^{m_2-1}) \quad (30)$$

$$\sigma_\theta = \frac{Pr^{m_1}\big(vm_1+(1-v)\big)(m_2(v-1)-1)\left(\frac{R_i}{R_o}\right)^{1-\beta} r^{\beta-1} - Pr^{m_2}\big(vm_2+(1-v)\big)(m_1(v-1)-1)\left(\frac{R_i}{R_o}\right)^{1-\beta} r^{\beta-1}}{(m_1(v-1)-1)(m_2(v-1)-1)\left(\left(\frac{R_i}{R_o}\right)^{m_1}-\left(\frac{R_i}{R_o}\right)^{m_2}\right)} \quad (31)$$

$$\sigma_\theta = \frac{\left(\frac{R_i}{R_o}\right)^{1-\beta} r^{\beta-1}(\chi_1-\chi_2)}{(m_1(v-1)-v)(m_2(v-1)-v)\left(\left(\frac{R_i}{R_o}\right)^{m_1}-\left(\frac{R_i}{R_o}\right)^{m_2}\right)} \quad (32)$$

$$\chi_1 = Pr^{m_2}\big(vm_2+(1-v)\big)(m_1(v-1)-v) \\ \chi_2 = Pr^{m_1}\big(vm_1+(1-v)\big)(m_2(v-1)-v) \quad (33)$$

3. Results and Discussion

The analytical solution proposed in the present study will be validated by comparing FEM and experimental analysis. In the FEM analysis, the cylinder is assumed to be an axisymmetric plane stress by creating layers of material with different stiffness, as has been done in a previous study [28]. Each layer has a thickness value of $(0.6 < {}^{r}/_{R_o} < 1)$ which refers to previous research [25].

The radial and hoop stress distributions are shown for each general inhomogeneity constant ($-2 < \beta < 2$). Meanwhile, the validation of the present study against experimental studies is by comparing it with previous research [27], which performed experiments on thick-walled cylinders by applying internal pressure caused by the penetration of a tapered cylinder.

3.1. FEM Validation

The finite element model developed in this study refers to the work of Gashemi [29], as presented in Table 1. The simulation employs the PLANE183 element type, with material properties defined by Young's modulus (E) and Poisson's ratio (v). Incorporates a quadrilateral mesh configuration with axisymmetric behavior and internal pressure in the FEM model was applied as a surface load. Figure 2 presents the model along with the corresponding meshing results.

Table 1. Model and **p**arameters [29].

Parameters	Symbol	Value	Unit
Internal Pressure	P	7	MPa
Inner Radius	R_i	30	mm
Outer Radius	R_o	50	mm
Inhomogeneity Constanta	β	-2, -1, 0, 1, 2	-
Poisson's Ratio	ν	0.3	-
Young's Modulus	E	72	GPa

Convergence tests have been conducted to evaluate the effect of the number of cylindrical layers on the stability of the stress values, as shown in Figure 3. The results indicate that convergence begins at a layer count of n = 20, but a more precise data stability occurs at n = 160. A comparison of the stress values from FEM in this study against reference studies can be seen in Table 2, with a maximum error rate of 4.32% for hoop stress. These results indicate that the accuracy of the FEM method in this study can be considered sufficient.

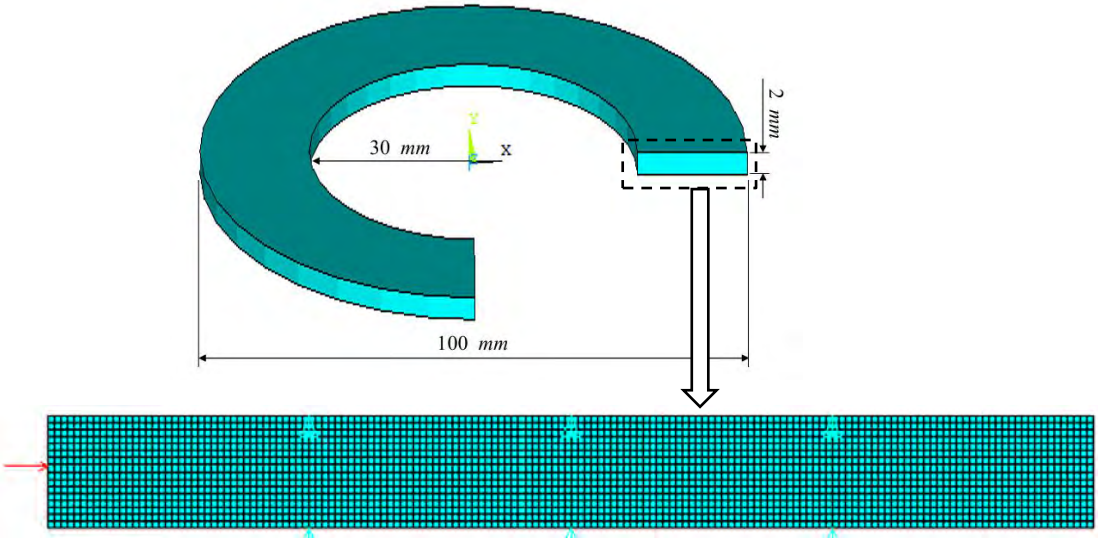


Fig. 2. The model, along with the corresponding meshing results

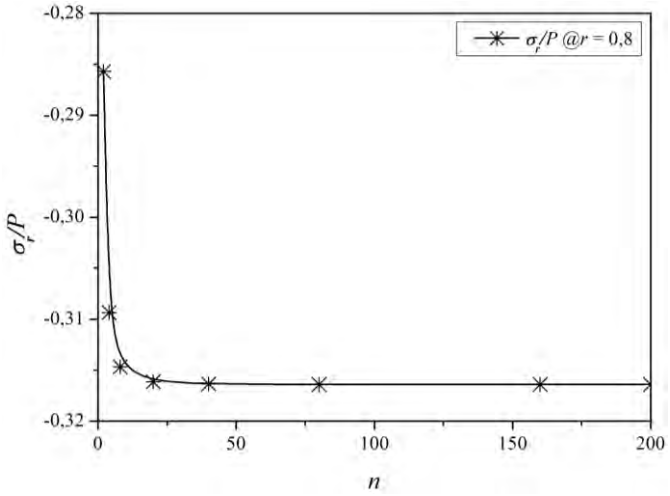


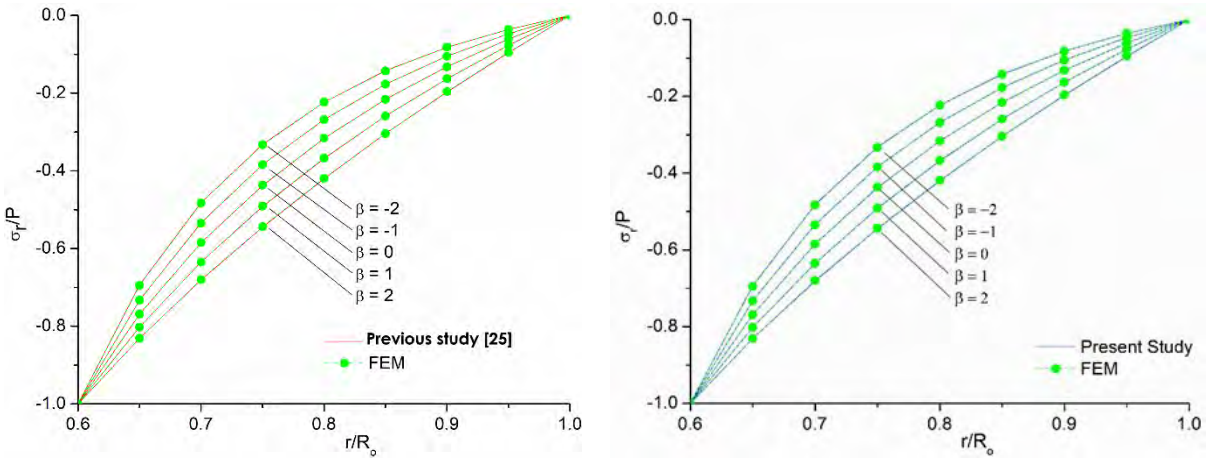
Fig. 3. Convergence Behavior of Stress Values to the Number of Cylinder Layers (n)

The next step is to validate the analytical solution developed in the present study against the FEM simulation results. The important themes discussed are radial and hoop stress distribution for general inhomogeneity constants. For radial stress, the solution previously proposed by [25] is the

same as the solution in the present study, as seen in Figures 4(a) and 4(b). Both solutions are valid when compared to FEM analysis; thus, there are no issues with these solutions and they are not important to discuss further. However, the problem is that the hoop stress distribution solution proposed by [25] is invalid when compared to the FEM analysis, as seen in Figure 5(a). For this reason, a new solution is proposed in the present study and proven to be valid for all inhomogeneity constants ($-2 < \beta < 2$), as can be seen in Figure 5(b).

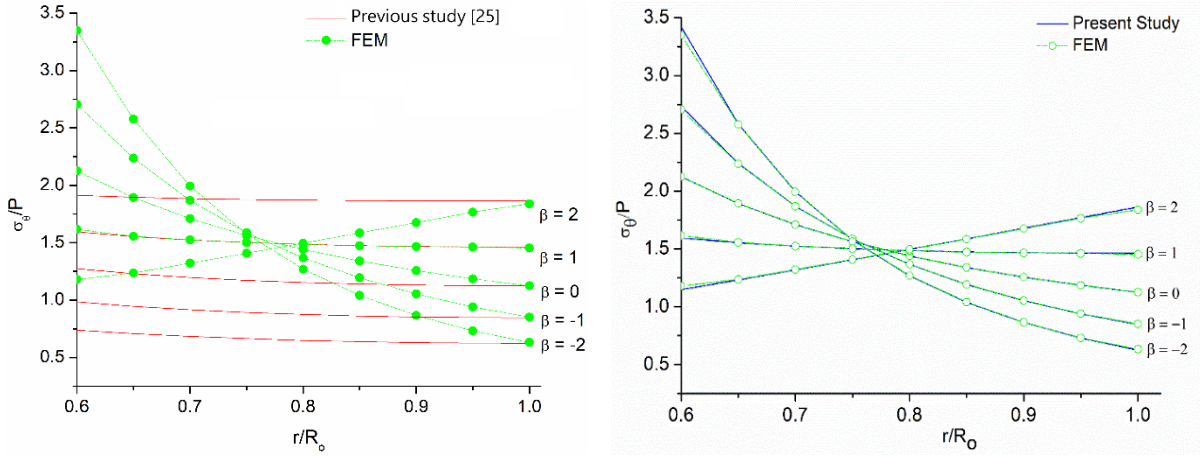
Table 2. A comparison of the stress values from FEM in this study against reference studies.

r/R_0	Present Study		Ghasemi[29]		Error (%)	
	σ_r/P	σ_θ/P	σ_r/P	σ_θ/P	σ_r/P	σ_θ/P
0.60	-0.9971	1.6757	-1.0000	1.6160	0.2857	3.6952
0.65	-0.8000	1.6243	-0.8020	1.5570	0.2494	4.3215
0.70	-0.6343	1.5857	-0.6350	1.5250	0.1125	3.9813
0.75	-0.4914	1.5571	-0.4910	1.5020	0.0873	3.6713
0.80	-0.3671	1.5357	-0.3670	1.4860	0.0389	3.3455
0.85	-0.2586	1.5200	-0.2590	1.4740	0.1655	3.1208
0.90	-0.1629	1.5100	-0.1630	1.4670	0.0876	2.9312
0.95	-0.0771	1.5029	-0.0770	1.4630	0.1855	2.7243
1.00	0.0000	1.4257	0.0000	1.4540	0.0000	1.9500



(a) (b)

Fig. 4. Validation of radial stress to FEM (a) Previous study [25], (b) Present study



(a) (b)

Fig. 5. Validation of hoop stress to FEM (a) Previous study [25], (b) Present study

Several noteworthy observations indicate that stress distribution can be effectively controlled through engineered material gradation using FGMs [30]; in particular, for hoop stress in FGM cylinders, a more uniform hoop stress distribution can be achieved, especially when the value of β equals 1 [31]. A recent numerical investigation by [32] also demonstrated that variations in the inhomogeneity parameter and Poisson's ratio significantly influence the thermoelastic stress and displacement fields in rotating thick-walled FGM cylinders, reinforcing the importance of accurate modeling in pressure vessel design under coupled mechanical and thermal loads

3.2. Experimental Validation

Experimental validation refers to previous research [27], with equipment as seen in Figure 6. Radial and hoop stresses are measured at several points on a cylinder made of homogeneous material (inhomogeneity constant $\beta = 0$). The penetration of a tapered cylinder results in pressure on the inner surface of the cylinder, which is considered to represent internal pressure. Several strain gauges were installed at the appropriate points and orientations to measure the radial and hoop strain within the range of $R_i = 90.5$ mm to $R_o = 140.5$ mm.

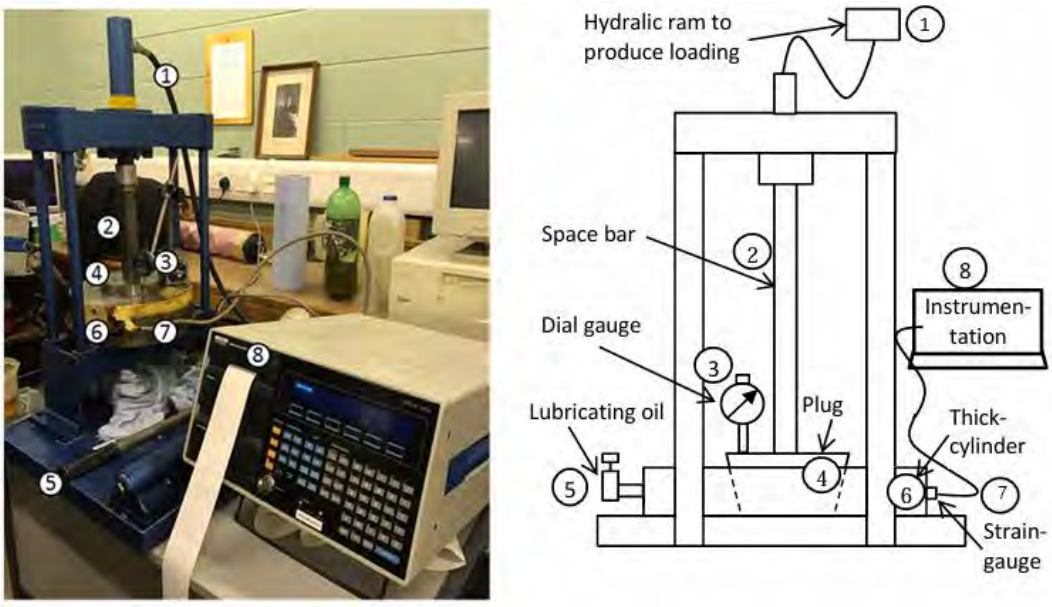


Fig. 6 Equipment used for the experiment and a schematic drawing showing all the parts of the apparatus and their interconnections [27]

Table 3. The strain gauge readings for variations in penetration depth

Penetration depth (mm)	0.96	1.92	2.64	3.26	4.48
Channel no.	Strain gauge readings				
1	-11	-30	-44	-55	-80
3	-16	-41	-61	-77	-111
5	-25	-55	-79	-99	-144
7	-30	-78	-117	-151	-220
9	-37	-110	-200	-264	-334
11	53	110	155	198	271
13	61	128	180	227	312
15	69	149	210	265	366
17	77	178	251	317	439
19	94	222	313	398	551

Table 3 shows the strain gauge readings for variations in penetration depth. In the experiment, channels 1, 3, 5, 7, and 9 are strain gauges used to measure radial stress, while channels 11, 13, 15, 17, and 19 are strain gauges used to measure hoop stress. For ease of understanding, the data in

Table 3 is rearranged to show the radial strain and hoop strain values at variations in radius values, respectively, as shown in Table 4.

Table 4. The radial strain and hoop strain values at variations in radius values

r (mm)	Types of strain gauges	Strain gauge readings on each space bar penetration (μm)				
		0.96 mm	1.92 mm	2.64 mm	3.26 mm	4.48 mm
90.5	ε_r	-37	-110	-200	-264	-334
	ε_θ	94	222	313	398	551
103.0	ε_r	-30	-78	-117	-151	-220
	ε_θ	77	178	251	317	439
115.5	ε_r	-25	-55	-79	-99	-144
	ε_θ	69	149	210	265	366
128.0	ε_r	-16	-41	-61	-77	-111
	ε_θ	61	128	180	227	312
140.5	ε_r	-11	-30	-44	-55	-80
	ε_θ	53	110	155	198	271

Radial stress is calculated by Equation (34), and hoop stress is calculated by Equation (35). Table 5 shows radial and hoop stress variations at radius (r) values.

$$\sigma_r = \frac{E}{1-v^2}(\varepsilon_r + v\varepsilon_\theta) \tag{34}$$

$$\sigma_\theta = \frac{E}{1-v^2}(\varepsilon_\theta + v\varepsilon_r) \tag{35}$$

Table 5. Radial and hoop stress at radius (r) values variations

r (mm)	Stress orientation	Stress value on each space bar penetration (MPa)				
		0.96 mm	1.92 mm	2.64 mm	3.26 mm	4.48 mm
90.5	σ_r	-2.011	-9.920	-24.251	-33.051	-38.560
	σ_θ	18.949	43.200	57.829	72.869	103.040
103	σ_r	-1.577	-5.623	-9.531	-12.777	-20.183
	σ_θ	15.543	35.337	49.349	62.103	85.257
115.5	σ_r	-0.983	-2.354	-3.657	-4.457	-7.817
	σ_θ	14.057	30.286	42.583	53.783	73.783
128	σ_r	0.526	-0.594	-1.600	-2.034	-3.977
	σ_θ	12.846	26.446	36.960	46.606	63.703
140.5	σ_r	1.120	0.686	0.571	1.006	0.297
	σ_θ	11.360	23.086	32.411	41.486	56.457

Table 6. The equivalent internal pressures

Space bar penetration (mm)	Internal Pressure (MPa)
0.96	3.13
1.92	15.15
2.64	40.05
3.26	55.40
4.48	61.65

The next step is to convert the depth of penetration of the space bar into internal pressure, assuming that the radial stress on the inner surface is equal to the internal pressure. The equivalence between the penetration depth of the space bar and the internal pressure is obtained from the regression process and is assumed to be a 2nd-order polynomial, as shown in Table 6.

Thus, the radial stress and hoop stress distribution graphs can be plotted with equivalent internal pressure, as shown in Figures 7, 8, 9, 10, and 11.

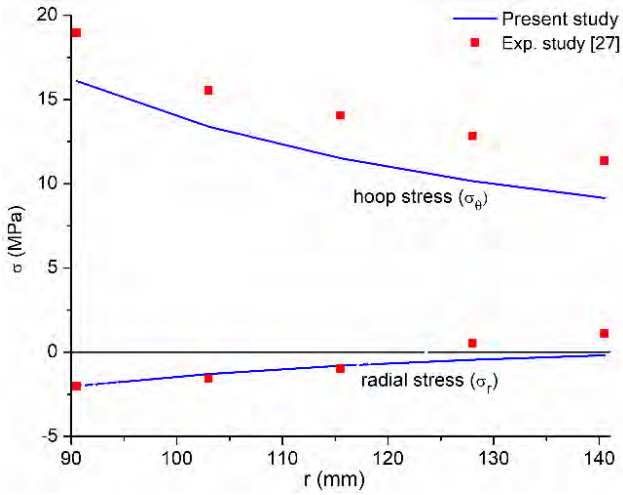


Fig. 7. Radial and hoop stress with a penetration of the space bar of 0.96 mm (P = 3.13 MPa)

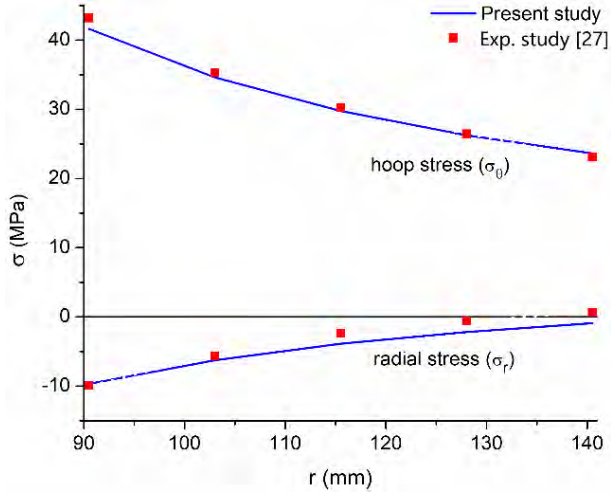


Fig. 8. Radial and hoop stress with a penetration of the space bar of 1.92 mm (P = 15.15 MPa)

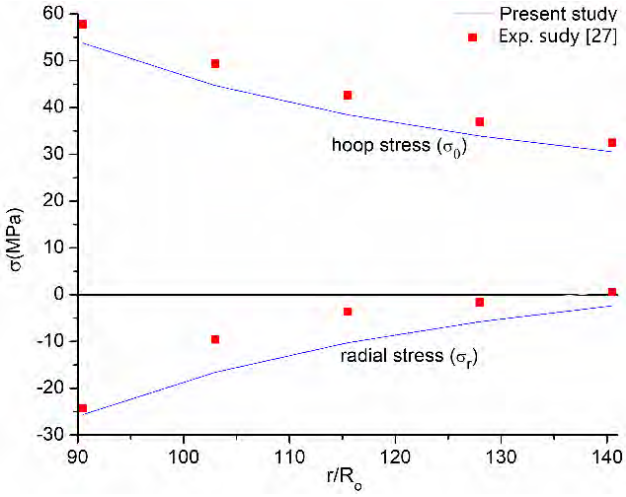


Fig. 9. Radial and hoop stress with a penetration of the space bar of 2.64 mm (P = 40.05 MPa)

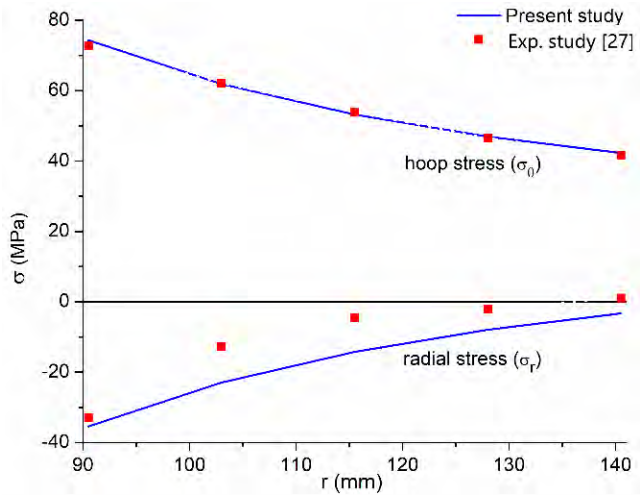


Fig. 10. Radial and hoop stress with a penetration of the space bar of 3.26 mm (P = 55.40 MPa)

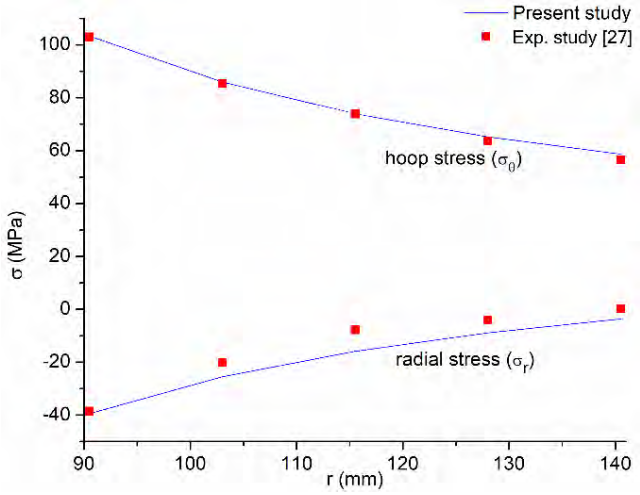


Fig. 11. Radial and hoop stress with a penetration of the space bar of 4.48 mm (P = 61.65 MPa)

The experimental validation conducted in this study has confirmed the reliability of the proposed analytical solution, although only in the homogeneous case (β = 0). For other values of β, further investigation remains to be conducted in the future. Additionally, the feasibility of using the tapered cylindrical penetration technique to simulate internal pressure in thick-walled cylinders has been acknowledged, as also reported by [33]. This approach is particularly valuable when direct pressurization is not practical, either technically or economically. Regression analysis, which links the depth of penetration with the equivalent internal pressure through a second-order polynomial, allows for the practical translation of experimental displacement measurements into stress conditions within the analytical domain. This mapping is crucial for bridging the gap between physical testing and theoretical modeling.

4. Conclusions

The use of functionally graded materials (FGMs) offers a strategic solution to meet the demands of modern industry, owing to their customizable nature that allows for specific property requirements in engineering applications. Previous researchers have proposed analytical solutions for stress distribution in the radial direction, but those solutions are not accurate for general inhomogeneity constants. The present study introduces a more accurate analytical solution to overcome these limitations. In this formulation, the characteristics of material inhomogeneity are defined using a power function, and internal pressure is applied under axisymmetric conditions.

The analytical solution in this present study has been validated with the finite element method (FEM) model, with a maximum error of less than 2.77%. The FEM model was created with sizes

and parameters referring to previous similar studies. The type of element used is PLANE183, defining material properties based on elastic modulus and Poisson's ratio. The model is divided into 160 layers based on convergence testing. The FEM results obtained have been consistent and valid compared to previous reference comparisons and are considered suitable for use. Furthermore, the validation of the experimental study also shows the accuracy of the proposed analytical solution, although it is limited only to homogeneous materials with an inhomogeneity constant β equal to zero. It is important to acknowledge that experimental validation for materials with non-zero β values has not been conducted, and further research is needed for the future.

The main contribution of this research lies in the specific boundary conditions: internal pressure is applied to the inner surface while the outer surface remains pressure-free. Caution should be emphasized when extending the application beyond these conditions. To strengthen the analysis, several previous studies involving FGM under various loading conditions have been reviewed to highlight the novelty and relevance of this work in advancing the analytical approach for graded materials. The proposed solution provides a reliable and practical framework for the design and evaluation of FGM cylinders, particularly in high-pressure applications where material gradation has a significant impact on structural behavior. Future research is expected to extend the experimental validation to a wider range of β values and investigate more complex boundary conditions, thus improving the general applicability of the developed analytical model.

Acknowledgement

The authors would like to acknowledge the support provided by Universitas Lampung through the Professorship Grant 2024, under Contract No. 539/UN26.21/PN/2024, dated April 24, 2024.

List of Notations

Symbol	Description	Unit
r	Radial coordinate	-
R_i	Inner radius of the cylinder	mm
R_o	Outer radius of the cylinder	mm
$u(r)$	Radial displacement as a function of r	-
σ_r	Radial stress	MPa
σ_θ	Hoop (circumferential) stress	MPa
$E(r)$	Young's modulus as a function of r	GPa
v	Poisson's ratio (assumed constant)	-
β	Inhomogeneity constant	-
A, B	Constants determined by boundary conditions	-
P	Internal pressure applied to the inner surface	MPa
ε_r	Radial strain	-
ε_θ	Hoop (circumferential) strain	-

References

[1] Karamanli A, Vo TP. Size-dependent behaviour of functionally graded sandwich microbeams based on the modified strain gradient theory. Composite Structures. 2020;246:112401. https://doi.org/10.1016/j.compstruct.2020.112401

[2] Mathew C, Ejiofor O. Mechanics and computational homogenization of effective material properties of functionally graded (composite) material plate FGM. Int J Sci Res Publ. 2023;13(9):128-50. https://doi.org/10.29322/IJSRP.13.09.2023.p14120

[3] El-Galy IM, Saleh BI, Ahmed MH. Functionally graded materials classifications and development trends from industrial point of view. SN Appl Sci. 2019;1(11):1378. doi:10.1007/s42452-019-1413-4. https://doi.org/10.1007/s42452-019-1413-4

[4] Wen Z, Li M. Compressive properties of functionally graded bionic bamboo lattice structures fabricated by FDM. Materials. 2021;14(16):4410. https://doi.org/10.3390/ma14164410

[5] Petit C, Montanaro L, Palmero P. Functionally graded ceramics for biomedical application: Concept, manufacturing, and properties. Int J Appl Ceram Technol. 2018;15(4):820-40. https://doi.org/10.1111/ijac.12878

[6] Jung W-Y, Han S-C. Transient analysis of FGM and laminated composite structures using a refined 8-node ANS shell element. Compos Part B Eng. 2014;56:372-83. https://doi.org/10.1016/j.compositesb.2013.08.044
[7] Dose G, Roccella S, Romanelli F. Engineering of a FGM interlayer to reduce the thermal stresses inside the PFCs. Appl Sci. 2022;12(20):10215. https://doi.org/10.3390/app122010215
[8] Sofiyev AH, Kuruoğlu N. The stability of FGM truncated conical shells under combined axial and external mechanical loads in the framework of the shear deformation theory. Compos Part B Eng. 2016;92:463-76. https://doi.org/10.1016/j.compositesb.2016.02.027
[9] Chu L, Dui G. Exact solutions for functionally graded micro-cylinders in first gradient elasticity. Int J Mech Sci. 2018;148:366-73. https://doi.org/10.1016/j.ijmecsci.2018.09.011
[10] Amos SO. Numerical analysis and material selection of functionally graded pipes based on metals and ceramics for deep offshore oil and gas operations in Gulf of Guinea. 2020 [cited 2024 Dec 17].
[11] Pachaiappan S, Chandrasekaran S. Numerical analysis of offshore topside with FGM under impact loads. Innov Infrastruct Solut. 2022;7(3):195. https://doi.org/10.1007/s41062-022-00802-2
[12] Wang ZW, Zhang Q, Xia LZ, Wu JT, Liu PQ. Stress analysis and parameter optimization of an FGM pressure vessel subjected to thermo-mechanical loadings. Procedia Eng. 2015;130:374-89. https://doi.org/10.1016/j.proeng.2015.12.230
[13] Habib E-S, El-Hadek MA, El-Megharbel A. Stress analysis for cylinder made of FGM and subjected to thermo-mechanical loadings. Metals. 2018;9(1):4. https://doi.org/10.3390/met9010004
[14] Ghannad M, Yaghoobi MP. 2D thermo elastic behavior of a FG cylinder under thermomechanical loads using a first order temperature theory. Int J Press Vessels Pip. 2017;149:75-92. https://doi.org/10.1016/j.ijpvp.2016.12.002
[15] Lo K-C, Lai H-Y. Corrosion enhancement for FGM coolant pipes subjected to high-temperature and hydrostatic pressure. Coatings. 2022;12(5):666. https://doi.org/10.3390/coatings12050666
[16] Yaghoobi MP, Ghannad M. An analytical solution for heat conduction of FGM cylinders with varying thickness subjected to non-uniform heat flux using a first-order temperature theory and perturbation technique. Int Commun Heat Mass Transf. 2020;116:104684. https://doi.org/10.1016/j.icheatmasstransfer.2020.104684
[17] Doan TN, Nguyen AT, Van Binh P, Van Hung T, Tru VQ, Luat DT. Static analysis of FGM cylindrical shells and the effect of stress concentration using quasi-3D type higher-order shear deformation theory. Composite Structures. 2021;262:113357. https://doi.org/10.1016/j.compstruct.2020.113357
[18] Shiyekar SM, Awari A. Static stress analysis of functionally graded cylindrical stiffened shells. ASPS Conf Proc. 2022;1(1):1847-52. https://doi.org/10.38208/acp.v1.727
[19] Sofiyev AH, Hui D. On the vibration and stability of FGM cylindrical shells under external pressures with mixed boundary conditions by using FOSDT. Thin-Walled Struct. 2019;134:419-27. https://doi.org/10.1016/j.tws.2018.10.018
[20] Han Y, Zhu X, Li T, Yu Y, Hu X. Free vibration and elastic critical load of functionally graded material thin cylindrical shells under internal pressure. Int J Struct Stab Dyn. 2018;18(11):1850138. https://doi.org/10.1142/S0219455418501389
[21] Gao G, Sun N, Shao D, Tao Y, Zhang H. Nonstationary response system for the stepped composite cylindrical shell with drop-off ply under moving random loads. Ocean Eng. 2024;298:117178. https://doi.org/10.1016/j.oceaneng.2024.117178
[22] Chen X, Drost L, Peters DJ. Hydrodynamic response of submerged floating tunnel in combined wave-current flows. In: Sapountzakis EJ, Banerjee M, Biswas P, Inan E, editors. Proc 14th Int Conf Vib Probl. Lecture Notes Mech Eng. Singapore: Springer; 2021. p. 807-22. https://doi.org/10.1007/978-981-15-8049-9_49
[23] Lin F, et al. Damage characteristics and dynamic response of RC shells subjected to underwater shock wave. Appl Sci. 2024;14(5):1878. https://doi.org/10.3390/app14051878
[24] Nugraha N, Akmal J, Lubis A. Submerged floating tunnel bridge (SFTB): A status report and evaluation of technology readiness level (TRL). J Integr Adv Eng. 2022;2(1):19-32. https://doi.org/10.51662/jiae.v2i1.35
[25] Tutuncu N, Ozturk M. Exact solutions for stresses in functionally graded pressure vessels. Compos Part B Eng. 2001;32(8):683-6. https://doi.org/10.1016/S1359-8368(01)00041-5
[26] Xie J, Hao S, Wang W, Shi P. Analytical solution of stress in functionally graded cylindrical/spherical pressure vessel. Arch Appl Mech. 2021;91(7):3341-63. https://doi.org/10.1007/s00419-021-01970-w
[27] Caela JG. Stress distribution in a tick cylinder. 2017 [cited 2024 Dec 17].
[28] Murti AW, Akmal J, Lubis A, Savetlana S. Exact and numerical solution for stress analysis on FGM cylindrical shell using axisymmetric element with plane stress. In: AIP Conf Proc. AIP Publishing; 2023. https://doi.org/10.1063/5.0115295
[29] Ghasemi AR, Kazemian A, Moradi M. Analytical and numerical investigation of FGM pressure vessel reinforced by laminated composite materials. 2014.

[30] Chitour M, Khadraoui F, Mansouri K, Rebai B, Menasria A, Zemmouri A, Touati S, Boumediri H. A novel high order theory for static bending of functionally graded (FG) beams subjected to various mechanical loads. Res. Eng. Struct. Mater., 2024; 10(4): 1523-1539. http://dx.doi.org/10.17515/resm2024.141me0104rs

[31] Sahu RK, Sondhi L, Bhowmick S, Madan R. Deformation and stress analysis of rotating functionally graded hollow cylindrical body for variable heat generation. Res. Eng. Struct. Mater., 2023; 9(2): 597-616. http://dx.doi.org/10.17515/resm2022.470me0713

[32] Das P, Benslimane A, Islam MA, Siddiquei AA, Rahman MM, Adil MM. Finite element analysis of a generalized rotating FGM vessel subjected to thermo-mechanical loadings: Effect of Poisson ratio and inhomogeneity parameters. Heliyon. 2024;10(11):e31833. https://doi.org/10.1016/j.heliyon.2024.e31833

[33] Amodu OA, Adamu AA, Anikoh GA. Investigation on the stress distributions in a thick-walled cylinder with internal pressure. 2025 [cited 2025 May 21].

Blank Page

Research on Engineering Structures & Materials
www.jresm.org
MIM Research Group

Research Article

Impact of the rigid piles on the dynamic response of the soil-inclusions-mattress-slab system under seismic excitations

Oussama Benmerabet [*,1,a], Salah Messioud [1,b], Rania Beghila [2,c], Daniel Dias [3,d]

[1]*LGCE Laboratory, Faculty of Sciences and Technology, University of Jijel, Algeria*
[2]*LEEGO Laboratory, Faculty of Civil Engineering, University of Sciences and Technology Houari Boumediene (USTHB), Algeria*
[3]*3SR Laboratory/Polytech, Grenoble Alpes University, France*

Article Info

Article History:

Received 24 Mar 2025

Accepted 02 June 2025

Keywords:

Code-Aster;
Numerical modeling;
Rigid inclusions;
Seismic loading;
Soil-structure interaction

Abstract

This paper presents a numerical model of the dynamic response of the soil-inclusions-mattress-slab system under seismic loading, with a particular focus on analyzing the influence of inclusions on the reinforcement system. Three-dimensional finite element numerical models with absorbing boundaries based on the direct method are utilized for this study using Code-Aster software. The analysis accounts for two different types of soil behavior: non-linear elastic and elasto-plastic. Six models were simulated in this study, each varying in the number of inclusions, to investigate how the number of inclusions impacts the overall behavior of the system and the variation in internal stresses and horizontal displacements within each inclusion. The objective of this numerical model is to study the influence of the number of inclusions on the dynamic response of a reinforcement system, for both elastic and elasto-plastic behaviors, using the Mohr-Coulomb criterion. The study's findings reveal that an increase in the number of inclusions leads to reduced stresses and displacements within the inclusions. Moreover, inclusions positioned closer to the perimeter of the inclusion network, farther from the point of loading application, experience lower stress levels and are less prone to displacements compared to those located at the network's center. Regarding the impact of considering elastic or elasto-plastic behavior, the results of elasto-plastic calculation are compared with those of non-linear elastic calculation. The results indicate that assuming elasto-plastic behavior in calculations results in decreased internal stresses rather than an increase in displacement.

© 2025 MIM Research Group. All rights reserved.

1. Introduction

Various compressible soils are commonly employed in civil engineering projects. The utilization of soft soil improvement techniques becomes essential as regions with suitable soil for constructing highways, railroads, and industrial networks become scarce. When the quality of these soils is inadequate, engineers opt for deep foundations to reach soil layers that offer better support. Addressing surface settlement issues can be achieved through the use of Rigid Inclusions (RIs). Additionally, this method is both efficient and eliminates the necessity for substituting soft soil [1-4].

The utilization of rigid inclusions as a soil reinforcement technique offers an intriguing alternative to conventional methods, such as pre-loading or vertical drainage. It addresses environmental concerns while optimizing costs and construction timelines. This approach can significantly

*Corresponding author: oussama.benmerabet@univ-jijel.dz
[a]orcid.org/0000-0003-3731-5121; [b]orcid.org/0000-0003-0368-9854; [c]orcid.org/0009-0006-8486-6531; [d]orcid.org/0000-0003-2238-7827
DOI: http://dx.doi.org/10.17515/resm2025-778st0324rs

enhance the initial bearing capacity of the soil and reduce foundation settlements under applied loads, thereby enhancing stability [5-8].

The process of reinforcement involves creating a composite foundation where the loads are distributed between the soil and the rigid inclusions. Compressible soil is strengthened by introducing a network of inclusions that traverse it, supported by a more rigid layer, along with a granular mattress positioned between the reinforced soil and the surface structure. Specifically, soil reinforcement encompasses various techniques aimed at incorporating vertical elements into the soil to improve its load-bearing capacity under static or dynamic loads, such as those exerted by embankments or surface foundations. It is also employed to counteract the pressure of soil in the case of support or stabilization works on natural slopes [2, 9, 10].

Structures supported by soils reinforced with rigid inclusions may encounter various types of loading, both static and dynamic. To gain a comprehensive understanding of the dynamic response of structures subjected to seismic loading, it is crucial to study the dynamic behavior of groups of rigid inclusions. In the past four decades, there has been a notable surge in the analysis of foundation behavior under dynamic stresses. Analytical methods have greatly benefited from the stringent safety requirements imposed on the design of particular types of structures [11].

The use of deep foundations in seismic regions raises several important questions, including the role of the mattress in altering the free-field response of the ground (amplification) and in distributing loads within the inclusions. In the case of rigid inclusions, direct contact between the structure and the inclusions is avoided because the distribution mattress acts as an intermediary [5]. The granular mattress, often referred to as the Load Transfer Platform (LTP), serves the purpose of transmitting the load applied at the surface to the heads of the inclusions through mechanisms such as the curved effect. This process is influenced by differential settlement between the inclusions and the compressible soil, as well as the friction within the granular soil. The mattress can be constructed using various materials, whether untreated or treated, such as lime or cement [12, 13]. This technique involves the integration of a grid of vertical rigid inclusions with a supporting layer and an intermediate mattress to create a system for distributing both vertical and horizontal stresses. The primary objective of this assembly is to facilitate the transfer of vertical loads from the surface to the supporting layer, consequently mitigating stresses on the compressible soil and minimizing settlement of the structure [14-16].

The analysis of how rigid inclusions respond to seismic forces requires solving a soil-structure interaction (SSI) problem that accounts for the unique components of the reinforcement system provided by the rigid inclusions. These components include the soil, the inclusions themselves, the distribution mattress, and the structure. This challenge is characterized by its three-dimensional and non-linear nature. SSI falls within the realm of applied mechanics, focusing on the development and examination of practical and theoretical methodologies for assessing structures subjected to dynamic loads while considering the behavior of both the soil and the structure [17-19].

In essence, SSI investigates how the ground's motion changes during an earthquake or under dynamic loads due to the presence of a structure. The significance of this interaction varies depending on factors such as the soil's properties, the structure's characteristics, and its foundation type. These structures encompass a wide range of applications, including nuclear power plants, power facilities, liquefied natural gas tanks (LNG), dams, and more [8, 20, 21]. In the early stages of research on soil-structure interaction (SSI), there was limited emphasis on analyzing high-rise buildings from an SSI perspective, primarily because they were classified as lightweight structures. Traditionally, seismic response evaluations of these structures were carried out without considering the influence of SSI. However, this perspective has evolved significantly due to damage assessment reports following recent devastating earthquakes, highlighting the substantial impact of SSI effects [8, 22-24].

Taking into account the influence of soil-structure interaction (SSI), the soil domain is typically characterized by an elasto-plastic behavior governed by the Mohr-Coulomb yield criterion. Addressing this complex issue requires a comprehensive investigation, including aspects such as defining seismic hazards and resulting ground motion, studying soil behavior under dynamic and cyclic loading, and assessing the response of open field soil and structures to seismic loads [19, 25].

In general, various approaches have been proposed for analyzing SSI and can be categorized into different methods: direct methods, substructure methods, and hybrid methods. Each of these methods corresponds to a specific representation of the soil-structure model [26-30].

The direct method, also known as global methods, is often considered the most rigorous approach for addressing SSI, especially in cases involving complex structural geometries and non-linear soil modeling. This method involves directly solving the motion equation of the soil-structure system. It simultaneously accounts for the behaviors and contact conditions of soil, foundation, and structural elements within the same analysis. These methods allow for the consideration of critical factors in SSI, including soil heterogeneity, the presence of water, the non-linear behavior of geomaterials, and soil-structure contact conditions [26, 31, 32].

This paper explores the dynamic response of soil-rigid inclusions-mattress-slab systems subjected to seismic loading. The investigation employs three-dimensional finite element numerical models with absorbing boundaries, utilizing the direct method. This work is oriented towards the qualification and quantification of solicitations and displacements in soil-piles-mattress-slab systems subjected to seismic loading, in order to study the effectiveness of soil reinforcement systems (soil-piles-mattress- slab), and to study the impact of the number of inclusions on the dynamic response of the system, for both elastic and elasto-plastic with Mohr-Coulomb criterion behaviors. The results of elasto-plastic calculation are compared with those of non-linear elastic calculation.

2. Numerical Study of The Soil–Pile–Mattress–Slab Interaction

2.1 Finite Element Method (FEM)

SSI analysis is categorized based on the method of analysis, treatment of the superstructure and soil, and the approach to handling interactions using various techniques. In SSI investigations, the primary computational techniques for discretizing the soil domain include the Finite-Element Method (FEM), Finite-Difference Method (FDM), and Boundary-Element Method (BEM). Among these, FEM has proven to be the most suitable approach for modeling and analyzing complex problems like SSI, covering a wide range of physical scenarios. It is a method used to approximate solutions within a spatial domain, allowing for the calculation of fields (scalars, vectors, tensors) that satisfy specific equations and imposed conditions. The versatility of this method has led to its increasing use in studying a diverse array of cases [32-37].

The Finite Element Method (FEM) is grounded in a straightforward concept: it involves dividing a complex shape into numerous elementary subdomains with simple geometric forms, known as finite elements, and connecting them at specific points referred to as "nodes." The process begins by constructing a mesh that incorporates the various elements of the system. Subsequently, material behavior laws for each component are selected, and finally, the problem is solved through numerical methods [27, 38].

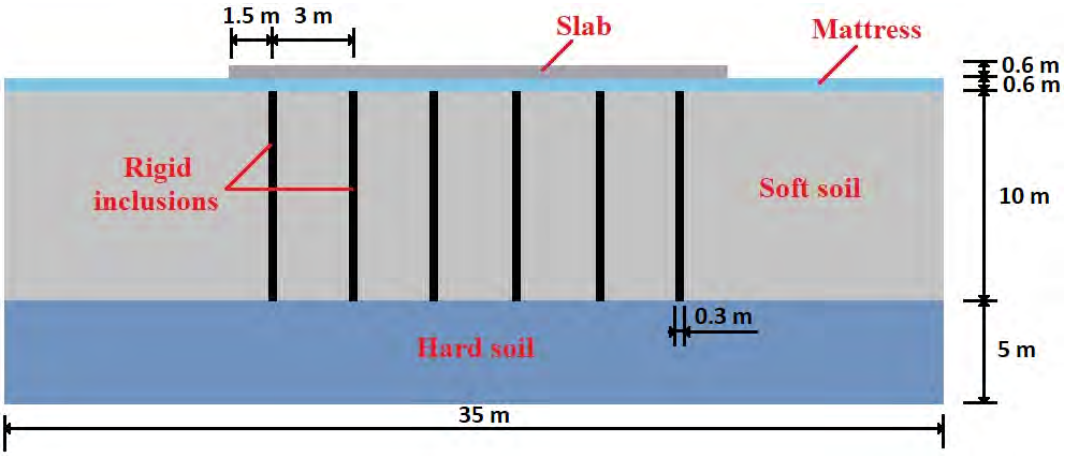
The rigid inclusion reinforcement system is composed of a mattress, which is further covered by a reinforced concrete slab and subjected to seismic loading. In this study, a 3D numerical modeling approach using the Finite Element Method (FEM) with absorbing boundaries is employed. Initially, the analysis considers the non-linear elastic behavior of the soil, followed by the consideration of elasto-plastic behavior. The modeling includes the representation of inclusions using bar elements, the slab using shell elements, and the soil and mattress using volume elements. Furthermore, the analysis accounts for complex conditions involving balance compatibility, material behavior, and boundary conditions [23, 39, 40].

Absorbing boundaries are an essential addition to this method because the numerical model cannot encompass the entire domain. To simulate the semi-infinite elastic space, Free-field boundaries are attributed to the vertical faces and to the bottom face of the numerical model. Paraxial elements are assigned to the free boundaries to answer soil-structure interaction problems and avoid wave reflection to satisfy the Sommerfeld conditions. These boundaries should be positioned at a significant distance from the structure to reduce computation time and prevent wave reflections at the soil-structure interface during the analysis [40-42]. The geometric characteristics of the model

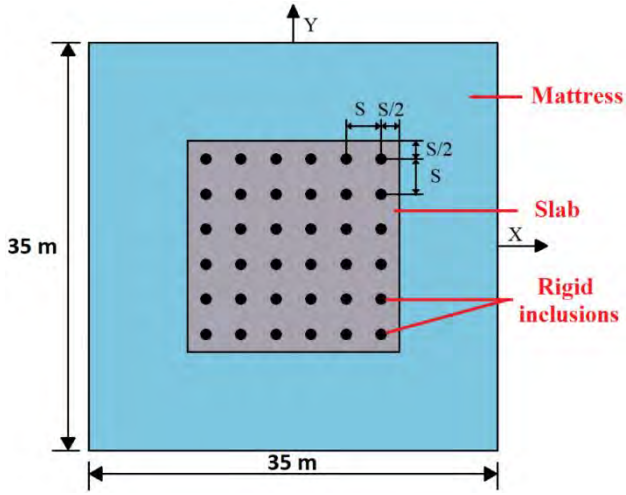
were determined using a parametric study to ensure the correct functioning of the absorbing boundaries.

2.2 Model Characteristics

A parametric study was conducted to determine the geometric properties of the model, ensuring the proper functioning of the absorbing boundaries. The maximum wavelength dictates the dimensions of the model as well as the element sizes. The soil volume consists of two layers with distinct characteristics. The base layer is a substratum measuring 35×35×5 meters, while the layer above is a 35×35×10 meters volume of compressible soil with unfavorable characteristics. To address the poor characteristics of the upper layer, it is reinforced with rigid concrete inclusions. These inclusions have a length of 10 meters, a circular section with a diameter of d = 0.3 meters, and are spaced at intervals of S = 3 meters. On top of the compressible soil layer, there is a load transfer mattress measuring 0.6 meters in thickness, which is further covered by a reinforced concrete slab also measuring 0.6 meters in thickness.



(a)



(b)

Fig. 1. Schematic representation of the analyzed systems: (a) Cross section of system. (b) Plan view and location of the vertical inclusions

At the bottom of the hard soil layer, which serves as the base for the systems under investigation, the seismic force is applied. Table 1 provides the mechanical characteristics of the soil layers and the transfer mattress. The choice of these properties was informed by the works of [43-45]. The damping ratio, angle of friction, angle of dilatancy, and cohesion are used in the calculation, which accounts for the elasto-plastic behavior of soils. Wave damping in soil generally results from its viscous properties, friction, and the development of plasticity. A linear elastic model for soil layers

does not explicitly represent viscosity. Therefore, 5% Rayleigh damping is introduced for all interactig elements.

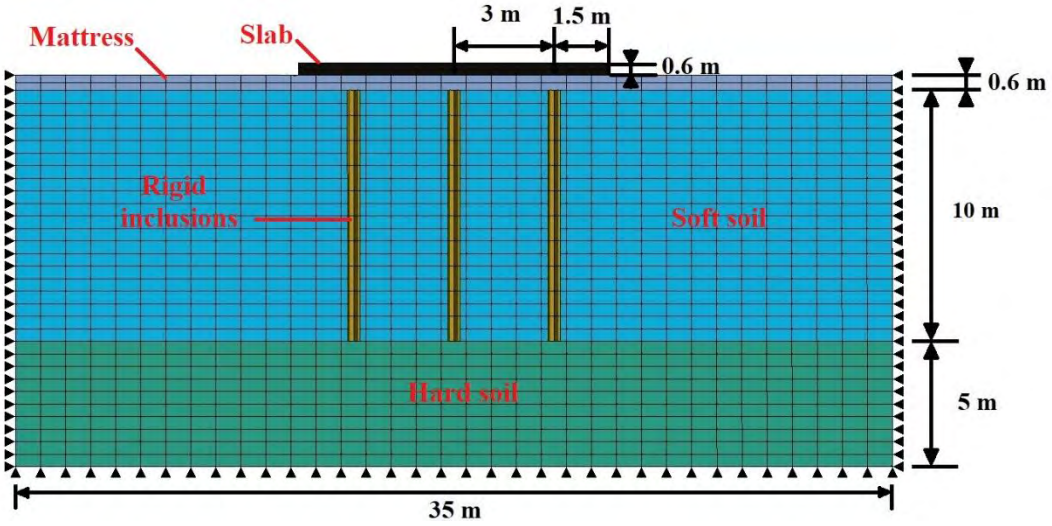
Table 1. Geo-mechanical parameters of the model elements.

Parameter / Element	Elastic modulus E (MPa)	Poisson ratio υ	Density ρ (kg/m³)	Cohesion, c (Pa)	Damping ratio ζ	Angle of friction, θ (°)	Angle of dilatancy, ψ(°)
Rigid inclusion	25000	0.25	2500	-	-	-	-
Slab	25000	0.25	2500	-	-	-	-
Mattress	50	0.4	2000	50000	0.5	25	10
Soft soil	10	0.4	1800	5000	0.5	25	10
Hard soil	100	0.4	2200	5000	0.5	25	10

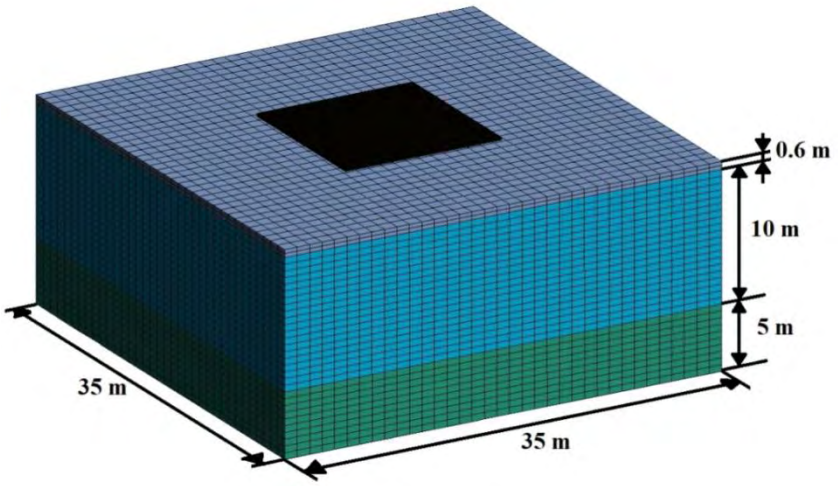
2.3 Methods of Analysis and Evaluation

Code-Aster is free Finite Element Analysis (FEA) software for numerical simulation in structural mechanics. This software provides around 400 different types of finite elements for discretizing solids and a large range of solvents, all of which have been subject to a rigorous and continuous verification and validation process. Developed since 1989 by EDF (Électricité De France Company) for the study of structure behavior by finite elements, it supports static, dynamic, and vibratory analysis of mechanically charged structures, as well as modal analysis. [45-47].

A study utilizing Code-Aster necessitates the implementation of a finite element mesh in conjunction with a command file to take advantage of the software's nonlinear capabilities. The distinctive elements of mooring system modeling, absent in the conventional Code-Aster workflow, have been incorporated by manually updating the command file with the requisite scripts. The command file adheres to the traditional fundamental stages of numerical simulations, commencing with the assimilation of the mesh, the choice of modeling, and the documentation of moments, materials, and initial and boundary conditions. [45, 47-50]. Initially, the geometrical characteristics of the model were determined with GMSH software, which is a prominent open-source 3D finite element mesh generator. The fundamental aim of this software is to deliver a rapid, agile, and user-friendly meshing tool with the capability of parametric input and flexible visualization. GMSH encompasses four modules, namely geometry, mesh, solver, and post-processing, that form the foundation of its architecture [51].



(a)



(b)

Fig. 2. Schematic view of the 3D numerical models and mesh distributions: (a) Half model view. (b) 3D view

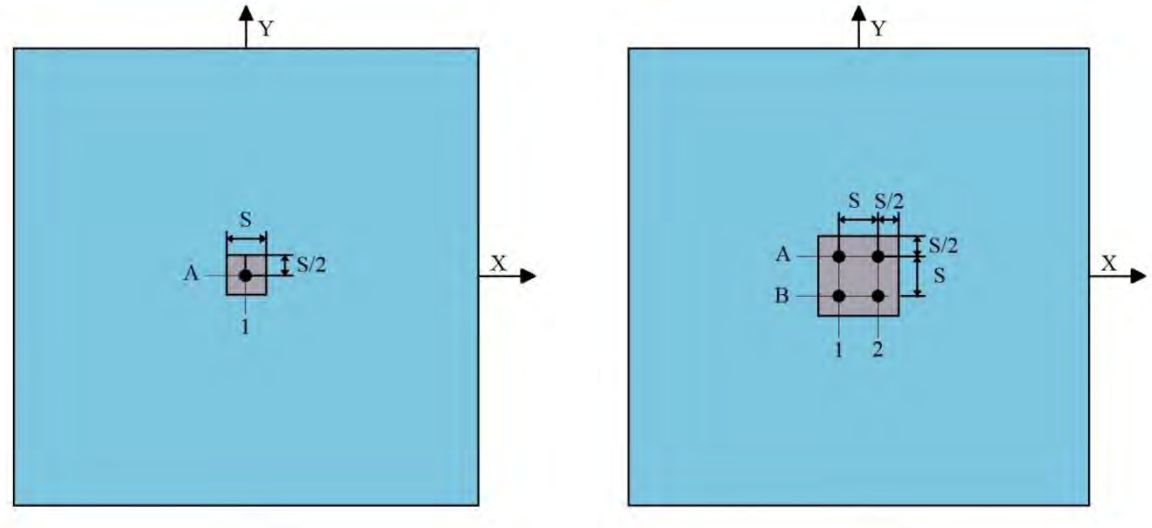
Figure 2 displays the model implemented in the numerical simulation. The magnitude of the mesh element ought to be minimized such that the mesh may effectively convey waves without any digital distortion. The dimensions of the mesh are contingent on the wave propagation speed and frequencies implicated [40, 44, 52]. Demonstrate that the dimensions of an element must be reduced to a range of one eighth to one tenth of the wavelength λ. As a result, the upper limit of the frequency that can be accurately simulated for a given mesh is established as follows [53]:

$$f = \frac{C_s}{10.\Delta l} \qquad with \qquad f = \frac{\omega}{2\pi} \tag{1}$$

Where, C_s: the wave propagation speed, Δl: the dimensions of the mesh component, ω : the excitation frequency.

2.4 Physical Models

In this study, six models were questioned while varying the number of inclusions in each model in order to study the impact of the number of inclusions on the overall behavior of the system and on the variation of the stresses taken up by each inclusion. Inclusions are represented in the Code-Aster by linear elements, while the soil and mattress have been represented through volume elements. Meanwhile, shell elements have been used to depict the slab.



(a) (b)

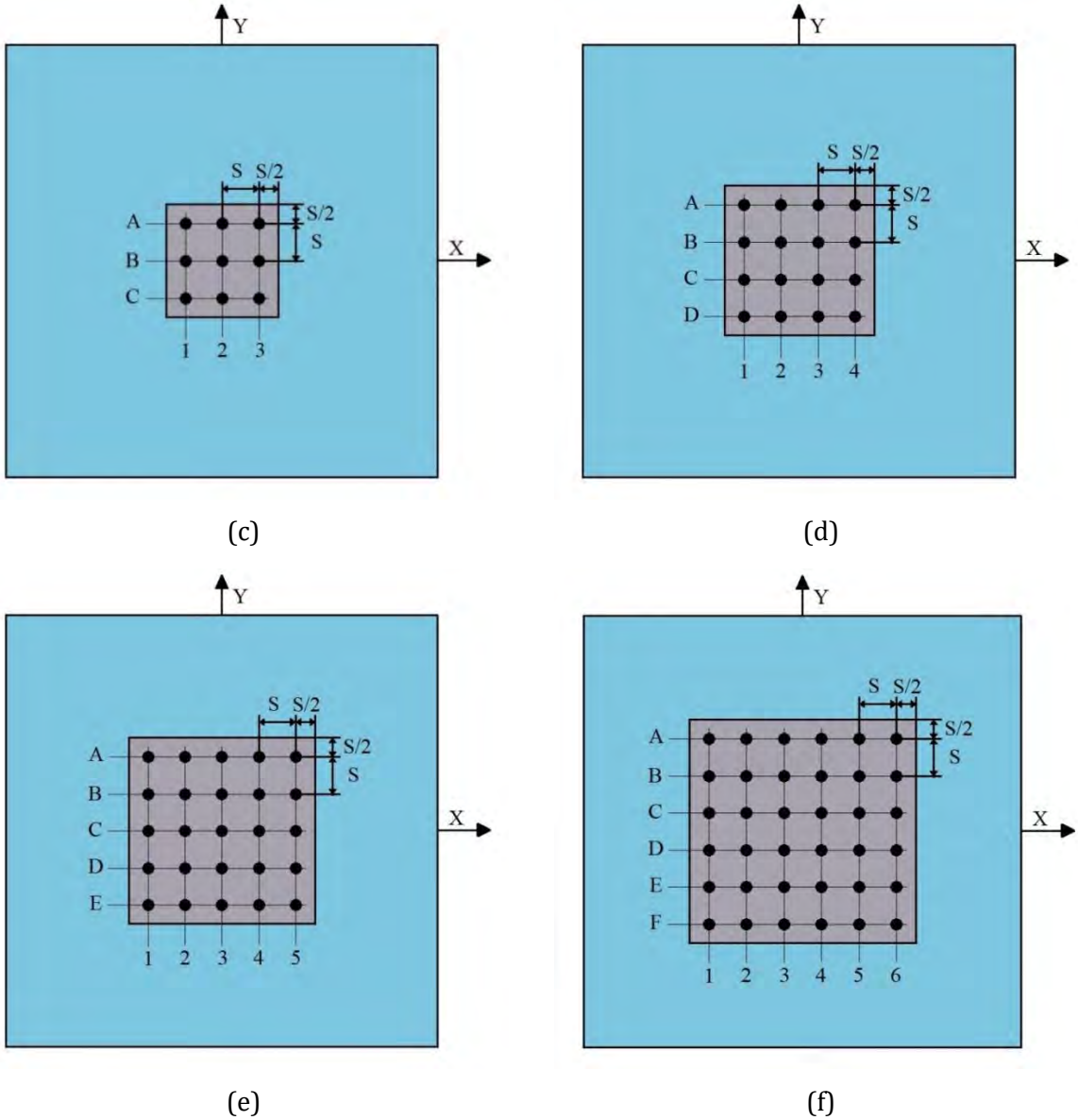


Fig. 3. Plan view of the six numerical models studied: (a) model 1 "one inclusion". (b) model 2 "4 inclusions". (c) model 3 "9 inclusions". (d) model 4 "16 inclusions". (e) model 5 "25 inclusions". (f) model 6 "36 inclusions"

The initial, second, and third models constitute a unified entity, featuring a singular inclusion, a 2x2 matrix of four inclusions, and a 3x3 matrix with a total of nine inclusions, correspondingly. Meanwhile, the fourth, fifth, and sixth models encompass configurations with 16 inclusions arranged in a 4x4 matrix, 25 inclusions forming a 5x5 matrix, and 36 inclusions structured in a 6x6 matrix, respectively. In the context of the first, third, and fifth models, the outcomes are derived from the central inclusion. In contrast, within the second, fourth, and sixth models, the results are determined based on one of the four inclusions situated at the center of the model, owing to their symmetrical arrangement. These models calculate stresses such as shear force and bending moment, as well as displacements, employing the Code-Aster software.

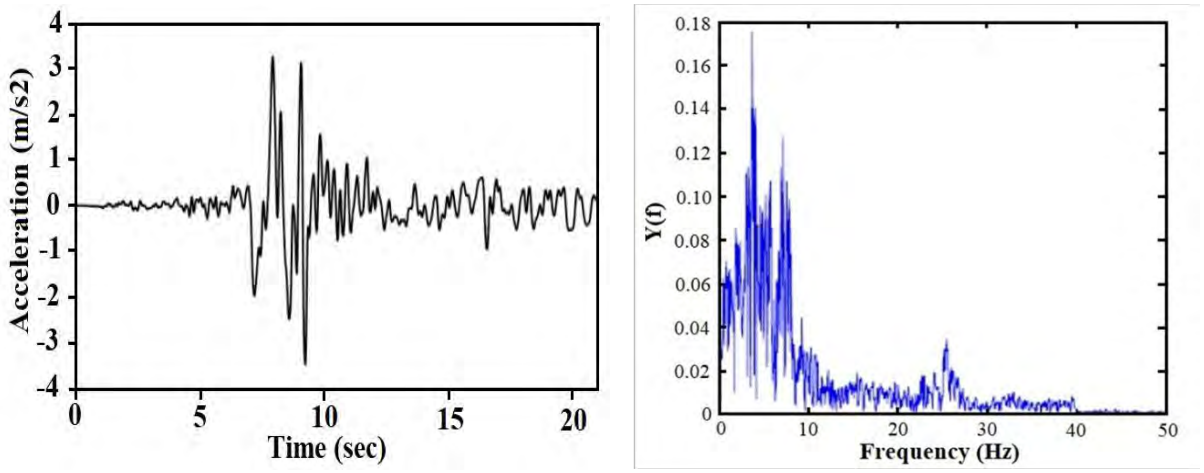
2.5 Seismic Loads

The seismic signal utilized in this study corresponds to the seismic activity observed in Nice, France. Its accelerogram aligns with the French design spectrum, as detailed in [54] and It has a maximum acceleration of 0.35g. This accelerogram spans a time history of 21 seconds, and you can find a visual representation of it in Fig. 4.a, Additionally, The Fourier amplitude of the uncorrected Nice record suggests that the maximum frequency fmax is below 5 Hz, as illustrated in Fig. 4.b [55,

56]. To generate comprehensive velocity profiles, our research approach involved amalgamating existing records. Subsequently, all nodes located along the model's lower boundary were subjected to these velocity profiles in the horizontal direction, following the methodology described by [44] We can compute the fundamental frequency of a soil layer using this formula: ω = 4 H/Vs

- H: the soil layer's total depth
- Vs: the shear wave velocity (m/s)

For lower damping values, the resonant frequency is roughly equal to the natural frequency



(a) (b)

Fig. 4. Seismic input signals of Nice: (a) Acceleration time history. (b) Fourier amplitude

3. Results and Discussion

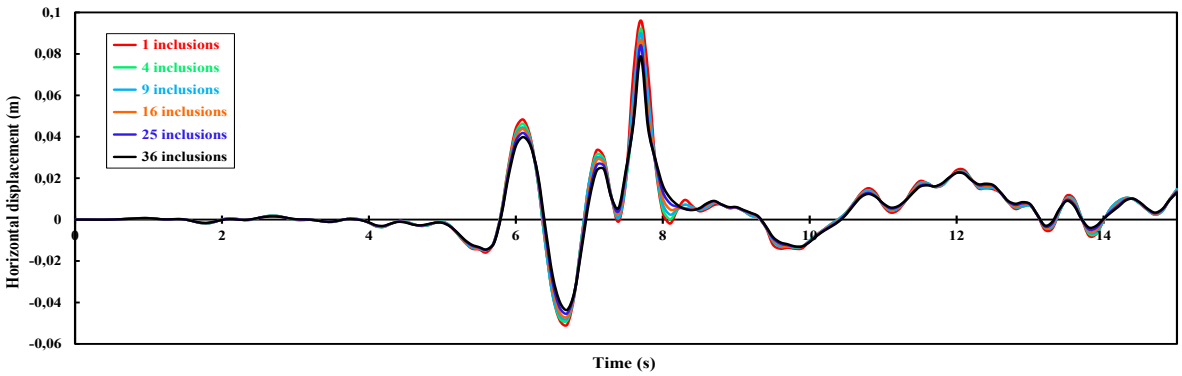
To justify the proper functioning of the proposed study, the numerical results for the proposed numerical model are compared and validated in the frequency domain with different numerical solutions formulated for pile groups system [44, 57]. The results of the dynamic stiffness matrix K_{ij} of a pile group are in good agreement with the results obtained by [58]. The dynamic impedance of a single pile and a cylinder pile is compared with those obtained by [58-61], respectively.

3.1 Non-linear Elastic Domain

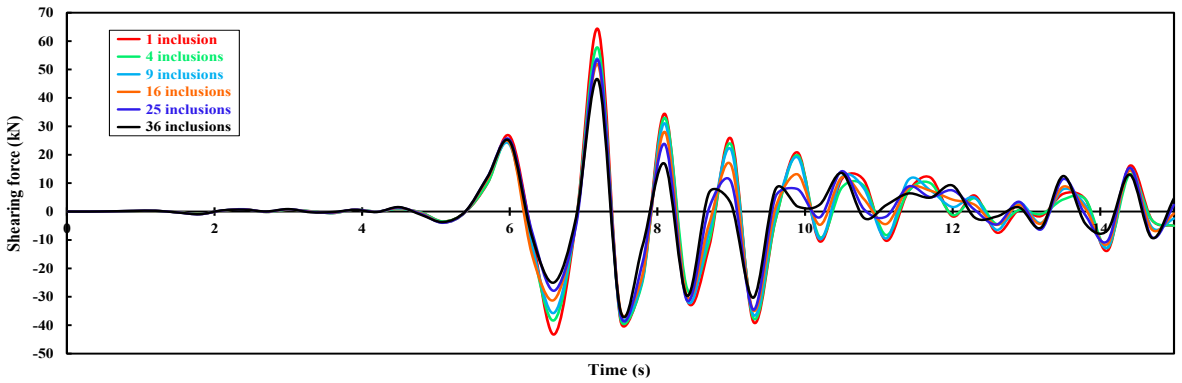
In the initial case, the influence of the number of inclusions on stresses such as shear force and bending moment, as well as horizontal displacements in non-linear elastic behavior was examined. The findings for the six models analyzed are presented in Figs. 6 and 7. The curves displayed illustrate the maximum outcomes of the horizontal displacement and stresses (shearing force and bending moment) in the central inclusion for each model based on the depth (i.e., the length of the inclusion).

3.1.1 The Variation of The Displacement and Internal Forces at The Head of The Central Inclusion as A Function of Time

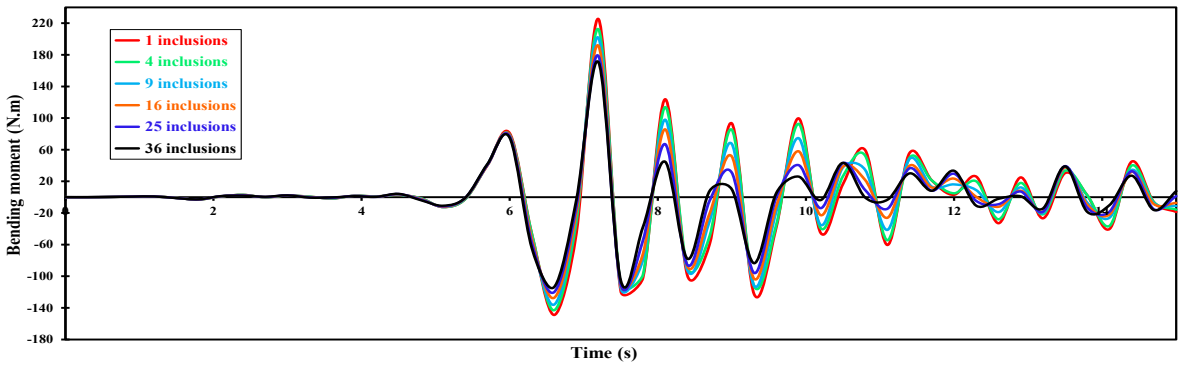
Figure 5 illustrates the time-history curve depicting the horizontal displacement and internal forces at the head of the central inclusion in the six models. Within a time, duration of 15 s, with a step of 0.01 s, this figure demonstrates that the evolution of internal forces and displacement aligns with the seismic loading, yielding nearly identical outcomes in all six models. It is worth noting that the initial model featuring a single inclusion exhibits the largest outcomes. As the number of inclusions increases, both the shear forces and bending moments, along with the horizontal displacement, diminish. The maximum results are observed between 7 and 8 seconds according to the time history (Fig. 5).



(a)



(b)

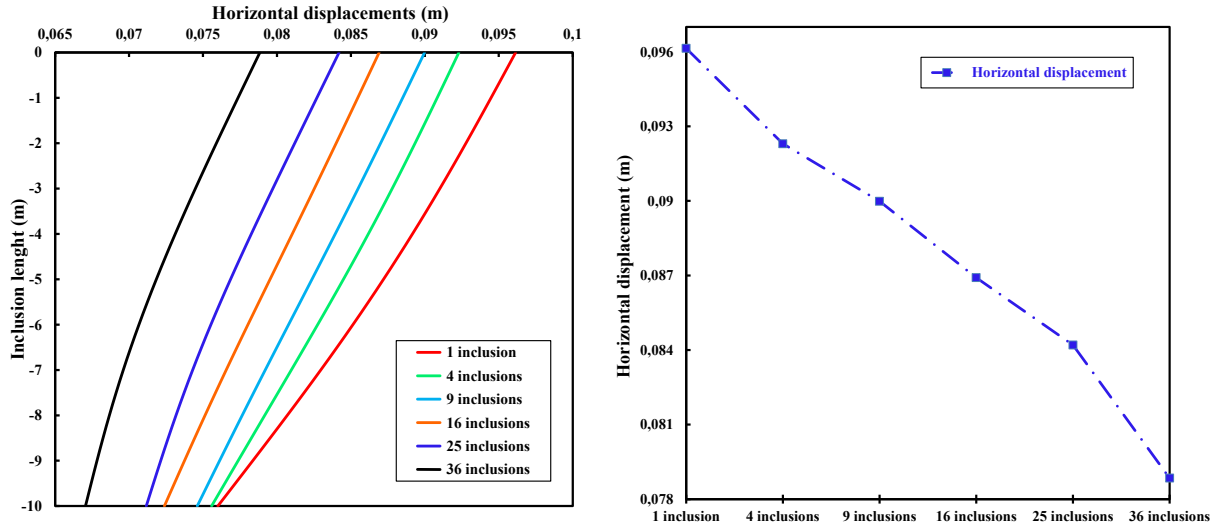


(c)

Fig. 5. The variation of the displacement and internal forces at the head of the central inclusion in the six models as a function of time: (a) Horizontal displacements. (b) Shearing force. (c) Bending moment

3.1.2 Horizontal Displacements

Figure 6 illustrates the displacements within the central inclusions of the six systems as a function of depth. Notably, the displacements within each inclusion exhibit a linear pattern, with the maximum displacement occurring at the head and gradually decreasing towards the minimum value at the tip. To provide specific values, for the "single inclusion" system, the maximum displacement at the inclusion is 0.096 meters at the head and decreases to 0.076 meters at the tip. These results vividly showcase how the number of inclusions within the reinforcing system impacts the variation in displacements. Moreover, it's evident that as the number of inclusions increases, the displacement at the inclusion head consistently decreases. This correlation underscores the influence of the inclusion count on the displacement behavior.



(a) (b)

Fig. 6. Impact of rigid inclusions on reinforcement system behavior: (a) The horizontal displacement of the central rigid inclusions for the 6 models. (b) Variation of the maximum horizontal displacement according to the number of inclusions

3.1.3 Bending Moments and Shear Forces

Figure 7 provides a visual representation of the shear force and bending moment profiles as a function of depth. When examining the central inclusion, which experiences the highest load in each model, a distinctive pattern emerges for the shear force. The shear force displays a linear relationship along the depth, with opposite signs in the upper and lower halves. At the head and foot of the inclusion, the maximum shear force is observed, with the head experiencing a greater force than the foot. This force remains nearly constant for depths shallower than 1 meter and subsequently decreases until it reaches zero at a depth of 4.5 meters, roughly halfway into the inclusion. Beyond this point, the force follows a similar trajectory but with a change in sign until it reaches its maximum value at the foot of the inclusion.

In the first model, specific values recorded for the shear force at different depths include 64 kN at the head, 0 kN at a depth of 5 meters, and -46.9 kN at the tip of the inclusion. These findings provide a comprehensive understanding of how shear forces vary with depth within the central inclusion. The bending moment profile within the inclusion exhibits an almost parabolic relationship, characterized by values of zero at both the top and bottom, with the peak typically occurring at the midpoint of the inclusion. A noteworthy example is observed in the "inclusion B2" within the third model, where the maximum bending moment reaches 160 kN at a depth of 5 meters. This phenomenon can be attributed to the absence of recesses or supports at the ends of the inclusion, causing it to behave akin to a simply supported beam. As a result, the bending moment distribution follows a classic parabolic pattern, with the highest moment occurring at the midpoint, a hallmark of such structural configurations.

Figures 7.c and 6.d provide a comprehensive view of the maximum variation in shear force and bending moment for each model, respectively. The values are determined from the head for shear force and at a depth of 5 meters for bending moment.

A consistent trend emerges from these figures, revealing that as the number of inclusions increases, the internal stresses decrease. This observation holds true for each individual computation, as depicted in the presented figures. Both the magnitudes of stresses and horizontal displacements show a diminishing trend with the progressive increase in the number of inclusions. This reduction in stress and displacement can be attributed to the fact that the total stress is distributed among all the inclusions within the system. Consequently, when the number of inclusions is augmented, the resultant stresses undergo a decrease, leading to a more evenly distributed load across the system.

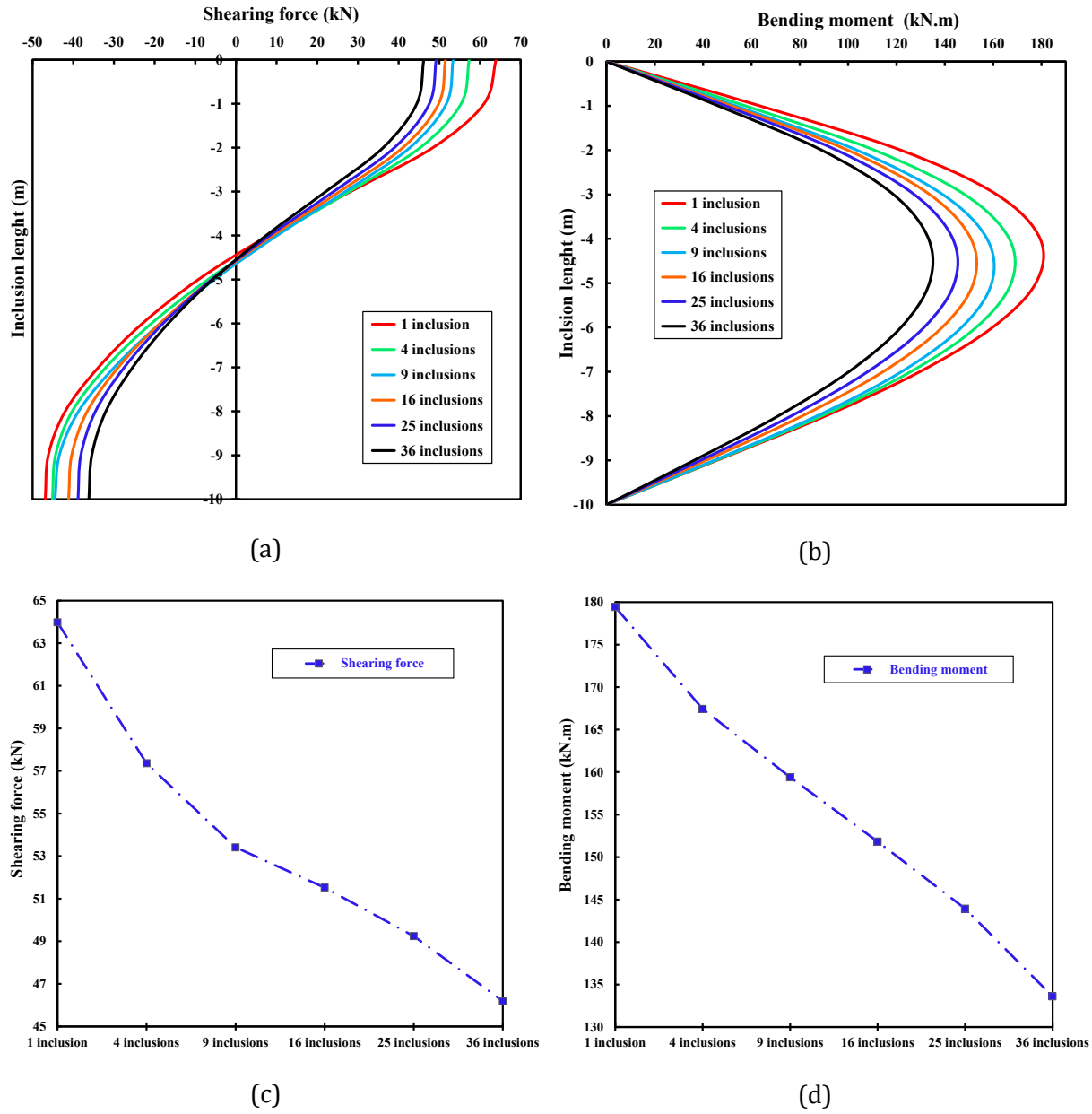


Fig. 7. Shearing force and bending moment: (a) Shearing force in the most solicited inclusion for the 6 models. (b) Bending moment in the most stressed inclusion for the 6 model. (c) Maximum shearing force for each inclusion, (at the head). (d) Maximum bending moment for each inclusion, (at 5 m)

3.1.4 The Effect of Inclusion Depth on The Variation of Displacements and Stresses

Figure 8 provides a comprehensive overview of horizontal displacement and stresses recorded at depths of 0 meters (the head of the inclusion), 2 meters, 5 meters, and 8 meters, focusing on the most stressed inclusion in each model. Several noteworthy trends can be observed: Decrease with Increased Inclusions: Across all depths, there is a consistent decrease in both displacements and stresses as the number of inclusions increases. This suggests that the addition of more inclusions in the system leads to a reduction in the observed displacements and stresses.

Horizontal displacement shows a diminishing trend as depth increases. For instance, in "model 3," the horizontal displacement of inclusion B2 measures 0.090 m at 0 meters, 0.087 m at 2 meters, 0.082 m at 5 meters, and 0.078 m at 8 meters. This indicates a decrease in horizontal displacement with greater depth. The bending moments exhibit a characteristic progression, starting from zero, reaching a maximum at the midpoint (5 meters), and then gradually decreasing. For example, in

the second model, the recorded bending moments at depths of 2 meters, 5 meters, and 8 meters are 111 kN.m, 167 kN.m, and 88.9 kN.m, respectively.

The shearing force profile differs from the bending moment. Initially, it decreases from the apex of the inclusion towards the center, nearly reaching zero. As an example, in the fifth model, inclusion C3 exhibits a force of 49.2 kN at the head of the inclusion and 39 kN at a depth of 2 meters, -5.95 kN at 5 meters, and subsequently increases while traversing almost identical values as observed in the upper region. At a depth of 8 meters, the shearing force equals -34.56 kN. These observations collectively highlight the influence of inclusion count and depth on displacement, bending moment, and shearing force patterns within the studied models.

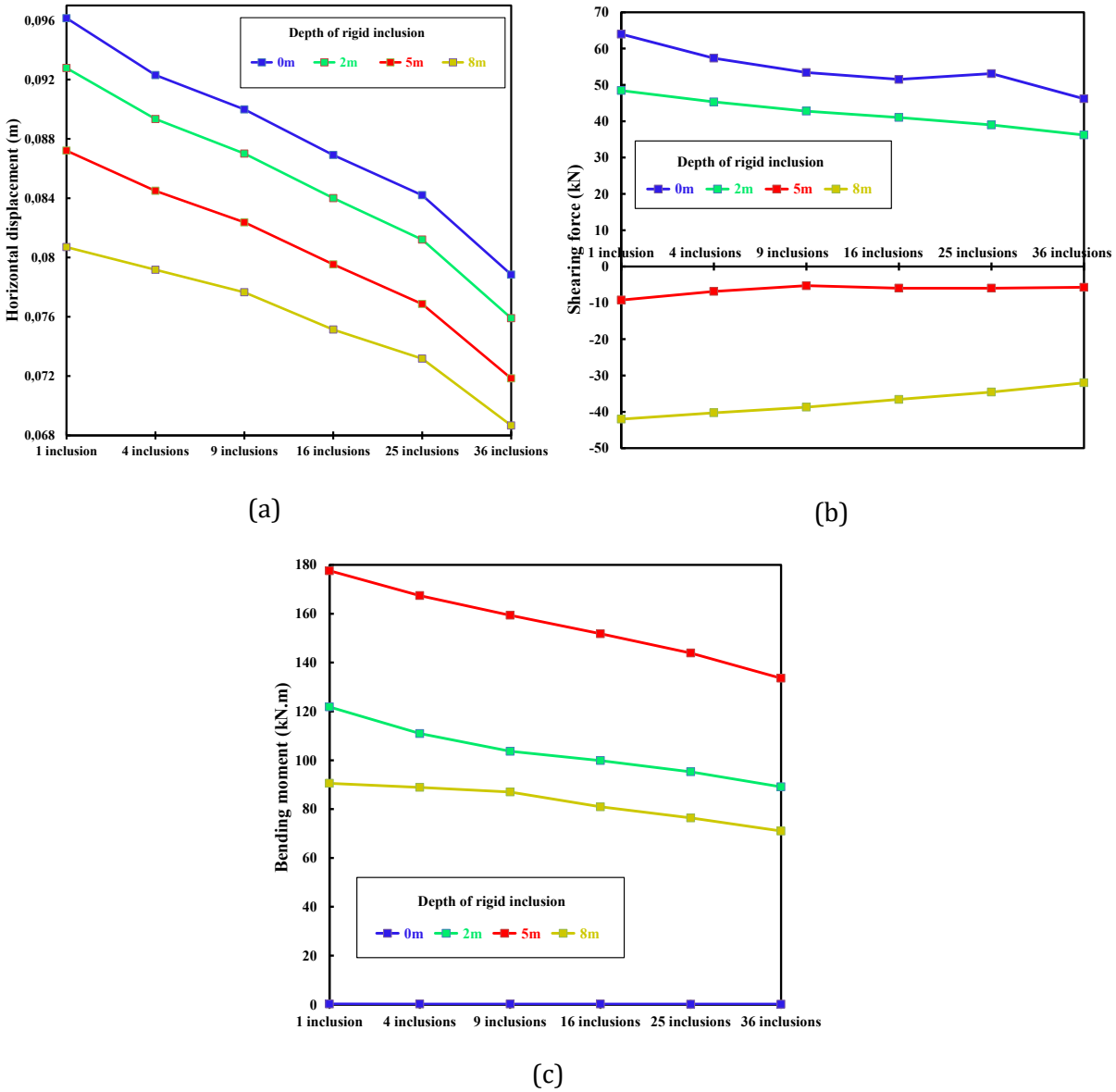
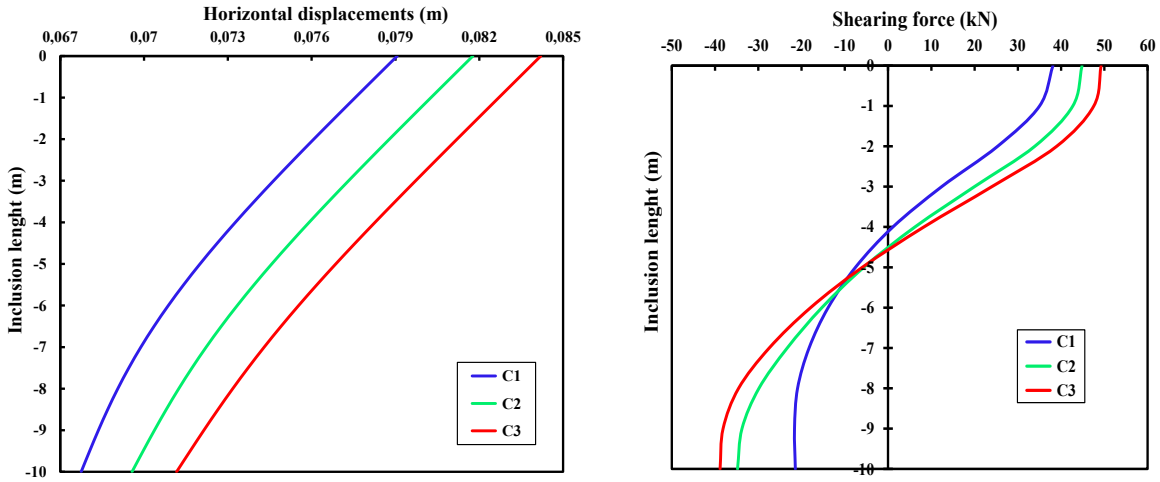


Fig. 8. The effect of inclusion depth on variation in displacements and stresses: (a) Horizontal displacement. (b) Shearing force. (c) Bending moment

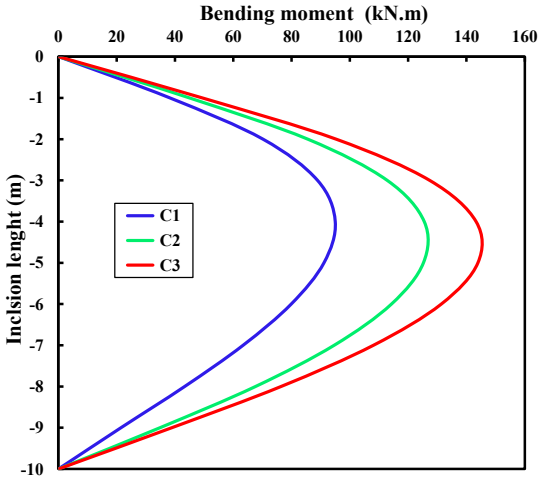
3.1.5 The Effect of The Inclusion Network's Position on The Horizontal Displacements and Solicitations

In order to assess the significance of inclusion placement on the variability of displacement and forces, we conducted an analysis by comparing the results obtained for the central-line inclusions of models 5 and 6:

- Model 5 (inclusions: C1, C2, and C3).



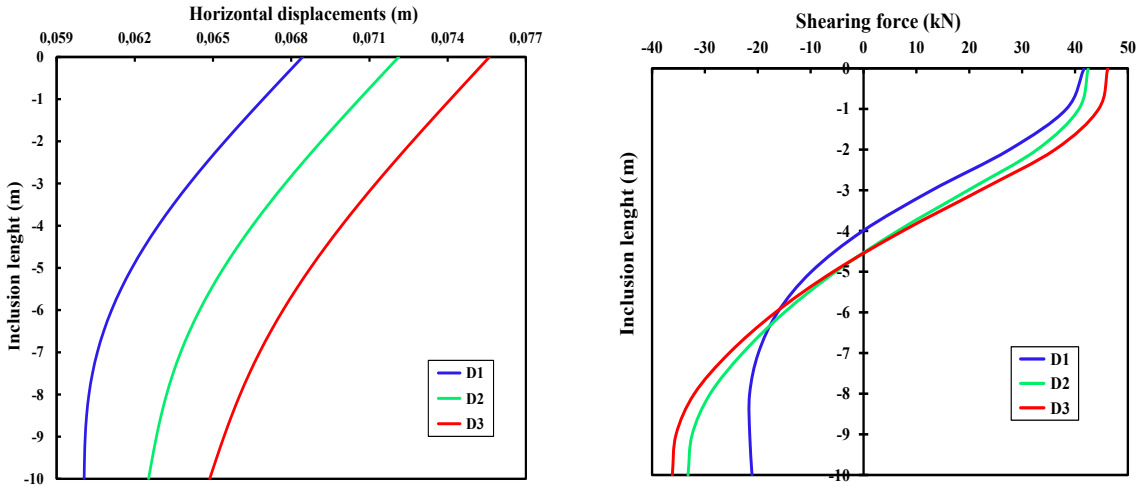
(a) (b)



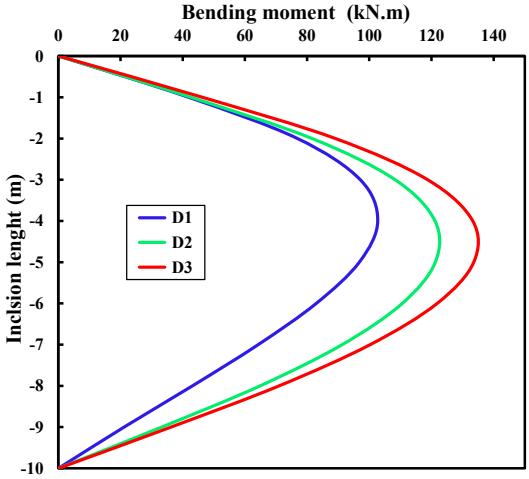
(c)

Fig. 9. The results of the central line inclusions according to the depth: (a) Horizontal displacement. (b) Shearing force. (c) Bending moment

- Model 6 (inclusions: D1, D2, and D3)



(a) (b)



(c)

Fig. 10. The results of the central line inclusions according to the depth: (a) Horizontal displacement. (b) Shearing force. (c) Bending moment

Figures 9 and 10 present a detailed overview of the horizontal displacements and stresses (shear forces and bending moments) along the central line of each model. Several key observations can be made from this analysis: It's important to note that all inclusions along the central line maintain a consistent spacing. A consistent trend is evident where horizontal displacements and stresses decrease as the inclusions approach the edge of the model. This phenomenon can be attributed to the application of earthquake forces to the middle of the substrate base, which is in contact with the soft soil. For instance, in model 5, at the head of the central line, inclusion C3 (located at the center of the model) records a horizontal displacement of 0.084 m. In comparison, inclusion C2 exhibits a displacement of 0.082 m, and inclusion C1 registers a lower value of 0.079 m. This trend highlights that the central inclusion experiences higher displacement compared to those further from the center. In model 6, at a depth of 8 meters, inclusion D3 shows a shearing force of -32 kN, inclusion D2 experiences -29 kN, while inclusion D1 has -21.5 kN. Regarding the bending moment at a depth of 2 meters in the same model, inclusion D3 records the highest value of 89.11 kN.m, followed by inclusion D2 at 81.61 kN.m, and inclusion C1 at 76.92 kN.m.

Central Inclusion Vulnerability: These results collectively indicate that the central inclusion is more susceptible to displacement and stress concentrations when compared to the other inclusions. The internal stresses decrease, and horizontal displacement reduces as one moves away from the center of the model, underscoring the importance of inclusion placement in assessing structural vulnerability. These findings contribute to a better understanding of how inclusion positioning impacts the behavior of the model under seismic loading, shedding light on the distribution of forces and displacements along the central line.

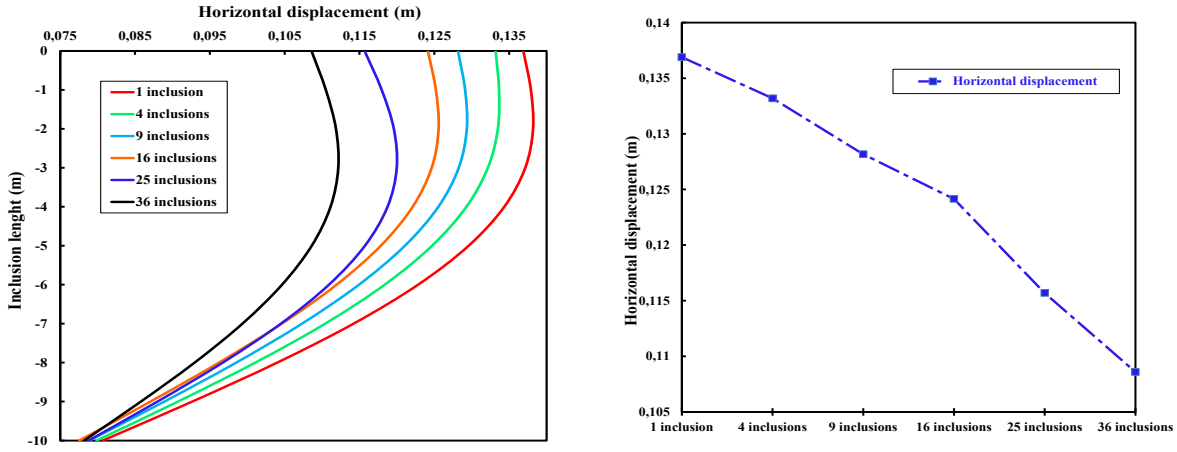
3.2 Elasto-Plastic Behavior

The investigation in question delves into the influence of different inclusion quantities on horizontal displacements and stresses, encompassing shear forces and bending moments. This analysis considers the elasto-plastic behavior of the soil. The curves presented in the following figures showcase the maximum results, which correspond to inclusions positioned in the middle, for each of the six models being studied. These curves are plotted with respect to depth, specifically the length of the inclusion. Subsequently, the maximum values are compared across each case to assess the impact of varying inclusion quantities on the observed outcomes.

Figures 11.a, 12.a, and 11.b provide a detailed illustration of the variations in displacement and stress (including bending moments and shear forces) concerning the depth of the most stressed inclusion for each corresponding model. Here are some key observations:

The displacement curve does not follow a linear pattern, unlike the initial behavior of the soil. Instead, it exhibits higher displacement values. This suggests that the soil behaves differently with

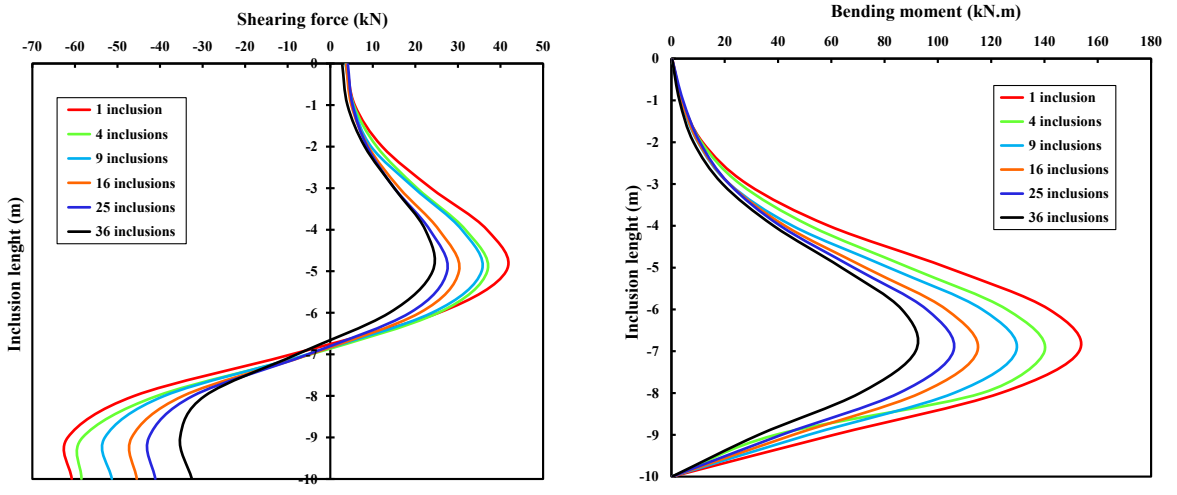
increased displacement values. The shear force curve showcases a distinctive pattern. Initially, it is relatively low at the inclusion head, followed by an increase to a peak value at a depth of 5 meters. Subsequently, it decreases to zero at 7 meters before rising again, with a different signal pattern towards the inclusion bottom. This complex behavior suggests changing forces within the soil layers. The bending moment follows an almost parabolic relationship, with the maximum value occurring at 7 meters and values of zero at both the top and bottom. For instance, in the case of "inclusion B2" within the third model, the maximum bending moment reached 129.4 kN.m at a depth of 7 meters.



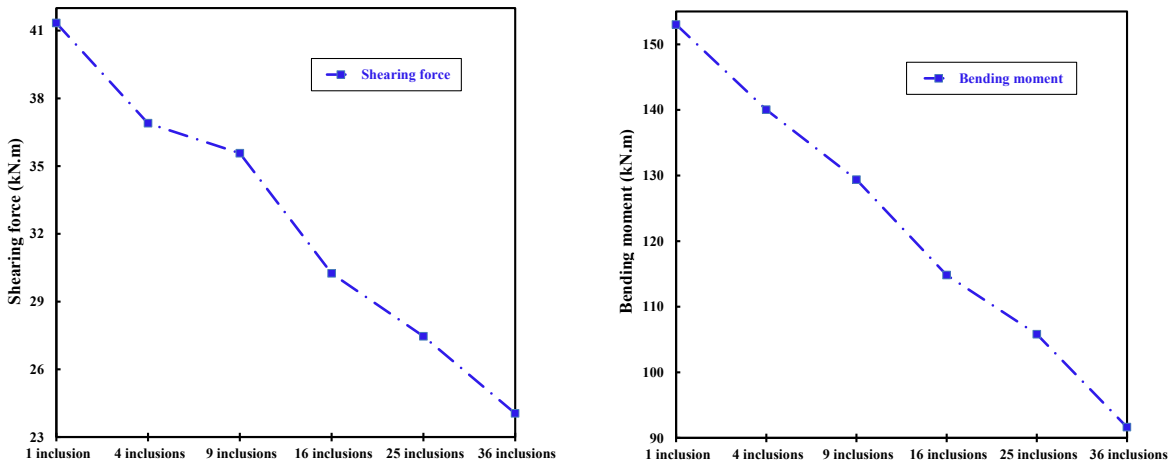
(a) (b)

Fig. 11. Impact of rigid inclusions on reinforcement system behavior: (a) The horizontal displacement of the central rigid inclusions for the 6 models. (b) Variation of the maximum horizontal displacement according to the number of inclusions

Now, turning to Figures 11.b, 12.c, and 12.d, these graphs display the maximum values of displacements and stresses for each model. The following observations can be made: It's evident that horizontal displacement, shear force, and bending moment exhibit an inverse proportionality concerning the increase in the number of inclusions. As the number of inclusions increases, the maximum values of these parameters decrease. This suggests that adding more inclusions leads to a reduction in displacement and stress levels, highlighting the effectiveness of inclusion strategies in mitigating structural loads and deformations. These findings contribute to a deeper understanding of the complex behaviors of soil, shear forces, and bending moments, and how they are influenced by the number of inclusions in the system.



(a) (b)



(c) (d)

Fig. 12. Bending moment and shearing force results in elasto-plastic behavior: (a) Variation of the shearing force according to the depth in the central inclusion for each model. (b) Variation of the bending moment as a function of the depth in the central inclusion for each mod. (c) Maximum shearing force (at the head of the central inclusion), for each model. (d) Maximum bending moment (at 5 M), for each model

3.3 Comparison Between Non-Linear Elastic and Elasto-Plastic Behavior

3.3.1 Comparison of The Maximum Results in Each Model

We examined the greatest outcomes in each model for displacement and internal forces in Fig.13 and Table 2 after computing each behavior separately. Figure 13.a indicates that the maximum values of the horizontal displacement in elasto-plastic behavior are larger than those of elastic behavior. Conversely, when we compared the results of bending moments and shear forces, we found that the elastic behavior had the largest values, as shown in Figure 13.b.

Table 2. The maximum results of each model in the two behaviors

	Horizontal displacement $\times 10^{-2}$ (m)		Shearing force $\times 10^{3}$ (N)		Bending moment $\times 10^{3}$ (N·m)	
	Elastic	Elasto-plastic	Elastic	Elasto-plastic	Elastic	Elasto-plastic
1 inclusion	9,61	13,69	63,98	41,34	179,43	153,02
4 inclusions	9,23	13,32	57,36	36,90	167,44	140,03
9 inclusions	8,99	12,82	53,41	35,58	159,40	129,37
16 inclusions	8,69	12,41	51,52	30,25	151,83	114,82
25 inclusions	8,42	11,57	49,24	27,46	143,93	105,81
36 inclusions	7,88	10,86	46,19	24,05	133,60	91,63

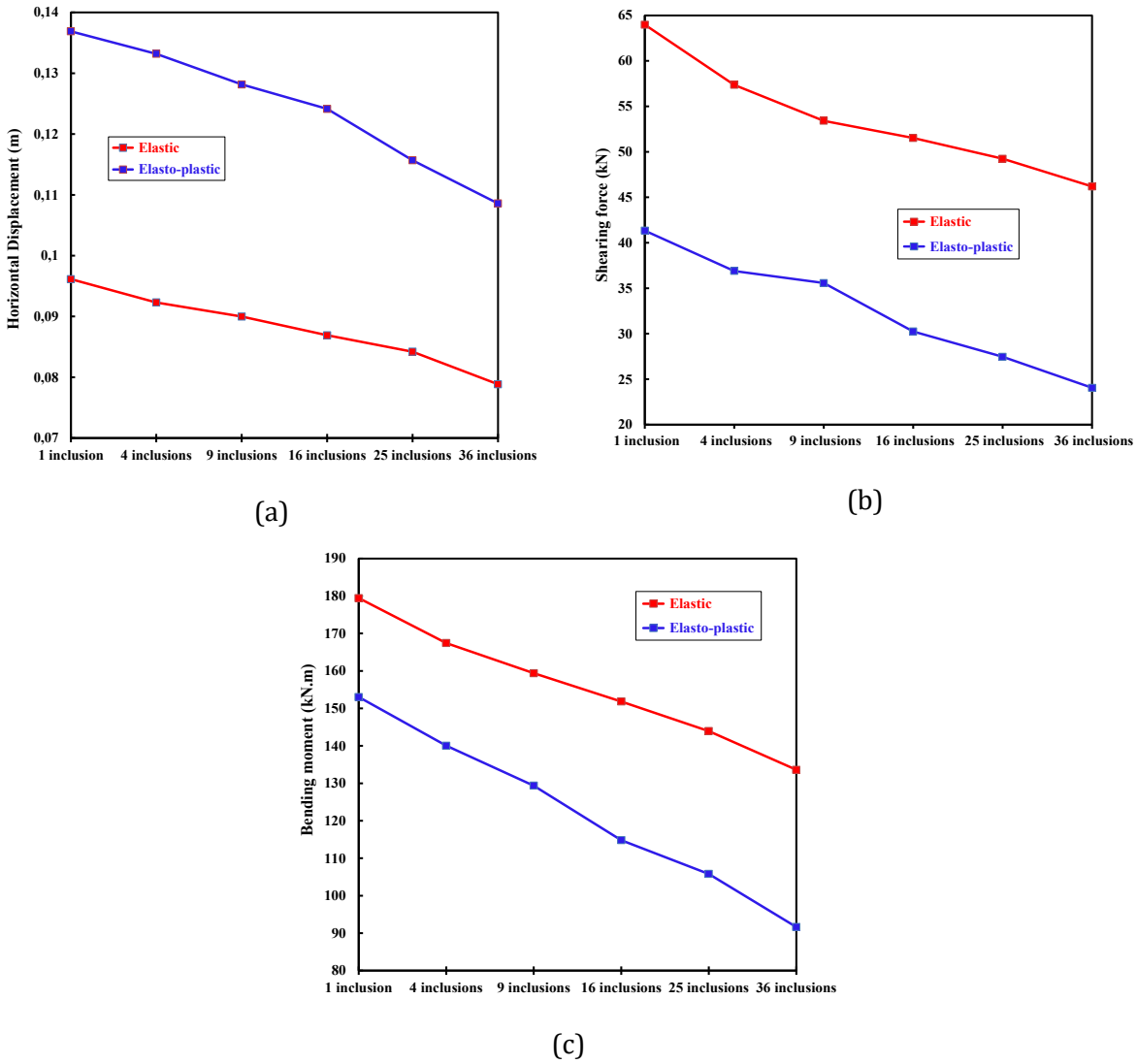


Fig. 13. Comparison between the maximum results of each model in non-linear elastic and elasto-plastic behavior: (a) Horizontal displacement. (b) Shearing force. (c) Bending moment

3.3.2 Comparison Between the Results of Model 4 In the Two Behaviors

In this section, we compare the results between the non-linear elastic and elasto-plastic behaviors of the soil using Model 4, which contains 16 inclusions. Figure 14 and Table 3 depicts the variations in displacement and internal stresses (including bending moments and shear forces) for both cases (non-linear elastic and elasto-plastic) with respect to the length of the inclusion. This comparison allows us to assess how the two different soil behaviors impact the structural response. Please refer to Figure 14 and Table 3 to analyze and interpret the specific findings and differences between the non-linear elastic and elasto-plastic simulations for Model 4.

The comparison between the results obtained for the non-linear elastic and elasto-plastic behaviors reveals notable differences. Here are the key findings from this comparison; horizontal Displacement (Fig. 14.a). In the elasto-plastic behavior case, horizontal displacement values are significantly higher than those observed in the non-linear elastic behavior. Furthermore, the displacement curves are not linear in the elasto-plastic case, indicating more pronounced deformation and structural response under elasto-plastic soil behavior.

Table 3. The results of the non-linear elastic and elasto-plastic behavior as a function of the depth in inclusion C2 of the 4th model.

Behavior	Depth (m)	Horizontal displacements × 10^{-2} (m)	Shearing force × 10^{3} (N)	Bending moment × 10^{3} (N·m)
Elastic	0 m	8,69	51,52	0,146
	3 m	8,25	25,46	133,78
	5 m	7,95	-59,57	151,83
	7 m	7,66	-28,95	114,43
	10 m	7,24	-41,13	0,071
Elasto-plastic	0 m	12,41	36,91	0,19
	3 m	12,47	16,25	21,79
	5 m	11,79	30,25	72,80
	7 m	10,46	-48,12	114,82
	10 m	7,75	-45,47	0,18

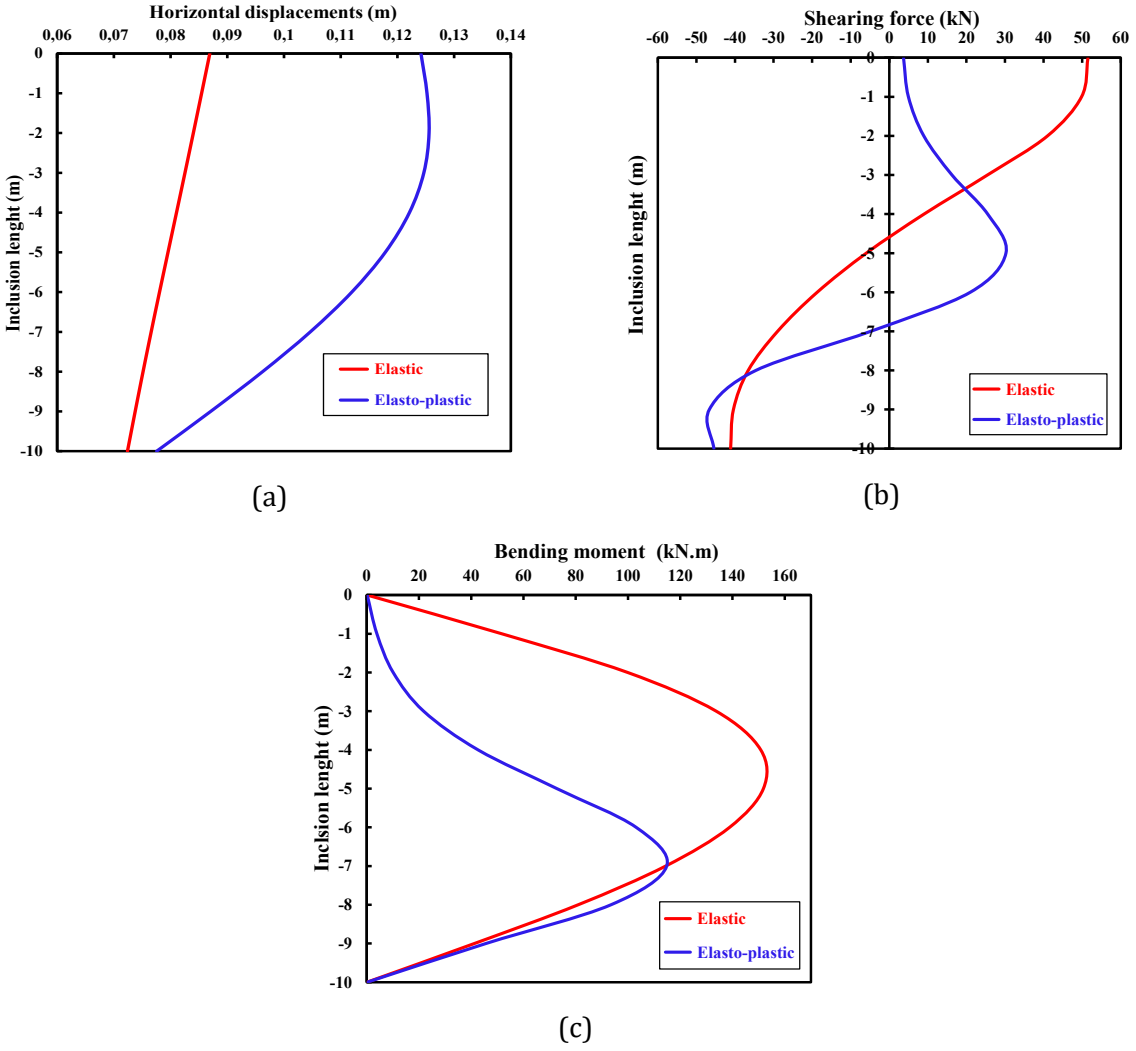


Fig. 14. The results of the comparison between non-linear elastic and elasto-plastic behavior as a function of the depth in inclusion C2 of the 4th model: (a) Horizontal displacements. (b) Shearing force. (c) Bending moment

In the non-linear elastic behavior, shear forces exhibit a peak value at the head of the inclusion, decrease towards zero at the middle, and then increase with negative values towards the bottom, though still lower than the top of the inclusion. In the elasto-plastic behavior, shear forces show weaker values at the inclusion head, followed by a gradual escalation towards the highest value at the midpoint. The shear forces then reach zero at a depth of 7 meters. This behavior suggests that under elasto-plastic conditions, there is a redistribution of forces with depth.

In the non-linear elastic behavior, the bending moment attains its maximum value at approximately the middle of the inclusion, reaching 152 kN.m. In the elasto-plastic behavior, the bending moment reaches its peak at a depth of 7 meters, corresponding to a value of 115 kN.m. Additionally, at the top and bottom of the inclusion, the values are nearly zero. This indicates that the elasto-plastic behavior leads to a different distribution of bending moments compared to non-linear elastic behavior.

Overall, the comparison underscores significant differences in the structural response between the non-linear elastic and elasto-plastic soil behaviors. The elasto-plastic behavior results in higher horizontal displacements, while the non-linear elastic behavior leads to higher shearing forces and bending moments. These findings emphasize the importance of considering soil behavior when assessing the response of structures subjected to seismic forces.

4. Conclusions

This article focuses on analyzing the behavior of reinforced soil with rigid inclusions under seismic stress conditions. The study particularly examines the influence of these inclusions on the reinforcement system, employing three-dimensional finite element numerical models with absorbing boundaries based on the direct method. The numerical models simulate various quantities of rigid inclusions, and horizontal displacements, as well as internal stresses, are computed using the Code-Aster software. The analysis takes into account two different types of soil behavior: non-linear elastic and elasto-plastic. Six different models are studied in this research, each varying in the number of inclusions.

The findings from this investigation can be summarized as follows:

- 1. Inclusion Quantity Effect: Increasing the number of inclusions within the system results in a reduction of stresses and horizontal displacements within these inclusions. This suggests that a higher number of inclusions contribute to a more effective reinforcement of the soil system under seismic forces.
- 2. Influence of Inclusion Position: Inclusions situated closer to the shore of the inclusion network, away from the point of applied load, experience lower stresses and horizontal displacements compared to those positioned at the center of the network. This highlights the significance of inclusion placement in the reinforcement system's response.
- 3. Comparison of Soil Behaviors: The study considers two soil behaviors, non-linear elastic and elasto-plastic. It is observed that in elasto-plastic soil behavior, the soil is more deformable, and its resistance is smaller than in the non-linear behavior.
- 4. Bending moments reach their maximum values at different depths in the two cases, with non-linear elastic behavior peaking at 5 meters and elasto-plastic behavior at 7 meters, albeit at a lower value.
- 5. The curve of shear force also exhibits distinct patterns in the two cases, with non-linear elastic soil showing a peak at the head of the inclusion and decreasing to zero at 5 meters, while elasto-plastic soil reaches zero at 7 meters.
- 6. Horizontal displacements differ in magnitude and curve shape between the two soil behaviors, with non-linear elastic soil following a linear curve and elasto-plastic soil exhibiting a non-linear trajectory.
- 7. In summary, this research provides valuable insights into the behavior of reinforced soil under seismic loading conditions, with a focus on the influence of rigid inclusions and the effects of different soil behaviors. The findings emphasize the importance of inclusion count, placement, and soil behavior in determining the structural response of such systems.

Acknowledgement

This work was supported and funded by the Directorate General for Scientific Research and Technological Development (DGRSDT, Algeria) and the Civil and Environmental Engineering Laboratory (LGCE) at the University of Jijel. These supports made this study and further research possible.

References

[1] Jenck O, Dias D, Kastner R. Two-dimensional physical and numerical modeling of a pile-supported earth platform over soft soil. J Geotech Geoenviron Eng. 2007 Mar;133(3):295-305. https://doi.org/10.1061/(ASCE)1090-0241(2007)133:3(295)

[2] Jenck O, Dias D, Kastner R. Three-dimensional numerical modeling of a piled embankment. Int J Geomech. 2009 May;9(3):102-12. https://doi.org/10.1061/(ASCE)1532-3641(2009)9:3(102)

[3] Briançon L, Dias D, Simon C. Monitoring and numerical investigation of a rigid inclusions-reinforced industrial building. Can Geotech J. 2015 Oct;52(10):1592-604. https://doi.org/10.1139/cgj-2014-0262

[4] Zhang J, An L, Li C, Dias D, Jenck O. Artificial neural network response assessment of a single footing on soft soil reinforced by rigid inclusions. Eng Struct. 2023 Apr;281:115753. https://doi.org/10.1016/j.engstruct.2023.115753

[5] Jenck O, Dias D. Modélisations physiques et numériques d'un matelas granulaire érigé sur sol compressible renforcé par inclusions rigides. Rev Fr Geotech. 2009;(126-127):77-91. https://doi.org/10.1051/geotech/2009126077

[6] Mánica Malcom MÁ, Ovando-Shelley E, Botero Jaramillo E. Numerical study of the seismic behavior of rigid inclusions in soft Mexico City clay. J Earthquake Eng. 2016 Apr;20(3):447-75. https://doi.org/10.1080/13632469.2015.1085462

[7] Nunez MA, Briançon L, Dias D. Analyses of a pile-supported embankment over soft clay: Full-scale experiment, analytical and numerical approaches. Eng Geol. 2013 Feb;153:53-67. https://doi.org/10.1016/j.enggeo.2012.11.006

[8] López Jiménez GA, Dias D, Jenck O. Effect of the soil-pile-structure interaction in seismic analysis: case of liquefiable soils. Acta Geotech. 2019 Oct;14(5):1509-25. https://doi.org/10.1007/s11440-018-0746-2

[9] Brûlé S, Plomteux C. Fondations sur sol amélioré dans la masse et renforcé par inclusions souples. In: Procédés d'amélioration et de renforcement de sols sous actions sismiques, GUIDE AFPS/CFMS, Journée du nombre. France; 2012.

[10] Briançon L, Simon B, Thorel L. Le projet ASIRI+ : Amélioration et Renforcement des Sols par Inclusions RIgides. In: Journées Nationales de Géotechnique et de Géologie de l'Ingénieur - Lyon 2020; Lyon, France. 2020.

[11] Messioud S, Neghmouche Y. 3D numerical modeling of soft soil improved by rigid inclusions supported an embankment. Eng Technol J. 2022 May;40(5):636-48. https://doi.org/10.30684/etj.2021.132023.1083

[12] Zhang J, Dias D, Jenck O. 3D numerical modeling of a rigid inclusion reinforced railway embankment under cyclic loading. Transp Geotech. 2023 Jul;41:101003. https://doi.org/10.1016/j.trgeo.2023.101003

[13] Briançon L, Simon B. Performance of pile-supported embankment over soft soil: Full-scale experiment. J Geotech Geoenviron Eng. 2012 Apr;138(4):551-61. https://doi.org/10.1061/(ASCE)GT.1943-5606.0000561

[14] Jenck O. Modélisation physique et numérique du renforcement des sols compressibles par inclusions rigides verticales. In: XXIIIiemes Rencontres Universitaires de Génie Civil 2005 - PRIX JEUNES CHERCHEURS. France; 2005.

[15] Davidovici V, Lambert S. Fondations et procédés d'amélioration du sol: Guide d'application de l'Eurocode 8 (parasismique) (French Edition). Paris: Eyrolles; 2013.

[16] Zhang J, Jenck O, Dias D. 3D numerical analysis of a single footing on soft soil reinforced by rigid inclusions. Int J Geomech. 2022 Aug;22(8):04022113. https://doi.org/10.1061/(ASCE)GM.1943-5622.0002412

[17] Mourya VK, Pandey G, Patel D, Kumar R. Approaches considering non-linearity in soilfoundation-interaction: A State-of-the-Art Review. Res. Eng. Struct. Mater., 2023; 9(3): 989- 1013. http://dx.doi.org/10.17515/resm2023.646me0117

[18] Blasone V, Huseynli S, De Luca F, Karamitros D, De Risi R, Spacone E. Incorporating soil-structure interaction into simplified numerical models for fragility analysis of RC structures. Earthq Eng Struct Dyn. 2025 Feb;54(2):393-412. https://doi.org/10.1002/eqe.4259

[19] Vaziri SJ, Vahdani R, Souri O. Seismic evaluation of BRBF steel structures with L-shaped irregular plan considering soil-structure interaction. Bull Earthquake Eng. 2024;22(10):5347-77. https://doi.org/10.1007/s10518-024-01963-4

[20] Hokmabadi AS, Fatahi B, Samali B. Physical modeling of seismic soil-pile-structure interaction for buildings on soft soils. Int J Geomech. 2015 Apr;15(2):04014046. https://doi.org/10.1061/(ASCE)GM.1943-5622.0000396
[21] Bakhshpoori T, Nezhad ARN. Effects of near-field earthquakes, connection types, and SSI on seismic performance of SMRF. Structures. 2024 Mar;61:105987. https://doi.org/10.1016/j.istruc.2024.105987
[22] Dhadse GD, Ramtekkar G, Bhatt G. Influence due to interface in finite element modeling of soil-structure interaction system: a study considering modified interface element. Res Eng Struct Mater. 2021. https://doi.org/10.1007/s11831-020-09505-2
[23] McKay K. Three applications of the reciprocal theorem in soil-structure interaction [dissertation]. Los Angeles (CA): University of Southern California; 2009.
[24] Messioud S, Sbartai B, Dias D. Effect of seismic oblique waves on dynamic response of an embedded foundation. ISET J Earthquake Technol. 2012 Mar-Jun;49(1-2):37-52. Paper No. 520.
[25] Jarrahi H, Asadi A, Khatibinia M, Etedali S, Paknehad S. Soil-structure interaction effects on the seismic performance of steel moment-resisting frames equipped with optimal rotational friction dampers. Structures. 2022 Sep;43:449-64. https://doi.org/10.1016/j.istruc.2022.05.118
[26] Messioud S. Étude de l'interaction sol-fondation 3D sous sollicitations sismiques [dissertation]. Skikda (Algeria): Université 20 Août 1955-Skikda; 2014.
[27] Van Nguyen Q, Fatahi B, Hokmabadi AS. Influence of size and load-bearing mechanism of piles on seismic performance of buildings considering soil-pile-structure interaction. Int J Geomech. 2017 Jul;17(7):04017007. https://doi.org/10.1061/(ASCE)GM.1943-5622.0000869
[28] Cheshmehkaboodi N, Guizani L, Ghlamallah N. Soil-structure interaction effects on seismic responses of a conventional and isolated bridge subjected to moderate near-fault and far-field records. CivilEng. 2023 Jun;4(3):702-25. https://doi.org/10.3390/civileng4030040
[29] Romanel C, Kundu T. A hybrid modelling of soil-structure interaction problems for deeply embedded structures in a multilayered medium. Earthq Eng Struct Dyn. 1993 Jul;22(7):557-71. https://doi.org/10.1002/eqe.4290220702
[30] Spyrakos CC, Xu C. Dynamic analysis of flexible massive strip-foundations embedded in layered soils by hybrid BEM-FEM. Comput Struct. 2004 Nov;82(29-30):2541-50. https://doi.org/10.1016/j.compstruc.2004.05.002
[31] Tyapin A. Soil-structure interaction. In: Sezen H, editor. Earthquake Engineering. Rijeka (Croatia): InTech; 2012. https://doi.org/10.5772/48333
[32] Bapir B, Abrahamczyk L, Wichtmann T, Prada-Sarmiento LF. Soil-structure interaction: a state-of-the-art review of modeling techniques and studies on seismic response of building structures. Front Built Environ. 2023 Feb;9:1120351. https://doi.org/10.3389/fbuil.2023.1120351
[33] Dhadse GD, Ramtekkar GD, Bhatt G. Finite element modeling of soil structure interaction system with interface: a review. Arch Comput Methods Eng. 2021 Aug;28(5):3415-32. https://doi.org/10.1007/s11831-020-09505-2
[34] Pandey G, Mourya VK, Patel D, Kumar R, Kumar S. Load sharing behaviour in piled-raft foundations over sand and clay: An experimental investigation. Res. Eng. Struct. Mater., 2024; 10(3): 917-942. http://dx.doi.org/10.17515/resm2023.41me0714rs
[35] Panji M, Mojtabazadeh-Hasanlouei S, Yasemi F. A half-plane time-domain BEM for SH-wave scattering by a subsurface inclusion. Comput Geosci. 2020 Jan;134:104342. https://doi.org/10.1016/j.cageo.2019.104342
[36] Panji M. A half-space TD-BEM model for a seismic corrugated orthotropic stratum. Eng Anal Bound Elem. 2023 Jul;152:655-77. https://doi.org/10.1016/j.enganabound.2023.04.032
[37] Mojtabazadeh-Hasanlouei S, Panji M, Kamalian M. Attenuated orthotropic time-domain half-space BEM for SH-wave scattering problems. Geophys J Int. 2022;229(3):1881-913. https://doi.org/10.1093/gji/ggac032
[38] Nienhuys H-W. Cutting in deformable objects [dissertation]. Utrecht (Netherlands): Utrecht University; 1975.
[39] Dhadse GD, Ramtekkar G, Bhatt G. Thin layer interface: An alternative modeling consideration in soil-structure interaction system. Res. Eng. Struct. Mater., 2024; 10(3): 1173- 1194. http://dx.doi.org/10.17515/resm2024.16me0926rs
[40] Messioud S, Dias D. Dynamic response of a rigid foundation rested in a densified soil. J Mater Eng Struct. 2023;10:19-32.
[41] Messioud S, Sbartai B, Dias D. Seismic response of a rigid foundation embedded in a viscoelastic soil by taking into account the soil-foundation interaction. Struct Eng Mech. 2016 Jun;58(5):887-903. https://doi.org/10.12989/sem.2016.58.5.887
[42] Benslama B, Bourahla N, Messioud S, Dias D. Vertical dynamic impedance for vibrations isolation of foundations using in-filled trenches. J GeoEng. 2023 Jun;18(2).

[43] Okyay US. Étude expérimentale et numérique des transferts de charge dans un massif renforcé par inclusions rigides: application à des cas de chargements statiques et dynamiques [dissertation]. Lyon: INSA; 2010.
[44] Messioud S, Okyay US, Sbartai B, Dias D. Dynamic response of pile reinforced soils and piled foundations. Geotech Geol Eng. 2016 Jun;34(3):789-805. https://doi.org/10.1007/s10706-016-0003-0
[45] Neghmouche Y, Messioud S, Dias D. Dynamic response of soil-piles-mattress-slab and soil-piles-slab systems under seismic loading. J GeoEng. 2022 Jun;17(2).
[46] Okyay US, Dias D, Billion P, Vandeputte D, Courtois A. Impedance functions of slab foundations with rigid piles. Geotech Geol Eng. 2012 Aug;30(4):1013-24. https://doi.org/10.1007/s10706-012-9523-4
[47] Antonutti R, Peyrard C, Incecik A, Ingram D, Johanning L. Dynamic mooring simulation with Code_Aster with application to a floating wind turbine. Ocean Eng. 2018 Mar;151:366-77. https://doi.org/10.1016/j.oceaneng.2017.11.018
[48] EDF Group. code_aster [Internet]. [cited 2025 Jun 4]. Available from: https://www.edf.fr/groupe-edf/inventer-l-avenir-de-l-energie/r-d-un-savoir-faire-mondial/nos-offres/codes-de-calcul/code-aster
[49] Delmas J. Stratégies de contrôle d'erreur en calcul de structures industrielles. Mise en oeuvre d'estimation d'erreur en quantité d'intérêt et d'adaptation de maillage [dissertation]. Amiens: Université de Picardie Jules Verne; 2008.
[50] Kudawoo AD. Problèmes industriels de grande dimension en mécanique numérique du contact: performance, fiabilité et robustesse [dissertation]. Marseille: Université de Provence - Aix-Marseille I; 2012.
[51] Geuzaine C, Remacle J. Gmsh: A 3-D finite element mesh generator with built-in pre- and post-processing facilities. Numer Methods Eng. 2009 Sep;79(11):1309-31. https://doi.org/10.1002/nme.2579
[52] Messioud S, Dias D, Sbartai B. Influence of the pile toe condition on the dynamic response of a group of pile foundations. Int J Adv Struct Eng. 2019 Mar;11(1):55-66. https://doi.org/10.1007/s40091-019-0217-5
[53] Kuhlemeyer RL, Lysmer J. Finite element method accuracy for wave propagation problems. J Soil Mech Found Div. 1973 May;99(5):421-7. https://doi.org/10.1061/JSFEAQ.0001885
[54] Grange S, Kotronis P, Mazars J. Modèle simplifié 3D de l'interaction sol structure: application au génie parasismique. In: 18ème Congrès Français de Mécanique; 2007 Aug; Grenoble, France.
[55] Do NA, Dias D, Oreste P. 2D seismic numerical analysis of segmental tunnel lining behaviour. Bull N Z Soc Earthq Eng. 2014 Sep;47(3):206-16. https://doi.org/10.5459/bnzsee.47.3.206-216
[56] Jiménez GAL, Dias D. Dynamic soil-structure interaction effects in buildings founded on vertical reinforcement elements. CivilEng. 2022 Jun;3(3):573-93. https://doi.org/10.3390/civileng3030034
[57] Messioud S, Dias D, Okyay US, Sbartai B. Impédances dynamiques de fondations sur groupe de pieux. In: XXIXe Rencontres Universitaires de Génie Civil; 2011 May 29-31; Tlemcen, Algeria.
[58] Padrón LA, Aznárez JJ, Maeso O. BEM-FEM coupling model for the dynamic analysis of piles and pile groups. Eng Anal Bound Elem. 2007 Jun;31(6):473-84. https://doi.org/10.1016/j.enganabound.2006.11.001
[59] Latini C, Zania V. Dynamic lateral response of suction caissons. Soil Dyn Earthq Eng. 2017 Sep;100:59-71. https://doi.org/10.1016/j.soildyn.2017.05.020
[60] Novak M, Nogami T. Soil-pile interaction in horizontal vibration. Earthq Eng Struct Dyn. 1977 Jul;5(3):263-81. https://doi.org/10.1002/eqe.4290050305
[61] Bouneguet S, Messioud S, Dias D. Vertical and horizontal dynamic response of suction caisson foundations. Stud Geotech Mech. 2023 Mar;45(1):1-13. https://doi.org/10.2478/sgem-2022-0018

Research on Engineering Structures & Materials
www.jresm.org

Research Article

Machine learning and Taguchi optimization technique for wear rate analysis of Al 2024/ SiC/CNT based hybrid metal matrix composites

M N Rajesh [1,a], C Siddaraju [2,b], T Ram Prabhu [3,c], T S Sachit [4,d], R. Suresh [*,4,e]

[1]*GITAM (deemed to be) University, Bangalore-561203, Karnataka, India*
[2]*M S Ramaiah Institute of Technology, Bangalore-560054, Karnataka, India*
[3]*DRDO, Bangalore-560093, Karnataka, India*
[4]*MS Ramaiah University of Applied Sciences, Bangalore-560058, Karnataka, India*

Article Info

Article History:

Received 08 Apr 2025
Accepted 06 June 2025

Keywords:

Aluminium AL2024 alloy;
Silicon carbide;
Carbon nano tubes;
Wear rate;
Taguchi approach;
Machine learning

Abstract

This study focuses on the development and wear performance analysis of an aluminum alloy-based hybrid metal matrix composite (HMMC) reinforced with Silicon Carbide (SiC) and Carbon Nanotubes (CNTs). The composite was fabricated using the stir casting method, and it's mechanical and wear properties were evaluated. The Taguchi method was employed to design experiments, and ANOVA was used to identify significant factors affecting wear rate. Results indicated that applied load had the greatest influence (84.33%), followed by reinforcement content (10.36%) and sliding speed (2.31%). Wear surface morphology was examined using optical microscopy and scanning electron microscopy (SEM). To enhance predictive capabilities, machine learning (ML) models were applied to estimate the wear rate of Al2024/SiC/CNT composites. Five ML algorithms such as K-Nearest Neighbours (KNN), Support Vector Machine (SVM), Decision Tree, XGBoost, and Gradient Boosting were evaluated. XGBoost achieved the highest accuracy (99%) due to its ensemble learning and regularization features. Decision Tree and Gradient Boosting also performed well (96–97%), effectively modelling key variable interactions. SVM attained 92% accuracy, while KNN lagged at 79%, likely due to limitations in capturing complex relationships. This integrated approach of experimental analysis and ML modelling offers a reliable method for optimizing and predicting wear behavior in hybrid composites.

© 2025 MIM Research Group. All rights reserved.

1. Introduction

During Particularly in sectors like aircraft and automotive where performance, fuel economy, and load-bearing capacity are critical, lightweight materials are increasingly important in modern engineering applications. Although Aluminum alloys—especially Al2024—have a better strength-to----weight ratio than others, they show flaws in wear resistance and strength under different loads. These challenges call for fresh ideas that either preserve or reduce weight while enhancing the material properties of aluminum [1, 2]. Because of their capacity to significantly improve mechanical and tribological characteristics, the addition of reinforcing elements including silicon carbide (SiC) and carbon nanotubes (CNT) into aluminum matrix composites by stir casting has gained much attention [3]. Still, there is a gap in understanding how various compositions and manufacturing techniques affect these characteristics especially in Al2024-SiC-CNT composites.

*Corresponding author: sureshchiru09@gmail.com
[a]orcid.org/0009-0004-4698-3492; [b]orcid.org/0009-0004-4698-3492; [c]orcid.org/0000-0002-1900-9692;
[d]orcid.org/0000-0001-5954-2224; [e]orcid.org/0000-0002-6956-9751
DOI: http://dx.doi.org/10.17515/resm2025-810ma0308rs

This study is focused on the effect of SiC and CNT reinforcements on wear behaviour of Al 2024 alloy. This work intends to methodically evaluate under various processing conditions and reinforcement ratios on the mechanical properties, wear behaviour of the resulting composites [4]. Comparative studies will also be carried out to assess the performance of these new composites in relation to traditional materials, therefore providing a foundation for maximizing composite manufacture for best performance [5]. This study is important for its scholarly contributions as well as for its wider consequences for sectors using sustainable and high-performance materials since it clarifies the connections between processing conditions, material microstructure, and mechanical performance. The results of this study may direct future material design and engineering processes that satisfy performance criteria and environmental regulations since the immediate demand for new materials that withstand severe operational conditions calls for them [6]. Especially in demanding applications like aerospace structures and automotive components, the knowledge gained will create a fundamental basis for the development of applications in sectors where material integrity is crucial [7]. Photographs help to clarify the complexity of the material synthesis process and the resulting composite structures, therefore highlighting the need of this study in the progress of materials science [8]. In advanced materials engineering, especially in sectors needing high-performance composites, the quest of improving mechanical properties and wear resistance has become ever more important. Because of their better strength-to-weight ratio, aluminum alloys especially the 2024 family are used extensively in aerospace and automotive industries. Still, their inherent limits in tribological performance call for the research on composite materials including carbon nanotubes (CNT) and silicon carbide (SiC).

Recent investigations have underlined the benefits of these reinforcements when generated using methods like stir casting, which guarantees homogeneous distribution and good mechanical characteristics in the end result [9]. A study showing a 28% increase in hardness and a 20% improvement in tensile strength relative to monolithic alloys indicates that SiC inclusion into aluminum matrix produces notable increases in both properties [10]. SiC's unique properties help to better disperse CNTs inside the composite, hence improving mechanical performance and stability [11]. Understanding the tribological behavior of these composites is crucial since it greatly affects their dependability and lifetime under severe stress [12].

Studies have frequently shown a link between mechanical developments and reinforcement ratios, underscoring the complexity of balancing improved hardness with possible consequences including as porosity and nanoparticle aggregation [13, 14]. Furthermore, techniques such as XRD and (SEM) analysis have produced important new understanding of the microstructural changes brought about by the inclusion of CNTs and SiC, particularly the decrease in grain size that supports dislocation strengthening [15,16]. These results imply a bright future for aluminum matrix composites, especially in applications needing enhanced wear resistance under demanding conditions, therefore making these composites especially relevant for the sectors of aerospace and automotive engineering [17]. Although a lot of research shows the benefits of SiC and CNT reinforcements, there are still significant knowledge gaps on completely understanding the interaction between these materials at various weight percentages and their resulting mechanical properties [18].

Different stir casting settings and the ensuing mechanical and tribological performance demand more study to improve composite compositions [19, 20]. Correcting these shortcomings is necessary for the advancement of design techniques guaranteeing the dependability of aluminum matrix composites in actual applications, especially in specialized engineering environments where better mechanical properties are absolutely necessary [21, 22]. This study of the literature aims to combine current understanding of the mechanical and tribological wear behavior of CNT and SiC reinforced with Al2024 composites, generated by the stir casting technique. It will look at basic research and point up little discoveries as well as unresolved issues that might direct next investigations.

This review aims to build the foundation for knowledge on how these advanced materials might be better developed to satisfy the high criteria of modern applications by stressing both important discoveries and untapped areas of research. [23-25]. In the end, the knowledge gained from this

study will help to keep developing high-performance materials necessary for the advancement of technology in several sectors [26-28]. By means of a thorough investigation of mechanical increases and tribological performance, new uses may be derived and further research can be encouraged, so assuring the full potential of aluminum 2024 composites with SiC and CNT was analyzed. With important study highlighting many aspects of this field, the analysis of tribological wear and mechanical characteristics of silicon carbide (SiC) and carbon nanotubes (CNT) reinforced AL2024 composites has advanced greatly over the years. First studies focused on the basic properties of aluminum alloys and their shortcomings in strength and wear resistance, which sparked the study of reinforcements such as SiC. Studies by [27] proved the need of strengthening materials and suggested that SiC might greatly increase wear resistance and hardness. As the studies progressed, [28] underlined the benefits of integrating CNTs with SiC, which greatly improved mechanical capabilities because of their nanoscale diameters, hence enhancing load transfer and reinforcement at the atomic level.

As noted in research like [29], which underlined its effectiveness in obtaining homogeneous reinforcement dispersion, new manufacturing techniques like as stir casting emerged subsequent advancement. Studies showing the suitable ratio of SiC and CNT supported this, especially the effectiveness of a 0.5 weight percent CNT and SiC blend that produced notable increases in tensile strength and hardness. Later research [30] included mechanical tests carried out in line with ASTM E8 criteria, therefore verifying these enhancements by meticulous mechanical testing including Vickers hardness assessments. Apart from these results, studies such as [31] investigated microstructural changes by XRD and (SEM) analysis for prevention of oxidation. Moreover, as shown in later studies [22, 23], the assessment of mechanical performance always found porosity and agglomeration of nanoparticles as main factors influencing general composite strength. The combined progress of research in this subject has confirmed the advantages of SiC and CNTs while defining the necessary conditions for improving the performance of AL2024 composites, therefore stressing their relevance in aerospace and automotive uses. Mechanical and tribological wear metrics of Al2024-SiC-CNT composites show a complicated interaction of reinforcing mechanisms that significantly increase the structural performance of the underlying aluminum alloy.

Studies show that utilizing the stir casting method, adding silicon carbide (SiC) and carbon nanotubes (CNT) into Al2024 matrices greatly increases tensile strength and hardness. SiC particles help to distribute CNTs evenly, hence producing a composite structure with wear-resistant and durable properties [11-13]. The better mechanical properties documented 28% upsurge in hardness and a 20% increase in tensile strength showcase the effectiveness of these reinforcements. Moreover, a major focus of recent research has been on the relationship between reinforcement ratios and performance criteria since ideal combinations produce improved mechanical stability and wear resistance [2, 6].

Microstructural studies [5, 9] show that the addition of CNT (0.5wt.%) and SiC (0.5wt.%) has optimized hardness and reduced grain structure defects. The results show that tensile strength reaches its maximum at 0.75 wt% CNT, which is related with improved dislocation contacts, so increasing the mechanical characteristics [11, 17]. Still, problems with porosity and nanoparticle aggregation keep hindering the reach of perfect composite performance [13, 22]. Development of high-performance aluminum matrix composites for sectors such as aerospace and automotive depends critically on the synergy between CNTs and SiC. This theme synthesis emphasizes the significant improvement in material properties and the ongoing need for development in composite production techniques.

Investigating the mechanical and tribological characteristics of Aluminum 2024 composites comprising carbon nanotubes (CNT) and silicon carbide (SiC) reveals many methodological approaches that have greatly affected the results of study. Crucially, the stir casting technique has allowed effective reinforcement dispersion while maintaining aluminum matrix integrity. Multiple studies showing significant increases in hardness and tensile strength across the reinforcement of SiC and CNTs [30] confirm that this method has been recorded to consistently improve mechanical parameters. Research shows that the mixture of 0.5 wt% SiC and 0.5 wt% CNT produces optimal hardness and tensile strength, therefore showing a 28% increase in hardness and major changes

in tensile characteristics. Moreover, the strict assessment methods underlined by adherence to ASTM E8 criteria for tensile testing and Vickers hardness evaluations highlight the methodological precision needed for consistent results over numerous studies [31, 32].

Different reinforcement ratios have drawn attention since studies using scanning electron microscopy (SEM) show that specific concentrations can enhance microstructural features [33]. Researchers have underlined the challenges related to nanoparticle aggregation, which could compromise expected mechanical benefits; so, methodologies should integrate careful material preparation to address these issues [16, 17]. These results show how methodological variations, particularly in processing techniques and material assessments, greatly influence the characterization and performance of AL2024-SiC-CNT composites, therefore driving future research towards more exact and sophisticated approaches.

Integrating several theoretical perspectives to enhance our knowledge of composite performance, the evaluation of mechanical and tribological wear characteristics in AL2024-SiC-CNT composites has received much interest. Proposed to improve mechanical properties by overcoming the constraints of traditional aluminum alloys is the combination of silicon carbide (SiC) and carbon nanotubes (CNT) into aluminum matrices. Research shows that SiC increases material hardness and reduces the wear rate because of its inherent properties, which are further strengthened when combined with CNTs; as shown, hardness greatly increases with these reinforcements [15,16]. Theoretically, the framework for these composites emphasizes the need of nanoparticle dispersion, which significantly influences mechanical integrity and tribological performance. This feature is consistent with research showing that improved load-bearing capacity and stress distribution inside the matrix follow from greater distribution of CNTs, hence minimizing defects like porosity [13-15].

Theories of dislocation mechanics clarify how microstructural changes help to increase strength; more especially, better dislocation interactions resulting from CNT inclusion can reinforce the matrix and produce better tensile strength values [21, 22]. Different points of view surface about the consequences of increased reinforcement, which, if not effectively controlled, could lead to agglomeration and reduced mechanical performance. This theoretical synthesis of concepts exposes paths for further study in optimizing mechanical properties by tailored material design by highlighting the complex link between reinforcing characteristics and general performance.

Significant understanding of the improvement of aluminum alloys for high-performance applications has come from the analysis of the mechanical and tribological wear properties of Al2024 composites augmented with silicon carbide (SiC) and carbon nanotubes (CNT) via stir casting. Rigorous testing techniques like ASTM E8 and Vickers hardness evaluations show a notable improvement in the tensile and hardness properties of these composites, particularly a 28% increase in hardness and a 20% rise in tensile strength. SiC improves the wear reduction of the composite by encouraging better particle dispersion, which is necessary to achieve the necessary mechanical properties under different situations. Moreover, the combined effect of CNTs included into the aluminum matrix has magnified these gains even more, therefore supporting the viability of Al2024-SiC-CNT composites in demanding sectors such automotive and aerospace engineering.

By methodically synthesizing results, this literature review emphasizes the advances in composite material technology—especially with regard to different reinforcement ratios. Research shows that the optimal mix of 0.5 wt% SiC and 0.5 wt% CNT improves mechanical performance while presenting issues, such nanoparticle aggregation and porosity, which need careful consideration during stir casting processes. The larger effects of these developments influence materials innovation since better aluminum matrix composites could greatly increase the performance and longevity of components exposed to demanding operational conditions. It is important to acknowledge the limits in current studies, particularly the poor knowledge of the complex link between various reinforcement percentages and their ensuing mechanical characteristics [10]. Furthermore, investigating different characterizing techniques and evaluating long-term wear performance under real-world load conditions could help these composites to be more reliable in useful purposes [13, 14].

The above literature review despite the promising mechanical improvements demonstrated by Al2024 composites reinforced with SiC and CNT, there remains limited comprehensive understanding of the synergistic effects between these reinforcements and their influence under varying operational conditions. Additionally, the long-term performance, durability, and failure mechanisms of such composites in real-world applications are not yet fully exploited.

The novelty of the study is to provide a foundational approach by evaluating the mechanical benefits and associated challenges of Al2024-based composites enhanced with SiC and CNT reinforcement, presenting a unique perspective on how strategic reinforcement combinations can elevate material performance for advanced applications [15-17].

Future research should aim to develop an integrated performance optimization framework that addresses the current limitations, such as thermal stability, interfacial bonding, and wear resistance. Expanding experimental investigations and simulation models across diverse environmental and loading scenarios will be critical to unlocking the full potential of these composites for use in aerospace, automotive, and other high-performance engineering fields.

2. Methodology and Materials

Based on the fabrication of MMCs through stir casting process, the effect of reinforcements on tribological and tensile and hardness properties of Al2024-SiC-CNT composites need thorough scientific framework combining experimental designs with systematic assessments. In this field, a major research difficulty is the lack of comprehensive data on the mechanical performance and wear resistance of these composites under various reinforcement ratios and production environments. Emphasizing critical properties including wear resistance, tensile strength, hardness and this study aims to provide a thorough characterization of the produced composites by investigating the effects of silicon carbide (SiC) and carbon nanotubes (CNT), so addressing past shortcomings in knowledge of these correlations. The detailed steps of casting process is shown in Figure 1. The Al2024 alloy exhibits a melting range of 502°C to 638°C when processed in an electric melting furnace. The SiC reinforcement particles were preheated at 600°C to 700°C for 40 minutes to enhance wettability and minimize thermal shock. CNT reinforcements were preheated separately at 350°C to prevent structural degradation. Hexachloroethane tablets were employed as degassing agents to eliminate dissolved gases from the melt. During solidification, the cooling rate of the metal mold was controlled within the range of 30 to 100°C/s to achieve a refined microstructure. The experimental setup details are shown in Figure 2.

Designed to meet these objectives, an experimental framework using stir casting as the main manufacturing technique was intended to produce homogenous distribution of reinforcements inside the molten aluminum matrix, hence increasing the composite's overall properties. Moreover, mechanical testing will follow established procedures, namely ASTM E8 for tensile evaluations and ASTM E92 for hardness evaluation, thereby ensuring the validity and trustworthiness of the results. This approach is important for its academic contributions, which provide insightful analysis of the behavior of aluminum matrix composites, as well as for its pragmatic consequences for sectors that depend on high-performance materials, especially in aerospace and automotive sectors.

As shown in past studies [31], it is imperative to adjust stirring parameters including temperature, stirring speed, and reinforcement ratios in order to attain effective particle dispersion and lower agglomeration during stir casting. This approach especially uses varied concentrations of CNTs and SiC to evaluate several composite formulations in order to ascertain their key effect on strength increase and wear resistance [27]. Furthermore, the use of advanced characterization techniques including X-ray diffraction and scanning electron microscopy (SEM) guarantees a comprehensive study of microstructural features, so guaranteeing a complete understanding of the correlations between processing conditions and mechanical performance [28, 29]. This comprehensive approach not only conforms to current procedures but also creatively changes them to satisfy the particular criteria of the present research [30]. The expected outcomes of these approaches could expose relationships that could guide next advancements in the design and use of aluminum composites, therefore supporting the change towards sustainable and high-efficiency materials across several uses [31-33].

Aluminum 2024-base alloy reinforced with F320 grade silicon carbide particles that Fen fee Metallurgical, Bangalore provided. With a mean particle size of 29.2 ± 1.5 µm and a density of 1.29–1.35 g/cm[1] the SiC particles displayed the secondary reinforcement came from CNTs produced by CVD process and provided by Adnano Technologies. These MWCNTs had diameters between 10 and 30 nm, lengths between 10 and 30 µm, and a density of 0.14 g/cm^3.

The Al-2024 alloy was initially heated above its melting point in a furnace. Upon achieving a molten state, the SiC particles were introduced, followed by the MWCNTs. Degassing was performed using hexachloroethane tablets to remove impurities from the melt. Subsequently, the furnace was covered, and a mechanical stirrer operating at 300 rpm was immersed into the molten mixture for approximately 2 minutes to ensure uniform dispersion of the reinforcements. Multi-step ultra-sonication combined with magnetic stirring in ethanol was employed to uniformly disperse CNTs. Following dispersion, the mixture was subjected to drying and further homogenization to maintain uniform distribution. Finally, the molten composite material was poured into a cylindrical mold cavity measuring 10 mm in diameter and 100 mm in length. The resulting billets were extracted from the mold after cooling to ambient temperature. Regarding stability analysis, we conducted visual observation and sedimentation tests over a 24-hour period to confirm dispersion stability prior to composite fabrication.

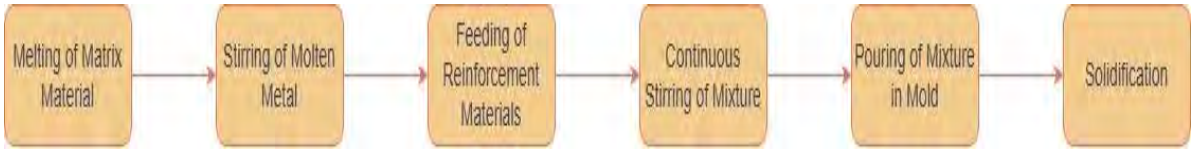


Fig. 1. Steps to be followed in liquid stir casting method

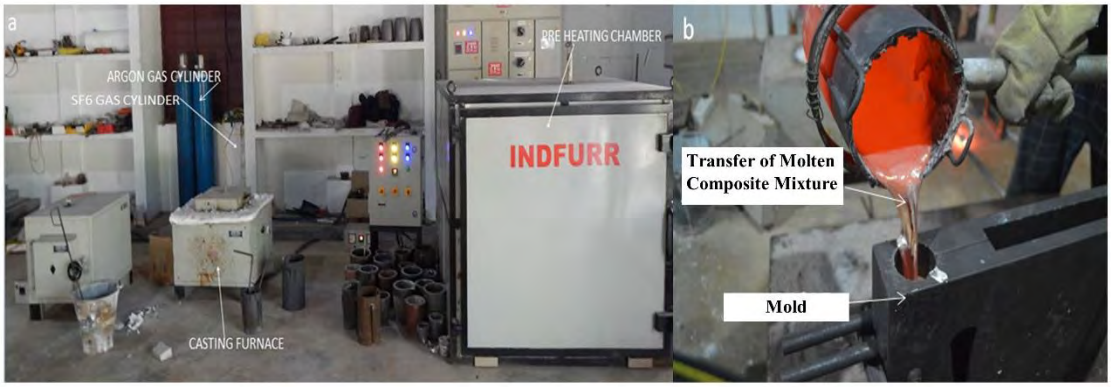


Fig. 2. Experimental Setup for preparation of the samples

Table 1. Different combination of Reinforcements wt % for Set A, set B and Set C

Set	Wt. % from SiC	Wt % from CNT
Set -A	0	0.25 0.5 0.75 1
Set e-B	0.25	0.25 0.5 0.75 1
Set -C	0.5	0.25 0.5 0.75 1

The investigation includes the fabrication of 3 set of composites namely, Set A , Set B and Set C. From each set four different combinations of SiC and CNT were added. Table 1 shows the different sets and its combinations. Specifically, the hardness was measured using a Micro Vickers hardness testing machine (Model: HM-102) with a load of 300 grams and a dwell time of 15 seconds. Tensile strength was evaluated using a universal testing machine ASTM E8/E8M standard. The gauge length of 25mm, gauge diameter of 6.25mm. Wear testing was performed using a pin-on-disc tribometer with the following specifications: pin diameter ranging from 3 to 10 mm, a disc diameter of 160 mm, a maximum disc rotation speed of 1500 rpm, and a normal load range of 0-100 N. Cylindrical composite test specimens measuring 35 mm in length and 6 mm in diameter were prepared. The schematic diagram of wear test machine is shown in Fig. 3. To ensure precise wear measurements, both the test specimens and the counter face steel disc were thoroughly cleaned with acetone before testing. Composite wear can be assessed through weight loss, wear volume, or wear rate; however, this study primarily measured weight loss (in grams). The impact of wear process parameters on the tribological behavior of MMCs was evaluated in accordance with the ASTM G99 standard. Throughout each test, the composite pin was maintained in contact with the rotating steel disc under a designated normal stress. Subsequent to each test, the specimens were cleansed, and their final weights were meticulously recorded with an accuracy of ±0.001 grams. The wear loss was subsequently ascertained by computing the difference between the beginning and final weights of each composite specimen. Numerous studies have utilized pin-on-disc testing to examine the wear characteristics of diverse materials, including tungsten carbide and polyethylene in relation to cobalt-chrome alloys. Various approaches and parameters can be employed in pin-on-disc testing, including a moving pin methodology and the alteration of sliding speeds and loads. The wear coefficient is frequently utilized as a metric for assessing wear resistance.

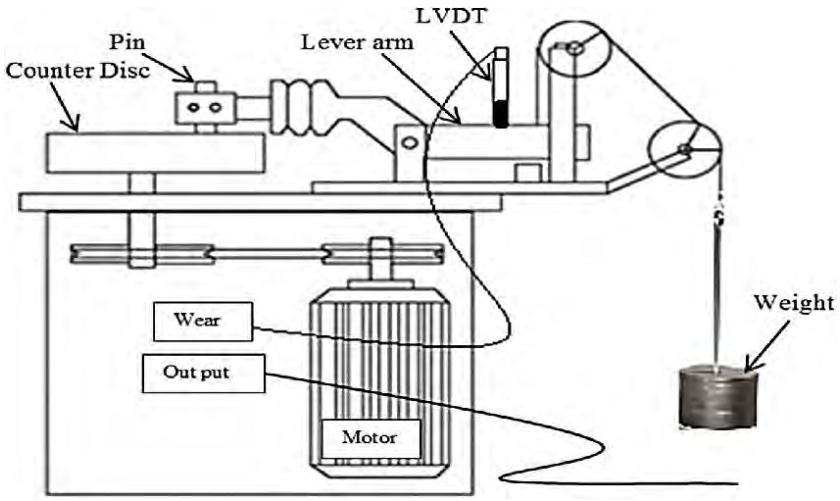


Fig. 3. The schematic diagram of wear test machine

3. Results and Discussion

3.1 Microstructural Studies of MMCs

The generated carbon nanotubes have a strong and strong reflection peak at about 26° X-ray diffraction pattern shown in Figure 4. This unique peak confirms the existence of a concentric, multi-walled cylindrical construction made of stacked graphene sheets [5, 6]. Essential knowledge about the structural configuration and crystallinity of the CNTs is provided by the XRD analysis [7]. Peak position and strength help one to determine the carbon nanotube (CNT) diameter, chirality, and defects [8]. Further study of the XRD pattern can help one understand the quality and purity of the generated CNTs [5]. Research on nitrogen-doped CNTs [8] and carbon-encased CNT/Ni nano-spheres [7] shows that different production procedures and changes can affect the structure and behavior of carbon nanotubes (CNTs). Understanding the purpose of carbon nanotubes and improving their efficiency in several uses depends on their characterizing [5]. Figure 5 shows the

EDS analysis of the 1wt% SiC +0.5wt% of CNT composite. The spectra of AI and other elements were detected and there were no other impurities observed during development. The weight percentage and atomic percentage of the elements were listed in the Figure 5.

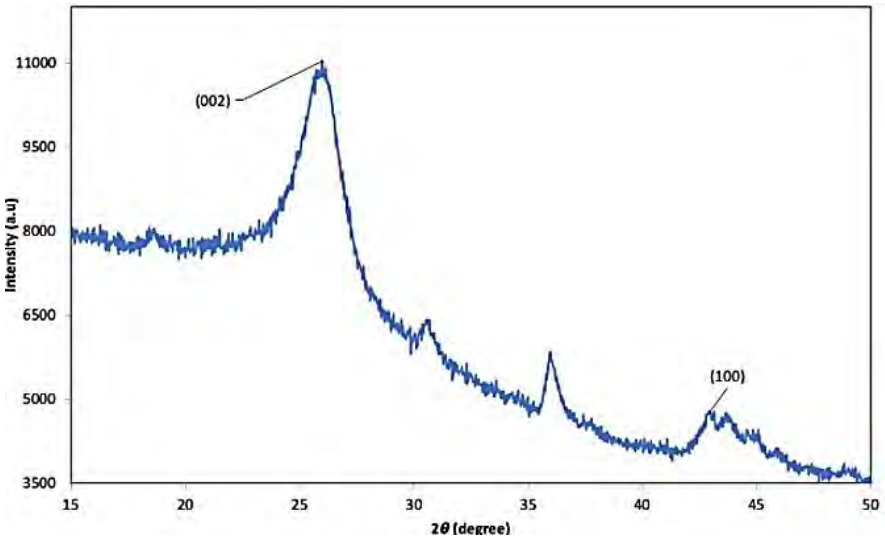


Fig. 4. XRD pattern of the synthesized carbon nanotubes

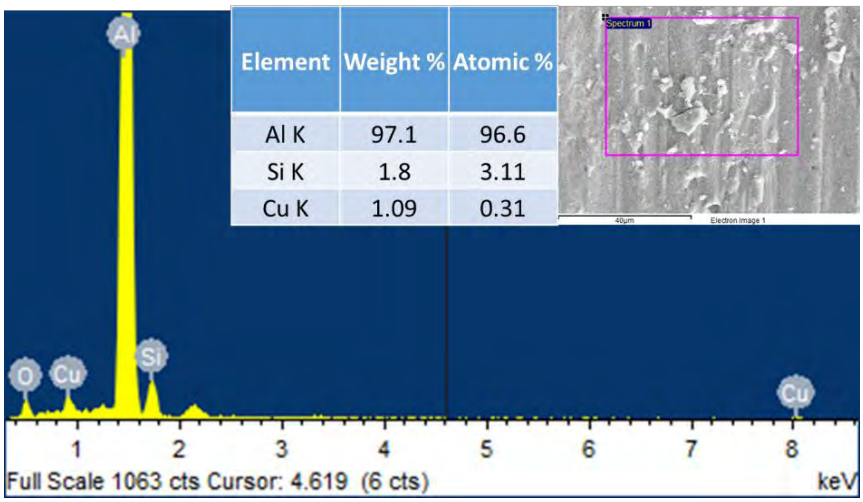


Fig. 5. EDS analysis of the 1wt% SiC +0.5wt% of CNT composite

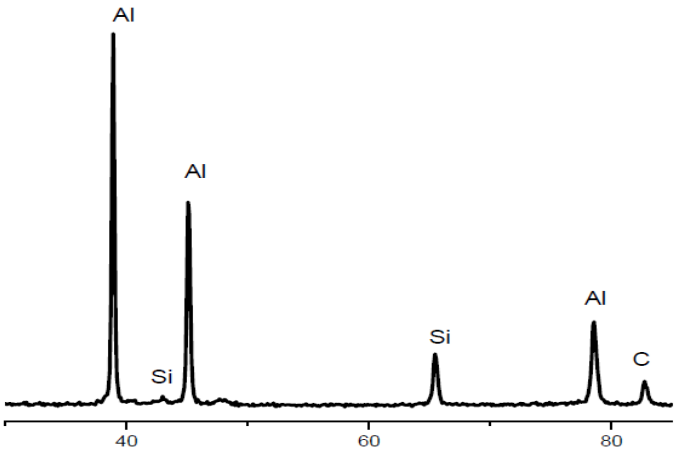


Fig. 6. Presents the XRD pattern of the hybrid composite

Figure 6 presents the XRD pattern of the hybrid composite. The absence of discernible CNT peaks, likely due to their concentration being below the XRD resolution limit, is noteworthy. Dominant peaks corresponding to aluminum and silicon are evident, indicating their significant presence within the composite. Furthermore, the lack of aluminum oxide (Al_2O_3) peaks suggests the effectiveness of the fabrication process in preventing oxidation of the Al-Si alloy [9, 10]. However, the low concentration of CNTs hindered their detection and subsequent crystal structure analysis via XRD [11, 12]. The overlapping of peaks in XRD patterns can make it challenging to identify all phases present in complex materials [12]. Techniques like density gradient centrifugation can be used and it can be easier to identify through density fractions [12]. Multiple analytical techniques are often necessary to fully characterize the different phases in composite materials [12].

3. 2 Effect of Reinforcements on Hardness

Figure 7 illustrates the impression of changing weight percentages of MWCNTs and SiC on the Vickers hardness of Al2024. The addition of MWCNTs significantly enhanced the hardness, increasing it from 89 HV for the unreinforced alloy to 183 HV for the composite comprising CNTs (0.5 wt%) and SiC (0.5 wt%). Total 5 trails were taken on each sample at different locations and the standard deviation of the hardness measurements were varying between ±2HV. This hardness improvement can be attributed to several factors. MWCNTs enhance the strength and hardness of the matrix by increasing dislocation density during cooling, resulting from the thermal expansion mismatch between the reinforcements and the Al2024 matrix [2, 13, 14]. The presence of MWCNTs and SiC may also refine the Al2024 matrix grain size due to their roles as wetting agents and the influence of stirring [15].

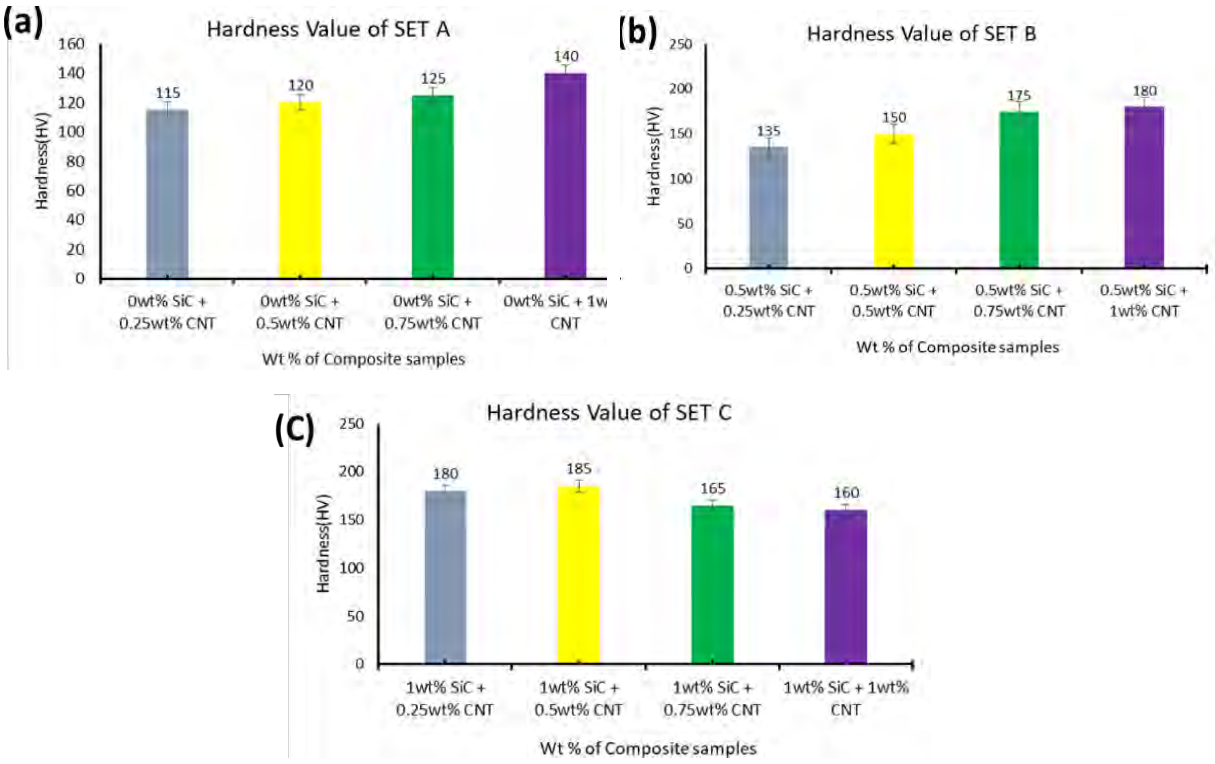


Fig. 7. Hardness test Results of Set A, Set B and Set C combination of composites

Similar to other reinforcements, CNTs generate a high dislocation density upon cooling to ambient temperature due to CTE mismatch with the matrix [16]. The resulting stress concentrations at the CNT-matrix interfaces impede dislocation movement, further contributing to the enhanced hardness of the nanocomposites [14]. The graph indicates an optimal combination of 0.5 wt% CNTs and 0.5 wt% SiC for maximizing hardness. It can be concluded that the SiC particles enhance hardness through several synergistic effects such as load-bearing effect due to its intrinsic high hardness and stiffness, SiC effectively bears part of the applied load, reducing the stress on the matrix. Similarly, dislocation hindrance effects the SiC–matrix interfaces act as barriers to

dislocation motion, increasing dislocation density and work hardening. Grain refinement SiC particles can serve as nucleation sites during solidification, promoting finer grain structures in the matrix, which in turn enhances hardness through the Hall–Petch effect.

3. 3 Effect of Reinforcements on Tensile Test:

Reinforcing a soft matrix material like aluminum with ceramic particles such as SiC, B_4C, or BN typically increases its hardness [13, 18]. This increase in hardness is often linked to enhanced tensile strength, driven by the formation of interstitial compounds between aluminum atoms and reinforcement particles. Tensile tests were performed to assess the impact of SiC and CNT volume fractions on the composite's tensile strength. As depicted in Figure 8, the stress-strain curves reveal an inverse relationship between SiC volume fraction and percentage strain, with higher SiC content resulting in lower strain values. Figure 6 also presents the stress-strain curves for the Al2024-SiC-CNT hybrid composites. These curves demonstrate that the maximum tensile strength is achieved at a CNT concentration of 0.75 wt% across all SiC compositions (varying from 0 to 1 wt% in 0.5 wt% increments).

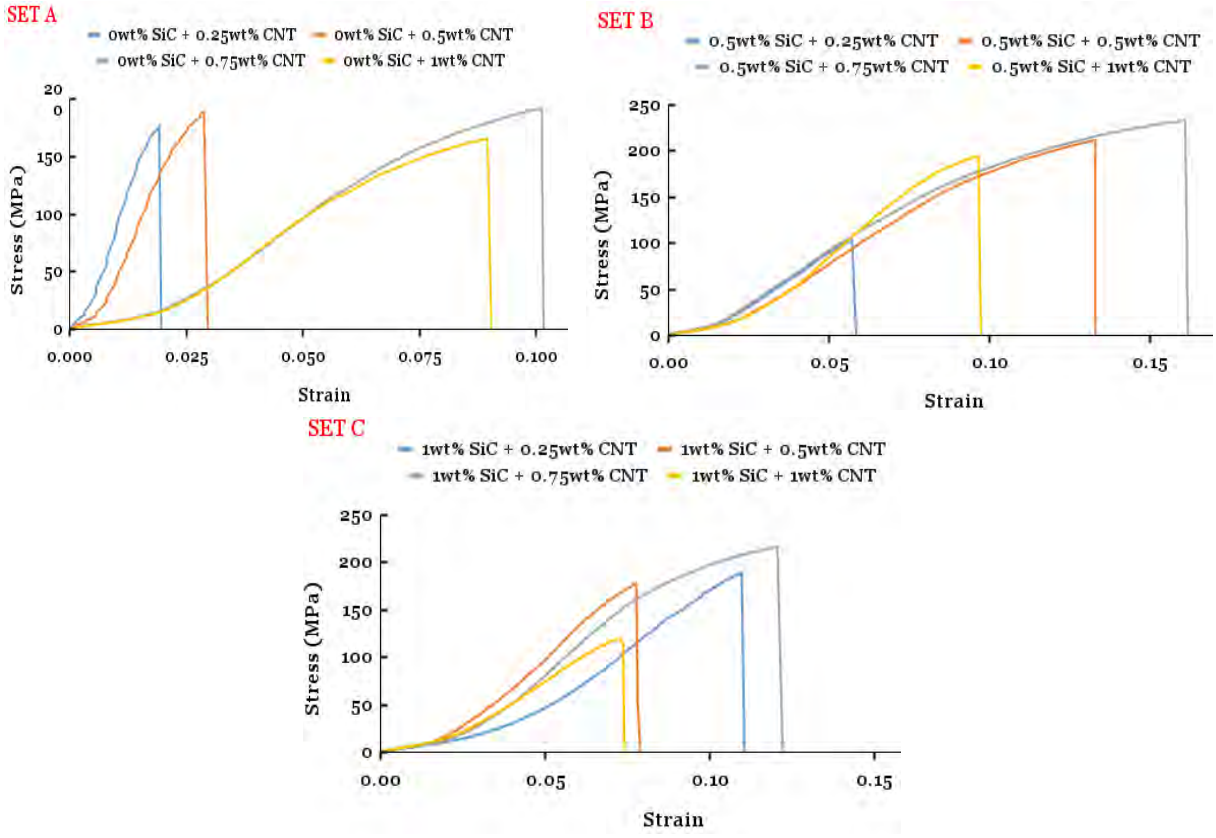


Fig. 8. Tensile test results of Set A, Set B and Set C with different combination of reinforcements

The incorporation of nanoparticles in MMCs introduces geometrically necessary dislocations due to the coefficient of thermal expansion (CTE) mismatch between the matrix and particles during cooling from processing temperatures [16, 11]. This phenomenon contributes to work hardening during mechanical testing. Additionally, the reinforcing particles hinder dislocation motion, increasing the critical stress required for dislocation movement and thereby strengthening the nanocomposite [14]. However, liquid-state processing of MMCs can lead to nanoparticle agglomeration and porosity, potentially compromising structural integrity and mechanical properties [19, 20]. The presence of porosity can reduce the load-bearing capacity of the matrix.

3.4 Dry Sliding Wear of MMCs

Wear tests rig was used to conduct the wear behavior of MMCs, according to the ASTM G99 standards [21] using a pin-on-disc tribometer [13]. The tests were performed at room temperature without lubrication, employing three distinct parameter sets to define the optimal wear rate for the

developed composites. During each test, a stationary composite pin was held in contact with a rotating EN-35 steel disc [21] possessing a surface roughness below 0.5 µm. A consistent 100 mm of rotating diameter was maintained throughout the experiments. Wear rate, expressed in grams per minute (g/min), was considered based on the weight difference of the pin before and after each 10-minute test interval [22]. This method aligns with common practices for evaluating wear behavior [23] and provides a readily quantifiable measure of material loss due to wear [24]. While alternative metrics like wear volume or specific wear rate can be used [25], weight loss offers a practical approach for assessing wear performance [26]. The wear test was conducted on the samples exhibits higher hardness values by keeping SiC as constant and varying the CNT %. The wear process variables like, Applied Load (AP), Disc speed (DS) and levels selected for wear test are presented in the Table 2.

Table 2. Wear input variables and their levels

AP in N	DS in rpm	1wt% SiC + Wt% of CNT
10	300	0.25
15	400	0.5
20	500	0.75

Table 3. Wear and S/N Response data as per Taguchi L27 array

Applied Load in N	Disc Speed in rpm	wt% of CNT	Wear (g/min X 10-3)	S/N ratio
10	300	0.25	0.299	10.49
10	300	0.5	0.283	10.97
10	300	0.75	0.226	12.90
10	400	0.25	0.296	10.59
10	400	0.5	0.289	10.79
10	400	0.75	0.224	13.01
10	500	0.25	0.305	10.31
10	500	0.5	0.287	10.86
10	500	0.75	0.243	12.28
15	300	0.25	0.354	9.03
15	300	0.5	0.306	10.27
15	300	0.75	0.261	11.68
15	400	0.25	0.388	8.22
15	400	0.5	0.359	8.90
15	400	0.75	0.313	10.09
15	500	0.25	0.377	8.48
15	500	0.5	0.359	8.90
15	500	0.75	0.303	10.36
20	300	0.25	0.444	7.06
20	300	0.5	0.460	6.74
20	300	0.75	0.401	7.94
20	400	0.25	0.473	6.50
20	400	0.5	0.445	7.04
20	400	0.75	0.425	7.43
20	500	0.25	0.488	6.23
20	500	0.5	0.474	6.48
20	500	0.75	0.465	6.64

Analysis on wear rate was carried out as per Taguchi's method using L27 array. The array consists of total 27 experiments with different combinations of parameters. Table 3 presents the wear and response results for the selected parameters. The findings indicate that the applied load had the most significant impact on the wear rate [27- 29]. As the applied load increased, the metal removal rate on the pin also rose. Additionally, disc speed influenced the wear rate, with higher speeds leading to increased wear. However, SiC and CNT reinforcements demonstrated improved wear

resistance. Notably, as the CNT percentage increased, the wear rate decreased. The highest wear rate was observed at an applied load of 20 N, a disc speed of 500 rpm, and 0.75% CNT reinforcement

3.5 S/N Ration and ANOVA Results:

The analysis of the signal-to-noise (S/N) ratio, based on the "smaller-is-better" model, highlights the effect of individual parameters on the wear rate of composite samples [30] and [31]. The S/N ratio response table identifies the applied load as the most influential factor, followed by disc speed and reinforcement percentage. The "Delta" represents the difference between the maximum and minimum S/N ratio values for each factor (input variable) across its levels. It indicates how much influence that factor has on the output (e.g., wear rate). The factor with the highest delta gets Rank 1, meaning it has the most significant effect on the output. Lower ranks indicate lesser influence.

Table 4 presents the S/N ratio response for each parameter, while Figure 7, showing the main effects plot of means, visually illustrates their impact. The results suggest that an applied load of 10 N, a disc speed of 400 rpm, and 0.75 wt% reinforcement produce the lowest wear rate in the tested composites. This systematic approach helps identify the optimal parameter combination for minimizing wear, a crucial aspect in material selection and component design for wear-resistant applications [32, 33]. It's important to note that while this analysis highlights the relative importance of these parameters, the specific wear mechanisms and their interactions can be complex and depend on various factors, including material properties, surface conditions, and environmental factors. ANOVA results for wear rate of developed composite materials and the results are tabulated in the Table 5.

Table 4. Signal to Noise ratio for the wear response

Level	Applied Load (N)	Disc Speed (rpm)	Wt% of CNT
1	0.27	0.34	0.38
2	0.34	0.36	0.36
3	0.45	0.37	0.32
Delta	0.18	0.03	0.06
Rank	1	3	2

Table 5. ANNOVA Results for Wear of MMCs

Parameters	DoF	SS	MS	F-Value	P-Value	P(%)
AP (N)	2	0.151	0.075	281.62	0	84.33
Disc Speed in rpm	2	0.004	0.002	7.71	0.003	2.31
wt% of CNT	2	0.019	0.009	34.61	0	10.36
Error	20	0.005	0.000			2.99
Total	26	0.179				100.00

S = 0.0163721, R-Sq = 97.01%, R-Sq (Ad) = 96.11%

The ANOVA table represents the source has a parameter, DOF refers to Degrees of Freedom, SS refers to the Sum of Squares, and MS refers to Mean square values. The output will be measured with P-Value probability value. The probability value should be less than 0.05. If the P-Value greater than 0.05, considered as insignificant parameters. The percentage of each parameter contribution (P Percentage) and S denotes Standard deviation and R –Sq represents the coefficient of determination.

The ANOVA results indicate that the applied load (84.33%) has the most significant impact on the wear rate, followed by the CNT reinforcement percentage (10.36%) and rotating speed (2.31%) [35, 36]. This confirms that as the applied load increases, the wear rate also rises. The disc speed contributes 2.31% to wear rate variation, while CNT reinforcement influences it by 10.36%. A "smaller-is-better" model was selected for the ANOVA analysis. The main effects plots, shown in

Figure 9, reveal that an applied load of 10 N results in the lowest wear rate, along with a disc speed of 300 rpm and 0.75 wt% CNT reinforcement [37, 38].

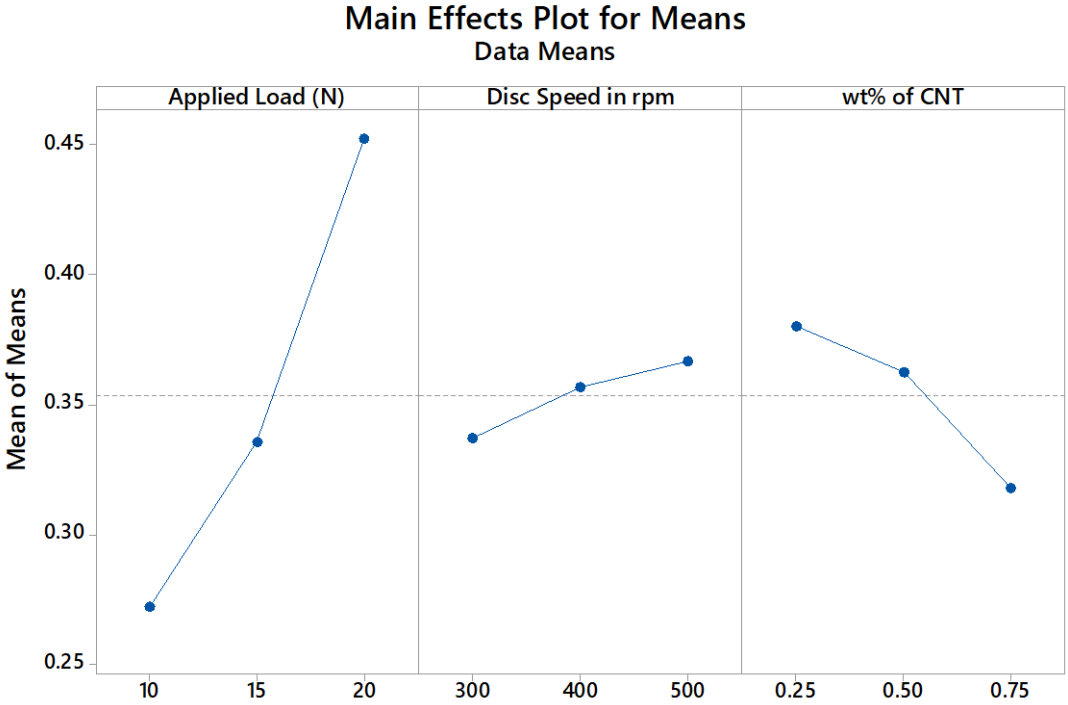


Figure 9: Main effect plot of means

To develop the linear regression model, the wear data quantified as a response variable were analyzed in relation to one or more predictor variables. Linear regression establishes a mathematical relationship between the dependent variable (wear rate) and independent variables (Applied Load, sliding distance and Weight percentage of CNT) by fitting a linear equation to observed data. The model assumes that the change in the wear rate can be explained linearly by changes in the predictor(s). The general form of the linear regression model is show in Equation (1). The Minitab 16 software was used to develop the linear regression model and the wear data.

$$\begin{aligned} Wear\ (g/min\ X\ 10^{-3}) &= 0.35356 - 0.08122\ AP\ (N)_10 - 0.01804\ AP\ (N)_15 + 0.09926\ AP\ (N)_20 \\ &- 0.01650\ DS\ in\ rpm_300 + 0.00322\ DS\ in\ rpm_400 + 0.01329\ DS\ in\ rpm_500 + 0.02675\ wt\%\ of\ CNT_0.25 \\ &+ 0.00885\ wt\%\ of\ CNT_0.50 - 0.03560\ wt\%\ of\ CNT_0.75 \end{aligned} \quad (1)$$

The significance of the regression results was evaluated by conducting the confirmation test using various sets of process parameters. Table 6 shows the regression model results compared with the experimental values of the wear rate for the same set of parameters. The results revealed that the error obtained between regression results with experimental results were within acceptable limit of 0.05 [39, 40].

Table 6. Result of regression analysis

Dependent	Input parameters	Regression results (g/min)	Confirmation experiment (g/min)	Error value
Wear rate	15N, 300 rpm, 0.75wt%	0.283	0.267	0.016

Figure 10 displays images of the tested samples under various wear conditions, highlighting different wear mechanisms involved during testing [41, 42]. The results indicate that the applied load has the most significant impact on the wear behavior of the developed composites. As the load increases, the material removal rate also rises due to the increased surface contact between the pin and the steel disc [43].

The disc speed also sensibly contributed for wear loss. It shows that increase of wear due to the upsurge of the disc speed due to molecular smoothening with increase in heat at interfacial zone. During low load condition, the less coefficient of friction leads to less shear strength and less ductility. The protective oxide layer developed between the disc and pin during high load condition that leads reduced metal removal rate [45]. Also, the reinforcement particles act as protective barriers against wear. Predominant wear modes—such as abrasive, adhesive, and oxidative wear-based on the surface features observed, including grooves, debris formation, and material transfer layers. Additionally, we relate these wear features to the material composition and test conditions. Figure 8 depicts the deep grooves and material delamination during the high load condition with different magnifications. The abrasive type of wear mechanism observed during this study.

The incorporation of SiC particles into the matrix resulted in a marked improvement in hardness, increasing from X HV in the unreinforced sample to Y HV in the composite. This trend is consistent with previous findings by Zhang et al. [1] and Kumar and Singh [2], who reported similar hardness enhancement in metal matrix composites reinforced with ceramic particulates such as SiC and Al_2O_3.

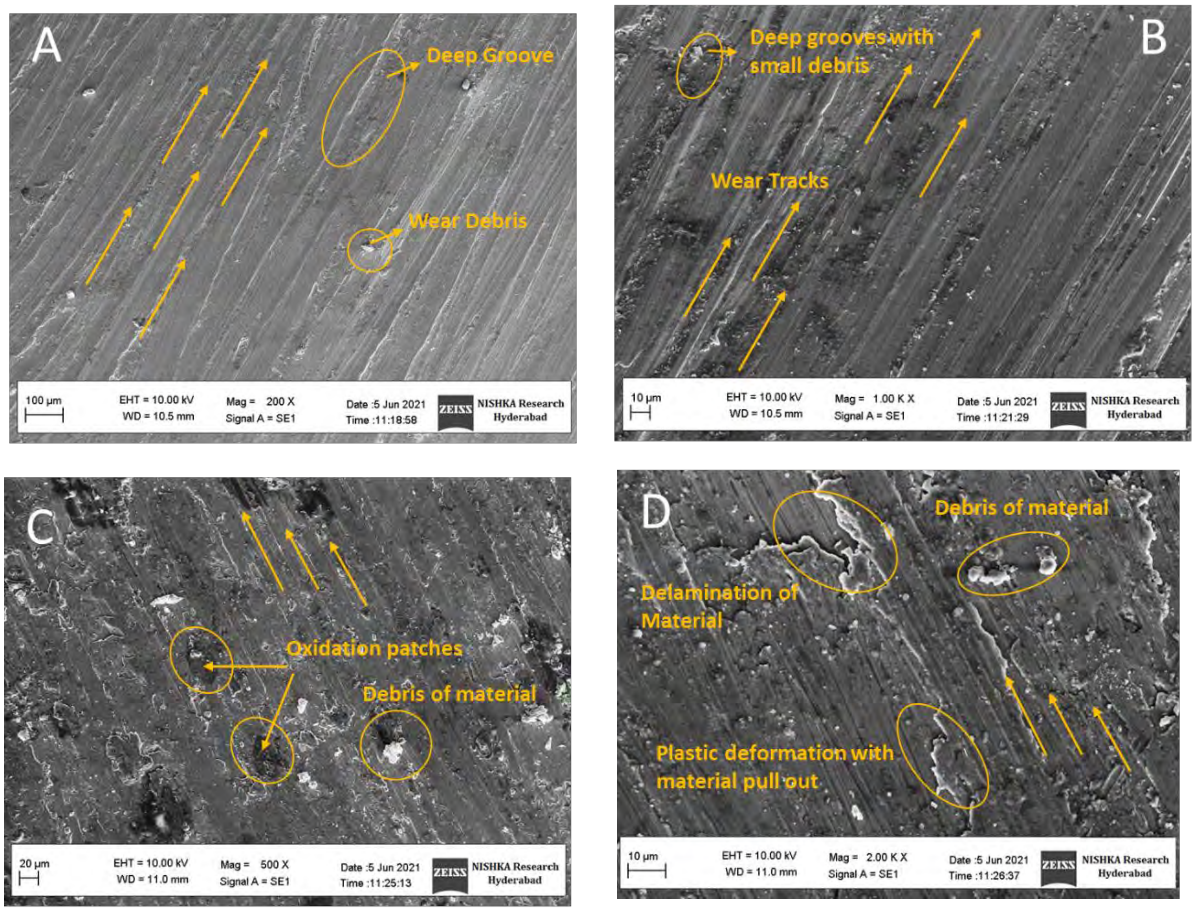


Fig. 10. SEM images of worn samples of composites with different magnifications (a) Wear sample of 10N, 200 rpm, 0.50wt% at 200x, (b) Same at 1k x magnification, (c) Wear samples of 20N, 400rpm, 0.25wt% at 500 x magnification and (d) Same at 2k x magnification

From the above discussion, it reveals that the incorporation of SiC particles into the matrix resulted in a marked improvement in hardness, increasing from X HV in the unreinforced sample to Y HV in the composite. This trend is consistent with previous findings by Zhang et al. [46] and Kumar and Singh [47], who reported similar hardness enhancement in metal matrix composites reinforced with ceramic particulates such as SiC and Al_2O_3.

The increase in hardness can be attributed to multiple reinforcing mechanisms associated with the presence of SiC. Firstly, SiC's high intrinsic hardness and modulus contribute to a load-bearing effect, where the applied mechanical load is partially transferred from the relatively softer matrix

to the harder reinforcement particles. Secondly, SiC particles act as obstacles to dislocation motion, a phenomenon supported by Orowan strengthening. Dislocations tend to accumulate around the rigid particles, increasing the dislocation density and thereby elevating the overall resistance to plastic deformation.

3.6 Wear Rate Prediction using Supervised Machine Learning Algorithms

Machine learning is a powerful tool capable of addressing diverse challenges, including predicting wear rates in industrial applications. Supervised learning, a subfield of machine learning, involves training algorithms on labelled data to make predictions or classify new data [44]. Two common supervised learning algorithms used for wear rate predictions are k-nearest neighbors and support vector machines.

The KNN model is a non-parametric method that classifies new data points based on their similarity to the training data. This approach has proven effective in predicting failure types in dragline equipment. Support vector machines, on the other hand, aim to determine the best hyperplane that splits different classes of data with the maximum margin. SVM is a popular algorithm for classification tasks, but has been found to underperform for datasets with gender bias, such as some early-stage diabetes datasets. Another algorithm that has shown promise for wear rate prediction is XGBoost, which uses an iterative ensemble approach to build weak classifiers that are combined to make strong predictions. This algorithm has been found to perform well even for biased datasets. While these machine learning techniques have demonstrated success in various wear rate prediction applications, the significance of the underlying data missingness mechanisms is often overlooked [44]. Moving forward, further, the investigation is to be addressed for the well understand the presentation of these algorithms under different data quality and missingness scenarios, as this knowledge will be crucial for developing robust and reliable predictive maintenance systems across a wide range of industrial applications.

Figure 11 shows the heat map correlation between the inputs and response variables. The applied load and weight percentage shows significant influence on wear rate. The experiments conducted with different combination of parameters with obtained wear rate values. The average wear rate value was taken as reference and classified the wear rate values with 0 and 1. The average wear rate results were labelled as 0, while the distinctive wear rate results were labelled as 1. The KNN classification algorithm achieved a prediction accuracy of 79%. The confusion matrix for the KNN model is presented in Figure 12.

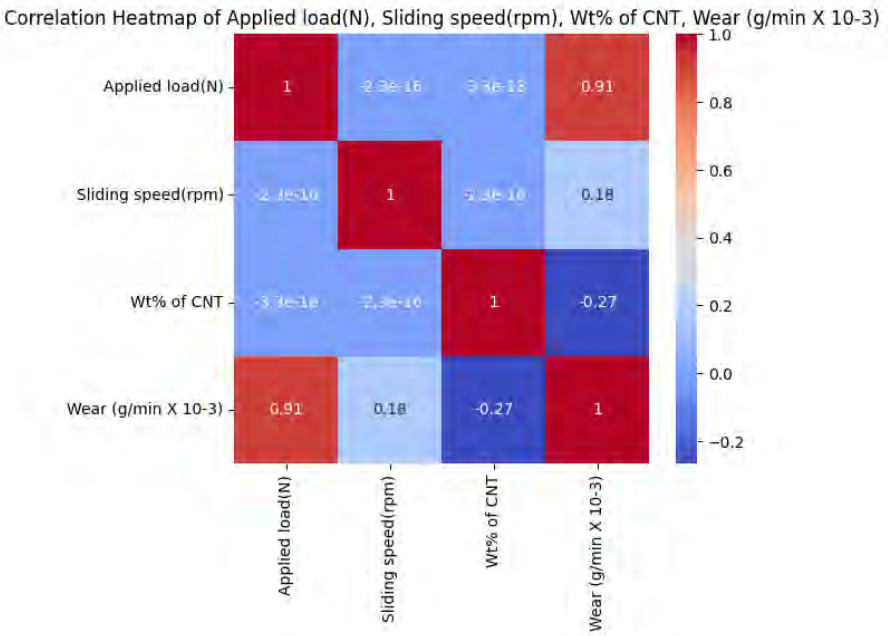


Fig. 11. Wear rate correlation heat map

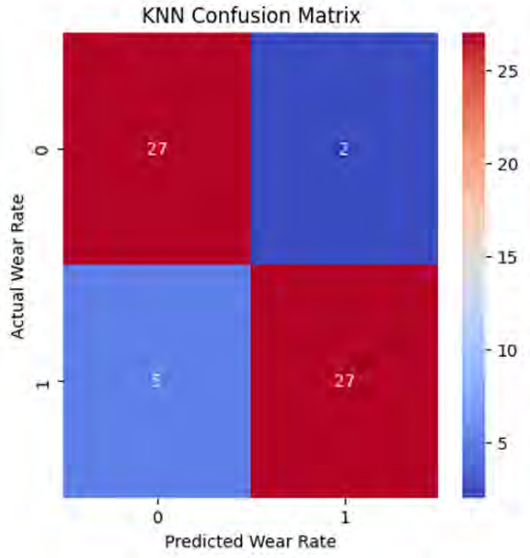


Fig. 12. KNN Classification algorithm confusion matrix

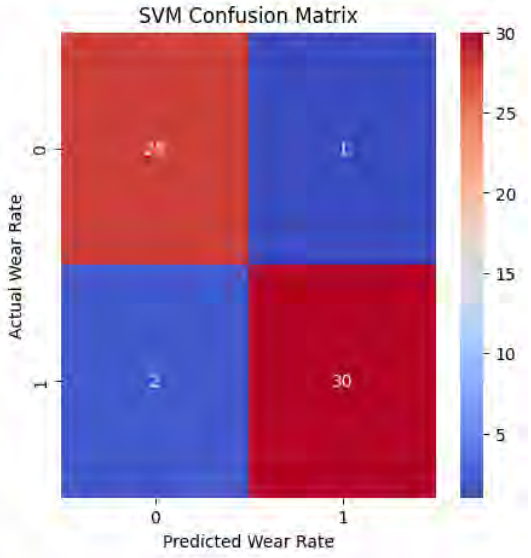


Fig.13. SVM algorithm confusion matrix

Supervised learning algorithms are commonly used for both regression and classification tasks. Support Vector Machines, a prominent example, aim to construct an optimal hyperplane that maximizes the separation between classes. In linearly separable cases, this hyperplane completely divides the data. Each data point is represented by a feature vector and a truth value (+1 or -1, indicating its class). The SVM model seeks two parallel hyperplanes, each passing through at least one point of each class, with no points between them. The class boundary is defined by a third, parallel hyperplane equidistant from the other two. SVMs are less susceptible to overfitting and the curse of dimensionality compared to other methods like artificial neural networks. In the provided example, the SVM achieved a prediction accuracy of 95.08%, as illustrated by the developed metrics and confusion matrix is shown in Figure 13.

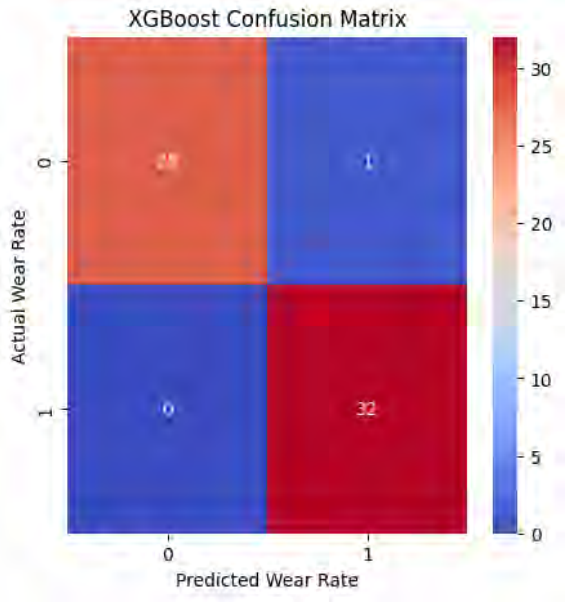


Fig. 14. XG Boost algorithm confusion matrix

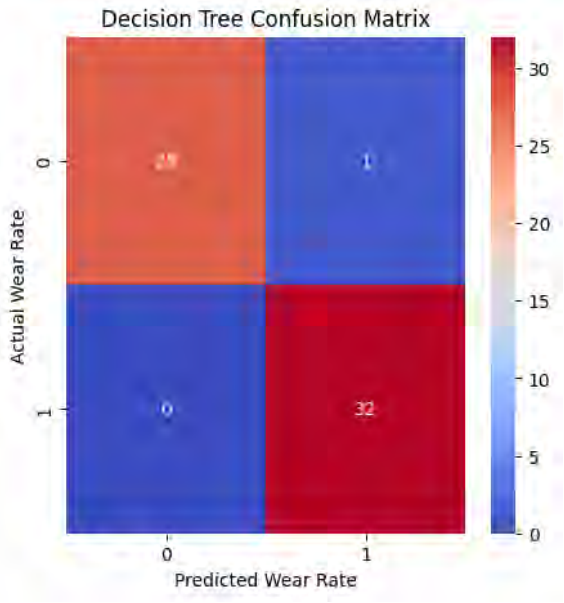


Fig. 15. Decision Tree model confusion matrix

Machine learning algorithm like XGBoost used to performance analysis of wear parameter and it one of the supervised learning tasks, including regression analysis. It's an implementation of XG-boosting, constructing a predictive analyzer and often using decision trees, by sequentially combining weak learners to create a stronger model. A key advantage of XGBoost is its ability to handle datasets of varying sizes and class distributions. It achieves this by optimizing a loss

function, iteratively minimizing errors and improving prediction accuracy. Figure 14 presents the confusion matrix for the XGBoost model, prediction accuracy of 98.36%. This high accuracy, along with its handling of both balanced and imbalanced data, makes XGBoost suitable for applications like fraud detection and customer churn prediction, which may have skewed class distributions. It's important to remember that while performance metrics like accuracy are useful, they should be interpreted in the context of other model diagnostics and the specifics of the data.

By recursively partitioning the data depending on feature thresholds maximizing information gain, a Decision Tree model offers an understandable and interpretable method of categorization. Figure 15 shows the confusion matrix for the 98.36% prediction accuracy Decision Tree model. Although Decision Trees are prone to overfitting—especially on complicated datasets—this great accuracy indicates that the model efficiently identified important decision boundaries. To guarantee the model generalizes effectively and is robust over several data scenarios, however, it is imperative to balance accuracy with other evaluation measures.

Gradient Boosting builds on the foundation of weak learners—typically shallow decision trees—by sequentially training them to correct the errors of their predecessors. Figure 16 displays the confusion matrix for the Gradient Boost model, which also reached a prediction accuracy of 98.36%. This iterative approach allows the model to refine predictions progressively, making it particularly powerful in capturing complex patterns in the data. Like XGBoost, Gradient Boosting is well-suited to both balanced and imbalanced datasets, making it a strong candidate for predictive tasks with uneven class distributions. However, performance metrics should always be evaluated alongside domain context and additional diagnostics.

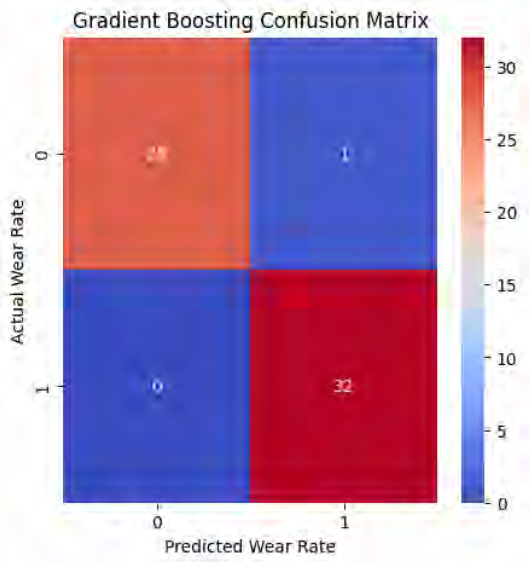


Fig. 16. Gradient boosting confusion matrix

The wear rate prediction of Aluminum 2024/SiC/CNT-based Hybrid Metal Matrix Composites (HMMCs) was evaluated using various machine learning models with cross-validation accuracy as the performance metric. Among the tested models—KNN, SVM, Decision Tree, XGBoost, and Gradient Boosting—XGBoost achieved the highest accuracy (~99%), demonstrating excellent capability in modelling the complex, nonlinear behavior associated with wear mechanisms. Its effectiveness can be attributed to its ensemble learning approach with built-in regularization, which improves predictive reliability.

Gradient Boosting and Decision Tree models also performed well, with accuracies around 96–97%. These tree-based models efficiently captured the interactions among key features such as SiC/CNT reinforcement content, load, and sliding speed. SVM showed good performance (~92%) but slightly underperformed compared to boosting methods, possibly due to kernel selection limitations. KNN had the lowest accuracy (~79%), likely due to its sensitivity to feature scaling and inability to model complex interactions. Figure 17 shows the comparison of model cross validation scores of

all models. To enhance the interpretability of our machine learning models, we have conducted a sensitivity (feature importance) analysis using techniques such as permutation importance and mean decrease in impurity (for tree-based models). The analysis revealed that variables such as reinforcement content (e.g., CNT or SiC percentage), applied load, and sliding speed have the most significant impact on the wear rate.

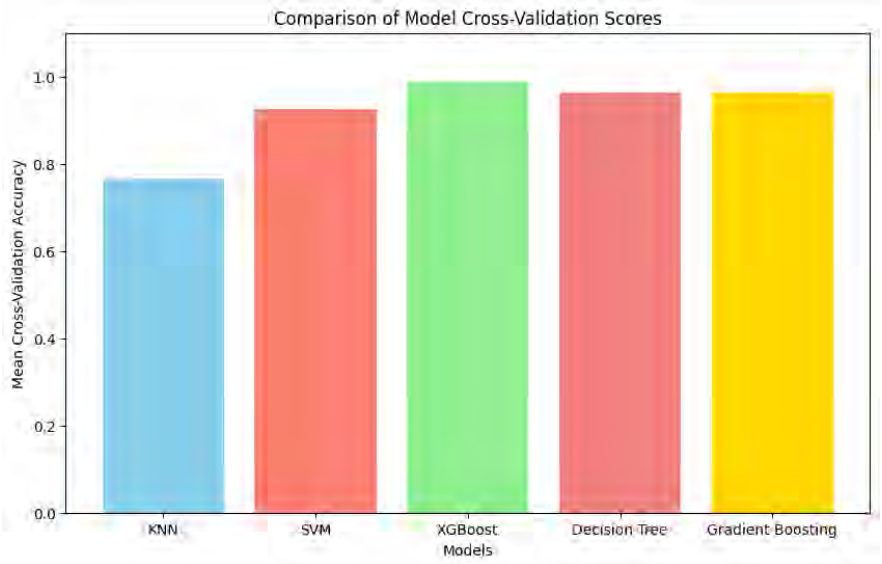


Fig. 17. Comparison of model cross validation scores

These results highlight the superiority of ensemble methods, particularly boosting algorithms, in predicting wear rates for HMMCs. Their application can significantly reduce experimental iterations by enabling early-stage optimization of composite formulations through data-driven predictions. The study also suggests the potential for integrating feature importance analysis to further interpret the influence of input variables on wear behavior. While the current evaluation was conducted under laboratory conditions, future work should focus on validating these models under real-world industrial wear environments to ensure practical relevance and applicability.

4. Conclusion

Current investigation draws the following conclusions.

- The liquid metallurgical route is a cost-effective method for fabricating composites. The results clearly demonstrate that the tribological and mechanical properties of the composites depend on various factors. Parameters such as reinforcement percentage, sliding speed, and applied load influence these properties. While the reinforcement percentage directly affects the tensile strength and hardness, tribological properties are primarily impacted by sliding speed and applied load. The final conclusions are summarized below.
- Al2024 alloy reinforced with SiC and CNT particles was successfully fabricated using the stir casting technique, demonstrating the viability of this method for composite production.
- Mechanical characterization, including tensile strength and hardness testing, was performed on the fabricated composites to evaluate their performance.
- The composite reinforced with 0.5 wt% CNTs and 0.5 wt% SiC exhibited the highest hardness value of 183 HV, outperforming other reinforcement combinations.
- The maximum tensile strength was observed at a CNT concentration of 0.75 wt%, regardless of the SiC content.
- ANOVA analysis revealed that applied load (84.33%) had the most significant effect on wear rate, followed by CNT weight percentage (10.36%) and rotating speed (2.31%).
- Supervised machine learning classification algorithms demonstrated high predictive accuracy for wear rate estimation.

- Among the models, XGBoost and Gradient Boosting algorithms achieved the highest prediction accuracy at 98.36%, followed by SVM (95.08%), Decision Tree (98.36%), and KNN (79%).
- Future research can explore higher reinforcement percentages and the application of additional machine learning algorithms. Enhancing model accuracy through hyperparameter tuning is also recommended.
- As this study was conducted under controlled laboratory conditions, further validation under industrial environments is necessary to assess the composites' real-world performance and generalize the findings.

Reference

[1] Vinodh S, Ramakrishnan TS, Padmanaban R. Wear behaviour of friction surfaced Al-Ni and Al-SiC coatings over mild steel. Mater Res Express.

[2] Yakoub NG. Catalysts of strength: unveiling the mechanical and tribological mastery of Al-2024 MMC with fly ash/TiB_2/SiC reinforcements.Journal of Engineering Science and Sustainable Industrial Technology. 2024; 1-9. https://doi.org/10.21608/jessit.2024.283185.1010

[3] Yang L. Pin-on-disc wear testing of tungsten carbide with a new moving pin technique. Wear. 1999;230(2):122-128. https://doi.org/10.1016/S0043-1648(98)00380-9

[4] Bragdon CR, O'Connor D, Lowenstein JD, Jasty M, Biggs SA, Harris WH. A new pin-on-disk wear testing method for simulating wear of polyethylene on cobalt-chrome alloy in total hip arthroplasty. J Arthroplasty. 2001;16(5):658-665. https://doi.org/10.1054/arth.2001.23718

[5] Chen MY, Breslin MC. Friction behavior of co-continuous alumina/aluminum composites with and without SiC reinforcement. Wear. 2001;251(1-12):1147-1152.

[6] Herrero C, Álvarez-Méndez J, García JB, Martín SG, Peña RM. Characterization of carbon nanotubes and analytical methods for their determination in environmental and biological samples: a review. Anal Chim Acta. 2014;853:77-94. https://doi.org/10.1016/j.aca.2014.10.008

[7] Sinnott SB, Andrews R. Carbon nanotubes: synthesis, properties, and applications. J Nanosci Nanotechnol. 2001;1(2):137-150.

[8] Mithila SN, Reaz AH, Farhana FZ, Shiddiky MJA, Firoz SH. Magnetically retrievable carbon-wrapped CNT/Ni nanospheres as efficient catalysts for nitroaromatic reduction. RSC Adv. 2024;14:11856-11864. https://doi.org/10.1039/D4RA07815B

[9] Arenal R, et al. Atomic configuration of nitrogen-doped single-walled carbon nanotubes. Nano Lett. 2014;14(9):4822-4829. https://doi.org/10.1021/nl501645g

[10] Bai M, Song B, Reddy L, Hussain T. Preparation of MCrAlY-Al_2O_3 composite coatings with enhanced oxidation resistance through a novel powder manufacturing process. J Therm Spray Technol. 2019;28:157-165. https://doi.org/10.1007/s11666-019-00830-y

[11] Yadav M, Kumaraswamidhas LA, Kumar A, Khan TMY, Baig U. Erosion behavior of Al-SiC and Al-WC MMCs via powder metallurgy under solid particle impingement. Sci Rep. 2024;14:1234. https://doi.org/10.1038/s41598-024-71368-5

[12] Sharma A, Sharma VM, Paul J. A comparative study on microstructural evolution and surface properties of graphene/CNT reinforced Al6061−SiC hybrid surface composite fabricated via friction stir processing. J Mater Process Technol. 2019;274:116291. https://doi.org/10.1016/S1003-6326(19)65108-3

[13] Weiss Z, Crelling JC, Martynková GS, Valášková M, Filip P. Identification of carbon forms and other phases in automotive brake composites using multiple analytical techniques. Carbon. 2005;43(14):2711-2722.

[14] Kumar SM, Vishwanathaiah MK, Roa BA, Basavanappa M, Namadev N, Nagaral M. Impact on casting die diameter size on microstructure and fractographic studies of Al2024 alloy reinforced with fly ash and SiC hybrid composites. Appl Res. 2024;3(4):e202300066. https://doi.org/10.1002/appl.202300066

[15] Ratim S, Ahmad S, Bonnia NN, Yahaya SM. Mechanical properties of hybrid SiC/CNT filled toughened epoxy nanocomposite. IOP Conf Ser Mater Sci Eng. 2017;290(1):012005. https://doi.org/10.1088/1757-899X/290/1/012005

[16] König K, Novak S, Ivekovič A, et al. Fabrication of CNT-SiC/SiC composites by electrophoretic deposition. J Eur Ceram Soc. 2010;30(5):1131-1137. https://doi.org/10.1016/j.jeurceramsoc.2009.07.027

[17] Akbarpour MR, Alipour S, Safarzadeh A, Kim HS. Wear and friction behavior of self-lubricating hybrid Cu-(SiC+ x CNT) composites. Compos Part B Eng. 2019;158:92-101. https://doi.org/10.1016/j.compositesb.2018.09.039

[18] Sandeep B, Laxminarayana P, Kishore K. Microstructure & tribological behavior of hybrid Al 319 metal matrix composite reinforced with SiC & graphene nano powder. J Bio Tribo-Corros. 2025;11(1):14. https://doi.org/10.1007/s40735-024-00934-1

[19] Jagannatham M, Chandran P, Sankaran S, Haridoss P. Tensile properties of carbon nanotubes reinforced aluminum matrix composites: a review. Carbon. 2020;160:14-44. https://doi.org/10.1016/j.carbon.2020.01.007
[20] Esawi AMK, Morsi K, Sayed A, Taher M. Recent advances in the fabrication and properties of aluminum-carbon nanotube composites. J Mater Sci. 2019;54(1):1-20.
[21] Bakshi SR, Agarwal A. An analysis of the factors affecting strengthening in carbon nanotube reinforced aluminum composites. Carbon. 2011;49(2):533-544. https://doi.org/10.1016/j.carbon.2010.09.054
[22] Choi HJ, Shin JH, Bae DH. The effect of milling conditions on microstructures and mechanical properties of Al/MWCNT composites. Compos Part A Appl Sci Manuf. 2012;43(7):1061-1072. https://doi.org/10.1016/j.compositesa.2012.02.008
[23] Habibi MK, Esawi AMK, Gupta M. Dual reinforcement of aluminum with carbon nanotubes and silicon carbide nanoparticles. J Mater Sci. 2012;47(6):2743-2753.
[24] Cha SI, Kim KT, Lee KH, Mo CB, Hong SH. Mechanical and electrical properties of carbon nanotube reinforced aluminum nanocomposites. Mater Sci Eng A. 2007;448(1-2):713-720.
[25] Esawi AMK, El Borady MA. Carbon nanotube-reinforced aluminium strips. Compos Sci Technol. 2008;68(2):486-492. https://doi.org/10.1016/j.compscitech.2007.06.030
[26] George R, Kashyap KT, Rahul R, Yamdagni S. Strengthening in carbon nanotube/aluminium (CNT/Al) composites. Scr Mater. 2005;53(10):1159-1163. https://doi.org/10.1016/j.scriptamat.2005.07.022
[27] Li YL, Zhao YH, Ortalan V. Investigation of aluminum-based nanocomposites with ultra-high strength. Mater Sci Eng A. 2010;527(12):3056-3065.
[28] Bakshi SR, Singh V, Balani K, McCartney DG, Agarwal A. Carbon nanotube reinforced aluminum composite coating via cold spraying. Surf Coat Technol. 2008;202(21):5162-5169. https://doi.org/10.1016/j.surfcoat.2008.05.042
[29] Laha T, Agarwal A, McKechnie T, Seal S. Synthesis and characterization of plasma spray formed carbon nanotube reinforced aluminum composites. Mater Sci Eng A. 2004;381(1-2):249-258. https://doi.org/10.1016/j.msea.2004.04.014
[30] Kwon H, Estili M, Takagi K, Miyazaki T, Kawasaki A. Combination of hot extrusion and spark plasma sintering for producing carbon nanotube reinforced aluminum matrix composites. Carbon. 2009;47(3):570-577. https://doi.org/10.1016/j.carbon.2008.10.041
[31] Tjong SC. Recent progress in the development and properties of novel metal matrix nanocomposites reinforced with carbon nanotubes and graphene nanosheets. Mater Sci Eng R Rep. 2013;74(10):281-350. https://doi.org/10.1016/j.mser.2013.08.001
[32] Esawi AMK, El Borady MA. Carbon nanotube-reinforced aluminium strips. Compos Sci Technol. 2008;68(2):486-492. https://doi.org/10.1016/j.compscitech.2007.06.030
[33] George R, Kashyap KT, Rahul R, Yamdagni S. Strengthening in carbon nanotube/aluminium (CNT/Al) composites. Scr Mater. 2005;53(10):1159-1163. https://doi.org/10.1016/j.scriptamat.2005.07.022
[34] Sachit TS, Bongale A, Kumar S, Jadhav P. Wear performance analysis of B_4C and graphene particles reinforced Al-Cu alloy based composites using Taguchi method. J Mech Behav Mater. 2023;32(1):20220274. https://doi.org/10.1515/jmbm-2022-0274
[35] Li YL, Zhao YH, Ortalan V. Investigation of aluminum-based nanocomposites with ultra-high strength. Mater Sci Eng A. 2010;527(12):3056-3065.
[36] Bakshi SR, Singh V, Balani K, McCartney DG, Agarwal A. Carbon nanotube reinforced aluminum composite coating via cold spraying. Surf Coat Technol. 2008;202(21):5162-5169. https://doi.org/10.1016/j.surfcoat.2008.05.042
[37] Laha T, Agarwal A, McKechnie T, Seal S. Synthesis and characterization of plasma spray formed carbon nanotube reinforced aluminum composites. Mater Sci Eng A. 2004;381(1-2):249-258. https://doi.org/10.1016/j.msea.2004.04.014
[38] Sachit TS, Khan MA. Effect of particle size on mechanical and tribological behavior of LM4/SiCp based MMC. Mater Today Proc. 2018;5(2):5901-5907. https://doi.org/10.1016/j.matpr.2017.12.189
[39] Kwon H, Estili M, Takagi K, Miyazaki T, Kawasaki A. Combination of hot extrusion and spark plasma sintering for producing carbon nanotube reinforced aluminum matrix composites. Carbon. 2009;47(3):570-577. https://doi.org/10.1016/j.carbon.2008.10.041
[40] Kumar PS, Sachit TS, Mohan N, Akshayprasad M. Dry sliding wear behaviour of Al-5Si-3Cu-0.5Mn alloy and its WC reinforced composites at elevated temperatures. Mater Today Proc. 2021;44:566-572. https://doi.org/10.1016/j.matpr.2020.10.351
[41] Sachit TS, Mohan N. Wear behavior of aluminum LM4 reinforced with WC and Ta/NbC hybrid nano-composites fabricated through powder metallurgy technique. FME Trans. 2019;47(3):406-412. https://doi.org/10.5937/fmet1903534S
[42] Tjong SC. Recent progress in the development and properties of novel metal matrix nanocomposites reinforced with carbon nanotubes and graphene nanosheets. Mater Sci Eng R Rep. 2013;74(10):281-350. https://doi.org/10.1016/j.mser.2013.08.001

[43] Song N, Liu H, Fang J. Fabrication and mechanical properties of multi-walled carbon nanotube reinforced reaction bonded silicon carbide composites. Ceram Int. 2016;42(1):351-356. https://doi.org/10.1016/j.ceramint.2015.08.117
[44] Sachit TS, Suresh R, Nagaraj T. Systematic wear rate analysis of Ti-6Al-4V based hybrid composites using Taguchi optimizer and machine learning classifiers. J Inst Eng India Ser D. 2025;1-13. https://doi.org/10.1007/s40033-025-00871-4
[45] Cai Y, Chen L, Yang H, et al. Mechanical and electrical properties of carbon nanotube buckypaper reinforced silicon carbide nanocomposites. Ceram Int. 2016;42(4):4984-4992. https://doi.org/10.1016/j.ceramint.2015.12.011
[46] Zhang Y, et al. Mechanical properties of SiC-reinforced aluminum matrix composites. Mater Sci Eng A. 2017;696:103-111.
[47] Kumar M, Singh R. Hardness and wear behavior of SiC-reinforced metal matrix composites. J Compos Mater. 2018;52(22):3093-3104.

Blank Page

Research on Engineering Structures & Materials
www.jresm.org

Review Article

Bamboo in construction: Mapping global trends, strategic clusters, and future research pathways

Sameh Fuqaha [*,a], Ahmad Zaki [b], Guntur Nugroho [c],

Department of Civil Engineering, Universitas Muhammadiyah Yogyakarta, Yogyakarta, Indonesia

Article Info

Article History:

Received 18 Apr 2025

Accepted 06 May 2025

Keywords:

Bamboo construction;
Sustainable materials;
Bibliometric analysis;
Green building

Abstract

As the construction industry intensifies its pursuit of sustainable and low-carbon alternatives to traditional materials, bamboo has emerged as a strategic resource owing to its rapid renewability, high strength-to-weight ratio, and superior environmental profile. This study presents a comprehensive bibliometric and thematic analysis of global research trends on bamboo construction, based on 1,456 peer-reviewed publications indexed in the Scopus database between 2019 and 2024. Using VOSviewer and the bibliometrix package in R, the analysis identifies three major thematic clusters: structural performance and mechanical behavior, sustainability and environmental applications, and microstructural characterization and advanced material development. The results highlight a sharp increase in scholarly output, with China, India, and Indonesia leading both in publications and citations, driven by strong policy initiatives and abundant bamboo resources. Despite significant advancements, critical gaps persist in standardization frameworks, long-term durability assessment, and integration with smart materials. This paper proposes future research pathways, including the development of hybrid composites, microstructural optimization, and regionally adaptive building codes. By systematically mapping the evolution, challenges, and opportunities in bamboo construction, the study offers a structured framework to accelerate bamboo's mainstream adoption as a high-performance, sustainable material in global infrastructure development.

© 2025 MIM Research Group. All rights reserved.

1. Introduction

The construction sector, responsible for 37-40% of global energy-related CO_2 emissions, is undergoing a profound transformation as it searches for alternatives to traditional high-impact materials like concrete, steel, and conventional timber[1]. Among the emerging contenders, bamboo has gained international attention for its unique blend of mechanical robustness, rapid renewability, and environmental compatibility [2]. As a natural, fast-growing grass with high strength-to-weight ratios and carbon sequestration potential, bamboo is increasingly viewed as a strategic bio-based material that aligns with global sustainability goals, particularly those related to climate resilience, circular economy, and low-carbon development [3].

Historically, bamboo has been used in vernacular construction across Asia, Africa, and Latin America, especially in low-income rural communities. However, in recent decades, its role has shifted from a traditional material to a focus of modern engineering and material science research. Innovations in laminated bamboo (thin layers of bamboo glued together for improved strength), bamboo scrimber (compressed bamboo strips bound with adhesive), and fiber-reinforced composites have unlocked new applications in structural frame, geotechnical foundations, seismic-resistant design, and green architecture [4]. Studies confirm that Engineered bamboo—bamboo

*Corresponding author: sameh.h.psc24@mail.umy.ac.id
[a]orcid.org/0009-0000-6914-7148; [b]orcid.org/0000-0003-1166-5078; [c]orcid.org/ 0000-0002-7881-6451;
DOI: http://dx.doi.org/10.17515/resm2025-825ma0418rs

processed into standardized structural elements—can achieve tensile strengths exceeding 200 MPa and compressive strengths of over 130 MPa, rivalling industrial-grade timber and approaching steel in performance under specific conditions [5]. Moreover, bamboo is known for its rapid maturation cycle—3 to 5 years versus decades for hardwoods—and its capacity to regenerate without replanting, making it a prime candidate for renewable construction materials [6].

Yet, despite the growing academic and commercial interest, bamboo's adoption in mainstream construction remains uneven and underutilized. Challenges persist regarding standardization, durability under climatic exposure, jointing systems, treatment protocols, and limited inclusion in national or international building codes [6]. Although ISO standards such as ISO 22156 and ISO 22157 define test methods for mechanical behavior and safety, bamboo is rarely included in performance-based structural design frameworks [7]. These limitations are exacerbated by bamboo's natural variability across species, geography, and processing techniques, leading to inconsistent mechanical behavior and variable structural reliability [8]. Moreover, Complexities in connection techniques-stemming from bamboo's hollow culm (stem) structure remain a major barrier to the development of prefabricated and modular bamboo systems, especially in multi-story construction [9].

In parallel, Bamboo, with its low embodied energy and potential for carbon sequestration, offers a unique convergence of ecological and mechanical benefits [10]. Lifecycle assessments (LCA), a method to evaluate environmental impacts across a product's lifespan, demonstrate that bamboo-based materials can reduce greenhouse gas emissions by up to 50% compared to concrete and steel, and bamboo cultivation itself supports biodiversity, soil restoration, and water retention [11,12]. Furthermore, innovations in composite engineering, nano-modification, and microstructural design have made bamboo increasingly competitive with synthetic and mineral-based construction alternatives, both in terms of performance and cost-efficiency.

This research aims to explore the evolving role of bamboo in construction by mapping current trends, identifying strategic clusters, and proposing future pathways. Emphasis will be placed on its mechanical performance, treatment advancements, code development, and practical integration into modern infrastructure. Through this approach, the study seeks to contribute to a more sustainable construction paradigm where bamboo becomes a mainstream, structurally reliable, and ecologically responsible material.

2. Standardization and Structural Applications of Bamboo in Construction

2.1 Bamboo Standards and Regulatory Codes

The formalization of bamboo standards was first initiated by the International Organization for Standardization (ISO) in 2004. During this year, ISO introduced three key documents concerning bamboo construction: ISO 22156, ISO 22157-1, and ISO 22157-2. These standards were primarily adapted from pre-existing timber guidelines to suit the unique characteristics of bamboo materials. ISO 22156 outlines the principles for the structural design of bamboo constructions, encompassing full culm, half culm, and laminated bamboo applications [13]. Meanwhile, ISO 22157-1 [14] and ISO 22157-2 [15] detail the procedures for testing the physical and mechanical properties of bamboo, including evaluations of moisture content, density, tensile strength, compressive strength, shear strength, and flexural strength.

As the use of bamboo in modern construction continues to expand, particularly in regions abundant with bamboo resources, many countries have undertaken the development of their own national standards [16–19]. These localized efforts aim to address specific species variations, environmental conditions, and construction practices unique to each country. Table 1 provides a summary of the current national and international standards governing bamboo specifications. These national and international standards represent important milestones in the effort to integrate bamboo as a legitimate construction material within formal building codes. However, continued collaboration is needed to harmonize testing procedures and design principles globally, ensuring bamboo's wider acceptance and safe application across diverse structural contexts.

Table 1. Summary of Existing Bamboo Construction Standards by Country

Country	Standard(s)	Reference
Philippines	PNS ISO 19624:2020 – Grading of bamboo culms; PNS ISO 22157:2020 – Determination of physical and mechanical properties of bamboo culms; PNS ISO 22156:2021 – Structural design of bamboo structures.	[20]
China	JG/T 199-2007 – Testing methods for physical and mechanical properties of bamboo used in building construction.	[21]
Colombia	NSR-10 G.12 – Guidelines for seismic-resistant structures using Guadua; NTC 5407 – Structural joints with Guadua angustifolia; NTC 5525 – Testing methods for Guadua properties.	[22]
Ecuador	NEC-SE-GUADUA – Structural design of Guadua structures; INEN 42 – Specifications for bamboo cane (Caña Guadua).	[23]
India	IS 6874:2008 – Method of tests for bamboo; IS 15912:2018 – Structural design using bamboo – Code of practice.	[24,25]
Peru	Reglamento Nacional de Edificaciones, Section III, Code E.100 – Design and construction with bamboo.	[26]
United States	ASTM D5456-21– Standard specification for evaluation of structural composite lumber products, including laminated veneer bamboo.	[16]
Bangladesh	Bangladesh National Building Code (BNBC) 2020, Part 6, Chapter 4 – Bamboo structures.	[27]
International	ISO 22156:2021 – Bamboo structures – Structural design; ISO 22157:2019 – Determination of physical and mechanical properties of bamboo culms – Test methods.	[25,28]

To address practical challenges associated with bamboo construction, several innovative approaches have been successfully demonstrated. For example, the Green School Bali showcased the use of boron salt preservation techniques and laminated bamboo composites to enhance structural durability under humid tropical conditions [6] . Similarly, the ZCB Bamboo Pavilion in Hong Kong utilized prefabricated laminated bamboo members and digital fabrication to overcome standardization and connection challenges [7]. These case studies indicate that through chemical treatment, engineered bamboo processing, and precision-based manufacturing, bamboo can achieve durability and mechanical stability comparable to conventional building materials. Future initiatives should integrate advanced preservation treatments and prefabricated modular systems to further improve the long-term performance and scalability of bamboo structures in modern construction.

2.2 Structural Applications of Bamboo in Construction

Bamboo is a versatile and sustainable material with significant potential for construction purposes. It can be used either in its natural form or as a processed material, depending on structural needs. The bamboo culm, whether used whole or modified, offers architectural flexibility while contributing socio-economic benefits due to its durability, availability, and relatively low cost [29]. Bamboo's unique properties make it a promising alternative to traditional construction materials, especially for organic-shaped and lightweight structures [30]. The various structural applications of bamboo are discussed in the following subsections.

2.2.1 Use of Full and Half Culm Bamboo

Whole bamboo culms are commonly used in architectural structures, scaffolding, and resort buildings, particularly in regions where bamboo is abundantly available. Full or split culms are connected to form columns, walls, roof purlins, and poles. The mechanical property of bamboo exhibits compressive strengths ranging between 56 MPa and 132.9 MPa, and tensile strengths between 71 MPa and 216 MPa, making it highly suitable for load-bearing applications [31].

However, the hollow structure of the culm presents challenges for creating effective joints, which often rely on simple binding methods like rope lashings[32].

Recent studies emphasize the critical role of nodes in enhancing the mechanical strength of bamboo elements, although these nodes complicate joint design [31]. To improve connection efficiency, techniques such as hose clamps, concrete infill, and bolted connections have been adopted. Hose clamps offer a quick and practical solution, whereas concrete infill methods strengthen the hollow structure, significantly increasing rigidity and load capacity [33]. These innovations have enhanced the structural reliability of bamboo elements in modern architectural and engineering applications.

2.2.2 Engineered Bamboo Products

Engineered bamboo refers to bamboo that has undergone industrial processing to enhance its structural performance. Common engineered bamboo products include laminated bamboo and bamboo scrimber, widely used in flooring, wall panels, and load-bearing applications. Laminated bamboo is produced by flattening bamboo culms into uniform strips, which are then bonded together using adhesives to create laminated boards [34,35]. Research indicates that Laminated bamboo demonstrates high compressive strength, especially when the load is applied parallel to the grain. For instance, matured glue-laminated bamboo has a compressive strength of 62.78 MPa, which is significantly higher than that of juvenile bamboo at 37.58 MPa [36]. Another study reports compressive strengths of 45.07 MPa parallel to the grain at 20°C, with variations depending on temperature [37]. Its orthotropic behavior, characterized by greater compressive strength along the grain, further enhances its structural applicability [38].

Moreover, bamboo's carbon footprint is substantially lower than that of steel and even better than traditional timber when lifecycle emissions are considered. Table 2 presents a comparative overview of bamboo composites, timber, and steel properties in construction applications, highlighting bamboo's strategic advantage in sustainable infrastructure development. As shown, bamboo composites exhibit tensile strengths comparable to timber (40–80 MPa) but possess a significantly lower elastic modulus (9 GPa) relative to steel (200 GPa) and timber (10–20 GPa) [39]. Despite this lower stiffness, bamboo's mechanical performance remains sufficient for many structural applications, especially when combined with its high strength-to-weight ratio. In terms of environmental impact, bamboo stands out with low CO_2 emissions and high renewability, offering a clear advantage over steel, which has a markedly higher carbon footprint [40]. From a cost perspective, bamboo composites are more expensive than local timber but remain cheaper than steel, positioning them as an economically viable material for sustainable construction [41]. Consequently, bamboo composites offer an optimal balance between mechanical performance, environmental sustainability, and affordability, making them an attractive alternative for structural elements such as floors, roofs, and lightweight frameworks.

Table 2. Comparative properties of bamboo composites, timber, and steel

Material	Tensile Strength (MPa)	Elastic Modulus (GPa)	Environmental Impact	Cost	Typical Applications
Bamboo Composites	40–80	9	Low CO_2 emissions, highly renewable	Higher than local timber, lower than steel	Structural elements, floors, roofs
Steel	370–700	200	High carbon footprint	Expensive	High-load, critical structures
Timber	40–80	10–20	Renewable but slower growth cycle	Affordable	Residential structures, bridges

2.2.3 Bamboo-Reinforced Concrete (BRC)

Bamboo's high tensile and compressive strengths along the longitudinal axis make it an effective substitute for traditional steel reinforcement in concrete structures. Bamboo strips or full culms, often treated to prevent termite attack, are embedded within concrete to form Bamboo-Reinforced Concrete (BRC). The performance of BRC beams closely resembles that of conventional reinforced concrete (RC) beams, particularly when treated with adhesives and hose clamps to improve bond strength and water resistance [42].

Experimental studies, such as those by Sutharsan et al. [43] demonstrate that bamboo reinforcement can enhance flexural strength by up to 77.7% compared to plain concrete. Bamboo is commonly used in beams (main bars and stirrups) and columns (main bars and hoops), offering structural behavior comparable to RC beams with lower reinforcement ratios [44]. Further improvements can be achieved through mechanical anchoring systems like rebar clamps [45]or hose clamps [46].

Bonding agents such as Sikadur 32-gel have been shown to enhance the bamboo-concrete interface, improving flexural strength performance [47]. Although BRC beams demonstrate significant strength improvements, steel-reinforced beams remain superior in terms of stiffness and ductility [48]. Bamboo has also proven effective in reinforcing slabs and shear walls, significantly improving flexural and shear capacities [49,50]. However, long-term performance is dependent on proper treatment and moisture protection

2.2.4 Bamboo Piles in Geotechnical Engineering

Bamboo piles have emerged as an eco-friendly alternative for lightweight foundation systems, particularly in soft soils [51]. Research shows that treated bamboo piles can achieve load capacities of approximately 75 kN in soft clay soils, maintaining strength even after extended environmental exposure [51]. Full-scale tests in the Philippines revealed service load capacities of up to 250 kN for bamboo piles in low-rise construction [52]. Moreover, bamboo piles enhance soil stability due to their rough surface texture, which improves frictional resistance. When bamboo piles were combined with lime stabilization, a 25% increase in soil bearing capacity [53].

Comparative studies confirm that bamboo piles can perform comparably to timber piles at a fraction of the cost, providing substantial environmental benefits [54] . Field trials in Indonesia reported a 35% reduction in settlement when using bamboo piles in untreated soft soils [55].

Despite their advantages, bamboo piles are vulnerable to biodegradation. Preservation methods, including chemical treatments (sodium borate, copper-chrome-arsenate)[56], thermal modification [57], and encapsulation with cementitious materials [58], have been shown to extend their lifespan significantly. Innovations like lime-soil caps combined with geotextile reinforcement further enhance their performance in challenging soil environments [59].

2.2.5 Bamboo Fiber Reinforced Concrete (BFRC)

The incorporation of fibers in concrete enhances its tensile strength and crack resistance. Traditionally, synthetic fibers such as glass, steel, and carbon have been used [60]. However, due to environmental concerns and the high cost of synthetic fibers, natural alternatives like wood, coconut, hemp, sisal, and bamboo are increasingly favored [61].

Bamboo fibers generally do not enhance the compressive strength of concrete and may even slightly reduce it. For instance, the compressive strength of bamboo fiber-reinforced lightweight aggregate concrete (LWAC) decreased by 3.6% to 11.1% with the addition of bamboo fibers [62]. Another study found that the compressive strength of bamboo scrimber decreased with increasing specimen size [63].

3. Primary Focus of Previous Reviews, Identified Gaps, and Research Questions

Table 3 presents a summary of key review articles on bamboo construction research published between 2019 and 2024. It highlights each study's thematic focus, methodological approach, and contributions to areas such as material innovation, structural performance, and environmental

sustainability. A review of the existing literature reveals a clear gap: few studies provide a comprehensive overview that traces the evolution of bamboo research while offering a structured and strategic classification of key developments. While many papers have investigated specific aspects—such as bamboo's mechanical properties, reinforcement potential, or its role in low-carbon construction, there remains a lack of integrative frameworks that connect these diverse strands into a cohesive understanding of the field.

Although previous reviews have provided valuable insights into bamboo's mechanical properties, reinforcement techniques, and sustainability applications, they often focus on isolated aspects without offering a holistic integration of the field. Specifically, prior studies tend to concentrate either on material performance, environmental potential, or structural applications in isolation, leaving a fragmented understanding of how bamboo research is evolving as a comprehensive construction solution. Furthermore, no existing review has systematically mapped the scientific landscape using bibliometric methods to identify thematic clusters, leading authors, institutional contributions, and future research pathways in bamboo construction. This study addresses these gaps by employing a data-driven bibliometric approach to not only analyze research output and collaboration networks but also to strategically classify emerging research fronts and propose targeted directions for advancing bamboo as a mainstream, sustainable construction material.

Table 3. Overview of review papers on bamboo construction

Ref	Year	Scope	The primary areas of discussion
[64]	2023	Structural performance and durability of bamboo	Summary of mechanical properties across bamboo species Discussion of structural adequacy and treatment methods Highlight of challenges in durability and standardization
[32]	2024	Connection techniques for raw bamboo	Review of 62 papers on raw bamboo connections Emphasis on failure modes and design limitations Recommendation for code development and research gaps
[65]	2023	Nanotechnology for bamboo improvement	Review of bamboo enhancement via nanomaterials Discussion of decay resistance and stability improvement Application of nano-cellulose and nano-lignin
[66]	2022	Amazon natural fibers in cementitious composites	Exploration of bamboo with Amazon natural fibers Use in cement-based composites for sustainability Emphasis on physical, chemical, and mechanical integration
[67]	2024	Mycelium composites with bamboo fibers	Discussion of bamboo-enhanced mycelium composites Mechanical and thermal benefits in sustainable design Focus on insulation, strength, and biodegradability
[68]	2024	Fiber-reinforced plywood including bamboo fibers	Analysis of fiber-reinforced plywood using bamboo Highlighted gains in strength and reduced material use Proposal for sustainable plywood applications

To address the identified research gap, this study is guided by a central research question: What are the emerging trends, strategic clusters, and future research directions in the field of bamboo construction? To support a structured and comprehensive analysis, this overarching question is divided into the following specific sub-questions:

- RQ1: How has research on bamboo in construction evolved over time, and what is the current state of the field?
- RQ2: Which countries, institutions, journals, and authors are most active and influential in advancing bamboo construction research?
- RQ3: What are the most cited and impactful publications that have shaped the development of this field?

- RQ4: What are the major research themes, innovation trends, and forward-looking topics that define the future landscape of bamboo construction?

To ensure clarity and logical flow, the remainder of this paper is structured as follows:

- Section 4 describes the research methodology employed, including data collection, processing, and analysis techniques.
- Section 5 presents the bibliometric analysis addressing the four research questions.
- Section 6 discusses strategic directions and emerging opportunities for future research in bamboo-based construction.
- Section 7 concludes the paper by summarizing the key insights and contributions.

4. Methodology

A bibliometric analysis was employed in this study to systematically explore and visualize the evolving landscape of research on bamboo in construction, with a focus on identifying thematic trends, mapping strategic clusters, and proposing future research pathways. Bibliometric analysis, a computer-assisted literature review technique, has been widely adopted for quantitatively assessing scientific progress and revealing knowledge structures across diverse fields [69,70]. This approach enables the identification of influential authors, institutions, countries, and emerging research fronts, while also highlighting gaps and underexplored areas within the domain of bamboo-based structural applications.

In constructing bibliometric networks, two principal counting methods are typically used: full counting and fractional counting. Full counting assigns equal weight to each occurrence and is favored for its interpretative simplicity. Fractional counting, on the other hand, distributes weights proportionally among co-authors or sources, making it suitable for nuanced attribution scenarios.

To implement this bibliometric analysis, the study utilized two established tools: VOSviewer, a well-known software for creating bibliometric maps, and the bibliometrix package in R, which supports in-depth statistical and network analysis [71]. These tools were applied to generate co-authorship networks, keyword co-occurrence maps, and citation analyses. In these visualizations, each node represents a research entity—such as an author, article, keyword, or institution—while edges denote relationships such as co-publications or shared thematic focus. The methodological framework of this research included: (1) data collection from a comprehensive scientific database, (2) performance analysis of core bibliometric indicators, (3) network mapping to reveal knowledge clusters, and (4) strategic interpretation to inform future directions in bamboo construction research.

4.1 Scope of the Study

This study aims to explore how bamboo is being used in the construction sector and how research in this area has evolved over time. By examining a wide range of publications, the analysis seeks to uncover key themes, trends, and research gaps related to bamboo in structural, geotechnical, and sustainable applications. The central question driving this investigation is: What are the major developments, research directions, and strategic focus areas in bamboo construction, and how can these insights help guide future studies?

4.2 Literature Search Strategy and Data Preparation

A critical component of this study involved selecting an appropriate and multidisciplinary data source to capture the breadth of research on bamboo in construction. Scopus was chosen as the primary database due to its extensive indexing of peer-reviewed journals across engineering, architecture, and environmental sciences, providing a comprehensive platform for conducting high-quality bibliometric analysis [72].

To retrieve relevant publications effectively, a structured search strategy employing Boolean operators was developed. Keywords were categorized into two main thematic groups. The first group targeted fundamental construction-related terms such as “bamboo construction,” “bamboo structure,” “bamboo building material,” and “bamboo pile,” ensuring the inclusion of studies focusing directly on bamboo’s application as a structural material. The second group encompassed

broader emerging themes, including "sustainability," "carbon reduction," "green materials," "reinforced concrete," "geotechnical engineering," and "engineered bamboo," aiming to capture literature situating bamboo within the context of sustainable development and material innovation. Using this dual-group keyword approach, a comprehensive search was conducted in Scopus. The initial search retrieved 1,545 publications, encompassing journal articles, reviews, and conference proceedings from diverse fields such as civil engineering, material science, environmental technology, and architecture. This broad initial dataset reflected the multidisciplinary interest in bamboo as a sustainable construction material.

To refine the search results and ensure data quality, a systematic filtering process was applied. The first filtering phase included only peer-reviewed journal articles and review papers, excluding conference papers, book chapters, and editorial materials. Publications were restricted to the English language to maintain consistency and accessibility across the dataset. No temporal restrictions were applied, allowing both foundational studies and recent developments to be captured. Following this, a second-level screening was conducted to ensure topical relevance. Publications that did not focus specifically on the structural, mechanical, or environmental aspects of bamboo in construction were excluded. Only studies directly contributing to bamboo's application as a construction material were retained, ensuring thematic consistency and scholarly relevance.

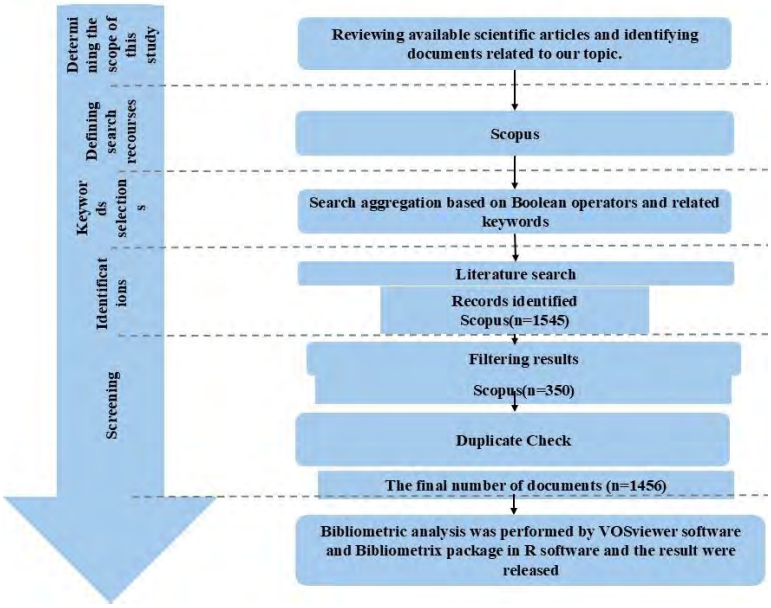


Fig. 1. Research framework outlining the sequential stages of the bibliometric analysis conducted in this study

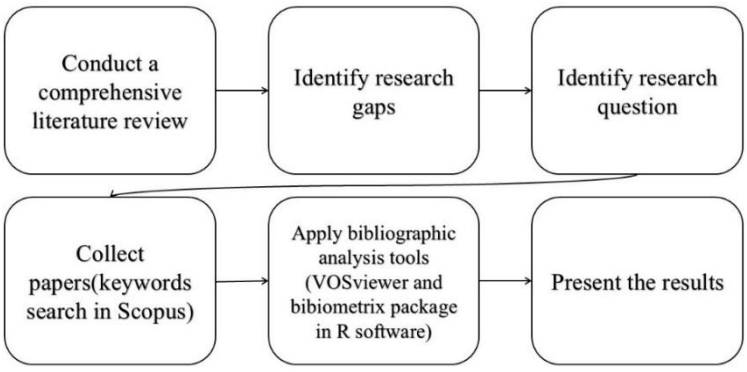


Fig. 2. Conceptual framework illustrating the linkages between past research trends, identification of strategic research clusters, and the formulation of future pathways for bamboo construction research

To finalize the dataset, a merging and deduplication process was undertaken using R software, following the bibliometric cleaning methodology outlined by Echchakoui [72]. This procedure removed duplicate entries and ensured the uniqueness of each document. After the cleaning process, the final dataset comprised 1,456 distinct publications, forming the analytical foundation for the bibliometric and thematic exploration presented in this study. To ensure a comprehensive review of the field, it was essential to select a reliable and multidisciplinary database. Scopus was chosen as the primary data source for this study because of its wide coverage of peer-reviewed literature across engineering, architecture, and environmental sciences. Its indexing quality and breadth of disciplines make it an ideal platform for bibliometric research on construction materials, especially bamboo [72].

The overall process employed in this research is summarized in a structured research framework (Fig. 1), which illustrates each step from database selection through data extraction, cleaning, and visual analysis. Additionally, a conceptual framework is presented (Fig. 2), demonstrating the logical progression of the study from mapping historical research trends to the identification of strategic clusters and the formulation of future research directions in the domain of bamboo-based construction.

4.3 Analysis and Review

The refined dataset was then analyzed using two powerful tools: VOSviewer and the bibliometrix package in R. These tools allowed for the creation of visual maps that revealed patterns in co-authorship, keyword usage, and citation behavior. Through these visualizations, it became possible to identify major research clusters, influential authors and institutions, and thematic areas that have gained attention over time. This analytical approach provided a data-driven, objective perspective on the current state of bamboo construction research.

5. Document Analysis

5.1 Trend Analysis

Analyzing publication trends offers valuable insights into the growth and evolution of a research field, revealing how academic interest has developed over time [70]. Fig. 3 illustrates the annual and cumulative publication trends in bamboo construction research from 2019 to 2024. The data demonstrate a clear and substantial increase in scholarly activity within this domain. From 2019 to 2021, the number of annual publications rose steadily, reflecting growing attention to sustainable and bio-based construction solutions. Although annual output from 2022 to 2024 stabilized somewhat, the cumulative publication curve shows a consistent and sharp upward trajectory—culminating in an overall growth of 156.6% over the six-year period.

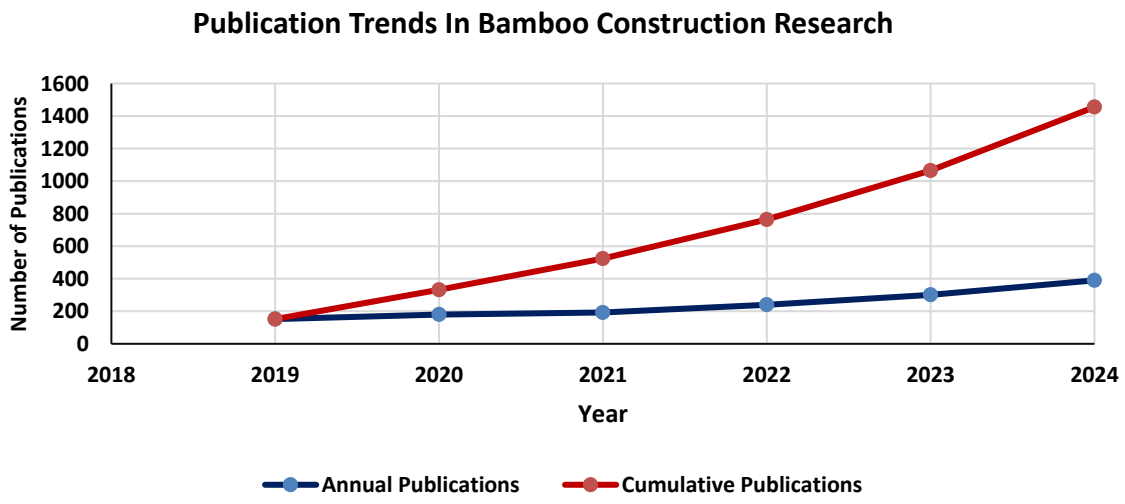


Fig. 3. Trends in research and developments in bamboo construction (2019–2024)

This upward trend underscores the increasing global recognition of bamboo as a viable, low-carbon construction material. The steady rise in research output reflects broader environmental concerns, the push for green infrastructure, and the demand for renewable alternatives to traditional building materials. The relative stabilization in annual publication counts in recent years may suggest a transition from exploratory research toward more focused investigations into structural performance, treatment technologies, and standardization frameworks.

5.2 State of Research and Developments

Understanding the geographical distribution of research contributions is key to mapping global innovation trends in bamboo construction. As illustrated in Fig. 4, China is the dominant contributor, accounting for 48.5% of all publications between 2019 and 2024. It is followed by India (17.9%) and Indonesia (10.4%), with other notable contributors including the United States (6.4%), Malaysia (4.7%), Brazil (4.1%), the United Kingdom (3.0%), and Italy (2.8%). These figures highlight a strong concentration of scholarly activity in Asia, particularly from countries that have abundant natural bamboo resources and are actively exploring sustainable construction practices.

In terms of impact, Fig. 5 presents the citation distribution by country. China again leads significantly, receiving 48.4% of all citations, reflecting not only its publication volume but also the influence and quality of its research. The United States ranks second with 13.0%, followed by India (10.4%), Malaysia (4.4%), and the United Kingdom (4.0%). Countries such as Australia, Indonesia, and Brazil also demonstrate strong visibility in citation impact, indicating the relevance of their contributions to the global discourse on sustainable and bio-based materials.

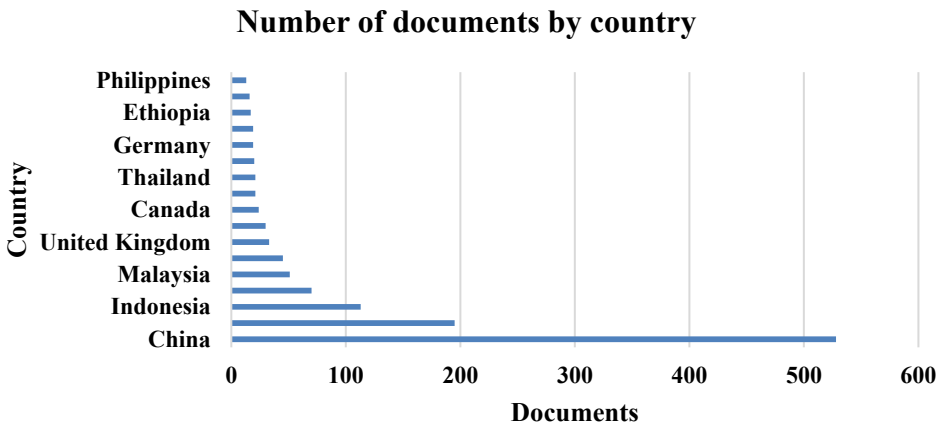


Fig. 4. Documents by country

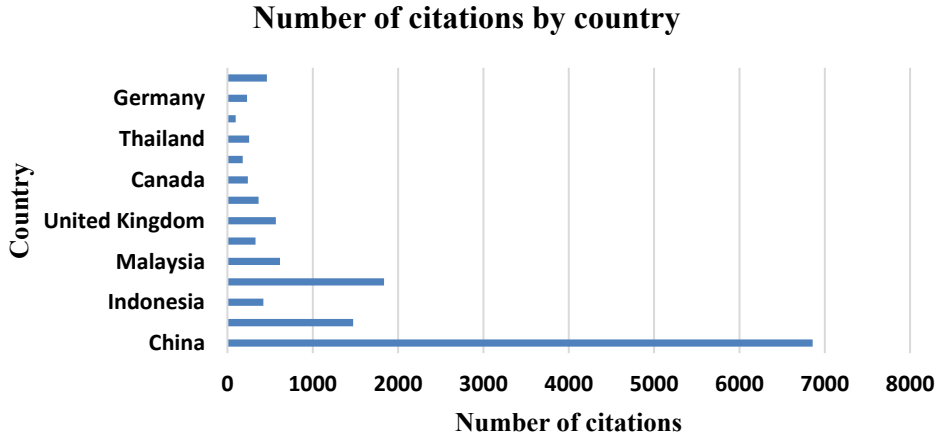


Fig. 5. Citations by country

The leadership of China, India, and Indonesia in bamboo construction research is underpinned by multiple factors. China has institutionalized bamboo development through national initiatives such as the "Bamboo Science and Technology Action Plan," encouraging academic research and industrial applications [73]. India's National Bamboo Mission, launched in 2018, provides policy incentives for bamboo cultivation and infrastructure development [74]. Indonesia benefits from rich native bamboo species diversity and active governmental support for green building practices using bamboo [75] These socio-economic and policy-driven factors, combined with historical usage of bamboo in vernacular architecture, explain the dominant research output from these regions.

Fig. 6 visualizes the international collaboration network in bamboo construction research. China appears as the central hub, engaging in frequent co-authorships with India, the United States, Malaysia, Indonesia, the United Kingdom, and Brazil. The dense network of linkages signifies a highly interconnected global research ecosystem, where advancements in material science, construction engineering, and sustainability policy are being collectively shaped.

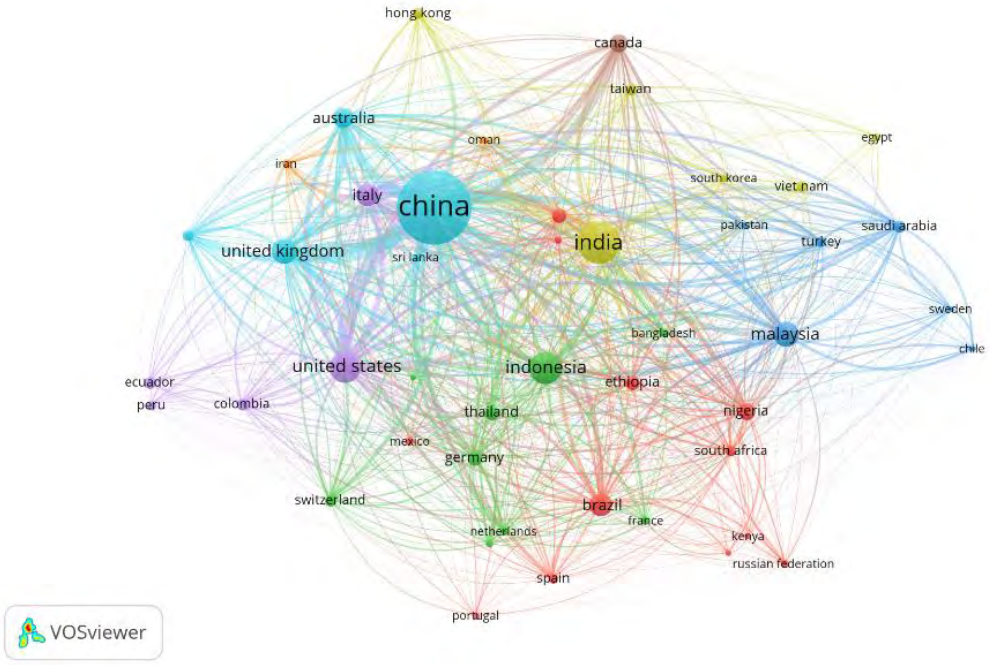


Fig. 6. Global collaboration network in railway safety research

This global collaboration map further reinforces the interdisciplinary and transnational nature of bamboo-related research. Contributions span from material performance and structural applications to emerging themes such as nanotechnology integration, engineered bamboo composites, and green infrastructure. The robust collaboration across continents suggests that bamboo construction is not merely a regional innovation, but a shared scientific pursuit aligned with broader global sustainability goals.

Table 4. Leading organizations in bamboo construction research

Organization	Articles
Research Institute of Wood Industry	13
Institute of Biomaterials for Bamboo and Rattan Resources	8
Institute of New Bamboo and Rattan Based Biomaterials	5
Civil Engineering Program	4
DICAM	4
Key Laboratory of Concrete and Prestressed Concrete Structures of the Ministry of Education	4
Key Laboratory of High Efficient Processing of Bamboo of Zhejiang Province	4
State Key Laboratory of Hydraulic Engineering Simulation and Safety	4
Laboratory of Biocomposite Technology	4
International Bamboo and Rattan Organization	3

The analysis of the most active organizations, as presented in Table 4, highlights the central role of leading institutions in advancing bamboo construction research. Key contributors include research entities such as the Research Institute of Wood Industry, the Institute of Biomaterials for Bamboo and Rattan, and the Institute of New Bamboo and Rattan Based Biomaterials. These organizations consistently contribute to the field by producing high-impact studies on bamboo's structural performance, durability, and integration into sustainable building systems. Their repeated engagement illustrates a strong institutional commitment to promoting low-carbon construction and innovation in bio-based materials.

Equally significant are the contributions of individual researchers, as summarized in Table 5. Scholars such as Li H. (65 articles), Wang X. (37 articles), Wang Y. (36 articles), and Li Z. (32 articles) emerge as the most prolific authors in the field. Their research spans a wide range of areas, including engineered bamboo composites, treatment techniques, connection technologies, and performance testing under various environmental conditions. These researchers play a critical role in shaping both the theoretical foundations and practical applications of bamboo in modern construction, often leading collaborative efforts across institutions and countries.

Table 5. Top authors in bamboo construction research

Author	Articles
Li H.	65
Wang X.	37
Wang Y.	36
Li Z.	32
Li X.	32
Wang Z.	30
Li Y.	29
Li J.	28
Zhang X.	28
Liu Y.	28

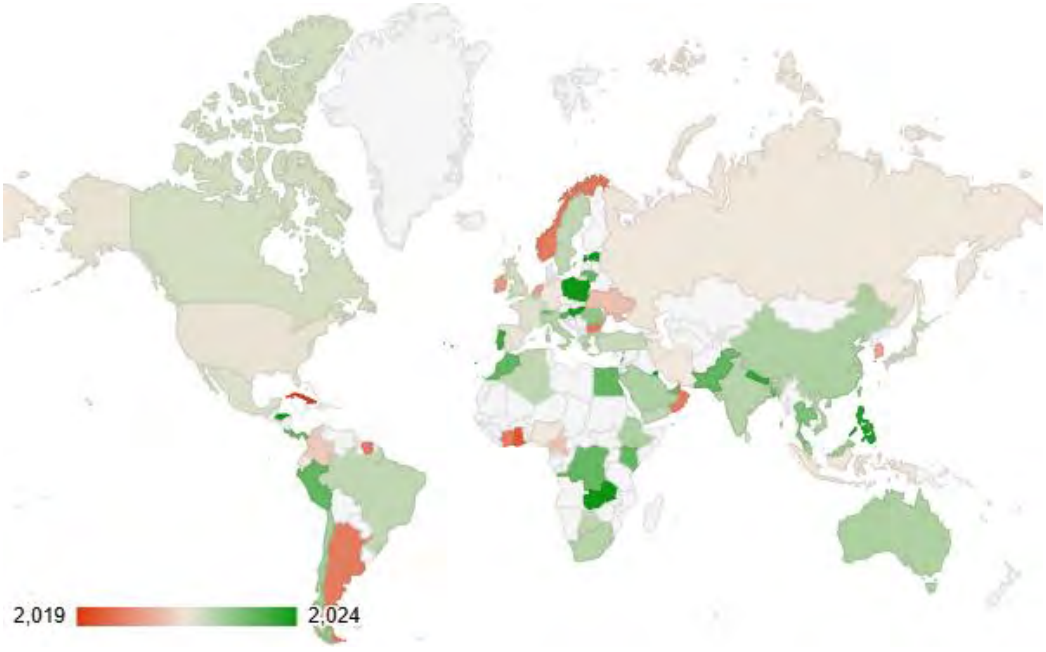


Fig. 7. Average publication year by country in railway safety research

From a global perspective, the country-level analysis presented earlier (Fig. 7) reveals a strong concentration of bamboo research in China (528 documents, avg. year 2022.2), followed by India (195 documents, avg. year 2022.1), Indonesia (113 documents, avg. year 2021.5), and the United States (70 documents, avg. year 2021.6). These countries are actively contributing to both

foundational research and technological innovation, driving the development of bamboo as a mainstream construction material. The presence of nations like Malaysia, Brazil, and the United Kingdom further reflects the growing international interest in sustainable building technologies.

Collectively, these findings demonstrate the collaborative and globally integrated nature of bamboo construction research. The sustained efforts of leading institutions and researchers, along with the growing participation of countries from Asia, the Americas, and Europe, underscore a shared recognition of bamboo as a key material in the transition toward greener infrastructure. This convergence of expertise and innovation continues to propel the field forward, laying the groundwork for scalable, climate-resilient, and low-impact construction solutions.

5.3 Citation Analysis of Literature

An essential consideration for researchers in the bamboo construction domain is identifying the most impactful publications that have significantly shaped the field's academic and technological progress. Citation analysis provides valuable insight into foundational studies, major breakthroughs, and emerging directions within bamboo-related research. Highly cited publications often serve as intellectual cornerstones, influencing both theoretical development and practical applications.

Table 6 presents the top-cited publications from the dataset, illustrating key developments in areas such as engineered bamboo composites, thermal and mechanical performance analysis, sustainable reinforcement materials, and novel material integration. Leading this list is the article titled "A Strong, Tough, and Scalable Structural Material from Bamboo" by Li et al., with 347 citations, underscoring its foundational role in demonstrating the mechanical viability of bamboo as a high-performance construction material. Another highly influential work, "Thermogravimetric Analysis Properties of Cellulose Fibers and Their Reinforcement in Polymer Composites" by Nurazzi et al., has received 271 citations, reflecting its impact in material characterization and thermal behavior analysis.

Also notable is the publication "Carbon Quantum Dots Supported AgI/ZnO/Phosphorus-Doped g-C3N4 Nanocomposite" by Hasija et al., with 220 citations, representing advancements in sustainable nanocomposite materials that include bamboo derivatives. Further, Thomas et al.'s article "Biomass Ashes from Agricultural Wastes as Supplementary Cementitious Materials" (205 citations) bridges waste valorization with cement replacement strategies, often synergistic with bamboo-based solutions. Moreover, Li et al.'s "Sustainable High-Strength Macrofibres Extracted from Natural Bamboo" (204 citations) highlights innovative approaches to enhancing fiber-based concrete performance.

Table 6. Highly Cited Publications in railway safety research

Ref	Title	Year	Total Citations	Source
[76]	A Strong, Tough, and Scalable Structural Material from Fast-Growing Bamboo	2020	347	Advanced Materials
[77]	Thermogravimetric analysis properties of cellulosic natural fiber polymer composites: A review on influence of chemical treatments	2021	271	Polymers
[78]	Carbon quantum dots supported AgI /ZnO/phosphorus doped graphitic carbon nitride as Z-scheme photocatalyst for efficient photodegradation of 2, 4-dinitrophenol	2019	220	Journal of Environmental Chemical Engineering
[79]	Biomass ashes from agricultural wastes as supplementary cementitious materials or aggregate replacement in cement/geopolymer concrete: A comprehensive review	2021	205	Journal of Building Engineering
[80]	Sustainable high-strength macrofibres extracted from natural bamboo	2022	204	Nature Sustainability

	Chemical Composition and Mechanical Properties of Natural Fibers	2020	155	Journal of Natural Fibers
[81]	Production of sustainable construction materials using agro-wastes	2020	153	Materials
[82]	Rapid Processing of Whole Bamboo with Exposed, Aligned Nanofibrils toward a High-Performance Structural Material	2020	152	ACS Nano
[83]	Flexural strength and ductility of moso bamboo	2020	150	Construction and Building Materials
[84]	Nano-Fe3O4/bamboo bundles/phenolic resin-oriented recombination ternary composite with enhanced multiple functions	2021	148	Composites Part B: Engineering

Fig. 8 shows how research on bamboo construction has been published across the five most active journals from 2019 to 2024. One journal that stands out is Construction and Building Materials, which shows steady and strong growth over the years—from just 5 articles in 2019 to 25 articles by 2024. This trend reflects the journal's central role in publishing high-quality studies focused on sustainable and innovative building materials. In contrast, IOP Conference Series: Earth and Environmental Science peaked early in 2020 but then declined, suggesting that researchers are increasingly moving towards permanent, peer-reviewed journal publications as the field matures.

Similarly, journals like Industrial Crops and Products and Journal of Building Engineering have shown significant growth, reflecting increased scholarly attention to bio-based construction materials and structural applications. Overall, this figure reflects a clear shift: researchers are increasingly choosing peer-reviewed journals over conferences to disseminate findings, and the body of work in bamboo construction is becoming more established and widely recognized.

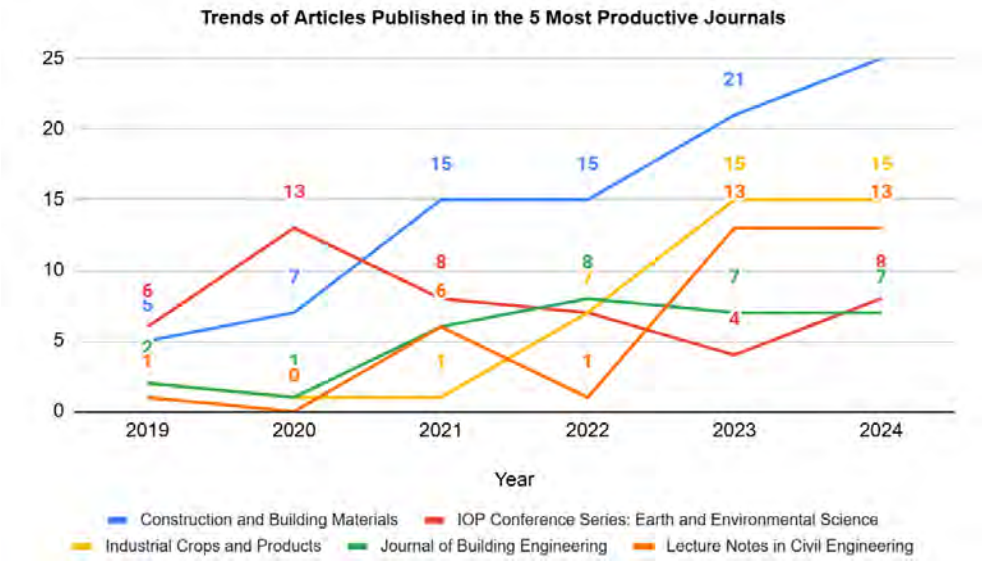


Fig. 8. Trends of Articles Published in the 5 Most Productive Journals (2019–2024)

5.4 Categorizing the Keywords

The keyword co-occurrence analysis, visualized in Fig. 9, provides a comprehensive view of the intellectual structure of bamboo construction research. This VOSviewer-generated map highlights the most frequently occurring terms and their interconnections across the literature. Based on proximity, co-usage, and network density, three primary thematic clusters emerge: (1) structural performance and mechanical behavior, (2) sustainability and environmental applications, and (3) microstructural characterization and advanced material development. Each cluster reflects a

specific domain of research emphasis, offering insight into both the depth and diversity of topics explored in this rapidly expanding field.

5.4.1 Cluster 1: Structural Performance and Mechanical Behavior

This cluster is one of the most rigorously studied areas in bamboo construction research, as reflected by the frequent co-occurrence of keywords such as compressive strength, tensile strength, bending strength, laminating, and mechanical properties. These terms emphasize the centrality of structural performance in bamboo-related research, particularly in the quest to develop bio-based alternatives to conventional construction materials.

One significant line of inquiry involves the development of lightweight yet strong and tough materials suitable for demanding structural uses. Innovations in bamboo-based composites demonstrate that through scalable processing techniques, these materials can achieve performance levels comparable to synthetic structural alternatives. Such advancements align with the pursuit of both high mechanical integrity and environmental responsibility [76]. Another area of research investigates the transformation of natural bamboo into high strength macrofibres. These studies highlight the structural advantages of natural fiber systems over petroleum-based synthetic fibers, especially in terms of tensile strength and sustainability. Bamboo-derived fibers have been shown to offer not only superior mechanical performance but also lower carbon footprints, making them viable for reinforcing composite systems [80].

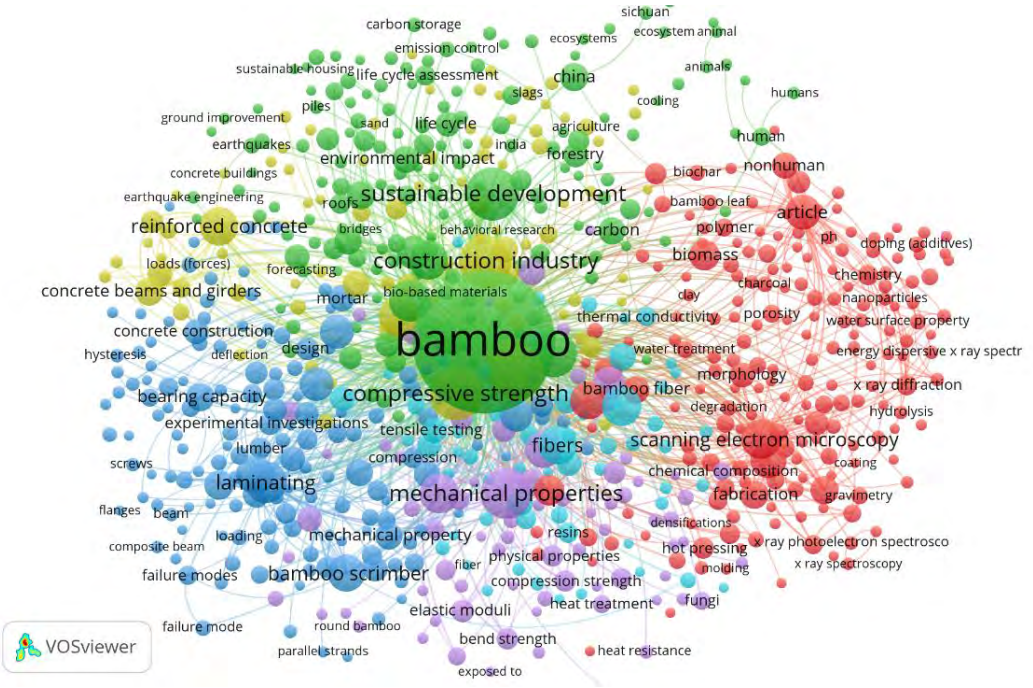


Fig. 9. Co-Occurrence Network of Keywords

The mechanical behavior of natural fibers—including bamboo—has also been extensively studied in terms of composition and durability. In these works, the structural integrity of bamboo is analyzed, and its suitability for engineering applications is confirmed through various stress tests. This includes assessments of tensile and compressive properties that are crucial for validating bamboo as a construction-grade material [85]

Recent investigations have further advanced understanding in this cluster. Bala et al. [86] explored the integration of bamboo reinforcement in geopolymer concrete, offering a novel low-carbon structural system that leverages bamboo's tensile capacity and the environmental benefits of alternative binders [86]. Similarly, Moujoud et al. [87] examined the performance of bamboo in load-bearing beams across various climatic conditions, focusing on shear capacity, bonding quality, and environmental durability. Seismic resilience is another emerging area of focus, with Wu et al. [88] demonstrating laminated bamboo's potential to absorb energy and resist deformation in frame structures under earthquake-like loading conditions.

Material innovation has also played a pivotal role in expanding bamboo's structural applications. Meng et al. [89] introduced nanoscale reinforcement strategies to enhance the performance of bamboo fiber composites, yielding lightweight panels with improved stiffness and fatigue resistance—characteristics crucial for prefabricated modular construction. Additionally, Xu et al. [90] investigated the bond performance between bamboo strips and various polymer adhesives, revealing key parameters that influence the interfacial strength and reliability of laminated systems.

Collectively, the research within this cluster substantiates bamboo's viability as a structurally competent and environmentally sustainable material for construction. The convergence of experimental, analytical, and materials engineering approaches has not only expanded bamboo's structural capabilities but has also laid the groundwork for standardized testing methods and performance-based design guidelines. As this research domain continues to evolve, it is expected that bamboo will increasingly serve as a key component in future-ready, low-carbon structural systems.

5.3.2. Cluster 2: Sustainability and Environmental Applications

The second major thematic cluster in bamboo construction research centers around the keywords *sustainable development*, *construction industry*, *carbon*, *bio-based materials*, and *environmental impact*. This cluster captures the growing interest in bamboo as a viable solution to reduce the ecological footprint of construction activities. In alignment with global sustainability goals and climate resilience strategies, bamboo is increasingly being investigated not only for its mechanical attributes but also for its environmental credentials—positioning it as both a high-performance and low-carbon alternative to traditional building materials.

Shi et al. [91] developed eco-friendly binderless bamboo fiberboards without synthetic adhesives, utilizing mechanical refining and hot-pressing techniques. Their results demonstrated strong bonding through natural lignin activation, resulting in high flexural strength and water resistance. The panels also exhibited excellent dimensional stability and biodegradability, presenting a low-toxicity insulation and paneling alternative for sustainable building design.

Han et al. [92] fabricated bamboo-inspired bio-composites that mimic the layered structure of natural bamboo. Through optimized lamination and water-activated bonding, they achieved materials with high toughness, vibration damping, and moisture resistance. The composites maintained mechanical integrity under varying humidity conditions, proving suitable for applications requiring both flexibility and climate responsiveness

Further expanding structural design applications, Xue et al. [93] constructed a modular building prototype known as "Bamboo Cubic," emphasizing carbon-neutral design through the use of locally sourced raw bamboo in prefabricated façades. Structural tests confirmed both compressive and lateral stability of the bamboo grid system. Life-cycle impact analyses showed significant reductions in construction-phase emissions and material waste, confirming the system's compatibility with net-zero housing initiatives.

In the geotechnical domain, Gidebo et al. [94] examined the stabilization of expansive soils using bamboo ash and agricultural by-products. Laboratory tests revealed improved shear strength, reduced plasticity index, and enhanced load-bearing performance of the treated soil layers. The study concluded that bamboo ash-based additives can replace industrial lime and cement in subgrade stabilization while lowering environmental impact and construction costs.

Han et al. [95] synthesized a bamboo-inspired structural composite using renewable cellulose nanofibrils. The composite achieved an outstanding balance of high tensile strength and flexibility. This was attributed to the hierarchical fiber arrangement modeled after bamboo's internal vascular system. Their results offer a blueprint for developing next-generation load-bearing elements from fully biodegradable, plant-derived resources. Cui et al. [96] introduced an innovative use of bamboo biomass in hybrid composite membranes for indoor air filtration and insulation, showing promise for bamboo's expansion into non-structural and passive energy systems. Finally, Lou et al. proposed the development of bamboo-based insulation panels designed for low-energy buildings,

combining affordability with excellent thermal resistance, thus bridging the gap between environmental performance and economic feasibility [97] .

Collectively, the studies within this cluster underscore bamboo's dual potential: it is both a technically viable material for structural applications and a key enabler of low-impact construction practices. Through applications ranging from reinforced concrete to thermal insulation and membrane technologies, bamboo's versatility continues to support the transition toward more circular, carbon-neutral, and eco-efficient construction systems. As climate change and resource scarcity drive global innovation, bamboo stands out as a strategic material capable of harmonizing environmental sustainability with practical engineering demands.

5.4.3 Cluster 3: Microstructural Characterization and Advanced Materials

The third thematic cluster centers on the microscopic and material science-based analysis of bamboo, with frequent keywords such as scanning electron microscopy (SEM), thermal conductivity, fabrication, porosity, and biomass. This area of research focuses on understanding the internal architecture of bamboo and its composites—investigating how thermal, chemical, and physical processing influence microstructural behavior, functional properties, and long-term performance. These insights are critical for optimizing bamboo's use in precision-engineered, high-performance construction systems.

Lv et al. [98] employed detailed microstructural imaging to explore bamboo-derived cellulose materials with superior piezo photocatalytic behavior. Their work identified that the alignment of nanoscale fibers and controlled porosity contributed to enhanced charge transfer and visible-light activity. This microstructural insight was crucial in optimizing bamboo-based hybrids for photocatalytic and sensor-integrated building materials. Wu et al. [99] fabricated a biomass cellulose-based adsorbent with tunable pore architecture. Using SEM and FTIR analysis, they demonstrated that precise control of internal cell wall thickness and surface functional groups significantly enhanced water absorption and thermal buffering capacities. These findings underscore how bamboo's hierarchical microstructure can be engineered for eco-friendly insulation and passive climate control in buildings.

Saravanan et al. [100] synthesized a hybrid material combining bamboo-derived nanocellulose and cassava tuber starch. Their analysis demonstrated a porous micro-network with strong interfacial compatibility and low thermal diffusivity. Mechanical tests and micro-imaging confirmed its suitability as a lightweight, biodegradable panel for thermal insulation and acoustic absorption in green construction. Niu et al. [101] integrated bamboo-derived cellulose nanocrystals into multifunctional membranes, significantly improving their mechanical integrity and filtration efficiency—demonstrating bamboo's potential in both structural and non-structural applications. Yang et al. [102] introduced a treatment method for round bamboo to enhance its dimensional stability and structural uniformity. The experimental work included cross-sectional imaging and thermal dimensional analysis, demonstrating that fiber shrinkage and deformation under moisture fluctuations could be effectively mitigated through chemical and thermal pretreatment. Additionally, Javadian et al. (2019) explored the effect of densification on bamboo, utilizing mechanical testing and SEM imaging to quantify improvements in strength and dimensional stability, confirming its suitability for load bearing uses [103].

These studies illustrate how bamboo's internal microarchitecture—characterized by fiber orientation, porosity, and cellular gradients—can be engineered to develop high-performance composites and bio-derived materials. By bridging microstructural design with environmental resilience and mechanical integrity, this research cluster supports the advancement of bamboo-based technologies for future-ready, sustainable construction systems.

6. Future Research Pathways in Bamboo Construction

Building upon the bibliometric analysis and thematic clusters identified in this study, several future research directions have emerged that merit focused investigation as in Fig. 10. These areas not only highlight gaps in current knowledge but also reflect the shifting needs of the construction industry as it moves toward more sustainable, high-performance, and resilient building solutions.

As bamboo gains global recognition as a viable alternative to conventional construction materials, further research is essential to unlock its full potential through technical innovation, material synergy, and regulatory advancement.

A key area of future research lies in the advanced modeling of engineered bamboo composites. While numerous studies have successfully characterized bamboo's mechanical properties under standard testing conditions, there remains a pressing need for high-fidelity models capable of simulating their behavior under complex stress states such as multi-axial loading, long-term fatigue, and seismic activity. However, current models often fall short in capturing degradation phenomena such as moisture cycling, creep deformation, and microbial attack. Incorporating artificial intelligence and machine learning into the predictive modeling of bamboo structures—trained on robust experimental datasets—could significantly enhance design reliability and long-term performance forecasting.

A second frontier involves the development of hybrid systems using bamboo in combination with other bio-based materials. The integration of bamboo with resources such as mycelium, recycled cellulose, and agricultural residues opens the door to creating multi-functional composites that combine mechanical strength with environmental compatibility. Nevertheless, challenges remain in scaling up fabrication processes and improving the bonding mechanisms at the interface of these natural materials. Research should prioritize optimizing matrix-fiber adhesion, evaluating long-term durability, and ensuring regulatory compliance of hybrid bamboo products for structural use.

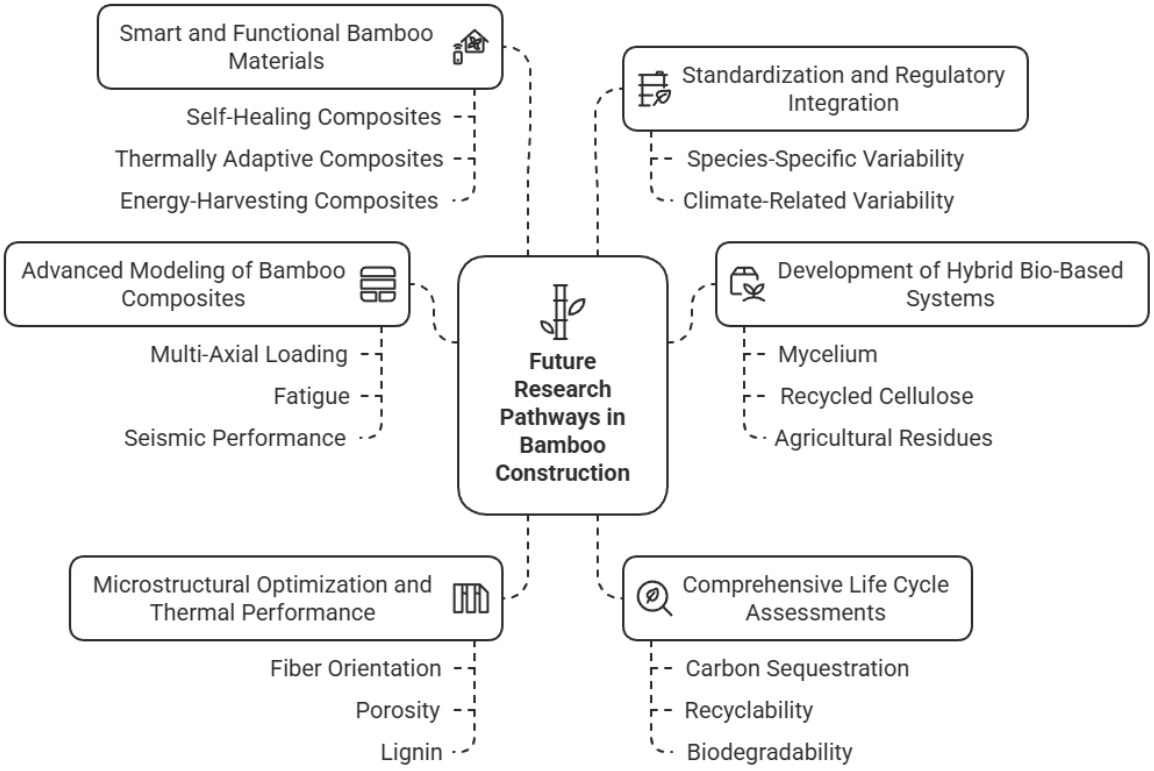


Fig. 10. Future research pathways in bamboo construction

In parallel, there is growing interest in microstructural optimization and thermal behavior enhancement of bamboo materials. Although techniques such as scanning electron microscopy (SEM) and X-ray diffraction have been widely employed to study bamboo's internal structure, few studies have successfully correlated microstructural parameters—such as fiber alignment, porosity, and lignin content—with macro-scale properties like thermal conductivity and dimensional stability. Future research should pursue integrative methods combining SEM, FTIR, and data-driven modeling to establish predictive frameworks for high-performance, thermally efficient bamboo building elements.

Despite bamboo's favorable material properties, its widespread adoption continues to be hindered by the absence of comprehensive and standardized building codes. Although ISO 22156 and 22157 provide baseline guidance, they do not account for species-specific variability or regional construction practices. Differences in treatment processes, environmental exposure, and mechanical performance further complicate the development of globally harmonized standards. Future efforts must focus on creating regionally adaptive design protocols, informed by rigorous experimental testing and lifecycle performance evaluations. Strong collaboration between material scientists, structural engineers, and policy-makers is essential to integrate bamboo into mainstream regulatory frameworks and ensure its safe, code-compliant application in construction.

Equally important is the need for more detailed and comprehensive life cycle assessments (LCAs). Although existing studies have established bamboo's role in reducing embodied carbon, most neglect broader environmental dimensions such as water usage, energy inputs across the supply chain, and end-of-life treatment. However, more work is needed to quantify the full ecological footprint of bamboo products, particularly in different climatic zones. Integrating bamboo into circular economy models—through recycling pathways, biodegradability testing, and carbon sequestration analysis—can strengthen its value proposition as a truly sustainable building material.

Finally, the frontier of smart and functional bamboo-based materials represents an exciting opportunity for interdisciplinary innovation. Emerging studies have begun to explore bamboo's potential as a base for sensors, actuators, and energy-harvesting systems. However, realizing these smart materials on a commercial scale will require overcoming challenges related to durability, cost, and integration with conventional building systems. Future research should investigate the feasibility of embedding responsive polymers, microcapsules, or energy storage elements within bamboo matrices to create self-healing, thermally adaptive, or even energy-producing construction elements.

7. Conclusions

This study provides a comprehensive bibliometric and knowledge-structure analysis of global research trends in bamboo-based construction between 2019 and 2024. Using a database of 1,456 peer-reviewed publications retrieved from Scopus and advanced mapping tools such as VOSviewer and bibliometrix in R, the research identified key thematic clusters in the domain. These clusters include structural performance and mechanical behavior, sustainability and environmental applications, and microstructural characterization and material innovation. The findings confirm that bamboo has gained increasing global attention as a sustainable construction material, supported by its mechanical strength, rapid renewability, and low environmental footprint.

Geographically, China, India, and Indonesia dominate publication and citation outputs, driven by abundant bamboo resources, government initiatives such as China's Bamboo Science and Technology Action Plan and India's National Bamboo Mission, and a growing emphasis on green construction strategies. Nevertheless, the bibliometric results also reveal critical research gaps that hinder bamboo's mainstream adoption in construction, particularly regarding international standardization, long-term durability assessment, scalability of engineered bamboo products, and lifecycle optimization methods. The limited integration of smart technologies, such as nano-enhancements and hybrid systems, further underscores the need for multidisciplinary research collaborations.

Beyond the bibliometric findings, a comparative evaluation between bamboo composites, steel, and timber highlights bamboo's competitive tensile strength, superior environmental performance, and promising cost-effectiveness, particularly in regions with limited access to traditional building materials. However, challenges related to quality consistency, market logistics, large-scale fabrication, and connection system standardization remain pressing concerns that must be addressed to ensure reliable and scalable applications.

Moving forward, future research should focus on developing regionally adaptive building codes, enhancing bamboo treatment and processing technologies, exploring bamboo's behavior under complex loading and environmental conditions, and advancing hybrid material systems to further improve performance and durability. Integrating bamboo construction into mainstream sustainable infrastructure solutions will also require strong policy support, education initiatives, and investment in industrial-scale production technologies.

In conclusion, bamboo has the potential to transition from a promising alternative to a key strategic material for achieving resilient, low-carbon, and sustainable infrastructure. Realizing this vision demands continued scientific innovation, strategic collaboration across sectors, and a commitment to advancing bamboo construction technologies globally.

Acknowledgement

The authors would like to express their sincere gratitude to Universitas Muhammadiyah Yogyakarta (UMY) for its valuable support and encouragement.

References

[1] Wan Q, Qian J, Baghirli A, Aghayev A. Green finance and carbon reduction: Implications for green recovery. Econ Anal Policy 2022;76. https://doi.org/10.1016/j.eap.2022.09.022
[2] Borowski PF, Patuk I, Bandala ER. Innovative Industrial Use of Bamboo as Key "Green" Material. Sustainability (Switzerland) 2022;14. https://doi.org/10.3390/su14041955
[3] Kaam R, Tchamba M, Nfornkah BN, Chimi Djomo C. Allometric equations and carbon stocks assessment for Bambusa vulgaris Schrad. ex J.C.Wendl. in the bimodal rainfall forest of Cameroon. Heliyon 2023;9. https://doi.org/10.1016/j.heliyon.2023.e21251
[4] Benedikter S, Truong TQ, Kapp G, Vasquez Coda ML. Towards an integrative perspective on commercialised wild-gathered bamboo use: insights into the extraction of lung bamboo in the Vietnamese uplands. Aust For 2022;85. https://doi.org/10.1080/00049158.2022.2137958
[5] Zheng Y, Zhou C, Wang Y, Zhang P. Strength design values of high-performance bamboo-based composite materials based on reliability requirements. Constr Build Mater 2023;368. https://doi.org/10.1016/j.conbuildmat.2023.130454
[6] Shu B, Xiao Z, Hong L, Zhang S, Li C, Fu N, et al. Review on the application of bamboo-based materials in construction engineering. J Renew Mater 2020;8. https://doi.org/10.32604/jrm.2020.011263.
[7] Harries KA, Rogers C, Brancaccio M. Bamboo joint capacity determined by ISO 22156 'complete joint testing' provisions. Advances in Bamboo Science 2022;1. https://doi.org/10.1016/j.bamboo.2022.100003
[8] Madhushan S, Buddika S, Bandara S, Navaratnam S, Abeysuriya N. Uses of Bamboo for Sustainable Construction—A Structural and Durability Perspective—A Review. Sustainability (Switzerland) 2023;15. https://doi.org/10.3390/su151411137
[9] Okolnikova GE, Weldelibanos GT, Kahsay HB, Gebrezgiabher AG. BAMBOO AS SUSTAINABLE MATERIAL FOR BUILDING CONSTRUCTION. Системные Технологии 2022. https://doi.org/10.55287/22275398_2022_1_73
[10] Chen Z, Ma R, Du Y, Wang X. State-of-the-art review on research and application of original bamboo-based composite components in structural engineering. Structures 2022;35. https://doi.org/10.1016/j.istruc.2021.11.059
[11] Zhang X, Xu J, Zhang X, Li Y. Life cycle carbon emission reduction potential of a new steel-bamboo composite frame structure for residential houses. Journal of Building Engineering 2021;39. https://doi.org/10.1016/j.jobe.2021.102295
[12] Zhao B, Yu Y, Xu Y, Guo H. Bamboo as a sustainable construction material for residential buildings in the cold and severe cold regions of China. Architectural Engineering and Design Management 2023. https://doi.org/10.1080/17452007.2023.2195614
[13] ISO. Bamboo- Determination of physical and mechanical properties - Part1: Requirements, ISO 22157-1:2004 (E). International Organization for Standardization, Geneva, Switzerland 2004.
[14] ISO (International Organization for Standardization). Bamboo —Determination of physical and mechanical properties - Part 1: Requirements. vol. 1. 2004.
[15] Standardization) I (International O for. TECHNICAL REPORT ISO 2011;2011.
[16] ASTM. ASTM D5456-21 Standard specification for evaluation of structural composite lumber products. American Society for Testing and Materials 2021.
[17] ISO-22157. INTERNATIONAL STANDARD Bamboo structures — Determination of physical and mechanical properties. Switzerland 2019;2019.

[18] ISO. Bamboo- Determination of physical and mechanical properties - Part1: Requirements, ISO 22157-1:2004 (E). International Organization for Standardization, Geneva, Switzerland 2004.
[19] Indian Standard. Method of Tests For Bamboo. IS 8242, New Delhi, India 2004.
[20] DTI-BPS adopts International Standards on bamboo structures 2020.
[21] JG/T 199-2007 – Testing methods for physical and mechanical properties of bamboo used in building 2007.
[22] Amede EA, Hailemariama EK, Hailemariam LM, Nuramo DA. A Review of Codes and Standards for Bamboo Structural Design. Advances in Materials Science and Engineering 2021;2021. https://doi.org/10.1155/2021/4788381
[23] ESTRUCTURAS DE GUADÚA - MIDUVI 2017.
[24] IS 15912:2018 – Structural Design Using Bamboo — Code of Practice 2018.
[25] ISO 22156:2021 – Bamboo structures – Structural design 2021.
[26] NORMA E.100 – Diseño y Construcción con Bamboo 2012.
[27] Bangladesh National Building Code (BNBC) 2020 2020.
[28] ISO 22157:2019 – Bamboo structures – Determination of physical and mechanical properties of bamboo culms – Test methods 2019.
[29] Manandhar R, Kim JH, Kim JT. Environmental, social and economic sustainability of bamboo and bamboo-based construction materials in buildings. Journal of Asian Architecture and Building Engineering 2019;18. https://doi.org/10.1080/13467581.2019.1595629
[30] Kathiravan NS, Manojkumar R, Jayakumar P, Kumaraguru J, Jayanthi V. State of art of review on bamboo reinforced concrete. Mater Today Proc, vol. 45, 2021. https://doi.org/10.1016/j.matpr.2020.03.159
[31] Chaowana K, Wisadsatorn S, Chaowana P. Bamboo as a sustainable building material—culm characteristics and properties. Sustainability (Switzerland) 2021;13. https://doi.org/10.3390/su13137376
[32] Aniñon MJC, Garciano LEO. Advances in Connection Techniques for Raw Bamboo Structures—A Review. Buildings 2024;14. https://doi.org/10.3390/buildings14041126
[33] Pradhan NPN, Paraskeva TS, Dimitrakopoulos EG. Quasi-static reversed cyclic testing of multi-culm bamboo members with steel connectors. Journal of Building Engineering 2020;27:100983. https://doi.org/10.1016/J.JOBE.2019.100983
[34] Shan B, Qiu J, Xu H, Li T, Xiao Y, Qin S, et al. Experimental research on standardized bamboo culm components for developing prefabricated bamboo building. Structures 2023;50. https://doi.org/10.1016/j.istruc.2023.02.046
[35] Liliefna LD, Nugroho N, Karlinasari L, Sadiyo S. Development of low-tech laminated bamboo esterilla sheet made of thin-wall bamboo culm. Constr Build Mater 2020;242. https://doi.org/10.1016/j.conbuildmat.2020.118181
[36] Appiah-Kubi E, Awotwe-Mensah M, Mitchual SJ. Assessment of physical and mechanical properties of juvenile and matured Bambusa vulgaris glue-laminated bamboo for structural applications in Ghana. Sustainable Structures 2023;3. https://doi.org/10.54113/j.sust.2023.000026
[37] Li H, Xu W, Chen C, Yao L, Corbi O. Effect of temperature on the compressive performance of laminated bamboo lumber. Proceedings of the Institution of Civil Engineers - Structures and Buildings 2024;177:1069–81. https://doi.org/10.1680/JSTBU.23.00034
[38] Tang G, Yin L, Li Z, Li Y, You L. Structural behaviors of bolted connections using laminated bamboo and steel plates. Structures 2019;20. https://doi.org/10.1016/j.istruc.2019.04.001
[39] Silva FJ, Rodrigues FC, Moreira LE. Buckling of masts of bamboos bundles. Key Eng Mater, vol. 634, 2015. https://doi.org/10.4028/www.scientific.net/KEM.634.379
[40] Desai A, Bheemrao N. Life cycle assessment of construction materials and its environmental impacts for sustainable development. Mater Today Proc, vol. 65, 2022. https://doi.org/10.1016/j.matpr.2022.07.171
[41] Kelkar BU, Shukla SR, Nagraik P, Paul BN. Structural bamboo composites: A review of processing, factors affecting properties and recent advances. Advances in Bamboo Science 2023;3. https://doi.org/10.1016/j.bamboo.2023.100026
[42] Muhtar. Experimental data from strengthening bamboo reinforcement using adhesives and hose-clamps. Data Brief 2019;27. https://doi.org/10.1016/j.dib.2019.104827
[43] Sutharsan R, Ramprasanna SR, Gnanappa SB, Ganesh AC. Experimental study on Bamboo as a reinforcing material in concrete. AIP Conf Proc 2020;2204:20024. https://doi.org/10.1063/1.5141561
[44] Mali PR, Datta D. Experimental evaluation of bamboo reinforced concrete beams. Journal of Building Engineering 2020;28. https://doi.org/10.1016/j.jobe.2019.101071.
[45] Experimental Strength Evaluation of Bamboo Reinforced Concrete Beams. International Journal of Advanced Trends in Computer Science and Engineering 2021;10. https://doi.org/10.30534/ijatcse/2021/571012021

[46] Muhtar, Murni Dewi S, Wisnumurti, Munawir A. The flexural behavior model of bamboo reinforced concrete beams using a hose clamp. MATEC Web of Conferences 2019;276. https://doi.org/10.1051/matecconf/201927601033
[47] Dixit A, Puri V. Bamboo bonding in concrete: A critical research. International Journal of Innovative Technology and Exploring Engineering 2019;8. https://doi.org/10.35940/ijitee.K1061.09811S19
[48] Mondal B, Maity D, Patra PK. Bond Behavior between Bamboo and Normal-Strength Concrete: Experimental and Numerical Investigation. Practice Periodical on Structural Design and Construction 2022;27. https://doi.org/10.1061/(asce)sc.1943-5576.0000715
[49] Wang Z, Wang M, Xu Q, Harries KA, Li X, Gao R. Experimental research on prestressed concrete hollow-core slabs strengthened with externally bonded bamboo laminates. Eng Struct 2021;244. https://doi.org/10.1016/j.engstruct.2021.112786
[50] Parasuram M, Baskaran K. Study on Bamboo and Steel As Hybrid Reinforcement for Concrete Slab. MERCon 2020 - 6th International Multidisciplinary Moratuwa Engineering Research Conference, Proceedings, 2020, p. 13–8. https://doi.org/10.1109/MERCon50084.2020.9185244
[51] Yusof ZM, Rozaini NAA, Zainorabidin A, Agung PAM. Settlement Performance of Bamboo Dendrocalamus Asper for Improving Peat Soil Reinforcement Stability. International Journal of Sustainable Construction Engineering and Technology 2023;14. https://doi.org/10.30880/ijscet.2023.14.05.030
[52] Widodo B, Pratikso, Rohim A. A Bearing Capacity of Bamboo Cluster Pile on Saturated Soft Soil Based on the Direct load Test and CPT'S Data. International Journal of Sustainable Construction Engineering and Technology 2022;13:390–8. https://doi.org/10.30880/ijscet.2022.13.04.033
[53] Madhushan S, Buddika S, Bandara S, Navaratnam S, Abeysuriya N. Uses of Bamboo for Sustainable Construction—A Structural and Durability Perspective—A Review. Sustainability (Switzerland) 2023;15. https://doi.org/10.3390/su151411137
[54] Wei Y, Ji X, Zhou M, Zhao L, Duan M. Mechanical properties of bamboo-concrete composite structures with dowel-type connections. Nongye Gongcheng Xuebao/Transactions of the Chinese Society of Agricultural Engineering 2017;33:65–72. https://doi.org/10.11975/j.issn.1002-6819.2017.03.009
[55] Nurdin S, Sawada K, Moriguchi S. Design Criterion of Reinforcement on Thick Soft Clay Foundations of Traditional Construction Method in Indonesia. MATEC Web of Conferences 2019;258. https://doi.org/10.1051/matecconf/201925803010
[56] Khatun R, Ahmmed E, Ferdousi S, Khan MAR, Hannan MO, Ashaduzzaman M, et al. Preservative treatment of the bamboos Dendrocalamus giganteus, Bambusa vulgaris and Gigantochloa nigrociliata. Advances in Bamboo Science 2025;11. https://doi.org/10.1016/j.bamboo.2025.100163
[57] Zhang Z, Wei Y, Wang J, Yi J, Wang G. Effect of thermal modification on axial compression properties and hardness of laminated bamboo. Constr Build Mater 2024;411. https://doi.org/10.1016/j.conbuildmat.2023.134747
[58] Gangorra LCC, Gomes BMDC, Hasparyk NP, Filho RDT. Analysis of the physical and mechanical properties of bamboo bio-concretes produced with fine particles as partial replacement of bio-aggregates | Análise das propriedades físico-mecânicas de bioconcretos de bambu produzidos com partículas finas em substi. Revista Materia 2024;29. https://doi.org/10.1590/1517-7076-RMAT-2024-0364
[59] Kumari M, Mondal S. Bamboo Strips as Eco-friendly Soil Reinforcement Material. Lecture Notes in Civil Engineering, vol. 154, 2022. https://doi.org/10.1007/978-981-16-1993-9_6
[60] Fahim M, Saeed M, Khan H, Gir A, Ullah S. Flexure Behavior of Carbon Fiber Reinforced Polymers Retrofitted RC Beams. Advances in Science and Technology Research Journal 2022;16. https://doi.org/10.12913/22998624/147337
[61] Tao Y, Hadigheh SA, Wei Y. Recycling of glass fibre reinforced polymer (GFRP) composite wastes in concrete: A critical review and cost benefit analysis. Structures 2023;53. https://doi.org/10.1016/j.istruc.2023.05.018
[62] Li H, Wei Y, Meng K, Zhao L, Zhu B, Wei B. Mechanical properties and stress-strain relationship of surface-treated bamboo fiber reinforced lightweight aggregate concrete. Constr Build Mater 2024;424. https://doi.org/10.1016/j.conbuildmat.2024.135914
[63] Li H, Zhang J, Xu G, Li H, Bai Y. Size effect on the compressive properties of neosinocalamus affinis-based bamboo scrimber. Wood Mater Sci Eng 2024. https://doi.org/10.1080/17480272.2024.2437683
[64] Madhushan S, Buddika S, Bandara S, Navaratnam S, Abeysuriya N. Uses of Bamboo for Sustainable Construction—A Structural and Durability Perspective—A Review. Sustainability (Switzerland) 2023;15. https://doi.org/10.3390/su151411137
[65] Paul D, Gaff M, Tesařová D, Hui D, Li H. Recent advancements in nanotechnology application on wood and bamboo materials: A review. Nanotechnol Rev 2023;12. https://doi.org/10.1515/ntrev-2022-0528
[66] de Lima TES, de Azevedo ARG, Marvila MT, Candido VS, Fediuk R, Monteiro SN. Potential of Using Amazon Natural Fibers to Reinforce Cementitious Composites: A Review. Polymers (Basel) 2022;14. https://doi.org/10.3390/polym14030647

[67] Voutetaki ME, Mpalaskas AC. Natural Fiber-Reinforced Mycelium Composite for Innovative and Sustainable Construction Materials. Fibers 2024;12. https://doi.org/10.3390/fib12070057
[68] Saal K, Kallakas H, Tuhkanen E, Just A, Rohumaa A, Kers J, et al. Fiber-Reinforced Plywood: Increased Performance with Less Raw Material. Materials 2024;17. https://doi.org/10.3390/ma17133218
[69] Aziminezhad M, Taherkhani R. BIM for deconstruction: A review and bibliometric analysis. Journal of Building Engineering 2023;73. https://doi.org/10.1016/j.jobe.2023.106683
[70] Taherkhani R, Aziminezhad M. Human-building interaction: A bibliometric review. Build Environ 2023;242. https://doi.org/10.1016/j.buildenv.2023.110493
[71] Rahman T, Zudhy Irawan M, Noor Tajudin A, Rizka Fahmi Amrozi M, Widyatmoko I. Knowledge mapping of cool pavement technologies for urban heat island Mitigation: A Systematic bibliometric analysis. Energy Build 2023;291. https://doi.org/10.1016/j.enbuild.2023.113133
[72] Burnham JF. Scopus database: A review. Biomed Digit Libr 2006;3. https://doi.org/10.1186/1742-5581-3-1
[73] Zhang X, Wen T, Li D, Li JW, Huo D, Jiang X, et al. Bamboo industry ecosystem structure and evolution: An example of Chishui city, Guizhou province, China. Shengtai Xuebao 2016;36. https://doi.org/10.5846/stxb201507171505
[74] Baksi S, Srivastava P. Bamboo: Technology Innovations Towards Value-Added Applications. Journal of Bamboo and Rattan 2021;20.
[75] Setiawati T, Mutaqin AZ, Irawan B, An'Amillah A, Iskandar J. Species diversity and utilization of bamboo to support life's the community of Karangwangi village, Cidaun sub-district of Cianjur, Indonesia. Biodiversitas 2017;18. https://doi.org/10.13057/biodiv/d180109
[76] Li Z, Chen C, Mi R, Gan W, Dai J, Jiao M, et al. A Strong, Tough, and Scalable Structural Material from Fast-Growing Bamboo. Advanced Materials 2020;32. https://doi.org/10.1002/adma.201906308
[77] Nurazzi NM, Asyraf MRM, Rayung M, Norrrahim MNF, Shazleen SS, Rani MSA, et al. Thermogravimetric analysis properties of cellulosic natural fiber polymer composites: A review on influence of chemical treatments. Polymers (Basel) 2021;13. https://doi.org/10.3390/polym13162710
[78] Hasija V, Sudhaik A, Raizada P, Hosseini-Bandegharaei A, Singh P. Carbon quantum dots supported AgI /ZnO/phosphorus doped graphitic carbon nitride as Z-scheme photocatalyst for efficient photodegradation of 2, 4-dinitrophenol. J Environ Chem Eng 2019;7. https://doi.org/10.1016/j.jece.2019.103272
[79] Thomas BS, Yang J, Mo KH, Abdalla JA, Hawileh RA, Ariyachandra E. Biomass ashes from agricultural wastes as supplementary cementitious materials or aggregate replacement in cement/geopolymer concrete: A comprehensive review. Journal of Building Engineering 2021;40. https://doi.org/10.1016/j.jobe.2021.102332
[80] Li Z, Chen C, Xie H, Yao Y, Zhang X, Brozena A, et al. Sustainable high-strength macrofibres extracted from natural bamboo. Nat Sustain 2022;5. https://doi.org/10.1038/s41893-021-00831-2
[81] Maraveas C. Production of sustainable construction materials using agro-wastes. Materials 2020;13. https://doi.org/10.3390/ma13020262
[82] Chen C, Li Z, Mi R, Dai J, Xie H, Pei Y, et al. Rapid Processing of Whole Bamboo with Exposed, Aligned Nanofibrils toward a High-Performance Structural Material. ACS Nano 2020;14. https://doi.org/10.1021/acsnano.9b08747
[83] Chen M, Ye L, Li H, Wang G, Chen Q, Fang C, et al. Flexural strength and ductility of moso bamboo. Constr Build Mater 2020;246. https://doi.org/10.1016/j.conbuildmat.2020.118418
[84] Lou Z, Han X, Liu J, Ma Q, Yan H, Yuan C, et al. Nano-Fe3O4/bamboo bundles/phenolic resin oriented recombination ternary composite with enhanced multiple functions. Compos B Eng 2021;226. https://doi.org/10.1016/j.compositesb.2021.109335
[85] Chokshi S, Parmar V, Gohil P, Chaudhary V. Chemical Composition and Mechanical Properties of Natural Fibers. Journal of Natural Fibers 2022;19. https://doi.org/10.1080/15440478.2020.1848738
[86] Bala A, Gupta S. Engineered bamboo and bamboo-reinforced concrete elements as sustainable building materials: A review. Constr Build Mater 2023;394. https://doi.org/10.1016/j.conbuildmat.2023.132116
[87] Moujoud Z, Sair S, Ait Ousaleh H, Ayouch I, El Bouari A, Tanane O. Geopolymer composites reinforced with natural Fibers: A review of recent advances in processing and properties. Constr Build Mater 2023;388. https://doi.org/10.1016/j.conbuildmat.2023.131666
[88] Wu F, Wei Y, Lin Y, Zhao K, Huang L. Experimental study of bamboo scrimber-filled steel tube columns under axial compression. Eng Struct 2023;280. https://doi.org/10.1016/j.engstruct.2023.115669
[89] Meng T, Ding Y, Liu Y, Xu L, Mao Y, Gelfond J, et al. In Situ Lignin Adhesion for High-Performance Bamboo Composites. Nano Lett 2023;23. https://doi.org/10.1021/acs.nanolett.3c01497
[90] Xu D, He S, Leng W, Chen Y, Wu Z. Replacing Plastic with Bamboo: A Review of the Properties and Green Applications of Bamboo-Fiber-Reinforced Polymer Composites. Polymers (Basel) 2023;15. https://doi.org/10.3390/polym15214276

[91] Shi J, Zhong T, Xu X, Wu J, Zou Y, Fei B, et al. Eco-friendly and special-shaped bamboo binderless fiberboards fabricated by self-bonding technology: Effect of bamboo fibers with different sizes. Ind Crops Prod 2023;194. https://doi.org/10.1016/j.indcrop.2023.116300
[92] Han S, Chen F, Yu Y, Chen L, Wang G. Bamboo-inspired strong, tough and stable composites derived from renewable bamboo. Ind Crops Prod 2023;194. https://doi.org/10.1016/j.indcrop.2023.116292
[93] Xue X, Zhou W, Sayed U, Feng Z, Li H, Li Y, et al. Design and construction of "Bamboo Cubic" facade with laminated bamboo lumber. Sustainable Structures 2023;3. https://doi.org/10.54113/j.sust.2023.000030
[94] Gidebo FA, Yasuhara H, Kinoshita N. Stabilization of expansive soil with agricultural waste additives: a review. International Journal of Geo-Engineering 2023;14. https://doi.org/10.1186/s40703-023-00194-x
[95] Han S, Chen F, Ye H, Zheng Z, Chen L, Wang G. Bamboo-Inspired Renewable, High-Strength, Vibration-Damping Composites for Structural Applications. ACS Sustain Chem Eng 2023;11. https://doi.org/10.1021/acssuschemeng.2c06490
[96] Cui C, Geng L, Jiang S, Bai W, Dai L, Jiang S, et al. Construction of hierarchical carbon fiber Aerogel@Hollow Co9S8 polyhedron for high-performance electromagnetic wave absorption at low-frequency. Chemical Engineering Journal 2023;466. https://doi.org/10.1016/j.cej.2023.143122
[97] Lou Z, Zheng Z, Yan N, Jiang X, Zhang X, Chen S, et al. Modification and Application of Bamboo-Based Materials: A Review—Part II: Application of Bamboo-Based Materials. Forests 2023;14. https://doi.org/10.3390/f14112266
[98] Lv H, Liu Y, Zhao P, Bai Y, Cui W, Shen S, et al. Insight into the superior piezophotocatalytic performance of BaTiO3//ZnO Janus nanofibrous heterostructures in the treatment of multi-pollutants from water. Appl Catal B 2023;330. https://doi.org/10.1016/j.apcatb.2023.122623
[99] Wu G, Zhou C, Li H, Xia S, Zhu Y, Han J, et al. Controlled fabrication of the biomass cellulose aerogel@ZIF-8 nanocomposite as efficient and recyclable adsorbents for methylene blue removal. Ind Crops Prod 2023;193. https://doi.org/10.1016/j.indcrop.2022.116169
[100] Saravanan KG, Kaliappan S, Natrayan L, Patil PP. Effect of cassava tuber nanocellulose and satin weaved bamboo fiber addition on mechanical, wear, hydrophobic, and thermal behavior of unsaturated polyester resin composites. Biomass Convers Biorefin 2024;14. https://doi.org/10.1007/s13399-023-04495-0
[101] Niu Y, Teng X, Gong S, Chen Z. A bimetallic alloy anchored on biomass-derived porous N-doped carbon fibers as a self-supporting bifunctional oxygen electrocatalyst for flexible Zn-air batteries. J Mater Chem A Mater 2020;8. https://doi.org/10.1039/d0ta03288c
[102] Yang X, Huang Y, Ye C, Lin X, Su N, Fei B. Improving the dimensional stability of round bamboo by environment-friendly modified rosin. Constr Build Mater 2023;365. https://doi.org/10.1016/j.conbuildmat.2022.130078
[103] Javadian A, Smith IFC, Saeidi N, Hebel DE. Mechanical properties of bamboo through measurement of culm physical properties for composite fabrication of structural concrete reinforcement. Front Mater 2019;6. https://doi.org/10.3389/fmats.2019.00015

Research on Engineering Structures & Materials
www.jresm.org

Research Article

Enhancing structural integrity of plastic concrete diaphragm walls in dams on thick alluvium: A numerical study of geometry and construction sequencing

Idrissa Ouedraogo [*,a], Anas Bahi [b], Latifa Ouadif [c]

L3GIE Laboratory, Mohammed V University, Mohammadia Engineering School, 10090 Agdal Rabat, Morocco

Article Info

Article History:

Received 30 Apr 2025

Accepted 28 July 2025

Keywords:

Concrete Face Rockfill Dam;
Alluvium;
Plastic concrete;
Diaphragm wall;
Geometric optimization;
Stress concentration;
Junction;
Junction angle;
Distortion

Abstract

Diaphragm walls are particularly useful in Dams laying on thick alluvial valleys, making it possible to connect the watertight components of the structure to the deep bedrock. This article analyses the case of a Concrete Face Rockfill Dam, resting on approximately 35 m of alluvium, where a soft concrete diaphragm wall was built to overcome tightness issues caused by the alluvium layer. The paper recalls the behavior of a plastic concrete diaphragm wall to analyze its dimensioning parameters, in order to propose a geometrically based design improvement. The study is based on numerical simulation, using Plaxis software. It emerges from the study that the area connecting the wall to the watertight organs of the dam constitutes its most critical part, where distortions reach 2%. The article thus proposes a softening of this junction. This design makes it possible to significantly reduce the concentration of deformations in that area. Applying this solution brings down the distortion to only 0,1%. Plus, the study shows that better results can be reached by having a strategic planning of the dike construction.

© 2025 MIM Research Group. All rights reserved.

1. Introduction

Dams are artificial barriers constructed in watercourses to create reservoirs for diverse purposes, including agriculture, hydroelectric power, domestic water supply, flood control, and recreational activities [1, 15]. However, geological investigations sometimes reveal challenges related to the watertightness of dam foundations. The Rhiss Dam in northeastern Morocco serves as the subject of this study. Geological assessments utilizing methods such as drilling and geophysical surveys have identified that the valley is filled with alluvial deposits overlying bedrock, reaching depths of up to thirty-five meters [5]. These alluvial soils, though recognized as productive and valuable for various uses, pose significant geotechnical challenges for dam foundations due to their permeability and high deformability [6, 7]. These characteristics not only compromise structural stability but also raise concerns related to soil liquefaction, especially in saturated conditions [1]. To address such risks, investigated vibro-compaction as a ground improvement technique for a similar sandy foundation in a Moroccan port area, suggesting important design parameters [14]. Liquefaction, a transient loss of soil strength in saturated conditions, has been characterized as a severe geohazard by Berkat et al. [16].

In response to seepage issues through alluvial foundations, Ouedraogo studied the use of a plastic diaphragm wall as a watertight barrier [1]. According to Hruban [17], such a diaphragm wall is "a wall constructed in a trench excavated mechanically from the surface", and it has been applied in various civil engineering contexts particularly for the formation of cofferdams to prevent seepage.

*Corresponding author: idr.oued07@gmail.com
[a]orcid.org/ 0009-0001-9410-7102; [b]orcid.org/ 0000-0002-1450-7254; [c]orcid.org/0000-0002-4613-1124;
DOI: http://dx.doi.org/10.17515/resm2025-858st0430rs

The structural behavior and performance of diaphragm walls have been the subject of several recent investigations. For instance, Jingwu Zhang et al., [2] analyzed lateral earth pressures on circular diaphragm walls and validated their analytical model with the Beam on Nonlinear Elastic Foundation (BNEF) method proposed by Wei He et al [3] Meanwhile, Yong Shao et al., [4] addressed leakage detection using Fiber Bragg Grating (FBG) sensing technologies. Despite these contributions, a specific phenomenon observed by Ouedraogo et al. [1] remains insufficiently explored: the accumulation of deformations at the junction between the concrete head block and the diaphragm wall body (Fig. 1). This localized distortion could critically affect the structural integrity of the diaphragm wall, yet few studies have quantitatively assessed or modeled its development.

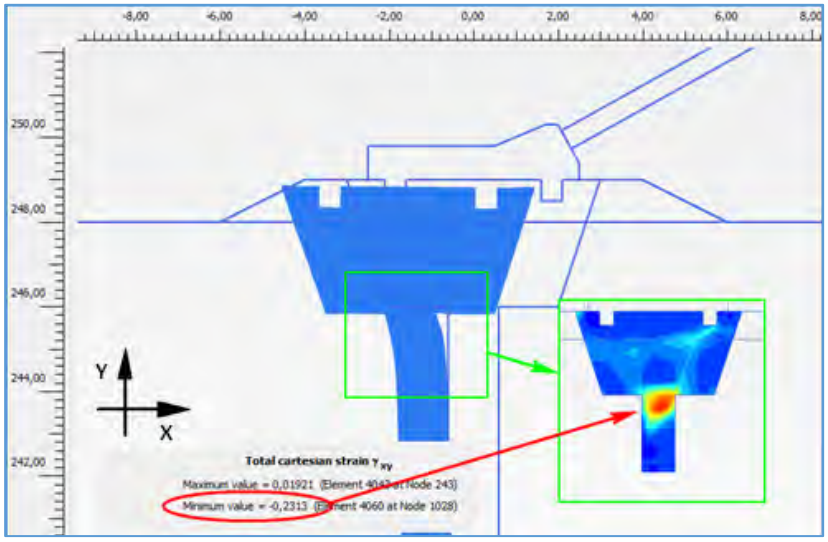


Fig. 1. Distortion accumulating in the junction of the concrete head block and the body of the diaphragm wall (adapted from [1])

The present study aims to investigate the deformation patterns observed at the junction between the concrete head block and the diaphragm wall, particularly in the context of thick alluvial layers such as those at the Rhiss Dam site. Using numerical modeling, the research simulates displacement and distortion fields within the diaphragm wall system, offering a detailed assessment of the structural behavior under geotechnical loading. The results confirm the presence of significant distortion concentrations at the junction points, reaching up to 2%, which pose a threat to the long-term performance of the wall. In response, two design optimizations were proposed. Most notably, smoothing the junction angle between the head block and the diaphragm wall body—a simple and cost-effective measure proved highly effective. This modification reduced the distortion at the upper junction point from 2% to just 0.1%, and also mitigated a secondary distortion peak at mid-height of the wall from 2.1% to 0.45%. These findings not only validate the initial observations by Ouedraogo et al. [1] but also offer practical engineering strategies to improve diaphragm wall integrity in similar geotechnical settings.

2. Materials and Methods

The subject of our investigation is the identical case as Ouedraogo et al. [1]. We adhered to a strict protocol that included bibliography research and comparisons of numerical analysis in order to achieve our original objective, which is to reduce the concentration of distortions at the junction points of the diaphragm wall (as it appears on Fig. 1). The analyses are made using Plaxis software.

2.1. Design of the Dam and the Diaphragm Wall

The paper investigates on a CFRD Dam (Concrete Faced Rockfill Dam). It was designed in accordance with the suggestions made by the CFBR (Comité Français des Barrages et Retenues) and the International Commission On Large Dams (ICOLD). The Dam's other components have

designed accordingly to [9, 10,12,13], which are indications provided by CIGB-ICOLD and CFBR for the design of CFRD dam components.

The dam is 85m high (with 8m crest) and laying on 35m of alluvium layer. The upstream facing is 1,8H/1V and the downstream facing is 2,35H/1V. Under the alluvium is the bedrock, composed of shale clay. Souileh et al., [18] found a permeability of $2.5x10^{-6}$ m/s for Khouribga shale clay, showing the tightness of that rock. The bedrock is indeed supposed to be watertight and incompressible. To connect the concrete face to the bedrock, a complex of plinth-concrete head block-diaphragm wall is constructed. The plinth and the concrete face are made with reinforced concrete while the diaphragm wall and its head block are in plastic concrete. This concept was explained by Ouedraogo et al, in his study [1].

The Dam was constructed using alluvium in the reservoir and shale clay from the bedrock. This has been made as ecofriendly procedure in order to utilize local construction materials. For instance, shale clay is encouraged to be used nowadays in Morocco, and prove high performance when used in concrete formulation. Indeed, Souileh et al., [19] found that clay shale-based concrete achieved a compressive strength of 12 MPa after seven days and 16 MPa after 28 days, meeting B25 concrete standards.

The diaphragm wall was constructed using a stair-step foundation that ensures a minimum anchoring of 1 m in the bedrock, and alternating main and secondary studs that are around 7 m wide each. It crosses the whole alluvium layer (35m) with 1m encoring in the shale bedrock. A layer of clayey silts, followed by a layer of coarse alluvium and finally a layer of alluvium, covers the fine (filtering) material that protects the concrete head block upstream. A cross-section of the diaphragm wall is shown in Figure 2.

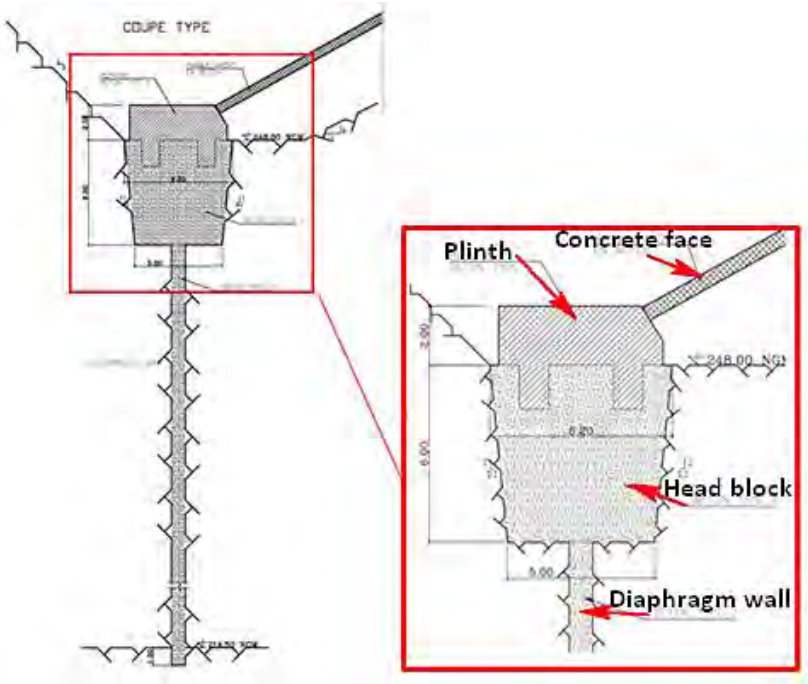


Fig. 2. Typical section of the diaphragm wall (adapted from [1])

In the current study, this conception has been maintained in order to be compared with an all-new design. This new design (solution 1. See §3.2) is indeed an enhanced one that makes it possible to mitigate distortions concentration at the junction point.

2.2. Numerical Analysis

We have employed finite elements-based numerical analysis to evaluate the diaphragm wall's capacity to withstand the constraints that it faces, where the loads listed below have been considered: water pressure and ground push and stop.

According Ouedraogo et al., [1], the water in the reservoir exerts a hydrostatic pressure equal to:

$$Pw = W.H \quad (1)$$

Where Pw is the hydrostatic pressure, W is the volume mass of water (1t/m3), and H is hydraulic load. The anchoring of the watertight break (diaphragm wall) in the bedrock and the permeability of the various horizons determine the hydraulic load (H) downstream of the diaphragm wall. The model computes it automatically. Due to nearly complete head loss in the bedrock, it is nearly constant between the diaphragm wall's downstream and the dam's downstream toe, and it is equivalent to the water level upstream of the dam [1]. Based on materials deformation and their limit resistance, the stresses that the ground applies to the diaphragm wall are automatically determined. As a result, the following factors determine the thrust and stop forces [1:

- Moduli of ground deformation.
- The soil's cohesiveness and friction angle.
- The wall's inertia.

The materials used in the model are adapted from [1] and their properties are shown on Tab 1, while Figure 3 shows the model, as simulated on Plaxis software.

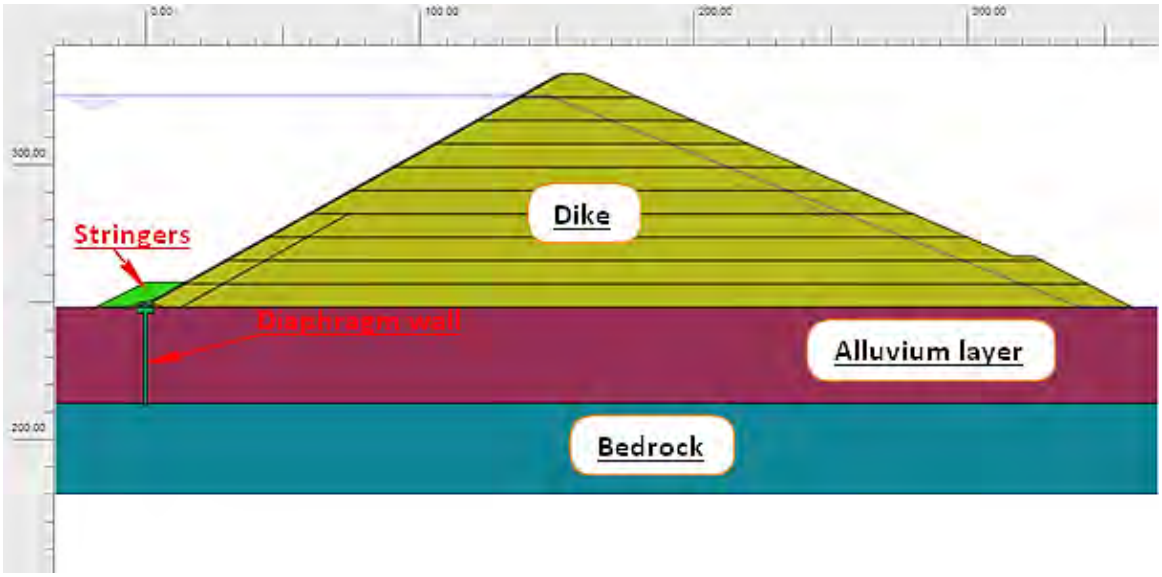


Fig. 3. Cross section of the model

Table 1. Materials used in the model and their parameters.

Materials	γ_{sec} (kN/m³)	n (%)	γ_{sat} (kN/m³)	K (m/s)	E (kN/m²)	C (kN/m²)	φ (°)	ν
Alluvium	21.0	10.0%	22.0	4.0E-05	2.0E+04	0.25*	39.00	0.25
Dike	23.2	10.0%	24.0	1.0E-04	1.0E+05	0.25*	39.00	0.3
Stringers	17.1	1.0%	17.20	1.0E-08	2.6E+04	50	26	0.19
Bedrock	21.0	1.0%	21.1	1.0E-09	3.0E+05	70	37.00	0.3
Diaphragm wall	23.2	1.0%	23.3	1.0E-08	4.0E+05	145	32	0.3
Plinth	24.5	0.1%	24.51	1.0E-11	2.2E+07	-	-	0.20
Concrete face	24.5	0.1%	24.51	1.0E-11	2.2E+07	-	-	0.20

In the current study, only construction and impoundment load cases are considered, while Ouedraogo et al., [1] include seismic analysis. The load cases considered are adopted from Ouedraogo et al., [1], who assume the construction of the diaphragm wall before the construction of the dam embankment. Displacements, stresses, and strains are calculated by considering the following cases:

- Step 1: “Construction of the diaphragm wall and the plinth”
- The earth pressures and the hydrostatic pressures are balanced on both sides (Upstream-downstream direction) of the diaphragm wall. The diaphragm wall is thus subjected to its own weight, the weight of the plinth, and friction with the alluvium [1].
- Step 2: “Step 1 + completion of the dam and the mask in 10 layers”
- The installation of the embankments for the construction of the dike is done gradually until reaching the crest of the dam. The thrust of the earth due to the weight of the dam downstream of the diaphragm wall induces a movement of the diaphragm wall upstream, in addition to settlement in the alluvial foundation [1].
- Step 3: “Step 2 + Installation of the upstream toe embankment”
- The placement of stringers at the upstream foot of the dam on the head of the diaphragm wall and the plinth constitutes an additional load for the diaphragm wall, causing its settlement and the one of the foundations.
- Step 4: “Step 3 + Impoundment of the dam up to the normal water level”
- To the forces due to load Step 3, are added the hydrostatic weight of the water above the plinth and the hydrostatic thrust resulting from the difference in the hydraulic load between the upstream and downstream of the diaphragm wall [1].

In accordance with the phasing given above, calculations have been made using Plaxis. Ouedraogo et al., [1] reported that has used Plaxis to analyse excavations supported with a diaphragm wall formed with rows of dry deep mixing columns [8]. Plaxis is indeed the model used by Ouedraogo in [1].

3. Results and Discussion

In the following paragraphs, we are going to show in the one hand the results of a similar modeling as studied by [1], to emphasize the accumulation of distortions at the junction points of the diaphragm wall. Then the distribution of displacements will allow us to give an explanation to that phenomenon. Understanding the magnitude and profile of these parameters is crucial for assessing Ouedraogo’s results. Indeed, ground movement potentially affects nearby structures [11]. In the other hand, we will study a geometry-based solution to tackle that issue. Finally, a second external solution will be investigated. This one is based on the planning related to the dike’s construction.

3.1. Structural Behavior of The Diaphragm Wall

The maximum displacements and distortions in the diaphragm wall are summarized in table.2 below. In order to visualize the evolution of the total displacements all along the construction of the dam, we made a plot of each phase. The results are shown on Figure 4. In this figure, Y coordinate are given on the cross section crossing the middle of the diaphragm wall as shown in right side of the figure.

It can be noticed on the figure that the construction of the dike engenders the displacement of the diaphragm wall accordingly. Hence, while the dike is getting higher, the diaphragm wall moves accordingly upstream. This corroborates the results given by Ouedraogo et al., [1]. Two points in the Y coordinate draw our attention: the points around Y=213m and Y=245m.

Although the relatively uniform variation of the displacements, theses to points stand out by the inflexion of all the curses. Indeed, at theses points, it can be noticed a change in the variation rate. Quantitatively, the curves vary smoothly from Y=208m to Y=213m, then the variation rate increases from Y =213m to Y =215m. Then it remains relatively smooth on the body of the diaphragm wall from Y =215m to Y =244m. At this point again, the same phenomenon is noticed: from Y =244m to Y =246m, the variation rate gets higher, and suddenly, decreases from Y =246m to Y =248m. In this last interval, it can be seen that the variation gets even negative, leading to a decrease of the displacement. This is more visible on the impoundment phase (refer to Figure 4). These particular intervals are emphasized on Figure 4 by vertical red barres.

Referring now to the corresponding position of these points on the diaphragm wall, it goes out that they are the anchoring points of the diaphragm wall: the first point is the anchoring with the bedrock (*Y*=213m), and the second is the anchoring with the head block(*Y*=246m). This is a proof

that the accumulation of the distortions at the anchoring points as stated in Ouedraogo et al., [1] is due to the sudden change in the displacement rate. In Figure5, we show the deformed mesh of the diaphragm wall, with emphasis to these two points. Note that the figure shows the true deformation, and an exaggerate one for visualization purposes, to present the deflexion at theses points.

Table 2. Calculation results -maximum deformations-

Load case	Corresponding Phase	U [cm]	Pu [cm]	γ_{xy} [%]	
1	Diaphragm Wall and plinth	1.19	1.19	0.021	-0.018
2	Dike and Mask	47.48	-	0.563	-2.475
3	Foot Embankment	49.09	7.21	0.579	-2.479
4	Impoundment	119.5	125.7	0.585	-2.504

Note: U is the total displacement, Pu is the total phase displacement, and γ_{xy} is the total strain (distortion).

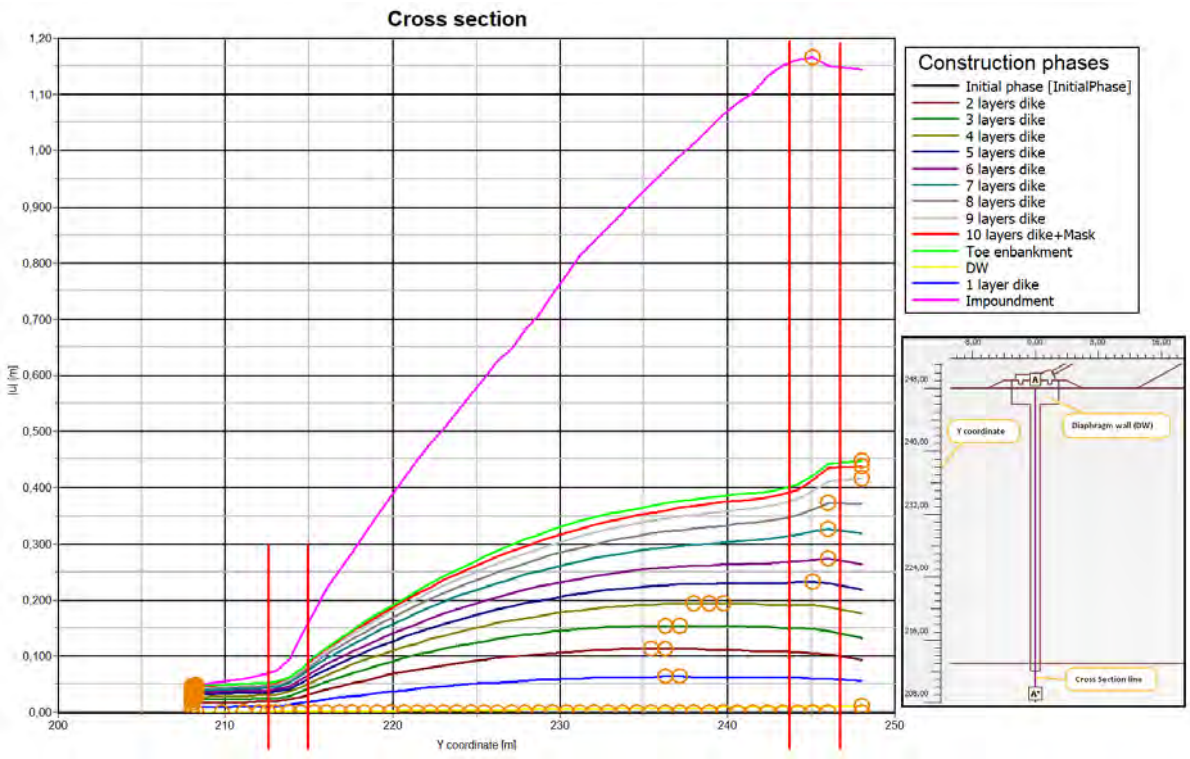


Fig. 4. Cross section of the diaphragm wall showing the evolution of total displacement (U) per phase

To support our point on the relationship between the displacements rate and the distortion accumulating to the junction points of the diaphragm wall, we have plotted the distribution of the distortions along the same cross section as the displacements one. Fig 6 shows that chart.

As it can be easily noticed, the same areas where displacements changed suddenly, the distortions get their maxima. For instance, around the junction points, all the curves get a peak. Although almost the whole curves have the same tendence, the impoundment one (the yellow curve) shows a different behaviour. Indeed, this curve shows, a pic at the middle of the diaphragm wall. Plus, although the pic at the junction points with the bedrock, the sign of the distortions from the bottom of the diaphragm wall (Y=208m) to Y=214,5m is opposite to their sign in the other curves. From Y=214,5m, all the distortions have the same sign.

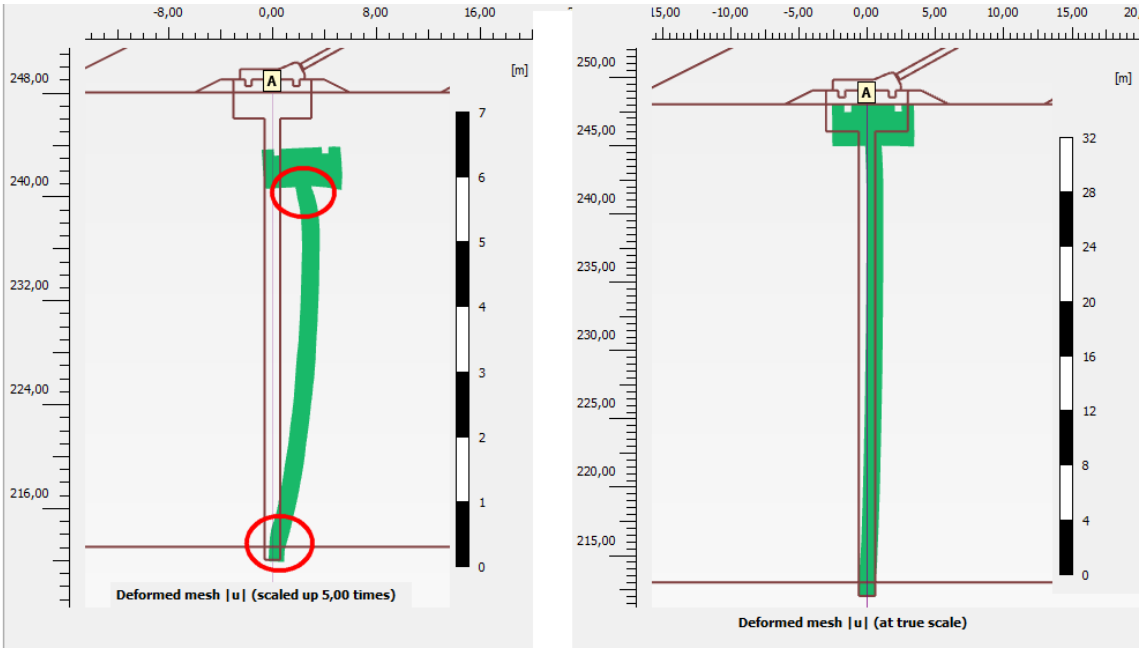


Fig. 5. Deformed mesh of the diaphragm wall at true scale (right) and scaled up 5times(left)

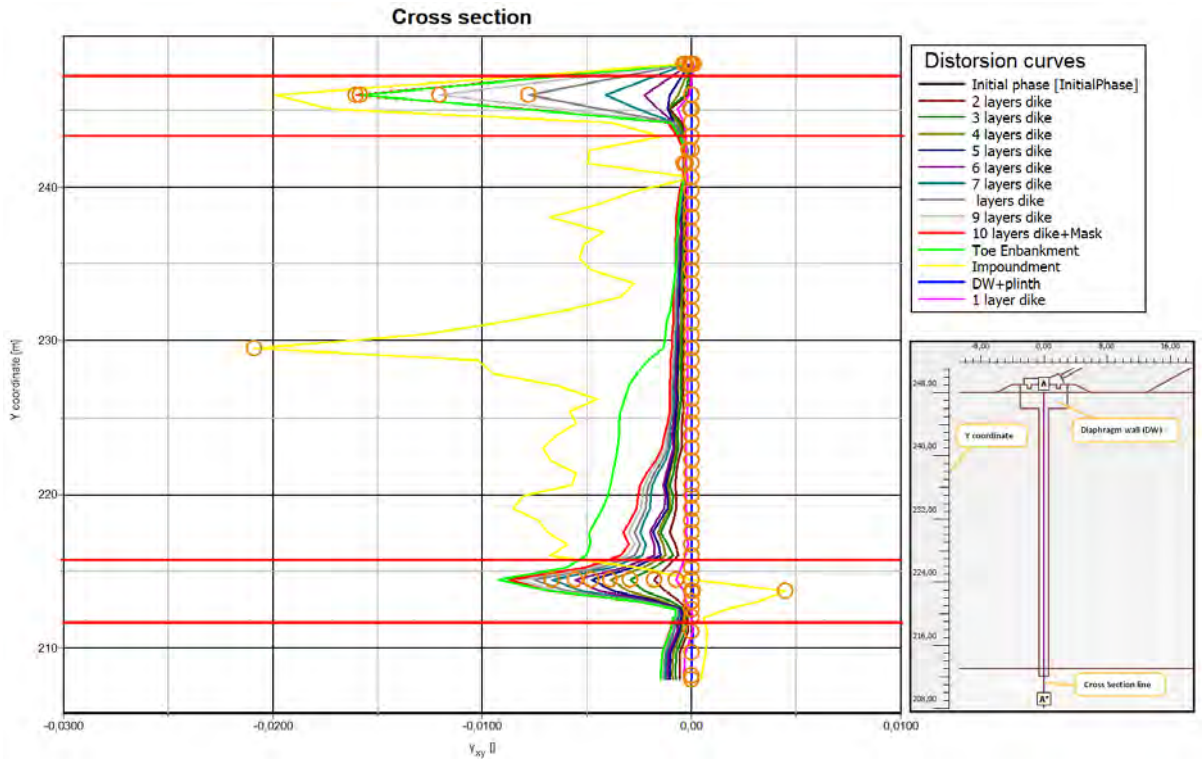


Fig. 6. Distribution of distortions on the body of the diaphragm wall

The change in behaviour of the impoundment curve is not irregular, because the impoundment changes the direction of the displacements in the diaphragm wall: while moving upstream during the dike construction, the diaphragm wall moves downstream during the impoundment. This result is also emphasized in Ouedraogo et al., [1]: "In fact, the hydraulic gradient between the upstream under the load of the reservoir and the almost drained downstream causes the wall to move widely downstream, thus exceeding its original axis". These changes in the displacements' direction explain the changes in the distortions and may be a reason of the impoundment curve's 3rd peak at the middle of the diaphragm wall.

Figures 7 and 8 are plots of the distortions' distribution on the body of the diaphragm wall. Note that only the last two phases are plotted. Figure7 shows the cross sections while Figure 8 shows the distribution on all the diaphragm wall.

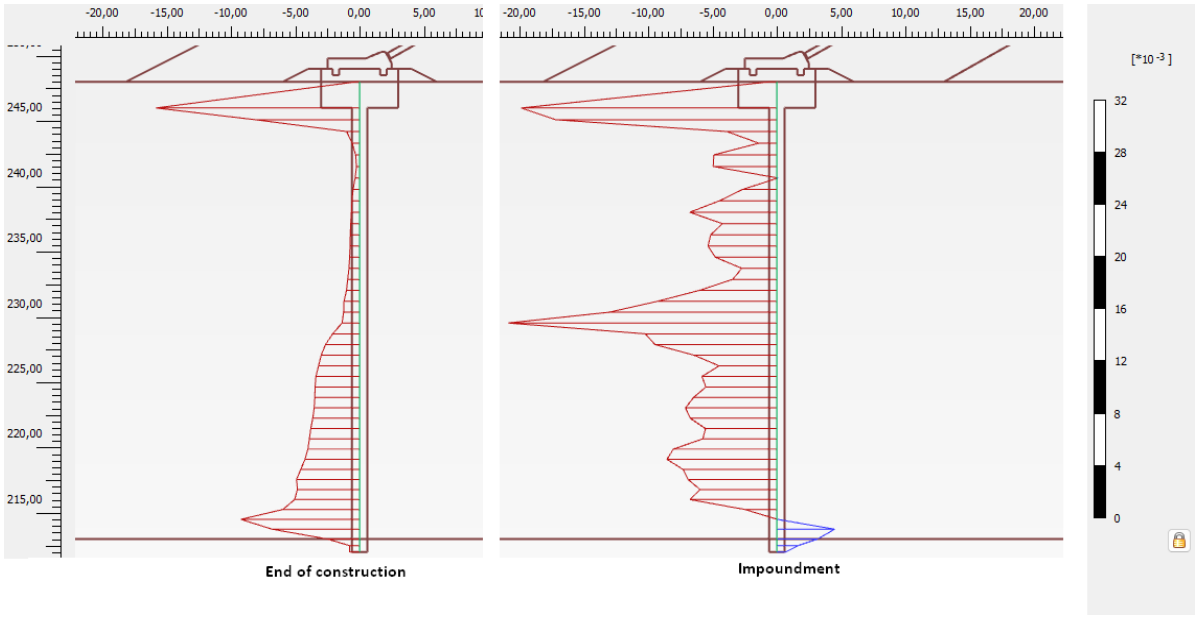


Fig. 7. Distribution of distortions on the body of the diaphragm wall -cross section view-

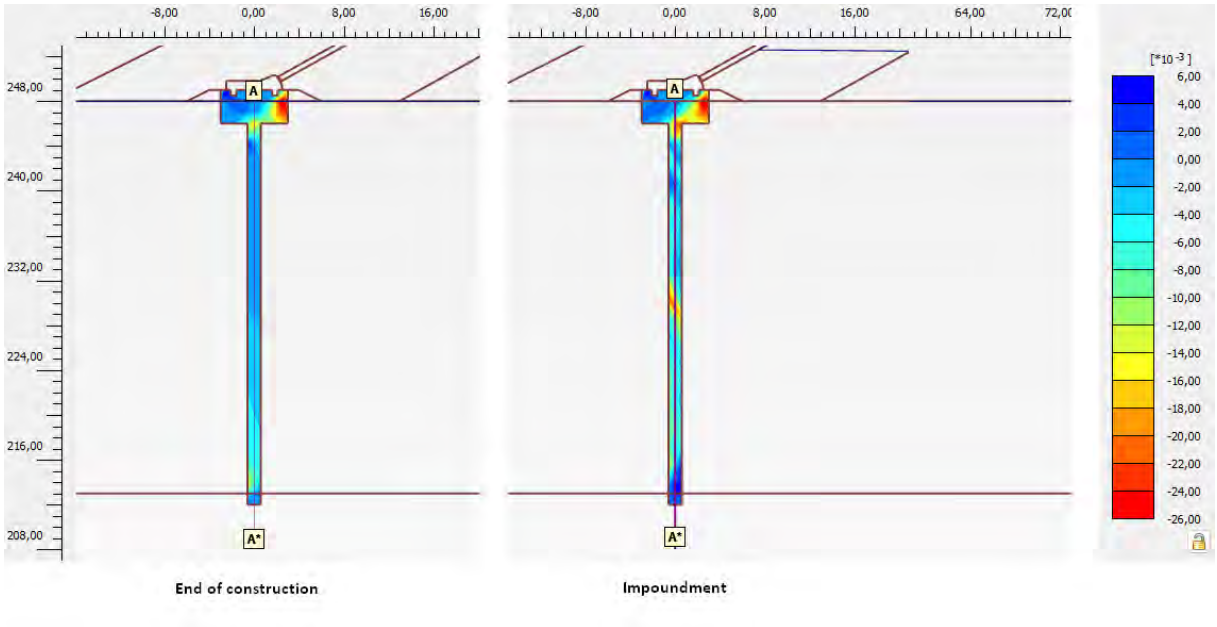


Fig. 8. Distribution of distortions on the body of the diaphragm wall -full chart view-

At this stage of our study, it is assumed that the distribution of displacement causes the diaphragm wall to accumulate strains at its anchoring points. While approaching the bottom point of the diaphragm wall seems difficult at this time of our investigations, here are several effective strategies to tackle the concentration of strains at the junction with the head block and drive meaningful change.

3.2. Effective Approaches to Address the Issue

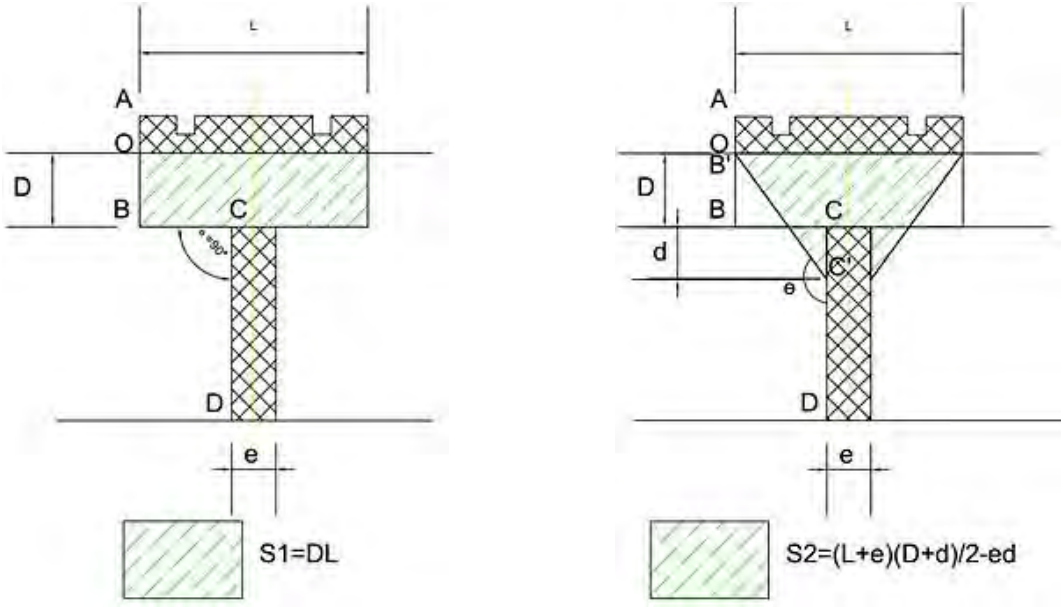
Two distinct yet complementary approaches to the problem mentioned above are provided in the paragraphs that follow.

3.2.1 Through Geometry Improvement

In this approach, we present a design adjustment to the head block. This new design consists in smoothing the junction, in other to avoid sudden break in the thickness of the diaphragm wall as a whole. Indeed, instead of having 90° joint between the head block and the body of the diaphragm wall, we propose to widen this angle.

3.2.1.1 Definition and Mathematical Concepts of The Approach

Referring to figure 9.a, let θ be the angle $\widehat{BCD}$. We assume to refer to θ as the junction angle. Considering points A and O fixed for design constraints (indeed, the area above O is supposed to be the anchor of the plinth), and 90° as the minimum value of θ, the angle θ can be widened by moving point B upward and/or moving C downward. In order to maintain an equal surface of the diaphragm wall, our approach consists in movement B at point B'=O and bringing down point C at C' as indicated on Fig 9. (b)



(a) (b)

Fig. 9. Definition of the junction angle ɵ : (a) ɵ=90°, (b) for any value of ɵ

The surface modification induced by the change in geometry concerns exclusively the surfaces *S1* and *S2*, as illustrated in Figure 9 a and b. Assuming parameters *L, D* and *e* fixed, to have the same surface from fig 9.a to fig 9.b ($S1 = S2$), we have to solve equation (2) for *d* (Note that the reason of the assumption "$S1 = S2$" is given at the end of paragraph 0).

$$D.L = \frac{(L+e).(D+d)}{2} - e.d \tag{2}$$

Where *L, D, e* and *d* are as defined on figure 9. Equation (2) can be simplified by solving for d, resulting in:

$$d(L-e) = D(L-e) \tag{3}$$

In practical applications, the value of $\boldsymbol{L}$ is greater than $\boldsymbol{e}$. Indeed, for CFRD dams' application, $\boldsymbol{e}$ varies from 1 to 2m while $\boldsymbol{L}$ is greater than 5m. Then, equation **(3)** can be divided by $(\boldsymbol{L}-\boldsymbol{e})$ leading to the result bellow:

$$L \gg e \Rightarrow (L-e) > 0 \tag{4}$$

$$(3)\ \&\ (4) \Longrightarrow d = D \tag{5}$$

So, having the same surface requires distance BB' equal to distance CC'. This can be geometrically interpreted as a 180° rotation of triangle OBO' around point O' both sides of the diaphragm wall as shown on Figure 10.

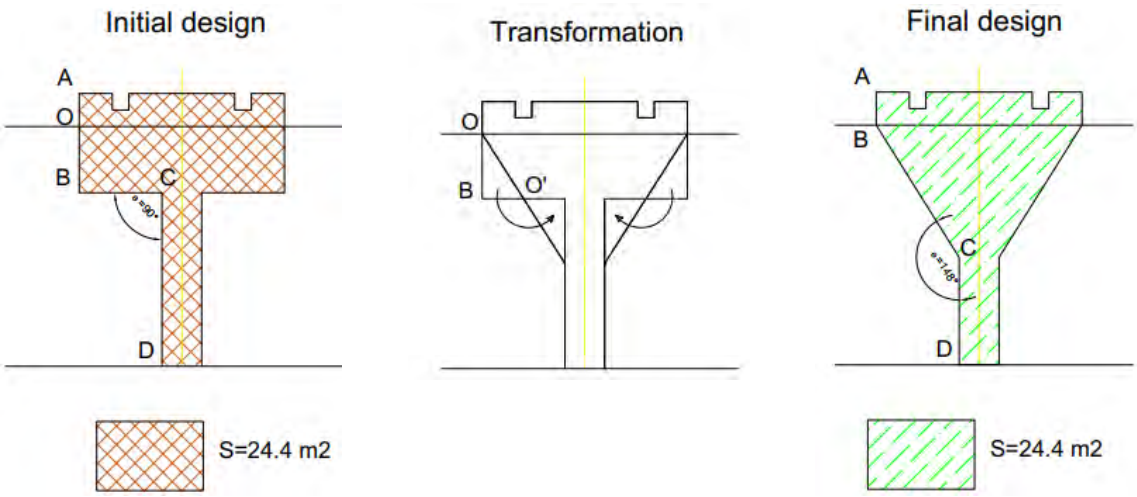


Fig. 10. Geometrical interpretation of the approach

From the results and figures above, a general expression of the junction angle $\boldsymbol{\theta}$ can be established as follows:

$$tan(\pi-\theta)=\frac{\frac{L-e}{2}}{D+d}=\frac{L-e}{2(D+d)} \Leftrightarrow \pi-\theta=atan\left(\frac{L-e}{2(D+d)}\right) \Leftrightarrow \theta=\pi-atan\left(\frac{L-e}{2(D+d)}\right) \quad (6)$$

$$\theta=\pi-atan\left(\frac{L-e}{2(D+d)}\right)$$

In the current study, the numerical values avec the parameters are as follow: $L=6.2m\,;e=1.2\text{m}\,;D=d=2.0\text{m}$. This leads to: $\theta=\pi-\text{atan}\left(\frac{6,2-1,2}{2*4}\right)=\pi-atan(0,625)\simeq 2.58299rad\asymp 148°$

3.2.1.2 Numerical Modelling and Analysis of The Solution

In this section, we are going to show the results of the numerical analysis of the solution described above. For practical raisons, we will focus on the two first and two last phases, meanwhile the diaphragm wall 's construction (Phase_1), the first 8.5m layer of the dike (Phase_2), the last construction phase (end of construction) and the impoundment phase. The analysis will consist in comparing the results of the new geometry (Solution 1) to the initial one studied by OUEDRAOGO et al., [1]. Due to Plaxis software restrictions, the curves have been plotted with excel software. Indeed, Plaxis doesn't allow plotting data from different projects files. So, the results have been copied from Plaxis to excel. Fig. 11 shows the displacements' curves of the initial geometry (Initial) and the solution described above (Solution 1).

Note that the curves with a square point type refer to the solution described above while the ones with cross type refer to the initial design. In a general view, the curves of the two designs have the same behavior. Still, some differences hide behind the details. Indeed, when we take a close look at the curves, some changes appear around the junction between the head block and the body of the diaphragm wall. For visual reasons, we have plotted only the two last phases around the junction on Figure 12.

As it can be seen on Figure 12, the curves' variation rate changes differently around the junction:

- End of construction phase: as for this phase, we note that the initial design's curve presents a sudden increase around Y=245m (remember that the junction is at Y=246m), while the Solution 1 design barely changes its behavior.
- Impoundment phase: although the two curves start decreasing the junction, each curve does it in a different way. Indeed, as shown on Figure12 ant Table 3, Solution 1 curve decreases

0,71% while Initial curve decrease 2,22%. The decrease of the two curves may seem tiny in terms of length, but seen from the rate perspective, Initial curve decreases 3 time faster than Solution 1 one. This result is particularly interesting given that these changes happen around the junction point.

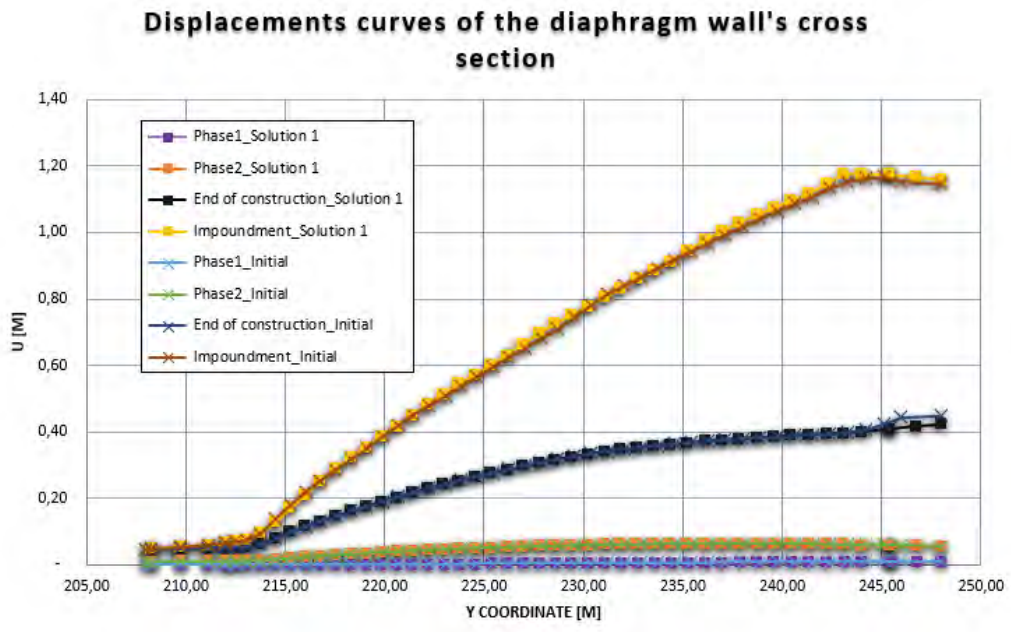


Fig. 11. Comparative curves of the displacements at the cross section of the diaphragm wall

Table 3. Variation rate of Initial and Solution 1 curves around the junction.

	$Y1$ (m)	$Y2$ (m)	ΔY (m)	$U1$ (m)	$U2$ (m)	ΔU (m)	$\frac{\Delta U}{\Delta Y}$ (%)
Initial	245.1	246.0	0.90	1.17	1.15	0.02	2.22
Solution 1	244.0	245.4	1.40	1,18	1,17	0.01	0.71

Note: $\Delta Y = Y2 - Y1$ and $\Delta U = U2 - U1$

These observations will help us to explain what happens in terms of distortion. Indeed, as we did with the displacements, we have plotted bellow the distortions' curves of the two designs (Initial and Solution 1) from the two last phases. Fig 13 shows the strains' (distortions') curves of the initial geometry (Initial) and the solution described above (Solution 1). The red circles and lines on the graph of Figure 13 emphasizes the distortions' peak areas on the diaphragm wall.

This graph shows that the peak at the junction point with the head block has been cleared in the Solution 1 design. Indeed, while the initial geometry's curves show a peak around Y=244m and Y=247m, the curves of Solution 1 show almost no change between the body of the diaphragm wall and the head block. Thus, smoothing the junction angle is an effective strategy to prevent distortion at the connection between the head block and the diaphragm wall's body. This proactive approach safeguards structural integrity for long-lasting performance.

By the way, this solution miraculously eliminates the peak at the middle of the diaphragm wall. Indeed, as we can see on Figure 13, the peak at the middle of the diaphragm wall is mitigated (from 2.1% to only 0.45%). However, it is essential to highlight that the impoundment curve's first peak at the junction with the bedrock has slightly increased (from 0,45% to 0,85%). Anyway, the new design's distortions never reach 1.0% (they vary from -0,95% to 0,85%) while the initial ones reach -2.1%.

- Figures 14 and 15 are plots of the distortions' distribution on the body of the diaphragm wall modeled with the smoothed junction angle's geometry for the last two phases. Figure14 shows the cross sections while Figure 15 shows the distribution on all the

diaphragm wall. Fig 15 shows a grouped view of the two geometries results. If $\theta < 148°$ then $S1 > S2$: this is a cheaper variant of our design (Solution 1), but is also less efficient,

- If $\theta = 148°$ then $S1 = S2$, corresponding to our design (Solution 1), described and analysed above,
- If $\theta > 148°$ then $S1 < S2$: in this case, the solution is more efficient but also more expensive.

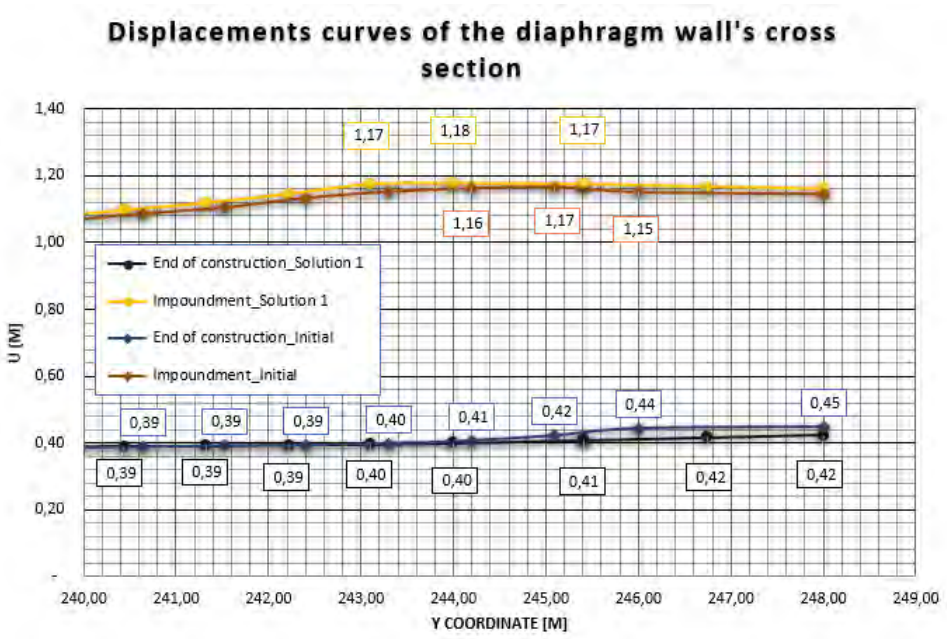


Fig. 12. Focus on last phases curves of the displacements

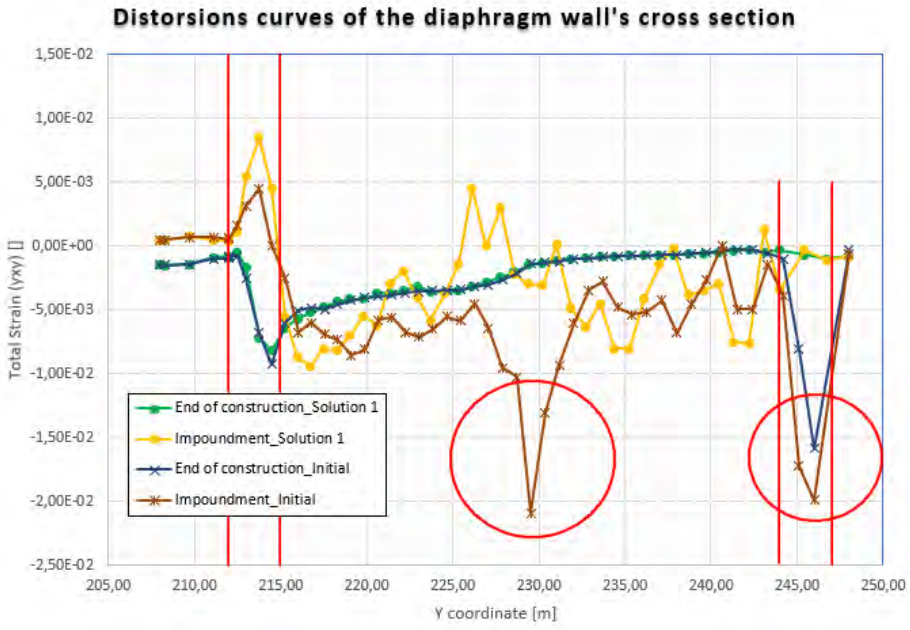


Fig. 13. Focus on last phases curves of the displacements

Now that our solution has proven itself, it is appropriate to clarify some assumptions that guided our approach. Specifically, when defining the junction angle, we assumed that surfaces S1 and S2, as depicted in Figure 9 a and b, should be equal. This assumption was not made randomly. Indeed, the amount of concrete required for this section of the plinth is determined by multiplying this surface area by the length of the plinth in the bank-to-bank direction. So, having these surfaces equal therefore ensures equality of cost between the two designs.

Furthermore, it is possible to evaluate the junction angle in terms of both cost-effectiveness and overall performance:

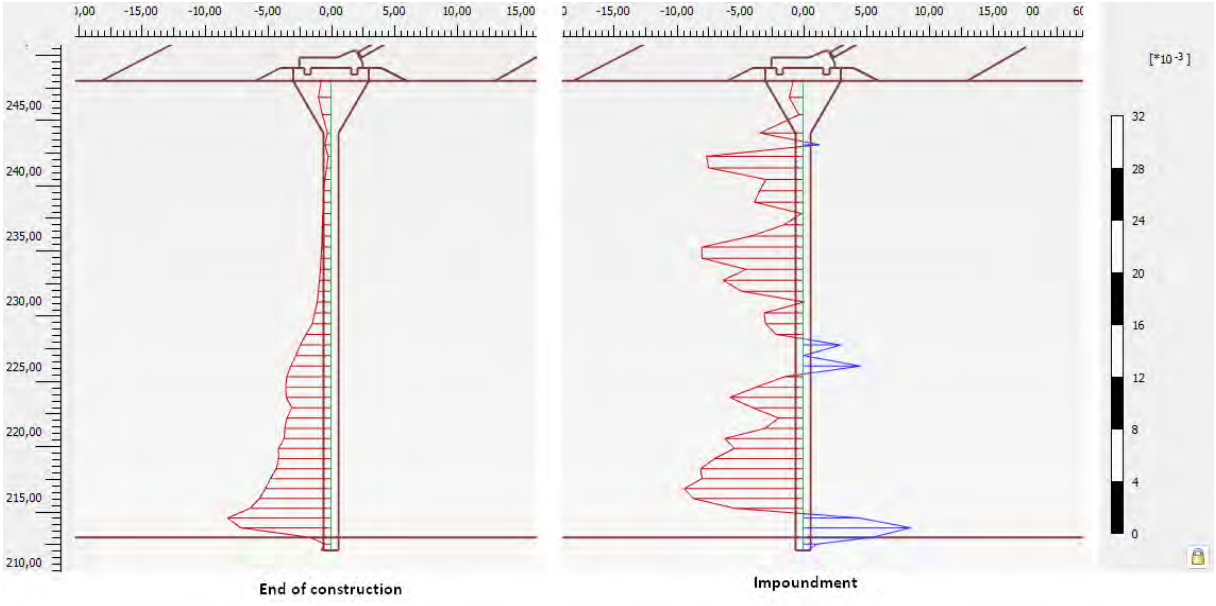


Fig. 14. Cross section view of the distortions' distribution on the body of the diaphragm wall - improved geometry-

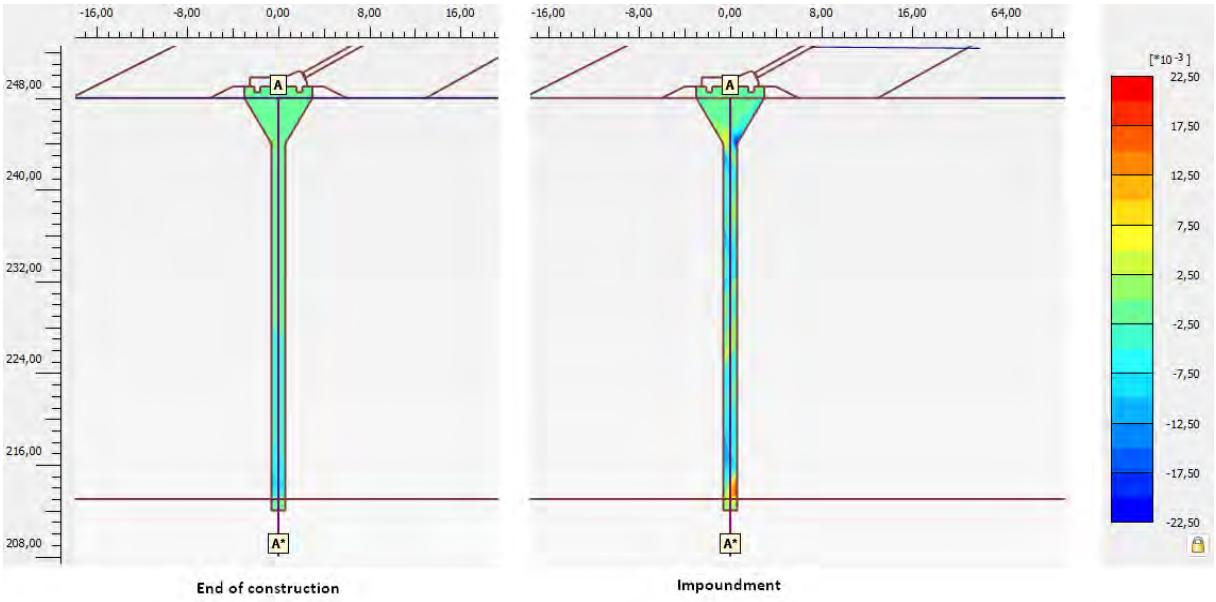


Fig. 15. Distribution of distortions on the body of the diaphragm wall -full chart view-

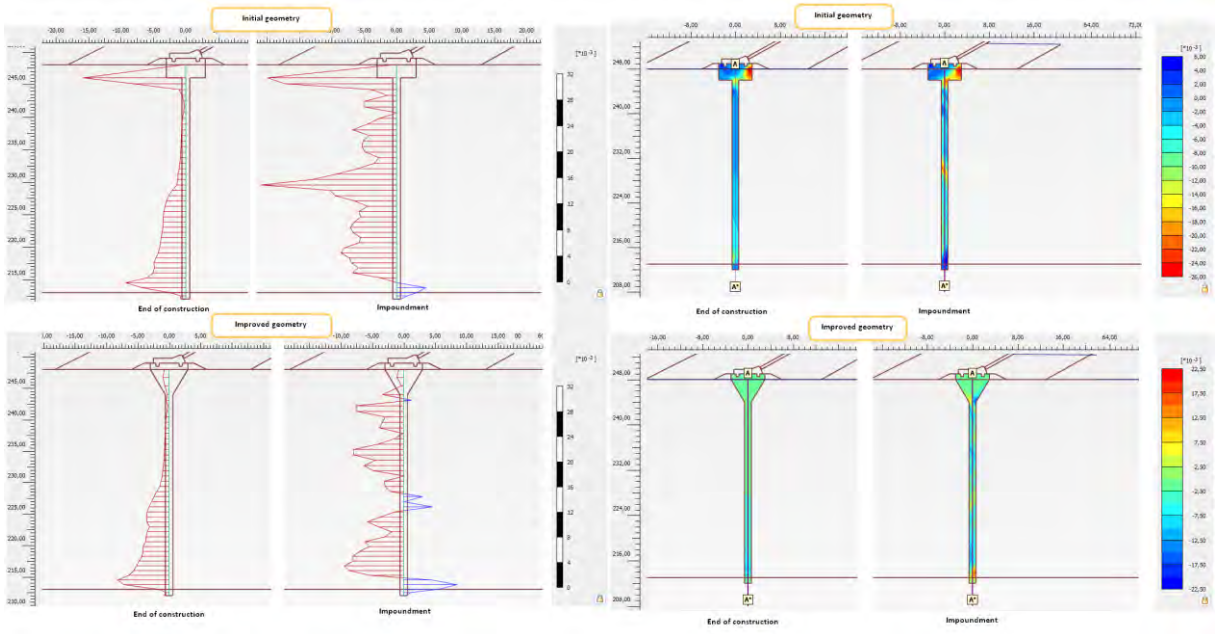


Fig. 16. Comparative views of initial and solution 1 ‘s distortions’ cross sections and cart

3.2.2 Through Planning the Dike Construction

This paragraph analyses a simple attempt to reduce the accumulation of deformations at the junction point by gradually charging the diaphragm wall. Indeed, as we are going the show, the peaks of distortions can be mitigated by planning strategically the dike’s construction.

To demonstrate that, we will compare the distortions field of two different ways of constructing the dike. For instance, it is necessary to present these ways of construction.

3.2.2.1 Geometrical Concept

The classic way consists in constructing the dike by full horizontal layers form upstream to downstream. Our approach consists in starting the dike’s construction at a certain distance from the diaphragm wall. This, to let the soil layer reorganize at a sufficient distance from the diaphragm wall in order to affect its body smoothly from the bottom to the head. For this application, we have chosen to begin the dike 10m far from the diaphragm wall for the first 4 layers of the dike.

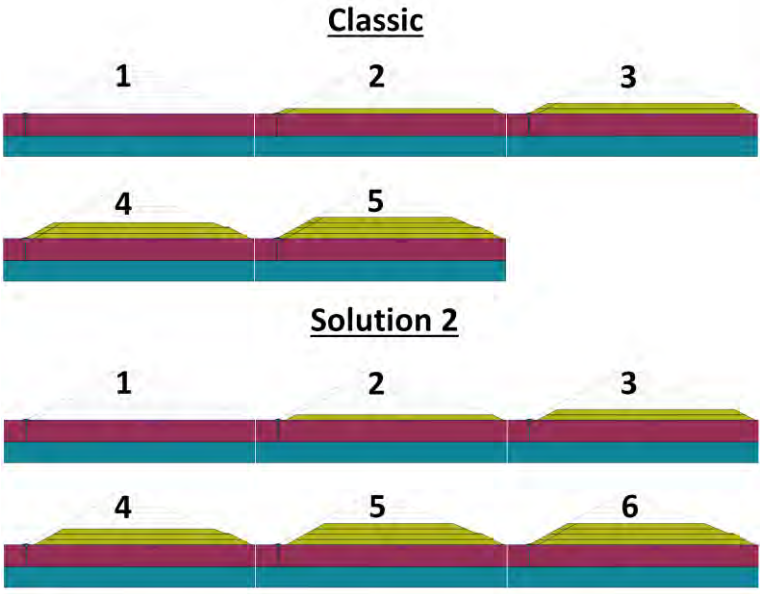


Fig. 17. Presentation of the two ways of the dike’s construction

Figure 17 shows the process of the dike's construction in the two ways. "Classic" is the way usually applied to construct dikes while "Solution 2" refers to our approach. Note that the figure only shows the first 4 layers of the dike. The next steps of the construction are the same, with each layer constructed as a whole. In the following, these two solutions are numerically simulated, and their results compared.

3.2.2.2 Analysis, Results, And Discussion Around the Two Planning's

This section focuses on the comparison of the distortions field of the two solutions. This comparison makes it possible to observe the reduction of distortions at the diaphragm wall's critical points. To focus on the principal results, we are going to show in the one hand the maximum displacements of the diaphragm wall in the two cases, and in the other hand, their distortions.

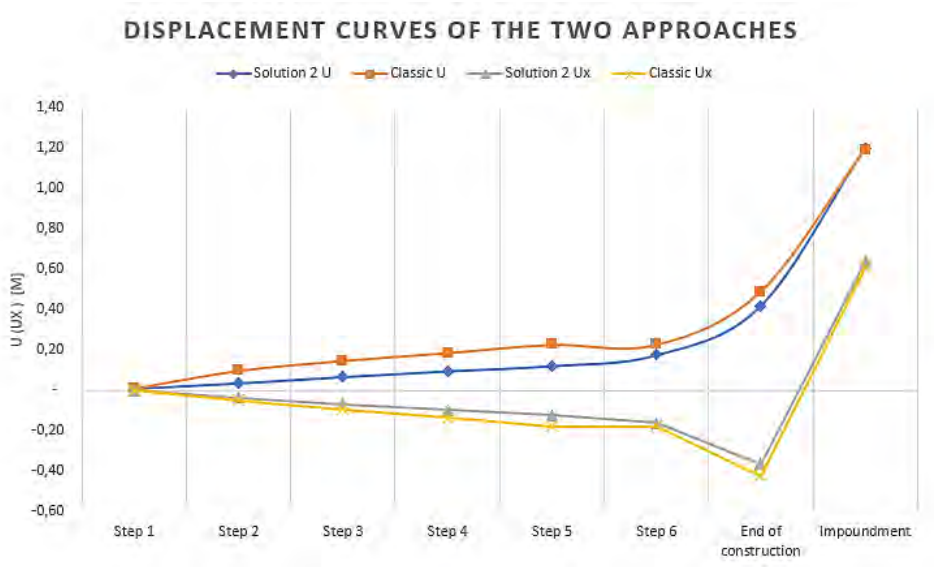


Fig. 18. Maximum displacements in the diaphragm wall U is the total displacement while Ux is the horizontal displacement

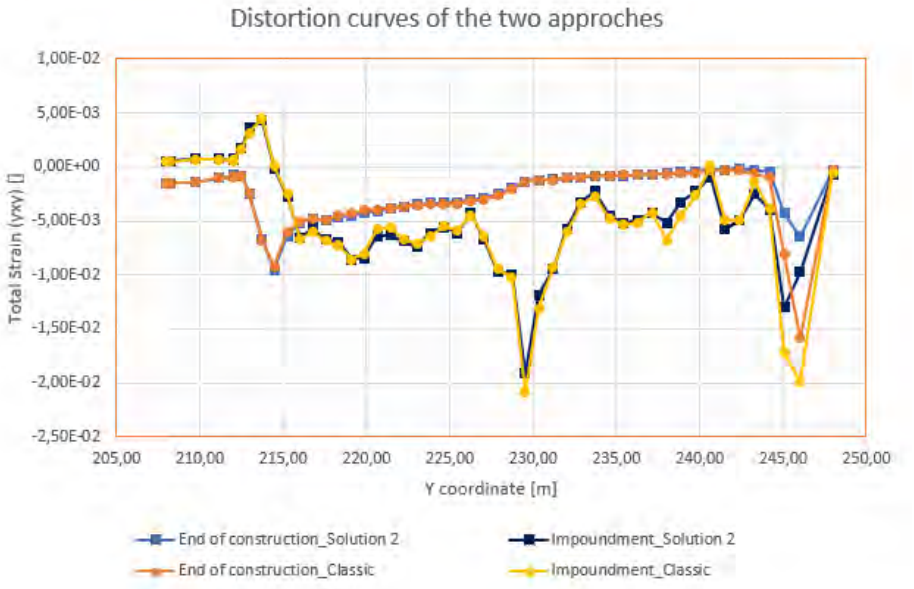


Fig. 19. Cross section of the diaphragm wall showing the distortions curves of the approaches

Figure 18 shows the maximum displacement curves of each approach. Note that Step 1 to 6 are as depicted on Figure 17. As it is easy to notice, the displacements curves of the Solution 2 approach are under the one of the Classic approaches for all the steps instead of impoundment. Meanwhile, during the dike's construction, the diaphragm wall is more deformed in the Classic process than in

The Solution 2 process. Note that this result is true for maximum displacement (U) and horizontal maximum displacement (Ux). Ux is negative because the diaphragm wall displaces upstream [1]. Nevertheless, the displacements are the same in the two approaches for the impoundment step. This is not a random outcome: in fact, it is the same state of constraints in the dam just before impoundment for the two cases. Coming now to the distortions, the results show that proceeding by Solution 2 process can help reduce the amount of the strains at the peaks. Fig 19 shows a comparative view of distortion curves of the two approaches. As we did in previous analysis, focus is made on the last phases: end of construction and impoundment.

According to the results shown on Figure 19, the distortions along the body of the diaphragm wall are almost the same for the two approaches, except some rare differences. Indeed, the curves related to the end of construction stage are nearly identical for the two approaches: the peaks happen at the same points and the values otherwhere are practically the same.

However, the values at the peaks make the difference. Solution 2 curves' peaks' values are less high than Classic ones. Indeed, when having a close glance to the peaks of the curves, we come to see that they (the peaks) are reduced from the top to the bottom of the diaphragm wall:

- Top peak : the peak at the head block junction is reduced more than a half at the end of construction in Solution 2 approach compared to it's value in Classic approch. Impoundment curves show a similar result, with the value reduced from a third;
- Middle peak : the peak occuring after the dam impoundment at the middle of the diaphragm wall remain on the two approaches. Anyway, we note a slight decrease from classic to solution 2 curves. No peak happens during the construction phase at the middle of the diapgragm wall;
- Bottom peak : finally, the peak at the bedrock junction of the diaphragm wall remain unchanged in the two approches, with nealy no anhancement.

These results show that starting the dam embankment at a certain distance from the diaphragm wall is a simple way to enhance its integrity by reducing both displacements and distortions. The results also show that the reduction of distortions is more pronounced at the top of the diaphragm wall and decreases from top to bottom. This effect may be due to the distance from which de embankment is started. While the current study shows the effect for 10m far from the diaphragm wall, starting at a longer distance may lead to more interesting results.

4. Conclusion

Based on numerical simulation, a diaphragm wall set upstream a high dam has been studied in this paper. The paper tackles a structural integrity issue highlighted by a recent similar study result. Indeed, in his 2025 study, OUEDRAOGO has raised the problem of concentrating distortions at critical points of soft diaphragm walls set on thick alluvium layers. The study consisted of investigating about that issue.

It comes out from the study that the concentration of distortions at the junction points (reaching 2%) is real and harmful to the diaphragm wall's long-lasting performances. Then, this paper proposed two effective ways to deal with the issue. Indeed, in the one hand, the paper proposes to smooth the junction angle between the head block and the body of the diaphragm wall. This simple and costless measure has proven significant results, helping to eliminate the distortions' concentrations at the upper junction point. The final distortion at the junction is only 0,1%. Plus, it helps in reducing another distortion peak that happens at the middle of the diaphragm wall, from 2,1% to 0,45%.

In the other hand, the paper demonstrates that strategically planning the dike construction is an effective way to deal with the same issue. Indeed, by starting the dike's construction far from the diaphragm wall, it is proved that the concentration of distortions around the junction point is mitigated. Although this trick helps to mitigate the concentration of strains during the construction stage, the impoundment phase requires a smooth junction point to avoid peaks on that junction and elsewhere on the diaphragm wall.

In sum, combining both solutions are highly recommended to effectively enhance the structural integrity of the diaphragm wall and ensure its durability for the long term. This integrated approach not only strengthens performance but also instills confidence in the diaphragm wall's longevity. Still, the anchoring point with the bedrock deserves to be investigated. The two solutions investigated above are yet incapable of reducing the concentration of distortions at this lower junction point.

Acknowledgement

I would like to thank Pr Latifa Ouadif for her indefectible help and comprehensiveness which lead to the realization of this work. I also thank Pr Anas Bahi for all the support he provides to me for my work. Finally, many thanks to everyone who helped me achieve this paper. A special thought to my wife and Dr Eddie Nébié.

References

[1] Oudraogo I, Ouadif L, Bahi A. Diaphragm wall behaviour under thick alluvium layer conditions. Civil Environ Eng. 2025;21(1):CEE_072524. https://doi.org/10.2478/cee-2025-0005
[2] Zhang J, Li M, Ke L, Yi J. Distributions of lateral earth pressure behind rock-socketed circular diaphragm walls considering radial deflection. 2022; 104604. https://doi.org/10.1016/j.compgeo.2021.104604
[3] He W, Luo C, Cui J, Zhang J. An axisymmetric BNEF method of circular excavations taking into account soil-structure interactions. 2017; 90:155-163 https://doi.org/10.1016/j.compgeo.2017.06.001
[4] Shao Y, Chen C, Lu Z, Zheng Y, Zhang Y. An intelligent leakage detection method for diaphragm wall joints based on fiber Bragg grating sensors and intelligent algorithms. 2022; 197; 111339. https://doi.org/10.1016/j.measurement.2022.111339
[5] Sari M, Seren A, Alemdag S. Determination of geological structures by geophysical and geotechnical techniques in Kirklartepe dam site (Turkey). 2020. https://doi.org/10.1016/j.jappgeo.2020.104174
[6] Boettinger JL. Alluvium and alluvial soils.Encyclopedia of Soils in the Environment. 2005; 45-49. https://doi.org/10.1016/B0-12-348530-4/00008-4
[7] DeJong JT, Sturm AP, Ghafghazi M. Characterization of gravelly alluvium.Soil Dynamics and Earthquake Engineering. 2016; 91:104-115. https://doi.org/10.1016/j.soildyn.2016.09.032
[8] Ignat R, Baker S, Larsson S, Liedberg S. Two and three-dimensional analyses of excavation support with rows of dry deep mixing columns. Computers and Geotechnics. 2015; 66: 16-302015. https://doi.org/10.1016/j.compgeo.2015.01.011
[9] CIGB-ICOLD. Bulletin 141: Concrete face rockfill dam: concepts for design and construction. 2010.
[10] CIGB-ICOLD. Bulletin 51: Matériaux de remplissage pour coupures étanches = Filling materials for watertight cut off walls. 1985.
[11] Aung AY, Kamchoom V, Aye ZZ. Diaphragm wall lateral movement in deep excavations in Bangkok clays: impacts and influencing factors. Can Geotech J. 2024.
[12] CIGB-ICOLD. Bulletin 150: Cutoffs for dams. CRC Press 2018. https://doi.org/10.1201/9781351035989
[13] CFBR. Recommandations pour la justification des barrages et des digues en remblai = Guidelines for the justification of embankment dams and levees. 2015.
[14] Mohamed B, Bahi L, Ouadif L, Bahi A, Sabihi A. Determination of vibro-compaction parameters by making a test board in a port site in Morocco. Civil Environ Eng. 2023;19(1):328-38. doi:10.2478/cee-2023-0029. https://doi.org/10.2478/cee-2023-0029
[15] Hanh DK, Truong DD, Bui KT. Application of numerical modeling and GIS for simulating inundation under dam failure scenarios. Civil Environ Eng. 2024;20(1):233-54. https://doi.org/10.2478/cee-2024-0019
[16] Berkat B, Akhssas A, Ouadif L, Bahi A. Assessment of liquefaction potential by comparing semi-empirical methods based on the CPT test. Civil Environ Eng. 2024;20(1):164-79. https://doi.org/10.2478/cee-2024-0014
[17] Hruban K. Methods of foundation engineering. Chapter 10. 1979.
[18] Souileh A, Mabrouk A, Ouadif L, El Hachmi D. Analysis of the geotechnical and mineralogical characteristics of the Settat-Khouribga shale clay for potential civil engineering applications. Res Eng Struct Mater. 2024;10(4):1699-716. https://doi.org/10.17515/resm2024.408ma0824rs
[19] Souileh A, Mabrouk A, Ouadif L, El Hachmi D, Chrachmy M, Benhaddou K. Building earthquake resilience with clay shale: pioneering sustainable concrete solutions with ecofriendly materials. Res Eng Struct Mater. 2024;10(4):1717-31. https://doi.org/10.17515/resm2024.479ea1007rs

Blank Page

Research on Engineering Structures & Materials
www.jresm.org

Research Article

Experimental evaluation on the durability characteristics of ternary blended concrete with ground granulated blast furnace slag and hydrated lime exposed to harsh environmental conditions

E. Dhanesh [a], M. Shanmugasundaram [*,b]

School of Civil Engineering, Vellore Institute of Technology, Chennai Campus, Tamil Nadu, India

Article Info

Article History:

Received 16 July 2025

Accepted 31 Aug 2025

Keywords:

Hydrated lime;
Ternary concrete mixes;
Slag;
Durability properties

Abstract

This study investigates the durability characteristics of ternary blended concrete prepared by partially substituting Ordinary Portland Cement (OPC) with Ground Granulated Blast Furnace Slag (GGBS) and Hydrated Lime (HL). Fifteen different mix combinations were developed by varying GGBS from 10% to 70% and HL from 10% to 20%, with a fixed water-to-binder ratio of 0.36. Durability characteristics of the ternary concrete mixes were evaluated using water absorption, permeability, rapid chloride penetration, acid resistance, and sulphate resistance tests. Among the fifteen designed mix proportions, the C40G50L10 blend (40% OPC, 50% GGBS, 10% HL) consistently produced superior durability characteristics. It achieved a 41% and 44% reduction in water absorption at 56 and 84 days, respectively, and a 47.4% and 40.2% decrease in water permeability compared to the control mix with 100% OPC. Chloride ion penetration was significantly reduced in the C40G50L10 mix, showing 428 and 386 coulombs at 56 and 84 days, reflecting a reduction of 58.3% and 55.2%, respectively. Furthermore, this mix also exhibited the least compressive strength reduction and weight loss under acid, sulphate, and chloride exposure, highlighting its resistance to chemical attack. Conversely, mixes with high GGBS (70%) and HL (20%) combined with low OPC (10%), such as C10G70L20, showed the highest deterioration, primarily due to inadequate matrix cohesion and increased porosity. The experimental findings demonstrate that optimizing OPC with GGBS and HL, particularly at a 40:50:10 ratio, produces concrete with enhanced durability characteristics, ideal for applications in chloride-heavy marine structures, sulphate-rich soil conditions, and acidic industrial environments exposed to aggressive conditions.

© 2025 MIM Research Group. All rights reserved.

1. Introduction

Concrete ranks as the second most consumed material globally after water, with an estimated annual production of nearly six billion tonnes, highlighting its widespread use in the construction industry [1]. Seeking to strike a balance between the growing needs of the construction industry and environmental sustainability is a big challenge to meet the demand for raw materials required for concrete and mortar [2]. Despite its widespread application, producing Ordinary Portland Cement (OPC), the key binding ingredient in concrete, is a primary source of anthropogenic carbon dioxide emissions, contributing approximately 7–8% of global carbon dioxide output [3]. Moreover, OPC manufacturing is energy-intensive and relies heavily on non-renewable raw materials. It is approximated that the production of one ton of cement results in the emission of about 0.8 to 0.9 tons of carbon dioxide into the atmosphere [4,5]. Given the growing environmental

*Corresponding author: shanmuga.sundaram@vit.ac.in
[a]orcid.org/0000-0002-1413-8495; [b]orcid.org/0000-0002-1387-7915
DOI: http://dx.doi.org/10.17515/resm2025-1033me0716rs

challenges, it is essential to explore alternative supplementary cementitious binders that offer similar mechanical performance and durability to conventional cement while reducing their ecological footprint [6]. In an effort to mitigate environmental impacts, numerous researchers have explored the incorporation of industrial by-products and waste materials like fly ash (FA) [7], ground granulated blast furnace slag (GGBS) [8], coal bottom ash (BA) [9], rice husk ash (RHA) [10], metakaolin (MK) [11], red mud (RM) [12], cement kiln dust (CKD) [13], waste glass powder (WGP) [14], silica fume (SF) [15], and sugarcane bagasse ash (SBA) [16] as alternative cementitious components for the development of environmentally sustainable concrete.

Due to its built-in hydraulic characteristics and proven pozzolanic behavior, GGBS has been extensively utilized as an alternative cementitious component in concrete production [17]. Its incorporation enhances the levels of alumina and silica within the mix, which in turn supports early-age strength development [18]. When used as a partial replacement for OPC, GGBS contributes to the formation of calcium-alumino-silicate-hydrate (C-A-S-H) gel, thereby improving the mechanical performance and durability of the composite [19]. This substitution leads to the formation of calcium aluminate or calcium sulfoaluminate phases [20], offering notable benefits such as reduced carbon emissions, enhanced compressive strength, improved resistance to tensile cracking, and decreased permeability and porosity through a refined microstructure [21,23].

Hydrated lime, typically available as a white powder or colorless crystalline substance, is produced by reacting quicklime with water. It has been observed that limestone-based fillers, such as hydrated lime, can improve both the mechanical strength and durability of concrete by refining the pore structure and enhancing compactness [24,25]. When introduced into OPC-GGBS systems, hydrated lime can enhance the pozzolanic reaction by supplying additional calcium hydroxide, promoting the formation of more calcium silicate hydrate (C–S–H) gels, and thereby improving the mechanical and microstructural performance of the composite [26].

Recent studies have highlighted the potential integration between HL and GGBS-based systems. For example, Ahmed [27] demonstrated that lime-slag limecrete mixes achieved compressive strengths above 25 MPa when optimally proportioned, indicating their feasibility as sustainable structural materials. Similarly, Bayat and Kashani [28] showed that incorporating HL with silica fume improved cohesiveness and rheological properties of cementitious mortars, supporting its role in advanced applications such as 3D printing. Shamseldeen and Dawood [29] further confirmed that partial replacement of cement with industrial by-products, including lime-based additives, enhances long-term strength and reduces carbon emissions by over 35%. In addition to these findings, our earlier study examined OPC–GGBS–HL ternary systems, where HL was shown to enhance workability, compressive strength, and microstructural performance by refining pore structure and promoting secondary gel formation [30]. While these outcomes confirmed the performance-enhancing role of HL, the focus remained on fresh, mechanical, and microstructural properties, with durability aspects receiving limited attention.

Previous investigations have also reported that durability improvements in blended concretes are most effective when GGBS replacement lies within the range of 40–70% of OPC, because of the enhanced pozzolanic activity and pore structure refinement [27, 28]. Similarly, HL additions above 20% resulted in excessive calcium hydroxide formation and increased porosity, whereas moderate HL levels of around 10% consistently improved performance in OPC–GGBS–HL systems [30]. Based on these important findings, the present study adopted substitution ranges of 10–70% GGBS and 10–20% HL to systematically evaluate both lower and higher replacement levels and identify the optimum blend for durability performance. Therefore, the present study investigates the feasibility of using HL as a partial binder replacement in ternary systems with OPC and GGBS, with a specific focus on durability. The study also aims to determine the optimum HL substitution level that can produce a durable and sustainable concrete matrix.

2. Experimental Program

2.1. Materials Used in the Study

This section presents a comprehensive overview of the physical and chemical properties of the raw materials used in formulating the ternary blended concrete, which includes OPC, GGBS, and HL. The OPC utilized in this study complies with IS: 269-2015 (Reaffirmed in 2020) specifications and is categorized as OPC 53 grade. GGBS used in the study was sourced from JSW Cements, Chennai, and HL was supplied by Astraa Chemicals, Chennai. To determine the chemical composition of the binder materials, X-ray fluorescence (XRF) analysis was performed, and the resulting oxide compositions are presented in Table 1. The XRF analysis revealed that the dominant oxides in GGBS were SiO_2 (34.60%), CaO (35.90%), and Al_2O_3 (20.42%). OPC was primarily composed of 60.31% CaO and 21.79% SiO2. In the case of HL, CaO was observed to be the primary component (69.82%), followed by very minor constituents, including Al_2O_3 and SiO_2.

Table 1. Physical and chemical characteristics of the binders employed in the study [30]

Oxide composition (%)	OPC	GGBS	HL
SiO_2	21.79	34.60	0.19
CaO	60.31	35.90	69.82
Al_2O_3	6.70	20.42	0.13
Fe_2O_3	3.80	0.64	0.15
MgO	1.72	6.01	0.52
SO_3	2.51	0.31	0.01
Na_2O	0.387	0.471	-
K_2O	0.42	0.491	0.03
Specific gravity	3.145	2.89	2.21
Color	Grey	Off white	White
Fineness (m^2/kg)	2.92	364	480

As per the specifications outlined in IS 383:2016, the fine aggregate used in this investigation was Manufactured Sand (M-Sand) with particle sizes passing through a 1.18 mm sieve, conforming to Zone II grading. The specific gravity of the fine aggregate was determined to be 2.63. The coarse aggregates, consisting of crushed stones procured from a local source, also adhered to the IS 383:2016 standards. The coarse aggregate blend included 20 mm and 12 mm nominal sizes, combined in 52% and 48% proportions, respectively.

2.2. Mix Proportion and Specimen Preparation

This study developed fifteen concrete mix designs, including a reference mix prepared by IS: 10262 guidelines [31]. The primary objective was to examine how varying levels of OPC replacement with GGBS (ranging from 10% to 70%) and HL (ranging from 10% to 20%) influenced key durability properties of ternary blended cement concrete mixes. All mixes were designed using M35 grade concrete, incorporating OPC of 53-grade. Notably, the authors previously investigated the same set of fifteen mix proportions to evaluate their workability, mechanical, and microstructural characteristics [30]. In continuation of that work, the present study focuses on assessing the durability performance of these established mixes. Although GGBS and HL generally increase water demand due to their physical and chemical characteristics, a constant water-to-binder ratio of 0.36 was maintained across all mixtures. To ensure adequate workability and retention time, a superplasticizer (Auromix 400) supplied by Fosroc Chemicals Private Limited was used uniformly at a dosage of 0.5% by weight of the binder. For all mixes, the quantities of binder, coarse aggregates, fine aggregates, and water were kept consistent at 400 kg/m^3, 1140 kg/m^3, 855 kg/m^3, and 144 kg/m^3, respectively, as presented in Table 2. The mix nomenclature follows the format CxGyLz, where C, G, and L represent the percentage contributions of OPC, GGBS, and HL, respectively (e.g., C40G50L10 denotes 40% OPC, 50% GGBS, and 10% HL).

Table 2. Mix proportion details for the ternary blended cement concrete mixes [30]

SI. No	Mix ID	OPC (kg/m³)	GGBS (kg/m³)	HL (kg/m³)	OPC (%)	GGBS (%)	HL (%)
1	C100	400	0	0	100	0	0
2	C80G10L10	320	40	40	80	10	10
3	C70G10L20	280	40	80	70	10	20
4	C70G20L20	280	80	40	70	20	10
5	C60G20L20	240	80	80	60	20	20
6	C60G30L10	240	120	40	60	30	10
7	C50G30L20	200	120	80	50	30	20
8	C50G40L10	160	200	40	50	40	10
9	C40G40L20	160	160	80	40	40	20
10	C40G50L10	160	200	40	40	50	10
11	C30G50L20	120	200	80	30	50	20
12	C30G60L10	120	240	40	30	60	10
13	C20G60L20	80	240	80	20	60	20
14	C20G70L10	80	280	40	20	70	10
15	C10G70L20	40	280	80	10	70	20

2.3. Testing Methods

To evaluate the durability performance of fifteen ternary concrete mixes, including a control mix, standard tests were conducted to assess resistance against deterioration mechanisms such as water penetration, water absorption, chemical attack, and chloride ion penetration. Water absorption was measured per ASTM C642 by comparing the weight of oven-dried concrete specimens before and after 24-hour water immersion, indicating the internal porosity. Water penetration was assessed as per DIN 1048 (Part 5), where concrete cubes were subjected to a water pressure of 5 bar for 72 hours, and the depth of water penetration was measured upon splitting the specimens. Chloride ion penetration was evaluated through the Rapid Chloride Penetration Test, following ASTM C1202, using cylindrical specimens exposed to a 60V DC for 6 hours across sodium chloride and sodium hydroxide solutions, with the total charge passed recorded to assess permeability.



Fig. 1. Effect Experimental test setup: (a) Water absorption test, (b) Rapid chloride penetration test, (c) Water penetration test, and (d) Acid and sulphate solution preparation

Acid resistance was tested by immersing standard-cured cubes in a 5% sulphuric acid solution, with mass and compressive strength losses monitored at 56 and 84 days. Sulphate resistance was similarly examined by submerging the specimens in a 5% sodium sulphate solution, with periodic solution replacement and stirring to prevent sedimentation, followed by strength and weight assessments at the same intervals. Finally, chloride resistance was assessed by immersing specimens in a 5% calcium chloride solution, observing variations in mass and compressive strength after 56 and 84 days of exposure. The photographs of the durability experimental setup used in the present investigation are presented in Fig. 1.

3. Results and Discussion

3.1. Effects of HL on The Water Absorption Properties of Ternary Concrete Mixes

Fig. 2 illustrates the water absorption of ternary concrete mixes in which OPC was partially substituted with varying amounts of GGBS and HL. The results, recorded after 56 and 84 days of water curing, show a general decline in water absorption characteristics as the GGBS content increases. However, HL content also plays a role in influencing this trend. Among all the mixes, C40G50L10 (containing 40% OPC, 50% GGBS, and 10% HL) exhibited the lowest water absorption values, 2.49% at 56 days and 2.08% at 84 days. These results represent a 41% and 44% reduction, respectively, compared to the control mix C100 (100% OPC), which showed absorption rates of 4.22% and 3.66% at the same time intervals. This demonstrates that the incorporation of 50% GGBS together with 10% HL effectively minimizes water ingress by refining the pore structure through pozzolanic reactions [32,33].

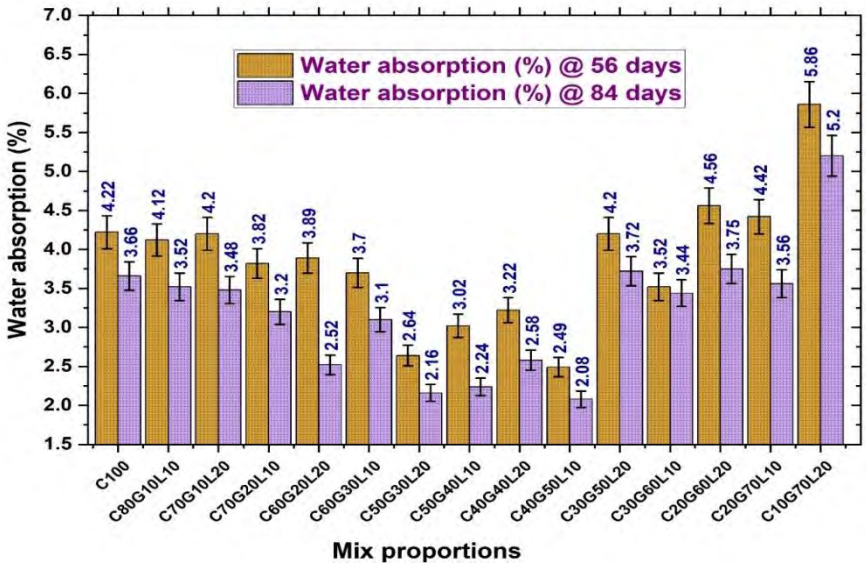


Fig. 2. Effect of HL and GGBS addition on the water absorption properties of ternary mixes

On the other hand, the mix C10G70L20 (10% OPC, 70% GGBS, 20% HL) recorded the highest absorption values, showing increases of 39% and 42% at 56 and 84 days, respectively, when compared with C100. This poor performance is mainly due to insufficient OPC for matrix development and the microstructural flaws introduced by excess HL, both of which increase permeability [34]. Notably, the C40G50L10 mix with 10% HL consistently outperformed similar mixes with 20% HL, such as the C50G30L20 mix, which had a slightly higher absorption rate of 2.64% in 56 days. This suggests that a moderate HL content (10%) is sufficient to refine the pore structure and reduce water absorption, whereas an excessive amount (20%) can compromise the mix by introducing microstructural flaws [35]. The test results confirm that C40G50L10 achieved more than a 40% reduction in absorption compared to the control mix, while C10G70L20 exhibited over 40% higher absorption. This quantitative contrast highlights the important role of balanced OPC–GGBS–HL proportions in achieving lower porosity and better water resistance.

The observed improvements in durability characteristics, particularly reduced water absorption and penetration in mixes containing 10% HL, were closely related to the microstructural

densification and enhanced pozzolanic activity. These mechanisms were confirmed in our earlier work (Dhanesh and Shanmugasundaram, 2023), where detailed SEM–EDS analysis established the role of HL in pore refinement and secondary C–S–H gel formation. A summary of the key microstructural findings and their durability implications is presented in Table 3, providing a direct correlation between microstructural evidence and the results of the present study.

Table 3. Summary of the microstructural observations from earlier research

Microstructural evidence	Observations	Durability implications
Refined pore structure with denser gel matrix	Attained with 10% HL in OPC-GGBS mix	Reduced water absorption and penetration
Formation of additional C-S-H and C-A-S-H gels	HL inclusion produced additional $Ca(OH)_2$ to activated GGBS	Enhanced chloride resistance
Presence of unreacted particles at 20% HL	Excess HL resulted in porosity	Increases permeability and reduces resistance in 20% HL mixes
Homogeneous matrix with low microcracks	Observed in mixes with 40% to 50% GGBS and 10% HL	Enhanced chemical resistance under acid and sulphate condition

3.2. Effects of HL on The Water Penetration Test Results of Ternary Concrete Mixes

Fig. 3 presents the water penetration performance of the ternary concrete mixes with varying proportions of OPC, GGBS, and HL. The permeability results measured after 56 and 84 days of curing demonstrate that the level of OPC replacement showed a notable effect on permeability results. Among all the mixes tested, C40G50L10 (comprising 40% OPC, 50% GGBS, and 10% HL) produced the lowest permeability values, 9.85 mm at 56 days and 7.6 mm at 84 days. These results indicate a significant reduction of 47.4% and 40.2%, respectively, compared to the control mix C100 (100% OPC), which exhibited permeability results of 18.7 mm and 12.7 mm at the same intervals.

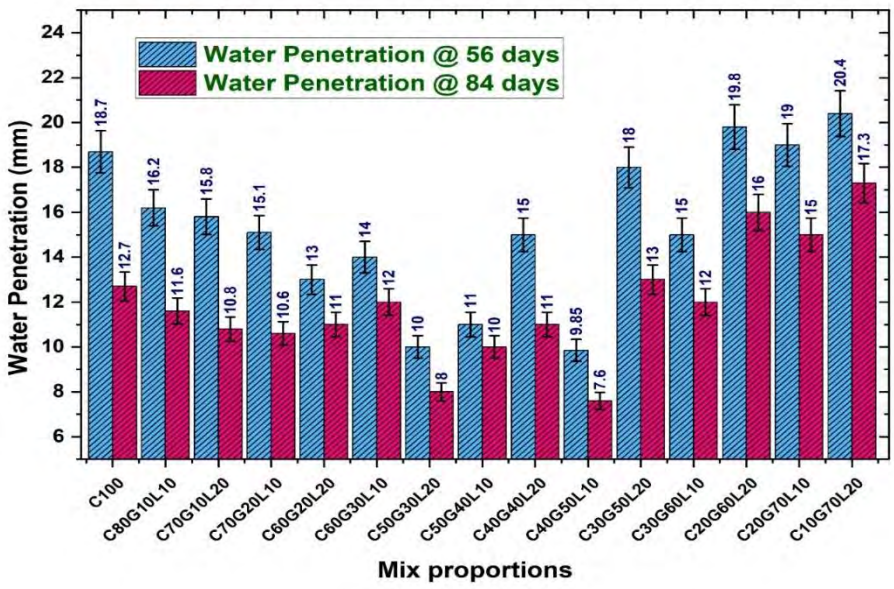


Fig. 3. Combined influence of HL and GGBS on the water penetration characteristics

The improved performance of the C40G50L10 mix is mainly because of the pozzolanic activity of GGBS, which refines the pore structure by filling capillary voids, while the inclusion of 10% HL further reduced water penetration by minimizing smaller pores [36], [37]. In addition, the 10% HL content further minimized water penetration by filling smaller pores present within the matrix. On the other side, the mix C10G70L20 (10% OPC, 70% GGBS, 20% HL) showed the highest penetration,

registering increase in the penetration results of 8.9% at 56 days and 36.3% at 84 days compared to the C100 mix. This poor performance is due to the low OPC content, which resulted in a weakly bonded microstructure with larger interconnected pores [38], [39]. Although HL can act as a filler, its benefit is limited when combined with excessive GGBS and low OPC, as this composition prevents effective densification [40]. The optimized C40G50L10 reduced water penetration depth by nearly half compared to the control mix, while the C10G70L20 mix exceeded the control mix by over 36% at 84 days.

3.3. Combined utilization of HL and GGBS on RCPT Performance of Ternary Mixes

Fig. 4 illustrates the RCPT results of ternary blended concrete mixes after 56 and 84 days of curing. The control mix C100 (100% OPC) illustrated the highest charge passed, measuring 1028 coulombs at 56 days and 865 coulombs at 84 days, which corresponds to the moderate chloride ion penetrability category as per ASTM C1202. The optimized blend C40G50L10 (40% OPC, 50% GGBS, and 10% HL) recorded the lowest values of 428 coulombs and 386 coulombs at 56 and 84 days, respectively, placing it in the low chloride ion penetrability range. This substantial reduction of 58.3% and 55.2% compared to the control mix indicates the importance of GGBS in refining the pore structure and limiting ion transport, while the inclusion of 10% HL further enhanced matrix densification through secondary reactions [28], [41].

Mixes containing 10% HL, such as C40G40L10, C50G40L10, and C60G30L10, consistently exhibited low chloride permeability, whereas 20% HL blends (e.g., C20G60L20, C10G70L20) remained in the moderate range. This indicates that while a moderate dosage of HL (10%) effectively complements the pozzolanic reaction of GGBS, higher HL content promotes the formation of excess calcium hydroxide, which increases pore connectivity and reduces durability [42], [43]. Based on the experimental results from 15 mixes, the ASTM-based classification confirms that ternary mixes with 10% HL provide optimal resistance against chloride penetration compared to both the control and higher HL (20%) blends. The test results indicate that the chloride ion penetration in the C40G50L10 mmix was reduced to below 400 coulombs at 84 days, while mixes with 20% HL exceeded 700 coulombs.

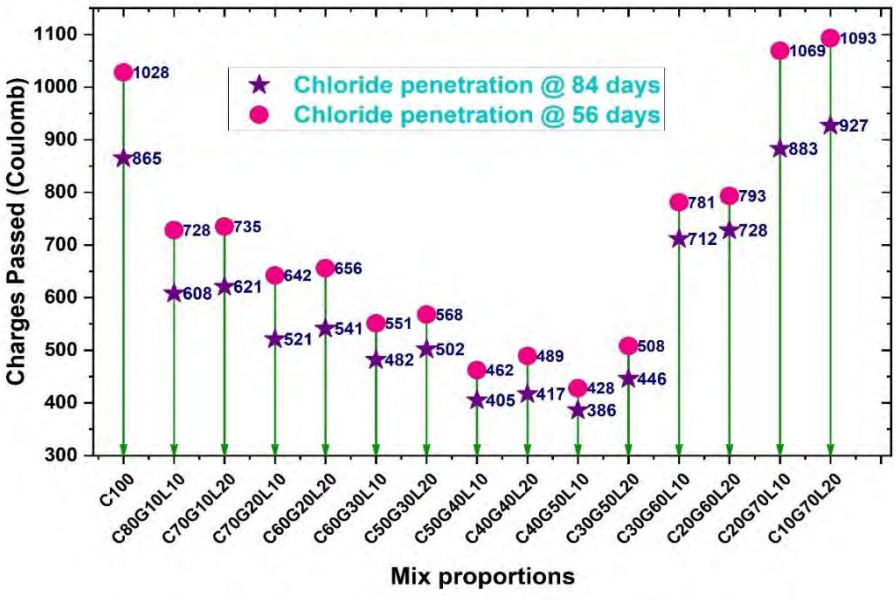


Fig. 4. Combined utilization of HL and GGBS on the chloride penetration of ternary mixes

3.4. Combined Impact of HL and GGBS on The Acid Resistance of Ternary Mixes

Fig. 5 presents the results of the acid resistance test on concrete mixes where OPC was partially replaced with varying substitution levels of GGBS and HL. Among the fifteen mixes, C10G70L20 (10% OPC, 70% GGBS, 20% HL) exhibited the highest loss in compressive strength, with reductions of 18.47% at 56 days and 33.62% at 84 days. In contrast, the C40G50L10 mix proportion (40% OPC, 50% GGBS, 10% HL) recorded the lowest strength loss at the same time intervals, 10.25% and

17.84%, respectively. The poor performance of C10G70L20 can be attributed to its very low OPC content, which plays a critical role in early-age strength development and acid resistance, coupled with excessive HL content (20%) that increased porosity [39], [44]. The superior performance of the C40G50L10 mix is mainly because of its well-balanced composition: 40% OPC ensures sufficient early strength and acid resistance, 50% GGBS contributes to long-term matrix refinement, and 10% HL likely helps reduce pore volume while supporting pozzolanic activity.

Fig. 6 presents the weight loss (%) experienced by the ternary mixes following acid exposure at the end of 56 and 84 days. Among the fifteen considered mixes, C40G50L10 demonstrated the least weight loss of 5.45% at 56 days and 7.42% at 84 days. In comparison, the control mix C100 exhibited weight losses of 8.12% and 10.58%, indicating reductions of 32.6% and 29.9%, respectively. C10G70L20 mix recorded the highest deterioration, with weight losses of 11.13% at 56 days and 14.95% at 84 days. These results suggest that despite high GGBS levels, the low OPC proportion and excessive HL dosage lead to unstable calcium hydroxide phases and inadequate matrix cohesion, thereby lowering acid resistance [45]. The C40G50L10 mix reduced the weight loss to below 8% and strength loss to below 18% after 84 days of acid exposure, whereas C10G70L20 showed nearly double the deterioration. This phenomenon indicated that limiting the 10% HL is very important for achieving better acid resistance in ternary blended systems.

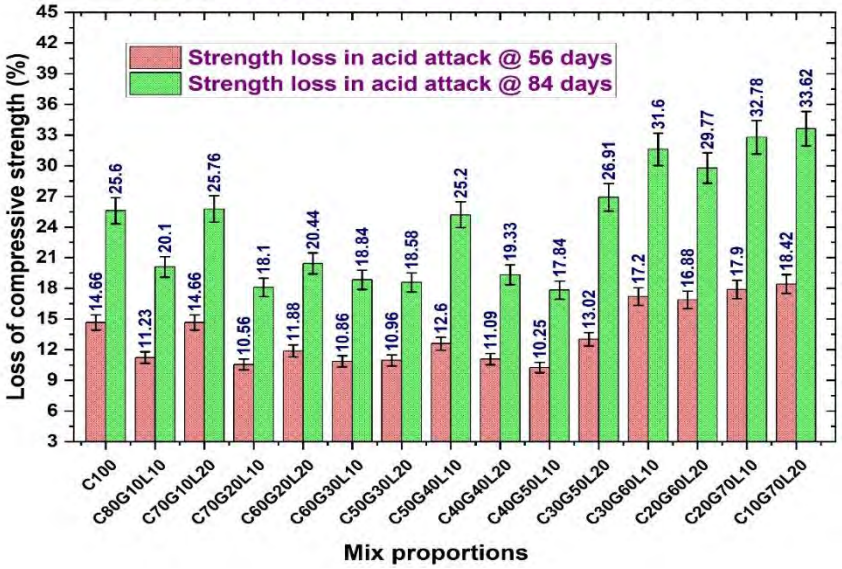


Fig. 5. Combined incorporation of HL and GGBS on the acid resistance test on ternary mixes

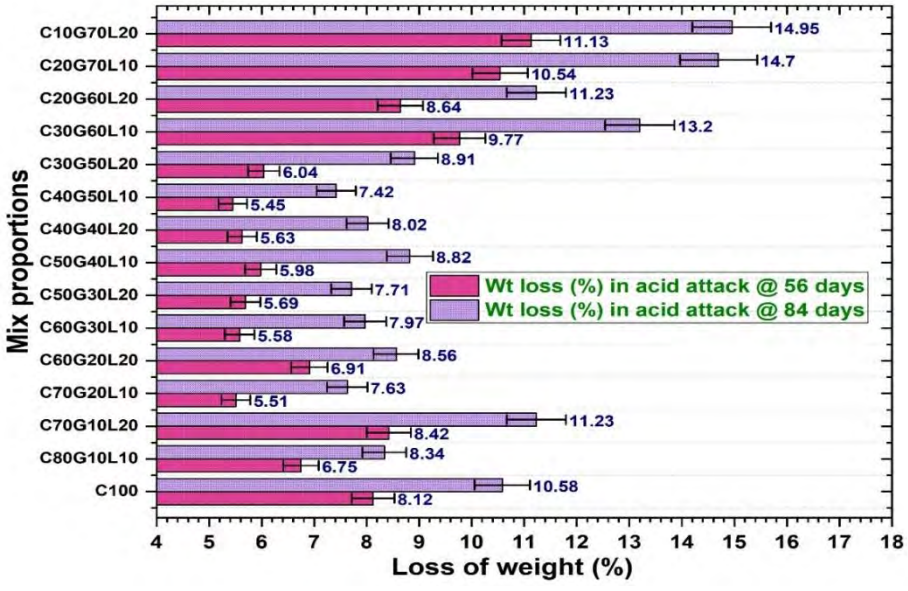


Fig. 6. Combined addition of HL and GGBS on the weight loss during acid attack

3.5. Influence of HL and GGBS Addition on The Sulphate Resistance Of Ternary Mixes

Fig. 7 illustrates the effect of incorporating GGBS and HL as partial replacements for OPC on sulphate resistance. The ternary mix comprising 40% OPC, 50% GGBS, 10% HL (C40G50L10) showed the lowest strength loss, with reductions of 3.56% at 56 days and 6.65% at 84 days, corresponding to 27.5% and 15.4% lower values compared to the control mix C100 (4.9% and 7.86%). On the other side, mix constituting 10% OPC, 70% GGBS, 20% HL (C10G70L20) recorded the highest strength loss of 5.1% and 9.10%, which represents an increase of 4.1% and 15.8% compared to the conventional mix (C100). The enhanced sulphate resistance of mixes like C40G50L10 and C50G40L10 is due to the pozzolanic action of GGBS, which helps create a denser internal structure and limits the formation of expansive compounds caused by sulphate reaction [46], [47]. However, in mixes with higher HL content, such as C10G70L20, the elevated porosity is attributed to the relatively weaker binding nature of HL, which results in deeper sulphate penetration, accelerating strength deterioration. Notably, mixtures containing 10% HL (e.g., C40G50L10, C50G40L10, C60G30L10) consistently retained more strength than those with 20% HL (C40G40L20, C50G30L20, C60G20L20), indicating that a moderate HL dosage may be optimal for improving sulphate environment [48], [49].

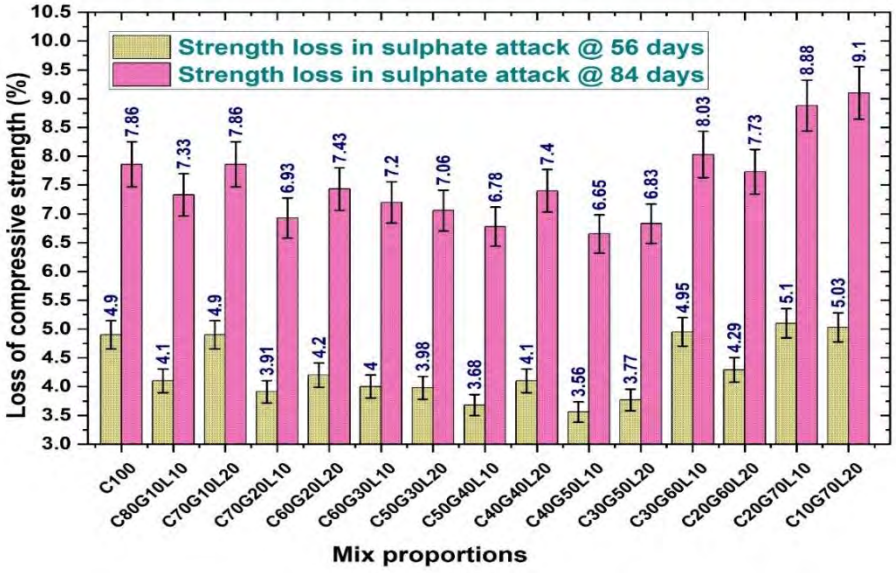


Fig. 7. Effect of HL and GGBS addition on the strength loss (%) during sulphate attack

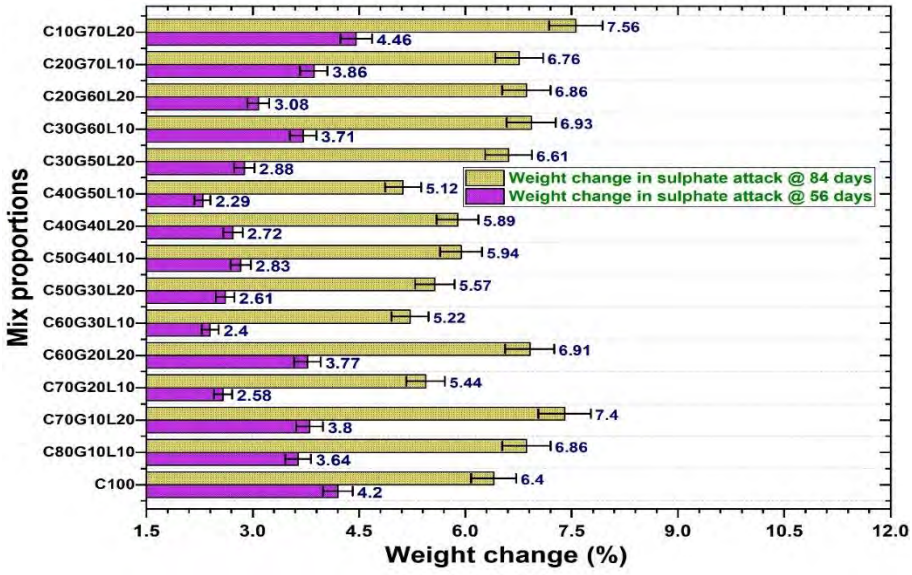


Fig. 8. Effect of HL and GGBS addition on the weight loss (%) during sulphate attack

Fig. 8 presents the percentage of weight loss experienced by the ternary concrete mixes after sulphate exposure at 56 and 84 days. Among the fifteen ternary mixes, C40G50L10 illustrated the lowest weight loss of 2.29% at 56 days (a reduction of 45.7% compared to C100) and 5.12% at 84 days (20.0% less than C100). The better performance of this mix is mainly due to the balanced combination of OPC, GGBS, and a moderate amount of HL, which enhances resistance to sulphate-induced degradation by reducing porosity and chemical penetration [50]. Conversely, the highest weight loss was observed in mix C10G70L20. Despite its high GGBS content, this mix exhibited marginally greater deterioration than the control, with weight losses of 4.46% at 56 days (6.2% higher than C100) and 7.56% at 84 days (18.4% higher). This suggests that the low OPC level and elevated HL dosage reduce the structural integrity of the matrix, allowing easier sulphate penetration [44].

3.6. Combined Influence of HL and GGBS on The Chloride Resistance of Ternary Mixes

The evaluation of chloride resistance of 15 ternary mix proportions, as depicted in Fig. 9, shows that the mix C40G50L10 (40% OPC, 50% GGBS, and 10% HL) recorded the lowest reduction in compressive strength of 3.63% at 56 days and 7.24% at 84 days, which is 30.3% and 10.0% lower than the control mix C100 (5.22% and 8.04%). On the other hand, the mix C20G70L10 (20% OPC, 70% GGBS, 10% HL) demonstrated the maximum reduction in strength, with losses of 5.7% and 9.51% at 56 and 84 days, indicating an increase of 9.2% and 18.4% over the control mix C100. The superior performance of C40G50L10 is mainly due to the ability of GGBS to bind chloride ions effectively, resulting in a compact microstructure that reduces chloride ingress and reinforcement corrosion. However, excessive GGBS proportion in C10G70L20 mix, reduces early-age strength and increases chloride-induced deterioration [51,52].

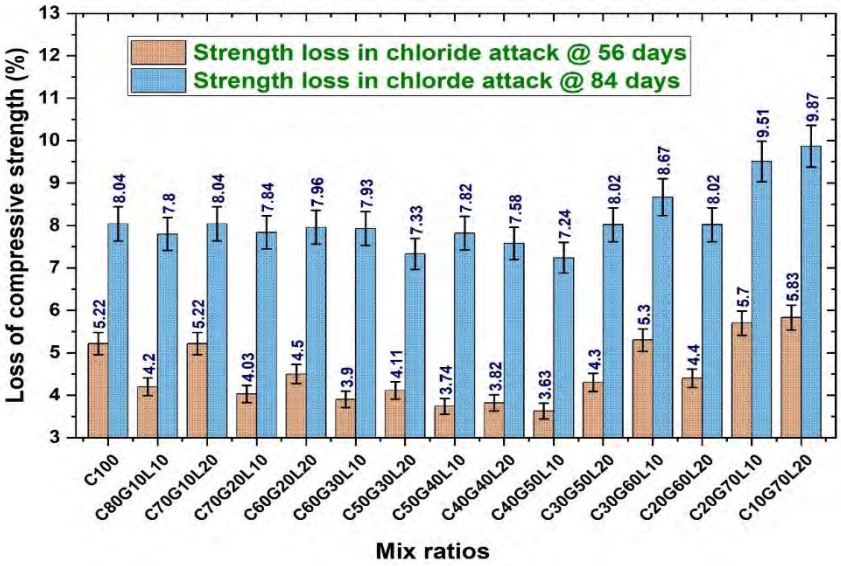


Fig. 9. Effect of HL and GGBS inclusion on the strength loss (%) during chloride attack

The mixes containing 10% HL (such as C40G50L10, C50G40L10, and C60G30L10) consistently retained more strength than the mixes incorporating 20% HL (C40G40L20, C50G30L20, and C60G20L20). This trend indicates that there may be an optimum HL content for resisting chloride attack, likely because moderate HL dosages contribute to pore structure refinement without significantly increasing permeability [53]. Fig. 10 supports these findings by illustrating weight loss percentages under chloride exposure. The C40G50L10 mix again performed best, with 3.26% loss at 56 days and 6.39% at 84 days, representing 20.7% and 18.1% reductions compared to C100 (4.1% and 7.8%). On the other hand, C20G70L10 exhibited the highest loss (5.7% and 9.51% at the same intervals), exceeding the control by 9.2% and 18.4%, respectively. Thus, chloride resistance is maximized with 50% GGBS and 10% HL, while excessive HL and very low OPC contents lead to performance deterioration.

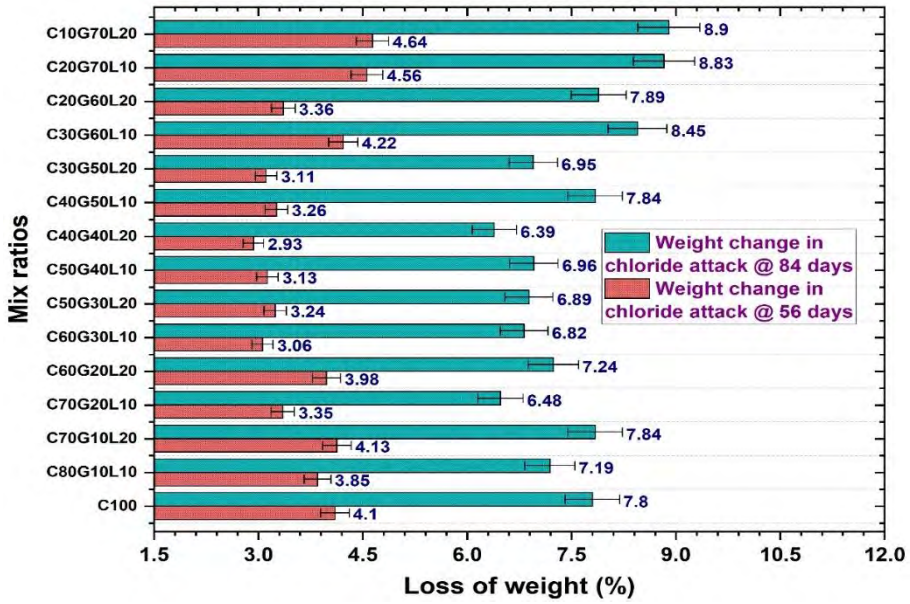


Fig. 10. Effect of HL and GGBS incorporation on the weight loss (%) during chloride attack

5. Conclusions

The study investigated the durability performance of ternary blended concrete incorporating varying proportions of GGBS and HL as partial replacements for OPC. The key findings are summarized as follows:

- Optimal Mix Performance: The C40G50L10 mix (40% OPC, 50% GGBS, 10% HL) exhibited superior durability across all tested parameters, achieving a 41% and 44% reduction in water absorption at 56 and 84 days, respectively, a 47.4% and 40.2% decrease in water permeability, and a 58.3% and 55.2% reduction in chloride ion penetration (428 and 386 coulombs) compared to the control mix (C100, 100% OPC).
- Role of GGBS: Higher GGBS content, particularly at 50% in the C40G50L10 mix, significantly enhanced durability by promoting pozzolanic reactions and reducing permeability, as evidenced by lower water absorption and chloride penetration values.
- Influence of HL Dosage: A moderate HL content of 10% (e.g., in C40G50L10, C50G40L10, C60G30L10) consistently outperformed mixes with 20% HL (e.g., C40G40L20, C50G30L20), indicating that 10% HL optimizes pore structure refinement.
- Poor Performance of High GGBS and HL Mixes: The C10G70L20 mix (10% OPC, 70% GGBS, 20% HL) showed the highest deterioration, with increased water absorption (39% and 42% higher than C100 at 56 and 84 days), water penetration (8.9% and 36.3% higher), and strength losses under acid (18.47% and 33.62%), sulphate (5.1% and 9.10%), and chloride (5.7% and 9.51%) exposures, attributed to insufficient OPC content and excessive HL-induced porosity.
- Chemical Resistance: The C40G50L10 mix demonstrated the least compressive strength reduction and weight loss under acid (10.25% and 17.84% strength loss; 5.45% and 7.42% weight loss), sulphate (3.56% and 6.65% strength loss; 2.29% and 5.12% weight loss), and chloride (3.63% and 7.24% strength loss; 3.63% and 7.24% weight loss) exposures, highlighting its suitability for aggressive environments.
- Practical Implications: The experimental findings of this study highlight that the C40G50L10 mix (40% OPC, 50% GGBS, 10% HL) provides a durable concrete matrix with excellent resistance to water ingress, chloride penetration, and chemical attack. This makes it highly suitable for marine structures exposed to seawater, foundations and substructures in sulphate-rich soils, and industrial environments prone to acidic exposure. By reducing permeability and enhancing chemical resistance, this mix can extend the service life of reinforced concrete structures while contributing to sustainability through lower OPC usage.

References

[1] Hawileh RA, et al. Effects of replacing cement with GGBS and fly ash on the flexural and shear performance of reinforced concrete beams. Pract Period Struct Des Constr. 2024 May;29(2). https://doi.org/10.1061/PPSCFX.SCENG-1339

[2] Vagestan PK, Periyasamy M, Shanmugasundaram V, Kumar TRS, Kumar KA, Tamilarasan A. Sustainable mortar design: optimizing performance with bamboo fiber and coal bottom ash using Taguchi and ANN. Emergent Mater. 2025 Jul. https://doi.org/10.1007/s42247-025-01177-7

[3] Cheah CB, Chung KY, Ramli M, Lim GK. The engineering properties and microstructure development of cement mortar containing high volume of inter-grinded GGBS and PFA cured at ambient temperature. Constr Build Mater. 2016 Sep;122:683-93. https://doi.org/10.1016/j.conbuildmat.2016.06.105

[4] Korde C, Cruickshank M, West RP. Activation of slag as partial replacement of cement mortar: Effects of superfine GGBS, temperature, and admixture. J Mater Civ Eng. 2020 Jul;32(7). https://doi.org/10.1061/(ASCE)MT.1943-5533.0003173

[5] Djeddou M, Amieur M, Chaid R, Mesbah HA. Development of eco-friendly self-compacting concrete using marble powder, blast furnace slag and glass fibre-reinforced plastic waste: Application of mixture design approach. Res. Eng. Struct. Mater., 2025; 11(1): 113-138. http://dx.doi.org/10.17515/resm2024.178ma0208rs

[6] Tang K, Wilkinson S, Beattie G. Effects of curing temperature on the hydration of GGBS concrete and the use of electron microscope particle analysis. Adv Cem Res. 2017;29(8). https://doi.org/10.1680/jadcr.16.00175

[7] Khan MNN, Kuri JC, Sarker PK. Effect of waste glass powder as a partial precursor in ambient cured alkali activated fly ash and fly ash-GGBFS mortars. J Build Eng. 2021 Apr;34:101934. https://doi.org/10.1016/j.jobe.2020.101934

[8] Manikandan P, Kumar VP, Vasugi V. Strength and microstructural characteristics of sustainable aluminosilicate binder using waste glass powder and ground granulated blast furnace slag. Innov Infrastruct Solut. 2025 Mar;10(3):105. https://doi.org/10.1007/s41062-025-01920-3

[9] Sandhu RK, Siddique R. Properties of sustainable self-compacting concrete made with rice husk ash. Eur J Environ Civ Eng. 2021;0(0):1-25.

[10] Vignesh R, Abdul Rahim A. Mechanical and microstructural properties of quaternary binder system containing OPC-GGBS-Metakaolin-Lime. In: Mater Today Proc. Elsevier Ltd; 2022 Jan. p. 970-5. https://doi.org/10.1016/j.matpr.2022.05.074

[11] Kumar BAVR, Ramakrishna G, Ajay CH. Performance evaluation of roller compacted concrete containing ferrochrome slag aggregates and red mud. Iran J Sci Technol Trans Civ Eng. 2022 Feb;49(1):467-85. https://doi.org/10.1007/s40996-024-01676-3

[12] Suthan Kumar N, Thanka Jebarsan V, Masi C. Effect of cement kiln dust and lignosulfonate on cement paste: a rheology and hydration kinetics study. Mater Res Express. 2023;10(10). https://doi.org/10.1088/2053-1591/ad020f

[13] Chandran P, Subhash N, Manikandan V, Vasugi V, Narendra S. Application of Taguchi approach to optimize the waste glass powder in developing eco-friendly ternary blended aluminosilicate matrix. Case Stud Constr Mater. 2024 Jun;21:e03398. https://doi.org/10.1016/j.cscm.2024.e03398

[14] Jung CT, Siang TC, Kwong TH, Boon K. Compressive strength and water absorption of mortar incorporating silica fume. Int J Civ Eng. 2019;6(8):39-43. https://doi.org/10.14445/23488352/IJCE-V6I8P106

[15] Cordeiro GC, Andreão PV, Tavares LM. Pozzolanic properties of ultrafine sugar cane bagasse ash produced by controlled burning. Heliyon. 2019;5(10):e02509. https://doi.org/10.1016/j.heliyon.2019.e02566

[16]Berkouche A, Belkadi A A, Aggoun S, Hammouche R, Benaniba S. Predictive modeling of glass powder and activator effects on slag-based geopolymers via central composite design. Res. Eng. Struct. Mater., 2025; 11(3): 1153-1178. http://dx.doi.org/10.17515/resm2024.337st0703rs

[17] Ofuyatan OM, Adeniyi AG, Ijie D, Ighalo JO, Oluwafemi J. Development of high-performance self compacting concrete using eggshell powder and blast furnace slag as partial cement replacement. Constr Build Mater. 2020 Sep;256:119459. https://doi.org/10.1016/j.conbuildmat.2020.119403

[18] Crossin E. The greenhouse gas implications of using ground granulated blast furnace slag as a cement substitute. J Clean Prod. 2015 May;95:101-8. https://doi.org/10.1016/j.jclepro.2015.02.082

[19] Karadumpa CS, Pancharathi RK. Influence of particle packing theories on strength and microstructure properties of composite cement-based mortars. J Mater Civ Eng. 2021 Oct;33(10). https://doi.org/10.1061/(ASCE)MT.1943-5533.0003848

[20] Peng Y, Ma K, Long G, Xie Y, Yu L, Xie Q. Effect of packing density according to CPM on the rheology of cement-fly ash-slag paste. J Mater Civ Eng. 2021 Aug;33(8). https://doi.org/10.1061/(ASCE)MT.1943-5533.0003823

[21] Taylor R, Richardson IG, Brydson RMD. Composition and microstructure of 20-year-old ordinary Portland cement-ground granulated blast-furnace slag blends containing 0 to 100% slag. Cem Concr Res. 2010 Jul;40(7):971-83. https://doi.org/10.1016/j.cemconres.2010.02.012
[22] Yazici H, Yardimci MY, Yiğiter H, Aydin S, Türkel S. Mechanical properties of reactive powder concrete containing high volumes of ground granulated blast furnace slag. Cem Concr Compos. 2010 Sep;32(8):639-48. https://doi.org/10.1016/j.cemconcomp.2010.07.005
[23] Cahyani RAT, Rusdianto Y. An overview of behaviour of concrete with granulated blast furnace slag as partial cement replacement. In: IOP Conf Ser Earth Environ Sci. IOP Publishing Ltd; 2021 Dec. https://doi.org/10.1088/1755-1315/933/1/012006
[24] Sahithi K, Priyanka GS. The effect of addition of limestone powder and granulated blast slag in concrete. Int J Comput Eng Res. 2015;2:1032-8.
[25] Jaafri R, Aboulayt A, Alam SY, Roziere E, Loukili A. Natural hydraulic lime for blended cement mortars: Behavior from fresh to hardened states. Cem Concr Res. 2019 Jun;120:52-65. https://doi.org/10.1016/j.cemconres.2019.03.003
[26] Ahmed A. Potential sustainable cement free limecrete based on GGBS & hydrated lime as an alternative for standardised prescribed concrete applications. Res Dev Mater Sci. 2021 Oct;15(5). https://doi.org/10.31031/RDMS.2021.15.000874
[27] Bayat H, Kashani A. Analysis of rheological properties and printability of a 3D-printing mortar containing silica fume, hydrated lime, and blast furnace slag. Mater Today Commun. 2023 Dec;37. https://doi.org/10.1016/j.mtcomm.2023.107128
[28] Fakhri RS, Dawood ET. Limestone powder, calcined clay and slag as quaternary blended cement used for green concrete production. J Build Eng. 2023 Nov;79. https://doi.org/10.1016/j.jobe.2023.107644
[29] Dhanesh E, Shanmugasundaram M. Prospective utilisation of hydrated lime as a performance enhancer in concrete. Mater Sci Technol. 2023 Nov;39(15):2062-73. https://doi.org/10.1080/02670836.2023.2188671
[30] Bureau of Indian Standards. IS 10262: Concrete mix proportioning - guidelines (second revision). New Delhi: BIS; 2019. p. 1-42.
[31] Divsholi BS, Lim TYD, Teng S. Durability properties and microstructure of ground granulated blast furnace slag cement concrete. Int J Concr Struct Mater. 2014 Jun;8(2):157-64. https://doi.org/10.1007/s40069-013-0063-y
[32] Manikandan P, et al. An artificial neural network based prediction of mechanical and durability characteristics of sustainable geopolymer composite. Adv Civ Eng. 2022;2022:1-15. https://doi.org/10.1155/2022/9343330
[33] Luo K, et al. Performance of hydraulic lime by using carbide slag. J Build Eng. 2022 Jul;51. https://doi.org/10.1016/j.jobe.2022.104208
[34] Bin Quraya A, et al. Experimental investigations of partial replacement of OPC with PFA and GGBS in cement mortar. IOP Conf Ser Mater Sci Eng. 2021 Feb;1058(1):012004. https://doi.org/10.1088/1757-899X/1058/1/012004
[35] Elavarasan S, Priya AK, Ajai N, Akash S, Annie TJ, Bhuvana G. Experimental study on partial replacement of cement by metakaolin and GGBS. In: Materials Today: Proceedings. Amsterdam: Elsevier; 2020. p. 3527-30. https://doi.org/10.1016/j.matpr.2020.09.416
[36] Li S, Sha F, Liu R, Li W, Li Z, Wang G. Properties of cement-based grouts with high amounts of ground granulated blast-furnace slag and fly ash. J Mater Civ Eng. 2017 Nov;29(11). https://doi.org/10.1061/(ASCE)MT.1943-5533.0002083
[37] Kyriakou L, Theodoridou M, Ioannou I. Micro-destructive evaluation of the mechanical properties of lime-based mortars. J Cult Herit. 2022 Nov;58:219-28. https://doi.org/10.1016/j.culher.2022.10.007
[38] Alyousef R, Abbass W, Aslam F, Gillani SAA. Characterization of high-performance concrete using limestone powder and supplementary fillers in binary and ternary blends under different curing regimes. Case Stud Constr Mater. 2023 Jul;18. https://doi.org/10.1016/j.cscm.2023.e02058
[39] Gunasekara C, Sandanayake M, Zhou Z, Law DW, Setunge S. Effect of nano-silica addition into high volume fly ash-hydrated lime blended concrete. Constr Build Mater. 2020 Aug;253. https://doi.org/10.1016/j.conbuildmat.2020.119205
[40] Zhang G, Peng GF, Zuo XY, Niu XJ, Ding H. Adding hydrated lime for improving microstructure and mechanical properties of mortar for ultra-high performance concrete. Cem Concr Res. 2023 May;167. https://doi.org/10.1016/j.cemconres.2023.107130
[41] Wu M, et al. The influence of chemical admixtures on the strength and hydration behavior of lime-based composite cementitious materials. Cem Concr Compos. 2019 Oct;103:353-64. https://doi.org/10.1016/j.cemconcomp.2019.05.008
[42] Anjos MAS, Camões A, Campos P, Azeredo GA, Ferreira RLS. Effect of high volume fly ash and metakaolin with and without hydrated lime on the properties of self-compacting concrete. J Build Eng. 2020 Jan;27. https://doi.org/10.1016/j.jobe.2019.100985

[43] Jung SH, Saraswathy V, Karthick S, Kathirvel P, Kwon SJ. Microstructure characteristics of fly ash concrete with rice husk ash and lime stone powder. Int J Concr Struct Mater. 2018 Dec;12(1). https://doi.org/10.1186/s40069-018-0257-4
[44] Ganesh P, Murthy AR. Tensile behaviour and durability aspects of sustainable ultra-high performance concrete incorporated with GGBS as cementitious material. Constr Build Mater. 2019 Feb;197:667-80. https://doi.org/10.1016/j.conbuildmat.2018.11.240
[45] Samad S, Shah A, Limbachiya MC. Strength development characteristics of concrete produced with blended cement using ground granulated blast furnace slag (GGBS) under various curing conditions. Sadhana. 2017 Jul;42(7):1203-13. https://doi.org/10.1007/s12046-017-0667-z
[46] Zhu H, Chen J, Li H. Effect of ultrafine pozzolanic powders on durability of fabricated hydraulic lime. Case Stud Constr Mater. 2022 Dec;17. https://doi.org/10.1016/j.cscm.2022.e01191
[47] Zhou YF, Li JS, Lu JX, Cheeseman C, Poon CS. Sewage sludge ash: A comparative evaluation with fly ash for potential use as lime-pozzolan binders. Constr Build Mater. 2020 May;242. https://doi.org/10.1016/j.conbuildmat.2020.118160
[48] Luo K, et al. Preparation and performances of foamed hydraulic lime. Constr Build Mater. 2021 Jul;290. https://doi.org/10.1016/j.conbuildmat.2021.123244
[49] Miah MJ, Huaping R, Paul SC, Babafemi AJ, Li Y. Long-term strength and durability performance of eco-friendly concrete with supplementary cementitious materials. Innov Infrastruct Solut. 2023 Oct;8(10):255. https://doi.org/10.1007/s41062-023-01225-3
[50] Maheswaran J, Chellapandian M, Arunachelam N, Hari MNT. Thermal and durability characteristics of optimized green concrete developed using slag powder and pond ash. Mater Res Express. 2023 Sep;10(9):095503. https://doi.org/10.1088/2053-1591/acf7b3
[51] Zhu J, et al. Effects of polycarboxylate superplasticizer on rheological properties and early hydration of natural hydraulic lime. Cem Concr Compos. 2021 Sep;122. https://doi.org/10.1016/j.cemconcomp.2021.104052

Research on Engineering Structures & Materials
www.jresm.org

Review Article

Reimagining steel slag in sustainable concrete: A bibliometric and experimental review

Osamah Ali [a], Pinta Astuti [*,b]

Department of Civil Engineering, Universitas Muhammadiyah Yogyakarta, Yogyakarta, Indonesia

Article Info

Article History:

Received 17 July 2025

Accepted 16 Aug 2025

Keywords:

Steel slag;
Sustainable concrete;
Cement replacement;
Durability performance;
Bibliometric analysis

Abstract

This review paper offers a comprehensive investigation into the use of steel slag in concrete, integrating bibliometric analysis with experimental findings to evaluate its performance, durability, and sustainability. Steel slag, a by-product of steel manufacturing, is generated in large volumes and presents environmental challenges due to improper disposal and leaching of harmful elements. Simultaneously, the construction industry's heavy dependence on Portland cement significantly contributes to global greenhouse gas emissions. Owing to its chemical similarity with cementitious materials, steel slag shows promise as a partial replacement for cement and natural aggregates. A bibliometric review of 880 Scopus-indexed publications reveals growing research interest worldwide—particularly in China, India, and Iraq—with main focus areas on mechanical properties, durability, and circular economy strategies. Experimental studies indicate that optimal replacement rates (10–15% for cement, 30–50% for aggregates) enhance compressive strength, chloride resistance, sulphate durability, and freeze–thaw performance. Treatments such as carbonation improve slag reactivity and stability. However, issues remain regarding workability, slag quality control, and extreme condition performance. Future research directions include smart concrete, geopolymer–slag hybrids, and nanomaterial enhancements. Life-cycle analysis and regulatory frameworks are essential for scaling adoption. Overall, steel slag presents a viable, sustainable solution in concrete, promoting resource efficiency and emission reduction.

© 2025 MIM Research Group. All rights reserved.

1. Introduction

The degradation of the ecological environment has emerged as a pressing concern in civil engineering. Alongside rapid economic advancement, the volume of industrial solid waste is escalating [1,2]. This surge poses substantial risks to ecological stability and environmental safety [3]. Among such wastes, steel slag and fly ash are generated in large quantities, making their effective disposal and reuse vital to environmental preservation. Unlike blast furnace slag, steel slag is a by-product of the steelmaking process and primarily comprises ferrites and calcium-bearing compounds formed during the cooling of molten steel [4]. Its heterogeneous composition necessitates tailored treatment and reuse strategies. Unfortunately, much of this waste is either landfilled or stored unsafely [5], leading to the leaching of alkaline substances and heavy metals [6], which threaten water quality, ecological integrity, and human and animal health [7,8]. This highlights the urgent need to develop sustainable management strategies for these materials to reduce their environmental footprint [9].

Cement-based materials continue to dominate the construction sector due to their mechanical and structural advantages. However, the production of Portland cement is resource-intensive, consuming vast amounts of raw materials and energy [10]. Additionally, it is a major contributor

*Corresponding author: pinta.astuti@ft.umy.ac.id
[a]orcid.org/0009-0009-4866-8791; [b]orcid.org/0000-0001-7465-6342
DOI: http://dx.doi.org/10.17515/resm2025-1037ma0717rv

to greenhouse gas emissions, with an estimated 0.79 tons of CO_2 released per ton of cement produced [11]. The cement industry is responsible for nearly 8–9% of global CO_2 emissions [12], prompting global discourse on more sustainable construction materials [13]. While industrial restructuring is imperative [14], efforts must also focus on the development of environmentally friendly, low-impact alternatives [15]. Minimizing resource consumption and emissions throughout the material lifecycle from production to disposal is essential, including strategies for recycling cementitious waste [16]. Thus, promoting energy efficiency and sustainable material use is becoming integral to the future of the construction industry [17].

Steel slag contains a wide range of chemical constituents, including major elements like Fe, Ca, Mg, and Si, along with trace components such as MnO_2 and Al_2O_3 [18]. Its composition features reactive phases like $CaSiO_3$ and SiO_2, closely resembling that of Portland cement [19]. Additionally, it includes mineralogical phases such as dicalcium silicate (C_2S), tricalcium silicate (C_3S), and calcium ferrite aluminate (C_4AF), which can actively participate in cement hydration [20]. Its SiO_2 content indicates promise as a filler material to improve the strength of cementitious composites [21].

Recent research has focused on advancing both cementitious and geopolymer composites through various material modifications. Notably, the chemical durability of geopolymers enhanced with silica fume and nano-silica has been studied under diverse curing regimes, offering insights into their resistance under aggressive environments [22]. Parallel investigations have explored the flexural behavior of self-compacting with steel fibers and silica fume, highlighting improvements in ductility and mechanical performance [23,24].

In the realm of construction applications, steel slag has emerged as a viable substitute for natural aggregates in structural concrete, subgrade layers, and railway ballast. Its mechanical characteristics are often comparable to those of traditional aggregates, reinforcing its role as a sustainable alternative [25,26]. Additionally, the integration of nanomaterials into geopolymer matrices continues to gain momentum, owing to their ability to refine microstructure and enhance performance [27].The use of steel slag in concrete systems presents a promising pathway for improving resource efficiency, reducing environmental pollution, and fostering industrial symbiosis between the steel manufacturing and construction sectors [28,29].

While numerous individual studies have investigated the use of steel slag in concrete, there remains a lack of comprehensive synthesis that integrates both quantitative bibliometric trends and technical performance evaluations across multiple domains—including workability, strength, durability, and microstructure. This review bridges that gap by combining a data-driven bibliometric analysis of 880 Scopus-indexed articles with a critical assessment of experimental findings. By mapping research evolution, international collaboration patterns, and emerging themes, this work not only identifies strategic research clusters and influential contributors but also highlights underexplored areas such as smart concrete, carbonation treatment, and slag quality standardization. Consequently, the research community benefits from a consolidated reference that supports evidence-based decision-making, guides future experimental design, and fosters collaborative innovation in sustainable concrete technologies.

2. Composition and Characteristics of Steel Slag

In the context of this study, the term “steel slag” refers to the by-product generated from steelmaking processes, particularly from basic oxygen furnaces (BOF) and electric arc furnaces (EAF). This type of slag is chemically and mineralogically distinct from ground granulated blast furnace slag (GGBFS), which is a by-product of pig iron production and widely used as a supplementary cementitious material. Unlike GGBFS, steel slag contains significant amounts of free lime (f-CaO) and magnesium oxide (MgO), which can lead to volumetric instability if untreated. Due to its complex mineral composition and variable chemistry, proper characterization and processing are essential before its application in cementitious systems.

2.1 Chemical and Mineral Composition

Steel slag, a by-product generated during steel production, is characterized by a complex mixture of chemical oxides. Dominant constituents typically include calcium oxide (CaO), silicon dioxide

(SiO_2), ferric oxide (Fe_2O_3), aluminum oxide (Al_2O_3), magnesium oxide (MgO), manganese oxide (MnO), ferrous oxide (FeO), and notably, free lime (f-CaO) [30]. The relative proportions of these oxides vary significantly depending on several factors, including the composition of the input materials, the specific steelmaking process used, and the type of steel produced [31].

In addition to its chemical complexity, steel slag also exhibits a diverse mineralogical profile. The primary crystalline phases commonly identified in slag include tricalcium silicate (C_3S), dicalcium silicate (C_2S), and dicalcium ferrite, alongside complex silicate compounds such as calcium–magnesium olivine and pyroxene derivatives [32]. A distinct feature of steel slag is the presence of the RO phase, which represents a solid solution composed primarily of MgO, FeO, and MnO, as well as unreacted free lime particles. The presence of these mineral phases is confirmed by X-ray diffraction (XRD) analysis, as illustrated in Fig. 1, which identifies dominant crystalline peaks corresponding to C_3S, C_2S, RO phase, and other silicate compounds. The typical morphology of steel slag, including the presence of angular particles and crystalline phases such as C_2S and RO compounds, is shown in Fig. 2.

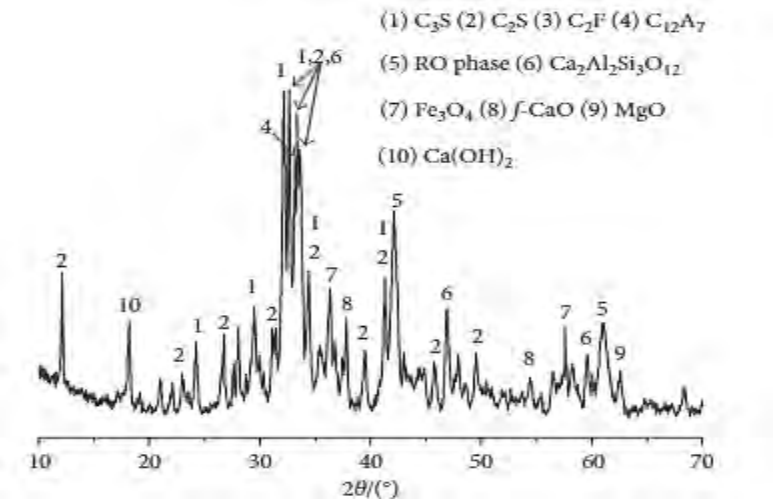


Fig. 1. X-ray diffraction (XRD) pattern of steel slag indicating dominant crystalline phases [33]

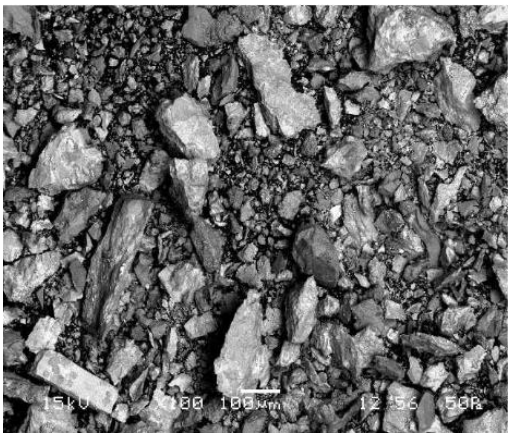


Fig. 2. Microstructure of steel slag [34]

The mineral composition of slag is closely tied to its basicity, which is typically expressed as the CaO/SiO_2 ratio [35]. As observed by Lin et al. [36], slags with lower basicity values tend to be rich in olivine, pyroxene, and RO phases. In contrast, medium to highly basic slags promote the crystallization of silicate-rich phases, such as C_3S and C_2S, which are relevant to the material's reactivity and cementitious potential. These trends are reflected in the representative chemical composition ranges summarized in Table 1, where the varying proportions of CaO and SiO_2 directly influence slag basicity and, consequently, the formation of specific mineral phases.

Table 1. Typical chemical composition ranges (wt.%) for various types of metallurgical slag [37]

Oxide	Range (wt.%)
CaO	40.04 - 50.64
MgO	6.40 - 7.12
Al2O3	22.84 - 41.73
SiO2	10.25 - 70.00
FeO	Up to 51.00
MnO	Trace amounts
P2O5	Trace amounts
K2O	Trace amounts
Na2O	Trace amounts
TiO2	Trace amounts
PbO	Higher in Pb smelting slags
ZnO	Trace amounts
Cr	Trace amounts
Ni	Trace amounts
V	Trace amounts

2.2 Physical Characteristics and Engineering Behavior

The physical appearance and density of steel slag vary with basicity and cooling conditions. Typically, the color transitions from dark gray or brown in low-basicity slag to light gray or white in high-basicity slag [38]. The bulk density of steel slag typically ranges from 3.1 to 3.6 g/cm^3. This range is supported by the specific gravity values mentioned in the abstracts, which indicate that steel slag has a high density compared to other materials. The moisture content of steel slag can vary between 3% and 8. This range is consistent with the findings in the abstracts, which discuss the water absorption properties and the impact of moisture content on the material's properties [39].

Steel slag exhibits three major engineering properties. First, its latent hydraulic activity stems from the presence of reactive silicate and aluminate minerals, which contribute to cementitious behavior under suitable conditions [40]. Second, the dimensional stability of steel slag is a concern due to its content of free CaO and MgO, which can hydrate over time, causing volumetric expansion. This poses a risk of cracking or instability in structures if the slag is not properly processed [41]. Third, the abrasion resistance of steel slag is influenced by its microstructure and mineral content. However, empirical studies have shown that its apparent poor wear resistance is often attributed to residual metallic iron particles rather than its crystalline phases. Specifically, grinding and sieving processes reveal that the coarse residue typically comprises iron, which deteriorates mechanical integrity when left unremoved [42].

3. Workability of Cement-Based Materials Containing Steel Slag

The fresh-state performance, or workability, of cementitious systems incorporating steel slag has been a central focus in numerous studies. A properly designed concrete mixture must demonstrate good cohesion, adequate flowability, and water retention without exhibiting bleeding or segregation. Researchers widely agree that optimizing the dosage and application method of steel slag is critical to achieving desirable workability in cement-based materials [43–48]. Table 2 maps the effects of steel slag substitution strategies on slump behavior and water demand. As shown, binder substitution with steel slag exhibits a non-linear trend: a 15% replacement improves slump due to better particle packing and lubricating effects, while 10% and 20% substitutions may reduce slump, likely due to insufficient or excessive particle interaction. When used as fine aggregate, steel slag improves workability up to an optimal replacement level of 30%, beyond which performance may decline. Conversely, using slag as coarse aggregate tends to deteriorate workability, attributed to its angular shape and higher density. In addition, the carbonation of steel slag introduces further complexity. Although it enhances early-age hydration, it also increases water demand, necessitating careful balance in mix design. These nuanced effects underscore the importance of

tailoring slag application to achieve desired fresh-state properties while maintaining compatibility with other mix components.

Table 2. Effect of steel slag utilization forms on fresh-state performance of cementitious materials, including setting time, slump, and hydration behavior

Steel Slag Usage Type	Replacement Level	Performance Indicator	Observed Effect (Fresh State)	Source
Cement replacement (SCM)	25%, 50%	Setting time; Hydration rate	Setting time significantly prolonged; early hydration kinetics noticeably slowed	[49]
Cement replacement (SCM)	25%, 50%	Setting time; Water demand	Setting was delayed, and required mixing water content was lowered by ~5–9% (reduced water demand)	[50]
Cement replacement (SCM)	30%	Setting time	Initial and final setting times extended by roughly 60% and 40% compared to plain cement (OPC)	[51]
Aggregate replacement	30%, 60% (fine aggregate)	Slump (workability)	Concrete maintained adequate slump at these replacement levels, indicating acceptable workability (steel slag concrete met standard slump requirements)	[52]
Aggregate replacement	10–50% (fine & coarse aggregate)	Slump (workability)	Concrete slump decreased significantly as steel slag content increased (e.g. from ~35 mm at 0% to ~3 mm at 50% coarse slag replacement. Very high slag replacement can lead to mix instability (segregation) due to the higher density of slag particles.	[53]

3.1 Steel Slag as a Binder Substitute

Martins [61] developed a blended binder using steel slag powder (SSP), cement, and linear alkylbenzene sulfonate (LAS). The introduction of SSP was shown to extend the setting time and modify the hydration process (Fig. 3). Interestingly, SSP improved the spread diameter of mortar mixtures, with the largest observed increase reaching 58.1 mm compared to mixtures using only Portland cement , confirming the trend reported by Bullerjahn [62].

Substituting cement with 10% steel slag generally results in a decrease in slump. This is supported by findings that incorporating steel slag reduces the workability of concrete, leading to a lower slump value. Specifically, one study noted a reduction in slump by up to 45.87% when 10% steel slag was used [54,55]. At 15% substitution, the slump increases. This could be due to the optimal balance between the cementitious properties of steel slag and the overall mix design, which might enhance the fluidity of the concrete mix. Although direct evidence for a 15% substitution is not provided, the trend of improved workability at certain substitution levels is noted in studies where steel slag improved the filling and passing ability of self-compacting concrete [56].Increasing the substitution to 20% results in another decrease in slump. This aligns with findings that higher proportions of steel slag can adversely affect the workability of concrete, leading to reduced slump values [54]. One study specifically mentioned that the workability of concrete decreases with increasing steel slag content, which supports the observed trend [57]. This behavior was attributed to multiple effects: (1) the filler effect, where slag particles provide nucleation sites that increase water demand; and (2) the ball-bearing effect, where smaller quantities of slag improve particle packing and enhance flowability [45]. The interaction between slag content and water availability plays a key role in modifying these rheological properties.

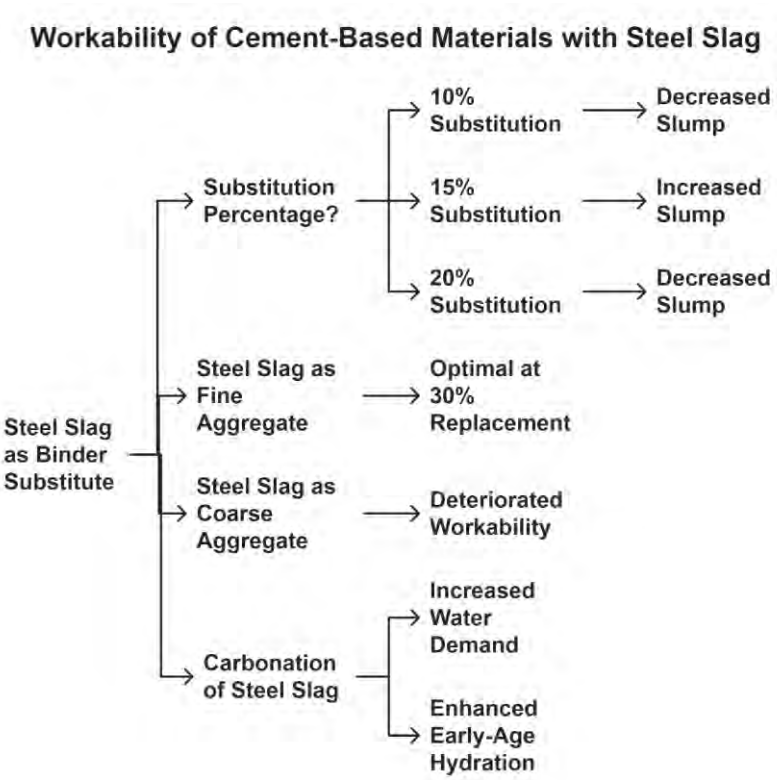


Fig. 3. Workability of cement-based materials with steel slag

3.2 Steel Slag as Fine and Coarse Aggregate

The use of steel slag as a replacement for natural aggregates—both fine and coarse—has been widely explored in concrete production. A study by Yehualaw et al. [58] evaluated the partial substitution of natural river sand with steel slag as fine aggregate. Their findings indicated that the concrete maintained acceptable workability, with slump performance more closely tied to the proportion of slag used rather than the water-to-cement (w/c) ratio. This emphasizes the importance of optimizing slag content to ensure consistent workability in structural applications. Supporting this, another investigation identified 30% replacement of natural sand with steel slag as an effective threshold, balancing both fresh properties and mechanical performance [59]. At this level, the concrete retained desirable slump values while benefiting from the strength-enhancing attributes of the slag particles.

Van Dao et al. [60] applied AI models to predict concrete properties with various mineral admixtures and confirmed that mixes containing steel slag consistently exhibited lower predicted slump values compared to mixes with fly ash or GGBS. The reduction in workability is also linked to the slower hydration kinetics of steel slag, which does not contribute significantly to early paste formation, causing stiffer fresh concrete. Moreover, Koniki et al. [61] highlighted that while geopolymer systems incorporating steel slag benefit from slag's latent hydraulic properties, higher dosages can still compromise flow without the use of superplasticizers.

Comparative analyses involving the replacement of both fine and coarse aggregates further reveal a decline in workability as the replacement percentage increases. However, fine aggregate substitution consistently outperforms coarse aggregate substitution in maintaining fresh concrete flow. This performance disparity is largely attributed to the particle angularity and grading of steel slag, which affect the internal friction and flow dynamics of the concrete mix [53].

3.3 Carbonation of Steel Slag and Its Impact

Carbonated slag increases the water demand for achieving standard consistency in cement mortars. This is attributed to the weight gain from carbonation, which correlates positively with the increased water requirement[62,63]. The carbonation process alters the microstructure of the

slag, leading to a refinement of the pore structure and an increase in specific surface area. This change in microstructure is likely responsible for the increased water demand, as more water is needed to wet the larger surface area and fill the refined pores[62].

Rui & Qian [64] evaluated the hydration response of cementitious systems containing CO_2-cured steel slag. The carbonated slag enhanced early-age hydration and shortened the setting time. steel slag processed with CO_2 fixation increased the specific surface area, which accelerated the cement hydration process by improving water absorption and reducing the availability of free water [65]. These findings indicate that carbonation pretreatment can significantly alter the fresh behavior of slag-containing concrete mixtures. Moreover, Gencel et al. [7] discussed how pre-wetting steel slag aggregate or using optimized gradation can mitigate workability loss. In high-performance concrete, partial replacement (up to 50%) tends to balance workability loss with mechanical and durability gains. This was corroborated by Nguyen et al.[66] , who reported that moderate slag aggregate content provided acceptable slump values when paired with appropriate water-reducing admixtures.

4. Influence of Steel Slag Incorporation on the Strength Properties of Cementitious Composites

In civil engineering applications, the mechanical behavior of materials remains a cornerstone for structural design and material selection. Key strength parameters compressive, tensile, and flexural serve as indicators of performance under both service and extreme conditions [67–71]. Table 3 outlines the impact of various steel slag applications on these strength characteristics. To complement this data, Fig. 4 illustrates the variation in compressive strength performance associated with different steel slag application methods. As shown, using steel slag as a 50% coarse aggregate replacement significantly enhances compressive strength, with results reaching up to 87.6 MPa. When steel slag undergoes carbonation treatment, the strength gain becomes even more pronounced, achieving a peak of 124.4 MPa, which demonstrates the synergistic effect of mineral reactivity and CO_2 curing. Other applications, such as 10% cementitious content or cement substitution, show moderate strength levels (42–49 MPa), while CO_2-cured composites yield intermediate performance at 72 MPa.

4.1 Steel Slag as a Cementitious Component

The effectiveness of steel slag as a cementitious material has been closely linked to its replacement level within the binder matrix. Studies indicate that compressive strength tends to peak around specific substitution thresholds. For instance, an optimal dosage of 10% steel slag has been reported to yield a 28-day compressive strength of 49.01 MPa, highlighting its potential to partially replace Portland cement without compromising structural performance [72].

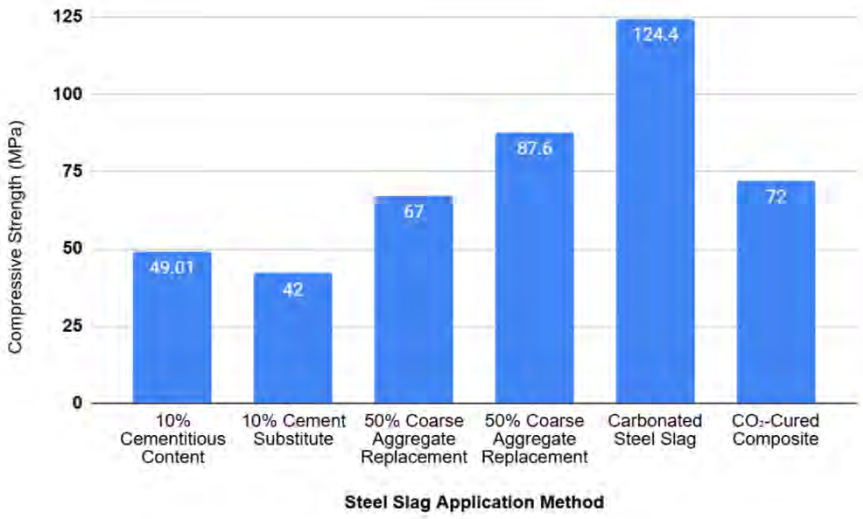


Fig. 4. Compressive strength improvements with steel slag

In a related study, Roslan evaluated steel slag powder as a partial cement replacement at levels of 5%, 10%, 15%, and 20%, identifying 10% substitution as the most effective, achieving 42 MPa at 28 days and a 27% improvement in early strength at 3 days compared to conventional concrete [73]. These results suggest that moderate slag inclusion can accelerate early hydration and enhance strength development. Beyond single-component replacement, steel slag has shown potential in hybrid binder systems. Ranjbar et al. [74] explored calcium carbonate-activated steel slag binders, observing improved microstructure and densification, which translated into higher long-term strength. Ganter et al. [75] examined steel slag combined with cement in stabilized soils and found that slag inclusion significantly enhanced the early and long-term strength, demonstrating promise for infrastructure applications beyond traditional concrete. Further performance enhancement is observed when steel slag is used in combination with ground granulated blast furnace slag (GGBFS) and desulfurized gypsum (DG). When applied as a coarse aggregate, this blended system demonstrated a 22.71% increase in compressive strength, reflecting synergistic effects between supplementary cementitious materials and the slag aggregate framework [76].

Table 3. Strength performance of cement-based composites incorporating steel slag as a partial binder or aggregate replacement

Steel Slag Usage Type	Replacement Ratio	Strength Parameter(s)	Performance Outcome	Reference
Cement replacement	5%, 10%, 15%, 20%	Compressive, flexural, splitting tensile	10% replacement provided peak strength: f_c= 42 MPa, f_t = 5.3 MPa, f_{ts}= 4.1 MPa	[73]
Coarse aggregate	40%, 45%, 50%	Compressive, splitting tensile	50% mix achieved f_c= 87.6 MPa, f_{ts}= 6 MPa (↑12.2% vs control)	[77]
Fine/coarse aggregate	Coarse: 0–80%, Fine: 0–60%	Compressive	Optimal at 50% coarse + 30% fine: f_c= 73.5–74.9 MPa (↑5–19% depending on age)	[78]
Carbonated slag additive	80%, 100% (14-day CO_2 curing)	Compressive	Improved strength; f_c= 72.0 MPa in slag–cement mixes after carbonation.	[79]
Carbonated slag additive	30% (15–240 min CO_2 curing)	Compressive at 3–90 days	Low-carbonated slag ↑ strength (↑8% at 28d); high-carbonated slag ↓ early but ↑ late strength (↑14.7% at 28d).	[80]

4.2 Steel Slag as Aggregate Replacement

Several studies have reported that substituting natural aggregates with steel slag enhances the mechanical performance of concrete, particularly in terms of compressive and flexural strength. For example, incorporating steel slag as a partial replacement for fine aggregates—up to 75%—has been shown to increase compressive strength by approximately 12% compared to conventional mixes [81]. A lower replacement ratio, such as 30%, has also produced favorable strength results when benchmarked against control specimens [82]. Additionally, the flexural performance improves with steel slag integration; a 75% substitution of both fine and coarse aggregates resulted in flexural strength gains of 13% and 15%, respectively [81]. Similar enhancements in tensile strength were observed across varying replacement levels [82].

Yang et al. [77] investigated the substitution of natural coarse aggregates with steel slag and assessed strength development over time. Their findings indicated that a 50% replacement ratio yielded optimal results, achieving 67 MPa compressive strength at 120 days—an 18.2% improvement over traditional concrete. This enhancement was linked to the formation of calcium aluminosilicate compounds during hydration, which contributed to a stronger bond between the aggregate and cement paste. However, beyond this optimal level, the strength benefit diminished due to reduced formation of calcium silicate hydrate (C–S–H) gel. In another study, Lai et al. [78]

examined combined replacement strategies involving up to 80% coarse and 60% fine aggregate substitution. The most effective mix—50% coarse and 30% fine replacement—achieved compressive strength increases of 5.32%, 5.76%, and 19.32% at 7, 28, and 90 days, respectively, highlighting the long-term performance benefits of optimized slag usage.

Meanwhile, Miah et al. [83] reported that partial replacement of natural coarse aggregate with untreated steel slag yielded significant enhancements in compressive, tensile, and flexural strength, indicating its robust structural potential. Work by Mekonen et al. [84] explored moderate substitution levels in reinforced concrete beams. Incorporating 30% steel slag as fine aggregate and 45% as coarse resulted in notable improvements: compressive strength rose at both 7 and 28 days, while flexural strength peaked around 45% replacement—suggesting optimal dosage windows. Table 4 presents a concise summary of key findings from recent studies on the use of steel slag as an aggregate replacement in concrete. The table highlights various replacement strategies—including partial and full substitutions of coarse and fine aggregates—and their corresponding effects on compressive, tensile, and flexural strength. These results demonstrate that optimized steel slag incorporation can significantly enhance the mechanical properties of concrete, offering promising pathways for sustainable construction practices.

Table 4. Summary of steel slag aggregate replacement levels and their associated performance impacts on concrete strength properties

Replacement Type & Level	Performance Impact
100% coarse + fibers	+70% to +170% compressive strength
60% carbonated SSFA	+1–7% compressive gain
Partial (30–45%) slag	Peak 28-day compressive/flexural strengths
25–100% slag pervious mix	Enhanced multi-modal strengths & abrasion resistance

4.3 Influence of CO_2 Treatment on the Functional Properties of Steel Slag

Carbonation increases the compressive strength of steel slag. For instance, carbonated steel slag aggregates showed a compressive strength improvement, with optimal conditions yielding a strength of 124.4 MPa [85]. Additionally, the use of chemical additives like EDTA and Na_2SO_4 further enhances compressive strength [86]. Carbonation reduces the expansion rate of steel slag, addressing the issue of harmful expansion due to free CaO. The formation of $CaCO_3$ during carbonation fills the pores, improving volume stability [87] The CO_2-cured composite reached up to 72.0 MPa in compressive strength [88], consistent with findings by Bukowski and Berger [89].

The effect of low- and high-carbonated steel slag (15 and 240 minutes, respectively) on cement mortars showed 5.3% and 8.0% increases in strength at 7 and 28 days, respectively. However, high-carbonated slag reduced early-age strength by 11.1% but enhanced later-age strength by 14.7% [80]. The early reduction was linked to excessive $CaSiO_3$ consumption reducing hydration reactivity, whereas the later gain stemmed from improved pozzolanic activity due to SiO_2 gel formation [90].

4.4 Optimal Compositions and Recommended Dosages for Steel Slag in Concrete

To facilitate practical implementation and support further research, this section summarizes optimal replacement levels of steel slag in concrete as reported across the literature. These numerical values offer guidance on effective dosages for various performance targets, ranging from mechanical strength to durability under harsh environmental conditions.

The literature consistently identifies 30% steel slag replacement of natural coarse aggregate as an effective threshold for improving compressive, tensile, and shear strength, particularly in structural concrete applications [91–93]. In sulfate-rich environments, increasing the replacement to 40% coarse aggregate has been shown to enhance resistance against chemical attack, improving the long-term performance of concrete exposed to wet–dry or saline cycles [94]. As for fine

aggregates, a replacement level of 30% also yields favorable results, contributing to increased compressive strength and enhanced durability [58,95].

When used as a partial cement replacement, steel slag powder demonstrates optimal performance at 20% substitution, enhancing compressive strength, dimensional stability, and long-term hydration [96]. In the case of ultra-high-performance concrete (UHPC) systems, steel slag powder shows improved synergy at a 30% binder replacement level, where it contributes to denser packing and better mechanical outcomes [97]. In self-compacting concrete (SCC), steel fibers derived from slag-enhanced mixes at a dosage of 2% by volume have been found to significantly boost ductility and strength while maintaining workability [98].

These recommended dosages provide a benchmark for mix design in both research and practice. While the optimal percentages may vary slightly depending on slag source, treatment method, and application type, the summarized data serve as a practical reference point for engineers, material scientists, and sustainability researchers aiming to integrate steel slag into durable and eco-efficient cementitious systems.

5. Long-Term Durability Characteristics of Cementitious Systems Incorporating Steel Slag

Ensuring long-term durability is critical for structural integrity and sustainability in concrete applications as in Table 5. This section highlights the performance of steel slag cementitious systems under durability-related stress conditions, including freeze–thaw cycles, sulfate attack, and permeability resistance [99–102]. Fig. 5 provides a visual summary of steel slag's impact on concrete durability across various conditions. As depicted, finer steel slag particles exhibit low resistance, often suffering from high mass and strength losses, particularly when subjected to repeated freeze–thaw cycles or aggressive chemical environments. Steel slag powder, while potentially useful as a partial cement substitute, tends to have lower resistance to chloride ion penetration, which may compromise durability in marine or saline-exposed structures.

Freeze–thaw resistance is a major concern for concrete exposed to cyclic freezing conditions, particularly in temperate and cold regions. Several studies have reported that replacing cement with 4–10% steel slag leads to excellent freeze–thaw performance, with the strength ratio remaining close to 100% even after 80 cycles [103]. When steel slag is used as fine or coarse aggregate at replacement levels of 20–60%, the concrete exhibited limited mass loss (2.2–3.0%) and retained a dynamic modulus in the range of 74.9–91.1% after up to 150 cycles [104]. These findings demonstrate the material's ability to resist microcracking and maintain elasticity under thermal stress, attributed to its dense microstructure and reduced pore connectivity.

Sulphate resistance, another critical durability indicator in environments subject to chemical exposure (e.g., coastal, saline, or sulphate-rich soils), also improved significantly with the use of steel slag. Concrete containing 30–90% slag as coarse aggregate maintained its mechanical properties over a 56-day exposure period, showing a three-phase behaviour in strength loss: an initial gain, a mild decline, and subsequent stabilization [105]. This pattern reflects the formation and densification of hydration products such as ettringite and C–S–H, which impede sulphate ingress and reduce cracking potential.

Regarding impermeability and porosity, steel slag incorporation—especially in the range of 0–80% for coarse and 0–60% for fine aggregates—contributes to substantial pore structure refinement. Microstructural investigations using SEM and mercury intrusion porosimeter revealed a notable decrease in harmful capillary pores and overall porosity, leading to improved compactness and reduced permeability [78]. Such characteristics are essential for enhancing resistance to chloride ion penetration and carbonation, particularly in marine and urban environments where durability dictates long-term performance.

Table 5. Performance of concrete with steel slag under freeze–thaw cycles, sulfate attack, and chloride permeability tests

Durability Parameter	Steel Slag Use Type & Replacement Level	Test Conditions / Parameters	Observed Durability Effect	Reference
Freeze–thaw resistance	Cementitious: 4%, 8%, 10%	30–80 cycles; strength ratio test	Strength ratio remained ~100% with increasing slag dosage	[103]
	Fine/coarse aggregate: 20%, 40%, 60%	Up to 150 cycles; dynamic modulus, weight loss	2.2–3.0% weight loss; modulus retained at 74.9–91.1% range	[104]
Sulfate resistance (wet–dry)	Coarse aggregate: 30%, 60%, 90%	56 days; compressive strength & modulus testing	Sulfate resistance improved; strength loss curve shows 3-phase behavior (initial ↑ then ↓)	[105]
Impermeability & porosity	Coarse: 0–80%, Fine: 0–60% (aggregate)	SEM & mercury intrusion analysis	Reduced harmful pores and total porosity; enhanced compactness and impermeability	[78]

5.1 Resistance to Freeze–Thaw Cycles

The incorporation of calcium sulfa-aluminate (CSA) cement in concrete formulations has been shown to significantly enhance durability under freeze–thaw conditions. In salt-rich environments, the number of freezes–thaw cycles endured by CSA-modified concrete increased from around 30 to 175, while in fresh water, it rose from approximately 150 to 300. These improvements are primarily attributed to the development of a denser interfacial transition zone (ITZ) and a reduction in matrix microcracking, both of which contribute to greater freeze–thaw resilience [106]. Abendeh et all. [81] investigated 0–75% replacement of fine and coarse aggregates with steel slag found up to 12% higher compressive strength at 75% replacement, coupled with superior freeze–thaw stability, as measured by ultrasonic pulse velocity retention after 250 cycles.

Steel slag, particularly when used as a fine aggregate at a 60% substitution level, has also demonstrated notable improvements in freeze–thaw resistance. Mixes incorporating this level of slag substitution exhibited minimal losses in both mass and compressive strength, along with elevated relative dynamic elastic modulus values, indicating strong resistance to structural degradation under cyclic thermal stresses [107].

5.2 Resistance to Sulfate-Induced Deterioration

The incorporation of steel slag as coarse aggregate in concrete has been shown to significantly improve resistance to sulfate-induced deterioration. In one study, concrete specimens with 60% steel slag replacement demonstrated a 20.7% increase in compressive strength when subjected to a 15% sulfate environment. This enhancement is primarily attributed to the presence of reactive mineral phases such as dicalcium silicate (C_2S) and tricalcium silicate (C_3S), which contribute to the formation of calcium silicate hydrate (C–S–H) gel, thereby improving structural integrity and reducing vulnerability to chemical attack. Further investigation by Cheng et al. [105] assessed sulfate durability under cyclic wetting and drying exposure. Their findings indicated that a 60% replacement level significantly increased the crack resistance coefficient (Kc), signifying enhanced resistance to sulfate ingress. The improved performance was linked to the hydration of free lime (f-CaO), which facilitated the formation of ettringite (AFt) and calcium hydroxide, leading to a denser microstructure and lower permeability.

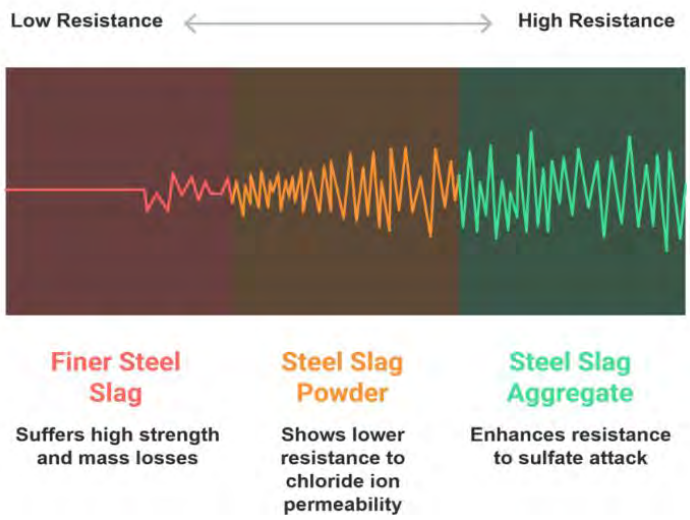


Fig. 5. Steel slag's impact on concrete durability under different conditions

Similarly, blended alkali-activated mixes composed of ground granulated furnace slag, lithium slag, and steel slag (GLS) achieved robust resistance to sodium sulfate attack, maintaining high compressive strength (> 70 MPa at 28 days) and showing minimal formation of expansive phases after prolonged exposure [108]. Another study focusing on cement mixes with 60% steel slag as aggregate confirmed that such mixes attained optimal sulfate resistance; the inclusion of slag's f-CaO hydration products enhanced internal densification, limiting sulfate ingress and reducing susceptibility to ettringite formation [109]. Finally, comparisons between steel-slag and natural-aggregate concretes immersed in sulfate-rich environments demonstrated that slag-containing concretes exhibited less surface deterioration and cracking under wetting–drying cycles, proving that steel slag contributes to denser microstructure and a more resistant interfacial transition zone—critical in halting sulfate penetration [110].

5.3 Chloride Permeability and Pore Structure

The use of steel slag, whether in the form of aggregate or powder, contributes to improved pore structure in concrete, particularly by reducing macro voids and refining capillary pores. This densification helps lower chloride diffusion coefficients and enhances the material's ability to bind chlorides, largely attributed to the presence of FeO-rich phases within the slag matrix [111]. Such effects are particularly beneficial in marine environments, where delaying chloride ingress is essential to minimizing corrosion risk and prolonging service life.

Chloride permeability performance varies depending on curing conditions and water-to-binder (w/b) ratios. In steam-cured mixes with steel slag, permeability remains moderate at higher w/b ratios but shows marked improvement when lower ratios are employed. When used in conjunction with ultrafine ground granulated blast furnace slag (UGGBS), the chloride resistance is further enhanced due to synergistic pore refinement and reduced ionic mobility [112].Meanwhile, investigations into alkali-activated mixtures containing steel slag showed that elevated slag content and optimized activator blends produced highly refined pore geometry, yielding low chloride diffusivity and superior permeability performance [113]. Other research confirmed that integrating iron and steel slag into concrete contributes to formation of dense, uniform interfacial transition zones and enhanced pore filling through secondary C–S–H and calcium carbonate, reducing total porosity and restricting pore connectivity [114].

Despite these advantages, long-term exposure studies have highlighted some limitations. Over a five-year period, concrete mixes containing steel slag powder exhibited lower resistance to chloride ion penetration than ordinary Portland cement (OPC) concrete. However, this drawback is mitigated when lower w/b ratios are used, suggesting that proper mix design can offset the material's inherent permeability issues [115]. Additionally, comparisons with other pozzolanic materials reveal that ground phosphate slag delivers superior chloride resistance compared to

ground granulated blast furnace slag (GGBS) or fly ash. This is attributed to its more compact and uniform pore network [116].

5.4 Microstructural Analysis via Scanning Electron Microscopy (SEM)

Scanning Electron Microscopy (SEM) offers a detailed view of the microstructure of concrete, particularly in assessing the influence of steel slag incorporation. It is frequently used to observe surface morphology, identify interfacial transitions, and detect microcracking or porosity that arise from hydration and drying processes. In concrete systems, the hydration of cement does not fully occupy the original water-filled voids, resulting in a network of pores ranging from a few nanometres to several microns, which directly impacts frost resistance and long-term durability. SEM analysis enables the visualization of these pore structures and microstructural changes caused by steel slag inclusion [104]. As shown in Fig. 6, notable differences can be observed between the control specimen (Fig. 6a) and the steel slag-modified concrete (Fig. 6b). The control sample exhibits visible microcracks and a loose matrix, indicating weaker interfacial bonding. In contrast, the steel slag-incorporated concrete shows a much denser and more compact structure, with tightly connected particles and fewer microcracks. This improved microstructure is attributed to the filler effect and nucleation sites provided by slag particles, which enhance hydration and packing density.

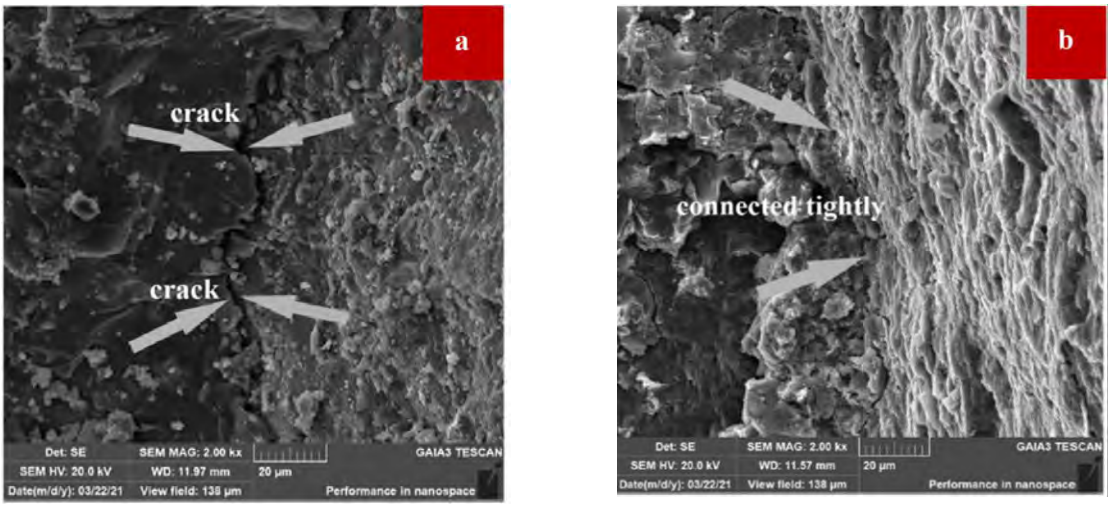


Fig. 6. SEM images of concrete: (a) Control mix with cracks; (b) Steel slag mix with dense, well-bonded structure [104]

6. Methodology

This study employed a bibliometric analysis to systematically examine the global research landscape surrounding the use of steel slag in concrete. The objective was to identify major thematic trends, uncover strategic research clusters, and chart future directions in this evolving field. Bibliometric analysis is a well-established, computer-assisted method for quantitatively evaluating scientific output. It enables researchers to track the development of knowledge domains, detect influential contributors, and expose underexplored areas [117,118]. Given its methodological rigor and capacity for large-scale synthesis, bibliometric analysis is increasingly recognized as a critical tool for strategic research planning across civil engineering and materials science disciplines.

The analytical framework in this study integrated two robust bibliometric tools: VOSviewer and the bibliometrix package in R. VOSviewer was used for visualizing bibliometric maps based on co-authorship, co-citation, and keyword co-occurrence data. The bibliometrix package, on the other hand, enabled comprehensive statistical evaluations and thematic classifications [119]. In constructing bibliometric networks, the study considered both full counting and fractional counting methods. Full counting assigns equal weight to all co-authors or keywords, offering a straightforward interpretation, while fractional counting apportions credit based on contribution,

providing more nuanced insights into collaboration patterns. The visual maps generated through these tools depict research entities such as authors, institutions, keywords, and journals as nodes, with their connections represented as edges signifying collaborative or thematic relationships.

The bibliometric methodology followed a structured multi-phase process. First, a dataset of relevant publications was retrieved from the Scopus database, chosen for its broad coverage of peer-reviewed literature in engineering, materials, and environmental science [120]. A dual-layered keyword search strategy was developed. The first layer targeted specific technical terms such as "steel slag concrete," "slag aggregate," "slag binder," and "slag replacement," while the second included broader sustainability terms like "green concrete," "waste utilization," and "low-carbon construction." This hybrid approach ensured that both technical performance and environmental implications of steel slag usage were captured.

The initial query retrieved 943 records. To ensure analytical reliability, a rigorous two-stage screening protocol was applied. In the first stage, only peer-reviewed journal articles and reviews were retained, excluding conference proceedings, book chapters, and editorials. Publications were restricted to the English language but included all years to allow longitudinal insights into research evolution. In the second stage, articles were evaluated for topical relevance, retaining only those that directly investigated the mechanical, durability, or environmental performance of steel slag in cementitious materials. The remaining dataset was refined further through dedication and metadata standardization using R, following the cleaning protocols outlined by Burnham [120]. This resulted in a final curated dataset of 880 unique publications. Additionally, Fig. 7 presents a conceptual framework linking historical research mapping with the identification of thematic clusters and the development of future research directions in the field of steel slag utilization in concrete.

These records formed the foundation for subsequent analyses. Using VOSviewer and bibliometrix, co-authorship networks were mapped to identify collaborative patterns among researchers and institutions, while keyword co-occurrence analysis revealed dominant and emerging themes in the literature. Citation analysis further highlighted seminal works and influential contributors. The integration of these methods provided a holistic view of the field, facilitating a data-driven exploration of both historical trajectories and emerging research frontiers in the utilization of steel slag for sustainable concrete production.

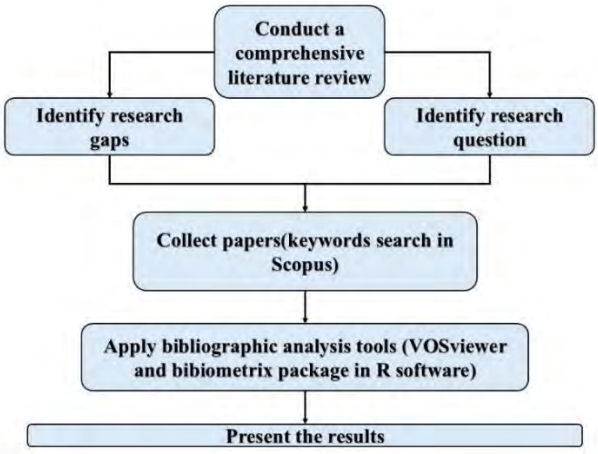


Fig. 7. Conceptual framework for bibliometric and experimental review of steel slag utilization in concrete

7. Document Analysis

7.1 Research Output Trends (2019–2024)

Analyzing publication trends provides critical insights into the evolution and maturity of research domain. Fig. 8 presents a detailed analysis of publication trends related to steel slag utilization in concrete from 2019 to 2023, capturing both annual outputs and cumulative growth. The data show

a steady increase in scholarly activity, with annual publications rising from 84 in 2019 to 169 in 2023, more than doubling over the five-year period. The cumulative number of publications reached 656 by 2023, highlighting a significant and sustained growth trajectory in the field.

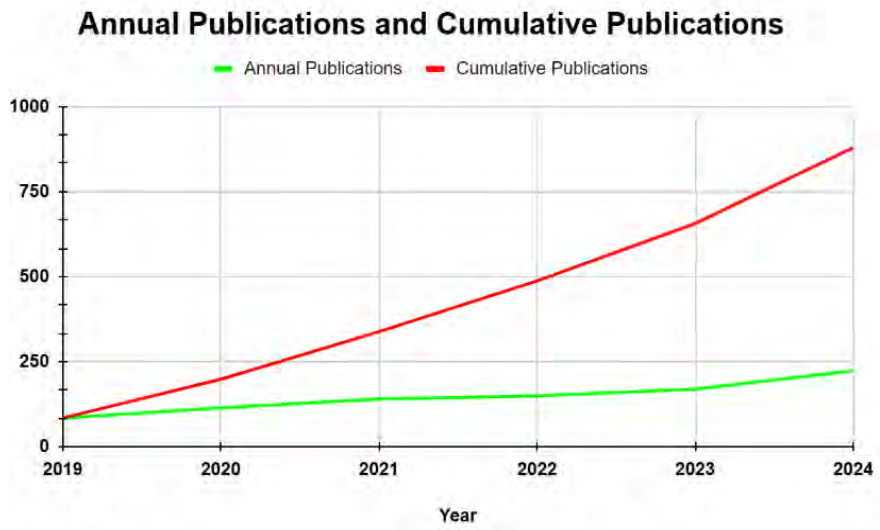


Fig. 8. Trend of publications on steel slag (2019–2024)

This upward trend indicates deepening academic interest in steel slag as a sustainable material in concrete production, driven by increasing global focus on circular economy practices and low-carbon construction alternatives. Although annual growth rates vary slightly from year to year, the consistent cumulative expansion points to the consolidation of steel slag research as a credible area within construction material science. The acceleration in annual outputs, particularly between 2021 and 2023, suggests an active shift from preliminary investigations to more advanced research addressing durability, mechanical performance, and environmental benefits.

The observed publication pattern reflects the rising importance of steel slag in addressing critical issues such as industrial waste management, resource efficiency, and cement reduction. Moving forward, research is likely to concentrate on optimizing slag processing techniques, enhancing its compatibility with supplementary cementitious materials, and assessing long-term structural performance under diverse environmental conditions. The cumulative publication surge affirms steel slag's emerging role in advancing sustainable and resilient infrastructure solutions.

7.2 Global Research Contributions by Country

Identifying the key contributing countries in the domain of steel slag utilization in concrete provides valuable insights into global research leadership, collaboration intensity, and knowledge dissemination. Fig. 9 and 10 offer a comparative analysis of the global distribution of research outputs and citation impacts in this field.

As presented in Fig. 9, China leads the global research landscape with 7,668 citations across 380 documents, indicating both prolific output and substantial scholarly influence. India follows with 1,844 citations from 163 publications, reflecting strong national commitment and growing visibility. Other notable contributors include Viet Nam (926 citations), Iraq (559 citations), and the United States (649 citations), each contributing significantly to the scientific discourse. Fig. 10 highlights the volume of publications by country. China again dominates with 380 documents, followed by India (163), South Korea (31), Viet Nam (32), and the United States (36), demonstrating concentrated research activity across Asia and North America. Countries like Australia, Saudi Arabia, Brazil, Malaysia, and Italy also show consistent engagement with 17–27 publications each, indicating broader international interest in steel slag applications.

Interestingly, there are discrepancies between publication counts and citation impact. For example, Germany and Portugal have fewer documents (9 and 21, respectively) but relatively high citations per paper, suggesting focused, high-impact studies. Similarly, Iraq and Viet Nam exhibit notable

citation strength despite smaller research volumes, likely attributed to internationally collaborative or innovative research outputs.

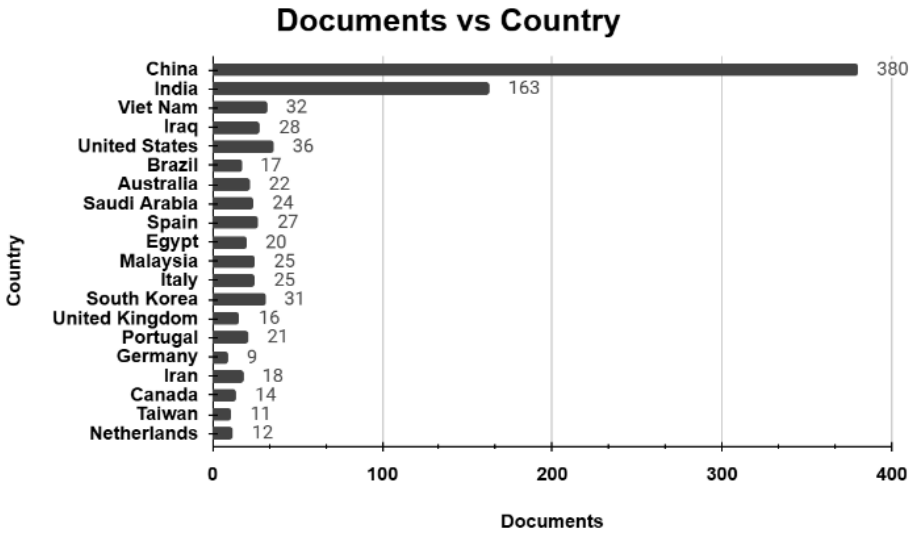


Fig. 9. Publication volume by country on steel slag concrete research

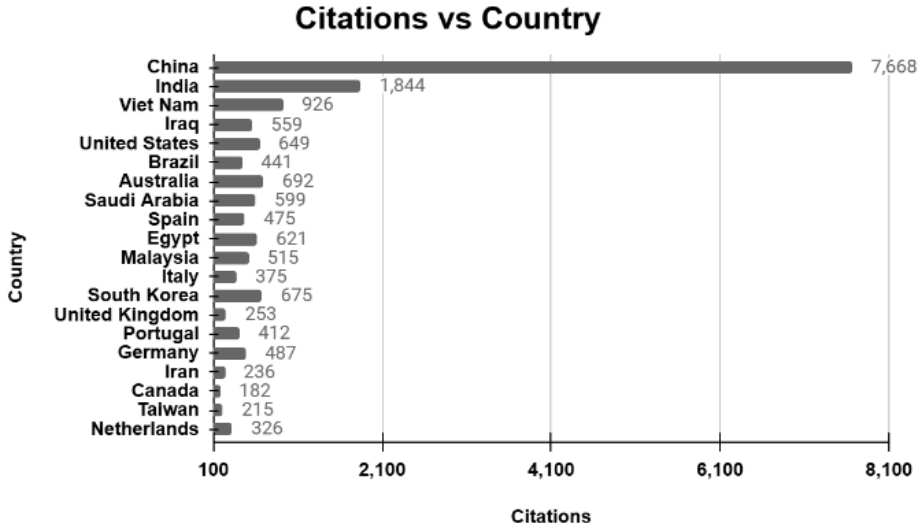


Fig 10. Citation impact of leading countries in steel slag concrete research

7.3 International Collaboration and Co-authorship Networks

The global distribution of research activity, as illustrated in Figure 11, highlights the highly interconnected and collaborative nature of the research landscape surrounding steel slag utilization in concrete. The visualization reveals dominant and densely linked research hubs, with China and India emerging as the most central and influential contributors evident from their large node sizes and extensive linkage with other countries. Other notable countries with strong collaborative networks include Iraq, Vietnam, South Korea, and the United States, indicating their significant roles in advancing knowledge through international partnerships.

The visual clustering of countries from different regions such as Europe (Germany, Italy, Portugal, Netherlands), Asia (China, India, Iraq, Malaysia, Vietnam), and the Middle East (Saudi Arabia, Egypt, Iran) underscores the global and multidisciplinary nature of the research community. The network density and cross-continental connections reflect a robust ecosystem of scientific exchange, where nations with varying technological capacities and research infrastructures collaborate on shared objectives, such as sustainable construction, circular economy practices, and low-carbon concrete solutions.

The sharp increase in publication volume reflects not only scholarly interest but also the rising industrial demand for steel slag as a sustainable construction material. As environmental regulations tighten and the push for low-carbon infrastructure accelerates, many countries are incentivizing the reuse of industrial by-products like steel slag in concrete and pavement applications. Global steel production continues to grow, generating over 250 million tons of slag annually—of which a substantial portion remains underutilized. This underlines the enormous untapped potential of steel slag in replacing natural aggregates and cement, particularly in emerging economies facing raw material scarcity. Based on current publication trajectories and global infrastructure trends, it is anticipated that steel slag utilization in cementitious systems could double within the next decade, especially with the adoption of smart concrete technologies, carbonation treatments, and circular economy frameworks.

7.4 Temporal and Geographic Distribution

Fig. 12 illustrates the global distribution of research activity on steel slag utilization in concrete between 2019 and 2024, with countries shaded according to their average publication year, indicating the recency and maturity of research engagement. The map highlights significant contributions from China and India, both of which demonstrate high publication volumes and recent research activity, with average publication years of 2022.09 and 2021.95, respectively. These countries also exhibit strong international collaboration, reinforcing their leadership roles in the global steel slag research network.

Notably, countries such as Canada (2022.83), Egypt (2021.82), and Brazil (2021.59) reflect sustained and timely engagement, suggesting their growing interest in sustainable construction materials. Australia (2021.00), while showing slightly earlier average activity, remains a consistent contributor to international efforts. This trend underscores the geographical expansion of scholarly participation, with newer entrants like Malaysia, Iran, and South Korea also playing increasingly prominent roles in regional research ecosystems.

The color gradient in the spatial visualization—ranging from earlier to more recent average publication years—demonstrates both the temporal dynamics and geographic breadth of research. Countries with darker shading reflect more recent academic focus, pointing to ongoing innovation and growing institutional attention. This global map reinforces the importance of cross-border collaboration and knowledge exchange, emphasizing how diverse nations are collectively contributing to the advancement of low-carbon, resource-efficient concrete technologies using steel slag.

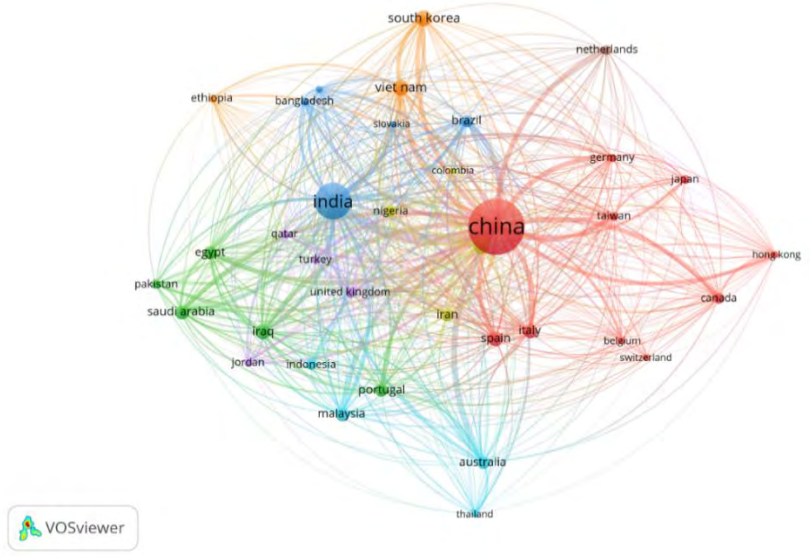


Fig. 11. Global co-authorship network showing collaboration intensity in steel slag research

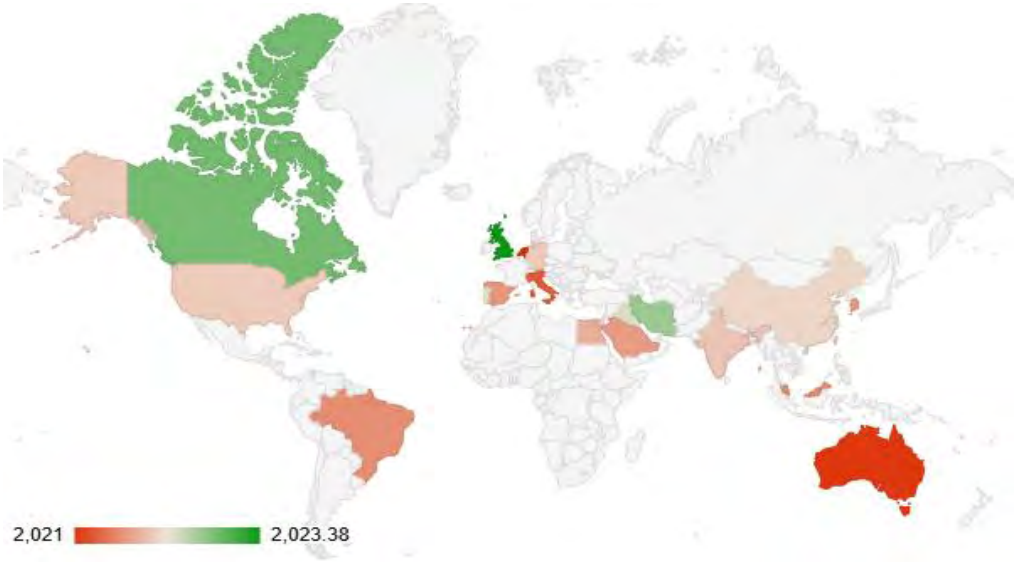


Fig. 12. Average publication year by country in steel slag concrete research (2019–2024)

7.5 Leading Institutions and Research Organizations

The analysis of institutional contributions to steel slag utilization in concrete research reveals a dynamic and globally interconnected academic landscape. Fig. 13 highlights the most active organizations in this domain, with the State Key Laboratory of Silicate Materials for Architectures at Wuhan University of Technology (China) leading with 25 publications and 624 citations, underscoring its central role in advancing sustainable construction materials. Following closely are prominent institutions such as the Civil Engineering Department, University of Sulaimani (Iraq) with 8 publications and 264 citations, and the Department of Highway and Bridge Engineering, Erbil Polytechnic University (Iraq) with 6 publications and a notable total link strength of 8,747, reflecting strong research connectivity and collaboration.

Several other institutions also demonstrate sustained contributions, including the School of Civil Engineering at Central South University (China), Soran University (Iraq), and Shenyang Jianzhu University (China), each with 6 publications, indicating robust regional engagement. Specialized research centers such as the State Key Laboratory of Solid Waste Reuse for Building Materials and the School of Civil and Resource Engineering at the University of Science and Technology Beijing further emphasize China's extensive investment in steel slag innovation. This institutional distribution reflects not only the multidisciplinary nature of steel slag research but also the growing global commitment to transforming industrial waste into high-performance construction materials. The breadth of contributing universities across Asia and the Middle East highlights an expanding international research network addressing critical challenges in cement reduction, resource recovery, and sustainable infrastructure development.

At the individual level, Fig. 14 highlights the most prolific authors contributing to the advancement of steel slag utilization in concrete. Ni, Wen leads the field with 13 publications, reflecting both consistent scholarly output and a strong presence in collaborative networks. Wu, Shaopeng follows closely with 11 publications, indicating sustained engagement in research focused on sustainable pavement and concrete materials. Other highly active contributors include Hamad, Samir M. and Mo, Liwu, each with 8 publications, suggesting their significant roles in advancing technical understanding and environmental applications of steel slag. Lai, M.H., also with 8 publications, has contributed notably to performance analysis and materials innovation. These leading researchers exemplify the growing depth and specialization within the field, driving innovation through both experimental research and international collaboration.

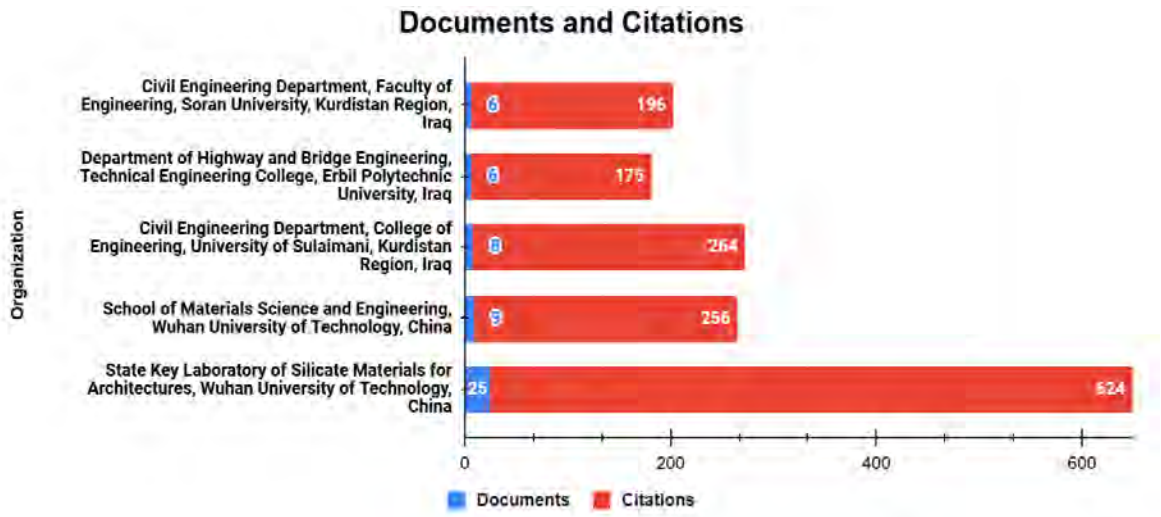


Fig. 13. Top contributing organizations in steel slag concrete research, with data on publications, citations, and research link strength

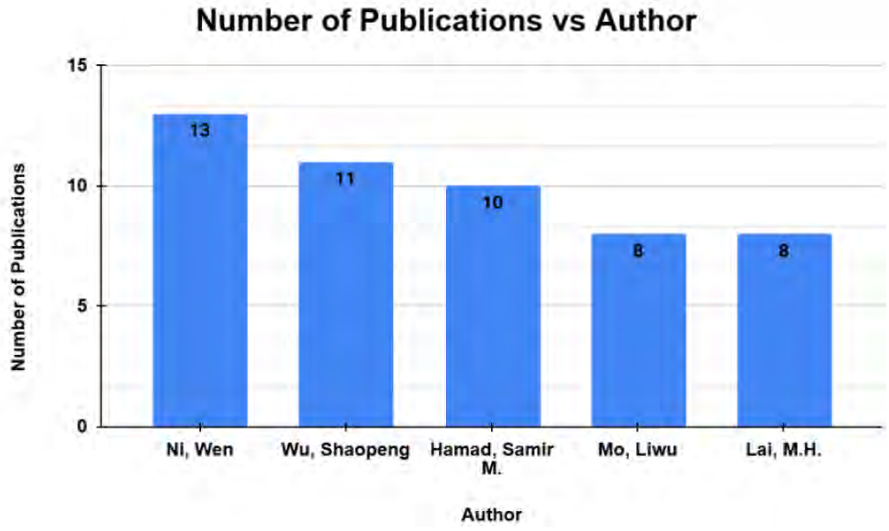


Fig. 14. Top five most active authors in steel slag research based on publication count

7.6 Citation Impact and Influential Publications

Another important consideration for researchers is identifying publications that have significantly contributed to advancing academic knowledge in the field of steel slag utilization in concrete. Citation analysis serves as a key indicator for determining the impact of scholarly work, revealing foundational studies, emerging research directions, and influential technological developments. Highly cited publications often represent pioneering research that has shaped scientific discourse and laid the groundwork for further innovation.

To identify the most influential articles and their contributions, Table 6 presents the top five highly cited publications in the domain. These studies encompass diverse themes such as material reuse, durability, mechanical performance, and sustainability in concrete production. The publication titled "Use of steel slag as sustainable construction materials for artificial reef: Engineering and ecological perspectives" by Song et al. leads with 286 citations, reflecting its groundbreaking role in both engineering application and ecological assessment. Closely following is the paper "Steel slag and its applications in cement and concrete technology: A review" by Gencel et al., also with 285 citations, which provides a comprehensive review of steel slag's performance as a cementitious material and aggregate substitute.

Another major contribution is the study by Van Dao et al., "Artificial intelligence approaches for predicting properties of concrete containing industrial waste: A review", which garnered 283

citations, showcasing the growing relevance of AI-based modeling in sustainable materials research. Also notable is "Recycling of steel slag aggregate in portland cement concrete: An overview" by Dong et al., with 196 citations, emphasizing the practical implications of steel slag in concrete recycling and infrastructure design. Finally, the study "Performance of geopolymer concrete containing steel slag aggregate: Mechanical and microstructural properties" by Aly et al., with 191 citations, highlights the integration of steel slag into geopolymer systems for enhanced sustainability and performance.

Table 6. Most highly cited publications on steel slag applications in concrete, indicating foundational contributions to the field

Ref	Title	Year	Total Citations
[121]	Use of steel slag as sustainable construction materials: A review of accelerated carbonation treatment	2021	286
[7]	Steel slag and its applications in cement and concrete technology: A review	2021	285
[60]	Artificial intelligence approaches for prediction of compressive strength of geopolymer concrete	2019	283
[122]	Recycling of steel slag aggregate in Portland cement concrete: An overview	2021	196
[123]	Performance of geopolymer concrete containing recycled rubber	2019	191
[124]	Preparation, microstructure and property of carbonated artificial steel slag aggregate used in concrete	2020	150
[125]	Strength performance of cement/slag-based stabilized soft clays	2019	145
[126]	Application of steel slag in cement treated aggregate base course	2020	143
[127]	Environmental benefit assessment of steel slag utilization and carbonation: A systematic review	2022	143
[78]	Improving mechanical behavior and microstructure of concrete by using BOF steel slag aggregate	2021	141

Fig. 15 illustrates the publication trends from 2019 to 2024 in the five most prolific journals contributing to research on steel slag utilization in concrete. The data clearly show that Construction and Building Materials stands out as the dominant publication outlet, with a strong and increasing output that peaked sharply at 40 publications in 2024, underscoring its central role in disseminating cutting-edge research on sustainable concrete technologies.

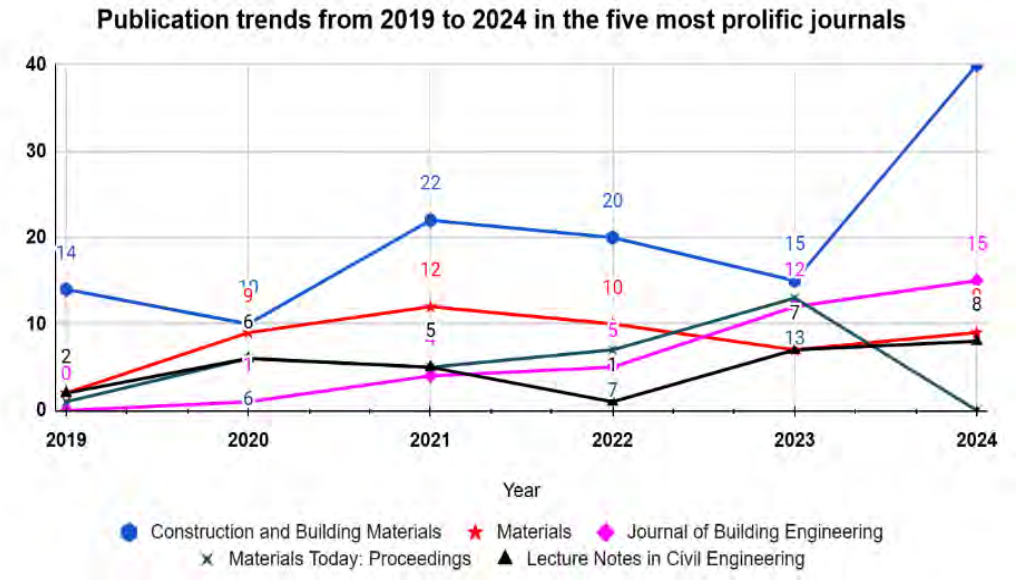


Fig. 15. Publication trends in the five most productive journals contributing to steel slag concrete research from 2019 to 2024

Materials follow as another key contributor, maintaining a steady upward trend in publication volume, particularly between 2020 and 2021, and sustaining consistent contributions through

2024. This highlights the journal's significance in addressing materials innovation and waste valorization in cementitious systems. Journal of Building Engineering shows a dramatic rise in output beginning in 2021, increasing to 15 publications by 2024, indicating growing attention to steel slag applications in practical and structural engineering contexts. Materials Today: Proceedings also demonstrated significant productivity, especially in 2023, with earlier peaks in 2020 and 2021, reflecting the importance for conference-based dissemination of emerging research. Meanwhile, Lecture Notes in Civil Engineering maintained stable activity throughout the period, with notable publication counts in 2020, 2021, and 2023, emphasizing its role in presenting steel slag research within academic and technical proceedings. Overall, these publication trends reveal the interdisciplinary and practice-oriented nature of steel slag research. The consistent and growing output across engineering and materials science journals underscores the critical role of these platforms in supporting sustainable construction innovation and circular economy approaches in civil infrastructure.

7.7 Keyword Co-occurrence and Thematic Clustering

The keyword co-occurrence network generated using VOSviewer, as shown in Fig. 16, reveals distinct clusters that reflect the thematic focus of steel slag research in concrete applications. These clusters emerge from the frequency and co-usage of keywords across hundreds of publications and represent the structure of scientific discourse in this field. Prominent terms such as "steel slag," "compressive strength," "durability," "concrete aggregates," and "hydration" dominate the network, indicating the core technical concerns related to mechanical performance, mix design, and material sustainability. The clustering also points to research pathways in waste valorization, microstructure evaluation, and structural optimization.

This cluster centers on the incorporation of steel slag in cementitious systems and the optimization of concrete mixtures. Core keywords include steel slag, concrete aggregates, cements, portland cement, coarse aggregates, and blast furnaces. Research in this area focuses on evaluating steel slag as a replacement for natural aggregates or as a supplementary cementitious material. Studies emphasize its influence on workability, setting time, and hardened properties Key challenges include ensuring particle compatibility, preventing excessive expansion due to free lime or magnesium oxide, and maintaining consistency across slag sources. Researchers are also investigating the role of hydration behavior and cement chemistry in mixtures with varying slag contents.

This cluster highlights performance-related themes such as compressive strength, tensile strength, durability, microstructure, and mechanical properties. These studies evaluate the effects of steel slag on the physical and structural behavior of concrete under short- and long-term loading. Advanced characterization techniques—such as scanning electron microscopy (SEM), X-ray diffraction (XRD), and ultrasonic pulse velocity (UPV)—are often used to investigate microstructural refinement, pore structure, and strength development. Numerous studies report that steel slag incorporation improves mechanical resilience due to its angularity, hardness, and mineral content. For example, reports increased compressive and tensile strength when steel slag is used as a coarse aggregate, particularly in synergy with fly ash or silica fume. Meanwhile, durability evaluations address carbonation resistance, sulfate attack, and freeze-thaw performance—key considerations in structural and pavement applications.

A third thematic group focuses on environmental concerns and sustainability frameworks. Dominant terms include recycling, sustainable development, construction industry, global warming, carbon dioxide, and carbonation. This cluster reflects the circular economy potential of steel slag and its role in reducing the carbon footprint of traditional Portland cement production. Researchers explore the lifecycle benefits of using industrial by-products, including lower greenhouse gas emissions, reduced reliance on virgin raw materials, and long-term resource efficiency. Studies such as emphasize the dual benefits of performance and environmental impact reduction, especially when slag is sourced from electric arc furnace (EAF) or blast furnace (BF) processes. The integration of steel slag into low-carbon construction strategies, combined with supportive policy and industry practices, underscores its growing relevance in achieving sustainability targets and enhancing the resilience of infrastructure.

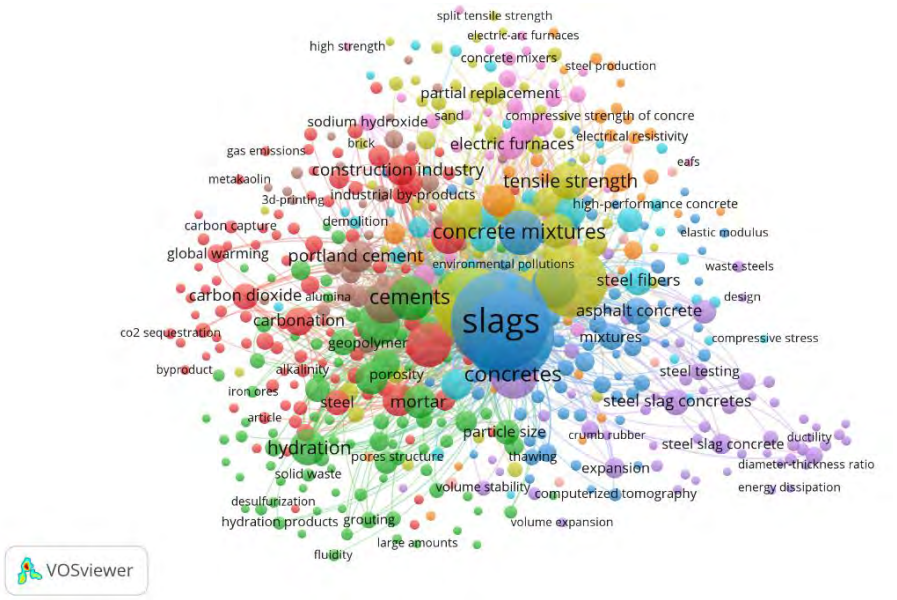


Fig. 16. Keyword co-occurrence network visualizing thematic clusters in steel slag research, generated using VOSviewer.

8. Future Research Pathways in Steel Slag Utilization in Concrete

Building upon the bibliometric findings and keyword clustering shown in Fig. 17, several underexplored and emerging directions in the field of steel slag-based concrete have been identified. These future research pathways not only reflect ongoing advances in sustainable construction materials but also align with global efforts to reduce industrial waste, decarbonize cement production, and enhance infrastructure resilience. As the construction industry seeks innovative, eco-efficient solutions, the following areas warrant focused investigation. With increasing demand for decarbonized materials, steel slag is expected to play a pivotal role in green construction strategies, especially as policy and performance standards evolve to support large-scale industrial reuse.

One promising avenue is the development of smart concrete systems using steel slag, particularly through the integration of embedded sensors and self-monitoring technologies. Despite the rising interest in structural health monitoring and durability tracking, there remains a gap in applying these innovations to slag-containing concrete. Future research should explore self-sensing concrete using conductive steel slag fillers, enabling real-time monitoring of crack formation, temperature, and stress conditions—especially in harsh environments or critical infrastructure applications.

Another important direction is the optimization of binder systems incorporating steel slag. While blended cements with fly ash, GGBS, and steel slag have demonstrated improved mechanical properties and durability, the performance of alkali-activated binders, geopolymers, and carbonated slag systems remains under-researched. Future studies should investigate how varying activation methods and mix proportions influence hydration kinetics, shrinkage behavior, and long-term performance across diverse exposure conditions.

Additionally, research should focus on long-term durability and microstructural evolution of slag-based concrete. Though compressive strength and tensile behavior are widely reported, fewer studies have examined sulfate attack, chloride ingress, alkali-silica reaction, or freeze-thaw resistance in slag-rich mixes. Life-cycle studies combining mechanical degradation with environmental exposure are essential to validate steel slag's reliability in large-scale structural applications.

A critical challenge remains in standardizing slag quality and treatment. Due to variations in chemical composition and mineralogy between blast furnace slag and electric arc furnace (EAF)

slag, establishing pre-treatment protocols (e.g., aging, carbonation, or magnetic separation) is key to ensuring consistent performance. Future research should establish internationally harmonized guidelines for slag classification, processing, and suitability for concrete production.

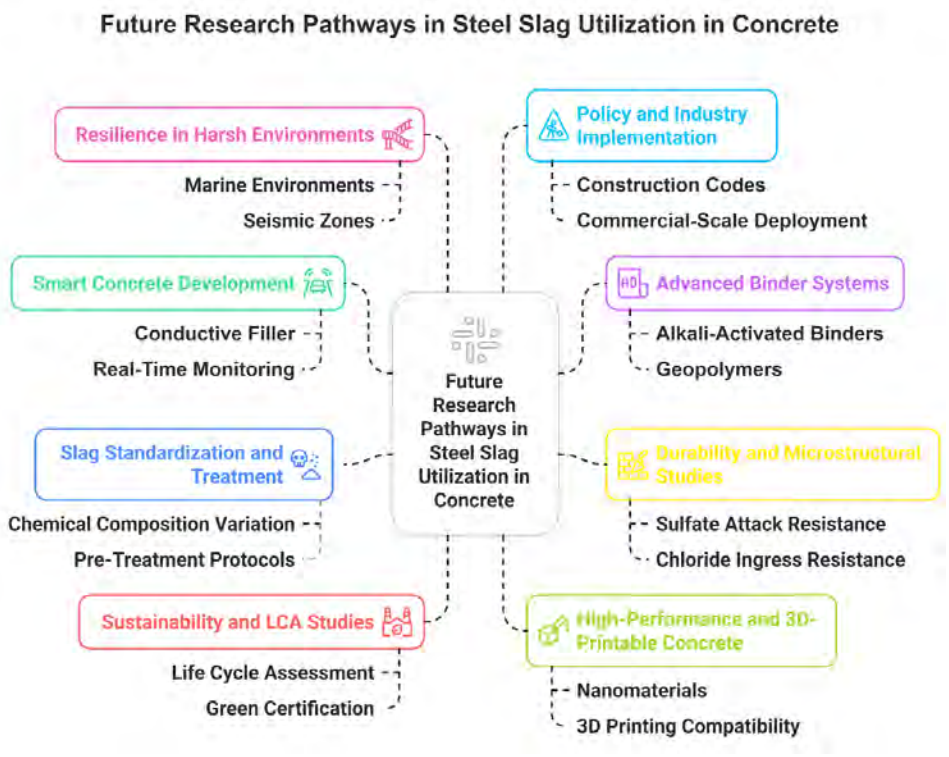


Fig. 17. Future research pathways in steel slag utilization in concrete

From a sustainability perspective, comprehensive life cycle assessment (LCA) and carbon footprint analysis of slag-concrete systems are urgently needed. While environmental benefits such as reduced clinker demand and waste reuse are well acknowledged, data on embodied energy, transport emissions, and economic feasibility remain limited. Future work should develop standardized LCA frameworks integrating environmental, economic, and social dimensions to support green certification and policy adoption.

Moreover, high-performance concrete (HPC) and ultra-high-performance concrete (UHPC) with steel slag present untapped potential. The synergy of steel slag with nanomaterials (e.g., nano-silica or graphene oxide), fiber reinforcements, or superplasticizers in HPC systems can yield advanced mechanical properties, ductility, and toughness. Investigations into 3D-printable slag-based concrete for digital construction could further revolutionize applications in sustainable building technologies.

Resilience under extreme environmental conditions—such as aggressive marine exposure, high thermal gradients, and seismic loading—is another vital frontier. Future studies should prioritize the adaptation of slag concrete for coastal defenses, transport infrastructure, and post-disaster reconstruction, ensuring durability and performance under climate-induced stressors.

Finally, there is scope for exploring policy frameworks and industry implementation models. Despite technical feasibility, widespread adoption of steel slag concrete faces regulatory, logistical, and market challenges. Research into construction codes, public procurement incentives, and supply chain optimization can facilitate the transition from lab-scale innovation to industry-wide application.

9. Conclusion

This study presents a holistic and multidisciplinary assessment of steel slag utilization in concrete, bridging bibliometric mapping with detailed experimental evidence to draw meaningful insights

for sustainable construction practices. Through the analysis of 880 Scopus-indexed publications and the critical synthesis of material performance data, the review provides a clear roadmap for transforming steel slag from a high-volume industrial by-product into a strategic component in low-carbon cementitious systems.

- Material Suitability and Composition: Steel slag, owing to its mineralogical composition—including reactive phases like C_2S, C_3S, and RO solids—exhibits promising cementitious and pozzolanic properties. Its high density, angularity, and latent hydraulic reactivity make it suitable for use as both binder and aggregate replacement, albeit requiring pre-treatment to mitigate expansion risks due to f-CaO and MgO.
- Workability Considerations: The fresh-state performance of slag-based concrete is highly dosage-sensitive. As a binder, steel slag enhances slump at around 15% replacement but reduces it at higher dosages. As fine aggregate, 30% substitution maintains cohesion and flowability. Coarse slag negatively affects workability due to angular morphology, though this can be offset using admixtures or optimized grading.
- Mechanical Performance Optimization: Experimental findings confirm that steel slag can significantly enhance mechanical properties. Optimal compressive strength (up to 124.4 MPa) was recorded in CO_2-cured mixes with 50% coarse aggregate replacement. Cement replacement at 10–15% consistently delivered compressive strengths above 42 MPa, while hybrid systems involving GGBFS or silica fume showed synergistic strength gains.
- Durability Enhancement: Durability outcomes further reinforce steel slag's suitability for long-life infrastructure. Notable improvements were observed in sulfate resistance, freeze–thaw durability, and chloride impermeability. SEM analysis confirmed denser microstructures with reduced pore connectivity, supporting long-term performance under aggressive environmental exposures.
- Optimal Compositions: Based on an extensive literature review, ideal substitution ratios include 10–15% for cement, 30% for fine aggregates, and 30–50% for coarse aggregates. In SCC and UHPC, 2% slag-derived steel fiber and 30% slag powder yielded high ductility and strength, supporting structural applications with enhanced sustainability.
- Bibliometric Insights: The bibliometric component highlighted exponential growth in steel slag research from 2019–2024, with China, India, and Iraq leading in both output and influence. Keyword clustering revealed thematic foci in mechanical performance, durability, and environmental optimization. VOSviewer analysis illustrated growing international collaboration and identified underexplored niches such as self-sensing concrete and slag–geopolymer synergy.
- Research Gaps and Future Pathways: Despite significant progress, several challenges remain. These include slag heterogeneity, lack of universal treatment standards, limited field-scale validations, and incomplete understanding of long-term performance under extreme conditions (marine environments, seismic zones). Future work must address smart concrete systems, nanomaterial integration, alkali activation mechanisms, and life-cycle cost–benefit analysis.
- Policy and Industry Relevance: From a policy perspective, encouraging steel slag usage through incentives, green labeling, and performance-based codes can accelerate market uptake. Industry implementation will benefit from robust standards, pre-treatment protocols, and validated mix designs tailored to regional material characteristics.

In conclusion, steel slag offers a high-potential route toward sustainable, durable, and resilient infrastructure. Through targeted optimization, interdisciplinary research, and policy support, this material can transition from an industrial burden into a key enabler of circular economy in the construction sector. This review provides a comprehensive foundation for researchers, engineers, and policymakers to collaboratively advance the large-scale adoption of steel slag in next-generation concrete systems.

Acknowledgement

The authors acknowledge that this study is supported by Universitas Muhammadiyah Yogyakarta.

References

[1] Chen J, Sun Y, Zhang Z. Evolution of trace elements and polluting gases toward clean co-combustion of coal and sewage sludge. Fuel 2020;280. https://doi.org/10.1016/j.fuel.2020.118685

[2] Nikitina N, Abdrakhimova E, Buynitsky G. Reducing ecological damage to flora and fauna through the use of waste from oil production as porous fillers in manufacturing. E3S Web of Conferences, vol. 389, 2023. https://doi.org/10.1051/e3sconf/202338902001

[3] Al-Taai SHH. Solid waste: A study of its concept, management methods, and environmental impacts. IOP Conf Ser Earth Environ Sci, vol. 1002, 2022. https://doi.org/10.1088/1755-1315/1002/1/012007

[4] Zhang R, Qureshi TS, Panesar DK. Use of industrial waste in construction and a cost analysis. 2021. https://doi.org/10.1016/B978-0-12-821730-6.00019-X

[5] Baalamurugan J, Kumar VG, Padmapriya R, Raja VKB. Recent applications of steel slag in construction industry. Environ Dev Sustain 2024;26. https://doi.org/10.1007/s10668-022-02894-3

[6] Zhao J, Hu W, Ni W, Guo J, Zhu W, Su S. The Effect of Removing Hard-to-Grind Minerals from Steel Slag on Efficient Grinding and Hydration Activity. Journal of Sustainable Metallurgy 2023;9. https://doi.org/10.1007/s40831-023-00728-8

[7] Gencel O, Karadag O, Oren OH, Bilir T. Steel slag and its applications in cement and concrete technology: A review. Constr Build Mater 2021;283. https://doi.org/10.1016/j.conbuildmat.2021.122783

[8] Ren Z, Li D. Application of Steel Slag as an Aggregate in Concrete Production: A Review. Materials 2023;16. https://doi.org/10.3390/ma16175841

[9] Li X, Gu X, Zhang W, Liu J, Li Z, Liu B. An ecological composites for a novel class of solid waste concrete. Mater Lett 2024;361. https://doi.org/10.1016/j.matlet.2024.136082

[10] Zhang T, Peng H, Wu C, Guo Y, Wang J, Chen X, et al. Process compatible desulfurization of NSP cement production: A novel strategy for efficient capture of trace SO2 and the industrial trial. J Clean Prod 2023;411. https://doi.org/10.1016/j.jclepro.2023.137344

[11] Fernández-Jiménez A, Garcia-Lodeiro I, Maltseva O, Palomo A. Sustainable Cements: Hybrid Alkaline Cements Overview. RILEM Bookseries, vol. 40, 2023. https://doi.org/10.1007/978-3-031-21735-7_68

[12] El Fami N, Ez-zaki H, Boukhari A, Khachani N, Diouri A. Influence of mechanical activation of fly ash on the properties of Portland cement mortars. Mater Today Proc, vol. 58, 2022, p. 1419–22. https://doi.org/10.1016/j.matpr.2022.02.340

[13] Fernández-Jiménez A, Garcia-Lodeiro I, Maltseva O, Palomo A. Sustainable Cements: Hybrid Alkaline Cements Overview. vol. 40. 2023. https://doi.org/10.1007/978-3-031-21735-7_68

[14] Belaïd F. How does concrete and cement industry transformation contribute to mitigating climate change challenges? Resources, Conservation and Recycling Advances 2022;15. https://doi.org/10.1016/j.rcradv.2022.200084

[15] Cabral JS, Menegatti CR, Nicolodelli G. Laser-induced breakdown spectroscopy in cementitious materials: A chronological review of cement and concrete from the last 20 years. TrAC - Trends in Analytical Chemistry 2023;160. https://doi.org/10.1016/j.trac.2023.116948

[16] El Messiry M, Al-Oufy A, Elmor M. Investigations of the recycling of airbag filters from the cement industry into fabric/polymer or fabric/cement composite materials. Discover Applied Sciences 2024;6. https://doi.org/10.1007/s42452-024-05632-8

[17] Barbhuiya S, Kanavaris F, Das BB, Idrees M. Decarbonising cement and concrete production: Strategies, challenges and pathways for sustainable development. Journal of Building Engineering 2024;86. https://doi.org/10.1016/j.jobe.2024.108861

[18] Haslinger G, Leuchtenmüller M, Steinlechner S. The Behaviour of Minor Metals in BOF Slag Under Different Additives. Minerals, Metals and Materials Series, 2023. https://doi.org/10.1007/978-3-031-22761-5_29

[19] Brand AS, Fanijo EO. A review of the influence of steel furnace slag type on the properties of cementitious composites. Applied Sciences (Switzerland) 2020;10. https://doi.org/10.3390/app10228210

[20] Wang Y, Zhao D, Li Z, Gao X, Shen W, Wang G, et al. Mineral Phase Transformation and Properties of Steel Slag in Process of Melting and Sintering. Bulletin of the Chinese Ceramic Society 2023;42

[21] Andrade FKG, Pires TAC, Silva JJR. Influence of silicon-dioxide nanoparticles in cementitious mortars: verification using x-ray diffraction, thermal analysis, physical, and mechanical tests. Mater Res Express 2023;10. https://doi.org/10.1088/2053-1591/acb4e1

[22] Paruthi S, Rahman I, Husain A, Hasan MA, Khan AH. Effects of Chemicals Exposure on the Durability of Geopolymer Concrete Incorporated with Silica Fumes and Nano-Sized Silica at Varying Curing Temperatures. Materials 2023;16. https://doi.org/10.3390/ma16186332

[23] Seshaiah B, Rao PS, Rao PS. Effect of mineral admixtures on the properties of steel fibre reinforced SCC proportioned using plastic viscosity and development of regression & ANN model. Computers and Concrete 2021;27:523–35. https://doi.org/10.12989/cac.2021.27.6.523

[24] Aowrangzib MA, Tangri A. Evaluation of strength properties of concrete by integrating different fibres with different aspect ratios. AIP Conf Proc, vol. 3100, 2024. https://doi.org/10.1063/5.0212623
[25] Januzzi RV, Costa LCB, Peixoto RAF, Cury AA. Study of the mechanical behavior of prisms composed by two blocks produced with electrical steel slag for structural masonry. Masonry International 2018;31:80–7
[26] Pernebekova G, Satyanaga A, Abishev R, Moon S-W, Kim J. Water characteristic curve and permeability function of steel slag. 2023. https://doi.org/10.1201/9781003299127-64
[27] Shi J, Shen Y, Zhang W, Fu Y, Kong X. Effects of three different nanomaterials on the properties and microstructure of sludge based geopolymers. Constr Build Mater 2024;414. https://doi.org/10.1016/j.conbuildmat.2024.134965
[28] Václavík V, Ondová M, Dvorský T, Eštoková A, Fabiánová M, Gola L. Sustainability potential evaluation of concrete with steel slag aggregates by the lca method. Sustainability (Switzerland) 2020;12. https://doi.org/10.3390/su12239873
[29] Tharun Teja G, Paluri Y, Pampana LD, Rebka Y. Evaluating the strength and durability characteristics of concrete incorporating steel slag, GGBS and silica fume. J Phys Conf Ser, vol. 2779, 2024. https://doi.org/10.1088/1742-6596/2779/1/012004
[30] Martins ACP, Franco de Carvalho JM, Costa LCB, Andrade HD, de Melo TV, Ribeiro JCL, et al. Steel slags in cement-based composites: An ultimate review on characterization, applications and performance. Constr Build Mater 2021;291. https://doi.org/10.1016/j.conbuildmat.2021.123265
[31] Jonczy I. Forms of occurrence of selected alloying elements in slag from an electric arc furnace. IOP Conf Ser Earth Environ Sci, vol. 261, 2019. https://doi.org/10.1088/1755-1315/261/1/012017
[32] Chen Y, Yang Q, Han F, Jiang L, Zhang L. Characterization and cementitious properties of BOF slag. vol. 680. 2016. https://doi.org/10.4028/www.scientific.net/KEM.680.462
[33] Liu J, Guo R. Applications of Steel Slag Powder and Steel Slag Aggregate in Ultra-High Performance Concrete. Advances in Civil Engineering 2018;2018. https://doi.org/10.1155/2018/1426037
[34] Murmu M. Evaluation Of Strength Characteristics Of Steel Slag Hydrated Matrix Master of Technology in Civil Engineering 2009.
[35] Chen Z, Liu J, Li R. Simulation and property prediction of MgO-FeO-MnO solid solution in steel slag. Mater Lett 2020;273. https://doi.org/10.1016/j.matlet.2020.127930
[36] Lin Y, Liu Y, Chou K, Shu Q. Effects of oxygen atmosphere, FeOx and basicity on mineralogical phases of CaO–SiO2–MgO–Al2O3–FetO–P2O5 steelmaking slag. Ironmaking and Steelmaking 2019;46. https://doi.org/10.1080/03019233.2018.1470362
[37] Xu J, Zhang J, Jie C, Liu G, Ruan F. Measuring and modeling of viscosities of selected CaO-MgO-Al 2O3-SiO2 slags. Adv Mat Res, vol. 152–153, 2011. https://doi.org/10.4028/www.scientific.net/AMR.152-153.782
[38] Yang G, Meng X, Yang R, Zeng R, Li W. Influence of Basicity on the Viscosity and Crystallization of Slag from the Double Slag Converter Steelmaking Process. JOM 2025;77:2383–91. https://doi.org/10.1007/s11837-025-07179-4.
[39] Kabeta WF, Lemma H. Modeling the application of steel slag in stabilizing expansive soil. Model Earth Syst Environ 2023;9:4023–30. https://doi.org/10.1007/s40808-023-01734-1.
[40] Zhang Y, Zhu G, Zhang Y, Wu X, Zhang F, Zhang J, et al. Hydration behavior and cementitious properties of steel slag: From an early age to a long-term. Case Studies in Construction Materials 2024;20. https://doi.org/10.1016/j.cscm.2024.e03066.
[41] Wu H, Xu F, Li B, Gao Q. Study on Expansion Rate of Steel Slag Cement-Stabilized Macadam Based on BP Neural Network. Materials 2024;17. https://doi.org/10.3390/ma17143558.
[42] Kalácska Á, De Baets P, Ben Hamouda H, Theuwissen K, Sukumaran J. Tribological investigation of abrasion resistant steels with martensitic and retained austenitic microstructure in single- and multi–asperity contact. Wear 2021;482–483. https://doi.org/10.1016/j.wear.2021.203980.
[43] Zhuang S, Wang Q. Inhibition mechanisms of steel slag on the early-age hydration of cement. Cem Concr Res 2021;140. https://doi.org/10.1016/j.cemconres.2020.106283.
[44] He J, Xiao R, Nie Q, Zhong J, Huang B. High-volume coal gasification fly ash–cement systems: Experimental and thermodynamic investigation. Constr Build Mater 2023;377. https://doi.org/10.1016/j.conbuildmat.2023.131082.
[45] Liu J, Wang M, Liu N, Teng L, Wang Y, Chen Z, et al. Development of ultra-fine SAP powder for lower-shrinkage and higher-strength cement pastes made with ultra-low water-to-binder ratio. Compos B Eng 2023;262. https://doi.org/10.1016/j.compositesb.2023.110810.
[46] Zang J, Li W, Shen X. The influence of steel slag with variable particle size distribution on the workability and mechanical properties of concrete. Ceramics Silikaty 2019;63:67–75. https://doi.org/10.13168/cs.2018.0046.
[47] Verma SK, Kodwani H, Asange S. Influence Of Aggregate Properties On Characteristics Of Concrete. Revista Romana De Materiale Romanian Journal of Materials 2022;52:293–302.

[48] Darwis Z, Fathonah W, Hadi F. Steel Slag's Physical And Chemical Impact On Concrete Workability And Strength As Fine Aggregate. J Teknol 2024;86:175–81. https://doi.org/10.11113/jurnalteknologi.v86.20423.
[49] Martins ACP, Franco de Carvalho JM, Duarte M do N, Lima GES de, Pedroti LG, Peixoto RAF. Influence of a LAS-based modifying admixture on cement-based composites containing steel slag powder. Journal of Building Engineering 2022;53. https://doi.org/10.1016/j.jobe.2022.104517.
[50] Bullerjahn F, Bolte G. Composition of the reactivity of engineered slags from bauxite residue and steel slag smelting and use as SCM for Portland cement. Constr Build Mater 2022;321. https://doi.org/10.1016/j.conbuildmat.2022.126331.
[51] Zhao Q, Pang L, Wang D. Adverse Effects of Using Metallurgical Slags as Supplementary Cementitious Materials and Aggregate: A Review. Materials 2022;15. https://doi.org/10.3390/ma15113803.
[52] Kang M, Kang MC, Yonis A, Vashistha P, Pyo S. Effect of steel slag on the mechanical properties and self-sensing capability of ultra-high performance concrete (UHPC). Developments in the Built Environment 2024;17. https://doi.org/10.1016/j.dibe.2024.100342.
[53] Subathra Devi V, Gnanavel BK. Properties of concrete manufactured using steel slag. Procedia Eng, vol. 97, 2014. https://doi.org/10.1016/j.proeng.2014.12.229.
[54] Darwis Z, Fathonah W, Hadi F. Steel Slag's Physical And Chemical Impact On Concrete Workability And Strength As Fine Aggregate. J Teknol 2024;86:175–81. https://doi.org/10.11113/jurnalteknologi.v86.20423.
[55] Mondragón DOC, Irigoin LG, Vásquez NRS, Chumacero JMG, Diaz ES, Pérez SPM, et al. Effect of steel slag and ceramic residues on the physical and mechanical properties of concrete. Engineering and Applied Science Research 2024;51:716–26. https://doi.org/10.14456/easr.2024.67.
[56] Pan Z, Zhou J, Jiang X, Zhuang Y, Zhang S, Si Q, et al. Investigating the effects of steel slag powder on the properties of self-compacting concrete with recycled aggregates. Constr Build Mater 2019;200:570–7. https://doi.org/10.1016/j.conbuildmat.2018.12.150.
[57] Abreha YB, Yifru BW, Yehualaw MD. Engineering Properties of Concrete with Partial Replacement Cement and Coarse Aggregate by Waste Glass Powder and Steel Slag Aggregate. 2023. https://doi.org/10.1007/978-3-031-33610-2_6.
[58] Yehualaw MD, Endale SA, Getahun S, Fantahun D, Vo D-H. Investigation on Utilizing of Steel Slag as a Partial Replacement of Natural River Sand as a Fine Aggregate in Concrete Production. 2023. https://doi.org/10.1007/978-3-031-33610-2_8.
[59] Ali AB, Sharif MB, Irfan-ul-Hassan M, Iqbal Y, Akmal U, Alabduljabbar H, et al. Coupled Effect of Polypropylene Fibers and Slag on the Impact Resistance and Mechanical Properties of Concrete. Materials 2022;15. https://doi.org/10.3390/ma15165654.
[60] Van Dao D, Ly HB, Trinh SH, Le TT, Pham BT. Artificial intelligence approaches for prediction of compressive strength of geopolymer concrete. Materials 2019;12. https://doi.org/10.3390/ma12060983.
[61] Koniki S, Prasad DR. Influence of hybrid fibres on strength and stress-strain behaviour of concrete under uni-axial stresses. Constr Build Mater 2019;207. https://doi.org/10.1016/j.conbuildmat.2019.02.113.
[62] Liu X, Wu P, Liu X, Zhang Z, Ai X. The Utilization of Carbonated Steel Slag as a Supplementary Cementitious Material in Cement. Materials 2024;17. https://doi.org/10.3390/ma17184574.
[63] Liu G, Wang J, Tang Y. Recycling and valorization of hydrated cement blends in mortars via semi-dry carbonation – The role of waste glass, granulated blast furnace slag and fly ash. Constr Build Mater 2023;401. https://doi.org/10.1016/j.conbuildmat.2023.132987.
[64] Rui Y, Qian C. CO2-fixing steel slag on hydration characteristics of cement-based materials. Constr Build Mater 2022;354. https://doi.org/10.1016/j.conbuildmat.2022.129193.
[65] Rui Y, Qian C, Zhang X, Ma Z. Different carbon treatments for steel slag powder and their subsequent effects on properties of cement-based materials. J Clean Prod 2022;362. https://doi.org/10.1016/j.jclepro.2022.132407.
[66] Nguyen-Sy T, Wakim J, To QD, Vu MN, Nguyen TD, Nguyen TT. Predicting the compressive strength of concrete from its compositions and age using the extreme gradient boosting method. Constr Build Mater 2020;260. https://doi.org/10.1016/j.conbuildmat.2020.119757.
[67] Wei X, Cai X, He Z, Tang S, Wu P, Su J. Effectiveness of fabricating high performance fiber reinforced cementitious composite (HPFRCC) using high volume steel slag powder. vol. 15. 2018. https://doi.org/10.1007/978-94-024-1194-2_15.
[68] Zhou L, Chen P, Hu C, Xia H, Liang Z, Rong B, et al. Hydration Hardening Characteristics of Steel Slag-Red Mud-Cement Based Composite Mortar | 钢渣-赤泥-水泥基复合砂浆的水化硬化特性. Bulletin of the Chinese Ceramic Society 2023;42:2837–45.
[69] Andrade HD, Costa LCB, Elói FPDF, Peixoto RAF, de Carvalho JMF, e Silva KDDC. Mechanical performance and resistance to carbonation of steel slag reinforced concrete. Constr Build Mater 2021;298. https://doi.org/10.1016/j.conbuildmat.2021.123910.

[70] Zhao Y, Zheng Y, Cui K, Shen P, Tao Y, Pan Z. Effect of Highly Reactive Carbonated Steel Slag on Hydration and Mechanical Properties of Cement Composites | 高活性碳化钢渣对水泥基复合材料水化与力学性能的影响. Bulletin of the Chinese Ceramic Society 2025;44:1306–27. https://doi.org/10.16552/j.cnki.issn1001-1625.2024.1524.
[71] Xue G, Fu Q, Xu S, Li J. Macroscopic mechanical properties and microstructure characteristics of steel slag fine aggregate concrete. Journal of Building Engineering 2022;56. https://doi.org/10.1016/j.jobe.2022.104742.
[72] Hou J, Liu J. Hydration activity and mechanical properties of steel slag used as cementitious materials. Environ Prog Sustain Energy 2022;41. https://doi.org/10.1002/ep.13756.
[73] Roslan NH, Ismail M, Abdul-Majid Z, Ghoreishiamiri S, Muhammad B. Performance of steel slag and steel sludge in concrete. Constr Build Mater 2016;104. https://doi.org/10.1016/j.conbuildmat.2015.12.008.
[74] Ranjbar N, Kuenzel C, Spangenberg J, Mehrali M. Hardening evolution of geopolymers from setting to equilibrium: A review. Cem Concr Compos 2020;114. https://doi.org/10.1016/j.cemconcomp.2020.103729
[75] Ganter D, Mielke T, Maier M, Lupascu DC. Bitumen rheology and the impact of rejuvenators. Constr Build Mater 2019;222. https://doi.org/10.1016/j.conbuildmat.2019.06.177
[76] Sun X, Li Y, Wei X, Yu J, Wang M. High contents of steel slag in the road concrete: Hydration mechanism, mechanical property and durability performance. Constr Build Mater 2023;400. https://doi.org/10.1016/j.conbuildmat.2023.132703
[77] Sai Keertan T, Pavan Kumar V, Bommisetty J, Ramanjaneyulu B, Ashok Kumar M. High strength fiber reinforced concrete with steel slag as partial replacement of coarse aggregate: Overview on mechanical and microstructure analysis. Mater Today Proc 2023. https://doi.org/10.1016/j.matpr.2023.03.687
[78] Lai MH, Zou J, Yao B, Ho JCM, Zhuang X, Wang Q. Improving mechanical behavior and microstructure of concrete by using BOF steel slag aggregate. Constr Build Mater 2021;277. https://doi.org/10.1016/j.conbuildmat.2021.122269
[79] Mo L, Zhang F, Deng M. Mechanical performance and microstructure of the calcium carbonate binders produced by carbonating steel slag paste under CO2 curing. Cem Concr Res 2016;88. https://doi.org/10.1016/j.cemconres.2016.05.013
[80] Liu P, Mo L, Zhang Z. Effects of carbonation degree on the hydration reactivity of steel slag in cement-based materials. Constr Build Mater 2023;370. https://doi.org/10.1016/j.conbuildmat.2023.130653
[81] Abendeh RM, Alhorani RAM, Ahmad HS, Baker MIB. Effect of steel slag as fine and coarse aggregate on pore structure and freeze-thaw resistance of high-strength concrete. Jordan Journal of Civil Engineering 2021;15:650–66.
[82] Yehualaw MD, Endale SA, Getahun S, Fantahun D, Vo D-H. Investigation on Utilizing of Steel Slag as a Partial Replacement of Natural River Sand as a Fine Aggregate in Concrete Production. 2023. https://doi.org/10.1007/978-3-031-33610-2_8
[83] Miah MJ, Miah MS, Sultana A, Shamim TA, Alom MA. The effect of steel slag coarse aggregate on the mechanical and durability performances of concrete. Key Eng Mater, vol. 833 KEM, 2020. https://doi.org/10.4028/www.scientific.net/KEM.833.228
[84] Mekonen TB, Alene TE, Alem YA, Nebiyu WM. Influence of Steel Slag as a Partial Replacement of Aggregate on Performance of Reinforced Concrete Beam. Int J Concr Struct Mater 2024;18. https://doi.org/10.1186/s40069-024-00698-5
[85] Yan Z, Fu W, Zhao L, Gao Z, Chen S, Wang Q, et al. Effect of Compaction Degree on the Carbonation Properties of Steel Slag. Materials 2025;18. https://doi.org/10.3390/ma18071629
[86] Deng J, Gu L, Yuan H, Zhang X, Zhang D. Enhanced carbonation of steel slag blocks using various chemical additives. Journal of Building Engineering 2025;105. https://doi.org/10.1016/j.jobe.2025.112518
[87] Ma J, Dai G, Wang X, Jiang F, Wang N, Zhao Y. Effect of Carbonation Treatment on the Properties of Steel Slag Aggregate. Materials 2023;16. https://doi.org/10.3390/ma16175768
[88] Men P, Wang X man, Liu D, Zhang Z, Zhang Q, Lu Y. On use of polyvinylpyrrolidone to modify polyethylene fibers for improving tensile properties of high strength ECC. Constr Build Mater 2024;417. https://doi.org/10.1016/j.conbuildmat.2024.135354
[89] Bukowski JM, Berger RL. Reactivity and strength development of CO2 activated non-hydraulic calcium silicates. Cem Concr Res 1979;9. https://doi.org/10.1016/0008-8846(79)90095-4
[90] Hu X, Yang B, Peng G, Zhong S, Zhang H. Investigation on hydration behavior and microscopic pore structure of early-age cement-based grouting material. Journal of Building Engineering 2023;80. https://doi.org/10.1016/j.jobe.2023.108050
[91] Bijalwan P, Kasilingam S. Mechanical characterization of the concrete mixture, including steel slag aggregate and steel fibres. In: R.K. DOBE, S.P. S, K. K, R. B, editors. Mater Today Proc, vol. 93, Department of Civil Engineering, Dr B R Ambedkar National Institute of Technology, Punjab, India: Elsevier Ltd; 2023, p. 201–10. https://doi.org/10.1016/j.matpr.2023.07.119

[92] Mitwally ME, Elnemr A, Shash A, Babiker A. Utilization of steel slag as partial replacement for coarse aggregate in concrete. Innovative Infrastructure Solutions 2024;9. https://doi.org/10.1007/s41062-024-01464-y
[93] Mitwally ME, Elnemr A, Shash A, Babiker A. Utilization of Steel Slag as Partial Replacement for Coarse Aggregate in Concrete. 2023 2nd International Conference on Smart Cities 4.0, Smart Cities 4.0 2023, German University In Cairo, Materials Engineering Department, Cairo, Egypt: Institute of Electrical and Electronics Engineers Inc.; 2023, p. 486–92. https://doi.org/10.1109/SmartCities4.056956.2023.10526048
[94] Olatoyan OJ, Okeyinka OM, Oluwafemi B, Oyewo ST, Olayanju OK, Kareem MA, et al. Investigation of tensile strength performance of green concrete incorporating steel slag. Hybrid Advances 2024;6. https://doi.org/10.1016/j.hybadv.2024.100186
[95] Guo Y, Xie J, Zhao J, Zuo K. Utilization of unprocessed steel slag as fine aggregate in normal- and high-strength concrete. Constr Build Mater 2019;204:41–9. https://doi.org/10.1016/j.conbuildmat.2019.01.178
[96] Chen W, Huo Z, Yang Z. Study on the Performance of Green Cement with Large Amount of Steel Slag Addition. IOP Conf Ser Earth Environ Sci, vol. 233, Xinjiang Communication Construction Group, Urumqi, Xinjiang, China: Institute of Physics Publishing; 2019. https://doi.org/10.1088/1755-1315/233/2/022015
[97] Shi K, Deng H, Hu J, Zhou J, Cai X, Liu Z. Effects of Steel Slag Powder Content and Curing Condition on the Performance of Alkali-Activated Materials Based UHPC Matrix. Materials 2023;16. https://doi.org/10.3390/ma16103875
[98] Singh S, Anand V. Optimizing self-compacting concrete with steel slag and fiber additions: enhancing fresh, mechanical, durability, and microstructural properties. Asian Journal of Civil Engineering 2025;26:683–99. https://doi.org/10.1007/s42107-024-01214-6
[99] Nirmala L, Tejaswini ML, Shilpa ML. An Investigation on the Mechanical and Durability Properties of Concrete Structures Incorporated with Steel Slag Industrial Waste. 2024. https://doi.org/10.1007/978-981-97-3654-6_3
[100] Barišić I, Zagvozda M, Marković B. Freeze–thaw resistance assessment of cement-bound steel slag aggregate for pavement structures. International Journal of Pavement Engineering 2019;20:448–57. https://doi.org/10.1080/10298436.2017.1309192
[101] Tang W, Sajjad U, Onaizi A, Amran M. Utilization of carbonated steel slag as fine sand in OPC concrete and mortar. Results in Engineering 2025;25. https://doi.org/10.1016/j.rineng.2024.103716
[102] Costa LCB, Nogueira MA, Andrade HD, Carvalho JMF de, Elói FP da F, Brigolini GJ, et al. Mechanical and durability performance of concretes produced with steel slag aggregate and mineral admixtures. Constr Build Mater 2022;318. https://doi.org/10.1016/j.conbuildmat.2021.126152
[103] Shan L, Li H, Zhao J, Zhang X, Kang X, Gao X, et al. Investigating on the Pavement Performance of Multi-Source Solid Wastes by Cement and Fly Ash. Materials 2023;16. https://doi.org/10.3390/ma16196556
[104] Wen Y, Sun H, Hu S, Xu G, Wu X, Song C, et al. Microstructure and life prediction model of steel slag concrete under freezing-thawing environment. Nanotechnol Rev 2021;10. https://doi.org/10.1515/ntrev-2021-0109
[105] Cheng X, Tian W, Gao J, Gao Y. Performance evaluation and lifetime prediction of steel slag coarse aggregate concrete under sulfate attack. Constr Build Mater 2022;344. https://doi.org/10.1016/j.conbuildmat.2022.128203
[106] Pang B, Zhou Z, Cheng X, Du P, Xu H. ITZ properties of concrete with carbonated steel slag aggregate in salty freeze-thaw environment. Constr Build Mater 2016;114:162–71. https://doi.org/10.1016/j.conbuildmat.2016.03.168
[107] Wang C, Zhou Y, Cao F, Wang G, Liu T, Wang X. Microstructure and damage evolution model of steel slag fine aggregates concrete under freezing-thawing environment | 冻融环境下钢渣细骨料混凝土微观结构及损伤演化模型. Yingyong Lixue Xuebao Chinese Journal of Applied Mechanics 2024;41:585–93. https://doi.org/10.11776/j.issn.1000-4939.2024.03.011
[108] Park M-S, Kim Y-S. A Study on the Sulfate Attack Resistance of Concrete Using EAF Slag as Fine Aggregate. Journal of the Korea Institute of Building Construction 2009;9. https://doi.org/10.5345/jkic.2009.9.1.081
[109] Cai X, Cao Z, Sun J, Wang H, Wu S. Influence of Steel Slag on Properties of Cement-Based Materials: A Review. Buildings 2024;14. https://doi.org/10.3390/buildings14092985
[110] Ali KS, Ishak NM, Mohd Ridzuan AR. Performance of concrete containing steel slag exposed to sulphate environment: A comparison of steel slag and natural aggregate use. ISBEIA 2011 - 2011 IEEE Symposium on Business, Engineering and Industrial Applications, 2011. https://doi.org/10.1109/ISBEIA.2011.6088883

[111] Costa LCB, Carvalho VR, Ferreira LC, Peixoto RAF, Baeta BEL. Utilizing steel slag to prolong the durability of reinforced concrete: Corrosion resistance mechanisms. Journal of Building Engineering 2024;98. https://doi.org/10.1016/j.jobe.2024.111505
[112] Han F, Liu J, He X, Song S. Experimental studies on the utilization of steel slag in the steam-cured concrete. Journal of Southeast University English Edition 2017;33:277–85. https://doi.org/10.3969/j.issn.1003-7985.2017.03.005
[113] Shi C. Strength, pore structure and permeability of alkali-activated slag mortars. Cem Concr Res 1996;26. https://doi.org/10.1016/S0008-8846(96)00174-3
[114] Aperador W, Bautista-Ruiz J, Sánchez-Molina J. Effect of Immersion Time in Chloride Solution on the Properties of Structural Rebar Embedded in Alkali-Activated Slag Concrete. Metals (Basel) 2022;12. https://doi.org/10.3390/met12111952
[115] Han F, Zhang Z. Properties of 5-year-old concrete containing steel slag powder. Powder Technol 2018;334:27–35. https://doi.org/10.1016/j.powtec.2018.04.054
[116] Ye JX, Wang YJ, Zhao S, Yang MC, Yang CH. Effect of ground phosphate slag on the resistance to chloride ion penetration of concrete. vol. 194–196. 2011. https://doi.org/10.4028/www.scientific.net/AMR.194-196.924
[117] Aziminezhad M, Taherkhani R. BIM for deconstruction: A review and bibliometric analysis. Journal of Building Engineering 2023;73. https://doi.org/10.1016/j.jobe.2023.106683
[118] Taherkhani R, Aziminezhad M. Human-building interaction: A bibliometric review. Build Environ 2023;242. https://doi.org/10.1016/j.buildenv.2023.110493
[119] Rahman T, Zudhy Irawan M, Noor Tajudin A, Rizka Fahmi Amrozi M, Widyatmoko I. Knowledge mapping of cool pavement technologies for urban heat island Mitigation: A Systematic bibliometric analysis. Energy Build 2023;291. https://doi.org/10.1016/j.enbuild.2023.113133
[120] Burnham JF. Scopus database: A review. Biomed Digit Libr 2006;3. https://doi.org/10.1186/1742-5581-3-1
[121] Song Q, Guo MZ, Wang L, Ling TC. Use of steel slag as sustainable construction materials: A review of accelerated carbonation treatment. Resour Conserv Recycl 2021;173. https://doi.org/10.1016/j.resconrec.2021.105740
[122] Dong Q, Wang G, Chen X, Tan J, Gu X. Recycling of steel slag aggregate in portland cement concrete: An overview. J Clean Prod 2021;282. https://doi.org/10.1016/j.jclepro.2020.124447
[123] Aly AM, El-Feky MS, Kohail M, Nasr ESAR. Performance of geopolymer concrete containing recycled rubber. Constr Build Mater 2019;207. https://doi.org/10.1016/j.conbuildmat.2019.02.121
[124] Mo L, Yang S, Huang B, Xu L, Feng S, Deng M. Preparation, microstructure and property of carbonated artificial steel slag aggregate used in concrete. Cem Concr Compos 2020;113. https://doi.org/10.1016/j.cemconcomp.2020.103715
[125] Liu L, Zhou A, Deng Y, Cui Y, Yu Z, Yu C. Strength performance of cement/slag-based stabilized soft clays. Constr Build Mater 2019;211. https://doi.org/10.1016/j.conbuildmat.2019.03.256
[126] Liu J, Yu B, Wang Q. Application of steel slag in cement treated aggregate base course. J Clean Prod 2020;269. https://doi.org/10.1016/j.jclepro.2020.121733
[127] Li L, Ling TC, Pan SY. Environmental benefit assessment of steel slag utilization and carbonation: A systematic review. Science of the Total Environment 2022;806. https://doi.org/10.1016/j.scitotenv.2021.150280

Research on Engineering Structures & Materials
www.jresm.org
MIM Research Group

Research Article

Enhancing mechanical properties of normal and lightweight concrete using ramie fiber-reinforced polymer

Parmo Parmo [*,a], Arqowi Pribadi [b], Noverma Noverma [c]

Dept. of Civil Engineering, State Islamic University of Sunan Ampel Surabaya, Surabaya, Indonesia

Article Info

Article History:

Received 26 July 2025

Accepted 09 Sep 2025

Keywords:

Compressive strength;
Flexural strength;
Normal and lightweight concrete;
Failure modes;
Ramie fiber-reinforced polymer

Abstract

This study determines the mechanical properties of normal and lightweight concrete strengthened with ramie fiber-reinforced polymer (RFRP) as an eco-friendly external confinement material. This research examines the tensile strength and modulus of RFRP, as well as the compressive strength, flexural strength, failure modes, stress-strain and force-displacement behaviors of both unstrengthened and strengthened cylindrical and beam samples. Cylinder and beam samples of normal and lightweight concrete were produced and strengthened using RFRP in different configurations (center strip and full jacketing for cylinders and bottom lamination for beams). The RFRP composites with 33.28 ± 4.11 MPa of tensile strength and 1064 ± 91.85 MPa of Young's modulus were used as a strengthened material. The results showed that, compared with unconfined samples, full RFRP jacketing improved the compressive strength by up to 47.9% in normal concrete and 30.2% in lightweight concrete. The flexural strength increased by 8.6% in normal concrete and 25.3% in lightweight concrete. The failure mode shifted from brittle cracking to more ductile and controlled failure in the strengthened samples. The study revealed that fiber confinement improved strain capacity with minimal impact on density, however, the enhancement effect may plateau depending on fiber configuration and concrete type. These findings demonstrate that RFRP is a promising, sustainable solution for enhancing structural performance, particularly in lightweight concrete applications where the strength-to-weight ratio is essential.

© 2025 MIM Research Group. All rights reserved.

1. Introduction

Lightweight concrete has long been utilized in construction due to its lighter weight and excellent thermal insulation properties. However, its lower mechanical properties, such as compressive strength, flexural strength, and elastic modulus, compared to conventional concrete pose challenges in its application for structural elements [1]. To address these limitations, various studies have been conducted on the use of natural fibers as reinforcing materials for concrete, such as jute, abaca, hemp, and cotton fibers. These fibers are not only environmentally friendly but also enhance the mechanical properties of concrete [2]. Bio-based fibers are recognized for their excellent tensile strength, high durability, and ecological properties, making them a promising alternative in the development of sustainable, high-performance composite concrete [3,4].

Lightweight concrete has the advantage of being lighter compared to normal concrete, which reduces structural and foundation costs in construction [5,6]. Nevertheless, it has inherent limitations compromising its performance in structural applications [7,8]. A promising solution involves employing natural fiber composites for strengthening concrete, which can not only increase its mechanical properties but also maintain its sustainability [9,10]. By bridging cracks

*Corresponding author: parmo_99@uinsa.ac.id
[a]orcid.org/0000-0003-0511-1925; [b]orcid.org/0009-0009-2273-3378; [c]orcid.org/0000-0002-0314-120X
DOI: http://dx.doi.org/10.17515/resm2025-1046me0726rs

and redistributing stress, natural fibers as external confinement significantly improves the strength, ductility, and durability of confined concrete.

Despite the success of strengthening systems by using synthetic materials, such as carbon fiber reinforced polymer (CFRP) [11], glass fiber-reinforced polymer (GFRP) [12], and aramid fiber-reinforced polymer (AFRP) [13], the current studies and investigations are turning toward for utilizing natural fibers as alternative of structural elements not only for strengthening existing elements but also for retrofitting utilization. Several previous studies have assessed the potential of natural fiber-reinforced polymer (NFRP) to enhance reinforced concrete elements such as columns [14,15], beams [16], and slabs [17].

The use of NFRP composites based on natural fibers like jute, sisal, hemp, abaca, or cotton for strengthening plain concrete to enhance its compressive and flexural strength has been confirmed in prior studies. Hussain et al. 2020 [18] reported that the use of NFRP composite based on hemp, cotton, and polyester fibers as a strengthened material could improve the ultimate strength, strain, and deformability of plain concrete. Furthermore, Sen and Paun 2015 [19] highlighted that there is a positive impact of NFRP based on sisal and jute fibers on the strength and modulus elasticity of the cylinder's concrete, with 66% and 48% improvement by sisal- and jute-NFRPs, respectively. On the other hand, Jirawattanasoumkul et al. 2019 [20] reported that the compressive strength of concrete confined with NFRP increases up to 25%, 28%, and 42% by using hemp-, jute-, and cotton-NFRPs, respectively. These studies underscore the potential of natural fibers to enhance the mechanical limitations of plain concrete while promoting the sustainable environment needs.

The NFRP-confined concrete notably increased its compressive strength. For instance, a study conducted by Amalia et al. (2024) [21] reported that the compressive strength of concrete confined by NFRP-based abaca fiber increased by up to 37% compared with that of unconfined concrete. Furthermore, Pimanmas et al. 2019 [22] demonstrated that both circular and square concrete samples exhibited significantly increased strength and deformability when sisal fibers were used for NFRP confinement. In addition, Antonio and Silva 2025 [23] noted that the thickness and number of layers play crucial roles in enhancing the compressive strength. Although extensive research highlights the benefits of NFRP in improving the performance of normal concrete, several gaps persist in optimizing NFRP based on ramie fibers confined in lightweight concrete.

The tensile strength of the RFRP laminate is assessed. The compressive and flexural strength of both normal and lightweight concrete is determined for specimens strengthened by RFRP. The hypothesis driving this work is that the use of RFRP to strengthen normal and lightweight concrete can significantly increase its compressive and flexural strength. The novelty of this study lies in its focus on NFRP based on ramie fibers, an underexplored yet promising natural reinforcement. This work seeks to address critical gaps in the field of optimizing natural fiber, particularly ramie, by exploring its application in lightweight concrete.

2. Experimental Details

2.1. Materials

Portland pozzolan cement (PPC) was utilized in this research as the primary binder material. The PPC is manufactured by grinding Portland cement clinker, gypsum, and several inorganic materials, such as blast furnace slag, pozzolans, silicate compounds, and limestone, with the combined content of inorganic materials ranging from 6% to 35% of the total mass [23]. This type of hydraulic cement is commonly available on the Indonesian market. In this study, the cement had a specific gravity of 3.02, a specific surface area of 327 m^2/kg, initial and final setting time of ≥ 45 minutes and ≤ 7 days (Table 1). The fine aggregate, which has a specific gravity of 2.78, a fineness modulus of 2.40, and an absorption rate of 2.1%, was prepared in accordance with ASTM C33/C33M-23 [24]. Two types of coarse aggregates were used in this study, gravel and pumice aggregates, which were produced according to ASTM C127-15 [25]. Gravel aggregates, with a specific gravity of 2.89, a bulk density of 1785 kg/m^3, an absorption rate of 1.89%, a fineness modulus of 0.8, and a maximum size of 12.7 mm, were utilized to produce normal concretes. Pumice aggregates were used to produce lightweight concrete with a specific gravity of 1.10, a bulk density of 559 kg/m^3, an absorption rate

of 35.4%, a fineness modulus of 0.7, and a maximum size of 10 mm. The physical properties of aggregates are shown in Table 2. The granulometry curves of the two kinds of aggregates are given in Fig. 1. The superplasticizers were added in the concrete mixture to improve workability and to reduce water content, which were compliant with ASTM C494/C494M-99a [26]. The materials used in this study to produce normal and lightweight concrete are shown in Fig. 2.

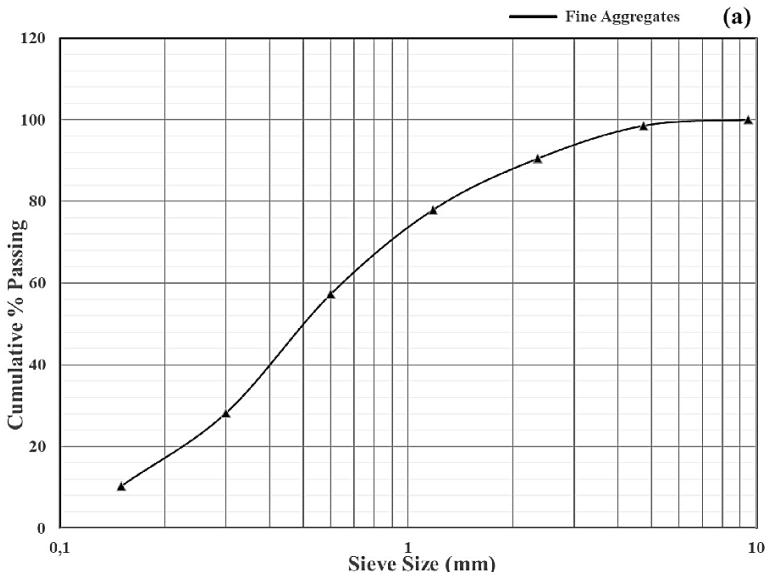
Table 1. Physical properties of PPC

Physical properties	Results
Specific gravity	3.02
Specific surface area, Blaine method (m^2/kg)	327
Initial setting time (minute)	≥ 45
Final setting time (hours)	≤ 7

Table 2. Physical properties of aggregates

Physical properties	Results		
	Sand	Gravel	Pumice
Specific gravity	2.78	2.89	1.10
Fineness modulus	2.40	0.80	0.70
Absorption (%)	2.1	1.89	35.4
Bulk density (kg/m^3)	1680	1785	559

In this study, the matrix of RFRP consisted of a two-component system comprising unsaturated polyester resin and hardener. The resin was manufactured by PT SHCP Indonesia with a density of approximately 1.10 g/cm^3. The methyl ethyl ketone peroxide was used as a hardener and was produced by the same manufacturer as the resin. The resin and hardener were mixed at a 50:1 weight ratio. The mixture had a pot life of approximately 30 minutes at room temperature. The woven ramie fiber fabric was utilized in this study, with a unit area weight of approximately 200 g/m^2. The average diameter of individual ramie fibers was about 160 to 200 μm (0.16 to 0.20 mm), varying in length from 40 to 200 mm. The single fiber tensile strength reported in the literature is 399.47 ± 178.74 MPa with a modulus of elasticity of 18.30 ± 7.88 GPa [27]. In the present study, the ramie fibers were used in their as-received condition without any chemical or surface pre-treatment.



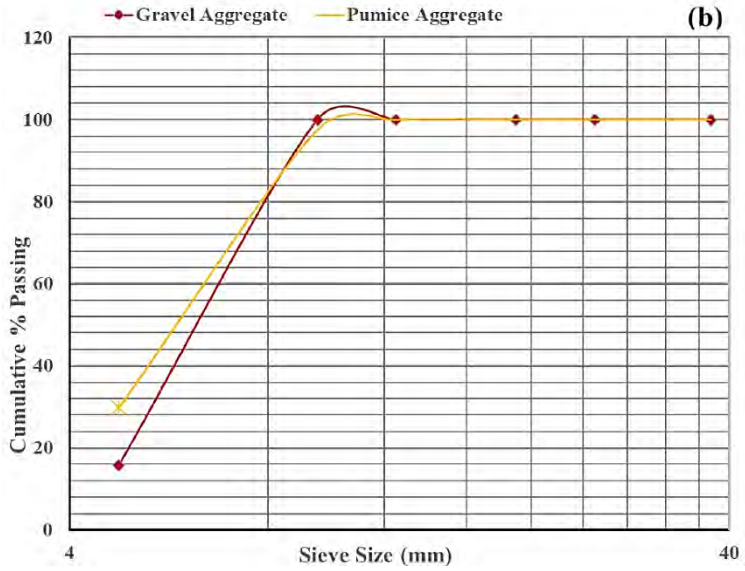


Fig. 1. Aggregate size distribution curves of (a) fine and (b) coarse aggregates

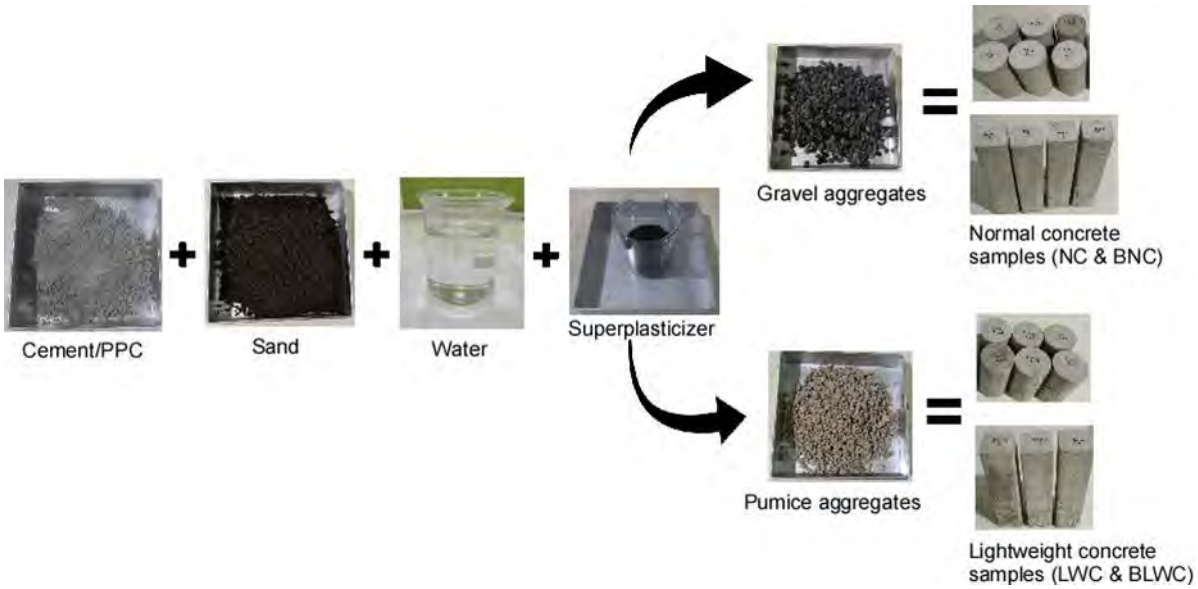


Fig. 2. Material mixes

2.2 Preparation of Samples

The RFRP coupon samples were prepared for conducting a tensile test by mixing polyester resin and hardener. The mixed resin and hardener were applied to the ramie fiber fabric utilizing the hand lay-up method to ensure proper impregnation of the fibers. After lay-up, the RFRP laminates were cured in an oven at a constant temperature of 50°C for 4 hours, and were then allowed to cure at ambient conditions for 2 hours to achieve sufficient cross-linking prior to the tensile test. Two formulations, normal concrete (NC) and lightweight concrete (LWC), were developed via the weight method in accordance with ACI PRC-211.1-22 [27] and ACI 211.2-98 [28], respectively. A suitable mixture of both the NC and LWC consists of 460 kg/m^3 of PPC, 648 kg/m^3 of fine aggregates, and 217 kg/m^3 of water. The W/C ratio and the superplasticizer were maintained at 0.46 and 1.5% by weight of the binder, respectively. The primary difference in the composition of the two types of concrete was in the use of coarse aggregates. The NC used gravel aggregates weighing 1038 kg/m^3, which was designed at a target density of 2300 kg/m^3 concrete. Moreover, the LWC utilized lightweight aggregates from pumice stone at 248 kg/m^3 with a target design density of 1600 kg/m^3 of lightweight concrete. Table 3 shows the mixed proportion details of the NC and LWC.

Table 3. Mixed proportions

Parameters	Mixes	
	NC	LWC
Target density (kg/m^3)	2300	1600
PPC (kg/m$^{3)}$	460	460
Water (kg/m^3)	217	217
W/C ratio	0.46	0.46
Fine aggregates (kg/m^3)	648	648
Gravel aggregates (kg/m^3)	1038	-
Pumice aggregates (kg/m^3)	-	248
Superplasticizer/SP (kg/m^3)	7	7

A total of 36 samples were produced, comprising plain cylindrical and beam of normal and lightweight concrete. The dimensions of the concrete samples were 55 × 110 mm (diameter × height) and 50 × 50 × 200 mm (width × depth × length) for the cylindrical and beam samples, respectively. Subsequent to the molding procedure, the samples were demolded and subjected to curing in a controlled environment at a consistent temperature of 23.0 ± 2.0 °C and a relative humidity of 95% for a duration of 28 days. The samples were prepared to be compatible for strengthening with RFRP after 28 days of curing. For the strengthened specimens, the surface of concrete was first roughened and cleaned to improve adhesion, followed by application of a thin primer coat of mixed resin. Additional mixed resin was spread, and the ramie fabric was placed by hand with longitudinal orientation, after a short dwell time of 2 minutes, ensuring uniform impregnation and removal of air voids using a roller. In this study, the mixed resin curing of the reinforced specimens was carried out in a drying oven for 4 hours at a constant temperature of 50^{o}C. The test programs are summarized in Table 4. The concrete samples were designated in such a way as to represent the research parameters. The cylindrical samples of the concrete control were labeled NC0 or LWC0. Cylindrical samples strengthened with RFRP strips were labeled NC1 or LWC1, whereas those with full jacketing strengthening were labeled NC2 or LWC2. For the beam samples, the concrete control samples were labeled BNC0 or BLWC0. The beams strengthened with one or two layers of RFRP laminates were designated BNC1 or BLWC1 and BNC2 or BLWC2, respectively, where BNC and BLWC refer to beam normal and lightweight concrete, respectively. The unstrengthened and strengthened concrete samples are shown in Fig. 3.

Table 4. Details of experimental tests

Specimen	Layers		Type	Number of specimens	Test
	Number	*Position*			
NC0	-	-	Cylinder	3	Compression
NC1	1	Center Strip	Cylinder	3	Compression
NC2	1	Full Jacketing	Cylinder	3	Compression
LWC0	-	-	Cylinder	3	Compression
LWC1	1	Center Strip	Cylinder	3	Compression
LWC2	1	Full Jacketing	Cylinder	3	Compression
BNC0	-	-	Beam	3	Third-Point bending
BNC1	1	Bottom Laminated	Beam	3	Third-Point bending
BNC2	2	Bottom Laminated	Beam	3	Third-Point bending
BLWC0	-	-	Beam	3	Third-Point bending
BLWC1	1	Bottom Laminated	Beam	3	Third-Point bending
BLWC2	2	Bottom Laminated	Beam	3	Third-Point bending

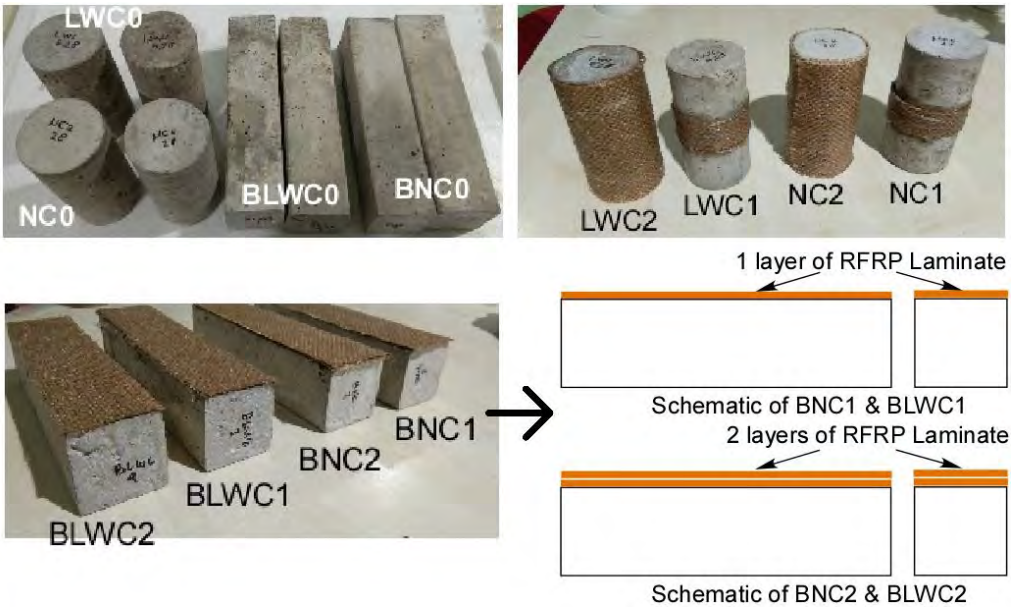


Fig. 3. Details of the unstrengthened and strengthened samples

The woven ramie natural fabric with a density of 1.52 g/cm^3 was used as a strengthened concrete combined with polyester resin as the RFRP. The average thickness of the one-layer RFRP composites was 1.65 mm. To obtain the mechanical properties of the RFRP composite, coupon samples with average widths and lengths of 15.0 mm and 150 mm, respectively, were prepared for tensile tests.

3. Experimental Methods

3.1 Ramie Composite Tensile Test

The RFRP coupon specimens, consisting of a single layer of ramie fiber fabric, had an average thickness of 1.65 mm, a width of 15 mm, and a length of 150 mm. Tensile tests of the RFRP composites were carried out using a 300 KN MTS electromechanical testing machine (Fig. 4a). The rate of pull was set at 0.1 mm/s for all sample tests. Five samples were subjected to these tensile tests, which were in compliance with ASTM D3039/D3039M-17 [29].

3.2 Compression Tests

Unstrengthened cylindrical samples of the NC and LWC samples were tested after 28 days of curing. For strengthened samples (center strips and full jacketing), compression tests were conducted after the curing of the mixed resin of RFRP was completed. In this study, the mixed resin curing of the reinforced or strengthened specimens was carried out in a drying oven at a constant temperature of 50^{o}C for 4 hours. Compression tests were conducted on all cylindrical samples via an MTS electromechanical testing machine in accordance with ASTM C39/C39M-23 [30]. The speed test of the testing machine was set at 0.5 mm/s during the compression test. Fig. 4b shows the compression test results for the cylindrical samples.

3.3 Third-Point Bending Tests

The beam specimens were tested with a span length of 170 mm. The same procedures were used with cylindrical samples for the drying process of strengthened beam samples in a drying oven. This third-point bending test, in accordance with ASTM C78/C78M-22 [31], was performed via an MTS electromechanical testing machine, and the speed test was set at 0.1 mm/s. Fig. 4c shows the third-point bending test of the sample beams.



(a) (b) (c)

Fig. 4. Experimental setup (a) Tensile test of ramie composites, (b) Compression test of cylindrical samples, and (c) Third-point bending test of beam samples

4. Results and Discussion

4.1 Tensile tests of the RFRP composites

The tensile test of the RFRP composite revealed several key mechanical properties that sustained a maximum load of 851 ± 87.2 N, with a corresponding tensile stress at a maximum of 33.28 ± 4.11 MPa. The Young's modulus was determined to be 1064 ± 91.85 MPa, and the tensile strain at break was recorded as 0.043 ± 0.004, at which point the composite failed due to rupture. The effects of stress and strain on the RFRP composite are shown in Fig. 5. The stress-strain curve exhibited a linear region followed by a gradual nonlinear behavior (or deformation) and an abrupt rupture, indicating brittle fracture characteristics of fiber-matrix composites.

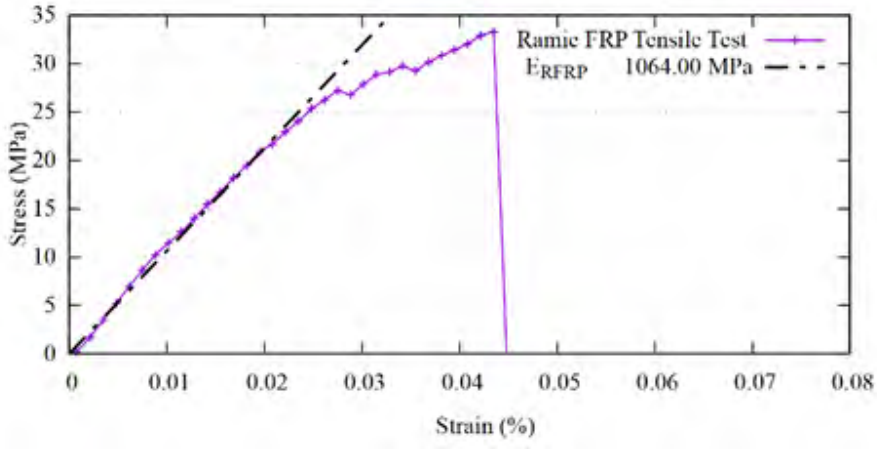


Fig. 5. Stress–strain curve of the RFRP composite

Fig. 6 shows the failure mode observed in the RFRP laminates. All the samples exhibited a characteristic failure pattern, with fractures occurring in the testing region rather than in the grasping area. The failure mechanism corresponds to the angular gauge middle (AGM) type, which originates a crack in a material's weak area, including a fractured fiber end or a matrix flaw [32]. The initial crack propagation in a particular direction is determined by the fiber orientation, the mechanical characteristics of the matrix, and the level of applied stress. If the crack propagates to a critical size, complete material failure will occur.



Fig. 6. Failure modes of RFRP under tensile test

4.2 Compressive Stress–Strain Curves and Strength

The stress–strain curves depicted in Fig. 7 provide a comprehensive understanding of the compressive behavior of the NC (Fig. 7a) and LWC (Fig. 7b) samples. The unstrengthened samples, NC0 and LWC0, exhibit the lowest peak stress and strain values, indicating limited compressive strength and ductility. Compared with the two strengthened samples, the NC0 sample exhibited a peak stress of 15.87 ± 1.20 MPa and a relatively brittle failure mode. The use of a one-layer center strip of RFRP (NC1) resulted in a slight increase in strength (16.96 ± 1.15 MPa) and an increased strain capacity of 28.52% compared to ultimate strain value of unconfined sample (NC0). The use of full jacketing of RFRP (NC2) significantly increased the strength and ultimate strain value, achieving a maximum compressive strength of 23.49 ± 0.85 MPa, which is a 48.02% increase over that of the NC0 sample in strength and an increased ultimate strain of 69.92% compared to NC0.

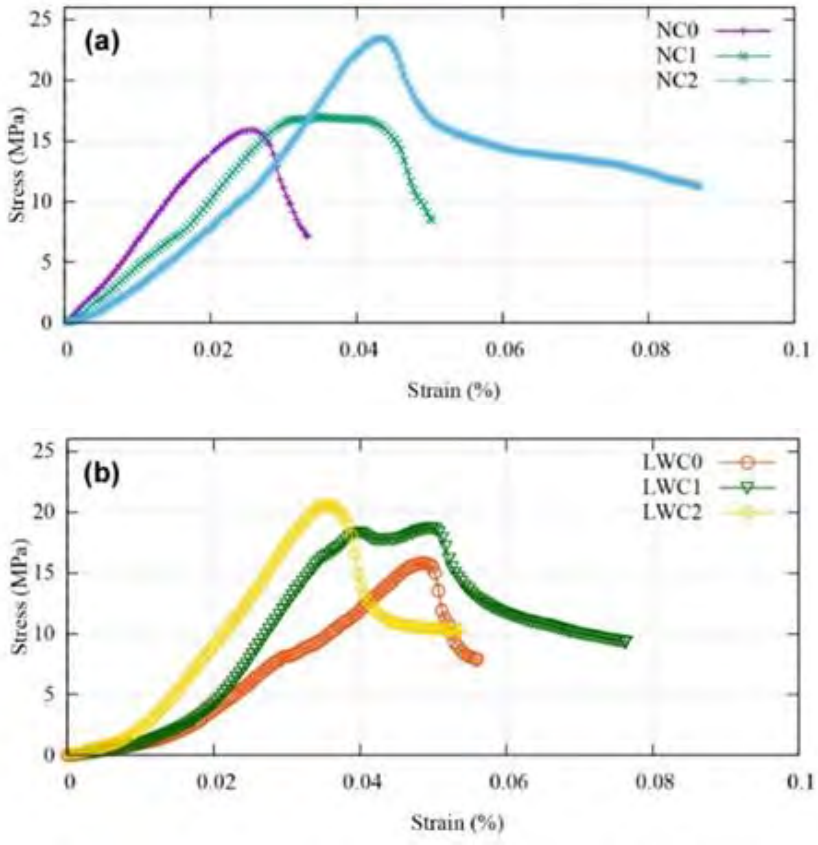


Fig. 7. Stress and strain curves in compression tests: a). normal, b). lightweight concrete

The superior performance of the full jacketing is attributed to more effective lateral expansion, and thus increases toughness. Likewise, the lightweight concrete samples (Fig. 7b) exhibited a consistent pattern. The unconfined sample (LWC0) exhibited a compressive strength of 15.85 ± 0.92 MPa. Following strengthening, LWC1 (center strip) increased to 18.43 ± 1.19 MPa, whereas

LWC2 (full jacketing) reached 20.63 ± 0.80 MPa, reflecting a 30.16% improvement in strength from the unconfined state. Fig. 8 visually confirms these findings by illustrating the relationship between the compressive strength and density across all the samples. Notably, while the normal concrete series had higher densities (~2200–2350 kg/m^3), the lightweight series remained at ~1700 kg/m^3, emphasizing the balance between strength gain and weight efficiency. These findings demonstrate that the use of ramie fibers, which are used for external jacketing in FRP systems, markedly improves the compressive performance of both normal and lightweight concrete. The results of this study are consistent with those of previous studies in which the compressive strength of concrete cylinders confined with NFRP increased by 28–42%, depending on the fiber type [20]. This encompasses not only an increase in the ultimate compressive strength but also significant increases in the strain capacity. This is particularly relevant for using lightweight concrete in structural applications, where the weight of the structure can be reduced without compromising its strength. The RFRP jacketing addresses these limitations by providing additional strength while maintaining structural integrity and offering an environmentally sustainable solution.

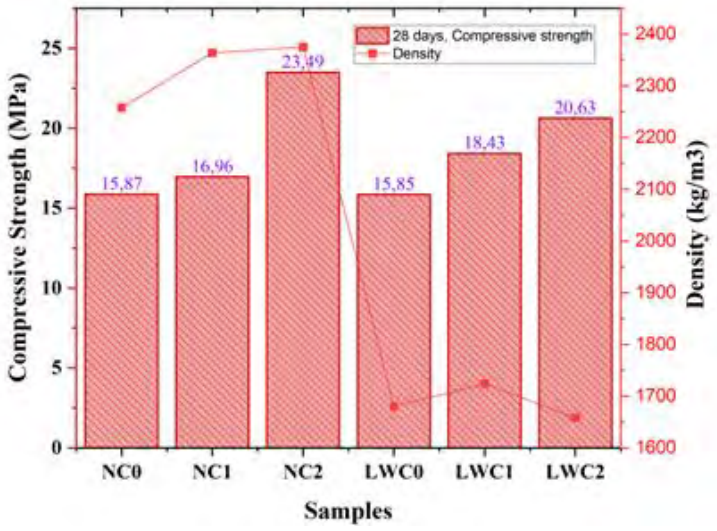


Fig. 8. Compressive strengths of the samples

4.3 Force vs Displacement Curves and Flexural Strength

The force and displacement responses of normal and lightweight concrete beams under third-point bending tests are shown in Fig. 9. The unstrengthened samples (BNC0 and BLWC0) exhibit brittle failure, characterized by abrupt load reductions and limited post-peak deformation, indicating low flexural strength, ductility, and capacity to absorb energy. One layer of RFRP on the BNC1 specimen provides moderate gains in peak force and displacement, while two layers on BNC2 yield the highest post peak force and substantial displacement increase. A similar trend is observed in lightweight concrete beams. The specimen with one layer of RFRP (BLWC1) shows moderate improvement, whereas two layers (BLWC2) significantly raise peak force capacity. The good performance of the two-layer of RFRP is attributed to improve stiffness, more effective crack bridging, and increased load distribution across the section. These findings also suggest that RFRP strengthened normal and lightweight concrete beams effectively inhibit crack propagation and sustain load-bearing capacity, as evidenced by an extended plateau in the post-peak region. This occurrence also indicates the role of fibers in sustaining load following matrix cracking.

Fig. 10 shows the flexural strengths of both the normal and lightweight beam samples in correlation with their densities. Compared with those of BNC2 and BNC0, the flexural strengths of the BNC samples increased from 3.85 ± 0.17 MPa (BNC0) to 4.14 ± 0.23 MPa (BNC1) and 4.18 ± 0.24 MPa (BNC2), corresponding to an increase of up to 8.6%. Due to its greater inherent stiffness and strength of normal concrete, the restricted supplementary effect of the RFRP and its flexural strength increased only slightly (8.6%). For lightweight beams, the flexural strength increased from 3.32 ± 0.15 MPa (BLWC0) to 4.12 ± 0.19 MPa (BLWC1) and 4.16 ± 0.32 MPa (BLWC2), indicating an

increase of approximately 25% without a substantial increase in density. In addition to improving strength and ductility, it preserves the low density of lightweight concrete, as shown in Fig. 10. This behavior could be attributed to the increased bond compatibility, stiffness contrast between the fiber and matrix, and the ability of RFRP to bridge cracks more effectively in lightweight concrete under flexural loading. This feature is crucial for structural design in seismic regions, where low mass and high energy dissipation are desired.

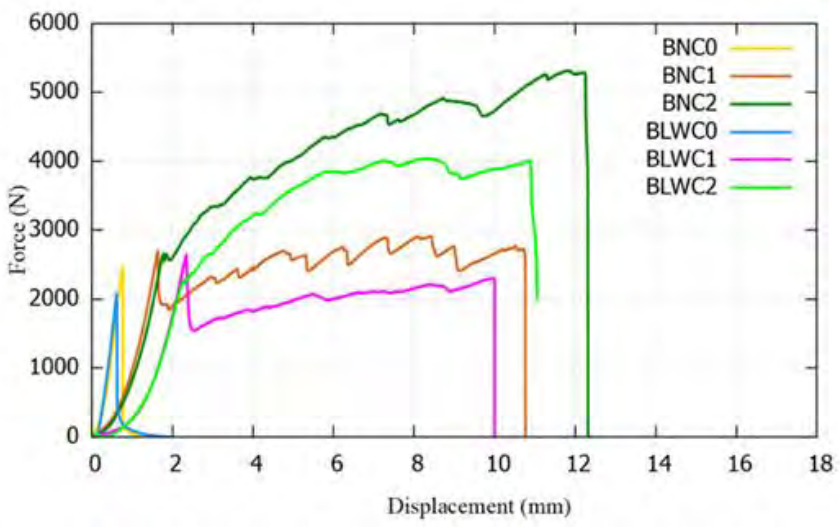


Fig. 9. Force vs. displacement curves of normal and lightweight concrete samples

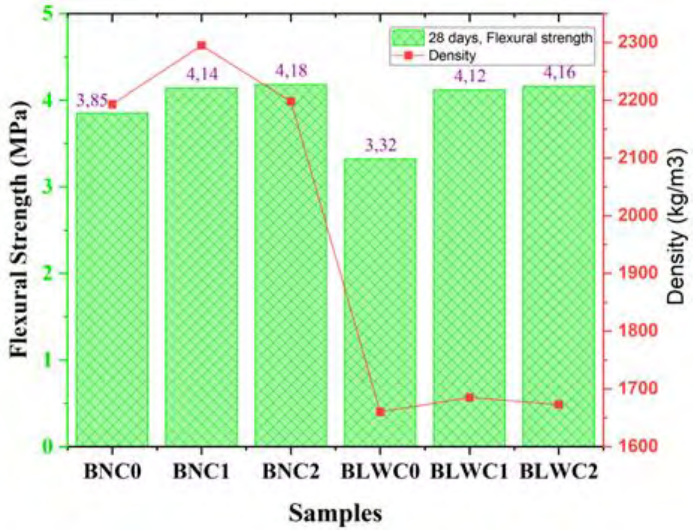


Fig. 10. Flexural strength of the samples

4.4 Failure Modes

The failure modes of the unconfined and RFRP-confined concrete cylinders in the NC and LWC series are illustrated in Fig. 11. The unconfined samples, NC0 and LWC0, displayed classic brittle failure, characterized by vertical cracking and crushing at the top edges. These cracks propagated rapidly after the peak load, confirming the typical brittle nature of plain concrete. In contrast, specimens with center strip RFRP confinement (NC1 and LWC1) exhibited partial crack control, characterized by vertical cracks, but less fragmentation and crushing at the top (NC1) and bottom (LWC1) edges. The RFPP strips around the midsection effectively delayed failure, particularly at the center of the samples, allowing them to retain their integrity longer under axial loading. The effect of RFRP was even more pronounced in specimens with full jacketing (NC2 and LWC2) confinement method. This method provided the greatest confinement, producing evenly distributed cracks and a more intact shape post-failure, suggesting enhanced strength and ductility.

Damage after the peak load was reached was observed in the overlapping RFRP section by debonding between confined layers. Overall, these findings align with previous studies, which have reported that natural fiber-confined concrete results in reduced crack width, produces more controlled failure patterns [20], and that full confinement restrains lateral expansion and delays crack propagation [22].



Fig. 11. Failure modes of unreinforced and strengthened NC and LWC cylinder samples

Fig. 12 shows the failure patterns of unstrengthened and RFRP-strengthened beams. The description of the beam failure modes is based on qualitative observations, as crack widths and propagation rates were not measured. The unstrengthened beams, BNC0 and BLWC0, exhibited a single crack at mid-span, typical of flexural failure under third-point loading. The cracks spread considerably through the depth of the beam, indicating brittle fracture of the samples. Compared with the unstrengthened samples, the single layers of the RFRP-strengthened samples (BNC1 and BLWC1) demonstrated more controlled cracking behavior. While major cracks still formed at the expected location, they appeared narrower and accompanied by distributed small cracks, especially at the RFRP-concrete interface. The presence of the RFRP laminate improved the load redistribution and crack-bridging capacity. In the concrete beams with two layers of RFRP (BNC2 and BLWC2), the failure modes were notably more constrained. The cracks were slightly narrower and more tortuous, indicating enhanced capacity and energy dissipation. On the other hand, the reduction in crack width and propagation confirms the effectiveness of multilayered fiber reinforcement in resisting tensile stresses. Previous investigations have documented these types of failure modes in natural FRP-strengthened concrete beams [3,33].



Fig. 12. Failure modes of the unstrengthened and strengthened beam samples

5. Conclusions

The mechanical of RFRP composite, normal and lightweight concrete strengthened with RFRP were investigated. The following conclusions were drawn in accordance with the experimental results:

- The tensile test of RFRP composite obtained several results such as 33.28 ± 4.11 MPa of tensile strength, 1064 ± 91.85 MPa of Young's modulus, and exhibited a characteristic failure pattern with fractures occurring in the testing rather than in the grasping area.
- The RFRP strengthening significantly enhanced both compressive and flexural performance. Compared with their unconfined counterparts, full jacketing with RFRP increased the compressive strength of cylindrical samples by up to 47.9% in normal concrete and 30.2% in lightweight concrete. The flexural strength of the beam samples

also increased, with BNC2 and BLWC2 exhibiting the greatest improvements of 8.6% and 25.3%, respectively.

- The stress–strain curves revealed that RFRP confinement increased both the peak stress and ultimate strain, particularly in the NC2 and LWC2 samples. Likewise, the load–displacement curves of the beam samples demonstrated increased load-bearing capacity and postpeak ductility with increasing layers of RFRP.
- Although the normal concrete samples exhibited greater overall strength due to greater density, the application of RFRP in lightweight concrete effectively closed the strength gap without significantly increasing the weight. This demonstrates the potential of the RFRP to decouple strength enhancement from density increase, making it highly advantageous for lightweight and sustainable construction.
- The failure mode shifted from brittle splitting or sudden crushing in the unconfined samples to more ductile and progressive response in the RFRP-confined samples. This behavior was reflected in the lengthened plateau region of the force-displacement curves, indicating enhanced energy absorption capacity. RFRP jacketing effectively bridged cracks and delayed their propagation, resulting in improved ultimate strain capacity and enhanced energy damping.
- The RFRP shows potential for retrofitting applications, particularly in normal and lightweight concrete, due to its ability to enhance strength and ductility. However, further studies are needed to address limitations associated with durability, long-term performance, and cost-effectiveness. Future research should investigate environmental exposure, economic feasibility, and full-scale structural applications to ensure its effectiveness for practical adoption in construction.

References

[1] Ozmen HB, Inel M. Effect of concrete strength and detailing properties on seismic damage for RC structures. Res Des. 2024;1(1):1-11. https://doi.org/10.17515/rede2024-005en1124rs

[2] Nwankwo CO, Ede AN, Olofinnade OM, Osofero AI. NFRP strengthening of reinforced concrete beams. IOP Conf Ser Mater Sci Eng. 2019;640(1). https://doi.org/10.1088/1757-899X/640/1/012074

[3] Yinh S, Hussain Q, Joyklad P, Chaimahawan P, Rattanapitikon W, Limkatanyu S, et al. Strengthening effect of natural fiber reinforced polymer composites (NFRP) on concrete. Case Stud Constr Mater. 2021;15(June). https://doi.org/10.1016/j.cscm.2021.e00653

[4] Parmo P, Hanus JL, Belayachi N, Bailly P. Effect of aggregate/binder ratio on mechanical and energy absorption properties of a straw-lime composite material. Constr Build Mater. 2023;400(March). https://doi.org/10.1016/j.conbuildmat.2023.132613

[5] Saad O, Ragab KS, Elnawawy O, Alharbi YR, Abadel AA, Talaat A, et al. Lightweight Structural Concrete. J Eng Res. 2023;11(1):52-66.

[6] Bozorgmehr Nia S, Nemati Chari M. Applied development of sustainable-durable high-performance lightweight concrete: Toward low carbon footprint, durability, and energy saving. Results Mater. 2023;20. https://doi.org/10.1016/j.rinma.2023.100482

[7] Suseno H, Soehardjono A. Evaluation of factors influencing the maximum crack width of pumice and scoria lightweight concrete one-way slabs. Eng Appl Sci Res. 2022;49(3):395 - 405.

[8] Sultan MA, Gaus A, Hakim R, Imran. Review of The Flexural Strength of Lightweight Concrete Beam Using Pumice Stone as of Substitution Partial Coarse Aggregate. Int J GEOMATE. 2021;21(85):154 - 159. https://doi.org/10.21660/2021.85.j2184

[9] Chen C, Yang Y, Zhou Y, Xue C, Chen X, Wu H, et al. Comparative analysis of natural fiber reinforced polymer and carbon fiber reinforced polymer in strengthening of reinforced concrete beams. J Clean Prod. 2020;263. https://doi.org/10.1016/j.jclepro.2020.121572

[10] Memon AH, Memon SA, Peerzada MH, Mangi SA, Muhammad K, Mujtaba G. Recent Eco-Friendly Developments in Personal Protective Clothing Materials for Reducing Plastic Pollution: A Review. Eng Technol Appl Sci Res. 2019;9(2):4012-8. https://doi.org/10.48084/etasr.2674

[11] Yahya Turki A, Al-Farttoosi MH. Investigation of the Stiffness and Ductility of Pre-Cracked RC Beams after repairing with CFRP using Different Strengthening Methods. Eng Technol Appl Sci Res. 2023;13(6):12423-6. https://doi.org/10.48084/etasr.6555

[12] Zendaoui A, Saadi M, Yahiaoui D, Amouri C. An Experimental and Analytical Study on the Compressive Behavior of Glass Fiber Reinforced Concrete (GFRC) confined with GFRP Composites. Eng Technol Appl Sci Res. 2024;14(6):17939-44. https://doi.org/10.48084/etasr.8750

[13] Toutanji H, Deng Y. Strength and durability performance of concrete axially loaded members confined with AFRP composite sheets. Compos Part BEngineering. 2002;33(4):255-61. https://doi.org/10.1016/S1359-8368(02)00016-1
[14] Yooprasertchai E, Wiwatrojanagul P, Pimanmas A. A use of natural sisal and jute fiber composites for seismic retrofitting of nonductile rectangular reinforced concrete columns. J Build Eng [Internet]. 2022;52(January):104521. https://doi.org/10.1016/j.jobe.2022.104521
[15] Ghalieh L, Awwad E, Saad G, Khatib H, Mabsout M. Concrete Columns Wrapped with Hemp Fiber Reinforced Polymer - An Experimental Study. Procedia Eng [Internet]. 2017;200:440-7. https://doi.org/10.1016/j.proeng.2017.07.062
[16] Saidi T, Hasan M, Amalia Z, Salsabila S. The analysis of the bond strength between natural fiber reinforced polymer (NFRP) sheets and concrete. Results Eng. 2023;18(March). https://doi.org/10.1016/j.rineng.2023.101124
[17] Nambiyanna B, Bakash MA, Reddy HNJ, Prabhakara R. Experimental investigation on flexural strengthening of RC slabs using natural fiber reinforced polymer composites (NFRPC). Asian J Civ Eng [Internet]. 2021;22(8):1581-93. https://doi.org/10.1007/s42107-021-00398-5
[18] Hussain Q, Ruangrassamee A, Tangtermsirikul S, Joyklad P. Behavior of concrete confined with epoxy bonded fiber ropes under axial load. Constr Build Mater [Internet]. 2020;263:120093. https://doi.org/10.1016/j.conbuildmat.2020.120093
[19] Sen T, Paul A. Confining concrete with sisal and jute FRP as alternatives for CFRP and GFRP. Int J Sustain Built Environ [Internet]. 2015;4(2):248-64. https://doi.org/10.1016/j.ijsbe.2015.04.001
[20] Jirawattanasomkul T, Ueda T, Likitlersuang S, Zhang D, Hanwiboonwat N, Wuttiwannasak N, et al. Effect of natural fibre reinforced polymers on confined compressive strength of concrete. Constr Build Mater. 2019;223:156-64. https://doi.org/10.1016/j.conbuildmat.2019.06.217
[21] Amalia Z, Saidi T, Hasan M, Al-Bakri NS, Fu L. The Impact of Fiber Density and Layering in NFRP on Confined Concrete Compressive Strength. J Civ Eng Forum. 2024;10(May):133-8. https://doi.org/10.22146/jcef.10408
[22] Pimanmas A, Hussain Q, Panyasirikhunawut A, Rattanapitikon W. Axial strength and deformability of concrete confined with natural fibre-reinforced polymers. Mag Concr Res. 2019;71(2):55-70. https://doi.org/10.1680/jmacr.17.00312
[23] Antonino JDP, Laroza Silva D. Axial Capacity Prediction of Concrete Externally Strengthened by Low-Cost Natural Fiber Reinforced Polymer Composite Utilizing Machine Learning Intelligence. In: ICACS 2024 - Proceedings of the 2024 8th International Conference on Algorithms, Computing and Systems. School of Graduate Studies, Mapua University, Manila, Philippines: Association for Computing Machinery, Inc; 2025. p. 36-42. https://doi.org/10.1145/3708597.3708603
[24] ASTM C33/C33M-23. Standard Specification for Concrete Aggregates. ASTM International, West Conshohocken, PA. 2023. p. 1-8.
[25] ASTM C127-15. Standard Test Method for Relative Density (Specific Gravity) and Absorption of Coarse Aggregate. ASTM International, West Conshohocken, PA. 2015. p. 1-5.
[26] ASTM C494/C494M - 99a. Standard Specification for Chemical Admixtures for Concrete. ASTM International, West Conshohocken, PA. 2001. p. 1-9.
[27] ACI Committee PRC-211.1-22. Selecting Proportions for Normal-Density and High-Density Concrete-Guide [Internet]. American Concrete Institute. 2022. p. 1-34. Available from: www.concrete.org
[28] ACI Committee 211.2-98. Standard Practice for Selecting Proportions for Structural Lightweight Concrete. American Concrete Institute. Detroit; 2004. p. 1-20.
[29] ASTM D3039/D3039M-17. Standard Test Method for Tensile Properties of Polymer Matrix Composit Materials. ASTM International, West Conshohocken, PA. 2017. p. 1-13.
[30] ASTM C39/C39M-23. Standard Test Method for Compressive Strength of Cylindrical Concrete Specimens. ASTM International, West Conshohocken, PA. 2023. p. 1-8.
[31] ASTM C78/C78M-22. Standard Test Method for Flexural Strength of Concrete (Using Simple Beam with Third-Point Loading). ASTM International, West Conshohocken, PA. 2022. p. 1-5.
[32] Fakhruddin, Mawaddah NA, Irmawaty R, Ngeljaratan LN. Physical and Mechanical Properties of Abaca Fiber Reinforced Polymer Composites for Sustainable Structural Application. Eng Technol Appl Sci Res. 2024;14(6):18955-60. https://doi.org/10.48084/etasr.8613
[33] Amalia Z, Saidi T, Hasan M, Al-Bakri NS, Fu L. The Impact of Fiber Density and Layering in NFRP on Confined Concrete Compressive Strength. J Civ Eng Forum. 2024;10(2):133-8. https://doi.org/10.22146/jcef.10408

Blank Page

Research on Engineering Structures & Materials
www.jresm.org

Research Article

Experimental and predictive assessment of recycled rubber-modified lightweight mortars

Luma Ahmed Aday [*,a]

Civil Engineering Department, College of Engineering, Al-Iraqia University, Baghdad, Iraq

Article Info

Article History:

Received 07 Aug 2025
Accepted 17 Sep 2025

Keywords:

Rubberized lightweight concrete;
Compressive strength prediction;
Physical and mechanical properties;
Artificial neural network

Abstract

This study examines lightweight cement mortars reinforced with Polyvinyl Alcohol (*PVA*) fibers to elucidate how introducing recycled rubber as a sand replacement influences microstructure-sensitive transport and load-bearing behavior. Using a standardized mix with a binary pozzolanic binder (Class F fly ash and silica fume), we assessed compressive and flexural strength, elastic modulus, stress–strain response, dry density, water absorption, and Ultrasonic Pulse Velocity (*UPV*). Increasing rubber fraction generally reduced strength and stiffness due to weaker interfacial bonding and elevated internal porosity; nevertheless, mortars with moderate rubber contents retained adequate strength while exhibiting enhanced plasticity/ductility, indicating potential for semi-structural use when properly optimized. An artificial neural network that ingests rubber content, dry density, water absorption, and UPV predicted 28-day compressive strength with high fidelity (R^2 = 0.94; MSE = 0.72MPa^2; MAPE = 1.87%), with *UPV* emerging as the most influential predictor. The combined experimental and data-driven findings provide non-destructive, *UPV*-anchored guidance for designing *PVA*-reinforced lightweight rubberized mortars for sustainable construction.

© 2025 MIM Research Group. All rights reserved.

1. Introduction

Lightweight concrete is characterized by its low density, typically less than 2000 kg/m^3, which is achieved by replacing conventional aggregates with lightweight materials such as recycled tire rubber. This reduction in mass contributes to lowering structural loads while maintaining the required mechanical performance. According to the American Tire Manufacturers Association, more than 300 million tires are discarded annually in the United States, with global figures exceeding 1.5 billion tires [1]. This environmental concern, along with rapid urbanization, has made waste tire management a pressing issue, prompting researchers to explore the use of recycled tires as partial replacements for traditional aggregates, with the dual objective of reducing environmental impact and improving concrete performance. One study showed that optimizing Tire-Derived Aggregate Concrete (TDAC) through particle grading, NaOH treatment, Supplementary Cementitious Materials (*SCMs*), and fiber reinforcement led to a 75.4% increase in compressive strength and a 465.6% improvement in toughness [2]. Other findings highlighted that since concrete strength is one of the most important parameters affecting structural performance, pretreatment of rubber with NaOH and silica significantly enhanced compressive strength and abrasion resistance, reaching 61.5 MPa at 10% replacement compared to untreated rubber concrete [3].

*Corresponding author: eng-luma00@aliraqia.edu.iq
[a]orcid.org/0000-0002-2689-4167
DOI: http://dx.doi.org/10.17515/resm2025-1063ma0807rs

Treated rubber (e.g., with NaOH or silane) maintained adequate compressive strength at up to 25% replacement. While replacing fine aggregate with rubber ash reduced flexural strength, the addition of rubber fibers improved mechanical properties and durability, as confirmed by microstructural analysis [4]. Furthermore, in addition, the incorporation of 1% rubber fibers by cement weight led to an improvement in compressive strength by 4.9% and flexural strength by 8.9%, while the splitting tensile strength decreased by approximately 12.4%. [5]. Rubberized concrete was also found to maintain acceptable strength levels up to 20% rubber content, although poor bonding with cement paste remains a challenge that warrants further investigation [6]. In contrast, rubberized concrete lost 54%–92% of its impact resistance and 21%–52% of its tensile strength when exposed to temperatures between 100–200 °C, with rubber chips performing better than crumb rubber [7]. The highest fracture resistance was observed at 30% RAP with 0% rubber, suggesting that rubber inclusion may not necessarily enhance fracture performance [8]. In another study, the addition of *PVA* fibers to rubberized concrete resulted in compressive strength of 49 MPa and improved durability [9]. Replacing fine aggregate with 5–15% recycled tire rubber or 35–100% expanded clay aggregates reduced density and strength while increasing porosity, with expanded clay performing better overall, making rubber more suitable for non-structural, eco-friendly applications [10]. Similarly, it was found that replacing fine aggregate with recycled rubber in self-compacting concrete performed better than coarse aggregate replacement [11]. It was also found that tire rubber can replace up to 7.5% of fine aggregate in M30 concrete without significantly affecting strength or durability [12], while improved durability was reported in aggressive environments at 2.5–7.5% rubber content due to reduced chloride penetration, acid attack, and strength loss [13]. Moreover, adding up to 10% rubber powder with a sand ratio of 33–36% improved impact resistance, noise reduction, and shrinkage behavior, although larger particle sizes and higher contents reduced strength and stiffness [14]. Treatment methods using silica fume and sulfuric acid significantly enhanced cement–rubber bonding in foam concrete, improving compressive strength by up to 56% [15]. Another study found that replacing coarse aggregate with 20% untreated rubber reduced compressive strength by 49%, but strength was restored to acceptable levels through compression casting using treated aggregates [16]. Combining NaOH-treated rubber with silica fume improved long-term durability and sustainability at 20–40% rubber content [17]. Studies [18,19] confirmed that adding fibers significantly enhances the mechanical and dynamic properties of rubberized concrete, helping to overcome the inherent strength limitations associated with rubber inclusion. High contents of crumb rubber (up to 40%) were found to significantly reduce strength by up to 50%; however, incorporating 0–5% treated rubber at a 0.4 water–cement ratio improved ductility by 86.2% and enhanced microstructural properties [20]. Low levels of fine (2–4 mm) or coarse (15 mm) rubber aggregates have been shown to enhance ductility and energy dissipation with minimal strength loss, making rubberized concrete a promising material for seismic and impact-resistant structures [21]. Additionally, concrete incorporating more than 80% crumb rubber exhibited reduced carbonation rates, while fiber-coated rubber (*FCR*) improved freeze–thaw and acid resistance by enhancing matrix cohesion [22]. Further, fiber-coated and polymer fiber-reinforced rubber concretes demonstrated enhanced durability and mechanical properties, although further research is needed to determine the optimal mix design [23]. Long-term performance improvements were also observed, including a 12% increase in compressive strength after 90 days [24]. While waste tire rubber typically reduces the mechanical strength of concrete, the use of appropriate treatment methods and moderate replacement ratios can significantly enhance both performance and sustainability [25]. Moreover, modifying rubberized concrete with 10% silica fume and 0.1% polypropylene fibers improved mechanical strength and microstructural integrity by reducing voids and limiting microcrack propagation [26]. These findings collectively provide dedicated support for the incorporation of recycled rubber in concrete, especially when combined with pozzolanic materials and fiber reinforcements. Recent advances in predictive modeling further support this direction. For instance, an *ANN* model accurately predicted the frost resistance of rubberized concrete (R^2=0.9825) based on mix proportions, rubber content, and freeze–thaw cycles, using relative dynamic elastic modulus as the durability metric [27]. Similarly, replacing 6% of aggregates with recycled rubber improved flexibility and crack resistance while maintaining similar performance to conventional concrete [28]. Machine learning models have also proven effective in predicting the mechanical properties of rubberized concrete at 28 days [29]. An

ANN model successfully predicted compressive strength using input parameters such as the water-to-cement ratio and granular skeleton, achieving a high correlation (up to 99.76%) and low error rates, potentially eliminating the need for extensive experimental testing. A broader comparative study [30] used *ANN*, Linear Regression (*LR*), Random Forest (RF), and M5P models to estimate the compressive strength of mortar modified with up to 7.5% crumb rubber, finding *ANN* to be the most accurate (R = 0.9998, RMSE ≈ 0.21). Moreover, [31] developed a Deep Neural Network (DNN) model using a comprehensive database of rubberized concrete mixes, achieving a high predictive accuracy (R^2 ≈ 0.99, RMSE < 0.13), outperforming traditional *ANN* and regression models.

In spite of all previous studies do not provide a systematic evaluation of lightweight mortars that pair sand-equivalent rubber (matched gradation and morphology to sand) with joint proportioning of SCMs, PVA fibers, and rubber under fixed mixing conditions thereby decoupling particle-size/surface effects from compositional effects across unexplored replacement ranges. This study addresses that gap by building response maps linking those joint proportions to mechanical and transport properties, UPV/NDT metrics, and ITZ features, delineating a balanced proportion window for practical and semi-structural applications and providing NDT-based mix guidance.

2. Methodology

2.1 Materials and Mix Design

This study endeavors to evaluate a series of lightweight concrete mixes to investigate the effects of replacing natural sand with Granulated Tire Rubber *(GTR)* on both mechanical performance and ultrasonic pulse transmission within a cementitious matrix. *GTR* was incorporated as a volumetric replacement for fine aggregate in incremental steps ranging from 0% to 30%, with a 5% increase in each mix. All concrete formulations were designed and tested according to ASTM C330/C330M [32] specifications, which define structural lightweight concrete as having a dry density less than 2000 kg/m^3. To maintain consistent bonding properties in all mixes, Type I Ordinary Portland Cement (*OPC*), conforming to ASTM C150, was used. In addition, two pozzolanic materials Class F fly ash conforming to ASTM C618 and silica fume conforming to ASTM C1240, were incorporated to improve microstructure and reduce porosity in the Interfacial Transition Zone (*ITZ*). Specifically, 25% of the cement content was replaced with fly ash, while silica fume contributed 8%, reducing the effective cement content from 400 kg/m^3 to 268 kg/m^3. Despite these substitutions, the total binder content was maintained at 400 kg/m^3, in line with ACI 211.2-98 [33]. properties of OPC, fly ash, and silica fume are summarized in Table 1.

Table 1. Physical and chemical properties of OPC, fly ash (FA), and silica fume

Property	Specific Gravity	SiO_2 (%)	Al_2O_3 (%)	Fe_2O_3 (%)	CaO (%)	MgO (%)	SO_3 (%)	LOI (%)	PAI at 7 days (%) (ASTM C311/C311 M)	Retained on 45 µm sieve (%)
OPC	3.15	20.5	4.8	3.2	63.7	1.5	2.7	1.5	-	-
Fly Ash	2.30	53.2	23.5	9.5	4.9	1.2	0.5	**1.9**	85.7	27
Silica Fume	2.21	92.0	1.0	0.5	0.2	0.3	0.1	1.0	112	7

Note: Properties as provided by the suppliers

PVA fibers were added at a constant volume ratio of 2% to all mixes. The main properties of PVA fibers are given in Table 2. A high-range water-reducing admixture (HRWRA), compliant with ASTM C494 Type F, was used to maintain workability without changing the water content. A constant water-to-binder (w/b) ratio of 0.45 was also adopted for all mixes to ensure uniform hydration and comparability of test results. . The recycled rubber was sourced from end-of-life vehicle tires and processed via mechanical shredding, magnetic separation, and sieving to produce clean, fine rubber granules. the recycled rubber particles ranged from 0.3 to 1.5 mm, which is comparable to the fine fraction of natural sand in terms of particle size distribution. Fig.1 displays the particle size distribution curves of both rubber and sand, demonstrating their comparable fineness and ensuring uniformity and reduced risk of segregation during mixing.

Table 2. Properties of polyvinyl alcohol (PVA) fibers

Length (mm)	Diameter (μm)	L/D	Density (g/cm^3)	Tensile Strength (MPa)	Modulus of Elasticity (GPa)	Elongation (%)
6.0	42.0	142	1.28	1700.0	57.0	6.0

Note: Properties as provided by the suppliers

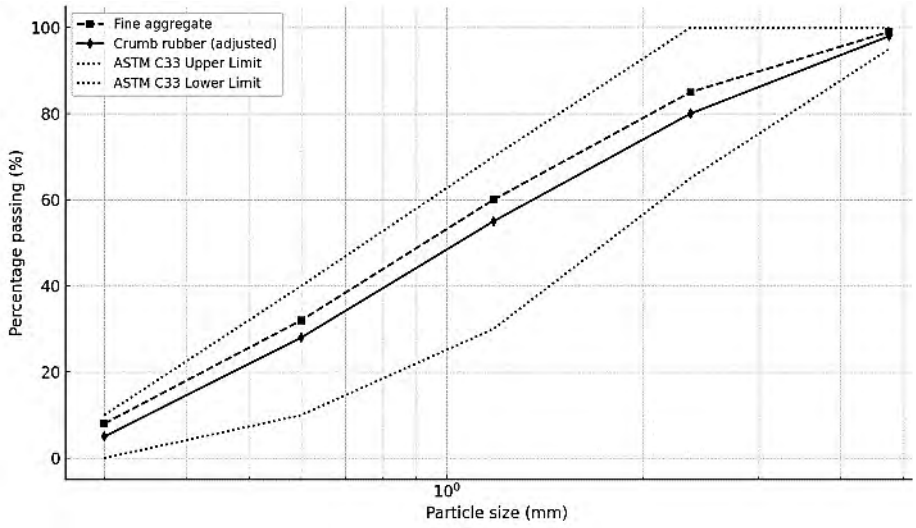


Fig. 1. Particle size distribution of fine aggregate and *GTR* with ASTM C33



(a) (b) (c) (d)

Fig. 2. Recycled and pozzolanic materials used in rubberized mortar mixtures (a) PVA, (b) ground tire rubber, (c)silica fume, and (d) fly ash

Table 3. Mix proportions of mortar specimens with varying rubber powder replacement levels-m^3

Mix ID	Rubber Replacement (%)	OPC (kg/m^3)	Fly Ash (kg/m^3)	Silica Fume (kg/m^3)	Water (kg/m^3)	Superplasticizer %	Sand (kg/m^3)	Rubber Powder (kg/m^3)	*PVA*% Fibers
R0	0	268	100	32	0.45	1.2	850	0	2%
R5	5	268	100	32	0.45	1.2	807	47	2%
R10	10	268	100	32	0.45	1.2	765	94	2%
R15	15	268	100	32	0.45	1.2	723	141	2%
R20	20	268	100	32	0.45	1.2	680	188	2%
R25	25	268	100	32	0.45	1.2	638	235	2%
R30	30	268	100	32	0.45	1.2	595	282	2%

The rubber powder, with a specific gravity of approximately 1.10, exhibited an irregular shape and a soft, elastic surface texture. In contrast, the natural sand used had a specific gravity of about 2.62.

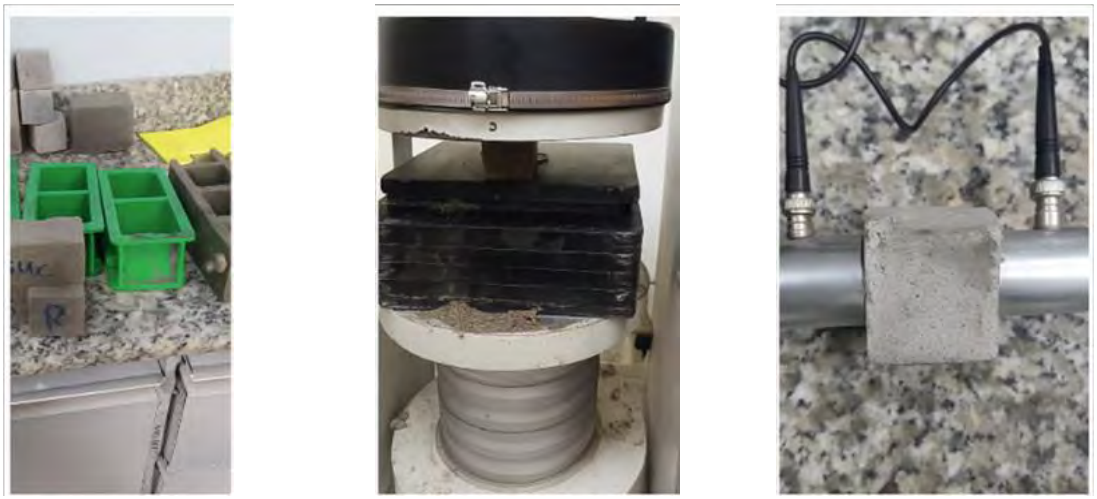
The proportions of the materials are summarized in Table 3. The materials are illustrated in (Fig 2.), which displays *PVA* fibers Fig. 2a, rubber granules Fig. 2b, silica fume Fig. 2c, and fly ash Fig. 2d.

2.2 Experimental Testing Program

An experimental program was designed to investigate the effect of Granulated Tire Rubber (GTR) on the mechanical and physical behavior of lightweight mortar. To ensure uniform dispersion of the components, a pan mixer was employed throughout the mixing process. The mixing procedure followed the guidelines of ASTM C192 with some modifications to accommodate the incorporation of rubber. The sequence consisted of dry mixing the natural aggregates and rubber particles for 1 minute, followed by the addition of cement, fly ash, and silica fume for another minute. Half of the mixing water was then introduced and mixing continued for 1 minute. Finally, the remaining water together with the High-Range Water-Reducing Admixture (HRWRA) was added, and mixing was extended for five minutes to obtain a homogeneous mixture.

The fresh mortar was cast into 50 × 50 × 50 mm cubes for compressive strength, dry density, water absorption, and ultrasonic pulse velocity (UPV) tests. Prisms of 40 × 40 × 160 mm were prepared for flexural strength tests, while cylinders of 100 × 200 mm were used for modulus of elasticity tests. All specimens were compacted using a vibration table to eliminate entrapped air and ensure consistency. After 24 hours of casting, the specimens were demolded and water-cured at [23 ± 2 °C] until the designated testing ages; laboratory handling/conditioning was conducted at [50 ± 5% RH] and [23 ± 2 °C]. The compressive and flexural strength tests were performed using a universal testing machine with a maximum load capacity of 2000 kN.

The tests were conducted in accordance with the relevant standards: compressive strength (ASTM C109) at 28 and 90 days, flexural strength (ASTM C348), modulus of elasticity (ASTM C469), ultrasonic pulse velocity (ASTM C597), and dry density and water absorption (ASTM C642) at 28 days. To ensure statistical validity and reliability, the average values were calculated from three specimens for each test. The Fig. 3 illustrates the laboratory workflow for rubberized mortar.



(a) (b) (c)

Fig. 3. Laboratory procedures for rubberized mortar testing

2.3 Prediction of Compressive Strength Using Artificial Neural Networks (ANN)

To complement the experimental results, a machine learning model was developed to explore the influence of selected physical parameters on the mechanical behavior of lightweight concrete using recycled rubber. This model utilized an *ANN* structured as a Multilayer Perceptron (*MLP*), with the primary objective of predicting the 28-day compressive strength. A notable advantage of this approach is its reliance on easily quantifiable input properties, reducing the need for repetitive and time-consuming laboratory tests. The *ANN* model was implemented using Python version 3.10 Supporting packages such as NumPy and Matplotlib were used to manage data preprocessing tasks

and facilitate graphical interpretation of the results. This predictive strategy provided a structured and efficient means of evaluating concrete performance based on experimental variables, complementing traditional testing procedures. The dataset contained 50 records. We randomly split the data into 70% training (n = 35), 15% validation (n = 8), and 15% testing (n = 7).The model relied on four input variables: *GTR* replacement ratio (%*GTR*), dry density, water absorption, and *UPV*. The network architecture consisted of three primary layers as shown in Fig. 4 .

- Input Layer: Comprising four neurons representing the following input variables:
  - *GTR* replacement percentage (%Rubber)
  - Dry density (kg/m^3)
  - Water absorption (%)
  - Ultrasonic pulse velocity (*UPV*, km/s)
- Hidden Layers:
  - The first hidden layer contains 8 neurons.
  - The second hidden layer also contains 8 neurons.
  - The *ReLU* (Rectified Linear Unit) activation function was applied in both hidden layers to enhance the model's ability to learn nonlinear relationships.
- Output Layer: A single neuron was used to represent the predicted value of compressive strength (fc) in megapascals (MPa).

Prior to training, all variables were normalized using the Min–Max Scaling technique according to the following formula:

$$X = [x_1, x_2, x_3, x_4]^T \tag{1}$$

Where; x_1: rubber content (%), x_2: dry density (kg/m^3), x_3: water absorption (%), x_4: ultrasonic pulse velocity (km/s).

Each feature was normalized using Min–Max scaling:

$$x_{i,norm}^{(n)} = \frac{x_i^{(n)} - x_{i,min}}{x_{i,max} - x_{i,min}}, \forall i = 1 \dots 4 \tag{2}$$

Where; $x_i^{(n)}$: the original value of feature i for sample n, $x_{i,min}$ and $x_{i,max}$: the minimum and maximum of feature i respectively. First hidden layer:

$$z_j^{(1)} = f\left(\sum_{i=1}^{4} w_{ji}^{(1)} x_i + b_j^{(1)}\right), j = 1,2, \dots,8 \tag{3}$$

Second hidden layer :

$$z_k^{(2)} = f\left(\sum_{j=1}^{8} w_{kj}^{(2)} z_j^{(1)} + b_k^{(2)}\right), k = 1,2, \dots,8 \tag{4}$$

Output layer:

$$\hat{y} = \sum_{k=1}^{8} w_k^{(2)} z_k^{(3)} + b^{(3)}) \tag{5}$$

Where; w , b *Weights and biases for layer,* f: *ReLU activation:* $f(x) = max(0, x)$

Training minimized the Mean Squared Error (*MSE*):

$$MSE = \frac{1}{N}\sum_{i=1}^{N} (y^{(i)} - \hat{y}^{(i)})^2 \tag{6}$$

Model accuracy was assessed using the coefficient of determination:

$$R^2 = 1 - \frac{\sum_{i=1}^{N}\left(y^{(i)} - \hat{y}^{(i)}\right)^2}{\sum_{i=1}^{N}\left(y^{(i)} - \overline{y}\right)^2} \quad (7)$$

Where; y^i*: actual value of sample I,* $\hat{y}^i$*: predicted value,* $\overline{y}$ *: mean of actual values, N: number of samples.*

The Mean Absolute Percentage Error (*MAPE*) was computed on the held-out test set:

$$MAPE\ \% = \sum_{i=1}^{N} \frac{100}{N} \left[\frac{\hat{y}^{(i)} - y^{(i)}}{y^{(i)}}\right] \quad (8)$$

Training used Adam (learning rate = 1e−3) with a batch size of 16. Training ran for up to 5,000 epochs with early stopping (patience = 100) based on validation loss to mitigate overfitting. Hyperparameters were tuned on a held-out validation set via guided trial-and-error within reasonable bounds; the final configuration was selected by the minimum validation *MSE*

The outputs were inverse-transformed to their original scale:

$$y^{actual} = \hat{y} \cdot (y^{max} - y^{min}) + y^{min} \quad (9)$$

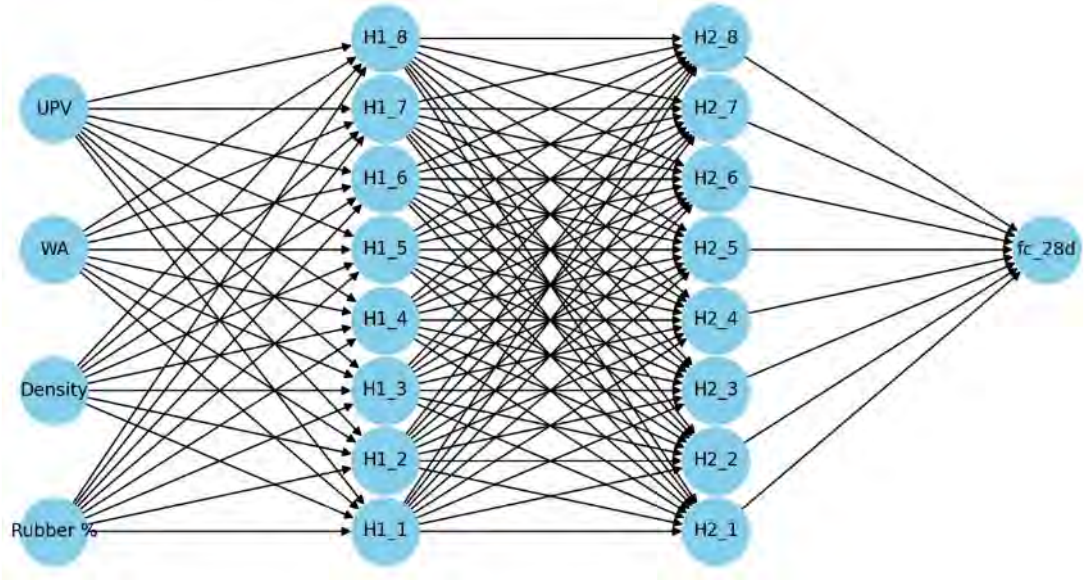


Fig. 4. Neural network architecture for predicting 28-day compressive strength

3. Result and Discussion

This section discusses the experimental results of the rubberized lightweight mortar mixtures, along with the predictive performance of the *ANN* model developed to estimate key mechanical parameters. The experimental tests provided a foundation for model training, and the *ANN*'s predictions were compared to the actual measured values to evaluate accuracy and generalization.

3.1 Compressive Strength Behavior

Compressive strength results at both 28 and 90 days including mean values, Standard Deviation (SD), and Coefficient of Variation (CoV) are presented in Table 4 and illustrated in Fig. 5. At 28 days, a progressive reduction in compressive strength was observed with increasing rubber powder replacement: approximately 14.5%, 23.8%, 31.2%, 40.0%, 48.1%, and 57.5% for R5–R30, respectively, compared to the reference mix R0. This trend is consistent with previous findings [39,40], which attributed the decline to the soft and hydrophobic nature of rubber particles that weaken the interfacial transition zone (ITZ), increase porosity, and reduce stiffness. Similarly, other studies [41,42] reported compromised mechanical performance due to weak rubber–cement bonding and

ineffective stress transfer across the matrix. Despite this strength degradation, CoV values for all mixes remained within the acceptable range of 4–6%, reflecting high internal consistency and effective compaction, supported by the use of HRWRA and well-dispersed PVA fibers. At 90 days, all mixes exhibited further strength gain over time. the reference mix R0 increased from 39.5 MPa at 28 days to 44.6 MPa at 90 days. Likewise, mix R5 improved from 33.8 to 40.4 MPa, R10 from 30.1 to 36.2 MPa, R15 from 27.2 to 33.1 MPa, R20 from 23.7 to 27.4 MPa, R25 from 20.5 to 21.9 MPa, and R30 from 16.8 to 19.2 MPa. This strength development is mainly attributed to the continuous hydration of unreacted cement particles, along with delayed pozzolanic reactions of fly ash and silica fume, which progressively consume calcium hydroxide and generate additional C–S–H gel. These secondary hydration products refine the pore structure, enhance the ITZ, and contribute to a denser microstructure, thereby improving long-term compressive strength. Nevertheless, the relative reductions compared to R0 at 90 days remained significant: 9.4% for R5, 18.9% for R10, 25.9% for R15, 38.5% for R20, 50.9% for R25, and 57.0% for R30.

These findings highlight a critical technical insight: although extended curing and refined mix design strategies particularly the inclusion of SCMs and PVA fibers can mitigate the negative effects of rubber inclusion to some extent, they cannot fully recover the structural integrity lost at higher rubber replacement levels. Thus, when incorporating recycled rubber into structural concrete, a careful balance must be maintained between sustainability goals and structural performance requirements.

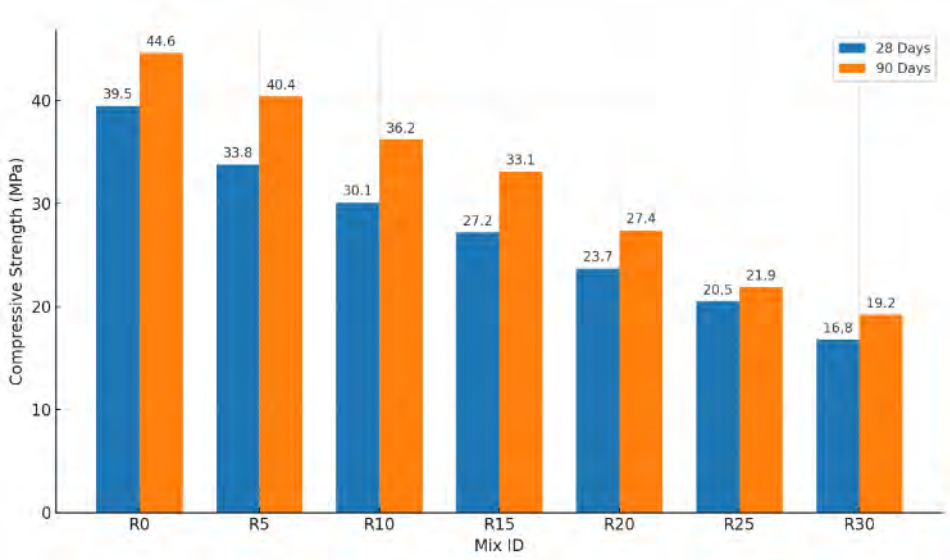


Fig. 5. Compressive strength test results

3.2. Elastic Modulus

Table. 4 presents the average values of the elastic modulus at 28 days. this property consistently decreases with increasing *GTR* replacement. Concrete mixes containing CR (*R5, R10, R15, R20, R25, and R30*) showed reductions in elastic modulus of approximately 8.5%, 15.4%, 21.6%,24.9%,30.9 and 37.9%respectively, compared to the reference mix (*R0*). This decline is mainly attributed to the inherently low stiffness of rubber particles and their weak interfacial bonding with the surrounding cementitious matrix, which compromises the concrete's resistance within the elastic range. Comparing the results across all mixtures reveals a clear inverse relationship between rubber content and elastic modulus higher replacement levels consistently led to lower stiffness. This trend is clearly illustrated in Fig. 6, which shows a steady degradation in elastic performance. These findings are in line with previous studies [43 ,44], which reported significant reductions in stiffness when rubber particles are incorporated, especially in lightweight concrete mixes.

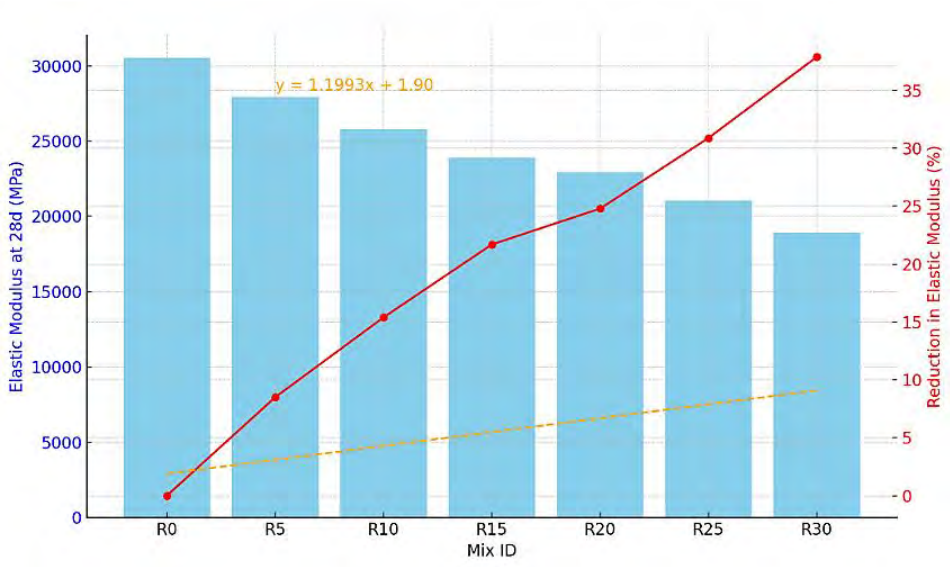


Fig. 6. Elastic modulus and reduction at 28 day

3.3 Stress–Strain Behavior

The stress–strain curves of the investigated mixes demonstrated a clear progression with increasing rubber content, as shown in Fig.7. The reference mix *R0*, representing lightweight concrete enhanced with *PVA* fibers and pozzolanic additives, displayed a sharply rising linear segment followed by a softening post-peak response characterized by moderate ductility. This behavior is largely attributed to the combined effects of *PVA* fibers, which help delay crack propagation and increase energy absorption, and the role of fly ash and silica fume in refining the cement matrix and improving interfacial bonding.

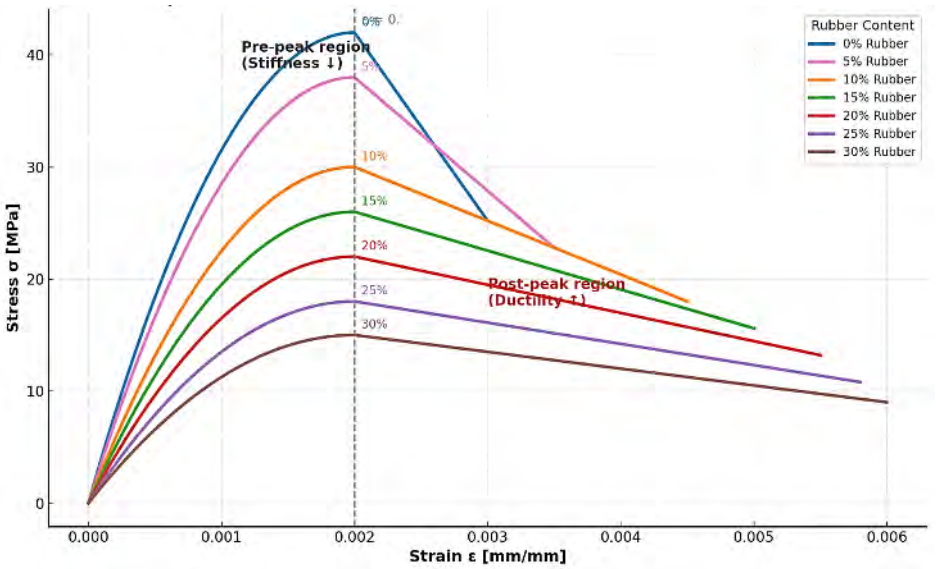


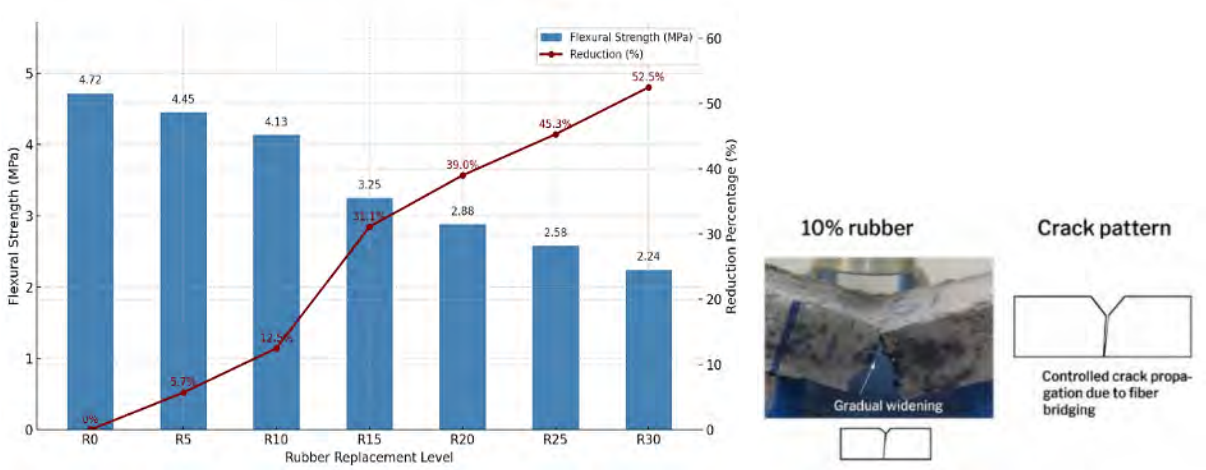
Fig. 7. Compressive stress-strain curves for reference concrete (R0) and rubberized concrete at 28 days

As outlined in Table 4, the recorded values for peak strain, ultimate strain, and peak stress align with the visual interpretations. A steady decline in peak compressive strength was observed as rubber content increased, while ultimate strain increased up to the *R10* mix before showing a reduction at higher replacement levels, indicating diminished ductility. As rubber content increased from *R5* to *R30*, a noticeable decrease in both peak strain and stiffness was evident, along with a steeper descending slope in the post-peak region most prominent in mixes *R25* and *R30*. This trend highlights a progressive weakening in structural integrity due to poor bonding between rubber

particles and the cementitious matrix, even though rubber inclusion contributed to greater deformability [45]. These observations are in agreement with previous research by [46- 49], which similarly found that the introduction of rubber into fiber-reinforced concrete results in a more ductile but less rigid compressive behavior.

3.4 Flexural Strength Behavior

The flexural strength at 28 days of the lightweight fiber-reinforced concrete mixes incorporating rubber exhibited a consistent decline as natural sand was progressively substituted with *GTR*, as depicted in Fig.8a, and summarized in Table 4. The control mix (R0) achieved 4.72 MPa, while mixes R5, R10, R15, R20, R25, and R30 recorded 4.45, 4.13, 3.25, 2.88, 2.58, and 2.24 MPa, respectively. With increasing rubber content from 5% to 30%, the strength reduced incrementally by approximately 7.8%, 12.5%, 20.8%, 34.5%, 44.1%, and 52.5%, respectively, compared to the reference mix. This downward trend is primarily attributed to the elastic nature of rubber particles and their inadequate adhesion to the cementitious matrix, which weakens the *ITZ* and raises the likelihood of microcracking under flexural loads. Nonetheless, the incorporation of 2% *PVA* fibers significantly enhanced post-cracking tensile performance through crack-bridging action, while the addition of pozzolanic materials such as fly ash and silica fume contributed to refining the cement matrix microstructure. Concrete mixes with moderate rubber content (*R5* to *R15*) demonstrated a favorable compromise between strength and ductility, making them suitable for lightweight structural elements where both mechanical strength and energy dissipation are required. As illustrated in Fig.8b, mixes like *R10* showed gradual and controlled crack propagation, reflecting improved post-cracking behavior due to the combined influence of fibers and rubber particles. These outcomes align with prior research by [50- 52], which emphasized the advantages of fiber–rubber hybrid systems in enhancing flexural toughness and ductility in concrete applications



(a) (b)

Fig. 8. (a) Flexural strength development of rubberized lightweight conrete and (b) crack pattern and fracture response of rubberized mortar under flexural loading

3.5 Interrelationship Between Physical Properties of Rubberized Lightweight Mortar

The integration of GTR into lightweight cementitious matrices significantly modifies their physical properties, particularly dry density, water absorption, and *UPV.* As shown in Fig.9, increasing the rubber content leads to a continuous decrease in dry density, primarily due to the low specific gravity of rubber granules (~1.10) compared to that of natural sand. This reduction in density is accompanied by a relative increase in water absorption, which is attributed to the rough and flexible surface of rubber particles that contribute to the formation of micro-voids within the cementitious matrix, thereby increasing overall porosity and disrupting the continuity of the internal concrete

structure. Parallel to this, UPV values also decline with increasing rubber replacement, reflecting a decrease in internal stiffness and homo-geneity caused by increased porosity [53,54]. To quantify the internal relationships between these variables, logarithmic regression models were applied. Dry density exhibited a strong inverse logarithmic relationship with water absorption, expressed by the model:

$$\rho = -501.32 \ln(WA) + 2496.73 \quad (10)$$

Similarly, *UPV* was found to exhibit a comparable logarithmic decline as water absorption increased:

$$UPV = -1.83 \ln(WA) + 5.46 \quad (11)$$

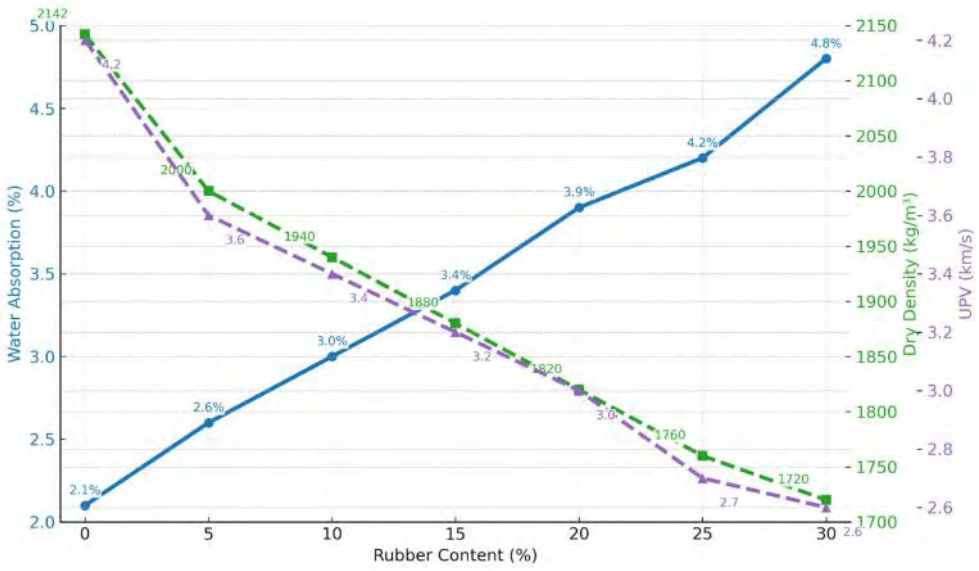


Fig. 9. Effect of rubber content on water absorption, dry density, and UPV at 28 days

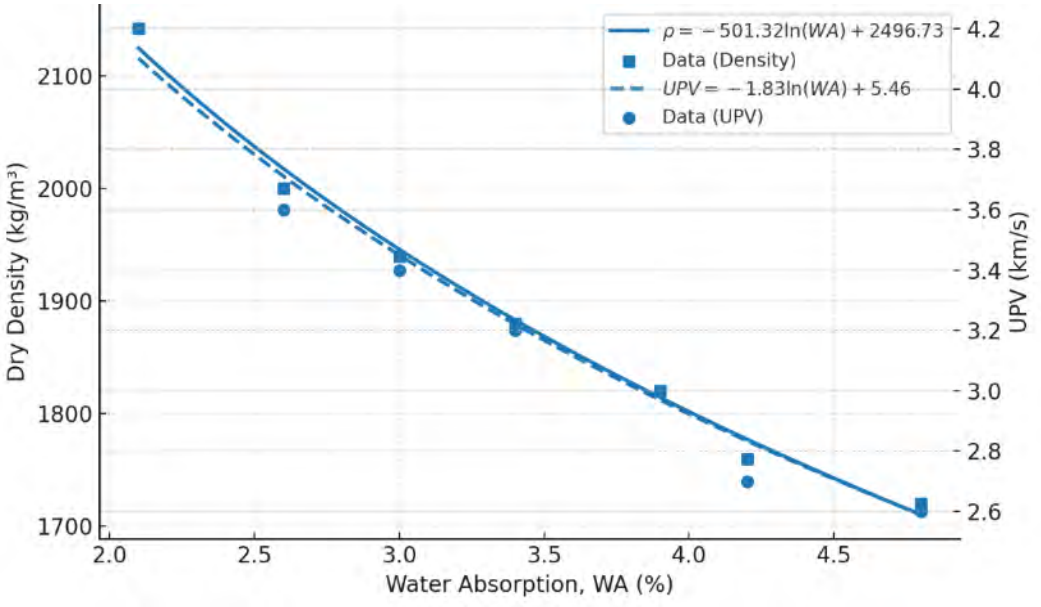


Fig. 10. Interrelationship between water absorption, dry density, and UPV

Both equations are depicted in (Fig.10) demonstrating high correlation coefficients ($R^2 > 0.98$), which indicates a strong interdependency among these physical parameters. Moreover, [55.56],

highlighted that the incorporation of mineral fillers and nano-sized pozzolans can refine the microstructure and partially mitigate the permeability effects induced by rubber inclusion. Notably, the UPV and density values remained within the acceptable limits for lightweight structural concrete up to 15% rubber replacement, as per ASTM C330/C330M, supporting the feasibility of using such modified mortars in structural and semi-structural applications. The established correlations confirm that water absorption is not only a durability-related indicator but also a reliable proxy for estimating other physical characteristics in rubberized lightweight mortar systems.

3.6 Analytical Evaluation and Comparative Performance of the ANN in Predicting 28-Day Compressive Strength

An *ANN* model was developed to predict the 28-day compressive strength of lightweight rubberized concrete, achieving R^2 = 0.94, *MSE* = 0.72 MPa^2, and *MAPE* = 1.87%, confirming high predictive accuracy up to 30% rubber replacement. The parity plot Fig. 11 shows close agreement between predicted and experimental values along the 1:1 line, indicating reliable performance and practical utility in reducing repetitive tests and expediting mix design. A typical decreasing trend in f_(c 28d) with increasing rubber content is observed, mainly due to loss of matrix cohesion, the elastic/hydrophobic nature of rubber, and increased porosity that weakens the ITZ. A one-at-a-time perturbation sensitivity analysis was conducted: each input (GTR content, dry density, water absorption, and UPV) was perturbed slightly while the others were held constant. The resulting change in the predicted 28-day compressive strength f_(c 28d) was recorded and used to rank input influence; as shown in Fig. 12, UPV was the most influential input, followed by dry density and water absorption.

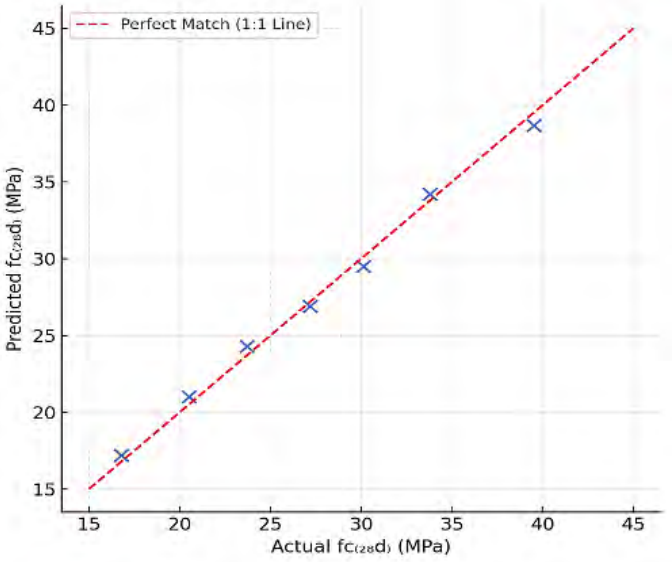


Fig. 11. Parity Plot: Predicted vs. Actual $f_{c\ 28d}$

Fig. 13 illustrates the joint effect of rubber content and UPV on $f_{c\ 28d}$: higher UPV combined with lower rubber content is generally associated with higher strength, highlighting the ANN's ability to capture nonlinear interactions. To further examine interrelationships, a Pearson correlation heatmap was constructed Fig. 14; its trends are consistent with the sensitivity ranking (rubber content negatively correlated with $f_{c\ 28d}$, *UPV* positively). Model accuracy and consistency were also verified through residual analysis (Fig. 15), where residuals are approximately normal and centered at zero, indicating unbiased predictions.

Table 4. Mechanical properties of rubberized lightweight mortar mixes (R0–R30)

Mix ID	Rubber Content [%]	Compressive Strength f_c				Modulus of Elasticity Ec	Peak Compressive Stress s_{max}			Deformation at Peak Compressive Stress e		Flexural Strength
		Mean $f_{c\,28d}$ [MPa]	$St.dev.$ $[MPa]$	CoV [%]	Reduction [%]	Mean Ec[MPa]	Mean s_{max} [MPa]	$St.dev.$ $[MPa]$	CoV [%]	Mean e		Mean Flexural Strength 28d (MPa)
R0	0	39.5	1.86	4.71	0	30518.18	41.93	3.28	7.82	0.000141		4.72
R5	5	33.78	1.67	4.94	14.48	27927.84	37.94	2.9	7.64	0.000283		4.35
R10	10	30.12	1.21	4.03	23.75	25814.97	29.95	2.3	7.68	0.000424		4.13
R15	15	27.18	1.31	4.81	31.19	23907.16	25.96	1.95	7.51	0.00057		3.74
R20	20	23.7	1.12	4.71	40	22930.09	21.96	1.45	6.6	0.00070		3.1
R25	25	20.52	0.99	4.8	48.05	21083.51	17.97	1.38	7.67	0.00085		2.64
R30	30	16.79	0.94	5.61	57.49	18933.14	14.98	1.25	8.34	0.00097		2.24

Note: Each mean value was calculated from three specimens (n = 3). Standard deviation (St. dev.) and coefficient of variation (CoV) were computed accordingly

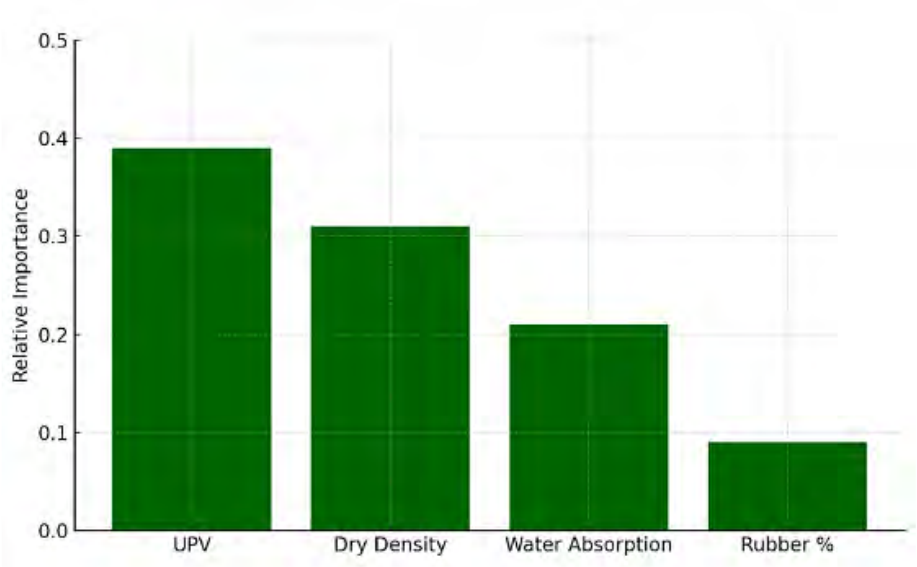


Fig. 12. Sensitivity Analysis of Inputs on $f_{c\ 28d}$

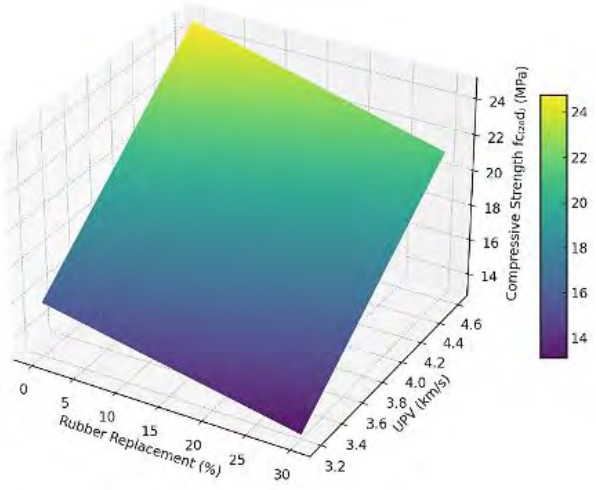


Fig. 13. Effect of rubber replacement (%) and UPV on 28-day compressive strength

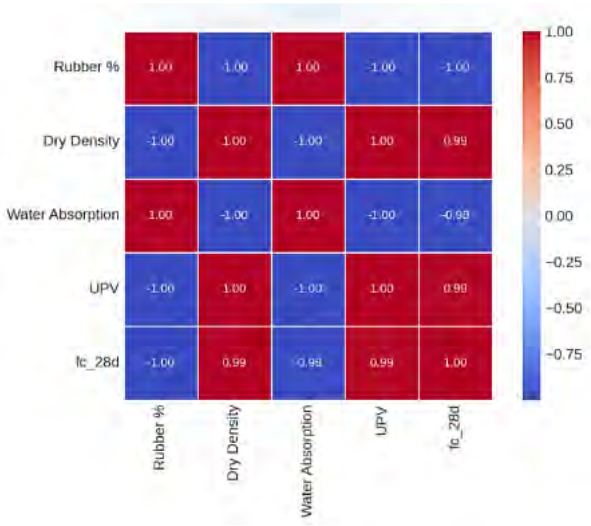


Fig. 14. Correlation Heatmap Between Input Features and $f_{c\ 28d}$

For benchmarking, the ANN was compared with third-order polynomial regression, Gaussian Process Regression (*GPR*), and Support Vector Machines (*SVMs*). The SVM used a radial basis function kernel,

$$K(x_i, x_j) = exp(-\gamma \parallel x_i - x_j \parallel^2) \quad 12$$

where γ controls the smoothness of the decision boundary and influences generalization. On the other hand, the *GPR* model employed a squared exponential covariance function:

$$k(x_i, x_j) = \sigma^2 exp\left(-\frac{(x_i - x_j)^2}{2l^2}\right) \quad 13$$

The ANN outperformed the baselines (R^2 = 0.94; MSE = 0.72). Polynomial regression achieved R^2 = 0.85; MSE = 1.10 MPa^2; GPR slightly exceeded SVM (R^2 ≈ 0.84–0.86; MSE ≈ 1.2–1.5 MPa^2), while SVM (RBF) yielded R^2 ≈ 0.82–0.83; MSE ≈ 1.6–1.9. These results highlight the superiority of the ANN for rubberized lightweight concrete and align with previous studies [57–59]. The developed

ANN thereby offers a reliable, cost-effective tool for predicting the mechanical performance of sustainable concrete mixtures, enabling in-silico screening to reduce trial batches and shorten design cycles.

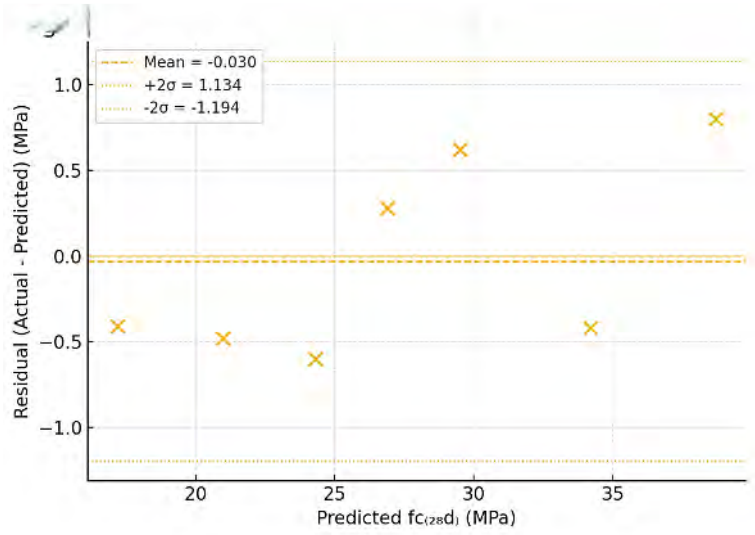


Fig. 15. Enhanced Residual Plot (with mean and ±2σ bands)

4. Conclusions

These conclusions stem from a comprehensive set of advanced laboratory experiments and predictive modeling aimed at assessing the behavior of lightweight mortar containing recycled rubber. The evaluation focused on essential mechanical and physical characteristics, while also examining the effects of key parameters on structural performance through the application of artificial intelligence methods. The principal outcomes of the study are summarized below:

- Strength loss with rubber replacement. At 28 days, compressive strength decreased from 39.5 MPa (R0) to 16.8 MPa (R30) (−14.5%, −23.8%, −31.2%, −40.0%, −48.1%, −57.5% for R5–R30). At 90 days, strengths increased to 44.6 MPa (R0) and 19.2 MPa (R30), but the relative reductions remained 9.4–57.0%. The reduction is linked to ITZ weakening, higher porosity, and the elastic/hydrophobic nature of rubber
- Rubber-enhanced mixtures demonstrated increased deformability, as shown by stress–strain analysis and a notable reduction in elastic modulus reaching up to 37.9 %. Although flexural strength declined with greater rubber content, the presence of 2% PVA fibers enhanced tensile resistance after cracking, improved ductility, and boosted energy absorption capabilities.
- Density, UPV, and absorption. Dry density fell from ≈2140 to ≈1720 kg/m^3 and UPV from ≈4.2 to ≈2.6 km/s as rubber increased from 0% to 30%, consistent with increased porosity and weaker internal continuity. Water absorption rose from ≈2.1% to ≈4.8%; using SCMs (fly ash, silica fume) with PVA fibers reduced pore connectivity and partially mitigated absorption.
- Peak strain showed a slight increase at moderate rubber levels before tapering off at higher replacement rates.
- Predictive modeling. The ANN predicted 28-day strength with R^2 = 0.94, MSE = 0.72 MPa^2, MAPE = 1.87%, outperforming polynomial regression, GPR, and SVM. Sensitivity analysis identified UPV as the most influential predictor of $f_{c\,28d}$, followed by dry density and water absorption.
- Semi-structural / non-critical structural uses: up to ≈15% *GTR* is a practical upper bound in this work, giving $f_{c\,28d}$≈27MPa, $f_{c\,90d}$ ≈33MPa, ρ≈1880kg/m^3,*UPV*≈3.2km/s, and water absorption ≈3.4%. These mixes balanced reduced density with acceptable strength and UPV for light-duty elements and energy-dissipative applications.

- Non-structural uses (blocks, infill, pavements, vibration-control layers): 20–30% GTR produced $f_{c\,28d}$≈24→17 MPa, UPV≈3.0→2.6km/s, ρ≈1800→1720kg/m^3, and higher water absorption (≈3.9–4.8%). These are suited to non-load-bearing or serviceability-driven applications.
- Replacing a portion of natural sand with granulated tire rubber repurposes end-of-life tires and curbs the extraction of virgin aggregates. The lower unit weight further decreases structural self-weight and can translate into reduced transport and handling impacts.
- the ANN model provides a robust and efficient substitute for extensive experimental testing, offering valuable support for sustainable concrete design and optimization.

References

[1] U.S. Tire Manufacturers Association (USTMA). Scrap Tire Management Summary. Washington (DC): USTMA; 2021. Available from: https://www.ustires.org

[2] Rodezno O.O, Rodriguez J, Nazari M. Transforming waste to strength: Experimental study and performance evaluation of tire-derived aggregate concrete for sustainable building solutions. *Case Stud Constr Mater*. 2025;22:e04826. DOI:10.1016/j.cscm.2025.e04826.

[3] Agrawal D, Ansari K, Waghe U, et al. Exploring the impact of pretreatment and particle size variation on properties of rubberized concrete. *Sci Rep*. 2025;15:11394. https://doi.org/10.1038/s41598-025-96402-y

[4] Guo S, Dai Q, Si R, Sun X. Evaluation of properties and performance of rubber-modified concrete for recycling of waste scrap tire. *J Clean Prod*. 2017;148:681–93. https://doi.org/10.1016/j.jclepro.2017.02.046

[5] Qader DN, Merie HD, Abdulhaleem KN. Impact of incorporating plastic fibers, walnut shells, and tire rubber fibers on the mechanical properties of concrete. *Electron J Struct Eng*. 2025. Available from: https://ejsei.com/EJSE/article/view/738

[6] Majain N, Radin JM, Ahmad MH, Zainal SMI, Sulaiman MF. The mechanical properties of concrete waste slurry containing steel fiber and rubber powder. In: *Cutting-Edge Advances in Nanofibers and Fibers: Shaping Future Applications*. Hershey (PA): IGI Global; 2025. p. 24. DOI:10.4018/979-8-3373-0230-0.ch015

[7] Makki OM. Heat influence on sustainable rubberized concrete mixes. *J Res Eng Struct Mater*. 2025. http://dx.doi.org/10.17515/resm2025-400ma0116rs

[8] Imani DM. Optimization of cementitious concrete mix design containing various percentages of recycled tire rubber granules and reclaimed asphalt pavement (RAP). *J Trans Infrastruct Eng*. 2025. 10.22075/jtie.2025.37190.1720

[9] Bheel N, Memon SA, Ali T, et al. Using optimization techniques on mechanical characteristics and sustainability assessment of rubberized concrete blended with PVA fiber through response surface methodology. *Int J CoCr Struct Mater*. 2024;18:59. https://doi.org/10.1186/s40069-024-00740-6

[10] Drebin Z, Bensaid S, Laidoudi B. Comparative study of the lightening of concrete through the use of recycled tire rubber and expanded clay aggregate. *Slovak J Civ Eng*. 2023;31(2):16–24. https://doi.org/10.2478/sjce-2023-0009

[11] Bušić R, et al. Recycled rubber as an aggregate replacement in self-compacting concrete—Literature overview. *Materials (Basel)*. 2018;11(9):1729. https://doi.org/10.3390/ma11091729

[12] Thomas BS, Gupta RC, Kalla P, Csetenyi L. Strength, abrasion and permeation characteristics of cement concrete containing discarded rubber fine aggregates. *Constr Build Mater*. 2014;59:204–12. https://doi.org/10.1016/j.conbuildmat.2014.01.074

[13] Thomas BS, Gupta RC, Panicker VJ. Recycling of waste tire rubber as aggregate in concrete: Durability-related performance. *J Clean Prod*. 2016;112:504–13. https://doi.org/10.1016/j.jclepro.2015.08.046

[14] Liu J, Li J, Xu Y, Ma S. Mechanical properties of cement concrete with waste rubber powder. *Appl Sci*. 2024;14(15):6636. https://doi.org/10.3390/app14156636

[15] Kashani A, Ngo T, Mendis P. Effects of surface treatments of recycled tyre crumb on cement–rubber bonding in concrete composite foam. *Constr Build Mater*. 2018;171:467–73. https://doi.org/10.1016/j.conbuildmat.2018.03.163

[16] Kazmi SMS, Abbas S, Munir MJ, Khitab A, Javed MF. Application of waste tire rubber and recycled aggregates in concrete products: A new compression casting approach. *Resour Conserv Recycl*. 2021;167:105353. https://doi.org/10.1016/j.resconrec.2020.105353

[**17**] Ince C, Shehata B, Derogar S, Ball R. Towards the development of sustainable concrete incorporating waste tyre rubbers: A long-term study of physical, mechanical & durability properties and environmental impact. *J Clean Prod*. 2021;334:130223. DOI:10.1016/j.jclepro.2021.130223

[**18**] Islam MMU, Li J, Roychand R, Saberian M. A comprehensive review on the application of renewable waste tire rubbers and fibers in sustainable concrete. *J Clean Prod*. 2022;357:131836. DOI:10.1016/j.jclepro.2022.133998

[**19**] Sheraz E, Ahmed A, Memon SA. Fresh and hardened properties of waste rubber tires-based concrete: A state of the art review. *SN Appl Sci*. 2023;5:119. https://doi.org/10.1007/s42452-023-05336-5

[**20**] Kilani M, Beroual A, Younes R. Effect of crumb rubber (CR) on concrete's and mortar's structural properties: A review. *Iran J Sci Technol Trans Civ Eng*. 2024. https://doi.org/10.1007/s40996-024-01647-8

[21] Karunarathna S, Linforth S, Kashani A, Liu X. Effect of recycled rubber aggregate size on fracture and other mechanical properties of structural concrete. *J Clean Prod*. 2021;313:127963. DOI:10.1016/j.jclepro.2021.128230

[**22**] Medina NF, Hernández-Olivares F, Frías M. Durability of rubberized concrete with recycled steel fibers from tyre recycling in aggressive environments. *Constr Build Mater*. 2023;391:132619. https://doi.org/10.1016/j.conbuildmat.2023.132619

[**23**] Liu J, Xu W, Li G, Chen B, Xiao Y, Huang H, Chen J. Performance and applications of polymer fiber rubber-reinforced concrete in civil engineering: A state-of-the-art review. *Polymers*. 2025;17(7):970. https://doi.org/10.3390/polym17070970

[**24**] Rashid K, Yazdanbakhsh A, Rehman MU. Sustainable selection of concrete incorporating recycled tire aggregate to be used as medium to low strength material. *J Clean Prod*. 2019;224:396–410. https://doi.org/10.1016/j.jclepro.2019.03.197

[**25**] Roychand R, Gravina RJ, Zhuge Y, Ma X. A comprehensive review on the mechanical properties of waste tire rubber concrete. *Constr Build Mater*. 2020;237:117651. https://doi.org/10.1016/j.conbuildmat.2019.117651

[**26**] Han C, Pang J, Hu S, et al. Study on static and dynamic mechanical properties and microstructure of silica fume–polypropylene fiber modified rubber concrete. *Sci Rep*. 2024;14:12573. https://doi.org/10.1038/s41598-024-63341-z

[**27**] Fu C, Li M. Frost resistance prediction for rubberized concrete based on artificial neural network. *Discov Appl Sci*. 2024;6:648. https://doi.org/10.1007/s42452-024-06357-4

[**28**] Vadivel TS, Suseelan A, Karthick K, et al. Experimental investigation and machine learning prediction of mechanical properties of rubberized concrete for sustainable construction. *Sci Rep*. 2024;14:22725. https://doi.org/10.1038/s41598-024-73504-7

[**29**] Bachir Rahali A, Mamoune Sidi Mohammed A, Trouzine H. Using artificial neural networks approach to estimate compressive strength for rubberized concrete. *Period Polytech Civ Eng*. 2018;62(4):858–65. https://doi.org/10.3311/PPci.11928

[**30**] Hurukadli P, Parashar B, Shukla BK, Sharma P, Sihag S. Predictive modeling of crumb rubber-modified mortar: Insights from ANN, LR, RF, and M5P methods. *Asian J Civ Eng*. 2025. https://doi.org/10.1007/s42107-025-01270-6

[**31**] Ly HB, Anh T, Mai HV, Van Quan T. Development of deep neural network model to predict the compressive strength of rubber concrete. *Constr Build Mater*. 2021;285:124081. https://doi.org/10.1016/j.conbuildmat.2021.124081

[**32**] ASTM C330/C330M-14. Standard Specification for Lightweight Aggregates for Structural Concrete. West Conshohocken (PA): ASTM International; 2014.

[**33**] ACI Committee 211. ACI 211.2-98: Standard Practice for Selecting Proportions for Structural Lightweight Concrete. Farmington Hills (MI): American Concrete Institute; 1998.

[34] ASTM C109/C109M-21. Standard Test Method for Compressive Strength of Hydraulic Cement Mortars (Using 2-in. or [50-mm] Cube Specimens). West Conshohocken (PA): ASTM International; 2021.

[35] ASTM C348-23. Standard Test Method for Flexural Strength of Hydraulic-Cement Mortars. West Conshohocken (PA): ASTM International; 2023.

[36] ASTM C469/C469M-14. Standard Test Method for Static Modulus of Elasticity and Poisson's Ratio of Concrete in Compression. West Conshohocken (PA): ASTM International; 2014.

[37] ASTM C597-22. Standard Test Method for Pulse Velocity Through Concrete. West Conshohocken (PA): ASTM International; 2022. .

[38] ASTM C642-21. Standard Test Method for Density, Absorption, and Voids in Hardened Concrete. West Conshohocken (PA): ASTM International; 2021. .

[39] Pham TM, Lee J, Pournasiri E, et al. Impact of rubber content on performance of ultra-high-performance rubberised concrete (UHPRuC). *Int J Concr Struct Mater*. 2024;18:59. https://doi.org/10.1186/s40069-024-00688-7

[40] He S, Jiang Z, Chen H, Chen Z, Ding J, Deng H, Mosallam AS. Mechanical properties, durability, and structural applications of rubber concrete: A state-of-the-art review. *Sustainability*. 2023;15(11):8541. https://doi.org/10.3390/su15118541

[41] Han C, Pang J, Hu S, et al. Study on static and dynamic mechanical properties and microstructure of silica fume–polypropylene fiber modified rubber concrete. *Sci Rep*. 2024;14:12573. https://doi.org/10.1038/s41598-024-63341-z

[42] Stojanovic M, Šupić S, Jankovic K, Bojovic D, Terzić A, Malešev M. Investigation of the mechanical properties of concrete incorporating recycled rubber particles. *Sci Sintering*. 2024;56(1):27–27. https://doi.org/10.2298/SOS240523027S.

[43] Jalal M, Nassir N, Jalal H. Waste tire rubber and pozzolans in concrete: A trade-off between cleaner production and mechanical properties in a greener concrete. *J Clean Prod*. 2019;238:117882. https://doi.org/10.1016/j.jclepro.2019.117882

[44] Lv J, Zhou T, Du Q, Wu H. Effects of rubber particles on mechanical properties of lightweight aggregate concrete. *Constr Build Mater*. 2015;91:145–9. https://doi.org/10.1016/j.conbuildmat.2015.05.038

[45] Eissa M, Habib A, Al Houri A, et al. Recent efforts on investigating the effects of recycled rubber content on the mechanical properties of structural concrete. *Discov Civ Eng*. 2024;1:16. https://doi.org/10.1007/s44290-024-00017-7

[46] Chen X, Ge G, Zhou Y, Pan S, Ren A. The effects of high-content rubber and steel fibers on the workability and mechanical properties of concrete. *Compos Adv Mater*. 2025;34. https://doi.org/10.1177/26349833251343228

[47] Strukar K, Kalman Šipoš T, Dokšanović T, Rodrigues H. Experimental study of rubberized concrete stress-strain behavior for improving constitutive models. *Materials*. 2018;11(11):2245. https://doi.org/10.3390/ma11112245

[48] Liu L, Guan Q, Zhang L, Liu C, Cai X, Chen X. Evaluation of the stress–strain behavior of rubberized concrete under quasi-static compression. *J Mater Civ Eng*. 2022;34(11). https://doi.org/10.1061/(ASCE)MT.1943-5533.0004480

[49] Walid M, Abdelrahman A, Kohail M, Moustafa A. Stress–strain behavior of rubberized concrete under compressive and flexural stresses. *J Build Eng*. 2022;59:105026. https://doi.org/10.1016/j.jobe.2022.105026

[50] Yildiz S, Guneyisi E. Static and dynamic behavior of fiber-rubber modified cementitious materials. *Sci Rep*. 2024;14:12573. https://doi.org/10.1038/s41598-024-63341-z

[51] El Naggar H, Abu Abdo AM. Properties and behavior of rubberized concrete enhanced with PVA fibers. *Buildings*. 2023;13(7):1681. https://doi.org/10.3390/buildings13071681

[52] Ge J, Mubiana G, Gao X, Xiao Y, Du S. Research on static mechanical properties of high-performance rubber concrete. *Front Mater*. 2024;11:1426979. https://doi.org/10.3389/fmats.2024.1426979

[53] Mohammed BS, Azmi NJ, Abdullahi M. Evaluation of rubbercrete based on ultrasonic pulse velocity and rebound hammer tests. *Constr Build Mater*. 2011;25(3):1388–97. https://doi.org/10.1016/j.conbuildmat.2010.09.004

[54] Shi M, Jeong D, Lee S, Choi Y. Relationship between UPV and strength of rubber concrete. *Defect Diffus Forum*. 2018;382:225–9. https://doi.org/10.4028/www.scientific.net/DDF.382.225

[55] Yasser N, Abdelrahman A, Kohail M, Moustafa A. Experimental investigation of durability properties of rubberized concrete. *Ain Shams Eng J*. 2023;14(6):102111. https://doi.org/10.1016/j.asej.2022.102111

[56] Gupta T, Chaudhary S, Sharma RK. Assessment of mechanical and durability properties of concrete containing waste rubber tire as fine aggregate. *Constr Build Mater*. 2014;73:562–74. DOI:10.1016/j.conbuildmat.2014.09.102

[57] Huang XY, Wu KY, Wang S, Lu T, Lu YF, Deng WC, Li HM. Compressive strength prediction of rubber concrete based on artificial neural network model with hybrid particle swarm optimization algorithm. *Materials*. 2022;15(11):3934. https://doi.org/10.3390/ma15113934

[58] Hasanipanah M, Abdullah RA, Iqbal M, Ly HB. Predicting rubberized concrete compressive strength using machine learning: A feature importance and partial dependence analysis. *J Sci Transp Technol*. 2023;3(1):27–44. https://doi.org/10.58845/jstt.utt.2023.en.3.1.27-44

[59] Choi Y, Kim IH, Lim HJ, Cho CG. Investigation of strength properties for concrete containing fine-rubber particles using UPV. *Materials (Basel)*. 2022;15(10):3452. https://doi.org/10.3390/ma15103452

Blank Page

Research on Engineering Structures & Materials
www.jresm.org

Research Article

Calibration of a general analytical model for the debonding strength of NSM-CFRP strip-concrete joints using particle swarm optimization

Sila Yaman [*,a]

Department of Civil Engineering, Süleyman Demirel University, Isparta, Türkiye

Article Info

Article History:

Received 05 Sep 2025

Accepted 25 Sep 2025

Keywords:

Intermediate crack (IC) debonding;
Particle swarm optimization;
NSM;
CFRP strip

Abstract

The use of FRP composites in the strengthening of existing structures has become increasingly common. In the strengthening of reinforced concrete (RC) elements using FRP through either the externally bonded reinforcement (EBR) or near-surface mounted (NSM) methods, the interface between the FRP and the concrete is typically the weakest link, which negatively affects the overall effectiveness of the strengthening technique. One of the primary damage mechanisms observed in RC members strengthened with NSM-CFRP strips is intermediate crack (IC) debonding. To estimate the maximum debonding resistance that develops in the NSM-CFRP strip against this type of failure, an existing analytical model in the literature was recalibrated using Particle Swarm Optimization (PSO). While preserving the original functional form proposed by the authors, four separate models were developed. The resulting coefficients and performance metrics (RMSE, MAE) were then compared with those of the existing model, which uses fixed coefficients reported in the literature, based on the same dataset. The recalibrated model achieved 6.9% improvement in MAE, demonstrating better prediction accuracy and more consistent performance across individual runs. These improvements can contribute to more efficient and reliable FRP strengthening designs by improving the accuracy of debonding strength estimation and enhancing economical design.

© 2025 MIM Research Group. All rights reserved.

1. Introduction

As reinforced concrete (RC) structures are exposed to increasing load demands or design deficiencies, their structural performance may gradually deteriorate. In such cases, strengthening techniques may become necessary to restore or enhance the load-carrying capacity, stiffness, or ductility - particularly to extend service life and improve safety under seismic or heavy loading conditions [1].

Recently, the use of Fiber Reinforced Polymer (FRP) composite materials in the strengthening of reinforced concrete (RC) structures has become increasingly widespread. There are two commonly adopted techniques for strengthening RC elements using composite materials: Externally Bonded Reinforcement (EBR) and Near Surface Mounted (NSM) methods [2-3]. In the EBR technique, FRP composites are bonded externally to the surface of the structural element, whereas in the NSM technique, FRP composites are embedded into grooves cut into the concrete cover and bonded using adhesives such as epoxy or repair mortars.

FRP composites are available in various forms, such as sheets, bars, and fabrics, and can be manufactured using different constituent materials, including carbon, glass, and aramid fibers.

*Corresponding author: silayaman@sdu.edu.tr
[a]orcid.org/0000-0003-3131-1090
DOI: http://dx.doi.org/10.17515/resm2025-1131an0905rs

Among these, Carbon Fiber Reinforced Polymer (CFRP) composites are the most widely used type. Compared to other types such as GFRP and AFRP, CFRP composites are preferred in structural strengthening applications due to their high tensile strength and stiffness, lower unit weight, resistance to corrosion, favorable performance under fire exposure, better fatigue performance, and more advanced manufacturing technologies. FRP materials exhibit linear elastic behavior up to their ultimate tensile strength, beyond which they fail abruptly and lose their load-carrying capacity.

In any strengthening application, it is ideal to fully utilize the mechanical properties of the FRP material [4]. In RC elements strengthened with FRP, the interface between the FRP and concrete is often the weakest link, and this interface plays a critical role in determining the effectiveness of the strengthening technique [5]. One of the major failure modes observed in elements strengthened with NSM-CFRP strips is known as intermediate crack (IC) debonding [6–8]. This failure typically occurs when a flexural or tensile crack in the concrete intersects the bonded CFRP strip. At the intersection point, cracks initiate at the FRP–concrete interface and often propagate into the surrounding concrete substrate [6]. If these interface cracks coalesce and reach the end of the CFRP strip, the deformation in the strip decreases significantly, leading to what is defined as "intermediate crack debonding" (IC debonding) [6, 9] (Fig. 1).



Fig. 1. Schematic illustration of the IC debonding failure mechanism (a) Initial state with applied load, (b) Development of flexural cracks intersecting the CFRP strip, (c) Initiation of debonding at the NSM-CFRP strip–concrete interface, (d) Propagation and coalescence of cracks leading to IC debonding failure

Several analytical models have been proposed in the literature to estimate the debonding strength at the NSM-CFRP interface, based on experimental studies [6, 10–17]. However, these models were generally calibrated using a limited number of experimental datasets. In the present study, the objective is to improve the accuracy of the model developed by Seracino et al. [6] by recalibrating its fixed parameters using Particle Swarm Optimization (PSO).

In recent years, the use of soft computing-based innovative approaches for solving civil engineering problems has been increasingly adopted [18–21]. In this context, artificial neural networks (ANNs) and/or machine learning (ML) techniques have been employed in various studies to predict or estimate key structural parameters, such as the compressive strength of concrete [22–24], the shear strength of reinforced concrete (RC) beams [25], the load-bearing capacity of strengthened RC slabs [26–27], and the required number of FRP layers for strengthening RC members or frames [28–29].

Li et al. [30] and Hu et al. [31] developed backpropagation neural network models to improve the accuracy of predicting debonding deformations in RC beams strengthened with FRP. Ghaidan et al. [32] applied multinomial logistic regression analysis to address the issue of concrete cover

separation - a premature failure mode observed in RC beams strengthened using NSM-FRP techniques.

Several studies in the literature have utilized Particle Swarm Optimization (PSO) for various structural engineering applications [33–34]. Ghodousian et al. [35] employed PSO to evaluate the interfacial bond strength of colored self-compacting concrete repair overlays. Mohammadizadeh and Esfandnia [36], as well as Wahab et al. [37], applied various metaheuristic algorithms, including PSO, to predict the compressive strength of reinforced concrete (RC) columns confined with FRP.

Nguyen and Lý [38] used Adaptive Neuro-Fuzzy Inference System (ANFIS) combined with PSO to estimate the bond strength between CFRP and concrete. Su et al. [39] proposed a backpropagation neural network model to predict the bond capacity at the NSM-CFRP-to-concrete interface. Kumar et al. [40] predicted the bond strength between FRP and concrete surfaces using Artificial Neural Networks (ANN), an optimized Artificial Bee Colony (ABC)-ANN, and Gaussian Process Regression (GPR). In a subsequent study, Kumar et al. [41] employed a PSO–optimized ANN approach. Pei and Wei [42] estimated this bond strength through an ant colony optimization-based ANFIS model. Zhang et al. [43] utilized six different ANN models. These models predict bond strength and shear capacity at the FRP–concrete interface. Tao and Xue [44] proposed a novel hybrid model. It integrates PSO with Random Forest (RF) techniques to predict FRP–concrete bond strength. Shbeeb et al. [45] applied both ANN and ANFIS methods. Xue et al. [46] validated the predictive capability of Multivariate Adaptive Regression Splines (MARS) and Wavelet Neural Network (WNN) algorithms for FRP–concrete bond strength. They also recalibrated these models using PSO. Moreover, Haddad et al. [47] employed artificial neural networks to determine the bond strength between EBR-FRP and heat-damaged concrete.

There are numerous studies in the literature predicting the debonding strength at the NSM-CFRP and concrete interface using artificial intelligence and optimization algorithms. However, research focusing on systematic improvement of existing analytical models through recalibration using methods such as Particle Swarm Optimization (PSO) remains limited. This study aims to improve the predictive accuracy of an existing analytical model [6] used to estimate the debonding strength at the NSM-CFRP strip–concrete interface. To this end, while preserving the original mathematical structure of the model, its constant coefficients were recalibrated using the Particle Swarm Optimization (PSO) technique. By adapting the model - originally proposed in the literature with fixed coefficients - to the available dataset through optimization, its prediction performance has been enhanced. During the calibration process, Root Mean Square Error (RMSE) and Mean Absolute Error (MAE) were used as cost functions, and two scenarios were considered: one with the first two geometric coefficients fixed, and one with them included as variables. As a result of the calibration, improvements of 0.73% in RMSE and 6.9% in MAE were achieved. Although these numerical differences may appear small, they can contribute to the design of CFRP-strengthened structures in a safer, more economical manner - avoiding unnecessary conservatism. In this respect, the study brings data-driven refinement to existing analytical models and enables more accurate predictions in structural engineering applications.

2. Material and Method

2.1. Material

Seracino et al. [6] proposed an analytical model to predict the debonding strength at the NSM CFRP strip - concrete interface using experimental data compiled from the literature. In the present study, the same experimental dataset was used to recalibrate the analytical model through the Particle Swarm Optimization (PSO) method. The experiments were conducted on CFRP strips embedded into concrete blocks using the NSM technique, and debonding strengths were obtained under push–pull loading conditions. The loading was uniaxial and applied in a monotonic (continuously increasing) manner. In the tested specimens, key parameters such as CFRP strip width (d_p), thickness (b_p), elastic modulus (E_p), embedment length (L), and concrete compressive strength (f_c) were varied. The ranges of these parameters are as follows: strip width (d_p), 9.95 - 20.47 mm; strip thickness (b_p), 1.2 - 2.9 mm; elastic modulus (E_p), 144600 - 162300 MPa; embedment length (L), 200 - 350 mm and concrete compressive strength (f_c): 30 - 65 MPa. These

parameters are the key factors influencing the debonding behavior at the NSM-CFRP interface and are critical for the calibration and validation of the model. The dataset used in this study consists of a total of 21 experimental tests, covering various combinations of the listed parameters. Statistical information related to these parameters and the corresponding experimental debonding strength results (P_{exp}) is provided in Table 1.

Table 1. Statistical data of the experimental dataset used in the study

	d_p (mm)	b_p (mm)	E_p (MPa)	f_c (MPa)	L (mm)	P_{exp} (kN)
Mean	14.51	1.33	161,195.24	43.48	233.33	47.63
Standard Error	1.03	0.08	831.36	2.51	11.09	4.14
Median	10.56	1.26	161,800.00	50.00	200.00	45.10
Standard Deviation	4.71	0.36	3809.75	11.52	50.83	18.97
Sample Variance	22.21	0.13	14,514,226.19	132.66	2583.33	359.83
Kurtosis	-1.97	20.76	20.81	-1.45	-0.46	-1.54
Skewness	0.30	4.54	-4.55	-0.12	1.08	0.33
Range	10.52	1.70	17,700.00	35.00	150.00	54.90
Minimum	9.95	1.20	144,600.00	30.00	200.00	23.00
Maximum	20.47	2.90	162,300.00	65.00	350.00	77.90
Sample Size			21			

2.2. Method

2.1.1 Analytical Model for Debonding Strength

Seracino et al. [6] proposed a generalized analytical model to predict the interfacial debonding strength (P_{IC}) of adhesively bonded strip–concrete interfaces. The model was developed by considering an idealized bond–slip relationship of the strip–concrete interface. It is a practical model applicable to strips used in both Externally Bonded Reinforcement (EBR) and Near Surface Mounted (NSM) techniques, and it depends solely on the strip geometry and material properties. The maximum debonding strength at the strip–concrete interface is expressed by Eq (1):

$$P_{IC}=\sqrt{\tau_{max}\times\delta_{max}}\cdot\sqrt{L_{per}\times E_p\times A_p} \quad (1)$$

$$L_{per}=2d_f+b_f \quad (2)$$

$$d_f=d_p+t_d,\quad b_f=b_p+2t_b \qquad (t_d=t_b=1) \quad (3)$$

$$A_p=b_p\times d_p \quad (4)$$

Fig. 2 schematically illustrates the debonding failure plane that occurs at strip-to-concrete interfaces and forms the conceptual foundation of the modeling approach adopted in this study. The debonding surface is defined as the mortar layer that separates from the concrete substrate while remaining attached to the CFRP strip. The transverse and longitudinal thicknesses of the mortar layer adhered to the strip are denoted as t_b and t_d, respectively. In the model proposed by Seracino et al. [6], these thicknesses are assumed to be constant and equal to 1 mm. The debonding surface is represented as a rectangular failure region characterized by its width (b_f) and depth (d_f), which are geometrically related to the dimensions of the NSM CFRP strip (b_p and d_p). The parameter L_{per} denotes the effective debonding length in the transverse section and plays a significant role in the transfer of shear stress along the interface. In this context, δ_{max} represents the maximum slip displacement that occurs at the interface prior to complete debonding, while τ_{max} denotes the corresponding maximum shear stress. Together, these two quantities define the energy dissipation capacity of the interface ($\tau_{max}\times\delta_{max}$), which is modeled as a function of the aspect ratio (φ_f) of the failure plane and the cylindrical compressive strength of concrete (f_c), as shown in Eq (5) and Eq (6). As illustrated in Fig. 2, this modeling approach assumes that debonding occurs along a well-

defined shear plane, the geometry of which governs the mechanical behavior of the bonded joint. Therefore, Fig. 2 not only serves as a conceptual basis for the analytical model but also helps visualize the physical meaning of the key parameters involved in the calibration process.

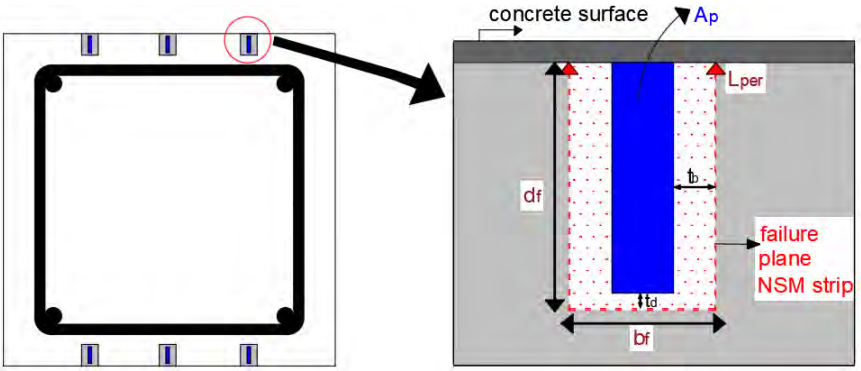


Fig. 2. IC Debonding failure plane of the strip embedded in the groove (tb = td = 1 mm) [6]

$$\varphi_f = \frac{d_f}{b_f} \tag{5}$$

$$\delta_{max} \times \tau_{max} = (C \times \varphi_f^m \times f_c^n) \tag{6}$$

Here, the constants C, m, and n were optimized using linear regression analysis. The values of δ_{max} and τ_{max}, which are necessary for determining the debonding strength, were obtained using Eq (7) and Eq (8), respectively.

$$\tau_{max} = (0.802 + 0.078\varphi_f) \times f_c^{0.6} \tag{7}$$

$$\delta_{max} = \frac{0.976\varphi_f^{0.526}}{0.802 + 0.078\varphi_f} \tag{8}$$

In the proposed analytical model for determining the debonding strength, the values of t_b and t_d are assumed to be constant and equal to one, as stated in the study. Accordingly, by modifying Eq (3), an expression containing constant coefficients is obtained (Eq 9).

$$d_f = d_p + 1, \quad b_f = b_p + 2 \tag{9}$$

Within the scope of this study, the calibration of the constant values in the analytical model (1 and 2 due to t_b and t_d; 0.976, 0.526, 0.802, 0.078, and 0.6) was performed using Particle Swarm Optimization (PSO). Since these values were originally treated as fixed coefficients in the model equations, they were redefined as variable parameters (K_1, K_2, ..., K_7) in the optimization process. This allowed the PSO algorithm to iteratively update their values during each run-in order to identify the optimal set of coefficients. Based on the original analytical formulation and the parameters described above, the modified model used in the optimization process is expressed in Eq 10. In this equation, the constants are replaced by optimization variables (K_1 to K_7) to allow for calibration using PSO:

$$P_{IC} = \sqrt{\left(\left(k_5 + k_6\left(\frac{d_p + k_1}{b_p + k_2}\right)\right).{f_c}^{k_7}\right).\left(\frac{k_3\left(\frac{d_p + k_1}{b_p + k_2}\right)^{k_4}}{\left(k_5 + k_6\left(\frac{d_p + k_1}{b_p + k_2}\right)\right)}\right).\sqrt{\left[2(d_p + k_1) + (b_p + k_2)\right].E_p.(d_p.b_p)}} \tag{10}$$

Table 2 presents the mapping between the parameters used in the PSO algorithm and their corresponding constants in the analytical model.

Table 2. Constants used in the model

PSO Parameter	K_1	K_2	K_3	K_4	K_5	K_6	K_7
Original Constant	1	2	0.976	0.526	0.802	0.078	0.6
Equation Number	Eq 9	Eq 9	Eq 8	Eq 8	Eq 7, Eq 8	Eq 7, Eq 8	Eq 7

K_1 and K_2 are geometric correction coefficients affecting the interaction area between the CFRP strip and concrete (related to the adhesive thickness and width). They replace the constants 1 and 2 in Eq 9. K_3 and K_4 represent the multiplier and exponent parameters used in the function defining the maximum shear displacement, which governs the deformation characteristics of the interface. K These replace the constants 0.976 and 0.526 in Eq 8. K_5 and K_6 are linear coefficients associated with φ_f in the maximum shear stress formula. They replace the values 0.802 and 0.078 in Eq 7 and Eq 8, respectively. K_7 is the exponential parameter reflecting the influence of concrete compressive strength and replaces the value 0.6 in Eq 7. These parameters are directly integrated into the mathematical formulation of the model and are optimized to enhance prediction accuracy.

2.2.2 Partical Swarm Optimization

Particle Swarm Optimization (PSO) is a nature-inspired metaheuristic optimization algorithm developed by Kennedy and Eberhart in 1995 [48]. The fundamental inspiration behind the algorithm is the collective behavior exhibited by flocks of birds or schools of fish while searching for food. Based on swarm intelligence, this algorithm is simple yet powerful [49–50]. PSO is widely used to solve nonlinear and complex problems in continuous or discrete parameter spaces.

PSO operates on a swarm consisting of individuals called "particles," which represent a set of potential solutions. Each particle corresponds to a point in the solution space and possesses certain velocity and position information. Over time, these particles move toward better solutions by learning from their own experiences as well as the best experiences of other particles in the swarm [51]. Fundamentally, PSO relies on particles adjusting their positions toward the best position found by any member of the swarm, and this process continues iteratively until the target is achieved [52]. The flowchart illustrating the steps of the algorithm is presented in Fig. 3.

In PSO, the initial position (Eq 11) and velocity (Eq 12) of each particle are first determined [53]. The fitness values of each particle, which lie within the defined boundary limits, are then calculated using Eq (13). In each iteration, the personal best (p_{best}) values - representing the best solution a particle has found so far - and the global best (g_{best}) values - representing the best solution found by any particle in the entire population - are identified. Based on these two best values, the velocities (Eq 14) and positions (Eq 15) of the particles are updated accordingly.

$$\begin{bmatrix} X_{11} & X_{12} & \dots & X_{1n} \\ .. & .. & \dots & .. \\ X_{m1} & X_{m2} & \dots & X_{mn} \end{bmatrix} \tag{11}$$

$$\begin{bmatrix} V_{11} & V_{12} & \dots & V_{1n} \\ .. & .. & \dots & .. \\ V_{m1} & V_{m2} & \dots & V_{mn} \end{bmatrix} \tag{12}$$

$$\begin{bmatrix} f(1) = f(X_{11}, X_{12}, \dots X_{1n}) \\ .. \\ f(m) = f(X_{m1}, X_{m2}, \dots X_{mn}) \end{bmatrix} \tag{13}$$

$$V_{id} = WV_{id} + c_1 rand_1(pbest_{id} - X_{id}) + c_2 rand_2(gbest - X_{id}) \tag{14}$$

$$X_{id} = X_{id} + V_{id} \tag{15}$$

Here, W represents the inertia weight; c_1 and c_2 are the acceleration (or scaling) coefficients; X_{id} denotes the position, and V_{id} denotes the velocity of the particle. The terms $rand_1$ and $rand_2$ are uniformly distributed random numbers between [0–1]. For problems with fewer parameters and low complexity, a larger inertia weight value may be used, whereas for more complex problems, a smaller value is generally preferred [54].

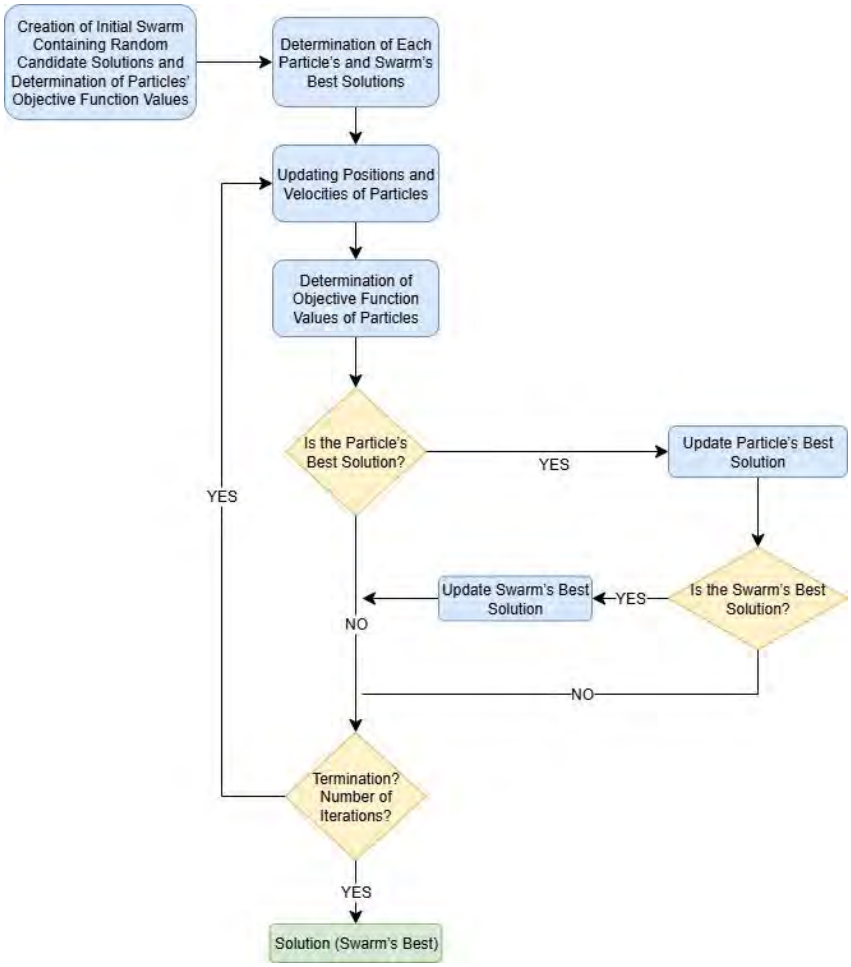


Fig. 3. Flowchart of the PSO algorithm [50]

To effectively operate the Particle Swarm Optimization (PSO) algorithm, an objective function is required to evaluate the performance of each possible parameter combination within the solution space. In this study, a PSO-based model was developed with the aim of modifying the constants in the analytical model proposed by Seracino et al. [6] to achieve results that more closely match the experimental data. The inertia weight (W) was set to 0.7. The cognitive (c_1) and social (c_2) acceleration coefficients were taken as 1.5. The swarm size (m) was fixed at 30 particles, and the maximum number of iterations was limited to 1000.

Two different error metrics were used to evaluate the predictive performance of the model: Mean Absolute Error (MAE) and Root Mean Square Error (RMSE). These error metrics are calculated based on the differences (i.e., errors) between the maximum load predicted by the PSO-calibrated model and the experimentally obtained load values.

2.2.3 Root Mean Square Error (RMSE)

RMSE is the square root of the mean of the squared errors. Since it involves squaring the errors, it penalizes larger errors more heavily.

$$RMSE=\sqrt{\frac{1}{n}\sum_{i=1}^{n}(P_i-P_i')^2} \tag{16}$$

2.2.4 Mean Absolute Error (MAE)

MAE is the mean of the absolute values of the errors. It directly reflects the magnitude of the model's prediction errors and treats all errors equally, regardless of their direction or size.

$$MAE = \frac{1}{n}\sum_{i=1}^{n} /P_i - P_i'/ \quad (17)$$

In both error metrics, values approaching zero indicate higher model accuracy. While MAE provides a general measure of the average error magnitude, RMSE reflects the model's sensitivity to larger deviations. In this study, RMSE and MAE were used as objective functions in the optimization process, and the aim was to identify the set of coefficients that minimize these error metrics.

2.2.5 Model Calibration

In this study, the original formula structure was preserved, and all models were calibrated using Particle Swarm Optimization (PSO). The general procedure involved in putting the data, running PSO with random initializations, calculating the selected error metric for each candidate coefficient set at every iteration, retaining the coefficient set with the minimum error, and outputting the best coefficients once the stopping criteria were met (Fig. 4).

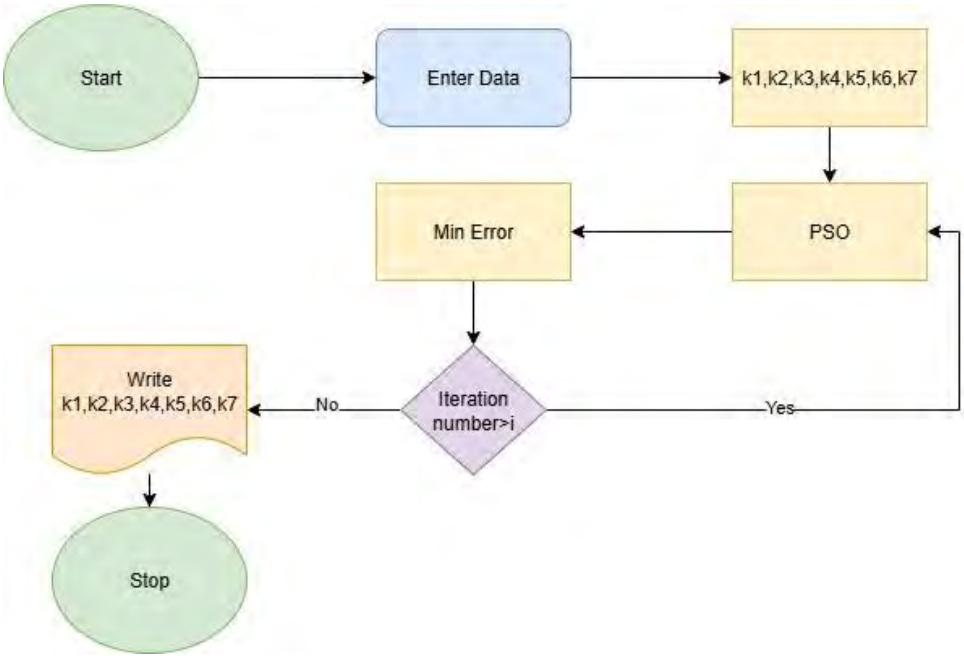


Fig. 4. Flowchart of the model calibration process

In this study, the termination criterion of the PSO algorithm was defined as reaching the maximum number of iterations. The error value was monitored by the decision-maker to evaluate the quality of the obtained solutions; however, no automatic error-based stopping condition was applied. PSO parameters remained consistent across all models to ensure that the comparison was based on the choice of error metric and the status of the first two coefficients. The optimization target was the "P_{IC}" value, which corresponds to the expression originally defined in Eq 1 and reformulated in Eq 10 for optimization purposes.

In the first model, the objective is to minimize the error according to the RMSE criterion. To ensure compatibility with the literature, K_1 and K_2 are kept fixed; PSO searches only over K_3 to K_7. In the flowchart, this is represented by the "PSO" block operating on a parameter set and the "Min Error = RMSE" evaluation. The second model also focuses on RMSE but allows K_1 and K_2 to be free parameters. Thus, PSO searches across all K_1 to K_7, enabling an independent investigation of the effect of including the first two coefficients in the calibration. The flow remains the same; only the dimension of decision variables increases. In the third model, the error criterion is selected as MAE. To maintain comparability with the literature, K_1 and K_2 are fixed; PSO works on K_3 to K_7. The difference in the flowchart is that the error is calculated as MAE in the "Min Error" step. Other steps remain unchanged. The fourth model uses MAE as the error criterion and also includes k_1 and k_2 in

the calibration; PSO optimizes all coefficients from K_1 to K_7. Thus, the effect of fixing or calibrating the first two coefficients on the MAE side is examined symmetrically alongside the RMSE side.

The software setup is consistent across all models. Each model is run with five independent trials; the best, average, and standard deviation values obtained in each trial were recorded for later reporting. Comparisons will be made along the axes of error metric selection (RMSE/MAE) and the status of coefficients K_1 and K_2 (fixed/free).

3. Results and Discussion

In this study, four models were developed using the same formula structure and all calibrated via Particle Swarm Optimization (PSO) models with fixed parameters K_1 = 1 and K_2 = 2, and free models where these two coefficients were also included in the calibration process. Regarding the error criterion, two models were optimized based on RMSE and two models based on MAE. The PSO search settings were kept constant throughout all experiments. Each model was run with five independent trials using different random initializations, and for each trial, the best (minimum), average, and standard deviation of the error values were reported (Table 3).

Table 3. Results of PSO analysis

Model	Independent Runs	K_1	K_2	K_3	K_4	K_5	K_6	K_7	RMSE	MAE
Model 1 K_1-K_2 fixed, optimized based on RMSE	1.	1.000	2.000	0.845	0.537	0.521	0.467	0.633	0.274	
	2.	1.000	2.000	0.845	0.537	0.462	0.761	0.633	0.274	
	3.	1.000	2.000	0.845	0.537	0.379	0.652	0.633	0.274	
	4.	1.000	2.000	0.845	0.537	0.610	0.613	0.633	0.274	
	5.	1.000	2.000	0.845	0.537	0.415	0.495	0.633	0.274	
	Standard Deviation	0.000	0.000	0.000	0.000	0.090	0.119	0.000	0.000	
	Mean	1.000	2.000	0.845	0.537	0.477	0.598	0.633	0.274	
Model 2 7-variable, optimized based on RMSE	1.	0.500	2.261	0.983	0.510	0.429	0.669	0.625	0.273	
	2.	0.500	2.312	0.988	0.512	0.271	0.496	0.624	0.273	
	3.	0.501	2.274	0.984	0.510	0.867	0.600	0.625	0.273	
	4.	0.500	2.161	0.975	0.505	0.325	0.844	0.626	0.273	
	5.	0.500	2.284	0.987	0.510	0.323	0.542	0.624	0.273	
	Standard Deviation	0.000	0.054	0.005	0.003	0.244	0.122	0.001	0.000	
	Mean	0.500	2.258	0.983	0.509	0.443	0.630	0.625	0.273	
Model 3 K_1-K_2 fixed, optimized based on MAE	1.	1.000	2.000	0.585	0.565	0.759	0.390	0.714		0.054
	2.	1.000	2.000	0.604	0.562	0.764	0.259	0.707		0.054
	3.	1.000	2.000	0.583	0.566	0.458	0.506	0.715		0.054
	4.	1.000	2.000	0.577	0.569	0.524	0.297	0.717		0.054
	5.	1.000	2.000	0.587	0.565	0.572	0.698	0.714		0.054
	Standard Deviation	0.000	0.000	0.010	0.003	0.138	0.163	0.004		0.000
	Mean	1.000	2.000	0.587	0.565	0.615	0.430	0.713		0.054
Model 4 7-variable, optimized based on MAE	1.	0.500	2.261	0.983	0.510	0.429	0.669	0.625		0.054
	2.	0.500	2.312	0.988	0.512	0.271	0.496	0.624		0.054
	3.	0.501	2.274	0.984	0.510	0.867	0.600	0.625		0.054
	4.	0.500	2.161	0.975	0.505	0.325	0.844	0.626		0.054
	5.	0.500	2.284	0.987	0.510	0.323	0.542	0.624		0.054
	Standard Deviation	0.000	0.054	0.005	0.003	0.244	0.122	0.001		0.000
	Mean	0.500	2.258	0.983	0.509	0.443	0.630	0.625		0.054
Coefficient from Literature	6.	1.000	2.000	0.976	0.526	0.802	0.078	0.600	0.275	0.058

The convergence consistency of the PSO runs was evaluated by analyzing the means and standard deviations of the coefficients (K_1–K_7) and the error values obtained from the five independent runs for each model. Overall, all four models demonstrated strong convergence stability, with most

coefficients and error metrics exhibiting near-zero standard deviations. In Model 1, K_1–K_4 and K_7 were highly stable, while K_5 (std ≈ 0.090) and K_6 (std ≈ 0.119) showed relatively higher variability. In Models 2 and 4, K_2 (std ≈ 0.054) and especially K_5 (std ≈ 0.244) displayed greater fluctuations, while the other parameters and error metrics remained consistent. In Model 3, K_3 and K_4 converged almost perfectly, with only K_5 (std ≈ 0.138) showing minor variability. The negligible variation in RMSE and MAE across all models confirms the reliability and reproducibility of PSO-based calibration. The obtained performance results and coefficient sets were compared with the existing method in the literature and its fixed coefficients, with the RMSE and MAE values of the reference method on the same dataset also presented. This approach clearly highlights the effects of treating the first two coefficients as adjustable and the choice of optimization criterion (RMSE/MAE).

Each of the four models was run using PSO with 5 independent trials, and the results were evaluated according to the model type using either RMSE or MAE. In the models optimized based on RMSE, the model with fixed K_1 and K_2 (RMSE–Fixed) consistently produced an RMSE of 0.274 across all trials, whereas the model with K_1 and K_2 treated as adjustable parameters (RMSE–Free) achieved an RMSE of 0.273 in every trial. This indicates that including K_1 and K_2 in the calibration yielded a small but consistent improvement of approximately 0.36% in RMSE. For the models optimized according to MAE, both the MAE–Fixed and MAE–Free models maintained a constant MAE value of 0.054 across all trials, suggesting that allowing K_1 and K_2 to vary did not provide any additional benefit within the reported precision for MAE. Although the coefficients in the models with adjustable parameters (particularly K_1–K_6) showed some variability across the five independent trials, the optimized error metrics (RMSE and MAE) remained highly consistent, with minimum, mean, and standard deviation values nearly identical. Given that the metrics did not vary over the 5 trials (min = mean = std ≈ 0), it can be concluded that PSO converged reliably for this problem. While parameter standard deviations are generally low, some degree of correlation among parameters may exist, which is common in multi-parameter calibrations. This likely contributes to the consistent error metrics despite small parameter variations. Overall, the results indicate reliable and reproducible convergence of the PSO algorithm. Examining the parameter patterns reveals that in the RMSE–Fixed model (with $K_1 = 1$ and $K_2 = 2$), the coefficients K_5 and K_6 were mainly adjusted between trials, whereas in the RMSE–Free model, K_1 converged around 0.500 and K_2 ranged approximately between 2.16 and 2.31. This suggests that setting the first two coefficients as adjustable redefined the equilibrium among the remaining coefficients (e.g., K_5 and K_6) and led to a slight reduction in RMSE. In the MAE group, the MAE–Fixed model highlighted bands of K_3 ≈ 0.58 – 0.60 and K_4 ≈ 0.56–0.57, while in the MAE–Free model, K_1 and K_2 again converged to similar ranges as in the RMSE–Free model, despite the MAE value remaining constant. This indicates that the MAE metric, which is more robust against outliers, did not reflect performance gains from allowing K_1 and K_2 to vary, whereas RMSE, being more sensitive to larger errors, showed a small but positive effect. In summary, treating K_1 and K_2 as adjustable parameters provided a marginal but consistent improvement in RMSE, while no significant difference was observed based on MAE.

When compared to the literature method coefficients ($K_1 = 1$, $K_2 = 2$, $K_3 = 0.976$, $K_4 = 0.526$, $K_5 = 0.802$, $K_6 = 0.078$, $K_7 = 0.600$) and performance values (RMSE = 0.275, MAE = 0.058), the PSO-based models demonstrated improvements: the RMSE–Fixed model reduced RMSE to 0.274, achieving approximately a 0.36% improvement, while the RMSE–Free model further reduced RMSE to 0.273, corresponding to about a 0.73% enhancement. For the MAE-focused models, both fixed and flexible cases resulted in an MAE of 0.054, representing a roughly 6.9% decrease compared to the literature. In other words, treating K_1 and K_2 as adjustable parameters produced a small but consistent additional gain in RMSE, whereas the MAE remained unchanged.

The 6.9% reduction in MAE indicates a significant improvement in the overall accuracy and consistency of the model, which is particularly advantageous when generalizing to different structural configurations. This enhancement contributes to more reliable safety assessments, reduced overdesign, and improved efficiency in the use of strengthening materials such as CFRP. These aspects highlight the practical engineering relevance of the improvements achieved through the proposed recalibration approach.

The prediction results obtained using the model parameters that showed the best performance through the PSO method are compared with the experimental data and presented in Fig. 5. The proximity of the data points to the linear reference line indicates the success of the calibration and that the model provides results closer to the experimental values.

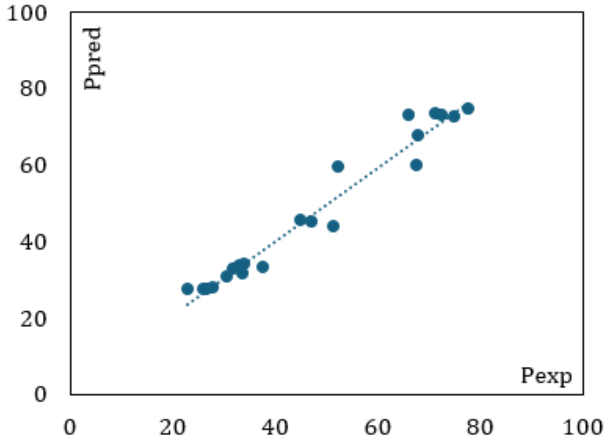


Fig. 5. Scatter plot of experimental vs. PSO-predicted IC debonding strength

4. Conclusion

In this study, the aim was to recalibrate an existing analytical model [6] in the literature that estimates the bond strength required to prevent debonding at the NSM-CFRP strip–concrete interface, using the Particle Swarm Optimization (PSO) algorithm. The original structure of the model was preserved. Four different model configurations were evaluated, in which the first two coefficients (K_1 and K_2) were kept constant or considered as optimization parameters. Each configuration was tested through five independent runs under identical PSO settings. Prediction accuracy was evaluated using Root Mean Square Error (RMSE) and Mean Absolute Error (MAE) metrics.

The results show that the PSO-based recalibration improves the predictive performance of the original model, particularly in terms of MAE. The 6.9% reduction in MAE represents a notable improvement in the model's overall consistency. The observed enhancement enables safer and more efficient structural design by reducing the need for excessive material use and improving the accuracy of performance predictions. These findings demonstrate the engineering relevance of the recalibrated model, offering practical benefits in real-world strengthening applications. Scatter plots comparing experimental and predicted loads confirm that the proposed models provide a closer fit to the experimental data. Moreover, the consistent performance across all five trials indicates that the PSO algorithm converged reliably for this specific problem.

The main contribution of this study is to demonstrate the applicability of metaheuristic optimization techniques such as PSO in calibrating bond strength models for NSM CFRP–concrete joints. Without adding complexity to the original model, it was shown that prediction accuracy can be improved by selectively recalibrating specific coefficients and choosing appropriate error metrics. This approach supports more reliable strength estimations, reduces overdesign, and promotes more efficient use of CFRP strips in strengthening applications.

However, the findings of this study are limited by the dataset and interface configuration used. The dataset is relatively small, and the calibration is restricted to specific NSM CFRP–concrete joint configurations. Future studies should aim to include broader datasets encompassing various concrete grades, groove dimensions, and different types and sizes of FRP materials. Additionally, testing other optimization methods or hybrid approaches may further enhance model performance and generalizability.

References

[1] Ozmen, H. B., & Inel, M. Effect of concrete strength and detailing properties on seismic damage for RC structures. Res Eng Des. 2024; 1 (1): 1-11. http://dx.doi.org/10.17515/rede2024-005en1124rs

[2] Sabau, C., Popescu, C., Sas, G., Schmidt, J. W., Blanksvärd, T., & Täljsten, B. (2018). Strengthening of RC beams using bottom and side NSM reinforcement. Composites Part B: Engineering, 149, 82-91. https://doi.org/10.1016/j.compositesb.2018.05.011

[3] Sagare, S. S., Kirthiga, R., & Elavenil, S. (2024). A state of art of review on strengthening of concrete structures using fabric reinforced cementitious matrix. Res. Eng. Struct. Mater, 10, 1231-1260. https://doi.org/10.17515/resm2024.133ma1226rv

[4] Al-Saawani, M. A., El-Sayed, A. K., & Al-Negheimish, A. I. (2015). Effect of basic design parameters on IC debonding of CFRP-strengthened shallow RC beams. Journal of Reinforced Plastics and Composites, 34(18), 1526-1539. https://doi.org/10.1177/0731684415593816

[5] Li, C., Zhao, Y., Wan, D., Han, X., Li, W., Tian, C., Whag, C., Chang, Z., & Huang, J. (2025). Parameter Analysis for the Flexural Performance of Concrete Beams Using Near-Surface Mounted-Strengthening Application. Buildings, 15(9), 1453. https://doi.org/10.3390/buildings15091453

[6] Seracino, R., Raizal Saifulnaz, M. R., & Oehlers, D. J. (2007). Generic debonding resistance of EB and NSM plate-to-concrete joints. Journal of Composites for Construction, 11(1), 62-70. https://doi.org/10.1061/(ASCE)1090-0268(2007)11:1(62)

[7] Bianco, V., Barros, J. A., & Monti, G. (2009). Bond model of NSM-FRP strips in the context of the shear strengthening of RC beams. Journal of Structural Engineering, 135(6), 619-631. https://doi.org/10.1061/(ASCE)0733-9445(2009)135:6(619)

[8] Zhang, S. S., Ke, Y., Smith, S. T., Zhu, H. P., & Wang, Z. L. (2021). Effect of FRP U-jackets on the behaviour of RC beams strengthened in flexure with NSM CFRP strips. Composite Structures, 256, 113095. https://doi.org/10.1016/j.compstruct.2020.113095

[9] Oehlers, D., & Seracino, R. (2004). Design of FRP and steel plated RC structures: Retrofitting beams and slabs for strength, stiffness and ductility. Elsevier.

[10] Ali, M. M., Oehlers, D. J., Griffith, M. C., & Seracino, R. (2008). Interfacial stress transfer of near surface-mounted FRP-to-concrete joints. Engineering structures, 30(7), 1861-1868. https://doi.org/10.1016/j.engstruct.2007.12.006

[11] Seracino, R., Jones, N. M., Ali, M. S., Page, M. W., & Oehlers, D. J. (2007). Bond strength of near-surface mounted FRP strip-to-concrete joints. Journal of Composites for Construction, 11(4), 401-409. https://doi.org/10.1061/(ASCE)1090-0268(2007)11:4(401)

[12] Oehlers, D. J., Rashid, R., & Seracino, R. (2008). IC debonding resistance of groups of FRP NSM strips in reinforced concrete beams. Construction and Building Materials, 22(7), 1574-1582. https://doi.org/10.1016/j.conbuildmat.2007.03.021

[13] Oehlers, D. J., Haskett, M., Wu, C., & Seracino, R. (2008). Embedding NSM FRP plates for improved IC debonding resistance. Journal of Composites for Construction, 12(6), 635-642. https://doi.org/10.1061/(ASCE)1090-0268(2008)12:6(635)

[14] Rashid, R., Oehlers, D. J., & Seracino, R. (2008). IC debonding of FRP NSM and EB retrofitted concrete: plate and cover interaction tests. Journal of Composites for Construction, 12(2), 160-167. https://doi.org/10.1061/(ASCE)1090-0268(2008)12:2(160)

[15] Zhang, S. S., Teng, J. G., & Yu, T. (2014). Bond strength model for CFRP strips near-surface mounted to concrete. Journal of Composites for Construction, 18(3), A4014003. https://doi.org/10.1061/(ASCE)CC.1943-5614.0000402

[16] Bilotta, A., Ceroni, F., Nigro, E., & Pecce, M. (2015). Efficiency of CFRP NSM strips and EBR plates for flexural strengthening of RC beams and loading pattern influence. Composite Structures, 124, 163-175. https://doi.org/10.1016/j.compstruct.2014.12.046

[17] D'Antino, T., & Pisani, M. A. (2020). General analytical model for the bond capacity of NSM FRP-concrete joints. Journal of Composites for Construction, 24(6), 04020065. https://doi.org/10.1061/(ASCE)CC.1943-5614.0001076

[18] Naderpour, H., Mirrashid, M., & Nagai, K. (2020). An innovative approach for bond strength modeling in FRP strip-to-concrete joints using adaptive neuro–fuzzy inference system. Engineering with computers, 36(3), 1083-1100. https://doi.org/10.1007/s00366-019-00751-y

[19] Milovancevic, M., Denić, N., Ćirković, B., Nešić, Z., Paunović, M., & Stojanović, J. (2021). Prediction of shear debonding strength of concrete structure with high-performance fiber reinforced concrete. Structures, 33, 4475-4480. https://doi.org/10.1016/j.istruc.2021.07.012

[20] Kumar, A., Arora, H. C., Kumar, K., Garg, H., & Jahangir, H. (2024). Development of efficient prediction model of FRP-to-concrete bond strength using curve fitting and ANFIS methods. Arabian Journal for Science and Engineering, 49(4), 5129-5158. https://doi.org/10.1007/s13369-023-08328-0

[21] Poonam, S. V. (2024). Response surface methodology use in optimization of concrete properties using blast furnace slag aggregate and recycled concrete sand. Res. Eng. Struct. Mater, 10(1), 111-133. https://doi.org/10.17515/resm2023.788me0614
[22] Sharma, K. K., Imam, A., Anifowose, F., & Srivastava, V. (2020). Compressive strength modeling of blended concrete based on empirical and artificial neural network techniques. Journal of structural integrity and maintenance, 5(4), 252-264. https://doi.org/10.1080/24705314.2020.1783120
[23] Imam, A., Salami, B. A., & Oyehan, T. A. (2021). Predicting the compressive strength of a quaternary blend concrete using Bayesian regularized neural network. Journal of Structural Integrity and Maintenance, 6(4), 237-246. https://doi.org/10.1080/24705314.2021.1892572
[24] Mohamed, O., Kewalramani, M., Ati, M., & Al Hawat, W. (2021). Application of ANN for prediction of chloride penetration resistance and concrete compressive strength. Materialia, 17, 101123. https://doi.org/10.1016/j.mtla.2021.101123
[25] Ebid, A. M., & Deifalla, A. (2021). Prediction of shear strength of FRP reinforced beams with and without stirrups using (GP) technique. Ain Shams Engineering Journal, 12(3), 2493-2510. https://doi.org/10.1016/j.asej.2021.02.006
[26] Zhang, S. Y., Chen, S. Z., Jiang, X., & Han, W. S. (2022). Data-driven prediction of FRP strengthened reinforced concrete beam capacity based on interpretable ensemble learning algorithms. Structures, 43, 860-877. https://doi.org/10.1016/j.istruc.2022.07.025
[27] Al-Hamrani, A., Wakjira, T. G., Alnahhal, W., & Ebead, U. (2023). Sensitivity analysis and genetic algorithm-based shear capacity model for basalt FRC one-way slabs reinforced with BFRP bars. Composite Structures, 305, 116473. https://doi.org/10.1016/j.compstruct.2022.116473
[28] Baji, H., Yang, W., & Li, C. Q. (2018). Optimal FRP-strengthening strategy for corrosion-affected reinforced concrete columns. Structure and Infrastructure Engineering, 14(12), 1586-1597. https://doi.org/10.1080/15732479.2018.1476560
[29] Mahdavi, G., Nasrollahzadeh, K., & Hariri-Ardebili, M. A. (2019). Optimal FRP jacket placement in RC frame structures towards a resilient seismic design. Sustainability, 11(24), 6985. https://doi.org/10.3390/su11246985
[30] Li, G., Hu, T., & Bai, D. (2021). BP Neural Network Improved by Sparrow Search Algorithm in Predicting Debonding Strain of FRP-Strengthened RC Beams. Advances in Civil Engineering, 2021(1), 9979028. https://doi.org/10.1155/2021/9979028
[31] Hu, T., Wang, J., Li, G., & Zheng, B. (2021). Prediction of Allowable Debonding Strain of FRP-Strengthened RC Beam Based on GA-BP Neural Network. IOP Conference Series: Earth and Environmental Science, 719(2), 022028. https://doi.org/10.1088/1755-1315/719/2/022028
[32] Ghaidan, D. J., Mohammed, H. J., & Salahaldin, A. I. (2024). Predicting Failure Modes of RC Beams Strengthening with FRP-NSM System: A Statistical Approach. International Journal of Sustainable Construction Engineering and Technology, 15(1), 226-240. https://doi.org/10.30880/ijscet.2024.15.01.016
[33] Jiang, W., Xie, Y., Li, W., Wu, J., & Long, G. (2021). Prediction of the splitting tensile strength of the bonding interface by combining the support vector machine with the particle swarm optimization algorithm. Engineering Structures, 230, 111696. https://doi.org/10.1016/j.engstruct.2020.111696
[34] Ji, W., Qin, Y., Liu, J., Zhang, X., & Zhou, H. (2025). Parameter inverse of fiber-cement matrix interface cohesive model based on PSO algorithm. Structural Concrete. https://doi.org/10.1002/suco.70148
[35] Ghodousian, O., Garcia, R., Shafaie, V., & Ghodousian, A. (2023). Interfacial bond strength of coloured SCC repair layers: an experimental and optimisation study. Journal of Structural Integrity and Maintenance, 8(3), 140-149. https://doi.org/10.1080/24705314.2023.2170620
[36] Mohammadizadeh, M. R., & Esfandnia, F. (2022). Predicting Compression Strength of Reinforced Concrete Columns Confined by FRP Using Meta-Heuristic Methods. Civil Engineering Infrastructures Journal, 55(1), 1-17. https://doi.org/10.22059/ceij.2021.304229.1685
[37] Wahab, S., Suleiman, M., Shabbir, F., Mahmoudabadi, N. S., Waqas, S., Herl, N., & Ahmad, A. (2023). Predicting confinement effect of carbon fiber reinforced polymers on strength of concrete using metaheuristics-based artificial neural networks. arXiv preprint arXiv:2403.13809. https://doi.org/10.48550/arXiv.2403.13809
[38] Nguyen, T. A., & Lý, H. B. (2021). Estimation of the bond strength between FRP and concrete using ANFIS and hybridized ANFIS machine learning models. Journal of Science and Transport Technology, 34-44. https://doi.org/10.58845/jstt.utt.2021.en.1.1.34-44
[39] Su, M., Peng, H., & Li, S. F. (2021). Application of an interpretable artificial neural network to predict the interface strength of a near-surface mounted fiber-reinforced polymer to concrete joint. Journal of Zhejiang University-SCIENCE A, 22(6), 427-440. https://doi.org/10.1631/jzus.A2000245
[40] Kumar, A., Arora, H. C., Mohammed, M. A., Kumar, K., & Nedoma, J. (2021). An optimized neuro-bee algorithm approach to predict the FRP-concrete bond strength of RC beams. IEEE Access, 10, 3790-3806. https://doi.org/10.1109/ACCESS.2021.3140046

[41] Kumar, A., Arora, H. C., Kapoor, N. R., & Kumar, A. (2024). Artificial neural network optimized with PSO to estimate the interfacial properties between FRP and concrete surface. Advances in Computers, 135, 497-527. https://doi.org/10.1016/bs.adcom.2023.11.014
[42] Pei, Z., & Wei, Y. (2022). Prediction of the bond strength of FRP-to-concrete under direct tension by ACO-based ANFIS approach. Composite Structures, 282, 115070. https://doi.org/10.1016/j.compstruct.2021.115070
[43] Zhang, F., Wang, C., Liu, J., Zou, X., Sneed, L. H., Bao, Y., & Wang, L. (2023). Prediction of FRP-concrete interfacial bond strength based on machine learning. Engineering structures, 274, 115156. https://doi.org/10.1016/j.engstruct.2022.115156
[44] Tao, L., & Xue, X. (2024). An improved random forest model to predict bond strength of FRP-to-concrete. Journal of Civil Engineering and Management, 30(6), 520-535. https://doi.org/10.3846/jcem.2024.21636
[45] Shbeeb, N. I., Katash, A. A., Oğuzmert, M., & Barham, W. S. (2024). Estimation of the bond strength of fiber-reinforced polymer bars in concrete using artificial intelligence systems. Buildings, 14(2), 369. https://doi.org/10.3390/buildings14020369
[46] Xue, X., Zhang, R., Chen, X., & Tao, L. (2024). Bond strength prediction of FRP reinforced concrete using soft computing techniques: X. Xue et al. Soft Computing, 28(19), 11553-11564. https://doi.org/10.1007/s00500-024-09904-8
[47] Haddad, R., Almasaeid, H., & Saeed, A. (2026). Predicting Bond Strength between Externally Bonded FRP and Heat-damaged Concrete Using ANN. Journal of Soft Computing in Civil Engineering, 10(1), e223688. https://doi.org/10.22115/scce.2025.1945
[48] Kennedy, J., & Eberhart, R. (1995). Particle Swarm Optimization. Proceedings of ICNN'95-International Conference on Neural Networks, 4, 1942-1948). https://doi.org/10.1109/ICNN.1995.488968
[49] Çevik, K., & Koçer, H. (2013). A Soft Computing Application Based On Artificial Neural Networks Training by ParticleSwarm Optimization. Süleyman Demirel University Journal of Natural and Applied Sciences, 17(2), 39-45.
[50] Derdiman, M. K. (2022). Reliability-Based Cross-Section Optimization of Cantilever Slabs Using Discrete PSO Algorithm. Journal of Engineering Sciences and Design, 10(3), 987-999. https://doi.org/10.21923/jesd.952838
[51] Saplıoğlu, K. (2025). Calibration of Linear Muskingum Model Coefficients and Coefficient Parameters Using Grey Wolf and Particle Swarm Optimization. Water Resources Management, 39(3), 999-1014. https://doi.org/10.1007/s11269-024-04063-9
[52] Özsağlam, M. Y., & Çunkaş, M. (2008). Particle Swarm Optimization Algorithm for Solving Optımızation Problems. Journal of Polytechnic, 11(4), 299-305.
[53] Saplıoğlu, K., Öztürk, T. S. K., & Acar, R. (2020). Optimization of open channels using particle swarm optimization algorithm. Journal of Intelligent & Fuzzy Systems, 39(1), 399-405. https://doi.org/10.3233/JIFS-191355
[54] Yazd, H. G. H., Arabshahi, S. J., Tavousi, M., & Alvani, A. (2015). Optimal designing of concrete gravity Dam using particle swarm optimization algorithm (PSO). Indian Journal of Science and Technology, 8(12), 1. https://doi.org/10.17485/ijst/2015/v8i12/70714

Research on Engineering Structures & Materials
www.jresm.org

Research Article

Investigation effect of metro entrance and exit construction on pedestrian overpass safety using numerical modelling and simulation

Ke Ji [a], BoiYee Liao [*,b]

Department of Engineering, International College, Krirk University, Bangkok, Thailand

Article Info

Article History:

Received 12 Aug 2025

Accepted 30 Sep 2025

Keywords:

Metro entrance and exit construction;
Pedestrian overpass safety;
3D numerical model;
Simulation analysis;
Nonlinear coupling algorithm

Abstract

Due to the complex working conditions of deep burial, proximity, and multiple interferences unique to subway engineering, the construction process inevitably causes additional deformation or even local damage to adjacent existing structures. In order to systematically study the settlement of pedestrian overpass foundation and deformation mechanism of upper structure caused by the construction of a certain subway entrance and exit, this paper takes the structural load characteristics and construction sequence of the subway entrance and exit as the starting point, integrates regional traffic organization and on-site construction constraints, and constructs a three-dimensional dynamic construction numerical model. The displacement response of pedestrian overpass foundation during the entire excavation and support loading process was accurately simulated using nonlinear coupling algorithm. The final results show that the established support system and construction parameter control provided best values in terms of horizontal and vertical displacements. The maximum horizontal displacement of the pedestrian overpass pile foundation induced by subway entrance and exit construction is 0.3 mm. The maximum vertical displacement of the main span pile foundation is 1.9 mm. Both values are considered lower than the standard limits, including the allowable total settlement value of the pile foundation of 127 mm and the horizontal displacement limit of the pile foundation of 31mm. The above results quantitatively verify the "controllability" of the impact of subway entrance and exit construction on the structural safety of pedestrian overpasses, which can provide theoretical basis and technical paradigm for risk assessment and dynamic control similar to adjacent construction.

© 2025 MIM Research Group. All rights reserved.

1. Introduction

During With the acceleration of urbanization, rail transit has become an important part of the urban traffic system, and more metros and tunnels are being developed and utilized [1]. Tunnel construction, especially in hilly areas, is mainly related to complex geology and uncertainty [2]. As the integration of urban underground transportation networks and underground spaces becomes increasingly close, the interference of adjacent building activities has a greater impact on existing infrastructure [3]. For example, urban bridges and subways often exhibit a closely coupled symbiotic relationship in spatial layout [4]. The internal forces of bridge structures are extremely sensitive to environmental disturbances, and even small changes in boundary conditions can cause a redistribution of the transmission path [5].

Urban metro construction, due to its long construction period and mostly in the bustling areas of the city, is mainly shallow buried and excavated [6]. According to the particularity of metro projects, shallow buried tunnels will affect the surface rock and soil, which may lead to ground

*Corresponding author: y5708211@gmail.com
[a]orcid.org/0009-0008-2185-7771; [b]orcid.org/0009-0002-3393-1701
DOI: http://dx.doi.org/10.17515/resm2025-1084st0812rs

collapse and road damage, and these factors will damage the structure of surrounding structures, making the impact of metro construction on the safety of adjacent buildings increasingly prominent [7]. He Y et al. [8] investigated the effect of subway foundation pit excavation and train-induced vibrations on adjacent architectural heritage through a case study of the City Square Station in Shaoxing. Li Q et al. [9] Explored the safety evaluation method for adjacent buildings during shield tunnel construction. Among them, the ground movement induced by metro construction and its impact on nearby buildings and the huge losses caused have made the accurate prediction of surface settlement and the provision of control standards a focus of research in the field of underground space engineering [10].

Zhou Limei [11] used numerical analysis and on-site detection to conduct safety impact analysis on the main risk points during the construction process of the station. Zhang JT et al. [12] analyzed the surface settlement caused by shallow tunnel excavation, as well as the deformation and internal forces of pile foundations. They found that the maximum horizontal displacement of the pile foundation (3.63 mm) exceeded the deformation control index (3 mm) and had a significant impact on the internal forces of adjacent pile foundations. Liu Z et al. [13] established the relationship between shield parameters and strata in finite element calculations, analyzing the impact of different shield parameters and support conditions on the force and deformation of existing viaduct group piles on both sides of the tunnel. Li L et al. [14] designed orthogonal experiments to analyze the sensitivity of parameters affecting buildings above the metro shield construction. Ju X [15] conducted research on the deformation impact of tunnel shield construction on surface structures and derived surface deformation formulas, obtaining a reasonable range of support parameters. Some scholars used numerical analysis software to conduct numerical analysis on the impact of urban metro construction on surface settlement [16]. Luo Q et al. [17] conducted a three-dimensional fine numerical simulation study on artificial freezing during the construction of subway pedestrian crossings. Yi LB et al. [18] used Midas/GTS software for finite element analysis to study the characteristics of displacement changes of the bridge deck, piers, abutments, and bridge piles during the construction process of the Beijing Extra Large Bridge of the Beijing Shanghai High speed Railway under the large section underground excavation section. Hu B et al. [19] used ABAQUS software to simulate the impact of soil disturbance caused by deep excavation on the displacement of underground pipelines. Zhou Y et al. [20] used finite element software ADINA for numerical simulation of excavation of foundation pits, analyzing the effects of horizontal and vertical displacement of foundation pits, as well as pre stress and angle of anchor rods on the displacement of support structures. The previous studies have significantly advanced the research on surface structure safety assessment during subway construction. However, there are still shortcomings in previous research on safety assessments of surface structures during subway construction. The assessments are data utilization, refined risk, multi-factor coupling, and surrounding buildings impact. Therefore, further and depth research is required in the structural safety field of the subway.

The safety of surface structures of metro construction excavation has always been a focus of many scholars and experts. This paper investigates the safety impact of a certain metro entrance and exit construction on a pedestrian overpass. It combines the structural characteristics of the pedestrian overpass and the spatial relationship with the metro entrance and exit. Furthermore, the current research aims to focus on the construction methods and characteristics of the metro entrance and exit using numerical modeling (three-dimensional finite element model) and simulation (Midas Gen 2022 structural analysis software). This study analyzes the adverse effects of metro entrance and exit construction on the pedestrian overpass. It focuses on the deformation of the pedestrian overpass step section and the main span foundation structure, and then it analyzes the structural safety of the pedestrian overpass.

2. Research Methodology

2.1 Project Overview

The construction site of a certain subway entrance and exit is located directly below a pedestrian overpass. The main span of the overpass is approximately 40.5 m. The subway entrance and exit

consist of a dark excavation section and a straight section, which are mainly composed of standard sections and civil air defense sections. Among them, the standard section is 8.0 m, and the civil air defense section is 9.0 m. The subway entrance and exit are positioned relative to the overpass pile foundation as shown in Fig. 1. The bottom of the pile foundation is 0.86 meters away from the net distance of the straight section of the subway entrance and exit. The escalator section is constructed to pass under the stair section of the pedestrian overpass, and the bottom of the main span pile foundation of the overpass partially overlaps with the local position of the foundation of the escalator section. The escalator section will directly cut off the overlapping pile foundation during excavation. Fig. 2 shows the longitudinal cross-sectional view of the subway entrance and exit and the overpass pile foundation.

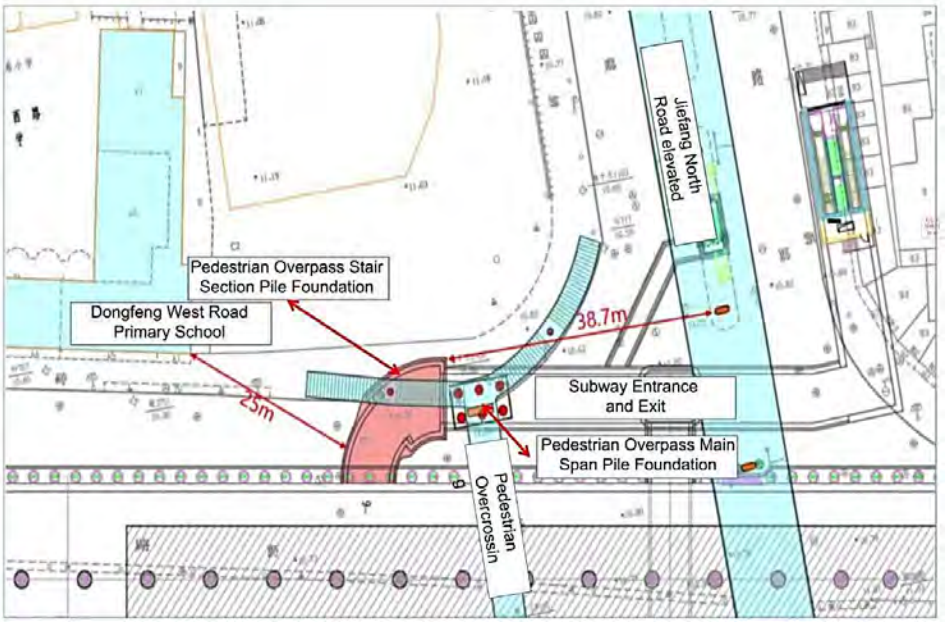


Fig. 1. Relative position of pile foundation of subway entrances and pedestrian bridge

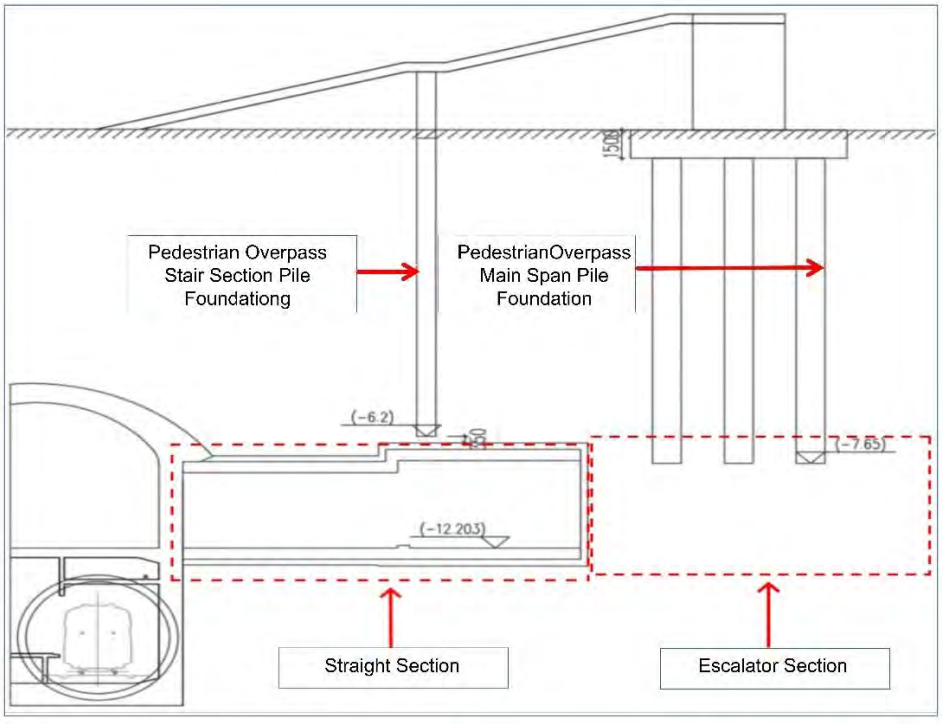


Fig. 2. Longitudinal section of pile foundation of subway entrance and exit and pedestrian bridge

2.2. 3D Modeling and Simulation

According to the three-dimensional relationship of pedestrian bridge and subway entrance and the construction characteristics, the 3D finite element calculation model is established. As shown in Fig. 3 is the 3D dimensional finite element integral model, and Fig. 4 shows the construction condition of subway entrance and exit. A three-dimensional finite element model was established using Midas Gen 2022 software, and solid elements were used for soil and bridge structures. The soil parameters of the model are detailed in Table 1, and the load parameters of the model are detailed in Table 2. The three-dimensional finite element model of this study is established based on nonlinear coupling algorithm, considering the soil structure interaction and the nonlinear contact between bridge pier foundation support structure. The computational model adopts the Mohr Coulomb criterion, which is based on the definition of ideal elastic-plastic behavior. For general nonlinear analysis of rocks and soils, this behavior is assumed. The results are completely reliable and therefore widely used to simulate most rock and soil types.

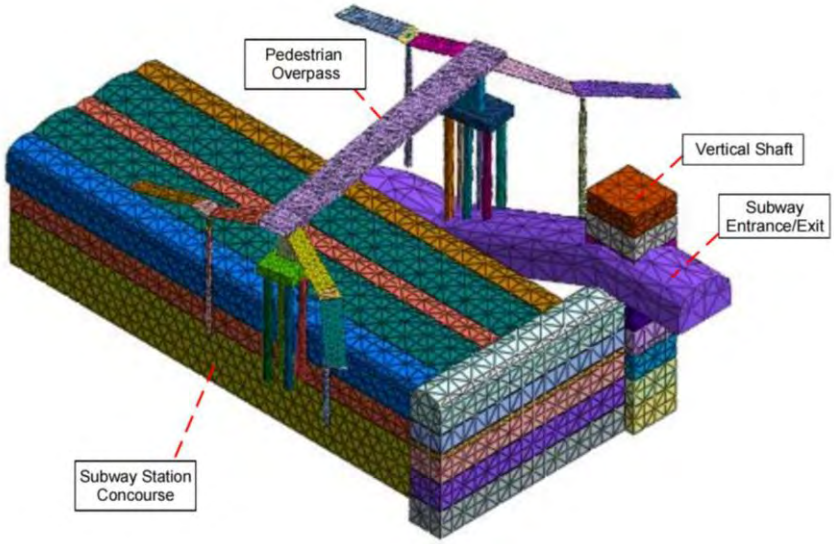


Fig. 3. 3D Finite element overall model

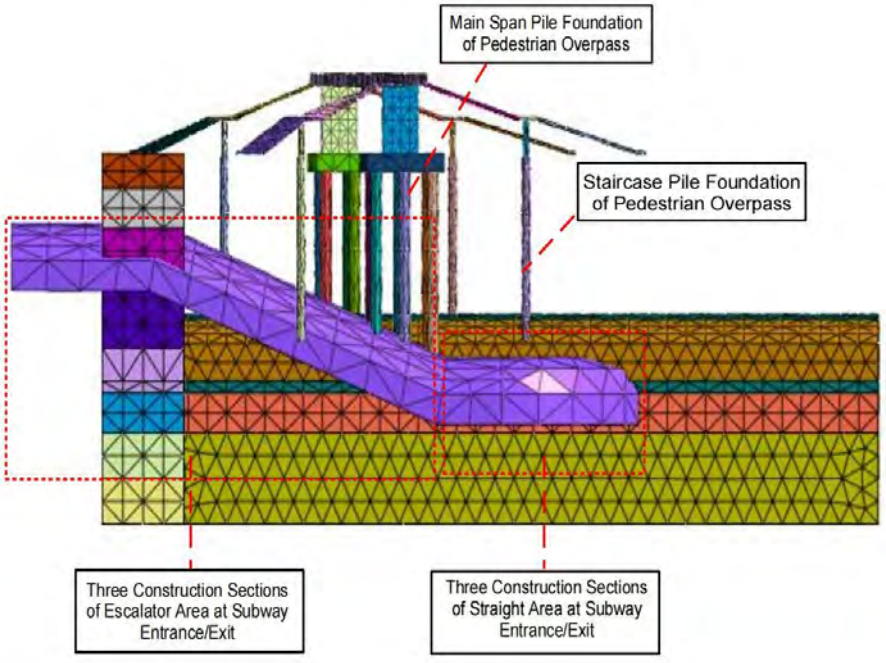


Fig. 4. Construction condition of the subway entrance and exit

Table 1. Soil parameters of the 3D finite element model

Soil layer name	Natural density (g/cm^3)	Side friction resistance (kPa)	Soil foundation coefficient (MPa/m)	Coefficient of earth pressure at rest
Plain fill	1.91	12	8	0.50
Silty fine sand	1.93	15	12	0.38
Plastic powdery clay	1.53	25	20	0.45
Silt	1.53	8	5	0.75
Mucky soil	1.77	8	7	0.75

Table 2. Load parameters of 3D finite element model

Load name	Load parameters
self-weight	The self-weight of reinforced concrete is calculated at 25 kN/m^3
Cover soil load	The soil cover weight is γ=20 kN/m^3, and under anti floating conditions, it is taken as γ=18 kN/m^3
Lateral soil and water load	Cohesive soil is calculated based on water and soil, while sandy soil is calculated based on water and soil
Water level	The water level on the outer side of the foundation pit is taken from the surface, and the inner side is 0.5 m below the bottom of the pit
Construction load	5 kPa

According to the relative position relationship between the straight section and the escalator section and the pedestrian overpass pile foundation, the excavation section of the straight section is divided into three construction processes, and the escalator section is also divided into three construction processes. The 3D dynamic construction simulation conditions of the influence of the subway entrance and exit construction on the pedestrian bridge foundation structure are shown in Table 3. The research flowchart of this article is shown in Fig. 5

Table 3. Construction conditions

Construction state	Main construction content
Working condition 1	Initial ground stress field analysis of the site
Working condition 2	Construction of the subway station hall was completed
Working condition 3	Initial construction of the straight section of the subway entrance and excavation 1
Working condition 4	Construction of the straight section 1 lining structure
Working condition 5	Initial construction of the straight section of the subway entrance and excavation 2
Working condition 6	Construction of the straight section 2 lining structure
Working condition 7	Initial construction of the straight section of the subway entrance and excavation 3
Working condition 8	Construction of the straight section 3 lining structure
Working condition 9	Initial construction of escalator section of subway entrance and excavation 1
Working condition 10	Construction of the lining structure of the escalator section 1
Working condition 11	Initial branch construction and excavation of escalator section of subway entrance and exit 2
Working condition 12	Construction of the lining structure of the escalator section 2
Working condition 13	Initial construction of escalator section of subway entrance and excavation 3
Working condition 14	Construction of the lining structure of escalator section 3

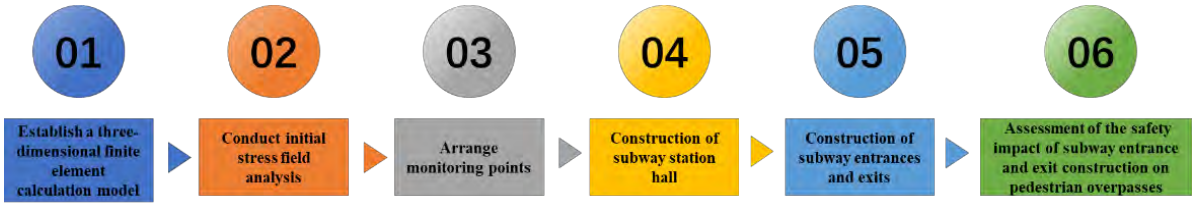


Fig. 5. Research flowchart

3. Results and Discussion

The influence of subway entrance and exit construction on the pedestrian bridge foundation has been investigated in X, Y, and Z directions using displacement results of 3D simulation analysis as shown in (Figs. 6-11). The staircase section and main span pile foundation displacements of pedestrian bridge under key working conditions during construction of subway entrance and exit are presented in Tables 4 and 5. From the data in Table. 4, it can be seen that the maximum X displacement of the staircase section pile foundation of pedestrian bridge is 0.2 mm, the maximum Y displacement is 0.4 mm, the maximum vertical displacement is 1.3 mm, and the maximum total displacement is 1.3 mm. From the data in Table. 5, it can be seen that the maximum X displacement of the main span pile foundation of pedestrian bridge is 0.3 mm, the maximum Y displacement is 0.4 mm, the maximum vertical displacement is 1.9 mm, and the maximum total displacement is 1.9 mm. According to the results in the Tables 4 and 5, during the construction of the proposed project, the maximum settlement of the main span pile foundation on the north and south sides of the adjacent foundations of the pedestrian bridge is 1.9 mm and 1.6 mm respectively, and the maximum settlement difference is 0.3 mm. The maximum settlement difference between the staircase section and the main span pile foundation is 0.6 mm.

Based on the three-dimensional simulation analysis of displacement results and on-site construction environment, this article analyzes the mechanism of settlement of pedestrian overpass foundations caused by subway entrance and exit construction as follows: (1) During excavation of foundation pits or subway entrance and exit construction, the original soil is removed, causing changes in the stress state of the surrounding soil, resulting in unloading rebound and lateral soil pressure reduction, which in turn causes settlement or uplift of the soil below the foundation of adjacent pedestrian overpasses; (2) If the foundation of a pedestrian overpass is located on a soil layer, soft soil layer, or mixed soil layer, and the subway construction disturbs these soil layers, it will cause a decrease in the local bearing capacity of the foundation and result in uneven settlement; (3) If precipitation or groundwater disturbance occurs during the construction process, it will cause a decrease in pore water pressure, leading to an increase in effective stress in the soil and further exacerbating settlement.

According to the industry standard of the People's Republic of China (Specifications for Maintenance of Highway Bridges and Culverts, JTG 5120-2021), the allowable total settlement value for simply supported bridge pile foundations is 127 mm, and the horizontal displacement limit for pile foundations is 31 mm. In view of the displacement of controllable, is far less than the allowable value of foundation deformation, so the subway entrance construction does not endanger the safety of the pedestrian bridge pile foundation. Therefore, it is considered that the construction of subway entrances and exits has little impact on the safety of the pedestrian bridge pile foundation. Therefore, it is suggested to pay close attention to the monitoring data of the bridge foundation in the construction process and carry out information construction.

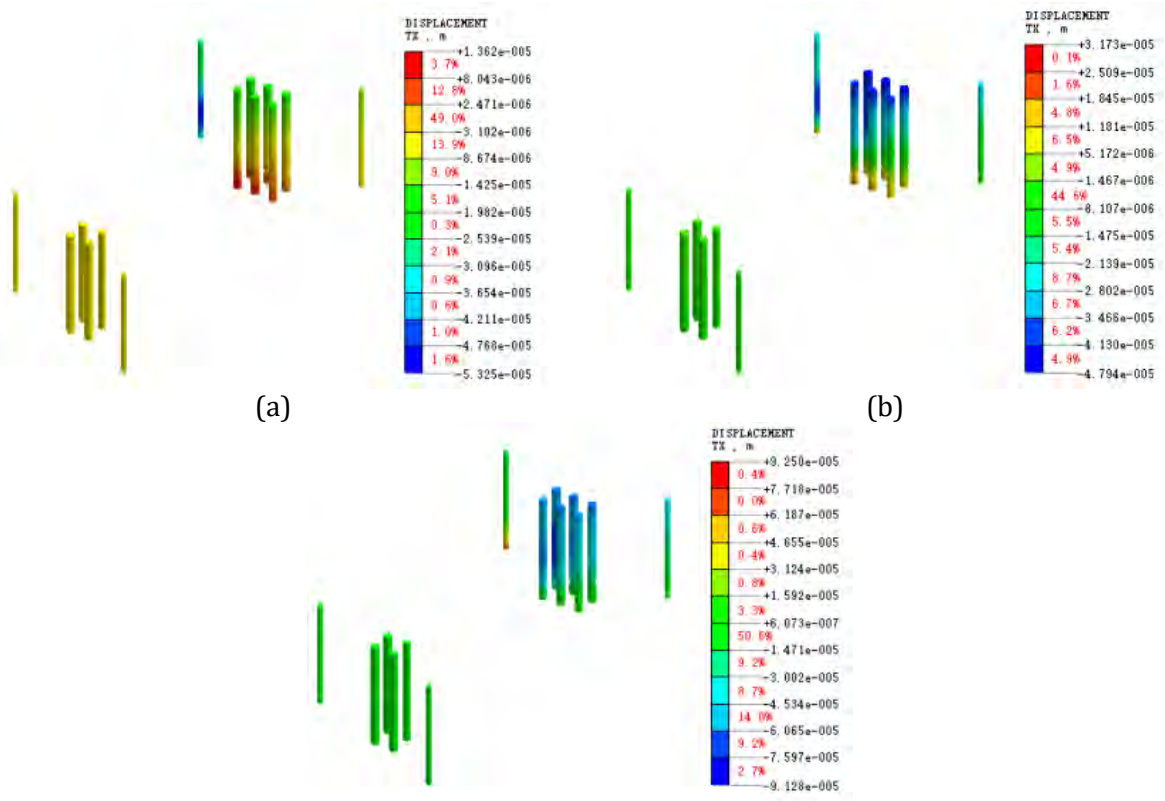


Fig. 6. X-direction displacements of pedestrian bridge pile infrastructure in (m) using initial support construction and excavation of subway entrance and exit straight sections (a) case 1 (b) case 2 (c) case 3

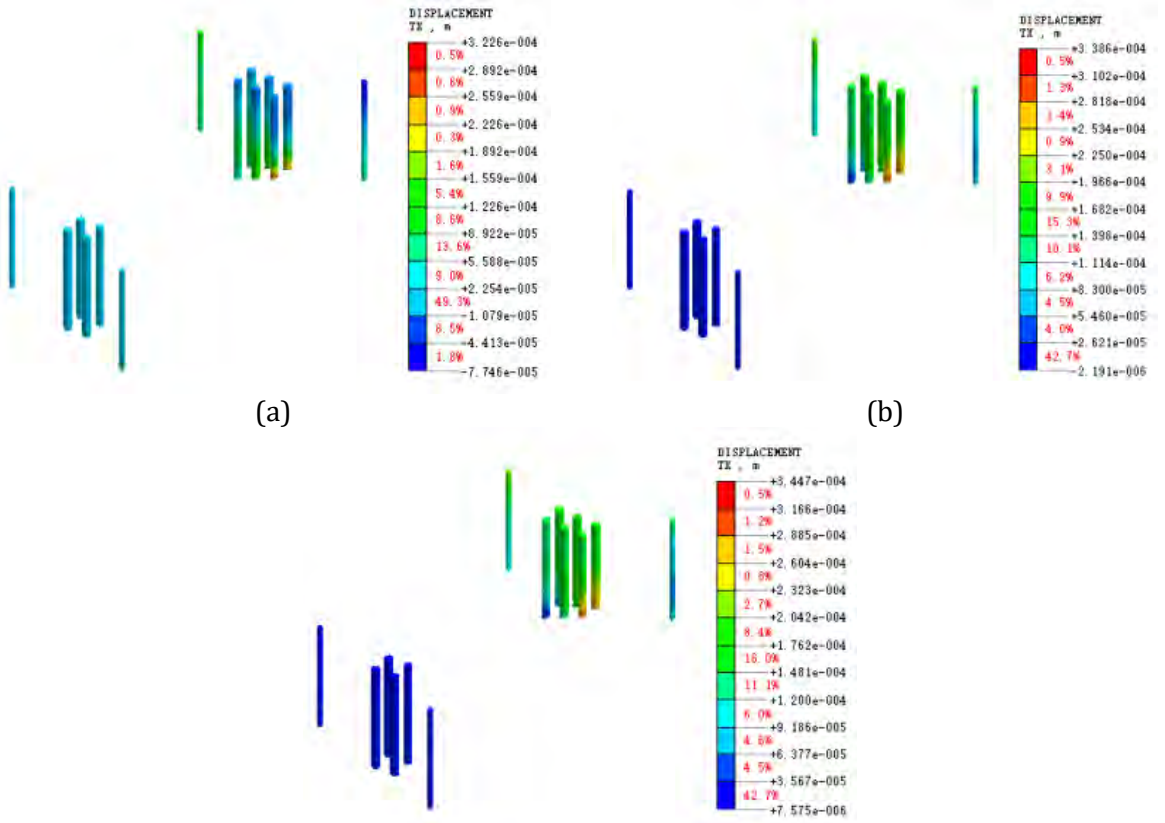
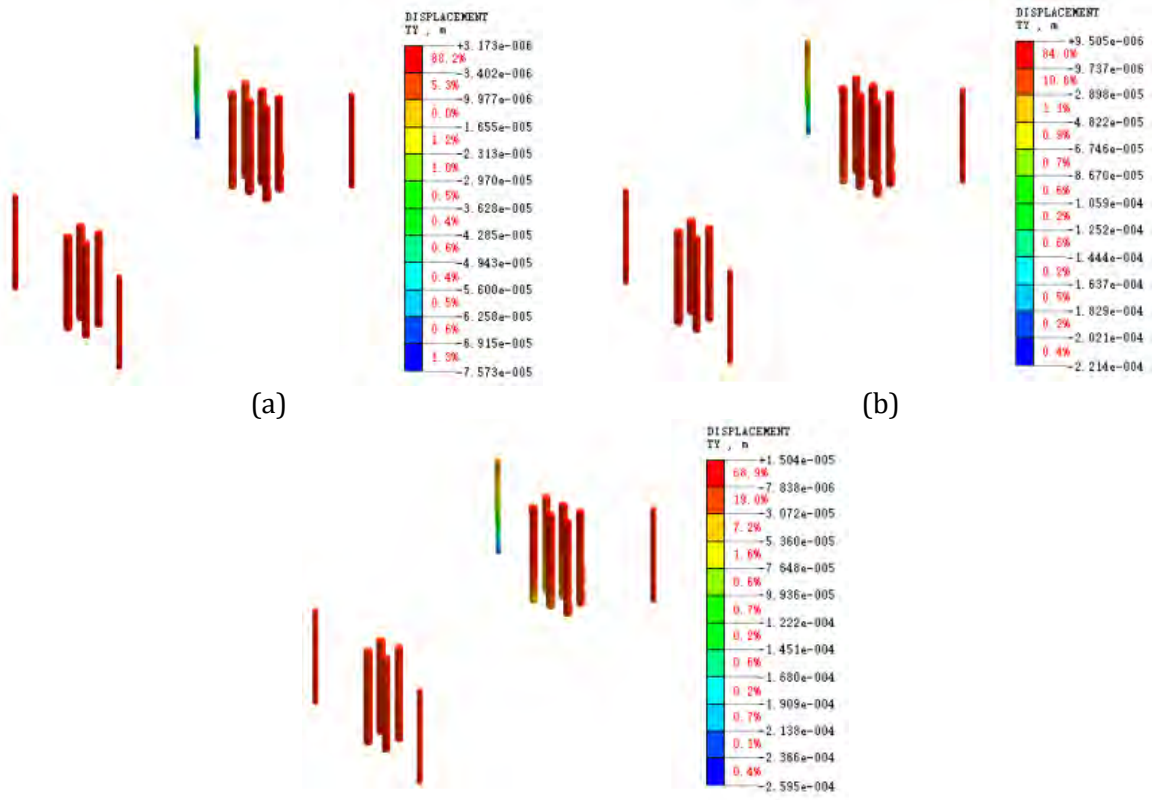


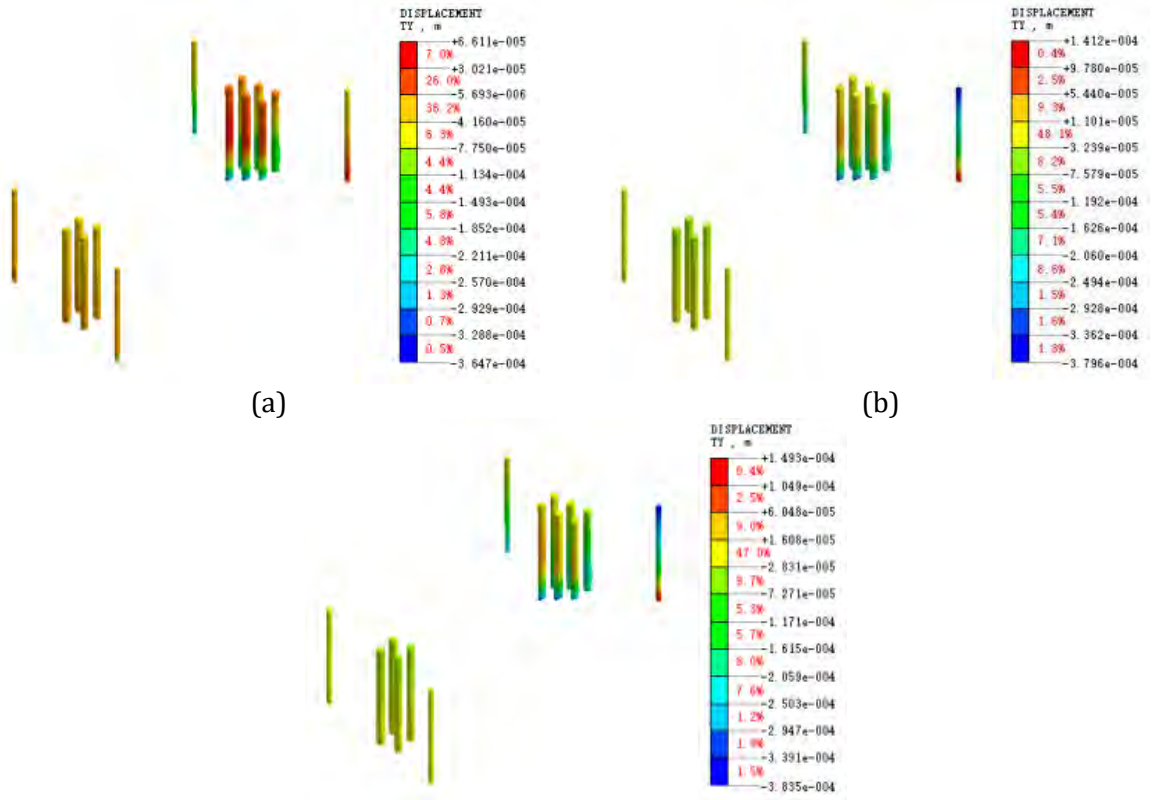
Fig. 7. X-direction displacements of pedestrian bridge pile infrastructure in (m) using initial support construction and excavation of escalator sections at subway entrance and exit (a) case 1 (b) case 2 (c) case 3



(a) (b)

(c)

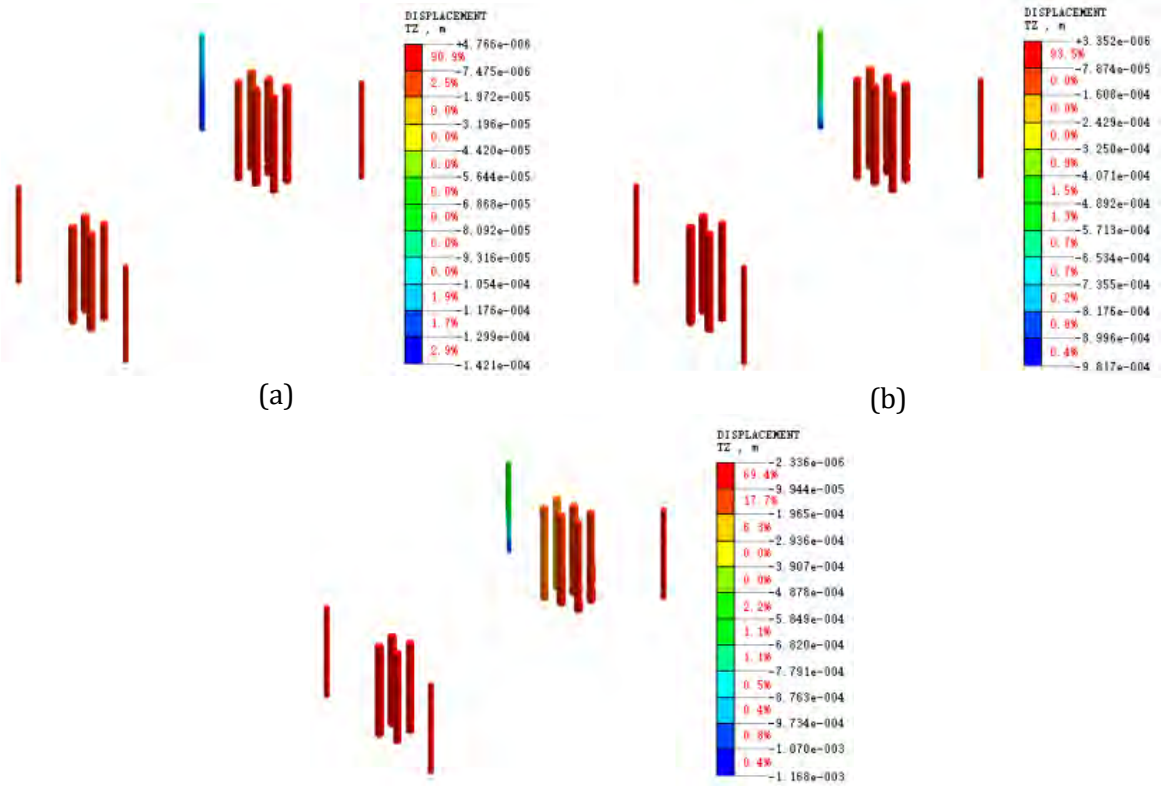
Fig. 8. Y-direction displacements of pedestrian bridge pile infrastructure in (m) using initial support construction and excavation of subway entrance and exit straight sections (a) case 1 (b) case 2 (c) case 3



(a) (b)

(c)

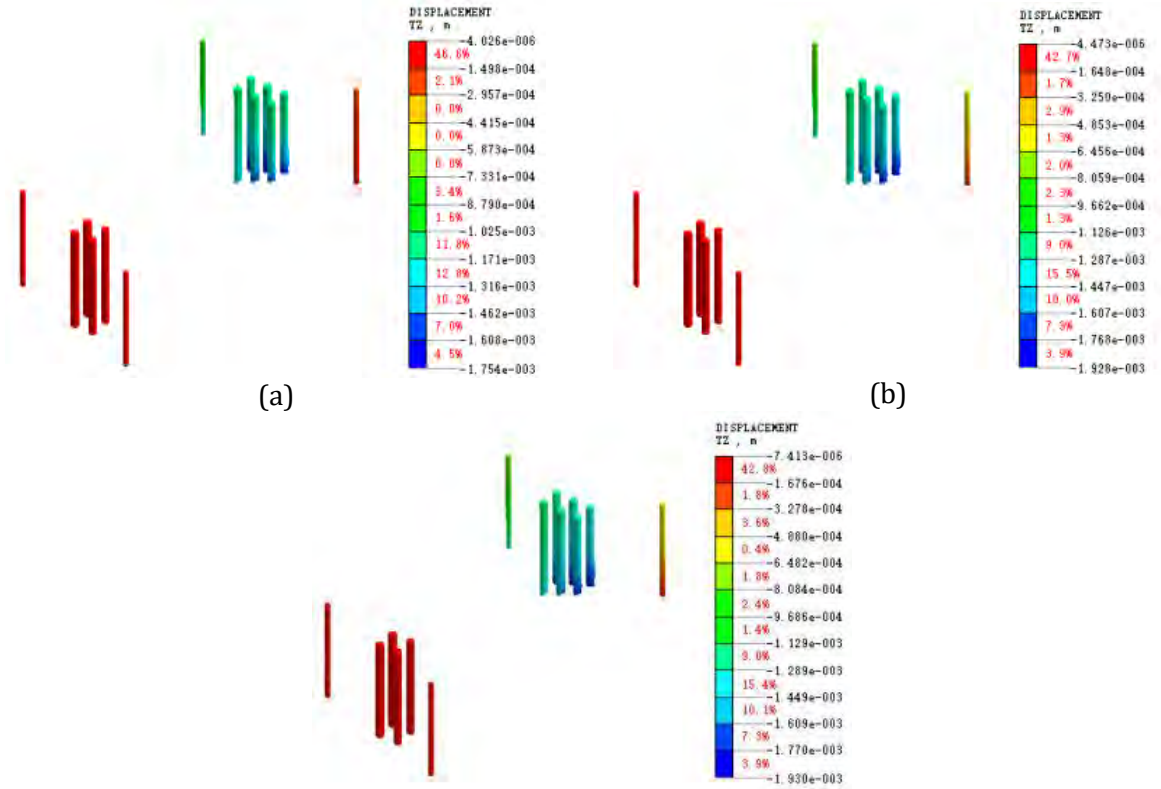
Fig. 9. Y-direction displacements of pedestrian bridge pile infrastructure in (m) using initial support construction and excavation of escalator sections at subway entrance and exit (a) case 1 (b) case 2 (c) case 3



(a) (b)

(c)

Fig. 10. Z-direction displacements of pedestrian bridge pile infrastructure in (m) using initial support construction and excavation of subway entrance and exit straight sections (a) case 1 (b) case 2 (c) case 3



(a) (b)

(c)

Fig. 11. Z-direction displacements of pedestrian bridge pile infrastructure in (m) using initial support construction and excavation of escalator sections at subway entrance and exit (a) case 1 (b) case 2 (c) case 3

Table 4. Staircase section pile foundation displacements of pedestrian bridge in (mm) during construction of subway entrance and exit

Calculation condition	Maximum displacements in mm			
	X displacement	Y displacement	vertical displacement	Total displacement
Construction of the subway station hall was completed	0.0	0.0	0.0	0.0
Initial construction of the straight section of the subway entrance and excavation 1	0.1	0.1	0.1	0.1
Construction of the straight section 1 lining structure	0.1	0.1	0.1	0.1
Initial construction of the straight section of the subway entrance and excavation 2	0.1	0.2	0.9	0.9
Construction of the straight section 2 lining structure	0.1	0.2	0.9	0.9
Initial construction of the straight section of the subway entrance and excavation 3	0.1	0.3	1.2	1.2
Construction of the straight section 3 lining structure	0.1	0.3	1.2	1.2
Initial construction of escalator section of subway entrance and excavation 1	0.1	0.3	1.3	1.3
Construction of the lining structure of the escalator section 1	0.1	0.3	1.3	1.3
Initial construction of escalator section of subway entrance and excavation 2	0.2	0.4	1.3	1.3
Construction of the lining structure of the escalator section 2	0.2	0.4	1.3	1.3
Initial construction of escalator section of subway entrance and excavation 3	0.2	0.4	1.3	1.3
Construction of the lining structure of the escalator section 3	0.2	0.4	1.3	1.3

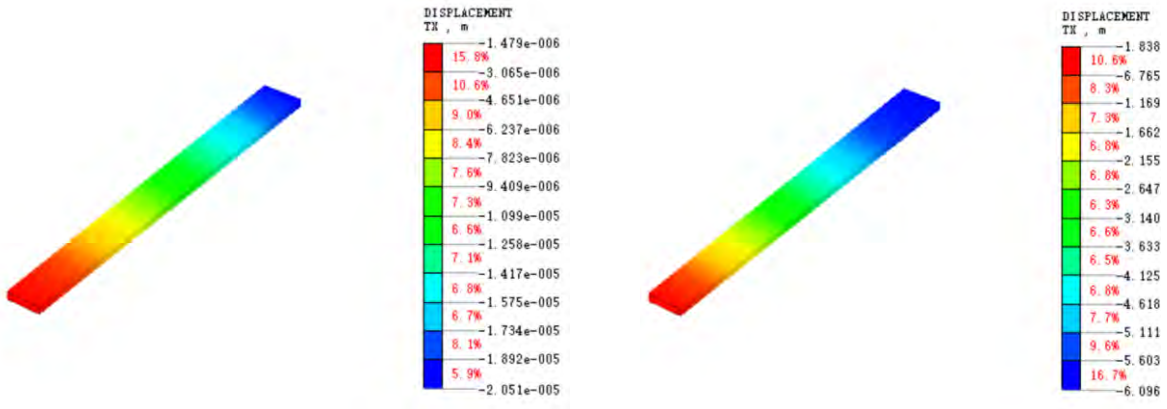
The influence of subway entrance and exit construction on the pedestrian bridge superstructure has been investigated in X, Y, and Z directions using displacement results of 3D simulation analysis as shown in (Figs. 12-17). The footbridge superstructure displacements under key working conditions during construction of proposed project are presented in Table. 6. The maximum X displacement of the upper part of the pedestrian bridge is 0.3 mm, the maximum Y displacement is 0.1 mm, the maximum vertical displacement is 1.3 mm, and the maximum total displacement is 1.3 mm.

Based on the three-dimensional simulation analysis of displacement results and on-site construction environment, this article analyzes the deformation mechanism of the upper structure of pedestrian overpasses caused by the construction of subway entrances and exits as follows: (1) The structure of pedestrian overpasses is sensitive to the difference in foundation settlement. If the settlement of the foundations on both sides is uneven, the upper structure of the pedestrian bridge will experience distortion, tilting, beam cracking, or node misalignment; (2) The construction of subway entrances and exits may be accompanied by pile loads, construction machinery loads, or temporary structural loads, which are transmitted through the soil to the foundation of the overpass, causing additional settlement and redistribution of structural internal forces; (3) Dynamic loads such as pile driving, blasting, and mechanical vibration during the construction process may cause instantaneous deformation or fatigue damage to the upper structure, especially steel structure overpasses that are more sensitive to vibration. During the construction of the subway entrance and exit structure, the reinforcement measures of the pile foundation and the main span and the bridge structure, the pile foundation and superstructure of the bridge are less affected by the construction. In view of the small displacement and force of the main span steel box

girder structure on the upper part of the pedestrian bridge induced by the subway entrance and exit construction, it is believed that the construction of the subway entrance and exit has little impact on the safety of the steel box girder structure on the upper part of the pedestrian bridge. It is suggested to pay close attention to the monitoring data of the bridge structure during the construction process and carry out information construction.

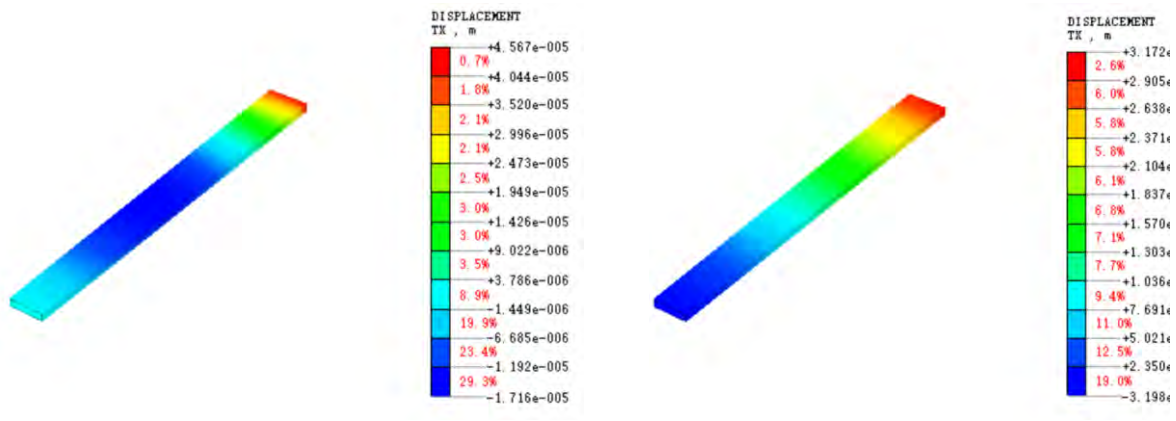
Table 5. Main span pile foundation displacements of pedestrian bridge in (mm) during subway entrance and exit construction

Calculation condition	Maximum displacements in mm			
	X displacement	Y displacement	vertical displacement	total displacement
Construction of the subway station hall was completed	0.0	0.0	0.0	0.0
Initial construction of the straight section of the subway entrance and excavation 1	0.1	0.1	0.1	0.1
Construction of the straight section 1 lining structure	0.1	0.1	0.1	0.1
Initial construction of the straight section of the subway entrance and excavation 2	0.1	0.1	0.1	0.1
Construction of the straight section 2 lining structure	0.1	0.1	0.1	0.1
Initial construction of the straight section of the subway entrance and excavation 3	0.1	0.1	0.3	0.3
Construction of the straight section 3 lining structure	0.1	0.1	0.3	0.3
Initial construction of escalator section of subway entrance and excavation 1	0.3	0.4	1.7	1.7
Construction of the lining structure of the escalator section 1	0.3	0.4	1.8	1.8
Initial construction of escalator section of subway entrance and excavation 2	0.3	0.4	1.9	1.9
Construction of the lining structure of the escalator section 2	0.3	0.4	1.9	1.9
Initial construction of escalator section of subway entrance and excavation 3	0.3	0.4	1.9	1.9
Construction of the lining structure of escalator section 3	0.3	0.4	1.9	1.9



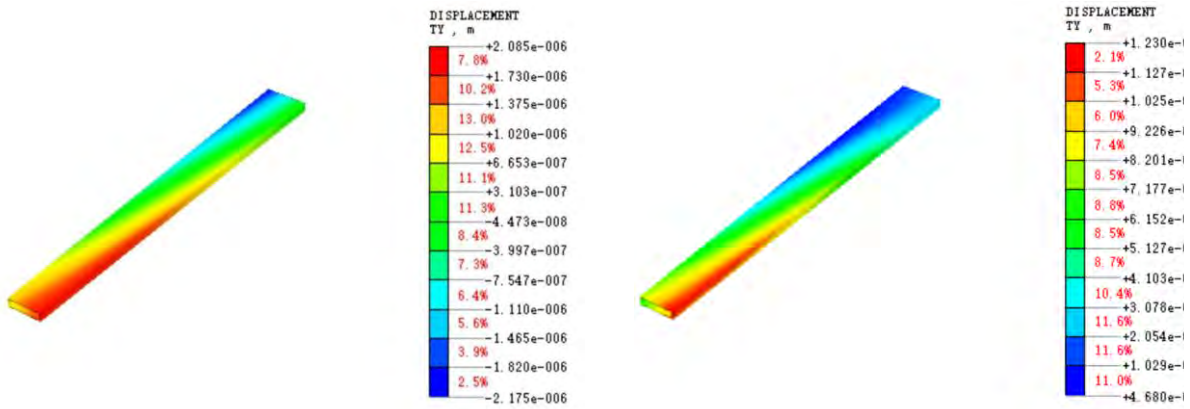
(a) (b)

Fig. 12. X-direction displacements of main span box beam structure of pedestrian overpass pile in (m) using initial support construction and excavation of subway entrance and exit straight sections (a) case 1 (b) case 2



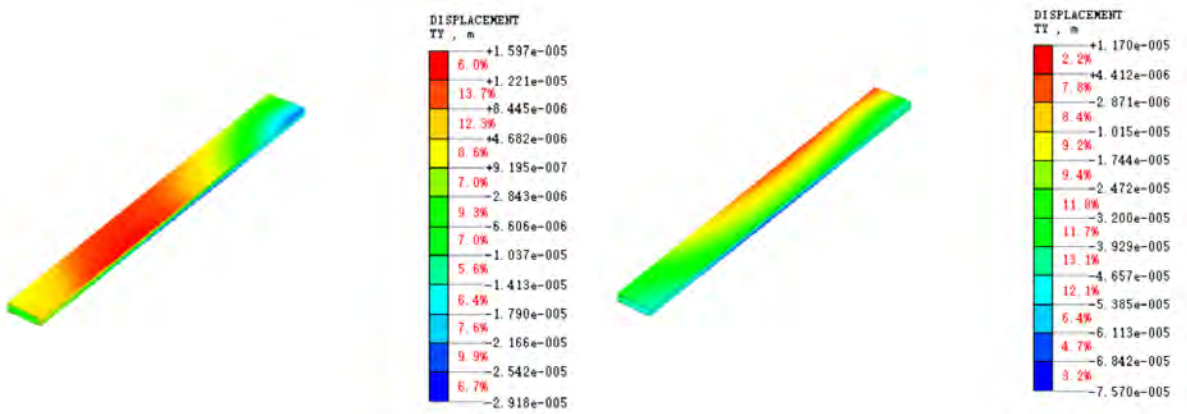
(a) (b)

Fig. 13. X-direction displacements of main span box beam structure of pedestrian overpass pile in (m) using initial support construction and excavation of escalator sections at subway entrance and exit (a) case 1 (b) case 2



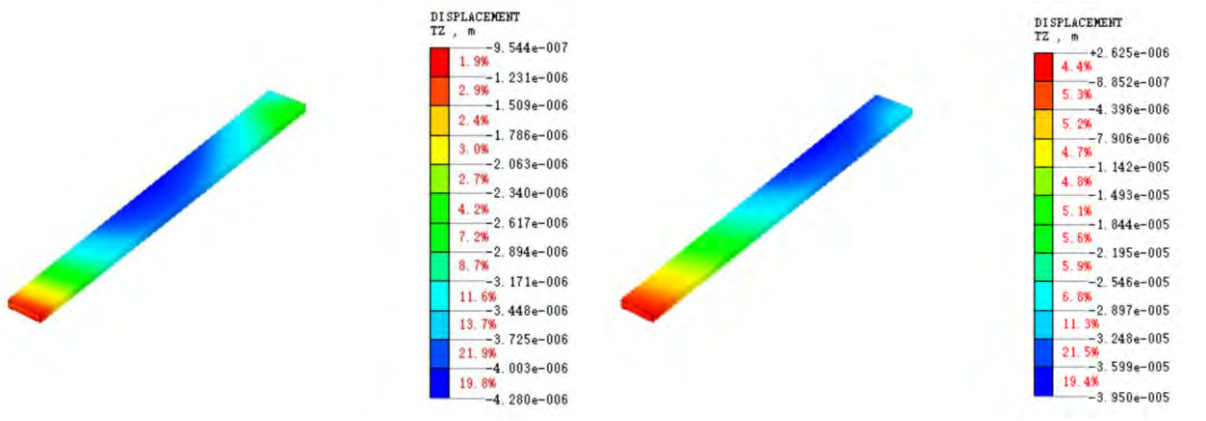
(a) (b)

Fig. 14. Y-direction displacements of main span box beam structure of pedestrian overpass pile in (m) using initial support construction and excavation of subway entrance and exit straight sections (a) case 1 (b) case 2



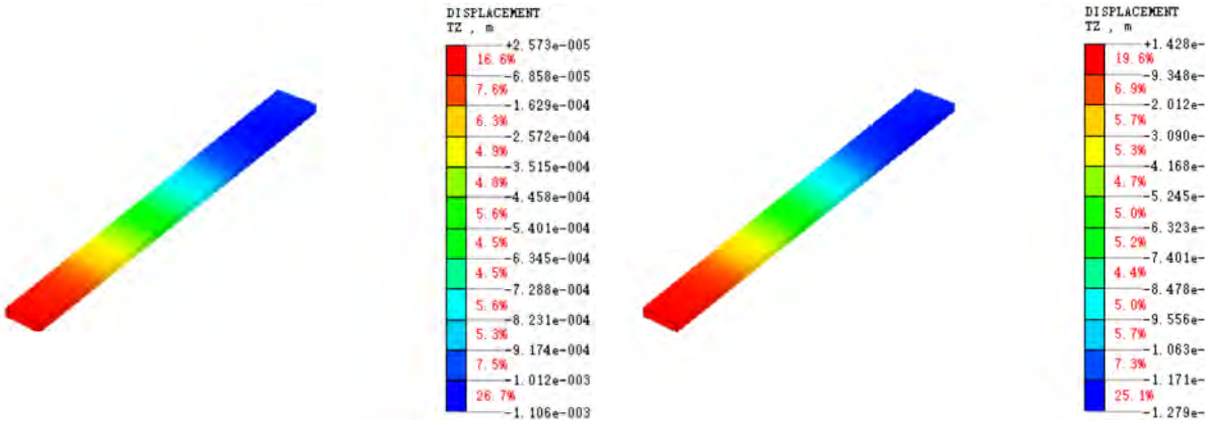
(a) (b)

Fig. 15. Y-direction displacements of main span box beam structure of pedestrian overpass pile in (m) using initial support construction and excavation of escalator sections at subway entrance and exit (a) case 1 (b) case 2



(a) (b)

Fig. 16. Z-direction displacements of main span box beam structure of pedestrian overpass pile in (m) using initial support construction and excavation of subway entrance and exit straight sections (a) case 1 (b) case 2



(a) (b)

Fig. 17. Z-direction displacements of main span box beam structure of the pedestrian overpass pile in (m) using initial support construction and excavation of escalator section at subway entrance and exit (a) case 1 (b) case 2

Table 6. Footbridge superstructure displacements in (mm) during construction of proposed project

Calculation condition	Maximum displacements in mm			
	X displacement	Y displacement	vertical displacement	Total displacement
Analysis of the initial ground stress field at the site	0.0	0.0	2.5	0.0
Initial construction of the straight section of the subway entrance and excavation 1	0.1	0.1	0.1	0.1
Initial construction of the straight section of the subway entrance and excavation 2	0.1	0.1	0.1	0.1
Initial construction of the straight section of the subway entrance and excavation 3	0.1	0.1	0.1	0.1
Initial support construction and excavation of escalator section at subway entrance and exit 1	0.1	0.1	1.1	1.1
Initial support construction and excavation of escalator section at subway entrance and exit 2	0.3	0.1	1.3	1.3

4. Conclusion

This article is based on the design characteristics of subway entrance and exit structures, and the structural characteristics of pedestrian overpasses. A three-dimensional dynamic construction numerical model is constructed using a nonlinear coupling algorithm to study the safety impact of subway entrance and exit construction on pedestrian overpasses. Based on the final results of this research, the following conclusions can be drawn:

- The unloading and disturbance of surrounding rock soil units caused by the construction of subway entrances and exits are the fundamental sources that induce additional responses from adjacent pedestrian overpasses.
- Disturbance stress is transmitted step by step through the "pile foundation–pier–upper structure", resulting in secondary internal force redistribution and cumulative deformation in key components of the bridge.
- When the deformation amplitude exceeds the threshold, it may endanger the safety of the bridge structure.
- The established support system and construction parameter control provided the best values for horizontal and vertical displacements.
- The maximum horizontal displacement of the pedestrian overpass pile foundation caused by the construction of subway entrances and exits is 0.3 mm.
- The maximum vertical displacement of the main span pile foundation is 1.9 mm.
- Both values of displacement are considered minimum than the allowable total settlement value of the pile foundation of 127 mm, and the horizontal displacement limit of the pile foundation of 31 mm.
- Strengthen the automation monitoring of key deformation parameters and set warning thresholds.
- Once the monitoring data approaches the threshold, emergency control measures should be immediately activated to ensure the functionality and safety of the surrounding structures during subway construction.

References

[1] Zheng G, Zhu HH, Liu XR, et al. Control of safety of deep excavations and underground engineering and its impact on surrounding environment. China Civil Engineering Journal,2016,49(6):1-24. http://manu36.magtech.com.cn/Jwk_tmgcxb/CN/Y2016/V49/I6/1

[2] Ganesh SI, Shailendra B, et al. Numerical analysis of surface settlement with saturated zone during urban tunnelling. Res. Eng. Struct. Mater., 2025. http://dx.doi.org/10.17515/resm2025-571st1219

[3] Gan BL, Zhang DM, Chen ZG, Huang ZK, et al. Resilience Evaluation of Existing Metro Stations Considering Adjacent Construction Disturbance Intensity: Methodology and Application. ASCE-ASME Journal of Risk and Uncertainty in Engineering Systems, Part A: Civil Engineering, 2025, 11(4): 1-10. https://doi.org/10.1061/AJRUA6.RUENG-1660

[4] Zhang Y, Su T. Research on nonlinear corrosion law of epoxy coating on steel bridges based on image processing. Res. Eng. Struct. Mater., 2025; 11(1): 287-304. http://dx.doi.org/10.17515/resm2024.219ma0325rs

[5] Avila V, Real M, Moura M. Computational study of the vertical impact coefficient on girders of pier access bridges. Res. Eng. Struct. Mater., 2019; 5(4): 367-377. http://dx.doi.org/10.17515/resm2019.99ms0128

[6] Vijaya B, Ranja B, Raja K. Development of traffic management evaluation framework during metro rail construction activities in urban location: case study of Patna metro rail project. Innovative Infrastructure Solutions, 2025, 10(9): 418-418. https://doi.org/10.1007/S41062-025-02216-2

[7] Brishti B, Gupinath B Sujit KB. Numerical Analysis of Ground Settlement Due to Twin Tunneling for Construction of the Kolkata East–West Metro: A Comparative Study. Indian Geotechnical Journal, 2025, (prepublish), 1-17. https://doi.org/10.1007/S40098-025-01365-6

[8] He Y, Liu B, Zhang H. Study on the effect of subway construction on adjacent architectural heritages and protection measures. Scientific Reports, 2025, 15(1):26847-26847. https://doi.org/10.1038/S41598-025-11831-Z

[9] Li Q, Liu Q, Liu XF, et al. Research Methods and Safety Evaluation of the Influence of Shield Construction on Adjacent Buildings. Municipal Engineering Technology, 2022, 40(6):74-79. https://doi.org/10.19922/j.1009-7767.2022.06.074

[10] Zhu CH, Li N. Estimation and Pattern Analysis of Maximum Ground Settlement Induced by Subway Construction. Chinese Journal of Rock Mechanics and Engineering, 2017, 36(S1): 3543-3560. https://doi.org/10.13722/j.cnki.jrme.2016.0651
[11] Zhou LM. Analysis and Evaluation of the Safety Impact of Subway Station Construction on Adjacent Structures. Journal of Wuhan Traffic University, 2020, 22(03):84-89. https://doi.org/10.3969/j.issn.1672-9846.2020.03.016
[12] Zhang JT, Pu ZH, Zhang YD, et al. Influence of shallow tunnel construction on adjacent pile foundation and reinforcement measures. Geotechnical Engineering Technique, 2025, 39(1): 56-61. https://doi.org/10.20265/j.cnki.issn.1007-2993.2023-0794
[13] Liu Z, He P, Zhang AQ, et al. Analysis of the Influence of Shield Tunnel Construction Process and Support Methods on the Pile Foundation of High-Speed Railway Viaduct Groups. Engineering Mechanics, 2016, 33(006): 219-2216. https://doi.org/10.6052/j.issn.1000-4750.2015.04.S045
[14] Li LH. Parametric Sensitivity Analysis of the Influence of Subway Shield Construction on Upper Buildings. Municipal Engineering Technology, 2022, 40(9): 132-136. https://doi.org/10.19922/j.1009-7767.2022.09.132
[15] Ju X. Analysis and Construction Control of Surface Settlement Induced by Double-Line Subway Shield Construction. Railway Standard Design, 2019, 63(8): 120-125, 139. https://doi.org/10.13238/j.issn.1004-2954.201809280003
[16] Li DP, Yan CH, Zhang S. Advances in researching influences of deep excavation on surrounding environment. Journal of Wuhan University, 2018, 51(8):659-668. https://doi.org/10.14188/j.1671-8844.2018-08-001
[17] Luo Q, Li J, Huang W, et al. Three-Dimensional Refined Numerical Modeling of Artificial Ground Freezing in Metro Cross-Passage Construction: Thermo-Mechanical Coupling Analysis and Field Validation. Buildings, 2025, 15(13): 2356-2356. https://doi.org/10.3390/BUILDINGS15132356
[18] Yi LB, Liu P, Du MF, et al. Influences of Underground Excavation Section on High-speed Railway Bridge: a Case Study of Beijing New Airport Line under Crossing Beijing Super-large Bridge of Beijing-Shanghai High-speed Railway. Tunnel Construction, 2018, 38(S2): 126-135. https://doi.org/10.3973/j.issn.2096-4498.2018.S2.018
[19] Hu B, Li XQ, Huang D. Safety Risk Analysis and Protective Control of Existing Pipelines Affected by Deep Pit Excavation in Metro Construction. Modelling and Simulation in Engineering, 2019(2019): 1-17. https://doi.org/10.1155/2019/3643808
[20] Zhou Y, Li K. Numerical simulation analysis of displacement of pile-anchor supporting structure for deep foundation pit based on excavation process. Journal of Lanzhou University of Technology, 2018, 44(5): 132-136. https://doi.org/10.3969/j.issn.1673-5196.2018.05.024

www.jresm.org

Research on Engineering Structures and Materials



Compendex on Engineering Village

Scopus®

EBSCO

DRJI

TÜBİTAK ULAKBİM

ProQuest

crossref

Google Scholar

Universal Impact Factor

Scientific Indexing Services

Journal Seeker Research Bible

CiteFactor Academic Scientific Journals

Elektronische Zeitschriftenbibliothek

Open Academic Journals Index

GIF GLOBAL IMPACT FACTOR

ASOS indeks

Cosmos

Publication Forum

INFOBASE INDEX

ROOTINDEXING JOURNAL ABSTRACTING AND INDEXING SERVICE

Scope Database Journal Indexing & Citation Analysis

Research Group

https://mimrg.net/